

















Carnegie  
Institution

Year Book 78

1978-1979







*Contents*

# *Carnegie Institution*

OF WASHINGTON

## *Year Book 78*

*1978–1979*



Carnegie  
Institution  
OF WASHINGTON



Year Book 78

Library of Congress Catalog Card Number 3-16716  
Braun-Brumfield, Inc., Ann Arbor, Michigan  
Issued December 1979

1978-1979



# *Contents*

Officers and Staff	v
Report of the President	1
Reports of Departments and Special Studies	1
Department of Embryology	3
Department of Plant Biology	109
Developmental Biology Research Group	239
Department of Terrestrial Magnetism	259
Geophysical Laboratory	429
Hale Observatories	709
Administrative Reports	801
Office of Administration	803
Bibliography	805
Report of the Executive Committee	807
Abstract of Minutes of the Eighty-Second Meeting of the Board of Trustees	809
Financial Statement	811
Articles of Incorporation	829
By-Laws of the Institution	833
Index of Names	839



Digitized by the Internet Archive  
in 2012 with funding from  
LYRASIS Members and Sloan Foundation



# *President and Trustees*

## PRESIDENT

James D. Ebert

## BOARD OF TRUSTEES

Frank Stanton  
*Chairman*

William C. Greenough  
*Vice-Chairman*

William T. Golden  
*Secretary*

Philip H. Abelson  
Robert O. Anderson  
J. Paul Austin<sup>1</sup>  
Lewis M. Branscomb  
John T. Connor  
John Diebold  
Michael Ference, Jr.  
Carl J. Gilbert  
Crawford H. Greenewalt  
Caryl P. Haskins  
William R. Hewlett  
William McChesney Martin, Jr.  
Franklin D. Murphy  
Walter H. Page<sup>2</sup>  
Robert M. Pennoyer  
Richard S. Perkins  
William M. Roth<sup>2</sup>  
Robert C. Seamans, Jr.  
Charles H. Townes  
Juan T. Trippe  
James N. White<sup>3</sup>

Henry S. Morgan  
Garrison Norton  
Charles P. Taft  
*Trustees Emeriti*

<sup>1</sup> Resigned November 17, 1978.

<sup>2</sup> Resigned May 1, 1979.

<sup>3</sup> Became Trustee Emeritus, May 1, 1979.



# Former Presidents and Trustees

## PRESIDENTS

Daniel Coit Gilman	1902–1904	Vannevar Bush	1939–1955
Robert Simpson Woodward	1904–1920	Caryl P. Haskins	1956–1971
John Campbell Merriam	1921–1938	Philip H. Abelson	1971–1978

## TRUSTEES

Alexander Agassiz	1904–1905	Robert A. Lovett	1948–1971
Lord Ashby of Brandon	1967–1974	Seth Low	1902–1916
George J. Baldwin	1925–1927	Wayne MacVeagh	1902–1907
Thomas Barbour	1934–1946	Keith S. McHugh	1950–1974
James F. Bell	1935–1961	Andrew W. Mellon	1924–1937
John S. Billings	1902–1913	John Campbell Merriam	1921–1938
Robert Woods Bliss	1936–1962	Margaret Carnegie Miller	1955–1967
Amory H. Bradford	1959–1972	Roswell Miller	1933–1955
Lindsay Bradford	1940–1958	Darius O. Mills	1902–1909
Omar N. Bradley	1948–1969	S. Weir Mitchell	1902–1914
Robert S. Brookings	1910–1929	Andrew J. Montague	1907–1935
Vannevar Bush	1958–1971	William W. Morrow	1902–1929
John L. Cadwalader	1903–1914	Seeley G. Mudd	1940–1968
William W. Campbell	1929–1938	William I. Myers	1948–1976
John J. Carty	1916–1932	William Church Osborn	1927–1934
Whitefoord R. Cole	1925–1934	James Parmelee	1917–1931
Frederic A. Delano	1927–1949	Wm. Barclay Parsons	1907–1932
Cleveland H. Dodge	1903–1923	Stewart Paton	1916–1942
William E. Dodge	1902–1903	George W. Pepper	1914–1919
Charles P. Fenner	1914–1924	John J. Pershing	1930–1943
Homer L. Ferguson	1927–1952	Henning W. Prentis, Jr.	1942–1959
Simon Flexner	1910–1914	Henry S. Pritchett	1906–1936
W. Cameron Forbes	1920–1955	Gordon S. Rentschler	1946–1948
James Forrestal	1948–1949	David Rockefeller	1952–1956
William N. Frew	1902–1915	Elihu Root	1902–1937
Lyman J. Gage	1902–1912	Elihu Root, Jr.	1937–1967
Walter S. Gifford	1931–1966	Julius Rosenwald	1929–1931
Cass Gilbert	1924–1934	William W. Rubey	1962–1974
Frederick H. Gillett	1924–1935	Martin A. Ryerson	1908–1928
Daniel C. Gilman	1902–1908	Henry R. Shepley	1937–1962
Hanna H. Gray	1974–1978	Theobald Smith	1914–1934
Patrick E. Haggerty	1974–1975	John C. Spooner	1902–1907
John Hay	1902–1905	William Benson Storey	1924–1939
Barklie McKee Henry	1949–1966	Richard P. Strong	1934–1948
Myron T. Herrick	1915–1929	William H. Taft	1906–1915
Abram S. Hewitt	1902–1903	William S. Thayer	1929–1932
Henry L. Higginson	1902–1919	James W. Wadsworth	1932–1952
Ethan A. Hitchcock	1902–1909	Charles D. Walcott	1902–1927
Henry Hitchcock	1902	Frederic C. Walcott	1931–1948
Herbert Hoover	1920–1949	Henry P. Walcott	1910–1924
William Wirt Howe	1903–1909	Lewis H. Weed	1935–1952
Charles L. Hutchinson	1902–1904	William H. Welch	1906–1934
Walter A. Jessup	1938–1944	Andrew D. White	1902–1916
Frank B. Jewett	1933–1949	Edward D. White	1902–1903
Samuel P. Langley	1904–1906	Henry White	1913–1927
Ernest O. Lawrence	1944–1958	George W. Wickersham	1909–1936
Charles A. Lindbergh	1934–1939	Robert E. Wilson	1953–1964
William Lindsay	1902–1909	Robert S. Woodward	1905–1924
Henry Cabot Lodge	1914–1924	Carroll D. Wright	1902–1908
Alfred L. Loomis	1934–1973		

Under the original charter, from the date of organization until April 28, 1904, the following were *ex officio* members of the Board of Trustees: the President of the United States, the President of the Senate, the Speaker of the House of Representatives, the Secretary of the Smithsonian Institution, and the President of the National Academy of Sciences.



## OFFICE OF ADMINISTRATION

*1530 P Street, N.W., Washington, D.C. 20005*

James D. Ebert	<i>President</i>
James W. Boise	<i>Bursar; Executive Secretary to the Finance Committee</i>
Christopher Wright	<i>Staff Member (Science Policy and Institutional Development)<sup>1</sup></i>
Franklin H. Portugal	<i>Historian</i>
Sheila McGough	<i>Publications Officer; Editor</i>
Kenneth R. Henard	<i>Assistant Bursar</i>
Susan Y. Vasquez	<i>Assistant to the President</i>
Joseph M. S. Haraburda	<i>Assistant to the Bursar</i>
Richard E. Hewitt	<i>Administrative Officer for Services</i>

---

Marshall Hornblower	<i>Counsel</i>
---------------------	----------------

## STAFF MEMBER IN SPECIAL SUBJECT AREAS

Roy J. Britten

## DISTINGUISHED SERVICE MEMBER IN SPECIAL SUBJECT AREA

Barbara McClintock

## RESEARCH ASSOCIATE AT LARGE

Harry E. D. Pollock

<sup>1</sup> Effective July 1, 1979.



Carnegie Institution of Washington adheres in all phases of its operations, including employment and educational programs, to a policy barring discrimination on the basis of race, religion, color, national or ethnic origin, sex, or physical handicap. In its educational programs it admits qualified students as fellows without regard to race, religion, color, national or ethnic origin, sex, or physical handicap to all the rights, privileges, programs, and activities generally accorded or made available to fellows at the Institution. It does not discriminate on the basis of race, religion, color, national or ethnic origin, sex, or physical handicap in administration of its educational policies, admissions policies, fellowship programs, and other Institution-administered programs.



*Carnegie  
Institution*

OF WASHINGTON

*Report* OF  
*THE President*

1978–1979







Now understand me well—It is provided in the essence of things, that from any fruition of success, no matter what, shall come forth something to make a greater struggle necessary.

*Walt Whitman*

INVETERATE READERS OF PRESIDENT'S REPORTS (if indeed so resolute a species exists) should be forewarned that the tone of this essay is optimistic, remarkably so for a statement written in October 1979. It could hardly be otherwise, for despite the economic and energy crises, the "crisis of confidence," and the repeated warnings of a national lag in technological innovation, the Institution's 77th year has been highly productive and satisfying—a true "season of opportunity." The evidence is clear: major discoveries, among which at least the most newsworthy have been Peter Bell's and Ho-Kwang Mao's production of solid hydrogen at room temperature, and Donald Brown's surprising demonstration that a control site for at least one animal gene is within the gene and not at one of its "ends"; substantial progress in major ongoing studies on more than a dozen fronts; the continuing renewal of the Institution's human resources, exemplified by the appointment of four uncommonly promising Staff Members in three of the Departments; and the recognition by several of the nation's major philanthropic foundations that our efforts are deserving of generous, unrestricted support.

To be sure, measured in dollars or man-years, our labors are a small fraction of the nation's total research effort. Yet there are new ideas to be generated, new courses to be charted, and new regions to be explored, for which the Institution is uniquely adapted. Despite the enormous growth of the nation's scientific enterprise, the Carnegie Institution has since its inception been the most fully independent research institution of national scope devoted to a wide range of research. We remain so, although in a fiscal sense we are no longer "fully independent," for 20 percent of moneys spent in 1978–1979 were from sources other than the Institution's own funds. Yet I see no evidence that the freedom of our scientists to choose and pursue their own lines of inquiry has been or need be compromised. I say "choose *and* pursue" deliberately, to emphasize the freedom of choice. It is one thing to be able to pursue an ongoing trail of research without distraction; it is something else again to be able to abandon a trail in midpassage and to start afresh on a new and, for whatever reason, more exciting tack. Our Staff Members can do just that. Physicists and physicians alike can become molecular biologists or biogeochemists of great distinction; new careers can be forged, new fields shaped.

I use the phrase "for whatever reason" because the factors influencing



the choice of a direction in research are many and varied; indeed they may be so subtle that even the investigator may be unaware of them. Many are driven, as one scientist puts it, "by that combination of raw curiosity and the search for utility that is so common in science." Others decry the search for utility: some disdain *any* suggestion that utility should influence the course of "pure" research, and some are concerned that the utilitarian argument has been overdone. The latter viewpoint is expressed forcefully in the text of Gerard Piel's address to the American Philosophical Society, "On Promoting Useful Knowledge." Expressing his concern that "the long-term objectives of science are crowded aside by the short-term and uncertain claims of an aggrandizing Federal government," Piel goes on to state his belief that "the general welfare of the country is thereby placed in jeopardy, and, prospectively, its capacity for self-government as well." Arguing that the increasing costs of scientific research have outrun all sources of funds except the federal government, and therefore that the scientific enterprise is irreversibly committed to support by the public treasury, he concludes that the autonomy of our universities must be secured on public approbation.

Piel has marshalled the evidence skillfully; I have read no more thoughtful summary of the ills besetting the scientific enterprise. He begins by tracing the evolution of the utilitarian argument: "It is, above all, the utility of science that warrants that support. From basic research through applied research through development, and sometimes by taxonomically more roundabout routes, science begets technology. On a progressive technology rest the prosperity, the material comfort, the health, and the defense of the nation."

But, he concludes, "the argument from utility has lost its magic." And, most crucially, "drift and change in the priorities of the Federal government and the waxing and waning of its agencies have exerted the dominant forces on the evolution of the universities and the work of their scientists." Even the vaunted peer review system comes in for criticism; Piel believes it favors recognized scientists engaged in established lines of work over young scientists seeking new departures.

Piel's is a serious indictment. Others carry the criticism further, attacking the government's "accountant's mentality"—the tendency to promulgate excessive and conflicting regulations, which sap the vigor of the scientific and technical enterprise. But before we return a verdict of guilty on all counts, let us test a different perspective.

Is my own optimism about the Institution unfounded? Have I been blind to the effects of funding pressures and the utilitarian arguments? Must our efforts ultimately and inevitably be shaped by the (often ill-defined) priorities of the federal government?

My answer to all these questions is simply, "No." But the reasons for



the existence of the Institution require that we not only assert our convictions but find ways of ensuring that our convictions are soundly based on reason and experience.

Our success in preserving the Institution's values is tied to the vitality of the nation's scientific enterprise as a whole. If indeed the United States is no longer at the leading edge of science and technology, we must spare no effort to identify the causes and take corrective measures.

The problems are real, but I would try to do more than add yet another voice to the clamor for superficial solutions. Perhaps because I have spent more than two decades in this unique Institution, I perceive the situation differently. It is true that the federal agencies that support research have taken on a growing "accountant's mentality." It is true that the scientific enterprise is the victim of excessive and conflicting regulation. However, I see the emphasis on immediate utilitarian priorities, narrow accountability, and excessive regulation as symptoms, not as causes; to me, they spring from a common base: the nation's "adversary mentality." There is widespread apprehension about both the costs and the precipitous social consequences of contemporary scientific inquiry and discoveries. We have yet to develop patterns of institutional independence and accountability that are appropriate to this new age.

Nor is the suspicion limited to the scientific enterprise. In today's emotional climate, we also make industry an adversary of government, of the larger society, and at times even of the science that begets its technology. I do not believe that our technology lag is the consequence of major and repeated failures in either basic research or its coupling with technology. I believe the roots of our difficulties lie in the failure of coupling between business planning and public need on the one hand and between business planning and research and development on the other.

The scientific community, industry, and the larger society are set up as adversaries rather than collaborators. The federal government is a partisan and inept referee. Unwilling to render unpopular decisions, it is inclined to pile regulation upon regulation.

Let us consider some of the conditions linking scientific research, industrial technology, and our governing institutions, which point to the need for more collaboration and less confrontation.

### *Basic Research in an Unsettled Future*

Just as I see the Institution's style and its approach to the conduct and funding of research as exemplary, I find the nation's basic research enterprise as a whole surprisingly healthy despite increasing concerns about reductions in support, increasing federal regulation, and misplaced priorities.

In the fields of cellular and molecular biology alone, the recombinant DNA methodology and the hybridoma techniques for producing monoclonal antibodies have revolutionized our approaches to understanding the mechanisms regulating gene action and cell structure and function. Moreover, in these fields the lag between new findings and their application is almost nonexistent. Processes for the mass production of hitherto scarce products—hormones and the like—are emerging swiftly. A gene has been injected into a defective living cell, curing that cell's fatal genetic flaw; new forms of organisms are being "tailor-made" for special purposes or for life in special environments.

These examples can be multiplied many times, in many fields, as our review of the year in the Institution's own Departments will attest.

What are the perils?

I see a need for pioneering independence in the prevailing peer review system. The problem is not just a failure of government; it is a failure of the scientific community itself, which has succumbed to the blandishments of "big science" and has overworked the concept of "critical mass." It is true that once a Brown or a Birnstiel has isolated a gene, or a Milstein has described a hybridoma producing a monoclonal antibody, more minds and more hands will isolate more genes and more antibodies. And they should. But opportunities for new departures must be increased. By maintaining the status quo, panels and study sections have in effect been setting national priorities, forgetting the subtle forces that shape the course of research—forces that are nourished in a climate of freedom and flexibility. The opinion of the scientific establishment, the public's needs, and economic forces, all may influence how we traverse a trail of research once it has been charted; but they often have little or no effect in establishing the starting point. The first experiments must be done, and they must be sound and reproducible, for if they are not, the opening of the field may be delayed.

Even critical findings may be untimely and fail to gain acceptance when they fall on minds unprepared for them. Illustrations are legion. The injection of genes may become commonplace in the 1980's, yet we recognized the "need" several decades ago. Another timely example may be the need to stimulate research on the regeneration of lost parts, especially limbs, in man. Public pressure is mounting for more research; but until recently the field was at a standstill, despite Marcus Singer's elegant demonstration of the role of nerves in amphibian limb regeneration some 25 years ago.

For an equally long time, evidence has been accumulating, much of it fragmentary but suggestive, that trans-cellular currents may play a key role in regeneration. For example, one can initiate a degree of regeneration in frog limbs by drawing currents through amputated "stumps." In a thoughtful review in *BioScience*, Borgens, Vanable, and Jaffe trace the



story of “bioelectricity and regeneration.” Despite its ancient and honorable history, the study of electrical phenomena in living organisms had not found great favor. Why? Clearly there was need. Economic forces do not appear to have held back research, nor do I detect any specific “negative pressure” from the scientific establishment. To be sure there was a healthy skepticism, but as good ideas slowly emerged they found support.

It was Lionel Jaffe and his colleagues and students who initiated the modern era in measuring currents in developing organisms with the introduction of an ultrasensitive vibrating electrode. It now appears that the surface potential differences along early regenerating salamander limbs (first described by Monroy in 1941) are produced by the skin and that they play a role in limb regeneration. It is suggested—but not yet established—that the role of the electrical field in evoking regeneration is the stimulation or direction of nerve growth. It appears that now, for the first time in several decades, a larger investment in research in regeneration might have a significant effect. And yet, it remains questionable whether the structure of the peer review system will facilitate development of these exciting possibilities.

The future directions of research will be shaped as much by choices made within the scientific enterprise as by any external factors.

### *The Coupling of Science and Technology*

Over a decade ago, the National Science Foundation published the first of its volumes *Technology in Retrospect and Critical Events in Science* (“TRACES”). The series traced key events leading to major technological innovations—magnetic ferrites, “the pill,” and the electron microscope, to name a few. I say “key events” rather than “key discoveries” or “key events in science” because once again we see the crucial interplay of science and social forces. Although the search for knowledge contributed to the origin of “the pill,” public need and opinion sparked by Margaret Sanger, and economic influences, were also highly significant influences. In TRACES we read,

Pincus has stated that the stimulus to his renewal of interest in the phenomenon of reproduction came from a 1951 visit by Sanger, who impressed upon him both the problem of women who needed to limit their families and the importance of the “population explosion.” From this meeting came a program supported by the Planned Parenthood Federation of America and G. D. Searle; the program led to confirmation of the action of progesterone reported in 1937, the action of certain progesterone derivatives, and the action of ovulation inhibitors in the rabbit as antifertility agents in the rat. Shortly thereafter, a sample of norethynodrel, among other steroids, was sent to Pincus and

Chang at the Worcester Foundation to be evaluated for anti-ovulatory and clinical effects and was found to be successful. These studies and the clinical research being conducted in the 1950's by Rock at the Brookline Free Womans Hospital in Brookline, Massachusetts, stimulated further investigation of ovulation inhibition. It was at this time, in 1952, that direct development of the oral contraceptive pill began.

These social and economic forces are necessary today for technological innovation, but as I have already remarked, the time lag between discovery and application is fast disappearing. In some fields it is so compressed that "basic" and "mission oriented" research are almost one. I have already spoken of the newly emerging genetic technology, a subject to which Donald Brown and his colleagues have made outstanding contributions. There are two other fields in which the world's needs and the frontiers of research are virtually the same: agriculture for arid regions, and the conservation and extension of mineral resources. In both, the Institution's programs are preeminent.

In his Lindbergh Lecture, "Science and Technology in a Conserving Society," Frank Press reminded us that of the approximately 350,000 plant species described by botanists only about 3,000 have been tried as sources of food and other useful materials. We cultivate only about 100 plant species on a large scale and, he goes on, about 90 percent of our food comes from only a dozen or so crops. Thus the urgency of identifying plants that can survive in, or can be adapted to, areas where it is difficult to cultivate today's conventional crops—the arid regions, for example, which constitute almost 19 million square miles, over one third of the Earth's land surface.

If we are to make better use of marginal land, we must learn how some plants manage to survive in harsh environments. During the past year, Olle Björkman and his colleagues in the physiological ecology group of the Department of Plant Biology have made substantial progress in understanding how certain plants can adapt to drastic changes in temperature and water availability. One such plant, commonly found as a highway planting in California, is the shrub called oleander. It is found throughout the state, from the desert regions to the mountains, and seems to thrive on neglect. What is happening when identical clones of oleander thrive both at temperatures approaching 120°F and at temperatures near 60°F?

It turns out that there are two major differences between the plants grown at hot and cool regimes. First, those plants from the cool regime can photosynthesize much more effectively at low temperature than can those from the warm regime. Indeed the plant from the cool regime achieves more than double the rate of photosynthesis of the warm-regime plant when both are tested near 65°F. It simply has a greater amount of



one particular limiting catalyst—almost two and one-half times as much. Otherwise there are no significant differences in the biochemical machinery for making additional biomass.

The other major difference between plants grown at warm and cool regimes is found when the plants are investigated at high temperature. Here the situation is reversed, the photosynthetic rate of the warm-regime plant far surpassing that of the cool. Again, the difference turns out to be relatively simple: the membranes from the high-temperature-grown plant are far more stable than those of the low-temperature-grown shrubs. It is only a small oversimplification to say that they develop membranes with a higher melting temperature.

Even more surprising is the finding that mature plants can adjust to dramatic temperature changes. Thus if a mature high-temperature-grown plant is moved to the low-temperature regime, the melting temperature of the membranes decreases (they must remain fluid at lower temperatures) and the amount of the limiting enzyme increases. These changes are rapid, and within a week or so the plant is completely adapted to its new regime. With the reciprocal change—a low-temperature plant moved to high temperature—the reciprocal changes in membrane properties and enzyme level occur.

It is clear that not all plants are as adaptable as oleander. However the plant breeder now has at hand simple tools for screening for such adaptability. The membrane properties can be studied in the field, and in seeking such desirable traits in crop plants (as ability to withstand high temperature and drought) the plants need no longer be grown through whole generations. They can be screened quickly at a young age, and the breeder knows precisely what to look for.

Inorganic minerals and nonrenewable resources may pose even greater problems for relating science to technological applications. Press argued in his Lindbergh Lecture that the crucial problem with respect to minerals consumption is not that we will run out of minerals in the immediate future, nor that we are in imminent danger of being prevented from acquiring them, but that the energy (hence economic) and environmental costs of obtaining them are becoming prohibitive; over one fifth of the nation's energy budget is now being spent on minerals production. Press may be correct on the first two counts if we choose to emphasize the *immediate* future. Before the year 2000, however, the world will probably experience mineral shortages as serious as the present oil crisis. The energy and environmental costs will continue to increase as lower grades of conventional ores are mined and nonconventional alternative sources are developed.

The growing restrictions on the use of mineral resources intensify the need to understand not only the accessible parts of the Earth's crust but

also the deeper crust, mantle, and core as these have affected the distribution of minerals. In doing so, it may also provide the basic underpinning for new technologies that will provide substitutes for existing metals. Currently in the Geophysical Laboratory significant attention is being focused on the detailed analysis of the properties of solid hydrogen, looking toward the possibility that a stable metallic hydrogen may be produced. Because metallic hydrogen is expected to be a superconductor, its potential application to the transport of electric energy is of uncommon interest.

Thus, the Institution's independence has enabled it to address scientific problems in fundamental ways, yet without precluding prompt application of the findings.

### *The Matter of "Regulation"*

The problem of regulation is in fact two problems, related but distinct. The first is the direct *regulation of research*. Jerome Wiesner, president of MIT, has observed that "universities have been beset in recent years by a barrage of independent and unrelated government actions that, often individually and certainly in the aggregate, have had an adverse impact on the health of the university. What we need, and what the country now needs, is regulation of regulation." It has been suggested that the business of regulating research is prospering at the expense of creative activity within universities and other centers of research.

The regulation of research is a symptom of the overselling of the utilitarian argument, of indiscriminate applications of social regulations meant to improve working conditions, and of a misconception about the nature of basic science, out of which arise continuing skepticism, even mistrust, toward science and scientists.

The second problem—the *regulation of industry*—is rooted in the difficulty of understanding the limits of science in making the necessary judgments about technology in relation to individual freedom and our collective future.

Frank Press has observed that

. . . because of the growing sensitivity of science today we are able to analyze and anticipate a greater number of risks, many stemming from scientific and technological advances that also promise great benefits. To complicate matters further, the risks and benefits do not necessarily accrue in the same time frame or to the same people. So once again we are involved with the age-old problems of "Faustian Bargains" and making decisions about activities which may not have a harmful impact for years, if not generations. Or for which the outcome, based on today's knowledge, is uncertain.



The methods of science cannot assure the safety of a product, nor can they provide a formula for the weighing of benefits and risks. It is nearly impossible to determine that a given environmental chemical, drug, or food will be neither carcinogenic, mutagenic, nor teratogenic. Nowhere is the difficulty of such assessment brought home more clearly than in relation to birth defects.

During the 1960's and 1970's, we searched for molecular mechanisms of birth defects, with more than a little success, especially for the 25 percent of defects that are genetic or chromosomal in origin. Such approaches will surely pay a handsome return as we evolve high technology treatments or cures. Barton Childs has emphasized, however, that a sizable proportion of the 65–70 percent of all birth defects of unknown etiology may well turn out to be the result of the action of “unpredictable sets of polymorphic genes” working under “unpredictable conditions.” Thus, the number of genotype-environment combinations will be large, increasing the difficulty of generalization, and making it probable that the cause of a given birth defect *may differ from individual to individual*.

Consider the contrasting stories of the dread thalidomide and the ubiquitous aspirin. By today's rigorous testing procedures requiring tests on primates, thalidomide would not have been marketed; but it passed the then existing “screens,” using mice, rats, and chick embryos, with flying colors. Aspirin has been considered “safe” since the very beginning. However, were it to appear today as a new drug, it might not reach the marketplace, for it is highly teratogenic in rats although safe in man. Aspirin is widely accepted, of course, and properly so, for its benefits clearly outweigh the risks, but the experience of geneticists would suggest that, however small, some risk exists that in some genotypes aspirin may be harmful.

How large is the problem, overall? How many times must one multiply this example to get the true picture of the dilemma of “regulation”? Perhaps it will suffice to point out that for one class of substances alone—the pesticides—the answer is 35,000 times.

Science provides ever more refined evidence of the consequences of industrial regulation. There is therefore no substitute for the open communications and the enlightened political processes by which our society must make increasingly difficult choices.

### *The Spirit of Collaborative Partnership*

. . . Upon this gifted age, in its dark hour,  
Rains from the sky a meteoric shower of facts. . . .  
They lie unquestioned, uncombined.  
Wisdom enough to leech us of our ill

Is daily spun; but there exists no loom  
To weave it into fabric. . . .

*Edna St. Vincent Millay*  
Huntsman, What Quarry?

Never in the history of American science has a set of problems demanded cooperative research and public understanding more than do the tasks now confronting us. And of all our needs, perhaps the greatest is for public understanding, which can emerge only from a truly effective synthesis of knowledge and collaboration among its users.

Frank Stanton, Chairman of the Institution's Board of Trustees, wrote eloquently of the risks in "labeling our times" when he observed that "we should resist the temptation to label our times the Age of Television. It really is an era of mass communication. Ours is not a television society but one in which attitudes and ambitions are shaped by information and impressions from all kinds of sources."

Nowhere is the tendency to label our times more dangerous than in the sciences. I am impatient with the Hydra-like notion that an Age of Discovery has given way to an Age of Perpetual Harvests with "mineral deposits that magically replenish themselves, a renewable food supply, and a power source that can provide free, fuelless energy until the end of time. . . ." We have sown, now shall we reap. Nonsense. Applied research, industrial development, and the art of medicine all spring from, are nourished by, and in turn nourish, basic science. Their further progress would eventually stagnate if basic research were long neglected.

Today, as Vannevar Bush wrote in *Endless Horizons*, "it is truer than ever that basic research is the pacemaker of technological progress. In the nineteenth century, Yankee mechanical ingenuity, building largely upon the basic discoveries of European scientists, could greatly advance the technical arts. Now the situation is different. A nation which depends upon others for its new basic scientific knowledge will be slow in its industrial progress and weak in its competitive skill." Man's progress depends upon a balanced effort resulting in both new knowledge and its innovative use. How is the balance to be sustained?

There must be a collaborative partnership of the research institution, the government, and the private sector. Industry must become a full partner, not merely a "user," and especially not an adversary. New connections must be forged between academic and industrial research centers. A wide range of cooperative programs must be emplaced; and, as in any true partnership, the needs of both parties must be taken into account. For healthy science the vital ingredients in the delicate process of creation (especially freedom of choice and a stable flow of support) must be preserved; and, meanwhile, industry has a right to a fair balance between risk and reward.



*The Stream of Knowledge*

While the artist's communication is linked forever with the original form, that of the scientist is modified, amplified, fused with the ideas and results of others, and melts into the stream of knowledge and ideas which forms our culture. The scientist has in common with the artist only this: that he can find no better retreat from the world and also no stronger link with the world than his work.

Max Delbrück

Delbrück's observation about the writings of scientists, made in the lecture he gave on receiving the Nobel Prize for physiology or medicine in 1969 (shared with Alfred Hershey and Salvador Luria), raises a delicate question, also touched upon in Hatten Yoder's introduction to the Report of the Geophysical Laboratory. What is the role of the annual reports of the Institution's Departments in the stream of knowledge?

It is true that, in Yoder's words, "increased speed of publication in the appropriate technical journals has reduced the need for extensive summaries of the large amount of work completed during the year." Thus increasingly, our annual reports will deal not with past and already cold events, but with work in progress. Over the years, few groups have worked as hard as the Institution's scientists to inform their peers and to expose their work to searching examination, a tradition to which we will hold fast. For it is through such searching examination that science advances, as ideas are "modified, amplified, and fused." Constant sifting and re-examination are crucial, of older concepts as well as the most recent observations, for, as Thomas Mann wrote, "the elements count for nothing, but that imaginative and fortunate combination counts for everything."

Our review of some of the year's research follows. I say "our" because I have drawn heavily from the Directors' statements; they, in turn, leaned on the detailed accounts by the Staff Members. As a Director, I was always concerned with the selection process whereby *some* examples of research were chosen. Today I am more concerned, for I have become ever more aware of the striking differences in the personal styles of scientists, of the boldness of some and the reticence of others to put forth untested ideas and data from experiments in progress. In his remarkable history of the revolution in biology, *The Eighth Day of Creation*, Horace Judson wrote, "as scientists understand very well—personality has always been an inseparable part of their styles of enquiry, a potent if unacknowledged factor in their results. Indeed, no art or popular entertainment is so carefully built as is science upon the individual talents, preferences and habits of its leaders."

*Astronomy at Hale*

As Philip Abelson once wrote, "To a considerable degree, the *Hale Observatories* have characteristics of a national astronomical facility." One might add, only half in jest, "without being funded as such." In the year under review, over 50 Staff Members, Staff Associates, and Fellows were active at Hale, along with 16 student observers. The Observatories provided opportunities for 75 guest investigators from 36 other institutions. Thus the Observatories' Report reflects the broad range of interests of nearly 150 observers. As the Director remarks, there has been a gradual shift of emphasis toward more distant objects such as galaxies and quasars, but important research continues on objects in our own solar system.

Astronomers have set themselves an extraordinary task: to understand a Universe that is ten trillion times larger than the solar system, that contains a billion trillion stars of which our Sun is one. They endeavor to answer questions about the birth and development of stars, the formation and evolution of galaxies, and the beginning and destiny of the Universe.

The astronomer is tackling these questions from a perch in the solar system, unable to move about the Universe in the way the experimental physicist moves about his world, the laboratory. The astronomer cannot manipulate the objects of interest and can only observe them, passively, by receiving and analyzing electromagnetic radiations, such as light, infrared, radio, x-ray, and gamma ray emission.

The physical complexity of astronomical objects usually allows only a partial understanding of their nature. Yet, the astronomer is often able to use poorly understood phenomena to advance knowledge elsewhere in the astronomical arena. An example is the chromospheric calcium emission in solar-type stars, which can be used in several ways.

Stars such as our Sun exhibit many absorption lines in their spectrum, as Fraunhofer first noted in 1811. The strongest absorption lines in the blue-ultraviolet part of the spectrum are due to calcium. In the center of these calcium absorption lines there appears a weak emission line due to calcium located in the chromosphere, an atmospheric layer of the Sun located above the light-emitting photosphere. Olin Wilson observed the calcium emission line in many stars in the 1960's, and he discovered with Carnegie Fellow Vainu Bappu that the width of this calcium emission line correlates well with the absolute luminosity of the star. Even though the effect is not physically well understood, it provides the astronomer's dream—a distance indicator. By observing this calcium emission line, the absolute magnitude of the star is obtained, and (by comparing the absolute magnitude with the observed apparent luminosity of the star) its distance. Since distance determinations in astronomy are difficult, such distance



indicators are particularly useful (in this particular case, application is limited because the chromospheric calcium emission line at the bottom of a deep absorption line is not easily observed).

Olin Wilson has been observing the chromospheric calcium line in 91 stars for about 10 years. He has noted that the emission has periodic variation in most stars, over time intervals from days to many years. About a dozen stars have essentially completed a cycle of variation with typical periods of from 7 to 10 years, and approximately as many probably exhibit cyclic variation with longer periods. Chromospheric activity in the Sun varies with the solar cycle, around 11 years, exhibited by sunspots and other solar activity. The cycles observed by Wilson are obviously the analog of the solar cycle. With so many more examples of this "solar cycle," the study of its nature is enormously enhanced.

Short-term variations in chromospheric emission noted by Wilson indicate time scales from one day to several months. Arthur Vaughan and George Preston will undertake further observations—essentially continuous over several months—to check for periodicity that can be associated with stellar rotation. This will give information about the rotation of solar-type stars that is now lacking. The Sun itself has a rotation period of almost a month.

Chromospheric emission can even be used to tackle questions about star births in the past. An important question in galactic evolution is how the birth rate of stars varies with time. We know that the Sun and the solar system were formed 4.6 billion years ago, whereas our Galaxy has probably existed for at least 15 billion years. Since the 1950's it has been possible to determine the age of star clusters. Studies of the chromospheric emission in stars belonging to such clusters show that its intensity slowly decreases with increasing age. Through this relationship one can estimate the age of an individual star by observing its chromospheric emission—averaged, of course, over years to avoid effects of cyclic variations. Vaughan and Preston will systematically observe stars in the solar neighborhood and, from the distribution of ages of the stars, will derive the birth rate of stars at different times in the past.

The remarkable power of chromospheric emission studies is being recognized by the astronomical community, and there are plans for extensive observational programs. All this is a deserved tribute to Olin Wilson, who retired five years ago.

As we noted above, distances to astronomical objects are difficult to measure. This is particularly the case in extragalactic astronomy. Edwin Hubble determined the distance of the Andromeda Nebula in 1924 by identifying and measuring in that galaxy Cepheid variables, whose intrinsic properties are known from studies of nearby representatives of this class of variable star. This was the final and definitive resolution of the

great debate between Shapley and Curtiss in 1920 as to the nature of the "nebulae."

By the late 1920's, Hubble had determined the distances of a number of galaxies. He announced in 1929 that galaxies are moving away from us with velocities proportional to their distances. This was the birth of the concept of the expanding Universe, no doubt the most important cosmological finding of the 20th century. The proportionality constant between velocity and distance is now called the Hubble constant. It corresponds to that velocity with which a galaxy at a distance of 1 million parsecs will move away from us as a consequence of the universal expansion. The work of Sandage and Tammann, reported in *Year Book 75*, resulted in a value of the Hubble constant of 50 km/sec per Megaparsec.

Sandage and Tammann assigned distances to individual galaxies based on characteristics of Cepheid variable stars, the brightest red stars, or the diameters of large ionized gas regions observed in these galaxies. For more distant galaxies, in which these objects cannot be individually discerned, the apparent brightness of the whole galaxy was used as a distance indicator.

Sandage reports this year on a further calibration of the luminosity of the brightest red stars. With Roberta Humphreys, he has isolated the brightest red stars in the nearby galaxy M33 (its distance is  $2\frac{1}{2}$  million light years). It required an extensive observational effort to separate the M33 red stars from the numerous red foreground stars belonging to our own Galaxy. The luminosity of the brightest red stars in M33 was found to be the same as that found by Sandage and Tammann in other galaxies, providing further confirmation of their usefulness as distance indicators.

Some astronomers are advocating values of the Hubble constant larger than that derived by Sandage and Tammann, up to 100 km/sec per Megaparsec. The value of the Hubble constant is of interest since it determines the time scale of the expanding Universe. In particular, if the average density of matter in the Universe is relatively low so that the mutual gravity of galaxies on each other does little to slow the expansion of the Universe, then the age of the expanding Universe is simply the inverse of the Hubble constant. This age is 20 billion years for the Sandage-Tammann value of the Hubble constant. For much larger values of the Hubble constant, the derived age of the Universe will be smaller than the derived age of the oldest stars in our Galaxy or the age of the chemical elements which have been created in the nuclear fires in the interiors of stars. Also, as noted by Tammann, for the larger values of the Hubble constant, distant galaxies will be typically smaller than our own Galaxy. And thus, a variety of arguments is brought to bear in discussions about the size and age of the Universe.

An extreme case of uncertainty about distance is presented by the qua-



sars, starlike objects with redshifts in their spectra corresponding to radial velocities equaling a large fraction of the velocity of light. Application of the Hubble law leads to distances of the quasars of 1–10 billion light years. Arp, however, has argued on the basis of photographs showing alignment between some quasars and nearby bright galaxies, that the redshifts cannot be distance indicators and that the quasars must be at distances similar to those of bright galaxies, i.e., around 100 million light years.

A new argument favoring the cosmological hypothesis of quasars has been developed on the basis of their space distribution. Green and Schmidt are in the process of completing a survey for bright quasars over 10,000 square degrees of the sky. They find that the number of quasars increases steeply with apparent magnitude, so steeply, in fact, that their space distribution cannot be uniform: The space density of quasars must increase sharply with distance from us. If quasars were relatively close to us, our location in the Universe would be a singular one—namely exactly at the density minimum in the quasar population. This is contrary to the principle that each observer in the Universe is equivalent. Only if, instead, quasars are exceedingly distant is this paradox resolved, since in that case light from quasars takes a large fraction of the age of the Universe to reach us. The density increase found by Green and Schmidt then refers to earlier cosmic times, which is entirely compatible with the concept of an evolving Universe.

### *Astronomy at DTM*

To the casual observer, the name of the *Department of Terrestrial Magnetism* (known affectionately throughout the scientific world as DTM) may seem an anachronism for a group conducting research on astronomy and the physics and chemistry of the Earth. However, the Department's Staff Members take pride in its glorious history and at times appear to enjoy the puzzlement the name evokes. Nor is the duality of the Department's research a recent phenomenon, for at times in the past the interests of its Staff were even more diverse.

As the Department's Director, George Wetherill, points out, there is today little cross-fertilization between galactic and extragalactic astronomy on the one hand, and geology on the other. Wetherill believes, however, that it is unlikely that this separation will always exist. Astronomers will learn more about how galaxies form and evolve, and this knowledge will increase our understanding of the history of the Earth, which badly needs the type of constraint that could be provided by knowledge of its initial conditions and of the physical and chemical environment wherein the Sun

and planets formed. Work is going forward on meteorites, lunar rocks, and the oldest rocks of the Earth, observations are proceeding relevant to star formation, and theoretical work is moving ahead on star and planet formation. But even now, our interpretation of the meteoritic isotopic data and the resulting time scale for the formation of the solar system is limited by uncertainty in the rate of heavy element formation in the Galaxy throughout its history. There is also observational evidence that the oldest stars in the disk of the Galaxy may not be significantly older than the well-established age of the solar system, and it is thus possible that the formation of the solar system is related to some unique event or environment in the history of the Galaxy. If so, present-day observation of star formation could lead to false inferences. Galactic events may even have been significant in more recent times. At the present time the supernova rate in the Galaxy is rapid—a supernova occurs within 50 light years of the Earth about once every 70 million years, which is, from the geological point of view, a short time.

This year, Rubin, Ford, and Thonnard report new observations which begin to establish relationships between observable parameters of spiral galaxies, such as mass, luminosity, velocity as a function of distance from the center of the galaxy, and the morphology of the galaxy. Last year these observers discussed similar results from a small sample of large galaxies. They were surprised to find that the rotation velocity continued to rise with increasing distance from the center of the galaxy. The fundamental laws of motion relate the rotation velocity at a given distance to the total mass of the galaxy within that distance from the center. Use of the laws of motion then led to the conclusions that the luminous mass in a galaxy is but a fraction of its total mass, and that the actual extent of a galaxy extends well beyond its optical boundaries. This year, the work was extended to include 21 smaller spiral galaxies, with similar results. When the rotational velocity is plotted against distance from the galactic nucleus, all galaxies, large and small, are found to fall nearly on a single curve, except for distances very near the nucleus. The principal difference between large and small galaxies appears to be simply that in large galaxies, the measurements can be made at greater nuclear distances.

In a separate report, Burstein and Krumm discuss their 21-cm radio observations of neutral hydrogen for a galaxy also studied by Rubin and Ford but of a type intermediate between spiral and elliptical. These observations permit measurement of rotation velocity well beyond the edge of the optical boundary of the galaxy. Again, no evidence is found for a decreasing velocity, indicating that the mass is not centrally concentrated.

The work of Burstein and Krumm on this galaxy, as well as observations reported by Gallagher, Faber, and Burstein on elliptical galaxies, sheds some light on various ways in which galaxies may evolve. The first



case is that of a moderate-size galaxy of a type transitional between elliptical and spiral. As we have already noted, the optically visible galaxy is accompanied by an unseen disk of neutral hydrogen several times the luminous mass and of much greater spatial extent. Because there are no plausible sources for this hydrogen in the vicinity of this galaxy, it seems that this disk has been present since the galaxy was formed. In contrast, the other galaxies studied are giant elliptical galaxies, and the measurements suggest that they may have acquired a large amount of their mass by tidal stripping of nearby galaxies.

*The early history of the solar system.* In spite of the reservations raised above (that there may be important differences between star formation in the Galaxy 4.5 billion years ago and star formation now), observational data relating to recent formation of stars of one solar mass represent the greatest single missing piece in the puzzle of the formation of the solar system and the Earth. Some observational data on the location of recent star formation within the Galaxy are provided by Lockman. However, there is much evidence that can be obtained from the solar system itself which has not yet been fully exploited.

One such line of evidence is provided by the residual population of small bodies, asteroids and comets, which remain after the formation of the solar system. Their abundance and orbital distribution can be observed today, and evidence regarding the past evolution of this population is available from the record of ancient impact cratering on the Moon, Earth, and planets. Theories for the formation of the solar system can be plausibly constrained by the requirement that the bodies which formed the planets evolve in a natural way to explain the observed population and impact effects of the small bodies.

One promising approach to solar system formation has been developed from qualitative beginnings into a quantitative theory by Safronov and his co-workers in Moscow. They argue for the formation of at least the inner terrestrial planets by a continuing sweeping up of small bodies by larger ones. When worked out quantitatively, this approach requires few free parameters and assumptions. This year, Wetherill reports an extension of this theory to include the fact that the accumulating bodies are not freely moving objects analogous to molecules in the kinetic theory of gases, but are constrained to move in Keplerian orbits about the Sun. The complications introduced by introducing this realistic requirement dictate a numerical approach to the problem, rather than the earlier analytical one. When this is done, it turns out that the predictions of the earlier theory are still valid. In addition, new effects, such as radial spread of the orbits of the accumulating bodies, are found. Although much work remains to be done, it appears that "ground rules" for this mode of planet

formation can be established. For example, it should be possible to say whether or not prior formation of the very large planets, Jupiter and Saturn, is necessary in the inner solar system to maintain the eccentric orbits needed for planetary encounters and accumulation.

Another line of direct evidence regarding the early solar system is from detailed measurements on meteorites. Some meteorites resemble material that crystallized from a liquid state, similar to volcanic rocks on the Earth or metal in a blast furnace. However, the majority are better described by the term "regolith," a generalization of the more familiar geological concept of "soil." Regoliths, which are mixtures of crystalline and glassy fragments and their disintegration products, form blankets on planetary surfaces. On the Earth, the abundant presence of water and the resulting weathering and erosion produce regoliths which usually are clay mineral deposits, the end product of the disintegration and transportation of terrestrial rocks. On the other hand, an airless planetary body like the Moon has a regolith consisting almost entirely of rock fragments formed by impact cratering. Moreover, the absence of a lunar atmosphere and magnetic field leads to exposure of the lunar regolith fragments to the solar wind and the energetic nuclear bombardment accompanying solar flare activity. The evidence for this exposure is preserved in the lunar regolith particles in a number of ways. For example, the penetrating nuclear bombardment produces tracks in these minerals, which can be observed in a microscope in much the same way that cosmic-ray scientists record these energetic particles in photographic film.

Many meteorites are regolithic assemblages remarkably similar to the lunar regolith. Others resemble it qualitatively, but not quantitatively. Still others are assemblages of fragmental material which are quite different. All these regolithic assemblages bear a record of the time and place of their formation, but the interpretation of this record is not simple.

Rajan, Kothari, and Scott are directing a variety of experimental techniques toward the goals of untangling this regolithic record and learning the time, place, and circumstances under which regoliths were developed. In some cases, it appears possible that we have in these meteorites samples of surface materials formed into a regolith during geologically recent times on the surface of an asteroid, in a way very similar to the way in which the lunar regolith is also being developed today. In other cases at least superficially similar, the regolith was more likely developed on an analogous surface but at a time more nearly contemporaneous with the formation of the solar system. Still other meteorites are probably relics of the even earlier original accumulation of the meteorite parent bodies. One technique, involving electron beam microanalysis of the distribution of nickel in the metallic grains of stone meteorites, is used by these workers to uncover the thermal history of the astronomical body from which these



meteorites were derived. In turn, this permits relating the body's thermal history to its metamorphic history, dated by radiometric and nuclear track techniques. The problem is obviously a complex one, but such measurements are providing detailed information about the solar system from times and distances inaccessible in any other way.

### *Physics and Chemistry of the Earth*

*New views of the Earth's mantle.* For more than a decade earth scientists have turned their attention toward the consequences of at least the outer regions of the Earth being a great "heat engine," powered by the release of nuclear energy from the radioactive disintegration of uranium, thorium, and potassium. The moving parts of the engine are the 50- to 100-km-thick solid plates of the oceanic lithosphere, which migrate horizontally for thousands of kilometers before they plunge into the Earth's interior at oceanic trenches; the more buoyant and thicker, slowly drifting "rafts" of continental lithosphere; the underlying plastic asthenosphere; and the deeper regions of the mantle where the return flow from trench to ridge takes place. In a general way this mechanism is well understood: heating at depth leads to rocks having lower density, greater buoyancy, and upward motion. Cooling near the surface of the Earth has the opposite effect. The result is the complex convective system summarized by the term "plate tectonics."

As Wetherill observes, these phenomena compose a uniformitarian process par excellence. Only by the use of highly sophisticated instruments is it possible to distinguish the flow of radioactive heat to the surface of the continent from the much greater background "noise" produced by variations in sunshine. The total kinetic energy associated with global plate motion is only about  $10^5$  joules, about enough to heat the water for a cup of tea. Yet in the last 200 million years these processes have broken the Americas from Europe and Africa, and scattered once-united Australia, Africa, Antarctica, South America, and India to their present locations.

This year the *Department of Terrestrial Magnetism* has directed considerable attention toward understanding the structure of the slab of oceanic lithospheric mantle along the western margin of South America. There, the collision between the oceanic and the continental lithosphere leads to subduction of the denser and less buoyant oceanic plate into the deeper mantle of the Earth. This is the only available example of a tectonic environment that, over the history of the Earth, must have played a major role in mountain building, ore formation, and the evolution of continents.

For some years workers at DTM and at Cornell University have inter-

puted seismic data from this region differently. The DTM group has argued that this subduction is "normal," i.e., similar to that found throughout the world in island arcs such as Japan, where the interaction is between two oceanic plates. In contrast, the Cornell group has maintained that in the regions of central Peru and central Chile the ocean-continent subduction is characteristically different: the subduction angle is very shallow, about  $10^\circ$ , in contrast with the normal subduction angle of  $30^\circ$ . Elsewhere, in the geographically intermediate region of southern Peru and northern Chile, both groups agree that the subduction angle is normal, i.e., about  $30^\circ$ . Acceptance of the shallow angle of subduction leads to the difficulty that its eastward continuation would require the South American continental lithosphere to be relatively thin, whereas DTM's seismic data indicates it is 300–400 km thick.

This year Hasegawa and Sacks describe a detailed reinvestigation of the seismic data in this region of subduction, resulting in conclusions which appear to reconcile the previous conflicting interpretations. It seems that both interpretations were partly true and partly false, and that, as usual, the real Earth fails to conform to simple models developed to interpret limited sets of data. By making use of the finer spatial resolution available by use of the densely spaced local earthquakes, the subducted slab has been mapped in more detail. It is found that for the first 100 km of descent, the slab enters at the normal  $30^\circ$  angle. However, below this depth it is bent to a nearly horizontal angle. This horizontal slab extends eastward about 300 km, and then dips steeply below the thick lithosphere of the principal portion of the South American continent. When viewed at the earlier lower resolution, the  $10^\circ$  subduction angle represents the averaged value of the initial steeper angle and that of the horizontal region. Snoke, Sacks, and James explain how this more refined picture of the subduction geometry fits in well with several lines of evidence obtained at DTM which supported the normal  $30^\circ$  subduction angle. This evidence correctly defined the steeply dipping initial portions of the subduction, but did not identify the horizontal portion.

Simple inspection of a map of western South America demonstrates that the downgoing slab of oceanic lithosphere has had, during the past several million years, a profound effect on the surface geology and geography of this region: it has produced the Andes mountains, the belt of active and dormant volcanoes, and the great thicknesses of volcanic deposits. It could be that these effects are primarily physical in origin, and that little new material is added to the continent by these processes. On the other hand, it is possible that the slab itself is melted, and that material derived from oceanic mantle is thereby injected into the crust of the continents, causing them to grow with time. As in most such problems, it is likely that neither of these simple pictures is really correct, but it is also likely that neither



has entirely missed the truth. Definition of more detailed mechanisms for volcanism and production of igneous rocks above subduction zones is at present a lively field of research in many laboratories.

In addition to petrological conclusions based on major elements, studies of trace elements and isotopic measurements are making major contributions toward the resolution of this problem. Last year James described work carried out in collaboration with Magaritz and Whitford, in which it was shown that the dominant element in the Andean volcanic rocks, oxygen, was clearly enriched in the heavy isotope  $^{18}\text{O}$ . These rocks were thereby shown to carry the isotopic signature of material from the continental crust, only a minor portion being derived from the oceanic lithosphere.

This year Tilton has presented the results of measurements of lead and neodymium isotopes from southern Peru and northern and central Chile, the region in Peru being the same as that examined by James. It also lies in the zone that seismologists agree is a "normal" subduction zone: a  $30^\circ$  subduction overlain by asthenospheric material, interpreted as partially melted mantle and hence a probable source of the volcanic lavas observed at the surface. Tilton's work strongly confirms James' conclusion that the continental crust has contributed to these volcanic rocks. The isotopic composition of their lead is totally unlike lead from oceanic regions, inasmuch as it is relatively depleted in  $^{206}\text{Pb}$  but not in  $^{208}\text{Pb}$ , showing that it came from a source region which has been depleted in uranium but not in thorium. The source of this lead is not oceanic and therefore must in some way be continental. The  $^{143}\text{Nd}/^{144}\text{Nd}$  data confirm this view. Tilton suggests that the most likely continental source is the lower crust. Although rocks known to be derived from the lower crust are poorly represented at the surface, those that are available provide evidence that they are the kind of rocks from which lead of this isotopic composition could be derived.

This detailed identification of the continental source region differs from that given earlier by James, who felt that the strontium isotopic compositions suggest that the continental contribution results from erosion of continental sediments into the oceanic trench at the continent-ocean boundary and subduction of these sediments along with the ocean lithosphere, followed by recycling of this continental material back to the continent by partial melting of the subducted materials.

Whitford and White describe neodymium and strontium isotope studies of oceanic subduction zones in Indonesia. One of these, the Sunda arc in Java, may be thought of as a "classical" oceanic island arc, a good candidate for comparison with the ocean-continent subduction in Peru. In this case, the strontium and neodymium isotope data show evidence that only a minor component is derived from the continental crust. The isotope

ratios conform to the trends previously associated with mantle rocks, and there is little doubt that the dominant source of these rocks is in the mantle of the Earth. On the other hand, the isotope ratios are also distinct from those of the mantle source associated with the most abundant ocean volcanic rock—the midocean ridge basalts. It appears that these lavas from the ridges are not simply derived by melting of the subducted oceanic lithosphere, but possibly involve the tapping of a deeper portion of the oceanic mantle that is less depleted in “crust-forming” elements with large ionic radii, e.g., K, Rb, and U. The other Indonesian arc studied by Whitford and White (the Banda arc) is anomalous in that it appears that continental crust is being subducted beneath oceanic mantle. This inference is supported by these isotopic studies, which reveal the effects expected for an admixture of material with a previous continental crustal history. A similar conclusion was reached by Magaritz, Whitford, and James two years ago using oxygen isotopic measurements. When results such as these are combined with similar work from other laboratories, one gets the feeling that the complexities of this new “mantle geology” will not prove overwhelming, and that combined application of the many tools of geochemistry and geophysics can reveal the characteristics of these rocks despite their occurrence deep within the Earth.

Within the ocean basins, far from subduction zones, large volumes of lava flow from the Earth’s interior to the surface. Along the axis of the midocean ridge system, these are the near-surface expression of the generation of new oceanic lithospheric plates, about 50 km in thickness, which on time scales of  $10^7$ – $10^8$  years migrate toward the trenches and associated subduction zones, where they are consumed. An account of a seismic investigation of such a spreading lithospheric plate is given by Evans and Sacks. Volcanic eruptions also occur on oceanic islands that are unrelated to the ridge system. Over the past 20 years, isotopic and trace element investigations have clearly shown that the mantle sources of these two types of oceanic volcanism are different. Those from the ridges appear to be derived from a much more homogeneous mantle source which has been depleted in the elements with large ionic radii—those needed to form basalts. The sources of the oceanic island volcanic rocks are much more heterogeneous, both chemically and isotopically. Furthermore, these sources do not appear to drift with the oceanic lithosphere and asthenosphere, but remain relatively fixed in the mantle, producing chains of islands (as found in Hawaii) as the oceanic lithosphere drifts by above their source. Although these matters are poorly understood, the mantle sources of these oceanic islands are usually thought to lie at great depth, below the asthenosphere. From these sources, material could rise toward the surface as “plumes” or “blobs.”

The full complement of trace element and isotopic techniques are now



being directed, both at DTM and in other institutions, toward the goal of replacing the present "cartoon models" for the formation of these oceanic igneous rocks, with some real understanding.

*Experimental studies.* Although seismic, electrical, magnetic, and other geophysical field measurements have been used in combination with telescope observations, meteorite compositions, and other indirect data to construct models of the Earth's interior, direct experimental data on materials that might be stable under the intense conditions of the Earth's interior are needed. With new techniques developed at the *Geophysical Laboratory* for experimenting with solids, liquids, and gases at pressures and temperatures as high as 1.7 Mbar and 4000°C, such data are becoming available.

This year Mao and Bell obtained the first systematic experimental data in the range 150–650 kbar at 1000°C, corresponding to a depth range in the Earth between 500 and 1700 km (which includes almost 60% of the Earth's volume). The experiments were run on compositions in the chemical system Mg-Fe-Si-O. Known minerals in this system, such as the pyroxenes, olivines, and garnets, were found to react and form new phase assemblages. The assemblages consist of phases with the perovskite structure but of pyroxene composition, plus phases in the magnesiowüstite series  $[(\text{Mg,Fe})_{1-x}\text{O}]$  and high-pressure phase of  $\text{SiO}_2$ , stishovite. The chemistry of these phases is complex, but a number of revealing findings have emerged from recent studies.

The pressures where the phase changes begin are between 180 and 200 kbar, corresponding to a depth of about 650 km in the Earth. At this depth a major seismic discontinuity is known. The new phases and assemblages are denser than their component oxides and other minerals previously thought stable in the deep mantle. The new phases were found to be stable under experimental conditions to 650 kbar. Perovskite-like and magnesiowüstite-like mineral structures are dominant, and one can conclude that most of the mantle is composed of those structures. Perhaps the most significant recent result is that the phase of perovskite structure is limited in composition to about 20% of the iron end-member (the  $\text{FeSiO}_3$  component), but the magnesiowüstite-type phase is not so limited, and thus there is a strong tendency for iron to leave the silicate phase and become concentrated in the oxide phase. This type of elemental partitioning or preferential chemical distribution is of great geochemical importance. It is apparently by this type of a major partitioning process that aluminum and calcium, for example, have been preferentially concentrated in the crust and relatively depleted in the upper mantle, whereas iron and magnesium are concentrated in the upper mantle relative to the crust. A similar condition may be postulated for the deep mantle, on the

basis of these data on the partitioning of iron and magnesium combined with the new data on the extensive stability of the perovskite and magnesiowüstite-type structures.

Such partitioning might have been significant in processes that originally formed the Earth, and indeed, in processes that maintain the distribution with depth of the major elements. In most theories of the formation of the Earth, the initial bulk composition is close to that of chondritic meteorites, a composition more iron-rich than the bulk composition of the mantle. In previous models a starting assemblage containing iron in the metallic state was used; however, no evidence for the large-scale separation of iron from magnesium or even from oxide minerals was available. Some models were based on disequilibrium requirements; others, on processes that included removing portions of the original bulk-accreted mass in order to achieve the present distribution of a central reduced core, a less reduced mantle, and an oxidized crust and atmosphere. A new model for the formation of the Earth based on experimental data includes the separation of iron-rich minerals to form the metallic core and yield a mantle residue close to that of the Earth today. The large density difference between the iron-rich oxides and the magnesium-rich silicates is sufficient to cause the separation. A later step of chemical disproportionation, whereby iron is extracted from the oxides, completes part of a cyclic process to stabilize the core, mantle, and crust. This model, the first to be constructed from experimental data, is an equilibrium model. The phases and the processes resulting from their unique properties must have played a significant role in forming the Earth and in stabilizing the present elemental distribution in the Earth.

*Application of flume studies to plate tectonics.* As we have already observed, the forces that drive tectonic processes are widely believed to stem from large-scale convection in the Earth's mantle. To recapitulate, this convection evidently features large cells in which hot material rises from depth, particularly along the midocean ridges, and spreads laterally, carrying with it the rigid outer Earth shell, or lithosphere, which includes the low-density rocks that form the continents. As the convecting material spreads, it cools by upward heat loss and its density increases, so that eventually it sinks back to depth, most commonly beneath island arcs and along continental margins. As it sinks, it is accompanied by slabs of the lithosphere that are said to be subducted as they move downward along inclined, seismically active structures called "Benioff zones." An especially puzzling feature of this system is that much of the world's most conspicuous magmatism, including such features as the highly explosive volcanoes of the present-day Pacific "Ring of Fire" and many of the giant granitic batholiths of ancient mountain belts, evidently occurs above



Benioff zones where cold rocks are descending into the mantle. It has not been clear how the heat that melts this magma originates in this environment.

In his work this year in the *Geophysical Laboratory*, Irvine has taken a novel approach to this problem through an experimental study of density currents. The currents are formed from silicone fluids in a small Plexiglas flume and are scaled to mantle conditions of size, density, and viscosity so that they flow at scaled velocities of a few centimeters per year, comparable to the rates at which sea floor spreads, continents drift, and lithosphere is subducted. The structure of the experimental current flow pattern is determined by means of visible tracer particles suspended in the silicone fluids and is illustrated using two alternative methods of flow visualization derived from fluid mechanics. The flow structure is then taken to represent mantle convection: upwelling of a low-density current in one method of visualization resembles the rise and spread of mantle material from beneath a midocean ridge; in the alternative method, the same current is seen to displace denser liquid in a way that compares with subduction.

Working from this framework, Irvine has developed tectonic models that appear to provide significant new insights into orogenic magmatism. In particular, he shows in his report that subduction probably occurs through the transfer of lithosphere *across* converging (descending) boundaries beneath convection cells, from the top of one cell into the body of its neighbor. He notes that, in the model convection system, rapid flow zones in the upwelling, spreading density currents have positions that compare with the locations of seismic low-velocity zones in the Earth's mantle, places where the mantle is believed to be partly melted, and he suggests that the Earth melting is the result of the release of pressure associated with rapid upward flow. Volcanic arc magmas seem reasonably portrayed as being released from the tips of mantle currents where flow within them divides or splits, and Irvine suggests that these currents also act, in effect, as focused heat sources in that they bring a continuing supply of hot mantle material into the lithosphere above Benioff zones where the heat may then melt the base of overlying continental crust to produce granitic intrusions. The models also provide different perspectives on such orogenic features as geosynclines and metamorphic belts, and some new possibilities are even raised regarding anorogenic magmatism, such as that yielding carbonatite and kimberlite intrusions.

*Isotopic studies of older rocks.* When isotopic geochemical and geochronological studies were started at DTM about 30 years ago, much of the emphasis was placed on older rocks of the Earth, particularly those in the Precambrian, ranging in age from 500 to 3000 million years. This

work resulted in delineation of the scope of Precambrian time and the distribution of these ancient rocks on the continents. With the advent of plate tectonics during the 1960's, attention shifted to the youngest rocks, particularly those from the oceanic regions. This shift took place because the "action"—the production and destruction of lithosphere—occurs in the young ocean basins. Although at least similar processes must also have occurred before the formation of the oldest preserved ocean basins about 200 million years ago, most of that record has now been lost. The surviving record will be found in the vestiges of old oceanic events preserved in the continents. Now that earth scientists are beginning to understand the processes occurring in the young oceans, it can be expected that there will be renewed interest in older rocks, making use of new insights into the Earth's fundamental tectonic processes from study of more recently formed rocks.

Three geochemical investigations involving older material are described in DTM's Report. Bugnon, Tera, and Brown report lead isotope measurements on 2640-million-year-old ores and their host rocks from the Abitibi greenstone belt in Ontario, which show that the mineralization and the formation of the rocks were very nearly contemporaneous. However, if one uses these data to calculate the isotopic composition of the lead in these rocks at the time of their formation, the material from which the rocks were derived appears to be about 2900 million years in age, according to the simplest models for evolution of the isotopic composition of lead in the Earth's mantle. The authors present some evidence that this is not a purely local phenomenon. Measurements of this kind will be used to provide information on the time scale for the evolution and early differentiation of the Earth's core and mantle.

Echeverría reports a geochemical investigation of an unusual type of magnesium-rich volcanic rock, spinifex-textured komatiite, of Tertiary (<60-m.y.) age from Colombia. These rocks have an unusually high melting range, and are almost entirely confined to the ancient Archean greenstone belts. The high mantle temperature required to form these rocks has been used as a constraint on the thermal evolution of the Earth. This work shows that very similar rocks can also be formed in relatively recent times. Investigation of such young komatiites will provide valuable data about the unusual mantle environment required to form these lavas and implications for the early history of the Earth.

In another study of older rocks, Mose has found billion-year-old Precambrian rocks, which intrude even older gneisses, under the Virginia Piedmont. In attempting to reconstruct plate tectonic events before formation of the present ocean basins, previous workers have concluded that the Virginia Piedmont was located on a young plate that collided with the



ancient North American plate during the Paleozoic. This work shows that the Piedmont rocks were also on a Precambrian plate of similar age, and may never have been separated from the North American plate.

*Stable isotopes in biogeochemical research.* Some elements of biogeochemical interest (hydrogen, carbon, oxygen, nitrogen, and sulfur) are mixtures of stable isotopes; that is, they contain atoms that differ only in their nuclear masses. For example, the element carbon has 98.6%  $^{12}\text{C}$  and 1.1%  $^{13}\text{C}$ ; hydrogen has 155 ppm heavy hydrogen (deuterium) and the remainder as hydrogen of mass 1. Molecules having different isotopic substitution ( $^{12}\text{CO}_2$  and  $^{13}\text{CO}_2$  or  $^1\text{H}^1\text{HO}$  and  $^1\text{H}^2\text{HO}$ ) are qualitatively identical in their chemical properties but have small quantitative physicochemical differences. In general, molecules containing the lighter isotopes react more rapidly than those having the heavier isotopes. Thus, during photosynthesis carbon dioxide with  $^{12}\text{C}$  is fixed into organic matter at a rate 2–3% faster than molecules with  $^{13}\text{C}$ .

As elements flow through the various geochemical cycles, isotope fractionation occurs in various steps resulting in characteristic labeling. These natural isotopic labels or tracers have proved to be extremely valuable in biogeochemical studies where stable carbon isotopes are used routinely. In the petroleum industry, for example, stable carbon isotopes are used to identify the source rocks of the crude oil that accumulates in a reservoir. Marine biologists use carbon isotopes to trace the sequence of changes in organic matter caused by living organisms growing and being consumed in the food chain.

In contrast to the highly developed field of carbon isotopes, little is known about hydrogen in organic matter, but it seems likely that this field will be particularly rewarding for determining source environment. There is a large body of information on the isotopic composition of natural waters. Sea waters of the temperate oceans have a nearly uniform hydrogen isotope ratio, but fresh waters are depleted in the heavy isotope and are highly variable. The hydrogen isotope ratio correlates with geographical position. Because plants derive their organic hydrogen from the environmental water, their hydrogen isotopes should reflect the location of their growth. A potential isotopic tracer therefore exists.

Estep and Hoering at the *Geophysical Laboratory* have begun to evaluate this potential research tool by measuring hydrogen isotope effects during photosynthesis in cultures of microalgae grown under controlled conditions. They have developed analytical procedures for the precision measurement of hydrogen isotope ratios on milligram quantities of organic matter. During photosynthesis algae incorporate “light” hydrogen at a rate 10–15% faster than “heavy” hydrogen. On the other hand, during

aerobic respiration, which predominates during periods of darkness, there is no isotope discrimination. Light-mediated chemical reactions are major factors controlling the hydrogen isotope composition of plants.

They also found that after hydrogen is bonded into natural macromolecules, it is stable against isotopic exchange with a large excess of water. After denaturation, i.e., alteration of the original state of the macromolecules, the organically bound hydrogen is more accessible and undergoes exchange. This observation will be significant in interpreting the observations on organic matter in sedimentary rocks.

The lipid fractions obtained from cultures, grown either photosynthetically or heterotrophically on glucose, are markedly depleted in the heavy isotope of hydrogen as compared with carbohydrates and proteins. The lipids contain fatty acids, waxes, and sterols where the hydrogen is bonded firmly to carbon and does not exchange with water. Thus the hydrogen isotopic ratios in lipids should be useful natural tracers for organic matter.

On the basis of the biochemistry of stable hydrogen isotopes obtained from experiments in the laboratory under controlled conditions, one can design experiments with natural populations of plants to determine how well their hydrogen isotopes correlate with their environmental waters. It is now possible to begin experiments on recent sediments to determine whether organic matter of terrestrial origin can be distinguished from that of marine origin.

Research in the field of stable oxygen isotopes in organic matter is at its beginnings, and experiments are being designed to study biological fractionation of oxygen isotopes. Oxygen is interesting because it has three major geochemical reservoirs significant in biogeochemistry— $\text{H}_2\text{O}$ ,  $\text{O}_2$ , and  $\text{CO}_2$ . Each of these reservoirs has a distinctive and widely different oxygen isotope ratio. Another potential tracer for organic substance therefore exists and is being exploited to ascertain the source of oxygen in the biogeochemical cycle. In short, the isotopes of C, O, H, N, and S are expected to provide many opportunities for determining the sources, rates, processes, alterations, and metamorphisms of organic substances now recognized throughout the entire geological sedimentary record.

*High-temperature solution chemistry.* Geochemistry is now on the verge of a new thrust into the understanding of many traditional geologic problems. With the application of theoretical transport models, one may be able to predict reaction mechanisms at metamorphic isograds and the evolution of various types of skarns, important in the formation of some ore deposits. Many such models involve the assumption of material transfer through a dispersed fluid phase in local equilibrium with neighboring solids. The relative fluxes of elements in pore fluids are highly dependent upon the concentration gradients of the dissolved solutes. Data from fluid



inclusions and from volcanic gases indicate that chloride can, in general, be assumed to be the most common anion in these natural supercritical solutions. Models based on these assumptions require data from experiments at elevated temperatures and pressures concerning the structure and thermodynamic properties of the electrolytic solutions as well as the solubilities of mineral phases.

Two general experimental methods have been employed at the *Geophysical Laboratory* to study solution equilibria at supercritical temperatures and pressures: (1) solubility studies using hydrothermal pressure vessels and (2) electrical conductance measurements. Theoretical approaches have been developed whereby data obtained from such studies can be extrapolated to temperature-pressure-compositional regions not amenable to experimentation.

With the development of the  $\text{Ag} + \text{AgCl}$  buffering technique by Frantz and Eugster, considerable progress has been made toward determining the solubilities of minerals containing alkali earths such as magnesium (Frantz and Popp) and calcium (Popp and Frantz), and containing iron (Boctor, Popp, and Frantz). The measurements were done at temperatures above  $300^\circ\text{C}$  and at pressures of 1000 and 2000 bars, conditions normally not investigated by solution chemists. From the results of these studies, the relative concentrations of solutes in fluids coexisting with mineral assemblages can be calculated. Magnesium and iron were found in minor abundance when compared with potassium, sodium, and calcium, and would, therefore, normally not be as easily transported by fluids altering rocks.

Electrical conductance studies have long provided the foundation for interpreting many of the above solubility studies by supplying information about the abundances of the different aqueous species. Solubility studies yield total concentrations of the elements in the quenched fluid, but to compute thermodynamic solubility constants from such data, knowledge of the distribution of the aqueous complexes must be known. Determination of the dissociation constants of the 1-1 electrolytes  $\text{HCl}$ ,  $\text{KCl}$ , and  $\text{NaCl}$  has shown a general trend that strong electrolytes (existing primarily as ions) at room temperature become weak electrolytes (existing primarily as associated molecules) with increasing temperature and decreasing density of  $\text{H}_2\text{O}$ . Frantz and Marshall measured the electrical conductances of the 2-1 electrolytes  $\text{CaCl}_2$  and  $\text{MgCl}_2$  up to 4000 bars and  $600^\circ\text{C}$ . They demonstrated for the first time that these strong electrolytic salts also become weak electrolytes with increasing temperature and decreasing density. They computed the two ionization constants for both salts and, using their results combined with the results of the solubility studies, characterized the  $\text{MgO-CaO-SiO}_2\text{-HCl-H}_2\text{O}$  fluids.

With the acquisition of these data, quantitative calculations modeling alterations of rocks described mainly by the system  $\text{MgO-CaO-SiO}_2\text{-H}_2\text{O-}$

CO<sub>2</sub> will be possible for the first time (if one assumes that the concentrations of magnesium and calcium carbonates in solution are small). By comparing the results of calculations using the multicomponent transport model of Frantz and Mao with natural systems that have undergone alteration under hydrothermal conditions (e.g., chert nodules in dolomitic limestones), it will be possible to determine the relative magnitudes of the fluxes (and diffusion coefficients) of the components in the intergranular fluid.

*A new approach to the chromatographic separation of optical isomers.* The existence of mirror-image isomers (enantiomers) of organic compounds has been known since the work of Louis Pasteur a century ago. It has been only within the last 15 years, however, that chromatographic methods have been available for the separation and quantitative determination of the isomeric ratios in a sample. Most of these methods require derivatization with optically active compounds, or preparation of optically active column supports or packings, in order to resolve the mirror-image isomers. Both approaches are time consuming and costly. A new approach has been devised in the *Geophysical Laboratory* by Hare and Gil-Av whereby an optically active compound (L-proline-copper complex) is added to the mobile phase of a liquid chromatography system using columns with readily available packing materials. With this system, underivatized amino acids can be resolved into their enantiomers quickly and efficiently, in fact so efficiently that it should be possible to prepare the pure enantiomers of several amino acids. The system has so far been used only for the separation of amino acid enantiomers but in principle is applicable to other classes of optically active organic compounds.

Laboratories in several disciplines are involved in amino acid studies, and interest in the distribution of amino acid enantiomers is widespread and growing dramatically. In living systems there is an almost exclusive preference for the L form. For example, proteins are biologically synthesized entirely from the L-isomers. The D-amino acids, the mirror-image isomers, however, do occur in biological peptides with antibiotic activity and in the cell walls of certain microorganisms. The presence of D-amino acids confers a resistance to many enzymatic processes that are active for only the L-forms. Many biological studies of amino acids involve work with D-amino acids, and the determination of the D to L ratios is essential. Synthetic peptides of biological interest incorporating D-isomers are receiving increasing attention to ascertain the biological effect of the configuration of the constituent amino acid residues. Questions have been raised as to the possible role of D-amino acids under pathological conditions.

Pure D or L forms can interconvert under some conditions to form a mixture of the isomers. This process is known as racemization and occurs,



for example, in biological tissues, during food processing, and in the amino acids of fossil shells, bones, and teeth. In organic geochemical studies, the increase in the D-amino acid isomers in the proteins and amino acids in fossil shells can be correlated with the age of the deposit. Use of the ratio of the D to L amino acids has proved a valuable aid in stratigraphic correlation and age estimates in deep sea cores, Pleistocene sedimentary sequences, and in particular the glacial and interglacial sequences in the Arctic. In the summer of 1979 an extensive mapping project on the glacial and interglacial deposits of Spitzbergen was carried out with a portable field instrument to obtain preliminary data on the amino acids and their enantiomers in fossil mollusc shells as an aid to stratigraphic correlation of isolated outcrops.

Another aspect of geochemical interest is the extraordinary stability of the complexes formed by the interaction of certain metallic ions and amino acids. Very specific interactions occur to form stable complexes that differ vastly in chemical and physical properties depending on the nature of the amino acids and metallic ions involved. Such complexes might be involved in geochemical transport and deposition of elements such as manganese, copper, zinc, and mercury, found in certain low-temperature ore deposits. Additionally, this work may lead to the development of certain organic materials that form complexes with metallic ions and may be used, therefore, to extract specific elements from mixtures of elements present in ores.

### *The Acquisition of Biological Specificity*

In the transformation of biology, the great underlying shift of view was the development of the concept of biological specificity. In the mid thirties, biologists and biochemists certainly spoke of specificity. They had to do so, for many of the phenomena they dealt with—genes (whatever they were in substance), enzymes and antibodies (known to be protein)—were highly specific in action. Yet specificity was really a term almost empty of meaning. When biochemists attempted to understand proteins, for example, they looked for general chemical rules for their assembly or for repeating physical units in their structure—and reported that they had found them, even though any such rules and units turned the notion of specificity into its opposite. Forty years later, biological specificity is richly stuffed with meaning.

*Horace Judson*

In one way or another the research of the *Department of Embryology* deals with “specificity.” Nerves grow to their target organs, molecules are assembled in exact locations within cells. There is specificity in the shape and movement of cells and in their interaction. Specificity is manifest in the expression of genes whose products determine the identity of cells,

tissues, and organisms. Understanding the molecular and cellular meaning of specificity in biological systems is the unifying theme of the Department, and provides a common goal for its members.

Kenneth Muller and his colleagues study nerves in the leech because the properties of single nerve cells with known connections can be analyzed more easily than those of complex nerve bundles of vertebrates. Regeneration of a single leech nerve cell can be observed over a period of months. It is possible to manipulate the cell and record the effects on regeneration. Thus this group seeks to understand the importance of target cells and glia on the specificity of nerve growth and on the formation and maintenance of synaptic connections.

Fambrough and his associates have developed methods of measuring rates of synthesis and degradation of specific surface proteins. These methods were first applied to the acetylcholine receptor because a protein,  $\alpha$ -bungarotoxin, interacts tightly and specifically with the receptor. These kinds of measurements were difficult to extend to other cell surface proteins because of the lack of specific probes. A new method devised by Milstein at the MRC Unit in Cambridge makes it feasible to obtain cells in culture that produce single monoclonal antibodies. These cells are called hybridomas, and Fambrough and his colleagues have produced hybridoma cell lines that are producing antibodies to surface proteins.

Rotundo has extended his studies of the important enzyme acetylcholinesterase. This enzyme can be secreted by cells or incorporated into their surface membranes, where it behaves as an integral membrane protein. The half-life of this enzyme localized in membranes is three times longer than the acetylcholine receptor—evidence that individual surface proteins can be metabolized independently.

Richard Pagano and his associates have developed methods for tagging lipids in various ways and introducing them specifically into the inner or outer leaflet of plasma membranes. Schroit has demonstrated that lipids in the outer leaflet can be capped. This observation bears on current hypotheses about the fluidity of lipids in plasma membranes and the possibility of a directional flow of molecules in the surface of a cell. Using these methods, Struck has found that the rate of exchange of lipids in the external leaflet of the plasma membrane with the interior of the cell is very slow, while that in the internal leaflet is rapid.

In order to explore the specificity of surface interactions when sperm fertilize eggs, Ward and his group have collected mutants of the nematode *C. elegans* that affect the fertility of sperm. Nelson has advanced the technology of sperm "culture" by discovering a means of inducing sperm motility in vitro with the ionophore monesin. Since active sperm are motile, this brings the technology a step closer to fertilization in vitro in *C. elegans*. The various mutants have characteristic and in some cases



aberrant responses to the ionophores. Morphological asymmetry of sperm is reflected in changes in surface and internal components. Argon has found that surface glycoproteins are redistributed in motile sperm. This is another descriptive tool with which to assay the mutant collection in the search for their underlying defects.

As we observed earlier in this essay, the detailed analysis of several multigene families encoding 5S ribosomal RNA has yielded some important and surprising discoveries. Peterson has completed the characterization of two of these gene families—there are now five that have been cloned by the recombinant DNA methodology and sequenced completely. There are striking differences between the spacer regions of somatic and oocyte-type gene families—the former being AT-rich, the latter GC-rich. The manipulation of one of these genes by Brown and his colleagues has demonstrated the remarkable finding that a region of about 30 nucleotides within the 5S gene controls its accurate expression. This finding suggests a mechanism for RNA polymerase recognition of a gene that is strikingly different from that of *E. coli* RNA polymerase and prokaryotic genes.

Two new undertakings are discussed in the Department's Report. Staff Associate Patricia Gearhart, a cellular immunologist, is interested in the repertoire of antibodies that can be elicited by a single antigen. In addition, she wishes to know how many immunoglobulin genes are expressed by a single cell.

S. McKnight, a Postdoctoral Fellow working with C. Croce, a Visiting Investigator from the Wistar Institute, is transforming animal cells with purified DNA, using a powerful new technique developed at Columbia University by R. Axel and his colleagues. A useful selectable marker is the gene for thymidine kinase. It can be obtained in large quantities from herpes simplex virus. By joining this gene to a bacterial plasmid a "double-headed" vector is obtained that, in theory, can be grown either in bacteria or in animal cells. Any other DNA fragment can be ligated to this vector and then introduced into an animal cell that lacks the thymidine kinase gene.

The departures of two Staff Members reflect continuing change in this Department. The Director, Donald Brown, is the only member remaining from a closely interacting group of four Staff Members who for more than ten years applied nucleic acid chemistry to isolated genes. As reported in *Year Book 77*, Igor Dawid moved to the National Cancer Institute in May 1978. In the fall of 1978 Ronald Reeder joined the faculty of the Hutchinson Cancer Research Institute in Seattle, Washington, and Yoshiaki Suzuki returned to Japan as a senior faculty member in the new National Institute for Basic Biology in Okazaki.

Ronald Reeder joined *Embryology* as a Postdoctoral Fellow in July 1967, and was appointed to the Staff in July 1969. He collaborated on some of

the early studies on purified ribosomal DNA of *Xenopus*. When restriction enzyme methodology became available, he carried out detailed analyses on the structure of this DNA. These studies elucidated the nature of length heterogeneity between repeating units of ribosomal DNA by showing that spacer regions contain simple sequences. Because ribosomal RNA genes (rDNA) are amplified in oocytes, they can be purified in their chromatin state. This enabled Reeder and his colleagues to begin characterizing the proteins associated with this DNA. Additional molecular detail of rDNA is presented in the Department's present Report, Barbara Sollner-Webb having localized and sequenced both the initiation and termination sites for rRNA synthesis, thus making it possible to analyze the developmental control of rRNA transcription.

In studies that have in many ways paralleled the investigations on ribosomal RNA genes, Yoshiaki Suzuki has studied the highly specialized structural gene for silk fibroin in *Bombyx mori*. His pioneering research over some ten years first resulted in the isolation and characterization of the silk fibroin messenger RNA, reported in 1972. Using this messenger RNA, Suzuki was then able to show that cells of *B. mori* have a single copy of the gene for this protein. In the last few years, Suzuki and his colleagues have cloned the silk fibroin gene by the recombinant DNA methodology and carried out detailed molecular characterization.

In their final report, Suzuki and his colleagues once again demonstrate the amazing power of the new molecular methods for analyzing genes and gene products. They have determined the "start site" for fibroin gene transcription, a remarkable feat considering that the gene is 16,000 nucleotides in size. The DNA sequence flanking the site of transcription initiation as well as the 5' end of the gene including the entire intervening sequence has been completed. In addition, they have developed an assay system that can detect accurate initiation events when they occur. Using these methods they have begun to study the developmental control of fibroin gene expression.

The departures of Dawid, Reeder, and Suzuki represent the end of an era for the *Department of Embryology* in which some of the earliest studies on purified eukaryotic genes of known function were carried out.

Two of these three positions have been filled. Nina Fedoroff joined the staff July 1, 1978, and in her first report as a Staff Member outlines her plans for analyzing controlling elements in maize. Her challenge will be to translate deductions made previously by cytogeneticists into molecular terms. The genetic systems used by Barbara McClintock to discover and describe controlling elements resulted in visible changes in the plant. The biochemical functions of these genes were not well understood. With the help of McClintock, Fedoroff hopes to produce strains of maize in which



controlling elements regulate genes that are amenable to study by biochemical methods.

Allan Spradling, currently a postdoctoral fellow of the Helen Hay Whitney Foundation in the Department of Biology at Indiana University, will take up residence by January 1980. Spradling studies the genes in *Drosophila* responsible for the egg shell proteins. This group of genes is expressed in only one cell type, and the proteins are synthesized according to a specific developmental timetable. Mutants have already been described that affect these proteins. Spradling's ability to do genetics of both the traditional and more "modern" molecular kinds lends exceptional promise to this work.

One of the Department's most able and dedicated workers, John Wiser, retired after 22 years of service. He has designed and fabricated specialized equipment that has met the most fastidious detail that highly critical scientists can devise. The great pride and skill that he has taken in his work has rewarded and inspired us all.

### *Plant Biology*

I have already discussed (p. 8) one of the principal accomplishments of the past year in the *Department of Plant Biology*—Björkman and Badger's discovery of thermal adaptation in mature leaves and Berry and co-worker's development of simple nondestructive techniques for following its course in time. The capacity for thermal acclimation is clearly much more widespread than originally expected, and the techniques for measuring it could be of considerable use to plant breeders searching for cultivars with improved resistance to high temperature and drought. Other groups in the Department have been equally productive. The careful quantitative studies of O<sub>2</sub> and CO<sub>2</sub> exchange in photorespiration do much to dispel any uncertainty about the dual role, both as oxygenase and as carboxylase, of the CO<sub>2</sub>-fixing enzyme in vivo. The successes in cloning both cDNA's and native plant DNA's should yield significant advances in our knowledge of patterns of transcription in development and of genome organization in plants, as well as in providing powerful tools for other kinds of genetic analysis and manipulation. A significant number of technical advances, many of them involving computer applications, should also be noted, as should the significant progress in characterization of a blue-light photoreceptor system in corn and the exploitation of a system for studying phytochrome in light-grown plants in the absence of chlorophyll.

Let us examine a few of these advances more fully. William Thompson

and his colleagues are continuing to probe the nature of plant genomes, their evolution, and their expression during development. Michael Murray and Thompson have now completed a characterization of the mung bean genome, using hybridization techniques to determine the length and linear distribution of repeated and unique DNA sequences in the nucleus. The mung bean genome itself contains only 0.5 pg per haploid nucleus, in contrast to the pea genome which is almost ten times as large. About 35% of the unique sequences in mung bean are between 300 and 1200 nucleotide pairs long, 18% between 1200 and 6700 nucleotide pairs long, and fully 46% are longer than 6700 nucleotide pairs. This genome organization stands in sharp contrast to that of pea in which the vast majority of the unique sequences are 300–400 nucleotide pairs in length. This great divergence in organization makes it unlikely that unique sequence length and distribution play any major role in regulation of gene transcription.

The Thompson group has also made substantial progress in cloning of plant DNA on bacterial plasmids. Debra Peters, Murray, and Thompson have developed the necessary technology to transcribe plant messenger RNA into complementary DNA (cDNA), and Richard Jorgensen and Thompson have succeeded in cloning such cDNA on bacterial plasmids. Indeed, with cloned cDNA made from pea leaf mRNA they were able to demonstrate substantial differences in levels of different messenger RNA's between leaves and buds. The technique involved making highly radioactive cDNA's from both leaf and bud messenger RNA's and then determining the relative degree of hybridization of these two different populations of cDNA with individual cloned cDNA from leaves. A total of 30 clones showed significant differences.

Richard Cuellar and Thompson report some initial success in cloning plant DNA directly via bacterial plasmids. In the past, such cloning has been achieved in other laboratories, but the length of the cloned pieces were always dismayingly shorter than the original plant DNA fragments used. This fragmentation is evidently at least partially a function of the genetic background of the host bacterial strain, and Cuellar and Thompson have now succeeded in obtaining cloned DNA's essentially the same length as the original plant DNA fragments inserted.

Heather Belford and Thompson report briefly on the extensive studies constituting Belford's thesis research on the genus *Atriplex*. Studies of degree of homology among single copy DNA's from a variety of *Atriplex* species suggest that most of these species must have arisen almost at the same time, by a radiative rather than a sequential process over millions of years. The results support the view reported previously that there is no need to hypothesize the independent evolution of C<sub>4</sub> photosynthesis twice within this genus. Diana Stein and Thompson also report evidence indicating the same sort of radiative process for the fern genus *Osmunda*,



suggesting further that the three species of the genus must have existed as separate evolutionary lines for at least 70 million years.

Finally, Jeffrey Palmer, Murray, and Thompson have determined that a significant fraction of the repeated DNA found in mung bean leaf preparations is chloroplast DNA. Using the high-resolution derivative analysis of melting curves developed last year by Cuellar, Ford, Briggs, and Thompson, they show that the component is largely lacking from nuclear preparations. They have developed very accurate techniques for quantitation of chloroplast DNA in various kinds of DNA preparations, and have shown that between pea and mung bean chloroplast DNA there is a high degree of sequence conservation. Though the results speak somewhat to problems of genome organization, the thrust promises to be more evolutionary in the future.

On the photoreceptor front, Mary Helen Goldsmith, first alone and then later with Roland Caubergs, continued to capitalize on her success in finding conditions to obtain flavin-mediated cytochrome reduction in corn membrane fractions reproducibly and to maximize the response. There is evidence, at least from studies of *Neurospora*, that such a system may be involved in blue-light photoreception in vivo. She and Caubergs report further evidence that the reaction is highly specific, involving probably only a single nonmitochondrial *b*-type cytochrome with an absorption maximum near 560 nm in the reduced form. They present quantitative evidence on the relative affinity of the system for exogenously added flavins. Caubergs, Goldsmith, and Briggs also report that in crude mitochondrial preparations light can cause the reduction of the mitochondrial cytochrome *aa*<sub>3</sub>, a reaction that completely overrides the photoreduction involving the *b*-type cytochrome. The mitochondrial reaction can be clearly distinguished from the nonmitochondrial, however. It differs spectrally, its photoreceptor moiety is readily washed out (that for the latter is tightly bound), its fractionation pattern is different, and its sensitivity to inhibitors is different.

Dina Mandoli and Briggs report some success in unraveling the complex kinetics and dose-response relationships for dark-grown oat seedlings exposed to red light. They noted an extreme sensitivity to the green safelight that resembled that reported last year by Quail and Briggs for potentiation of sensitivity to gravity in corn roots by light. In another study on the influence of light on growth, Holly Gorton and Briggs report that the preemergent herbicide Sandoz, which inhibits synthesis of visible-absorbing carotenoids both in light and dark and hence leads to complete photo-destruction of chlorophyll in the light, has no qualitative or quantitative effect on three different phytochrome-mediated reactions in light-grown corn seedlings. These are promotion of coleoptile growth, promotion of mesocotyl elongation, and suppression of anthocyanin synthesis. The re-

sults encourage the expectation that Sandoz may be used to determine ways in which chlorophyll affects phytochrome photoequilibria in vivo by its screening properties.

Among the technical achievements deserving of mention are the following: Jeanette Brown has developed and modified techniques for obtaining preparations of photosynthetic pigment complexes which show far more normal absorption and fluorescence properties than in the past. This separation of a portion of the photosynthetic apparatus from the whole without serious disruption of the relationships between the component molecules should greatly enhance elucidation of the nature of pigment interactions in photosynthesis. Brown and Richard Hart have also designed and constructed a simple and inexpensive hydraulic apparatus to operate a French pressure cell. James Collatz, Badger, Celia Smith, and Berry have developed a sensitive and very useful radioimmune assay for the enzyme ribulose biphosphate carboxylase-oxygenase, based on an analog of ribulose biphosphate which can be labeled with  $^{14}\text{C}$  and which binds irreversibly to the enzyme. Geoffrey Harvey has developed a technique involving computer analysis of cytochrome difference spectra. The method is useful for quantitating photosynthetic cytochromes more precisely than previously possible. Fork, Glenn Ford, and Benny Catanzaro have developed a microprocessor-based spectrofluorimeter and interfaced it to the Department's central minicomputer, greatly increasing the versatility of the system and increasing time-sharing possibilities. In addition, Shmuel Malkin, Ford, and Fork have adapted the computer for direct determination of photosynthetic unit size from fluorescence-rise kinetics, on the basis of the report last year of the advantages of this fluorescence method (by Malkin, Ford, and Armond). Finally, Peter Quail has implemented the immunoaffinity technique for purification of the photomorphogenic pigment phytochrome from higher plants, a technique developed by Lee H. Pratt and his students at Vanderbilt, and is using it in attempts to localize phytochrome receptor sites on specific membrane fractions.

## LOSSES

It is with a deep sense of loss that I record the resignation of four Trustees of the Institution, James N. White, J. Paul Austin, Walter H. Page, and William M. Roth. Mr. White, who has served the Institution with great distinction as a Trustee for over 22 years and as the Board's Chairman, 1965–1970, has been named Trustee Emeritus.

The Office of Administration is not the same without Marjorie Walburn and Mary Hedger, who have retired. Miss Walburn served the Institution with distinction in many capacities for 32 years, most recently as Assistant



to the President, 1962–1978. Mrs. Hedger's devoted service, first as Secretary and later as Administrative Assistant to the Bursar, also spanned nearly 32 years.

### . . . AND GAINS

I have already reported the appointment of Allan Spradling in the Department of Embryology. Typhoon Lee was appointed a Staff Member of the Department of Terrestrial Magnetism. Lee, who most recently held a Robert R. McCormick Fellowship at the Enrico Fermi Institute at the University of Chicago, was the codiscoverer of the  $^{26}\text{Mg}$  anomaly in meteorites. He took his Ph.D. from the University of Texas at Austin, in 1977, receiving the 1978 Robert J. Trumpler Award "for outstanding doctoral dissertation research in astronomy" from the Astronomical Society of the Pacific. At DTM, Lee will work on the application of high-precision mass spectrometry to problems of solar system origins.

Marilyn Estep, a biochemist, from the Marine Science Institute at the University of Texas at Port Aransas, received her Ph.D. from the University of Texas in 1977. From July 1978 to July 1979, Estep was a Post-doctoral Fellow at the Geophysical Laboratory. Her studies of the hydrogen isotope content of organic material in plants and sedimentary rocks, and of biomineralization by algae, have been highly productive and I am happy to report that she will remain on the Laboratory's Staff.

Christopher Wright began his appointment as Staff Member for Science Policy and Institutional Development in July 1979. Wright came to the Institution from the Congressional Office of Technology Assessment, where he worked on national research and development priorities. Previously, from 1958 to 1972, he directed Columbia University's Institute for the Study of Science in Human Affairs and its predecessor, the Council for Atomic Age Studies. Wright will explore the general health of the national and international scientific and technological enterprise, with particular emphasis on policies and programs affecting science institutions. He will also examine the extent to which scientific knowledge shapes public policy, especially in the earth sciences.

Two other appointments deserve special mention. Mrs. Susan Vasquez was appointed Assistant to the President in midsummer 1978, and Mr. Montgomery S. Bradley has returned to the Institution as Special Assistant for the Corporate Sponsors Program.

The following honors were awarded to Staff Members during the year:

Hatten S. Yoder, Jr., Director of the Geophysical Laboratory, was elected to the American Philosophical Society in April. On May 9, he was

elected a Fellow of the American Academy of Arts and Sciences. Later that month, he received the Wollaston Medal, the senior award of the Geological Society of London. Former members of the Laboratory who have received the medal are A. L. Day, N. L. Bowen, and C. E. Tilley.

Olle Björkman of the Department of Plant Biology was elected to the National Academy of Sciences on April 24, 1979. Election signifies "distinguished and continuing contribution in original research." Björkman has worked many years studying the mechanisms of photosynthesis, primarily in studies of how plants adapt to stressful environments.

Maarten Schmidt, Director of Hale Observatories, was appointed a Knight in the Order of the Netherlands Lion by Queen Juliana of the Netherlands. The Order is the highest civil award of the Netherlands. The American Astronomical Society awarded Dr. Schmidt the Russell Lectureship, the most prestigious award of the Society.

An asteroid was named for George Wetherill, Director of the Department of Terrestrial Magnetism, in July. Noted for his work on isotopic age determination, meteorites, and the origin of the terrestrial planets, Wetherill has been a leading student of the dynamical evolution of orbits of meteorites and planet-crossing asteroids.

Charles T. Kowal of the Hale Observatories received the James Craig Watson Award from the National Academy of Sciences in April. Mr. Kowal was honored for his discovery of Chiron, a new asteroid-like object in the solar system.

James A. Rose of the Hale Observatories received the Dirk Brouwer Prize for a contribution of unusual merit to astronomy from the President and Fellows of Yale University in March.

Peter M. Bell of the Geophysical Laboratory was awarded the Apollo Principal Investigator's Award from NASA in June.

George W. Corner, Director Emeritus of the Department of Embryology, received the Henry Gray Award for 1979 from the American Association of Anatomists. The award recognized "sustained and meritorious service to the entire scientific community through scholarly accomplishments in original investigations, teaching, and writing in the field of anatomy."

Barbara McClintock, Distinguished Service Member of the Institution at Cold Spring Harbor, New York, received the Louis and Bert Freedman Foundation Award for Research in Biochemistry at the New York Academy of Sciences' 161st meeting in December 1978. Dr. McClintock was cited for her imaginative and original research on the complex mechanisms involved in the transfer and expression of genetic information. She received honorary Doctor of Science degrees from Harvard and Rockefeller Universities in June 1979.

Vera Rubin of the Department of Terrestrial Magnetism received an



honorary Doctor of Science degree from Creighton University for her achievements in astronomy, and James D. Ebert received the honorary degree Doctor of Laws from Moravian College in June. Ebert was reelected to a second term of membership in the Institute of Medicine.

*James D. Ebert*

## FACULTY, FELLOWS, AND STUDENTS

1978-1979

## DEPARTMENT OF EMBRYOLOGY

Baltimore, Maryland

*Director*

Donald D. Brown

*Staff Members*

Douglas M. Fambrough

Nina V. Fedoroff

Kenneth J. Muller

Richard E. Pagano

Ronald H. Reeder

Yoshiaki Suzuki

Samuel Ward

*Staff Associate*

Patricia Gearhart

*Senior Fellows*

B. E. H. Maden

Carlo M. Croce

*Fellows*

Saoko Atsumi

Ellen Bayne

Edward H. Birkenmeier

Daniel Bogenhagen

Peter Botchan

Salvatore T. Carbonetto

Ellen Elliott

Laurence J. Korn

Steven McKnight

Yasumi Ohshima

Ronald Peterson

Thomas Roberts

Richard Rotundo

Alex Sandra

Alan Schroit

Sheryl Scott

Barbara Sollner-Webb

Douglas Struck

Masaaki Tsuda

Yoshihide Tsujimoto

Harvey Wahn

Eric Wakshull

*Students*

Yair Argon

John M. Gardner

Elizabeth Gavis

Robert Hipskind

Gregory A. Nelson

Shigeru Sakonju

## GEOPHYSICAL LABORATORY

Washington, D.C.

*Director*

Hatten S. Yoder, Jr.

*Emeritus*

Gordon L. Davis

Elburt F. Osborn

Emanuel G. Zies

*Staff Members*

Peter M. Bell

Francis R. Boyd, Jr.

Felix Chayes

John R. Brady

Larry W. Finger

John D. Frantz

P. Edgar Hare

Robert M. Hazen

Thomas C. Hoering

T. Neil Irvine

Ikuo Kushiro

Ho-Kwang Mao

Robert H. McCallister

Tsutomu Murase

Bjørn Mysen

Douglas Rumble III

Friedrich A. Seifert

David Virgo

*Research Associates*

Robert K. Popp

Bruno A. Simons

Takehiko Yagi



*Fellows*

Nabil Z. Boctor  
 Marilyn L. F. Estep  
 Anthony A. Finnerty  
 Hiroyuki Fukuyama  
 Wendy J. Harrison  
 James D. Hoover  
 Richard H. Kingsley  
 Charles A. Lawson  
 Joseph F. Mammone  
 Shirley A. Rawson  
 Shiv K. Sharma  
 Frank S. Spear  
 Eiichi Takahashi  
 Richard F. Wendlandt

*Students*

Pamela R. Baur  
 Heather D. Boek  
 Julia A. Carey  
 Julia D. Pasteris  
 Noreen C. Tuross  
 Jonathan K. Powell

# HALE OBSERVATORIES

Pasadena, California

*Director*

Maarten Schmidt

*Staff Members*

Halton C. Arp  
 Horace W. Babcock  
 Judith G. Cohen  
 Jesse L. Greenstein  
 James E. Gunn  
 Robert F. Howard  
 Jerome A. Kristian  
 Robert B. Leighton  
 Gerry Neugebauer  
 J. Beverley Oke  
 S. Eric Persson  
 George W. Preston  
 Allan R. Sandage  
 Wallace L. W. Sargent  
 Leonard Searle  
 Stephen A. Sheckman

Arthur H. Vaughan  
 James A. Westphal  
 Harold Zirin

*Staff Associates*

Robert J. Brucato  
 Charles T. Kowal  
 Jean J. Lorre  
 Keith W. Matthews  
 B. Thomas Soifer  
 John T. Trauger  
 Michael W. Werner

*Senior Fellows*

Alan M. Dressler  
 Thomas R. Geballe  
 Ronald L. Moore  
 Robert J. Zinn

*Fellows*

Thomas B. Ake III  
 Peter L. Cottrell  
 Gary S. DaCosta  
 A. Ger de Bruyn  
 Richard F. Green  
 Frank P. Israel  
 Robert C. Kennicutt, Jr.  
 Barry J. LaBonte  
 Stefan Mochnecki  
 Jeremy R. Mould  
 Larry D. Petro  
 Michael Rich  
 James A. Rose  
 Anneila I. Sargent  
 Robert Schommer  
 Robert Shaw  
 Jack W. Sulentic  
 Peter L. Young

*Carnegie-Chilean Fellow*

Guido Garay

*Student Observers*

Graham Berriman  
 Kirk D. Borne  
 France A. Cordova  
 Boris Gokham  
 John G. Hoessel  
 Keith Horne  
 Stephen M. Kent  
 Matthew Malkan

Daniel Nadeau  
 Jeffrey R. Pier  
 Douglas M. Rabin  
 Abhijit Saha  
 Donald P. Schneider  
 William L. Sebok  
 Richard A. Wade  
 Howard K.-C. Yee

DEPARTMENT OF PLANT  
 BIOLOGY  
 Stanford, California

*Director*

Winslow R. Briggs

*Director Emeritus*

C. Stacy French

*Emeritus*

William M. Hiesey

*Staff Members*

Joseph A. Berry  
 Olle Björkman  
 Jeanette S. Brown  
 David C. Fork  
 Malcolm A. Nobs  
 William F. Thompson

*Research Associate*

Michael G. Murray

*Senior Fellows*

W. J. S. Downton  
 Mary Helen Goldsmith  
 John L. Hess  
 Jacob Levitt  
 Shmuel Malkin  
 Peter H. Quail  
 John K. Raison

*Fellows*

Paul A. Armond  
 Murray R. Badger  
 Roland Caubergs  
 Geoffrey Harvey  
 Richard A. Jorgensen

Anastasios Melis  
 Carl S. Pike  
 Gijsbert van Ginkel

*Students*

Heather S. Belford  
 Michael R. Blatt  
 G. James Collatz  
 Richard Cuellar  
 Holly Gorton  
 Dina F. Mandoli  
 Jeffrey Palmer  
 Richard Preisler  
 Jeffrey R. Seemann  
 William Williams

DEPARTMENT OF  
 TERRESTRIAL MAGNETISM  
 Washington, D.C.

*Director*

George W. Wetherill

*Distinguished Service Member*

Merle A. Tuve

*Emeritus*

Scott E. Forbush  
 Richard B. Roberts

*Staff Members*

L. Thomas Aldrich  
 George E. Assousa  
 Louis Brown  
 W. Kent Ford, Jr.  
 Albrecht W. Hofmann  
 David E. James  
 Alan T. Linde  
 R. Sundar Rajan  
 Vera C. Rubin  
 I. Selwyn Sacks  
 Fouad Tera  
 Norbert Thonnard  
 Kenneth C. Turner

*Research Associates*

Albert Jambon  
 Leonidas Ocala



Rambabu P. Ranganayaki  
Frederick J. Ryerson

*Visiting Investigators*

Akira Hasegawa  
Douglas G. Mose  
George R. Tilton

*Senior Fellow*

Edward R. D. Scott

*Fellows*

David Burstein  
Bruce W. Carney

Lina María Echeverría  
John R. Evans  
W. Daniel Heinze  
William Herbst  
Brajesh K. Kothari  
Felix J. Lockman  
Richard A. Lux  
Douglas O. ReVelle  
William M. White  
David J. Whitford

*Student*

Marie-France Bugnon





# *Reports of Departments and Special Studies*

Department of Embryology

Department of Plant Biology

Developmental Biology Research Group

Department of Terrestrial Magnetism

Geophysical Laboratory

Hale Observatories





# *Department of Embryology*

*Baltimore, Maryland*

Donald D. Brown

*Director*



Department of Embryology staff, June 1979. *Bottom row, left to right:* Yair Argon, Ellen Bayne, Jeffrey Mauvais, Thomas Roberts, Allan Schroit, Ginny Selby, Susan Satchell, John Pazdernik, Barbara Sollner-Webb, Eddie Jordan. *Second row:* Richard Grill, Gregory Nelson, Richard Rontundo, Eric Wakshull, Ellen Elliott, Eileen Hogan, Betty Phebus, Patricia Gearhart, Sheryl Scott, Shigeru Sakonju, Thomas Malooly, Kenneth Muller. *Third row:* Nina Fedoroff, Clint Miller, John Jones, John Wiser, Sam Ward, Richard Pagano, Donald Brown, William Duncan, Barbara Thomas, Thomas Miller, Edward Birkenmeier, Ronald Peterson, Steven McKnight, Daniel Bogenhagen, Alice Mabin, Carlo Croce.



# Contents

Introduction . . . . .	7
Interactions between Nerve Cells and Their Synaptic Targets . . . . .	9
Regeneration in the absence of the target neuron . . . . .	12
A contact inhibition between nerve cell axons? . . . . .	13
The distribution of synapses between neurons can modulate synaptic transmission . . . . .	16
Branch-point failure modulates synaptic transmission from touch sensory neurons to S-cells . . . . .	16
An interneuron mediates the direct electrical connection between touch sensory neurons and the S-cells . . . . .	19
Activation of a portion of the synapses between a sensory and a motor neuron . . . . .	19
Role of glia in nerve regeneration . . . . .	20
The development of skin innervation patterns in the chick . . . . .	20
Studies on Nerve and Muscle Membranes . . . . .	21
Construction of continuous cell lines secreting monoclonal antibodies . . . . .	22
Chick embryo muscle acetylcholinesterase . . . . .	27
Properties of cell surface AChE . . . . .	27
Synthesis of cell surface AChE . . . . .	28
Degradation of cell surface AChE . . . . .	29
Purification of AChE . . . . .	30
Organization, Dynamics, and Metabolism of Cell Surface Phospholipids . . . . .	31
Formation of asymmetric phospholipid vesicles . . . . .	32
Incorporation of fluorescent phospholipids into intact cells by vesicle-cell fusion and vesicle-cell lipid exchange . . . . .	33
Lipid capping in lymphocytes . . . . .	37
The distribution of Tnp-DOPE at the cell surface . . . . .	40
Genetic Dissection of Cell Morphology . . . . .	43
Nematode sperm motility . . . . .	44
The acquisition of sperm asymmetry . . . . .	48
Sperm lectin receptors . . . . .	49
Expression of Antibody Variable and Constant Regions during B-Cell Differentiation . . . . .	52
The dynamics of C <sub>H</sub> expression during intraclonal differentiation . . . . .	53
Correlation of membrane C <sub>H</sub> class to secreted C <sub>H</sub> class . . . . .	54
Diversity of V regions of antibodies to phosphorylcholine . . . . .	55
A V <sub>H</sub> region is shared by IgM and IgA . . . . .	56
Introduction of Isolated DNA Sequences . . . . .	56
Controlling Elements in Maize . . . . .	61

<i>Xenopus</i> Ribosomal DNA . . . . .	65
Methylation of <i>X. laevis</i> rDNA . . . . .	65
The 5.8S-28S gap . . . . .	65
Methylation map of rRNA . . . . .	66
Atypical properties of Region IV . . . . .	66
Nucleotide sequence of regions of the <i>Xenopus laevis</i> ribosomal DNA . . . . .	67
Transcription initiation region . . . . .	67
Nontranscribed spacer . . . . .	69
Transcription termination region . . . . .	69
Formamide sequencing gels . . . . .	71
 The Dual 5S RNA Gene System in <i>Xenopus</i> . . . . .	 71
The characteristics and sequences of <i>X. laevis</i> trace oocyte 5S DNA and <i>X. laevis</i> somatic 5S DNA . . . . .	 72
Organization of the <i>Xenopus borealis</i> oocyte-specific 5S RNA gene family . . . . .	75
In vitro genetics of 5S DNA . . . . .	75
Deletions of the 5' end of the gene . . . . .	75
Deletions of the 3' end of the gene . . . . .	78
The preparation and transcription of 5S RNA "maxi-genes" . . . . .	80
A termination mutant of 5S DNA . . . . .	81
Identification of factors required for accurate transcription of 5S RNA genes . . . . .	81
Transcription initiation in extracts of nuclei from <i>Xenopus</i> oocytes . . . . .	82
 Structural and Functional Studies of the Fibroin Gene . . . . .	 84
Structural analysis of the fibroin gene . . . . .	86
Precise localization of the 5' and 3' coding-intervening junctions . . . . .	86
Characteristics of the intervening sequence in the fibroin gene . . . . .	86
RNA-RNA splicing and sequences at the coding-intervening junctions . . . . .	89
Determination of the cap locus of the fibroin gene . . . . .	89
The 5' flanking sequence . . . . .	91
A presumed initiation site of the fibroin gene transcription . . . . .	92
Initiation of fibroin gene transcription by purified RNA polymerase II from wheat germ . . . . .	 96
 The Collection of Human Embryos . . . . .	 101
Developmental stages in human embryos . . . . .	101
Development of the nervous system . . . . .	101
Development of the cardiovascular system . . . . .	102
Visitors . . . . .	102
 Staff Activities . . . . .	 102
 Bibliography . . . . .	 103
 Personnel . . . . .	 106



## INTRODUCTION

In one form or another the research projects of this Department deal with "specificity." Nerves can grow to their target organs; molecules are assembled in exact locations within cells. There is specificity in the shape and movement of cells and in the interaction of cells. Specificity is studied in the expression of genes whose products determine the identity of cells, tissues, and whole organisms. Understanding the molecular and cellular meaning of specificity in biological systems unites the various research projects in this Department and provides our common goal.

Kenneth Muller and his colleagues study nerves in the leech because the properties of single nerve cells with known connections can be analyzed more easily than those of complex nerve bundles of vertebrates. Regeneration of a single leech nerve cell can be observed over a period of months. It is possible to manipulate the cell and record the effects on regeneration. Thus, Muller's group seeks to learn the importance of target cells and glia on the specificity of nerve growth and on the formation and maintenance of synaptic connections.

Fambrough and his associates have developed methods to measure rates of synthesis and degradation of specific surface proteins. These methods were first applied to the acetylcholine receptor because a protein,  $\alpha$ -bungarotoxin, interacts tightly and specifically with the receptor. These kinds of measurements were difficult to extend to other cell surface proteins because of the lack of specific probes. A new method devised by C. Milstein at the MRC Unit in Cambridge makes it feasible to obtain cells in culture that produce single monoclonal antibodies. These cells are called hybridomas, and Fambrough and his associates have produced hybridoma cell lines that are producing antibodies to surface proteins.

R. Rotundo has extended his studies

with the important enzyme acetylcholinesterase. This enzyme can be secreted by cells or incorporated into their surface membranes. In the latter case it behaves as an integral membrane protein. The half-life of this enzyme localized in membranes is three times longer than that of the acetylcholine receptor—evidence that individual surface proteins can be metabolized independently.

R. Pagano and his colleagues have developed methods for tagging lipids in various ways and introducing them specifically into the inner or outer leaflet of plasma membranes. A. Schroit has demonstrated that lipids in the outer leaflet can be capped. This observation bears on current hypotheses about the fluidity of lipids in plasma membranes and the possibility of a directional flow of molecules in the surface of a cell. Using these methods, D. Struck has found that the rate of exchange of lipids in the external leaflet of the plasmid membrane with the interior of the cell is very slow, while that in the internal leaflet is rapid.

In order to explore the specificity of surface interaction when sperm fertilize eggs, S. Ward and his associates have collected mutants of the nematode *C. elegans* that affect the fertility of sperm. G. Nelson has advanced the technology of sperm "culture" by discovering a means to induce sperm motility in vitro with the ionophore monesin. Since active sperm are motile, this brings them a step closer to fertilization in vitro, which is not now possible in *C. elegans*. The various mutants have characteristic and in some cases aberrant responses to the ionophores. Morphological asymmetry of sperm is reflected in changes in surface and internal components. Y. Argon has found that surface glycoproteins are redistributed in motile sperm. This is another descriptive tool with which to assay the mutant collection in the search for their underlying defects.

There have been important advances in the past year in the detailed analysis of several multigene families encoding 5S ribosomal RNA. R. Peterson has completed the characterization of two of these gene families—there are now five that have been cloned by the recombinant DNA methodology and sequenced completely. There are striking differences between the spacer regions of somatic and oocyte-type gene families, the former being AT-rich, the latter GC-rich. Beginning manipulation of one of these genes has demonstrated the remarkable finding that RNA polymerase probably binds to a DNA region of about 30–40 nucleotides within the gene itself. This finding suggests an enzymatic mechanism for RNA polymerase recognition of a gene, a mechanism very different from that of *E. coli* RNA polymerase and prokaryotic genes.

Two new projects are discussed in this Report. P. Gearhart, a Staff Associate, is a cellular immunologist interested in the repertoire of antibodies that can be elicited by a single antigen. In addition she is investigating how many immunoglobulin genes are expressed by a single cell.

S. McKnight, a Postdoctoral Fellow, and C. Croce, a Visiting Investigator from the Wistar Institute, are transforming animal cells with purified DNA. This powerful new technique was developed at Columbia University by R. Axel and his colleagues. A useful selectable marker is the gene for thymidine kinase. It can be obtained in large quantities from herpes simplex virus. By joining this gene to a bacterial plasmid a “double-headed” vector is obtained that in theory can be grown either in bacteria or in animal cells. Any other DNA fragment can be ligated to this vector and then introduced into an animal cell that lacks the thymidine kinase gene.

The departures of two Staff Members this year reflects continuing change in the Department. The Director is the only member remaining from a closely inter-

acting group of four Staff Members who for more than ten years applied nucleic acid chemistry to isolated genes. Igor Dawid went to the National Cancer Institute in May 1978. In the fall of 1978 Ronald Reeder joined the faculty of the Hutchinson Cancer Research Institute in Seattle, Washington, and Yoshiaki Suzuki returned to Japan as a senior faculty member in the new National Institute for Basic Biology in Okazaki.

Ronald Reeder came to this Department as a postdoctoral student in July 1967, and was appointed to the staff in July 1969. He collaborated on some of the early studies on purified ribosomal DNA of *Xenopus*. When restriction enzyme methodology became available, he carried out detailed analyses on the structure of this DNA. These studies elucidated the nature of length heterogeneity between repeating units of ribosomal DNA by showing that spacer regions contain simple sequences. Because ribosomal RNA genes (rDNA) are amplified in oocytes, they can be purified in their chromatin state. This enabled Reeder and his colleagues to begin characterization of the proteins associated with this DNA. Additional molecular detail of rDNA is described in this Report. B. Sollner-Webb has localized and sequenced both the initiation and termination sites for rRNA synthesis. This makes possible studies on the developmental control of rRNA transcription.

In studies that have in many ways paralleled the investigations on ribosomal RNA genes, Yoshiaki Suzuki has studied the highly specialized structural gene for silk fibroin in *Bombyx mori*. His research, carried out in this Department over the past ten years, first resulted in the isolation and characterization of the silk fibroin messenger RNA reported in 1972. Using the messenger RNA, he was able to show that cells of *B. mori* have a single copy of the gene for this protein. In the last few years, Suzuki and his colleagues have cloned the



silk fibroin gene by the recombinant DNA methodology and carried out detailed molecular characterization.

In their final report, Suzuki and his colleagues once again demonstrate the amazing power of the new molecular methods for analyzing genes and gene products. They have determined the start sites for fibroin gene transcription, a remarkable feat considering that the gene is 16,000 nucleotides in size. The DNA sequence flanking the site of transcription initiation as well as the 5' end of the gene including the entire intervening sequence, has been completed. In addition, they have developed an assay system that can detect accurate initiation events when they occur. Using these methods they have begun to study the developmental control of fibroin gene expression.

The departures of Dawid, Reeder, and Suzuki represent for this Department the end of an era, one in which some of the earliest studies on purified eukaryotic genes of known function were carried out.

Two of these three positions have been filled. Nina Fedoroff joined the staff on July 1, 1978, and her first report is included here. She describes her plans for analyzing controlling elements in maize. Her challenge will be to translate deductions made previously by cytogeneticists into molecular terms. The genetic systems used by Barbara McClintock to discover and describe controlling elements resulted in visible changes in the plant. The biochemical functions of these

genes were not well understood. With the help of Dr. McClintock, Fedoroff hopes to produce strains of maize in which controlling elements regulate genes that are easier to study using biochemical methods.

Allan Spradling, currently a postdoctoral fellow of the Helen Hay Whitney Foundation in the Department of Biology at Indiana University, will join the Department by January 1980. Spradling studies the genes in *Drosophila* responsible for the egg shell proteins. This group of genes is only expressed in one cell type, and the proteins are synthesized according to a specific developmental timetable. Mutants have already been described that affect these proteins. Spradling's ability to do genetics of both the traditional and molecular kinds lends exceptional promise to this work.

One of our most able and dedicated employees, John Wiser, retired from the Department this summer after 22 years of service. He has designed and fabricated specialized equipment to meet the most fastidious detail that highly critical scientists can devise. His great pride and skill in his work has rewarded and inspired us all.

Grants from the National Institutes of Health supported in part the research programs of Brown, Gearhart, Muller, Pagano, Reeder, Suzuki, and Ward. Fambrough's research has benefited from a grant by the Muscular Dystrophy Association.

*Donald D. Brown*

## INTERACTIONS BETWEEN NERVE CELLS AND THEIR SYNAPTIC TARGETS

*K. J. Muller, E. J. Elliott, S. A. Scott, and B. E. Thomas*

During development the nervous system is wired together by the selective growth of its constituent nerve cells, or neurons. The survival of axonal lines of communication and sometimes of neu-

rons themselves depends in large measure on the ability of the growing axons to connect with suitable targets. Even in the brains of adult vertebrates it is possible for some neurons whose axons have been

severed to regenerate those axons to again form functional synapses, the links that carry nerve impulse information from cell to cell. Most studies of axon growth and regeneration in nervous systems have dealt with populations of neurons. This has made it difficult to determine whether regenerating neurons connect with the same targets they had contacted previously and whether targets play a role in directing axon growth toward them.

In order to tackle problems of growth and regeneration at the level of single neurons, we have turned to the relatively simple nervous system of a segmented worm, the medicinal leech. Although it has perhaps one millionth the number of neurons we do, the leech still contains more than 10,000 nerve cells, each contacting a highly select population of targets. Signaling in the leech nervous system operates on the same principles found in higher nervous systems. For example, information is passed from cell to cell by electrical synapses, which carry currents directly from one neuron to the next, and by chemical synapses, where transmitter molecules released by one cell diffuse a short distance to the next cell to activate receptor molecules in its membrane. Physical properties of the neurons, such as their size and shape, make it possible to identify the same nerve cell from one leech to the next. The distinctive functions and synaptic connections of many cells have been learned and are remarkably consistent between animals. We now know that injured neurons can regenerate connections with their normal complement of target neurons, and that the regenerating axons reach their appropriate targets by selective growth along their original pathways (*Year Book 76*, *Year Book 77*). This degree of experimental resolution has not yet been possible in other systems.

The same system of neurons that has provided a detailed picture of regenera-

tion now permits us to examine the role of the synaptic target in both regeneration and maintenance of synaptic connections. We have confirmed the preliminary observation reported last year that a severed axon can regenerate to its normal site of synapse when its target has been destroyed. Because the axon both starts and stops growing just as it would in the presence of the target, we conclude that the presence of the target is not necessary for accurate regeneration. During normal regeneration there is a high degree of specificity, and this precision is not relaxed when the target is destroyed. The neurons we have studied do not make aberrant synapses.

Although an intact cell in the adult shows no measurable response to the loss of its target, we have made the surprising discovery that injury to the cell will prompt an entirely intact axon to grow toward the missing target. Because this phenomenon, known as sprouting, does not occur when the axon is in contact with the target, the target cell must normally provide a contact inhibition of axon growth.

Identified sensory neurons in the leech were used in the first demonstration that single neurons could reconnect with their original synaptic targets. Although under many conditions the neuron is the unit of function in the nervous system, it is becoming increasingly clear that different parts of a single neuron can and often do act independently of one another. This suggests that if during regeneration two neurons manage to synapse with each other but do not establish the original distribution of contacts between them, full function might not be restored. We have begun to examine how a sensory neuron's shape and the distribution of its branches affect the normal flow of electrical information at its many synapses. The characteristic patterns that we have measured both physiologically and morphologically provide a baseline to study whether the specificity



of regenerating connections that occurs between single cells can be traced to the subcellular level.

Other work in the laboratory has focused on neuroglial cells, which constitute half the volume of the nervous sys-

tem and envelop neurons, and on the role of neuroglia in nerve regeneration. In addition, work has begun on the formation of connections by developing sensory neurons in the hind limb of the chick.

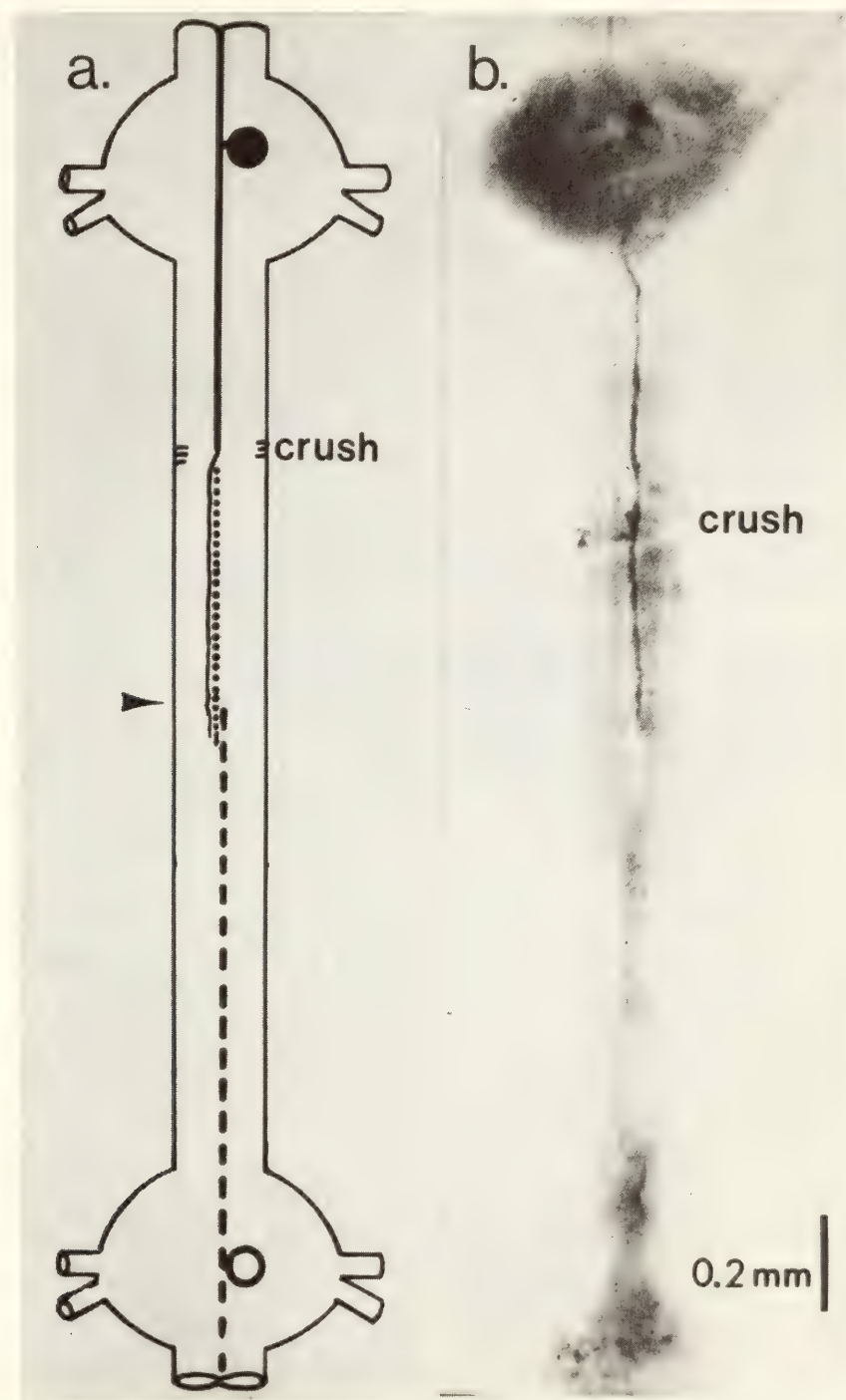


Fig. 1. (a) Regenerating neuron in the ganglion at the top (anterior) in one month grows across the crush, along its severed distal stump (dotted line), and stops at the original synaptic region in the connective midpoint even when the target neuron (dashed line and open circle) has been selectively destroyed. (b) The regenerating neuron has been marked with intracellular injection of horseradish peroxidase 45 days after its axon was severed (*crush*) and the posterior S-cell (in lower ganglion) killed by intracellular injection of protease. Further growth is not seen. Arrowhead in (a) indicates location of cross sections in Fig. 2.

## REGENERATION IN THE ABSENCE OF THE TARGET NEURON

*K. J. Muller, S. A. Scott, and B. E. Thomas*

Our understanding of the details of regeneration has gained much from studies on one particular neuron, the S-cell. The nervous system of the leech is a chain of 21 nearly identical segmental ganglia, or neuron clusters, distributed along the length of the animal, and larger fused ganglia at the head and tail. There is one S-cell in each segmental ganglion, and it extends an axon halfway to the next ganglion anteriorly and posteriorly along the connective axon bundles to make an electrical synapse with the next S-cell (Fig. 1). Because the S-cell axon is the largest in the connective and occupies a distinctive position in Faivre's nerve, the unpaired median bundle of about a hundred axons, the S-cell's axon can be readily distinguished in either the light or the electron microscope. S-cells studied with microelectrodes can be selectively stained if they are injected with the marker horseradish peroxidase (HRP). With these techniques we have previously shown that when the S-cell axon is severed by crushing or cutting the connective, the axon sprouts fine processes at the crush and shrinks in caliber. The portion of the axon that is cut away from the rest of the cell, the severed distal stump, survives for weeks and continues to be capable of signaling to the next S-cell across the original synapse. One or a few fine regenerating sprouts find the distal stump and grow along it to synapse with the next S-cell within a month of making the lesion. In about half the cases examined the regenerating neuron first synapses with its severed distal stump, thereby rapidly restoring the connection between S-cells before the two cells have had a chance to contact one another directly.

The electrical synapses between S-cells

have been demonstrated by passing currents between recording microelectrodes. We recently also used the dye Lucifer Yellow, which can cross between electrically coupled cells, to show the formation and presence of electrical synapses between S-cells. This technique has been especially useful in confirming that the adjacent S-cell is the only cell with which the regenerating neuron synapses, and that synapses are sometimes made upon its own severed distal stump.

We have been able selectively to remove single S-cells from the nervous system by destroying the cell with intracellular injection of a protease. All branches of the injected cell are destroyed, but other cells electrically coupled to it are apparently unaffected. Therefore, killing one S-cell does not cause the adjacent S-cell to either extend or retract its "unused" axon. But if this axon is severed, it will regenerate in a normal fashion even though it has no target. We have examined 21 preparations at times ranging from four days to six months after destroying one S-cell with protease injection and severing the S-cell axon that had been linked to it by crushing the connective (Fig. 1). The severed distal stump survives for up to two months and provides a pathway along which the injured S-cell regenerates. The regenerating axon is tipped with a growth cone (Fig. 2), which is filled with a characteristic smooth membranous reticulum that is universally found in the tips of growing axons. Using the growth cone as an index for when the regenerating axon stops growing (Fig. 2), we have not seen the axon regenerate beyond the severed distal stump or the normal region of synapse midway along the connective to the next ganglion. Intracellular injections of Lucifer Yellow dye show that just as during normal regeneration the growing axon sometimes synapses with its severed distal stump. However, the dye never passes into other axons in the connective, indicating that



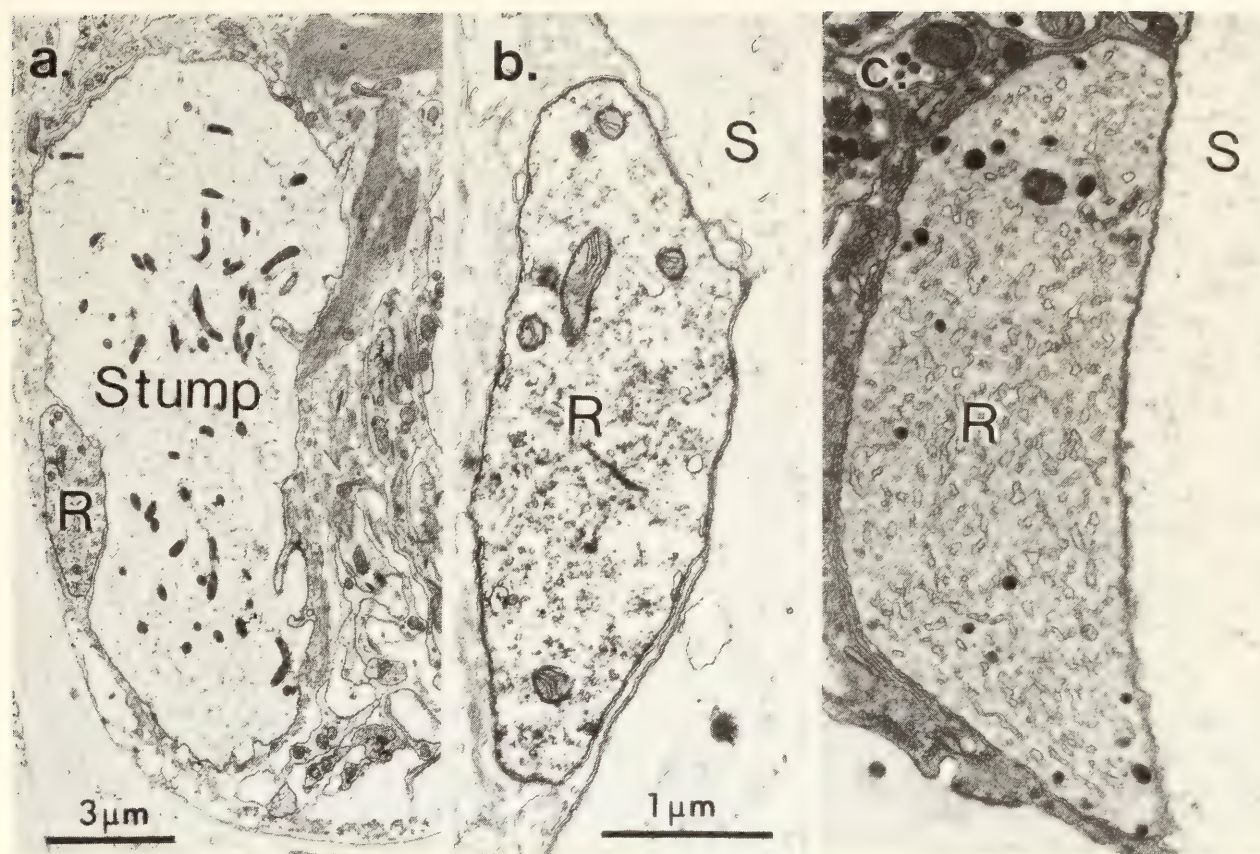


Fig. 2. (a) Six weeks after its target has been killed and its axon severed, the regenerating neuron (*R*) has grown to the normal region of synapse (arrowhead, Fig. 1a) near the end of its severed distal stump, where it has stopped. (b) Same section at higher magnification shows that in the axon tip (*R*) there is little of the smooth membranous reticulum found in growth cones at earlier times, such as that in (c), 24 days. *R*, tip of regenerating axon; *S*, severed distal stump. Same scale in (b) and (c).

when the S-axon fails to contact its normal synaptic target, it does not make similar synapses with alternative targets.

Although no other cell replaces the cell that is destroyed, it is possible to circumvent the missing neuron via normal pathways. Figure 3 shows that even in the absence of an S-cell, it is possible to activate the next S-cell along the chain of ganglia by using a sufficiently strong stimulus. The synaptic potential that gives rise to the nerve impulse shows that this activation is not direct; it is through preexisting pathways that can be demonstrated after acute injury to the S-cell.

Our finding that regenerating axons grow to the normal site of synapse but not beyond agrees with results of McMahan and co-workers on the neuromuscular junction in the frog, where end-

plate specializations of the basal lamina provide cues to regenerating motor neurons. While neurons in the central nervous system do not have a basal lamina, in the leech there is a persistent distal axon stump. Whether the stump or something else acts as a signpost to the growing axons remains to be determined, but the target S-cell is not essential.

#### A CONTACT INHIBITION BETWEEN NERVE CELL AXONS?

*K. J. Muller, S. A. Scott, and B. E. Thomas*

Normally during axonal regeneration in the leech, injury to one axon of a cell prompts only the injured axon to grow and restore its original connections. Other branches of the same cell which remain in synaptic contact with their targets are

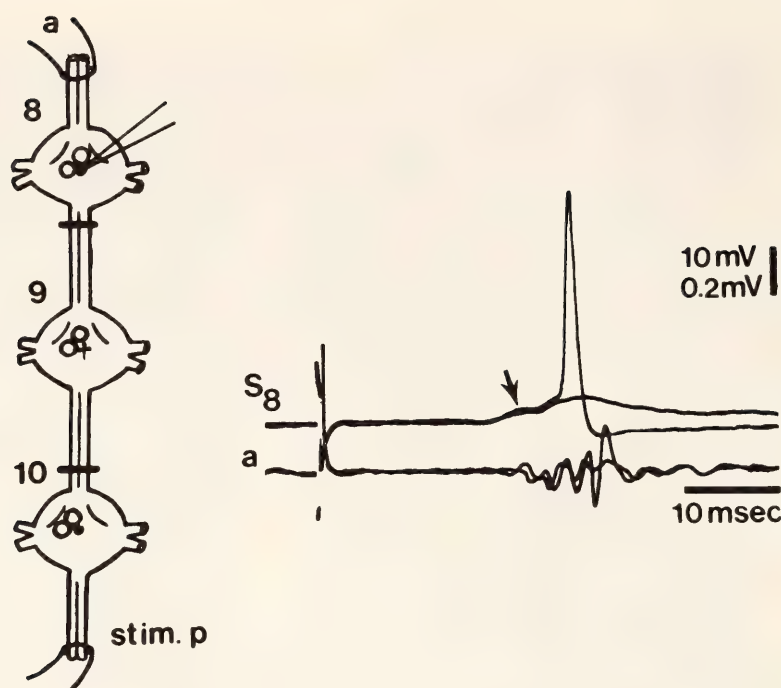


Fig. 3. Regeneration of pathways that allow activation of S-cells when one S-cell has been killed. A stimulus to the posterior (*stim p*) connective of ganglion 10, stronger than that required to activate  $S_{10}$ , activates neurons that have regenerated across crushes (bars) between ganglion 8 and 10. The stronger of two stimuli to these axons produces a large enough synaptic potential (arrow at  $S_8$ ) in the S-cell in ganglion 8 to generate nerve impulse. The impulse is then recorded with a suction electrode applied to the anterior connective (*a*); the recording at *a* shows that many axons are candidates for participants in this excitatory pathway.

apparently unaffected. We have discovered that an intact axon can under such conditions be made to grow by removing its target. This finding was unexpected because target removal is by itself not sufficient to cause growth.

For our experiments we have used S-cells, whose electrical synapses with adjacent S-cells and capacity for regeneration are well studied. In the 11 cells examined for periods of less than three weeks to several months, we found that the intact axon can be induced to sprout if its target is removed by protease injection and another, remote axon of the cell injured to encourage regeneration (Fig. 4). The sprouting axon grows along the pathway occupied by the destroyed cell's axon (Fig. 5) and can extend to twice its usual length, to the next ganglion. The same type of growth cone that we see in regenerating axons is seen in the sprouting axons (Fig. 4). Unlike normal re-

generation, however, the intact axon does not shrink in caliber, but the newly sprouted branch is as thin as regenerating branches are. Preliminary evidence indicates that the time course of sprouting is slightly delayed with respect to regeneration. Injections of Lucifer Yellow dye show that the sprouted axon does not form similar electrical junctions with other neurons in place of the lost input, nor does it contact the S-cell on the other side of the destroyed neuron. Control experiments indicate that neither a cessation of electrical input nor simple disconnection from the cell body of the next S-cell are sufficient to make an intact axon grow in an otherwise regenerating cell. Although some of the sprouted intact axons might in time retract their sprouts, we have seen fully extended axons later than three months.

There is some parallel between these findings and the properties of neurons in



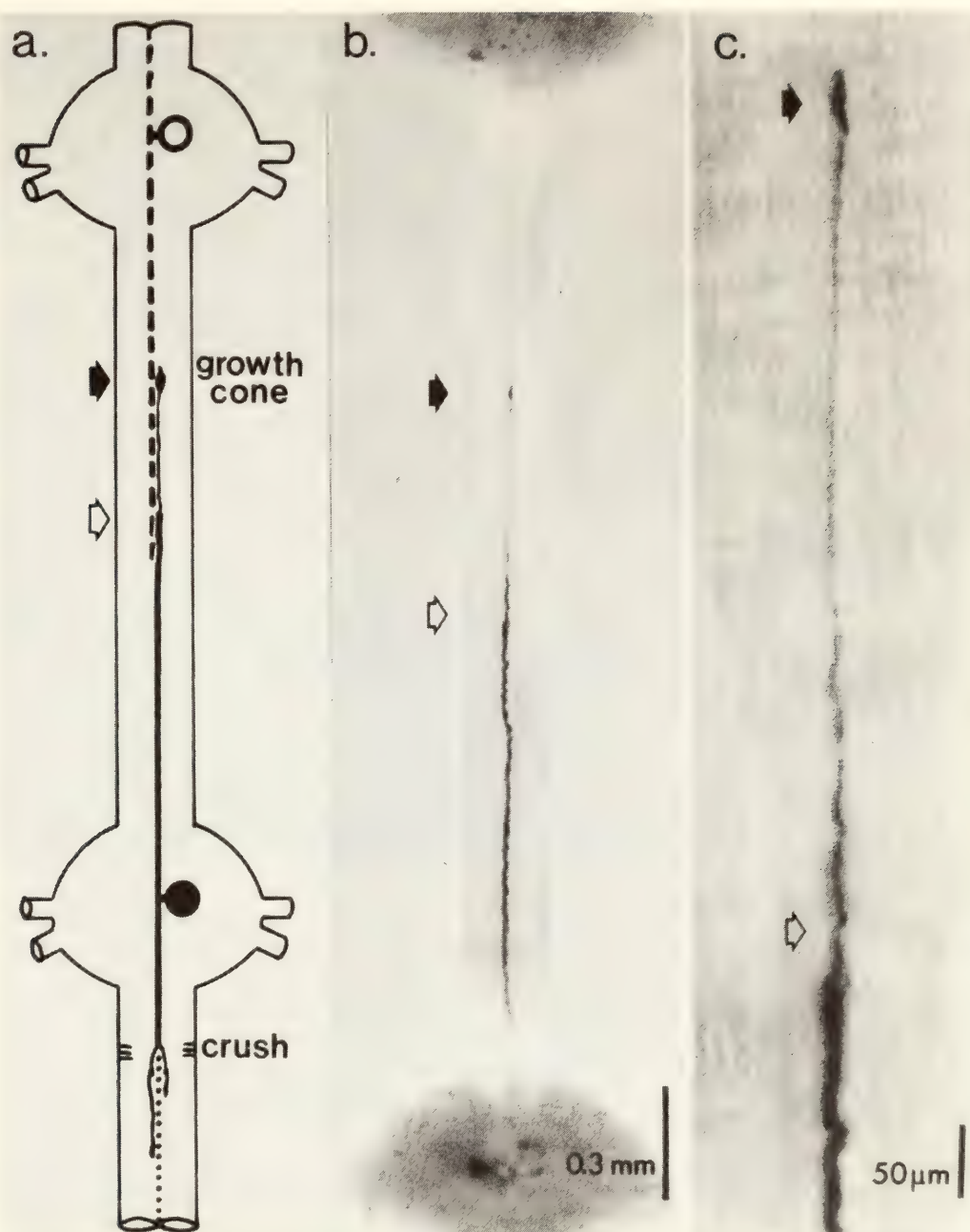


Fig. 4. An intact axon can be made to sprout when its synaptic contact is removed. (a) The neuron in the ganglion at top (anterior) was injected with protease, which destroyed the entire cell (dashed line and open circle). A distant axon of the adjacent S-cell was then severed by crushing the connective (*crush*). The injured axon regenerated normally along its severed distal stump (dotted line), and the intact axon that had been in contact with the killed cell at the connective midpoint (open arrow) grew along the connective toward the ganglion of the killed cell. (b) The sprouting neuron was marked by intracellular injection of horseradish peroxidase 25 days after its posterior axon (not visible) was severed. (c) The sprouted axon is seen at higher magnification, showing the enlarged growth cone (solid arrow). Because this tissue was not cleared, it could be observed later in the electron microscope.

developing nervous systems, a similarity that does not exist unless the adult neuron is primed to grow by injury somewhere on its arborization. Developing neurons in the brain that fail to contact

their normal targets often continue to grow until they find a suitable target, or failing that, they retract their axons and sometimes die. While sprouting S-cells have not been seen to make alternative



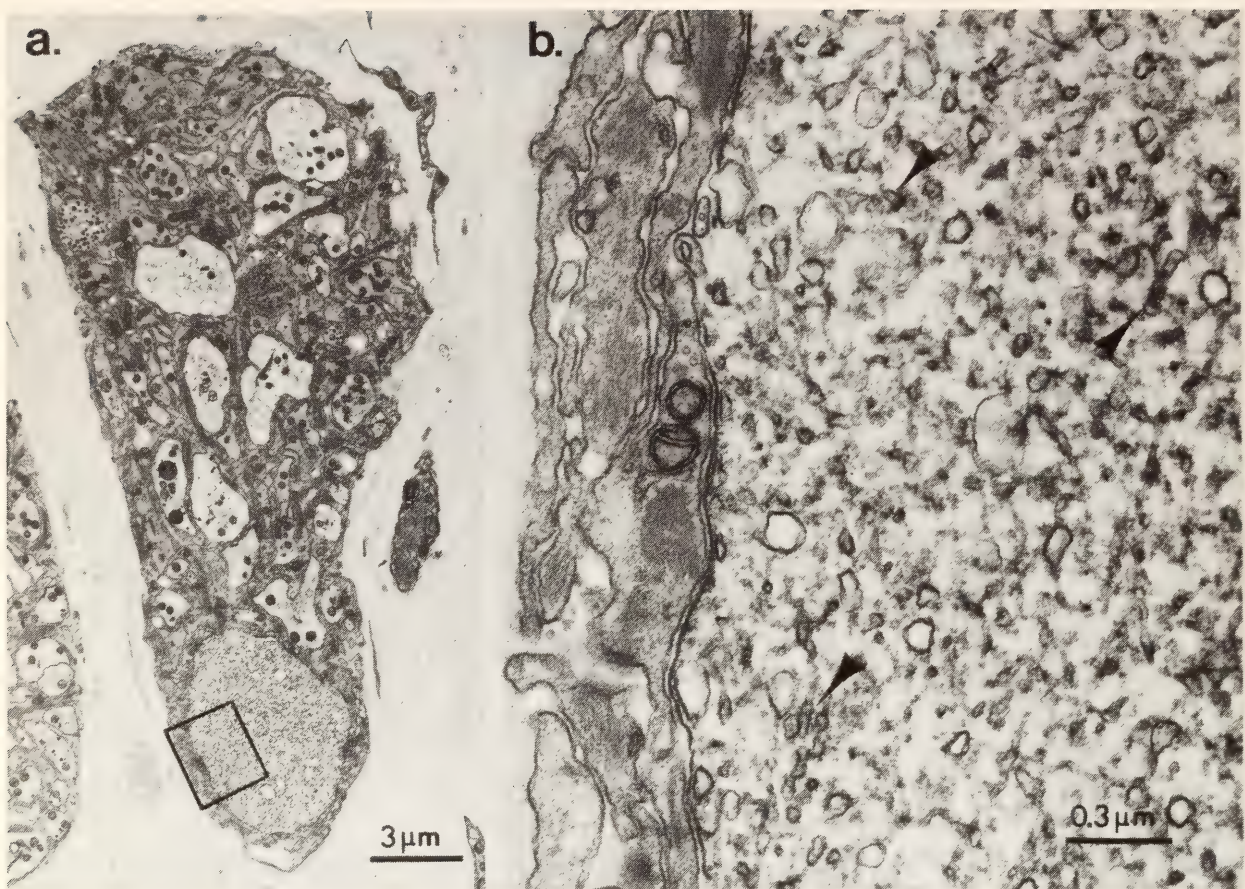


Fig. 5. The axon that sprouts in response to the loss of synaptic contact grows along the path of the destroyed cell. The sprouted neuron was marked by intracellular injection of horseradish peroxidase 38 days after the adjacent S-cell was killed. This cross section of Faivre's nerve was cut through the growth cone of the sprouted axon, which is located at the dorsal position in Faivre's nerve that had been occupied by the killed cell (a). The growth cone contains much smooth membranous reticulum characteristic of the tips of growing axons, as shown in (b), enlargement of boxed region of (a).

contacts or to retract, it may be that some percentage will exhibit the plastic properties that we have already described for S-cells that have long before lost contact with their targets (*Year Book 75*).

#### THE DISTRIBUTION OF SYNAPSES BETWEEN NEURONS CAN MODULATE SYNAPTIC TRANSMISSION

*K. J. Muller and S. A. Scott*

#### *Branch-point Failure Modulates Synaptic Transmission from Touch Sensory Neurons to S-cells*

Although a neuron's shape is widely held to be inextricably linked to its function, there are some aspects of the link

that have been suspected but not well demonstrated. A synaptic connection between two neurons generally appears to the neurophysiologist as a unitary electrical event, the postsynaptic potential, that is, the excitation of one cell produces a single response in another. Yet a look with the microscope at the number of possible sites of interaction between two cells can reveal that the physiologists' unitary event is in fact the sum of many local interactions. A single neuron may make many synapses upon another cell, and although these synapses may often act in concert, there are likely to be natural circumstances in which certain synapses of a cell are selectively activated.



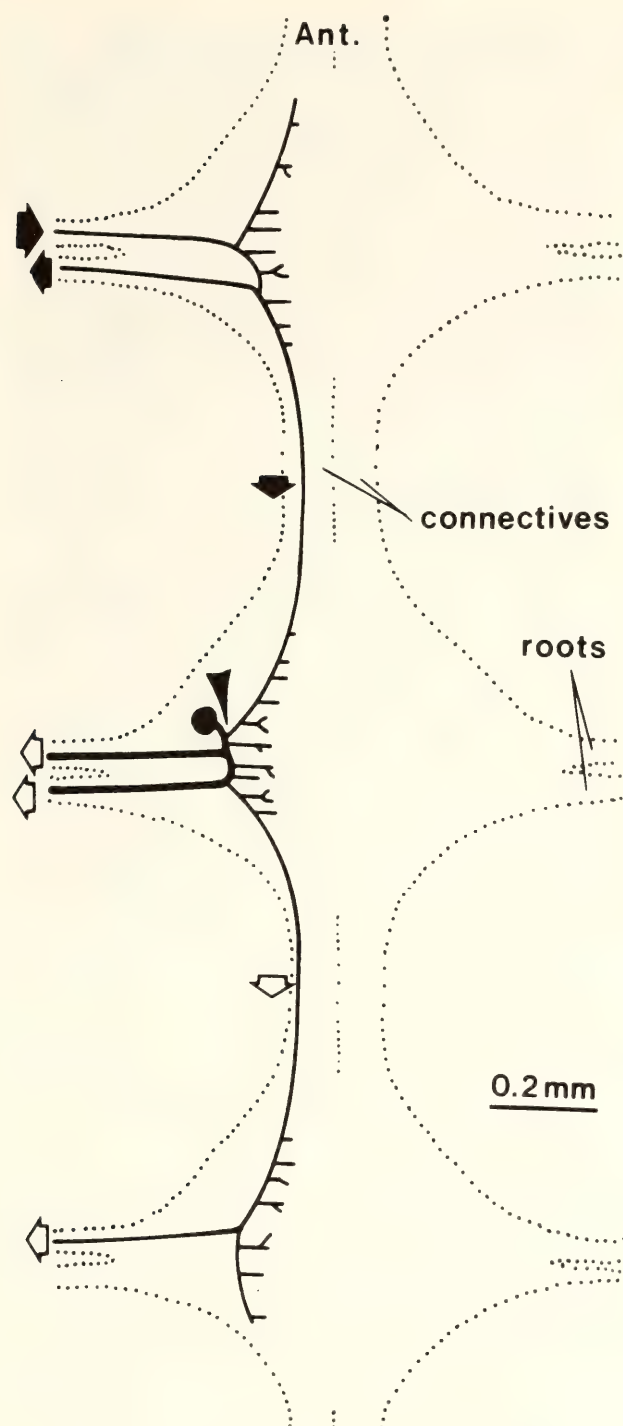


Fig. 6. Each touch sensory neuron arborizes in three ganglia and innervates skin through roots of its own and adjacent ganglia. In this schematic diagram, dots outline ganglia and connectives; the distance between ganglia is not drawn to scale and is typically 5 mm. Nerve impulses may enter the central nervous system along any axon, depending upon which portion of the receptive field is stimulated. When, for example, a patch of skin innervated through the most anterior root is stimulated, impulses propagate in the directions indicated by arrows. If the neuron becomes hyperpolarized, as may occur during a train of impulses, then impulses may be blocked at the

The touch sensory neurons in the leech are examples of such cells. Each touch cell innervates a characteristic patch of skin (its receptive field) with axons that travel to the periphery via axon bundles called roots, which not only leave the cell's own ganglion but also extend from the anterior and posterior adjacent ganglia (Fig. 6). A single impulse activated in a touch cell anywhere in its receptive field is ordinarily equally effective in reaching the cell's synaptic terminals. However, it has been shown by D. Van Essen and K.-W. Yau that after only a few impulses in the touch cell a sodium pump is activated. Activation of the pump changes the excitability of the cell so that impulses in small branches fail to invade large branches, but impulses can always travel from large branches to small. Such impulse failure at a branch-point can occur for impulses generated, for example, in the anterior portion of a touch cell's receptive field (Fig. 6). We would predict that impulses blocked at the branch-point would reach only a small portion of the cell's synaptic terminals. The branch-point in this case acts as a switch and effectively changes the size of the cell's receptive field.

To show that the switch affects synaptic integration in the nervous system and therefore has functional effects, we have examined the excitation of S-cells. The S-cell in turn activates L-motor neurons that shorten the animal. This chain of excitatory actions mediates reflex shortening of the leech. By recording simultaneously with microelectrodes placed in the cell bodies of a touch cell and an S-cell, we can show that activation of the touch cell tends to activate

branch-point where the thinner axon meets a thicker one (at arrowhead in the central ganglion). Open arrows indicate pathways that under such conditions cease conducting impulses from the anterior ganglion. Short secondary branches within each ganglion are locations of synaptic terminals.

the S-cell and that the postsynaptic potential produced is an electrical synaptic potential—that is, currents can spread directly from the touch cell to the S-cell. The synapse does not work in reverse, so S-cell impulses do not excite touch cells. Because the connection is electrical, conditions that normally reduce or block chemical synaptic transmission, such as bathing the preparation in solutions containing 15 mM magnesium ions, have no effect on the postsynaptic potential. To selectively stimulate touch cells, we touched the skin with an electromechanically driven stylus and, by simultaneously recording from the appropriate nerve root, confirmed that we were not activating other touch cells that might affect our recordings (Fig. 7). We found that when impulses fail at a branch-point, and therefore reach only some of the synaptic terminals of the touch cell, the synaptic potential in the

S-cell is correspondingly reduced. The localized action of the nerve impulse, even at electrical synapses, has been shown by control experiments. We can artificially block nerve impulses that enter the cell's own ganglion along the roots to prevent them from reaching any synaptic terminals by passing negative currents in the cell, and the blocked impulses produce no synaptic potential. Furthermore, experiments like those in Fig. 7b can demonstrate that the synaptic potential is generated exclusively by the touch cell from which we are recording. These experiments show, therefore, that branch-point failure modulates synaptic transmission under natural conditions. These results are important not only for what they tell us about mechanisms by which the nervous system handles information but also because they provide a finer test of the specificity with which cells regenerate connections.

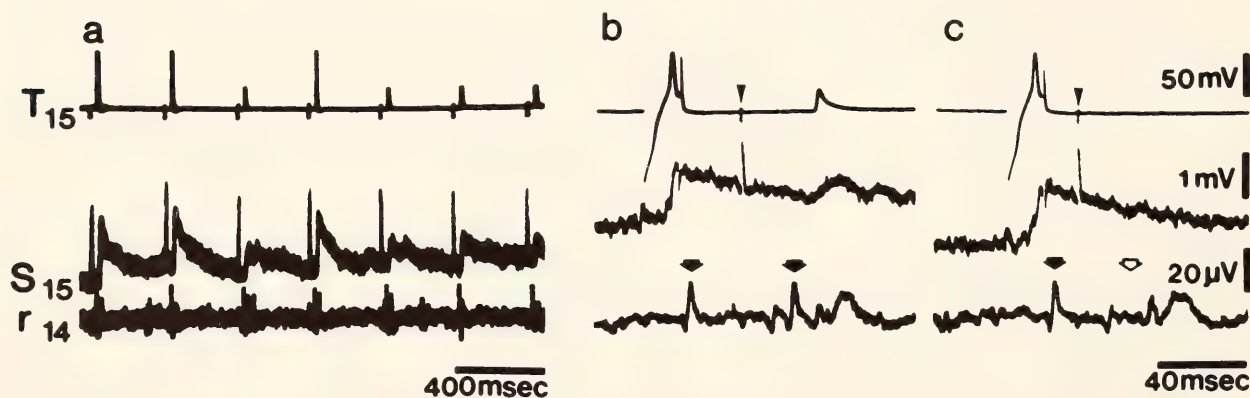


Fig. 7. The nerve impulses in a touch cell evoke smaller synaptic potentials in the S-cell when the touch cell impulses fail to propagate beyond central branch-points. (a) Oscilloscope recording depicts a train of impulses initiated in the lateral touch cell of ganglion 15 ( $T_{15}$ ) when the most anterior receptive field of the cell is stimulated. Impulses in the cell traverse the roots of ganglion 14 ( $r_{14}$ , also solid arrows in (b) and (c)) on their way to ganglion 15 (see also Fig. 6);  $T_{14}$  was not stimulated, since its large impulse is not recorded in  $r_{14}$ . The third, fifth, sixth, and seventh impulses in the train are reduced owing to branch-point failure, and the synaptic potentials they evoke in the S-cell ( $S_{15}$ ) are accordingly reduced. Stimulus artifacts precede the impulses by about 40 msec and appear as sharp vertical lines in  $T_{15}$  and  $S_{15}$ , (b) and (c). A collision between an impulse evoked in  $T_{15}$  with the recording microelectrode and the impulse evoked in the skin eliminates the synaptic potential produced by touching the skin and shows that the peripherally evoked synaptic potential is caused entirely by the lateral T-cell in ganglion 15. The arrowhead indicates the timing of the stimulus to the skin. If the stimulus is presented soon after the impulse is produced in the cell body, a collision results, preventing the nerve impulse from entering the root of ganglion 14 at open arrow in (c) and therefore from activating a synaptic potential. Ganglia bathed in 15 mM  $Mg^{++}$ .



*An Interneuron Mediates the  
Direct Electrical Connection between  
Touch Sensory Neurons and the S-cells*

Although currents can be made to pass from ventral and lateral touch sensory neurons to S-cells, the cells are not in direct contact with one another, as can be demonstrated by injecting them with the marker horseradish peroxidase, which completely fills each cell (Fig. 8a). The physiological link is a pair of interneurons that are electrically coupled to touch cells and S-cells. When the S-cell is injected with the fluorescent dye Lucifer Yellow, the pair of interneurons also fills with the dye (Fig. 8b). We have been able to record from and characterize the interneurons by fluorescence microscopy. When both interneurons are destroyed by intracellular injection of protease, the synaptic connection between touch cells and the S-cell is selectively broken, demonstrating conclu-

sively the role of the interneurons as an essential link in what by other criteria appears to be a monosynaptic connection. Because the synaptic inputs of the touch cells are distributed upon the interneuron, it would seem that the primary effects of branch-point failure in the touch cell are therefore on synaptic transmission to the interneuron, and that any modulation is then reflected to the S-cell.

*Activation of a Portion of the  
Synapses between a Sensory and a  
Motor Neuron*

In collaboration with Dr. Eduardo Macagno at Columbia University, we have been studying the distribution of chemical synapses between a pressure (P) sensory neuron and the longitudinal (L) motor neuron. The effects of branch-point failure, described above for touch sensory neurons, have been shown also

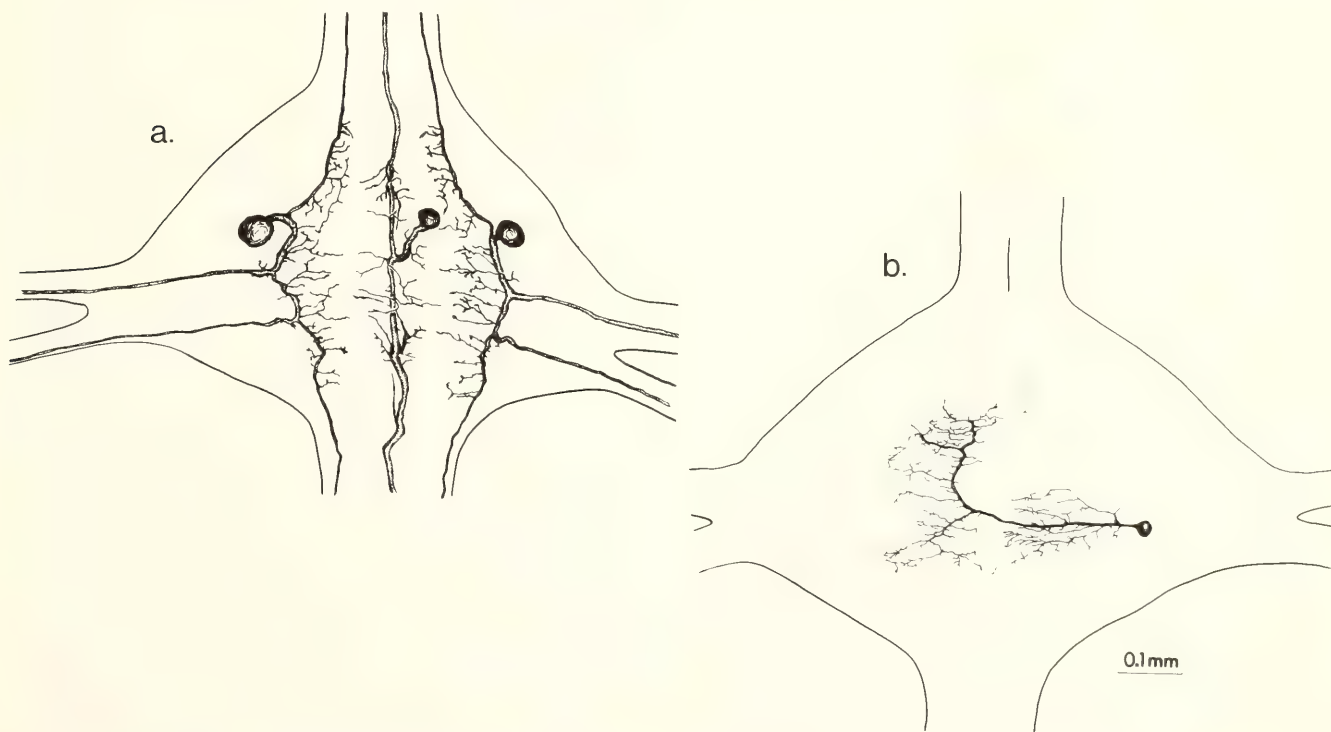


Fig. 8. The electrical connection between the touch sensory neurons and S-cell is mediated by an interneuron. (a) Two touch sensory cells and an S-cell were stained using intracellular injection of horseradish peroxidase, and their processes were traced with *camera lucida*. The cells do not touch one another and have a normal appearance. In this preparation the interneurons in (b) were killed the day before by intracellular injection of protease, which eliminated the electrical connection. In order to stain the interneuron in (b) it was first identified as a fluorescent cell body after the S-cell to which it is electrically coupled was injected with fluorescent dye Lucifer Yellow.

for pressure cells, with the advantage that the P-cell synapses are truly monosynaptic and (because they are chemical and have distinct specializations) can be easily seen in the electron microscope. The capacity of P-cells to regenerate synaptic connections with L-cells will also be useful in our analysis of the interactions between the cells. Our preliminary results are that the P-cell can be selectively activated by electrical stimulation of the skin. Impulses that fail at central branch-points activate a select group of synaptic terminals, resulting in a partial or in a nearly complete reduction of the excitatory postsynaptic potential in the L motor neuron, depending upon whether an anterior or a posterior receptive field is stimulated. These physiological findings are in agreement with the distribution of contacts between the P and L neurons and should provide a means for analyzing the extent of synapse regeneration.

#### ROLE OF GLIA IN NERVE REGENERATION

*E. J. Elliott and K. J. Muller*

Glia, the non-neuronal cells that ensheath neurons, are believed to play a role in nerve regeneration. In the leech *Hirudo medicinalis*, we are studying the glial cells of the lateral connectives to determine how these cells behave after injury, what mechanisms of repair they use, and whether they actively contribute to regeneration of severed axons.

We have crushed the connective in two places to create an isolated glial stump, separated from both its nucleus and from contact with the adjacent glial cell. Some of the injured neurons in the crushed connective can form electrical synapses with their severed axons and thereby restore function (*Year Book* 76). We wanted to know whether glial cells, which normally make electrical junctions with one another, also can regenerate after such a crush by forming electrical junctions with their anucleate stumps or

whether they grow new processes to replace the old. The glial stump survives for at least two months, which is comparable to survival times for the severed stumps of large axons. We have found that the fluorescent dye Lucifer Yellow readily passes between glia in the leech *Haementaria ghilianii* (a preparation that permits a direct test of electrical coupling between glial cells in an intact connective). Lucifer Yellow injected into the nucleated portion of a severed connective glial cell in *Hirudo* did not pass into the stump, and dye injected into the stump did not pass into the proximal part of the glial cell or into the adjacent glial cell. This result suggests that although glial stumps survive, electrical connections are not formed between them and the nucleated portion of the cell. More dye-injection experiments will be performed to determine whether this result is always obtained, and electrophysiological recording will be done to test directly whether electrical coupling is established between glial cells and their stumps. We plan to study next whether the ensheathing glial cell is important for survival of axonal stumps.

#### THE DEVELOPMENT OF SKIN INNERVATION PATTERNS IN THE CHICK

*S. A. Scott*

Sensory innervation of the skin is supplied by axons whose cell bodies reside in the dorsal root ganglia (DRG's). Axons from each DRG innervate a characteristic region of skin, referred to as a dermatome. Very little is known about the development of dermatomes and how growing DRG neurons recognize the correct region of skin. This is an important problem, both because the precision with which DRG neurons innervate the skin is critical in determining the normal functioning of the sense of touch and, more generally, because we know little about target recognition by developing neurons. Even at an elementary level it



seems equally likely, for example, (1) that the DRG neurons are specified to innervate a particular region of skin no matter what route their axons must take to get there and (2) that their starting point and some quality of the pathway they follow in the limb direct the growing neurons.

We have recently begun to investigate the development of dermatomes in the chick hind limb. This preparation was chosen because in chick embryos it should be possible surgically to manipulate the DRG neurons, the skin, and the limb at early developmental stages before the skin is innervated. A comparison of the dermatomes established in operated embryos with those observed normally should provide insight into how

growing sensory neurons reach the correct region of skin during normal development.

The approach we are taking is to record with suction electrodes from the axon bundle comprising each dorsal root. We then stimulate the skin of the hind limb and map the region of skin in which stimulation evokes nerve impulses for each dorsal root. The experiments are being made in isolated limb-nerve preparations of embryos from various developmental stages, and the maps are used to chart the normal course of dermatome development. Although recordings have been made from embryos as young as 10 days, full dermatome maps have not yet been obtained.

## STUDIES ON NERVE AND MUSCLE MEMBRANES

*E. K. Bayne, J. M. Gardner, R. Rotundo, E. Wakshull, and D. M. Fambrough,  
with the technical assistance of D. Somerville*

In the genesis of tissue and organ structure and in the genesis of the organism as a whole there must be extensive communication between the component parts, the cells. Such communication can involve cell movements, recognition of various signals, formation of cell associations, and elaboration of asymmetries, to name but a few events whose underlying mechanisms probably lie primarily at some level other than the level of genetic regulation. Since many of these events involve cell-cell interactions and the formation of specialized cell contacts, it is reasonable to suppose that features of the cells' surfaces and of the extracellular matrices are principal components. In the past few years we have focused our studies upon certain glycoproteins that occur in the surface membranes of muscle fibers and neurons or in the extracellular surround of these cells. These glycoproteins (the acetylcholine receptor, the molecular forms of the

acetylcholinesterases, and the  $\alpha$ -bungarotoxin binding receptor of sympathetic neurons) are key components of the contact regions between neurons and between neuron and muscle fiber.

The acetylcholine receptors of skeletal muscle have been our longest-term focus of study. In past Reports we have described our studies of the number and distribution of receptor sites in adult muscle, in embryonic muscle, and in denervated adult muscle fibers. We have also described many aspects of receptor function during development, the involvement of acetylcholine receptors in some human neuromuscular diseases, and the effects of innervation and of muscle activity on the distribution of receptor sites. But the aspect of our studies that is of most interest has to do with the events involved in the biosynthesis of receptors, their transport to the surface membrane and incorporation into it, and the subsequent degradation of receptor

molecules. These events are likely to be similar to the events involved in membrane protein metabolism in all cells. It is this set of events, summed over all of the cell surface proteins, that establishes the cell surface phenotype and thus the appearance of the cell to its neighbors and the ability of the cell to perceive exogenous signals. In this Report we describe some new observations which extend our studies to encompass some of the other surface proteins of skeletal muscle. We wish to determine to what extent we can generalize from our knowledge of acetylcholine receptors.

In *Year Book 77* we described a new immunological technique (devised by Kohler and Milstein) for generating immunological probes for cell surface components. During the past year we have made a major effort to develop the new immunological techniques to the point where they can be applied to problems of membrane structure, function, and metabolism in skeletal muscle and neurons. This effort has yielded a set of ligands specific for components on skeletal muscle fibers and also a ligand for one component residing in the extracellular matrix of muscle tissue. Several of the ligands are now prepared in quantity and are being used to map the distribution of the target antigens on the muscle cells in tissue culture and to characterize the chemical nature of the antigens and probe the function of each antigen.

Further information has been obtained about the cellular distribution of the acetylcholinesterases. The molecular forms of acetylcholinesterase located on the cell surface have been examined in most detail, and some preliminary evidence suggests a surprisingly long metabolic lifetime for these molecules, significantly longer than the lifetime of the acetylcholine receptors in the same surface membrane. This difference in lifetime is not explained by anything we know about membrane turnover in skeletal muscle. If the difference is real, then we must conclude that the cells regulate the quantity

of each cell surface component not only by setting rates of biosynthesis but also by setting degradation rates. We have no clues as to how this might be accomplished. Exploring this mystery is a top-priority matter for the coming year. We plan to measure the turnover rates of each of the membrane antigens for which we now have immunological probes. We hope to find a correlation between some property of each antigen and its turnover rate.

#### CONSTRUCTION OF CONTINUOUS CELL LINES SECRETING MONOCLONAL ANTIBODIES

*E. K. Bayne, E. Wakshull, J. M. Gardner,  
and D. M. Fambrough*

The technique recently introduced by Kohler and Milstein for fusing myeloma and spleen cells to produce antibody-secreting hybridoma cells has great potential for studies of cell surfaces. By cloning selected hybrids, one can establish continuous cell lines that secrete antibodies against individual surface components. Purified immunogens need not be used to obtain monoclonal antibodies. We have adopted this technique to examine chick muscle membrane antigens.

Over the past year we have been successful in generating a variety of hybrid lines which secrete anti-chick muscle membrane antibodies. Our basic immunization and screening strategies for obtaining such lines were summarized in *Year Book 77*. Only minor modifications of the described procedures have been made. The spleen cells used in the fusions were obtained from mice that had been immunized with crude homogenates of either leg muscle taken directly from 14-day chick embryos or with crude homogenates of prefusion myoblast cultures. The myoblast cultures were established from mechanically dissociated 10–12 day chick embryo leg muscle, and were enriched for myoblasts (versus fibroblasts)



by a preplating step. Three different myeloma cell lines have been employed as fusion partners: (1) P3X63 Ag8, a myeloma that secretes an IgG of unknown target specificity; (2) P3-NS1-1-Ag 4-1, a variant of (1) which synthesizes a  $\kappa$  light chain; and (3) SP2/0-Ag 14, a line which makes no immunoglobulin of its own but is permissive for secretion of antibody when hybridized with spleen cells. The fusagen in all cases was polyethylene glycol, and the fusion products were divided into multiwell costar plates and grown in hybrid selective medium.

Hybridoma-conditioned medium was screened for the presence of anti-chick muscle membrane antibodies by indirect immunoassays (see *Year Book 77* and legend to Fig. 9 for details). Briefly, hybridoma medium was incubated with either crude muscle membrane preparations or intact muscle cultures. The membranes or cultures were then washed and incubated with  $^{125}\text{I}$ -labeled goat anti-mouse Fab in order to detect bound hybridoma antibody. Since the assay with intact cultures presumably detects only external antigens, hybridomas testing positive in this assay were chosen for

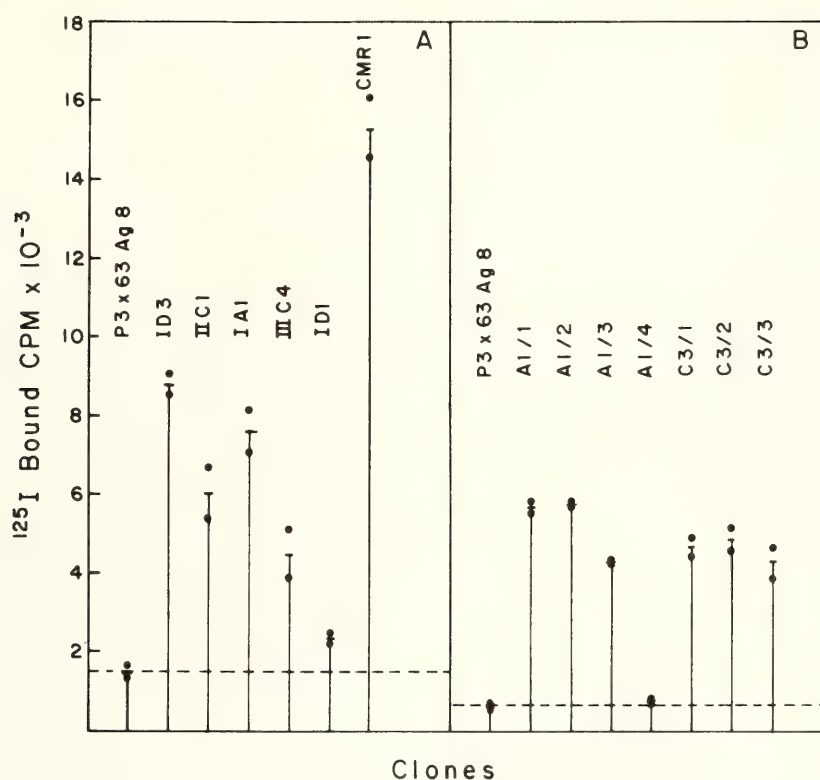


Fig. 9. Assays of hybridoma-conditioned medium for antibody binding to chick muscle cultures. Cultures were washed in Hanks balanced salt solution containing 0.1% bovine serum albumin (Hanks-BSA) for 10 minutes prior to the assay. Each 35-mm culture was incubated at room temperature with 0.5 ml hybridoma medium for 2 hours. The cultures were then washed thoroughly in Hanks-BSA and incubated with  $^{125}\text{I}$ -labeled goat anti-mouse Fab for 2 hours. After extensive washing the cultures were solubilized in 1N NaOH and radioactivity in the samples measured. Medium from P3X63 Ag 8 cultures was used as a control for nonspecific binding of immunoglobulin. (A) A typical assay of medium from hybridoma lines which had been maintained in culture for a minimum of 8 months. The relative levels of binding observed have remained fairly constant. All lines but B1 have been cloned at least twice. (B) Assay of clones derived from two separate wells, A1 and C3, after fusion of SP2/0 myeloma cells to spleen cells from a mouse immunized with homogenates of myoblast cultures. In this case, binding of antibody to prefusion cultures was measured, whereas in (A) postfusion cultures were used as the target for antibody binding. All clones but A1/4 were scored as positive. (Points represent duplicate assay plates; lines are drawn to averages).

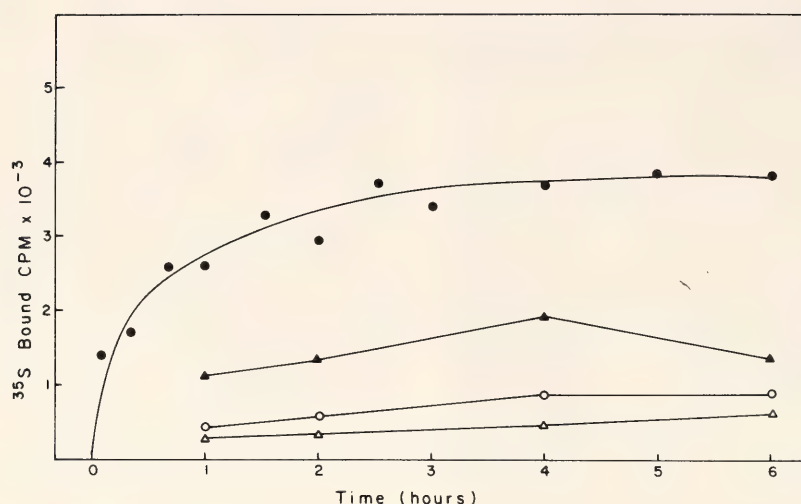


Fig. 10. Binding of  $^{35}\text{S}$ -methionine-labeled IIC1 antibody to postfusion chick muscle cultures (●). Controls measuring antibody binding to collagen-coated dishes without cells (△) and controls measuring the binding of boiled antibody to muscle cultures (○) were performed. The effect of a 2-hr incubation of the muscle cultures with unlabeled IIC1-conditioned culture medium prior to addition of the labeled IIC1 antibody is also shown (▲). All points represent the average of triplicates. See text for further details.

cloning in soft agar. The clones were then similarly screened, and positives were selected for further study. Figure 9 shows typical results obtained in assays of hybridoma-conditioned medium from clonally derived hybrid cell cultures.

Following cloning, the types of antibodies produced by various hybrids were analyzed in a number of ways. Incubation of hybrid cells with  $^{35}\text{S}$ -methionine provided a means of obtaining labeled antibody. Sucrose density gradient centrifugation of such antibody identified clones secreting antibody with a sedimentation coefficient of 7s (IgG), as well as clones producing 19s (IgM) antibody. All the clones illustrated in Figure 9B, for example, have been shown to secrete IgG, whereas with the exception of CMR1 the clones in 9A produce IgM. Such classification was confirmed by SDS-PAGE of the  $^{35}\text{S}$ -labeled antibodies and by indirect immunoassays using  $^{125}\text{I}$ -labeled antibody directed against specific immunoglobulin classes.

In other studies  $^{35}\text{S}$ -labeled immunoglobulin has been used for direct examination of antibody binding to chick muscle cultures. The results of one such experiment are presented in Fig. 10.  $^{35}\text{S}$ -

labeled antibody from clone IIC1 (an IgM secretor) was prepared by ammonium sulfate precipitation followed by fractionation on a Biogel A1.5 M column and incubated at room temperature with muscle cultures. After various times of incubation, cultures were washed extensively and solubilized, and the radioactivity was counted. As seen in Fig. 10, the binding of the  $^{35}\text{S}$ -labeled IIC1 antibody saturated in about two hours. Controls measuring the binding of antibody to collagen-coated culture dishes (preincubated overnight with complete medium) and controls measuring the binding of heat-denatured  $^{35}\text{S}$ -antibody (used at the same concentration as the native antibody) indicated that most of the binding was specific. In addition, preincubation of the muscle cultures with unlabeled IIC1-conditioned medium significantly lowered subsequent binding of the labeled antibody (Fig. 10). Preincubation with other hybridoma supernatants, on the other hand, did not affect binding of  $^{35}\text{S}$ -labeled IIC1 antibody (data not shown).

Characterization of the antigens to which the hybridoma antibodies bind is still in its initial stages. One approach



that has yielded considerable information is autoradiography. Muscle cultures incubated in hybridoma-conditioned medium and  $^{125}\text{I}$ -goat anti-mouse Fab have demonstrated varying distributions of antigens recognized by different hybridoma antibodies.

An example of these differences is illustrated in Fig. 11. IIC1 antibody binds preferentially to myotubes with little or no binding to fibroblasts. Preliminary evidence further suggests that the antigen is present on prefusion myoblasts (data not shown), but additional work is necessary to confirm this result. In contrast to clone IIC1, CMR1 appears to bind preferentially to cell-free areas of the culture dish (see below). Work is in progress to further elucidate species, tissue, and developmental specificities of different hybridoma antibodies.

Biochemical properties of the antigens

are also being examined. The binding of antibody from a number of clones, for example, has been shown to be sensitive to pretreatment of membranes with trypsin. In other analyses, pretreatment of intact muscle cultures with 1% Triton X-100 significantly reduced binding of C3/1-3 antibodies while not seriously altering the binding of CMR1. Several interesting experiments with this latter clone have given some clues to the identity of this antigen.

The finding that CMR1 recognized an antigen distributed in cell-free areas of chick muscle cultures, together with the observation that the antigen is largely resistant to removal by non-ionic detergent extraction, led us to postulate that CMR1 antibody was binding to an intercellular matrix component. Fibronectin (also referred to as cell surface protein, CSP, or large external transformation

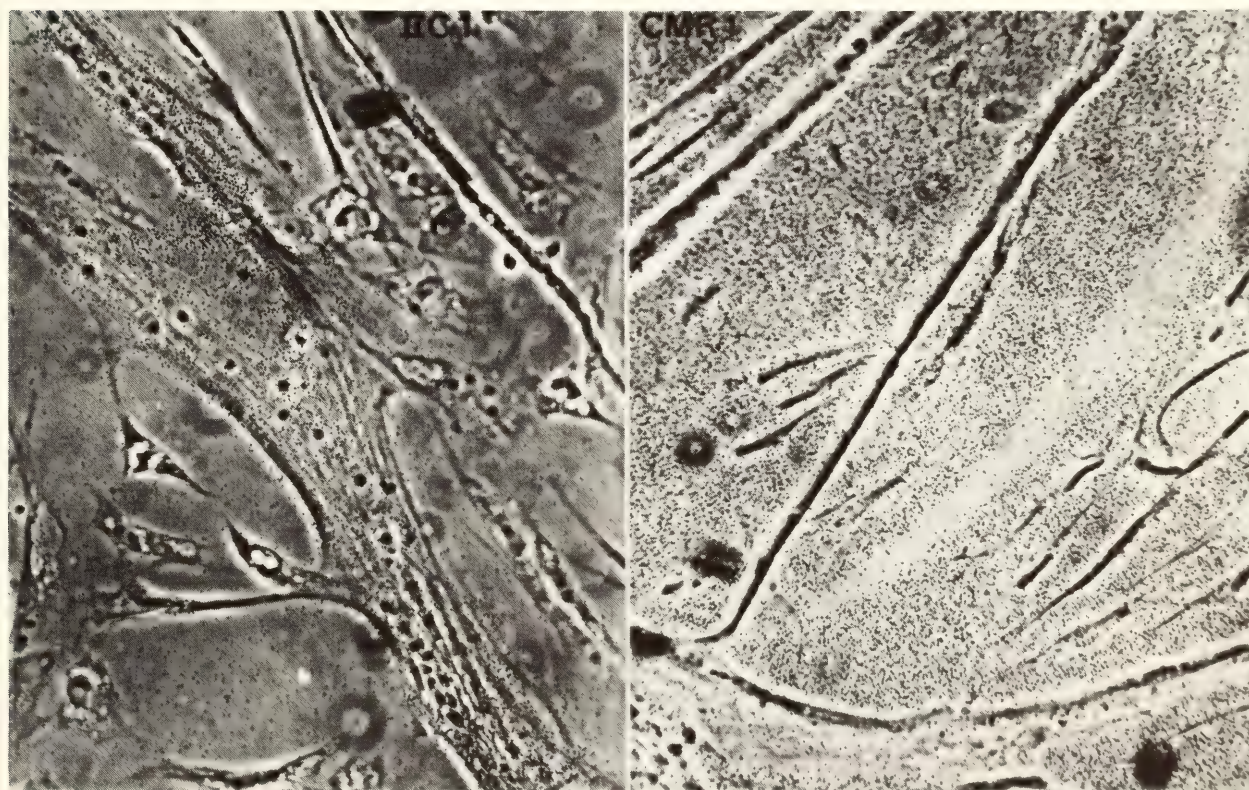


Fig. 11. Autoradiographs of cultures that were exposed first to hybridoma-conditioned culture medium and then to  $^{125}\text{I}$ -labeled goat anti-mouse Fab. Silver grains in cultures incubated with IIC1 antibody (at left) are located predominantly over myotubes. Silver grains produced in autoradiographs of cultures incubated with CMR1 antibody (at right) are primarily over the substratum. Grains are greatly reduced in number, however, in areas where myotubes have been dislodged.



sensitive protein, LETS) is the major glycoprotein found in intercellular matrices associated with a wide variety of cell types including muscle and fibroblasts and thus represents a likely target for CMR1. To test this hypothesis, fibronectin was prepared from urea extracts of confluent cultures of embryonic chick fibroblasts and subsequently purified by affinity chromatography on immobilized collagen agarose columns. Fibronectin obtained in this manner was essentially homogeneous, as analyzed by SDS polyacrylamide gel electrophoresis. Taking advantage of the affinity of fibronectin to gelatin (denatured collagen), a simple solid-phase radioimmunoassay was devised. Purified fibronectin (10  $\mu$ g/ml) was absorbed to culture dishes coated with denatured collagen. After incubation of the dishes with fibronectin for 12 hours at 4°C, followed by extensive washing with buffer to remove unbound protein, the dishes were incubated with conditioned medium from the CMR1 cell line. Bound hybridoma antibody was then detected, utilizing <sup>125</sup>I-labeled goat anti-mouse Fab. The results of this indirect immunoassay are shown in Table 1 and indicate that absorption of fibronectin to collagen-coated dishes significantly increased the binding of CMR1 antibody. Controls in which IIC1 hy-

bridoma supernatant was used in place of CMR1 antibody and controls in which first antibody was omitted altogether were performed. Also consistent with the hypothesis that fibronectin is the target antigen of CMR1 was the observation that culture dishes pretreated with either collagen alone or collagen followed by fibronectin show a dramatic increase in CMR1 binding after incubation with phosphate-buffered saline containing 10% horse serum. Cold insoluble globulin, the plasma form of fibronectin, is present in serum in relatively high concentrations, and it is probable that the absorption of this protein to the dishes is responsible for the enhanced antibody binding. Experiments to further analyze the specificity of the interaction between CMR1 antibody and fibronectin are in progress. If the CMR1 antibody (obtained by immunizing mice with a crude embryonic chick muscle membrane preparation) is indeed fibronectin specific, it should prove useful in studies of the extracellular matrix of muscle cells in vivo and in vitro.

Finally we should point out that while the described studies have been carried out using antibodies secreted by hybridomas into their culture medium, such antibodies are present only at low concentrations. To obviate this problem, hy-

TABLE 1. Antibody Binding to Fibronectin on Culture Dishes\*

Collagen + Fibronectin			Collagen			Collagen + Fibronectin PBS-10% Horse Serum	Collagen + PBS-10% Horse Serum
CMR1†	IIC1	...	CMR1	IIC1	...	CMR1	CMR1
921‡	392	116	365	398	119	2593	2636

\* Collagen-coated 35-mm plastic culture dishes were either pretreated with fibronectin, as described in the text, or used directly. In some cases, such dishes were further treated with PBS containing 10% horse serum for 30' at room temperature. Dishes were then treated with hybridoma antibody for two hours; washing and subsequent incubation with <sup>125</sup>I-labeled goat anti-mouse Fab for two hours followed.

† Antibody assayed.

‡ Values represent the average of assays in triplicate (cpm).



bridoma clones have been injected intraperitoneally into mice in order to induce the formation of ascites tumors. The peritoneal fluid obtained from the tumor-bearing mice may contain antibody titers over  $1000\times$  higher than those found in culture supernatants. IIC1 ascites fluid, for example, was found to contain 1.8 mg IgM/ml. This antibody has been partially purified and demonstrates specific binding to chick muscle.

We plan to use monoclonal antibodies to study the metabolism and regulation of a variety of muscle surface components. It will be of interest to determine whether various membrane glycoproteins are processed independently or whether generalized mechanisms exist. Further, since it has been shown that multivalent ligands often induce clearing of their receptors from the cell surface, it may be possible to determine the function of antigens by assaying for effects of monoclonal antibodies on various surface-mediated phenomena.

#### CHICK EMBRYO MUSCLE ACETYLCHOLINESTERASE

*R. Rotundo*

Acetylcholinesterase (AChE) is an enzyme which exists as a family of molecular forms in all cholinergically innervated tissues and whose forms can be distinguished by their sedimentation coefficients. This family of enzymes is developmentally regulated, both during the period of myogenic cell fusion and during innervation when the incoming neuron exerts a profound effect on the amount of this enzyme synthesized and on the appearance of particular molecular forms and their localization. In cultured muscle cells, this enzyme exists as both a surface membrane protein and a secretory protein (*Year Book 76*), thus enabling us to study the relationships between the synthesis and transport of membrane and secretory proteins and to compare these to the production of another well-studied

membrane protein, the acetylcholine receptor (Devreotes and Fambrough, *Year Book 75*, *Year Book 76*, *Year Book 77*).

In previous Reports (*Year Book 76*, *Year Book 77*) we described the various molecular forms of AChE found in chick embryo leg muscle *in ovo* and *in vitro*, their rates of synthesis, transport, and secretion, and their subcellular distribution. In cultured muscle cells two AChE forms predominate, the 11.5S and the 7.1S molecular forms. The kinetics of transport and release of the secreted AChE molecules paralleled that of the transport and insertion into the plasma membrane of the acetylcholine receptor and suggested that the processes of transport of membrane and secreted proteins were metabolically coupled. This past year our studies have focused on the cell surface AChE molecules, their molecular forms, and their synthesis and accumulation on the plasma membrane.

#### *Properties of Cell Surface AChE*

One question of importance in these studies is the nature of the association of cell surface AChE with the muscle cells. Membrane proteins are generally viewed as belonging to two classes: integral membrane proteins whose peptide chains actually traverse the lipid bilayer, and peripheral proteins, whose persistence on the surface of the lipid bilayer is via interactions with other membrane-associated molecules. A third category can also be discerned—those proteins bound either ionically or covalently to the extracellular matrix. To categorize cell surface AChE, we have treated muscle cultures with solutions of high ionic strength (i.e., 1 M NaCl), EDTA (10 mM), various sugars, including d-mannose, N-acetyl-d-glucosamine, d-glucosamine, and  $\beta$ -d-fructose (all at 1.0 mM), and the non-ionic detergent Triton X-100. Only the detergent was capable of solubilizing the cell surface AChE, indicating that this pool of enzyme is tightly associated with the plasma membrane. Al-

TABLE 2. Effect of DFP Pretreatment on Cell Surface AChE Accumulation in Culture\*

Pretreatment	Post-treatment Medium	Cell Surface AChE (% Control)	Total AChE (% Control)
HBSS	EMEM 210	100 ± 7	100 ± 3
HBSS	DFP/EMEM 210	99 ± 6	90 ± 1
10 <sup>-4</sup> M DFP	EMEM 210	88 ± 4	103 ± 3
10 <sup>-4</sup> M DFP	DFP/EMEM 210	76 ± 9	86 ± 2

\* Myogenic cells from 11-day-old chick embryo leg muscle were divided into two identical aliquots and treated with either HBSS alone or HBSS with 10<sup>-4</sup> M DFP for 15 minutes. The cells were then washed with 3 × 5 ml EMEM 210; each batch was subdivided into two equal portions and resuspended in either EMEM 210 or DFP-treated EMEM 210. The muscle cells were plated at a density of about 4 × 10<sup>5</sup> cells per culture dish and grown for three days before assaying for surface and total AChE activity.

though it behaves under all conditions like an integral membrane protein, we cannot yet rule out the possibility that the AChE molecule itself is a peripheral membrane protein which interacts in some special manner with a second protein embedded in the lipid bilayer.

A second series of studies involved comparing membrane-bound with detergent-solubilized enzyme with respect to catalytic efficiencies. In these experiments we found no differences in the kinetic properties of the two preparations; this result indicates that the association with membranes does not affect the active sites of the enzyme.

#### *Synthesis of Cell Surface AChE*

The cell surface acetylcholinesterase in cultured muscle cells could arise from one of three possible sources: (1) the enzyme is synthesized *in ovo* and is deposited on the muscle cells' membranes prior to their removal for culturing; (2) the AChE is derived from the culture medium, which contains very large quantities of this enzyme; or (3) the surface AChE is synthesized by the muscle cells in culture and is somehow deposited on the cell surface. To test these hypotheses, myogenic cells obtained from 11-day-old chick embryo leg muscle were treated prior to culturing with either Hank's Balanced Salt Solution (HBSS) or the

same solution containing 10<sup>-4</sup> M diisopropylfluorophosphate (DFP), an irreversible inhibitor of all cell-associated AChE. The cells were then cultured in either regular medium (EMEM 210) or medium pretreated with DFP to remove all endogenous esterase activity. Table 2 shows the results of this experiment. Since cells that had been pretreated with DFP and grown in esterase-free medium recovered their surface and total enzyme pools almost completely, the surface AChE molecules could only have arisen from a pool of molecules synthesized by the cells in culture. The slightly lower values of AChE found in cells grown in DFP-treated medium are related to the depletion of some essential nutrients during preparation of the medium.

In order to determine which molecular forms of AChE are located on the cell surface, we took advantage of the fact that DFP is a lipid-soluble irreversible inhibitor of the enzyme, whereas another inhibitor, BW284c51, is easily reversible and does not penetrate the plasma membrane. By preincubating the muscle cells in BW284c51 to block the surface enzyme, treating with DFP to irreversibly inactivate the intracellular enzyme molecules, then washing out both inhibitors, only the surface enzyme remains active. By analyzing the remaining AChE activity by velocity sedimentation (Fig. 12), we found that both the 11.5S and 7.1S



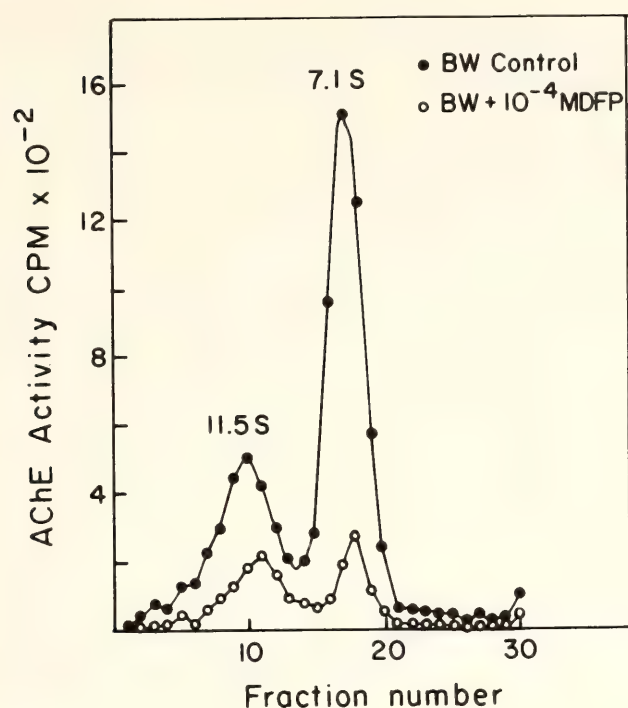


Fig. 12. Molecular forms of acetylcholinesterase on the muscle cell surface. Muscle cultures were washed and covered with 1 ml HBSS containing 0.5 mg/ml BW184c51 to protect the cell surface enzyme from inactivation. Half of the cultures were then covered with an additional 1 ml HBSS containing  $2 \times 10^{-4}$  M DFP; the remaining half received HBSS alone. After a 15-min incubation at room temperature, the cultures were washed, extracted in buffered detergent solution, and analyzed by velocity sedimentation on linear sucrose gradients.

forms are on the muscle cell membrane. In this experiment approximately 30% of the total cells' contents of AChE are accounted for by the protected forms, which is in good agreement with our earlier estimates of subcellular distribution (*Year Book 76*).

The accumulation of cell surface AChE during muscle cell development in culture is depicted in Fig. 13. During the first three days in vitro, the myogenic cells are proliferating and fusing to form the multinucleated myotubes characteristic of differentiated muscle. There is only a low level of surface AChE synthesis (data not shown). Following this period of cell differentiation, there is a large accumulation of AChE molecules on the cell surface occurring over several days. The rates of synthesis of the

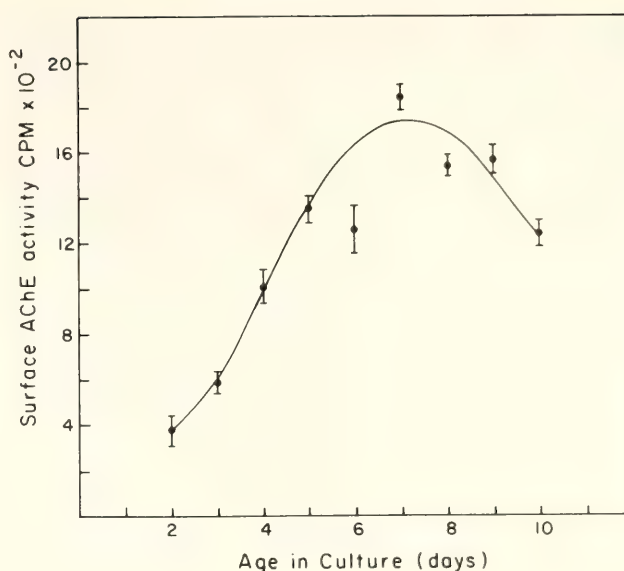


Fig. 13. Development of cell surface acetylcholinesterase activity in culture. Chick muscle cultures were prepared from 11-day-old chick embryo leg muscle. At the indicated times, three muscle cultures were washed to remove medium esterases and assayed for cell surface AChE, as described in *Year Book 76*.

surface molecules can easily be studied by treating the cultures with DFP and measuring the rate of return of enzyme activity. In these types of experiments we always observe a rapid but partial recovery of surface enzyme during the 18–24 hours following DFP. In our experiments to date, however, we have never observed a complete recovery of surface enzyme. The reasons for this lack of total recovery are under investigation.

#### *Degradation of Cell Surface AChE*

We have previously shown that AChE in cultured muscle cells exists as both a rapidly turning over internal pool and an external, surface membrane pool with a slower half-life (*Year Book 76*, *Year Book 77*). The internal pool provides mainly the secreted AChE forms, which are released at the rate of approximately 10% of total cell contents per hour; only a small portion of this internal pool is subsequently deposited on the surface membrane. To study the degradation of the external surface enzyme we used a procedure that involves first labeling the

cells with  $^3\text{H}$ -DFP, then washing out any unreacted labeled material. Since the  $^3\text{H}$ -DFP is covalently linked to the active site of the enzyme, the degradation of AChE can then be studied simply by observing the loss of protein-bound  $^3\text{H}$ -DFP. The kinetics of degradation of surface AChE are illustrated in Fig. 14; the initial portion of the curve showing a rapid loss of  $^3\text{H}$ -DFP is associated with the depletion of the internal pool of secreted AChE molecules. The second portion of the curve is the first-order exponential decrease of the surface-bound enzyme. The approximate half-life of the surface enzyme under these conditions is 55 hours, or three times that of the acetylcholine receptor (*Year Book 75*, *Year Book 76*, *Year Book 77*). That these observations are not due to a direct effect of DFP on the degradation of membrane proteins is illustrated by the fact that DFP has no effect upon the synthesis, transport, accumulation, or degradation of the acetylcholine receptor.

#### *Purification of AChE*

Obtaining the various molecular forms of AChE in pure preparations has become an important aspect of our research program, not only to further characterize this family of molecules but also to produce specific antibodies for use in a wide variety of experiments ranging from tissue localization studies to the identification of in vitro mRNA translation products. This has proved to be a difficult task because of the many forms of the enzyme and the fact that even within a given group there is some heterogeneity with respect to glycosylation. We have, how-

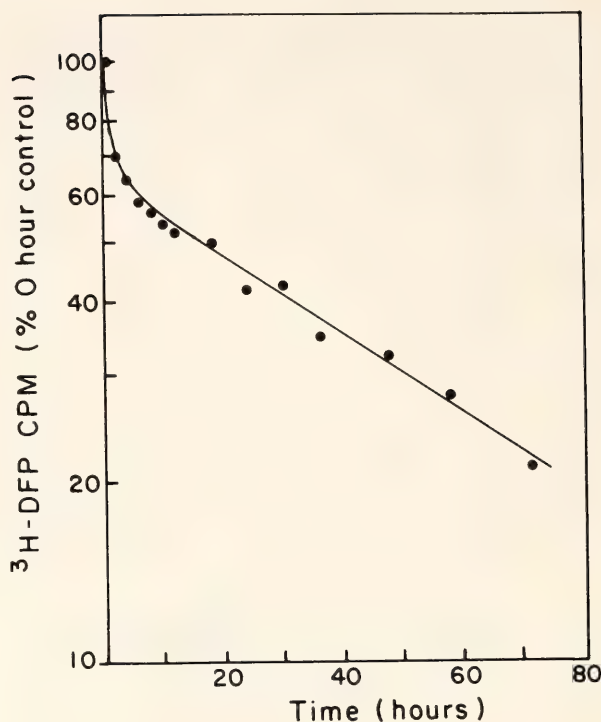


Fig. 14. Degradation of chick muscle culture acetylcholinesterase. Chick embryo muscle cultures were washed and labeled by incubating for 30 min with  $2.6 \times 10^{-7}$  M  $^3\text{H}$ -DFP at room temperature (total label = 1  $\mu\text{Ci}$ ). The cultures were then washed with medium to remove any unreacted  $^3\text{H}$ -DFP and returned to the incubator. At the indicated times, four cultures were removed, washed, and extracted in buffered detergent solution at 1 ml per culture. The cells were scraped into solution; the proteins were extracted and precipitated with acetone, dissolved in 1 M NaOH, and counted in a scintillation spectrometer. All values are expressed as percent of the 0-hr control value, and the half-life is calculated by regression analysis of the linear portion of the curve.

ever, established a protocol for the isolation and purification of the 19.5S and 11.5S molecular forms of AChE which will yield sufficient quantities of the proteins for further analysis.



## ORGANIZATION, DYNAMICS, AND METABOLISM OF CELL SURFACE PHOSPHOLIPIDS

*R. E. Pagano, A. J. Schroit, D. K. Struck, and O. C. Martin  
with the technical assistance of B. Smith and W. Duncan*

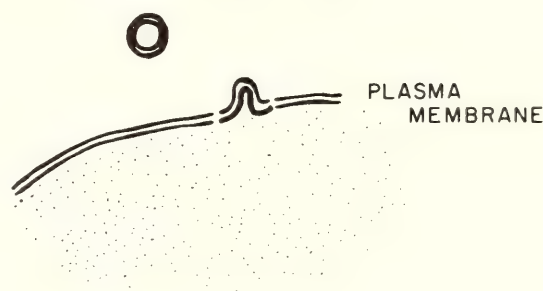
We continue our studies on the organization, dynamics, and metabolism of cell surface lipids in eukaryotic cells. As discussed more fully in *Year Book 77*, there are several important membrane-related questions of general interest to the cell biologist which are under study. Briefly, we seek to determine (1) whether lipid components in the two halves of the plasma membrane are processed and metabolized differently from one another, (2) whether plasma membrane lipids are in a state of flow which can result in the patching and capping of cell surface proteins, and (3) whether deliberate perturbation of the plasma membrane lipid asymmetry can be recognized by the cell and restored to normal by the cellular metabolic machinery. Each of these questions could be addressed if it were possible to selectively integrate exogenous phospholipid molecules into the inner or outer leaflets of the plasma membrane of a living cell.

We now have evidence that appropriately tagged lipids—namely radio-labeled or fluorescently labeled lipids, or lipids that bear an antigenic determinant—can be selectively introduced into either the outer or inner leaflets of the plasma membranes of mouse lymphocytes or Chinese hamster fibroblasts after the exchange or fusion of artificially generated lipid vesicles with the cell surface. Thus, as illustrated schematically in Fig. 15, following vesicle-cell fusion, lipid molecules residing on the external leaflet of the vesicle surface would be expected to be delivered predominantly to the external leaflet of the plasma membrane bilayer, while lipids residing on the inner leaflet of the vesicle bilayer should be delivered predominantly to the cytoplasmic leaflet of the cell surface mem-

brane. Thus, by using lipid vesicles in which one of the lipid components is asymmetrically distributed across the vesicle bilayer, one could hope to selectively deliver lipid molecules to the inner or outer halves of the plasma membrane bilayer. In contrast, vesicle-cell exchange (Fig. 15) results predominantly in the introduction of vesicle lipids into the outer leaflet of the cell surface membrane, as documented previously by this laboratory (*Year Book 77*).

In this year's report we present a general method for the construction of asymmetric vesicles, one which is proving useful in examining the fate of lipids in the two halves of the plasma mem-

### VESICLE-CELL FUSION



### VESICLE-CELL EXCHANGE

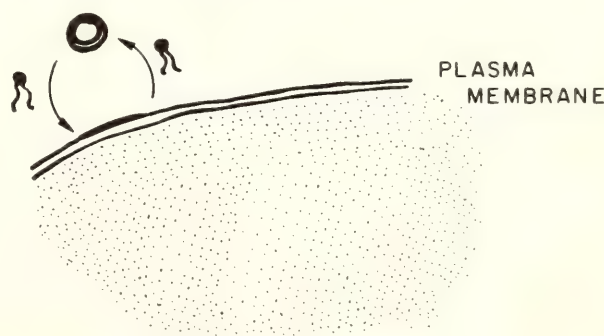


Fig. 15. Schematic representation of asymmetric delivery of vesicle lipid components to the cell surface following vesicle-cell fusion and vesicle-cell lipid exchange.

brane. Using this method and related techniques in conjunction with fluorescently labeled lipids, Douglas Struck reports the most interesting and unexpected finding that lipids inserted into the inner and outer halves of the plasma membrane of cells are processed by the cell very differently. Lipids inserted into the outer leaflet appear to remain restricted to the cell surface for hours, whereas lipids inserted into the inner half of the plasma membrane bilayer are rapidly equilibrated with lipid pools within the cytoplasm of the cell.

In related studies, Alan Schroit reports on the dynamics of exogenous lipids that have been inserted into the outer leaflet of the plasma membrane of mouse lymphocytes. Using hapten-conjugated lipids and appropriate immunochemical methods, he finds that these foreign lipids are rapidly capped to one pole of the cell surface, similar in many respects to the capping of cell surface (glyco)proteins reported extensively by many other laboratories. This finding of lipid capping is extremely important in terms of our current thinking about the organization and structure of membranes. How can these foreign lipids, which cannot span the plasma membrane bilayer and thus cannot be directly linked with the cytoskeleton which is generally thought to be responsible for the capping of cell surface antigens, exhibit many of the properties of capping of macromolecules in the cell surface? This unexpected result raises the possibility that another kind of mechanism, designated "lipid flow," might play an important role in the dynamics of the cell surface.

#### FORMATION OF ASYMMETRIC PHOSPHOLIPID VESICLES

*R. E. Pagano and O. C. Martin*

Small unilamellar vesicles are first generated by sonication from egg- or dioleoyl-phosphatidylcholine (EPC or DOPC) in an aqueous buffer by stand-

ard procedures. Elution behavior on Sepharose 4B and negative staining electron microscopy confirm the existence in the preparations of unilamellar vesicles, designated recipient vesicles, approximately 250–500 Å in diameter. A second, donor lipid which is to be asymmetrically inserted into the external leaflet of the vesicle bilayer, is dried down from an organic solvent under a stream of argon gas and subsequently put under vacuum to remove residual solvent. The lipid is then solubilized in dilute detergent (0.1% deoxycholate or 10 mM n-octyl-D-glucoside) and mixed with a concentrated suspension of the preformed recipient EPC or DOPC vesicles.\* The vesicle-detergent suspension is then applied to a Sepharose 4B column and the small unilamellar vesicles, which distribute with the internal volume of the column and elute as a broad symmetrical peak, are pooled and dialyzed overnight against a balanced salt solution to remove residual amounts of detergent. When radiolabeled (or fluorescent) donor lipids are used, the pattern of radioactivity (or fluorescence) precisely follows the optical density pattern characteristic of a sonicated vesicle preparation eluting from a Sepharose 4B column (see Fig. 16). Donor lipids may be chemically distinct from the lipids of the recipient vesicles. Thus a variety of fluorescently tagged and spin-labeled phospholipids, as well as radiolabeled phosphatidylcholine (PC) or phosphatidyl ethanolamine (PE) have been used. Experiments employing radiolabeled detergents demonstrate that less than 1 molecule of detergent per 6000 lipid molecules contaminates the vesicle preparation.

Ongoing experiments strongly suggest that the donor lipids are preferentially inserted into the external leaflet of the vesicle bilayer. This was shown in an experiment in which a PE molecule bear-

\* Standard conditions: 0.25 ml of 30 mg/ml vesicle suspension mixed with 0.125 ml detergent-solubilized donor lipid (75 µg).



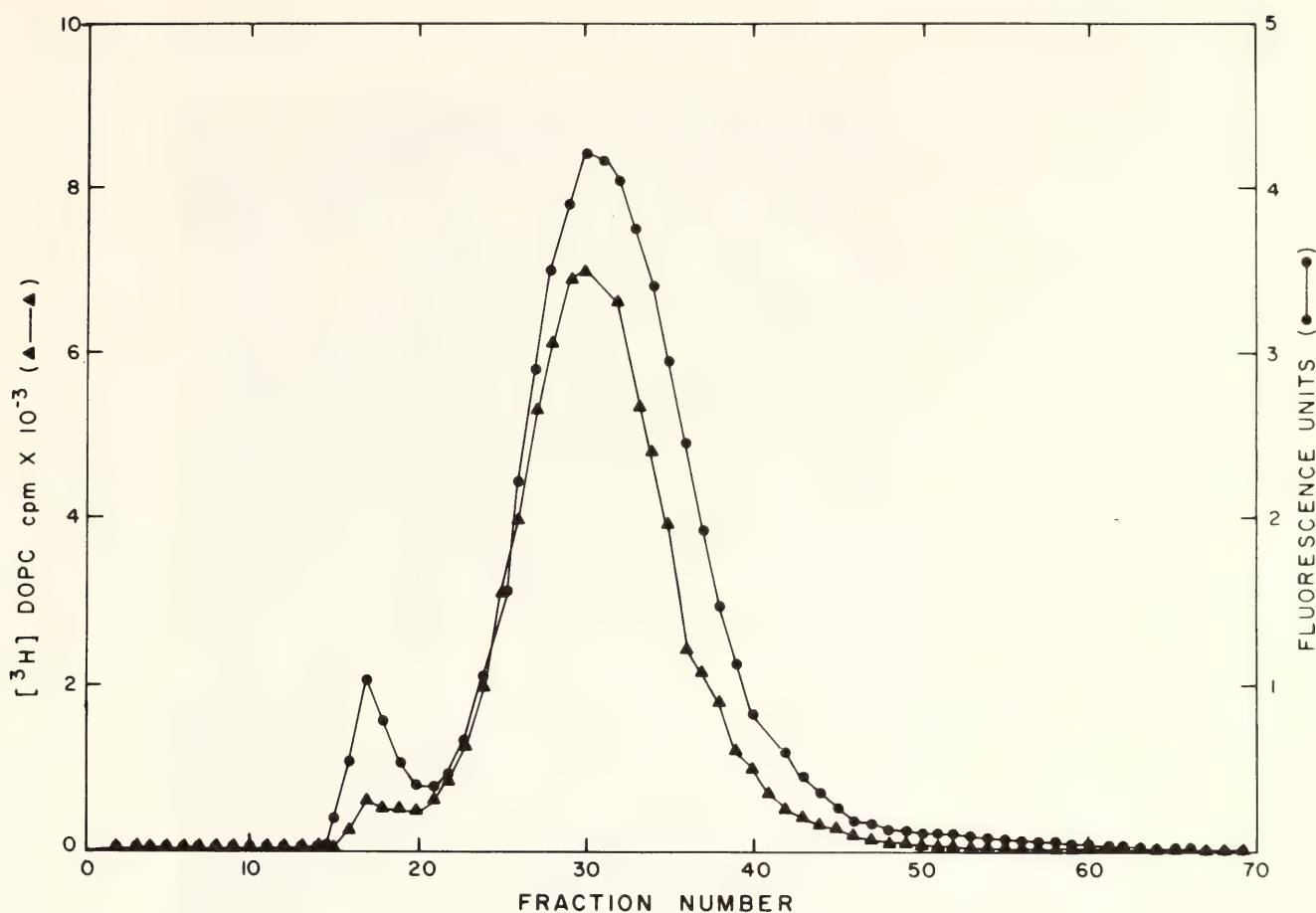


Fig. 16. Sepharose 4B profile of sonicated EPC vesicles containing an asymmetrically incorporated, fluorescently tagged phospholipid.

ing a fluorescent group on its acyl chain was introduced into EPC recipient vesicles using either deoxycholate or n-octyl glucoside. Following vesicle formation, the vesicles were derivatized with trinitrobenzene sulfonic acid (TNBS). TNBS reacts covalently with the primary amino group of PE, converting it to a trinitrophenylated derivative, designated Tnp-PE. Under appropriate conditions, TNBS has been shown not to penetrate the vesicle bilayer, and thus it can be used to measure any asymmetry in the PE distribution across the vesicle membrane. As seen in Fig. 17, most of the fluorescent PE present in asymmetric vesicles could be derivatized by TNBS, thus confirming its asymmetric distribution in these preparations. In contrast, in control uniform vesicle preparations made by direct sonication of a mixture of PE and EPC, only about half the fluorescent lipid was accessible to label-

ing by TNBS. Additional studies to examine the disposition of other types of donor lipids in these vesicle preparations are in progress. The behavior of asymmetric fluorescently labeled vesicles with cells is described below.

#### INCORPORATION OF FLUORESCENT PHOSPHOLIPIDS INTO INTACT CELLS BY VESICLE-CELL FUSION AND VESICLE-CELL LIPID EXCHANGE

*D. K. Struck*

Previous studies from this laboratory have shown that small unilamellar vesicles consisting of lipid molecules in a "fluid" state (above their phase transition temperature) interact with cultured Chinese hamster V79 fibroblasts by two distinct mechanisms. At low temperatures, a process known as lipid exchange is predominant. The exchange process

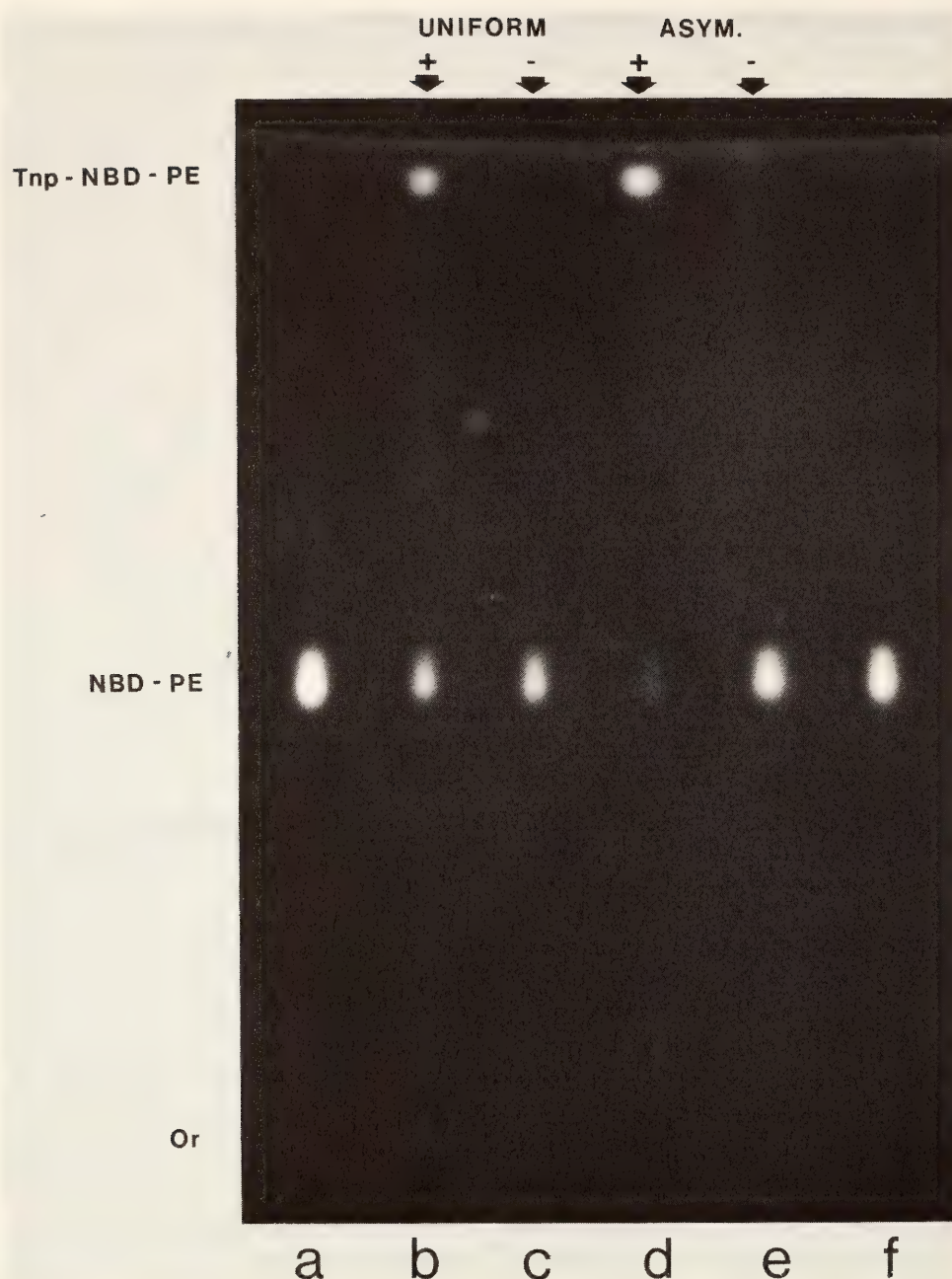


Fig. 17. Thin-layer chromatogram of the lipids extracted from small unilamellar vesicles bearing a "uniform" and an "asymmetric" distribution of the fluorescent phospholipid, 1-acyl-2-(N-4-nitrobenzo-2-oxa-1,3-diazole)-aminocaproyl phosphatidylethanolamine (NBD-PE). Aliquots of each vesicle suspension were reacted with TNBS to determine the sidedness of the NBD-PE. Lanes *a* and *f* = NBD-PE standards. Lanes *b* and *c* = EPC vesicles containing a uniform or symmetrical distribution of NBD-PE across the membrane. Lanes *d* and *e* = EPC vesicles containing NBD-PE added to the vesicles via detergent. Lanes *b* and *d* represent lipid extracts from vesicles treated with TNBS. Note that in the detergent-treated vesicles nearly all of the fluorescent PE can be converted to the Tnp-derivative, suggesting its asymmetric distribution in these preparations, whereas in the uniformly labeled vesicles only about 50% of the NBD-PE is accessible to TNBS.

has several distinctive characteristics: (1) only lipid molecules residing in the outer leaflet of the vesicle bilayer are involved, (2) the exchange appears to be highly specific with respect to the nature of the polar head group of the lipid mole-

cules involved (i.e., vesicle phosphatidylcholine exchanges only with cell phosphatidylcholine and not with other cell surface phospholipid species), and (3) exchange occurs without net transfer of lipid mass between vesicles and cells. At



higher temperatures, lipid vesicle-cell fusion is the mechanism by which vesicle phospholipids become cell associated. Fusion can be distinguished from exchange, since (1) there is a net transfer of lipid from vesicle to cell, (2) lipids from both the inner and outer leaflets of the vesicle bilayer are incorporated into cellular membranes, and (3) fusion has no specificity with regard to the polar head groups involved. In our current investigations, we have utilized fluorescent phospholipids to examine further the processes of lipid exchange and vesicle-cell fusion.

When vesicles containing a fluorescent phosphatidylcholine derivative (NBD-PC) are incubated with V79 fibroblasts at low temperature, the fluorescent lipid is rapidly transferred to the cells. In these experiments, the fluorophore is covalently attached to one of the fatty acid constituents of the probe molecule. Examination of the cells by fluorescence microscopy indicates that the fluorescent lipid is located at the periphery of the cell (Fig. 18a), as would be expected if

lipid exchange were operative. This peripheral fluorescence is rapidly internalized if the cells are shifted to a higher temperature at which endocytosis and pinocytosis are known to occur (Fig. 18b). Of interest is the fact that this internalized fluorescence is very granular in appearance, with the majority of the lipid probe restricted to one or a few sites within the cell.

That the peripheral fluorescence shown in Fig. 18a actually represents NBD-PC incorporated into the outer leaflet of the plasma membrane of the fibroblasts is supported by the following observations. First, when vesicles containing both NBD-PC and a tetramethylrhodamine derivative of phosphatidylethanolamine (TMR-PE) in which the fluorophore is coupled to the polar head group of the lipid are incubated with cells at low temperature, essentially no TMR-PE becomes cell associated while all the cells exhibit a bright ring fluorescence caused by NBD-PC. This immediately excludes the possibility that vesicles containing these fluorescent lipid analogs fuse with,

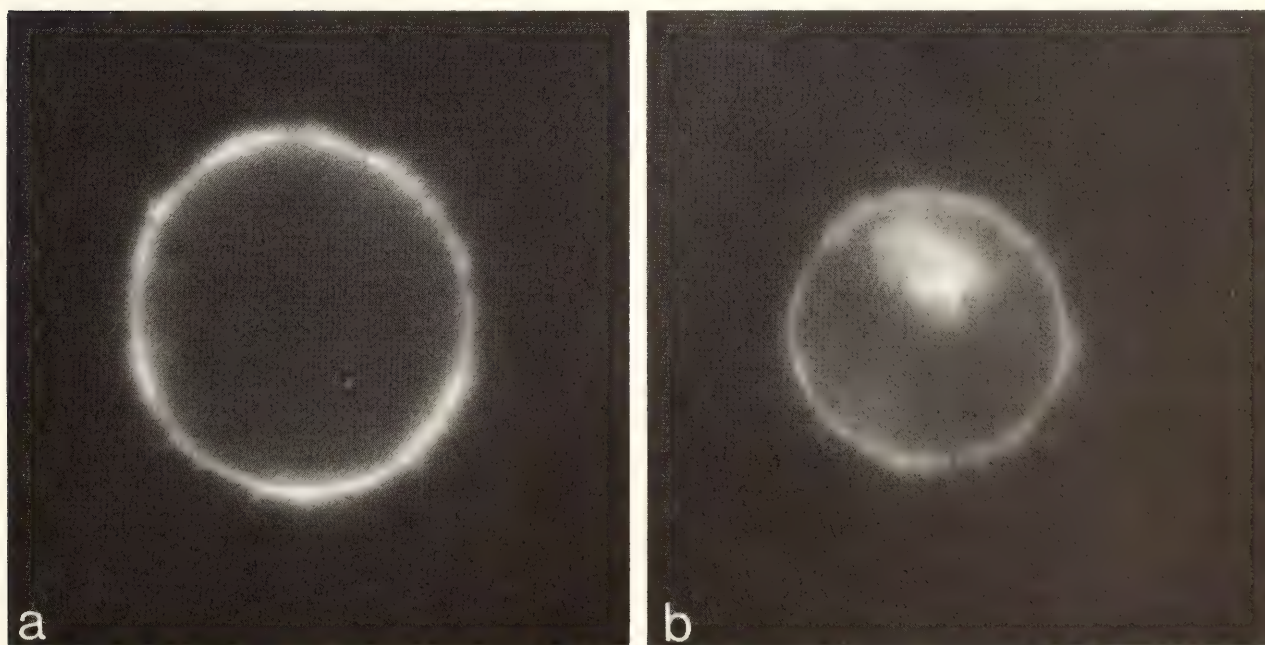


Fig. 18. Interaction of vesicles containing NBD-PC with cells at low temperature. V79 cells were incubated with vesicles for 60 min at 2°C, washed, and then observed by fluorescence microscopy. Cells were photographed (a) immediately after washing and (b) after a 60-min incubation at 37°C after the final wash.



adsorb to, or are endocytosed by the cells under the conditions employed. This finding further documents the specificity of lipid exchange, since TMR-PE is a probe having a modified polar head group which has no natural analog in normal cells, while NBD-PC has the naturally occurring choline moiety at this position. Second, the NBD-PC that becomes cell associated at low temperature can be completely removed by incubating the fluorescent cells with vesicles consisting solely of dioleoyl-phosphatidylcholine under conditions favoring lipid exchange. This result demonstrates that lipids incorporated into cells by the exchange process are inserted into the cell surface in a manner which allows them to participate in the exchange process. It should be noted that the internalized fluorescence shown in Fig. 18b cannot be removed by a similar treatment, indicating that lipids residing in intracellular membranes do not participate in the exchange process. From these observations we conclude that vesicle constituents are integrated into the outer leaflet of the plasma membrane of these cells. Qualitatively similar results have been obtained using a phosphatidylethanolamine derivative, NBD-PE, where the fluorophore is coupled to a fatty acyl residue of the molecule.

The ability to preferentially incorporate fluorescent phospholipids into the plasma membrane has enabled us to measure the lateral diffusion rates of these molecules in the plasma membrane of intact cells by the technique of fluorescence photobleaching. These measurements are the first obtained in which the probe molecule is a phospholipid rather than a lipophilic dye where the orientation of the dye in the membrane and its subsequent behavior may not reflect that of structurally distinct molecules such as phospholipids. Our preliminary data indicate that both NBD-PC and NBD-PE rapidly diffuse in the plane of the plasma membrane (Table 3), although their diffusion rates appear to be substantially

lower than those reported for lipophilic dyes ( $\sim 10^{-8}$  cm<sup>2</sup>/sec). In addition, it appears that NBD-PE may diffuse at a significantly faster rate than NBD-PC.

Fluorescent phospholipid derivatives have also been useful in determining the fate of vesicle lipids that become cell associated via vesicle-cell fusion. When cells are incubated with NBD-PC-containing vesicles at 37°C, three distinct types of cell-associated fluorescence are observed: (1) a uniform peripheral ring, (2) a granular internal component, and (3) a diffuse, more nearly uniform internal component (Fig. 19a). If the vesicle-cell incubation is carried out in the presence of metabolic inhibitors (2-deoxyglucose and sodium azide), the appearance of the granular internal fluorescence is markedly diminished (Fig. 19b). We tentatively conclude that this granular fluorescence is associated with internalization of fluorescently labeled plasma membrane by endocytosis (see also Fig. 18). In contrast, the diffuse internal fluorescence is not affected by these inhibitors. Consequently, it does not represent lipid that is internalized by an energy-dependent process. Instead, we believe that this component of the

TABLE 3. Diffusion Rates of Fluorescent Phospholipids in the Plasma Membrane of V79 Fibroblasts as Measured by Fluorescence Photobleaching\*

Lipid Probe	Temperature of Measurement (°C)	Diffusion Constant (cm <sup>2</sup> /sec)
NBD-PC	22	$1.96 \times 10^{-9}$
NBD-PE	22	$3.08 \times 10^{-9}$
NBD-PE	37	$3.84 \times 10^{-9}$

\* Cells were incubated with vesicles containing either NBD-PC or NBD-PE at 2°C for 60 minutes, washed, and subjected to photobleaching analysis. Cells were mounted for observation in a fluorescence microscope and illuminated with the 488.0-nm line of a krypton-argon laser passed through a 40× oil immersion objective lens and focused to a 1.1-μ spot on the specimen. Bleach times were 200 msec.



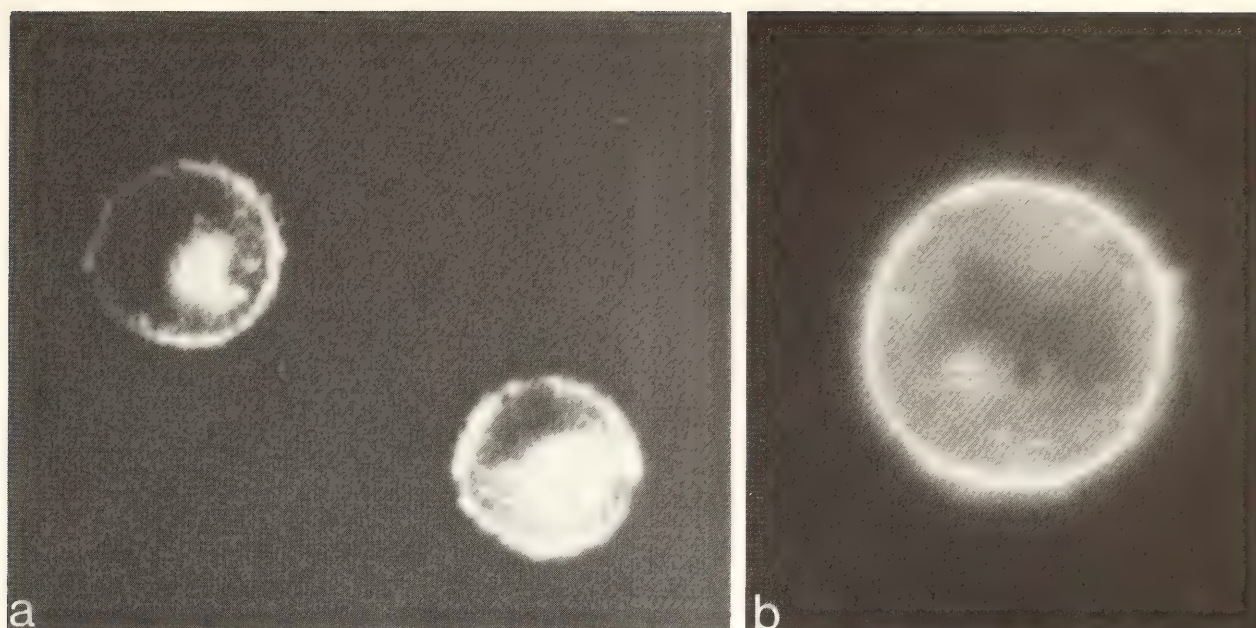


Fig. 19. Interaction of vesicles containing NBD-PC with cells at high temperature. V79 cells were incubated with NBD-PC-containing vesicles for 30 min at 37°C in the absence (a) or presence (b) of 25 mM deoxyglucose and 10 mM sodium azide. The cells were then washed and immediately photographed.

cell-associated fluorescence is the result of a rapid equilibration of NBD-PC introduced into the inner leaflet of the plasma membrane during the fusion event with the vast excess of phospholipid present in intracellular membranes. Such a process might be mediated by intracellular phospholipid-exchange proteins isolated from a variety of eukaryotic sources. If this proposal is correct, it would appear that the two leaflets of the plasma membrane are metabolically independent. This could in part explain the origin of the known compositional asymmetry of the plasma membranes of various eukaryotic cells. Finally, the ring fluorescence seen in Fig. 19 (a and b) is probably due to the presence of NBD-PC in the outer leaflet of the plasma membrane. Supporting this conclusion is the fact that these rings can be "removed" by incubation of the labeled cells with dioleoylphosphatidylcholine vesicles at low temperature (Fig. 20) through the lipid exchange process discussed above. Note that the pattern of internal fluorescence is not altered by this procedure.

The present studies in combination with previous reports from this laboratory indicate that it is feasible to insert defined phospholipid molecules into the plasma membrane of intact cells using vesicle-cell interaction. This possibility should allow studies on the environment, metabolism, and fate of individual plasma membrane phospholipid species. We hope that future studies bear out our current optimism.

#### LIPID CAPPING IN LYMPHOCYTES

*A. J. Schroit*

We have previously shown it to be possible to integrate haptenated phospholipids into the plasma membrane of Chinese hamster fibroblasts by transfer of the lipid from small unilamellar vesicles (liposomes). We have also shown that the incorporated phospholipid antigen, N-2,4,6 trinitrobenzyl dioleoylphosphatidylethanolamine (Tnp-DOPE), diffuses freely in the plane of the membrane and is capable of undergoing an antibody-mediated redistribution in the presence of divalent antihapten antibodies.



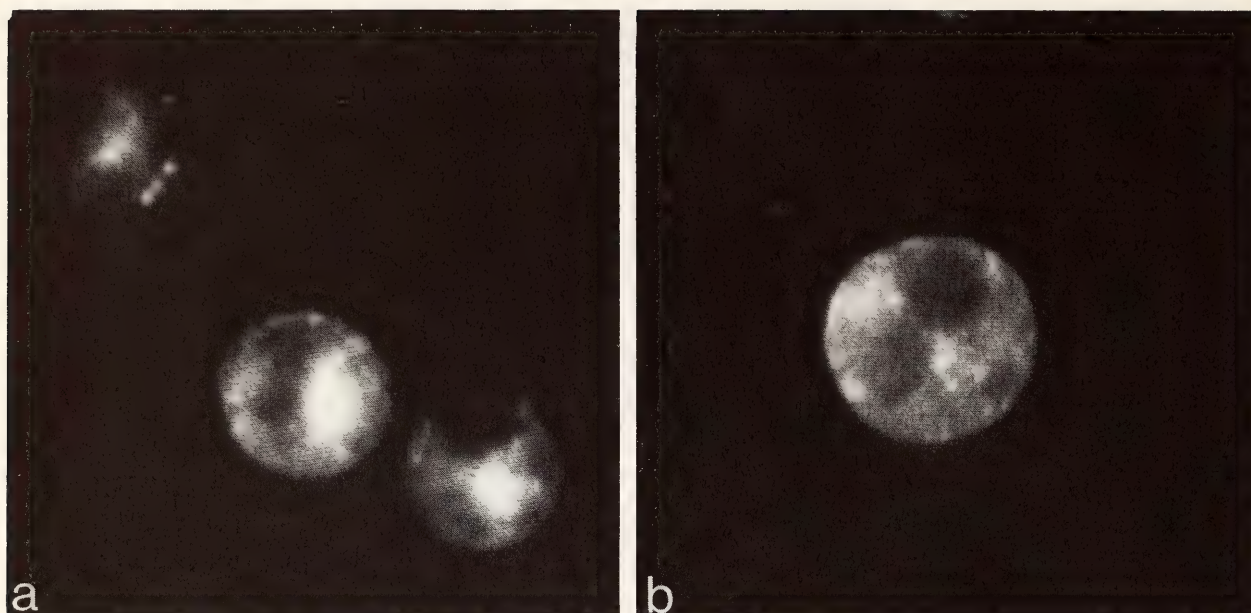


Fig. 20. Removal of cell surface NBD-PC by incubation of fluorescent cells with dioleoylphosphatidylcholine vesicles at low temperature. Cells were incubated as in Figure 19 in the absence (a) or presence (b) of 25 mM deoxyglucose and 10 mM sodium azide. The cells were then washed and incubated with dioleoylphosphatidylcholine vesicles for 30 min at 2°C, washed, and immediately photographed.

During the last year these studies have been extended to another cell system, the mouse T-lymphocyte, which serves a central role in a variety of immunological phenomena. In order to obtain many cells of reasonable purity we have chosen to use a model system, the EL-4 T-lymphocyte lymphoma line, which is cultivated *in vivo* in the ascites form. The way the Tnp-DOPE vesicles interact with lymphocytes was determined by incubating cells with vesicles containing the haptenated lipid on the external leaflet of the vesicle bilayer. The results presented in Table 4 demonstrate that significant amounts of lipid become cell associated within 1 hour at 0° and 37°C. It is interesting to note that the ratio of DOPE to Tnp-DOPE in the cells was nearly identical to that of the original vesicle suspension and that the presence of metabolic inhibitors during the incubation period had little effect on the absolute and relative amounts of lipid taken up by the cells. The foregoing results suggest that the Tnp-DOPE vesicles are being taken up as intact structures, and are

consistent with vesicle-cell fusion, adsorption, endocytosis, or some combination of these processes. However, it appears that endocytosis can be ruled out as a significant factor of vesicle uptake in this system, since the presence of metabolic inhibitors during the incubation period had only minimal effects.

Additional evidence strongly suggesting that the lipid vesicles are not simply adhering as intact entities to the lymphocyte surface was obtained from experiments with vesicles containing entrapped self-quenching concentrations of the water-soluble fluorophore carboxyfluorescein (Table 5). The rationale behind these experiments is that if intact vesicles were adhering to the cell surface, the addition of detergent to lyse the cells would result in dilution of the vesicle-entrapped fluorophore and would result in increased fluorescence intensity. If, on the other hand, vesicle lipids were simply being transferred to the lymphocyte surface, little or no fluorophore should become cell associated and the addition of detergent should not result in any in-



TABLE 4. Uptake of Haptenated Phospholipid by EL-4 Cells

	Cell-Associated Lipid cpm/10 <sup>7</sup> Cells*		
	Tnp-DOPE	DOPE	DOPE/ Tnp-DOPE
Vesicles	...	...	0.60
EL-4 incubated 0°C	22305	14305	0.64
EL-4 incubated 37°C	37742	23446	0.62
EL-4 incubated 37°C + inhibitor†	32405	18618	0.57

\* Cells were incubated with vesicles composed of Tnp-<sup>3</sup>H DOPE; DOPE (external leaflet) and <sup>3</sup>H DOPE; DOPC (internal leaflet) for 1 hr.

† Cells were coincubated with vesicles and 5 mM NaN<sub>3</sub> and 50 mM deoxyglucose.

crease in the intensity of the fluorescence. The results of these experiments (Table 5) strongly suggest that the Tnp-DOPE vesicles do not associate with lymphocytes via cell-vesicle adhesion. This is in contrast to the increase in fluorescence found upon detergent lysis of lymphocytes treated at 0°C with vesicles composed of saturated lipids [Tnp-dipalmitoylphosphatidylethanolamine (Tnp-DPPE)] which have been shown to preferentially adhere to cell surfaces (Table 5).

Other control experiments were carried out in order to rule out the possibility that Tnp-DOPE vesicles were taken up by a stable vesicle-cell adsorption. Scanning electron micrographs of EL-4 cells treated with Tnp-DOPE vesicles failed

to reveal any vesicles or vesicular-like material adsorbed to the cell surface, although adherent vesicles composed of saturated lipids (Tnp-DPPE) are readily visible by this technique (Fig. 21). Furthermore, transmission electron micrographs of lymphocytes incubated with these vesicles and stained with rabbit anti-Tnp antibodies followed by ferritin-conjugated anti-rabbit antibodies demonstrated the absence of vesicular structures at the cell surface, although large amounts of ferritin were present. These findings are consistent with our previous observations that vesicles composed of saturated or unsaturated lipids preferentially adsorb or fuse/exchange, respectively, with the cells (*Year Book 76, Year Book 77*).

TABLE 5. Release of Carboxyfluorescein from Cell-Associated Vesicles

	Relative Fluorescence*		Net Increase
	—Triton	+Triton	
<i>Control Vesicles</i>			
Tnp-DPPE/DPPC	0.05	3.5	70
Tnp-DOPE/DOPC	0.06	1.73	28.8
<i>Vesicle-Treated Cells†</i>			
Tnp-DPPE/DPPC	0.13	4.7	36.1
Tnp-DOPE/DOPC	1.9	3.6	1.9

\* Arbitrary units.

† Vesicles containing 200 mM CF composed of saturated (Tnp-DPPE/DPPC) or unsaturated (Tnp-DOPE/DOPC) lipids were incubated with EL-4 cells at 0°C for 1 hr. The cells were then washed and the relative fluorescence of 10<sup>6</sup> cells was determined before and after the addition of Triton X-100 (2% final concentration).



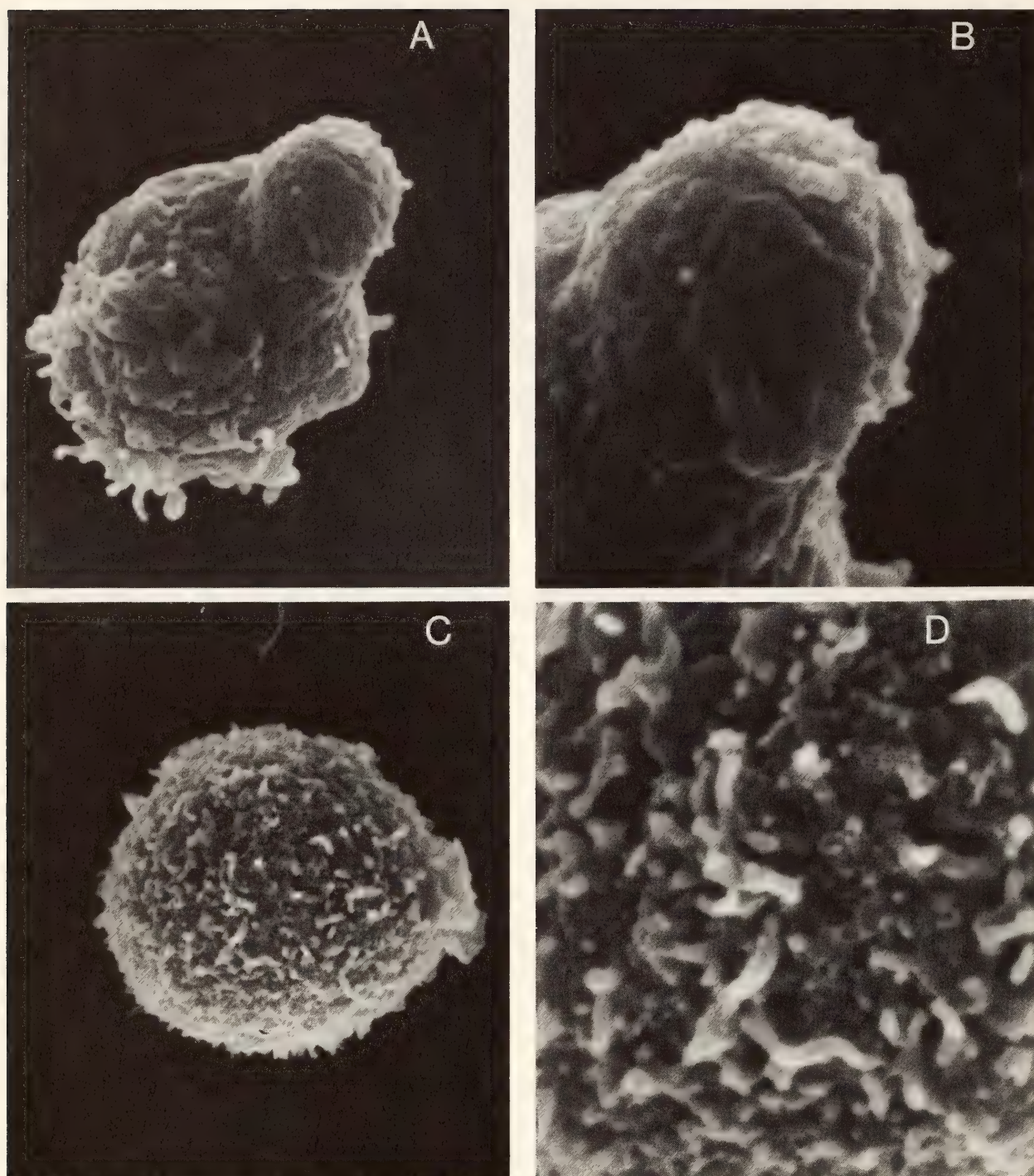


Fig. 21. Scanning electron micrographs of vesicle-treated EL-4 cells. (A), (B) Tnp-DOPE/DOPC vesicles; (C), (D) Tnp-DPPE/DPPC vesicles.

*The Distribution of Tnp-DOPE  
at the Cell Surface*

The distribution of the exogenously supplied Tnp-DOPE in the plasma membrane of the vesicle-treated lymphocytes was determined by staining the cells with fluorescein-conjugated anti-Tnp antibodies. It should be emphasized that the

antibody treatments were carried out at 0°C to prevent redistribution of the haptenated lipid in the cell surface (see below). Lymphocytes treated with Tnp-DOPE vesicles for 1 hour at 37°C were washed and stained at 0°C with the fluorescent antibodies. The distribution of the lipid hapten in the cell surface was then determined by fluorescence micros-



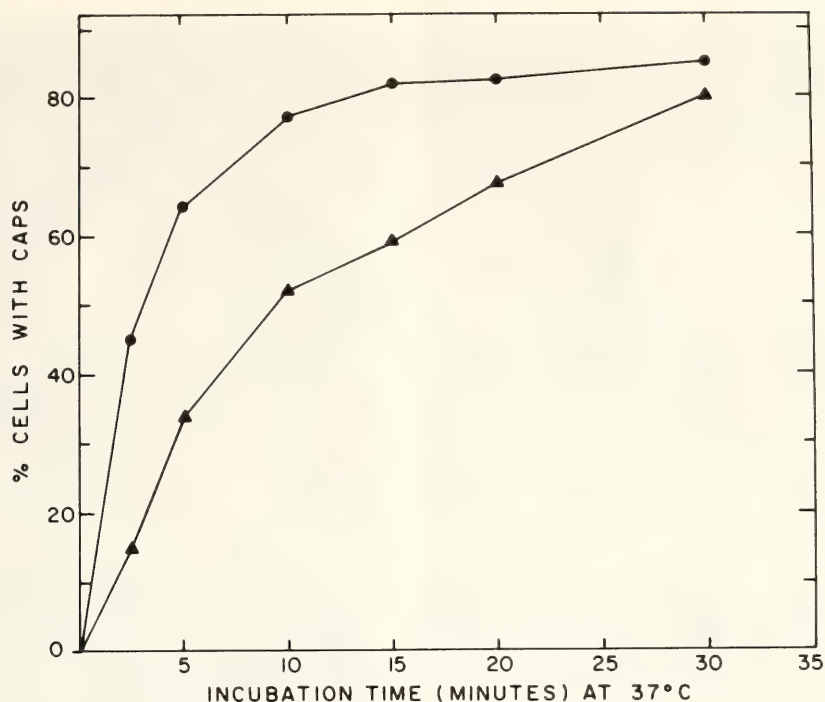


Fig. 22. Capping of Tnp-DOPE in EL-4 cells: vesicle-treated (Tnp-DOPE/DOPC) cells were incubated at 37°C for various periods in the presence (●—●) or absence (▲—▲) of Tnp antibodies.

copy, which revealed the lipid to be in a highly patched or capped form. Although the capping of the lipid could be completely inhibited by adding metabolic inhibitors to the incubation medium, this result excluded the possibility of carrying out any detailed analysis on the rate and general characteristics of the capping phenomena in these cells. The following experiments were therefore carried out on the cells incubated with vesicles at 0°C, a procedure which inhibited redistribution of the inserted Tnp-DOPE.

Lymphocytes treated with Tnp-DOPE at 0°C were washed free of excess vesicles and then incubated at 37°C for various periods of time. The percentage of capped cells was then determined after staining with fluorescein antibody in the cold. Figure 22 shows that within 30 minutes at 37°C more than 80% of the lymphocytes have confined the haptenated lipid to a cap, the remainder of the cell surface being void of the Tnp-DOPE. This phenomena of lipid capping was completely inhibited by sodium azide or

cytochalasin B. On the other hand, if the lipids were allowed to cap following treatment of the cells with anti-Tnp antibody, the rate of capping was much faster. Thus by using this technique one could easily distinguish between a relatively slow antibody-independent capping and a fast antibody-dependent capping (Fig. 22). In either case the sequence of events leading to formation of the cap is similar to the sequence in the capping of a variety of cell surface receptors: one observes the progression of a uniformly labeled cell transform into a spotty ring, to large aggregates, and finally to a cap, which may coincide with the formation of a uropod (Fig. 23). It should be noted that a uniform distribution of the fluorescent antibody on the cell surface is difficult to obtain, and patching appears to progress relatively well even at 0°C. This finding suggests that the precise mechanism of lipid capping may be different from those mechanisms postulated to be responsible for the capping of a variety of cell surface re-

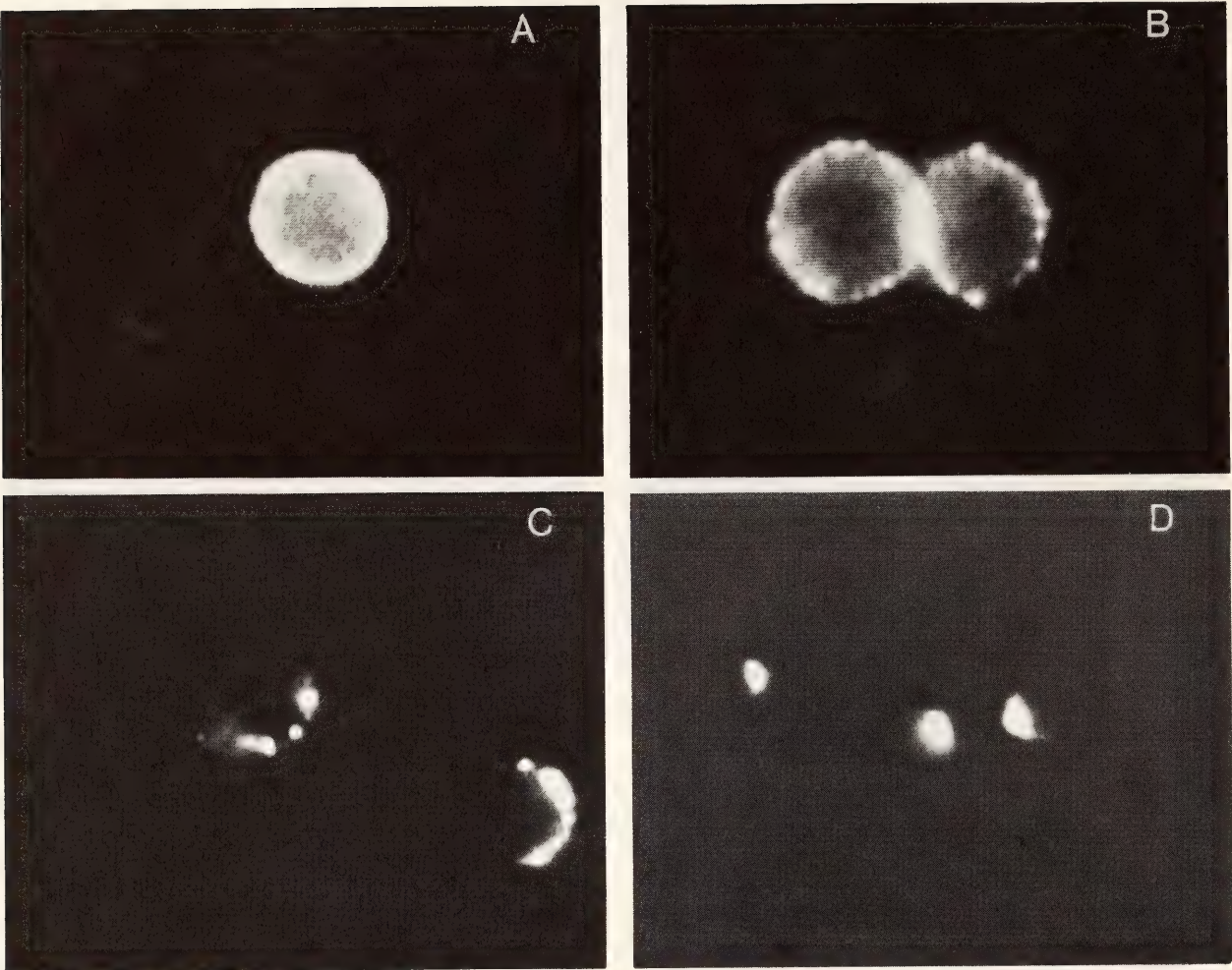


Fig. 23. Redistribution of Tnp-DOPE in EL-4 cells: vesicle-treated cells were incubated with fluorescein anti-Tnp for 20 min at 0°C. The cells were then washed, and incubated at 37°C for 0 (A), (B), 1 (C), or 5 (D) min.

ceptors. The capping of lipids requires metabolic energy, as it is completely inhibited by cold temperatures and by a variety of metabolic inhibitors. The capping process is also extremely sensitive to cytochalasin B, a microfilament disrupting agent. On the other hand, capping is not inhibited by the microtubule depolymerizing vinca alkaloids; nor is it affected by local anesthetics, in contrast to the capping of some lymphocyte surface antigens (Table 6). It is difficult to see just how a lipid molecule can be capped by the cell, as cross linking does not appear to be a prerequisite for this process, although it is enhanced by it. Furthermore, the sensitivity of the process to cytochalasin B

TABLE 6. Effects of Various Drugs and Experimental Manipulations on the Capping of Tnp-DOPE on EL-4 Cells

Treatment*	Cells with Caps (%)
0°C	0
37°C	>85
Xylocaine (10 <sup>-4</sup> M)	>85
Chlorpromazine (10 <sup>-4</sup> M)	>85
Cytochalasin B (10 µg/ml)	< 5
Colchicine (10 <sup>-4</sup> M)	>85
Cytochalasin B + colchicine	0
NaN <sub>3</sub> (0.2%)	< 5

\* Tnp-DOPE/DOPC vesicle-treated cells (1 hr at 0°C) were stained with fluorescein-conjugated anti-Tnp antibodies for 20 min at 0°C. The cells were washed, suspended in the various solutions, and incubated at 37°C for 15 min.



suggests that microfilaments may play a role in this process, although whether microfilaments control lipid mobility directly or indirectly remains to be shown.

Experiments to determine how this process proceeds are now in progress. It is possible that the integrated vesicular lipids exist in the form of molecular clusters in the cell membrane and behave like multivalent antigens. This would explain the differences in the rate of capping in the presence and absence of divalent anti-Tnp antibodies. As microfilaments probably do not transverse the

plasma membrane, however, it is unclear just how such structures can react with the outer half of the lipid bilayer (those lipids detected by the anti-Tnp antibodies). Alternatively, our findings are consistent with the possibility that there is a continuous, directed flow of cell surface lipids, which Bretscher and others have postulated to be responsible for the general capping of cell surface receptors. To test this possibility, experiments are now in progress to quantify the rates of lateral diffusion and flow of lipids in the cell surface.

## GENETIC DISSECTION OF CELL MORPHOLOGY

*Samuel Ward, Yair Argon, Gregory Nelson, Thomas Roberts*

Most differentiated cells have a distinct morphology that enables them to perform their specialized functions. They acquire this morphology during development by the expression of distinct gene products and the localization of gene products to specific parts of the cell. In asymmetric cells, such as neurons, many gene products must be localized. But which gene products are these? How is the information that determines their localization specified? What guides them to their final location and what holds them there? And how does this localization generate the cell's final form?

We have been attempting to answer some of these questions by studying mutants that alter the morphology of a differentiated cell. By analyzing mutant cells biochemically and histologically we hope to identify gene products that are asymmetrically localized and that function to determine the shape of a cell. By examining the morphological consequences of mutations altering these gene products, we hope to deduce the normal function of the mutated products.

The organism we study is the soil nematode *Caenorhabditis elegans*. It was chosen because it is readily grown in the

laboratory and is ideal for mutant isolation and genetic manipulation. The nematode cell we have been studying is the sperm. Sperm were chosen because they have a specialized morphology, they can be isolated in sufficient quantities for biochemical characterization, and because sperm-defective mutants can be recognized by their sterile phenotype.

In the previous report (*Year Book 77*) we described the isolation and initial characterization of nine fertilization-defective (*fer*) mutants that had defective sperm. We have since isolated five more, so that a total of 11 *fer* genes have been identified. Table 7 summarizes some of the properties of these mutants. During the past year, several important advances have aided our analysis of mutant and wild-type sperm. The discovery of proper conditions for studying sperm motility and development in vitro has enabled detailed comparisons of mutant and wild-type sperm (see Nelson, below); the detection of lectin receptors, which could be studied histochemically on the sperm surface and biochemically on fractionated components, allows correlation between biochemical and morphological studies (Argon, below); the

TABLE 7. Fertilization-Defective Mutants\*

Gene	Alleles	Morphological Defect	Motility
<i>fer-1</i> I	<i>hc1ts</i> ; <i>hc13ts</i> ; <i>hc24ts</i> ; <i>hc8</i>	short pseudopod; no MO fusions	pseudopods move, no translocation
<i>fer-2</i> IV	<i>hc2ts</i>	variable; defective pseudopods	none
<i>fer-3</i> I	<i>hc3ts</i>	short aberrant pseudopods; inclusions	mostly nonmotile
<i>fer-4</i> V	<i>hc4ts</i>	smooth pseudopods; 43 nM tubules	none
<i>fer-5</i> IV	<i>hc23ts</i>	few pseudopods; few MO fusions; inclusions	none
<i>fer-6</i> I	<i>hc6ts</i>	few pseudopods; inclusions	none
<i>fer-14</i> X	<i>hc14</i>	normal by SEM	normal
<i>fer-15</i> II	<i>hc15ts</i>	...	normal

\* Fertilization-defective (*fer*) genes are listed with a roman numeral designating their linkage group. Alleles are independently isolated mutations in each gene; ts means temperature sensitive, other alleles are absolute and are maintained as balanced heterozygotes. Morphological defect summarizes the appearance of mutant sperm by scanning and transmission electron microscopy. Motility summarizes their movement. Three additional *fer* genes have been identified: *fer-7* (*hc34ts*) I, *fer-10* (*hc10ts*) IV, and *fer-9* (*hc9*) V; but their sperm have not been studied.

identification of an internal membrane complex in the sperm suggests a mechanism for asymmetrical arrangement of cell organelles (see Ward, below); the installation of a scanning electron microscope has allowed us to describe the morphology of mutant and wild-type sperm in more detail. Figure 24 shows the appearance of wild-type sperm and some of the mutant sperm.

NEMATODE SPERM MOTILITY

Greg Nelson

Nematode sperm are intriguing cells because they undergo a dramatic terminal differentiation, which produces a mature spermatozoan capable of rapid movement over large distances and cap-

able of specific interactions with the ovum. The ease of genetic manipulation of *C. elegans* makes its sperm a unique model for genetic analysis of cell motility that might identify the gene products necessary for movement. The transparency of the worm allows study of motility in vivo and the results described below show that motility can be studied and manipulated in vitro as well.

Sperm can be prepared for in vitro examination by dissecting them from males into a medium of low osmotic strength supplemented with protein. This medium permits the development of primary spermatocytes into haploid spermatids and promotes the active motility of mature spermatozoa.

When round young virgin males are



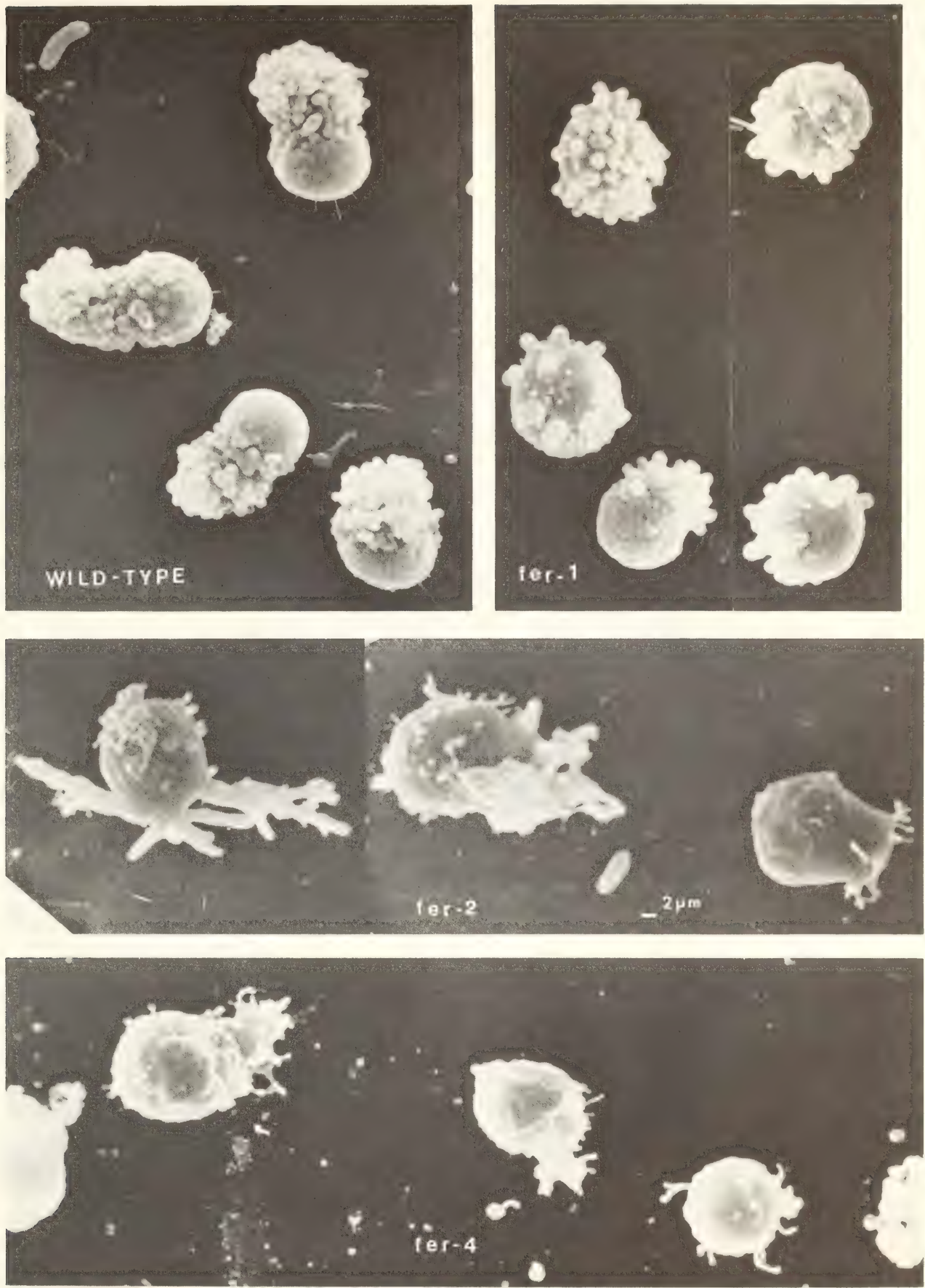


Fig. 24. Scanning electron micrographs of wild-type and mutant sperm. Bar = 2  $\mu$  for all sperm.



dissected, hundreds of spermatids are released into the medium. These are small, round cells, 4  $\mu\text{m}$  in diameter, whose surfaces contain a few randomly located microvilli. Spermatids are completely sessile.

If, however, sperm are obtained from older, actively mating males, a different result is obtained. Strikingly asymmetric, motile spermatozoa are released whose external morphology is shown in Fig. 24. Spermatozoa possess a single prominent

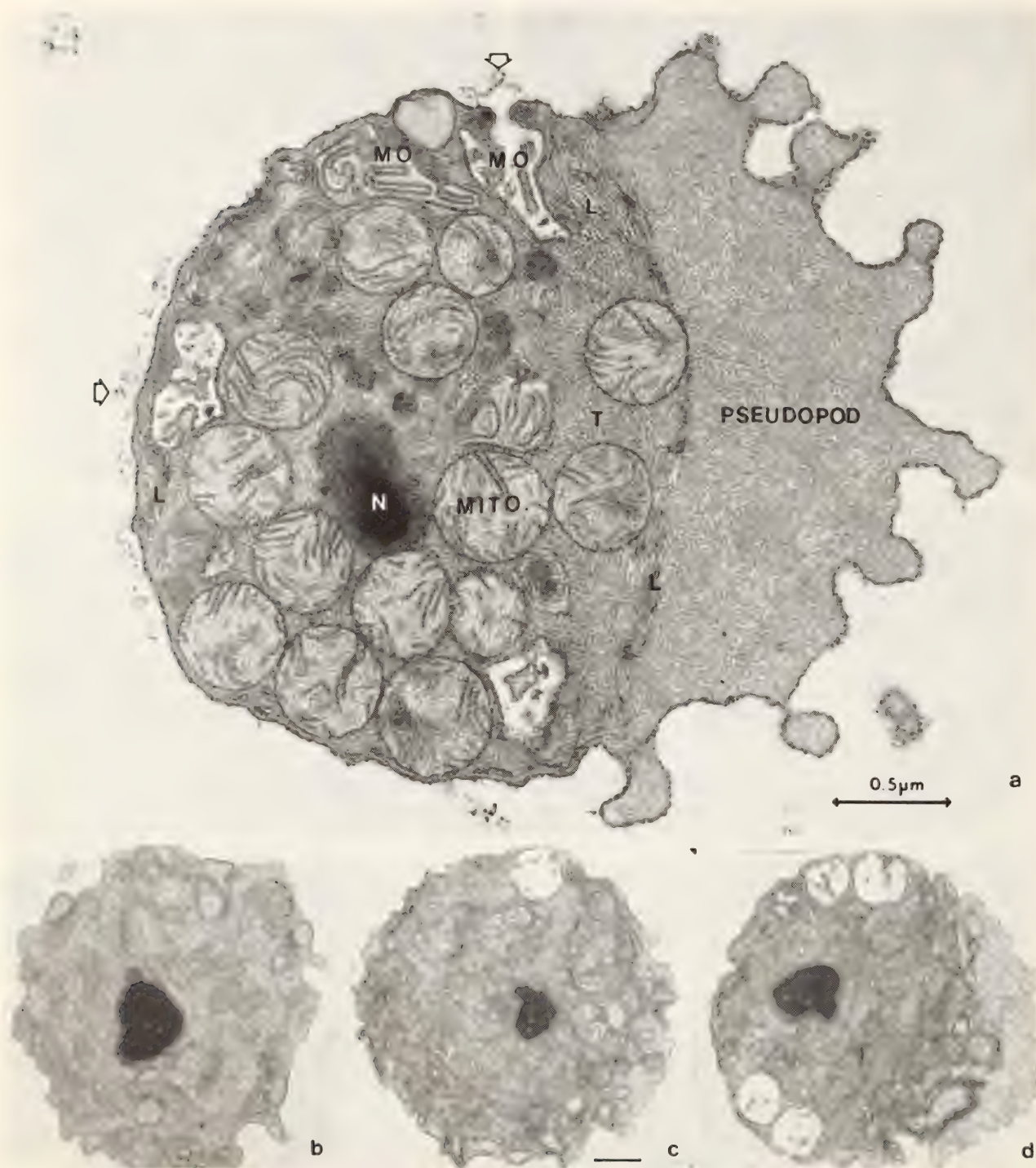


Fig. 25. Transmission electron micrographs of sperm. (a) Mature spermatozoa. *N* = nucleus, *MO* = membranous organelle, *L* = lamellar membrane, *T* = tubular elements, *mito* = mitochondria. Arrows show filamentous material released by *MO* fusion. The plane of section does not pass through the entire pseudopod, so it appears short. (b) Spermatid. (c) Early stage in pseudopod formation showing pseudopod on the right side of cell separated from organelles by the lamellar membrane. (d) Later stage of pseudopod formation.



pseudopod on their leading edges, which may extend several microns from the cell body. These pseudopods are studded with numerous stubby "projections." Transmission electron microscopy shows that all subcellular organelles are located in the hemispherical cell body (Fig. 25), whereas the pseudopod is composed of an amorphous or granular material devoid of filaments under all fixation conditions tested.

Spermatozoa move in the direction of their pseudopods at rates up to  $10\text{ }\mu\text{m}/\text{min}$ , which is comparable to the fastest amoeboid metazoan cells. As they move, the pseudopods change shape, and the projections are seen to move back toward the cell body at speeds comparable to the cell's forward movement (Fig. 26). When the pseudopod changes shape and makes new attachments with the substrate, the direction of motion of the cell changes, with the cell body tagging along behind the pseudopod. Trailing retraction fibers which may be relics of old attachments (Fig. 24) are occasionally seen. Sperm may also change direction abruptly when their pseudopods detach from the substrate. They swirl and ruffle until new attachments are formed and

the cell makes a beeline in another direction. Motility of sperm in vitro looks identical to that observed in vivo. Both qualitatively and quantitatively, the motility of *C. elegans* sperm resembles that of mammalian white blood cells.

The age and mating experience of the male are two critical physiological factors which control the activation of spermatids into spermatozoa. The results of several experiments suggest that, as in the parasitic nematode *Ascaris*, a substance made in the male vas deferens is released into the lumen of the gonad during copulation and triggers spermatids to mature into spermatozoa. We have screened numerous biologically active chemicals and extracts from nematodes and have recently succeeded in triggering this final maturation of sperm in vitro using the ionophore monensin. Monensin is known to transport monovalent cations across cell membranes and has a preferential affinity for sodium. Concentrations of the ionophore from  $10^{-7}$  to  $10^{-6}$  molar are maximally effective in inducing rapid pseudopod formation within 6 minutes of application. The effect is sensitive to external sodium and potassium concentration. Sperm acti-

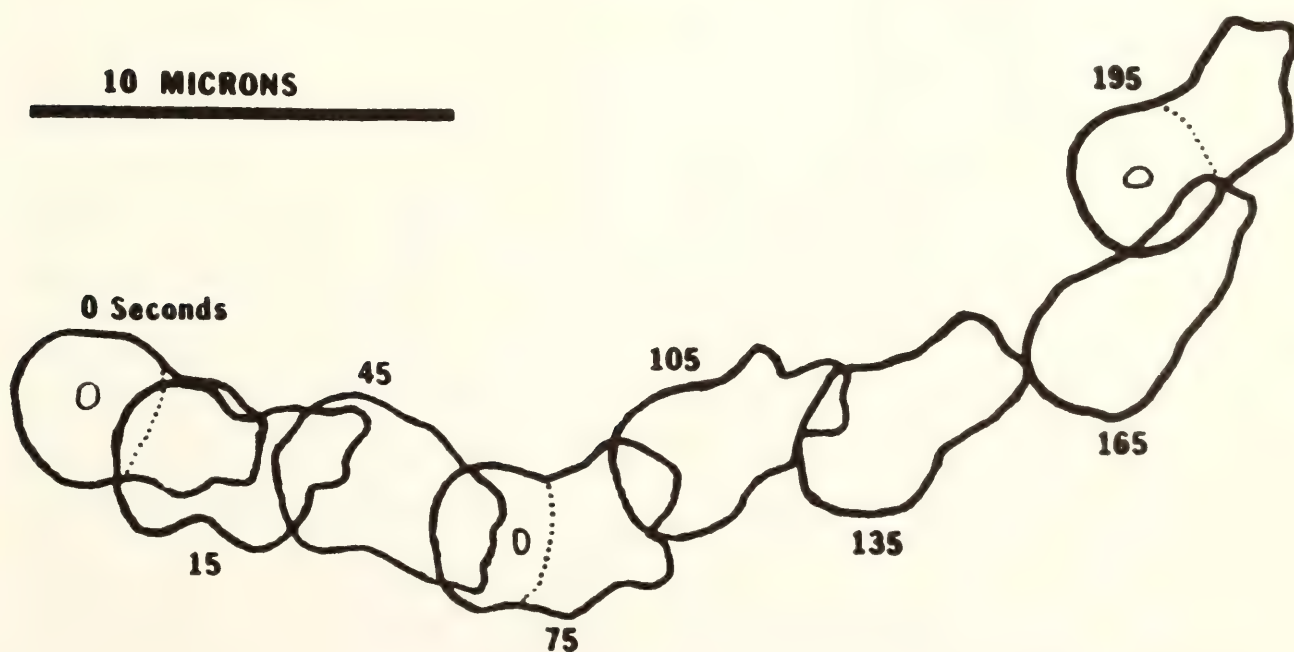


Fig. 26. Outlines of spermatozoa moving on a glass substrate as recorded on time-lapse video tape.

vated by monensin appear identical in morphology and behavior to mating-activated cells.

Mutants have begun to give us some insight into the genetic control of cell motility. Most *fer* mutants have sperm motility defects (Table 7). For example, *fer-1* mutants are capable of producing sperm that are activated by mating but fail to produce normal pseudopods. These cells possess a small cluster of pseudopodial projections at one end and are capable of developing motive force because they twitch and twirl, but they cannot direct their movement owing to an undersized pseudopod. In contrast, the *fer-4* mutant produces sperm with large pseudopods that are deficient in projections and do not move at all. These results show that the pseudopodial projections are essential for motility. In addition to the *fer* mutants, other investigators have isolated mutations in 14 genes which disrupt body muscles in *C. elegans*. Mutants in 11 of these genes were examined for sperm motility defects to help define the genetic relationship(s) between muscle and nonmuscle cell motility. Sperm in all 11 mutants were found to be normal.

To gain a more fundamental understanding of sperm motility, we carried out pharmacological, histochemical, and biochemical studies on sperm from *C. elegans* and the related nematode *Ascaris lumbricoides*. *Ascaris* sperm were examined because they are available in large quantities for biochemical studies. *Ascaris* sperm resemble *C. elegans* sperm in behavior and morphology, with the important exception that in *Ascaris* sperm, pseudopods contain some microfilaments. The protein actin, which is ubiquitous and highly conserved in all species, was the first target of these investigations because of its supposed role in nonmuscle cell motility.

Cytochalasins B, D, and E—drugs that disrupt cytoplasmic actin microfilaments in many cell types—have no effect on mature spermatozoa, although they quickly

inhibit cleavage in spermatocytes. Actin filaments can be identified histochemically by proteolytic fragments of muscle myosin which bind to actin filaments to give distinctive arrowhead structure. Filaments in the cortex of spermatocytes were decorated by myosin, but no decorated filaments were found in mature spermatozoa. Direct immunofluorescent staining of *C. elegans* and *Ascaris* sperm with fluorescent anti-actin antibodies reveals staining in the pseudopods of *Ascaris* sperm but not in *C. elegans* sperm.

Two-dimensional gel electrophoresis of sperm proteins, using nematode muscle actomyosin as a standard, indicates that little if any ( $< 1\%$  cell protein) protein in sperm migrates at the expected molecular weight (43,000) and isoelectric point (pH 5.5–5.7) for actin.

A sensitive assay for actin which measures the inhibition of DNaseI enzymatic activity failed to indicate the presence of any actin in sperm and further suggested the presence of a sperm component capable of releasing the inhibitory action of rabbit actin on the enzyme.

Taken together, these observations suggest that unlike other cells, nematode sperm are capable of rapid amoeboid movement with little or no actin.

## THE ACQUISITION OF SPERM ASYMMETRY

*Samuel Ward*

The scanning electron micrograph shown in Figure 24 reveals that the sperm is a highly asymmetric cell with an actively motile pseudopod on one side and a rigid cell body on the other. Figure 25 shows a transmission electron micrograph of a section through a similar cell. The pseudopod contains an amorphous granular cytoplasm devoid of filaments and organelles, whereas the cell body contains the nucleus, mitochondria, membranous organelles (MO), cytoplasmic tubular (T) structure, and a complex internal membrane lamellae (L) that appears to extend around the organelles and



is concentrated between the cell body and the pseudopod.

In order to understand how this asymmetry arises, we have studied the processes of spermatogenesis (formation of the haploid spermatid) and spermiogenesis (maturation of the spermatid to a motile spermatozoa) in detail. Four haploid spermatids are produced simultaneously by budding from one spermatocyte. A residual body containing unneeded cell components, ribosomes, rough endoplasmic reticulum, and golgi bodies, is left behind. After budding, the spermatids mature somewhat and accumulate in the male until copulation triggers them to complete spermiogenesis and become motile spermatozoa. Serial-section reconstruction of nine spermatids reveals that they are essentially spherically symmetric cells. The mitochondria and MO's are distributed uniformly around the central nucleus, and there is no hint of a pseudopod or site of pseudopod formation. The internal lamellar membrane extends around the periphery of the cytoplasm (Fig. 25b).

When the spermatid matures, the pseudopod begins to extend from one side of the cell (Fig. 25c) and the membranous organelles begin fusing at the other side. The internal membrane appears to accumulate between the organelles and the pseudopod, and builds up there as shown in a later stage of pseudopod extensions (Fig. 25d). The recent discovery that this maturation can be triggered in vitro (Nelson) will allow more complete description of the intermediate stages.

The fusion of the MO's and the extension of the pseudopod occur simultaneously in all normal cells, and this has led other workers to propose that the MO fusion caused pseudopod extension. The phenotypes of two mutants show that this is not the case in *C. elegans*. The sperm of *fer-1* mutants form pseudopods that are shorter than wild-type but still motile. However, their MO's never fuse with the plasma membrane (Year Book 77). In contrast, sperm of *fer-2* often

have most of their MO's fused but rarely extend pseudopods. These mutants reveal then that MO fusion is neither necessary nor sufficient for pseudopod extension, although it may be necessary to extend full-length pseudopods.

It has been proposed that the direction of pseudopod extension in other motile amoeboid cells is determined by the position of centrioles that organize the microtubular cytoskeleton to direct pseudopod extension. We have carefully examined the position of the centrioles in 40 spermatozoa with pseudopods. The position or orientation shows no correlation with the direction of pseudopod extension. In addition, the normal sperm have no detectable microtubules, so a conventional cytoskeleton cannot be involved in pseudopod extension.

These negative correlations caused us to examine the internal laminar membrane in more detail. It appears to accumulate preferentially between the pseudopod and the organelles during pseudopod extension as shown in Fig. 25 (b and c). The arrangement of this membrane structure is altered in some of the sperm that fail to form pseudopods owing to mutations in genes *fer-2*, *fer-5*, and *fer-6*. However, there is considerable variation in morphology of these mutant sperm, so this result is not easy to interpret. Further studies of the structure, composition, and dynamics of this internal membrane during in vitro maturation will be made.

## SPERM LECTIN RECEPTORS

*Yair Argon*

The spermatozoa of *C. elegans* exhibit distinct morphological asymmetry, as described above. The sperm membrane around the pseudopod is a dynamic structure that ruffles, changes shape, and mediates the cell's adhesion to substrate. In contrast, the membrane around the cell body appears rigid. The previous reports dealt with the cytoplasmic structures



that underlie this asymmetry. I am interested in determining if the membranes of the two parts of the cell differ in protein composition. If differences occur, I would like to identify the specific proteins involved and see if their presence or arrangement is altered in mutant sperm which exhibit abnormal morphology.

I chose to use lectins as ligands to identify surface molecules. Lectins are plant proteins that bind to specific carbohydrate residues on glycoproteins and glycolipids. I tested the binding of eight fluorophore-tagged lectins to live spermatids and spermatozoa, using fluorescence microscopy. Four of them stained spermatids brightly in a uniform ring of fluorescence; these were wheat-germ agglutinin (WGA), *Ricinus communis* agglutinin (RCA<sub>60</sub>), soy bean agglutinin (SBA), and *Lens culinaris* agglutinin (LCA). Spermatozoa, however, stain asymmetrically with all four lectins—the fluorescence intensity on the cell body is 3–5 times higher than on the

pseudopod. An example is shown in Fig. 27.

In addition to surface staining, Fig. 27 shows that WGA also stains a series of bright spots inside the cell. There are 10–25 spots per cell and they are confined to the cell body, adjacent to the cell membrane. These spots have never been observed in spermatocytes or in spermatids and are absent from spermatozoa of mutants in the gene *fer-1* in which the membraneous organelles (MO) remain unfused. I conclude from all these observations that the fluorescent spots represent the fused MO's. This identification of fused MO's by light microscopy will provide a useful method for screening mutant sperm that are defective in this membrane fusion process. Examination by electron microscopy of cells stained with ferritin-labeled WGA reveals that at least part of the asymmetric staining is due to staining of the MO contents which are released around the cell body.

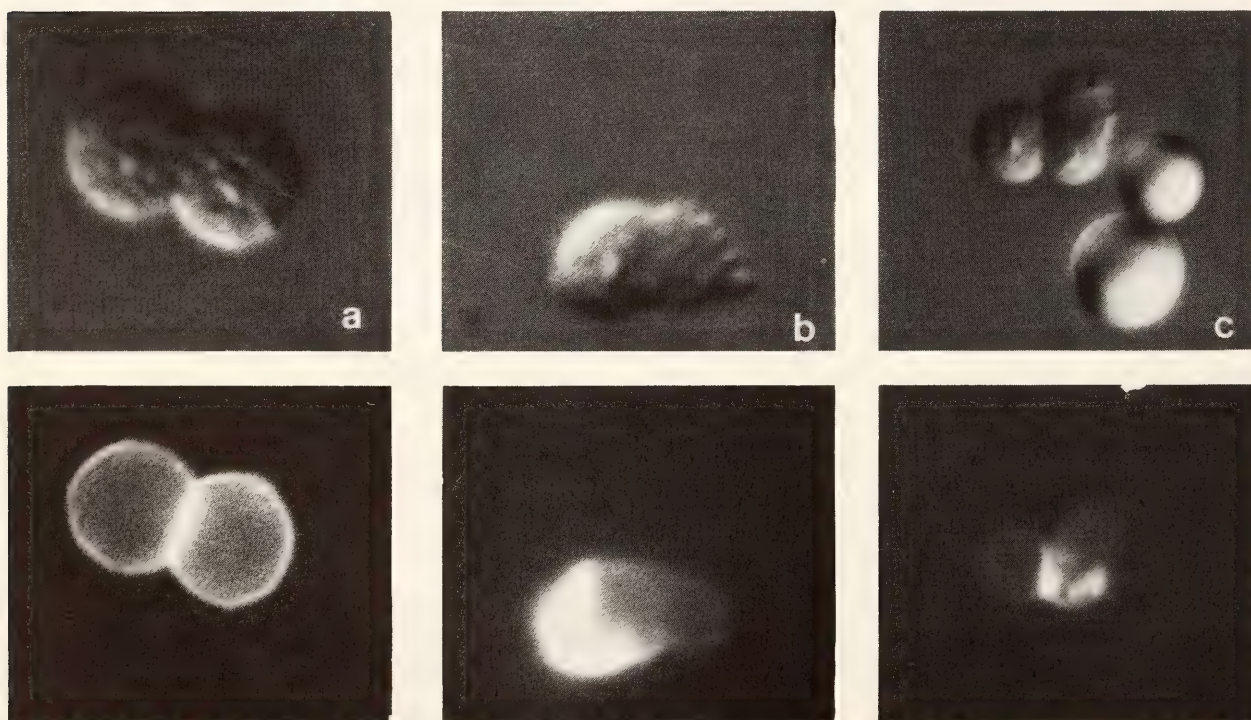


Fig. 27. Wild-type spermatids and spermatozoa stained with TRITC-WGA. Nomarski and fluorescence pairs of same cells. (a) Spermatids, magnification  $\times 1260$ . (b) Spermatozoan, magnification  $\times 1260$ . (c) Spermatozoan showing dotted staining in the cell body, while adjacent spermatid is surface-stained only. Bright spheres are latex beads. Magnification  $\times 680$ .



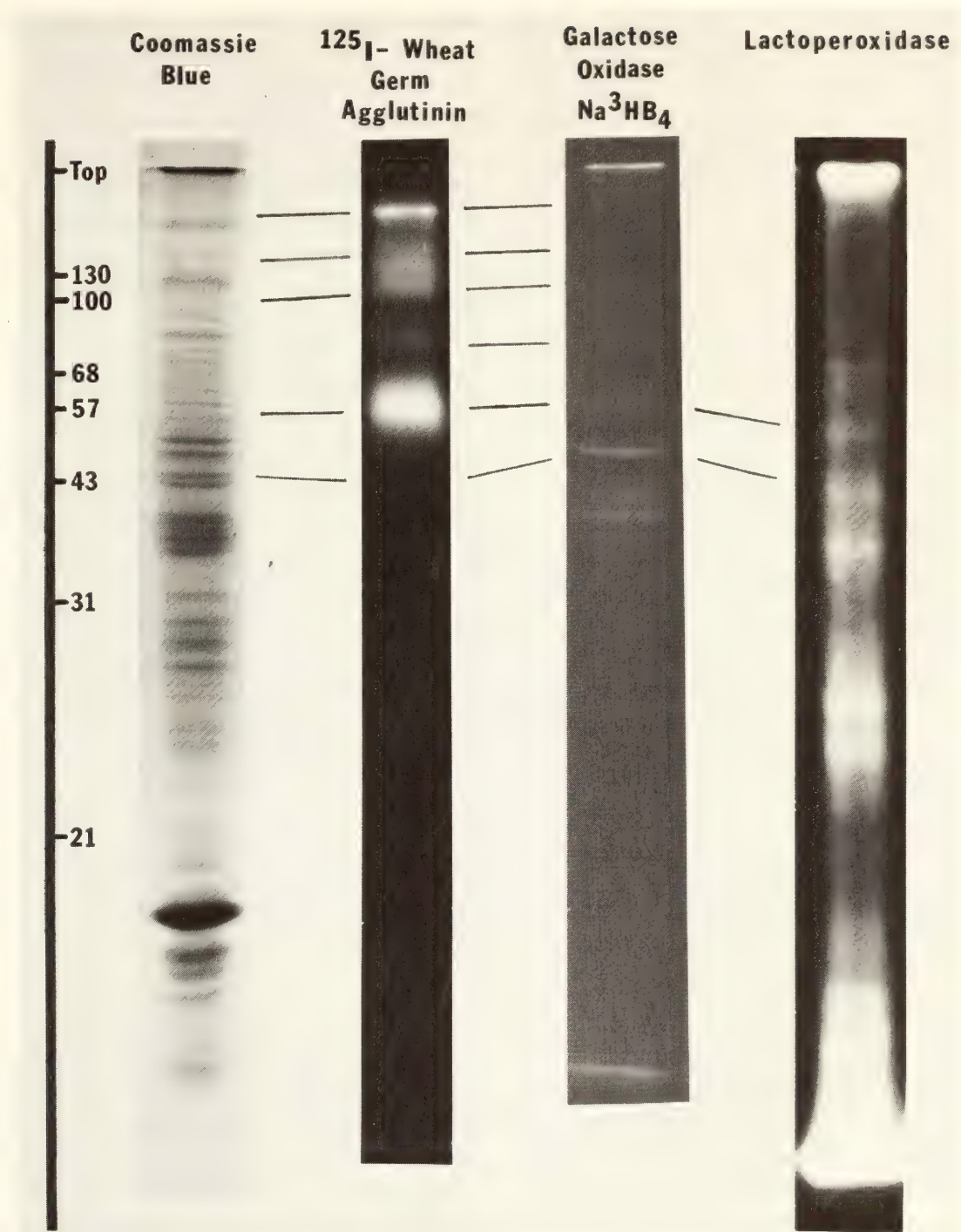


Fig. 28. SDS-PAGE of sperm proteins from wild-type males grown at 25°C. Molecular weight markers are shown on the left scale. The second lane was stained with <sup>125</sup>I-WGA after fixation and equilibration. The third and fourth lanes show surface-labeled sperm proteins detected by fluorography and autoradiography, respectively. The tops of the lanes were aligned. Because of their different lengths, bands with similar relative mobility are indicated with lines.

Since spermatids bind lectins uniformly but spermatozoa bind them asymmetrically, I asked if there is redistribution of lectin receptors upon activation of spermatids. Greg Nelson's recent discovery that the ionophore monensin can induce pseudopod formation provides a way of

probing such redistribution. When spermatids are first reacted with fluorescent WGA, LCA, or SBA and then treated with ionophore, a crescent of fluorescence is observed on the cell body and no fluorescence is detected on the pseudopod of cells induced to become spermat-

zoa. MO staining is also observed, so that fusion must occur during ionophore activation. Unactivated spermatids remain uniformly stained in the presence of ionophore. These observations imply that lectin receptors on the spermatid surface are confined to the cell body during extension of pseudopods. When the spermatids are first reacted with non-fluorescent WGA, induced to form pseudopods with ionophore, and then stained with fluorescent WGA, faint fluorescence is detected over the entire surface of spermatozoa. Unactivated cells show no fluorescence. This observation suggests that, in addition to the confinement of preexisting lectin receptors, new receptors are added to the cell membrane during pseudopod formation.

To determine the nature of the WGA receptors, I used the technique of Burridge, in which SDS-PAGE gels of sperm proteins were stained with  $^{125}\text{I}$ -lectin and

stained bands identified by autoradiography. Seven lectin-binding bands in the molecular weight range of 50–200 k were identified. All of them are presumably surface glycoproteins because they can be labeled on intact cells by the galactose oxidase- $\text{Na}^3\text{HB}_4$  treatment. All these glycoproteins can also be labeled by lactoperoxidase iodination of cells (Fig. 28).

These studies show that the morphological asymmetry of *C. elegans* spermatozoa is reflected in molecular asymmetry of the sperm membrane. A set of surface glycoproteins undergo redistribution during activation of the sperm, resulting in an asymmetric distribution in the cell membrane. Their role in the final shape of the spermatozoan and their relation to the function of the sperm motility and fusion with ova will be analyzed using the sperm-defective mutants that have been isolated.

## EXPRESSION OF ANTIBODY VARIABLE AND CONSTANT REGIONS DURING B-CELL DIFFERENTIATION

*Patricia J. Gearhart*

The immunoglobulin system has provided fascinating insights into gene expression during cell differentiation and gene diversity. The antibody molecule is comprised of two types of polypeptides, light (L) and heavy (H) chains. All polypeptides are divided into an  $\text{NH}_2$ -terminal variable (V) region and a  $\text{COOH}$ -terminal constant (C) region. Multiple genes code for V and C regions. In addition to the large number of V genes that code for antigen-combining sites, the murine H-chain locus has as many as 10 C genes ( $\text{C}_\text{H}$ ) which determine the class of immunoglobulin molecule (e.g., IgM, IgG, IgA, IgD, or IgE).

As precursors (B-cells) to antibody-secreting cells have the potential to respond to an antigen by producing antibodies of several immunoglobulin classes,

it is of basic interest to study what determines which  $\text{C}_\text{H}$  region is expressed during cell differentiation. The control of  $\text{C}_\text{H}$ -region expression is being approached (1) by establishing the dynamics of antibody expression during the differentiation of a clone and (2) by correlating the class of surface immunoglobulin on a cell to that produced by its clonal progeny after antigen stimulation.

The immune system is unique in that it can generate as many as  $10^5$ – $10^8$  antibodies with different antigen-combining sites. However, many of our concepts of V-region diversity are based on the amino acid sequences of randomly produced myeloma proteins, which may represent only a selected population of immunoglobulins. Diversity among functional antibodies is being studied by



determining the amino acid sequence of V regions of antibodies produced in response to an antigenic stimulus. A comparison of the antibody V-region repertoire to the myeloma repertoire will indicate if they are equivalent or if antibodies are more diverse than the known sequences of myeloma proteins would predict.

### *The Dynamics of C<sub>H</sub> Expression during Intraclonal Differentiation*

Recent findings indicate that many B-cells have the potential to generate a clone of antibody-secreting cells producing several heavy-chain classes. Thus a single B-cell, after antigen stimulation, undergoes 6–8 divisions, and its clonal progeny produce IgM, IgG1, and IgA, which all have the same V-region antigenic determinants (idiotype), as measured by an anti-V region antisera (Fig. 29). The V and C genes for the H-chain polypeptide are located on a single chromosome, as shown in Fig. 30. As a B-cell

Heavy chain chromosome

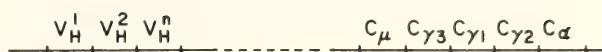


Fig. 30. Murine chromosome containing the V and C genes for the H chain.

is committed to expressing only one V region during its lifetime, the question arises how a V<sub>H</sub> gene can be associated with several C<sub>H</sub> genes during clonal expansion.

In collaboration with Julia Hurwitz and John Cebra at the Johns Hopkins University, I have examined the cells within clones producing multiple-immunoglobulin classes to determine (1) if cells produce one class per cell or two classes per cell and (2) if cells have the same potential at different times in clonal development to produce two classes per cell. The splenic focus technique of isolating single B-cells, developed by N. Klinman at Scripps Clinic, was used to prepare murine spleen fragments containing clones producing anti-phosphorylcholine (PC) antibody of the  $\mu$ ,  $\gamma$ 1, and  $\alpha$  classes. Fragments were dissociated and cells were stained with rhodamine, fluorescein, and <sup>3</sup>H-labeled antibodies to detect anti-PC antibody, and C <sub>$\mu$</sub>  and C <sub>$\alpha$</sub>  regions. The results in Table 8 indicate that (1) the majority of cells within clones secreting IgM, IgG1, and IgA produce only one class at a time, (2) 10–30% of cells stain for two heavy-chain classes, suggesting that cells switch during differentiation, and (3) the proportion of cells stained for both IgM and IgA decreases with time from 30% on day 7 after antigen stimulation to 10% on day 12.

Several molecular models can be used to explain multiple C<sub>H</sub> expression by a single cell. First, a V<sub>H</sub> gene may be duplicated and inserted next to each C<sub>H</sub> gene so that several V-C pairs can be transcribed simultaneously. Second, a V<sub>H</sub> gene may switch from one C<sub>H</sub> gene to

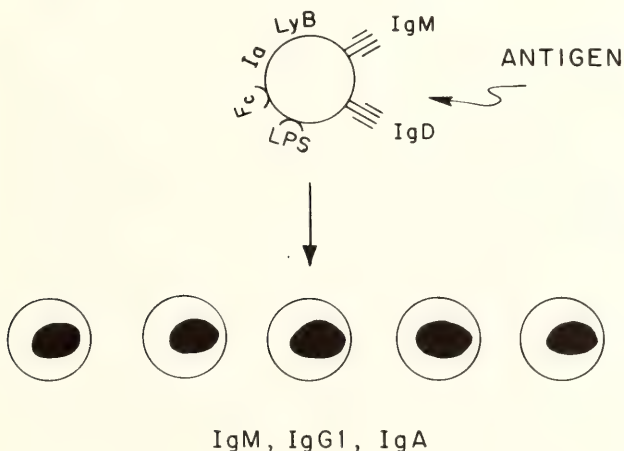


Fig. 29. Antigen stimulation of a B-cell followed by clonal expansion. A B-cell, bearing surface proteins such as immunoglobulin IgM and IgD, Ia and LyB antigens, and receptors for lipopolysaccharide and the Fc region of immunoglobulin, is triggered to divide after binding to antigen by its immunoglobulin receptors. The cell undergoes 6–8 divisions to generate a clone of cells secreting IgM, IgG1, and IgA antibodies, which all have the same V-region antigenic determinants as the precursor B-cell.

TABLE 8. Cells Containing IgM and IgA from Clones Secreting Several Immunoglobulin Classes\*

Cytoplasmic Staining of Cells Containing Anti-PC Antibody	Days after Antigen Stimulation	
	7	12
IgM only	7/46† (15%)	6/84 (7%)
IgA only	8/46 (17%)	23/84 (27%)
Other‡	17/46 (37%)	47/84 (56%)
Both IgM and IgA	14/46 (30%)	8/84 (10%)

\* Culture fluids from spleen fragments containing B-cell clones were assayed by radioimmunoassay six days after antigen stimulation to detect those fragments secreting anti-PC antibody of  $\mu$ ,  $\gamma 1$ , and  $\alpha$  H-chain classes. Some fragments were dissociated on day 7, and the cells were placed on a slide and stained for cytoplasmic immunoglobulin. Other fragments were dissociated on day 12 and stained. Cells were stained with PC conjugated to goat immunoglobulin followed by rhodamine-labeled rabbit anti-goat immunoglobulin, fluorescein-labeled rabbit anti-mouse IgM, and  $^3\text{H}$ -labeled rabbit anti-mouse IgA. After scoring cells for fluorescein and rhodamine fluorescence, slides were dipped in emulsion, and autoradiographs were developed one week later to detect IgA-containing cells.

† Data represent the number of cells stained for anti-PC antibody and the indicated immunoglobulin class, divided by the total number of cells stained for anti-PC antibody. The results are from 14 clones.

‡ Cells may contain IgG. The analysis is being continued to detect cells containing both cytoplasmic IgG and IgA.

another, and a cell staining for two classes contains the long-lived mRNA from a previous V-C joining as well as mRNA from the current V-C pair. Third, a long mRNA molecule which encodes information for the  $V_H$  region and several  $C_H$  regions may be differentially spliced to generate information for several immunoglobulin classes. Fourth, both maternal and paternal chromosomes may be activated so that one chromosome has rearranged to a V- $C_\mu$  pair and the other chromosome has rearranged to

a V- $C_\alpha$  pair. Although other investigators have shown that plasma cells secrete immunoglobulin from only one chromosome containing the  $C_H$  genes, cells from a developing clone may not be committed to transcription from a particular chromosome early in differentiation.

A test of the last model of multiple  $C_H$  expression by both chromosomes was made by collecting antibody from clones derived from  $F_1$  (BALB/c  $\times$  C57BL/6) mice and analyzing H-chain classes by radioimmunoassay for the presence of BALB/c or C57BL/6 alleles.  $C_H$  regions are polymorphic among strains of mice, and antibodies can be raised to recognize the antigenic differences of alleles. The results in Table 9 show that in a  $F_1$  clone making both IgG1 and IgA antibody, all of the antibody with  $C_{\gamma 1}$  and  $C_\alpha$  regions comes from one parental H-chain chromosome. All of the cells from a clone secreting several immunoglobulin classes are therefore committed to expressing  $C_H$  regions from only one chromosome.

#### *Correlation of Membrane $C_H$ Class to Secreted $C_H$ Class*

Some 80% of splenic B-cells have two classes of membrane immunoglobulin per cell—IgM and IgD (which is not secreted) (Fig. 29); 10% have IgG membrane immunoglobulin; and 10% have IgA. In collaboration with John Cebra, I am separating cells according to membrane H-chain class and analyzing the secreted antibody of daughter cells to determine if the class of membrane immunoglobulin on a B-cell will predict what class is secreted by the clonal progeny of that cell. Spleen cells are stained with rhodamine-labeled anti- $\mu$  (or anti- $\gamma 1$  or anti- $\alpha$ ), and the positively and negatively stained cells are separated in a fluorescence-activated cell sorter at the Johns Hopkins Medical School. IgM- (or IgG1- or IgA-) bearing cells are then stimulated in vitro with antigen, and the secreted antibody of each clone is analyzed for heavy-chain class by radioim-



TABLE 9. Immunoglobulin Classes Produced by F<sub>1</sub> Clones Come from One Chromosome

CB6F <sub>1</sub> /J Clone*	Nanograms Anti-PC Antibody†					
	Total IgG1	IgG1 <sup>a</sup>	IgG1 <sup>b</sup>	Total IgA	IgA <sup>a</sup>	IgA <sup>b</sup>
1	3.6	5.6	0	8.0	8.0	0
2	2.8	2.4	0	4.0	5.4	0
3	2.0	4.4	0	1.0	0.8	0
4	3.4	0	2.4	2.6	0	3.0
5	0.8	0	1.1	6.0	0	6.0
6	0.5	0	2.3	4.0	0	4.0

\* The data shown are representative of analyses of antibody from 14 clones from two F<sub>1</sub> (BALB/c × C57BL/6) donor mice. BALB/c mice have IgC<sub>H</sub><sup>a</sup> alleles and C57BL/6 mice have IgC<sub>H</sub><sup>b</sup> alleles. One half of the clones produced antibody with IgC<sub>H</sub><sup>a</sup> determinants and the other half produced antibody with IgC<sub>H</sub><sup>b</sup> determinants.

† Total IgG1 and IgA was determined by adding aliquots of culture fluids from clones to PC-bovine serum albumin-coated plastic microtiter plates, and detecting bound antibody with <sup>125</sup>I-labeled rabbit anti-mouse IgG1 or IgA. The following antisera were used to detect IgC<sub>H</sub> alleles: C57BL/6 anti-BALB/c IgG<sup>a</sup>, BALB/c anti-C57BL/6 IgG<sup>b</sup> (both antisera were graciously furnished by Mel Bosma, Institute for Cancer Research, Philadelphia), A/He anti-BALB/c IgA<sup>a</sup>, and rabbit anti-C57BL/6 IgA<sup>b</sup>, which was extensively absorbed by John Cebra to remove crossreactive antibody. All four antisera were demonstrated to be specific for the appropriate IgC<sub>H</sub> allele. The allotype of heavy-chain classes was determined by (1) adding aliquots of monoclonal culture fluids to PC-bovine serum albumin-coated plastic plates, (2) glutaraldehyde fixation (2.5 × 10<sup>-5</sup> M), (3) adding anti-allotype antisera, (4) glutaraldehyde fixation, and (5) adding <sup>125</sup>I-labeled rabbit anti-mouse IgG2 to detect anti-allotype antisera to IgG<sup>a</sup>, IgG<sup>b</sup>, and IgA<sup>a</sup> alleles, or <sup>125</sup>I-labeled goat anti-rabbit immunoglobulin to detect antisera to the IgA<sup>b</sup> allele. None of the clones produced IgG2 anti-PC antibody. Antibody was quantified from standard curves, using known quantities of antibody from C57BL/6 or BALB/c clones.

munoassay. With this protocol, we can analyze individual cells and their clonal progeny in a system where three heavy-chain classes can be expressed. The experiments are in preliminary stages, but one prediction might be that  $\mu$ -bearing cells are the precursors of clones producing several immunoglobulin classes, and  $\gamma$ 1 or  $\alpha$ -bearing cells are a more committed cell type and may secrete only IgG1 or IgA.

*Diversity of V Regions of  
Antibodies to Phosphorylcholine*

An animal responds to an antigenic determinant with a heterogeneous array of antibody molecules. A knowledge of the phenotype of V regions an animal

uses to respond to an antigen may be useful in studying the number and organization of germline genes at the DNA level. In a project done in collaboration with N. Johnson and L. Hood at Caltech, we studied diversity among antibodies produced in response to PC for two reasons: first, the amino acid sequence of five myelomas that bind PC is known and provides a basis of comparison and, second, analyses of the antigenic determinants on V regions and different affinities of antibodies for PC indicated that the repertoire of V regions would be heterogeneous. The sequences of several antibodies would indicate whether they resemble the V regions of PC-binding myeloma proteins or if antibodies are more diverse.

BALB/c mice were immunized with PC, and hybrid cells were made from spleen cells and nonimmunoglobulin-secreting myeloma cells. Ten hybridoma cell lines have been cloned and antibodies have been characterized for immunoglobulin class, V-region antigenic determinants, and affinity for PC. Cells have been grown in mice as tumors, and the antibody was purified on a PC-conjugated Sepharose column. H and L chains were separated and sequenced by N. Johnson at Caltech.

Preliminary results show that the V regions of H and L chains fall into three categories: (1) antibodies that have H- and L-chain sequences similar to those of the T15 myeloma, which is commonly found in anti-PC antisera, (2) antibodies that have L chains structurally similar to McPC 603, a PC-binding myeloma that has V-region antigenic determinants not commonly detected in the response to PC, and (3) an antibody that has an unusual  $\lambda$  L chain and an H chain belonging to a different subgroup than the PC-binding myelomas. The results suggest that antibodies produced by mice in response to PC will resemble those sequences already seen in PC-binding myelomas as well as new sequences. This analysis is being continued on more anti-PC antibodies to examine

patterns of diversity in the framework, hypervariable, and joining regions of the V region.

#### *A $V_H$ Region Shared by IgM and IgA*

It has been proposed that a  $V_H$  region can be associated with more than one  $C_H$  region, based on evidence of sharing of V-region antigenic determinants by IgM, IgG, and IgA antibodies, and the partial amino acid sequences of IgM, IgG, and IgA myeloma proteins. The issue of whether a complete  $V_H$  region can be joined to more than one  $C_H$  region is critical in considering one possible role of the putative joining (J) segment on the H chain, which contains the last 20 amino acids of the V region. Different J-coding genes may join to each  $C_H$  gene, so that a  $V_H$ - $C_\mu$  polypeptide would contain a different J segment than a  $V_H$ - $C_\alpha$  polypeptide.

The data in Fig. 31 demonstrates that a complete  $V_H$  sequence from residues 1–120 is shared by T15 (an IgA myeloma) and M-2 (an IgM hybridoma). The sequence data proves that one complete  $V_H$  region, including the putative J segment, is associated with both  $C_\mu$  and  $C_\alpha$  regions. This strongly suggests that a  $V_H$  gene can be rearranged next to any  $C_H$  gene on the heavy-chain chromosome.

## INTRODUCTION OF ISOLATED DNA SEQUENCES INTO CULTURED EUKARYOTIC CELLS

*Steven L. McKnight and Carlo Croce  
with the technical assistance of Bob Kingsbury*

During the past year we have been trying to develop a means to assay the expression of isolated structural genes. Structural genes, whose products are the messenger RNA's of eukaryocytes, are transcribed by RNA polymerase II. Although exciting advances have been made by Brown and his colleagues (*Year Book 77*, *Year Book 78*) regarding the in

vitro expression of isolated "polymerase III" genes, and by Reeder and Hipkind (*Year Book 77*), who have been studying the expression of a "polymerase I" gene in vitro, efforts to reconstitute faithful in vitro expression of structural genes have met with only modest success. Instead of attempting to construct a "test-tube" reaction assay, we are introducing



SAME  $V_H$  REGION IS SHARED BY  $C_\mu$  AND  $C_\alpha$

	1	30	60	90	120
T15 $V_H$	EVKLVESGGGLVQPGGSLRLSCATSGFTFSDFYMEWVRQPPGKRLEWIAASRNKANDYTTEYSASVKGRFIVSRDTSQSILYLQMNALRAEDTAIYYCARDYYGSSYWFYFBVWGAGTT				
M-2 $V_H$	-----				

Fig. 31. Complete amino acid sequence identity of  $V_H$  regions from IgM and IgA. The entire  $V_H$  region of T15, an IgA myeloma protein, is identical to that of M-2, an IgM antibody produced by hybridoma cells from BALB/c mice, indicating that the same  $V_H$  region can be shared by two immunoglobulin classes.

isolated structural genes into living cells by DNA-mediated transformation.

Richard Axel and his colleagues at Columbia University have shown that exogenous DNA can be stably introduced into cultured eukaryotic cells. The prototype system employs the herpes simplex virus type I (HSV1) thymidine kinase (tk) gene to transform tk-deficient ( $tk^-$ ) mouse fibroblasts to the tk positive ( $tk^+$ ) genotype. This selective system is particularly valuable, since  $tk^+$  cells will grow in medium containing hypoxanthine, aminopterin, and thymidine (HAT), but die when exposed to medium containing bromodeoxyuridine (BrdU). The reverse behavior is observed for  $tk^-$  cells.

We reasoned that the HSV-tk gene could be used to construct a “double-headed” vector: that is, a vector that could be introduced into and recovered from both eukaryotic and prokaryotic cells. We produced such a vector by inserting the HSV-tk gene into the prokaryotic plasmid pBR322. The vector can be maintained in bacteria, recovered in large quantities, and used to transform  $tk^-$  eukaryotic cells to the  $tk^+$  genotype. Now we are trying to recover the integrated vector from the genome of transformed  $tk^+$  cultured cells.

Figure 32 shows a restriction endonuclease map of an internal segment of HSV1. The map was prepared by Dr. Gary Hayward of the Johns Hopkins

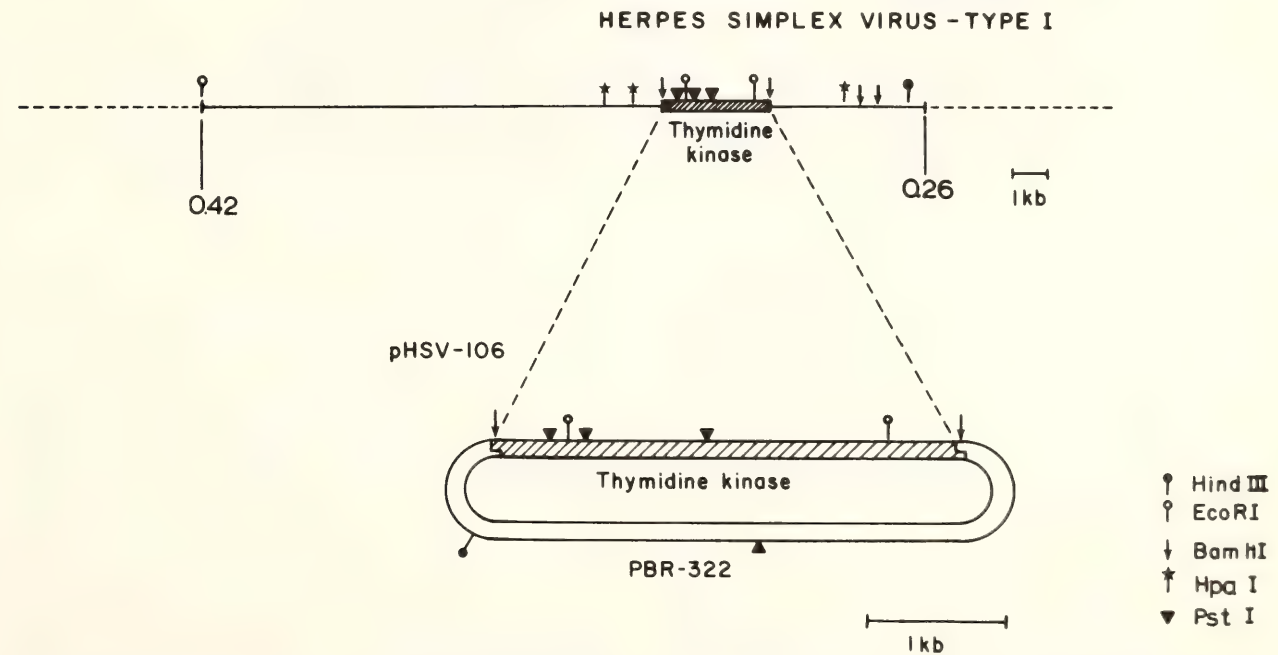


Fig. 32. A restriction enzyme map of an internal segment of HSV1 (upper diagram). Numbers below the HSV1 diagram refer to map units on intact viral DNA. The lower diagram shows a restriction enzyme map of plasmid pHSV-106. The plasmid contains a segment of HSV1 DNA inserted within the tetracycline-resistance gene of pBR322.

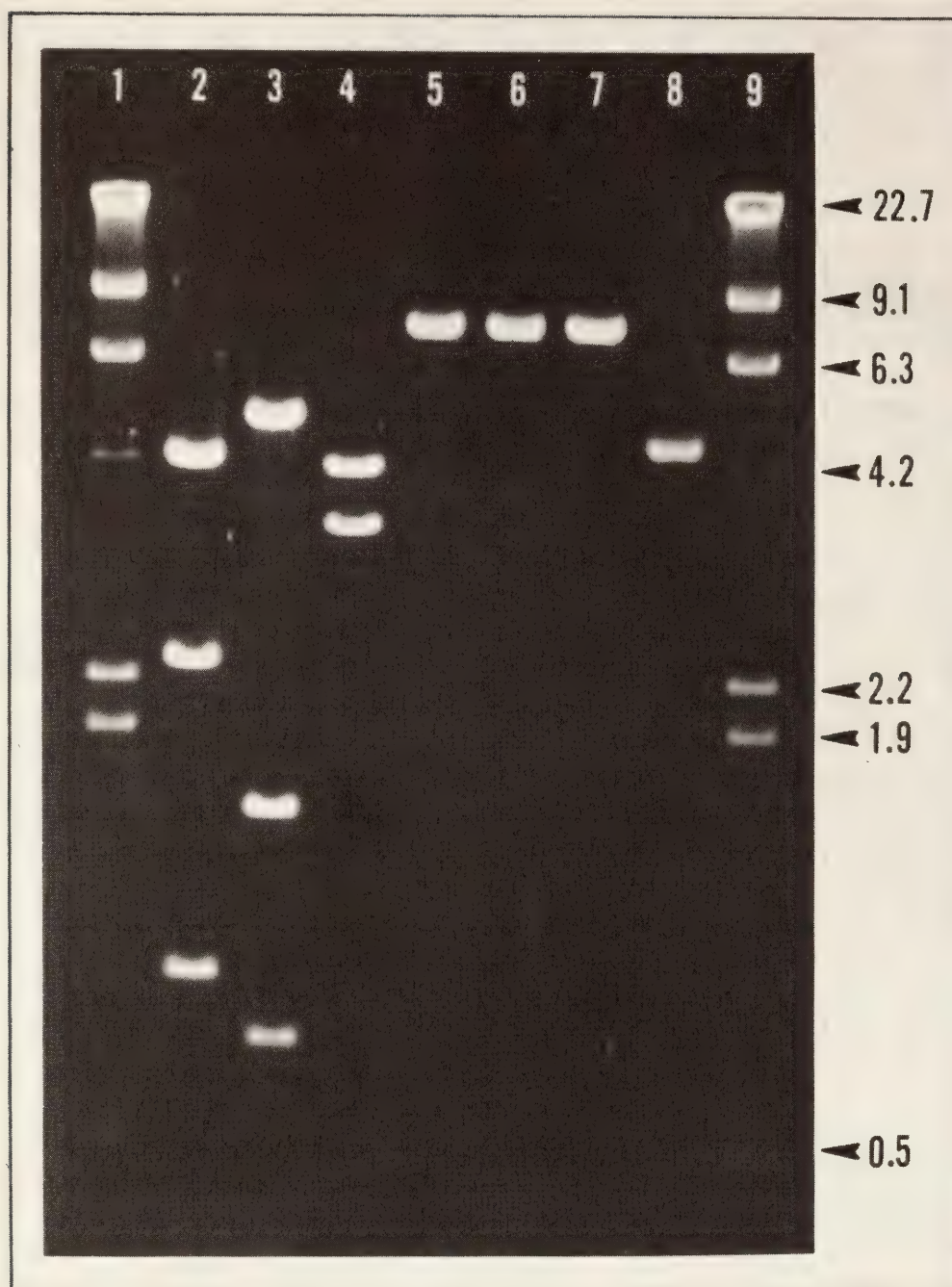


Fig. 33. Photograph of an agarose electropherogram upon which various restriction endonuclease digests of pHSV-106 were separated. DNA bands are visualized by ethidium bromide staining. Bacteriophage  $\lambda$  DNA digested with Hind III was electrophoresed in lanes 1 and 9 to provide molecular weight markers. Numbers adjacent to  $\lambda$  digestion products are estimated fragment sizes in kilobase pairs. Lanes 2-7 show restriction patterns of pHSV-106 after cleavage with Eco RI, Pst I, Bam HI, Pvu I, Sal I and Hind III, respectively. The latter three restriction enzymes cut once in the plasmid DNA but do not cut within the inserted HSV-tk DNA. Intact pHSV-106 DNA was run in lane 8.

University Medical School. In order to clone the tk gene we first digested HSVI DNA with the restriction enzyme Hpa I. Subsequent to this step the tk gene resided on a DNA fragment 8.3 kilobase (kb) pairs in length (see Fig. 32). The

8.3-kb fragment was separated from the remaining digestion product by agarose gel electrophoresis, recovered from the gel, and further digested with Bam HI. Axel and his colleagues had shown previously that the tk gene is contained



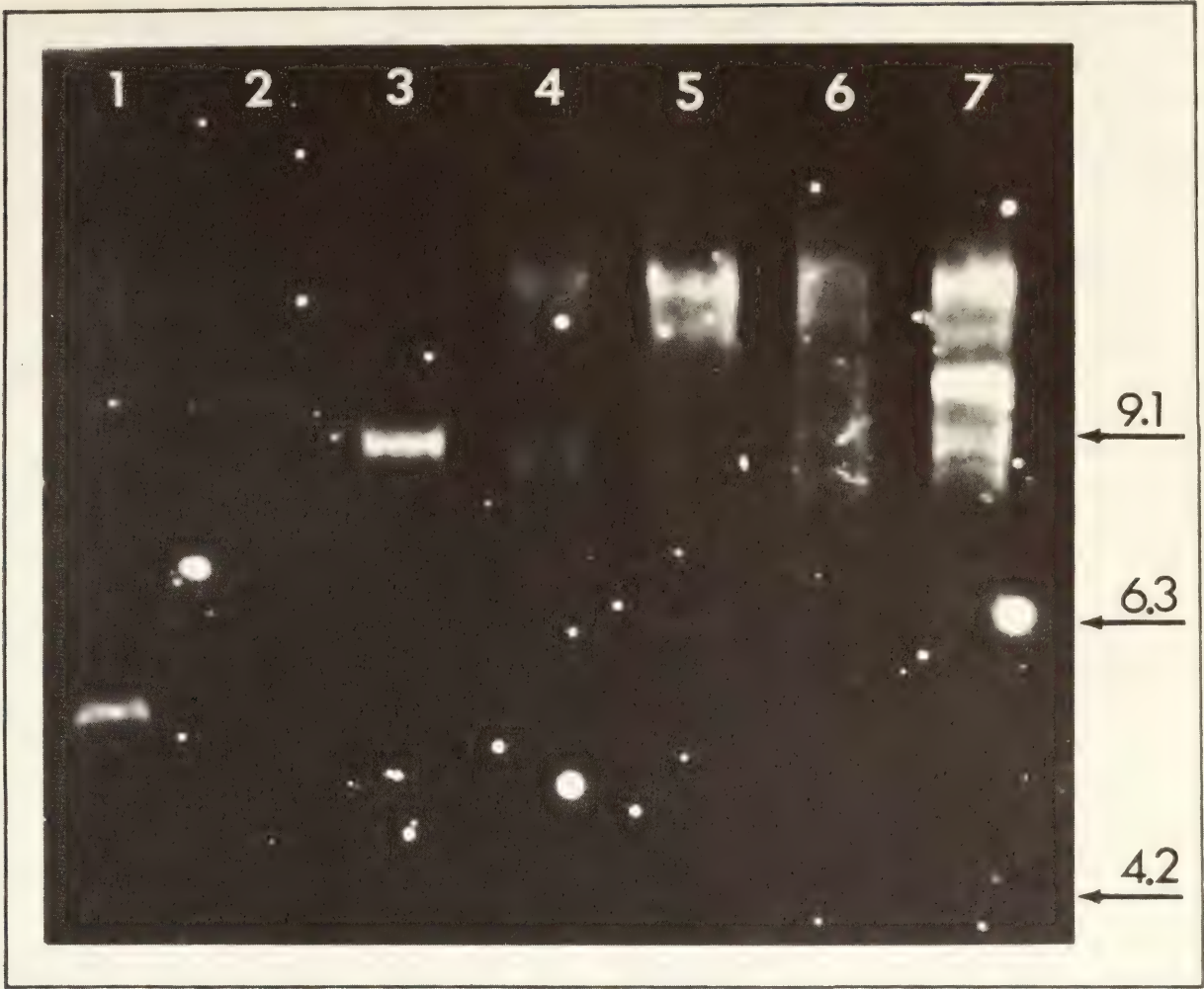


Fig. 34. HSV tk-specific DNA sequences detected in transformed cell DNA's digested with Kpn I. High molecular weight DNA was prepared from seven HSV tk-transformed clones. DNA was digested with Kpn I and electrophoresed on an alkaline, 0.75% agarose gel. The DNA was transferred to a nitrocellulose filter by the "Southern blotting" procedure, and incubated with <sup>32</sup>P pHSV-106 DNA under conditions that allow DNA/DNA hybridization. After extensive washing, the filter was exposed to Kodak x-ray film for 4 days. Bands reflect DNA sequences complementary to pHSV-106 DNA. Numbers above arrows refer to molecular weight markers as estimated in kilobases.

within a 3.4-kb DNA fragment produced by Bam HI digestion of the 8.3-kb Hpa I fragment. We introduced the 3.4-kb Bam HI fragment into the prokaryotic plasmid pBR322 by ligating it to the Bam HI linear form of the plasmid. These recombinants were used to transform *E. coli* HB-101. An isolate, termed pHSV-106, contained the 3.4-kb HSV Bam HI fragment inserted into the tetracycline-resistance gene of the plasmid. By digesting pHSV-106 with a variety of restriction enzymes we assigned the orientation of the inserted HSV-tk fragment (see Figs. 32 and 33).

The biological activity of the tk gene in recombinant form in pHSV-106 has been confirmed by incubating tk<sup>-</sup> mouse fibroblasts with the intact vector and with vector DNA digested with a variety of restriction enzymes. Intact pHSV-106 DNA, or the DNA cleaved with either Bam HI or Hind III, can transform tk<sup>-</sup> cells to tk<sup>+</sup> (Table 10). Alternatively, when pHSV-106 DNA digested with either Eco RI or Pst I is incubated with tk<sup>-</sup> fibroblasts, no tk<sup>+</sup> colonies appear when the cells are selected in HAT medium. Both Eco RI and Pst I cleave the 3.4-kb insert at

TABLE 10. Transformation of Mouse tk<sup>-</sup> Cells to tk<sup>+</sup>\*

pHSV-106 DNA	tk <sup>+</sup> colonies/10 <sup>6</sup> cells
Intact Plasmid	2.0
Bam HI digested	11.4
Hind III digested	3.3
Eco RI digested	0
Pst I digested	0

\*For each experiment 10<sup>7</sup> tk<sup>-</sup> mouse fibroblasts (10<sup>6</sup> cells/35-mm petri dish) were incubated with a total of 10μg intact or restricted pHSV-106 DNA along with 500 μg of high-molecular-weight mouse DNA derived from tk<sup>-</sup> cells. After 4 hours at 37°C the cells were placed in fresh, nonselective medium. After 24 hours cells were placed in HAT medium, which was changed at 3-day intervals. Plates were scored 15 days after transformation.

multiple sites probably within the tk gene (see Fig. 32).

We have used the “Southern transfer” technique to determine whether authentic transformants have been generated rather than revertant survivors. pHSV-106 DNA, labeled with <sup>32</sup>P to a high specific activity, was incubated with nitrocellulose filters to which the restricted DNA of seven transformant clones had been transferred. Each of the seven transformant clones contain specific DNA sequences complementary to HSV-tk DNA (Fig. 34). DNA from the parental tk<sup>-</sup> cells have no sequences complementary to the HSV-tk gene.

To obtain a more useful transformation vector we constructed a derivative of pHSV-106 that contains the HSV-tk DNA fragment inserted at the unique Eco RI site of pBR322 (Fig. 35). This recombinant DNA (termed pTK-101) has intact tetracycline and ampicillin drug resistance genes. Thus, other DNA sequences can easily be introduced into this vector. Furthermore, having both drug resistance markers intact should facilitate the retrieval of the recombinant molecule from eukaryotic cells.

We are interested in using the pHSV-

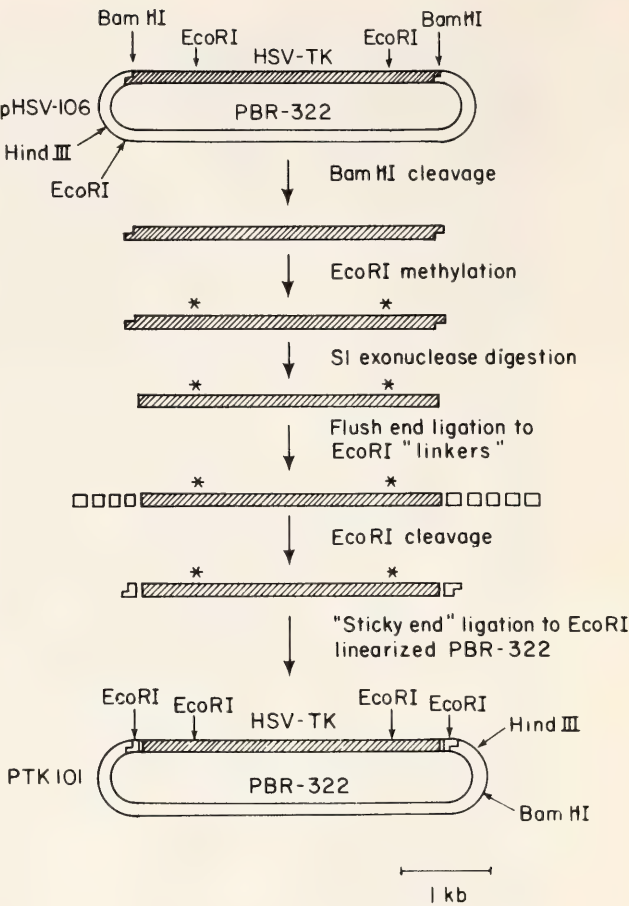


Fig. 35. The scheme used to transfer the HSV-tk sequence from the Bam HI restriction enzyme site of pBR-322 to the Eco RI site. The 3.4-kb tk insert was isolated from pHSV-106 by Bam HI digestion and agarose gel electrophoresis. The two internal Eco RI sites of the tk sequence were then protected by Eco RI methylase (asterisks denote methylated Eco RI sites). Subsequently, the single-strand specific exonuclease, S1, was used to render flush termini, and the fragment was ligated to synthetic Eco RI “linker” DNA molecules that had been terminally labeled with <sup>32</sup>P. The fragment was separated from contaminating “linkers” by agarose gel electrophoresis, eluted from the gel, and digested with Eco RI. This product was subsequently ligated to Eco RI linearized pBR322 DNA. The resulting plasmid, termed pTK-101, was isolated after transformation of *E. coli* strain HB-101.

106 and pTK-101 vectors to introduce isolated eukaryotic genes into cultured cells. There are two ways to accomplish this objective. First, an isolated eukaryotic gene can be inserted directly into one of the vectors by in vitro recombination. We have constructed a variety of recom-



binants of this sort that contain genomic segments of human ribosomal DNA, human  $\beta$ -globin DNA, and rabbit  $\beta$ -globin DNA, as well as one that contains a synthetic DNA sequence prepared from mouse immunoglobulin mRNA inserted into pHSV-106. Such derivatives are currently being used to transform various tk<sup>-</sup> cell cultures. Alternatively, two unlinked DNA's can be added to tk<sup>-</sup> cell cultures. Axel has recently shown that the incidence of co-transfer of independent DNA markers is remarkably high. In other words, after incubation with a mixture of tk DNA and some other pure DNA sequence, most tk<sup>+</sup> transformants contain both DNA's integrated into their genome. Inasmuch as tk<sup>+</sup> transformants contain multiple copies of the HSV-tk

sequence (see Fig. 34), the high incidence of co-transfer is not surprising.

Assuming we are able to introduce structural genes by one of the two approaches mentioned in the preceding paragraph, it will be interesting to study their expression. For instance, will the rabbit  $\beta$ -globin gene be expressed when introduced into a mouse erythroleukemic background or a fibroblastic background? Similarly, will an isolated mouse  $\lambda$  chain immunoglobulin gene be expressed when transplanted into a mouse myeloma cell synthesizing  $\kappa$  chain? If the answers to these questions are positive, it may be possible to alter the purified structural gene and retest the mutant genes in this manner to localize DNA sequences responsible for gene expression.

## CONTROLLING ELEMENTS IN MAIZE

*Nina Fedoroff and Jeff Mauvais*

Controlling elements in maize are genetic units capable of integrating in or very near a locus and imposing on it a precise, although altered, pattern of expression in development. A controlling element comprises at least one or two, and probably more, genes capable of transposing as a unit. Expression of the protein encoded by the locus, as judged by the level of the product whose synthesis is catalyzed by the enzyme encoded by the locus, may or may not be affected by integration of the controlling element. The potential for expression of the locus is, however, changed in a clonal fashion during development, producing plant parts that are mosaic for expression of the gene. Many genetically stable derivatives of such loci have been obtained, in each of which the potential for expression of the locus is altered in a very precise manner with respect to timing and frequency in development, the portion of the tissue affected, and the final level of gene expression. Such derivatives com-

prise, in essence, a set of developmental alleles of a locus, each responsible for a particular pattern of gene expression in the mature plant. Much of the genetic information available on controlling elements was obtained by B. McClintock of this Institution, and the reader is referred to successive Year Books, beginning with *Year Book 45* (1946), for detailed genetic analyses of controlling elements in maize.

Two categories of controlling element systems have been described: "autonomous" and "two-element." The system described above is termed autonomous because all of the information specifying the pattern of gene expression in development resides at the locus itself. In a two-element system, the controlling element resides at a different location than the locus whose developmental pattern of expression it controls. It is thought that two-element systems arise from one-element systems by transposition of a portion of the controlling element away

from the locus, leaving behind the genetic information required for the locus to continue responding to the gene products of the controlling element.

Three different controlling element systems have been studied in detail, though there are several others in maize. The three are termed "Dotted" (Dt), "Activator-Dissociation" (Ac-Ds), and "Suppressor-mutator" (Spm). Although each has properties unique to it, they share the common attribute of conferring precise developmental patterns of gene expression on loci under their control. Each is a self-contained system. Loci responsive to one controlling element system are not responsive to the others. Thus sequences in the DNA which mediate the effect of the controlling element system on gene expression appear to be specific to each system. The Spm controlling element system has been chosen as the focus of the present study because of its phenotypic richness and the extensive genetic information that exists on its mode of action.

The minimal composition of the Spm controlling element system, as defined by McClintock's genetic analyses, is represented schematically in Fig. 36. It comprises a regulatory element (Spm) and a controlled locus. The controlled locus has been modified in some way, bringing it under the control of Spm. This modifi-

cation is termed the "receptor" and is believed to be a DNA sequence foreign to the locus. The regulatory component influences expression of the controlled gene whether it is located in the immediate vicinity of the gene or elsewhere in the chromosome complement. In the absence of Spm, the expression of a controlled locus containing a receptor element may be unaltered from the wild-type level, or the locus may be expressed at some reduced level. In some alleles, the controlled locus appears not to be expressed at all in the absence of Spm. When Spm is introduced into the same nucleus as a controlled locus by an appropriate genetic cross, the basal level of expression of the locus is inhibited by the suppressor moiety of the Spm. The potential for expression of the gene is subsequently restored in a clonal fashion during development of the organism under the influence of the mutator component of Spm. It is hypothesized that the event which restores the potential of the gene for subsequent expression is the excision of the receptor element from the controlled locus. For some controlled loci, there are many alleles, each relatively stable genetically and showing a unique and consistent pattern of gene expression in the presence and absence of Spm. Each allele exhibits a particular level of gene expression in the absence of

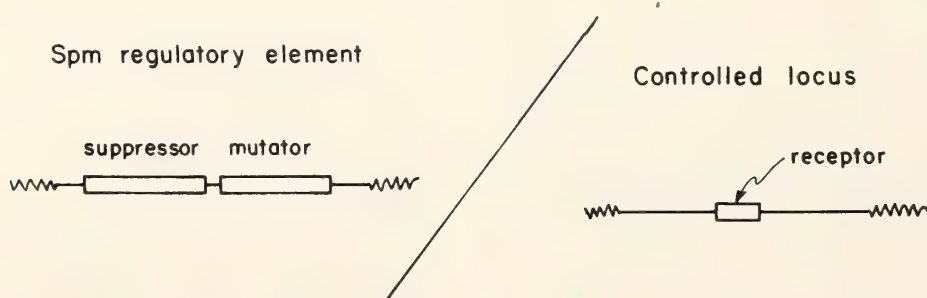


Fig. 36. Minimal composition of the Spm controlling element system. The Spm controlling element system comprises a *regulatory* component and a *receptor* component integrated in or near a controlled locus. The two known, genetically distinct functions of the regulatory component are designated the *suppressor* and the *mutator* (represented by open boxes). Additional sequences associated with the controlling element and possibly containing additional genes are represented by solid lines; the contiguous chromosomal sequences are represented by irregular lines. The receptor, whose nature is unknown, is represented by a box, the controlled locus by a solid line, and adjacent chromosomal sequences by an irregular line.



Spm and a characteristic time and frequency of occurrence of the mutator-catalyzed event restoring the potential for gene expression.

There are also altered forms of the regulatory component. The Spm component can undergo changes of phase from active to inactive. Although an inactive Spm can be identified genetically, it has no effect on the controlled locus. From analyses of Spm "mutants" which undergo frequent changes of phase, it has been inferred that the expression of the mutator function is contingent on expression of the suppressor function. An altered form of the Spm element has been analyzed in which expression of the mutator function appears to be delayed in development. A fundamental property of Spm is its ability to transpose. The chromosomal location of an Spm is sufficiently stable so that in most cases it can be mapped by conventional genetic techniques. In a small fraction of the progeny of a given Spm-containing plant, however, it is found that the Spm is lost, translocated to a new position, or present in more than the original number of copies.

We have undertaken to extend the analysis of controlling elements to the molecular level. The choice of controlling elements for molecular analysis is based on the conviction that they represent fundamental mechanisms for the developmental programming of genes. An awareness of the paramount importance of genetic analyses in our present understanding of prokaryotic gene regulation underlies the choice of maize as an experimental system for the present studies. It is in maize that controlling elements have received the keenest genetic study, and the wealth of existing genetic information on their mode of action will provide an indispensable base for the interpretation of molecular data. The major difficulties in the isolation and study of controlling elements are twofold. First, no gene product is known by which a controlling element can be identified and

isolated. Hence this isolation must be accomplished indirectly by isolating a gene containing a controlling element. Second, the loci which have yielded the most genetic information on controlling elements and which are likely to be the most useful in reconstruction experiments for reasons of ready visualization are those in the anthocyanin pigment pathways. It is already clear that the enzymes of the anthocyanin pigment pathways are not among the most abundant proteins in tissues which express the pigments. Spm, the controlling element system described above, has been studied almost exclusively in connection with genes in the anthocyanin pigment pathways.

Our initial efforts in gaining access to the molecular basis of controlling element function are progressing along several lines. A major effort is under way in collaboration with Dr. Barbara McClintock to obtain maize strains in which the Spm controlling element has transposed and become associated with loci that produce abundant, already identified gene products. These include the shrunken 1 (Sh1) locus, encoding a sucrose synthetase which is the most abundant soluble endosperm protein, and shrunken 2 (Sh2), encoding a subunit of an ADP glucose pyrophosphorylase. The enzymatic product of the Sh2 locus is likely to be less abundant than that of the Sh1 locus. Its importance stems from the fact that mutable alleles of the locus are more easily recognized phenotypically than mutable alleles of the Sh1 locus. In addition, it is located less than half of a recombination unit from the A1 locus of the anthocyanin pigment pathway. Isolation of the Sh2 gene may well facilitate isolation of the A1 locus, for which there exists a large variety of controlling element alleles having different patterns of gene expression in development. We are also attempting to derive Spm-controlled alleles of the Bronze (Bz) locus, the single locus in the anthocyanin pigment pathway for which an



enzymatic activity has been identified. It encodes a flavonoid glucosyl transferase, which carries out the terminal glycosylation step in anthocyanin pigment biosynthesis.

The first year's work in the laboratory has had several objectives. These include purification of the flavonoid glucosyl transferase, development of novel approaches to the identification of the protein product of the A1 locus, and development of maize tissue cultures.

The flavonoid glucosyl transferase is present in an active form in mature, dehydrated maize kernels. A large supply of mature kernels was prepared for this purpose during the summer of 1978 by Drs. E. H. Coe and M. G. Neuffer of the University of Missouri. Immature kernels were also harvested at various times after pollination and frozen in liquid nitrogen for future isolation of the mRNA encoding the glucosyl transferase as well as other endosperm proteins. The glucosyl transferase has been purified to near homogeneity by standard chromatographic procedures, including DEAE cellulose, CM cellulose, hydroxylapatite, and affinity chromatography. Sufficient amounts of the purified enzyme for antibody production should be available in the near future.

One approach that we have begun to develop toward the identification of gene products whose enzymatic activities are unknown relies on comparative gel electrophoretic analysis of proteins from tissues that have the product and those that lack it. In the case of the A1 locus, we are comparing the proteins from pigmented and unpigmented sectors of the aleurone layer from single kernels. The reason for using single kernels is that each kernel is genetically homogeneous, having developed from a single nucleus. The pigmented and unpigmented sectors in the aleurone layer of Spm-controlled A1 alleles are known to result from the action of the mutator and suppressor functions of Spm, respectively. That is, in the unpigmented sectors A1 gene ex-

pression is inhibited by the suppressor moiety of Spm, while in the pigmented sectors gene expression has been restored under the influence of the mutator component. Although the molecular basis of Spm action is not understood, the genetic studies strongly favor the hypothesis that the suppressor affects gene expression at the transcriptional level. It also appears likely from these studies that Spm is active throughout the kernel. Finally, the Spm controlling element system, unlike the Ac-Ds system, does not cause frequent chromosome breaks. Hence pigmented and unpigmented sectors of the aleurone layer of a single kernel having an A1 locus controlled by Spm are likely to differ from each other largely or solely by the presence and absence, respectively, of the A1 gene product. We have therefore developed procedures for labeling the proteins of the aleurone layer in vivo with tritiated amino acids and analyzing the labeled proteins on two-dimensional gels. Briefly, sectors of the fragile aleurone and overlying pericarp layers are dissected together from kernels taken from ears harvested 28–30 days after pollination. Pigmented and unpigmented sectors of the same size and from comparable locations on the kernel are removed and placed in individual wells of a microtiter dish. Several microliters of a buffer solution containing one or several tritiated amino acids are applied to the aleurone layer, and the dish is covered and incubated at 30°C for several hours. The aleurone layer is then separated from the underlying pericarp, homogenized in a solution suitable for direct analysis of the proteins by isoelectric focusing, and frozen in liquid nitrogen for later analysis by isoelectric focusing and SDS polyacrylamide gel electrophoresis. We have found that the labeled amino acids are readily incorporated into protein, and we are able to obtain several microcuries of labeled protein from a single aleurone sector.

Maize tissue culture is not an exten-



sively developed field, and our initial efforts in this area have concentrated on the development of rapidly and reproducibly growing maize cells. We have recently succeeded in establishing vigorously growing cultures from immature maize embryos, kindly supplied by Drs. E. H. Coe and M. G. Neuffer. We have also established tobacco and soy bean cultures and plan to explore techniques for using these cultures as feeder cells to clone single maize cells. Our eventual objective in this area is to develop cultures which grow as suspensions of either

single cells or very small aggregates and which can be used for the introduction of foreign DNA. These are particularly difficult tasks with maize, since maize cells neither grow as well in culture as certain other types of plant cells nor recover as readily from the cell wall removal procedures that have been used to obtain protoplasts capable of taking up exogenously supplied substances. Our efforts will be directed at the development of techniques for rendering the cell membrane accessible while minimally disturbing cell wall structure.

### *Xenopus* RIBOSOMAL DNA

*R. H. Reeder, B. E. H. Maden, and B. Sollner-Webb*

#### METHYLATION OF *X. laevis* rDNA

*B. E. H. Maden and R. H. Reeder*

Understanding the function and assembly of animal cell ribosomes should be aided by knowledge of the primary structure of rRNA and ribosomal precursor RNA. Combined RNA and DNA sequencing techniques are likely to contribute toward this end. We have explored the usefulness of the following combined approach. rRNA is hybridized to restriction fragments of rDNA, unhybridized regions are removed by trimming with ribonuclease, and the hybridized RNA is eluted and examined by fingerprinting analysis.

*Year Book 77* described preliminary experiments of this nature, using the cloned *X. laevis* rDNA fragments Xlr11 and Xlr14. (For a more detailed report, see Maden and Reeder, *Nucleic Acids Res.*, 6, 817, 1979). We have now purified five restriction fragments from the above clones and have inserted them separately into the plasmid pBR 322. The subcloned fragments define regions I–V of the *X. laevis* ribosomal transcription unit in Fig. 37. Region VI was subcloned by Dr. Barbara Sollner-Webb as

described elsewhere in this Report. Each subcloned region contains one or more features of biological interest, and together the subclones encompass the complete ribosomal transcription unit. For example, region I contains the external transcribed spacer and the 5' part of the 18S gene, region II the middle part of the 18S gene, and so forth. The following examples illustrate findings so far obtained from RNA hybridization experiments.

#### *The 5.8S–28S Gap*

The internal transcribed spacer is usually conceived as the region between the 18S and 28S genes (or the corresponding region in ribosomal precursor RNA). This conception is somewhat imprecise, as the region contains the 5.8S RNA sequence, and the distance between the 5.8S and 28S sequences is unknown. The 5.8S–28S cleavage event is one of the last steps in ribosome maturation in animal cells. Precise knowledge of this region would therefore be of interest in relation to the control of ribosome formation. It was recently shown that the 5.8S gene terminates approximately 130

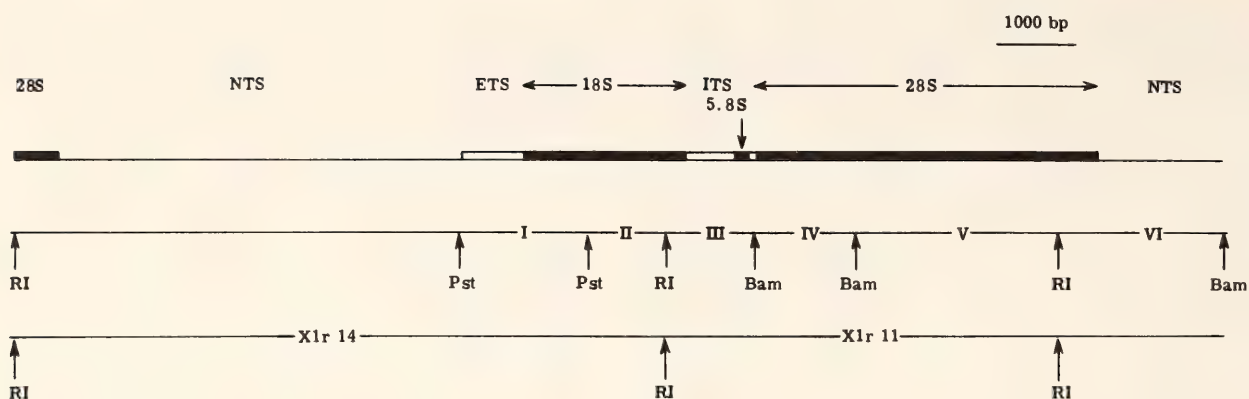


Fig. 37. Diagram illustrating slightly more than one repeat of rDNA in *X. laevis*. The middle line is composite: Regions *III*, *IV*, and *V* were subcloned from Xlr14. Region *VI*, which was subcloned by Dr. Barbara Sollner-Webb, is here shown to the right of region *V* to emphasize its effective contiguity with the other subclones.

nucleotides to the left of the Bam site that separates regions *III* and *IV* in Fig. 37 (Boseley *et al.*, *Nucleic Acids Res.*, 5, 1121, 1978). The present analysis has revealed that the 5' terminal nucleotide of 28S RNA, pUp, hybridizes to region *IV* and not to region *III*. Therefore, a substantial spacer of at least 130 nucleotides separates the 5.8S and 28S genes. This region is being further examined with a view to complete molecular characterization.

#### Methylation Map of rRNA

An enigmatic feature of eukaryotic rRNA is its characteristically high content of modified nucleotides. Knowledge of the locations of the modified nucleotides along the primary sequence may provide insight into the molecular basis and biological role of secondary modification events during ribosome maturation. A detailed map of the distribution of modified nucleotides along *X. laevis* 18S and 28S RNA is being constructed by hybridizing rRNA to the various subclones and to restriction fragments thereof, followed by fingerprinting analysis of the hybridized regions. Modified nucleotides are found in moderately high abundance in all three main regions of 18S RNA and in regions *V* and *VI* of 28S RNA, and the locations of distinctive methylation sites are being discovered.

For example, a sequence containing three methyl groups in a row, Am-Gm-Cm-A, which is present in the 28S RNA of most vertebrates, was erroneously assigned by one group of workers to the 5' end of the molecule. The present analysis reveals clearly that it is located in region *V*, the central region.

#### Atypical Properties of Region *IV*

This substantial region comprising > 1000 nucleotides at the 5' end of 28S RNA differs from all other major rRNA regions studied in possessing a higher GC content (70%) and very few modified nucleotides (probably fewer than five). There are hints from various lines of evidence that this 5' region of 28S RNA may be less highly conserved in evolution than the remainder of ribosomal RNA. Further characterization of this region, including comparative studies, will be of interest in relation both to rRNA function and to evolution of the rRNA genes.

In addition to the experiments described here, these and similar subclones are likely to find broad applications in studies of ribosome structure and assembly by other methods, including DNA sequence analysis and the development of assays for rRNA transcription and processing.



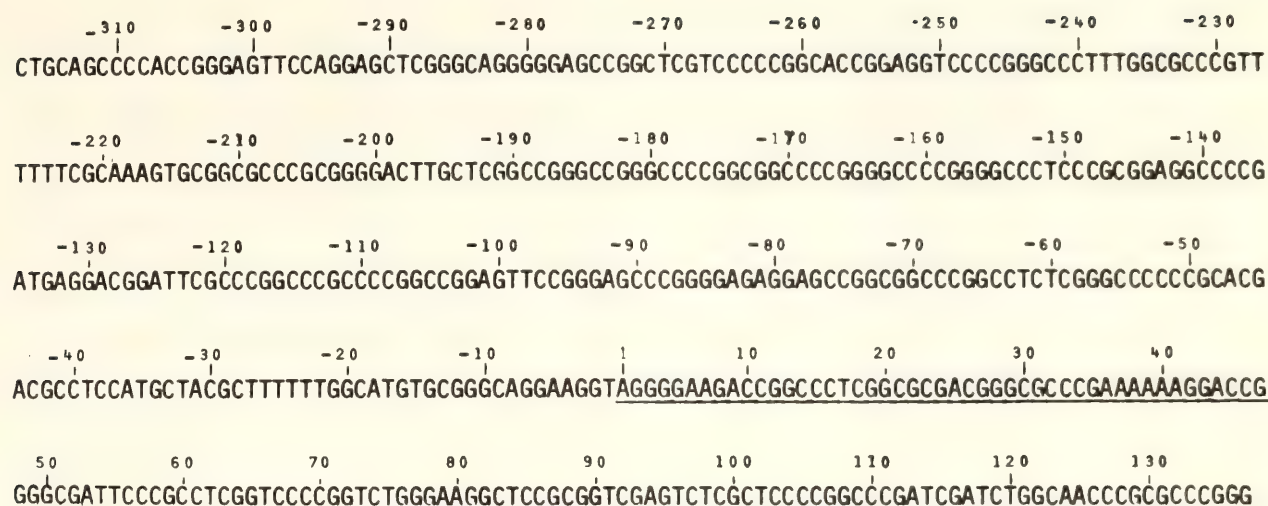


Fig. 38. The sequence of the noncoding strand of rDNA, clone pXlr14, was determined by the method of Maxam and Gilbert (*Methods Enzymol.*, 65, in press, 1979). Nucleotides -245 to +80 were confirmed by sequencing in the two opposite directions; positions +80 to +120 were sequenced from both a 5' and 3' label in the same direction.

#### NUCLEOTIDE SEQUENCE OF REGIONS OF THE *Xenopus laevis* RIBOSOMAL DNA

Barbara Sollner-Webb and Ronald H. Reeder

##### *Transcription Initiation Region*

The largest known precursor to *Xenopus laevis* 18S and 28S rRNA's sediments as a 40S species (Landesman and Gross, *Devel. Biol.*, 18, 571, 1968). Two years ago we demonstrated that the 5' termini of 40S RNA are polyphosphorylated, indicating that 40S RNA is the primary transcript of the ribosomal DNA (rDNA) (*Year Book* 76), and last year we reported studies that localize the nucleotide encoding the 5' end of 40S RNA to a 221-base-pair Sma I fragment of the rDNA (*Year Book* 77). We have now sequenced this region of the DNA and determined the position in this sequence where transcription begins.

The sequence of a 450-nucleotide region of *Xenopus laevis* rDNA that includes the 221-base-pair Sma I fragment has been determined for clone pXlr14 (Fig. 38). This sequence is numbered relative to the transcription initiation site (designated +1), as will be justified in the following paragraphs. The Sma I fragment extends from position -87 to +134.

We mapped the 5' end of 40S RNA on

this DNA by two methods. One method makes use of the single-strand specificity of S1 nuclease. The coding strand of the 221-nucleotide Sma I fragment was hybridized to 40S RNA, and the hybrid was treated with S1 nuclease. Single-stranded DNA that extends beyond the region of RNA-DNA duplex is thereby removed; the length of the resultant DNA should correspond to the distance between the 5' end of the Sma fragment and the nucleotide encoding the 5' end of 40S RNA. Using 25 units of S1 nuclease, the protected DNA forms two bands when electrophoresed on a sequencing gel (Fig. 39). This DNA was sized by electrophoresis alongside the coding strand of the Sma I fragment which had been chemically cleaved for sequence determination. The fragments protected from S1 nuclease are seen to be 134-135 nucleotides long: i.e., their 3' termini correspond to position -1 and +1 of the DNA sequence (Fig. 38).

In the other method of mapping the 5' end of the RNA, reverse transcription was employed. The 221-nucleotide Sma I fragment was cleaved with the Hae II, and the right-hand fragment was isolated and hybridized with 40S RNA. The 3' terminus of this DNA, which is recessed in the hybrid, was extended with reverse transcriptase, using the 40S RNA as



Fig. 39. Location of 5' terminus of 40S RNA. The 221-nucleotide Sma I fragment was labeled at the 5' terminus. The coding strand was isolated, hybridized to 40S RNA, and treated with 25 units S1 nuclease/100  $\mu$ l reaction. Alternatively the Sma fragment was cleaved with Hae II, the right-hand fragment was hybridized to 40S RNA, and the 3' end of the DNA was extended using reverse transcriptase. The duplexes were denatured and the DNA electrophoresed on a urea-containing 8% acrylamide gel.

template. Reaction conditions which favor full-length transcripts were used. Again the length of the resultant DNA should measure the distance from the Sma I site (position +134) to the nucleotide encoding the 5' end of 40S RNA. When sized by electrophoresis, the reverse transcript is seen to be a homogeneous band, 134 nucleotides in length (Fig. 39). Thus, if reverse transcriptase synthesized out to the 5' end of the RNA, this RNA should be encoded by the DNA sequence starting at position +1.

We have sequenced the 5' end of 40S RNA and find that it does in fact

uniquely correspond to the DNA sequence starting at position +1. We earlier reported that AAG was the 5' trinucleotide of in vitro-capped 40S RNA (*Year Book 76*). Unfortunately, a one-nucleotide error was made in sizing the RNase T1 product, causing an error in this sequence determination. We have now repeated and extended the sequencing of polyphosphate-bearing 40S RNA molecules. The 5' termini of these molecules were radioactively labeled in vitro using the *Vaccinia* virus capping enzymes. The RNA was fully or partially digested with various RNase's and the 5' oligonucleotide was sized both on urea-DEAE columns and on sequencing gels. The sequence AGGGGP<sub>4</sub>Q was determined for the polyphosphorylated 40S RNA (P stands for purine, Q for pyrimidine). However, 75% of 40S RNA molecules are not polyphosphorylated. Their 5' termini were labeled using polynucleotide kinase. By RNase digestion and gel electrophoresis, AGGGGAAGAQQ was shown to be the sequence of the 5' end of bulk 40S RNA. Inspection of Fig. 38 shows that the oligonucleotide AG<sub>4</sub>P<sub>4</sub>Q is found only once in the Sma I fragment, starting at position +1.

We therefore conclude that rRNA transcription starts at the nucleotide designated +1 in the DNA sequence (Fig. 38). Bulk 40S RNA also starts with this nucleotide. Since the DNA fragments generated by S1 nuclease and reverse transcriptase are the same length (Fig. 39), we may further conclude that the first 134 nucleotides of the transcribed region contain no oligonucleotides that are spliced out in the mature 40S RNA.

This study reports the first RNA polymerase I initiation site that has been located and sequenced. Synthesis of 40S RNA starts at a purine, which is preceded by a pyrimidine. This is the same sequence configuration noted by Korn (*Year Book 77*) for the start sites of genes transcribed by RNA polymerase III and by *E. coli* RNA polymerase. This similarity suggests that pyrimidine-



purine start sites may be a general feature of several classes of RNA polymerase. In contrast, other oligonucleotides conserved specifically in the region of prokaryotic RNA polymerase or RNA polymerase III initiation sites (Pribnow, *Proc. Nat. Acad. Sci. USA*, 72, 784, 1975; Korn, *Year Book* 77) are not found in the region of the rRNA initiation site. The region immediately surrounding the rRNA initiation site is richer in A+T residues than are the flanking regions (>40% A+T from -47 to +9, ~20% A+T from -377 to -48 and -10 to +137). It has been suggested that local regions of relatively higher A+T content may aid prokaryotic RNA polymerase in initiating on DNA (Botchan, *J. Mol. Biol.*, 105, 161, 1976), and they could conceivably function similarly in the eukaryotic system. Finally, only one start site was detected for *Xenopus* rDNA, in contrast to the two start sites of the *E. coli* rRNA cistron *rrnB* (Glaser and Cashell, *Cell*, 16, 111, 1979).

We have sequenced the 221-nucleotide Sma I fragment which encodes the 5' end of 40S RNA from another rDNA clone, pXlr12. There is only one difference from the sequence of pXlr14: a T replaced the A at position +53 in Fig. 38. Boseley *et al.* (*Cell*, 17, 19, 1979) have sequenced this region from yet another *X. laevis* rDNA clone, pCD4, the sequence of which appears to be identical to that of pXlr12. This suggests that the sequence of the transcription initiation site may be highly conserved within the species *Xenopus laevis*.

#### Nontranscribed Spacer

The nontranscribed spacer of *Xenopus laevis* is occasionally interrupted by Bam HI sites (Botchan, *Year Book* 75). We have determined the nucleotide sequence from clone pXlr14, starting at the proximal Bam HI site (position -1147) and moving toward the transcription initiation region. The nucleotide sequence of positions -127 to +4

around the transcription initiation site is repeated from -1147 to -1017 with <10% mismatches. However, we have been unable to detect RNA whose 5' terminus is homologous to this region of the spacer. This extends the observation of Boseley *et al.* (*Cell*, 17, 19, 1979) that the region around the Bam HI sites of clone CD4 has a similar sequence to a region deduced to be in the vicinity of the transcription initiation site. These authors have also sequenced several of the repetitive elements in region D of the nontranscribed spacer of clone CD4 (Fig. 40). We have shown that clone pXlr14 contains these same kinds of repetitive elements between the proximal Bam HI site and initiation region (Fig. 40). Ten complete repetitive elements are found in pXlr14 from -1016 to -159. The sequence of 1100 nucleotides in the spacer of pXlr14 is diagrammed in Figure 40.

#### Transcription Termination Region

Ribosomal RNA transcription is known to terminate within ~200 nucleotides of the single Hind III site of *X. laevis* rDNA (Reeder *et al.*, *Year Book* 75; Botchan, *Year Book* 75). The sequence of rDNA clone pXlr14 has been determined around the Hind III site and is shown in Fig. 41. The 3' end of 40S RNA was mapped on the DNA, using the S1 nuclease technique described earlier. When a Hinf I fragment (-73 to ~+290) was hybridized to 40S RNA and treated with 30 units of S1, the resultant DNA was 74 nucleotides long. Analogy to the similar experiment at the 5' end of the gene suggests that the 3' end of 40S RNA is encoded by positions -1 or +1 within the Hind III site (Fig. 41).

When this S1 experiment is repeated, also using 28S RNA and various amounts of S1 nuclease, the 3' terminus of 28S RNA is seen to be identical to the 3' terminus of 40S RNA. This confirms, on the nucleotide level, that nucleotides are

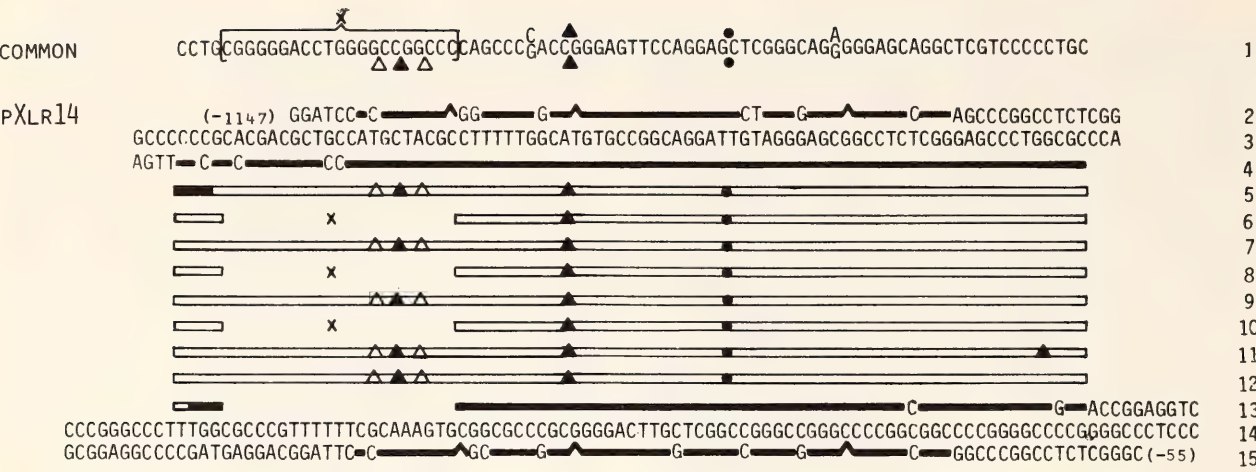


Fig. 40. Nontranscribed spacers of pXlr14. A number of repeating elements of the spacer of rDNA clone pCD4 have been sequenced by Boseley *et al.* (*Cell*, 17, 19, 1979), the common sequence of which is shown in line 1. A 21-base-pair deletion/insertion allows the element to exist in both a 61- and 81-base-pair form. Restriction enzyme cuts are as indicated: Pst I, X (when the 21-base-pair segment is not there); Hae III, Δ; Hap II, ▲; Alu I, ●. Below, the sequence of clone pXlr14 is aligned to emphasize the repetitive elements of its spacer; nucleotides -1147 to -55 are shown on continuous lines. Sequenced regions are represented by solid bars where they agree with the sequence of line 1 and by letters where they differ. Regions that have not been sequenced, represented by hollow bars, are aligned by their restriction enzyme cleavage sites.

not lost from the 3' end of 40S RNA on the production of mature 28S RNA.

There is evidence that the Hind III site also marks the region where transcription terminates. Trendelenberg and Gurdon (*Nature*, 276, 292, 1978) have demonstrated that rDNA clone pXlr101 supports the production of normal-size transcription units even though the pMB9 vector is inserted into the Hind III site of the rDNA. Thus, unless a fortuitous RNA polymerase I termination sequence

occurs in pMB9 near the Hind III site, the rRNA transcription termination site must reside upstream from or within the Hind III site.

The DNA sequence around the Hind III site is very similar to the termination sequences recognized by *E. coli* RNA polymerase and by RNA polymerase III (Korn, *Year Book* 77). It has a T cluster in an AT-rich region, preceded by a dyad symmetry in a somewhat GC-rich region (Fig. 41). This result increases the prob-

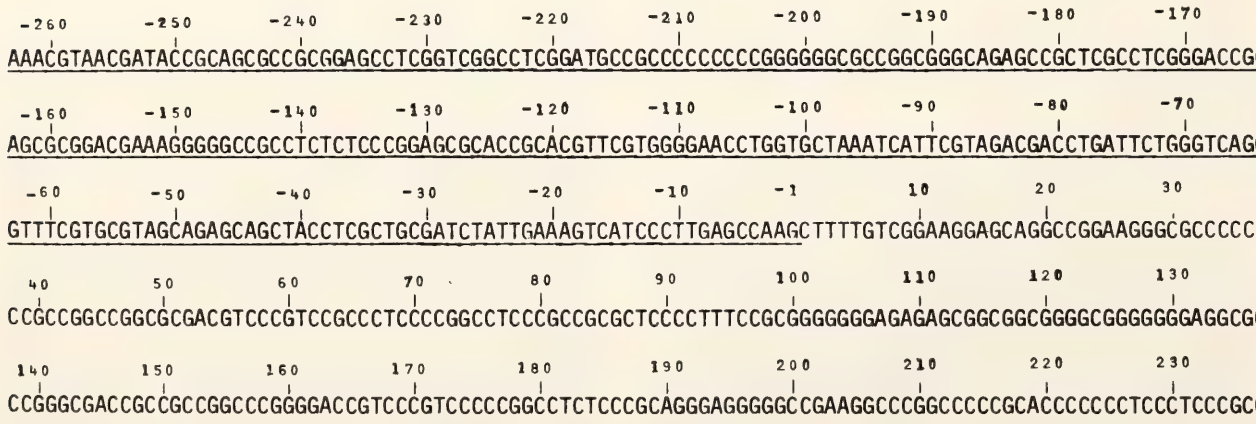


Fig. 41. Transcription termination region. The sequence of the noncoding strand of rDNA, clone pXlr14 was determined. Nucleotides -206 to +161 were confirmed by sequencing in the two opposite directions. Numbering is relative to the dyad axis of the Hind III site.



ability that the termination sites for various RNA polymerase classes share similar features.

### *Formamide Sequencing Gels*

In the course of sequence determination of the very G+C rich *X. laevis* rDNA, it became apparent that regions of secondary structure were forming during electrophoresis of the base-specific cleavage products. This causes DNA fragments of differing length to comigrate rather than appear as successive bands on the gel. The result is that the nucleotide positions corresponding to the distal portion of the dyad symmetric region are omitted from the sequence determination. When a DNA region is sequenced in opposite directions, the "ends" of the secondary structure are at different nucleotide positions and the

artifact is readily discerned as a region that differs in apparent sequence in the two determinations. This is not the case when a region is sequenced in the same direction from both the 3' and 5' termini. 8 M urea-containing gels run at ~35 V/cm have been reported to melt out such DNA structures (Sanger and Coulson, *FEBS Letters*, 87, 107, 1978). However, in the G+C-rich rDNA some secondary structure remains, even in 9 M urea gels run at ~45 V/cm. 90% formamide reduces the  $T_m$  of DNA by 40° more than 9 M urea does, and we have found that DNA sequences can easily be determined on 90% formamide containing 20% acrylamide gels with a Tris-borate buffer. These gels require no aging time, they produce sharp, well-resolved bands, and they allow the rDNA sequence to be determined without any evidence of artifacts due to secondary structure.

## THE DUAL 5S RNA GENE SYSTEM IN *Xenopus*

*D. D. Brown, E. Birkenmeier, D. Bogenhagen, L. J. Korn,  
E. Jordan, R. Peterson, and S. Sakonju*

Our goal has been to characterize the multigene families encoding the two kinds of 5S ribosomal RNA synthesized by two species of *Xenopus* (*X. laevis* and *X. borealis*). We then wish to reconstruct in vitro the molecular controls that regulate their expression in the living cell. This report represents a turning point in this project. What may be the final "characterization" studies are described, as are the first attempts to carry out in vitro genetics on cloned single repeating units of 5S DNA. Individual repeating units of five different multigene families of 5S DNA have now been cloned by the recombinant DNA methodology and sequenced completely. R. Peterson describes the isolation and sequence of two 5S DNA's from *X. laevis*—the minor oocyte-specific 5S DNA (Xlt) and the somatic 5S DNA (Xls). Characteriza-

tion of the other three 5S DNA's (Xlo, Xbo, and Xbs 5S DNA's) have been described in previous Reports. This has enabled us to compare multigene families under different control from the same species (Xls vs. Xlo, for example) and families with the same control from different species (Xls vs. Xbs, for example).

The opportunity to study the expression of these genes is afforded by an in vitro extract from oocyte nuclei (*Year Book* 77) that supports the accurate synthesis of 5S RNA from these purified genes in their recombinant form. Birkenmeier has begun fractionating this nucleoplasmic extract and has been able to separate a factor from the RNA polymerase activity. In the absence of the factor, the enzyme synthesizes RNA but not 5S RNA. Adding back the factor results in 5S RNA synthesis. Additional

improvements in the in vitro assay enable us to determine accurate initiation of transcription in the absence of termination (Korn and Birkenmeier). We have learned that initiation of transcription by RNA polymerase III is usually at purine residues.

Deleted 5S RNA genes have been prepared enzymatically and tested in the in vitro extract by Sakonju and Bogenhagen. This has led to the remarkable finding that accurate initiation of transcription by polymerase requires a region within the gene from approximately +50 to +80. Thus, removal of either the first or last third of the gene does not stop specific initiation of transcription. In the case of the 5' deletions, Sakonju shows that initiation begins at about 50 nucleotides upstream from the recognition site even if the DNA located there is not 5S DNA. Bogenhagen finds that deletions into the gene from the 3' end destroy the termination site but do not alter initiation until more than one third of the gene has been lost. In addition he has introduced a 20-base-pair insert into the first third of the gene. This "maxi-gene" causes initiation of transcription to occur about 20 nucleotides into the gene. An interpretation of these first in vitro genetic studies is that the polymerase binds to a region of about 30–40 nucleotides near the middle of the gene; it initiates at a purine about 50 nucleotides upstream. The exact sequence of the initiation site is not important as long as the first nucleotide transcribed is a purine. Termination of transcription requires the cluster of four T's at the 3' end of the gene and perhaps additional sequences within the gene.

THE CHARACTERISTICS AND SEQUENCES  
OF *X. laevis* TRACE OOCYTE 5S DNA  
AND *X. laevis* SOMATIC 5S DNA

*R. C. Peterson and D. D. Brown*

There are at least three multigene families encoding 5S RNA in the frog

*Xenopus laevis*. All three families are expressed in the developing oocyte of this animal, but only one type is expressed in somatic cells. The major and minor (trace) oocyte-specific 5S RNA's are transcribed from families with the largest number of 5S RNA genes, and they are termed Xlo and Xlt 5S DNA, respectively. These genes have been purified previously from genomic *X. laevis* DNA, and repeating units of Xlo 5S DNA have been cloned as recombinant molecules (*Year Book* 75). Xlt 5S DNA contains about one tenth the number of repeating units as does Xlo 5S DNA.

Recently a third set of 5S rRNA genes was detected in *X. laevis* DNA (*Year Book* 77). This gene family is present in fewer copies than either of the two oocyte-specific types. It has now been shown that this third gene family encodes the 5S RNA that is expressed in somatic cells.

The genes for the *X. laevis* somatic type 5S RNA (Xls 5S DNA) have not been purified to homogeneity from genomic DNA, since they make up such a small fraction of the total DNA of a cell. However Xls 5S DNA has been partially purified and then cloned by recombinant DNA methods. For this purpose it was necessary to separate the somatic 5S RNA genes from Xlo and Xlt 5S DNA, since all three types of 5S DNA will hybridize to the <sup>125</sup>I-labeled 5S RNA used as a probe. Actinomycin D-CsCl gradient centrifugation was used in the purification of the somatic 5S RNA genes from embryonic DNA of *X. laevis*. Under these conditions, Xlo 5S DNA bands at a density heavier than the main band of DNA, while the Xlt and Xls somatic 5S DNA's band at a density lighter than the main band. The fractions that contain Xlt and Xls 5S DNA were pooled and rerun on an identical actinomycin D-CsCl gradient in order to remove the Xlo 5S DNA entirely. The DNA from this second gradient was then cut with the restriction endonuclease Hind III. This enzyme cleaves the so-



matic 5S DNA once every repeat to give a fragment 850–900 base pairs long, but it cuts Xlt 5S DNA infrequently. After cleavage with Hind III, most of the Xlt 5S DNA could be removed from the smaller Xls 5S DNA fragments by electrophoresis on a 1.4% agarose gel. The DNA fragments about 800–1000 base pairs long were extracted from the gel and joined to the plasmid pBR322 at the Hind III site. These recombinant molecules were cloned in *E. coli* strain HB-101, and individual colonies were screened by the colony hybridization technique using  $^{125}\text{I}$ -labeled 5S RNA as a probe. The plasmids from some of these clones contained a single fragment of DNA about 850 base pairs long inserted at the Hind III site. These recombinant DNA's supported the synthesis of 5S RNA when added to extracts of oocyte nuclei. The 5S RNA synthesized in this system was determined to be the somatic type by

two-dimensional fingerprint analysis. A single cloned repeating unit of Xls 5S DNA has been sequenced completely by the chemical cleavage method and is shown in Fig. 42.

The *X. laevis* somatic 5S RNA gene has a repeat length of 882 base pairs and contains 57% guanine and cytosine bases. The somatic 5S RNA gene from *X. laevis* is only one nucleotide different from that of the somatic 5S RNA gene from *X. borealis* (Xbs). A direct comparison of DNA sequences that flank the 5S RNA genes in the two kinds of 5S DNA shows about 72% homology. Many of the mismatches are single base differences, and some of these may be due to sequence heterogeneity within the families. The sequences of Xls and Xbs 5S DNA were determined from single cloned fragments and therefore may not be identical to the predominant sequence.

In addition to single base differences

```

      20      40      60      80
AAGCTTGGCCTCTCAGCAAAATGTCGAGTGGAAAAAGGCTTTTTGTGTCTGCCTCAGACACAAAAGGAAAGGGCCTTTTCTCAGGAGG
    100      120      140      160      180
TGAGCAGCAAGCTGGACTCTGGGATGGCGCTGGAAGTGATCTGCCCCTTGGATTTTGTCTGGACACTTTGATGCAAGGGCTATCCTGAGCT
    200      220      240      260
GACAAGGGCCATGGGAGGGGGCGGGGGGGGTTGAAGAGAACAAGCTGTCCAATTGTAGGCAGTGTCAATTCGCTAGCGGCGGCCGTAGCA
    280      300      320      340      360
AATAAGGTCCCGTCTTGATAGAAAAGGGCATGAAGTGGTGGGGGGTGGGGAAAGGGCAGTTTGAGCCTTTTCTGCGGTTGCCCCCGGT
    380      400      420      440
CAGGCCCCGAGCTGGAGTAGGCAGCTGGGATTTGGCCTCCAGTATATGCGGTCTTAAGAAGGTTATGAGTGAGCTGGAGAGAGGGCAGAG
    460      480      500      520      540
GGGTGTAAGTACAGGGGTGAAAGGGATGGAGGAGCTGAGGTAGGCGGGCCGGCTGTCCAGGCTGGGGTTTTTATCTTGGGGAAAAGAGC
    560      580      600      620
CCTGCATGGGGAGGAGCTGGGCCCAAGAAGGCAGCACAGAGGAGGAAAAAGTCAGCCTTGTGTTCGCCTACGGCCACACCACCTGAAA
    640      660      680      700      720
GTGCCCGATCTCGTCTGATCTCGGAAGCCAAGCAGGGTCGGGCCTGGTTAGTACTTGATGGGAGACCGCCTGGGAATACCAGGTGTCGT
    740      760      780      800
AGGCTTTTGCACTTTGCCCTTCTGAGCAGCAGGGGGCAGTCTCCTCCTGCTTTTTCTTCCCGCAACAGCCAGACAGCTAGCTGCCTGA
    820      840      860      880
TAGAGACCCCCACCCCTGTAAGGGAGCCACTCCATACGCTGAACTGTACACCTGCGGGCCTTGCCAGGAC(AAGCTT)

```

Fig. 42. The nucleotide sequence of a single cloned repeating unit of *X. laevis* somatic (Xls) 5S DNA. Only the noncoding strand is shown, and the 5S RNA gene sequence is underlined.

between the somatic 5S DNA sequences from these two species, there are several differences which appear to have arisen from insertions or deletions. The sequences that have been inserted or deleted are not homologous to each other or to other regions within the repeating unit. Thus, there appear to be at least two mechanisms by which the 5S DNA has diverged between these two closely related species—insertion or deletion of oligonucleotides and single base changes.

The Xlt 5S DNA is cleaved in some repeats by the restriction endonuclease Hind III. Complete digestion with this enzyme results in DNA fragments that contain various numbers of repeats, although most of the genes are present in fragments longer than 4000 base pairs. When the DNA from actinomycin D-CsCl gradients was cut with the enzyme Hind III, the digestion of Xlt 5S DNA resulted in some fragments only slightly longer than the Xls 5S DNA repeat. The Xlt 5S DNA repeat has been shown to be about 350 base pairs long, and thus three tandem repeats would give a fragment length of about 1000 base pairs. This Xlt 5S DNA fragment was extracted from an agarose gel along with the somatic 5S DNA fragment and cloned as a recombinant molecule. The Xlt 5S DNA fragment was detected in purified plasmids by its length difference from the somatic 5S DNA fragment. A two-dimensional fingerprint of the 5S RNA transcribed from these recombinant

plasmids showed that this fragment encoded Xlt 5S RNA. The DNA sequence of Xlt 5S DNA was determined by the chemical-sequencing method, and the sequence of a single repeating unit is shown in Fig. 43. There is one difference in the coding portion of the gene and the sequence of Xlt 5S RNA that had been previously proposed (Brown *et al.*, *Cell*, 12, 1045, 1977). The Xlt 5S DNA spacer is rich in A and T nucleotides and shares some sequence homologies with the spacer from Xlo 5S DNA. The region 5' to the gene is also very similar to the corresponding region of the Xlo 5S DNA. The 3' flanking sequence of Xlo 5S DNA is very much like its own spacer region, while Xlt 5S DNA contains a different oligonucleotide sequence flanking the 3' end of the gene. This difference in the sequence immediately following the gene may influence the termination of transcription.

The restriction endonuclease Hind III recognition site is located seven nucleotides in front of the site of transcription initiation of Xlt 5S DNA. A single base change, G to A, accounts for the heterogeneity at this position in the multigene family. Another sequence recognized by the restriction enzyme Ava II is located 30 bases in front of the transcription initiation site and is present in most if not all repeats of the Xlt 5S DNA. Thus, base heterogeneity is more prevalent at the Hind III site within the spacer than at the Ava II site.

```

      20      40      60      80
TTCAAATTTTCACCTTTTCATTTTTTTTAACATTTTGCACTTTATTTTTTACACAGCACCGCCACAGGTCCAAAAGGCCAAAGTGCC
      100      120      140      160      180
AAGCTTCATCGCCTACGGCCACACCACCTGAAAGCGCCGATCTCGTCTGATCTCGGAAGCGATCCAGGGCCGGGCTGGTTAGTACCT
      200      220      240      260
GGATGGGAGACCGCTGGGAATACCGGGTGTCTAGGCTTTTTAGCCGTTGCCATTTTTTAACATTTTCATGTTTTCACTCTTTTTTT
      280      300
TCCACTGCGCGCATGCGTCAGGAAGCCGCAAAGAGCCATTTT

```

Fig. 43. The nucleotide sequence of a single repeating unit of *X. laevis* oocyte-specific trace (Xlt) 5S DNA. Only the noncoding strand is shown, and the 5S RNA gene sequence is underlined.



Fragments from the spacer regions of Xlt and Xls 5S DNA have been cloned separately and provide hybridization probes that are specific for the individual gene families. Analysis of each of these families after restriction enzyme digestion, gel electrophoresis, and blotting onto nitrocellulose filters shows that both Xls and Xlt 5S DNA's consist of homogeneous length repeats. This is in contrast to Xlo 5S DNA that is heterogeneous in length. The presence of a 15-nucleotide-long sequence, repeated various numbers of times within the spacer portion of Xlo 5S DNA, accounts for this length heterogeneity (see *Year Book 76*). Neither Xlt or Xls 5S DNA have an identifiable, simple sequence repeat within their spacers.

#### ORGANIZATION OF THE *Xenopus borealis* OOCYTE-SPECIFIC 5S RNA GENE FAMILY

*L. J. Korn and D. D. Brown*

The most complex of the five 5S DNA multigene families that we have studied is the one specifying the major 5S RNA synthesized by oocytes in *X. borealis* (Xbo 5S DNA). Although this DNA was isolated and partly characterized several years ago (*Year Book 71*), it was not until the availability of restriction endonucleases that its organization could be studied (*Year Book 75*). Repeating units of Xbo 5S DNA consist of one or more closely spaced 5S RNA genes interspersed with variable-length spacer regions. The spacers themselves contain a 21-nucleotide simple sequence that repeats variable numbers of times within a spacer.

One cloned fragment of Xbo 5S DNA has been sequenced (*Year Book 77*). It contains three 5S RNA genes. The first gene (referred to as gene one) has the sequence of the major 5S RNA found in oocytes; the second and third genes differ from gene one by 2 and 15 nucleotides, respectively. These nucleotide differences result in changes in restriction enzyme sites that have enabled us to measure the abundance of each kind of

gene and their order in the genomic Xbo 5S DNA. The following conclusions describe the nonrandom order of genes one and three in the gene clusters.

About 25% of all repeating units have a single copy of gene one. The majority if not all of the clusters with more than one gene, have one copy of gene three, and it is always at the end of the gene cluster in the sense of transcription. The sequences that flank gene three have also diverged from those that flank gene one. We believe that gene three has diverged from gene one and spread throughout the multigene family by unequal crossing over. Its specific location at the end of each gene cluster would result from a restriction that would require a gene three to cross over only with another gene three, not with a gene one. These restrictions on the interaction of different regions of this multigene family can account for the complexity of Xbo 5S DNA and the arrangement of the different repeated sequences within it.

#### IN VITRO GENETICS OF 5S DNA

*S. Sakonju, D. Bogenhagen, and D. D. Brown*

We have used the in vitro transcription system (*Year Book 77*) as an assay system to localize the regions in 5S DNA that direct accurate initiation and termination of transcription. Cloned repeating units of the five 5S DNA multigene families are transcribed faithfully into 5S RNA by the nuclear extract. We have chosen to carry out a systematic deletion and mutation analysis on the plasmid pXbs1 (a single repeating unit of *X. borealis* somatic 5S DNA cloned in the plasmid pBR322) because more than 80% of the RNA transcribed from it in vitro is 5S RNA (see *Year Book 77*).

#### *Deletions of the 5' End of the Gene*

*S. Sakonju*

Deletions from the 5' side of the Xbs gene were generated by digesting a gel-

purified restriction enzyme fragment containing 102 base pairs of the 5' flanking region with exonuclease III to various extents (Fig. 44). The conditions for Exo III digestion were chosen such that the end points of the deletions were distributed over the 5' flanking region and the 5S RNA gene. The single-stranded regions that remain after Exo III digestion were cleaved by S1 nuclease to form flush ends. Synthetic Hind III linker DNA was ligated onto these molecules. They were then cleaved with the enzyme Hind III and ligated to pBR322. Since the deleted molecules have Hind III sites on both ends after linker ligation, they recombine in both orientations with Hind III cut pBR322. Cloned deleted molecules were screened for size and their ability to support 5S RNA synthesis in the *in vitro* transcription system. In order to obtain deletions in a specified region of 5S DNA, recombinant DNA from pooled clones was isolated and then digested with Hind III, and the inserts were sized on an acrylamide gel. Fragments corresponding to the desired extent of deletion were excised and eluted from the gel and recloned with pBR322. The orientation of the insert and the end points of each deletion were determined by digesting the recombinant plasmid with Hae III and sizing the altered fragments on a 10% acrylamide gel. The end points can be mapped by this procedure with the accuracy of up to  $\pm 1$  nucleotide.

We have tested 13 different clones whose deletion end points map at various points along the 5' flanking region and found that they all support accurate synthesis of 5S RNA. The largest extragenic deletion characterized so far leaves only one base pair of 5S DNA immediately in front of the first nucleotide of the gene. The deletion end points of a -11 clone (5' flanking region is deleted except for 11 base pairs in front of the gene) and a +3 clone (the entire 5' flanking region plus the first two base pairs of the gene are deleted) were con-

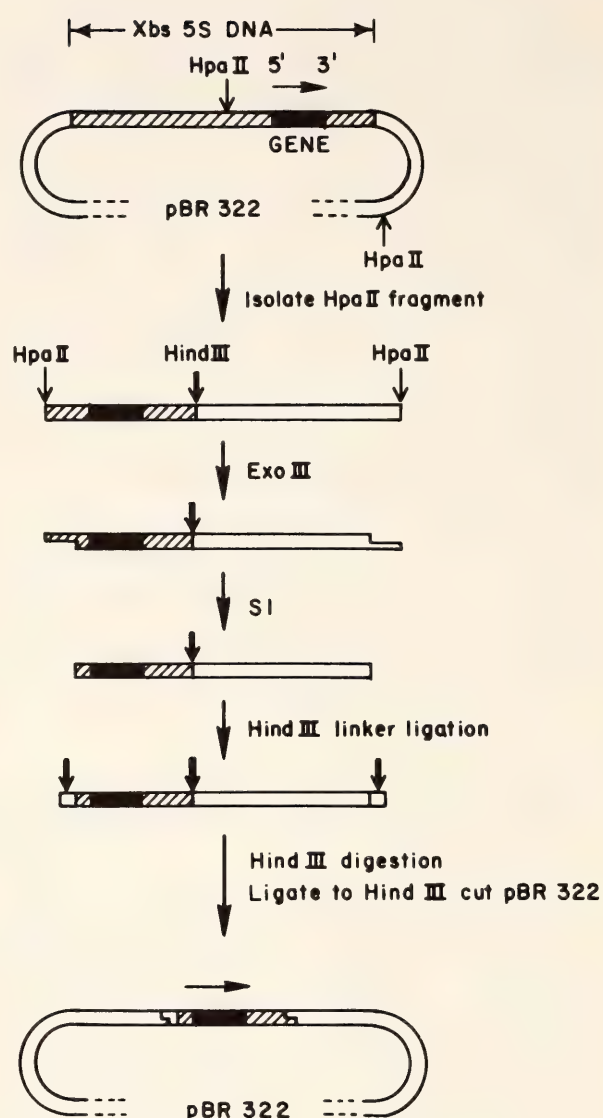


Fig. 44. The method for producing fragments of 5S DNA with deletions toward the 5' side of the gene (see text for details).

firmed by direct DNA sequencing. 5S RNA synthesized from a -11 clone has been analyzed by two-dimensional electrophoresis of T1 digestion products and it is identical to Xbs 5S RNA.

The transcription of 5S RNA from deleted 5S DNA is unlikely to be due to the presence of a fortuitous promoter sequence in the plasmid DNA for the following reasons. (1) Deleted 5S DNA can be ligated to the plasmid in two possible orientations, placing two different plasmid sequences in front of the 5S DNA. Recombinant plasmids in both orientations support 5S RNA synthesis. (2) The insert of a -11 clone was excised by



Hind III digestion and purified on an acrylamide gel. This 276-mer linear fragment containing only 11 base pairs of 5S DNA and three base pairs plus four single-stranded nucleotides derived from the DNA linker flanking the gene on its 5' end, supports 5S RNA synthesis, albeit at much reduced efficiency.

When we tested deleted molecules whose end points mapped as far as +47 into the 5S RNA gene, we were surprised to find that RNA of approximately 5S size was synthesized (Fig. 45). We isolated eight such clones in which the plas-

mid and DNA linker were joined to between +1 and +47 of the gene. The "5S" RNA synthesized from a +47 clone has been analyzed by two-dimensional fingerprinting. All characteristic T1 oligonucleotides from +47 to the 3' end of authentic 5S RNA are present. The oligonucleotides in the region from +1 to +46 of 5S RNA are absent, but they are replaced by ones predicted from the known sequence of approximately 50 nucleotides of plasmid and linker DNA that adjoin the remnant of the 5S RNA gene. Transcription is not likely to be due to

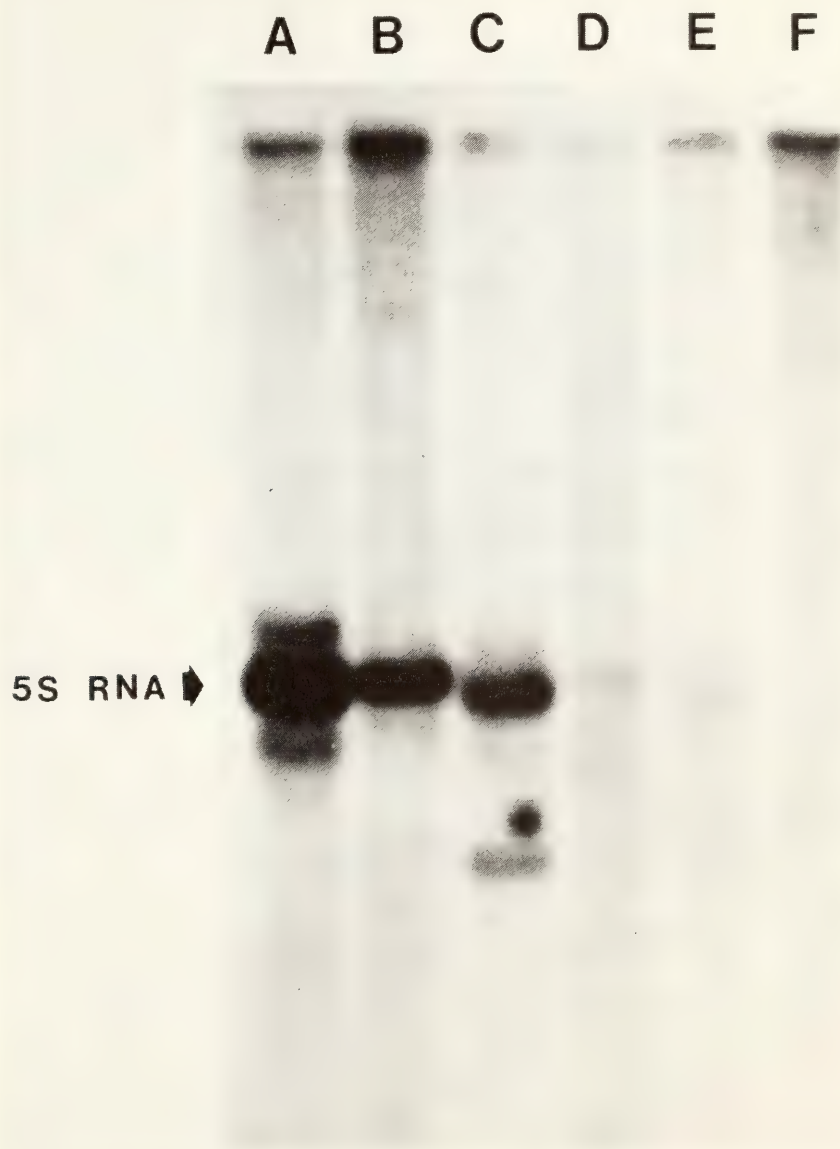


Fig. 45. Autoradiogram of  $^{32}\text{P}$ -labeled RNA synthesized in vitro using different deleted 5S DNA's as templates. RNA was electrophoresed on a 10% nondenaturing acrylamide gel. A. pXbs1 containing a complete 5S repeating unit. B and C. +47 deletion inserted at two different orientations into pBR322. D. +64 deletion. E. +77 deletion. F. Deletion to five base pairs past the end of the 5S RNA gene.

the fortuitous presence of a plasmid sequence with promoter function, since the synthesis of discrete "5S" RNA is observed with inserts in both orientations. Furthermore, D. Bogenhagen has shown that 5S DNA cloned at a *Sau*3A site at +40 of the 5S RNA gene into the *Bam* HI site of pBR322 supports "5S" RNA synthesis. Thus, transcription initiation can occur within a third region of the plasmid. Deletion molecules whose end points map at +59, +64, and +77 support little or no synthesis of "5S" size RNA (Fig. 46). Therefore, we conclude that the sequence necessary for 5S RNA transcription must reside within the 5S RNA gene itself, and the 5' border of the promoter sequence must be somewhere between +47 and +59 of the gene sequence (Fig. 46). The discrete "5S" RNA size transcript from intragenically deleted 5S DNA indicates that the importance, if any, of a specific sequence for transcription initiation is minimal. Rather, the initiation of 5S RNA transcription may be dictated by less specific requirements such as the presence of a purine at a certain distance upstream from the promoter sequence. Further-

more, it presents another piece of evidence that 5S RNA is a primary transcript and not processed, at least on its 5' side, from a precursor molecule. It seems unlikely that precursor molecules with different sequences would all be processed to mature molecules of the same size.

Our *in vitro* transcription system is not designed to be a quantitative assay. Therefore, even though some deletion mutants seem to be less efficient as transcription templates, we do not yet know whether this decrease represents the loss of a sequence that affects transcription.

### *Deletions of the 3' End of the Gene*

*D. Bogenhagen and D. D. Brown*

Our collection of 5' deletion mutants has shown that a control region for RNA synthesis is located within the *Xbs* 5S RNA gene, in contrast to prokaryotic models of transcription. However, 5S RNA transcription termination may be more predictable by analogy to prokaryotic models. In *Year Book 77*, Korn and Brown compared the sequences of several

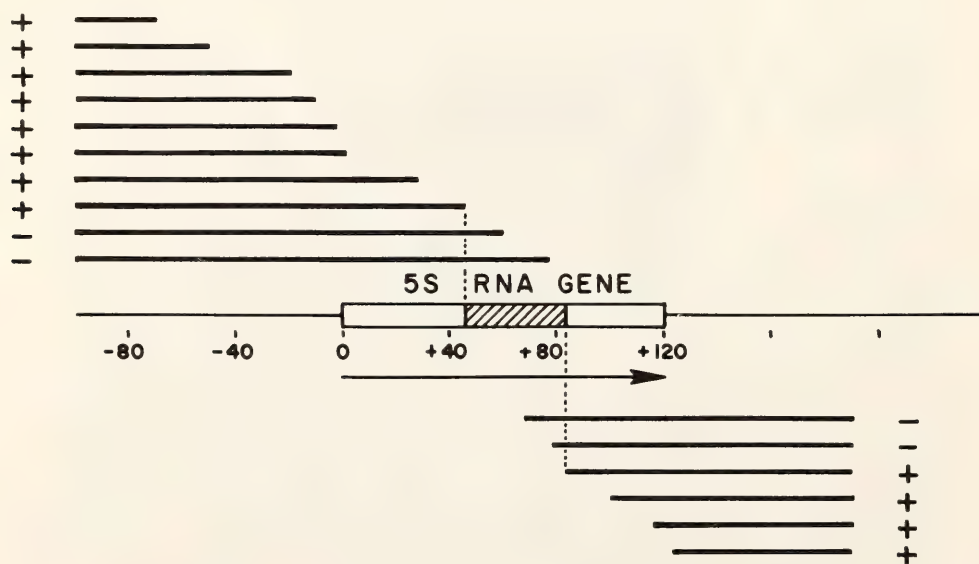


Fig. 46. A summary of 5' and 3' deletions into the 5S RNA gene of *Xbs*1. The 5S RNA gene is represented as a block, and the arrow denotes the direction of RNA transcription. The extent of 5' and 3' deletions is shown as lines above and below the diagram of the gene, respectively. Deletion mutants that still initiate at specific locations are scored with a plus sign; those that do not are scored with a minus sign. The assays for each kind of deletion are described in the text. The cross-hatched part of the gene is the putative promoter.



*Xenopus* 5S RNA genes as well as that of the 5.5S RNA of adenovirus, another RNA polymerase III product. They found the following similarities to prokaryotic termination sites: (1) a dyad symmetry element within the gene ending about 10 nucleotides from the terminus and (2) termination within a cluster of T-residues (on the noncoding strand). In addition, the five *Xenopus* 5S genes share considerable homology to the sequence TTXACTTTTGCCATTC in the 17 residues following the gene. Thus, a set of 5S RNA genes containing successively larger 3' deletions will lack, first the extragenic 3' homology region, then the T-cluster, and later the dyad symmetry element. Large deletions that remove sequences necessary for termination may be expected to allow faithful initiation without termination, resulting in long RNA transcripts.

We cloned a large number of 5S genes with varying degrees of 3' deletion, using an approach similar to that described for 5' deletions. We began with a fragment of Xbs1 DNA of fixed orientation, having a Hind III site approximately 57 nucleotides in front of the gene (i.e., on the 5' side) and a Bam HI site in the 3' flanking sequence. This gene was cloned as a Bam HI–Hind III insert in the plasmid vector pBR322. A heterogeneous pool of deletions was produced by cutting with Bam HI to expose the 3' side of the gene, then digesting with Exo III, followed by nuclease S1. Bam HI linkers were added by blunt-end ligation using T4 DNA ligase. This heterogeneous pool of deletion mutants was fractionated on the basis of size in a polyacrylamide gel into extragenic and intragenic deletions, and recloned in pBR322. Individual clones were isolated, and the extent of deletion was determined by sizing the Sau3A restriction fragment beginning at residue 40 within the gene and ending within the Bam HI linker.

These 3' deletions fall into two classes that require separate methods of analysis

of their in vitro transcription products. The largest extragenic deletion capable of supporting accurate termination of transcription that has been found ends about four nucleotides beyond the end of the gene. We conclude that the DNA sequence beyond the T-cluster in the spacer is not absolutely required for accurate 5S RNA termination, although it may influence the efficiency of termination. Genes with larger deletions that remove the T-cluster do not make discrete 5S size transcripts. However, to show that these intragenic deletions are transcription *termination* mutants, it is necessary to demonstrate that transcription *initiation* is not severely affected. This is not a trivial distinction, since we have shown that the promoter is located within the 5S RNA gene. If sequences important for termination overlap significantly with the intragenic promoter, it may be impossible for 3' intragenic deletions to promote initiation. We have developed several procedures to assay for specific initiation in the absence of specific termination. One of these is described elsewhere in this Report. Another convenient method has been the inclusion of a nucleotide analogue, cordecypin triphosphate, in the in vitro transcription reaction. This analogue is an RNA chain terminator whose incorporation in the place of adenylylate residues in a growing RNA transcript stops chain elongation. The pattern of chain-terminated intermediates in Xbs 5S RNA synthesis can be resolved as a characteristic ladder-like pattern on denaturing polyacrylamide gels. Using this assay procedure, we have shown that several mutants lacking the normal T-cluster support accurate initiation but fail to terminate transcription. Figure 46 shows that 5S RNA genes ending approximately between residues 82 and 115 allow accurate initiation at the beginning of the 5S RNA gene, whereas more extensive deletions do not. For example, a gene with an intact 5' flanking sequence and the first 5' 78 nucleotides of the gene does not

support initiation in the 5S RNA gene. It is a control mutant. These data complement data derived from analysis of 5' deletions, by indicating that a DNA region in the center of the gene is essential for transcription initiation.

The summary of both 5' and 3' deletions indicates that a region approximately bordered by +50 to +53 at its 5' end and +78 to +82 at its 3' end is required for specific binding of RNA polymerase III for accurate transcription initiation (Fig. 46). The initiation of transcription does not require a specific "initiation sequence" but seems to occur at a specified distance from the binding site. Termination of transcription requires the full 3' end of the gene including the T-cluster.

### *The Preparation and Transcription of 5S RNA "Maxi-Genes"*

*D. Bogenhagen*

To generate greater diversity of 5S RNA gene mutants, a modified Xbs 5S RNA gene containing a single Bam HI restriction endonuclease cleavage site was constructed (Fig. 47). The starting material for this recombination was one of the altered Xbs genes cloned by S. Sakonju. This DNA fragment contains a full-length 5S RNA gene flanked by 50 nucleotides on its 5' end and 39 nucleo-

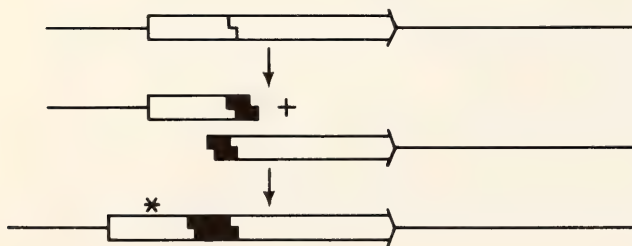


Fig. 47. Construction of a 5S "maxigene." The Hind III insert of a 5' deletion mutant of Xbs 5S DNA is shown with a staggered cut site for Sau3A. The two Hind III/Sau3A gene fragments were cloned separately, reisolated, and reunited to produce a "maxigene" containing a 20-nucleotide insert. The asterisk denotes the new initiation site for transcription of the altered gene.

tides at its 3' end. The gene supports 5S RNA transcription in the in vitro extract and contains a single Sau3A restriction site ( $\downarrow$ GATC) that is cleaved to produce the same "sticky end" as Bam HI ( $G\downarrow$ GATCC). The isolated Hind III insert was cleaved with Sau3A, and the fragments ligated to synthetic decanucleotide DNA linkers. These commercially available Bam HI linkers had been ligated previously to form oligomers and then cleaved with Bam HI to generate the "sticky ends." The 5' third and 3' two-thirds of the gene were then cloned separately as Bam HI-Hind III fragments in the vector pBR322. Since both fragments have different restriction sites on each end, they can be recombined or modified without change in their orientation.

The two gene fragments were religated and cloned as a Hind III insert in pBR322 to produce a 5S "maxigene" with an insertion of 20 nucleotides (containing a single Bam HI site). This "maxigene" might be expected to direct synthesis of a 140-nucleotide transcript in the germinal vesicle extract. However, the discrete, stable "maxigene" transcript did not migrate substantially slower than Xbs 5S RNA on a 95% formamide denaturing polyacrylamide gel. The fingerprint of a T1 RNase digest of this RNA lacked the three 5' oligonucleotides of a normal Xbs 5S RNA transcript. The primary maxigene transcript was labeled at the 5' terminus by including  $\gamma$ - $^{32}\text{P}$ -ATP in the in vitro transcription system, and the RNA was gel isolated and subjected to end-group analysis by complete digestion with pancreatic RNase and S1 nuclease and thin-layer chromatography. The majority of transcripts were initiated with A and a minority with G residues. This result suggests that transcription initiates within the oligonucleotide AAAG at gene positions 22-25. Thus it appears that insertion of a 20-nucleotide intervening sequence at residue 40/41 of a 5S RNA gene causes RNA polymerase III to ignore the usual transcription start



site and to initiate instead at purine residues approximately 20 nucleotides downstream within the gene sequence. This result further suggests that the mechanism of transcription initiation by RNA polymerase III may involve recognition of an intragenic control site more than 50 nucleotides from the site of initiation.

### *A Termination Mutant of 5S DNA*

*D. D. Brown and E. Jordan*

Using the oocyte-injection method we had found one cloned repeating unit of *X. laevis* oocyte-specific 5S DNA (Xlo6) that made less 5S RNA than other cloned repeats. This DNA has been tested in the nuclear extract. Compared to other cloned repeating units of *X. laevis* oocyte 5S DNA, Xlo6 synthesized less than half as much 5S RNA. RNA transcription reads through the termination site and stops at other T-clusters in the spacer region. We have sequenced the DNA on both sides of the termination site in Xlo6. The sequence is identical to that of other repeating units of Xlo 5S DNA except for a single nucleotide change (Fig. 48). The fourth T in the cluster at the termination site is changed to a C-residue. This result emphasizes the importance of the T-clusters for accurate termination—a fact that had been inferred from the presence of four or more T-residues at the ends of all 5S RNA genes that have been studied to date (see *Year Book 77*).

### IDENTIFICATION OF FACTORS REQUIRED FOR ACCURATE TRANSCRIPTION OF 5S RNA GENES

*E. Birkenmeier*

Our previous results demonstrated that a nucleoplasmic extract of *Xenopus laevis* oocyte nuclei could accurately transcribe exogenously added 5S RNA genes (*Year Book 77*). Since then, all known 5S RNA gene families of *Xenopus laevis* and *Xenopus borealis* have been

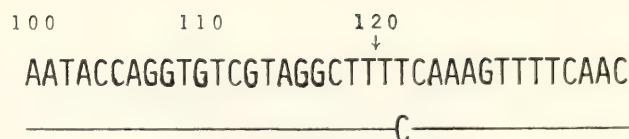


Fig. 48. The sequence of a termination mutant of *X. laevis* oocyte 5S DNA. The upper line is the dominant sequence surrounding the termination site of the 5S RNA gene in Xlo 5S DNA. The sequence of Xlo6 (below) is identical except for a T→C change in the last T at the termination site. The arrow denotes where most transcription events terminate. Sequences of the noncoding strands are shown. Transcription is from left to right.

accurately transcribed in vitro. Because the extract transcribes both oocyte-type and somatic-type genes, it is not known whether the factors required for faithful transcription in vitro are the same for all gene families. In order to begin to answer this question, two types of experiments have been used.

The first type was to see if addition of purified RNA polymerase III to the in vitro transcription reaction increased the amount of 5S RNA synthesized. If it did, then one would be able to add back various nuclear proteins to pure RNA polymerase III until accurate 5S RNA synthesis was achieved. The unexpected result was that while addition of RNA polymerase could double total RNA synthesis, there was no increase in 5S RNA synthesis. Similar results were obtained even if the template DNA was preincubated in the reaction mixture before addition of the RNA polymerase. Presumably, some alteration in the enzyme occurred during its purification that could not be reversed by incubation in the nucleoplasmic extract.

Therefore, a second type of approach was used. We began to fractionate the extract. This was done to see whether components required for accurate 5S RNA synthesis could be separated from RNA polymerase III. The RNA polymerase in the extract bound to a DEAE-cellulose column. No polymerase activity was found in the flow-through material.



Fig. 49. Autoradiogram of an electrophoretic gel of [ $^{32}$ P]-RNA synthesized in vitro. The recombinant plasmid pXbs1 containing one *Xenopus borealis* somatic type 5S RNA gene was the template. In channel A the RNA polymerase recovered after chromatography on two DEAE-cellulose columns was incubated with pXbs1. In channel B the material that flowed through the first DEAE-cellulose column was added to the reaction mixture. 21% more acid-insoluble [ $^{32}$ P]-counts were incorporated into total RNA for the reaction without the flow-through material (channel A).

RNA polymerase was then eluted from the column with 140 mM  $\text{NH}_4\text{Cl}$ . The enzyme now showed a fivefold decrease in the amount of 5S RNA synthesized. Normal levels of 5S RNA synthesis were restored by adding back the flow-through material from the column.

To better characterize this flow-through fraction, it was necessary to obtain an RNA polymerase III fraction that synthesized no 5S RNA. This was accomplished by passing the extract through a Bio Gel A 0.5-m column. The enzyme eluted from the column in the void volume and was concentrated by chromatography on DEAE-cellulose. This enzyme synthesized no 5S RNA. If, however, the flow-through fraction described above was added to this enzyme, faithful transcription of 5S RNA genes was restored. Similar results were obtained when the RNA polymerase was chromatographed on two consecutive DEAE-cellulose columns (Fig. 49). Thus, it is now possible to have a partially pure RNA polymerase III preparation that makes no 5S RNA unless the DEAE-cellulose flow-through material is present. With this assay it should be possible to purify the components in the flow-through fraction that are required for accurate 5S RNA synthesis.

#### TRANSCRIPTION INITIATION IN EXTRACTS OF NUCLEI FROM *Xenopus* OOCYTES

L. J. Korn, E. H. Birkenmeier, D. D. Brown,  
and E. Jordan

Faithful transcription is the result of accurate initiation and termination of RNA synthesis. The oocyte nuclear extract carries out both of these events when 5S DNA is added as a template and synthesizes 5S RNA (*Year Book* 77). If initiation or termination of transcription is not accurate, acrylamide gel electrophoresis does not yield much information on the specificity of transcription, since the RNA is heterogeneous in size. For this reason we have developed



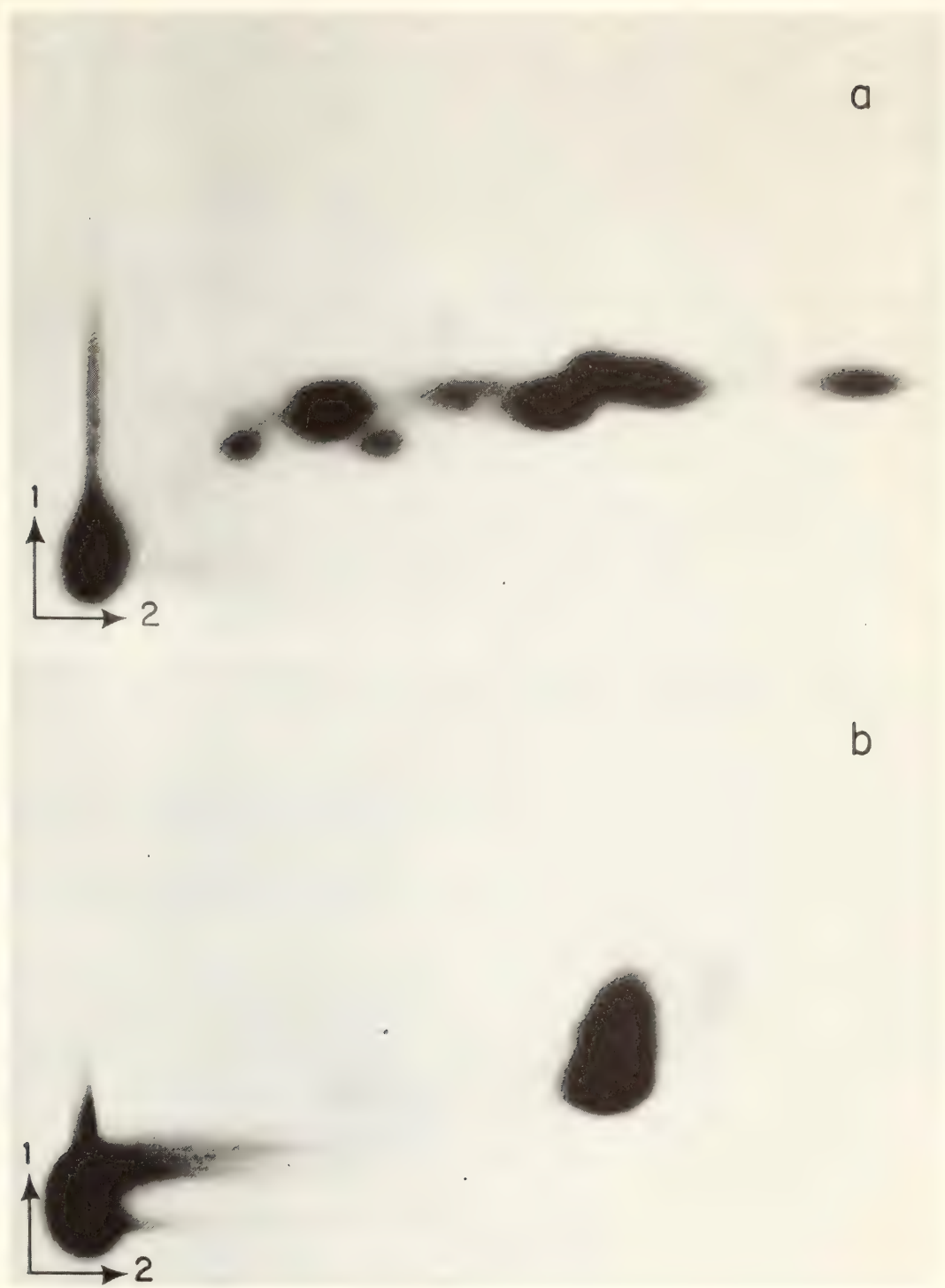


Fig. 50. Two-dimensional thin-layer chromatography on PE1 plates of RNA labeled with  $\gamma$ - $^{32}\text{P}$ -ATP in the in vitro extract. The labeled RNA was digested with pancreatic RNase. The templates used were (a) the plasmid pBR322, (b) pXbs1.

an initiation assay that does not rely on accurate termination. The assay requires that the first nucleotide of all transcripts be labeled. Since only the first nucleotide of the RNA retains all three phosphates, it can be identified after hydrolysis of the RNA. The first nucleotide is labeled

by adding  $\gamma$ - $^{32}\text{P}$ -ATP as one of the nucleoside triphosphates in the reaction mixture. We found that the radioactivity is rapidly distributed to all four ribonucleoside triphosphates in the mixture, thus providing  $\gamma$ - $^{32}\text{P}$ -labeled substrates for all RNA initiation events. Further-

more, the label is not transferred to the  $\beta$  or  $\alpha$  positions during the incubation procedure. The radioactive RNA transcribed from different 5S DNA-containing plasmids was digested with pancreatic RNase to generate 5' oligonucleotides. These oligonucleotides were separated by two-dimensional chromatography. There are at least eight different oligonucleotides characteristic of the multiple start sites in the plasmid vector (Fig. 50a). However, when this same plasmid has a single 5S DNA insertion (Fig. 50b), there is only one major oligonucleotide. Additional studies show that this oligonucleotide begins with a G-residue, and it migrates at the position expected for pppGpCp—the predicted oligonucleotide derived from the 5' end of 5S RNA by cleavage with pancreatic RNase. Therefore, transcription from the 5S DNA-containing plasmid starts only at the beginning of the 5S RNA gene, and initiation of transcription within the plasmid is suppressed. Analysis of the plasmid transcripts shows that they all begin with purines.

The requirement for initiation of transcription at a purine residue is demonstrated by an altered 5S RNA gene that is present in a cloned fragment of *X. borealis* oocyte 5S DNA. Among the several nucleotide changes between this gene (gene three) and the

most abundant 5S RNA gene sequence are the first nucleotide of the gene and several upstream from the gene (Fig. 51). The first nucleotide is changed to a pyrimidine (G→C) and the nucleotide at  $-1$  is changed to a purine (T→A). This gene is transcribed into an RNA of about the same length as 5S RNA by the nuclear extract. Analysis of this RNA shows that transcription of gene three begins at the purine located at  $-1$  rather than at the pyrimidine present at  $+1$ .

The initiation assay has been used to test a number of altered 5S RNA genes that do not support the synthesis of 5S RNA. The results show that at least some of these genes still initiate accurately but have defective termination sites.

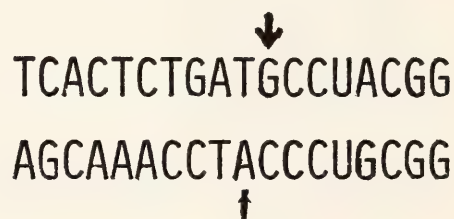


Fig. 51. The sequence of the initiation site of gene one (upper) and gene three (lower) of a cloned fragment of *X. borealis* oocyte-specific 5S DNA. The arrows show where the initiation of transcription occurs in these two genes, and transcription is from left to right. Sequences of the noncoding strands are shown.

## STRUCTURAL AND FUNCTIONAL STUDIES OF THE FIBROIN GENE

*Y. Suzuki, M. Tsuda, Y. Tsujimoto, Y. Ohshima, and P. E. Giza*

Since 1968 we have been trying to understand the regulation of a tissue-specific gene, the silk fibroin gene of *Bombyx mori*. The task is still incomplete, but this report is the final one by our group within the Department. We describe the sequence of a region flanking the 5' end

of the gene that includes the putative promoter region. The presumed transcription initiation site has been determined, and a promising in vitro transcription system is described that initiated RNA synthesis on the correct strand at about the correct site.



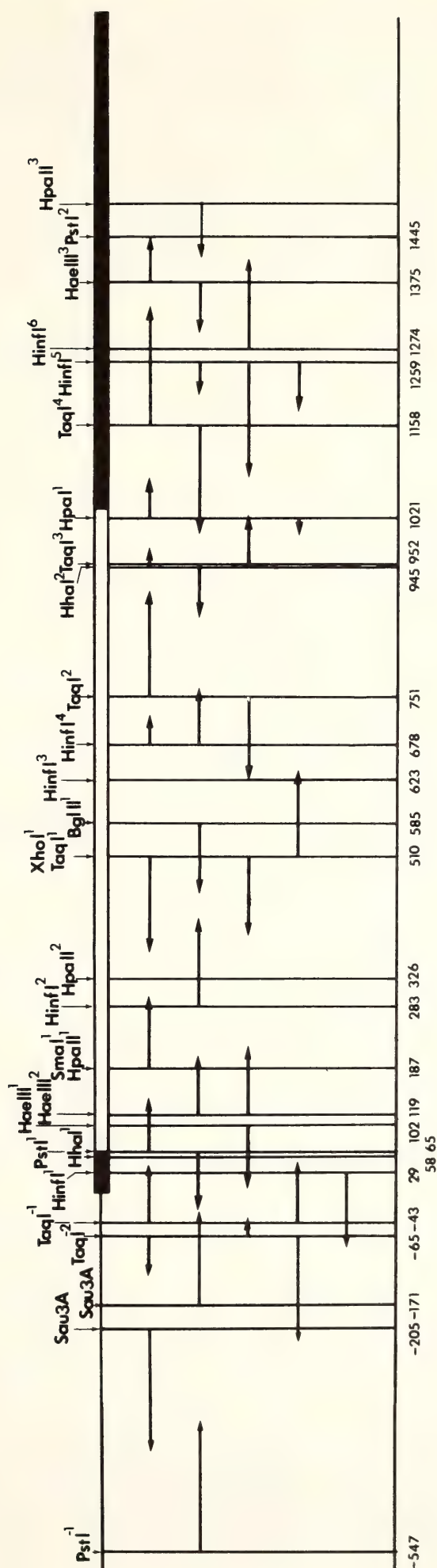


Fig. 52. Restriction map and sequencing strategy of the intervening sequence and neighboring regions of the fibroin gene. The upper part represents the restriction map of the region encompassing the intervening sequence of the fibroin gene, with the 5' end of the transcription unit at the left. The boxed regions indicate the gene, and the open box shows the intervening sequence. The cleavage sites of restriction enzymes are numbered from the cap locus, and their positions are shown at the bottom of the figure by the distance (in bases) on the non-coding strand from the cap locus. The arrows indicate the regions sequenced and directions of the respective sequencing. Only two sites cleaved by *Sau3A*, which were used for DNA sequencing, are shown.

## STRUCTURAL ANALYSIS OF THE FIBROIN GENE

*Y. Tsujimoto and Y. Suzuki*

In *Year Book 77* we described some results of the structural analysis of the fibroin gene. We describe here additional sequencing information from a genomic recombinant DNA (pFb29) and a cDNA copy of fibroin mRNA, including the intervening sequence and its borders as well as the 5' flanking region, which is expected to contain a promoter for RNA polymerase and regulatory signals for transcription.

Although fibroin is known to consist mostly of repetitious glycine-alanine residues, the N-terminal amino acids of fibroin or its precursor are not known. The DNA sequence permits some conclusions about the protein sequence.

### *Precise Localization of the 5' and 3' Coding-Intervening Junctions*

The restriction map of the intervening sequence and its neighboring regions is shown in Fig. 52. The nucleotide sequences from -552 to +1497 (calling the cap locus +1) was determined for a cloned genomic fibroin gene (pFb29) (Fig. 53).

As described in *Year Book 77*, the fibroin gene is interrupted by a 1-kb intervening sequence near the cap locus. To locate more precisely the 5' and 3' junctions of the coding-intervening sequence, we first carried out S1 mapping experiments, as described by Berk and Sharp (*Cell*, 12, 721, 1977), using fibroin mRNA and cloned genomic DNA. The result is that the 5' coding-intervening junction is located about 68 bases downstream from the 5' end of the gene, and the 3' junction is about 10 bases downstream from the Hpa I site at +1021 (see Fig. 52). To pinpoint these junctions in the DNA sequence, the nucleotide sequence of mRNA that does not contain the intervening sequence has been determined. We sequenced the comple-

mentary DNA (cDNA) synthesized in vitro from fibroin mRNA, using reverse transcriptase. The cDNA primed with a DNA fragment labeled at the Taq I site was sequenced by Maxam and Gilbert's method (*Proc. Nat. Acad. Sci. U.S.A.*, 74, 560, 1977) and compared with the sequence of the genomic fibroin gene (Fig. 54). The sequence of cDNA coincides perfectly with the genomic sequence from +1160 (Taq I cleavage site) to +1034 (shown by arrows in Fig. 54) but then changes at +1033. The cDNA sequence also corresponds to the genomic sequence from +64 to the 5' end of the gene. The result indicates that the fibroin gene contains a 970-base-long extra sequence that is not present in mRNA. Since the sequence CAG repeats at both 5' and 3' coding-intervening junctions (see Fig. 53), the positions where the intervening sequence starts and terminates are at 64-66 and at 1034-1036 bases downstream from the 5' end of the gene, respectively.

### *Characteristics of the Intervening Sequence in the Fibroin Gene*

The intervening sequence is 64% AT, and the two mRNA coding regions are 53% AT (+1 to +66) and 57% AT (+1037 to +1498). The 5' flanking sequence (-1 to -552) is AT rich (70% AT). It is not known whether this intervening sequence is within the protein coding region because the location of the initiation codon for fibroin is not known. As shown in Fig. 53, the nucleotide sequence from +1448 to +1498 corresponds to the repetitious glycine-alanine peptide that is characteristic of fibroin. When nucleotide codons are read upstream in phase, possible initiation codons (AUG) appear at nucleotide positions +1301, +1232, +1184, and +25. In nearly all eukaryotic mRNA, the 5' proximal AUG is the initiation codon (Kozak, *Cell*, 15, 1109, 1978). In fibroin mRNA, the AUG at +25 is the most 5' proximal one. These facts strongly sug-



CT  
GA

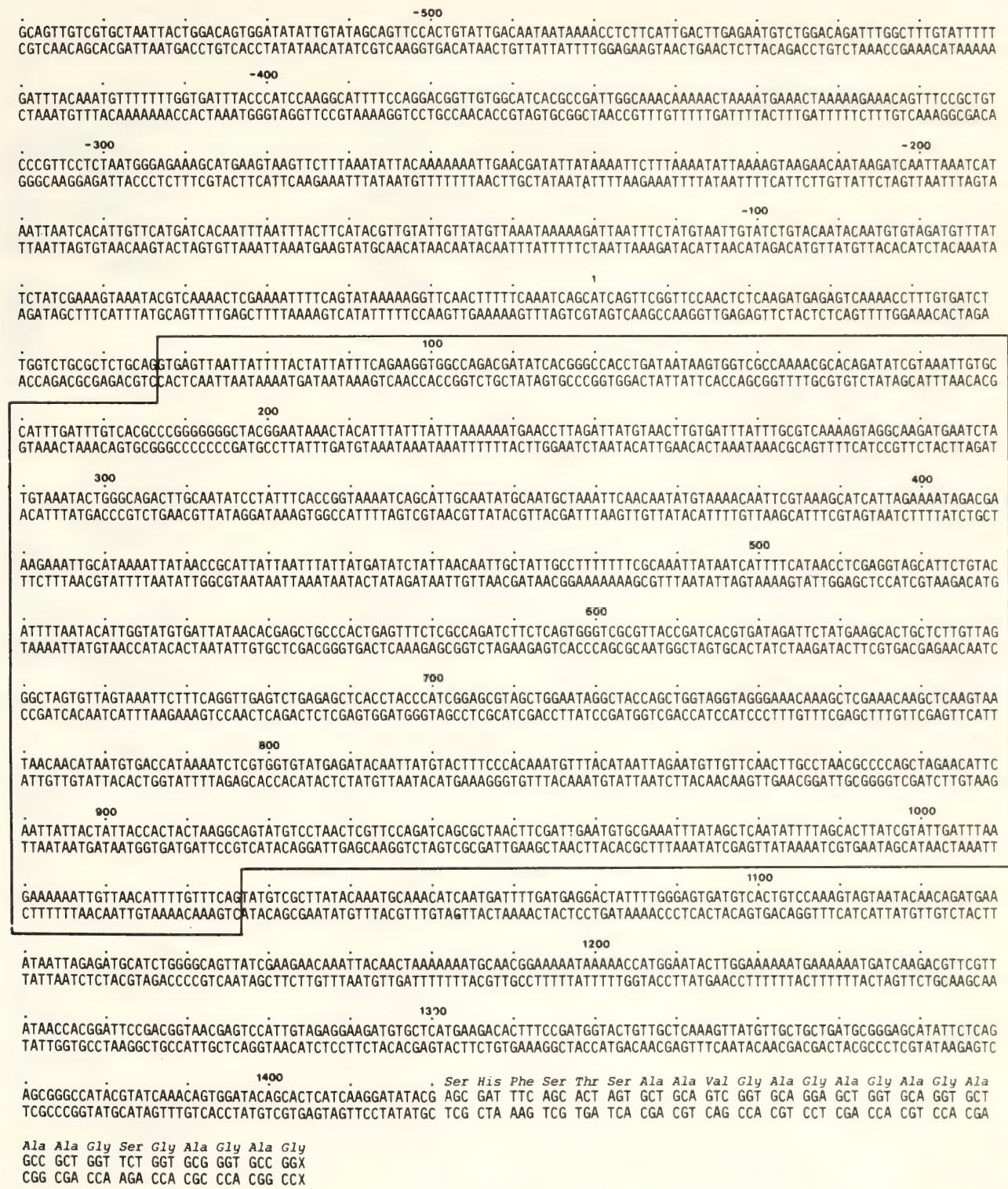


Fig. 53. The complete nucleotide sequence of the intervening sequence of the fibroin gene with its neighboring sequences. The boxed region is the intervening sequence of 970 bases. Amino acid residues are also shown above the sequence that immediately precedes and codes the repetitious glycine-alanine peptide.

gest that the AUG at +25 is the initiation codon for fibroin, and the intervening sequence is within the protein coding region. If that is the case, either fibroin or its precursor peptide should have a leader peptide of a maximum of 158 amino acid residues that is of the non-(gly-ala) type. It is interesting to



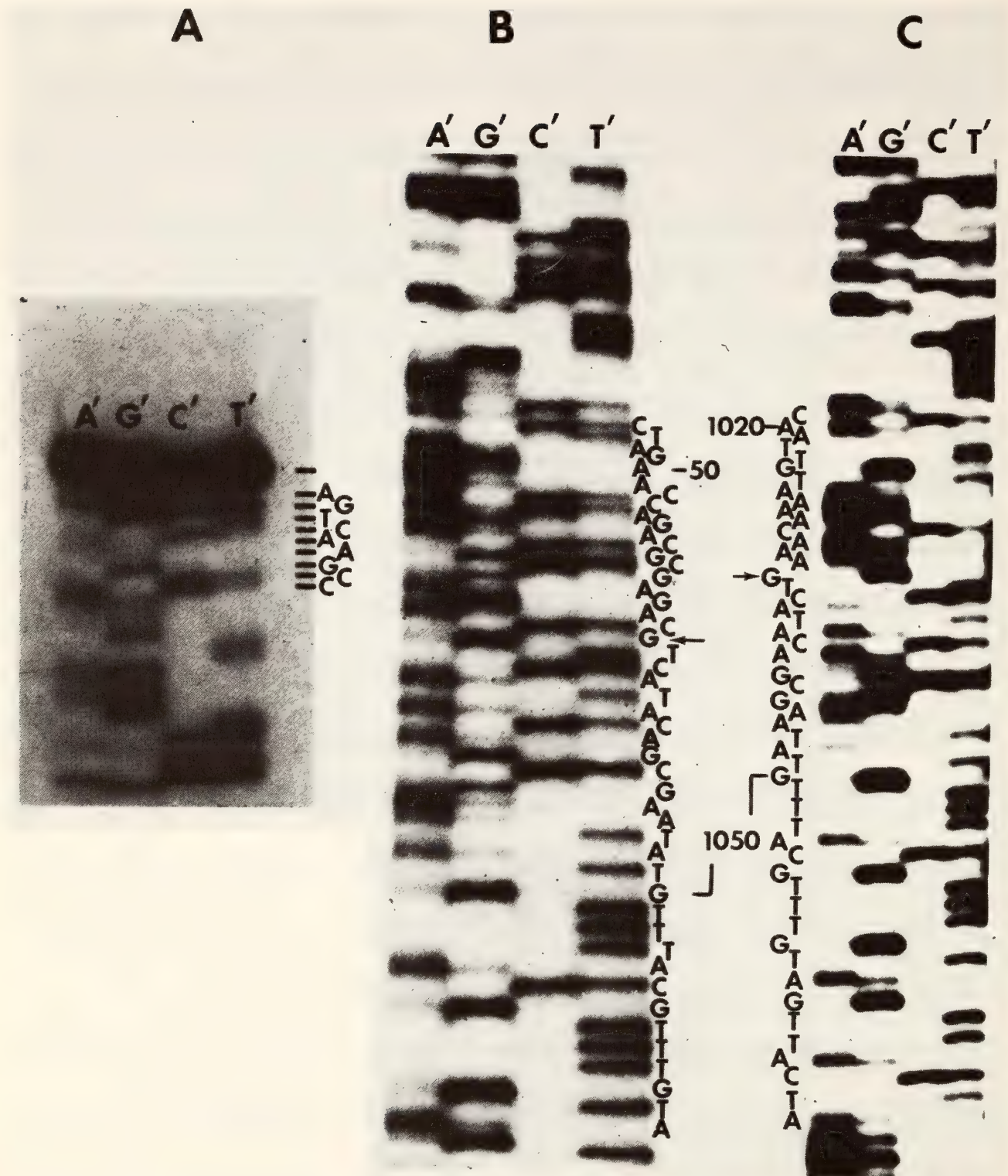


Fig. 54. Autoradiograms for determination of nucleotide sequences of cDNA and the cloned genomic gene. (A and B) The sequence corresponds to mRNA coding sequence. (C) A restriction fragment, Alu I-Taq I (Alu I is at +976, and the Taq I site was labeled with <sup>32</sup>P), containing the 3' coding-intervening junction, was sequenced. The numbers indicate the distance of the sequence from the 5' end of the gene. The arrows represent the position where the sequence of cDNA no longer corresponds to the sequence of cloned genomic DNA.

note that the presumed leader peptide contains a hydrophobic peptide at its N-terminus, which is characteristic of secretory proteins and is suggested to be

necessary for the transfer of a protein across a membrane (Blobel *et al.*, *J. Cell Biol.*, 67, 835, 1975). It is interesting to speculate whether



the intervening sequence could encode a protein. The intervening sequence of the fibroin gene contains 16 possible initiation codons (16 AUG) and 65 termination codons (16 UAG, 32 UAA, 17 UGA) for protein synthesis. All possible initiation codons are followed by termination codons in phase within the intervening sequence. The largest potential polypeptide encoded by the intervening sequence is 60 amino acid residues long. It has never been tested whether this peptide is actually synthesized.

### *RNA-RNA Splicing and Sequences at the Coding-Intervening Junctions*

The nucleotide sequence at the coding-intervening junction would be expected to have a signal for splicing of the RNA. We notice the following features of the sequence. The first is its homology with the coding-intervening junctions of many eukaryotic genes. The fibroin gene, an insect single-copy gene, shares homologous sequences at its coding-intervening junctions with those of avian and mammalian genes (W. Gehring, *Nature*, 275, 3640, 1978), as shown in Fig. 55. This homology suggests that these sequences may play an important role in splicing precursor transcripts to mature RNA and that a similar mechanism or a similar enzyme is involved in the splicing of many different genes. The splicing mechanism thus seems to be conserved during evolution.

The second feature is that the intervening sequence of the fibroin gene contains a long inverted repeat (17 base match out of 23 bases) at its extremities, as shown in Fig. 56. This situation is not restricted to the fibroin gene, since inverted repeats that are more poorly matched have been observed at similar positions in the intervening sequence of many other genes, including mouse and rabbit  $\beta$ -globin, mouse immunoglobulin, and ovalbumin genes. The fibroin mRNA sequence next to the intervening sequence

can be drawn into a secondary structure, so that the intervening sequence is extruded out of a folded mRNA sequence (C. Mak and M. Philipp, personal communication). The secondary structure extends from nucleotide position +9 to +139 of the mRNA sequence. This kind of secondary structure might facilitate the removal of the intervening sequence from a precursor transcript.

In prokaryotes, some transposable elements are able to integrate into many different loci in the genome (for a review, see Kleckner, *Cell*, 11, 11, 1977). The 5' and 3' extremities of one of the prokaryotic transposable elements, IS1 (Ohtsubo and Ohtsubo, *Proc. Nat. Acad. Sci. U.S.A.*, 75, 615, 1978), show some sequence homology with the sequence of the eukaryotic coding-intervening junctions, especially the 5' junction as shown in Fig. 55. Thus, eukaryotic intervening sequences and prokaryotic transposable elements might have shared a common origin. The integration of IS1 sequence into the genome results in the generation of direct repeats of nine bases (Grindley, *Cell*, 13, 419, 1978; Calos *et al.*, *Cell*, 13, 411, 1978). The direct-repeat sequences can also be seen at the boundaries of eukaryotic intervening sequence (Fig. 55).

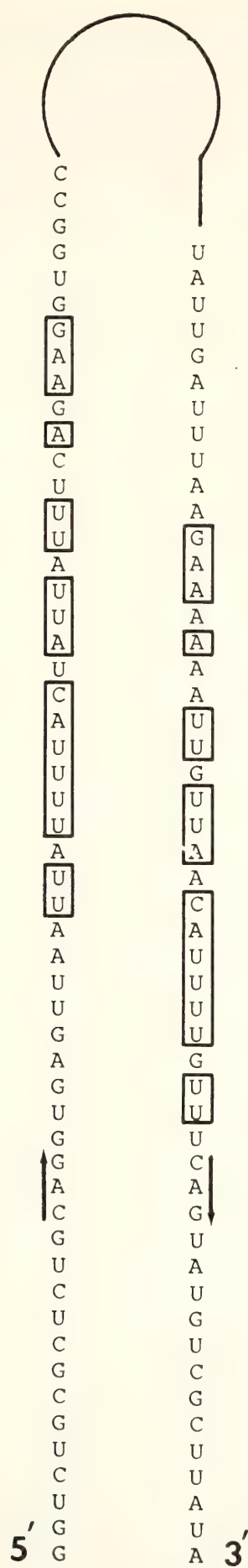
### *Determination of the Cap Locus of the Fibroin Gene*

In *Year Book 77*, we described the location of the 5' end of fibroin mRNA in the DNA sequence. However, the ATCAG sequence that corresponds to the 5' end of fibroin mRNA is present in tandem as ATCAGCATCAG (−6 to +5 bases in Fig. 53) around the 5' end of the gene. We tentatively identified the second ATCAG sequence as the cap locus of the gene.

The cDNA described above represents a full-length copy of fibroin mRNA. In order to determine the 5' end of the gene, we asked where the 3' end of cDNA







terminated. As shown in Fig. 54, DNA sequencing of cDNA terminates at +1. Unless there is steric hindrance for cDNA synthesis near the 5' end of fibroin mRNA, the result indicates that the second ATCAG corresponds to the 5' end of fibroin mRNA.

The sequence at the 5' end of mRNA can be folded into a secondary structure as shown in Fig. 57. The  $\Delta G$  value for the secondary structure is estimated as  $-16.8$  kcal, or  $-0.37$  kcal per nucleotide, according to the calculation outlined by Tinoco *et al.* (*Nature New Biol.*, 14, 40, 1973). Thus the secondary structure is thermodynamically stable, although its existence in vivo is not proven.

We also note a sequence with extensive complementarity to the 3' end of the 18S ribosomal RNA (Hagenbüchle *et al.*, *Cell*, 13, 551, 1978), as shown in Fig. 57.

*The 5' Flanking Sequence*

We note that the seven-nucleotide sequence TATAAAA, which is similar to the "Pribnow box" sequence found in prokaryotic DNA, is present at  $-30$  to  $-24$  in the 5' flanking sequence of the fibroin gene (Tsujimoto and Suzuki, *Cell*, 16, 425, 1979). The same or a similar sequence is also observed at the equivalent position in other eukaryotic genes including mouse  $\beta$ -globin (Konkel *et al.*, *Cell*, 15, 1125, 1978), and adenovirus late gene (Ziff *et al.*, *Cell*, 15, 1463, 1978). These findings and a tentative mapping of the transcription initiation site of the fibroin gene (Tsuda *et al.*, this Report) strongly suggest that the 5' flanking sequence immediately preceding the mRNA coding region includes a promoter. In prokaryotic promoters, in ad-

Fig. 56. The inverted repeat sequence at the extremities of the intervening sequence of the fibroin gene. The arrows indicate a CAG sequence that repeats at the 5' and 3' coding-intervening junctions. The inverted repeat sequence is boxed.

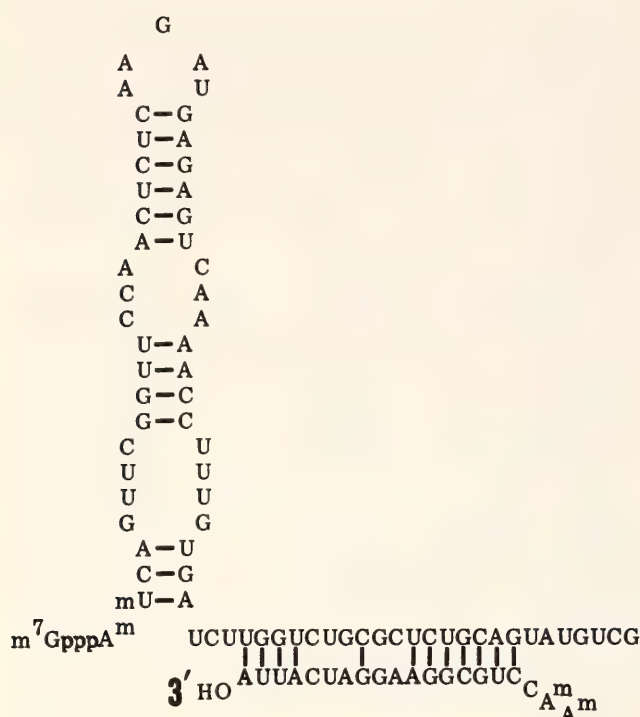


Fig. 57. Possible secondary structure at the 5' end of fibroin mRNA, and complementarity between fibroin mRNA and the 3' end of 18S ribosomal RNA. The sequence from +2 to +46 of fibroin mRNA can be drawn into a secondary structure. The fibroin mRNA possesses 12 nucleotides complementary to the 3' end of 18S ribosomal RNA at +50 to +66.

dition to the "Pribnow box," the sequence around -35 is also necessary for transcription initiation (Gilbert, in *RNA Polymerase*, 193, 1976). According to Scherer *et al.* (*Nucleic Acids Res.*, 5, 3759, 1978), a sequence around -35 that is required for transcription is 5'GTTG-TTGACATTTT3'. It is interesting to note that a similar sequence 5'TGTGT-AGATGTTTAT3' is observed at -85 to -71 in the 5' flanking sequence of the fibroin gene. Thus, eukaryotic promoters for RNA polymerase II and prokaryotic promoters might have some basic common features.

Konkel *et al.* (*Cell*, 15, 1125, 1978) have noted that the DNA region that precedes and overlaps the cap locus of several mammalian genes, including  $\beta$ -globin, immunoglobulin, and adenovirus genes, shows sequence homology. However, the fibroin gene does not reveal such a homology with the mammalian

genes (4 bases of the fibroin gene match the 12 bases of the prototype sequence; 10-12 bases match out of 12 bases in the case of the mammalian genes). If the homologous sequence mentioned by Konkel *et al.* has biological significance as a promoter, the sequence difference between the fibroin gene and the mammalian genes might reflect species difference or imply that the sequence conserved among the mammalian genes is required only for transcription of those genes.

#### A PRESUMED INITIATION SITE OF THE FIBROIN GENE TRANSCRIPTION

M. Tsuda, Y. Ohshima, and Y. Suzuki

One approach to elucidate the mechanisms of specific gene transcription is to establish a faithful in vitro transcription system. For this purpose it is essential to know the initiation site for in vivo transcription. In globin mRNA maturation, the 15S precursor RNA is assumed to be processed to the 10S mature globin mRNA by splicing of the intervening sequence (Tilghman *et al.*, *Proc. Nat. Acad. Sci. U.S.A.*, 75, 1309, 1978). We searched for transcripts that include the intervening sequence of the fibroin gene, and mapped the 5' end of these transcripts.

We have not yet determined whether the primary fibroin RNA transcript begins at the site corresponding to the cap locus (Fig. 58a) or at a distant site in the 5' flanking sequence. To detect a possible precursor that could have its 5' end initiated outside the cap locus, a good DNA probe for hybridization mapping should contain the cap locus and a long flanking sequence. For this purpose, we prepared the 6.2-kb Xho I-Eco RI fragment that had been labeled only at the Xho I end on the coding strand (Fig. 58a). Since the Xho I site is within the intervening sequence (position +514), mature fibroin mRNA cannot protect the label at the Xho I site from digestion



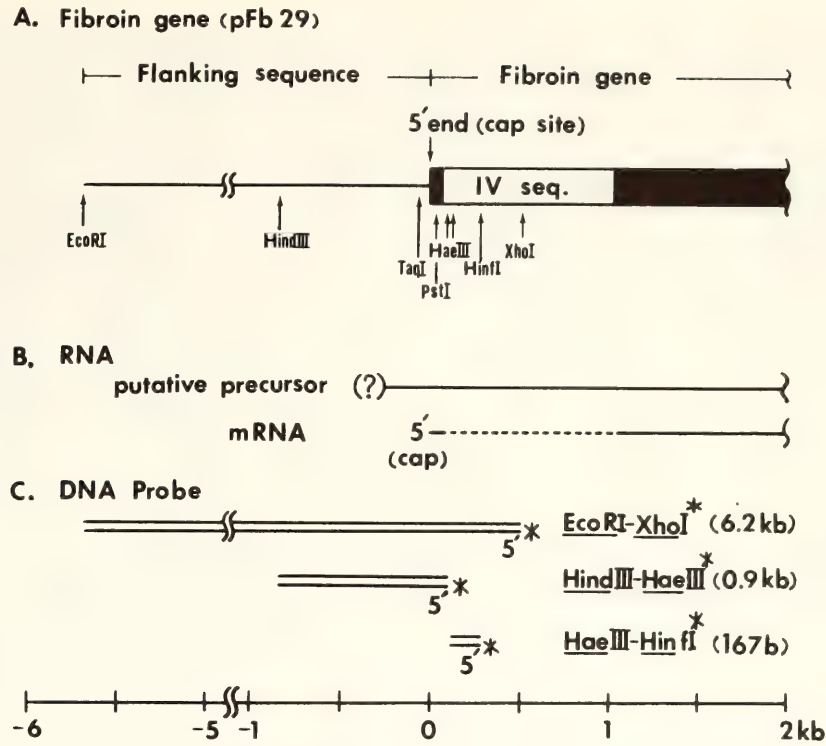


Fig. 58. Experimental design to map the transcription initiation site of the fibroin gene. (A) The black-boxed regions indicate the portions of the fibroin gene corresponding to the mature mRNA sequence, and the open box (*IV seq.*) indicates the intervening sequence (+65 to +1035). (B) The dotted line indicates the region corresponding to the intervening sequence. The question mark means the 5' end of the precursor RNA to be determined. (C) The location of the <sup>32</sup>P-label is denoted by \* in the line.

with nuclease S1 after DNA-RNA hybridization. However, a precursor of the fibroin mRNA that includes the intervening sequence (Fig. 58b) should protect the label from nuclease S1 digestion.

RNA purified from nuclei of posterior silk glands of middle fifth instar larvae were hybridized with the Eco RI-Xho I fragment using conditions described by Casey and Davidson after heat denaturation (Casey *et al.*, *Nucleic Acids Res.*, 4, 1539, 1977). Single-stranded DNA's were digested with nuclease S1, and the size of the undigested radioactive DNA's were analyzed by 1.5 alkaline agarose gel electrophoresis. As shown in Fig. 59a, a prominent band of 0.5 kb appeared. When an excess amount of the purified fibroin mRNA was used for hybridization (lane 6), the 0.5-kb band was not observed. When a similar nuclear RNA preparation from the middle silk glands, where silk fibroin mRNA is not detected, was used, this band was not detected

(lane 7). For further analysis the total cellular RNA preparation extracted from posterior silk glands was used for hybridization in order to avoid degradation of RNA during isolation of the nuclei (Fig. 59c, lane 2).

A band near the origin of the gel, which comigrates with the untreated Eco RI-Xho I fragment (Fig. 59a, lane 8), and a smear below it are common to the hybridization with any other RNA preparations used here. Since the full-size band and the smear appeared also after hybridization at 55°C when the 0.5-kb band was not detected, they might be due to the reassociation of DNA fragments during the hybridization reaction. Next, we prepared the Eco RI-Xho I fragment and slightly digested its 3' ends with exonuclease III. If reassociated DNA fragments accounted for the resistant radioactive DNA described above, the label at the 5' end of exonuclease III-digested fragments should be sensi-

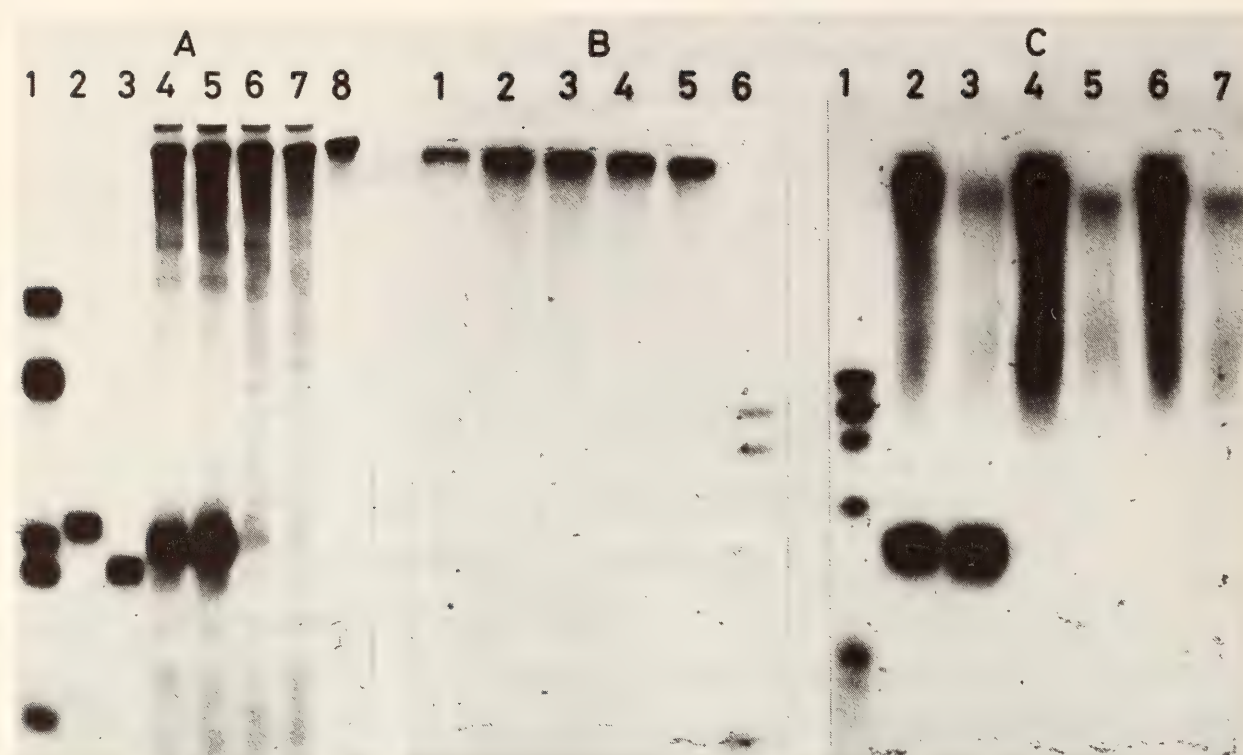


Fig. 59. Autoradiograms of 1.5% alkaline agarose gels (the S1 nuclease experiment). (A) SV40 Hind III fragments end-labeled with  $^{32}\text{P}$  (lane 1), Taq I-Xho I\* (—41 to +514, lane 2), Pst I-Xho I\* (+62 to +514, lane 3), and Eco RI-Xho I\* (6.2 kb, lane 8) fragments were run as size markers. Eco RI-Xho I\* fragments were hybridized with nuclear RNA (lanes 4 and 5) from posterior silk glands, purified fibroin mRNA (lane 6), or nuclear RNA from middle silk glands (lane 7). (B) Eco RI-Xho I\* fragments treated with exonuclease III electrophoresed on an alkaline agarose gel. (C) Eco RI-Xho I\* fragments were hybridized with total cellular RNA from posterior silk glands (lane 2), total cellular RNA from middle silk glands (lane 4), or *E. coli* tRNA (lane 6). Eco RI-Xho I\* fragments treated with exonuclease III were hybridized with total cellular RNA from posterior silk glands (lane 3), total cellular RNA from middle silk glands (lane 5), or tRNA (lane 7).

tive to nuclease S1. On the other hand, the labeled DNA-RNA hybrid molecules should be protected from nuclease S1 digestion. As shown in Fig. 59c (lanes 3, 5, 7), the full-size band and the smear disappeared drastically, while the intensity of the 0.5-kb band protected by hybridization with RNA from the posterior silk glands did not change (lanes 2, 3). From these results, we conclude that the full-size band and the smear were due to the reassociation of DNA fragments, and that the only DNA band protected by RNA is the single one estimated to be 0.5 kb.

The 0.5-kb band means that transcripts including the intervening sequence exist in the RNA from posterior silk glands and that their 5' end is close to or at the

cap site. We attempted to map the precise localization of the 5' end of the transcripts on a DNA-sequencing gel. We prepared Hind III-Hae III\* fragments labeled only at the Hae III site of the coding strand (Fig. 58c), and hybridized the DNA with nuclear RNA from the posterior silk glands; the preparation was then digested with nuclease S1. Once again it was demonstrated that the 5' end of transcripts that included the intervening sequence were located within six bases of the cap locus.

At this point we had not ruled out the possibility that a larger precursor containing a leader sequence originated from a distant site in the flanking sequence upstream from the cap locus. In that case, the DNA-RNA hybrid would



be unable to form at the site preceding the cap locus and nuclease S1 would cleave the single-stranded DNA region, giving a 0.5-kb band. Another possibility is that an unpaired region might form during hybridization owing to the high AT sequence just outside the cap locus, and nuclease S1 could cleave this region. To check these possibilities we tried to map the 5' end of the transcripts, using a reverse transcription method.

For this purpose, we prepared Hae III-Hinf I fragment (167 bases, +120 to

+286) (Fig. 58c) as a primer for reverse transcription. The fragment was derived from the intervening sequence region and labeled at the position +286. The labeled primer was hybridized with the total cellular RNA from posterior silk glands, the primer was extended with reverse transcriptase, and the products were treated with alkali and run on a 10% polyacrylamide/7M urea gel. As shown in Fig. 60, we detected a discrete band roughly estimated at 280–290 bases, corresponding to the distance from the Hinf

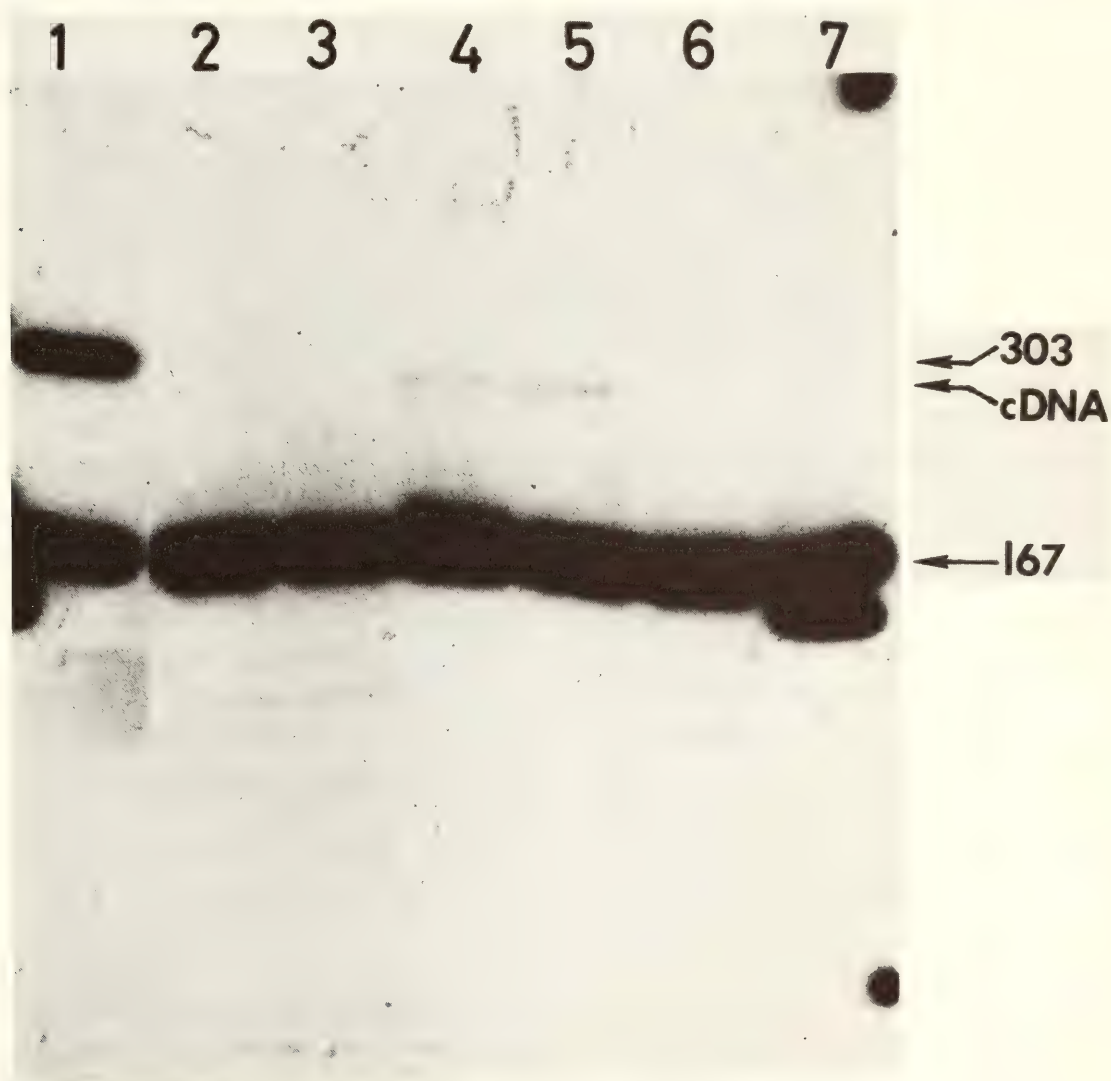


Fig. 60. Autoradiogram of polyacrylamide urea gel (the reverse transcription experiment). A size marker (303 bases) was run together with Hae III-Hinf I\* fragments (167 bases) (lane 1). Radioactive DNA was hybridized with RNA from posterior silk glands (lanes 2–5). Radioactive DNA after hybridization (lane 2), hybridization and incubation without reverse transcriptase (lane 3), and hybridization and incubation with reverse transcriptase (lanes 4 and 5) were run on a 10% polyacrylamide 7 M urea gel. Materials after hybridization with tRNA and incubation without reverse transcriptase (lane 6), and hybridization and incubation with reverse transcriptase (lane 7) were run on a gel. Reverse transcription reactions were incubated for 5 hours at 37°C using 16 units reverse transcriptase (lanes 4, 5, and 7).

I site to the cap site (lanes 4, 5). Since no other band than the 280–290 base band was detected even after prolonged exposure of the autoradiograph, the result given by the S1 experiment shown in Fig. 59 is confirmed, and we conclude that the 5' end of the transcripts including the intervening sequence is around the cap site.

To know whether there could be transcripts including the intervening sequence that are larger than the mature fibroin mRNA (16 kb), we checked the size of transcripts that protected the 0.5-kb band by the S1 nuclease method. A total RNA preparation from posterior silk glands was sedimented in a 15–30% sucrose gradient after disaggregation by heating. The RNA giving the 0.5-kb band was most concentrated in the large RNA fraction (>40S). To analyze further the size of the large RNA giving the 0.5-kb band, we collected the RNA fractions from about 36 mg of total cellular RNA and sedimented it again in a 15–30% sucrose gradient after disaggregation by heating. The S1 experiment indicated that the 0.5-kb band was produced most strongly by RNA fractions with a size that included the mature fibroin mRNA (16 kb). We conclude that there are large transcripts that could accommodate the entire mRNA sequence (16 kb) and intervening sequence (1 kb), and we assume that these transcripts containing the intervening sequence are precursors to mature fibroin mRNA.

From these results, we assume that the initiation site of fibroin gene transcription is the cap site, and the promoter sequence for initiation exists near the cap locus of the gene.

#### INITIATION OF FIBROIN GENE TRANSCRIPTION BY PURIFIED RNA POLYMERASE II FROM WHEAT GERM

*M. Tsuda and Y. Suzuki*

We have been trying to establish an in vitro fibroin gene transcription system

by reconstituting mixtures containing the cloned fibroin gene with essential components. In these experiments we tested whether extracted RNA polymerase form II (RPase II) has the intrinsic capability for selective and accurate transcription. As described in the last Report, partially purified RPase II from the posterior silk glands of *B. mori* was unable to transcribe selectively the coding strand of the fibroin gene, although purified wheat germ RPase II showed a slight preference for the coding strand (about threefold). Then we checked the effect of  $Mn^{++}$  on total RNA synthesis and on strand selectivity. As shown in Table 11, when  $Mn^{++}$  was removed from the reaction, *B. mori* RPase II was unable to transcribe the pFb29 DNA (twisted circular form), while wheat germ RPase II still revealed about half of the activity found in the presence of  $Mn^{++}$ . If  $Mn^{++}$  could activate transcription nonspecifically in vitro, the transcription ratio of coding strand to noncoding strand given by wheat germ RPase II should increase in the absence of  $Mn^{++}$ . In addition, we sought to reduce nonspecific transcription by including a preincubation step before the reaction (see legend to Table 11). As shown in Table 11, removal of  $Mn^{++}$  increased the ratio to about tenfold coding-to-noncoding strand preference transcription.

Next, we checked the initiation site of the RNA synthesized by wheat germ RPase II. As reported in the last section, we had obtained evidence suggesting that the initiation of fibroin gene transcription in vivo occurs at the cap locus. As shown in Fig. 61, the RNA synthesized when  $Mn^{++}$  was omitted gave a discrete band similar in size to the 0.5-kb band given by the in vivo RNA from posterior silk glands (Fig. 61C, lane 2). The result indicates that wheat germ RPase II can initiate transcription from a discrete site around the cap locus with high fidelity. The 0.5-kb band was not synthesized



TABLE 11. Fidelity of Transcription of the Fibroin Gene by Different RNA Polymerases\*

RPase	Preincu- bation	Mn <sup>++</sup>	Total Synthesis (cpm)	Hybridization		Ratio
				Coding	Non- coding	
<i>B. mori</i> RPase II	—	+	5,990			
		—	60			
<i>E. coli</i> RPase	—	+	1.35 × 10 <sup>6</sup>			
		—	1.36 × 10 <sup>6</sup>			
wheat germ RPase II	—	+	132,000			
		—	72,900			
	—	+	326,000	28,600	15,900	1.79
		—	207,000	27,600	10,800	2.57
	+	+	137,000	10,400	6,170	1.68
		—	13,200	1,200	117	10.2

\* The reaction mixture containing pFB29 and RNA polymerase was preincubated for 5 min at 26°C in the absence of XTPs. ATP and GTP were added to the reaction, and the mixture was incubated for 5 min. The reaction was then started at 26°C by adding CTP, UTP, and labeled UTP. The incubation was for 30 min at 26°C. The radioactive RNA synthesized in vitro was hybridized with the Hind III-Eco RI fragment that contains most of the fibroin gene sequence (described in *Year Book 77*).

in the absence of preincubation and in the presence of Mn<sup>++</sup> (Fig. 61B, lane 3)—conditions that gave a low coding strand selectivity (Table 11). When the reaction was achieved in the presence of Mn<sup>++</sup> without preincubation, the 0.5-kb band was not detected. From these results, we concluded that wheat germ RPase II was able to initiate fibroin gene transcription at one or a few sites near the cap locus. The RNA synthesized by *E. coli* RPase did not give the 0.5-kb band, although another discrete band as large as about 2 kb was detected (Fig. 61, lanes 6, 7).

In all the experiments described above, we used the substrate concentration, 30 μM each of ATP, GTP, and CTP, and 2.5 μM of UTP. The concentration is lower than that used by other workers. So we checked the effect of higher substrate concentrations (600 μM each of ATP, GTP, and CTP, and 30 μM of UTP) on the 0.5-kb band transcription. As shown in Fig. 62, the RNA synthesized using higher substrate concentra-

tion did not give the 0.5-kb band even when the amount of RPase II was increased fivefold (lanes 5, 6). Total RNA synthesis was about 20 times higher in the high substrate concentration, and the size distribution of the product RNA was large enough to give the 0.5-kb band.

The pFb29 plasmid DNA carries a fibroin gene that was isolated from the posterior silk glands where the fibroin gene is actively expressed, while the pBF41 plasmid DNA (a gift from J. Morrow and T. Mukai) has a fibroin gene isolated from pupa where the fibroin gene is known not to be expressed. No difference was found in the structure around the cap locus between pFb29 DNA and pBF41 DNA, using restriction mapping and sequencing analysis (see *Year Book 77*). We checked the template activity of pBF41 for 0.5-kb band transcription. The pBF41 DNA as well as pFb29 DNA worked as an effective template for 0.5-kb band transcription. Therefore, we conclude that there is probably no significant structural change

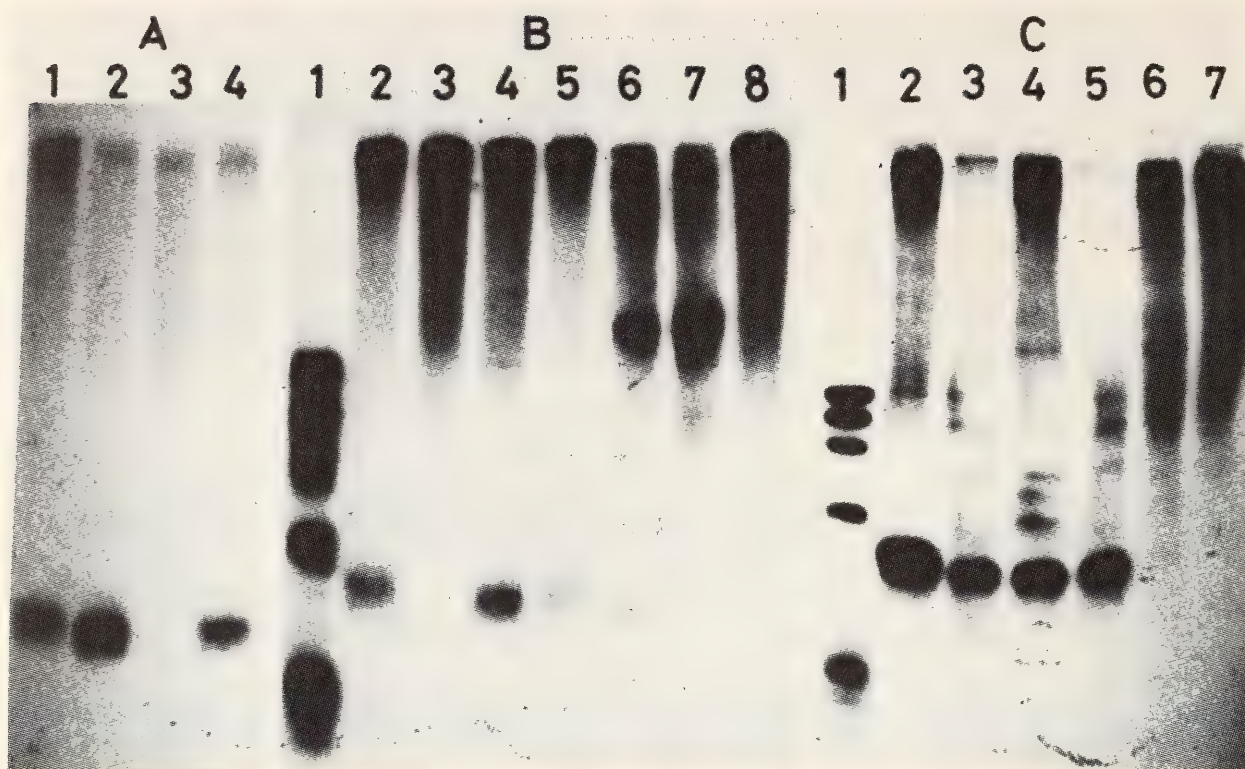


Fig. 61. The "0.5-kb band transcription" by wheat germ RNA polymerase II. (A) Total cellular RNA from posterior silk glands (lanes 1 and 4), RNA synthesized in vitro by wheat germ RPase II (lane 2) or *E. coli* tRNA (lane 3) was used for hybridization with Eco RI-Xho I\* fragments. (B) End-labeled  $\phi$ X174 Hae III fragments were run as size markers (lane 1). Total cellular RNA from posterior silk glands (lanes 2 and 5), RNA synthesized by wheat germ RPase II (lane 3, without preincubation, with  $Mn^{++}$ ; lane 4, with preincubation, without  $Mn^{++}$ ), RNA synthesized by *E. coli* RPase (lane 6, without preincubation, with  $Mn^{++}$ ; lane 7, with preincubation, without  $Mn^{++}$ ), and *E. coli* tRNA (lane 8) were used for hybridization. (C)  $\phi$ X174 Hae III fragments were run as size markers (lane 1). Total cellular RNA from posterior silk glands (lane 2), RNA synthesized by wheat germ RPase II (lane 3, with preincubation, without  $Mn^{++}$ ; lane 6, without preincubation, with  $Mn^{++}$ ), or *E. coli* tRNA (lane 7) was used for hybridization.

in pBF41 DNA compared to pFb29 DNA. When a linear molecule of pFb29 DNA produced by Eco RI cleavage was used as a template, the 0.5-kb band was not detected.

To know the initiation site accounting for 0.5-kb band transcription more precisely, we mapped the 5' end of the 0.5 kb RNA transcripts, using reverse transcription (see the previous section). As shown in Fig. 63, we detected a discrete band (280–290 bases long) when the total cellular RNA from posterior silk glands was used for hybridization (lane 4). A discrete band was also detected when the RNA synthesized in vitro was used. However, its size was smaller (lanes 1, 2) than the one given by the in vivo

RNA from posterior silk glands. It was roughly estimated to be about 250–260 bases long, so its 5' end maps around position +30. After a prolonged exposure of the autoradiography, a faint band was detectable at the expected size position (280–290 bases). From this result, we conclude that wheat germ RPase II initiated transcription at a discrete site 30 nucleotides downstream from the cap locus.

We have not yet succeeded in faithful transcription of the fibroin gene by RPase II from the posterior silk glands of *B. mori*. As shown in Table 11, partially purified *B. mori* RPase II was unable to transcribe pFb29 DNA in the absence of  $Mn^{++}$ . The inability might



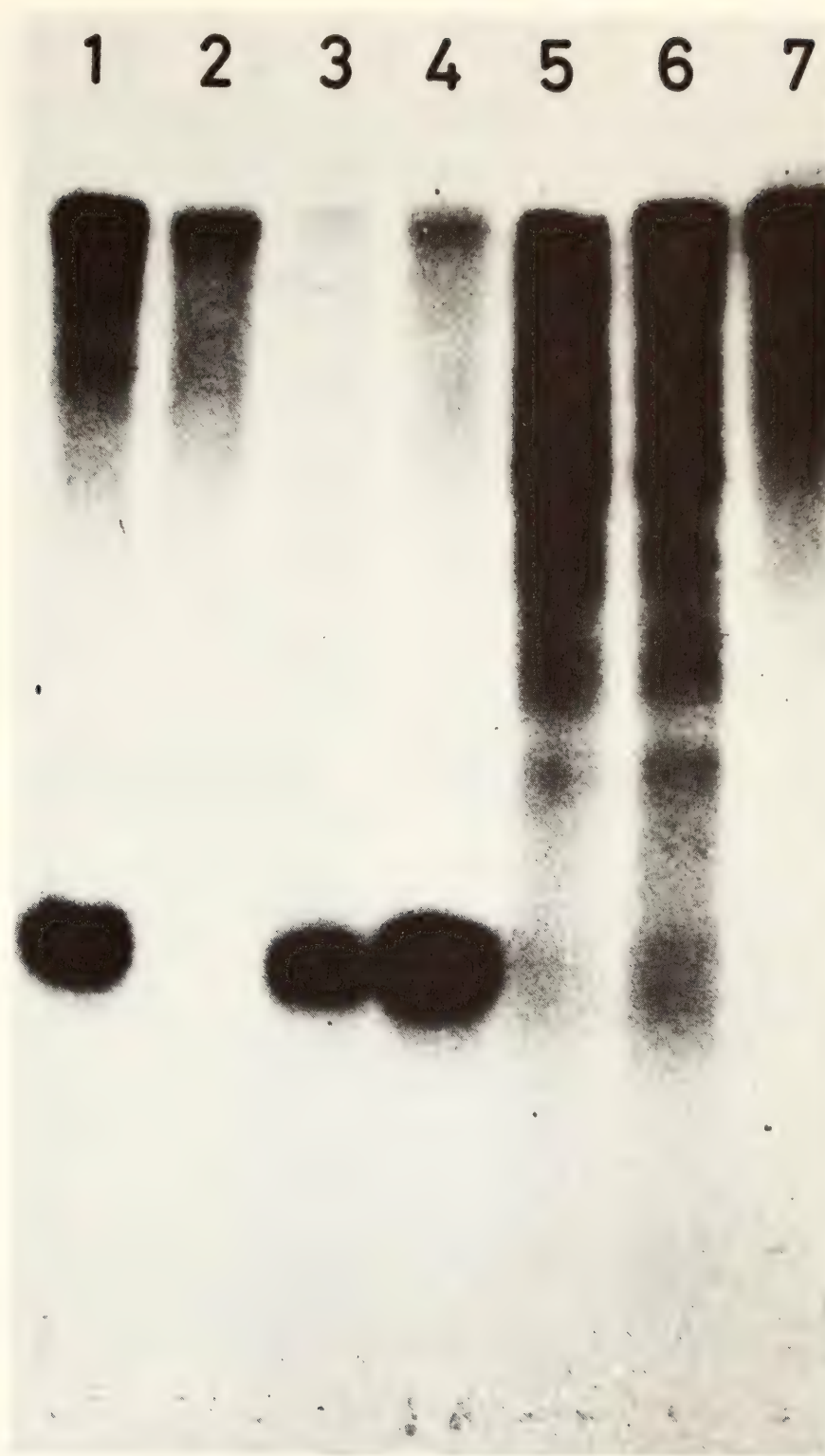


Fig. 62. Effect of substrate concentration on "0.5-kb band transcription." Total cellular RNA from posterior silk glands (lane 1), RNA synthesized by 25  $\mu$ l of wheat germ RPase II sol. in 1.5  $\mu$ M each of ATP, GTP, CTP, and 1.25  $\mu$ M of UTP (lane 2), RNA synthesized by 5  $\mu$ l (lane 3) or 25  $\mu$ l (lane 4) of wheat germ RPase II sol. in 30  $\mu$ M each of ATP, GTP, CTP, and 2.5  $\mu$ M of UTP, RNA synthesized by 5  $\mu$ l (lane 5) or 15  $\mu$ l (lane 6) of wheat germ RPase II sol. in 600  $\mu$ M each of ATP, GTP, CTP, and 50  $\mu$ M of UTP, or *E. coli* tRNA (lane 7) was used.

be caused by the procedure of RPase II solubilization (Sklar *et al.*, *J. Biol. Chem.*, 251, 3794, 1974), which is dif-

ferent from that of wheat germ RPase II (Jendrisak *et al.*, *Biochemistry*, 14, 4639, 1975). Therefore, a dissociation of

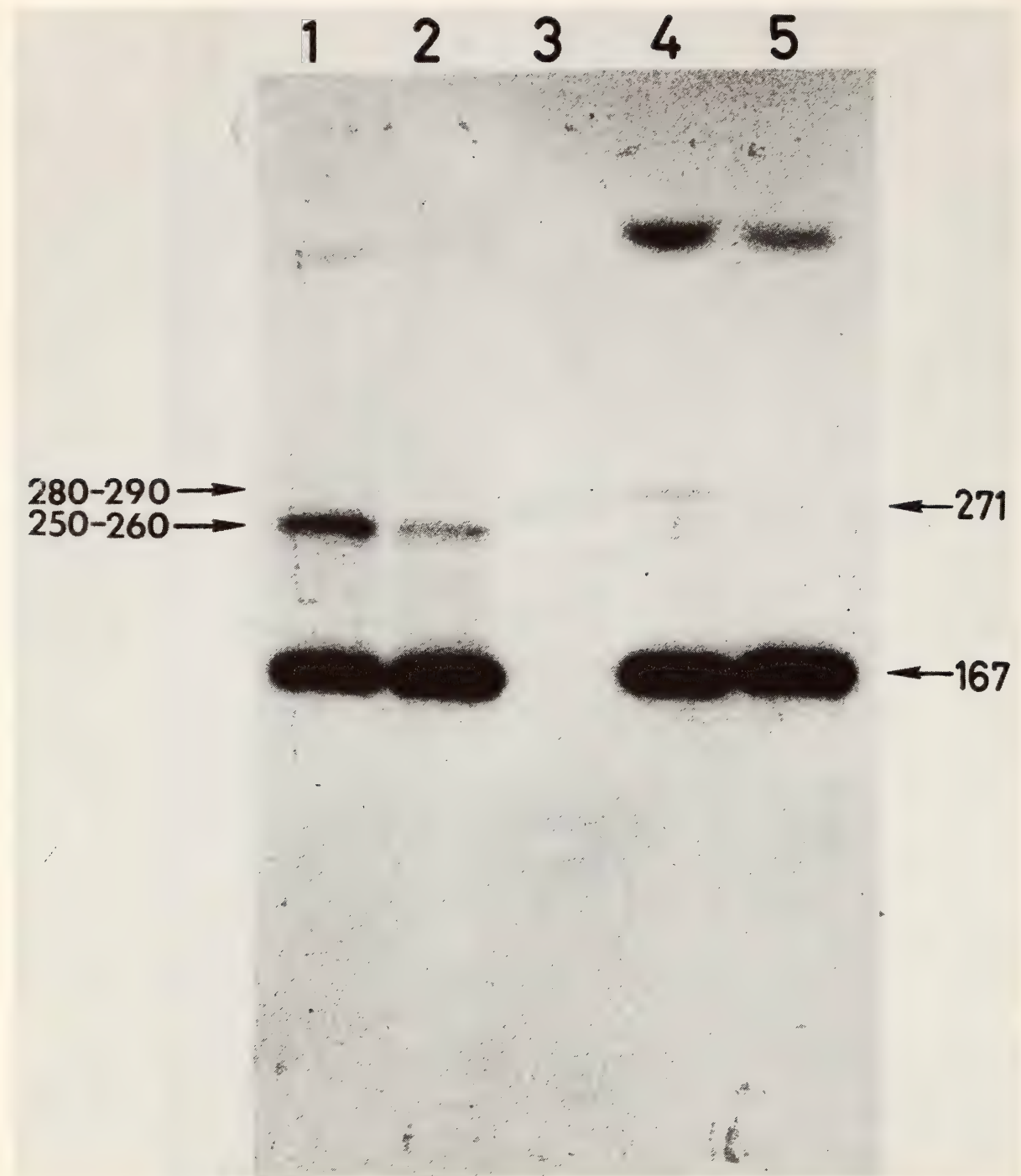


Fig. 63. Mapping of the 5' end of the 0.5-kb band by reverse transcription. RNA (330 pmoles) synthesized in vitro was divided into two fractions, and reverse transcription proceeded for 2.5 hours using 4 units of reverse transcriptase (lane 2) or for 5 hours using 12 units reverse transcriptase (lane 1). Total cellular RNA from posterior silk glands (lane 4) or *E. coli* tRNA (lane 5) was used for hybridization. End-labeled  $\phi$ X174 Hae III fragments were run as size markers (lane 3).

some component from *B. mori* RPase II might occur during solubilization, which is responsible for transcribing the double-stranded DNA. In fact, fractions that regain *B. mori* RPase II activity in the absence of  $Mn^{++}$  were detected in phosphocellulose chromatography of the

flow-through fraction after DEAE-cellulose chromatography during the *B. mori* RPase II purification. Currently we are modifying the purification procedure of *B. mori* RPase II with the hope that factors required for faithful transcription of the fibroin gene will be preserved.



## THE COLLECTION OF HUMAN EMBRYOS

*Ronan O'Rahilly*

The embryological collections, both human and comparative, are housed at the University of California, Davis, and all inquiries as well as requests for permission for publication should be addressed to Professor R. O'Rahilly, Carnegie Laboratories of Embryology, University of California, Davis, California 95616.

DEVELOPMENTAL STAGES IN  
HUMAN EMBRYOS

The revision of stages 10 to 23 and the tabulation of the timing and sequence of developmental events in staged human embryos are being pursued. The digestive system has been published recently, and an account of vertebral development is awaiting publication; the reproductive and endocrine systems are being prepared. The computerized catalogue of Carnegie specimens established by Dr. Alexander Barry has been extended to include other collections, such as that at the University of Michigan, Ann Arbor, and the Hooker-Humphrey collection of the University of Alabama at Birmingham.

Mr. Osborne O. Heard (Hayden Lake, Idaho), who made practically all the superb reconstructions of the Carnegie collection over a period of 42 years in Baltimore, visited Davis for a week. During his visit he reminisced about Drs. Mall and Streeter, and discussed the technique of Born reconstructions; he is writing an account of this technique that will include a number of unpublished details.

## DEVELOPMENT OF THE NERVOUS SYSTEM

The project on the developmental neurobiology of primates has been

strengthened by the arrival of Dr. Fabiola Müller from the University of Basel. Dr. Müller, who has specialized in modern techniques of graphic reconstruction, is preparing three-dimensional views of the brain at stages 9 and 23 and of the skull at stage 23. These precise and time-consuming reconstructions will form part of a proposed atlas of the prenatal development of the human brain, already begun by R. O'Rahilly and the late Ernest Gardner.

Collaboration with Professor W. Woźniak (Poznań) continues, and light and electron microscopic studies of neural cells in the spinal ganglia of human embryos and early fetuses, as well as a related investigation of the developing spinal cord, are in press.

Dr. Mary E. Desmond, in collaboration with R. O'Rahilly, spent the summer of 1978 in a study of the growth of the human brain during the much-neglected embryonic period proper. Linear axes and areas of major subdivisions of the brain were measured in 27 Born reconstructions, 61 coronally sectioned embryos, and 60 sagittally sectioned embryos from Carnegie stages 11 to 23 (3½–8 postovulatory weeks). It was found that the increase in length and width of the prosencephalon is proportional to that of the crown-rump length. The presumptive temporal and fronto-occipital diameters increase at the same rate as in the fetal period. The mesencephalon grows more rapidly in both length and height during the embryonic than during the fetal period. The height of the vermis cerebelli increases steadily throughout the embryonic period proper.

In addition to the studies of the skeletal covering of the brain by O'Rahilly and Müller, Dr. David B. Meyer (Wayne

State University, Detroit) continues his studies of the vertebral column.

#### DEVELOPMENT OF THE CARDIOVASCULAR SYSTEM

Dr. Alexander Barry is taking a further look at the detailed development of the aortic arches (a subject on which he has published previously). Dr. Pieter A. deVries continues his observations of the early development of the human heart (stages 9 to 11) with particular attention to the truncus arteriosus, and subsequent changes in the outflow tract (stages 12

to 18). Drs. Grover M. Hutchins and G. William Moore (Johns Hopkins) are advancing their important studies of normal and abnormal cardiac development.

#### VISITORS

Visitors who studied the collection included Dr. Mary E. Desmond (Villanova, Pennsylvania), Dr. Grover M. Hutchins (Baltimore), Dr. David B. Meyer (Detroit), Dr. G. William Moore (Baltimore), Dr. Jean Moore (La Jolla), and Dr. W. Woźniak (Poznań).

#### STAFF ACTIVITIES

During the year staff members participated as chairmen or speakers at the following conferences: Gordon Research Conferences on Animal Cells and Viruses, Nuclear Proteins and Gene Expression, Biological Regulatory Mechanisms, Nucleic Acid, Chromatin, Immunology, and Lipid Metabolism; Cold Spring Harbor Symposium; VII International Congress of Pharmacology in Paris; Pontifical Academy of Science; AAAS Symposium on Neuroscience and Disease; Annual Meeting of the American Society for Cell Biology; ICN-UCLA Meetings on Eukaryotic Gene Regulation and T and B Lymphocytes; International Society for Differentiation; British Society for Developmental Biology; Society for Neuroscience.

Lectures were given at Johns Hopkins University, Cold Spring Harbor Laboratories, Salk Institute, Princeton University, The Hutchinson Cancer Research Institute, University of Texas, Vanderbilt University, Duke University, St. Vincent Hospital in Indianapolis, University of Colorado, Baylor Medical School, Albert Einstein Medical School, Armed Forces Medical School, St. Louis Medical School, University of Virginia,

University of Illinois, Brandeis University, University of Pennsylvania, National Institutes of Health, The Roche Institute of Molecular Biology, University of Iowa, California Institute of Technology, Massachusetts Institute of Technology, Merck, Sharpe and Dohme Research Laboratories, Medical College of Pennsylvania, University of Tennessee, University of California at Irvine and Davis, Stanford University, University of Paris, University of Vermont, Harvard Medical School, Brookhaven National Laboratories, and the University of Chicago.

Members of the staff served on the Developmental Biology and Cell Biology Study Sections of the National Science Foundation, on the selection committee for the Newcomb Cleveland Prize of the AAAS, on an advisory committee to the Office of Technology Assessment for the Congress, and on the executive committee of the Johns Hopkins Immunology Council. A staff member serves as Chairman of the Membrane Biophysics Subgroup of the Biophysical Society. Additional consulting activities include membership on the visiting committees to the Roche Institute of Molecular Biology,



the Biology (Chairman) and the Biochemistry Departments of Harvard University, and the Board of Scientific Counselors of the National Institute of Child Health and Development.

Even though the Editor of *Developmental Biology* has moved to NIH, the office remains here in this Department and is ably run by Barbara Melnick.

### Seminars

The Department offers at least two seminars each week, one of them usually presented by a scientist from outside the Department. This year 41 invited speakers from the Baltimore scientific community lectured. The second annual Mini-Symposium was entitled "Developmental Neurobiology." The five principal speakers were G. D. Fischbach and D. D. Potter, Harvard Medical School; D. Purves, Washington University Medical School; D. Kankel, Yale University; and L. Hall, Massachusetts Institute of Technology. The following visitors spoke on occasions other than the Mini-Symposium: I. B. Thompson, M. Potter, R. Rees, J. Seidman, E. Long, M. Gellert,

P. Qasba, J. Piatagorsky, M. Bina-Stein, and G. Khoury, all from the National Institutes of Health; P. Malan, Harvard University; G. Rubin, Sidney Farber Cancer Center; H. Noll, Northwestern University; W. Thompson, Department of Plant Biology, Carnegie Institution; H. Koenig, University of Paris; U. J. McMahan, Stanford University; W. Nichols, University of California at Davis; R. Baserga, Temple University; W. Jelinek, Rockefeller University; A. S. Spirin, Moscow; A. Spradling, Indiana University; K. Karrer, University of Indiana; D. Kuffler, Stanford University; W. Bender, Stanford University; K. Yamamoto, University of California at San Francisco; N. Kalderon, Rockefeller University; M. Kuno, University of North Carolina; R. Hynes, Massachusetts Institute of Technology; P. Wensink, Brandeis University; R. Wall, University of California at Los Angeles; G. Fink, Cornell University; G. Albrecht-Buehler, Cold Spring Harbor Laboratory; D. Forman, Naval Medical Research Institute; T. Honjo, Tokyo University; G. Georgiev, Molecular Biology Institute, Moscow; and K. Skriabin, Molecular Biology Institute, Moscow.

### BIBLIOGRAPHY

- Barry, A., and A. R. Burdi, Catalogue of human embryos. *Anat. Rec.*, 193, 476-477, 1979.
- Birkenmeier, E. H., D. D. Brown, and E. Jordan, A nuclear extract of *Xenopus laevis* oocytes that accurately transcribes 5S RNA genes. *Cell*, 15, 1077-1086, 1978.
- Botchan, P., see Reeder, R. H.
- Brown, D. D., Developmental genetics by gene isolation: The dual 5S RNA gene system in *Xenopus*. In *Mechanisms of Cell Change*, J. Ebert and T. Okada, eds., John Wiley & Sons, Inc., New York, pp. 65-70, 1979.
- Brown, D. D., and J. B. Gurdon, Cloned single repeating units of 5S DNA direct accurate transcription of 5S RNA when injected into *Xenopus* oocytes. *Proc. Nat. Acad. Sci. U.S.A.*, 75, 2849-2853, 1978.
- Brown, D. D., see also Birkenmeier, E. H., Fedoroff, N. V., Gurdon, J. B., and Korn, L. J.
- Burdi, A. R., see Barry, A.
- Carbonetto, S., and D. M. Fambrough, Synthesis, incorporation into plasma membrane and turnover of  $\alpha$ -bungarotoxin receptors in chick sympathetic neurons. *J. Cell. Biol.*, 81, 555-569, 1979.

- Carbonetto, S., see also Muller, K. J.
- Card, D. L., see Fambrough, D. M.
- Cebra, J. J., see Gearhart, P. J.
- Dawid, I. B., P. K. Wellauer, and E. O. Long, Ribosomal DNA in *Drosophila melanogaster*. I. Isolation and characterization of cloned fragments. *J. Mol. Biol.*, 126, 749-768, 1978.
- Dawid, I. B., see also Wahli, W. and Wellauer, P. K.
- Desmond, M. E., and R. O'Rahilly, The growth of the human brain during the embryonic period proper. *Anat. Rec.*, 193, 521, 1979.
- Devreotes, P. N., see Fambrough, D. M.
- Fambrough, D. M., Control of acetylcholine receptors in skeletal muscle. *Physiol. Rev.*, 59, 165-227, 1979.
- Fambrough, D. M., P. N. Devreotes, J. M. Gardner, and D. Card, The life history of acetylcholine receptors. Progress in brain research. In *The Cholinergic Synapse*, Tucek, ed., 49, pp. 325-334, 1979.
- Fambrough, D. M., see also Carbonetto, S., Gardner, J. M., and Linden, D. C.
- Fedoroff, N. V., Deletion mutants of *Xenopus laevis* 5S ribosomal DNA. *Cell*, 16, 551-563, 1979.
- Fedoroff, N. V., On spacers. *Cell*, 16, 697-710, 1979.
- Fedoroff, N. V., The structure of deletion derivatives of a recombinant plasmid containing the transposable element Tn9 in the spacer sequence of *Xenopus laevis* 5S DNA. *Cold Spring Harbor Symp. Quant. Biol.*, 43, 1978.
- Gardner, J. M., and D. M. Fambrough, Properties of acetylcholine receptor turnover in cultured embryonic muscle cells. In *Maturation of Neurotransmission*, A. Vernadakis, E. Giacobini and G. Filogamo, eds., Karber Press, Basel, pp. 31-40, 1978.
- Gardner, J. M., and Fambrough, D. M., Acetylcholine receptor degradation measured by density labeling: Effects of cholinergic ligands and evidence against recycling. *Cell*, 16, 661-674, 1979.
- Gardner, J. M., see also Fambrough, D. M., and Linden, D. C.
- Gearhart, P. J., and J. J. Cebra, Differentiated B lymphocytes. Potential to express particular antibody variable and constant regions depends on site of lymphoid tissue and antigen load. *J. Exp. Med.*, 149, 216-227, 1979.
- Gurdon, J. B., and D. D. Brown, The transcription of 5S DNA injected into *Xenopus* oocytes. *Devel. Biol.*, 67, 346-356, 1978.
- Gurdon, J. B., see also Brown, D. D.
- Hipskind, R., see Reeder, R. H.
- Jaggi, R. B., see Wahli, W.
- Jordan, E., see Birkenmeier, E. H.
- Korn, L. J., and D. D. Brown, Nucleotide sequence of *Xenopus borealis* oocyte 5S DNA: Comparison of sequences that flank several related eukaryotic genes. *Cell*, 15, 1145-1156, 1978.
- Lew, K. K., see Nelson, G. A.
- Linden, D. C., and D. M. Fambrough, Biosynthesis and degradation of acetylcholine receptors in rat skeletal muscles. Effects of electrical stimulation. *Neuroscience*, 4, 527-538, 1979.
- Linden, D. C., J. M. Gardner, and D. M. Fambrough, Some observations on denervation supersensitivity in skeletal muscle. In *Advances in Pharmacological and Therapeutic Receptors*, J. Jacobs, ed., Pergamon Press, Oxford, 1978.
- Long, E. O., see Dawid, I. B.
- Maden, B. E. H., and R. H. Reeder, Partial mapping of methylated sequences in *Xenopus laevis* ribosomal RNA by preparative hybridization to cloned fragments of ribosomal DNA. *Nucleic Acids Res.*, 6, 817-830, 1979.
- Müller, F., The human chondrocranium at the end of the embryonic period proper. *Anat. Rec.*, 193, 750, 1979.
- Muller, K. J., Synapses between neurones in the central nervous system of the leech. *Biol. Rev.*, 54, 99-134, 1979.
- Muller, K. J., and S. Carbonetto, The morphological and physiological properties



- of a regenerating synapse in the C.N.S. of the leech. *J. Comp. Neurol.*, 185, 485-516, 1979.
- Nelson, G. A., K. K. Lew, and S. Ward, Intersex, a temperature-sensitive mutant of the nematode *Caenorhabditis elegans*. *Devel. Biol.*, 66, 386-409, 1978.
- Ohshima, Y., see Suzuki, Y.
- O'Rahilly, R., Le développement prénatal. *C'est Pour Quand*, 2, 20-23, 1979.
- O'Rahilly, R., The timing and sequence of events in the development of the human digestive system and associated structures during the embryonic period proper. *Anat. Embryol.*, 153, 123-136, 1978.
- O'Rahilly, R., see also Desmond, M. E.
- Pagano, R. E., Interactions of phospholipid vesicles with mammalian cells *in vitro*. In *Mechanisms of Cell Change*, J. Ebert and T. Okada, eds., John Wiley and Sons, New York, pp. 199-213, 1979.
- Pagano, R. E., see also Sandra, A., and Schroit, A. J.
- Reeder, R. H., B. Sollner-Webb, R. Hipskind, H. L. Wahn, and P. Botchan, Structure and function of *Xenopus* ribosomal genes. In *Differentiation and Development*, F. Ahman, T. Russel, J. Schultz, and R. Werner, eds., Academic Press, Inc., New York, 15, pp. 335-352, 1978.
- Reeder, R. H., H. L. Wahn, P. Botchan, R. Hipskind, and B. Sollner-Webb, Ribosomal genes and their proteins from *Xenopus*, *Cold Spring Harbor Symp. Quant. Biol.*, 42, 1167-1177, 1977.
- Reeder, R. H., see also Maden, B. E. H.
- Ryffel, G. U., see Wahli, W.
- Sandra, A., and R. E. Pagano, Liposome-cell interactions. Studies of lipid transfer using isotopically asymmetric vesicles. *J. Biol. Chem.*, 254, 2244-2249, 1979.
- Schroit, A. J., and R. E. Pagano, Introduction of antigenic phospholipids into the plasma membrane of mammalian cells: Organization and antibody-induced lipid redistribution. *Proc. Nat. Acad. Sci. U.S.A.*, 75, 5529-5533, 1978.
- Sollner-Webb, B., see Reeder, R. H.
- Suzuki, Y., and Y. Ohshima, Isolation and characterization of the silk fibroin gene with its flanking sequences. *Cold Spring Harbor Symp. Quant. Biol.*, 42, 947-957, 1977.
- Suzuki, Y., see also Tsujimoto, Y.
- Tartof, K. E., see Wellauer, P. K.
- Tsujimoto, Y., and Y. Suzuki, Structural analysis of fibroin gene and its flanking sequences. *Int. Conf. Mol. Devel. Biol. Insects, Abst.*, 10, 1978.
- Tsujimoto, Y., and Y. Suzuki, Structural analysis of the fibroin gene at the 5' end and its surrounding regions. *Cell*, 16, 425-436, 1979.
- Tsujimoto, Y., and Y. Suzuki, Structure and function of the silk fibroin gene. *Protein Nucl. Acid Enzyme Tokyo*, 24, 83-95, 1979 (in Japanese).
- Wahli, W., I. B. Dawid, T. Wyler, R. B. Jaggi, R. Weber, and G. U. Ryffel, Vitellogenin in *Xenopus laevis* is encoded in a small family of genes. *Cell*, 16, 535-549, 1979.
- Wahli, W., G. U. Ryffel, T. Wyler, R. B. Jaggi, R. Weber, and I. B. Dawid, Cloning and characterization of synthetic sequences from the *Xenopus laevis* vitellogenin structural gene. *Devel. Biol.*, 67, 371-383, 1978.
- Wahn, H. L., see Reeder, R. H.
- Ward, S., Nematode chemotaxis and chemoreceptors. In *Taxis and Behavior* (Receptors and Recognition, Series B. Volume 5), G. L. Hazelbauer, ed., Chapman and Hall, London, pp. 143-168, 1978.
- Ward, S., see also Nelson, G. A.
- Weber, R., see Wahli, W.
- Wellauer, P. K., and I. B. Dawid, Isolation and sequence organization of human ribosomal DNA. *J. Mol. Biol.*, 128, 289-303, 1979.
- Wellauer, P. K., and I. B. Dawid, Ribosomal DNA in *Drosophila melanogaster*. II. Heteroduplex mapping of cloned and uncloned rDNA. *J. Mol. Biol.*, 126, 769-782, 1978.
- Wellauer, P. K., I. B. Dawid, and K. D. Tartof, X and Y chromosomal ribosomal

DNA of *Drosophila*: Comparison of spacers and insertions. *Cell*, 14, 269-278, 1978.

Wellauer, P. K., see also Dawid, I. B.

Wyler, T., see Wahli, W.

## PERSONNEL

Year Ended June 30, 1979

(including those whose services ended during the year)

### *Research Staff*

Donald D. Brown, Director  
Douglas M. Fambrough  
Nina V. Fedoroff  
Kenneth J. Muller  
Richard E. Pagano  
Ronald H. Reeder<sup>1</sup>  
Yoshiaki Suzuki<sup>2</sup>  
Samuel Ward

### *Staff Associate*

Patricia Gearhart

### *Research Associates (Extramural)*

Bent G. Böving, Detroit, Michigan  
Igor B. Dawid, Bethesda, Maryland  
Robert L. DeHaan, Atlanta, Georgia  
Arthur T. Hertig, Boston, Massachusetts  
Irwin R. Konigsberg, Charlottesville, Virginia  
Ronan O'Rahilly, Davis, California  
Elizabeth M. Ramsey, Washington, D.C.  
Ronald H. Reeder, Seattle, Washington  
Yoshiaki Suzuki, Okazaki City, Japan

### *Postdoctoral Fellows and Grant-Supported Associates*

Saoko Atsumi, Fellow of Carnegie Institution of Washington<sup>3</sup>  
Ellen Bayne, Fellow of Carnegie Institution of Washington  
Edward H. Birkenmeier, U.S. Public Health Service Grant (Brown)  
Daniel Bogenhagen, Fellow of Helen Hay Whitney Foundation and Carnegie Institution of Washington

<sup>1</sup> To August 31, 1978.

<sup>2</sup> To November 30, 1978.

<sup>3</sup> To September 30, 1978.

Peter Botchan, Fellow of the U.S. Public Health Service and Carnegie Institution of Washington<sup>4</sup>

Salvatore T. Carbonetto, Fellow of the U.S. Public Health Service and Carnegie Institution of Washington<sup>5</sup>

Ellen Elliott, U.S. Public Health Service Grant (Muller)

Laurence J. Korn, Fellow of Helen Hay Whitney Foundation and Carnegie Institution of Washington<sup>6</sup>

Steven McKnight, Fellow of Helen Hay Whitney Foundation and Carnegie Institution of Washington

Yasumi Ohshima, Fellow of Carnegie Institution of Washington<sup>7</sup>

Ronald Peterson, Fellow of Helen Hay Whitney Foundation and Carnegie Institution of Washington

Thomas Roberts, U.S. Public Health Service Grant (Ward)

Richard Rotundo, Fellow of Muscular Dystrophy Association of America, Inc., and Carnegie Institution of Washington

Alex Sandra, U.S. Public Health Service Grant (Pagano)<sup>8</sup>

Alan Schroit, U.S. Public Health Service Grant (Pagano)

Sheryl Scott, Fellow of U.S. Public Health Service and Carnegie Institution of Washington

Barbara Sollner-Webb, Fellow of U.S. Public Health Service and Carnegie Institution of Washington

Douglas Struck, Fellow of the American Cancer Society and Carnegie Institution of Washington

<sup>4</sup> To December 31, 1978.

<sup>5</sup> To April 30, 1979.

<sup>6</sup> To April 30, 1979.

<sup>7</sup> To July 31, 1978.

<sup>8</sup> To August 18, 1978.



Masaaki Tsuda, U.S. Public Health Service Grant (Suzuki)<sup>9</sup>  
 Yoshihide Tsujimoto, U.S. Public Health Service Grant (Suzuki)<sup>10</sup>  
 Harvey Wahn, U.S. Public Health Service Grant (Reeder)<sup>11</sup>  
 Eric Wakshull, Fellow of Muscular Dystrophy Association of America, Inc., and Carnegie Institution of Washington

### *Students*

Yair Argon, Graduate, Harvard University  
 John M. Gardner, Graduate, Johns Hopkins University  
 Elizabeth Gavis, Undergraduate, Cornell University  
 Robert A. Hipskind, Graduate, Johns Hopkins University<sup>11</sup>  
 Gregory A. Nelson, Graduate, Harvard University  
 Shigeru Sakonju, Graduate, Johns Hopkins University

### *Visiting Investigators and Extramural Collaborators*

J. Cebra, Baltimore, Maryland  
 P. Chatelain, Brussels, Belgium  
 E. H. Coe, St. Louis, Missouri  
 C. Croce, Philadelphia, Pennsylvania  
 J. B. Gurdon, Cambridge, England  
 L. Hood, Pasadena, California  
 J. Hurwitz, Baltimore, Maryland  
 N. Johnson, Pasadena, California  
 E. Macagno, New York, New York  
 B. E. H. Maden, Glasgow, U.K.  
 B. McClintock, Cold Spring Harbor, New York

<sup>9</sup> To March 31, 1979.

<sup>10</sup> To March 31, 1979.

<sup>11</sup> To September 30, 1978.

<sup>12</sup> To July 6, 1978.

M. G. Neuffer, St. Louis, Missouri  
 H. Shin, Baltimore, Maryland

### *Clerical and Technical Staff*

Elaine S. Asch, Senior Technician<sup>12</sup>  
 James H. Blackwell, Custodian  
 Paul Blackwell, Custodian (part-time)  
 Sharon Bodmer, Technician<sup>13</sup>  
 Joan Cartwright, Technician<sup>14</sup>  
 Scott Downing, Technician<sup>15</sup>  
 William H. Duncan, Senior Technician  
 Ernestine V. Flemmings, Laboratory Helper  
 Paul E. Giza, Technician<sup>16</sup>  
 Richard D. Grill, Photographer  
 Virginia Hicks, Laboratory Helper  
 Mary E. Hogan, Technician  
 William L. Johnson, Custodian<sup>17</sup>  
 John E. Jones, Custodian  
 Eddie Jordan, Senior Technician  
 Robert Kingsbury, Technician  
 Catherine R. Lane, Librarian (part-time)  
 Alice H. Mabin, Laboratory Helper  
 Thomas F. Malooly, Business Manager  
 Ona Martin, Technician  
 Jeffrey Mauvais, Technician  
 Clinton E. Miller, Technician  
 Thomas F. Miller, Custodian  
 Joyce Patterson, Laboratory Helper  
 John Pazdernik, Building Engineer  
 Betty Lou Phebus, Bookkeeper/Clerk  
 Susan D. Satchell, Secretary  
 Patricia Schmidt, Secretary  
 Ginny Selby, Secretary (part-time)  
 Bessie Smith, Laboratory Helper  
 Delores Somerville, Senior Technician  
 Barbara Thomas, Technician  
 John Wiser, Machinist

<sup>13</sup> To September 8, 1978.

<sup>14</sup> To December 14, 1978.

<sup>15</sup> To May 15, 1979.

<sup>16</sup> To November 23, 1978.

<sup>17</sup> To June 30, 1978.











# *Department of Plant Biology*

*Stanford, California*

Winslow R. Briggs

*Director*





# Contents

Introduction (Briggs) . . . . .	113	Phase separation temperatures of phospholipids from warm and cool climate plants (Pike and Berry) . .	163
Light-inducible cytochrome reduction in membranes from corn coleoptiles: cytochrome difference spectra and sensitization by exogenous flavin (Goldsmith, Caubergs, and Briggs)	118	Enhancement of high temperature stability of protein-protein interactions by deuterium oxide (Armond and Hess) . . . . .	168
Light-inducible cytochrome reduction in membranes from corn coleoptiles: fractionation and inhibitor studies (Caubergs, Goldsmith, and Briggs)	121	A radioimmune assay for RuP <sub>2</sub> carboxylase protein (Collatz, Badger, Smith, and Berry) . . .	171
Immunoaffinity purification of phytochrome (Quail and Briggs) . . .	126	Direct measurement of photorespiration as a function of CO <sub>2</sub> concentration (Berry and Badger) . . . . .	175
Irradiation-enhanced phytochrome pelletability: filtration and mixing experiments (Quail and Briggs) . .	129	Phase transitions in thylakoid membranes and vesicles prepared from lipids separated from <i>Synechococcus lividus</i> grown at 55° and 38°C (Fork and van Ginkel) . . . . .	178
Phytochrome responses in light-grown green and achlorophyllous corn seedlings (Gorton and Briggs) . .	134	Kinetic identification of component X as P430: acceptor of photosystem I (Hiyama and Fork) . . . . .	180
Shibata shift in corn seedlings grown with and without Sandoz (Gorton and Briggs) . . . . .	138	Light-induced formation of oxygen radicals in systems containing chlorophyll (van Ginkel and Raison) . . . . .	183
Growth characteristics of etiolated <i>Avena sativa</i> L. (cv. Lodi) in response to red and green light (Mandoli and Briggs) . . . . .	140	Spectral studies of triton-solubilized chlorophyll-proteins from <i>Euglena</i> and antenna chlorophyll from spinach (Brown) . . . . .	189
Time course of thermal acclimation of the photosynthetic apparatus in <i>Nerium oleander</i> (Björkman and Badger) . . . . .	145	Analysis of photosynthetic cytochrome content with a spectrophotometer-computer interfaced system (Harvey) . . . . .	194
Viscotropic denaturation of chloroplast membranes and acclimation to temperature by adjustment of lipid viscosity (Raison and Berry) . .	149	Measurements with a microprocessor-based fluorescence spectrophotometer made on the blue-green alga <i>Anacystis nidulans</i> above and below the phase transition temperature (Fork, Ford, and Cantanzaro) . .	196
Dissociation of supramolecular complexes in chloroplast membranes: a manifestation of heat damage to the photosynthetic apparatus (Armond, Björkman, and Staehelin) . . .	153	Computer-assisted measurements of parameters of the rise curve of fluorescence (Malkin, Ford, and Fork) . . . . .	199
Field studies of acclimation to high temperature: winter ephemerals in Death Valley (Seemann, Downton, and Berry) . . . . .	157		

Photosynthesis bibliographic file update —June 1979 (Brown) . . . . .	202	five host strains of <i>Escherichia coli</i> (Cuellar, Selker, and Thompson) .	215
A motor-driven hydraulic press for the French press (Brown and Hart) .	202	Single-copy DNA homologies and the phylogeny of <i>Atriplex</i> (Belford and Thompson) . . . . .	217
Long-period interspersions in the mung bean genome (Murray and Thompson) . . . . .	204	Studies in the Osmundaceae: single-copy DNA comparisons (Stein and Thompson) . . . . .	223
The use of cDNA for study of tran- scribed sequences (Peters, Murray, and Thompson) . . . . .	208	Studies on chloroplast DNA of mung bean and pea (Palmer, Murray, and Thompson) . . . . .	226
Isolation of <i>Pisum sativum</i> gene sequences exhibiting altered levels of expression during leaf development (Jorgensen and Thompson) . . .	212	Bibliography . . . . .	231
Cloning of plant DNA: comparison of		Speeches . . . . .	234
		Personnel . . . . .	237



## INTRODUCTION

Over the past few years the Department of Plant Biology has been making a major effort to understand the ways in which the photosynthetic apparatus adapts to temperature change. Most of the effort has focused on adaptation to high temperature, but there have been studies related to chilling resistance as well. A striking feature of the findings is that in individual species that have a high adaptive capacity the nature of the short-term acclimation is very similar to the evolutionary adaptations found in plants acclimated to high or low temperature but incapable themselves of any major biochemical adjustment to temperature change.

The research effort in this area during the past year has been intensive, and several remarkable findings have emerged. Much of the study has focused on *Nerium oleander*, a hardy shrub found last year to be unusually capable of thermal acclimation. Olle Björkman and his colleagues reported last year that if oleander plants were grown at different temperatures, they had quite different characteristics: plants grown at low temperatures had far greater photosynthetic capacity at low and moderate temperatures than did those grown at high temperatures, and the difference could be accounted for almost entirely on the basis of one limiting enzyme in the reactions of carbon dioxide fixation—fructose diphosphate phosphatase—over twofold higher in the plant from the cooler regime. Ribulose biphosphate carboxylase-oxygenase, the actual CO<sub>2</sub>-fixing enzyme, was also higher but not sufficiently high to account for the 2.5-fold difference in photosynthetic capacity. This year Björkman and Murray Badger report the surprising finding that even mature oleander leaves can adapt completely if moved from a cool to a hot growth regime or vice versa. When

the temperature shift is downward, the half-time for adaptation is about four or five days, but when the shift is upward, the half-time can be two days or less. Paralleling the changes in photosynthetic capacity are changes in activity of both fructose diphosphate phosphatase and ribulose biphosphate carboxylase-oxygenase. Other enzymes for carbon dioxide fixation do not change significantly.

There was another reported difference between oleander plants grown in cool and in warm regimes: plants from cool regimes sustained thermal damage to their photosynthetic apparatus at significantly lower temperatures than those from warm regimes. These differences could be ascribed to differences in chloroplast membrane stability with increasing temperature. The chloroplast membranes from cool-regime plants underwent thermal denaturation at far lower temperatures than those from their warm-regime counterparts. John Raison and Joseph Berry have now studied both the integrity of the photosynthetic apparatus in intact leaves (by monitoring fluorescence, a component of which shows a dramatic increase upon thermal damage to the system, while increasing leaf temperature), and the properties of the chloroplast polar lipids as temperature increases. Denaturation occurred at the same lipid fluidity for all plants. However, warm-regime plants had lipids that were less fluid at any temperature tested than those of cool regime plants. These differences in lipid properties are sufficient to account for differences in membrane thermal stability. In experiments paralleling those of Björkman and Badger, they sampled cool-regime plants moved to a warm regime and vice versa. Thermal acclimation in the mature leaves occurred as effectively for the integrity of the photosynthetic apparatus and for lipid fluidity (which probably underlies



this integrity) as it did for the photosynthetic enzymes. The kinetics of all of these changes were similar.

Finally, Paul Armond, Björkman, and Andrew Staehelin (at the University of Colorado) used freeze-fracture techniques followed by electron microscopy to look directly at chloroplast membranes for any structural differences related to differences in temperature regime during growth. Cool-regime plants exposed to high temperature showed a significant decrease in the size of particles detectable on the appropriate chloroplast membrane face, without any change in particle number. These particles are thought to be aggregates of the various pigment-protein complexes, and the size decrease could represent detachment of portions of the light-harvesting pigment system. This interpretation is consistent with results of fluorescence studies by Armond and Schreiber made two years ago which led to the same suggestion.

Mature oleander leaves thus have the capacity not only to change the levels of two important photosynthetic enzymes but to change their membrane properties as well in response to changes in temperature. The way the temperature change is sensed and the biochemical mechanisms by which this information regulates levels on photosynthetic enzymes on the one hand and the pattern of membrane synthesis and turnover on the other remains elusive.

Whatever the membrane differences are, they must in some way involve differences in hydrophilic/hydrophobic interactions of membrane components. Carl Pike and Berry measured the phase separation temperatures by cooling the extracted phospholipids from cool- and warm-regime oleander while monitoring the fluorescence of a probe very sensitive to lipid state. The phase separation temperature for lipids from cool-regime plants was fully 10°C lower than that for warm-regime plants, further evidence of substantial differences in membrane

properties brought about by different growth temperatures. Indeed, Pike and Berry showed that in general phase separation temperatures were lower for species adapted to cool climates than for those adapted to warm. Armond and John Hess showed that substitution of D<sub>2</sub>O for water increases the thermal stability of photosynthetic membranes from both cool- and warm-regime oleander. D<sub>2</sub>O is thought to alter in some fashion the hydrophilic/hydrophobic forces that stabilize the protein-protein interactions required for integrity of the photosynthetic apparatus.

Jeffrey Seemann, John Downton, and Berry extended the various techniques developed with oleander and other plants to field studies of a group of annual species in Death Valley, California. They discovered that the capacity for dramatic thermal acclimation was widespread among them. An important technical advance came from their careful documentation that a sharp rise in the temperature-versus-fluorescence curve provided an accurate index for the occurrence of thermal damage to the photosynthetic apparatus at the temperature at which the rise occurred. Thus they could follow acclimation in the field by making simple fluorescence measurements from time to time rather than being required to make elaborate measurements of photosynthetic gas exchange as a function of leaf temperature. They found that the break point in the fluorescence-versus-temperature curve declined consistently with increasing altitude (and decreasing temperature) for one species, and that another species subjected to normal Death Valley water stress had significantly higher break-point temperatures than watered individuals. Clearly, capacity to acclimate while growing or mature may be of great importance to plants surviving in environments in which temperatures are high and water is scarce.

The complexities of changes in mem-



brane properties with alteration in growth temperature are underlined by experiments with a thermophilic alga by David Fork and Gijsbert van Ginkel. They followed chlorophyll fluorescence in photosynthetic membranes and in vesicles prepared from the lipids of these membranes as a function of temperature change. Although there were good correlations between certain temperatures showing change in photosynthetic activities and phase transition temperatures of the lipids, such correlations were not always found. Thus there are still unresolved puzzles in the process of thermal acclimation.

Several other photosynthetic investigations merit note before we move to other research areas at the Department of Plant Biology. The primary electron acceptor components for photosystem I of photosynthesis have been very difficult to resolve and have only recently yielded in several laboratories to electron-spin resonance spectroscopy at low temperature. Tetsuo Hiyama and Fork have now demonstrated that one of these components is probably a moiety showing a difference spectrum peak near 430 nm, which has been studied spectrophotometrically at temperatures above freezing for several years. Thus one of the components of this electron acceptor (and possibly others as well) is now far more accessible to investigation than previously.

Van Ginkel and Raison have continued studies begun last year on oxygen and proton uptake by chloroplasts, photosystem I particles, and chlorophyll-lipid vesicles, using techniques to trap free radicals into stable derivatives for electron-spin resonance spectroscopy. Their results suggest that in the presence of ascorbate the reactions result from the reaction of ascorbate with hydroxyl radical formed by the interaction of photoexcited chlorophyll with oxygen and the resulting generation of superoxide.

Berry and Badger have continued a

long-standing project to resolve the pathway of oxygen uptake in photorespiration, an area of not inconsiderable controversy. By use of a heavy isotope of oxygen and mass spectrometry, coupled with CO<sub>2</sub> analysis, they were able to show that on increasing external CO<sub>2</sub>, the resulting increase in net CO<sub>2</sub> fixation by the intact leaf of a C<sub>3</sub> plant was exactly matched by a decrease in the uptake of O<sub>2</sub> in photorespiration. These results provide further strong evidence that photorespiration is regulated by CO<sub>2</sub> and O<sub>2</sub> concentrations by direct effects of these molecules on the reactions catalyzed by the enzyme ribulose biphosphate carboxylase-oxygenase.

During the past year, there have been a number of technical achievements worthy of mention here. Jeanette Brown has developed and modified techniques for obtaining preparations of photosynthetic pigment complexes which show far more normal absorption and fluorescence properties than in the past. Thus separation of a portion of the photosynthetic apparatus from the whole without serious disruption of the relationships between the component molecules should greatly enhance elucidation of the nature of pigment interactions in photosynthesis. Brown and Richard Hart have also designed and constructed a simple and inexpensive hydraulic apparatus to operate a French pressure cell. James Collatz, Badger, Celia Smith, and Berry have developed a sensitive and very useful radioimmune assay for the enzyme ribulose biphosphate carboxylase-oxygenase, based on an analog of ribulose biphosphate which can be labeled with <sup>14</sup>C and which binds irreversibly to the enzyme. Geoffrey Harvey has developed an analytical technique involving computer analysis of cytochrome difference spectra. The method is useful for quantitating photosynthetic cytochromes more precisely than previously possible. Fork, Glenn Ford, and Benny Catanzaro have developed and interfaced a microproces-



sor-based spectrofluorimeter to the Department's central minicomputer, greatly increasing the versatility of the system and increasing time-sharing possibilities. In addition, Shmuel Malkin, Ford, and Fork have adapted the computer for direct determination of photosynthetic unit size from fluorescence rise kinetics, on the basis of the report last year of the advantages of this fluorescence method (by Malkin, Fork, and Armond). Peter Quail has implemented the immuno-affinity technique for purification of the photomorphogenic pigment phytochrome from higher plants, a technique developed by Lee H. Pratt and his students at Vanderbilt, and is using it in attempts to localize phytochrome receptor sites on specific membrane fractions.

William Thompson and his colleagues are continuing to probe the nature of plant genomes, their evolution, and their expression during development. Michael Murray and Thompson have now completed a characterization of the mung bean genome, using hybridization techniques to determine the length and linear distribution of repeated and unique DNA sequences in the nucleus. The mung bean genome itself contains only 0.5 pg per haploid nucleus, in contrast to the pea genome, which is almost ten times as large. About 35% of the unique sequences in mung bean are between 300 and 1200 nucleotide pairs long, 18% between 1200 and 6700 nucleotide pairs long, and fully 46% are longer than 6700 nucleotide pairs. This genome organization stands in sharp contrast to that of pea, in which the vast majority of the unique sequences are 300 to 400 nucleotide pairs in length. This great divergence in organization makes it unlikely that unique sequence length and distribution play any major role in regulation of gene transcription.

The Thompson group has also made substantial progress in the cloning of plant DNA on bacterial plasmids. Debra Peters, Murray, and Thompson have developed the necessary technology to

transcribe plant messenger RNA into complementary DNA (cDNA), and Richard Jorgensen and Thompson have succeeded in cloning such cDNA on bacterial plasmids. Indeed, with cloned cDNA made from pea leaf mRNA they were able to demonstrate substantial differences in levels of messenger RNA's between leaves and buds. The technique involved making highly radioactive cDNA's from both leaf and bud messenger RNA's and then determining the relative degree of hybridization of these two different populations of cDNA with individual cloned cDNA from leaves. Thirty clones showed significant differences.

Richard Cuellar and Thompson report some initial success in cloning plant DNA directly via bacterial plasmids. In the past, such cloning has been achieved in other laboratories, but the length of the cloned pieces were always dismayingly shorter than the original plant DNA fragments used. This fragmentation is evidently at least partially a function of the genetic background of the host bacterial strain, and Cuellar and Thompson have now succeeded in obtaining cloned DNA's essentially the same length as the original plant DNA fragments inserted.

Heather Belford and Thompson report briefly on the extensive studies constituting Belford's thesis research on the genus *Atriplex*. Studies of degree of homology among single-copy DNA's from a variety of *Atriplex* species suggest that most of these species must have arisen almost at the same time, by a radiative process rather than by a sequential process over millions of years. The results support the view reported previously that there is no need to hypothesize the independent evolution of C<sub>4</sub> photosynthesis twice within this genus. Diana Stein and Thompson also report evidence indicating the same sort of radiative process for the fern genus *Osmunda*, suggesting further that the



three species of the genus must have existed as separate evolutionary lines for at least 70 million years.

Jeffrey Palmer, Murray, and Thompson have determined that a significant fraction of the repeated DNA found in mung bean leaf preparations is chloroplast DNA. Using the high-resolution derivative analysis of melting curves developed last year by Cuellar, Ford, Briggs, and Thompson, they show that the component is largely lacking from nuclear preparations. They have developed very accurate techniques for quantitation of chloroplast DNA in various kinds of DNA preparations, and have shown that between pea and mung bean chloroplast DNA there is a high degree of sequence conservation. Though the results speak somewhat to problems of genome organization, the thrust promises to be more evolutionary in the future.

The Director would be remiss if he failed to mention activities in his own laboratory. Mary Helen Goldsmith, first alone and later with Roland Caubergs, continued to capitalize on her success in finding conditions to obtain flavin-mediated cytochrome reduction in corn membrane fractions reproducibly and to maximize the response. There is evidence, at least from studies of *Neurospora*, that such a system may be involved in blue light photoreception in vivo. She and Caubergs report further evidence that the reaction is highly specific, involving probably only a single nonmitochondrial *b*-type cytochrome with an absorption maximum near 560 nm in the reduced form. They present quantitative evidence on the relative affinity of the system for exogenously added flavins. Caubergs, Goldsmith, and Briggs also report that in crude mitochondrial preparations light can cause the reduction of the mitochondrial cytochrome *aa*<sub>3</sub>, a reaction that completely overrides the photoreduction involving the *b*-type cytochrome. The mitochondrial reaction can be clearly distinguished

from the nonmitochondrial, however. It differs spectrally, its photoreceptor moiety is readily washed out (that for the latter is tightly bound), its fractionation pattern is different, and its sensitivity to inhibitors is different.

Dina Mandoli and Briggs report some success in unraveling the complex kinetics and dose-response relationships for dark-grown oat seedlings exposed to red light. They noted an extreme sensitivity to the green safelight that resembled that reported last year by Quail and Briggs for potentiation of sensitivity to gravity in corn roots by light. In another study on the influence of light on growth, Holly Gorton and Briggs report that the pre-emergent herbicide Sandoz, which inhibits synthesis of visible-absorbing carotenoids both in light and dark and hence leads to complete photodestruction of chlorophyll in the light, has no qualitative or quantitative effect on three different phytochrome-mediated reactions in light-grown corn seedlings. These are promotion of coleoptile growth, promotion of mesocotyl elongation, and suppression of anthocyanin synthesis. The results encourage the expectation that Sandoz may be used to determine ways in which chlorophyll affects phytochrome photoequilibria in vivo by its screening properties. Gorton and Briggs also report that the complex spectral shifts that follow initial protochlorophyll transformation to chlorophyll by irradiation of dark-grown seedlings are unaffected by Sandoz. Evidently these reactions do not involve carotenoids.

A number of things stand out among the accomplishments of the past year. Of great potential importance is the discovery of thermal adaptation in mature leaves and the development of simple nondestructive techniques to follow its course in time. The capacity for thermal acclimation is clearly much more widespread than originally expected, and the techniques for measuring it could be of considerable use to plant

breeders searching for cultivars with improved resistance to high temperature and drought. The careful quantitative studies of O<sub>2</sub> and CO<sub>2</sub> exchange in photorespiration do much to dispel any uncertainty about the dual role, both as oxygenase and as carboxylase, of the CO<sub>2</sub>-fixing enzyme in vivo. The successes in cloning both cDNA's and native plant DNA's should yield significant advances in our knowledge of patterns of transcription in development and of genome organization in plants as well as providing powerful tools for other kinds of genetic analysis and manipulation. A

significant number of technical advances, many of them involving computer applications, should also be noted, as should the significant progress in characterization of a blue-light photoreceptor system in corn and the exploitation of a system for studying phytochrome in light-grown plants in the absence of chlorophyll.

This Director has in the past occasionally succumbed to the urge to show more than a little pride in the accomplishments of the Department, and this year is no exception. The reports below are in large part responsible.

*Winslow R. Briggs*

# LIGHT-INDUCIBLE CYTOCHROME REDUCTION IN MEMBRANES FROM CORN COLEOPTILES: CYTOCHROME DIFFERENCE SPECTRA AND SENSITIZATION BY EXOGENOUS FLAVINS

*Mary Helen M. Goldsmith, Roland J. Caubergs, and Winslow R. Briggs*

In our first report of light-inducible cytochrome reduction in membranes from corn coleoptiles and *Neurospora mycelium* (Brain *et al.*, 1977) we noted the difficulties of obtaining reproducible results with corn membrane fractions. Last year (Goldsmith and Briggs, *Year Book* 77, pp. 347–353) we reported the conditions necessary to obtain the desired reproducibility: glucose plus glucose oxidase, which both lowers oxygen tension and produces a small amount of H<sub>2</sub>O<sub>2</sub>; EDTA, which in some manner facilitates electron transfer both from an endogenous flavin and from exogenously added flavins to the cytochrome on photoexcitation; and temperatures below 10°C. We also reported that light-minus-dark difference spectra in the Soret region showed a difference peak near 429 nm regardless of whether the cytochrome reduction was photosensitized by endogenous flavin, added riboflavin, or added methylene blue. This difference peak could be readily distin-

guished from the dithionite reduced-minus-oxidized peak at 426 nm, representing the bulk of the cytochrome present. More detailed studies of the methylene blue-sensitized reaction have appeared elsewhere (Britz *et al.*, 1979).

We report here additional spectral studies in the region of the cytochrome alpha band and quantitative studies on the effect of added flavins. All techniques for growing corn seedlings, harvesting coleoptiles, preparing the various membrane fractions, and measuring the light-induced absorbance changes are described elsewhere (Brain *et al.*, 1977; Britz *et al.*, 1979). Additional studies on another light-inducible cytochrome reduction that is most likely mitochondrial and on the distribution of the non-mitochondrial system on preliminary fractionation are reported in the following article (Caubergs *et al.*, this *Year Book*).

The spectral studies in the Soret region, presented last year (*Year Book* 77,



pp. 347–353), show that the major cytochrome components in the  $21,000 \times g$  pellet from corn homogenates (21KP) are not photoreduced by blue light and have a difference band 3 nm to shorter wavelengths than that of the photoreducible cytochrome. These observations, however, do not eliminate the possibility that the endogenous flavin, riboflavin, or methylene blue may each be acting on two or more *different b*-type cytochromes—all minor components, all nonmitochondrial, and all with difference bands near 429 nm. Thus it was important to investigate difference spectra in the alpha band region where such different *b*-type cytochromes might be expected to have distinguishable difference maxima. Difference spectra between 500 and 600 nm obtained with each of the three photoreceptors are shown in Fig. 1. In all three cases the difference maximum is a sharp peak near 560 nm for the alpha band, with a broad maximum between 520 and 540 in the beta region. Thus it seems highly likely that all three photoreceptors are interacting with the same *b*-type cytochrome. Evidence that all three photoactivities (as well as that for FMN) partition in the same manner on differential centrifugation is presented in the following paper (Caubergs *et al.*, this Year Book).

We reported last year that the endogenous photoreceptor for cytochrome reduction was bound tightly enough to remain with the particulate fraction on resuspension and recentrifugation. It was therefore of interest to determine whether or not added exogenous flavin would also become tightly bound. For the experiment shown in Table 1 a  $21,000 \times g$  pellet was suspended in buffer, recentrifuged at  $21,000 \times g$  for 20 min, and then resuspended for spectral assay. Photoactivity was measured before and after adding riboflavin to a final concentration of  $3 \mu\text{M}$  (first line, Table 1). The expected tripling of cytochrome reduction was obtained. The sample con-

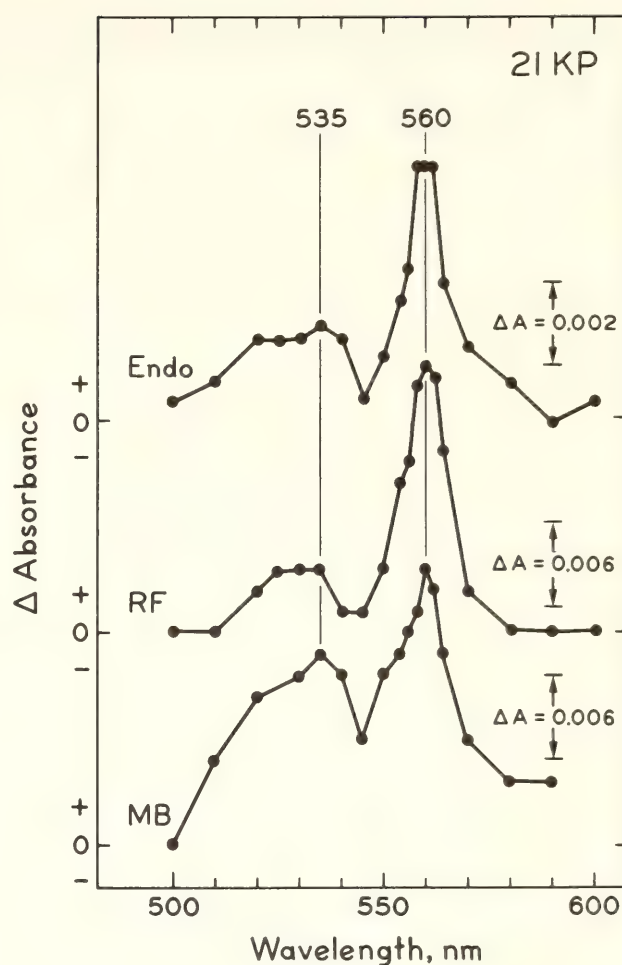


Fig. 1. Difference spectra obtained in the alpha-band region when endogenous photoreceptor (Endo), riboflavin (RF) or methylene blue (MB) served as photosensitizer. Perkin-Elmer 356 Spectrophotometer was in dual beam mode with one wavelength fixed and the other variable. For endogenous photoreceptor and riboflavin, fixed wavelength was 600 nm. For methylene blue, it was 500 nm. Glucose oxidase, 1 mg/ml;  $\beta$ -D-glucose, 8 mg/ml; EDTA, 25 mM; riboflavin, when present,  $5 \mu\text{M}$ ; methylene blue, when present,  $2 \mu\text{M}$ ; protein concentrations between 3.5 and 4.0 mg/ml. Samples, washed 21KP's obtained on different days. Sample temperature,  $7^\circ\text{C}$ .

taining the added riboflavin was then diluted with buffer, centrifuged a third time at  $21,000 \times g$  for 20 min, and again resuspended for assay before and after adding riboflavin to the same concentration (second line, Table 1). This washing procedure reduced the absorbance change threefold, suggesting that the riboflavin might have been entirely washed away, leaving only endogenous photoreceptor. This hypothesis is con-

TABLE 1. Effect of Washing on Photoreduction of Membrane-Bound Cytochrome by Added Riboflavin\*

	Protein mg/ml	Absorbance Change, units $\times 10^3$ /mg protein†	
		Before Adding Riboflavin	After Adding Riboflavin
Original washed pellet	3.55	1.14	3.21
Rewashed and resuspended pellet	2.70	0.94	3.11

\* Sample temperature 7°C. Absorbance measured in the Soret region of the spectrum in the presence of 25 mM EDTA, 1 mg/ml glucose oxidase, 8 mg/ml  $\beta$ -D-glucose, and 1 mM KCN. Sample: washed and resuspended 21KP. Riboflavin where present, 3  $\mu$ M.

† A unit of the photoactive system is defined as that amount which in the presence of optimal EDTA, glucose oxidase, glucose, and KCN concentrations, yields a  $\Delta(A_{428} - A_{410})$  of 1.0 when suspended in 1 ml and measured through a 1-cm pathlength.

firmed by the restoration of the reaction to the same level as previously obtained upon readdition of riboflavin.

Since the glucose oxidase itself contained a tightly bound flavin, FAD, as its prosthetic group (Swoboda, 1969), it was necessary to determine whether or not this FAD was itself acting as a photosensitizer. We therefore compared its effectiveness with that of another oxidase system, galactose plus galactose oxidase. The latter enzyme contains not FAD but copper as its prosthetic group (Hamilton *et al.*, 1973). Dose-response curves from threshold to near light saturation were obtained for the cytochrome reduction by varying the length of the light exposure from 1 to 100 s, ( $14 \text{ Wm}^{-2}$ ) with either the glucose oxidase or galactose oxidase systems present. The two dose-response curves were essentially indistinguishable (results not shown). Thus it is an enzymatic role of the glucose oxidase rather than a possible photosensitizing role that permits us to observe light-inducible cytochrome reduction when this enzyme and its substrate are present. Although it seems likely that it is the oxygen-scavenging activity that is required to allow measurable amounts of reduced cytochrome to accumulate in the light, a role for the  $\text{H}_2\text{O}_2$

generated has not been rigorously eliminated.

We then investigated the relative effectiveness of several different flavins in photosensitizing the cytochrome reduction. The results are shown in Fig. 2. Riboflavin and FMN were equally effective, with  $K_M$  values of 0.63 and 0.67  $\mu$ M, respectively. FAD was significantly less effective, with  $K_M$  near 1.9  $\mu$ M. The intercepts for maximum possible reduction for all three added flavins are identical, indicating that all three are probably interacting with the same cytochrome.

#### REFERENCES

- Brain, R. D., J. A. Freeberg, C. V. Weiss, and W. R. Briggs, *Plant Physiol.*, **59**, 948-952, 1977.
- Britz, S. J., E. Schrott, S. Widell, and W. R. Briggs, *Photochem. Photobiol.*, **29**, 359-365, 1979.
- Hamilton, G. A., J. De Jersey, and P. K. Adolf, in *Oxidases and Related Redox Systems*, T. E. King, H. S. Mason, and M. Morrison, eds., pp. 103-119, University Park Press, Baltimore, 1973.
- Swoboda, B. E. P., *Biochim. Biophys. Acta*, **175**, 365-379, 1969.
- Wilkinson, G. N., *Biochem. J.*, **80**, 324-332, 1961.



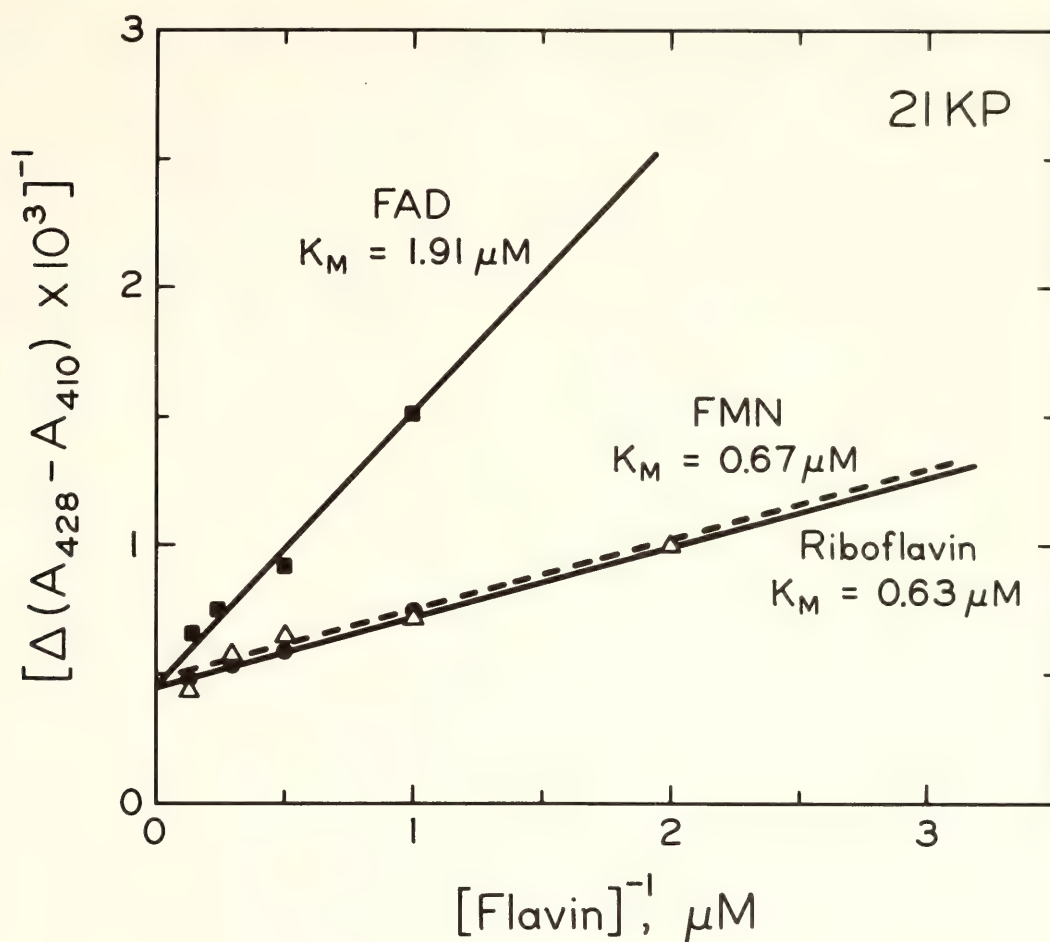


Fig. 2. Double reciprocal plots showing the effect of varying the concentration of several flavins on blue light-induced cytochrome reduction. Glucose oxidase, 1 mg/ml;  $\beta$ -D-glucose, 8 mg/ml; EDTA, 25 mM; protein concentrations, 5.7 mg/ml. Sample, unwashed 21KP, no KCN.  $K_M$  standard errors, 0.08, 0.26, and 0.33; intercept standard errors, 0.06, 0.21, and 0.13 for riboflavin, FMN, and FAD, respectively. Calculated after Wilkinson (1961). Sample temperature 7°C.

## LIGHT-INDUCIBLE CYTOCHROME REDUCTION IN MEMBRANES FROM CORN COLEOPTILES: FRACTIONATION AND INHIBITOR STUDIES

*Roland J. Caubergs, Mary Helen M. Goldsmith, and Winslow R. Briggs*

In previous reports (Goldsmith and Briggs, *Year Book* 77, pp. 347-353; Goldsmith *et al.*, this *Year Book*) we have partially characterized a system exhibiting reduction of a *b*-type cytochrome upon photoexcitation of a tightly bound endogenous photoreceptor, exogenously added riboflavin, or exogenously added methylene blue in a membrane fraction obtained from corn coleoptiles. We have also reported the conditions

required to obtain the reaction reproducibly and to maximize it; and we have presented evidence from washing experiments that the endogenous photoreceptor is tightly bound. In the present paper, we report photoreduction of cytochrome *aa<sub>3</sub>* in unwashed resuspended mitochondrial pellets, and we demonstrate that washing eliminates this photoactivity. We also report fractionation and inhibitor studies that clearly distinguish

it from the system involving the *b*-type cytochrome. Finally we present further evidence (see Caubergs *et al.*, *Year Book 77*, pp. 356–357) that the endogenous photoreceptor is a flavin.

The techniques for growing seedlings, preparing the various membrane fractions, obtaining difference spectra, and measuring light-induced cytochrome reduction are described elsewhere (Brain *et al.*, 1977; Britz *et al.*, 1979; Goldsmith and Briggs, *Year Book 77*, pp. 347–353). All inhibitors were made up in aqueous solution except for antimycin A, which was dissolved in ethanol. Control experiments indicated that the amount of ethanol added to the preparations with antimycin A had no detectable effect on cytochrome photoreduction.

Our normal method for measuring these light-induced absorbance changes involves setting the Perkin-Elmer 356 spectrophotometer in the dual-beam mode with the beams adjusted to 428 and 410 nm, respectively. The difference in absorbance between the two is determined after dark equilibration and immediately after saturating actinic light. The  $\Delta(A_{428} - A_{410})$  is thus determined for light-minus-dark conditions. If a *b*-type cytochrome with a Soret difference peak near 429 is reduced in light, this value is positive. Often, however, strong negative signals were obtained when the sample was an unwashed pellet enriched for mitochondria (9KP, see Jesaitis *et al.*, 1977). The light-minus-dark difference spectrum for this change is shown in Fig. 3. Instead of a difference maximum near 429 nm, there is a clear minimum and the maximum is instead at 445 nm. This difference spectrum is characteristic of the mitochondrial constituent, cytochrome *aa*<sub>3</sub> (Lemberg and Barrett, 1973). The photoreceptor for this reaction has not been identified. However, it may be residual endogenous soluble flavin in the unwashed pellet: Schmidt and Butler (1976) have reported nonspecific reduction of cytochrome *c* by photoexcited

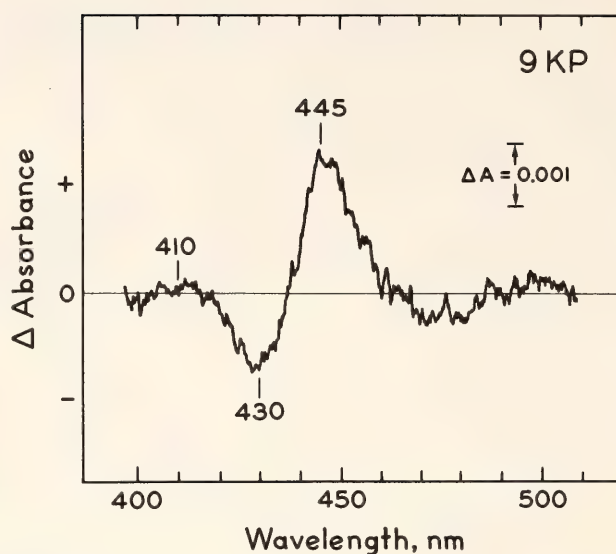


Fig. 3. Light-minus-dark difference spectrum for unwashed 9KP. Glucose oxidase, 1 mg/ml;  $\beta$ -D-glucose, 8 mg/ml; EDTA 25 mM; protein concentration, 14.7 mg/ml; sample temperature, 7°C. Scan rate, 480 nm/min.

riboflavin; Goldsmith *et al.* (this *Year Book*) have reported that enhancement of photoreduction of the *b*-type cytochrome by added flavin can be eliminated by washing the 21KP membranes; and we can likewise eliminate all photoactivity for reduction of cytochrome *aa*<sub>3</sub> by the same washing procedure with the 9KP, while retaining photoreduction of the *b*-type cytochrome (data not shown).

In addition, as shown by the results in Fig. 4, the photoreduction of cytochrome *aa*<sub>3</sub> can be distinguished readily from that of the *b*-type cytochrome on the basis of differential sensitivity to inhibitors. Although the 9KP contains some of the *b*-type cytochrome plus its tightly bound photoreceptor, it is not normally seen in an unwashed 9KP, since the cytochrome *aa*<sub>3</sub> reaction dominates (Fig. 4, top traces). Unlike the cytochrome *b* system, however, which is very sensitive to salicylhydroxamic acid (SHAM) (Caubergs *et al.*, *Year Book 77*, pp. 356–357; see also below), the cytochrome *aa*<sub>3</sub> system is unaffected by SHAM at a concentration as high as 1 mM (Fig. 4, center traces). If KCN is added instead of SHAM, however, the



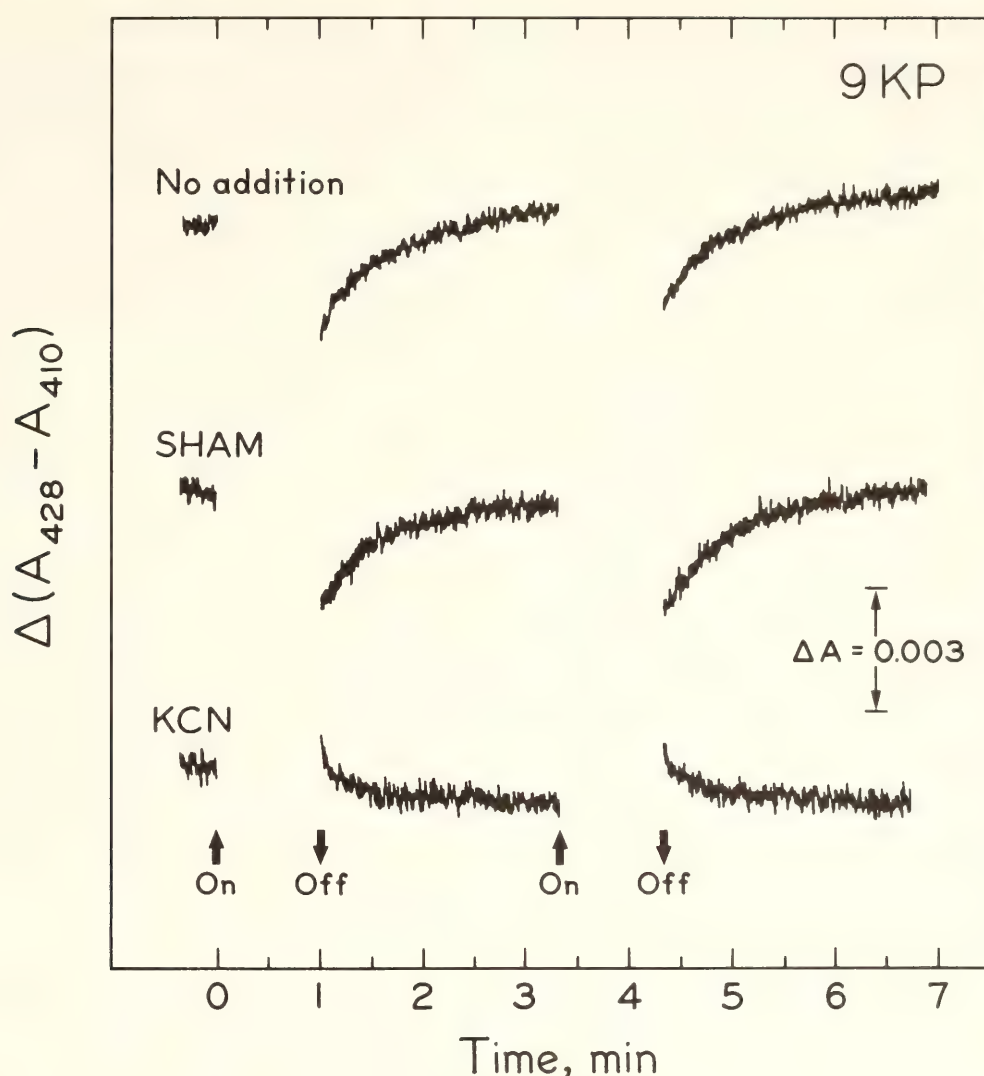


Fig. 4. Differential effects of SHAM and KCN on photoreduction of cytochrome  $aa_3$  (negative signals) and a  $b$ -type cytochrome (positive signals). Glucose oxidase, 1 mg/ml;  $\beta$ -D-glucose, 8 mg/ml; EDTA, 25 mM; protein concentration, 14.7 mg/ml; sample temperature, 7°C. The upper and center traces represent the same sample before (upper) and after (center) addition of SHAM (to 1 mM). The lower traces represent another aliquot from the same 9KP preparation following addition of KCN (to 1 mM) instead of SHAM.

mitochondrial system is completely blocked. Photoreduction of the  $b$ -cytochrome persists, and a positive signal is obtained (Fig. 4, bottom traces).

The lack of any effect of cyanide on photoreduction of the  $b$ -type cytochrome was demonstrated further by experiments with the washed 21KP, the fraction most enriched for this system. The influence of riboflavin concentration on photoreduction was tested as before (Goldsmith *et al.*, this *Year Book*) with or without 1 mM KCN present. The  $K_M$

values for riboflavin did not differ significantly (0.97 and 1.10, respectively), nor did the maximum photoreduction obtainable with saturating riboflavin (results not shown). Difference spectra obtained in the alpha band region upon photoexcitation of the endogenous photoreceptor (no added flavin) were identical with or without KCN (1 mM). Peak heights were the same, and the difference maximum was at 560 nm in both cases (see Goldsmith *et al.*, this *Year Book*).

The specific photoactivity for reduc-

tion of the *b*-type cytochrome in various particulate fractions was investigated after differential centrifugation. The tissue homogenate was centrifuged successively at 2000, 9000, 21,000, and 50,000 × *g* for 10, 15, 20, and 90 min, respectively. Of the pellets obtained (designated 2, 9, 21, and 50KP, respectively), the 2KP was discarded and the other three resuspended for photoassay and protein determination. The results of several such experiments are shown in Table 2. The first four experiments show the specific photoactivities when the photosensitizer is the endogenous photoreceptor only, and the fifth experiment shows specific photoactivity with added riboflavin (3 μM), or FMN (2 μM). Also shown for comparison (last two columns, Table 2) are specific photoactivities in similar corn membrane fractions when methylene blue (5 μM) is

the photosensitizer (Widell *et al.*, *Year Book* 77, pp. 344–347) and specific photoactivities in *Neurospora* membrane fractions with endogenous photoreceptor only (Brain *et al.*, 1977). In all cases, maximal specific photoactivity was found in the 21KP, with a variable but lesser value for the 50KP, and about one-third the enrichment in the 9KP. Since the 9KP is known to be enriched for mitochondria (Jesaitis *et al.*, 1977) and the 50KP for endoplasmic reticulum (Cross and Briggs, 1979; *Year Book* 77, pp. 353–356), the photoactivity cannot be assigned solely to either of these membranous components. In summary, the photoreduction of cytochrome *aa*<sub>3</sub> described here differs from that of the *b*-type cytochrome in at least four ways: (1) *aa*<sub>3</sub> is mitochondrial, while the *b*-type does not fractionate with mitochondrial markers. (2) *aa*<sub>3</sub> is cyanide sensitive and SHAM

TABLE 2. Specific Photoactivity (units × 10<sup>3</sup>/mg protein) for Reduction of a *b*-Type Cytochrome in Fractions Obtained by Differential Centrifugation\*

	Photoreceptor							
	Endogenous Flavint†				RF†	FMN†	Endogenous	
							MB†	Flavint‡
	Exp. 1	Exp. 2	Exp. 3	Exp. 4	Exp. 5	Exp. 5	Exp. 6	Exp. 7
9KP	4.8 (31)	7.8 (30)	7.1 (28)	6.8 (30)	11.9 (33)	9.6 (32)	9.8 (21)	49.0 (38)
21KP	15.4 (100)	25.9 (100)	25.0 (100)	21.7 (100)	35.6 (100)	29.7 (100)	46.7 (100)	130.1 (100)
50KP	12.4 (80)	16.8 (65)	14.0 (56)	14.1 (65)	31.0 (87)	29.3 (98)	29.4 (63)	64.0 (49)

\* Units of activity as in Goldsmith *et al.* (this *Year Book*, Table 1). In experiments 1–5, glucose oxidase was 1 mg/ml; β-D-glucose, 8 mg/ml; EDTA, 25 mM; sample temperatures, 7°C. All pellets were washed by recentrifugation and resuspension. KCN was present with the 9KP samples for the experiments with riboflavin and FMN only. For experiments 6 and 7, the pellets were unwashed, glucose and glucose oxidase were not present, EDTA concentration was 3 mM, and cyanide was not used. Experiment 6 is from Widell *et al.* (*Year Book* 77, pp. 344–347) and experiment 7 from Brain *et al.* (1977). Numbers in parentheses are activities relative to that in the 21KP normalized to 100.

† Organism: Corn.

‡ Organism: *Neurospora*.



insensitive, while the *b*-type is the opposite for both inhibitors. (3) *aa*<sub>3</sub> has a difference maximum at 445 nm, *b*-type at 429 nm. (4) The photoreceptor moiety for *aa*<sub>3</sub> is not tightly bound, and hence is lost if the membranes are recentrifuged and resuspended once, while that for the *b*-type will survive at least two such washings with an insignificant loss of activity because its photoreceptor is very tightly bound.

A series of experiments was conducted to determine the sensitivity of photo-reduction of the *b*-type cytochrome to a further series of inhibitors in the absence of any added photosensitizer. The first three inhibitors, phenylacetic acid, sodium iodide, and sodium azide, might all be expected to inhibit reactions involving flavin in the triplet state. Phenylacetic acid reacts with triplet flavin to form a covalent bond (Hemmerich *et al.*, 1976), and both iodide ion and azide are effective in depopulating flavin triplets (see Heelis *et al.*, 1978). All three inhibitors were effective on the present system, with *K*<sub>I</sub> values of 40 mM, 50 mM, and 2 mM, respectively. SHAM, ineffective on photoreduction of the mitochondrial cytochrome *aa*<sub>3</sub>, as mentioned above, was extremely effective on the present system with a *K*<sub>I</sub> near 14  $\mu$ M (see Caubergs *et al.*, *Year Book* 77, 356–357). Antimycin A, which blocks electron transport between mitochondrial *b* and *c* cytochromes (Lemberg and Barrett, 1973) was completely ineffective at a concentration (10  $\mu$ M) sufficient in our hands to block mitochondrial electron transport completely (results not shown), although higher concentrations (40  $\mu$ M and above) did give up to 80% inhibition of photoreduction of the *b*-cytochrome.

Several experiments were carried out with inhibitors when exogenous photosensitizers had been added. Azide was equally effective whether exogenous flavin (1  $\mu$ M FMN) was present or not, not a surprising result in view of its

known action on flavins. SHAM was ten-fold less effective with exogenous flavin (3  $\mu$ M riboflavin), a difference not readily explainable without further knowledge of the mechanism of action of the various inhibitors in the hydroxamic acid family. Iodide is equally effective whether endogenous photoreceptors or methylene blue (excited by red light) are used for cytochrome reduction, suggesting that it may also depopulate triplets of methylene blue, a possibility that remains to be tested. Finally, phenylacetic acid also inhibits the reaction when methylene blue is the photoreceptor, though it is threefold less effective than when endogenous photoreceptor is used. The precise nature of the reaction between methylene blue and phenylacetic acid is not clear at present, but since this dye and flavins share common structural properties and have very similar photochemistry, formation of a covalent link between the phenylacetic acid and a triplet state of methylene blue should be considered.

#### REFERENCES

- Brain, R. D., J. A. Freeberg, C. V. Weiss, and W. R. Briggs, *Plant Physiol.*, **59**, 948–952, 1977.
- Britz, S. J., E. Schrott, S. Widell, and W. R. Briggs, *Photochem. Photobiol.*, **29**, 359–365, 1979.
- Cross, J. W., and W. R. Briggs, *Planta*, in press, 1979.
- Heelis, P. F., B. J. Parsons, G. O. Phillips, and J. F. McKellar, *Photochem. Photobiol.*, **28**, 169–173, 1978.
- Hemmerich, P., V. Massey, and G. Weber, *Nature*, **213**, 728–730, 1967.
- Jesaitis, A. J., P. R. Heners, R. Hertel, and W. R. Briggs, *Plant Physiol.*, **59**, 941–947, 1977.
- Lemberg, R., and J. Barrett, *Cytochromes*, Academic Press, London, 1973.
- Schmidt, W., and W. L. Butler, *Photochem. Photobiol.*, **24**, 71–75, 1976.

## IMMUNOAFFINITY PURIFICATION OF PHYTOCHROME

Peter H. Quail and Winslow R. Briggs

Conventional phytochrome purification is lengthy and laborious. Moreover, with some starting material, notably *Avena*, preparations of undegraded phytochrome obtained in this manner are routinely not completely homogenous (Pratt, 1978). Hunt and Pratt (1979) have recently developed an immunoaffinity purification procedure that enables the preparation of mg lots of 95–100% pure phytochrome in 2–3 hr starting with the relatively crude fraction (5–8% pure) obtained from brushite chromatography in the first step of the conventional procedure (Rice *et al.*, 1973). Our laboratory, in close collaboration with Dr. Pratt and colleagues, has also recently implemented the immunoaffinity method for phytochrome purification from *Avena*.

The protocol followed is described in detail by Hunt and Pratt (1979). Briefly, the procedure is as follows: Phytochrome purified by conventional means is both immobilized on Sepharose beads and

used to raise antiserum. Antiphytochrome immunoglobulins (IgG's) are purified from the antiserum by sequential adsorption to and desorption from the Sepharose-immobilized phytochrome by formation and disruption of the antibody-antigen complex. The monospecific antibodies thus obtained are in turn covalently linked to Sepharose beads. These immobilized antiphytochrome IgG's are then used repeatedly for phytochrome purification by specific immunoadsorption from relatively crude fractions, thereby completing the cycle.

In the present study purified *Avena* phytochrome (Pratt, 1978) was used to raise rabbit antiserum. About 10 mg of monospecific antiphytochrome IgG's were extracted from 25 ml of this antiserum with a column of ~10 mg of Sepharose-immobilized phytochrome provided by Dr. L. H. Pratt (Hunt and Pratt, 1979). These monospecific antibodies were immobilized on CNBr-activated Sepharose 4B and have been

TABLE 3. Representative Immunoaffinity Purification Balance Sheet\*

Phytochrome Fraction	mg	SAR†	Percent
Applied to beads	12.8	0.07	100
Not adsorbed during initial incubation	4.8	...	38
Eluted by 1 M NaCl wash	1.3	...	10
Eluted by 3 M MgCl <sub>2</sub> before (NH <sub>4</sub> ) <sub>2</sub> SO <sub>4</sub> precipitation	2.1	...	16
Eluted by 1 M formic acid before (NH <sub>4</sub> ) <sub>2</sub> SO <sub>4</sub> precipitation	3.2	...	25
Total recovered from column prior to (NH <sub>4</sub> ) <sub>2</sub> SO <sub>4</sub> precipitation	11.4	...	89
(NH <sub>4</sub> ) <sub>2</sub> SO <sub>4</sub> -precipitated phytochrome from MgCl <sub>2</sub> elution	1.4	0.85	11

\* The purification was performed using monospecific antiphytochrome IgG's covalently coupled to Sepharose 4B. See text for details of protocol.

† SAR = specific absorbance ratio =  $\frac{A_{667}}{A_{280}}$



used thus far to prepare in several successive runs a total of ~15 mg phytochrome of >95% purity.

Table 3 shows the balance sheet from a typical purification run. The protocol was as follows: an aliquot of 12.8 mg brushite-purified phytochrome (1.22 mg/ml; specific absorbance ratio (SAR) = 0.07) was incubated for 15 min at 4°C with 10 mg Sepharose-immobilized monospecific antiphytochrome IgG's. The buffer phase containing unadsorbed protein was drained and assayed for phytochrome (4.8 mg). After thorough washing of the column with buffered 1 M NaCl to remove nonspecifically adsorbed proteins (including 1.3 mg phytochrome), the remaining immunospecifically adsorbed pigment was eluted successively with 3 M MgCl<sub>2</sub> (2.1 mg) and 1 M formic acid (3.2 mg). Both lots were concentrated by ammonium sulfate (200 gm/l) precipitation. A final yield of 1.4 mg MgCl<sub>2</sub>-eluted phytochrome with an SAR of 0.85 and >95% homogeneous on SDS gels (see below) was obtained. This amount represents 11% of the pigment initially applied to the beads, 21% of that estimated to have been bound immunospecifically, and a yield of 145

μg phytochrome/mg immobilized IgG's. About 10% of the original pigment is unaccounted for at the end of the incubation and elution steps. A further loss occurs upon (NH<sub>4</sub>)<sub>2</sub> SO<sub>4</sub> precipitation. This loss is routinely 25% of that phytochrome initially eluted from the column by MgCl<sub>2</sub>.

Table 4 indicates the range of values obtained over 12 purification runs for some of the parameters of the procedure. In the range studied, the yield of MgCl<sub>2</sub>-eluted phytochrome per mg immobilized IgG's increased with increasing amounts of brushite phytochrome applied to the same beads. There is, as expected, however, a concomitant decline in the yield as expressed per mg of brushite phytochrome applied as this ratio of brushite phytochrome to immobilized IgG increases. The SAR remained nearly constant from run to run with no apparent influence of the ratio of brushite phytochrome to immobilized IgG's. These SAR values agree well with those of Hunt and Pratt (1979) and are slightly higher than those previously reported for conventional purifications of undegraded phytochrome (Rice *et al.*, 1973; Pratt, 1978). Together with the high degree of

TABLE 4. Ranges and Means of Values Obtained for Some Parameters of Phytochrome Immunopurification Procedure\*

Parameters		Range	Mean
Ratio	$\frac{\text{brushite phytochrome applied (mg)}}{\text{immobilized IgG (mg)}}$	0.67–1.73	1.02
Yield	$\frac{\text{MgCl}_2 \text{ eluted phytochrome}}{\text{brushite phytochrome applied}} \times 100$	8.6–17.9	13.5
Ratio	$\frac{\text{MgCl}_2 \text{ eluted phytochrome } (\mu\text{g})}{\text{immobilized IgG (mg)}}$	95–168	125
SAR	$\frac{A_{667}}{A_{280}}$	0.79–0.88	0.84
Ratio	$\frac{\text{MgCl}_2 \text{ eluted phytochrome}}{\text{Formate eluted phytochrome}}$	0.18–0.47	0.40

\* The data were obtained over 12 successive runs analogous to that outlined in Table 3.

homogeneity observed on SDS gels (see below), the SAR values suggest that minimum spectral denaturation has occurred. The ratio of  $\text{MgCl}_2$ -eluted to formate-eluted phytochrome was not correlated with the ratio of brushite phytochrome to immobilized IgG's. Indeed, for 10 of the 12 runs the  $\text{MgCl}_2$ -eluted to formate-eluted ratio lay between 0.37 and 0.47 despite the larger range indicated in Table 4. On this basis, no marked decline was evident in the capacity of the beads to bind phytochrome over the 12 runs mentioned.

Ten mg of  $\text{MgCl}_2$ -eluted phytochrome from the best preparations were pooled and covalently linked to Sepharose 4B (Hunt and Pratt, 1979). The degree of purity of this pool is shown by the SDS gel profile in Fig. 5. The major band, presumably representing the 120,000-dalton native phytochrome monomer, contains >95% of the protein on the gel. Two minor bands are indicated by the arrows. The higher mobility band is suspected to be the commonly observed 60,000-dalton discrete proteolytic cleavage product of phytochrome (Gardner *et al.*, 1971). The low-mobility component may also be derived from the phytochrome in the preparation, as it is sometimes observed to increase in quantity upon storage (R. Hunt, personal communication). No verified explanation for this observation is yet available.

The immobilized phytochrome shown in Fig. 5 has been used to prepare a further 12 mg of monospecific antiphytochrome IgG's from a separate 18 ml batch of antiserum, thereby completing the cycle. With both purified antigen and antibody immobilized on separate Sepharose columns, we now have the capacity for relatively rapid purification of either complementary molecule.

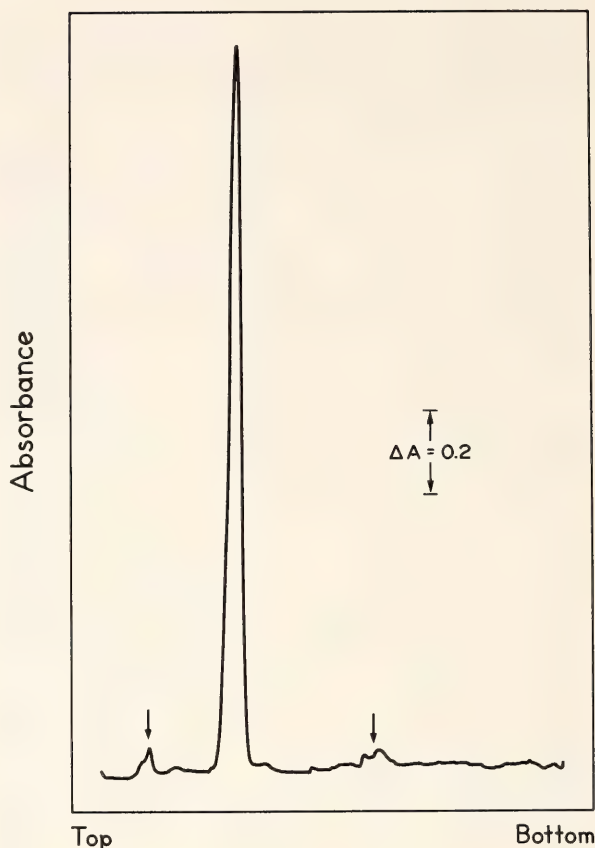


Fig. 5. SDS polyacrylamide gel electrophoresis of 20  $\mu\text{g}$  immunoaffinity-purified *Avena* phytochrome ( $\text{MgCl}_2$  eluted) prepared according to Hunt and Pratt (1979). The profile here represents an aliquot taken from a pool of 10 mg phytochrome accumulated over several purifications and has a SAR of 0.83.

#### REFERENCES

- Gardner, G., C. S. Pike, H. V. Rice, and W. R. Briggs, *Plant Physiol.*, **48**, 686-693, 1971.
- Hunt, R. E., and L. H. Pratt, *Plant Physiol.*, in press, 1979.
- Pratt, L. H., *Photochem. Photobiol.*, **27**, 81-105, 1978.
- Rice, H. V., W. R. Briggs, and C. J. Jackson-White, *Plant Physiol.*, **51**, 917-926, 1973.



# IRRADIATION-ENHANCED PHYTOCHROME PELLETABILITY: FILTRATION AND MIXING EXPERIMENTS

Peter H. Quail and Winslow R. Briggs

Irradiation-enhanced phytochrome pelletability in *Avena* is a manifestation of a prior rapid Pfr-mediated intracellular event (Quail and Briggs, 1978). The precise relationship between the physical association observed as pelletability in the test tube and the preceding intracellular event remains obscure (Pratt, 1978; Quail and Briggs, 1978; Boeshore and Pratt, 1978). In particular it is uncertain whether this association actually occurs in the cell and is preserved upon

homogenization in the presence of the requisite 10 mM divalent cation (Pratt and Marmé, 1976; Quail, 1978) or occurs artifactually during homogenization.

Two approaches to this problem have been attempted here. First, tissue homogenates prepared in the absence of exogenous divalent cation were rapidly passed through membrane filters, and phytochrome retention with the particulate material on the filter was determined. From the earlier observation (Quail,

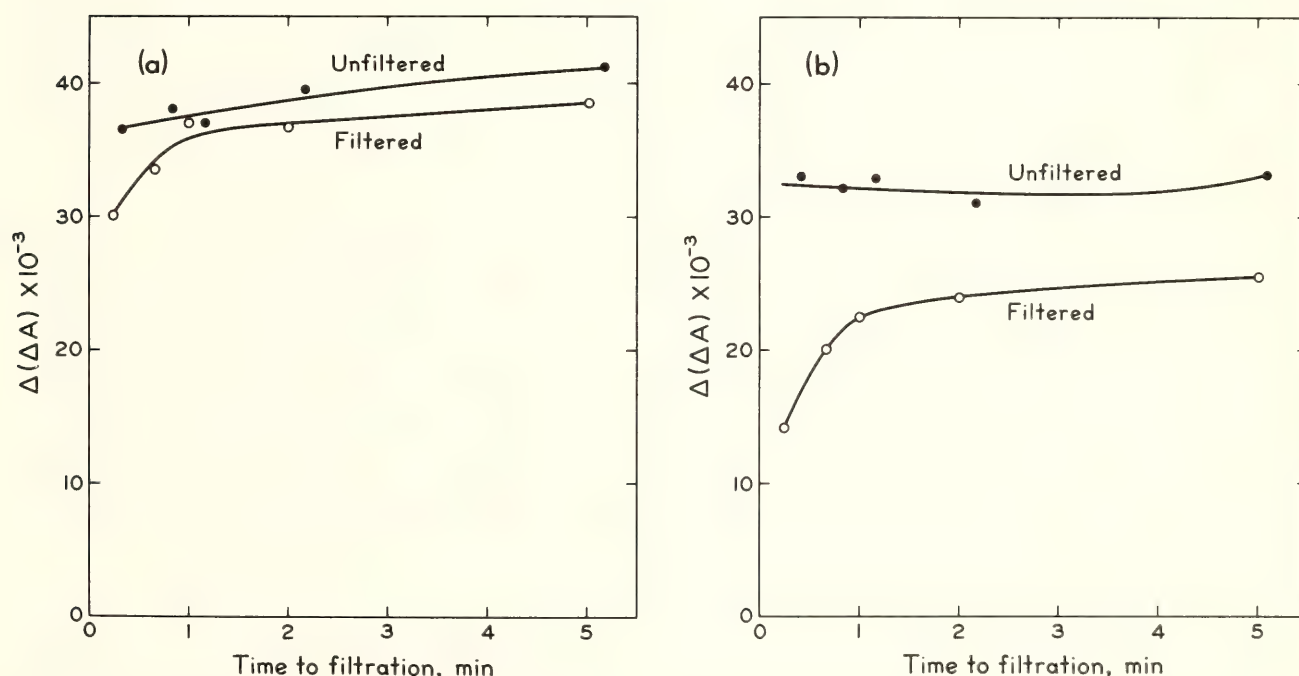


Fig. 6. Phytochrome content of *Avena* homogenates before and after filtration as a function of time from homogenization in  $Mg^{2+}$ -free medium. (a) unirradiated controls; (b) tissue irradiated with a saturating pulse (10 s) of 660-nm light at 25°C with a subsequent 60 s darkness before cooling and extraction. Growth of tissue, irradiation conditions, extraction medium, and phytochrome assay were as previously described unless otherwise indicated (Quail and Briggs, 1978). Tissue was homogenized with an Ultra-Turrax blender in  $Mg^{2+}$ -free medium directly in a syringe for 5 s starting at time zero. At the times indicated, the homogenate was passed either (1) only through a porous 35- $\mu m$  plastic disk to remove large debris (= "unfiltered") or (2) sequentially through both the porous plastic and a 0.2- $\mu m$  cellulose acetate filter combined with a Whatman GFC prefilter (= "filtered"). A three-way stopcock permitted alternate collection of filtered and unfiltered samples from the same initial homogenate at the times shown. A fresh cellulose acetate-GFC filter combination was used for each time point. The first filtered sample was collected at 15 s from the onset of homogenization.

1978) that delayed posthomogenization  $Mg^{2+}$  addition leads to a rapid decline (first 1–2 min) in pelletability, we anticipated that the filtration procedure might distinguish between the two above-mentioned extreme alternatives. If pelletability results from a preformed but rapidly labile association that is stabilized by exogenous  $Mg^{2+}$ , then a rapidly declining retention of phytochrome on the filter would be expected. If, instead, pelletability is the product of a  $Mg^{2+}$ -induced, posthomogenization association predetermined in the cell by some intrinsic but labile configurational change in the phytochrome molecule itself, then no irradiation-enhanced filter retention of phytochrome would be expected. Moreover, in the latter eventuality the rapid passage of the particle-free filtrate into a  $Mg^{2+}$ -containing vessel might preserve the postulated labile phytochrome configuration for subsequent analysis in the absence of any induced association with particulate material.

The data obtained do not conform to either of these predicted patterns. Figure 6(a) and (b) indicate the amount of phytochrome detectable in homogenates of dark control and red-irradiated tissue, respectively, before and after filtration through 0.2- $\mu$ m cellulose acetate filters with increasing time from the onset of a 5-s homogenization in  $Mg^{2+}$ -free media. From data like these we determined the proportion of phytochrome retained on the filter as a function of time from homogenization (Fig. 7). The percent retention is enhanced by *in vivo* irradiations, but no decline in the irradiation-enhanced increment relative to dark controls is observed between 15 s and 5 min from the onset of homogenization. A rapid decline in phytochrome retention is in fact observed over the first 60 s, but this occurs in all fractions, irradiated or not, so the incremental difference remains constant. A general decline in protein retention on the filter from  $\sim 40\%$  to  $\sim 26\%$  over the first 1–2 min from

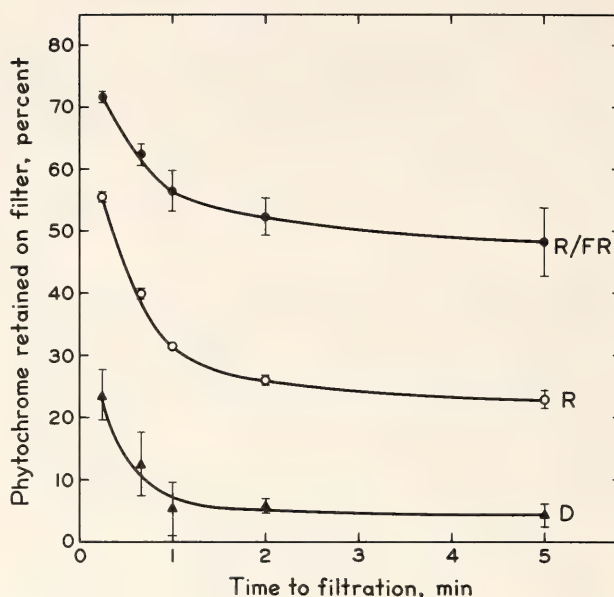


Fig. 7. Proportion of phytochrome retained on 0.2- $\mu$ m cellulose acetate filters as a function of time from the start of homogenization in  $Mg^{2+}$ -free media. D = unirradiated control tissue; R = 10 s (saturating) 660-nm light at 25°C plus 60 s darkness before cooling and homogenization; R/FR = 10 s (saturating), 660-nm light plus 60 s dark plus 30 s far red light (saturating), all at 25°C. Homogenization and filtration procedures as in Fig. 6. The percent phytochrome retained was calculated from curves like those in Fig. 6 as

$$\frac{(\text{unfiltered}) - (\text{filtered})}{(\text{unfiltered})} \times 100.$$

The unfiltered value used for each filtered time point was obtained by taking the mean of the two unfiltered time points on either side of the relevant filtered value (except for the first filtered value, where only the first unfiltered value was used). This procedure was necessary to account for the tendency for the unfiltered  $\Delta(\Delta A)$  values to increase slightly with time in some experiments (Fig. 6a).

homogenization is also observed, however, indicating that this effect is not specific to phytochrome. Inclusion of  $Mg^{2+}$  in the extraction buffer eliminates the overall decline in phytochrome retention so that it remains relatively constant at  $\sim 75\%$  for both R and R/FR irradiated tissue and at 10–20% for dark controls over the period studied (data not shown). The latter result is consistent with data commonly obtained by centrifugation. Taken together the above data indicate that if the binding event



occurs *in vitro*, it has gone to completion within the first 15 s from cell disruption, but they do not permit a distinction to be made between *in vivo* and *in vitro* binding.

In the second approach, irradiated and nonirradiated lots of *Avena* shoot tissue were either (a) combined physically and subsequently homogenized together in the same vessel or (b) homogenized separately and the extracts subsequently mixed (Fig. 8). Phytochrome pelletability in all four sets of extracts thus generated was then determined. All homogenizations were performed in the presence of 10 mM  $Mg^{2+}$ .

The rationale for these experiments resides in the observation that, under the extraction conditions used, a maximum of ~60% of the extractable phytochrome can be induced to pellet by *in vivo* irradiations (Pratt and Marmé, 1976; Quail, 1978; Quail and Briggs, 1978). One testable hypothesis for this apparent ceiling is that pelletability does indeed result from the *in vitro* binding of *in vivo*-modified phytochrome to particulate material but that the number of effective binding sites is limited. The ratio of particulate material to *in vivo*-irradiated phytochrome molecules at the moment of cell breakage can be effec-

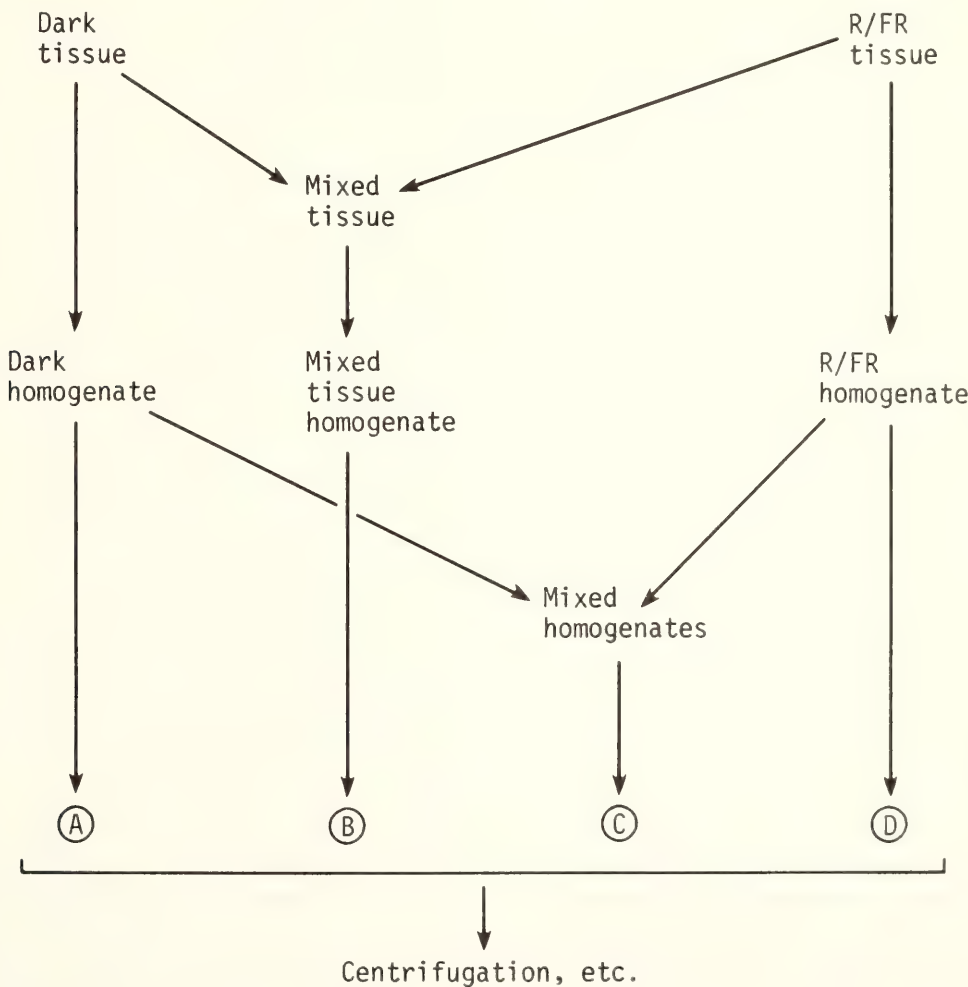


Fig. 8. Example of protocol followed routinely in mixing experiments. Subsamples of irradiated (R/FR here) and control (D here) tissue were either (1) extracted separately (A) and (D) or (2) mixed in varying proportions and then extracted together in the same vessel (B). Aliquots of the homogenates from the unmixed tissues were also mixed (C) in the same proportion as for the mixed tissue in (B). Each of the four samples (A) through (D) were then tested for phytochrome pelletability as previously described (Quail and Briggs, 1978). The extraction medium contained 10 mM  $Mg^{2+}$ .

tively increased by mixing control with irradiated tissue for simultaneous homogenization. This procedure provides maximum opportunity for the normally unpelletable 40% phytochrome to interact with excess potential binding material right from the onset of homogenization.

In the present study ratios of control to irradiated tissue ranging from 4:6 to 9:1 were examined. In all cases the pelletability observed was equal to the arithmetic mean of the values obtained for the two sets of tissues *separately* homogenized and tested for pelletability in the normal way without mixing. This observation is most readily appreciated from the data in Table 5, where the ratio of control to irradiated tissue was 1:1.

TABLE 5. Phytochrome Pelletability in Extracts from *Avena* in a Mixing Experiment Performed According to the General Protocol Outlined in Fig. 8\*

Treatment	Pelletability (%)	
	Measured	Arithmetic Mean
Dark Control (D)	3.1	33.3
Mixed tissue (D + R) homogenate	32.8	
Mixed homogenates (D+R)	35.1	
Red-irradiated tissue (R)	63.4	
Far-red control (FR)	3.2	31.6
Mixed tissue (FR+R/FR)	32.1	
Mixed homogenates (FR+R/FR)	34.8	
Red + Far-red-irradiated tissue (R/FR)	60.0	

\* Tissue and homogenates were mixed where indicated in a ratio of 1:1. Procedures for irradiation, extraction, and determination of phytochrome pelletability were as previously described (Quail and Briggs, 1978). All irradiations were given to intact tissue at 25°C under conditions designed to maximize pelletability (R = 10 s 660 nm light; R/FR = 10 s 660 nm + 60 s dark + 30 s far red; FR = 30 s far red). The arithmetic mean value indicated was derived from the two values obtained separately for the unmixed control and the irradiated samples.

The results of the complete range of ratios examined are combined in Fig. 9. It is clear that the data points show strong agreement with the theoretical curve (solid line) that represents the simple arithmetic mean expected from the physical mixing of two behaviorally noninteractive populations of molecules. The data do not correlate with the other extreme theoretical curve (dashed line) constructed on the premise that particulate material from control tissue has an *in vitro* binding capacity equivalent to that from irradiated tissue and would therefore bind all excess unbound molecules from irradiated tissue at any ratio of control to irradiated tissue greater than ~40:60. Moreover, there is no apparent influence of the form of the phytochrome from irradiated tissue at the time of homogenization (Fig. 9). The same results are obtained whether the pigment is present as Pfr or "cycled" Pr (Quail *et al.*, 1978; Boeshore and Pratt, 1978).

These data indicate that the observed limit to the pelletability inducible in irradiated tissue does not result from a limited number of nonspecific particulate binding sites to which predisposed phytochrome molecules have access during or after homogenization. Thus it seems possible that if the responsible binding event does occur *in vitro*, it is complete within a few seconds and apparently is not indiscriminant with respect to particulate fractions. While the hypothesis that binding does occur *in vivo* obviously remains the most attractive one, it is not possible from these data to preclude the following alternatives: (a) that there are two populations of phytochrome molecules in irradiated tissue—60% that bind *in vitro* and 40% that do not; (b) that there is some Pfr-mediated *in vivo* alteration in the particulate fraction destined to bind phytochrome upon homogenization. Particulate material from control tissue would lack this induced alteration and therefore lack the capacity to bind phytochrome in the mixing experiments.



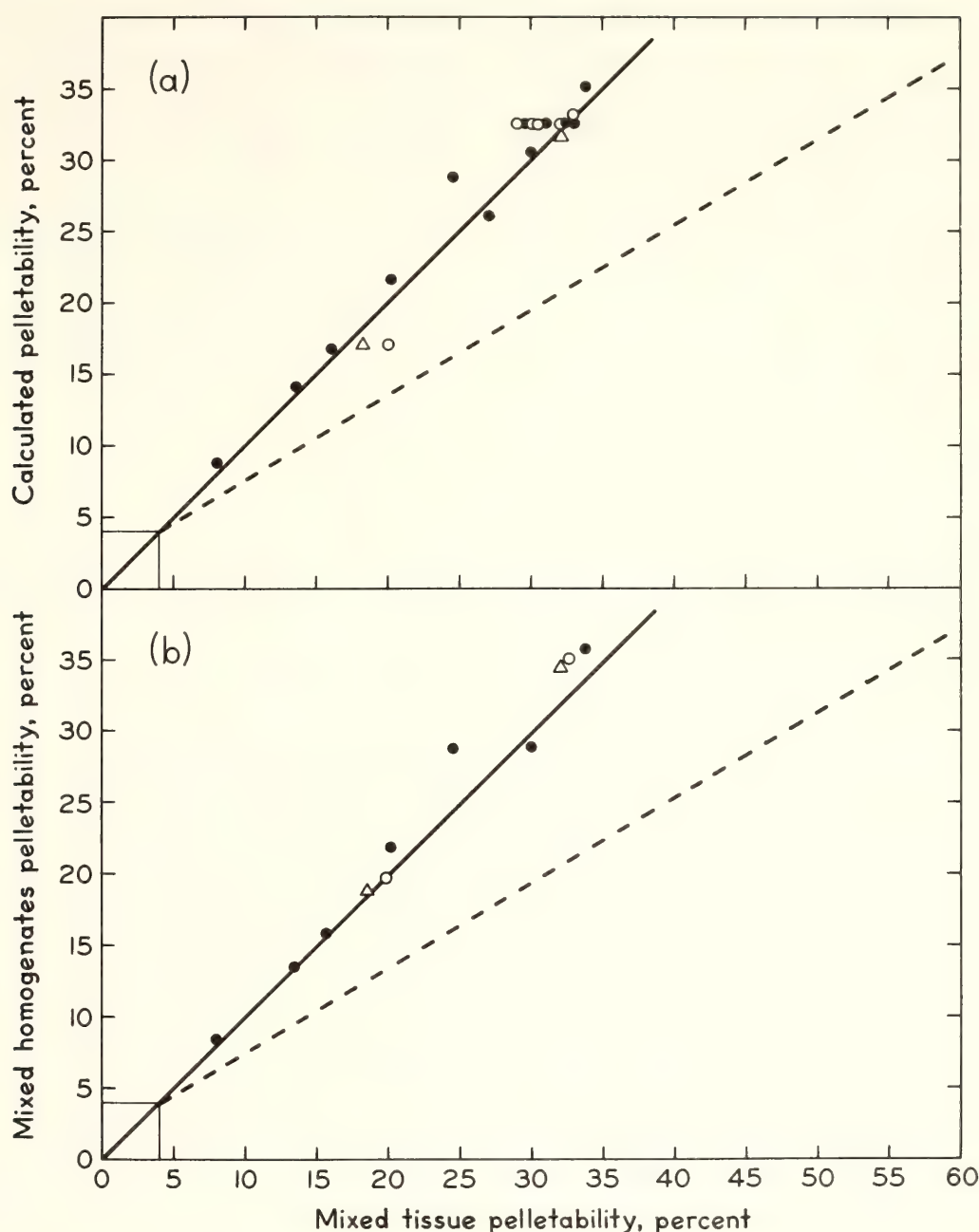


Fig. 9. The effect of tissue and homogenate mixing on phytochrome pelletability in *Avena*. Control (D and FR) and irradiated (R and R/FR) tissue and homogenates derived separately therefrom were mixed in ratios ranging from 4:6 to 9:1 according to the general scheme in Fig. 8. Other conditions were as in Table 5. Mixtures tested were R + D, R/FR + D and R/FR + FR. The pelletability obtained in the mixed tissue homogenate (i.e. (B), Fig. 8) is plotted (a) against the pelletability *calculated* to be the arithmetic mean of the separately centrifuged homogenates ((A) and (D) in Fig. 8); and (b) against the pelletability *observed* when the homogenates are physically mixed before centrifugation ((C) in Fig. 8). Symbols are observed data. Solid line is the theoretical curve obtained when the two populations of phytochrome molecules comprising the mixture behave totally independently with regard to the pelleting process. Dashed line is the theoretical curve derived on the premise that phytochrome from irradiated tissue can bind *in vitro* equally well to particulate material from control and from irradiated tissue. In this case, the former tissue is considered to provide "unoccupied" binding sites for the ~40% unpelletable pigment normally observed with irradiated tissue alone under these conditions. Assuming complete linearity, all molecules from irradiated tissue should be bound at a ratio slightly greater than 40:60 for control:irradiated tissue (when the 3-4% control pelletability is taken into account).

## REFERENCES

- Boeshore, M. L., and L. H. Pratt, *Plant Growth and Light Perception. Selected Topics from Annual European Symposium on Photomorphogenesis*, pp. 117–136, B. Deutch, B. I. Deutch, and A. O. Glydenholm, eds., Aarhus, Denmark, 1978.
- Pratt, L. H., *Photochem. Photobiol.*, **27**, 81–105, 1978.
- Pratt, L. H., and D. Marmé, *Plant Physiol.*, **58**, 686–692, 1976.
- Quail, P. H., *Photochem. Photobiol.*, **27**, 147–153, 1978.
- Quail, P. H., and W. R. Briggs, *Plant Physiol.*, **62**, 773–778, 1978.
- Quail, P. H., W. R. Briggs, and L. H. Pratt, *Carnegie Inst. Washington Year Book 77*, 342–344, 1978.

## PHYTOCHROME RESPONSES IN LIGHT-GROWN GREEN AND ACHLOROPHYLLOUS CORN SEEDLINGS

Holly L. Gorton and Winslow R. Briggs

For the past 35 years, much research on phytochrome has been carried out with etiolated seedlings rather than light-grown plants. The assay used to measure the amounts of the two forms of phytochrome, Pr and Pfr, is spectral, and chlorophyll fluorescence interferes with the measurement (Pratt, 1978; Jose *et al.*, 1977). To study the phytochrome system in light-grown plants, one must either find a way to grow achlorophyllous seedlings in the light or use a nonspectral assay. Hunt and Pratt (1977) have developed a sensitive radioimmunoassay that is capable of measuring the very small amount of phytochrome in light-grown plants, but the assay measures only the total amount of phytochrome and cannot distinguish between Pr and Pfr. The spectral assay is the only way known to measure photoconversion and photoequilibria of phytochrome.

One way to obtain achlorophyllous seedlings is to grow the plants on Sandoz 9789 ((4-chloro-5-methylamino)-2-( $\alpha,\alpha,\alpha$ -trifluoro-*m*-tolyl)-3(2H)-pyridizine), a pre-emergent, chlorosis-inducing herbicide. Sandoz blocks the desaturation steps of carotenoid biosynthesis (Bartels and McCullough, 1972). Without carotenoids to protect against photo-

oxidation, any chlorophyll present becomes bleached in the light (Wolff and Witt, 1972). The amount of chlorophyll in Sandoz-treated seedlings is insignificant, so it is possible to measure phytochrome in them using standard spectral techniques (Jabben and Deitzer, 1978). Jabben and Deitzer (1979) have looked at several phytochrome-mediated photomorphogenic systems in dark- and light-grown seedlings grown with and without Sandoz. Only one intensity was used to induce each response measured, and dose-response curves were not reported. Thus, although Sandoz did not block phytochrome action, a Sandoz-induced change in sensitivity of the phytochrome system cannot be ruled out by their results.

Before doing a spectroscopic examination of the phytochrome in the achlorophyllous light-grown seedlings as it changes in response to actinic irradiation, it is necessary to determine whether or not the Sandoz itself alters the phytochrome system in light-grown plants. Hence, dose-response curves for several responses of light-grown corn seedlings to end-of-day far-red (FR) irradiation and subsequent reversal by red (R) irradiation have been obtained.

Corn was chosen because Sandoz pro-



duced achlorophyllous tissue at a concentration that did not significantly alter the growth of the seedlings in the dark (data not shown). Corn seeds (Bear Hybrid 610  $\times$  08) were imbibed at room temperature for 3 hr in water or  $10^{-4}$  M Sandoz before planting on one layer of Kimpak moistened with the appropriate solution. Seeds were germinated for 24 hr in the dark, then grown on an 8-hr light/16-hr dark cycle. White light ( $16 \text{ W m}^{-2}$ ) was provided by five 40-W Sylvania fluorescent lamps. The temperature was maintained at  $27^{\circ}\text{C}$  during germination and the subsequent light/dark cycles. After one light/dark cycle, seedlings were transferred to glass vials filled with 0.65% agar, with or without  $10^{-4}$  M Sandoz. Seedlings with roots 2–3 cm long were chosen for transfer.

After five days, Sandoz-treated seedlings contained less chlorophyll than could be detected by *in vivo* spectroscopy. The leaves were completely white. While there was no difference in elongation of seedlings grown with and without Sandoz in the dark, leaf growth was slightly (less than 20%) slower in Sandoz-treated seedlings in the light. Presumably this effect is caused by limited carbohydrate supplies in the achlorophyllous seedlings, which cannot photosynthesize.

FR and R light treatments were given at the end of the second, third, and fourth 8-hr white light periods. The FR light was supplied by two GTE Sylvania high-output fluorescent bulbs (F48T12/E-5346/VHO). These bulbs have maximal output at about 745 nm. One layer of 1/8-inch "black" Plexiglas (FRF 700; Westlake Plastics, Lenni Mills, PA) was used to filter out mercury lines and any other radiation with wavelengths shorter than 700 nm. The R light source used to test reversibility of effects caused by end-of-day FR irradiation consisted of four Sylvania warm white fluorescent bulbs (F20T12WW) and a red Plexiglas filter (Rohm and Hass No. 2423). R irradiations were begun within 30 seconds of the

termination of a 40-second FR irradiation ( $\log \text{ nE cm}^{-2}$ , 2.4).

Seedlings were irradiated in groups of 15 to 20. They were harvested after five days' growth. The seedlings were dissected, and the mesocotyls and coleoptiles were laid on clear plastic sheets and photocopied to facilitate length measurement. Coleoptiles were then frozen in liquid nitrogen and lyophilized. Anthocyanins were extracted from the dry tissue with *n*-propanol:HCl:water (18:1:81), with 3 ml of solvent for about 50 mg of tissue (dry weight). The tissue was extracted for 12–24 hr at  $4^{\circ}\text{C}$ . Extracts were then filtered through a Whatman GF/A glass filter and a Millipore HA filter to remove particles that might cause turbidity. Spectra of the extracts were taken between 450 and 670 nm, and the absorption at the anthocyanin peak (520–522 nm) above absorbance at 650 was determined.

If the seedlings were given FR light at the end of the day, several responses were observed. Both mesocotyl and coleoptile elongation were stimulated by end-of-day FR treatments, and the amount of anthocyanin in the coleoptiles was greatly decreased. Dose-response curves for the end-of-day FR effect on anthocyanin in coleoptiles of seedlings grown with or without Sandoz are shown in Fig. 10.

Dose-response curves for the mesocotyl (about 70–80% increase in length) and coleoptile (about 15% increase in length) were also obtained (data not shown). Even at the highest dose of FR ( $\log \text{ nE cm}^{-2}$ , 3.9) neither the mesocotyl or coleoptile elongation responses seemed to be saturated, although the anthocyanin response was clearly saturated by a dose of about  $1000 \text{ nE cm}^{-2}$  (Fig. 11). Threshold end-of-day FR doses for stimulation of mesocotyl and coleoptile elongation and the decrease in anthocyanin in the coleoptiles are shown in Table 6. Thresholds were roughly estimated by extrapolating the log-linear portions of the dose-response curves through a line represent-

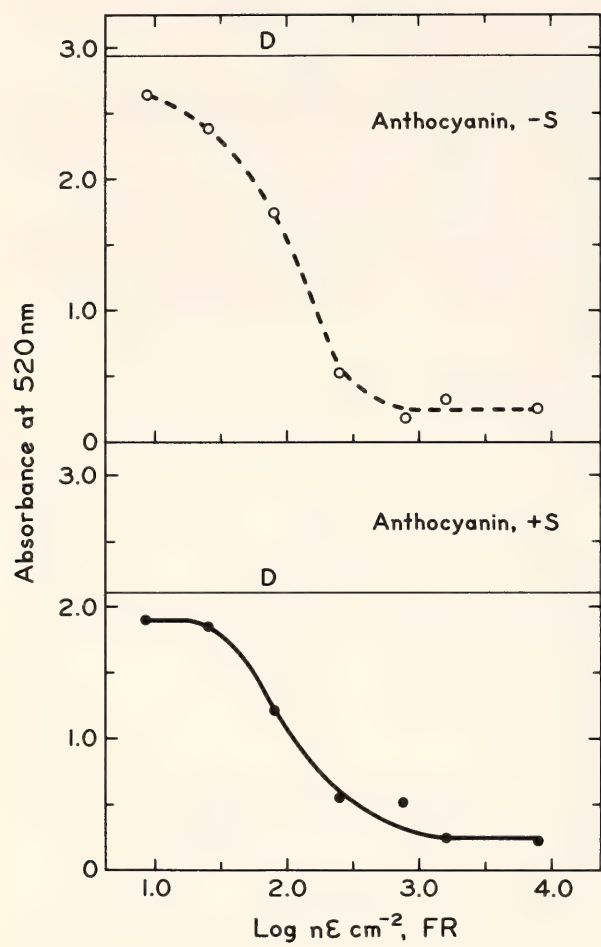


Fig. 10. Dose-response curves for the effect of end-of-day FR irradiation on the anthocyanin content in coleoptiles of light-grown corn. Seedlings were grown either with (+S) or without (−S) 10<sup>−4</sup> M Sandoz.

ing the dark control. Although there are too few points for a more precise determination of the threshold, the two curves shown in Fig. 10 are clearly superimposable. There were no significant differences between thresholds for any of the three responses either with or without Sandoz.

Dose-response curves for R reversal of

TABLE 6. Approximate Threshold FR Doses, log nE cm<sup>−2</sup>

	Meso- cotyl	Coleop- tile	Antho- cyanin
− Sandoz	1.5 ± 0.1	1.6 ± 0.2	1.3 ± 0.3
+ Sandoz	1.5 ± 0.2	1.5 ± 0.2	1.3 ± 0.2

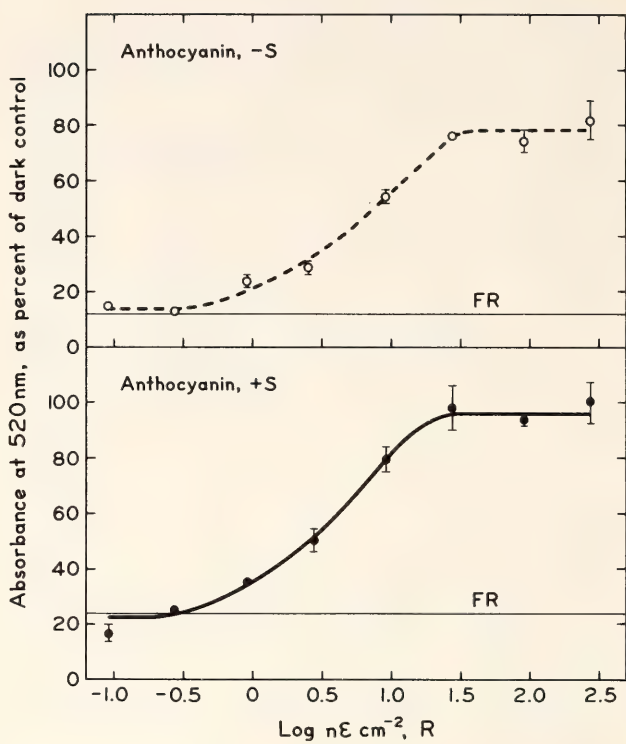


Fig. 11. Dose-response curves for R reversal of the end-of-day FR effect on the anthocyanin content in coleoptiles of light-grown corn. Seedlings were grown either with (+S) or without (−S) 10<sup>−4</sup> M Sandoz. FR dose, log nE cm<sup>−2</sup>, 2.4. Vertical bars indicate standard errors.

FR inhibition of anthocyanin formation in seedlings grown with and without Sandoz are presented in Fig. 11. Again, the curves for mesocotyl and coleoptile stimulation are not shown. All three responses to end-of-day FR could be fully reversed by R. Values for threshold and saturating R doses for the three responses in seedlings grown with and without Sandoz are given in Table 7. No significant differences in responses were seen between any of the treatments.

According to these data, Sandoz has no significant effect on the phytochrome system in light-grown plants grown under our conditions. The absolute level of anthocyanin is about 25% less in the Sandoz-treated seedlings than in the untreated controls, but this decrease is not attributable to a change in sensitivity of the phytochrome system. Absolute coleoptile and mesocotyl lengths were not affected by the Sandoz.



TABLE 7. Approximate Threshold and Saturating R Doses for Reversal of End-of-Day FR Irradiation, log nE cm<sup>-2</sup>

	Mesocotyl	Coleoptile	Anthocyanin
— Sandoz			
Threshold	−0.5 ± 0.1	−0.2 ± 0.2	−0.5 ± 0.1
Saturation	1.4 ± 0.1	1.3 ± 0.2	1.4 ± 0.1
+ Sandoz			
Threshold	−0.5 ± 0.1	−0.2 ± 0.2	−0.5 ± 0.1
Saturation	1.3 ± 0.2	1.2 ± 0.2	1.4 ± 0.1

It is significant that neither of the responding organs in the untreated seedlings contain much chlorophyll. Since chlorophyll and phytochrome both absorb strongly at 660 nm, chlorophyll is thought to screen phytochrome in green leaves, making larger doses of R necessary to achieve the same amount of photoconversion (Jose and Schäfer, 1978; Monteith, 1976). If this screening is significant, differences should show up in the dose-response curves for R reversal of end-of-day FR effects in green and achlorophyllous seedlings. Achlorophyllous seedlings should be more sensitive to R light. Since we see no difference in the phytochrome responses of green and Sandoz-treated seedlings, the amount of chlorophyll must be sufficiently low in the photoreceptive organ(s) to be unimportant in screening or the phytochrome must be situated in an unscreened location. Thus far the photoreceptive organs have not been conclusively identified.

Phytochrome-mediated responses to end-of-day FR are being sought in the leaves of light-grown corn. Leaf growth is often inhibited by end-of-day FR, but the variability is great. A biochemical response might prove more useful. It

would then be possible to obtain a direct measure of the extent of screening of phytochrome by chlorophyll in the same leaf.

REFERENCES

Bartels, P. G., and C. McCullough, *Biochem. Biophys. Res. Comm.*, 48, 16–22, 1972.

Hunt, R. E., and L. H. Pratt, *Plant Physiol.*, 59s, 100, 1977.

Jabben, M., and G. Deitzer, *Photochem. Photobiol.*, 27, 799–802, 1978.

Jabben, M., and G. Deitzer, *Plant Physiol.*, 63, 481–485, 1979.

Jose, A. M., and E. Schäfer, *Planta*, 138, 25–28, 1978.

Jose, A. M., D. Vince-Prue, and J. R. Hilton, *Planta*, 135, 119–123, 1977.

Monteith, J. L., in *Light and Plant Development*, H. Smith, ed., Butterworths, Boston, Mass., 447–460, 1976.

Pratt, L. H., *Photochem. Photobiol.*, 27, 81–105, 1978.

Wolff, C., and H. T. Witt, in *Proceedings of the Second International Congress on Photosynthesis Research*, G. Forti, M. Avron, and A. Melandri, eds. Dr. W. Junk N. V. Publishers, The Hague, 931–936, 1972.

## SHIBATA SHIFT IN CORN SEEDLINGS GROWN WITH AND WITHOUT SANDOZ

*Holly L. Gorton and Winslow R. Briggs*

In the preceding article (Gorton and Briggs, this *Year Book*) we describe the use of a pre-emergent herbicide, Sandoz, to grow achlorophyllous plants in the light. Here we study the photoconversion of protochlorophyllide to chlorophyllide and the resulting spectral shifts in leaves from etiolated seedlings grown with and without Sandoz.

Carotenoids are normally present in etiolated grass seedlings. Bartels and McCullough (1972) found both xanthophylls and  $\beta$ -carotene in etiolated wheat shoots. Bartels and Hyde (1970) reported that in etiolated seedlings grown on  $10^{-4}$  M Sandoz, the amount of colored carotenoids present was about 4% of the control level in untreated seedlings. Uncolored carotenoid precursors accumulated instead (Bartels and McCullough, 1972). We found a similar decrease in colored carotenoids in 4-day corn seedlings imbibed for 3 hours and grown ( $27^{\circ}$  in the dark) in the presence of  $2 \times 10^{-4}$  M Sandoz. Quantitative measurement of the carotenoids was not done, but it was evident from *in vivo* spectroscopy that the absorption pattern typical of carotenoids between 400 and 500 nm was indistinct, if the peaks were indeed present. The leaves from treated seedlings did not have the yellow appearance of normal etiolated leaves. It was difficult to separate the contributions to blue absorption made by carotenoids, protochlorophyll, and cytochromes by *in vivo* spectroscopy. They were all of the same order of magnitude in Sandoz-treated plants. It was clear, however, that the concentration of carotenoids, which normally absorb much more strongly than the protochlorophyll or cytochromes, was greatly reduced by Sandoz.

When etiolated seedlings are given a

brief flash of red or blue light, protochlorophyllide, which absorbs maximally at about 650 nm, is photoreduced to chlorophyllide, which absorbs at about 685 nm. The absorption maximum of chlorophyllide then shifts to about 670 nm in the dark. This shift, termed the Shibata shift after its discoverer, represents a change in the molecular environment rather than the structure of the chlorophyllide (Shibata, 1957). The nature of the molecular change that takes place during the Shibata shift is unknown. In light-grown plants carotenoids are important components of chloroplast grana. During greening they must become closely associated with chlorophyll for energy transfer to occur. It is possible that carotenoids might in some way be involved in the Shibata shift.

We therefore examined the Shibata shift using 4-day corn seedlings grown with and without Sandoz to see if it would occur even though the normal complement of carotenoids was vastly altered and reduced. The kinetics of the Shibata shift were studied in etiolated corn leaves excised from plants grown with or without  $2 \times 10^{-4}$  M Sandoz. Actinic irradiation was given while the samples were in a Perkin-Elmer dual-wavelength spectrophotometer. Irradiation coming from the actinic light was passed through a blue filter (Corning 9782) and reflected from a half-silvered mirror onto the sample. Actinic irradiation was blocked from the photomultiplier by a red cutoff filter (Schott RG-2). Intensity of the blue light at the plane of the sample was  $3300 \text{ ergs cm}^{-2} \text{ s}^{-1}$ . The measuring beam passed through the half-silvered mirror to strike the samples. With this arrangement, it was possible to irradiate the samples with actinic blue



irradiation and simultaneously measure the increase in absorption at 690 nm, compared to a reference wavelength (720 nm) as photoconversion from protochlorophyllide to chlorophyllide took place. Saturation of the photoconversion occurred within 5 minutes. As the Shibata shift progressed, absorption at 690 decreased in subsequent darkness. The half-times for the Shibata shift were variable but in general longer in Sandoz-treated leaves than in untreated controls.

Spectra of the protochlorophyllide and chlorophyllide peaks before actinic irradiation of leaves from Sandoz-treated seedlings immediately after irradiation and after the Shibata shift had occurred are shown in Fig. 12. For these experiments the red filter was removed. Simultaneous actinic irradiation and measurement were not necessary. The spectra show that a nontransformable protochlorophyllide (Shibata, 1957) peak, the transformable protochlorophyllide peak, the chlorophyllide peak formed immediately upon irradiation, and the peak formed after the Shibata shift had occurred were at 630, 648, 684, and 669 nm, respectively. Some resynthesis of the transformable protochlorophyllide is seen in the spectrum taken 15 minutes after actinic irradiation.

Spectra for leaves from untreated plants were essentially identical to those shown in Fig. 12. There was no significant difference in the amount of protochlorophyllide present in the treated or control leaves. Peak wavelengths were identical for the initial transformable protochlorophyllide, untransformable protochlorophyllide, chlorophyllide formed immediately upon phototransformation, chlorophyllide found upon completion of the Shibata shift, or protochlorophyllide resynthesized in the dark during the Shibata shift, whether or not Sandoz was present. It is therefore unlikely that carotenoids play an important

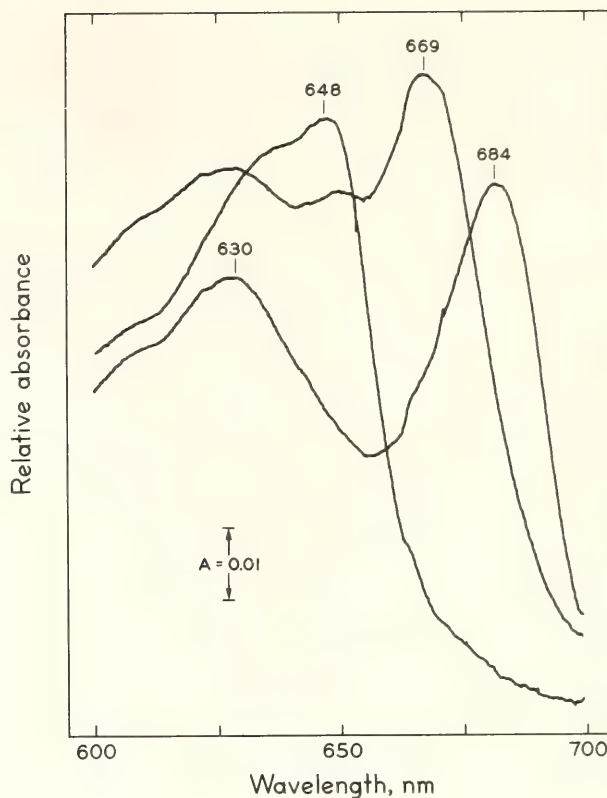


Fig. 12. In vivo absorption spectra of leaves from etiolated corn plants treated with  $2 \times 10^{-4}$  M Sandoz. Leaves were harvested under dim green light, cut to 1-cm lengths, and sandwiched between two pieces of transparent plastic which fit in the cuvette holder. The field was defined by a 6-mm hole in a piece of black tape on one of the plastic pieces. The rolled leaves were arranged to cover the hole as evenly as possible. Usually 5 segments of leaf were sufficient. Spectra were taken: A, before 2.5 minutes actinic blue irradiation; B, immediately after actinic irradiation; and C, 15 min after the termination of actinic irradiation. All spectra shown are from same sample.

role in the "changing molecular environment" that produces the shift.

#### REFERENCES

- Bartels, P. G., and A. Hyde, *Plant Physiol.*, **45**, 807-810, 1970.
- Bartels, P. G., and C. McCullough, *Biochem. Biophys. Res. Comm.*, **48**, 16-22, 1972.
- Shibata, K., *J. Biochem., Tokyo*, **44**, 147-173, 1957.

## GROWTH CHARACTERISTICS OF ETIOLATED *Avena sativa* L. (cv. LODI) IN RESPONSE TO RED AND GREEN LIGHT

*Dina F. Mandoli and Winslow R. Briggs*

Recently, Blaauw and Blaauw-Jansen (1975) and Vanderhoef *et al.* (1979) have shown that red light dose-response curves for elongation growth of etiolated oat and corn tissues are multiphasic. Oat mesocotyl suppression is triphasic, with the first detectable response at  $10^{-3}$  and final saturation near  $10^7 \mu\text{W s cm}^{-2}$ . Blaauw *et al.* (1968 and 1978) characterize the first phase of mesocotyl suppression, which reduces mesocotyl length to 85% of the dark control, as irreversible by far-red light and inducible by several wavelengths of light (660, 735, 770, 790 nm). The second phase of oat mesocotyl suppression, which reduces mesocotyl length to 50% of the dark control, is characterized by far-red reversibility, and the third (to 5% of dark control) by its time dependence. Oat coleoptile stimulation parallels this pattern, although the magnitude of the response is not as dramatic (Blaauw *et al.*, 1968). In corn, Vanderhoef *et al.* (1979) find that mesocotyl suppression by red light occurs in two steps similar in magnitude to the 50% and 95% mesocotyl suppression found in oat (Blaauw *et al.*, 1968). They did not detect in corn the very sensitive phase found in oats (yielding the first 15% of suppression). If such a response is present in corn, they may have saturated it with their green "safe" lights (see below). Generally, the characteristics of the two phases of the mesocotyl responses described for corn were similar in magnitude, R/FR reversibility, and time dependence to those described in oat (Vanderhoef *et al.*, 1979). Corn coleoptiles, however, show no response at all to red light for doses from  $10^0$  to  $10^5 \text{ nE cm}^{-2}$  (Vanderhoef, unpublished).

It is well known that tissue age determines to a large extent the response of

that tissue to light (Went, 1941). Thomson (1950) provided evidence that oat development is generally accelerated by white light and that responses of coleoptile, mesocotyl, and leaf tissue depend largely on how old they are at the time of treatment, i.e., whether they are undergoing elongation or division growth (Thomson, 1951). In characterizing any morphogenetic response, tissue age is important for reproducibility and response optimization. This report presents red light dose-response curves for oat mesocotyls and coleoptiles in a growth system in which uniform growth has been achieved and individual seedlings rather than groups of plants can be analyzed (*cf.* Blaauw *et al.*, 1975). Some effects of green light and tissue age are presented.

### METHODS

Groups of 20 dry, unhusked oat seeds (*Avena sativa* L., cv. Lodi) were held embryo-up on glass plates with masking tape and imbibed for  $\frac{1}{2}$  hr in distilled water in this position. Seedlings were grown on these glass plates at a 30- to 45-degree angle at  $28^\circ\text{C}$  in darkness with 85% humidity. Plates of 20 seedlings each were treated 24 hr before harvest. Seedlings were photocopied and measurements taken directly from these images with an Alvin planimeter or a computerized digitizer. Data points are usually the average of 50–100 seedlings, and standard errors less than 5%. Incandescent light filtered through Roehm and Haas red Plexiglas (No. 2444) provided broad-band red light; percent transmittance with a Corning 7-56 cut-off filter (visible-absorbing, infrared-transmitting) was zero. Overhead gold fluorescent tubes filtered through one layer each



Roehm and Haas blue (No. 2424) and green (No. 2092) plastic provided 0.002 nE cm<sup>-2</sup> s<sup>-1</sup> green “safe” light at bench level. All light intensities were measured with a Licor radiometer (Model No. LI-185A).

RESULTS AND DISCUSSION

Growth in total length of etiolated Lodi oat remains linear from about 56 to 122 hours after the start of imbibition and then dropped to slightly less than half the initial rate (Table 8).

Since moving seedlings from light-tight growth cabinets into 85% humidity and green “safe” light (total dose 7.2 nE cm<sup>-2</sup>) could change the rate of increase in total length (Table 8), green light and handling effects were monitored as a source of variability in all subsequent experiments.

Although total length of oat seedlings increases linearly from 54 to 122 hours, mesocotyls and coleoptiles show maximal growth at different times. From 15% to 30% mesocotyl suppression and 10–20% coleoptile stimulation are commonly seen as a result of a 10-min green light exposure (Fig. 13).

Growth rates (cm/24 hr) of dark-grown mesocotyls were maximal between 70 and 96 hr in age. Growth rates declined thereafter until by 122 hr, meso-

cotyl growth had ceased. The coleoptile growth rate continued increasing slowly between 64 and 96–98 hr, when it reached a maximum. Between 98 and 122 hr of growth in the dark, growth rate tapered off. A total dose of 4.0 nE cm<sup>-2</sup> of red light suppresses mesocotyl elongation and slightly stimulates coleoptile elongation but does not change the pattern of morphogenesis during the 24 hr immediately after treatment. Although similar data have been obtained by Thomson (1954) for Victory oat, direct comparisons are impossible, since an incandescent source of unspecified intensity was used. Dark-grown Victory oat mesocotyls showed a maximum rate of cell division from 2½ to 3 days and a maximal rate of elongation of both whole mesocotyls and individual cells from roughly 2 to 6 days (Thomson 1954). Thomson (1950 and 1954) concluded that the effect of white light on oat seedlings is to accelerate their development over the course of several days. This effect on oat development is not clearly evident in either her data at 24 hr after treatment with white light or in those presented here for red light. Green light may delay the time of maximal elongation rate for the mesocotyl (Fig. 13), but the effect of morphogenetically active wavelengths of light on the rate of development of oat seedlings remains unresolved from these studies.

TABLE 8. Linear Regression and Regression Coefficients for Total Length of Oat Seedlings

	56–122 hr	r <sup>2</sup>	122–144 hr	r <sup>2</sup>
Dark control*				
Exp. 1	y = − 7.28 + 0.15x	0.98		
Exp. 2	y = − 7.77 + 0.16x	0.98		
Pseudoillumination†				
Exp. 1	y = − 8.65 + 0.16x	0.96	y = 3.64 + 0.06x	0.90
Exp. 2	y = − 11.00 + 0.19x	0.96	y = 4.20 + 0.06x	0.64

\* Undisturbed dark-grown plants (dark controls).

† Pseudoilluminated seedlings are those that were removed from light-tight growth cabinets to a bench under overhead green “safe” light (Schiff, 1972) for 10 minutes. Humidity remained at or above 85%. During these 10 minutes, groups of seedlings were moved into position for red-light illumination but were not illuminated.

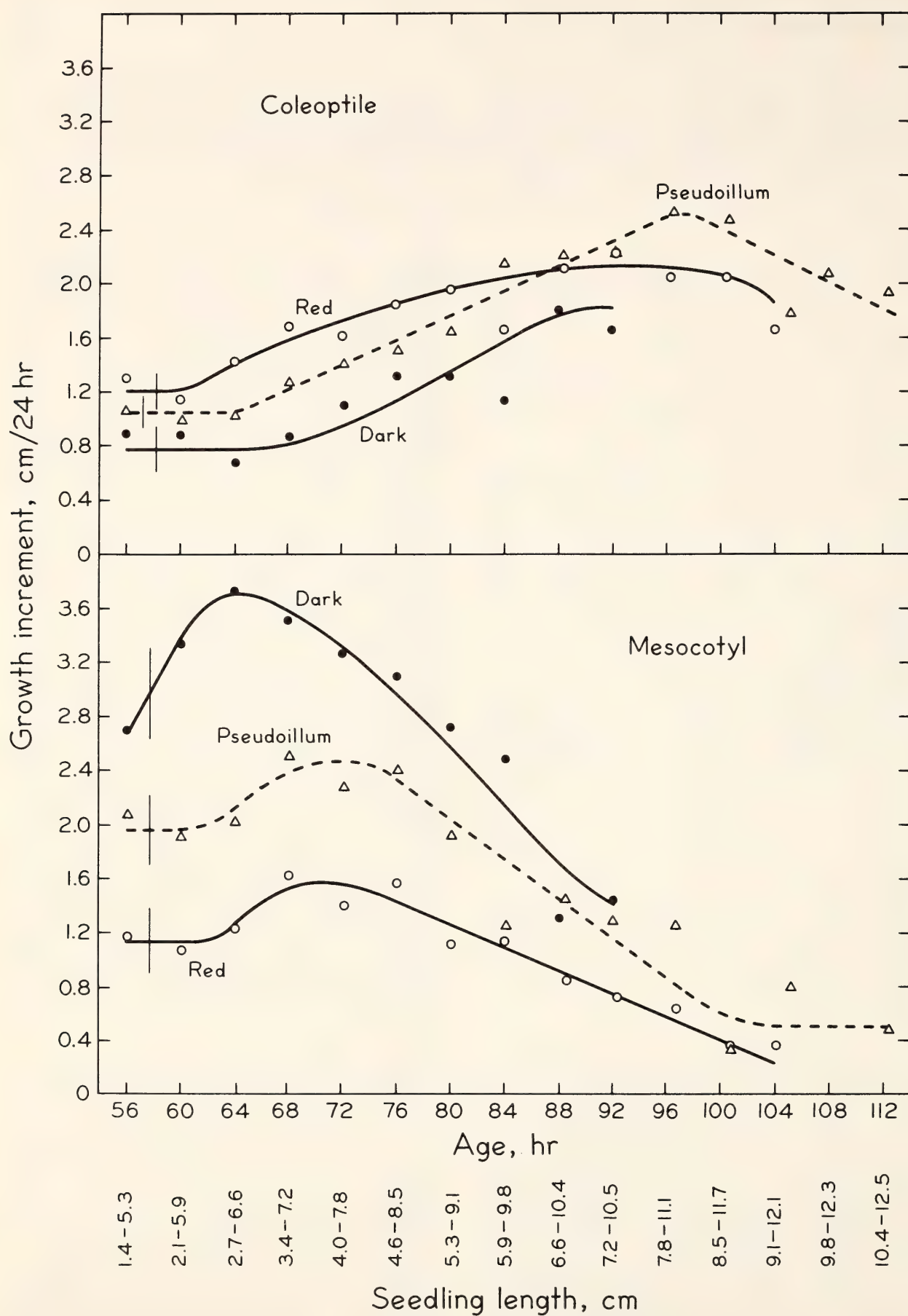


Fig. 13. Growth increments of mesocotyls and coleoptiles were measured 24 hours after treatment and plotted as a function of age at the time of treatment. Age was measured from the start of imbibition. Approximate total seedling lengths are also indicated along the abscissa. Red light dose was 20 s duration for a total dose of  $4.0 \text{ nE cm}^{-2}$ . Vertical bars represent the range of values obtained in replicate experiments.



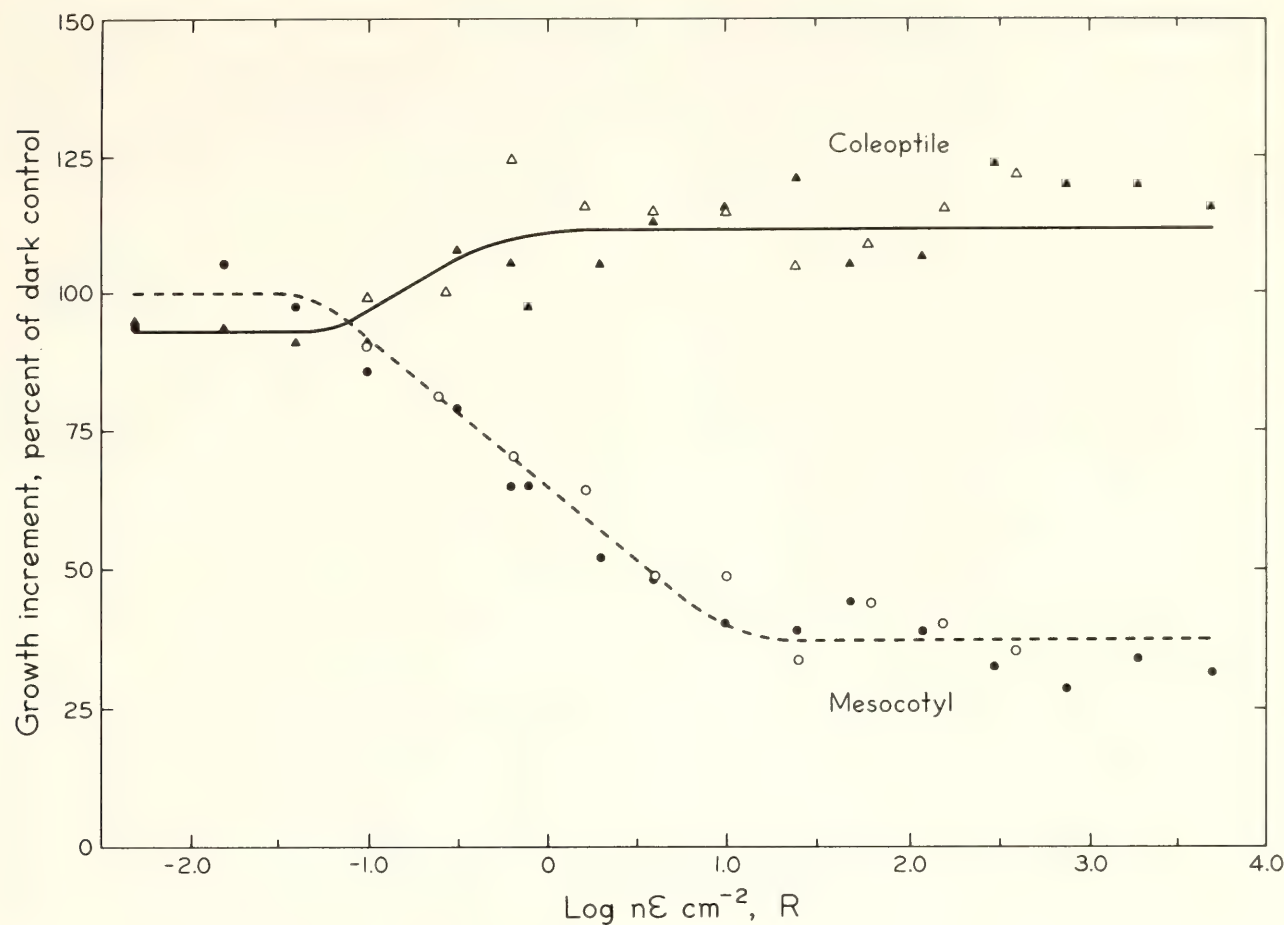


Fig. 14. Effect of red light on mesocotyl and coleoptile growth. Pulse duration constant at 20 s and intensity varied with neutral density filters [ $\Delta$ ]. Intensity constant at 0.005, 0.63 or 15.0 nE cm<sup>-2</sup> s<sup>-1</sup> and pulse duration varied from 1 to 360 s [o].

Reciprocity is demonstrated from  $2.0 \times 10^{-2}$  to almost  $10^4$  nE cm<sup>-2</sup> for both mesocotyl suppression and coleoptile stimulation (Fig. 14). The threshold for mesocotyl suppression occurs at  $4.0 \times 10^{-1}$  nE cm<sup>-2</sup> and saturation at 16 nE cm<sup>-2</sup> (Table 9). A slight (15%) stimulation of elongation rate of the coleoptile is discernible over this dose range. However, the response appears to become saturated over a surprisingly small dose range (from  $4.0 \times 10^{-1}$  to 2.5 nE cm<sup>-2</sup>).

TABLE 9. Mesocotyl Elongation Suppression by Red Light\*

	Blaauw <i>et al.</i> 1968	This report 1979	Vanderhoef <i>et al.</i> 1979
	Oat (Victory)	Oat (Lodi)	Corn (WF9 $\times$ Bear 38)
Phase 1			
Threshold	-5.74	...	...
Saturation	-2.26	...	...
Phase 2			
Threshold	-1.56	-1.6	-2.14
Saturation	1.74	1.8	1.5

\* The third phase of mesocotyl suppression is not included in this table because it is likely to be a time-dependent phenomenon. Units: log nE cm<sup>-2</sup>.

Variability within these measurements will have to be reduced before any conclusions can be drawn.

Preliminary dose-response curves for seedlings that were 60, 72, 82, 96, and 104 hours old at the time of treatment show that the mesocotyl response does not vary as a function of age until the mesocotyl ceases to grow (104 hr old). Coleoptile stimulation, however, may show an age-dependent effect on the dose response to red light; red light at the earliest age tested (60 hr) seems to be more effective in stimulating growth. These age-dependent responses might be expected from previous work on Victory oats (Thomson, 1950, Fig. 2, 3; Thomson, 1959, Fig. 1).

Blaauw *et al.* (1968) showed that the first phase in mesocotyl suppression reduced growth of Victory oat mesocotyls by only 15% from the dark control, and that wavelengths at 735, 770, and 790 as well as 660 are all effective in eliciting this response. Since low doses of green "safe" light ( $0.08 \text{ nE cm}^{-2}$ ) suppress mesocotyl elongation for Lodi oats and may slightly stimulate coleoptile elongation (Fig. 14), this response to green light may be identical with the first response seen in Victory oat by Blaauw *et al.* (1968). Quail has observed a similar low dose effect of green "safe" lights in potentiating corn root geotropism (*Year Book* 77, pp. 336-339). Dose response curves for green light are being characterized for Lodi oats.

The second phase of mesocotyl suppression by red light has a threshold at  $4.0 \times 10^{-1} \text{ nE cm}^{-2}$  (Fig. 14) and becomes saturated at  $8.0 \times 10^1$ . At saturation, mesocotyls show 50% suppression of growth over controls. Blaauw *et al.* (1968) report values of  $4.0 \times 10^{-1}$  and  $6.3 \times 10^1 \text{ nE cm}^{-2}$  for threshold and saturation of Victory oat mesocotyls. Vanderhoef *et al.* (1979) show a threshold at  $1.4 \times 10^{-2} \text{ nE cm}^{-2}$  and saturation for 50% corn mesocotyl suppression at  $3.8 \times 10^1 \text{ nE cm}^{-2}$  (Table 9).

The time-dependent response that re-

sults in 95% suppression of both corn and oat mesocotyl elongation (Vanderhoef *et al.*, 1979, and Blaauw *et al.*, 1968, respectively) can be induced with doses as low as  $1.3 \times 10^{-2} \text{ nE cm}^{-2}$ , provided that ample time is allowed for potentiation of the response. Preliminary data indicate that Lodi oats will show a similar time-dependent response curve. The time course of this potentiation has not been explored. It may be that the expression of this response also requires a longer time, especially in the coleoptile (*cf.* Thomson, 1950, Fig. 2A and B).

## CONCLUSIONS

The pattern and time course of oat mesocotyl and coleoptile development are similar in Lodi and Victory cultivars. Etiolated mesocotyls show maximal elongation growth a full day before the coleoptiles. Red and green light do not change these developmental patterns, only the magnitude of the growth. Threshold and saturation values for this complex red light-induced mesocotyl response are in good agreement with published values.

## REFERENCES

- Blaauw, O. H., Blaauw-Jansen, G., and van Leeuwen, W. J., *Planta*, 82, 87-104, 1968.
- Blaauw, O. H., Blaauw-Jansen, G., *Zeit. Pflanzen. Bd.*, 76. S., 333-338, 1975.
- Schiff, J. A., in *Methods in Enzymology*, 24 (B), 321-322, A. San Pietro, ed., Academic Press, N. Y., 1972.
- Thomson, B., *Amer. J. Bot.*, 37, 284-291, 1950.
- Thomson, B., *Amer. J. Bot.*, 38, 635-638, 1951.
- Thomson, B., *Amer. J. Bot.*, 41, 326-332, 1954.
- Vanderhoef, L., Quail, P., and Briggs, W. R., *Plant Physiol.*, 63, 1062-1067, 1979.
- Went, F. W., *Amer. J. Bot.*, 28, 83-95, 1941.



TIME COURSE OF THERMAL ACCLIMATION OF THE PHOTOSYNTHETIC APPARATUS IN *Nerium oleander**Olle Björkman and Murray Badger*

As reported last year (*Year Book 77*, pp. 262–276) the Old World desert shrub *Nerium oleander* possesses a large capacity for photosynthetic acclimation over a wide temperature range. This ability may be present in many evergreen desert shrubs which, in their native habitats, are subject to a large seasonal variation in temperature regime (Mooney, Björkman, and Collatz, 1978; Percy, 1977). Our previous studies with *N. oleander* showed that cloned individuals grown under a 20°C day/15°C night regime had at least twice as high a photosynthetic capacity at 20°C as individuals grown under a regime of 45°C day/32°C night. Conversely, individuals grown under the hot regime had about twice the photosynthetic rate at 45°C of those grown under the cool regime.

The superior photosynthetic capacity at low temperature of the 20°C-grown compared with the 45°C-grown plants was found to be unrelated to stomatal or other leaf factors that influence the diffusion transport of CO<sub>2</sub> into the chloroplasts or to differences in leaf anatomy, amount of photosynthetic machinery per leaf area, capacity for photosynthetic electron transport and photophosphorylation, or to a general increase in the level of enzymes of photosynthetic carbon metabolism. Of the 13 carbon cycle enzymes examined, only two, Ru-P<sub>2</sub> carboxylase and Fru-P<sub>2</sub> phosphatase, showed substantial differences in activity between plants grown under the two contrasting regimes. Only Fru-P<sub>2</sub> phosphatase was affected by growth temperature to an extent comparable to photosynthetic capacity, suggesting that the level of this enzyme may be a key factor in photosynthetic acclimation to low temperature.

The superior photosynthetic performance at high temperatures of the 45°C-grown plants was found to be primarily a result of increased heat stability of the chloroplast membrane-bound reactions, especially of photosystem II-driven electron transport and noncyclic photophosphorylation. This and other evidence indicates that acclimation to high temperatures involves a change in the physical properties of the thylakoid membrane. The work of Raison and Berry (*Year Book 77*, pp. 276–282) further revealed that the thylakoid membrane polar lipids of 45°C-grown *N. oleander* plants are more viscous than the corresponding lipids from the 20°C-grown plants (when measured at the same temperature), resulting in a partial compensation for the change in lipid viscosity at the growth temperature. Such viscosity changes provide an attractive explanation for the observed differences in heat stability of overall photosynthesis and electron transport reactions.

The adaptive significance of photosynthetic acclimation to temperature is obviously to maintain a productive photosynthetic rate throughout the seasonal cycle of temperature variation in the field. In our previous studies the experimental plants had been continuously grown under different temperature regimes for several months, and the leaves used for various measurements had experienced their entire development from apical meristem to mature leaf under the designated temperature regime. Since the longevity of *N. oleander* leaves usually exceeds an entire year, we considered it important to assess the time scale over which developing and mature leaves are capable of acclimating to a *change* in the growth temperature regime.

In the present experiments, cloned plants were grown as previously reported (Year Book 77, pp. 262–276) under either a 20°C day/15°C night or a 45°C day/32°C night regime. The development of individual leaves was observed twice weekly, and leaves were considered to have reached full maturity when no further expansion in area, increase in leaf thickness, or change in photosynthetic capacity (measured at 20°C) could be detected. Measurements on leaves of the same age and developmental stage as the attached leaves used for the determinations of photosynthetic characteristics showed that chlorophyll and protein content as well as Ru-P<sub>2</sub> carboxylase and Fru-P<sub>2</sub> phosphatase activity had reached a constant level when increase in leaf area and thickness had ceased. The potted plants were then transferred either from the 45°C to the 20°C growth regime or vice versa. Photosynthetic capacity at 20°C, the activities of several enzymes, and certain other leaf parameters were monitored for two weeks following the transfer.

As shown in the upper part of Fig. 15, the photosynthetic capacity of mature intact leaves developed under either the hot or the cool regime was capable of changing after transfer to the reciprocal regime. The photosynthetic capacity of mature leaves of plants developed under the 45°C growth regime increased after transfer to the 20°C regime so that after 12–14 days this capacity was indistinguishable from that of plants that had been continuously maintained under the 20°C regime. Conversely, within 12–14 days after transfer of plants grown under the 20°C regime to the 45°C regime the photosynthetic capacity of the intact leaves gradually decreased to the level found in the plants maintained at 45°C.

In another series of experiments (data not shown) it was also found that the optimum temperature for whole leaf photosynthesis (measured at high CO<sub>2</sub> pressure) showed an increase of 6–9°C within 10 days or less after the plants

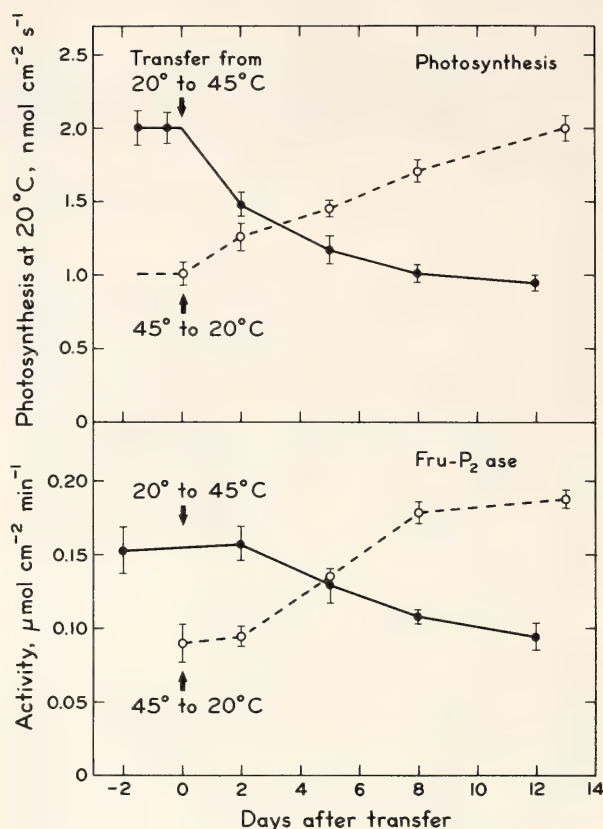


Fig. 15. Changes in photosynthetic capacity, measured at a leaf temperature of 20°C, 200 nE cm<sup>-2</sup> s<sup>-1</sup> and 330 μbar CO<sub>2</sub>, and the activity of Fru-P<sub>2</sub> phosphatase, measured at 30°C, following transfer of *N. oleander* plants from a 45°C day/32°C night growth regime to a 20°C day/15°C night growth regime, and reciprocally. Photosynthesis was followed on three separate, mature attached leaves over the entire period of the transfer time-course. Enzyme activity was determined on a sample of three equivalent leaves at each time point.

were moved from the cool to the hot regime, while transfer in the other direction caused a gradual decline in the optimum temperature.

These results demonstrate that in *N. oleander* even mature leaves have a high potential for photosynthetic temperature acclimation. In spite of the drastic changes in growth temperature regime to which the plants were subjected in these experiments, full acclimation was completed within two weeks. Thus, the much more gradual seasonal changes experienced by plants in the field should allow them to maintain complete adaptation to the thermal regime existing at any time



of the year. The ability of an evergreen plant to adjust its photosynthetic characteristics in the ways described here is undoubtedly an important factor enabling the plant to cope with large temporal temperature variations within a single habitat and to succeed in different habitats having widely diverse temperature regimes.

As shown in the lower part of Fig. 15, the increase in photosynthetic capacity (measured at 20°C) after transfer of 45°C-grown plants to the 20°C-grown regime was closely correlated with an increased level of Fru-P<sub>2</sub> phosphatase activity. After transfer from the 20°C to the 45°C regime there is an immediate reduction in photosynthetic capacity which is not accompanied by a change in Fru-P<sub>2</sub> phosphatase activity, but subsequent changes in photosynthesis and Fru-P<sub>2</sub> phosphatase are closely matched. The initial rapid fall in photosynthesis following the abrupt increase in temperature from 20°C to 45°C is probably caused by an inactivation of photosystem II-driven electron transport occurring before the photosynthetic machinery has had time to acclimate to the increased temperature. As shown in Table 10, after a period of 12–14 days following the transfers, the Fru-P<sub>2</sub> phosphatase activities of leaves that were mature before the time of transfer were very similar to

those of new leaves that had developed after the transfers as well as to those of leaves that were kept constant at the appropriate regime throughout the experiments.

Of the other enzymes examined in this study, Ru-P<sub>2</sub> carboxylase activity shows changes that correlate with but are less pronounced than the changes in photosynthetic capacity and Fru-P<sub>2</sub> phosphatase activity. The remaining enzymes, 3-PGA kinase, phosphoglucomutase and phosphohexose isomerase have very similar activities in leaves grown under the two temperature regimes, and they show only small changes after transfer from the cool to the hot regime and vice versa (Fig. 16).

The close correlations between the changes in the activities of Fru-P<sub>2</sub> phosphatase, and to a lesser extent Ru-P<sub>2</sub> carboxylase, and the changes in photosynthetic capacity provide additional support for the concept that these enzymes may be rate limiting for photosynthesis at low and moderate temperatures and that regulation of their synthesis, especially Fru-P<sub>2</sub> phosphatase, may be a key factor in photosynthetic acclimation.

Another important factor in photosynthetic acclimation is the increase in the optimum temperature for photosynthesis which is observed as early as a

TABLE 10. Activities of Enzymes of Photosynthetic Carbon Metabolism of *Nerium oleander* Leaves before and after Transfer of Plants for 12–14 Days to a Contrasting Temperature Regime

Enzyme activity,* nmol sec <sup>-1</sup> g <sup>-1</sup> fresh wt.						
		Fru-P <sub>2</sub> phosphatase	Ru-P <sub>2</sub> carboxylase	3-PGA kinase	P-hexose isomerase	P-glucos mutase
45°C	20°C	1.50 → 3.12 (3.33)†	5.10 → 7.77 (8.38)	51.7 → 64.5 (63.9)	5.32 → 6.55 (5.85)	4.17 → 5.27 (4.43)
20°C	45°C	2.52 → 1.56 (1.47)	8.06 → 5.50 (3.47)	63.1 → 59.5 (43.3)	5.43 → 5.00 (4.45)	4.53 → 3.67 (3.00)

\* Activities were measured at 30°C as described earlier (*Year Book* 76, pp. 346–354).

† Values in parentheses are for new leaves developed after transfer.

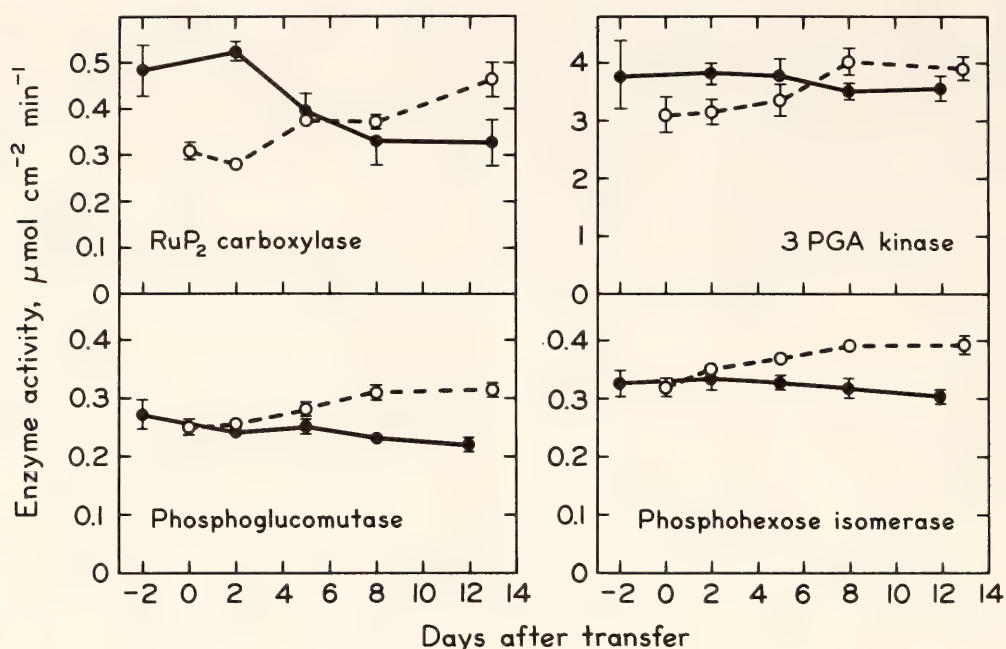


Fig. 16. Changes in the activities of Ru-P<sub>2</sub> carboxylase, 3- PGA kinase, phosphoglucomutase and phosphohexose isomerase, following transfer of *N. oleander* plants as indicated in Fig. 15.

few days after transfer of the plants from the cool to the hot regime. This upward shift in the temperature at which photosynthesis reaches its maximum rate is the result of two factors: (1) the decreased photosynthetic capacity discussed in previous paragraphs and (2) an increased high-temperature stability of the photosynthetic machinery. As was mentioned in the introduction, our previous work has shown that *N. oleander* plants grown at high temperature possess an increased heat stability of photosystem II-driven electron transport, and it has been suggested that this increased heat stability may be related to the increased viscosity of the chloroplast membrane lipids found in the high temperature-grown plants. The studies of Berry and Raison (this *Year Book*) with the same plant materials and conditions used for the transfer experiments reported

here indicate that substantial increases in the heat stability of the chloroplast membranes and in the viscosity of the membrane lipids accompany this upward shift in the optimum temperature for whole leaf photosynthesis which takes place after transfer of the plants from the 20°C to the 45°C growth regime. These results provide further evidence that changes in the physical properties of these lipids may play an important role in photosynthetic acclimation to high temperature.

#### REFERENCES

- Mooney, H. A., O. Björkman, and G. J. Collatz, *Plant Physiol.*, **61**, 406–410, 1978.  
 Percy, R. W., *Plant Physiol.*, **59**, 795–799, 1977.



## VISCOTROPIC DENATURATION OF CHLOROPLAST MEMBRANES AND ACCLIMATION TO TEMPERATURE BY ADJUSTMENT OF LIPID VISCOSITY

John K. Raison and Joseph A. Berry

In a previous paper (*Year Book 77*, pp. 276–282), we reported that the microviscosities of liposomes prepared from polar lipids of *Nerium oleander* grown either at low (20°C/15°C day/night) or high (45°/32°C) temperatures were different. The lipids of high temperature-grown plants were more viscous than those of low temperature-grown plants. We speculated that if there were a limiting minimum viscosity for membrane stability, then the high temperature-grown plants would reach this viscosity at a temperature about 10°C higher than the low temperature-grown plants.

We report here additional studies relating to this hypothesis of a minimum limiting viscosity for stability and to the concept that the adaptive modification of membrane stability in some species is accomplished by modification of membrane viscosity.

### METHODS

Cloned plants of a single genotype of *Nerium oleander* were grown in growth cabinets at 20°/15°C or 45°/32°C (day/night) temperature (*Year Book 77*, pp. 262–276). Chloroplast lipids were also extracted, purified, and studied as described (*Year Book 77*, pp. 276–282). The temperature threshold for denaturation of the chloroplast membranes was determined from studies of the temperature-versus-fluorescence course from intact attached leaves according to the method of Schreiber and Berry (1977). Details of this procedure are described by Seemann *et al.* (this *Year Book*).

### RESULTS

The temperature-versus-fluorescence course for intact leaves of *N. oleander* grown at either 20° or 45° day temperature are shown in Fig. 17. The sharp increase in fluorescence which occurs as the temperature of the leaf is increased is most likely the result of denaturation of the light-harvesting pigment system of the membranes (Armond *et al.*, this *Year Book*). The threshold temperatures for this denaturation can be estimated as 43° and 53°C from Fig. 17 for the 20°- and 45°C-grown plants, respectively. This result thus indicates that at least the integrity of the light-harvesting pigment system in chloroplast membrane is stable to a temperature 10°C higher in high temperature-acclimated than low temperature-acclimated plants.

We have determined the molecular motion of a probe within the hydrophobic region of chloroplast membrane lipid vesicles of these plants by use of EPR spin labels (see Fig. 18). In this report we focus upon studies with liposomes prepared from chloroplast polar lipids. Studies not detailed here have convinced us that the apparently lower molecular motion (greater viscosity) of the corresponding chloroplast membrane (see *Year Book 77*, 276–282) is an artifact arising from binding of the spin label probe to the membrane proteins. The resulting EPR spectra of chloroplasts are a composite of mobile probe in lipid and immobilized probe bound to protein.

Results of studies with chloroplast polar lipids are shown in Fig. 18. The molecular motion has been expressed as the motion parameter ( $\tau$ ), which is calcu-

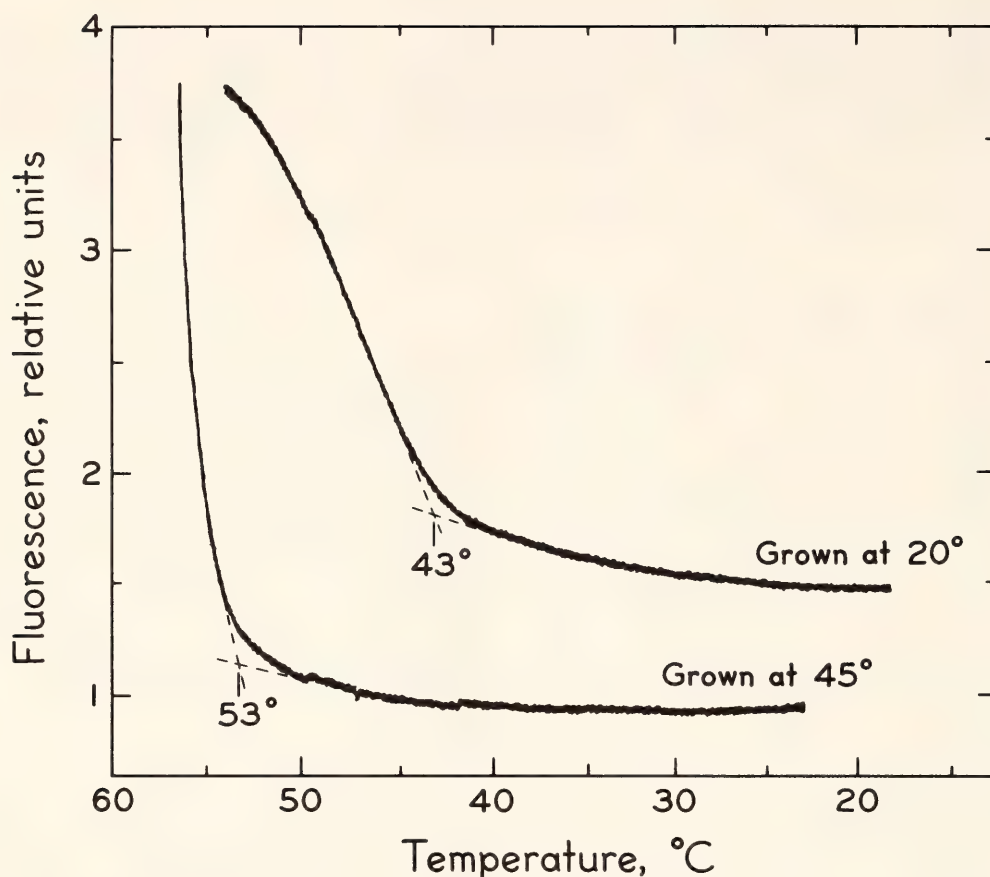


Fig. 17. Change in the relative fluorescence yield from chlorophyll in whole attached leaves of *Nerium oleander* as a function of leaf temperature. Plants were grown either at 45°/32°C day/night temperatures or 20°/15°C.

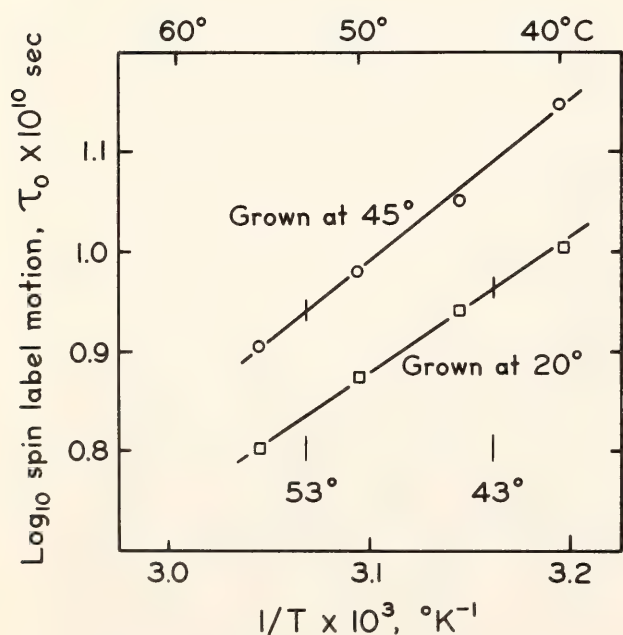


Fig. 18. The motion of the spin label derivative of methyl stearate, 3-oxazolidinyloxy-2-(10 carbmethoxydecyl)-2-hexyl-4, 4-dimethyl (12 NS) incorporated into chloroplast polar lipid suspensions prepared from plants of *N. oleander* grown at 20°/15°C or 45°/32°C. The

lated as described elsewhere (*Year Book* 77, pp. 276–282). The value of this parameter is a function of viscosity. However, the concept of a quantitative measurement of viscosity in an anisotropic medium such as a membrane bilayer has been questioned recently (Schreier *et al.*, 1978). We therefore do not report results in absolute units of viscosity (poise) as we did previously. In a qualitative sense, however, the lower the value of  $\tau$  the lower the relative viscosity. The data presented in Fig. 18 thus indicate that at any temperature between 30° and 55°C the relative viscosity of membrane lipids from 45°C-grown plants is greater than that of the 20°C-grown plants. The motion param-

standard deviation for measurements of the motion parameter ( $\tau$ ) was  $\pm 0.05 \times 10^{-10}$  at 50°C and  $\pm 0.2 \times 10^{-10}$  at 20°C for both preparations.



eter ( $\tau$ ) follows the Arrhenius relationship, and a straight line connecting these data can be used to interpolate the value of  $\tau$  at any temperature within the range of the measurements.

If the temperature thresholds for denaturation of the corresponding chloroplast membranes as determined in Fig. 17 are used to estimate the value of  $\tau$  at the denaturation temperature (from Fig. 18) we arrive at the same value ( $8.6$  to  $8.8 \times 10^{-10}$  s) for the two preparations. This result implies that denaturation of the chloroplast membrane may be controlled by molecular motion or viscosity within the hydrophobic region of the membrane.

Similar studies with additional species have been conducted, and the results are summarized in Table 11. Shown are the species, the growth conditions, the threshold temperature for denaturation ( $T_c$ ), and the motion parameter at the threshold temperature (the critical motion parameter,  $\tau_c$ ). The value of  $\tau_c$  ranges between  $7.9$  and  $10.0 \times 10^{-10}$  s, but paired determinations with the same species acclimated to different temperatures are within  $0.2 \times 10^{-10}$  s. This result indicates that for a given species the value of  $\tau_c$  is fairly constant. There are somewhat larger differences between species, however. One might expect this result, since other factors such as differ-

ences in the primary structure of the proteins of the membrane must be considered when comparing across species boundaries. The value of  $\tau_c$  for all of these species is nevertheless quite similar with a mean of  $9.0 \pm 0.8 \times 10^{-10}$  s. The standard deviation corresponds to about  $\pm 3^\circ\text{C}$  if the variation is considered instead in terms of the threshold temperature (estimated from the slope of the lines in Fig. 18). The error in determination of  $T_c$  is about  $\pm 1^\circ\text{C}$ .

Another perspective from which to examine the relationship between thermal stability and membrane lipid viscosity is provided by kinetic studies of acclimation following a sudden change in growth temperature. *N. oleander* plants grown at either  $45^\circ$  or  $20^\circ\text{C}$  can be transferred to the reciprocal growth regime, and over a period of time these plants will acclimate to their new growth conditions such that they assume properties quite similar to control plants that have developed entirely at that temperature (see Björkman *et al.*, this *Year Book*). Studies of the change in  $T_c$ ,  $\tau$  at a given temperature ( $45^\circ\text{C}$ ) and  $\tau_c$  during reciprocal transfer experiments are shown in Fig. 19. The thermal stability ( $T_c$ ) adjusts rapidly upward or downward upon transfer. This process is very rapid, with acclimation approximately half complete after one day. Rapid and

TABLE 11. Threshold Temperature for Denaturation and the Corresponding Motion of the Spin Label 12 NS in Chloroplast Polar Lipids of Test Plant at That Temperature

Species	Growth Temperature (°C)	$T_c$ (°C)	$\tau_c$ ( $\times 10^{-10}$ s)
<i>Spinacea oleraceae</i>	*	43	9.6
<i>Atriplex sabulosa</i>	20/15	45	9.5
<i>Atriplex lentiformis</i>	20/15	44	9.8
<i>Atriplex lentiformis</i>	40/25	50	10.0
<i>Tidestromia oblongifolia</i>	†	48.5	7.9
<i>Tidestromia oblongifolia</i>	45/32	52.3	8.0
<i>Nerium oleander</i>	20/15	43	8.8
<i>Nerium oleander</i>	45/32	53	8.6

\* Greenhouse approx. 25/20°C.  
† Collected in Death Valley, CA, Dec. 17, 1979, approx. 20/5°C.

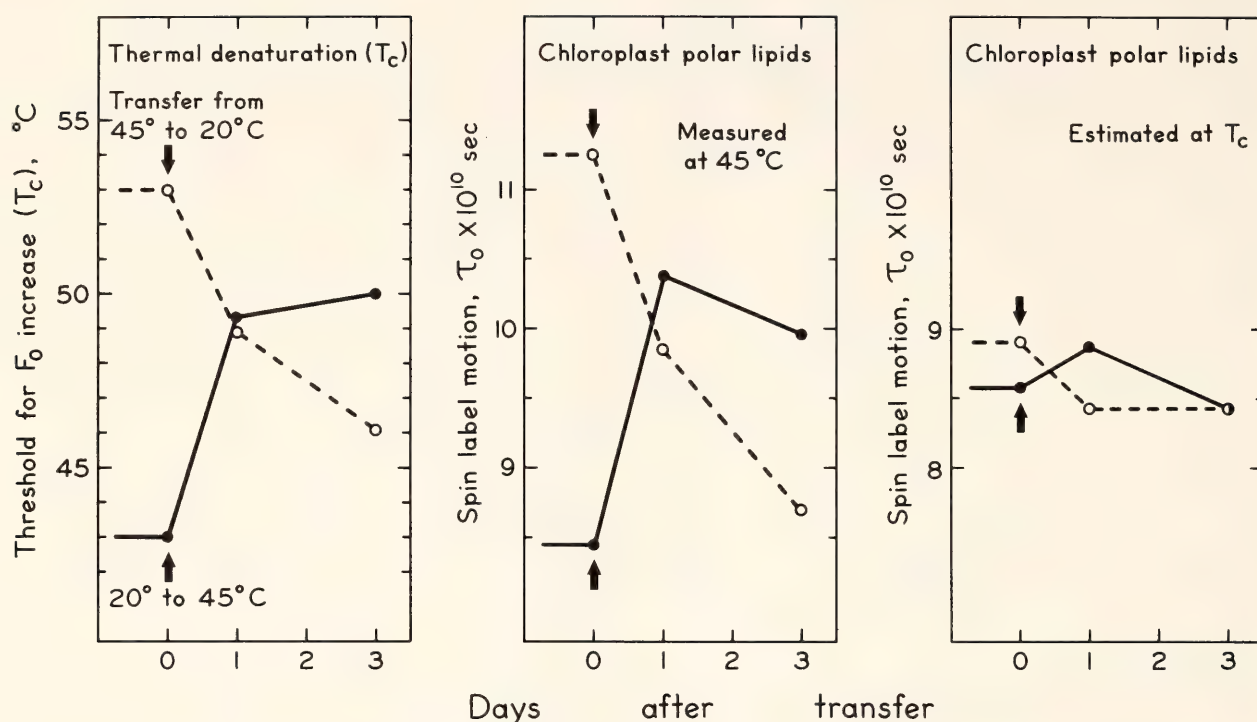


Fig. 19. Changes in thermal stability, motion parameter of chloroplast polar lipids at 45°C, and critical motion parameter,  $\tau_c$ , for chloroplast membrane stability, determined after transfer of *N. oleander* plants from 45°/32° to 20°/15°C and the reciprocal. The parameters reported were determined from data sets analogous to those in Figures 17 and 18 obtained from samples taken at each time point.

corresponding changes in the value of  $\tau$  measured at 45°C were also observed. These indicate that during acclimation the lipid viscosity increased upon transfer from low to high temperature and decreased upon transfer from high to low temperature. This adjustment is such that the interpolated critical lipid motion parameter ( $\tau_c$ ) was nearly constant at  $8.6 \pm 0.2 \times 10^{-10}$  s for all determinations of  $\tau_c$ . The deviation corresponds to less than  $\pm 1^\circ\text{C}$  in the value of  $T_c$ .

We conclude that lipid properties do in fact determine the thermal stability of the chloroplast membrane. Other factors such as genetic differences in homologous proteins among plants or in the nature of the aqueous environment (see Armond

and Hess, this *Year Book*) may also affect this stability. Acclimation of the plants studied appears, however, to occur by modification of lipid properties. The mechanisms that sense the change in temperature and lead to modification of the lipids are not identified in these studies, nor are the lipid modifications characterized. These are clearly important biochemical features of this mechanism which merit future research.

#### REFERENCES

- Schreiber, U., and J. A. Berry, *Planta*, **136**, 233–238, 1977.  
Schreier, S., C. F. Polnaszek, and I. C. P. Smith, *Biochim. Biophys. Acta*, **515**, 375–436, 1978.



## DISSOCIATION OF SUPRAMOLECULAR COMPLEXES IN CHLOROPLAST MEMBRANES: A MANIFESTATION OF HEAT DAMAGE TO THE PHOTOSYNTHETIC APPARATUS

Paul A. Armond, Olle Björkman, and L. Andrew Staehelin\*

In analyzing the thermal response of photosynthesis, we have observed that the onset of inhibition of photosynthesis at high temperatures is accompanied by functional alterations of the interactions among the pigment-protein complexes of the chloroplast membrane. These alterations, primarily decreases in the efficiency of excitation energy transfer, are detected as changes in the chlorophyll fluorescence emission characteristics of whole leaves (Schreiber and Berry, *Year Book 75*, pp. 323–327) as well as isolated chloroplasts (Armond *et al.*, *Year Book 76*, pp. 335–341). Such changes in the fluorescence emission have been interpreted as indicating a functional dissociation of the bulk light-harvesting chlorophylls from the reaction center complexes (Schreiber and Armond, *Year Book 76*, pp. 341–346).

To investigate the possible structural changes that may accompany the physiological damage in chloroplast membranes, we analyzed the chloroplast membranes of *Nerium oleander* by freeze-fracture electron microscopy. *N. oleander* provides an ideal system for such a study because it can acclimate to different growth temperatures. The use of leaves from *N. oleander* plants grown under temperature regimes of 20°C/15°C and 45°C/32°C allows the comparison not only of physiologically damaged membranes to undamaged ones but also of membranes with different thermal stabilities that have been pretreated at the same temperature.

Previous studies have identified the

particles of the exoplasmic fracture face (EF: the fracture face of the inner membrane leaflet) as being composed of the photochemically active core complex of photosystem II, surrounded by aggregates of the light-harvesting pigment-protein complex (Armond *et al.*, 1977). Since the interpretation of the fluorescence changes indicates a functional dissociation of these integral membrane components (Schreiber and Armond, *Year Book 76*, pp. 341–346), we have concentrated our attention on the particles of the EF fracture face.

Chloroplasts were isolated from leaves of *N. oleander* grown at 20°C/15°C or 45°C/32°C day/night temperature regime and pretreated at temperatures from 40°C to 55°C as described (Björkman *et al.*, *Year Book 77*, pp. 262–276). This temperature range encompasses the span from physiologically undamaging (for samples from both growth regimes) to inhibition of photosynthesis greater than 80% (for the 20°C/15°C-grown material). Samples in which the grana structure was maintained, as well as experimentally unstacked chloroplast membranes, were prepared for freeze-fracture as described elsewhere (Armond *et al.*, 1977). Samples in which the thylakoids were maintained in a stacked condition were qualitatively analyzed for heat-induced morphological alterations. Quantitative analyses of the micrographs (particle size and density measurements) were performed on the more homogeneous material provided by the unstacking process. Freeze-fracture nomenclature is according to Branton *et al.* (1972). The samples are designated in the figures by the daytime growth temperature (20°C or 45°C) followed by the pretreat-

\* Department of Molecular, Cellular, and Developmental Biology; University of Colorado, Boulder, Colorado.



ment temperature (the indicated pretreatment temperatures of 40.7, 48.8, and 55.2 for the 20°C material and 41.6, 49.2,

and 55.5 for the 45°C-grown material are the average of five measurements taken during the 10-minute pretreatment).

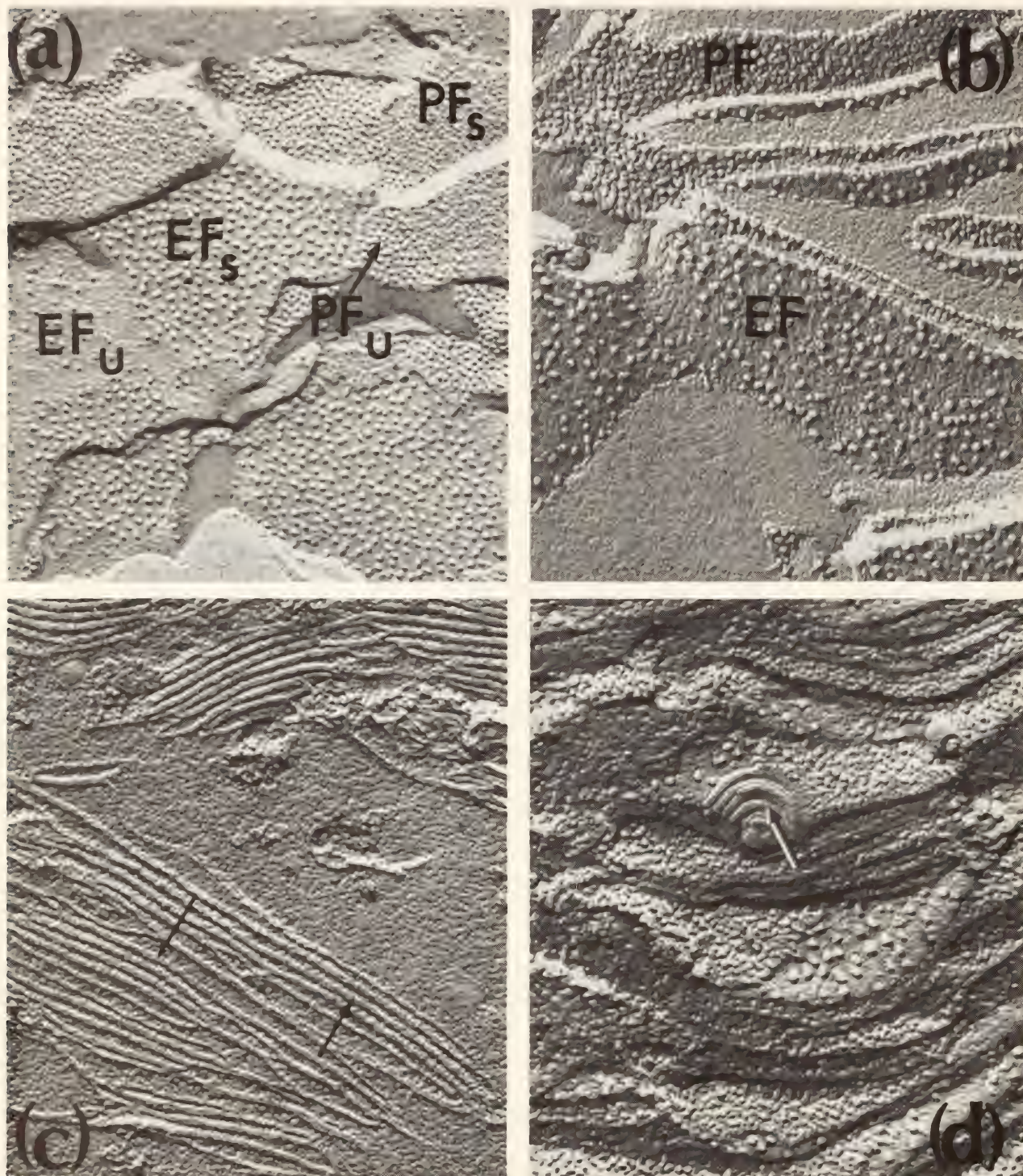


Fig. 20. Freeze-fractured thylakoid membranes isolated from leaves of *N. oleander*. (a) Normal freeze-fracture morphology exhibited by the 45/41.6 sample with a clear differentiation of the membrane into stacked ( $EF_s$ ,  $PF_s$ ) and unstacked ( $EF_u$ ,  $PF_u$ ) regions. (b) Experimentally unstacked sample (45/41.6) exhibiting an even distribution of particles on both  $EF$  and  $PF$  faces (compare with a). (c, d) Heat-damaged membranes (20/55.2) exhibiting distortion of grana stacks into long appressed regions (c) and the appearance of pure lipid myelin figures indicative of membrane damage (d). Magnification equals  $\times 62,000$  (a);  $\times 94,000$  (b, d);  $\times 49,000$  (c).



A qualitative examination of the micrographs revealed a normal freeze-fracture morphology for the 45/41.6 (Figure 20A), 45/49.2, and 20/40.7 samples. The fracture face of the outer membrane leaflet (protoplasmic or PF) and the fracture face of the inner membrane leaflet (exoplasmic or EF) exhibited a normal differentiation into stacked ( $EF_s$ ,  $PF_s$ ) and unstacked ( $EF_u$ ,  $PF_u$ ) membrane regions. When the thylakoids were unstacked, this differentiation was lost, and the EF particles that were normally aggregated into the stacked regions of the chloroplast membrane became homogeneously distributed on the EF fracture face (45/41.6, Fig. 20B).

Among the remaining samples, a notable distortion of the chloroplast membranes was observed in the 20/55.2 sample (Fig. 20C, D). The most distinguishing feature of this damage was the replacement of the normal grana structure by expansive regions of membrane appression (Fig. 20C). Among heat-induced anomalies in the chloroplast structure was the appearance of myelin figures contiguous with the plastid membranes, presumably formed by the coalescing of lipids that had leaked out of the membrane (Fig. 20D).

Quantitative analysis of the micrographs included both particle size frequency histograms of the EF fracture face and particle density measurements of both the EF and PF fracture faces. The particle size frequency histograms for the samples from the 20°C-grown material demonstrate a progressive loss of EF particles from the larger particle size classes as the temperature of the pretreatment was increased (Fig. 21). This loss indicates that the components of the EF particles, presumed to be the light-harvesting complex and the photosystem II core complex, may become physically dissociated as a result of the heat pretreatment. The magnitude of this dissociation can be more easily seen by subtracting the 20/40.7 histogram from

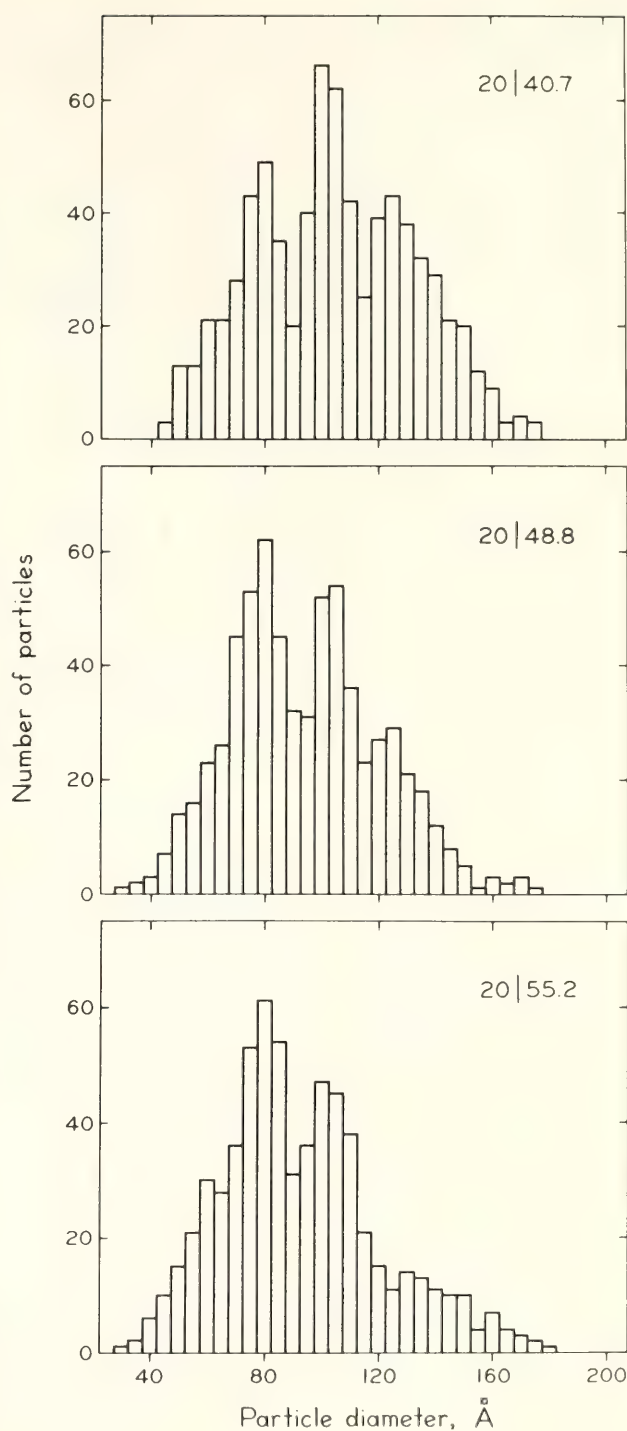


Fig. 21. Histogram of particle size classes on the EF fracture face of chloroplasts isolated from 20°C-grown *N. oleander* leaves pretreated at 40.7°C, 48.8°C, and 55.2°C. Note the progressive loss of particles from the larger size classes with increasing pretreatment temperature.

the 20/49.2 and the 20/55.2 histograms, producing the "difference histograms" of Fig. 22. A substantial loss in the number of particles in size classes greater than 90 Å diameter occurs with pretreatment

at 48.8°C and 55.2°C for the 20°C-grown material (Fig. 22). The degree of alteration in the 45/55.5 sample was similar to that for the 20/48.8; the 45/49.2 was indistinguishable from the 45/41.6 (data not shown).

The particle density measurements (Table 12) did not reflect the large changes observed in the particle size measurements. Only small and insignificant variations existed among the particle densities both for the EF and the PF faces. These data indicate that once the components of the EF particles dissociate, the smaller component parts are not detectable as distinct freeze-fracture particles on either fracture face. Although it is possible that the PF particles increased in diameter, the nature of the

TABLE 12. Particle density on the fracture faces of *N. oleander* thylakoid membranes.\*

Growth Temp (°C)	Treatment Temp (°C)	Particles per micron <sup>2</sup> ± SD	
		EF	PF
20	40.7	1656 ± 162	5433 ± 280
	48.8	1665 ± 178	5677 ± 291
	55.2	1629 ± 176	5843 ± 315
45	41.6	1764 ± 143	5789 ± 385
	49.2	1783 ± 154	5787 ± 381
	55.5	1715 ± 143	5876 ± 385

\* The chloroplasts were isolated from leaves pretreated at the indicated temperatures and experimentally unstacked.

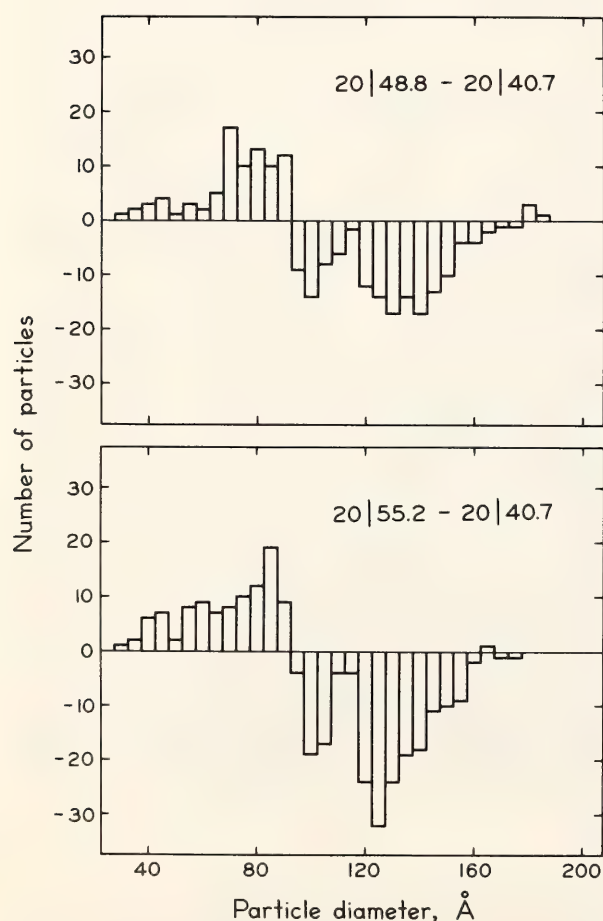


Fig. 22. Difference histograms produced by subtracting the 20/48.8 and 20/55.2 histograms from the 20/40.7 histogram of Fig. 21. The loss of particles in size classes >90 Å is clearly evident.

PF fracture face precludes the accurate measurements necessary to examine this alternative.

These data demonstrate that the heat-induced damage to the photosynthetic apparatus involves not only a functional dissociation of the light-harvesting complex from the photosystem II complex but a physical dissociation as well. It is also evident that the enhanced thermal stability of photosynthesis in the 45°C-grown material is accompanied by a greater stability of the interactions of these integral membrane protein complexes. It is possible that the proteins themselves are altered in some way by the process of acclimation. However, the lipid composition and fluidity changes in the membranes of *N. oleander* grown under the two thermal regimes (Raison and Berry, *Year Book* 77, pp. 276–282) could account for the stability differences. Although the light-harvesting complex and photosystem II complex are integral membrane components and the association between them is probably governed by hydrophilic interactions, the interactions of this supramolecular complex with the other components of the membrane are dominated by hydrophobic interactions. The relative strengths of these interactions can be



altered by changing the temperature. When temperature is increased, the hydrophilic interactions decrease and the hydrophobic interactions are enhanced. If these interactions become sufficiently unbalanced, integral membrane protein complexes tend to dissociate, an event which was observed in the chloroplast membranes of *N. oleander*. The process of acclimation by alteration of the lipid composition and fluidity of the membrane may result in changes in the balance of the hydrophobic and hydrophilic interactions in such a way as to enhance

the apparent stability of the integral membrane protein complexes.

#### REFERENCES

- Armond, P. A., L. A. Staehelin, and C. J. Arntzen, *J. Cell Biol.*, **73**, 400–418, 1977.
- Branton, D., S. Bullivant, N. B. Gilula, M. J. Karnovsky, H. Moor, K. Mühlethaler, D. H. Northcote, L. Packer, B. Satir, P. Satir, U. Speth, L. A. Staehelin, R. L. Steere, and R. S. Weinstein, *Science*, **190**, 54–56, 1975.

### FIELD STUDIES OF ACCLIMATION TO HIGH TEMPERATURE: WINTER EPHEMERALS IN DEATH VALLEY\*

*Jeffrey R. Seemann, W. J. S. Downton and Joseph A. Berry*

The winter and spring ephemerals that occasionally produce spectacular floral displays in the deserts of California experience an extreme change of environmental conditions during their short growing season. In Death Valley, this season begins with winter rains, and during the early part of the season the temperatures are low with occasional frosts. Temperatures climb steadily during the spring and in some seasons may approach 50°C within six to eight weeks after the rains that bring about germination. These extremes of temperature impose limits on the time available for growth and the rate of photosynthetic carbon gain during the growing season. Physiological mechanisms that might permit the plants to prolong their growing season or otherwise increase their carbon gain during this short period of growth might be important adaptations for these ephemeral species.

\* This research was supported by the Science and Education Administration of the U.S. Department of Agriculture under Grant No. 5901-0410-8-0128-0 from the Competitive Research Grants Office.

Mooney *et al.* (1976) reported that the species *Camissonia claviformis* has exceptionally high rates of photosynthesis. This capacity may be an adaptation to the short growing season. Pike *et al.* (this *Year Book*) have examined the phase boundaries of membrane lipids from a number of cool season and warm season species, including several winter ephemerals from Death Valley. These species are apparently distinct from other ephemeral species that germinate during warmer periods in that the lipid phase separation temperatures are near or below 0°C. It is thought that the low phase separation temperature may be an adaptation to growth at low ambient temperatures.

In this paper we examine performance of a number of these winter and spring ephemerals at high temperatures. The objective of these studies was to determine the physiological limits to performance at high temperature and to identify mechanisms that may adapt these plants to the increasing temperature during their growing season.

Previous studies have identified photo-

synthesis as one of the processes most sensitive to high temperature (*Year Book 74*, pp. 751–759). Characteristics of the photosynthetic membranes have been identified as important determinants of the capacity to maintain photosynthetic performance at high temperature (*Year Book 75*, pp. 400–407, and Raison and Berry, this *Year Book*).

The most direct measure of temperature tolerance can be obtained by measurement of net photosynthetic carbon dioxide fixation as a function of temperature under otherwise nonlimiting conditions. The temperature optimum is the most obvious feature of the photosynthetic temperature-response curve. As discussed previously (*Year Book 77*, pp. 262–276), shifts in the temperature optimum can best be attributed to differences in the thermal stability of the photosynthetic apparatus. The steep decline of photosynthesis at temperatures in excess of the temperature optimum is attributed to the instability of the photosynthetic membranes. The temperature at which nonreversible inhibition of photosynthesis is detected (*Year Book 74*, pp. 751–759 and Percy *et al.*, 1976) and the temperature at which photosynthesis falls to half its optimum value (Bauer, 1978) have been taken as indices of thermal stability of the photosynthetic apparatus. These parameters allow one to distinguish between plants on the basis of their thermal stability and to quantify plant modifications that affect thermal stability.

Another approach is based upon the observations of Schreiber and Berry (1977) that there are large changes in the fluorescence of chlorophyll in an intact leaf when the photosynthetic apparatus of that leaf is denatured by high temperature. While this measurement can be made more rapidly than direct measurement of photosynthetic performance, it is difficult to relate to photosynthetic performance without some di-

rect studies of photosynthesis utilizing the same material.

We have applied both gas exchange and fluorescence techniques to the study of high temperature tolerance of several species of winter and spring ephemerals. These measurements were conducted with field-grown plants that developed either under natural conditions or within an experimental garden in Death Valley. The measurements were made during late April of 1979. High leaf temperatures are likely to occur at this time, and mechanisms that would enable plants to extend their tolerance to high temperature would probably be expressed at this time.

Photosynthesis studies were conducted with attached leaves of field-grown plants as described (*Year Book 75*, pp. 410–413). All studies reported here were conducted at full sunlight (intensities of  $180\text{--}200\text{ nE cm}^{-2}\text{s}^{-1}$ ) provided from a high pressure metal-arc lamp.  $\text{CO}_2$  concentration was maintained at  $700\text{--}900\text{ }\mu\text{bar}$ , nearly rate-saturating for these  $\text{C}_3$  species. We chose to use rate-saturating rather than normal ambient  $\text{CO}_2$  concentrations, since high  $\text{CO}_2$  eliminates effects of differences in stomatal conductance on photosynthesis and photorespiration which might obscure the direct effects of temperature on the photosynthetic apparatus (see *Year Book 77*, pp. 262–276).

Fluorescence studies were conducted with whole leaves. Intact plants or branches of plants were excised and recut under water, kept in a plastic bag, and transported to the fluorescence equipment. The measurements were made by enclosing a leaf in a water-jacketed and stirred cuvette. The temperature of the cuvette was increased at  $1^\circ\text{C}/\text{min}$  using a temperature circulator. The temperature was measured by a thermocouple appressed to the leaf, and fluorescence was monitored through a narrow band-pass interference filter ( $\lambda^{\text{max}} = 690\text{ m}\mu$ ). Fluorescence excitation was  $1 \times 10^{-11}$



$E\text{ cm}^{-2}\text{s}^{-1}$  broad-band blue light (Corning 9782 filter). These signals were displayed on an x-y recorder yielding a fluorescence-versus-temperature course. Air within the cuvette was humid, and the petiole of the leaf was kept immersed in water during the fluorescence-versus-temperature measurement. Water potentials were measured by psychrometry.

### RESULTS

The temperature response curve and corresponding fluorescence-versus-temperature course for leaves of the same plants of *Abronia villosa*, *Cucurbita palmata*, *Geraea canescens*, *Malvastrum rotundifolium*, and *Phacelia crenulata* are shown in Figs. 23 and 25. The breakpoint of the fluorescence-versus-temperature course obtained by extrapolation of the linear segments of the curve (see

Fig. 23 for examples) corresponds closely to the temperature at which photosynthetic  $\text{CO}_2$  fixation falls to half its maximum value for each of these species.

There are substantial differences in the thermal responses of the leaves of these species. The differences are reflected in the fluorescence-versus-temperature courses. These fluorescence measurements have proved to be quite reproducible, with variation in breakpoint temperature of not more than  $\pm 1^\circ\text{C}$  for similar leaves of the same plant. These results indicate that the fluorescence assay can be used with some confidence to determine the high-temperature tolerance of similar plants. Since photosynthesis falls steeply at superoptimal temperatures and becomes almost irreversibly inhibited at high temperature (Bauer, 1978), we are confident that differences among plants in the breakpoint of the fluores-

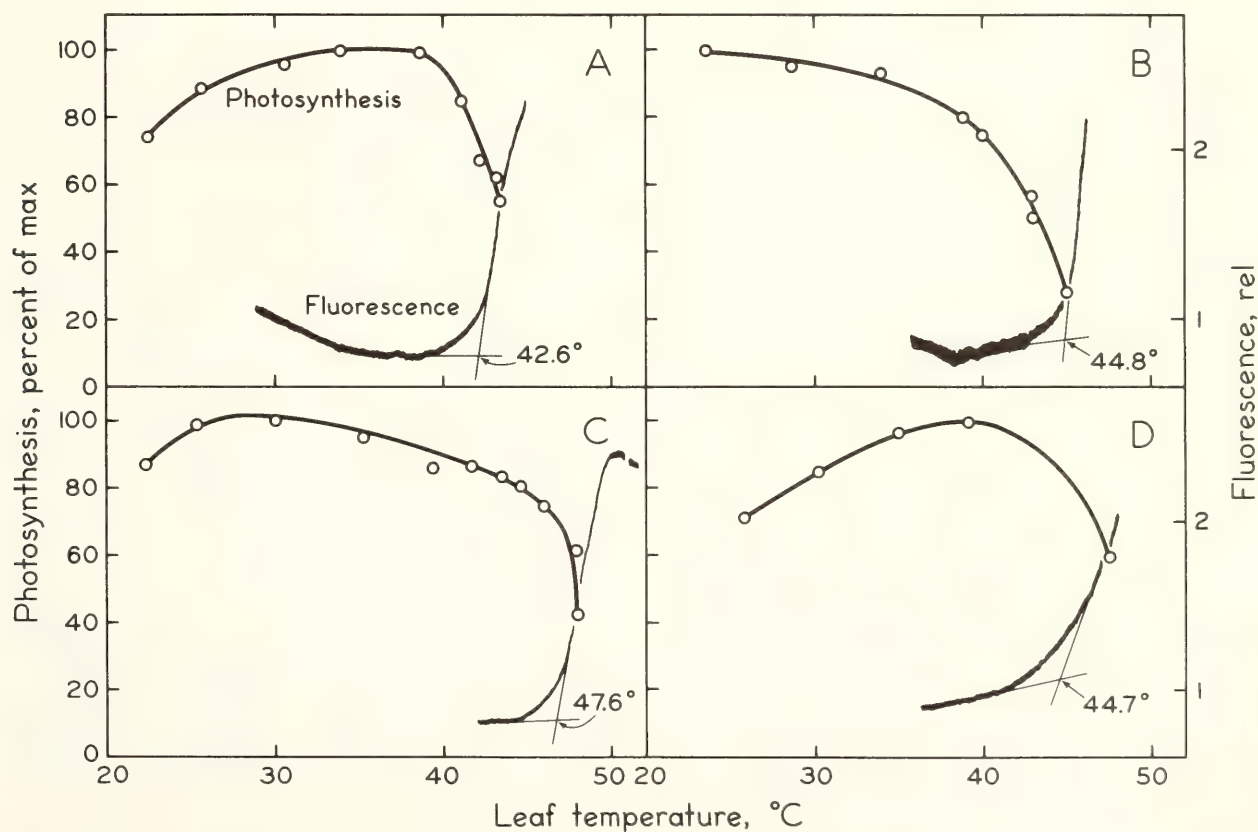


Fig. 23. Photosynthesis temperature curves and fluorescence-versus-temperature courses determined for leaves of the same plants of (A) *Phacelia crenulata*; (B) *Malvastrum rotundifolium*; (C) *Abronia villosa*; (D) *Cucurbita palmata*. Photosynthesis was determined at 21%  $\text{O}_2$  and 700–900  $\mu\text{bar}$   $\text{CO}_2$ ; maximum rates were 3.4, 7.0, 7.0, and 5.9  $\text{nmol cm}^{-2}\text{s}^{-1}$  for A, B, C, and D, respectively. Fluorescence yields are expressed in relative units.

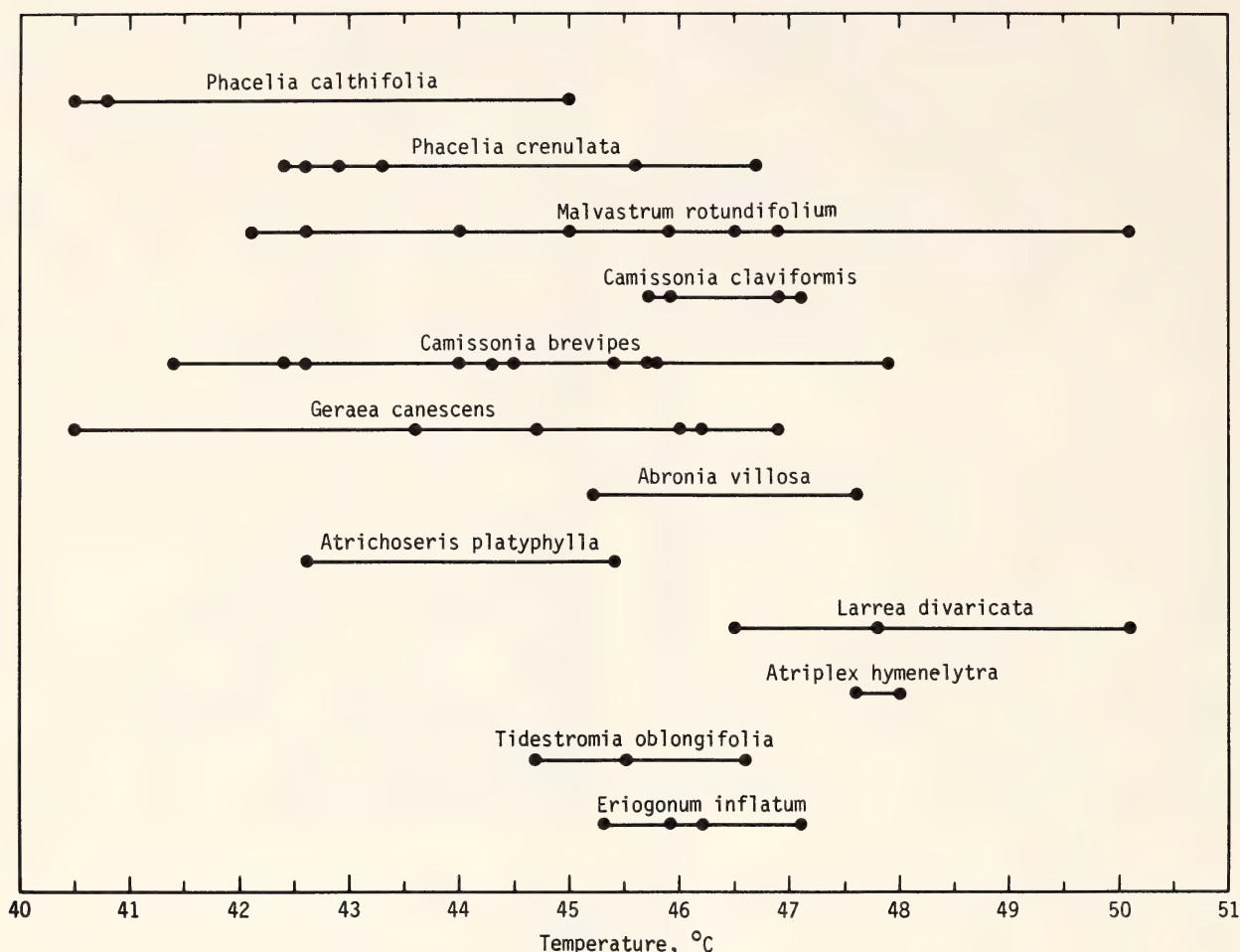


Fig. 24. The thermal stability of both annual and perennial species collected in Death Valley National Monument. The breakpoint of the fluorescence-versus-temperature course is plotted by species for each separate collection.

cence-versus-temperature course are ecologically significant.

We used the fluorescence assay to examine the high-temperature tolerance of the more common annuals and native perennials growing under natural conditions. The results are summarized in Fig. 24, which plots the breakpoint of the fluorescence-versus-temperature course by species. It is evident that there is a great deal of variation among plants of the same species and that there are not clear differences between species. The temperature tolerances of the annuals overlap those of perennials such as *Larrea divaricata*, *Atriplex hymenelytra*, or *Tidestromia oblongifolia*, which will continue growth into the summer, unlike the annuals. Taken as a group, however, the annuals show a lower temperature

tolerance than the perennials (breakpoints  $44.8 \pm 2.1^{\circ}\text{C}$ ,  $n = 50$  vs.  $47.1 \pm 1.6^{\circ}\text{C}$ ,  $n = 20$ , respectively).

The large variation in temperature tolerance among plants of the same species was not entirely random. We noted two trends, one with elevation and the other with water status, which offered an explanation for some of the variation.

*Camissonia brevipes*, an annual that occurs over a wide range of elevations, was collected along two gradients extending from sea level to about 1200 m. Along each gradient we found a consistent decrease in thermal stability with increasing elevation. Linear regression of the data indicated a  $-3.1^{\circ}\text{C}$  change in the fluorescence-versus-temperature breakpoint per 1000 m ( $r^2 = 0.88$ ). Since the plants were carefully selected to



avoid differences in water status or phenology, it is reasonable to assume that the differences in thermal stability reflect a plant response to a gradient in leaf temperature with elevation.

Such elevational temperature gradients could explain only part of the variation observed, however. Plants of *Geraea canescens* growing with ample water in our experimental garden were found to have lower thermal stability than plants growing under obvious drought stress on natural sites at the same elevation. The latter plants had received only natural precipitation (26 mm at the Death Valley Weather Station for the season) and were at a lower water potential than the plants in the garden (Table 13). The plants growing in the natural area had become adapted to the lower water availability by osmotic adjustment such that they maintained a positive turgor, presumably by mechanisms similar to those described by Jones (1979). The drought-stressed plants had also apparently acclimated to a higher temperature. Fluorescence-versus-temperature courses for the amply watered plant in the garden and a drought-stressed plant are shown in Fig. 25A. Comparison of the photosynthesis responses to increases in leaf temperature of the watered and drought-stressed plants (Fig. 25B) con-

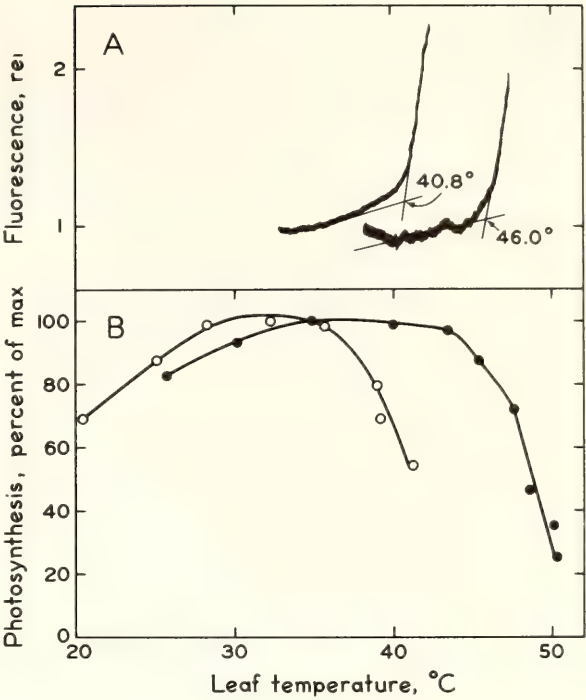


Fig. 25. The fluorescence-versus-temperature courses (A) and the photosynthesis temperature-response curves (B) of leaves of *Geraea canescens* plants growing either with abundant water (○) or under drought stress (●).

firm that the drought-stressed plant was able to maintain photosynthetic activity to a higher temperature than the watered plant, as predicted by fluorescence-versus-temperature courses.

While it is possible that the difference observed between drought-stressed plants and watered plants is directly related to water status, it seems more likely that the difference is indirect, caused by changes in leaf temperature. *Geraea*, like most other winter and spring ephemerals, may have rather large leaves. If transpiration is rapid, the loss of latent heat may cause leaf temperature to fall below air temperature. Leaf temperatures several degrees below ambient have been observed with a number of desert species (Smith, 1978). Ball (personal communication) has observed that well-watered *Geraea* may have a leaf temperature substantially below ambient, while drought-stressed *Geraea* leaves do not. This is no doubt caused by differences in the rate of transpiration, which affects the leaf energy balance. During mid-day

TABLE 13. A Summary of Water Relations and Photosynthetic Characteristics of Leaves of *Geraea canescens*\*

	Garden	Field
Photosynthesis, nmol cm <sup>-2</sup> s <sup>-1</sup> (at temperature optimum)	5.3	6.2
Inhibition of photosynthesis, °C (50% of maximum)	41	48
Fluorescence-versus-temperature °C (break point)	41	46
Water potential, bars	-3.6	-21.8
Osmotic potential, bars	-8.8	-25.9
Turgor pressure, bars	5.2	4.1

\* Plants were growing either with abundant water in the experimental garden or without supplemental water in a natural area.

when temperature and radiation are highest, for any given ambient air temperature the watered plant will have a lower leaf temperature than a drought-stressed plant. The magnitude of this difference can be quite large (5–10°C) and is comparable to the difference in ambient temperature which might be expected along a large (1000–2000 m) elevational gradient.

This difference in thermal response, which is apparently linked to water status, is probably a significant factor in thermal acclimation. When we applied water to drought-stressed plants of *Geraea*, there was a rapid increase in water potential, and after four days we noted a 4°C change in the apparent thermal stability from fluorescence-versus-temperature courses. The difference between leaf temperature and air temperature during mid-day was larger for the watered plants ( $-3.9 \pm 0.6^\circ\text{C}$ ,  $n = 4$ ) than for unwatered control plants ( $-2.0 \pm 1.1^\circ\text{C}$ ,  $n = 3$ ).

The large variation among individual plants in their apparent thermal stability (Fig. 24) could be explained by the hypothesis that the plants are each responding to their own thermal environment. We have observed that elevation and water status may both contribute to these differences in a consistent way. The variation in temperature tolerance observed therefore indicates that these annuals are capable of acclimating to temperature change. The general features of this acclimation process appear to be similar to that described in laboratory studies with the desert perennial *Nerium oleander*. In this species, membrane lipid composition adjusts rapidly to a change in thermal regime to com-

pensate partially for effects of the temperature change upon lipid properties (Raison and Berry, this *Year Book*).

The results presented here suggest that the desert annuals may also change their lipid composition in such a way as to increase their tolerance to high temperature as temperature increases. Preliminary experiments with *Geraea canescens* verify that differences in growth temperature result in differences in the thermal stability of its membranes. This adjustment may be rather rapid ( $t_{1/2}$  for *N. oleander* of 24 hours, Berry and Raison; Björkman *et al.*, this *Year Book*), and provided that leaf temperatures do not increase dramatically over a short period, the annual plants may be able to adjust their properties to their current thermal regime. The long-term temperature tolerance of these species may thus be considerably greater than would be indicated by a single measurement at an arbitrary time. Such changes in plant properties with growth temperature appear to play an important role under natural conditions in adapting these ephemeral species to their rapidly changing environment.

#### REFERENCES

- Bauer, H., *Physiol. Plant.*, **44**, 400–406, 1978.
- Jones, M. M., and H. M. Rawson, *Physiol. Plant.*, **45**, 103–111, 1979.
- Mooney, H. A., J. Ehleringer, and J. A. Berry, *Science*, **194**, 322–324, 1976.
- Pearcy, R. W., J. A. Berry, and D. C. Fork, *Plant Physiol.*, **59**, 873–878, 1976.
- Schreiber, U., and J. A. Berry, *Planta*, **136**, 233–238, 1977.
- Smith, W. K., *Science*, **201**, 614–616, 1978.



PHASE SEPARATION TEMPERATURES OF PHOSPHOLIPIDS  
FROM WARM AND COOL CLIMATE PLANTS*Carl S. Pike and Joseph A. Berry*

## INTRODUCTION

The physical state of membrane lipids has been suggested to be a major determinant of the lower temperature limit for a species' growth or survival. Comparisons in various crop plants of the temperature dependence of membrane lipid physical state and of various membrane-linked biochemical processes have indicated a correlation between the lipid phase transition temperature and an increase in the activation energy of various reactions (Raison, 1974). A sharp change in the temperature dependence of spin label motion in mung bean lipids corresponded to the lower limit of seedling growth (Raison and Chapman, 1976). The lipid phase change temperature in several *Passiflora* species corresponded to their temperature preferences for growth (Patterson *et al.*, 1976).

In these studies we have used the fluorescent membrane probe *trans*-parinaric acid, a polyene fatty acid that would be expected minimally to perturb the lipid orientation. The fluorescence intensity and polarization of the probe in membranes or lipid vesicles can provide information on phase separation temperatures; the polarization ratio is used as an expression of fluidity (Sklar *et al.*, 1979). The *trans* isomer, which has a strong preference for the solid phase in a mixed system, can detect a few percent solid but becomes insensitive to the formation of solid lipid above about 50%. The *cis* isomer has a very slight preference for the fluid phase (Sklar *et al.*, 1979).

Most studies on plant lipids as related to chilling sensitivity and resistance have dealt with crop plants, which have undoubtedly been extensively modified by

artificial selection. Our investigations focus on wild plants, since the temperature responses of their lipids might more closely reflect the constraints of natural selection in the native habitat. Wherever possible, plants were grown from seed at the same temperature, so we could focus on genetic rather than environmentally induced differences in lipid physical properties.

## METHODS

For plants grown from seed in the laboratory, controlled environment chambers were used to grow warm- and cool-climate plants under the same conditions. For plants collected in Death Valley, the mean daily maximum and minimum temperatures for the months in which the collections were made are indicated below.

Lipids were isolated from leaf tissue as described by Raison and Berry (*Year Book* 77, pp. 276–282). The lipid extract was chromatographed on Bio-Sil A, and the phospholipid-rich methanol fraction was used in fluorescence studies. Liposomes were prepared as described by Raison and Berry.

Measurements were made with a Perkin-Elmer MPF-3L fluorescence spectrophotometer. The excitation and emission monochromators were set at 320 and 420 nm, respectively. The excitation beam was passed through a polarizing prism (Karl Lambrecht and Co.); the emitted light was passed through a plastic polarizer (Edmund Scientific) and a 350-nm cut-off filter. The cuvette holder was temperature regulated; temperatures were measured with a copper-constantan thermocouple in the sample. All temperature scans were made in the ascending

direction. Fluorescence intensity was measured with the emission polarizer oriented parallel ( $I_{\parallel}$ ) and perpendicular ( $I_{\perp}$ ) to the orientation of the excitation polarizer. Plots were made of  $\log I_{\parallel}$  as a function of reciprocal temperature and of the polarization ratio ( $I_{\parallel}/I_{\perp}$ ) as a function of temperature. Changes in slope of these plots were used to determine the phase separation temperature. For a given sample the two methods usually agree within  $1^{\circ}\text{C}$  of each other. Likewise, the reproducibility of replicate experiments was within  $1^{\circ}\text{C}$ .

## RESULTS AND DISCUSSION

### Phase Separation Processes

The change in *trans*-parinaric acid fluorescence with the phase separation process in membrane phospholipids is exemplified by the results with maize (Fig. 26). The change in slope of the

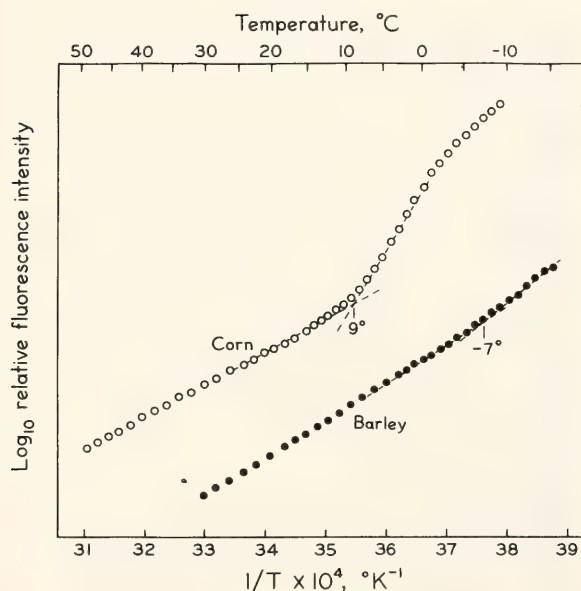


Fig. 26. Arrhenius plots of *trans*-parinaric acid fluorescence intensity of corn and barley phospholipid vesicles. The phospholipids were dispersed by gentle sonication in 0.1 M Tris-HCl buffer, pH 7.2, containing 5 mM  $\text{Na}_2\text{EDTA}$  and 25% or 33% (V/V) ethylene glycol. A suspension containing 400  $\mu\text{g}$  lipid per 3 ml of buffer was labeled with 0.7  $\mu\text{g}$  of *trans*-parinaric acid. Polarized light at 320 nm was used to excite the sample, and fluorescence was measured at 420 nm, with the excitation polarizer parallel to the emission polarizer.

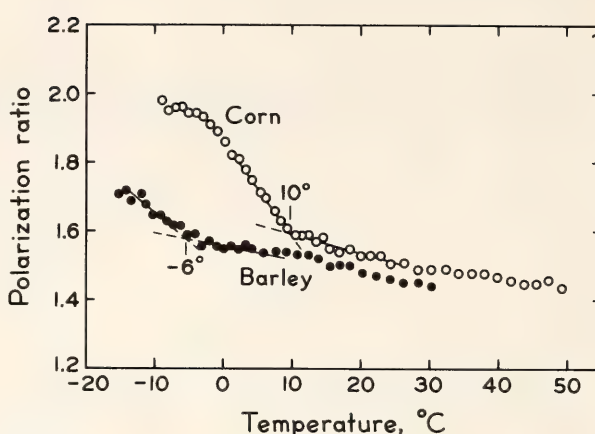


Fig. 27. *Trans*-parinaric acid fluorescence polarization of corn and barley phospholipid vesicles. Fluorescence emission was measured with the polarizer parallel ( $I_{\parallel}$ ) and perpendicular ( $I_{\perp}$ ) to the orientation of the excitation polarizer. The polarization ratio is  $I_{\parallel}/I_{\perp}$ .

fluorescence intensity versus temperature curve (an Arrhenius plot) occurs at  $9^{\circ}\text{C}$ , in good agreement with ESR determinations. A sharp discontinuity at  $10^{\circ}\text{C}$  is seen in the polarization ratio plot (Fig. 27). These changes suggest the occurrence of a change in fluidity. The slope change seen at around  $25\text{--}35^{\circ}\text{C}$  with certain ESR probes (Raison and Chapman, 1976; Raison and Berry, *Year Book* 77, pp. 276–282) is not observed with *trans*-parinaric acid; we do not know what sort of physical change is detected by those ESR probes.

The low polarization ratio above  $10^{\circ}\text{C}$  indicates a fluid probe environment (Sklar *et al.*, 1979). We interpret the slope change at  $10^{\circ}\text{C}$  as indicating the beginning of the appearance of detectable solid as the temperature is lowered, since *trans*-parinaric acid is sensitive to a few percent solid (Sklar *et al.*, 1979). This interpretation is supported by studies in which the phase separation process of *Anacystis nidulans* membranes was observed by freeze-fracture electron microscopy and the properties of extracted phospholipids were studied with *trans*-parinaric acid (Armond and Staehelin, 1979; Raison *et al.*, 1980). In Fig. 27 the leveling off of the polarization ratio of the maize lipids at about



2.0 (seen at about  $-5^{\circ}\text{C}$ ) does not indicate the completion of solidification. In model systems, Sklar *et al.* (1979) found that the leveling off with *trans*-parinaric acid occurred at about 50% solid; the *cis* isomer could indicate the completion of solidification, which might not occur in corn phospholipids until about  $-20^{\circ}\text{C}$ .

The intensity (Fig. 26) and polarization ratio (Fig. 27) plots for barley phospholipids indicate slight discontinuities at about  $-6^{\circ}\text{C}$ . The polarization ratio shows that even below that point the barley lipids are not very ordered compared to the corn lipids.

*Phase Separation Temperatures of Warm- and Cool-Climature Plants*

Table 14 shows the phase separation temperatures for phospholipids from several grasses generally considered warm- and cool-temperature active. The warm-climate species show considerably higher separation temperatures.

Mojave Desert dicots, chiefly annuals, were selected to exemplify the winter- and summer-active floras (Shreve and Wiggins, 1964; Mulroy and Rundel,

1977). As shown in Table 15, the winter-active species showed phospholipid phase separations at  $3^{\circ}\text{C}$  or lower. These plants seem well adapted to the typical winter thermal regime in the Death Valley area, where the mean daily minimum temperature in the coolest months is  $3^{\circ}\text{C}$ . For most of the summer-active species, separation temperatures of  $10^{\circ}\text{C}$  or higher were observed. *Tidestromia oblongifolia* (a winter-dormant perennial) showed a separation temperature of  $12^{\circ}\text{C}$  when grown under optimal conditions ( $45^{\circ}\text{C}/32^{\circ}\text{C}$ ). For phospholipids from leaves collected in December (just before they are shed), the separation temperature was  $7^{\circ}\text{C}$ . The low separation temperature for *Atriplex elegans elegans* is an exception and may indicate that it is not necessary for a summer-active species to have a high phase-separation temperature. Although this plant is part of the summer flora in the Mojave Desert, it can also be found during the winter (Shreve and Wiggins, 1964). Its phase separation behavior may reflect a genetic adaptation to the coolest conditions the plant might experience. The elevated phase separation temperatures generally observed with summer-active species could reflect the absence of low temperatures during the growth period or may be related to adaptation of the plant to high temperature. We have found no winter-active plants with high separation temperatures. This observation suggests a direct relationship between the occurrence of low temperatures and natural selection for lipids with a low phase-separation temperature.

The observation of marked differences in separation temperatures between warm- and cool-climate plants contradicts the failure to detect such differences with ESR reported by Raison and Berry (Year Book 77, pp. 276–282). Raison, however, recently surveyed a wide range of native Australian plants and obtained results comparable to our present findings.

TABLE 14. Phospholipid Phase Separation Temperatures for Annual Grasses

Species*	Separation Temperature† ( $^{\circ}\text{C}$ )
Cool Climate	
<i>Avena fatua</i>	−9
<i>Avena sativa</i>	−11
<i>Bromus rigidus</i>	−10
<i>Hordeum vulgare</i>	−6
Warm Climate	
<i>Chloris virgata</i>	4
<i>Digitaria sanguinalis</i>	8
<i>Panicum texanum</i>	7
<i>Zea mays</i>	9

\* All plants were grown at constant  $27^{\circ}\text{C}$  and a 16 hr photoperiod.

† Determined as the average value from *trans*-parinaric acid fluorescence intensity and polarization ratio plots of data from 2 samples.

TABLE 15. Phospholipid Phase Separation Temperatures for Desert Dicots

Species	Growth Conditions*	Separation Temperature† (°C)
Cool Climate		
<i>Atriplex elegans fasciculata</i>	L 28C/21C	2
<i>Boerhaavia annulata</i>	DV 19C/3C	2
<i>Camissonia claviformis</i>	DV 22C/6C	-3
<i>Cryptantha angustifolia</i>	L 28C/21C	2
<i>Eriogonum inflatum</i>	DV 22C/6C	-4
<i>Lepidium lasiocarpum</i>	L 28C/21C	-1
<i>Perityle emoryi</i>	L 28C/21C	3
Warm Climate		
<i>Atriplex elegans</i> ssp. <i>elegans</i>	L 28C/21C	-1
<i>Boerhaavia coccinea</i>	L 28C/21C	12
<i>Mollugo verticillata</i>	L 28C/21C	17
<i>Pectis papposa</i>	L 28C/21C	13
<i>Portulaca oleracea</i>	L 28C/21C	11
<i>Tidestromia oblongifolia</i>	L 45C/32C	12
<i>Tidestromia oblongifolia</i>	DV 19C/3C	7

\* For laboratory-grown plants (L), the growth chamber day and night temperatures are given (16 hr photoperiod). For plants collected in Death Valley (DV), the mean daily maximum and minimum temperatures for the month of collection are given.

† Determined as in Table 14.

#### Phase Separation Temperatures in Plants Capable of Acclimating to a Wide Range of Temperatures

We have investigated the phase separation temperatures of phospholipids from leaves of *Nerium oleander* plants grown at 20°C/15°C and 45°C/32°C as a laboratory model for a very adaptable plant. As shown by the polarization ratio plots (Fig. 28), the phase separation temperatures were about -3°C and 7°C, respectively. The fluorescence intensity plots, not shown, gave similar values, as have recent ESR studies by Raison and Berry; these results cause us to question the values reported last year (Raison and Berry, *Year Book* 77, pp. 276-282). A similar difference was observed with chloroplast phospholipids. Thus, the acclimation of oleander involves alterations of membrane lipid physical properties, in addition to alterations of various functional properties (Björkman *et al.*, *Year Book* 77, pp.

262-276). The change in membrane lipid physical properties may be involved in the change in thermal behavior of various membrane-linked biochemical processes.

Björkman *et al.*, (*Year Book* 77, pp. 262-276) have shown that the acclimation of oleander to these contrasting

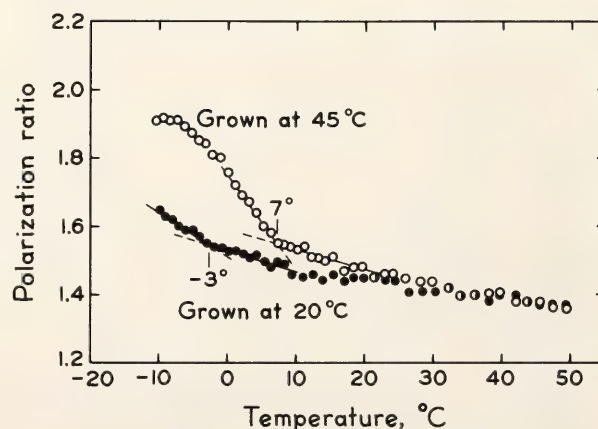


Fig. 28. *Trans*-parinaric acid fluorescence polarization of phospholipids from *Nerium oleander* grown at 45C/32C and 20C/15C.



thermal regimes involves a substantial alteration in the thermal stability of the photosynthetic apparatus. Raison and Berry (this *Year Book*) report that the stability of thylakoid membranes differs by about 10°C between the 45°C/32°C and 20°C/15°C plants, and that there is a comparable shift in membrane lipid viscosity. Thus, we have demonstrated changes in both the low-temperature and the high-temperature lipid physical properties. Studies of other widely tolerant species should indicate if these two sets of changes generally occur together, a situation which would suggest a common basis in a changed lipid composition.

To extend the studies on the acclimation of oleander, we are investigating the phase separation temperatures of phospholipids from several Death Valley plants that are active throughout the year (*Atriplex hymenelytra*, *Heliotropium curassavicum*, *Larrea divaricata*, and *Psathyrotes ramosissima*). When sampled in January, the separation temperatures were all at 1°C or below. Thus, we suggest that both annuals and perennials, when growing in cool conditions, synthesize a phospholipid mixture with a low phase-separation temperature. These four species will be sampled again in the summer. Desert perennials, such as *Larrea divaricata* (Mooney *et al.*, 1978) and *Atriplex lentiformis* (Pearcy *et al.*, 1977), have been shown to exhibit substantial seasonal changes in photosynthetic properties. There are seasonal changes in the chemical composition of *A. lentiformis* lipids, an indirect indication of changes in physical properties (Pearcy, 1978).

#### CONCLUSIONS

We suggest that the phase separation observed at about 10°C in typical chilling-sensitive plants represents the beginning of the appearance of ordered

(gel-phase) lipid. This solidification is not completed until well below 0°C. These processes are shifted to lower temperatures in typical cool-climate species. Our proposal, which differs from the assignment of slope changes based on ESR (Raison, 1974; Raison and Chapman, 1976; Raison and Berry, *Year Book* 77, pp. 276–282) ought to be tested by other methods.

Adaptation of plant species to growth at low temperature is accompanied by (and may require) a low phospholipid phase separation temperature, while adaptation to growth at high temperature is usually associated with a higher phase separation temperature. It appears, therefore, that plants normally growing in a certain environment synthesize a mixture of phospholipids that will not phase-separate in the usual thermal regime. These results suggest that natural selection has acted upon the phase separation temperature of membrane lipids; but other lipid properties are also important. Present techniques can only study the bulk lipid properties. If a rough lower limit for normal function is set by the phase separation, then an important question is, what processes are incompatible with solidification?

#### ACKNOWLEDGMENTS

We thank R. Simoni for a supply of *trans*-parinaric acid, and J. Ehleringer and M. Nobs for seeds.

#### REFERENCES

- Armond, P. A., and L. A. Staehelin, *Proc. Nat. Acad. Sci. USA*, 76, 1901–1905, 1979.
- Mooney, H. A., O. Björkman, and G. J. Collatz, *Plant Physiol.*, 61, 406–419, 1978.
- Mulroy, T. W., and P. W. Rundel, *Bio Science*, 27, 109–114, 1977.

- Patterson, B. D., T. Murata, and D. Graham, *Aust. J. Plant Physiol.*, **3**, 435–442, 1976.
- Pearcy, R. W., *Plant Physiol.*, **61**, 484–486, 1978.
- Pearcy, R. W., J. A. Berry, and D. C. Fork, *Plant Physiol.*, **59**, 873–878, 1977.
- Raison, J. K., *R. Soc. NZ Bull.*, **12**, 487–497, 1974.
- Raison, J. K., J. A. Berry, P. A. Armond, and C. S. Pike, in *Adaptations of Plants to Water and High Temperature Stress*, P. Kramer and N. Turner, eds., Wiley-Interscience, New York, in press, 1980.
- Raison, J. K., and E. A. Chapman, *Aust. J. Plant Physiol.*, **3**, 291–299, 1976.
- Shreve, F., and I. L. Wiggins, *Vegetation and Flora of the Sonoran Desert*, Stanford University Press, Stanford, CA, 1964.
- Sklar, L. A., G. P. Miljanich, and E. A. Dratz, *Biochemistry*, **18**, 1707–1716, 1979.

## ENHANCEMENT OF HIGH TEMPERATURE STABILITY OF PROTEIN-PROTEIN INTERACTIONS BY DEUTERIUM OXIDE

Paul A. Armond and John L. Hess

The investigations of the thermal response of photosynthesis have included field studies as well as analysis of the photosynthetic apparatus of plants grown in carefully controlled environments (see *Year Book 77*, pp. 262–276). The studies of the biochemical and biophysical responses of the photosynthetic apparatus to temperature have also included examinations of the thermal response of membranes. The investigations of Raison and Berry (*Year Book 77*, pp. 276–282) and Pike and Berry (this *Year Book*) emphasize the important effect that alterations in the physical properties of membrane lipids have on the thermal response of photosynthesis. It was determined that the differences in the response of photosynthesis to temperature between different plant species can be correlated with differences in membrane fluidity and phase transition temperatures.

The fluidity of the membrane lipids and the amphipathic nature of lipid molecules have a profound effect on the proteins associated with membranes, particularly those that are integral membrane proteins. As was observed by Armond *et al.* (this *Year Book*), a manifestation of heat damage to the photo-

synthetic membranes of *Nerium oleander* was a high-temperature induced dissociation of the light-harvesting complex from the photosystem II reaction center complex. Since it has been observed that hydrophilic interactions are reduced and hydrophobic interactions are enhanced by increasing temperature (Oakenfull and Fenwick, 1977), these results were interpreted as a high-temperature induced decrease in the hydrophilic interactions between the constituent subunits of the supramolecular complexes and an increase in the interactions of the hydrophobic portions of the protein complexes with the surrounding lipid molecules. If this interpretation is correct, then the observed changes in membrane stability that occur with photosynthetic acclimation to temperature or the difference between the thermal stability of warm and cool season plants may result from alterations in the balance of hydrophobic and hydrophilic interactions, upon which physiological protein-protein and protein-lipid interactions depend.

Substitution of D<sub>2</sub>O for H<sub>2</sub>O alters the balance between the hydrophobic and hydrophilic interactions, which may result in an increased strength of hydro-



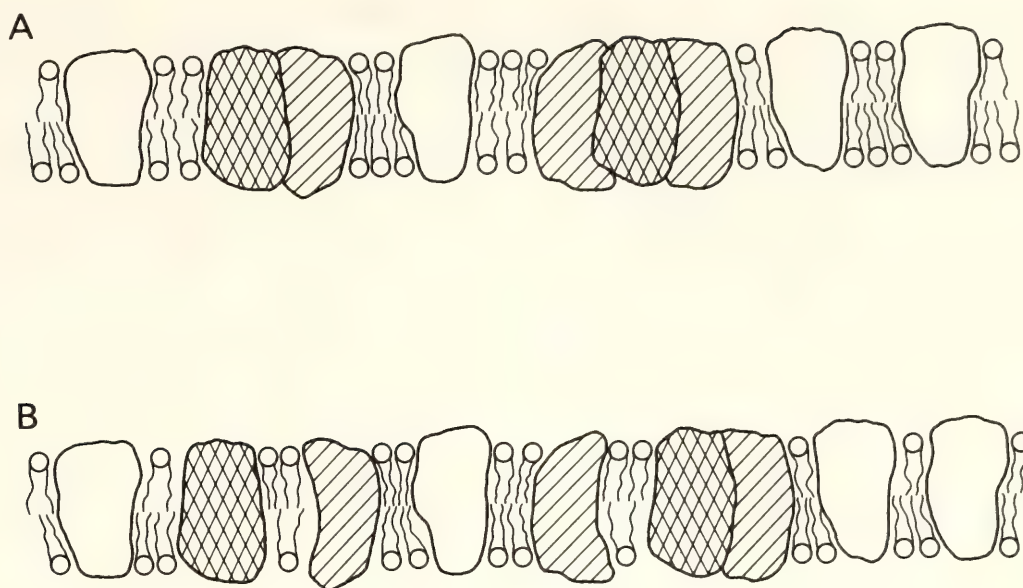


Fig. 29. Model of the chloroplast membrane of *Nerium oleander*. The interactions of the photosystem II core complex (double hatch) and the light-harvesting complex (single hatch) can be used to study protein-protein interactions in an environment dominated by the surrounding lipids (A). As temperature is increased, the interactions between these integral membrane complexes decrease, resulting in a dissociation of the light-harvesting complex from photosystem II (B).

philic interactions (Oakenfull and Fenwick, 1975; Némethy and Sherga, 1964). To examine the result of D<sub>2</sub>O-enhanced hydrophilic interactions on protein-protein interactions of two integral membrane complexes, the chloroplasts of *N. oleander* were used. In the chloroplasts of higher plants, the light-harvesting complex normally maintains a close association with the photosystem II core complex (Fig. 29A). At high temperatures, these two components can dissociate (Fig. 29B), resulting in changes in light-harvesting efficiency. The interaction of the light-harvesting complex with the photosystem II core complex can be monitored by observing the  $F_0$  level of chlorophyll *a* fluorescence. Changes in this type of fluorescence are indicative of functional (Armond *et al.*, *Year Book* 76, pp. 335–341) as well as morphological (Armond *et al.*, this *Year Book*) dissociation of the light-harvesting complex from photosystem II.

Interactions between proteins in which lipids play no direct role can be examined in the phycobilisomes of the blue-green

alga *Anacystis nidulans*. The phycobilisome, a larger peripheral membrane complex, contains the major light-harvesting pigments (phycocyanin and allophycocyanin), and normally transfers the excitation energy absorbed by these pigments to an integral membrane complex containing chlorophyll (Gantt *et al.*, 1979). An increase in the level of allophycocyanin fluorescence with increased temperature indicates a disruption of the normal excitation energy transfer pathway.

The effect of D<sub>2</sub>O on protein-protein interactions was examined for isolated chloroplasts from *N. oleander* grown at 20°C/15°C and 45°C/32°C (Björkman *et al.*, *Year Book* 77, pp. 262–276) and from *A. nidulans* grown at 28°C and 38°C (Murata and Fork, *Year Book* 74, pp. 766–776). The experimental procedure involved resuspending chloroplasts or algal cells in a medium containing 10 mM MgCl<sub>2</sub> and 100 mM KCl in either H<sub>2</sub>O or D<sub>2</sub>O (90%). The temperature of the suspensions was slowly increased (~1°C/min) and either  $F_0$  fluorescence

of chlorophyll *a* at 685 nm, or allophycocyanin fluorescence at 655 nm was monitored.

The light-harvesting complex photosystem II interactions in the 20°C-grown *N. oleander* chloroplasts were substantially enhanced by the substitution of D<sub>2</sub>O for H<sub>2</sub>O in the medium (Fig. 30A). This increased stability was of a similar magnitude to the stability enhancement

that results from acclimation to a 45°C growth temperature (compare the D<sub>2</sub>O-*F*<sub>0</sub> response of Fig. 30A with the H<sub>2</sub>O-*F*<sub>0</sub> curve of Fig. 30B). The 45°C sample also showed an enhanced stability of the light-harvesting complex photosystem II interactions although of a somewhat lesser magnitude.

The temperature-dependent increase of allophycocyanin fluorescence was also affected by the substitution of D<sub>2</sub>O for H<sub>2</sub>O (Fig. 31). The efficient energy transfer from the allophycocyanin of the phycobilisome to the chlorophyll of the inte-

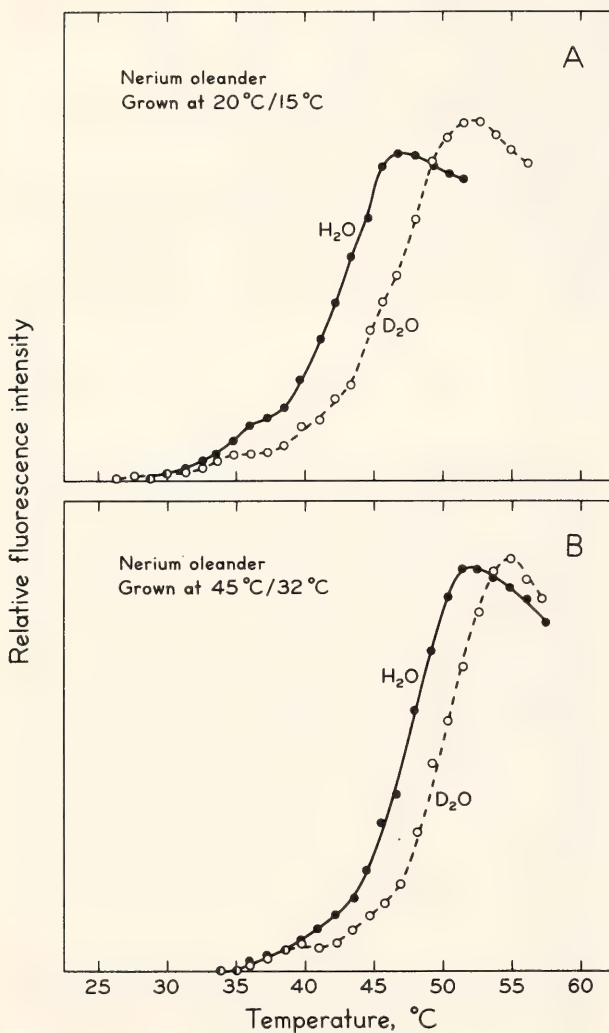


Fig. 30. The response of the *F*<sub>0</sub> level of chlorophyll *a* fluorescence in chloroplasts of *Nerium oleander*. The chloroplasts were isolated from leaves of plants grown at either 30°C/15°C (day/night) (A) or 45°C/32°C (B) and resuspended either in H<sub>2</sub>O or in D<sub>2</sub>O. Measurements were made with a Perkin-Elmer spectrofluorometer MPF-3L with a Balzer 2.5% neutral density and Corning 4-96 filter covering the excitation slit, and a Corning 2-58 filter over the emission slit. Excitation wavelength was 440 nm with a 3-nm slit width. Emission was a broad band at 685 nm.

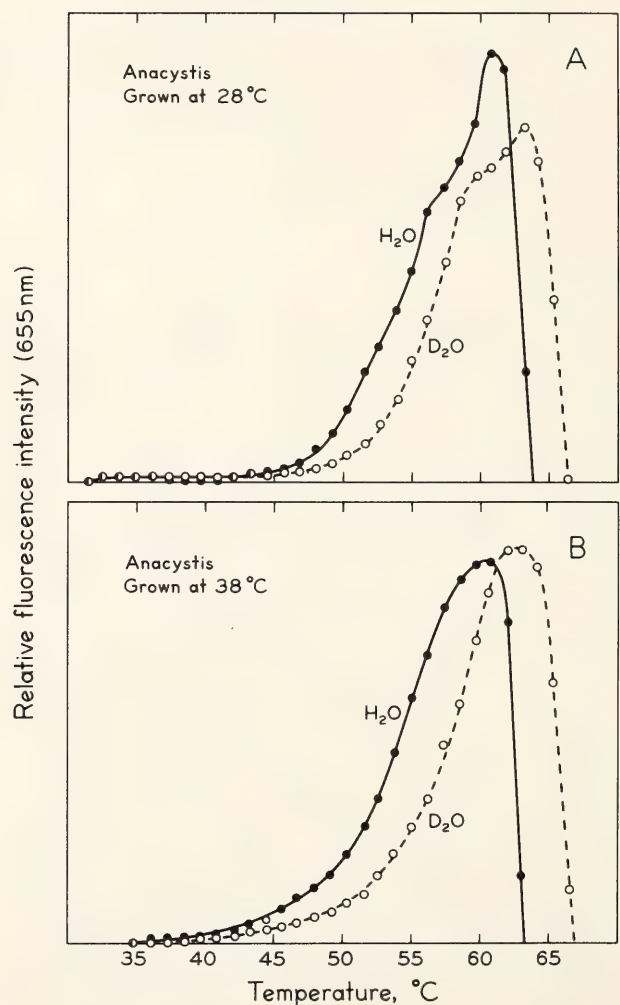


Fig. 31. Alterations in the level of phycocyanin fluorescence induced by heating cells of *Anacystis nidulans*. The substitution of D<sub>2</sub>O for H<sub>2</sub>O resulted in increased stability of energy transfer from phycocyanin to chlorophyll for both the 28°C-grown cells (A) and 38°C-grown cells (B). Excitation was at 600 nm (4 nm slit width) and emission at 655 nm (4 nm slit width).



gral membrane protein complex was stable to higher temperatures when the cells were in the presence of D<sub>2</sub>O. With the exception of some differences in curve shape, however, there were no significant differences in the stability of this process between cells grown at 28°C (Fig. 31A) or at 38°C (Fig. 31B).

These results indicate that the effect of membrane lipid fluidity on physiological activity of membranes may be specifically at the level of the hydrophobic/hydrophilic interactions of the membrane components. The changes in membrane fluidity which occur during the process of photosynthetic acclimation and the differences in fluidity which exist between plant species that are cool- or warm-season active (Pike and Berry, this *Year Book*) have the potential to affect the balance of hydrophobic and hydrophilic interactions. As would be expected, the results also show that membrane lipids have greater influence on protein complexes that are in an environment dominated by lipids (integral membrane complexes) than on peripheral complexes. The proteins themselves may not necessarily undergo any change when acclimation occurs.

Membrane properties (Murata and Fork, *Year Book* 77, pp. 289–291) and lipid composition (Holton *et al.*, 1964) in *A. nidulans* are altered in response to differences in growth temperature. However, the thermal stability of excitation energy transfer from allophycocyanin to chlorophyll was not affected by growth temperature but was significantly stabilized by the presence of D<sub>2</sub>O. The effect of D<sub>2</sub>O in this system is interpreted as an alteration of the hydrophilic/hydrophobic forces that stabilize the protein-protein interactions required for efficient excitation energy transfer.

#### REFERENCES

- Gantt, E., C. A. Lipschultz, J. Grabowski, and B. K. Zimmerman, *Plant Physiol.*, **63**, 615–620, 1979.  
Holton, R. W., H. H. Blecker, and M. Onore, *Phytochemistry*, **3**, 592–602, 1964.  
Némethy, G., and H. A. Scheraga, *J. Chem. Phys.*, **41**, 680–689, 1964.  
Oakenfull, D., and D. E. Fenwick, *Aust. J. Chem.*, **28**, 715–720, 1975.  
Oakenfull, D., and D. E. Fenwick, *Aust. J. Chem.*, **30**, 741–752, 1977.

### A RADIOIMMUNE ASSAY FOR RuP<sub>2</sub> CARBOXYLASE PROTEIN

*G. James Collatz, Murray Badger, Celia Smith, and Joseph A. Berry*

We report here the development of a new technique for determination of the amount of RuP<sub>2</sub> carboxylase protein in crude preparations of soluble protein. The technique is based upon the observation of Wishnick *et al.* (1970) that an analog to the transition state of the carboxylation reaction, carboxyribitol bisphosphate (CRP<sub>2</sub>), binds stoichiometrically to the enzyme. [<sup>14</sup>C]-labeled CRP<sub>2</sub> is added to a protein preparation, and the CRP<sub>2</sub>-RuP<sub>2</sub> carboxylase complex formed is separated from unbound CRP<sub>2</sub>

by immunoprecipitation. This radioimmune assay is simple and accurate, and there is sufficient antigenic similarity among RuP<sub>2</sub> carboxylase from different species that the immuno-precipitation can be used with enzymes from a wide range of species other than that used in preparation of the antiserum. The molar concentration of active sites of RuP<sub>2</sub> carboxylase can be determined directly in a crude preparation, and the technique permits measurement of catalytic site concentration or density in photosyn-

thetic tissue. When coupled with assays of catalytic activity, it permits measurement of the catalytic efficiency of the active sites (turnover number,  $s^{-1}$ ). Routine assays of these parameters are being used to survey for possible differences in the catalytic efficiency of RuP<sub>2</sub> carboxylase among species and in studies of the factors that control RuP<sub>2</sub> carboxylase activity in vivo.

#### MATERIALS AND METHODS

Crude extracts of leaf protein were prepared as described elsewhere (*Year Book* 76, p. 350), and RuP<sub>2</sub> carboxylase activity was assayed according to Lorimer *et al.* (1977). Spinach RuP<sub>2</sub> carboxylase was prepared from fresh spinach leaves (*Spinacea oleracea* hybrid 102) as described by Paulsen and Lane (1966). This enzyme was judged homogeneous by SDS-polyacrylamide gel electrophoresis.

Antiserum was prepared by injecting a young female rabbit with a dispersion of 5 mg of the purified spinach carboxylase with Freund's complete adjuvant (Grand Island Biological Supply Co.). The injection was repeated at monthly intervals except that Freund's incomplete adjuvant was used in place of the complete adjuvant. Serum was collected one week after the injections.

[<sup>14</sup>C]-labeled carboxyribitol bisphosphate was prepared essentially as described by Rabin *et al.* (1958). First, 17.2  $\mu$  mol of RuP<sub>2</sub> (Sigma) was reacted with 19.1  $\mu$  mol of [<sup>14</sup>C]-NaCN (New England Nuclear, 52.44  $\mu$  Ci/ $\mu$  mol) for 16 hr at room temperature. The reaction was stopped by the addition of 3.5 ml of 1% formic acid and taken to dryness under vacuum twice on a rotary film evaporator. The yield of conversion of RuP<sub>2</sub> to [<sup>14</sup>C]-CRP<sub>2</sub> was greater than 98%, and the specific radioactivity was 120 dpm/pico mol. The product was dissolved in buffer (50 mM HEPES, pH 7.8, 10 mM MgCl<sub>2</sub>, 0.25 mM EDTA) to give a final concentration of 2 mM CRP<sub>2</sub>.

Immunoprecipitates were formed by

incubating a sample containing 1–40  $\mu$ g of RuP<sub>2</sub> carboxylase in 50  $\mu$ l of buffer (60 mM HEPES pH 7.2, 10 mM MgCl<sub>2</sub>) and 25  $\mu$ M CRP<sub>2</sub> with 100  $\mu$ l of rabbit antiserum for 1½ hr at 37°C in 400  $\mu$ l microcentrifuge tubes. The precipitate was collected on Millipore filters (type EH, 0.5  $\mu$ ) and washed with 0.85% NaCl. The filters, 1.0 ml of 0.2 N NaOH and 6 ml of a water-miscible scintillation fluid were counted in a scintillation counter.

#### RESULTS

Control experiments in which RuP<sub>2</sub> carboxylase was omitted or in which serum from a rabbit that had not been sensitized to RuP<sub>2</sub> carboxylase was used in place of the antiserum indicated very little nonspecific binding of CRP<sub>2</sub> to the filters. When purified spinach RuP<sub>2</sub> carboxylase was incubated with CRP<sub>2</sub> and the antiserum, a quantitative relationship between the <sup>14</sup>C bound to the filters and the amount of RuP<sub>2</sub> carboxylase present in the incubation was observed, as shown in Fig. 32. One can calculate that 7.55 mol of CRP<sub>2</sub> were bound per

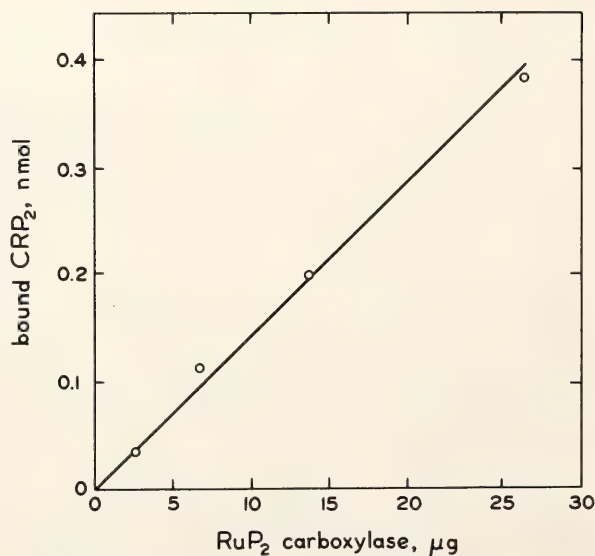


Fig. 32. Recovery of (<sup>14</sup>C)-CRP<sub>2</sub> with immuno-precipitates of purified spinach carboxylase as a function of RuP<sub>2</sub> carboxylase added to the incubation medium. The slope of the line indicates 7.55 mol of CRP<sub>2</sub> bound per mol of enzyme added.



550,000 daltons of purified spinach carboxylase. This result is in agreement with that of Wishnick *et al.* (1970), who conclude that there are eight binding sites per mol of enzyme. Presumably these binding sites are identical with the catalytic sites.

Studies of the conditions required for binding confirmed that magnesium is needed for irreversible binding of  $\text{CRP}_2$  to the enzyme and that binding becomes saturated at very low concentrations of free  $\text{CRP}_2$  ( $< 10 \mu\text{M}$ ). The presence of inorganic phosphate in the millimolar range which might be expected to compete with  $\text{CRP}_2$  for binding had the effect of changing the number of binding sites per mol enzyme for  $\text{CRP}_2$  at concentrations in excess of 1 mM (data not shown). The basis of this effect is not known. It should cause no difficulty with the assay procedure, however, provided that care is taken to exclude significant levels of inorganic phosphate. Possible interference by other phosphorylated compounds that might be present in the assay mixture should be investigated.

Studies with enzyme preparations having different histories and different apparent catalytic efficiency yielded a constant stoichiometry of binding, suggesting that the binding of the analog to the enzyme does not require a completely competent catalytic site. However, no experiments involving chemical modification of the protein were conducted.

These results indicate that with appropriate precautions this procedure can be used to determine spinach  $\text{RuP}_2$  carboxylase protein quantitatively. To examine the possibility of extending the technique to measure the concentration of  $\text{RuP}_2$  carboxylase from species other than spinach, we purified small quantities of  $\text{RuP}_2$  carboxylase from crude extracts of several species by centrifugation on a linear sucrose density gradient (0.2–0.8 M sucrose, 50 mM Tricine pH 7.6, 20 mM  $\text{MgCl}_2$ , 5 mM DTT and 0.25 mM EDTA) at 45,000 rpm for 2½ hr in a Sorvall TV850 vertical rotor. The  $\text{RuP}_2$

carboxylase protein separated from other proteins of the extract. Total protein of the carboxylase-containing fraction was determined by the Lowry procedure (Lowry *et al.*, 1951, and Paulsen and Lane, 1966), and  $\text{RuP}_2$  carboxylase by the  $\text{CRP}_2$ -immunoprecipitation procedure. There was good agreement between the two techniques, as shown in Fig. 33, and the amount of  $\text{CRP}_2$  bound per  $\mu\text{g}$  of  $\text{RuP}_2$  carboxylase protein was identical ( $8.2 \pm 0.6 \text{ mol/mol}$ ) for all species up to at least 20  $\mu\text{g}$  of carboxylase per assay. Apparent saturation of the assay for species such as *Nerium oleander* or *Phacelia pedicellata* at high levels of carboxylase was a consequence of incomplete precipitation of the  $\text{RuP}_2$  carboxylase- $\text{CRP}_2$  complex by the antiserum. Differences in the observed titer among the species are probably related to differences in the number of antigenic determinants observed with Ouchterlony analysis (data not shown). Even the carboxylase from species such as *Chlamydomonas reinhardtii*, which differed antigenically from spinach, could be assayed if care was taken to ensure that the concentrations of carboxylase did not exceed the linear range.

Experiments with crude protein extracts also yielded linear regions followed by saturation. (Fig. 34 shows the results with two of the species.) It is concluded that the slope of the linear portion of the curve reflects the amount of  $\text{RuP}_2$  carboxylase in the extract. This value may be related to the  $\text{RuP}_2$  carboxylase activity of the extract, and this value may be used to obtain the specific activity or catalytic efficiency of the enzyme.

Measurements of the catalytic efficiency of  $\text{RuP}_2$  carboxylase in crude extracts of spinach leaves were comparable (3.0–3.2  $\mu\text{mol/min mg RuP}_2$  carboxylase at 30°C) to the highest values we have obtained with freshly purified spinach carboxylase. The apparent catalytic efficiency of  $\text{RuP}_2$  carboxylase has ranged from 1.0 to 3.4  $\mu\text{mol/min mg RuP}_2$  carboxylase in crude extracts from 20 plant

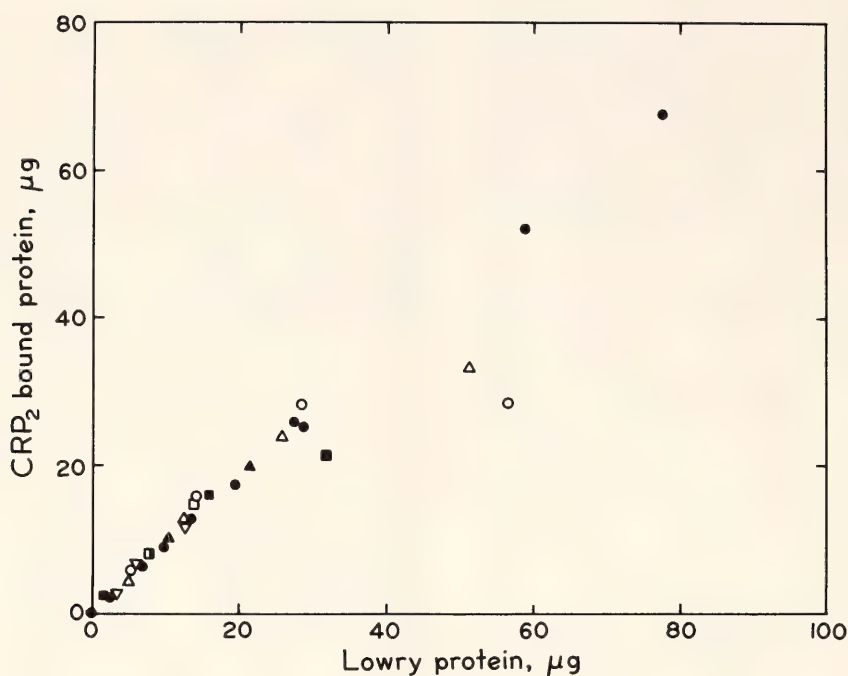


Fig. 33. RuP<sub>2</sub> carboxylase protein measured by the radioimmune assay (CRP<sub>2</sub> bound protein) and measured by the Lowry procedure according to Paulsen and Lane (1966) on preparations of RuP<sub>2</sub> carboxylase purified by ultracentrifugation from several species. ● *Spinacea oleracea*, ∇ *Ranunculus californicus*, ■ *Nerium oleander*, □ *Phacelia calthifolia*, ▲ *P. crenulata*, ○ *P. pedicellata*, △ *Cucurbiata palmata*.

species examined. It is not known whether this variation is the consequence of differences among species in the intrinsic efficiency of the native enzyme or is due to partial inactivation of the enzyme during extraction. The measurements for a given species, however, have been reproducible. For all C<sub>3</sub> species of higher plants examined so far, RuP<sub>2</sub> carboxylase accounted for 38–55% of the soluble leaf protein and 16–22% of the total leaf protein. Threefold differences in the catalytic efficiency of RuP<sub>2</sub> carboxylase protein would have important implications for the total protein economy of the plant, since the carboxylase constitutes such a large proportion of the total protein.

There have been many studies of changes in RuP<sub>2</sub> carboxylase activity with development, senescence, and stress treatments (Kawashima and Wildman, 1970). Fewer of these studies have examined changes in the quantity of RuP<sub>2</sub> carboxylase protein. The use of this technique should permit routine determination of RuP<sub>2</sub> carboxylase activity,

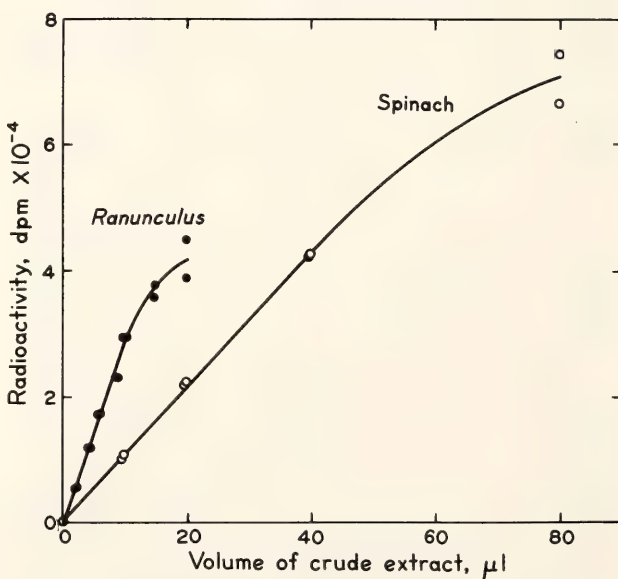


Fig. 34. Radioimmune assay for RuP<sub>2</sub> carboxylase protein on crude extracts of leaves of *Spinacea oleracea* (spinach) and *Ranunculus californicus*. The slope of the line corresponds to 1.66 μg/μl for *Ranunculus* and 0.61 μg/μl for *Spinacea oleracea*. Specific activities were 3.4 and 2.9 μmol CO<sub>2</sub> fixed per mg RuP<sub>2</sub> carboxylase at 30°C for *Ranunculus* and spinach, respectively.



quantity, and catalytic efficiency with treatment. It should thus be possible to determine whether changes in activity are a result of changes in the amount of carboxylase protein or of activation or inactivation of existing protein.

The principal application of this technique to our own work has been to assist in interpreting studies of the steady-state pool size of  $\text{RuP}_2$  during photosynthesis. As pointed out last year (*Year Book* 77, pp. 248–251), a significant portion of the measured pool of  $\text{RuP}_2$  in photosynthetic tissue is probably not free but is bound to the  $\text{RuP}_2$  carboxylase enzyme. Thus, in order to assess the extent to which the rate of carboxylation may be limited by  $\text{RuP}_2$  concentration, it is necessary to know both the concentration of catalytic sites and the  $\text{RuP}_2$  concentration. The radioimmune procedure is being used to obtain these measurements of active site concentration. With spinach tissue we obtain about 50 nmol of active sites/mg chl. This number of active sites is approximately equal to that of  $\text{RuP}_2$  observed in spinach cells at saturating light and ambient  $\text{CO}_2$  and  $\text{O}_2$  concentrations (*Year Book* 77, pp. 248–251). Higher concentrations were observed in low  $\text{O}_2$  and  $\text{CO}_2$ . Thus, together with measurements of the active site concentration, it may be concluded that photosynthesis by these spinach cells was probably not rate limited by  $\text{RuP}_2$  at low  $\text{O}_2$  and  $\text{CO}_2$ . However, as  $\text{CO}_2$  is increased even at rate-saturating light intensity, the steady-state pool of  $\text{RuP}_2$  falls below the concentration of active sites. This indi-

cates that the carboxylase is no longer rate saturated by  $\text{RuP}_2$  and photosynthesis is limited by the rate of supply of  $\text{RuP}_2$ . Preliminary experiments conducted with plants growing under natural conditions indicate that photosynthesis may be  $\text{RuP}_2$  carboxylase-limited at full noon in some species, while it may be limited by the supply of  $\text{RuP}_2$  under identical conditions in other species. It is expected that application of these techniques in studies of the control of photosynthesis by environmental factors will permit better insights into the biochemical mechanisms involved.\*

\* This research was supported in part by the Science and Education Administration of the U.S. Department of Agriculture under Grant No. 5901-0410-0128-0.

#### REFERENCES

- Kawashima, N., and S. G. Wildman, *Annu. Rev. Plant Physiol.*, **21**, 325–358, 1970.
- Lorimer, G. H., M. R. Badger, and T. J. Andrews, *Anal. Biochem.*, **78**, 66–75, 1977.
- Lowry, O. H., N. J. Rosenbrough, A. L. Farr, and R. J. Randall, *J. Biol. Chem.*, **193**, 265–275, 1951.
- Paulsen, M. J., and M. D. Lane, *Biochemistry*, **5**, 2350–2357, 1966.
- Rabin, B. R., D. P. Shaw, N. G. Pon, J. M. Anderson, and M. J. Calvin, *J. Amer. Chem. Soc.*, **80**, 2528–2532, 1958.
- Wishnick, M., M. D. Lane, and M. C. Scrutton, *J. Biol. Chem.*, **245**, 4939–4947, 1970.

### DIRECT MEASUREMENT OF PHOTORESPIRATION AS A FUNCTION OF $\text{CO}_2$ CONCENTRATION\*

*Joseph A. Berry and Murray R. Badger*

In a previous study (Berry *et al.*, 1978) we demonstrated the use of the

\* These studies were conducted in the Department of Environmental Biology, Australian National University, Canberra, Australia.

stable isotope  $^{18}\text{O}$  as a tracer for studying the rate and pathway of photorespiration. The results obtained in that study were entirely consistent with the hypothesis, originally advanced by Bowes *et al.*

(1971), that photorespiration in higher plants is directly linked to the oxygenase activity of ribulose-1, 5-bisphosphate ( $\text{RuP}_2$ ) carboxylase-oxygenase. This enzyme catalyzes the oxygenolytic cleavage of  $\text{RuP}_2$  yielding phosphoglycolic acid, the presumed substrate for photorespiration, and 3-phosphoglycerate. When this reaction is conducted in the presence of  $^{18}\text{O}$ -labeled  $\text{O}_2$ , there is fixation of a single atom of oxygen from molecular oxygen into the carboxyl group of phosphoglycolate (Lorimer *et al.*, 1973). When intact leaves of  $\text{C}_3$  plants are permitted to photorespire in  $[\text{O}^{18}]\text{-O}_2$ , rapid fixation of oxygen into the carboxyl oxygen of glycolate, glycine, serine, glycerate, and 3-phosphoglycerate was observed (Berry *et al.*, 1978). Also, the yield of incorporation of oxygen into the above photorespiratory intermediates was high (at least 60% in intact leaves, 95% with chloroplasts), indicating that all or nearly all of the glycolate metabolized in photorespiration was derived from a reaction that results in the fixation of oxygen, such as the  $\text{RuP}_2$  oxygenase reaction.

Studies of the kinetics of  $\text{RuP}_2$  oxygenase activity in vitro indicate that  $\text{CO}_2$  is a competitive inhibitor of this reaction as well as a substrate for the alternative carboxylation reaction (Badger and Andrews, 1974; Laing *et al.*, 1974). This finding leads to the prediction that photorespiration of intact leaves of higher plants should be inhibited by high  $\text{CO}_2$  if the source of glycolate for photorespiration is the  $\text{RuP}_2$  oxygenase reaction. The studies reported in the previous paper (Berry *et al.*, 1978) were conducted at the  $\text{CO}_2$  compensation concentration and do not address this prediction. This paper presents preliminary results of measurements of photorespiration by exchange of isotopic oxygen as a function of  $\text{CO}_2$  concentration. These studies confirm that high concentrations of  $\text{CO}_2$  inhibit photorespiration in  $\text{C}_3$  plants.

## METHODS

Mass spectrometric techniques were used as described previously (Berry *et al.*, 1978) except that the leaf cuvette was modified to permit measurement and control of the  $\text{CO}_2$  concentration to which the leaf was exposed during measurement of isotopic oxygen exchange. This modification permitted  $\text{CO}_2$  to be added to the closed compartment to replace that fixed by the leaf, and  $\text{CO}_2$  concentration to be measured by an infrared  $\text{CO}_2$  analyzer included in the gas flow circuit. Provided that the rate of  $\text{CO}_2$  addition was less than the rate-saturated capacity for  $\text{CO}_2$  uptake of the leaf enclosed in the cuvette, a steady-state  $\text{CO}_2$  concentration was established within the cuvette. This concentration could be manipulated by adjusting the rate of  $\text{CO}_2$  addition, and at constant rates of addition the steady-state  $\text{CO}_2$  concentration remained constant. Pure  $\text{CO}_2$  was added through a stainless steel capillary tube that had been crimped to restrict flow to  $4 \mu\text{l s}^{-1}$  at an applied pressure of 40 psi. The rate of addition was adjusted by adjusting the pressure applied to the capillary. The capillary flow versus pressure was calibrated by means of precision mixing pumps and checked at frequent intervals during the study.

Leaves of *Hirschfeldia incana*, *Spinacea oleracea*, or *Amaranthus edulis* were detached under water and the petiole recut under water. The detached leaves were kept with their petioles immersed in distilled  $\text{H}_2\text{O}$  and illuminated with about  $20 \text{ nE cm}^{-2}\text{s}^{-1}$  for several minutes to ensure that the supply of water to the leaf had not been disrupted during detachment. The leaf was placed in the cuvette with its petiole immersed in a potometer well. The cuvette was closed and the atmosphere within replaced by a mixture of Argon and  $[\text{O}^{18}]\text{-labeled O}_2$  (99 atom %). The partial pressures of  $^{18}\text{O}_2$  ( $m/e = 36$ )  $^{16}\text{O}_2$  ( $m/e = 32$ ) Ar ( $m/e = 40$ ) and  $\text{N}_2$  ( $m/e = 28$ ) were monitored continuously on the four col-



lectors of a MAT-Varian GD150/4 mass spectrometer. These measurements permitted detection of leaks ( $N_2$ ); drift in the sensitivity of the analyzer (Ar), and simultaneous measurement of oxygen uptake and production. We found it necessary to permit the pressure to equalize between the cuvette and the atmosphere every 10 min. Results were calculated essentially as described previously except that net  $CO_2$  uptake was estimated from a pressure-versus-flow calibration of the capillary leak and from the pressure of  $CO_2$  required to maintain a given steady-state  $CO_2$  concentration.

## RESULTS

Figure 35 illustrates the results obtained under rate-limiting light intensities with a detached leaf of *Hirschfeldia incana* maintained under illumination at  $20 \text{ nE cm}^{-2}\text{s}^{-1}$ . The rate of photosynthetic oxygen production is independent of the  $CO_2$  concentration at these conditions. This result is expected, since the rate of electron transport is light limited and unaffected by the nature of the acceptor for these electrons. The net rate of  $CO_2$  uptake, however, is dramatically affected by the  $CO_2$  concentration. At the  $CO_2$  compensation point there is of course no net uptake of  $CO_2$ , and this uptake increases hyperbolically with increasing  $CO_2$  concentration. This result is similar to that reported by Ehleringer and Björkman (1977), who examined the quantum yield for  $CO_2$  fixation by leaves of  $C_3$  plants. They hypothesized that the increased  $CO_2$  uptake at high  $CO_2$  concentrations under light-limited conditions was the result of inhibition of photorespiration by high  $CO_2$ . Measurement of photorespiratory oxygen uptake, also shown in Fig. 35, confirms this hypothesis. Increases in the net uptake of  $CO_2$  correspond exactly to decreases in the uptake of  $O_2$  such that the net exchange of  $O_2$  and  $CO_2$  are mirror images of each other [(net  $O_2$  exchange) = -(net  $CO_2$

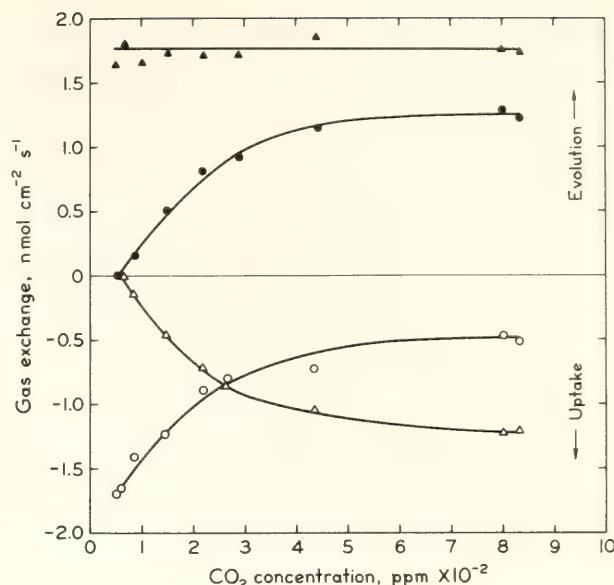


Fig. 35. Simultaneous measurement of: oxygen uptake (○); oxygen production (▲); net oxygen production (●), and net  $CO_2$  uptake (△) by a detached leaf of *Hirschfeldia incana* as a function of  $CO_2$  concentration. Measurements were conducted at  $25^\circ C$  and a light intensity of  $20 \text{ nE cm}^{-2}\text{s}^{-1}$ .

exchange)] over this range of  $CO_2$  concentrations.

Measurements conducted with the  $C_4$  plant *Amaranthus edulis*, which is thought to have reduced photorespiration and the quantum yield of which is independent of  $CO_2$  concentration (Ehleringer and Björkman, 1977), did not show  $CO_2$ -dependent oxygen uptake (data not shown). The fixation of  $^{18}O_2$  and the flux of  $^{18}O$  into glycine were compared in intact spinach leaves (Lorimer, Berry, and Osmond, unpublished), and the results of these studies confirm that inhibition of  $O_2$  uptake by high  $CO_2$  concentrations corresponds to inhibition of the photorespiratory flux of  $O_2$  into glycine.

## CONCLUSIONS

These results provide conclusive proof that photorespiration in  $C_3$  plants is inhibited by high  $CO_2$  concentrations. This result provides further evidence that photorespiration is regulated by  $CO_2$  and  $O_2$  concentration through their effect on

the reactions catalyzed by RuP<sub>2</sub> carboxylase-oxygenase as described by Lorimer *et al.* (1978).

## REFERENCES

- Badger, M. R., and T. J. Andrews, *Biochem. Biophys. Res. Commun.*, **60**, 204–210, 1974.
- Berry, J. A., C. B. Osmond, and G. H. Lorimer, *Plant Physiol.*, **62**, 954–967, 1978.
- Bowes, G., W. L. Ogren, and R. H. Hageman, *Biochem. Biophys. Res. Commun.*, **45**, 716–722, 1971.
- Ehleringer, J., and O. Björkman, *Plant Physiol.*, **59**, 86–90, 1977.
- Laing, W. A., W. L. Ogren, and R. H. Hageman, *Plant Physiol.*, **54**, 678–685, 1974.
- Lorimer, G. H., T. J. Andrews, and N. E. Tolbert, *Biochemistry*, **12**, 18–23, 1973.
- Lorimer, G. H., K. C. Woo, J. A. Berry, and C. B. Osmond, in *Photosynthesis*, **77**, D. O. Hall, J. Coombs, and T. W. Goodwin, eds., pp. 311–322, The Biochemical Society, London 1978.

# PHASE TRANSITIONS IN THYLAKOID MEMBRANES AND VESICLES PREPARED FROM LIPIDS SEPARATED FROM *Synechococcus lividus* GROWN AT 55° AND 38°C

David C. Fork and Gijsbert van Ginkel

We have been investigating the relationship between the physical phase of the thylakoid membrane lipids and photosynthetic activity in a variety of plants (*Year Book 74*, 766–776; *Year Book 75*, 465–472; *Year Book 76*, 220–235; *Year Book 77*, 283–291). Recently we have studied the obligate thermophilic blue-green alga *Synechococcus lividus*, which can grow photosynthetically at extremely high temperatures (Fork *et al.*, 1979). This alga was found to contain only four major lipids: monogalactosyldiglyceride (MGDG), digalactosyldiglyceride (DGDG), sulfoquinovosyldiglyceride (SL), and phosphatidylglycerol (PL). Moreover, the fatty acid composition of these lipids is very simple and consists of only saturated and monounsaturated fatty acids of the type 16:0, 18:0 and 16:1, 18:1, respectively.

Studies of photosynthetic activity as a function of temperature with cells grown at 55°C revealed discontinuities in Arrhenius plots at 43°C and perhaps at 26°C for electron transport between the two photosystems of photosynthesis (measured as cytochrome *f* reduction) and a

discontinuity at 44°C for the State 1–State 2 shift in light energy redistribution between the two photosystems (Fork *et al.*, 1979). For cells grown at 38°C the breaks in the Arrhenius plots for electron transport appeared around 37°C and possibly at 27°C and for the State 1–State 2 shift the break points were seen near 37°C and possibly at 25–27°C (Fork *et al.*, 1979).

Phase transitions in intact cells were detected by following the fluorescence of chlorophyll *a* in cells to which DCMU [3-(3,4-dichlorophenyl)-1,1-dimethylurea] had been added to eliminate fluorescence variations produced by electron transport (Murata *et al.*, 1975). Cells grown at 55°C showed a phase transition at 40–43°C. However, for cells grown at 38°C no clear maxima or shoulders that indicate phase transitions were seen in the curves of fluorescence as a function of temperatures, although maxima or shoulders were seen around 25°C.

In this investigation we prepared thylakoid membranes from *S. lividus* grown at 55°C and 38°C essentially according to the procedures described by Ono and



Murata (1979) by using lysozyme treatment followed by physical disruption in the French pressure cell. Lipids from cells grown at both temperatures were extracted in chloroform/methanol (2:1) and fractionated on silicic acid columns using chloroform to elute neutral lipids, acetone to elute glycolipids (MGDG,

DGDG, and SL), and methanol to elute the phospholipids (PL). Lipid vesicles were prepared from the separated lipids by shaking and sonicating them in buffer solution. The temperature dependence of fluorescence was measured in thylakoid membrane preparations after addition of DCMU (Fig. 36).

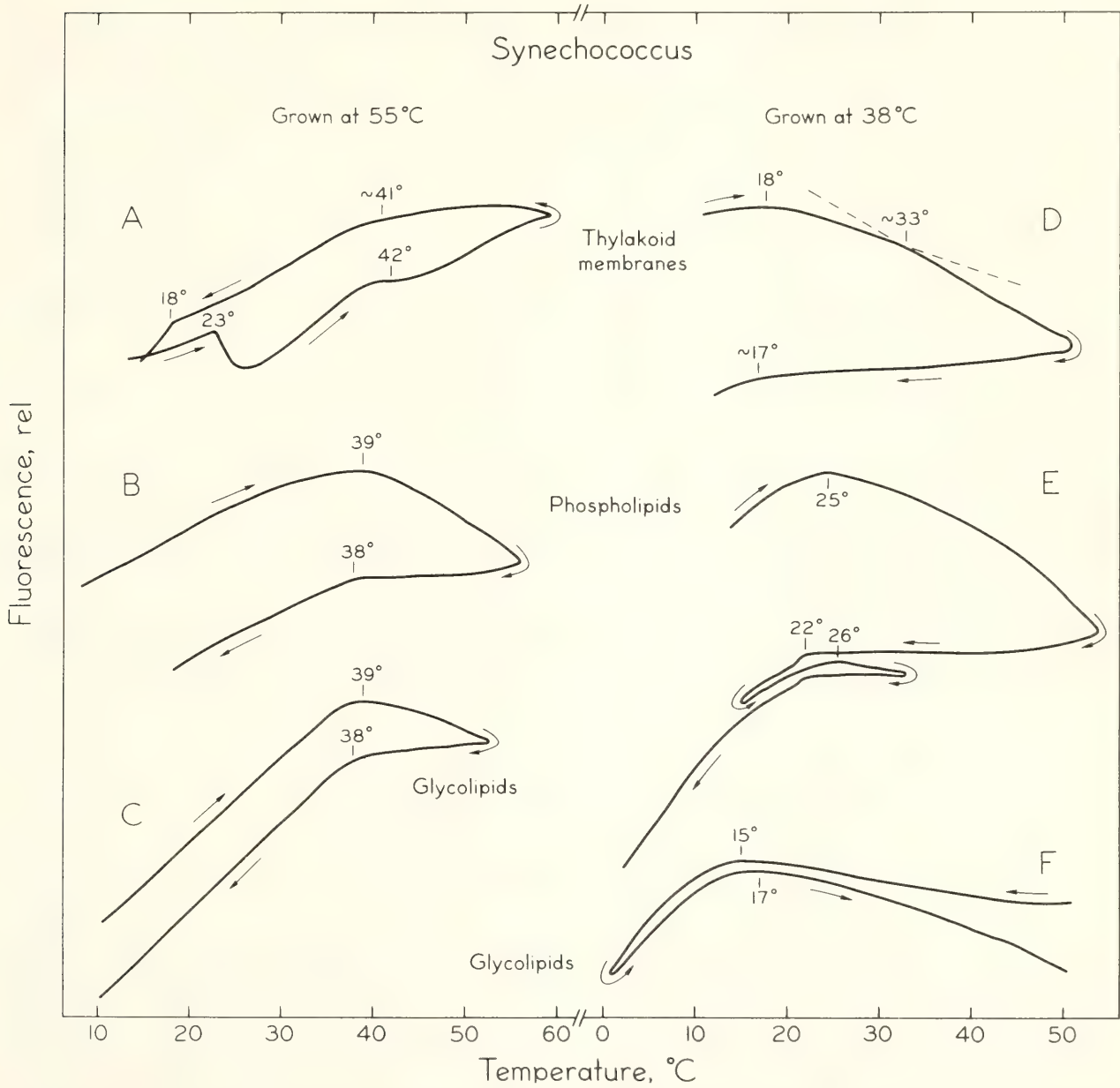


Fig. 36. Temperature dependence of chlorophyll *a* fluorescence in thylakoid membranes and in vesicles prepared from lipids extracted from cells of *Synechococcus lividus* grown at 55°C and 38°C. Thylakoid membranes were treated with 20  $\mu$ M DCMU to inhibit electron transport. The separated phospholipids and glycolipids containing a small amount of added sunflower chlorophyll *a* were suspended in 10  $\mu$ M phosphate buffer (pH 6.5), shaken with glass beads, and sonicated for several minutes to form vesicles. The lipid:chlorophyll ratio (W/W) was 400:1 for parts B and C, 100:1 for part E, and 60:1 for part F. Fluorescence was excited at 430 and 433 nm and measured at 684 and 672 nm on thylakoid membranes and lipid vesicles, respectively. Arrows indicate the direction of the temperature change.

In thylakoid membrane preparations made from cells grown at 55°C a peak or shoulder was seen near 23° and 42°C upon increasing the temperature and at 41° and 18°C upon decreasing the temperature (Figure 36A). Phase transitions in the range 37–39°C were seen in the phospholipid and glycolipid vesicle preparations made from lipids extracted from *Synechococcus* grown at the same temperature. No changes were seen around 25°C. Thus it would appear likely that the changes of photosynthetic activity around 40–43°C seen in cells results from phase transitions in the bulk lipids of the thylakoid membranes. The phase transitions of the lipid vesicles are a few degrees below the transitions observed in vivo. The difference may be caused by extraction and purification of these lipids from other thylakoid membrane components that may alter the characteristic behavior of lipids in vivo as a function of temperature.

The thylakoid membranes prepared from cells grown at 38°C had a broad shoulder and a peak near 33° and 18°C, respectively (Figure 36D), while the vesicles prepared from the phospholipids had reversible phase transitions at 22°C upon decreasing the temperature and at

24.5–25.5°C upon increasing the temperature. The glycolipids (Figure 36F), by contrast, more closely matched the result obtained from the thylakoid membranes (Figure 36D) and had a broad transition centered around 15–17°C. There was no evidence for a shoulder at higher temperatures. As mentioned previously, the Arrhenius plots of photosynthetic activity indicated breaks near 37° and 27°C.

Although there is a good correlation between the temperature at which changes of photosynthetic activities are seen in cells grown at 55°C and the temperatures of the phase transitions in these cells, thylakoid membranes and lipid vesicles, such an association has yet to be made for cells grown at 38°C. Further studies are in progress to provide answers to these questions.

#### REFERENCES

- Fork, D. C., N. Murata, and N. Sato, *Plant Physiol.*, **63**, 524–530, 1979.  
 Murata, N., J. H. Troughton, and D. C. Fork, *Plant Physiol.*, **56**, 508–517, 1975.  
 Ono, T., and N. Murata, *Biochim. Biophys. Acta*, **545**, 69–76, 1979.

### KINETIC IDENTIFICATION OF COMPONENT X AS P430: ACCEPTOR OF PHOTOSYSTEM I

*Tetsuo Hiyama\* and David C. Fork*

The primary photochemical reaction of photosystem I in green plant photosynthesis involves the photooxidation of the photochemical reaction center pigment, P700, most likely a form of chlorophyll *a* with the concomitant reduction of the primary electron acceptor, the identity of which is still unclear. In recent years four possibilities for the primary acceptor have been proposed: (1)

an iron-sulfur center called Center A by Malkin and Bearden (1971); (2) another iron-sulfur center, called Center B by Evans *et al.* (1974); (3) a center called component X by McIntosh *et al.* (1975); and (4) a pigment called P430 by Hiyama and Ke (1971).

None of these proposed acceptors has been isolated and characterized according to its chemical identity. All of them except P430 require for their detection the technique of electron paramagnetic

\* Department of Biochemistry, Saitama University, Urawa, Japan.



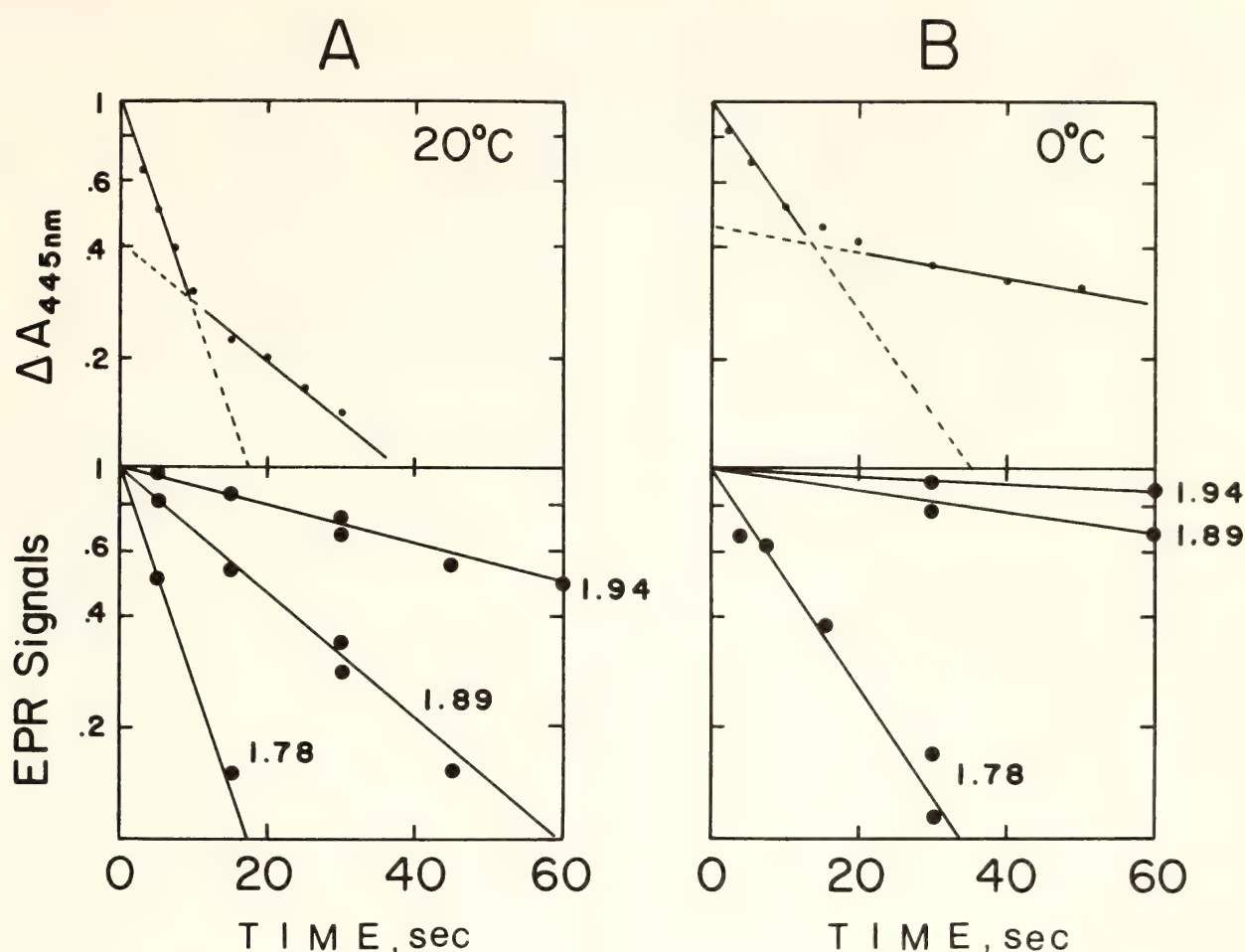


Fig. 37. A comparison of the recovery kinetics on semi-logarithmic plots of the absorbance changes at 445 nm and epr signals at  $g = 1.78, 1.89$ , and  $1.94$ . The reaction mixture contained Fraction C prepared from *Nostoc muscorum* (see text),  $550 \mu\text{g}$  chlorophyll;  $50 \text{ mM}$  Tricine buffer, pH 7.6;  $10 \text{ mM}$   $\text{MgCl}_2$ ;  $200 \mu\text{M}$  sodium dichlorophenol-indophenol;  $10 \text{ mM}$  sodium ascorbate,  $13 \text{ units/ml}$  glucose oxidase,  $10 \text{ mM}$  glucose; and  $0.1 \text{ mg/ml}$  catalase. The epr spectra were recorded at a sample temperature of  $20^\circ\text{K}$ , a magnetic field modulation of  $10 \text{ Gauss}$  at  $100 \text{ KHz}$  and at a microwave power of  $13 \text{ mW}$ . The peak heights at each  $g$  value in the first derivative epr spectra were normalized at  $0 \text{ s}$  and plotted on a relative scale. The kinetics of absorbance changes at  $445 \text{ nm}$  induced by continuous illumination were followed in the dark as described in the text. Optical pathlengths,  $1 \text{ mm}$ .

resonance (epr) spectroscopy at extremely low temperatures that can be attained only by using liquid helium. P430, on the other hand, has been studied extensively by spectrophotometric methods at room temperatures but not at temperatures below the freezing point. Thus the relationship of P430 with other species that have been detected only by the cryogenic epr technique has not yet been established.

In this study, we employed special experimental conditions, under which the rates of light-induced changes and subsequent dark relaxations at physiological temperatures were slow enough so

that the kinetics could be studied not only by spectrophotometry but also by cryogenic epr spectroscopy in combination with a quick-freeze technique.

In these experiments the reaction mixture consisted of membrane fragments of a blue-green alga, *Nostoc muscorum* (Arnon *et al.*, 1974) under strictly anaerobic conditions, and a highly efficient electron donor system (2,6-dichlorophenol indophenol and ascorbate) with no external electron acceptor. The sample was illuminated by intense red light for 30 seconds either at  $20^\circ\text{C}$  or  $0^\circ\text{C}$ , then quickly frozen in liquid nitrogen in the subsequent dark period. Epr spectra

were recorded subsequently with this frozen sample at liquid helium temperatures.

The companion absorption change measurements, also at 20° and 0°C, were done with the same sample used in the epr experiments. After illumination (30 s), measurements of the dark-recovery kinetics of the 445-nm absorbance change were made in a high sensitivity spectrophotometer equipped with a temperature control (Murata and Fork, 1975).

Figure 37 compares the kinetics of the dark recovery of Center A ( $g = 1.94$ ), Center B ( $g = 1.89$ ) and Component X ( $g = 1.78$ ) detected by epr and the dark recovery kinetics of the 445-nm absorbance change. It should be noted that kinetics of the absorbance changes ( $\Delta A$  445 nm) were biphasic, particularly at 0°C. More importantly, the fast phase of these absorbance changes corresponds kinetically to the recovery of Component X ( $g = 1.78$ ) both at 20° and at 0°C. The slow phase in the figure seemed to correspond kinetically with Center B.

Moreover, the difference spectrum of the fast phase, shown in Figure 38, closely resembled that of P430, obtained by using flash kinetic spectroscopy in the original P430 study (Hiyama and Ke, 1971a). The spectrum of the slow phase was quite different, however (Figure 38).

From these results, we conclude that Component X, which was detected first by epr in 1975 (McIntosh *et al.*, 1975), is most likely P430, which was studied spectrophotometrically several years earlier (Hiyama and Ke, 1971 and 1971a). By combining the evidence for both P430 and Component X, we propose that P430 (Component X) is more closely associated with the primary acceptor of photosystem I than is Center A or B, or that it may be the primary acceptor itself. Such evidence includes the extremely low redox potential obtained for Component X (McIntosh *et al.*, 1975) and extensive evidence obtained at room temperatures for P430

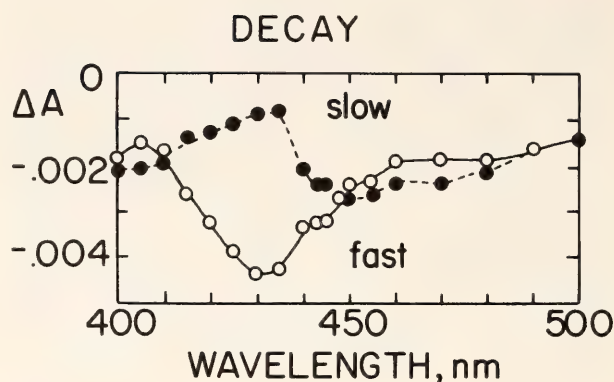


Figure 38. Difference spectra of the fast and slow decay phases of the 445-nm absorbance change produced in *Nostoc* particles as described in the text. The "fast" phase was the difference between the 10 and the 0 s points after the cessation of illumination. The "slow" phase was the difference between the 10 s point and the dark baseline.

(Hiyama and Ke, 1971a). Furthermore, the information on the  $g$  values ( $g = 1.78, 1.88, 2.08$  for Component X) and the optical difference spectrum (a broad negative peak around 430 nm for P430) will also help to elucidate the chemical identity of P430.

More details of this study will be reported in *Arch. Biochem. Biophys.*, in press, 1979. The work was supported in part by a T. H. Foundation grant and by a National Science Foundation grant (76-84395) to Professor D. I. Arnon.

#### REFERENCES

- Arnon, D. I., B. D. McSwain, H. Y. Tsujimoto, and K. Wada, *Biochim. Biophys. Acta*, **357**, 231–245, 1974.
- Evans, M. C. W., S. G. Reeves, and R. Cammack, *FEBS Lett.* **49**, 111–114, 1974.
- Hiyama, T., and B. Ke, *Proc. Nat. Acad. Sci. USA*, **68**, 1010–1013, 1971.
- Hiyama, T., and B. Ke, *Arch. Biochem. Biophys.*, **147**, 99–108, 1971a.
- Malkin, R., and A. J. Bearden, *Proc. Nat. Acad. Sci. USA*, **68**, 16–19, 1971.
- McIntosh, A. R., M. Chu, and J. R. Bolton, *Biochim. Biophys. Acta*, **376**, 308–314, 1975.
- Murata, N., and D. C. Fork, *Plant Physiol.*, **56**, 508–517, 1975.



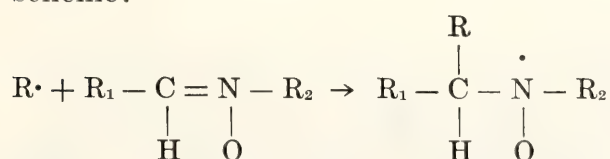
# LIGHT-INDUCED FORMATION OF OXYGEN RADICALS IN SYSTEMS CONTAINING CHLOROPHYLL

*Gijsbert van Ginkel and John K. Raison*

Last year we reported (van Ginkel, Brown, and van Ginkel, *Year Book 77*, pp. 294–302) that isolated photosystem I particles show enhanced light-induced  $H^+$ - and  $O_2$ -uptake in the presence of ascorbate upon combination with artificial vesicular lipid membranes or Triton X-100 micelles. Since uncouplers had no effect and the same photochemical reactions also occur in chlorophyll-lipid vesicles, there is no direct correlation with the photochemistry of PS-1. It has been suggested that the described photochemical reactions are caused by the reaction of ascorbate with oxygen radicals formed upon interaction of chlorophyll and oxygen in light (van Ginkel, 1979).  $O_2^-$ ,  $HO_2^\bullet$ ,  $OH^\bullet$ , and singlet oxygen were considered likely candidates for the reactive oxygen radicals. Because the lifetime of these oxygen radicals is generally very short, their concentration is too low to be detected directly by, for example, epr spectroscopy. Therefore, indirect methods are usually applied to demonstrate their formation.

This problem has been overcome by the introduction of the spin-trap technique, which has been applied to biological systems (Harbour and Bolton, 1975; Saprin and Piette, 1977). Most of the spin-traps used are molecules containing an NO-group, which, upon addition of a labile free radical, form stable nitroxides that accumulate and can easily be detected by epr.

The general mechanism of spin-trapping can be illustrated by the following scheme:



Such a reaction scheme involves the

trapping of a reactive free radical by an addition reaction so that a more stable radical is produced which is detectable by epr spectroscopy. Since both the  $\beta$ -proton hyperfine splitting and the nitrogen hyperfine splitting of the nitroxide spin-adduct are very sensitive to the nature of  $R^\bullet$  (Janzen and Liu, 1973) this information can in favorable cases be used to identify  $R^\bullet$ . However, the technique has some limitations, depending on the spin-trap and the reaction conditions used (Lai and Piette, 1977; Buettner and Oberley, 1978; Saprin and Piette, 1977).

With the spin-trap 5,5'-dimethyl-1-pyrroline-1-oxide (DMPO) Harbour and Bolton showed that chloroplasts produce superoxide in light (Harbour and Bolton, 1975). In a more recent publication the same investigators obtained evidence, also with DMPO, that hydroxyl radicals are produced in light by chlorophyll in 4% Triton X-100, chloroplasts, and chromatophores of *Rhodospseudomonas spheroides* (Harbour and Bolton, 1978). In the case of chlorophyll in Triton X-100 no DMPO-superoxide spectrum was detected, whereas in chloroplasts only a very small hydroxyl adduct was observed.

We carried out the investigations described here to identify the oxygen radicals that are formed upon interaction of photosystem I particles, chlorophyll-lipid vesicles, or chloroplasts with oxygen in light. For that purpose the spin-traps phenyl tertiary butylnitron (PBN) and DMPO were used as well as the spin-probe 1,2-dihydroxybenzene-3,5-disulfonate (Tiron). The latter has been reported to be an  $O_2^-$ -specific spin-probe (Greenstock and Miller, 1975; Miller and Macdowall, 1975).

## MATERIALS AND METHODS

Photosystem I particles were isolated according to the procedure of Shiozawa *et al.* (1974). The characteristics of these particles have been described elsewhere (Brown and van Ginkel, *Year Book* 77, pp. 298–302; van Ginkel and Brown, 1978; van Ginkel, 1979).

Spinach chloroplasts were isolated according to standard procedures (Waring blender, cheese cloth filtration, centrifugation) in a medium containing 0.4 M sucrose, 50 mM phosphate pH 7.5. After the chloroplasts had been washed twice in the grinding medium, they were stored on ice in the dark in a medium containing 0.2 M KCl, 2 mM phosphate pH 7.5.

Osmotically shocked chloroplasts were prepared by resuspending them in distilled water and then putting them on ice for half an hour in the dark. The thylakoid membrane fragments were collected by centrifugation and stored in 0.2 M KCl, 2 mM phosphate pH 7.5 on ice in the dark.

Photosystem I lipid vesicles or chlorophyll-lipid vesicles were prepared by means of the French press method or by sonication, as described before (van Ginkel, *Year Book* 77, pp. 294–297, van Ginkel, 1979).

Epr spectra were recorded on a Varian E 112 spectrometer connected to a Nicolet

1180 computer for signal averaging. The samples were flushed with oxygen for about 2–3 minutes before being irradiated in the cavity of the epr spectrometer. The samples were irradiated with red light (Schott RG-2 filter) from a Leitz slide projector containing a 500 W tungsten bulb. The light source was placed about 60–80 cm from the sample in the cavity. Pulse-radiolysis measurements were done with a 2-MeV Van de Graaff accelerator from the Department of Molecular Biophysics, State University of Utrecht, The Netherlands.

## RESULTS

*Data Obtained with PBN*

A known amount of solid PBN was dissolved directly in a given sample to a final concentration of 0.12–0.15 M. Care was taken to exclude methanol, which forms an adduct with PBN (Saprin and Piette, 1977). With chloroplasts, whether they were whole or broken, no epr spectrum could be obtained at all with PBN, presumably because any PBN radicals would be immediately reduced by photosynthetic reductants formed upon irradiation of chloroplasts. Control experiments showed that other epr probes used for measuring the viscosity of lipid membranes (Raison and Berry, *Year Book*

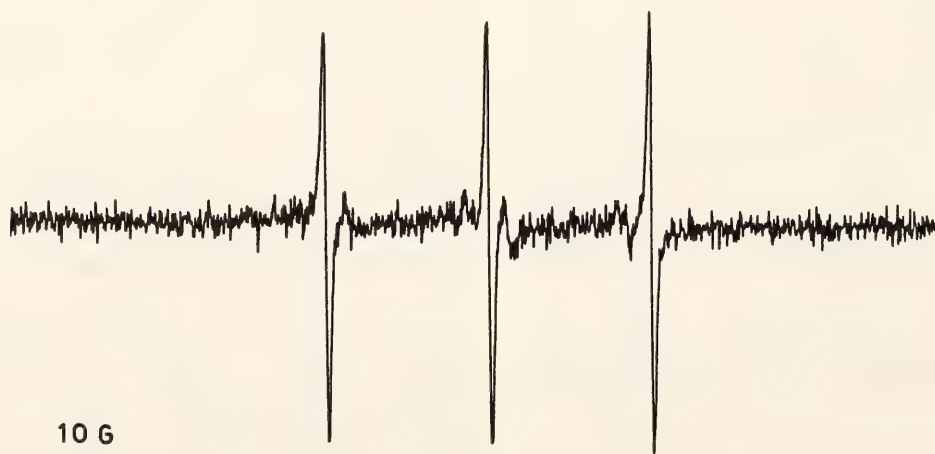


Fig. 39. epr spectrum obtained upon irradiation of PS-I lipid vesicles ( $30 \mu\text{g chl}\cdot\text{ml}^{-1}$  or chlorophyll-lipid vesicles ( $100 \mu\text{g chl}\cdot\text{ml}^{-1}$ ) in 15–25 mM phosphate buffer pH 7.5 in the presence of oxygen and 0.12 M PBN. Formation of the spectrum occurs in the presence or absence of 0.1–0.2 mM methyl viologen and 5–20 mM  $\text{K}_4\text{Fe}(\text{CN})_6$ .



77, pp. 276–282) are destroyed very rapidly (presumably by reduction) by these chloroplasts in light.

In contrast, irradiation of photosystem I lipid vesicles and chlorophyll-lipid vesicles with PBN resulted in a product whose spectrum is shown in Fig. 39. Formation of this spectrum is completely inhibited by catalase but not by superoxide dismutase (SOD). This observation as well as the shape of the spectrum indicate that Fig. 39 is not the spectrum of a PBN-radical adduct but is very probably the spectrum of a peroxide-induced disintegration product of PBN. Evidence obtained by other investigators supports this conclusion (L. H. Piette, personal communication). We conclude that PBN is not a useful spin-trap in investigations of systems containing chlorophyll.

#### *Data Obtained with DMPO*

DMPO is readily soluble in water, and the spectra of its adducts are fairly distinct. However, DMPO also has some

limitations that require experimental precautions (Lai and Piette, 1977, Buettner and Oberley, 1978). When chloroplasts were illuminated in the presence of DMPO and  $\text{CN}^-$  to inhibit catalase and SOD activities of the intact chloroplast (van Ginkel and Brown, 1978), we obtained an epr spectrum as shown in Fig. 40a. This is probably a mixed spectrum of DMPO-superoxide and DMPO-OH adducts. We reach this conclusion from comparison of this spectrum with a number of published DMPO spectra (Harbour and Bolton, 1978; Buettner and Oberley, 1978, 1979; Buettner *et al.*, 1978; Lai and Piette, 1977, 1978). The spectrum of Fig. 40a contains a very distinct contribution of the DMPO-OH adduct, a result that is not surprising. Under conditions in which catalase and SOD are inhibited, the iron-catalyzed Haber-Weiss and Fenton reaction may produce hydroxyl radicals (Lai and Piette, 1978; Buettner *et al.*, 1978; Koppenol and Butler, 1977). We were unable to obtain an epr spectrum of

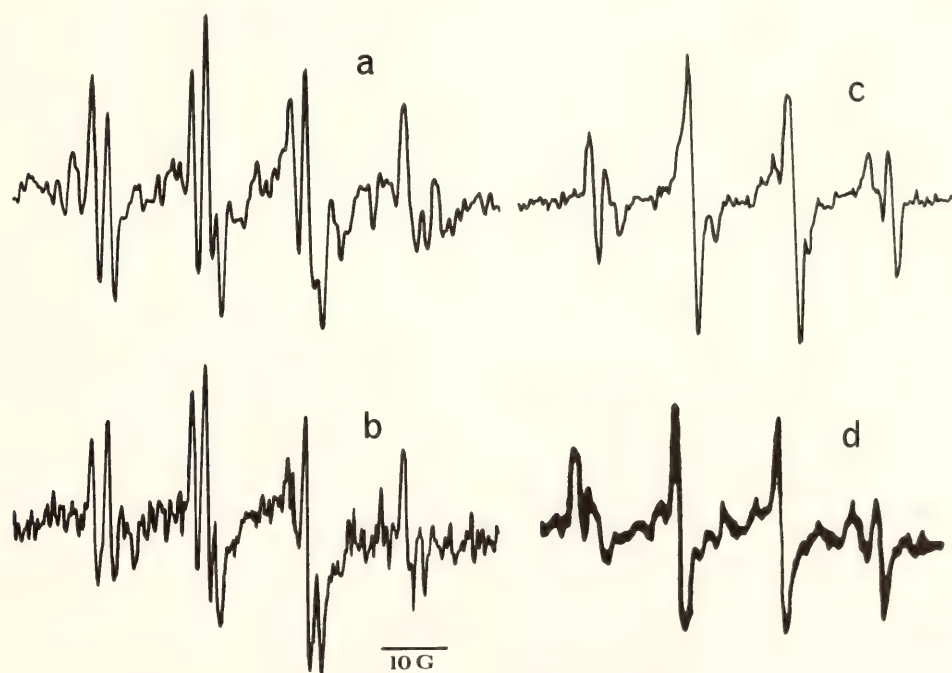


Fig. 40. epr spectra obtained upon irradiation of (a) chloroplasts ( $100 \mu\text{g chl}\cdot\text{ml}^{-1}$ ) + 5 mM KCN, (b) PS-I particles ( $30 \mu\text{g chl}$ ) + 5 mM KCN, (c) chlorophyll-lipid vesicles ( $100 \mu\text{g chl}\cdot\text{ml}^{-1}$ ) in the presence of oxygen and DMPO (10–25 mM). Spectrum (d) is a photographic copy of a mixed DMPO-OH-DMPO-superoxide spectrum published by Buettner *et al.* (1978); see their figure 1c. This spectrum was obtained upon incubation of DMPO in the presence of xanthine-xanthine oxidase and  $10^{-4}$  M iron (II)-ions.

DMPO-superoxide only, like that reported by Harbour and Bolton (1975), under our reaction conditions with chloroplasts.

In the presence of DMPO, photosystem I particles yield an epr spectrum identical to the one obtained with chloroplasts (Fig. 40b). This result suggests that superoxide and hydroxyl radical formation in the chloroplast is caused by the photochemistry of photosystem I. It is not definite proof, however, as is shown by the epr spectrum obtained upon irradiation of chlorophyll-lipid vesicles in the presence of DMPO (Fig. 40c). Although this spectrum differs slightly from the spectra shown in Figs. 40a and 40b, it could also be considered a mixed DMPO-OH-DMPO-superoxide spectrum, being identical to a mixed spectrum of these adducts published by Buettner *et al.* (1978) (see their fig. 1c). For comparison we have plotted their spectrum in Fig. 40d.

If the interpretation of this spectrum by Buettner *et al.* is correct, our results indicate that chlorophyll in an artificial lipid membrane also catalyzes the formation of superoxide and hydroxyl radicals upon interaction with oxygen in the light. Therefore, one cannot exclude the possibility that light-induced formation of these radicals in chloroplasts or chloroplast fragments is catalyzed, at least in part, by chlorophyll that is not connected with the photosynthetic pathway. This is especially likely with thylakoid membranes obtained as a result of harsh mechanical or detergent treatments.

Formation of superoxide in chlorophyll-lipid vesicles, which was reported before on the basis of data obtained with SOD (van Ginkel, 1979) can be explained in two ways:

1. Chlorophyll excited by light directly transfers an electron to oxygen. An increasing amount of data show that chlorophyll in an artificial lipid membrane catalyzes light-induced electron transfer to appropriate electron acceptors (Oettmeier *et al.*, 1976; Toyoshima *et al.*, 1978;

Tomkiewicz and Corker, 1974), indicating that this is a possible mechanism. However, there may be another mechanism involved.

2. Superoxide could be formed as a secondary product by the reaction of hydroxyl radicals with hydrogen peroxide. The rate constant of this reaction is very low for an OH• reaction ( $k \approx 1 \times 10^7 \text{ M}^{-1}\text{s}^{-1}$ ; see Farhataziz and Ross, 1977). It is doubtful, therefore, that this reaction can produce superoxide in sufficient amounts to permit detection with DMPO. Another complication here is that the lifetime of the DMPO-superoxide adduct is very short (Buettner and Oberley, 1978) and DMPO itself is labile in certain buffers (Lai and Piette, 1977). Therefore, low superoxide concentrations can easily escape detection with DMPO. This may be the reason that Harbour and Bolton (1978) did not observe formation of the DMPO-superoxide adduct upon irradiation of chlorophyll in 4% Triton X-100, although on the basis of their proposed reaction mechanism, formation of superoxide could be expected by the reaction between OH• and  $\text{H}_2\text{O}_2$  mentioned above.

In our view these arguments lend support to the first explanation. However, further investigations are necessary to establish the exact reaction mechanism.

#### *Data Obtained with Tiron*

Tiron has been introduced as a spin-probe for  $\text{O}_2^-$  because it is rapidly oxidized by  $\text{O}_2^-$  to its semiquinone, a stable free radical at pH 7 with a characteristic epr spectrum (Miller and Rapp, 1973; Greenstock and Miller, 1975). It has been used to demonstrate superoxide formation in chloroplasts (Miller and Macdowall, 1975).

Therefore, we also used Tiron for our samples. In all our experiments with chloroplasts, photosystem I particles, and chlorophyll-lipid vesicles we obtained an epr spectrum that was indicative of the formation of the Tiron-semiquinone (Fig. 41a). Addition of catalase or SOD to



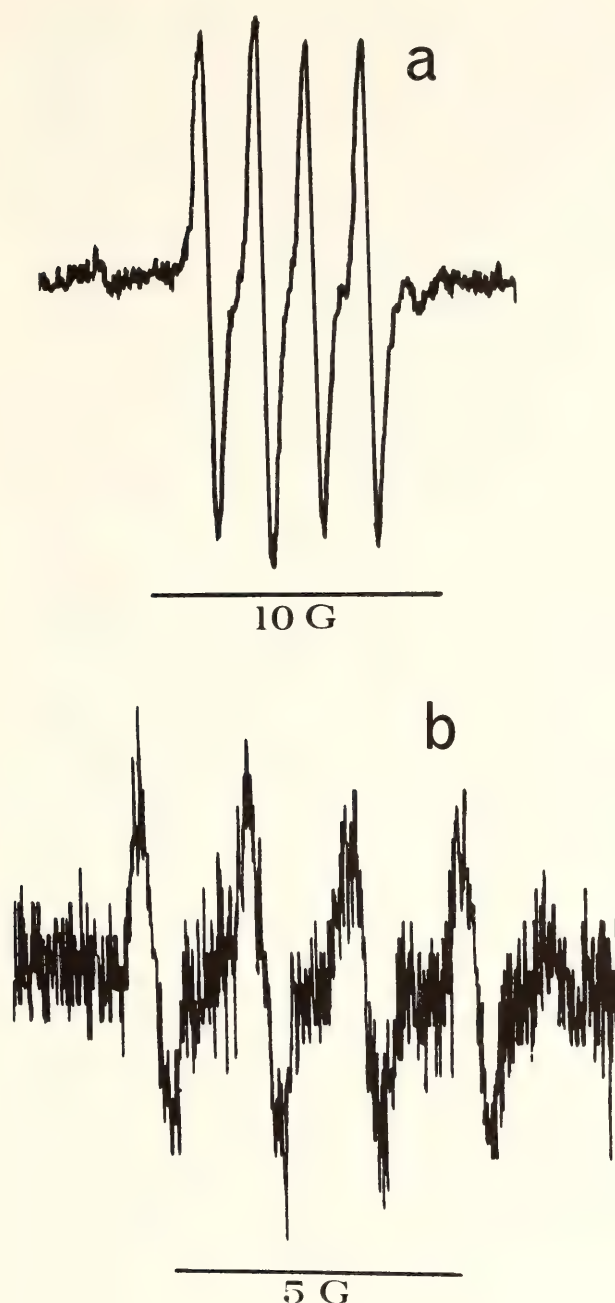


Fig. 41. epr spectrum obtained upon irradiation of chloroplasts, PS-I particles or chlorophyll-lipid vesicles in the presence of oxygen and Tiron (4 mM). The spectrum shown (41a) is the one obtained with chlorophyll-lipid vesicles ( $200 \mu\text{g chl}\cdot\text{ml}^{-1}$ ). Measurement of this curve under identical conditions, but in the presence of 20 mM thiourea, yields an epr spectrum as shown in Fig. 41b. Ethanol in a final concentration of 1% has a similar effect.

chlorophyll-lipid vesicles does not significantly change the intensity of the Tiron-semiquinone epr spectrum, whereas hydroxyl radical scavengers such as thiourea or ethanol strongly affect the formation of the Tiron semiquinone (Fig.

41b). These data suggest that OH-radicals can also oxidize Tiron to its semiquinone at a high rate, yielding the same epr spectrum as that produced when Tiron is oxidized by  $\text{O}_2^-$ .

Pulse-radiolysis measurements done with Dr. Johan van Leeuwen, Department of Molecular Biophysics, State University of Utrecht, The Netherlands, showed that the rate constant for the reaction of Tiron with OH $\cdot$ -radicals is  $8.2 \times 10^9 \text{ M}^{-1}\cdot\text{s}^{-1}$ , a rate constant of  $6.6 \times 10^9 \text{ M}^{-1}\cdot\text{s}^{-1}$  being taken for the reaction of  $\text{CNS}^-$ -ions with OH $\cdot$  (Farhataziz and Ross, 1977).

Greenstock and Miller (1975) measured a rate constant of  $5.0 \times 10^8 \text{ M}^{-1}\cdot\text{s}^{-1}$  for the oxidation of Tiron by  $\text{O}_2^-$ . Our data therefore indicate that the reactivity of Tiron with hydroxyl radicals is much higher than with  $\text{O}_2^-$  and the compound is not a specific spin-probe for  $\text{O}_2^-$  at all. This conclusion is supported by data from a recent publication of Bors *et al.* (1979). These investigators found rate constants of  $1.0 \times 10^9 \text{ M}^{-1}\cdot\text{s}^{-1}$  and  $1.0 \times 10^7 \text{ M}^{-1}\cdot\text{s}^{-1}$  for the reaction of Tiron with OH $\cdot$  and  $\text{O}_2^-$ , respectively. They suggested that ultimately the same semiquinone is formed upon the reaction of Tiron with OH $\cdot$  as upon the reaction of Tiron with  $\text{O}_2^-$ . This suggestion agrees with our observations.

## CONCLUSIONS

The data with DMPO show that hydroxyl and superoxide radicals are formed upon irradiation of chloroplasts, PS-1 particles, and chlorophyll-lipid vesicles. The stimulation of light-induced  $\text{H}^+$ - and  $\text{O}_2$ -uptake in PS-1 lipid vesicles or PS-1 Triton X-100 micelles in the presence of ascorbate, reported before (Brown and van Ginkel, *Year Book* 77, pp. 298–302; van Ginkel, 1979), is therefore very probably caused by the reaction of ascorbate with hydroxyl radicals, which are formed upon the interaction of solubilized chlorophyll and oxygen in

light. Data in the literature indicate that this reaction may cause the observed effects (Fessenden and Verma, 1978; Bielski *et al.*, 1971; Biaglow *et al.*, 1976; Redpath and Wilson, 1973). The reaction is very rapid ( $k = 1.3 \times 10^{10} \text{ M}^{-1}\cdot\text{s}^{-1}$ , see Farhataziz and Ross, 1977). It can explain the inhibiting effect ascorbate has on the photooxidation of chlorophyll, also reported by van Ginkel (1979), since ascorbate scavenges the  $\text{OH}\cdot$  radicals before they are able to react with chlorophyll.

Harbour and Bolton (1978) also suggested that the hydroxyl radical may play a key role in the destruction of chlorophyll. Because the reactivity of ascorbate with hydroxyl radicals is so much higher than with  $\text{O}_2^-$  [ $k = 1.3 \times 10^{10} \text{ M}^{-1}\cdot\text{s}^{-1}$  versus  $2 \times 10^5 \text{ M}^{-1}\cdot\text{s}^{-1}$ , respectively (Farhataziz and Ross, 1977; Nishikimi, 1975), it seems likely that ascorbate is more important as a scavenger for  $\text{OH}\cdot$  in the chloroplast, whereas  $\text{O}_2^-$  is removed by SOD present in photosynthetic membranes (Asada *et al.*, 1977).

Further investigations are required to determine the extent of stimulation either by  $\text{OH}$  radicals or by superoxide of light-induced  $\text{O}_2$  uptake by ascorbate in chloroplasts. The latter reaction is generally assumed to be entirely responsible for that phenomenon (Epel and Neumann, 1973; Allen and Hall, 1973, 1974).

On the basis of the inhibitory effect of azide (a known quencher of singlet oxygen; see Krinsky, 1977) on light-induced  $\text{H}^+$  and  $\text{O}_2$  uptake in chlorophyll-lipid vesicles, one of us suggested that part of the oxidation of ascorbate was caused by singlet oxygen (van Ginkel, 1979). However, the data presented here indicate that the inhibition of these photochemical reactions by azide is probably caused by the competition between azide and ascorbate for the  $\text{OH}$  radicals that have rate constants for reaction with  $\text{OH}\cdot$  of  $k = 1.1 \times 10^{10} \text{ M}^{-1}\cdot\text{s}^{-1}$  and  $k = 1.3 \times 10^{10} \text{ M}^{-1}\cdot\text{s}^{-1}$ , respectively (Farhataziz and Ross, 1977).

The experimental data obtained with PBN show that this compound is not a useful spin-trap in systems containing chlorophyll, since reduction or decomposition reactions prevent the formation of PBN-radical adducts that can be detected by epr spectroscopy.

The results presented also show that Tiron cannot be used as a specific spin-probe for  $\text{O}_2^-$ , since the reactivity of Tiron with  $\text{OH}$  radicals is much higher than with  $\text{O}_2^-$ . Recent data in literature support this conclusion. The Tiron-semiquinone epr spectra obtained with chloroplasts, photosystem I particles, and chlorophyll-lipid vesicles are therefore probably caused entirely by the reaction of hydroxyl radicals with Tiron.

Tiron is a useful epr probe for  $\text{OH}$ -radicals but only if sufficient amounts of SOD are present to prevent oxidation of Tiron by  $\text{O}_2^-$ .

#### ACKNOWLEDGMENTS

We wish to thank Professor R. Holm and Professor S. Boxer of the Chemistry Department at Stanford University for making the Varian E 112 spectrometer available to us, and Dr. Jeanette S. Brown and Ms. Patricia Sullivan for providing PS-1 particles for study.

#### REFERENCES

- Allen, J. F., and D. O. Hall, *Biochem. Biophys. Res. Commun.*, **52**, 856–862, 1973.
- Allen, J. F., and D. O. Hall, *Biochem. Biophys. Res. Commun.*, **58**, 579–585, 1974.
- Asada, K., S. Kanematsu, and K. Uchida, *Arch. Biochem. Biophys.*, **179**, 243–256, 1977.
- Biaglow, J. E., B. Jacobson, and C. Koch, *Biochem. Biophys. Res. Commun.*, **70**, 1316–1323, 1976.
- Bielski, B. H. J., D. A. Comstock, and R. A. Bowen, *J. Amer. Chem. Soc.*, **93**, 5624–5629, 1971.
- Bors, W., M. Saran, and C. Michel, *Bio-*



- chim. Biophys. Acta*, 582, 537-542, 1979.
- Buettner, G. R., and L. W. Oberley, *Biochem. Biophys. Res. Commun.*, 83, 69-74, 1978.
- Buettner, G. R., L. W. Oberley, and S. W. H. Chan Leuthauser, *Photochem. Photobiol.*, 28, 693-695, 1978.
- Buettner, G. R., and L. W. Oberley, *FEBS letters*, 98, 18-21, 1979.
- Epel, B. L., and J. Neumann, *Biochim. Biophys. Acta*, 325, 520-529, 1973.
- Farhataziz, and A. B. Ross, *Selected specific rates of reactions of transients from water in aqueous solution. III. Hydroxyl radical and perhydroxyl radical and their radical ions*, NSRDS-NBS 59, National Bureau of Standards, Washington, 1977.
- Fessenden, R. W., and N. C. Verma, *Biophys. J.*, 24, 93-101, 1978.
- Greenstock, C. L., and R. W. Miller, *Biochim. Biophys. Acta*, 396, 11-16, 1975.
- Harbour, J. R., and J. R. Bolton, *Biochem. Biophys. Res. Commun.*, 64, 803-807, 1975.
- Harbour, J. R., and J. R. Bolton, *Photochem. Photobiol.*, 28, 213-235, 1978.
- Janzen, E. G., and J. L. I. Ping Liu, *J. Magn. Resonance*, 9, 510-513, 1973.
- Koppenol, W. H., and J. Butler, *FEBS letters*, 83, 1-6, 1977.
- Krinsky, N. I., *Trends in Biochemistry*, 2, 35-38, 1977.
- Lai, Ching-san, and L. H. Piette, *Biochem. Biophys. Res. Commun.*, 78, 51-59, 1977.
- Lai, Ching-san, and L. H. Piette, *Arch. Biochem. Biophys.*, 190, 27-38, 1978.
- Miller, R. W., and U. Rapp, *J. Biol. Chem.*, 248, 6084-6090, 1973.
- Miller, R. W., and F. D. H. Macdowall, *Biochim. Biophys. Acta*, 387, 176-187, 1975.
- Nishikimi, M., *Biochem. Biophys. Res. Commun.*, 63, 463-468, 1975.
- Oettmeier, W., J. R. Norris, and J. J. Katz, *Z. Naturforsch.*, 31c, 163-168, 1976.
- Redpath, J. L., and R. L. Wilson, *Int. J. Radiat. Biol.*, 23, 51-65, 1973.
- Saprin, A. N., and L. H. Piette, *Arch. Biochem. Biophys.*, 180, 480-492, 1977.
- Shiozawa, J. A., R. S. Alberte, and J. P. Thornber, *Arch. Biochem. Biophys.*, 165, 388-397, 1974.
- Tomkiewicz, M., and G. Corker, In *Proc. Third Intern. Congr. Photosynthesis Res.*, Avron, M., ed., Elsevier Amsterdam, The Netherlands, pp. 265-272, 1974.
- Toyoshima, Y., and M. Sukigara, *Sixth Intern. Biophysics Congr.*, Kyoto (Japan), Sept. 3-9, Book of Abstracts, 248 pp., 1978.
- van Ginkel, G., and J. S. Brown, *FEBS letters*, 94, 284-287, 1978.
- van Ginkel, G., *Photochem. Photobiol.*, 1979, in press.

## SPECTRAL STUDIES OF TRITON-SOLUBILIZED CHLOROPHYLL-PROTEINS FROM *Euglena* AND ANTENNA CHLOROPHYLL FROM SPINACH

J. S. Brown

Spectroscopic investigations of chlorophyll in biological systems have been carried on in this department for many years. Eventually these studies should lead to a better understanding of the state of chlorophyll in membranes and of the initial steps in photosynthesis.

High pigment concentration and particle size, which can cause flattening of absorption bands, reabsorption of fluorescence, and errors from differential light scattering, may complicate interpretation of spectral measurements of leaves, algae, or even large chloroplast fragments. To

minimize these artifacts, we have been trying to prepare smaller pigmented fractions that retain their original function and state at the molecular level.

Recent results of resonance Raman spectroscopy (Lutz, 1977) have indicated that most of the chlorophyll in plant membranes is bound to protein, and essentially none is covalently linked with itself. Because most chl-protein complexes are strongly hydrophobic, detergent action is necessary to dissociate them. Absorption and fluorescence spectra of chl-protein complexes, dissociated by Triton X-100 and isolated by hydroxylapatite (HAP) chromatography, have been published in *Year Book 73*, p. 694; *Year Book 74*, p. 779; *Year Book 75*, p. 460; and *Year Book 76*, p. 209.

Although these recent studies avoided the errors caused by particle size, new problems may have been introduced by detergent action, which can change the state of chlorophyll and its attachment to proteins. Therefore, new detergent procedures for isolating chl-proteins and ways to characterize them spectroscopically are being investigated.

## RESULTS AND DISCUSSION

### *Effect of Triton on Euglena Chloroplast Membranes*

Absorption, fluorescence excitation, and emission spectra of *Euglena* chloroplasts before and after treatment with

Triton are shown in Fig. 42. The complex absorption spectrum of chloroplast fragments (Fig. 42A) is typical of *Euglena* cells that, because of light-limited growth, have relatively little chl *b* (chl *a/b* = 10). When a computer analysis of a similar spectrum was carried out by French *et al.* (1972), chl *a* components were distinguished with absorption maxima at 662, 670, 678, 683, 692, and 703 nm in addition to chl *b* at 652 nm. The fluorescence emission spectrum was also recorded previously (Brown and Michel-Wolwertz, 1968). New observations are that the emission spectrum is independent of exciting wavelength between 400 and 500 nm and that the absorption and fluorescence excitation spectra are not coincident in this same region. Comparison of the absorption band centered at 436 nm with the excitation maximum at 443 nm suggests that a form of chl *a* absorbing near the latter wavelength is the primary source of emission. No doubt there are several forms of chl *a* absorbing in this region, but their spectral overlap with each other and the carotenoids is too great for them to be distinguished in these curves. The lack of an excitation band at 495 nm indicates that there is little if any energy transfer between carotenoid and chl *a*, but the broad shoulder on the excitation curve between 460 and 490 nm shows some transfer between chl's *b* and *a*.

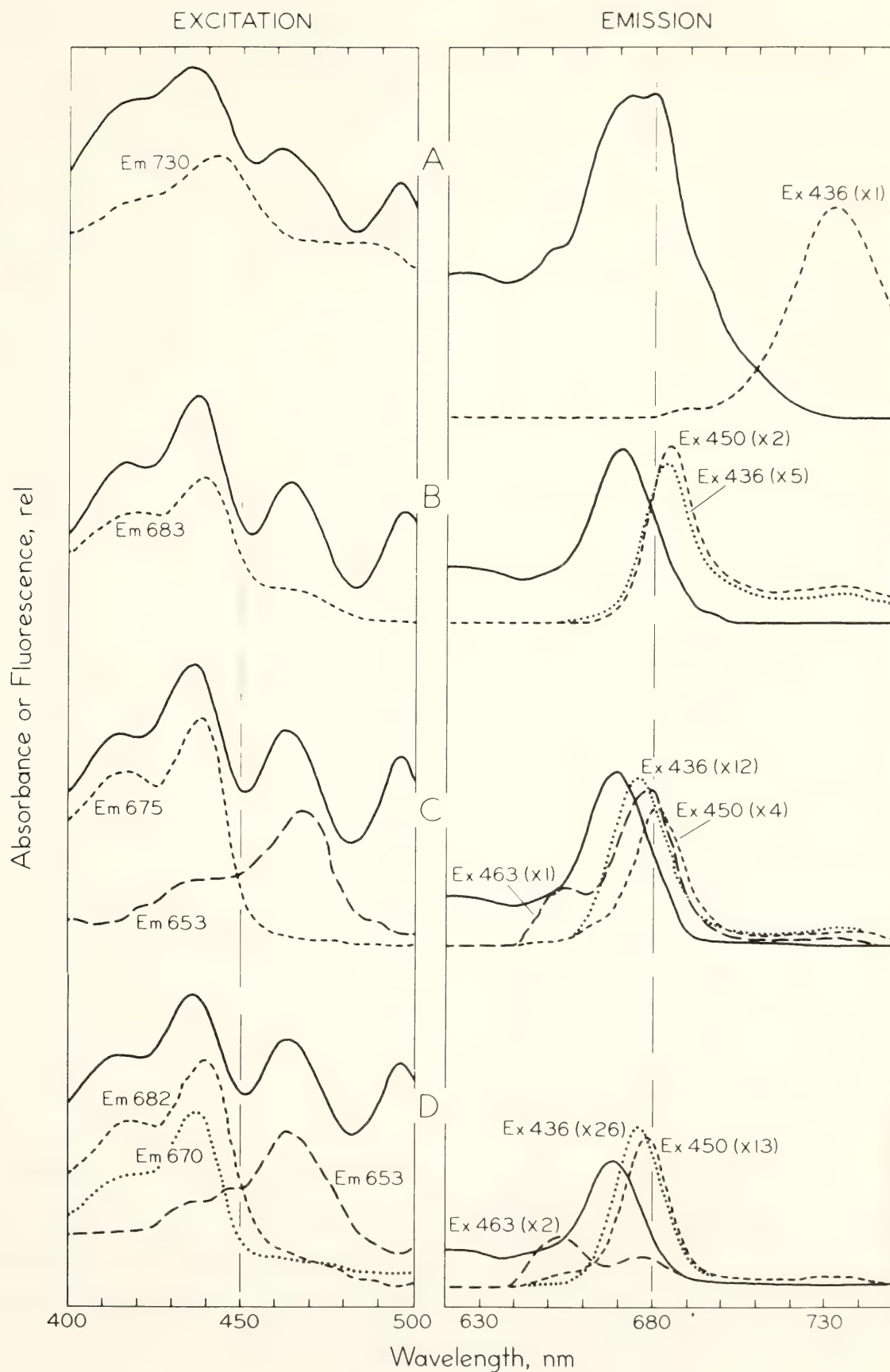
An extract of these membranes in 0.5% Triton (Triton:chl = 10, wt:wt) was made by the same procedure described

Fig. 42. Absorption (solid line), fluorescence excitation and emission (broken lines) spectra of *Euglena* chloroplast membranes broken in a French pressure cell. Emission wavelengths for excitation spectra and exciting wavelengths for emission spectra are shown adjacent to curves. For all fluorescence spectra, the slit width of the fixed wavelength was 5 nm and that of the variable wavelength, 3 nm. The numbers in parentheses indicate the factor by which the area under each emission spectrum should be multiplied to compare the relative fluorescence yields on a chlorophyll basis. The absorption spectra (slit width < 1 nm at peak wavelengths) were measured at approx.  $-185^{\circ}$  C and the fluorescence spectra at  $-196^{\circ}$  C. All fluorescence spectra were corrected for the wavelength sensitivity of the apparatus. (A) Untreated membrane fragments; (B) membrane fragments in 0.5% Triton X-100; (C) in 1% Triton X-100; (D) in 1% Triton after passage through HAP.



below with spinach chloroplasts, and its spectra are shown in Fig. 42B. In work to be reported elsewhere, this extract was fractionated by sucrose density gradient

centrifugation, and three distinct green bands were recovered. The major fraction (near the top of the gradient) corresponded in several respects to a light-



harvesting chl-protein (LHC)\* found in higher plants (Burke *et al.*, 1978), and spectra of the total 0.5% Triton extract in Fig. 42B mainly reflect the presence of this fraction. The absorption band in the red spectral region is simplified, and both absorption and fluorescence emission are considerably blue-shifted compared to spectra of the untreated membranes. Also there is a small shift to a shorter wavelength for maximal emission and a large increase in yield when fluorescence is excited at 436 nm rather than 450 nm. Factors in parentheses on the figure are inversely proportional to the chlorophyll concentration and instrument sensitivity and can be used to compare the relative emissions of different samples. Although there is a relative decrease in absorption near 445 nm, and the excitation maximum is blue-shifted, the shoulder near 445 nm and another around 470 nm indicate some excitation energy transfer from chl's *a* and *b* to the form of chl *a* that emits near 683 nm.

When *Euglena* membranes were further dissociated in 1% Triton (Triton:chl = 75, wt:wt), the spectra shown in Fig. 42C were obtained. These spectra are more blue-shifted, and the fluorescence yield from 436-nm excitation is considerably higher—characteristics to be expected from chlorophyll in solution. Much of the chlorophyll has probably become detached from protein and solubilized into detergent micelles. The emission band near 653 nm, preferentially excited by 463 nm, indicates the solubilization of chl *b*, which absorbs in this region. However, the fact that excitation at 450 nm induces emission near 681 nm shows that some chl *a* is still bound to protein.

When a chloroplast extract in 1% Triton is passed through an HAP column, most but not all of the chl-proteins adhere. Spectra of an eluate from such a

column are typical of solubilized chl's *a* and *b* (Fig. 42D). Because the emission from 450-nm excitation is slightly red-shifted relative to emission from 436-nm excitation, a small portion of a chl-protein (probably LHC) must have passed through the column along with the detergent-solubilized pigment.

These results suggest two different effects of Triton on chloroplast membranes. At low concentration (<0.5%) and ionic strength this detergent causes at least some of the antenna chl-proteins, cytochrome *b<sub>6</sub>-f* complexes, and photosystem I particles to dissociate from the membrane and from one another. A small amount of pigment is also either solubilized in the detergent micelles or sufficiently altered in its binding to protein to lower the probability of energy transfer between molecules. At higher concentrations of Triton (about 1%), the membranes are completely dissociated; some P700-chl *a*-protein complexes (chl *a*:P700 = 30–40) remain intact, but much of the chlorophyll is solubilized.

Because chlorophyll in solution has a slightly higher absorption coefficient and much higher fluorescence yield than when it is closely associated with protein, emission from the former state overshadows the latter in spectra of mixtures when excited where both states absorb. However, because the chl-proteins absorb at longer wavelengths in the blue spectral region, their emission can be excited preferentially. This finding has helped to characterize three different chl-proteins from *Euglena* (to be reported elsewhere). One appears to be an antenna, or light-harvesting, chl *a-b*-protein; another is a P700-chl *a*-protein; and a third, CPa<sub>1</sub>, was reported previously (Year Book 73) after its isolation by HAP chromatography. Because CPa<sub>1</sub> has now also been detected in the lowest sucrose gradient band, the possibility is greater of its being a real membrane component and not an artifact of the isolation procedure.

\* LHC = light-harvesting chl-protein complex, also CPa<sub>1</sub>.



## ANTENNA CHLOROPHYLL FROM SPINACH

A chl-protein complex with a very low chl *a* to *b* ratio and no apparent photochemical activity has been isolated from several plants by solubilization in SDS\* and chromatography on HAP (Kung and Thornber, 1971) and more recently by solubilization in Triton and centrifugation through a sucrose density gradient (Burke *et al.*, 1978). This complex comprises more than 50% of the total chlorophyll in most plants studied and has been called the antenna, or light-harvesting, complex (LHC, originally CP II). Although the absorption and fluorescence of CP II from tobacco and *Chlamydomonas* were published in *Year Book 73*, p. 694, and *Year Book 74*, p. 781, those preparations had been treated with SDS, which may have altered the native complex more than the milder acting Triton. Therefore, spectra of LHC isolated from spinach chloroplasts according to Burke *et al.* (1978) were measured.

An essential step of this procedure is the initial thorough washing of isolated chloroplasts with EDTA to remove most of the cations and cause the grana lamellae to unstack. Such washed spinach chloroplasts were suspended in 0.5% Triton X-100, stirred at 26°C for 15 min, and centrifuged at  $27,000 \times g$  for 10 min. Aliquots of the supernatant were layered over a gradient of 0.1 to 1.0 M sucrose in 0.5% Triton, and the tubes were centrifuged at  $178,000 \times g$  (av.) in a Sorval TV 850 rotor for 4.5 hr. A broad, highly fluorescent green band remained near the top of the gradient while heavier green particles, enriched in photosystem I, sedimented to a layer just above a dense sucrose cushion. The broad upper band contained the LHC. Its absorption and fluorescence emission spectra are shown in Fig. 43A.

According to Burke *et al.*, a more purified LHC complex can be sedimented from the upper gradient band of pea

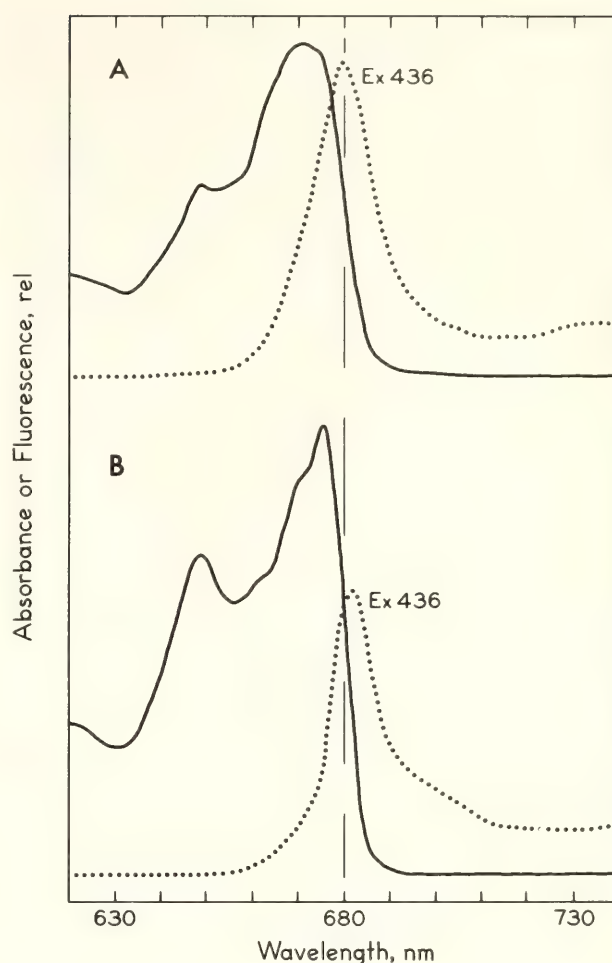


Fig. 43. Absorption (solid line) and fluorescence emission (dotted line) spectra of spinach chloroplast fractions. (A) Upper centrifugal fraction from a sucrose gradient; (B) LHC precipitated from (A) by cations. Conditions for measuring spectra as in Fig. 42.

chloroplasts by adding  $\text{MgCl}_2$  and KCl to give 10 mM and 100 mM, respectively, and then centrifuging at  $9000 \times g$  for 10 min. When we tried this technique with spinach, no sediment was observed initially; but after spinning at  $27,000 \times g$  for 25 min, a small amount of LHC was obtained. This sediment was homogenized in 10 mM phosphate, pH 7.6, and its absorption and fluorescence emission spectra were also measured at low temperature. The spectra are shown in Fig. 43B. The ratio of chl *a* to *b* was 2.08 for the gradient band and 1.35 for the purified LHC; the relative fluorescence yield was more than twice as great in the gradient band as in the purified complex.

\* SDS = sodium lauryl sulfate.

In another experiment we added  $\text{MgCl}_2$  and KCl (to 10 and 100 mM) to the upper gradient band and dialyzed the preparation overnight against 2 mM phosphate buffer, pH 7.6 containing the same concentrations of salts. The LHC precipitated during this procedure, and by centrifugation more than 30% of the chlorophyll in the upper gradient band was recovered in the sediment with a chl *a* to *b* ratio of 1.20. The absorption spectrum of this LHC fraction was essentially the same as that shown in Fig. 43B. In addition, comparison of this spectrum in the blue region with a spectrum of the supernatant from which this LHC was sedimented showed a clear difference at 478 nm. Because both fractions probably contained the same carotenoids, the 478-nm band can be attributed to chl *b*.

Sodium lauryl sulfate was added to a suspension of LHC to give 0.1%, and low-temperature spectra were measured of aliquots after 5, 15, and 30 min incubation at about 20°C. A time-dependent disappearance of the 676-nm peak and 663-nm shoulder occurred while the 670-nm and 650-nm bands became prominent. The final spectrum in SDS was very similar to the spectrum of CPII published in *Year Book 73*, which had also been treated by SDS. Spectra in Fig. 43B of purified LHC prepared after Triton dissociation may therefore be more representative of the native ab-

sorption and fluorescence emission for antenna chlorophyll.

The fact that cytochromes *f* and *b<sub>6</sub>* cochromatograph with the P700-chl *a* protein (CPI) on hydroxylapatite has been discussed previously (*Year Book 77*, p. 298). Because these cytochromes remain in the upper part of the sucrose gradient, CPI free of cytochrome can be obtained by subsequent HAP chromatography of the lower layer of green particles after dialysis to remove the sucrose and addition of Triton (final conc. 1%) to dissociate the particles.

These studies have shown that certain chl-protein complexes that comprise part of photosynthetic membranes can be characterized by spectral analyses and distinguished from detergent-solubilized chlorophyll.

#### REFERENCES

- Burke, J. J., C. L. Ditto, and C. J. Arntzen, *Arch. Biochem. Biophys.*, **187**, 252-263, 1978.
- Brown, J. S., and M. R. Michel-Wolwertz, *Biochim. Biophys. Acta*, **153**, 288-290, 1968.
- French, C. S., J. S. Brown, and M. C. Lawrence, *Plant Physiol.*, **49**, 421-429, 1972.
- Kung, S. D., and J. P. Thornber, *Biochim. Biophys. Acta*, **253**, 285-289, 1971.
- Lutz, M., *Biochim. Biophys. Acta*, **460**, 408-430, 1977.

### ANALYSIS OF PHOTOSYNTHETIC CYTOCHROME CONTENT WITH A SPECTROPHOTOMETER-COMPUTER INTERFACED SYSTEM

*Geoffrey W. Harvey*

The photosynthetic cytochromes have been analyzed in chloroplast membranes with several variations of the technique outlined by Bendall *et al.* (1971). The method requires manual analysis of com-

plex difference spectra, a laborious procedure that greatly reduces the speed of analysis. A cytochrome analysis is reported here which takes advantage of computer assistance to average differ-



ence spectra, subtract baseline spectra, and analyze complex spectra for component cytochromes.

A chloroplast membrane fraction in which the photosynthetic cytochromes predominated was used in the analysis. Neither respiratory nor microsomal cytochromes were detected. All assays were made in Jensen-Bassham (1966) buffer 1, pH 6.5. Chlorophyll was determined by the technique of Arnon (1949). Suspensions containing 42.5–85  $\mu\text{g}/\text{ml}$  chlorophyll were used for difference spectra.

A Perkin-Elmer 356 dual-beam spectrophotometer operated in the split beam mode and interfaced with a Hewlett-Packard 2116C computer, collected both baselines and chemically oxidized-minus-reduced spectra. Cytochrome  $c_{554}$  was determined in a suspension made to 1% Triton X-100. After a stable baseline was recorded in the computer, the oxidant (potassium ferricyanide) and reductant (hydroquinone) were added to separate cuvettes to a final concentration of 2 mM. After 1 minute, several spectra were recorded and averaged and the baseline subtracted to give the difference spectrum. Cytochrome  $b_{559,\text{HP}}$  ferricyanide-versus-hydroquinone difference spectra were determined with osmotically shocked chloroplast membranes in suspensions containing no detergent. Difference spectra for cytochromes  $b_{559,\text{LP}}$  and  $b_{563}$  were determined in suspensions identical to the  $b_{559,\text{HP}}$  samples except that they contained 2 mM hydroquinone and 400 units/ml catalase. After determination of the baseline, 0.5 mg/ml sodium dithionite was added to one cuvette, and the difference spectra were recorded several times in the next 10 minutes (Bendall *et al.*, 1971).

Cytochrome  $c_{554}$  and  $b_{559,\text{HP}}$  concentrations were calculated from the  $\alpha$  band peak heights and the extinction coefficients 17.7 and 20  $\text{cm}^2/\text{mmole}$ , respectively (Bendall *et al.*, 1971). Care was taken to subtract the cytochrome  $c_{554}$  component from the cytochrome  $b_{559,\text{HP}}$

spectra. Hydroquinone-dithionite difference spectra, which no longer evidenced shifts between successive spectra in either peak heights or wavelength maxima, were treated with the RESOLV program described by Cuellar *et al.* (1978) and French *et al.* (Year Book 67, pp. 536–546). Absorption maxima of 531 and 559 for the  $b_{559,\text{LP}}$  and 536 and 563 for the  $b_{563}$  were used. Half bandwidths of 10 nm for the  $\alpha$  and 20 nm for the  $\beta$  bands were used (Cramer and Whitemarsh, 1977). Since little latitude was allowed for alteration of bandwidths or wavelength maxima, the variable altered by the program was peak height. After the best possible fit of the curve was achieved, cytochrome  $b_{559,\text{LP}}$  and  $b_{563}$  were calculated from the  $\alpha$  band peak height using the extinction, 20  $\text{cm}^2/\text{mmole}$  (Bendall *et al.*, 1971).

Photosynthetic cytochromes were measured in solutions containing one half to one fourth the chlorophyll content recommended by Bendall *et al.* (1971). Very sharp difference spectra were obtained by using the computer to average both baselines and oxidized-versus-reduced difference spectra and to make the necessary subtractions. The final difference spectra can be obtained quickly. Additionally the chloroplast membrane preparation can be fairly crude. However, phenolic substances and some as yet uncharacterized membrane constituents present in some species can alter absorption markedly with introduction of the oxidant or reductant. These artifacts mask shifts attributable to cytochromes. For reference, osmotically shocked membranes (1:10 dilution in distilled water) were compared with a destacked membrane preparation. Both treatments provided identical cytochrome values. A major benefit of employing the spectrophotometer-computer interface is the ease with which the RESOLV program can be used to obtain the component cytochrome  $b_{559,\text{LP}}$  and  $b_{563}$  spectra. Previously, a more laborious method based upon the

time-dependent reduction of the two *b* types of dithionite was employed (Bendall *et al.*, 1971). In the three cases where the two techniques were compared, the results were similar.

The computer-assisted collection, averaging, and subtraction of scans significantly decreases the time required for analysis of the photosynthetic cytochromes of crude chloroplast membrane preparations. Employing the RESOLV technique for separation of the absorption due to overlapping bands of  $b_{559,LP}$  and  $b_{563}$  in the hydroquinone-versus-dithionite spectra is easier than the plotting technique and just as accurate.

## REFERENCES

- Bendall, D. S., H. E. Davenport, and R. Hill, in *Methods in Enzymology*, A. San Pietro, ed., Vol. 13: Photosynthesis Part A. Academic Press, New York 327–343, 1971.
- Cuellar, R. E., G. A. Ford, W. R. Briggs, and W. F. Thompson, *Proc. Nat. Acad. Sci. U.S.A.*, 75, 6026–6030, 1978.
- Cramer, W. A., and J. Whitemarsh, *Annu. Rev. Plant Physiol.*, 28, 133–172, 1977.
- Jensen, R. G., and J. A. Bassham. *Proc. Nat. Acad. Sci. U.S.A.*, 56, 1095–1101, 1966.

## MEASUREMENTS WITH A MICROPROCESSOR-BASED FLUORESCENCE SPECTROPHOTOMETER MADE ON THE BLUE-GREEN ALGA *Anacystis nidulans* ABOVE AND BELOW THE PHASE TRANSITION TEMPERATURE

David C. Fork, Glen A. Ford, and Benny Catanzaro

In studies of the effect of temperature on the physical state of thylakoid membrane lipids and on photosynthesis it is useful to have an apparatus that can measure fluorescence emission spectra conveniently and quickly on small samples whose temperature can be changed over a wide range and to have access to a computer capable of acquisition and manipulation of the resulting fluorescence data. We have made some preliminary measurements using the blue-green alga *Anacystis nidulans* to obtain fluorescence emission spectra above and below the phase transition temperature of the thylakoid membrane lipids.

For this purpose we have assembled a microprocessor-based fluorescence emission spectrophotometer that uses a small monochromator (Jarrell-Ash, 0.25 m Ebert) having a 13-bit digital shaft encoder (Norden, ADC-13-BNRY-E attached to its motorized wavelength drive. This shaft encoder provides a digital

indication of wavelength position with a resolution of 0.065 nm.

The fluorescence signal is detected by a gallium arsenide photomultiplier (Hamamatsu TV, R666S) having an essentially flat spectral response over the wavelength range of about 500–800 nm. The signal is digitized by a 12-bit analog-to-digital (A/D) converter (Philbrick-Teledyne) when pulsed by appropriate control signals.

Both digital signals are interfaced to a single board microcomputer (Intel, SDK85). The board contains a microprocessor (Intel 8085), 4096 bytes of RAM (read-write) memory for data storage, 768 bytes of RAM memory for application program storage, 2048 bytes of EPROM (read only) memory for system utility routines, and associated input-output ports for sensory and control lines. Once the desired starting and ending wavelengths for a set of scans has been entered, an application program



continuously senses the current wavelength position and at appropriate and precise wavelength intervals reads the A/D converter and stores this fluorescence information in memory.

The data stored in the microcomputer can be displayed on a storage oscilloscope or an x-y recorder. For this purpose a 12-bit digital-to-analog converter (DAC) and a remote start signal allow the contents of memory to be displayed under program control.

The microprocessor system as it is most commonly used runs under the control of a master program (MICRO) contained in the laboratory's central computer (*Year Book* 77, pp. 305-307), a Hewlett/Packard 2116C minicomputer. Communication between the two systems is achieved via a parallel interface consisting of 16 input, 16 output, and 2 control lines. This enables the transfer of fluorescence data from the microcomputer to the central computer for storage on magnetic disk or more complex data reduction. Likewise, stored or reduced data may be retrieved from the central system and transferred to the microcomputer memory, ready for plotting. Space is currently allocated in the Hewlett/Packard system to store fifty fluorescence emission curves, each consisting of 2048 data points.

The master program, MICRO, allows the use of simple commands to load the microprocessor with different application programs, to modify wavelength scan parameters, to transfer curves between systems, and to manipulate the spectral data. Spectral manipulation may involve subtracting or dividing spectra by one another, normalizing or averaging spectra, computing derivative spectra, or smoothing noisy spectral data. One of the curves stored on the disk holds the spectrum obtained with a standard lamp and another holds all the factors needed to correct the fluorescence measurements at each wavelength interval.

A quartz sample cuvette consists of an

8-mm open thermostated tube with a water jacket for temperature control. The bottom of the cuvette is sealed with an 8-mm quartz rod that serves as an optical guide to conduct actinic light to a 0.5-ml sample located above it. Another 8-mm rod fused on the side of the sample chamber and at right angles to the actinic rod conducts fluorescence to the entrance slit of the monochromator adjusted to pass a half bandwidth of 3.6 nm. Alternatively, the sample can be illuminated and fluorescence conducted to the monochromator via a branched fiber optical system (Schott) designed by Dr. R. Strasser. For living cells the sample in the thermostated cuvette can be kept aerobic by using a thin vibrating rod that stirs the sample.

Figure 44 shows the fluorescence emission spectra of *Anacystis nidulans* cells grown at 38°C and measured above and below the phase transition temperature (around 24°C: Murata, Troughton, and Fork, 1975; Ono and Murata, 1979). The spectrum measured at 38°C (Fig. 44A) had emission bands at 656 and 682 nm that are produced by allophycocyanin and chlorophyll *a*, respectively (Gray and Gantt, 1975; Mimuro and Fujita, 1977; Murata, Nishimura, and Takamiya, 1966) and is similar to fluorescence spectra previously reported for this organism (Murata, 1977).

The same sample used for the measurement of the spectrum shown in Figure 44A was cooled in the dark at a rate of about 0.5°C/min to 10°C and the fluorescence spectrum again measured. Figure 44B shows that at this temperature the 682-nm fluorescence band was increased. The difference spectrum in Figure 44D (10°C curve minus 38°C curve) shows a peak at 682 nm, suggesting that chlorophyll *a* fluorescence increases when *Anacystis* cells are cooled below the phase transition temperature. This effect is reversible. The fluorescence emission spectrum obtained after the cells had been warmed again to 38°C was almost

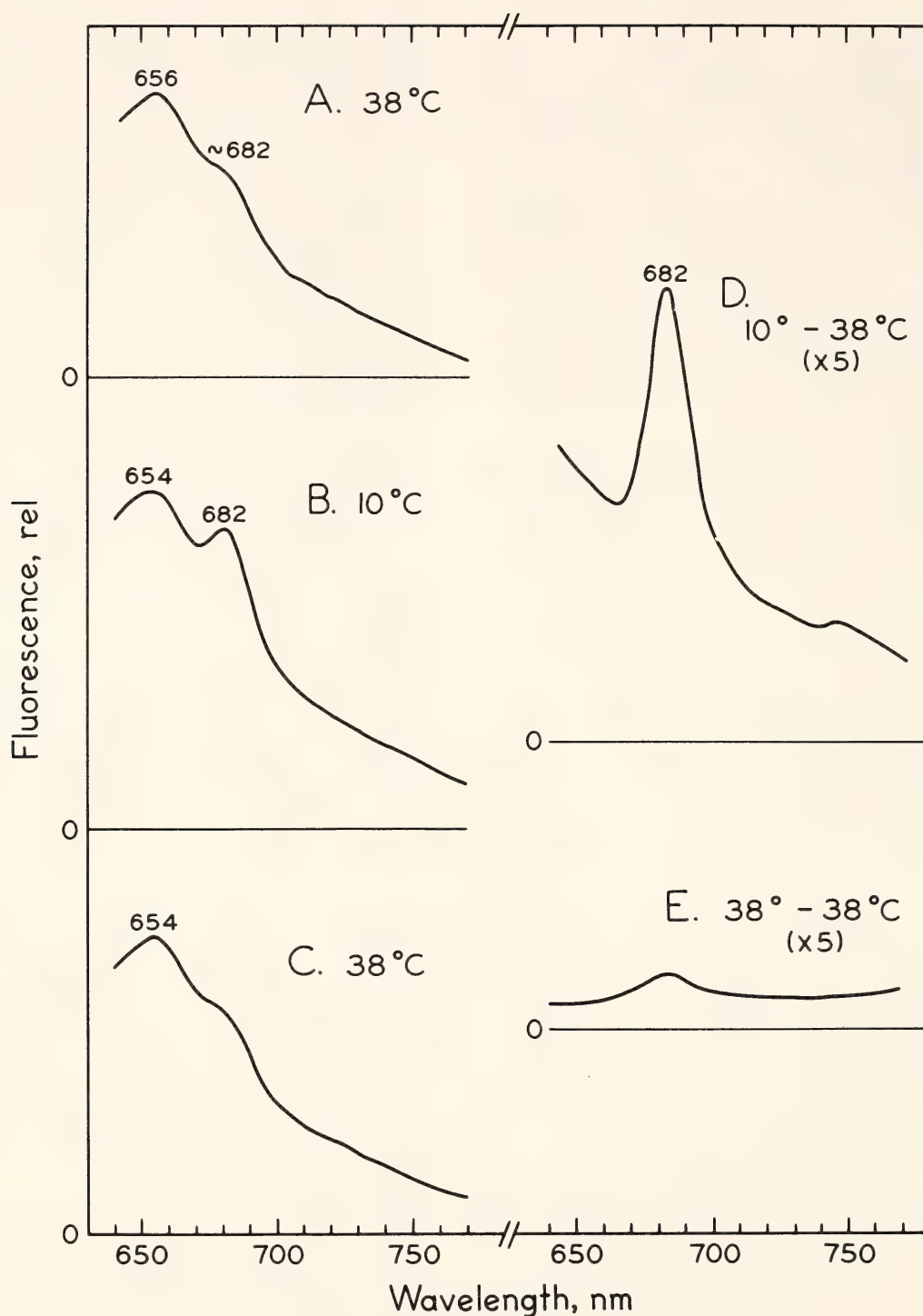


Fig. 44. Fluorescence emission spectra measured at 38° and 10°C in *Anacystis nidulans* grown at 38°C. No DCMU added. The spectra were corrected for the spectral sensitivity of the photomultiplier and the monochromator by use of a standard lamp. The cell suspension was diluted to an absorbance of 0.2 at 678 nm (1 cm cell). The excitation light was obtained by filtering white light through a Calflex C heat-reflecting filter and Corning glass filters CS 3-66 and 4-96 and had a half bandwidth of 22 nm and a fluence of 4000 mW cm<sup>-2</sup>.

identical to the original curve. Figure 44E shows little difference between the two 38°C curves.

Cooling *Anacystis* below its phase

transition temperature mimics the effect of DCMU (3-(3,4-dichlorophenyl)-1,1-dimethylurea) (Murata, 1977), which is thought to inhibit electron transport



near the reaction center of photosystem II, thus blocking the trapping of excitation energy by this photosystem (Duysens and Sweers, 1963; Murata and Takamiya, 1967). We found previously that at near 24°C a transition of the thylakoid membrane lipids from the liquid crystalline to the phase separation state gives rise to changes in activity of many photosynthetic parameters. In an earlier study (Year Book 74, 766–776; Murata, Troughton, and Fork, 1975) it was suggested that one of the important effects of cooling *Anacystis* below its phase transition was to slow down the reoxidation of the lipophilic electron carrier, plastoquinone. The fluorescence results described above are consistent with this hypothesis, since an accumulation of reduced plastoquinone at temperatures below the phase transition temperature would give rise to an accumulation of reduced Q (the primary acceptor of photosystem II) and result in enhanced fluorescence from chlorophyll *a*.

## REFERENCES

- Duysens, L. N. M., and H. E. Sweers, in *Studies on Microalgae and Photosynthetic Bacteria*, Japanese Society of Plant Physiologists, eds., pp. 353–372, Univ. Tokyo, 1963.
- Gray, B. H., and E. Gantt, *Photochem. Photobiol.*, 21, 121–128, 1975.
- Mimuro, M., and Y. Fujita, *Biochim. Biophys. Acta*, 459, 376–389, 1977.
- Murata, N., in *Photosynthetic Organelles: Structure and Function*, S. Miyachi, S. Katoh, Y. Fujita, and K. Shibata, eds., pp. 9–13, Japanese Society of Plant Physiologists, Tokyo, 1977.
- Murata, N., M. Nishimura, and A. Takamiya, *Biochim. Biophys. Acta*, 126, 234–243, 1966.
- Murata, N., and A. Takamiya, *Plant and Cell Physiol.*, 8, 683–694, 1967.
- Murata, N., J. H. Troughton, and D. C. Fork, *Plant Physiol.*, 56, 508–517, 1975.
- Ono, T., and N. Murata, *Biochim. Biophys. Acta*, 545, 69–76, 1979.

## COMPUTER-ASSISTED MEASUREMENTS OF PARAMETERS OF THE RISE CURVE OF FLUORESCENCE

*Shmuel Malkin, Glenn A. Ford, and David C. Fork*

The concept of the photosynthetic unit (PSU) introduced by Emerson and Arnold (1932) relates the number of functional chlorophyll molecules associated with each reaction center of photosynthesis. We were interested in developing a technique to measure the PSU size *in vivo* accurately and quickly in a routine way and we wanted to be able to use intact material such as leaves or algae. Measurements of this kind are important when dealing with questions such as the relationship between the PSU size and the rate of photosynthesis. The size of the PSU has an important bearing on considerations of plant pro-

ductivity as well as on the adaptation of plants to different environments.

The accurate quantitative determination of the PSU size is not a trivial problem. Although a number of methods have been used, each has difficulties often leading to results that are only rough approximations. It was our purpose to develop a convenient and reliable procedure to determine the PSU size *in vivo* by following fluorescence induction in intact plant material. This technique has already been applied to measure PSU size for isolated chloroplasts (Malkin and Kok, 1966; Dubertret and Joliot, 1974; Armond *et al.*, 1976).

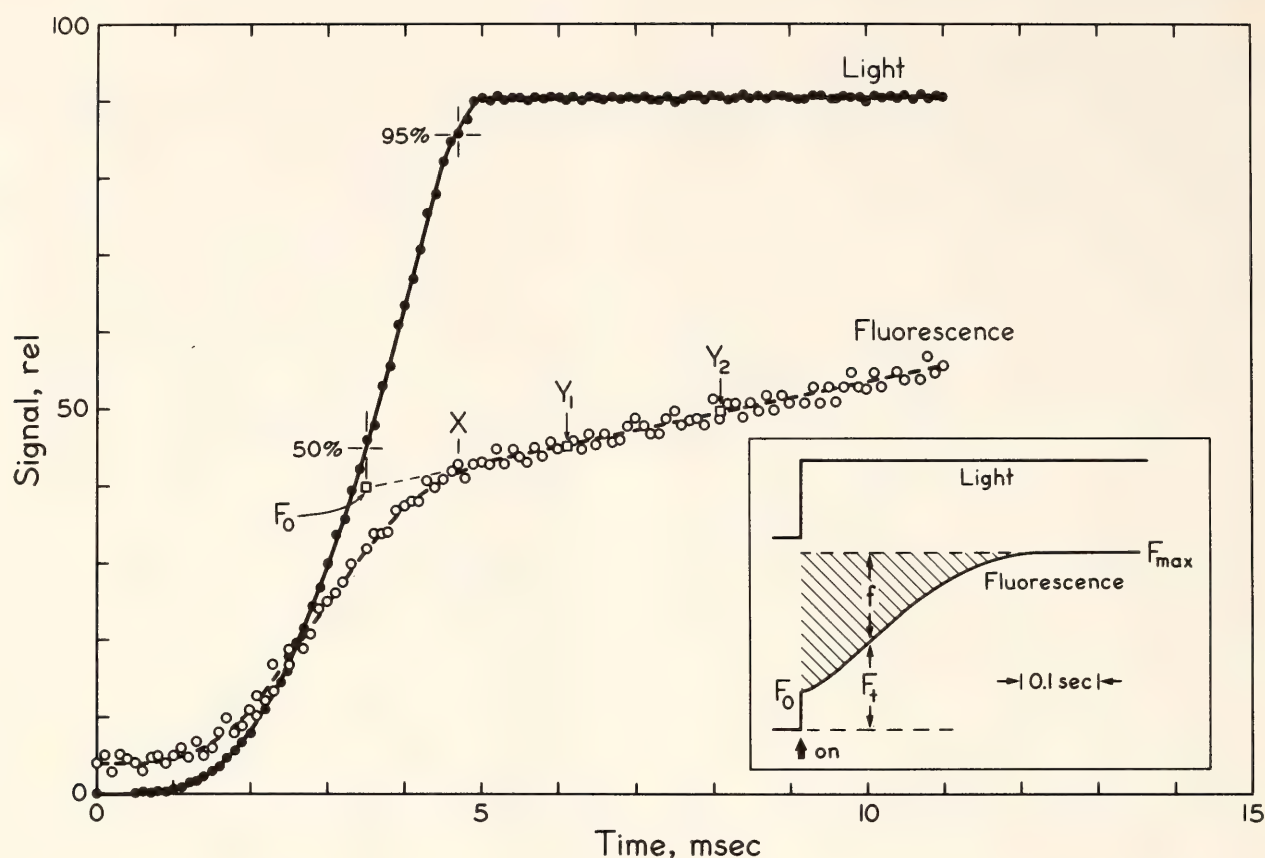


Fig. 45. Plot of the digital points obtained during the recording of time courses of fluorescence and of the actinic light used to produce the fluorescence. The time interval between the points is  $100\ \mu\text{s}$ . Spinach chloroplasts in  $20\ \mu\text{M}$  DCMU. Insert: Diagrammatic representation of time courses of fluorescence and of actinic light. See text for definition of terms.

Typically, upon illumination of dark-adapted plants fluorescence is at its minimum level ( $F_0$ ), and after some period of illumination fluorescence increases to a maximum steady-state level ( $F_{\text{max}}$ ) (Fig. 45). It is thought (Zankel and Kok, 1972) that this fluorescence rise curve seen in the presence of the inhibitor DCMU reflects the conversion of the reaction centers of photosystem II from the active to the inactive or reduced form. For a given absorbed light intensity ( $I_{\text{abs}}$ ) the average time of the fluorescence rise  $\bar{t}$  is related to the number of reaction centers ( $n$ ) by the formula of Malkin and Kok (1966):

$$n = \alpha_2 \phi_2 I_{\text{abs}} \bar{t}$$

where  $\alpha_2$  is the fraction of absorbed light delivered initially to photosystem II and  $\phi_2$  is the maximum photochemical efficiency of photoreaction II. For our ex-

periments we wanted to be able to measure  $\bar{t}$  rapidly and accurately. This quantity is found by determining the area above the time course of fluorescence that is bounded by the fluorescence axis at time zero and the line  $F = F_{\text{max}}$  when the value  $F_{\text{max}} - F_0$  is normalized to unity.

For this purpose we have adapted techniques used previously for computer analysis of spectroscopic measurements (Year Book 77, pp. 307–310). Two analog signals were monitored simultaneously during the measurements; one from a photomultiplier that followed the kinetics of fluorescence and another from a photocell that measured the intensity and the beginning and end of the illumination period. The analog data from these two channels were digitized into 1024 points for each curve by the HP-91000A Analog Subsystem (Year Book



77, pp. 305–307). The time resolution was 100  $\mu$ s.

Computer calculation of the area over a fluorescence rise curve is a simple process, since the curve is defined by a large number of points. In this case the area can be accurately approximated as the sum of the individual rectangles defined by the time intervals and the fluorescence. This task, however, was complicated by the finite opening time ( $\sim 3$  ms) of the shutter that controlled the actinic light. The initial kinetics of fluorescence were thus somewhat distorted. Since the opening time of the shutter was short compared to the total induction time, it was possible to find the  $F_0$  level by extrapolating back linearly to a point in time when the actinic light intensity was at 50% of its maximum value. To obtain this point the data from the channel monitoring the actinic light were examined first (Fig. 45). The value for the maximum light intensity was obtained by averaging a number of points 20 msec after the start of the shutter opening. This procedure ensured that the shutter was fully open and that the light intensity had attained its maximum value. The points corresponding to the 50% and 95% light intensity levels were then determined as shown in Fig. 45. Fig. 45 also shows the digital values obtained from the fluorescence signal. The value of fluorescence that corresponded in time to the 95% light intensity value was found ( $x$ ). Ten fluorescence points were averaged to give the point  $Y_1$ . After 20 points further in time along the fluorescence curve another nine points were averaged to give  $Y_2$ . A line fitted through  $Y_1$  and  $Y_2$  was extrapo-

lated back to the point in time corresponding to 50% light intensity. The fluorescence at this time was taken as  $F_0$ . The area of the trapezoid bounded by  $F_0$ ,  $Y_1$ , and  $F_{\max}$  was then found. Rectangular integration provided the remaining area above the fluorescence rise curve and this was added to the trapezoidal area to give the total area (the shaded area shown in the insert of Fig. 45). The program (FAREA) produced values for  $F_0$ ,  $F_{\max}$ ,  $\text{Area}_{\text{total}}$ , and  $1 - F_0/F_{\max}$  (a measure of the photochemical efficiency of photoreaction II). Another program (SAREA) provided values at 50 time intervals along the fluorescence rise curve for  $F$  (defined as  $F_{\max} - F_t/F_{\max} - F_0$ , see insert) and the values  $1 - \text{Area}/\text{Area}_{\max}$  allow estimation of the probability of energy transfer to another reaction center if a photon reaches a closed reaction center of photosystem II (Joliot and Joliot, 1964).

#### REFERENCES

- Armond, P. A., C. J. Arntzen, J. M. Briantais, and C. L. Vernotte, *Arch. Biochem. Biophys.*, **175**, 54–63, 1976.  
Dubertret, G., and P. Joliot, *Biochim. Biophys. Acta*, **357**, 399–411, 1974.  
Emerson, R., and W. Arnold, *J. Gen. Physiol.*, **16**, 191–205, 1932.  
Joliot, A., and P. Joliot, *Compt. Rend.*, **258**, 4622–4625, 1964.  
Malkin, S., and B. Kok, *Biochim. Biophys. Acta*, **126**, 413–432, 1966.  
Zankel, K. L., and B. Kok, in *Methods of Enzymology*, Vol. XXIV, *Photosynthesis and Nitrogen Fixation, Part B*, A. San Pietro, ed., pp. 218–237, Academic Press, N.Y., 1972.

## PHOTOSYNTHESIS BIBLIOGRAPHIC FILE UPDATE— JUNE 1979

*J. S. Brown*

The computer-based bibliographic information retrieval file described in *Year Book 72*, p. 407, and *Year Book 75*, p. 479, has continued to grow, with more than 9000 references concerning photosynthetic electron-transport intermediates, pigments and light reactions, chloroplast and chromatophore activity, microalgae, culture, fractionation procedures, and more. Although we continue to control the contents and build the PLANTBIO File, the Research Libraries

Group, Inc., at Stanford is supporting the cost of continuous on-line service. Also, they have added a title-word search capability in addition to the category and author searching previously available.

You may contact The Research Libraries Information Network (RLIN), Stanford, CA 94305, (Tel.: 415/497-0652) for an account number and information about searching this File from your own nearest library terminal.

## A MOTOR-DRIVEN HYDRAULIC PRESS FOR THE FRENCH PRESS

*J. S. Brown and R. W. Hart*

The effective disintegration of plant cells and organelles with minimal loss of activity was an early interest of Dr. C. Stacy French and this department. A mechanical device was constructed and tested in collaboration with Mr. Harold Milner. With this device a cell or chloroplast suspension can be forced through a fine needle-valve by high pressure (*Year Book 48*, p. 88; Milner *et al.*, 1950; French and Milner, 1955). The pressure to operate this device was supplied by a simple, hand-pumped hydraulic jack. The American Instrument Company, which manufactures the French Press, gave one of their models to the department a few years ago.

Our use of the French Press, especially to break unicellular algae and last year to form lipid vesicles (*Year Book 77*, p. 294), has remained intensive. Although we recognize the value of exercise, we decided to mechanize the hydraulic press and constructed an apparatus from com-

ponents described below and shown in Fig. 46 for less than half the current cost of the commercially available, assembled machine.

We are indebted to Mr. Charles W. Anderson of Hydraulic Controls, Inc., Emeryville, CA, for obtaining and assembling the following components: pump motor—Delta Power Hydraulic Co., Model B1 and B174; directional control valve—Rexroth, type WMM 10; relief valve—Sun, Model RPGC KAN CCC; gauge—Marsh, HO278, 0 to 3000 psig; hydraulic cylinder—Sheffer, Model HH, 3000 psi series.

This assembly has a 2½-inch drive piston and gives 491 lb force per 100 psi. With the Aminco cylinder having a 1-inch diameter bore, the pressure on a sample over the needle valve is  $4.91/0.78 = 6.25$  times the gauge reading in psi. (To convert psi to newtons/m<sup>2</sup>, multiply by  $6.89 \times 10^3$ .) Similarly for our old assembly with a ¾-inch plunger, the



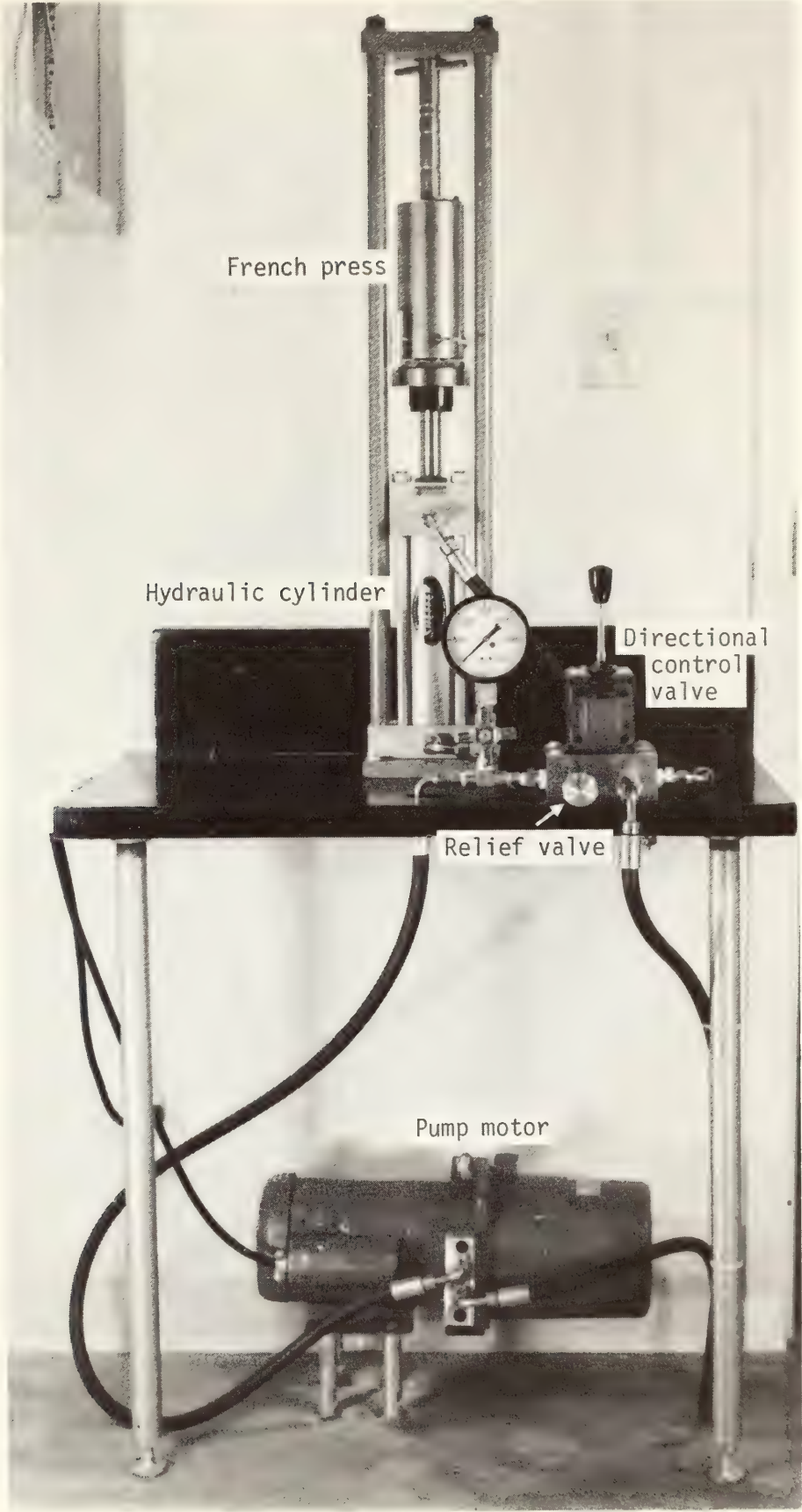


Fig. 46. Hydraulic press assembly.

pressure is 11.1 times the gauge reading.  
To operate the press, one merely turns on the motor switch and moves the con-

trol valve handle forward to compress the sample and backward to reduce the pressure. The desired gauge pressure to

be maintained automatically can be initially adjusted and set with the handle in the backward position. The pump quickly readjusts to a preset pressure when the needle-valve is opened; and the motor is reasonably quiet.

## REFERENCES

- French, C. S., and H. W. Milner, *Methods Enzymol.*, **I**, 64–67, 1955.  
 Milner, H. W., N. S. Lawrence, and C. S. French, *Science*, **111**, 633–634, 1950.

## LONG-PERIOD INTERSPERSION IN THE MUNG BEAN GENOME

*M. G. Murray and W. F. Thompson*

The linear arrangement of repetitive and single-copy DNA sequences is receiving considerable attention in our efforts to understand the evolution and function of the genome. Two basic patterns of sequence interspersion have been identified. In many organisms repeated sequences are interspersed with single-copy sequences which are generally  $\leq 2500$  nucleotide pairs in length. This pattern is termed short-period interspersion (Davidson *et al.*, 1975). The widespread occurrence of the short-period pattern suggests that it may have some functional significance. Britten and Davidson (1969) have proposed that interspersed repeats might function in the coordinate regulation of unlinked genes. However, in a recent review, Davidson *et al.* (1977) suggest that only a small fraction of the observed short-period interspersion is attributable to presumptive regulatory repetitive elements adjacent to genes. Moreover, an increasing number of organisms are being found which show long-period interspersion wherein single-copy sequences may exceed 10,000 nucleotide pairs without interruption by repeated sequences. In addition to the insect genomes where long-period interspersion was first identified (Manning *et al.*, 1975; Crain *et al.*, 1976), the pattern has now been found in avian (e.g., Arthur and Strauss, 1978), fungal (Hudspeth *et al.*, 1977), and nematode (Schachat *et al.*, 1978) genomes. Most of the higher plant genomes that have been

examined have been shown to conform to the short-period interspersion pattern (reviewed in Thompson and Murray, 1979). However, this sample includes only nine species, and we cannot yet generalize that all plants show short-period interspersion.

In assessing the significance of sequence interspersion in higher plants we have been conducting parallel studies on two legumes, the pea and the mung bean. We have shown previously that the pea (*Pisum sativum*) genome contains about 4.5 pg of DNA per haploid nucleus and is more extensively interspersed, with shorter intervals, than the genome of any other organism (Murray *et al.*, 1978). Most of the single-copy sequences in pea are 300–400 nucleotides in length, and we are unable to find any single-copy sequences longer than 1000 nucleotide pairs. The mung bean (*Vigna radiata*) is a member of the same subfamily (Fabaceae) but differs dramatically in both genome size and in the pattern of sequence interspersion. Haploid mung bean nuclei contain about 0.5 pg of DNA, and almost half of the single-copy sequences are longer than 6700 nucleotides.

Single-copy and repetitive sequences in mung bean DNA were characterized by reassociation kinetics (Murray *et al.*, 1979). Reassociation experiments with 300-nucleotide-long fragments of total mung bean DNA and a purified single-copy fraction show that the most slowly



reassociating sequences do so at a rate of  $0.0016 \text{ L mol}^{-1} \text{ s}^{-1}$  when assayed with hydroxylapatite. This rate is about 105 times slower than that observed for *E. coli* DNA fragments included in the same mixture, so we may calculate that the mung bean genome has a kinetic complexity 105 times greater than that of *E. coli*, of about  $4.7 \times 10^8$  nucleotide pairs (0.48 pg) per haploid nucleus. This value is in good agreement with cytochemical measurements on our material (M. D. Bennett, personal communication). The mung bean genome is thus about nine times smaller than the pea genome; it is the smallest higher plant genome that has been extensively characterized.

Repeated sequences constitute about 35% of mung bean DNA, in contrast to a value of 70% for the pea genome. Although the reassociation of mung bean repeated sequences can be described with a single theoretical second-order component, experiments with isolated kinetic fractions indicate that there is actually a distribution of repetition frequencies ranging from about 50 to several thousand copies per haploid genome. Studies on the thermal stability of reassociated repeats show that there is also a broad range in the degree of mismatch (see Palmer *et al.*, this *Year Book*). Leaf DNA preparations contain an additional 11% of rapidly reassociating sequences which can be shown to be derived from chloroplast DNA rather than nuclear repeats (Palmer *et al.*, this *Year Book*).

The degree of interspersion of repeated and single-copy sequences was determined from the reassociation kinetics of radioactively labeled tracers of differing lengths. Fig. 47 depicts the reassociation kinetics of 300-, 1200-, and 6700-nucleotide-long tracers in the presence of an excess of 300-nucleotide-long unlabeled fragments. In each experiment, the data have been fitted with three theoretical second-order components, but only the single-copy component is shown. In ar-

riving at these solutions, we fixed the single-copy rates at those predicted for single-copy sequences of the indicated lengths. In a tracer-driver reassociation 1200-nucleotide single-copy sequences are expected to react with a rate constant of 0.0064 ( $= 1200/300 \times 0.0016$ ), and 6700-nucleotide single-copy DNA should reassociate with a rate of 0.036 ( $= 6700/300 \times 0.0016$ ) (see Murray *et al.*, 1978).

As tracer length is increased from 300 to 1200 nucleotides, the fraction of the fragments showing single-copy kinetics drops from 65% to 42%. Consequently, 23% ( $= 65-42\%$ ) of the 1200-nucleotide-long fragments contain single-copy sequences contiguous with repeated sequences, and we can calculate that about 35% ( $= 23/65\%$ ) of the single-copy sequences are interspersed with repeats at distances of 300 to 1200 nucleotides. At a fragment length of 6700 nucleotides, 30% of the fragments reassociate with the predicted single-copy kinetics, and thus 18% ( $= 42-30/65\%$ ) of the single-copy sequences are interspersed with repeats at distances of 1200 to 6700 nucleotides. The remaining 46% ( $= 30/65\%$ ) of the single-copy sequences must be interspersed only at distances exceeding 6700 nucleotide pairs, if at all. These data show that while there clearly is some short-period interspersion in the mung bean genome, there is also a substantial amount of long-period interspersion.

It is significant that the mung bean genome is the smallest well-characterized higher plant genome and that it shows the most extensive long-period interspersion. Previously, a significant amount of long-period interspersion had been clearly shown in only one other higher plant that also has a small haploid DNA content (0.8 pg). About 20% of the cotton genome is composed of single-copy sequences  $\geq 4000$  nucleotides in length (Walbot and Dure, 1976). All other higher plant genomes that have

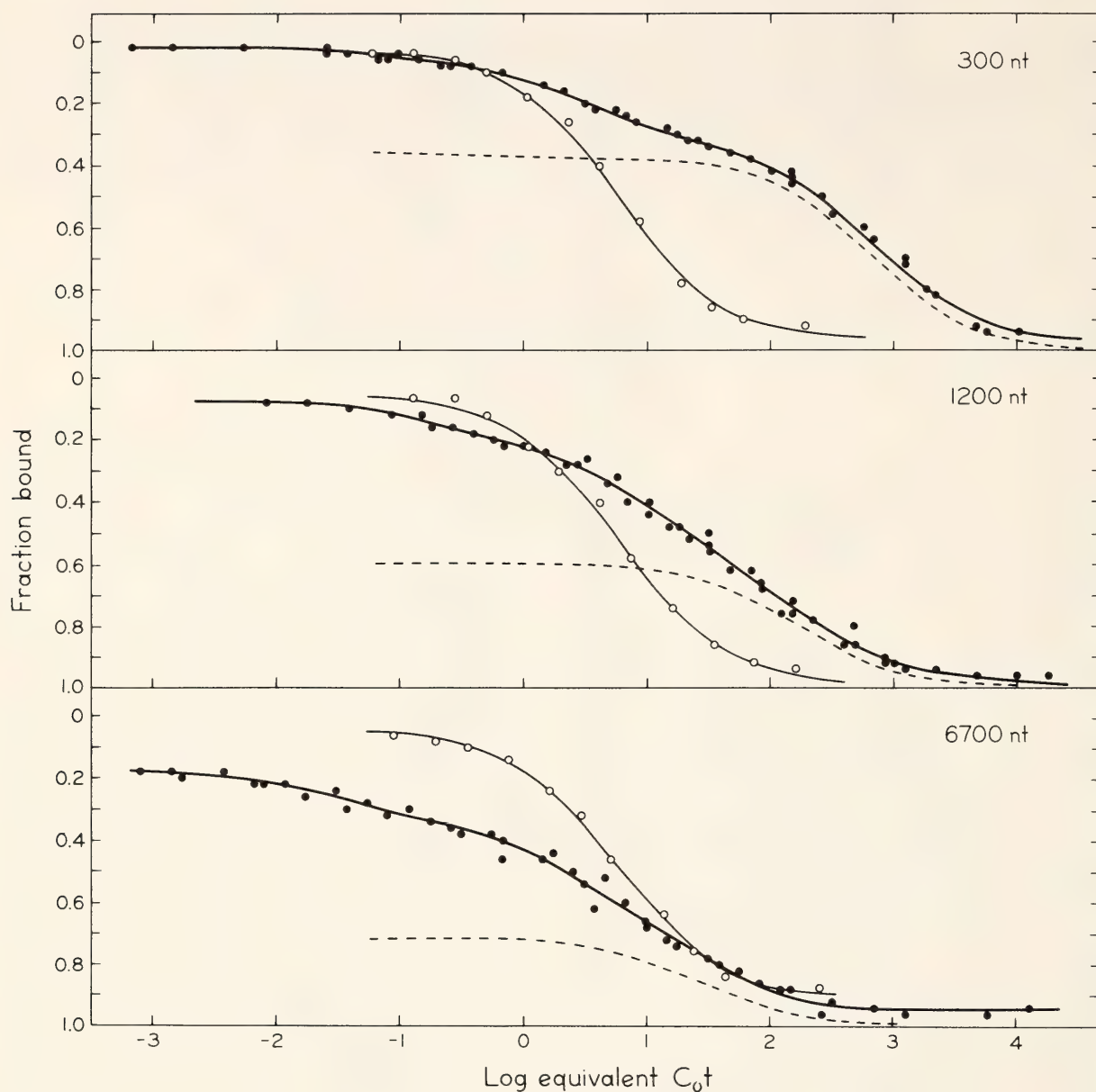


Fig. 47. Reassociation kinetics of mung bean fragments of different lengths. The reassociation kinetics of  $^3\text{H}$ -mung bean tracers with starting fragment lengths of 300, 1,200 or 6,700 nucleotides were determined in the presence of excess unlabeled 300 nucleotide fragments using techniques described in Murray *et al.* (1979).  $^{14}\text{C}$ -*E. coli* DNA was included in all mixtures to provide an internal rate standard. Data were analyzed in terms of three theoretical second-order components and the single-copy components are indicated with dashed lines. Single-copy rates were fixed at those predicted for the indicated fragment lengths as described in the text. All fragment lengths were measured after incubation to the approximate  $C_{0t_{1/2}}$  of the single-copy reaction in each series to compensate for size degradation upon incubation. Degradation was significant only in the longest tracer.

been examined are larger than 1 pg and show extensive short-period interspersions (reviewed in Thompson and Murray, 1979). Thus in plants there appears to be some correlation between the relative genome size and the pattern of sequence organization. This hypothesis is strengthened by data from the animal kingdom,

and the Dipteran insects provide a striking example. The housefly genome is some eight times larger than that of the fruitfly and, while the housefly shows short-period interspersions the fruitfly shows long-period interspersions exclusively (Crain *et al.*, 1976; Manning *et al.*, 1975).



The fact that organisms of similar biological complexity such as fruitflies and houseflies or peas and mung beans differ so dramatically in patterns of sequence organization makes it increasingly difficult to support the hypothesis that the short-period pattern required is for gene regulation. We think that different patterns of sequence interspersion might be more readily explained by largely stochastic processes of molecular evolution such as sequence amplification and translocation. Flavell and colleagues (Smith *et al.*, 1976; Flavell *et al.*, 1977) have shown that these processes have played an important part in the evolution of modern cereal grains.

Comparisons of the genome size and the fraction composed of single-copy sequences in higher plants indicate that most of the additional DNA in the larger genomes is composed of repeated sequences (Thompson and Murray, 1979). Much of the excess DNA may correspond to what Hinegardner (1976) has termed "secondary DNA," or DNA that serves no strongly sequence-dependent biological function. One would predict that in a small, largely single-copy genome such as that of the mung bean, translocation events would intersperse single-copy sequences with other single-copy sequences more often than with repeated sequences and thus not result in extensive repeat-single-copy interspersions. However, as larger genomes evolve by processes including frequent amplification and re-amplification, the probability of translocations leading to short-period repeat-single-copy interspersions increases.

At present, we believe that processes of amplification and translocation in secondary DNA provide a more reasonable explanation than any regulatory model for the differences we see between the mung bean and pea genomes. This view does not exclude the possibility that regulatory mechanisms have evolved to capitalize on emerging patterns of sequence arrangement. However, much

additional work will be required before we can distinguish patterns that may have specific regulatory significance from those that merely reflect the evolutionary processes active in eukaryotic DNA.

#### REFERENCES

- Arthur, R. R., and N. A. Strauss, *Can. J. Biochem.*, **56**, 257–263, 1978.
- Britten, R. J., and E. H. Davidson, *Science*, **165**, 349–357, 1969.
- Crain, W. R., E. H. Davidson, and R. J. Britten, *Chromosoma (Berl.)*, **59**, 1–12, 1976.
- Davidson, E. H., G. A. Galau, R. C. Angerer, and R. J. Britten, *Chromosoma*, **51**, 253–259, 1975.
- Davidson, E. H., W. H. Klein, and R. J. Britten, *Dev. Biol.*, **55**, 69–84, 1977.
- Flavell, R. B., J. Rimpau, and D. B. Smith, *Chromosoma (Berl.)*, **63**, 205–222, 1977.
- Hinegardner, R., in *Molecular Evolution*, pp. 179–199, F. J. Ayala, ed., Sinauer Associates, Inc., Sunderland, Mass., 1976.
- Hudspeth, M. E. S., W. E. Timberlake, and R. B. Goldberg, *Proc. Nat. Acad. Sci. U.S.A.*, **74**, 4332–4336, 1977.
- Manning, J. E., C. W. Schmidt, and N. Davidson, *Cell*, **4**, 141–155, 1975.
- Murray, M. G., R. E. Cuellar, and W. F. Thompson, *Biochemistry*, **17**, 5781–5790, 1978.
- Murray, M. G., J. D. Palmer, R. E. Cuellar, and W. F. Thompson, *Biochemistry* (in press), 1979.
- Schachat, F., D. J. O'Connor, and H. F. Epstein, *Biochim. Biophys. Acta*, **520**, 688–692, 1978.
- Smith, D. B., J. Rimpau, and R. B. Flavell, *Nucleic Acids Res.*, **3**, 2811–2825, 1976.
- Thompson, W. F., and M. G. Murray, in *The Biochemistry of Higher Plants: A Comprehensive Treatise*, VI (in press), A. Marcus, ed., Academic Press, New York, N.Y., 1979.
- Walbot, V., and L. S. Dure, *J. Mol. Biol.*, **101**, 503–536, 1976.

## THE USE OF cDNA FOR STUDY OF TRANSCRIBED SEQUENCES

*Debra L. Peters, Michael G. Murray, and William F. Thompson*

The proper functioning of a cell is dependent upon regulating the expression of its genes, and various processes of cellular differentiation and development are likely to involve large shifts in gene expression. In animal systems it has been shown that development often requires activating the transcription of large numbers of genes (e.g., Axel *et al.*, 1976; Harding *et al.*, 1977).

The role of transcriptional control in development has not been as thoroughly studied in plant systems. An ideal system to study is one with several normal physiological or morphological changes that can be triggered by an easily regulated physiological amount of inducer. An ideal inducer, the dose of which can be accurately controlled, is light.

In plants one of the more obvious developmental transitions triggered by light is the greening process. This process leads to a number of morphological changes such as leaf expansion, hook opening, and the cessation of stem elongation, in addition to chloroplast development. The array of responses leads one to suspect that greening is the result of many changes, both quantitative and qualitative, in the products of transcription. A system involving many transcriptional changes allows for the study of developmentally regulated messenger RNA populations as well as specific messengers.

Thompson and Cleland (1972) used filter hybridization techniques to demonstrate a change in repetitive sequence transcripts when pea seedlings were exposed to white light. Subsequent studies with beans (e.g., Smith, 1976; Klein and Pine, 1977; Malcolm and Russell, 1974) have shown that the polysome/monosome ratio increases after irradiation of etiolated seedlings. We have found that

buds from peas grown in the dark for six days have a polysome/monosome ratio of 0.5 to 0.6. It is interesting to note that hook material from dark-grown pea seedlings has a polysome/monosome ratio of 1.9–2.3, making it imperative to exclude hook tissue when effects of light on bud polysome content are being studied, particularly since hooks contain far more polysomes per gram of tissue than buds.

If, after the six-day dark period, the seedlings are exposed to continuous white incandescent and fluorescent light, the polysome/monosome ratio steadily increases, reaching a ratio of approximately 2.2 after 8 hr of illumination. After 12 hr of illumination the ratio is 3.5. The marked increase in polysome ratio of pea buds in response to light has prompted our investigation of light-induced messenger RNA populations.

A useful technique for characterizing messenger RNA populations is to hybridize a labeled DNA probe with an excess of RNA. RNA sequences complementary to the DNA probe will form hybrids, the rate of hybrid formation being dependent upon the initial concentration of RNA. The DNA probe complementary to mRNA (cDNA) is synthesized using avian myeloblastosis virus (AMV) reverse transcriptase (RNA-dependent DNA polymerase; Faras *et al.*, 1972). The template is polysomal poly-(A)-containing mRNA primed with oligo-(dT).

To isolate polyribosomes, tissue is homogenized in 3 volumes of 50 mM Tris, pH 8.5; 50 mM KCl; 20 mM MgOAc; 10 mM dithiothreitol (DTT); 250 mM sucrose; plus 30 mM VOSO<sub>4</sub> and 30 mM UMP (see below). The homogenate is strained through one



layer of Miracloth and clarified by centrifugation at  $16K \times g$  for 10 min. The clarified supernatant is then layered over a discontinuous sucrose shelf and polysomes are pelleted as described by Gray and Cashmore (1976). The polysome pellet is suspended in oligo-(dT)-cellulose binding buffer (Aviv and Leder, 1972), digested with 10–20  $\mu\text{g}/\text{ml}$  of proteinase K for 30 min at  $37^\circ\text{C}$ , and poly-(A) mRNA is isolated on oligo-(dT) cellulose as described by Aviv and Leder (1972).

During the isolation of polysomes one must take steps to inhibit ribonuclease activity. Jackson and Larkins (1976) reported that homogenization of tobacco leaves in buffer containing 400 mM KCl and 200 mM Tris pH 9.0 decreases ribonuclease degradation of polysomes. Egberts *et al.* (1977) have reported on the effectiveness of  $\text{VOSO}_4$  and UMP, which combine to form a transition state analog, as a ribonuclease inhibitor. Table

TABLE 16. The Effect of  $\text{VOSO}_4$ -UMP on Endogenous Ribonuclease Activity\*

$\text{VOSO}_4$ -UMP (mM)	Percentage CPM remaining	
	Buffer I	Buffer II
0	67	45
4	78	68
10	78	78
20	81	91
30	73	104
40	82	102
60	82	104

\* One gram of mung bean leaf tissue was homogenized in 10 ml of buffer containing 20 mM  $\text{MgOAc}$ –0.25 M sucrose–10 mM DTT–0.5% DOC–0.5% Triton X-100 and either 200 mM Tris pH 8.5–300 mM KCl (buffer I) or 50 mM Tris pH 8.5–50 mM KCl (buffer II).  $^3\text{H}$ -poly-(U) was added to the clarified homogenate after the indicated amount of 1 M  $\text{VOSO}_4$  and 1 M UMP were added. Samples were incubated at  $37^\circ\text{C}$  for one hour. The reaction was stopped by the addition of cold TCA to 5%. The precipitate was collected on glass fiber filters, and the amount of precipitable  $^3\text{H}$ -poly-(U) remaining was determined by scintillation counting.

16 shows the effect of varying amounts of  $\text{VOSO}_4$ -UMP on the degradation of poly-(U) by endogenous mung bean ribonucleases. As shown in the table, a modified Jackson and Larkins homogenization buffer (buffer I) is not sufficient for complete inhibition of mung bean homogenate ribonuclease activity. Although it appears superior to the low KCl–low Tris buffer (buffer II) in the absence of  $\text{VOSO}_4$ -UMP, complete inhibition was not obtained with buffer I even in the presence of high concentrations of the transition state analog. However, when the low KCl–low Tris buffer is used, 30 mM  $\text{VOSO}_4$ -UMP inhibits ribonuclease activity by 100%. In pea homogenate, 10 mM  $\text{VOSO}_4$ -UMP is apparently sufficient for 100% inhibition.

After investigating the effects of various parameters on the size and quantity of cDNA, we settled upon the following synthesis conditions: 0.05 M Tris, pH 8.3; 6 mM  $\text{MgCl}_2$ ; 0.02 M DTT; 0.5 mM dGTP, dATP, dTTP, and dCTP; 250 units/ml AMV reverse transcriptase; 5  $\mu\text{g}/\text{ml}$  oligo-(dT), and 10  $\mu\text{g}/\text{ml}$  poly-(A) mRNA. The labeled nucleotide is generally  $^3\text{H}$ -dCTP. The reaction is incubated at  $42^\circ\text{C}$  for 30 min. In our hands, these conditions produce cDNA copies of 90–100% of cowpea mosaic virus mRNA templates, with the majority of the cDNA being full length (4800 to 6400 nucleotides) as measured by agarose gel electrophoresis with glyoxal as denaturant (McMaster and Carmichael, 1977). When pea leaf poly-(A) mRNA is used as template, 60–80% of the message is copied; cDNA sizes range from 300 to 4000 nucleotides, with a mass average of 800 nucleotides.

Once the cDNA is isolated from the mRNA template and unincorporated nucleotides, it can be used for analysis of message populations. Such analyses are often made by hybridizing the cDNA to the template mRNA. Plots of the product of RNA concentration and time ( $R_0t$ ) versus the percentage hybridiza-

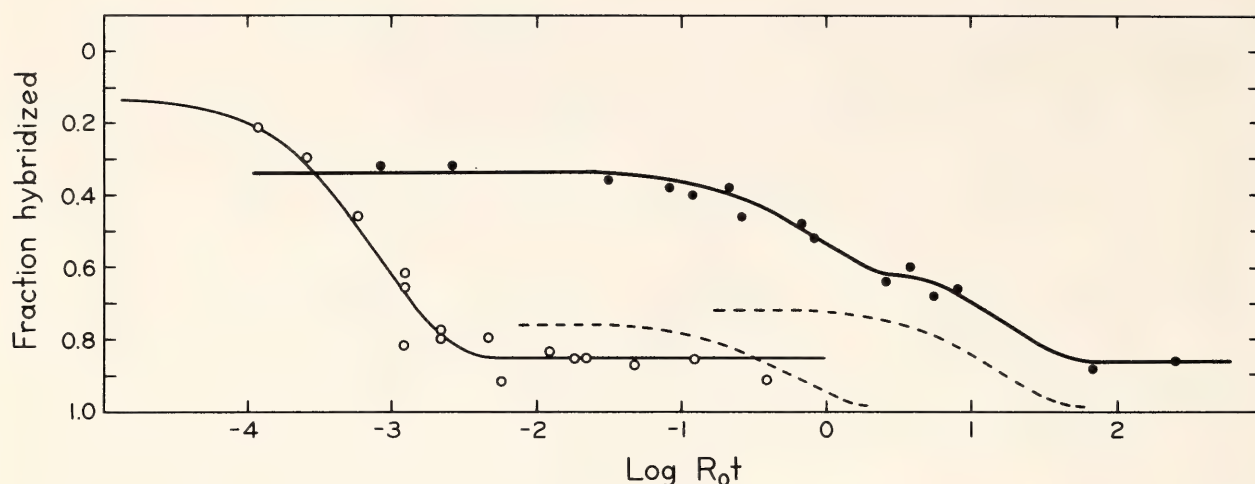


Fig. 48. Hybridization of pea bud mRNA and cDNA.  $^3\text{H}$ -cDNA was synthesized from poly-(A)-mRNA extracted from the terminal buds of pea seedlings grown for six days in the dark and then illuminated with white incandescent and fluorescent light for 24 hr. The average length of the pea cDNA was 650 nucleotides. To provide a kinetic standard,  $^3\text{H}$ -cDNA synthesized from cowpea mosaic virus mRNA was reacted with its template mRNA under similar conditions. Hybridizations were carried out in 0.6 M NaCl; 10 mM PIPES, pH 6.7; 0.1 mM EDTA; 0.1% SDS at 70° C. Hybridization was monitored by hydroxylapatite column chromatography. The solid lines represent computer-derived, least squares fits assuming a single theoretical pseudo-first order component for the cowpea reaction (O) and two components (indicated by dashed lines) for the pea cDNA reassociation (●). Complexity measurements are based on the following equation:

$$\text{Component complexity} = \frac{K_{\text{cowpea}}}{K_{\text{pea component}}} \times \frac{\text{Complexity of cowpea (} = 10,000 \text{)}}{\text{fraction cDNA hybridized}}$$

tion are called  $R_0t$  curves. Since the rate of the reaction is dependent upon the concentration of RNA, the relative abundance of different classes of RNA in the message population can be ascertained; those RNA species present in the population in multiple copies will hybridize with the cDNA at a faster rate than will those transcripts present in one or a few copies.

The amount of hybridization is assayed by hydroxylapatite column chromatography. Samples are incubated in NaCl-PIPES buffer (see Fig. 48) at 70°C for varying amounts of time. At the end of the incubation period the sample is diluted in 100 vols of 0.12 M sodium phosphate buffer. The samples are loaded on hydroxylapatite at 60°C. Under these conditions hybridized cDNA molecules will bind to the column, whereas single-stranded molecules will be washed through. Hybrids are then removed by

an additional wash with 0.12 M sodium phosphate at 98°–100°.

The kinetics of hybridization of pea bud cDNA with an excess of the template mRNA preparation are shown in Fig. 48. About 52% of the cDNA hybridizes between  $R_0t$  values of  $4 \times 10^{-1}$  to  $2.6 \times 10^2$ . Approximately 34% of the cDNA has already reacted at a  $R_0t$  value of  $2.6 \times 10^{-4}$ , suggesting that there is an extremely abundant fraction in the RNA preparation. (Analysis of the probe revealed only 5% zero-time binding, or foldback, sequences.) Although the nature of the highly abundant fraction is unknown, it is possible that it represents rRNA contamination.

By least-squares procedures (Pearson *et al.*, 1977), we can fit the data with a curve composed of two pseudo-first-order components. The slow component includes 28% of the cDNA and has a rate constant of  $0.057 \text{ M}^{-1} \text{ s}^{-1}$ . This



component has a kinetic complexity of  $5.7 \times 10^7$  nucleotides (calculated against cDNA/RNA hybridization kinetics of cowpea mosaic virus as a standard). The fast component has a rate constant of  $1.49 \text{ M}^{-1} \text{ s}^{-1}$ , and a kinetic complexity of  $1.86 \times 10^6$  nucleotides. These complexity estimates are only approximate, since the cowpea data was obtained from a separate experiment and there may actually be more than two mRNA frequency classes.

Fourteen percent of the cDNA appears to be unreactable and may represent cDNA's that are too small to form hybrids able to bind hydroxylapatite under the conditions used. It may be argued that the 14% unreactable fraction could represent a very high complexity component. However, one can estimate that the high complexity ( $5.7 \times 10^7$  nucleotides) component fitted by the computer represents 1.2% of the pea genome, or about 57,000 messengers 1000 nucleotides in length. This preliminary estimate of gene number is higher than usual (see Kiper, 1979) and can be viewed as an upper limit, making it unlikely that a third, higher complexity component

will be resolved at higher  $R_0t$  values.

The cDNA sequences representing transcripts of individual genes can also be cloned in *E. coli* by recombinant DNA techniques (see Jorgensen, this *Year Book*). Once a number of different clones are established, those messengers that are light induced or repressed can be scored and isolated. The kinetics of light induction or repression can then be followed at the polysomal message level as well as the HnRNA and RNP level. The cloned cDNA sequences can also be used for examining the nature of the genomic DNA sequences that code for the mRNA's as well as the DNA sequences that surround light-regulated messengers.

cDNA probes are also useful for examining the nature of the DNA sequences that code for mRNA's. Figure 49 shows such an experiment designed to determine whether mRNA's are transcribed from single-copy or repetitive sequences. The reassociation kinetics of cDNA were followed in the presence of excess genomic DNA, and the data have been analyzed in terms of two theoretical second-order components.

About 18% of the cDNA reassociates

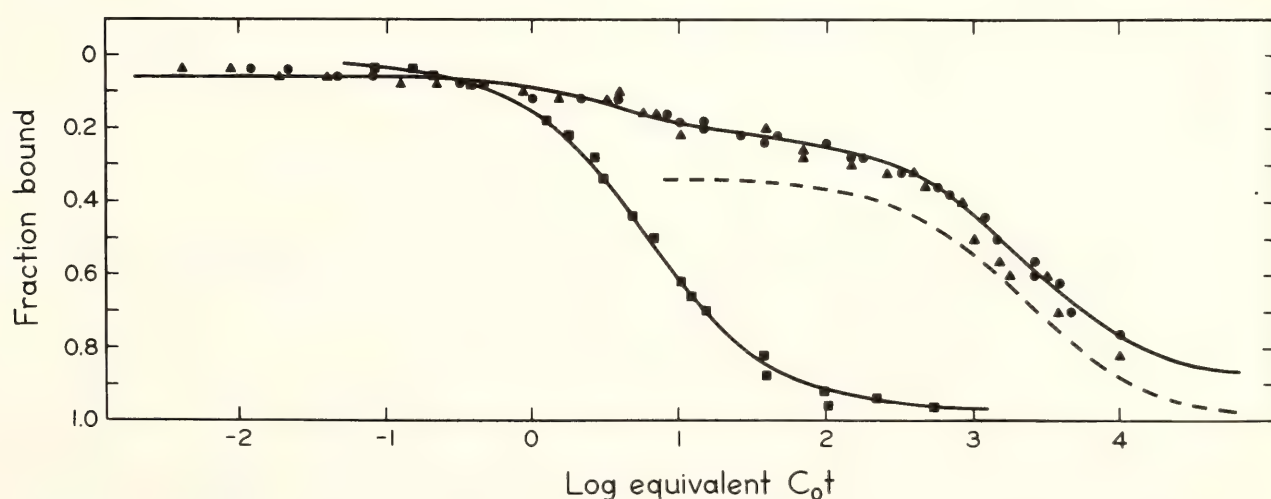


Fig. 49. Reassociation kinetics of cDNA synthesized from mRNA of pea buds. The reassociation kinetics of 650-nucleotide-long  $^3\text{H}$ -cDNA were followed in the presence of a 3,000-fold excess of 300-nucleotide-long unlabeled total DNA fragments as described previously (Murray *et al.*, 1978).  $^{14}\text{C}$ -*E. coli* DNA fragments (■) were included in the reaction mixtures to provide an internal kinetic standard. Reassociations were carried out at  $T_M-25$  (○) and  $T_M-35$  (▲), and analyzed in terms of two second-order components. For simplicity, the curve through the data points represents only the  $T_M-25$  solution.

more rapidly than would be expected for single-copy sequences. Whether the rapidly reassociating material is truly representative of mRNA's that are transcribed from repetitive sequences or is merely rRNA contamination is under investigation. About 11% of the cDNA is unretractable because DNA sequence excess was not obtained for mRNA's present in more than about 700 copies per cell.

About 71% of the cDNA tracer (80% of the total reaction) reassociates at a rate of  $0.0004 \text{ M}^{-1} \text{ s}^{-1}$ . Since single-copy sequences of this length (600 nucleotides) would reassociate at the same rate (Murray *et al.*, 1978), most of the mRNA's represented in the cDNA preparation are transcribed from single-copy sequences. Very similar results are obtained regardless of whether reassociation is performed at  $25^\circ$  or  $35^\circ\text{C}$  below the  $T_m$  of pea DNA, again indicating that most mRNA's are transcribed from single-copy sequences.

#### REFERENCES

- Aviv, H., and P. Leder, *Proc. Nat. Acad. Sci. U.S.A.*, **69**, 1408–1412, 1972.
- Axel, R., P. Feigelson, and G. Schutz, *Cell*, **7**, 247–254, 1976.
- Egberts, E., P. B. Hackett, and P. Traub, *Hoppe-Seylers Z. physiol. Chem.*, Bd 358, p. 475–490, 1977.
- Faras, A. J., J. M. Taylor, J. P. McDonnell, W. E. Levinson, and J. M. Bishop, *Biochemistry*, **12**, 2334–2341, 1972.
- Gray, R. E., and A. R. Cashmore, *J. Mol. Biol.*, **108**, 595–608, 1976.
- Harding, J. D., R. J. McDonald, A. E. Przybyla, J. M. Chirgwin, R. L. Pictet, and W. J. Rutter, *J. Biol. Chem.*, **252**, 7391–7397, 1977.
- Jackson, A. O., and B. A. Larkins, *Plant Physiol.*, **57**, 5–10, 1976.
- Klein, A. O., and K. Pine, *Plant Physiol.*, **59**, 767–770, 1977.
- Kiper, M. *Nature*, **278**, 279–280, 1979.
- Malcolm, A. A., and D. W. Russell, in *Mechanisms of Regulation of Plant Growth*, R. L. Bielecki, A. R. Ferguson, M. M. Cresswell, eds. Bulletin 12, The Royal Society of New Zealand, Wellington, 333–338, 1974.
- McMaster, G. K., and G. G. Carmichael, *Proc. Nat. Acad. Sci. U.S.A.*, **74**, 4835–4838, 1977.
- Murray, M. G., R. E. Cuellar, and W. F. Thompson, *Biochemistry*, **17**, 5781–5790, 1978.
- Pearson, W. R., E. H. Davidson, R. J. Britten, *Nucleic Acid Res.*, **4**, 1727–1731, 1977.
- Smith, H., *Eur. J. Biochem.*, **65**, 161–166, 1976.
- Thompson, W. F., and R. Cleland, *Plant Physiol.*, **50**, 289–292, 1972.

### ISOLATION OF *Pisum sativum* GENE SEQUENCES EXHIBITING ALTERED LEVELS OF EXPRESSION DURING LEAF DEVELOPMENT

*Richard Jorgensen and William F. Thompson*

Further advances in the study of gene organization and expression in higher plants will be enhanced by the isolation of individual genes and their RNA transcripts. Such purified materials will be of great value in elucidating the organization of gene-containing regions of the genome as well as the mechanisms of

gene expression and control during development. To achieve the isolation of individual genes of *Pisum sativum* (the garden pea) we have employed a gene "cloning" strategy as a first step. This approach involves the in vitro enzymatic synthesis of double-stranded DNA complementary to polyadenylated (poly-A)



mRNA molecules, followed by linkage of these synthetic DNA molecules to a bacterial plasmid and propagation of the hybrid plasmids in *Escherichia coli* (*E. coli*). Individual bacterial clones isolated in this manner contain sequences complementary to a single mRNA from the population of mRNA's initially employed and at the same time complementary to the gene which encodes that mRNA. Plasmid DNA's purified from these bacterial clones are useful as probes for studying the structure and expression of individual genes.

The procedure we used to clone pea poly-(A) mRNA sequences is a modification of an unpublished procedure of D. Kemp and J. Lis, obtained from G. Guild and M. Wolfner (personal communication). Briefly, double-stranded complementary DNA (cDNA) molecules were produced by a three-step synthesis using poly-(A) mRNA isolated from pea leaf tissue as template (see Peters *et al.*, this *Year Book*). The first step involves synthesis of cDNA from poly-(A) mRNA using AMV reverse transcriptase under the same conditions as described by Peters *et al.* Synthesis of the second strand of the double-stranded cDNA molecule is accomplished by means of a "self-priming" reaction in which the 3' end of the reverse transcriptase-synthesized cDNA "folds back" and anneals to a short complementary sequence near the 3' end. This "fold-back" structure is capable of priming *E. coli* DNA polymerase I, which then synthesizes the complementary second strand to produce a double-stranded molecule terminated at one end by a short single-stranded loop. In the third step, these molecules are treated with the single-strand nuclease S1, which acts to remove the loop, leaving a "flush-ended" double-stranded DNA molecule that can be joined to a bacterial plasmid and thereby propagated in *E. coli*. With this procedure we synthesized 0.38  $\mu\text{g}$  double-stranded cDNA from 1  $\mu\text{g}$  pea leaf poly-(A)

mRNA. The number average length of this cDNA was approximately 400 base pairs. So far about 70 clones have been derived from about 10 nanograms of the synthetic DNA preparation.

The first aspect of gene expression we have begun to investigate using cDNA clones as probes is the differential abundance of individual poly-(A) mRNA's in different tissues of the pea. It is possible to obtain semiquantitative measurements of the relative amounts of a single species of mRNA in different populations by using a technique called colony hybridization (Grunstein and Hogness, 1975). The principal advantage of this method is that it allows one to screen rapidly hundreds of cloned sequences to determine the relative amounts of RNA homologous to each clone. Bacterial colonies are grown in a grid-like pattern on nitrocellulose filters, and the DNA in each colony is then fixed to the filter *in situ*. These filters can be used to measure the abundance of sequences homologous to a given cloned sequence in different RNA populations by preparing highly labeled probes from the RNA's, hybridizing the probes to the filter-bound cloned DNA sequences, and estimating the amount of hybridization to the DNA in each colony by autoradiography. Comparison of the levels of RNA's in different populations is accomplished by hybridizing different populations to replicate filters.

Figure 50 shows the results of a colony hybridization experiment in which 50 cDNA clones were analyzed for their ability to hybridize to mRNA's from mature leaf tissue and bud tissue (from 8-day-old etiolated seedlings given 6 hr light immediately before harvest) from peas.

Thirty of the 50 clones hybridize to a level detectable in this assay, either to leaf or to bud mRNA probe: 29 to leaf RNA and 22 to bud RNA. In addition, the RNA's homologous to each of these 30 clones were present at different levels

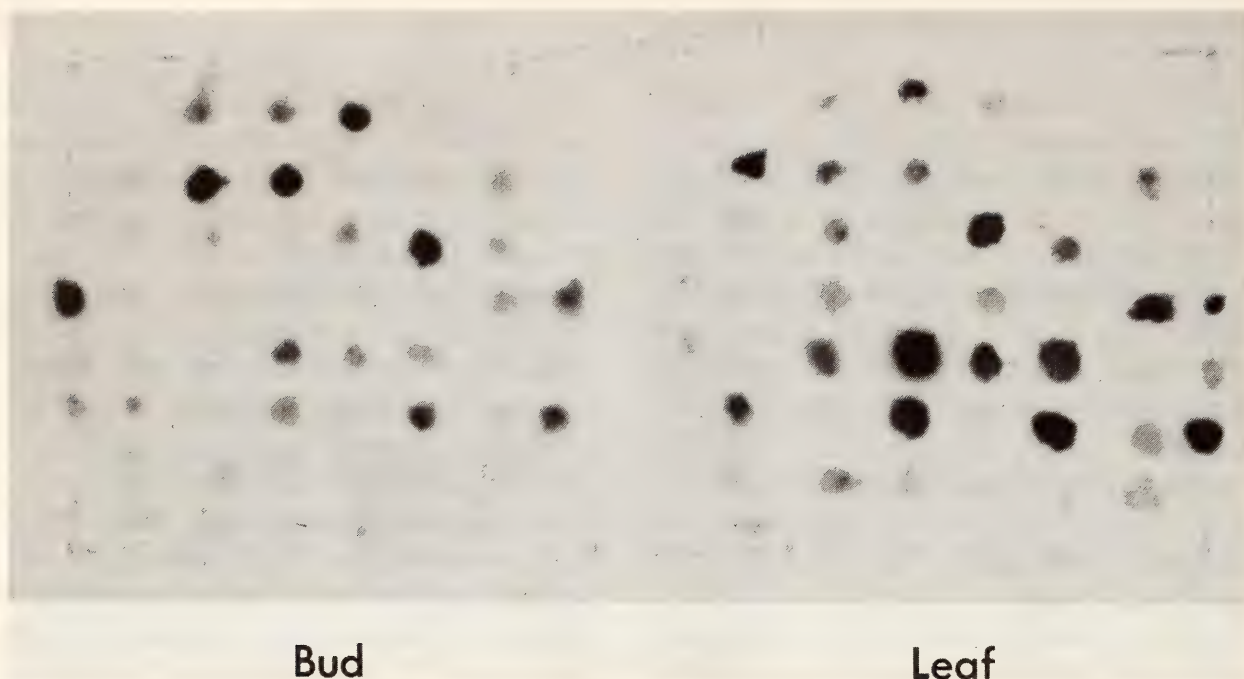


Fig. 50. Autoradiograph of two nitrocellulose filters containing 51 cDNA clones hybridized to pea bud (left) and leaf (right) messenger RNA sequences labeled by synthesis of single-stranded cDNA with  $^{32}\text{P}$ -labeled precursors. The conditions of hybridization were: 50% formamide, 0.75 M NaCl, 75 mM Na citrate, 50 mM Na  $\text{PO}_4$ , pH7, 42°C, 38 hr. Colony imprints were made by replica plating onto the filter so that each filter carries the 51 colonies in the same configuration. For reference, the first row carries 4 clones; the second and third, 6 each; fourth, fifth and sixth, 8 each; the seventh, 6; and the eighth, 5. Autoradiography was for 50 hr at  $-20^\circ\text{C}$  with Kodak X-omat R film and a du Pont Lightning Plus intensifying screen.

in leaf and bud tissue, as judged by comparison of the intensities of the autoradiographic signal produced by the same cDNA clone hybridized to probes representing the two different RNA populations. Although all the cDNA clones were isolated from leaf mRNA, only 23 of these 30 messages were more abundant in leaf than in bud mRNA populations; the other seven were more abundant in bud than in leaf populations. Furthermore, there is significant variation in the intensities of signals given by different cDNA clones in the same hybridization reactions, suggesting that many of these clones derive from independent messages. It should be noted that tissue-specific differences in message levels reflect changes only in the relative abundance of a given message in the two populations of messages and not necessarily in the absolute amount of a particular message in each cell. In other words, an increase in the signal of one message in the colony hybridization assay may be

the result of either an increase in the level of that message or a decrease in the level of other messages in the cell.

In summary, we have isolated sequences homologous to pea leaf mRNA by a cDNA cloning procedure, and have shown that at least 30 of these clones are homologous to RNA's whose level is different in populations of pea leaf and bud poly-(A) mRNA's. We plan to extend this analysis to many hundreds of pea cDNA clones to establish classes of messages distinguished by their levels in developing leaf and bud tissue. We hope that this approach will lead to the identification of the major species of messenger RNA's that are developmentally controlled in the growing leaf.

#### REFERENCE

- Grunstein, M., and D. Hogness, *Proc. Nat. Acad. Sci. U.S.A.*, **72**, 3961-3965, 1975.



CLOWING OF PLANT DNA: COMPARISON OF FIVE HOST STRAINS OF *Escherichia coli*

Richard E. Cuellar, Eric U. Selker, and William F. Thompson

INTRODUCTION

In order to study the sequence arrangement of plant DNA's, we have in the past used the methods of DNA reassociation and thermal denaturation. In those studies (Murray *et al.*, 1978; *Year Book* 76, pp. 240-255; *Year Book* 77, pp. 316-332) total genomic DNA could be studied in some detail by fractionation into components of differing kinetic complexities or thermal stabilities. A limitation of such techniques is that obtaining "discrete" components for use as probes is difficult, and therefore descriptions of a genome obtained from such studies cannot go beyond the sequence "family" level. Even with such limitations it has been possible to show that the pea genome, for example, is complex: consisting of a "spectrum" of repetitive sequence "families" with a broad range of repetition frequencies. Recombinant DNA technology allows one to clone discrete fragments of DNA in amounts necessary to study genome organization at the sequence level. Recent studies of the sea urchin took advantage of discrete cloned sequences to investigate its complex genome. As in the pea genome, sea urchins contain a broad spectrum of repetitive sequence families (Klein *et al.*, 1978; Moore *et al.*, 1978).

We report here some preliminary results in the cloning of pea DNA, and progress in the development of useful cloning systems for the study of plant DNA. Our approach was to survey a number of host strains of *Escherichia coli* which would tolerate the presence of recombinant plasmids containing plant sequences without causing deletions of the original sequence. This study was necessitated by early results indicating that fragments of pea DNA produced by the restriction enzyme EcoRI in the plasmid pACYC184 would undergo deletion at high frequency when cloned in host strain ES89.

Our survey included all the strains listed in Table 17. We examined the strains with respect to transformation frequency of covalently closed circular (ccc), linearized, and recircularized plasmid pACYC184, and transformation efficiency with respect to cloned *E. coli* fragment and cloned pea DNA fragments. Transformation frequency varied from  $1.0 \times 10^6$  to  $1.5 \times 10^6$  transformants per  $\mu\text{g}$  of ccc plasmid for strains HB101, SK1592, and ES89, and from  $5 \times 10^5$  to  $8 \times 10^5$  transformants per  $\mu\text{g}$  for ES4 and SK2267. Recircularized plasmid DNA transformed cells at approximately 10% of these levels for each strain. Recombinant plasmids containing *E. coli*

TABLE 17. Host Strains of *E. coli*

Strain	Genotype							
ES4 (c600)	Bl-	leu-	thr-	trp $\Delta$ E5			rK-	mK+
ES89 (c600)	Bl-	leu-	thr-	trp-			rK-	mK+
SK1592	F-	gal-	thi-	Trp	end A-	sbc Bl5	hsd R4	hsd M+
SK2267	same as SK 1592, with additional lesion <i>recA1</i>							
HB101 (c600)	Bl-	leu-	thr-	Pro-	SuII,	recA-	rK-	mK-

DNA fragments transformed cells at from  $5.2 \times 10^3$  per  $\mu\text{g}$  in strain HB101, to  $1.1 \times 10^3$  per  $\mu\text{g}$  for the remaining strains. Recombinant plasmids containing plant DNA fragments transformed cells at approximately one-fourth the frequencies seen for plasmids containing *E. coli* DNA. Thus the results vary a great deal from strain to strain.

The most striking difference is seen by comparing the size distributions of fragments recovered after cloning in strains HB101 and ES89. Fig. 51 shows integral frequency distributions for fragments cloned in ES89 and HB101, along with a plot of the distribution of original fragment sizes in a limit EcoRI digest of

pea DNA. One might expect that a population of cloned fragments would approximate the EcoRI "spectrum," if ligation, transformation, and subsequent propagation are operating as nondiscriminatory processes. It is clear that the clones from HB101 approach such a distribution and those obtained in ES89 do not. We have also observed that some of the "small" cloned sequences derived from ES89 show significant hybridization to bands of much higher molecular weight when assayed by the Southern hybridization technique (Southern, 1975). We are in the process of testing cloned fragments from HB101 but do not have the results at this time.

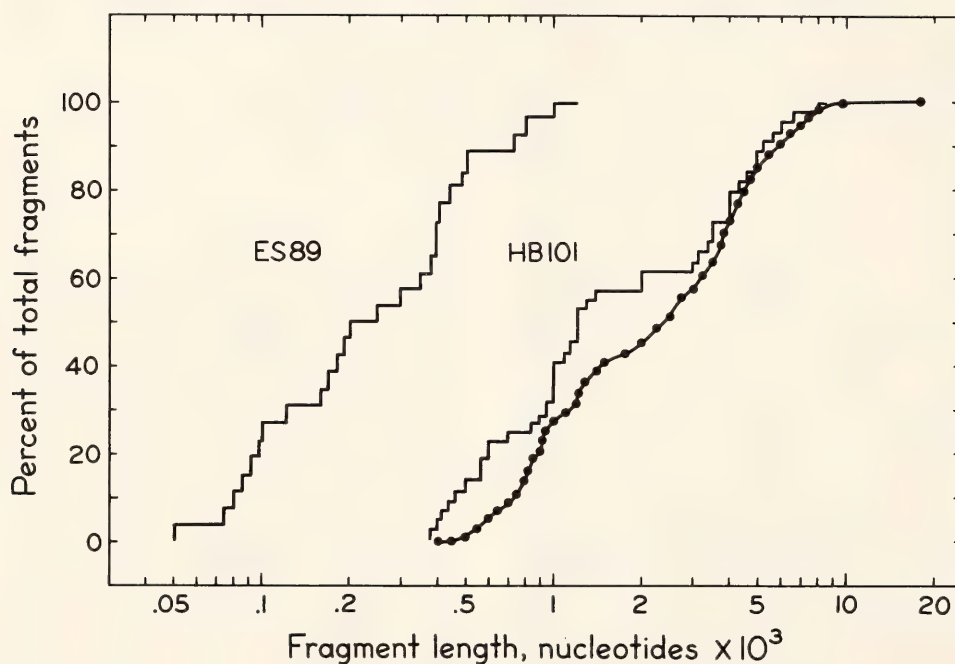


Fig. 51. Comparison of EcoRI restriction fragment sizes from two host strains of *E. coli*. Native pea DNA and pACYC184 DNA were separately limit-digested with EcoRI endonuclease (New England Biolabs). Upon completion of digestion, EcoRI was inactivated by the addition of 1/20 volume of 100:1 ethanol:diethylpyrocarbonate and heating to 70°C for 10 min. Six  $\mu\text{g}$  EcoRI-cleaved pea DNA and one  $\mu\text{g}$  plasmid DNA were combined in ligation buffer (20 mM Tris pH 7.5, 10 mM  $\text{MgCl}_2$ , 1 mM dithio-threitol, 1 mM  $\text{Na}_2\text{EDTA}$ , 0.05 M ATP) and incubated in the presence of  $\sim 0.2$  units of T4 ligase (New England Biolabs) at 15°C for 5 hours. One fifth of the ligation mixture was used to transform 0.2 ml of competent cells (Mandel and Higa, 1970). Transformants were selected on L. B. plates containing 10  $\mu\text{g}/\text{ml}$  tetracycline (Sigma) and recombinants were screened on plates containing 25  $\mu\text{g}/\text{ml}$  chloramphenicol. Plasmids were prepared from chloramphenicol sensitive colonies by the quick lysate procedure (Cameron, *et al.*, 1970) as modified for plasmids (S. Rothstein, personal communication). Whole ccc plasmid sizes were determined by agarose gel electrophoresis, using ccc pACYC184 monomers and dimers, and  $\phi\text{X174}$  am3 rf I DNA as standards. Insert lengths were also determined by EcoRI cleavage and subsequent sizing by 2% agarose or 8% polyacrylamide gel electrophoresis. (●) EcoRI fragments of total pea DNA.



Table 17 shows the genetic backgrounds of the host strains used in this study. HB101 and ES89 differ in several ways, including *recA*. Recombination-deficient *recA*<sup>-</sup> strains of *E. coli*, including HB101, do not form "figure 8" molecules (recombination intermediates composed of two molecules joined at a region of homology) when compared to wild type or *recBC*<sup>-</sup> strains (Potter and Dressler, 1976). If the loss of pea DNA sequences is a recombination-induced deletion, then the deletion could be mediated to some extent by a process involving the *recA* function. We are in the process of screening recombinant plasmids propagated in ES4, SK2267, and SK1592. Preliminary sizing of whole recombinant plasmids suggests that SK2267 can tolerate plasmids containing fragments of larger size than ES89.

We have little understanding of the deletion phenomenon we observe. We do know that plant DNA differs from other DNA's in the extent of sequence repetition (repetitive sequence complements of more than 70% are common) and in the extent of methylation. Whether or not these features are related to the observed phenomenon is not known.

## ACKNOWLEDGMENTS

We would like to thank Sidney Kushner for strains SK2267 and SK1592, Eric Selker for strains ES89 and ES4, and Dan Stinchcomb for strain HB101. We would also like to thank Richard Jorgensen for stimulating discussions and valuable advice in this study.

## REFERENCES

- Cameron, J. R., P. Philippsen, and R. W. Davis, *Nucleic Acids Res.*, **4**, 1429-1448, 1977.
- Klein, W. H., T. L. Thomas, C. Lai, R. H. Scheller, R. J. Britten, and E. H. Davidson, *Cell*, **14**, 889-900, 1978.
- Mandel, M., and A. Higa, *J. Molec. Biol.*, **58**, 159-162, 1970.
- Moore, G. P., R. H. Scheller, E. H. Davidson, and R. J. Britten, *Cell*, **15**, 649-660, 1978.
- Murray, M. G., R. E. Cuellar, and W. F. Thompson, *Biochemistry*, **17**, 5781-5790, 1978.
- Potter, H., and D. Dressler, *Proc. Nat. Acad. Sci. U.S.A.*, **73**, 3000-3004, 1976.
- Southern, E. M., *J. Molec. Biol.*, **98**, 503-517, 1975.

SINGLE-COPY DNA HOMOLOGIES AND THE PHYLOGENY OF *Atriplex*

Heather S. Belford and William F. Thompson

In continuing our effort to clarify phylogenetic relationships among C3 and C4 species of the genus *Atriplex*, we have now examined both single-copy sequence homology and cross reactivity in some detail for eight species. *A. fruticulosa* (C<sub>4</sub>), *A. phyllostegia* (C<sub>3</sub>), *A. serenana* (C<sub>4</sub>), and *A. truncata* (C<sub>4</sub>) are classified in the subgenus Obione and *A. hortensis* (C<sub>3</sub>), *A. rosea* (C<sub>4</sub>), *A. sabulosa* (C<sub>4</sub>), and *A. triangularis* (C<sub>3</sub>) in Euatriplex. Single-copy sequence DNA from spinach (*Spinacia oleracea*), which also belongs

to the family Chenopodiaceae, was included to provide an extrageneric comparison.

Total DNA was extracted from mature leaf tissue of each species. Single-copy sequences were purified by hydroxylapatite fractionation and labeled in vitro with <sup>14</sup>C-dCTP or <sup>3</sup>H-dCTP via an oligonucleotide-primed reaction with *E. coli* DNA polymerase I (modified from Murray *et al.*, *Year Book* **76**, 262-267). Homologous and heterologous labeled single-copy tracers were mixed with ex-

cess unlabeled total *Atriplex* DNA in such proportions that the tracers were too dilute to reassociate significantly except with the unlabeled “driver” DNA sequences. Technical details of these and other procedures have been described (Belford, 1979; Belford and Thompson, in preparation).

TABLE 18. Haploid Genome Size, Single-Copy Fraction and Single-Copy Complexity\*

Species	Haploid Genome 10 <sup>8</sup> NTP	Single-Copy Fraction	Single-Copy Complexity, 10 <sup>8</sup> NTP
<i>A. serenana</i>	4.1	0.30	1.2
<i>A. fruticulosa</i>	3.5	0.40	1.4
<i>A. rosea</i>	4.0	0.37	1.5
<i>A. sabulosa</i>	4.1	0.39	1.6
<i>A. phyllostegia</i>	4.6	0.41	1.9
<i>A. hortensis</i>	7.3	0.28	2.0
<i>A. truncata</i>	5.6	0.38	2.1
<i>A. triangularis</i>	6.9	0.31	2.1
spinach	7.9	0.26	2.1
<i>E. coli</i>	0.045	1.00	0.045

\* Genome size, single-copy fraction, and single-copy complexity were derived from single-copy tracer and total DNA reassociation kinetics as measured by hydroxylapatite chromatography. The fraction of single-copy DNA may thus be somewhat underestimated if very short single-copy sequences are interspersed with repeats.

TABLE 19. Estimates of Interspecific Cross Reactivity

Species A	Species B	Driver A		Driver B	
		Fraction	NTP × 10 <sup>-8</sup>	Fraction	NTP × 10 <sup>-8</sup>
<i>A. rosea</i>	<i>A. sabulosa</i>	0.72	1.1	0.81	1.2
	<i>A. triangularis</i>	0.55	1.2	0.75	1.1
		0.59			
	<i>A. hortensis</i>	0.58	1.2	0.64	1.0
	<i>A. fruticulosa</i>	0.55	0.8	0.60	0.9
		0.56			
	<i>A. truncata</i>	0.53	1.1	0.62	0.9
	<i>A. serenana</i>	0.64	0.8	0.47	0.7
		0.56		0.45	
		0.63			
	<i>A. phyllostegia</i>	0.26	0.6	0.26	0.4
		0.33			
	spinach	0.12	0.2	0.21	0.3
<i>A. serenana</i>	<i>A. fruticulosa</i>	0.96	1.3	...	...
		0.89			
	<i>A. sabulosa</i>	0.81	1.3	...	...
	<i>A. truncata</i>	0.72	1.5	0.93	1.2
	<i>A. triangularis</i>	0.56	1.4	...	...
	<i>A. hortensis</i>	0.46	0.9	...	...
	<i>A. rosea</i>	0.47	0.7	0.64	0.8
		0.45		0.56	
				0.63	
	<i>A. phyllostegia</i>	0.28	0.5	0.41	0.5
	spinach	0.18	0.4	0.22	0.3



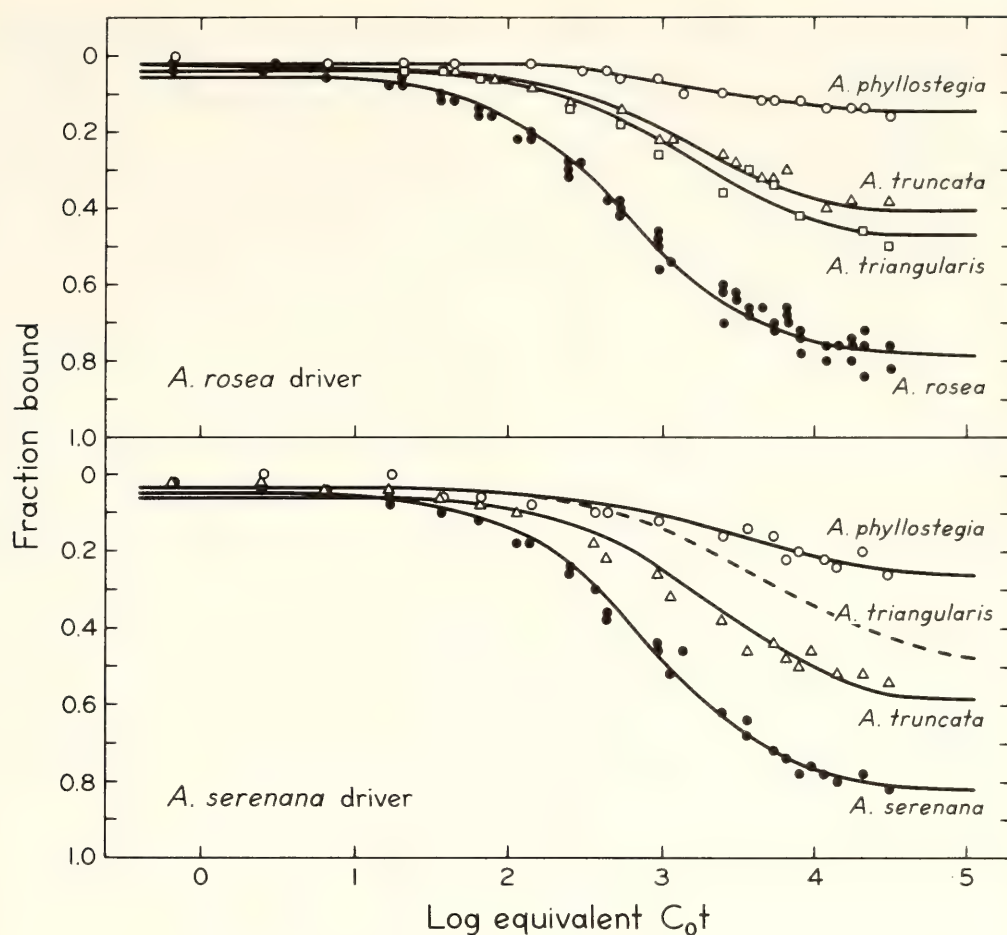


Fig. 52. Reassociation kinetics of homologous and heterologous single-copy tracers with excess total DNA from *A. rosea* (top panel) and *A. serenana* (bottom panel). The homologous reaction data have been fitted with ideal second-order components according to the least squares computer program of Pearson *et al.* (1977). Heterologous reaction data were fitted by means of a similar program (Galau *et al.*, 1976; Belford and Thompson, *Year Book* 76, 246–252) modified to take into account the retardation of heterologous reassociation resulting from base sequence mismatch (Bonner *et al.*, 1973). The *A. triangularis* curve in the bottom panel is actually the theoretical single-copy component of a two-component fit, since a small amount of repetitive sequence contamination was present in this tracer.

Genome size and single-copy fraction measurements are summarized in Table 18. Single-copy complexity is estimated from the product of these two values. All the *Atriplex* species and spinach have small genomes in comparison with many other plants (Bennett and Smith, 1976). Moreover, it is observed that *A. fruticulosa*, *A. serenana*, *A. sabulosa*, and *A. rosea* contain only about 75% as much single-copy DNA per haploid genome as do the other four *Atriplex* species and spinach.

Figure 52 illustrates the kinetics of several interspecific reactions, and estimates of interspecific cross reactivity are summarized in Table 19. While spe-

cies pairs previously proven capable of producing fertile sexual hybrids (*A. serenana*  $\times$  *A. fruticulosa* and *A. rosea*  $\times$  *A. sabulosa*; Nobs, *Year Book* 75, 421–423) show high cross reactivity, high values are also observed for other species pairs that are not known to do so (e.g., *A. serenana*  $\times$  *A. sabulosa* or *A. truncata*). Thus high cross reactivity is not closely correlated with the ability to produce fertile progeny.

If the broad range of cross reactivities were simply the result of sequence divergence by random base substitution, the single-copy sequences able to hybridize between species should also show a broad range of base sequence mis-

match, with increasing base substitution paralleling decreasing cross reactivity. Mismatch in interspecific hybrids was measured by comparing the thermal stabilities of duplexes formed by heterologous and homologous single-copy tracers reassociated simultaneously with the same unlabeled DNA. The difference between the average thermal stabilities of these duplexes ( $\Delta T_E$ ) should be proportional to the percentage of mismatched base pairs in the interspecific products. Under the thermal elution conditions we used (Murray *et al.*, 1978; see also Martinson and Wagenaar, 1977), a 1°  $\Delta T_E$  indicates approximately 2% mismatch (Belford, 1979 and in preparation). The  $\Delta T_E$  results for *Atriplex* interspecific hybrids are summarized in Table 20. Out of an experimentally possible range of perhaps 20°C, most *Atriplex*  $\Delta T_E$  values fell between 5° and 6.5°C. The two species pairs that showed both high DNA cross reactivity and the ability to form fertile sexual hybrids (*A.*

*fruticulosa*  $\times$  *A. serenana* and *A. rosea*  $\times$  *A. sabulosa*) had  $\Delta T_E$  values of 4.0°–4.5°, and the largest  $\Delta T_E$  observed for any pair of species was only 8.2°C.

Thus the broad range of *Atriplex* cross reactivities does not appear to be attributable to simple base-substitution events. Instead, we believe the spectrum of cross reactivities is probably the result of widespread and random deletion events. For example, the ancestral genome from which modern *Atriplex* species were derived may have been larger than those of the present-day species. In the course of evolution, different sequences could have been deleted from different genomes, with the result that many are now found in only one member of a given species pair. Since base substitutions—but not necessarily deletion events—are thought to occur at a constant rate in evolution, we considered the  $\Delta T_E$  values rather than the cross reactivity estimates in developing a phylogenetic scheme for *Atriplex* species.

All species in this study were compared with the same two reference species. Possible divergence-time relationships therefore fall into only three categories: a given lineage may have originated before the separation of lines leading to the reference species, at the same time as this separation, or at some later time. If genetic isolation was a unique and permanent event, and mutations have accumulated at the same rate in different lines, then the  $\Delta T_E$  relationships should also fall into three classes. In the case of a lineage originating before the reference species, the  $\Delta T_E$  should be equal for both references but greater than that between the reference species themselves. Species whose origin was contemporary with that of the references should also have equal  $\Delta T_E$  values, but they should be the same as the  $\Delta T_E$  between references. When a given lineage originated from one of the reference lines later in evolution it should show a smaller  $\Delta T_E$  when compared to that

TABLE 20. Summary of  $\Delta T_E$  Measurements

Tracer A	Tracer B	Corrected* $\Delta T_E$ , °C	
		Driver A	Driver B
<i>A. rosea</i>	<i>A. sabulosa</i>	4.5	4.0
	<i>A. triangularis</i>	5.0	6.5
	<i>A. truncata</i>	5.2	6.5
	<i>A. phyllostegia</i>	5.5	4.2
	<i>A. hortensis</i>	6.2	5.4
	<i>A. serenana</i>	6.5	6.7
	<i>A. fruticulosa</i>	7.2	7.5
	spinach	8.2	4.2
<i>A. serenana</i>	<i>A. fruticulosa</i>	4.4	...
	<i>A. truncata</i>	5.0	4.2
	<i>A. sabulosa</i>	5.0	...
	<i>A. hortensis</i>	5.2	...
	<i>A. phyllostegia</i>	5.7	4.7
	<i>A. rosea</i>	6.7	6.5
	<i>A. triangularis</i>	8.2	...
	spinach	4.4	6.0

\*  $\Delta T_E$  values were corrected for the contribution of any tracer sequences reassociating at low *cot* values as described by Belford and Thompson (*Year Book* 76, pp. 246–252).



reference species, but the  $\Delta T_E$  observed with the other reference should still be equal to that between the references themselves.

These theoretical  $\Delta T_E$  relationships are indicated by the heavy solid lines in the matrix diagram of Figure 53. The two arcs define points equidistant from each reference. Where these arcs intersect, the  $\Delta T_E$  for each reference is the same as that between references. Dashed lines and circles have been used to indicate the  $1^\circ$  range of experimental error we observe in actual measurements. Given this range, all the *Atriplex* species

can be considered to fit the predicted pattern for simple divergence relationships (although the fit for *A. triangularis* and *A. sabulosa* is only marginal; see below). *A. phyllostegia* and *A. hortensis* are located close to the intersection point, indicating that the species became isolated from the *A. rosea* and *A. serenana* lines at about the same time as or shortly after these lineages separated from each other. The *A. truncata* lineage may have originated at about this time or perhaps somewhat later, while the placement of the *A. fruticulosa* range across the *A. serenana* leg of the matrix clearly sug-

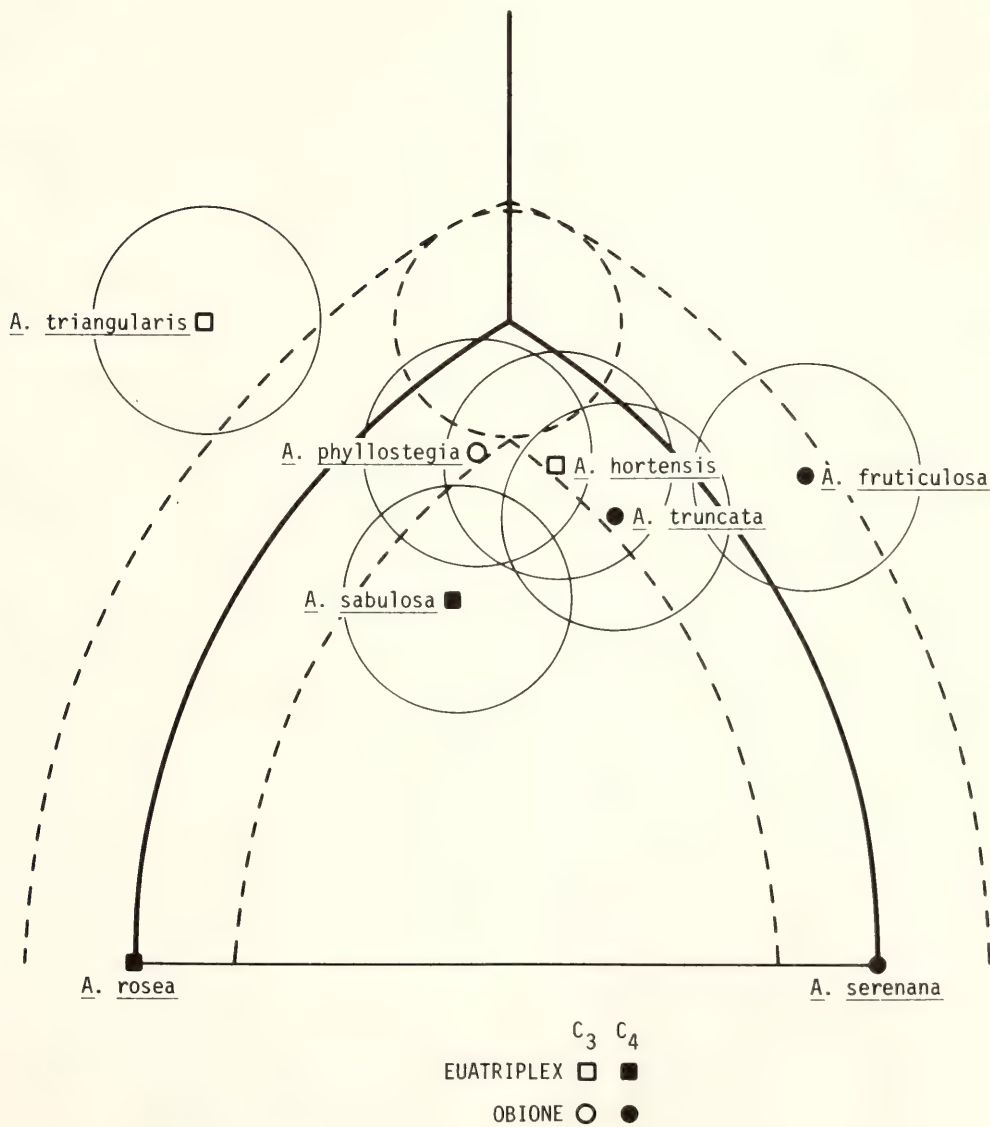


Fig. 53. Location of the *Atriplex* species on the theoretical matrix described in the text. Linear distances between any two species positions are proportional to the  $\Delta T_E$  measurements for the interspecific hybrids. Circles and dashed lines indicate a  $\pm 1^\circ$  error range. Actual  $\Delta T_E$  values are given in Table 20.

gests that *A. fruticulosa* diverged from the *A. serenana* after the *A. serenana* line had separated from that of *A. rosea*.

The overlap of *A. triangularis* and *A. sabulosa* ranges with that of the *A. rosea* leg might also be interpreted to suggest that these species diverged from the *A. rosea* lineage after the *A. rosea* and *A. serenana* lines had become independent. However, these overlaps are not great, which leads us to consider an alternative hypothesis involving secondary exchanges of genetic material. It may be that *A. triangularis* first separated from *A. serenana* and *A. rosea* before they separated from each other. At some later time, secondary gene exchange may have occurred between *A. triangularis* and *A. rosea*, reducing the apparent base-sequence divergence measurable for this species pair. Similarly, the *A. sabulosa* ancestor may have retained the ability to interbreed with both *A. rosea* and *A. serenana* lines for some time after the separation of the two species, so that the divergence between *A. sabulosa* and either reference appears to be less than the divergence between the references themselves.

The *Atriplex*-spinach reactions showed much more than the usual variation in  $\Delta T_E$  values, a result which is probably attributable to the low levels of cross reaction obtained in these experiments. Nevertheless, it is interesting to note that all the spinach-*Atriplex* values are in the same range as those between *Atriplex* species. Since it is unlikely (though not impossible) that spinach and some *Atriplex* species shared a common ancestor more recently than other *Atriplex* species pairs, one interpretation of the spinach results is that there may be a small subset of single-copy sequences which has been more strongly conserved than total single-copy DNA in spinach and *Atriplex* genomes. Further investigation of this possibility should prove interesting. However, at present, the main significance of these observations is as an illus-

tration of the importance of measuring cross reactivities as well as hybrid thermal stability.

Several conclusions from these studies appear to be of general interest. First, the range of cross reactivities we observed was unusually broad and was not associated with a similar degree of variation in hybrid thermal stability. Several authors have reported consistently high levels of cross reactivity within genera of animals (e.g., Rice, 1972; Shields and Straus, 1975; Sohn *et al.*, 1975), which may indicate that deletion events have been less important in the evolution of these genera than they have in *Atriplex*. In addition, our hybrid thermal stability measurements indicate that lines leading to many present-day *Atriplex* species probably originated during a single period of rapid speciation. This group includes *A. rosea*, *A. serenana*, *A. hortensis*, *A. phyllostegia*, and perhaps *A. truncata*; *A. triangularis* may have originated even earlier. Even the first four species, whose placement is most certain, include representatives of both subgenera. Thus, the subgeneric distinction proposed by Hall and Clements (1923), with its implication of a gradually reticulating phylogenetic "tree," is not supported by our data. Furthermore, since the same four species also include representatives of both  $C_3$  and  $C_4$  photosynthetic pathways, it appears logical to assume that  $C_4$  photosynthesis first appeared in *Atriplex* at about this time. In the context of the phylogenetic history derived from our molecular data, it is no longer necessary to postulate a polyphyletic origin for  $C_4$  photosynthesis within *Atriplex*.

#### REFERENCES

- Belford, H. S., Thesis, University of Massachusetts, 1979.
- Bennett, M., and J. B. Smith, *Phil. Trans. Royal Soc. Lond., B* 274, 227-273, 1976.
- Bonner, T. I., D. J. Brenner, B. R. Neu-



- feld, and R. J. Britten, *J. Mol. Biol.*, **81**, 122–135, 1973.
- Galau, G. A., M. E. Chamberlin, B. R. Hough, R. J. Britten, and E. H. Davidson, in *Molecular Evolution*, F. J. Ayala, ed., Sinauer Associates, Sunderland, Mass., 1976.
- Hall, H. M., and F. E. Clements, *Carnegie Inst. Wash. Pub.* **326**, 1923.
- Martinson, H. G., and E. B. Wagenaar, *Biochim. Biophys. Acta*, **474**, 445–455, 1977.
- Murray, M. G., R. E. Cuellar, and W. F. Thompson, *Biochemistry*, **17**, 5781–5790, 1978.
- Pearson, W. R., E. H. Davidson, and R. J. Britten, *Nucleic Acids Res.*, **4**, 1727–1735, 1977.
- Rice, N. R., *Brookhaven Symp. Biol.*, **23**, 44–78, 1972.
- Shields, G. F., and N. A. Straus, *Evolution*, **29**, 159–166, 1975.
- Shon, U.-I., K. H. Rothfels, and N. A. Straus, *J. Mol. Evol.*, **5**, 75–85, 1975.

## STUDIES IN THE OSMUNDACEAE: SINGLE-COPY DNA COMPARISONS

*Diana B. Stein\* and William F. Thompson*

Earlier DNA sequence comparisons using total DNA from three species of *Osmunda* indicated that the DNA's of these species were similarly diverged (*Year Book* **76**, 252–255). Such evidence suggests that lines leading to *Osmunda cinnamomea*, *O. regalis*, and *O. claytoniana* probably separated from a common ancestor at about the same time. To verify this earlier conclusion and to obtain an estimate of the rate of nucleotide substitution in this group, comparisons have now been made using a tracer enriched for single-copy sequences.

DNA was isolated as described earlier (Stein and Thompson, 1978), and other procedures are fully described in Stein *et al.* (1979). Reassociation was carried out in a buffer consisting of 1.0 M NaCl, 50% formamide, and 10 mM piperazine-N,N'-bis [2-ethanesulfonate], pH, 6.7–6.9. The melting temperature ( $T_m$ ) of sheared native DNA in this solvent was determined optically to be 63°C. Bacterial DNA incubated in our buffer at 42°C reassociates approximately 3.5 times faster than in 120 mM sodium phosphate at 60°. To isolate a DNA frac-

tion enriched for unique sequences, aliquots of total DNA were denatured by heating at 85°C and reassociated at 42°C to a  $C_0t$  of 600. The aliquots were rapidly chilled in ice water, diluted 200-fold with 120 mM sodium phosphate buffer, and passed over hydroxylapatite at 60°C. The unbound fraction containing primarily the unreassociated single-copy sequences was then subjected to agarose gel exclusion chromatography (Bio-Gel A 1.5m) to remove low molecular weight material. DNA in the exclusion peak was iodinated according to procedures modified from Orosz and Wetmur (1974) or used to prepare complementary tracer with DNA polymerase I (Murray *et al.*, *Year Book* **76**, 262–267).

Reassociation kinetics of  $^{125}\text{I}$ -tracer prepared from *O. claytoniana* DNA are shown in Fig. 54. The tracer data were fitted with theoretical second order components using a computerized least-squares procedure (Pearson *et al.*, 1977). The best fit was obtained with a 17% repeated component and 26% unreactable (degraded) DNA. In this solution 77% of the reactable tracer reassociates as a single component (dashed line) with a rate constant of  $2.9 \times 10^{-4}$ . Examination of the data for total DNA

\* Department of Botany, University of Massachusetts, Amherst.

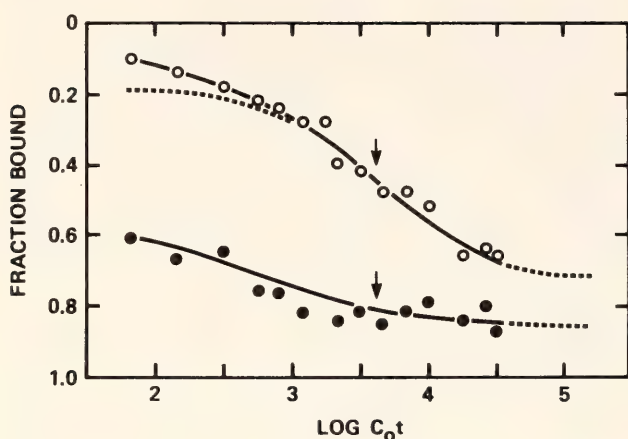


Fig. 54. Reassociation kinetics of *O. claytoniana* unlabeled DNA fragments (●) and  $^{125}\text{I}$  tracer enriched for single-copy sequences (○). Triplicate samples were heat denatured and incubated to various  $C_0t$  values at  $T_M - 21^\circ$  prior to hydroxylapatite fractionation. The dashed line represents a theoretical second-order component with a rate constant of  $2.9 \times 10^{-4}$  in the solvent used (see text). Arrows indicate the  $C_0t_{1/2}$  for this component.

in the lower curve indicates that such slowly reassociating fragments constitute a very small fraction of the total population and thus that the tracer has been substantially enriched for single-copy DNA. Controls showed less than 2.5% tracer self-reassociation.

The rate of reassociation for the major component illustrated in Fig. 54 is about 2000 to 3000 times slower than that expected for *E. coli* DNA fragments in the same buffer. Assuming this component of the tracer is single-copy DNA, we calculate that the haploid genome of *O. claytoniana* contains on the order of 1 to  $1.5 \times 10^{10}$  nucleotide pairs. No chemical or cytophotometric determination of nuclear DNA content is available for any of the *Osmunda* species. Sparrow *et al.* (1972) reported a value of  $4.8 \times 10^{10}$  nucleotide pairs for *O. cinnamomea* from measurements of nuclear volume. The difference between this value and our kinetic estimate does not appear to us to be unreasonable, given the high degree of uncertainty associated with both types of measurement. However, accurate determinations of nuclear DNA

content in these ferns must await careful chemical and/or cytophotometric measurements.

For thermal stability measurements,  $^{125}\text{I}$ -*O. claytoniana* single-copy tracer was mixed in a 1:2500 ratio with driver DNA from each of the three species of ferns. These mixtures were reassociated to a  $C_0t$  of 16,000 and the resulting duplexes subjected to thermal elution from hydroxylapatite to obtain the profiles shown in Fig. 55. The  $T_E$  of the reassociated *O. claytoniana* single-copy DNA was  $81^\circ\text{C}$ . Native DNA had a  $T_E$  of  $86^\circ\text{C}$ . Under ideal conditions, single-copy sequences should reassociate to give well-paired duplexes with a  $T_E$  nearly equal to that of native DNA. However, the tracer used here was 230 nucleotides long prior to its final incubation, and a period of 120 hr was necessary to reach  $C_0t$  16,000; during this time significant additional degradation would be expected. Thus, we expect this tracer to form very short duplexes with correspondingly lower thermal stabilities. In

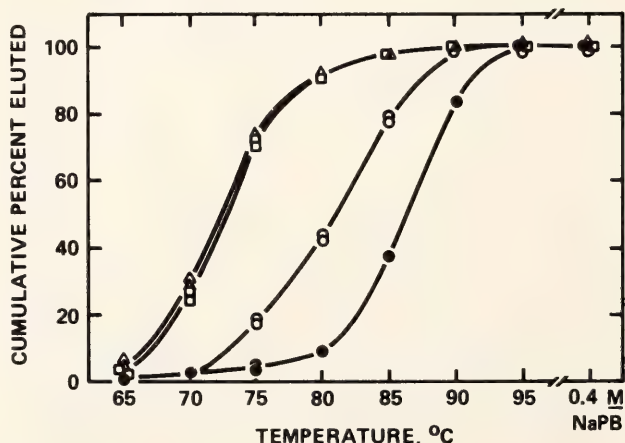


Fig. 55. Hydroxylapatite thermal elution profiles for native *O. claytoniana* DNA fragments (●) and duplexes formed between the *O. claytoniana*  $^{125}\text{I}$  tracer of Fig. 54 and unlabeled DNA from *O. claytoniana* (○), *O. cinnamomea* (△) or *O. regalis* (□). Triplicate samples were denatured, reassociated ( $C_0t = 16,000$ ), and applied to hydroxylapatite as described in the text. Single strands were removed with 0.12 M sodium phosphate buffer at  $60^\circ$ , and the remaining was DNA eluted with the same buffer at a series of temperatures.



addition, the few repetitive sequences remaining in the tracer may form mismatched duplexes which would also contribute to the  $T_E$  depression.

It is clear, however, that the interspecific duplexes formed between *O. claytoniana* single-copy tracer and *O. regalis* or *O. cinnamomea* DNA have essentially the same thermal stability, with  $\Delta T_E$  values of 8.3° and 8.5°C, respectively, indicating equal sequence divergence between *O. claytoniana* and the other two species. Reciprocal crosses of *O. regalis* tracer with unlabeled *O. claytoniana* DNA and *O. cinnamomea* tracer with unlabeled *O. claytoniana* driver also showed *O. claytoniana* DNA to be equidistant from the other two species.

These results support the phylogeny derived previously from data on unfractionated DNA, in which lines leading to all three modern species are assumed to have diverged at about the same time. Such a phylogeny is easily reconciled with the fossil evidence (C. Miller, personal communication), since the Tertiary fossil considered ancestral to modern *O. claytoniana* might well have belonged to a line of evolution which originated much earlier than previously supposed. In this case the *O. claytoniana* line could have diverged at about the same time as the *O. cinnamomea* line. This interpretation of the fossil record also suggests that all three evolutionary lines have been separated for at least 70 million years.

The data obtained with single-copy-enriched tracers can also be used to estimate the rate of base substitution in the *Osmundas*. A  $\Delta T_E$  of 8.5°C represents about 8.5% mismatch in the interspecific duplexes (Bonner *et al.*, 1973), and thus about 4.25% base substitution in the

DNA of each species. If one considers that the species diverged about 70 million years ago, then single-copy sequences in the *Osmundas* appear to have undergone approximately  $4.25/70 = 0.06\%$  substitution per million years. Similar estimates of single-copy base-substitution rates have not yet been made for any other plant group. Although slower than the rates reported for some animal groups (e.g., Angerer *et al.*, 1976; Galau *et al.*, 1976; Laird *et al.*, 1969), the rate of change estimated for *Osmunda* DNA is very close to that observed in primates (Kohne, 1970).

#### REFERENCES

- Angerer, R. C., E. H. Davidson, and R. J. Britten, *Chromosoma*, **56**, 213–226, 1976.
- Bonner, T. I., D. J. Brenner, B. R. Neufeld, and R. J. Britten, *J. Mol. Biol.*, **81**, 122–135, 1973.
- Galau, G. A., M. E. Chamberlin, B. R. Hough, R. J. Britten, and E. H. Davidson, in *Molecular Evolution* (F. J. Ayala, ed.), Sinauer Associates, Sunderland, Mass., 1976.
- Kohne, D. E., *Quart. Rev. Biophysics*, **33**, 327–375, 1970.
- Laird, C., B. L. McConaughy, and B. J. McCarthy, *Nature*, **224**, 149–154, 1969.
- Orosz, J. M., and J. G. Wetmur, *Biochemistry*, **13**, 5467–5473, 1974.
- Pearson, W. R., E. H. Davidson, and R. J. Britten, *Nucleic Acids Research*, **4**, 1727–1735, 1977.
- Sparrow, A. H., H. J. Price, and A. G. Underbrink, *Brookhaven Symp. Biol.*, **23**, 451–494, 1972.
- Stein, D. B., and W. F. Thompson, *Plant Science Letters*, **11**, 323–328, 1978.
- Stein, D. B., W. F. Thompson, and H. S. Belford, *J. Mol. Evol.*, in press, 1979.

## STUDIES ON CHLOROPLAST DNA OF MUNG BEAN AND PEA

Jeffrey D. Palmer, Michael G. Murray, and William F. Thompson

Recent studies from this laboratory suggest that chloroplast DNA comprises a significant fraction of mung bean leaf DNA. Optical reassociation measurements with mung bean leaf DNA at various temperatures indicate that up to 17% can be attributed to a component of precisely the kinetic complexity of chloroplast DNA (Preisler and Thompson, 1978). This fraction reassociates at only 5° below the  $T_m$  of native mung bean DNA, indicating that it contains little or no base pair mismatch, as expected for chloroplast DNA (Kolodner and Tewari, 1975). Murray *et al.* (1979) also found an additional 11% repeat fraction in total leaf DNA which is not present in root DNA.

In this report we further analyze the contribution of chloroplast DNA to leaf DNA from mung bean by using the high resolution melting technique of Cuellar *et al.* (1978a and 1978b) and by directly quantitating the amount of chloroplast DNA with a purified chloroplast DNA probe. This probe is also used to examine the amount of chloroplast DNA in pea leaves and to study the degree of sequence homology between mung bean and pea chloroplast DNA's.

### METHODS

Purification of leaf and embryo DNA's, preparation of radioactively labeled tracers, shearing, and fragment length measurements have been detailed previously (Murray *et al.*, 1978). A mung bean nuclear fraction was obtained by pelleting a leaf homogenate through 60% sucrose and then extensively washing with 3% Triton X-100 until all green color was removed. Mung bean chloroplasts were purified by flotation in su-

crose (Manning *et al.*, 1971). DNA was isolated from the nuclear and chloroplast lysates by two rounds of CsCl-ethidium bromide centrifugation and further purified by treatment with RNase, pronase, chloroform/octanol extraction and hydroxylapatite chromatography.

### RESULTS

Indirect evidence for a large chloroplast DNA component in mung bean leaves was gained by comparing the proportions of leaf and nuclear DNA's that reassociate at repetitive  $C_0t$ 's and by examining the thermal stabilities of these reassociated repeats. We expected that a DNA of low kinetic complexity like chloroplast DNA, if present as a large percentage of total DNA, would reassociate with repetitive kinetics and that the homogeneous nature of the chloroplast DNA population would be reflected by the presence of an additional high thermal stability component when we melted these reassociated repeats.

Figure 56 shows that a putative chloroplast DNA component does indeed make a dramatic contribution to the thermal stability profile of reassociated repeats in mung bean leaf tissue. Note that reassociation and melting were carried out in 2.4 M tetraethylammonium chloride, a solvent that abolishes the effect of base composition on thermal stability (Melchior and Von Hippel, 1973; Chang *et al.*, 1974), permitting high-resolution denaturation analysis, which reflects only mismatch and fragment length effects (Cuellar *et al.*, 1978a, 1978b). Leaf preparations are 27.8% base-paired after incubation to  $C_0t$  9.5 (uncorrected) while nuclear preparations are 20.8% base-paired after incubation



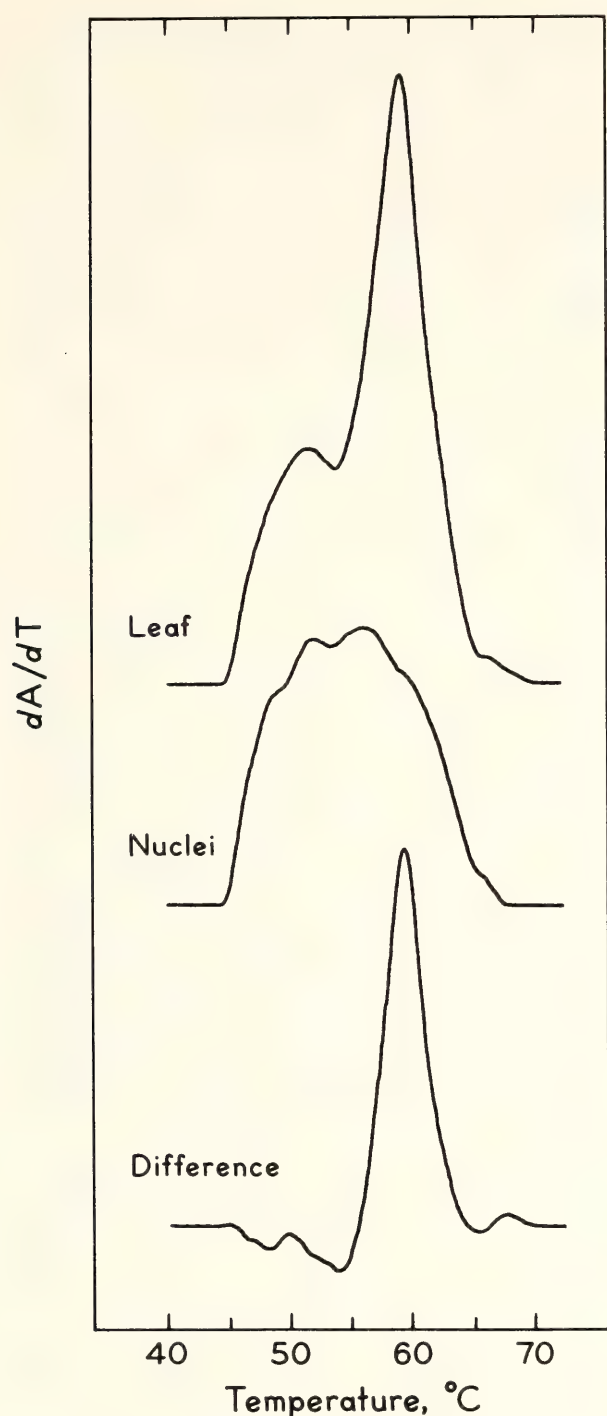


Fig. 56. Thermal stability of reassociated repeated sequences in mung bean leaf and nuclear preparations. Total leaf or nuclear DNA fragments 300 nucleotides long were re-associated in 2.4 M tetraethylammonium chloride to  $C_0t$  9.5 or 6.5 (uncorrected), respectively. Thermal denaturation was carried out in the same solvent with a Gilford 2527 thermal programmer. First derivative profiles were obtained as described previously (Cuellar *et al.*, 1978a, 1978b) and adjusted so that the area under the curves is proportional to the total hyperchromicity. The lower profile shows the difference between the two preparations (leaf minus nuclear). The hyperchromicity of re-

to  $C_0t$  6.5 (uncorrected). The 7% additional base-paired material cannot be explained by the different  $C_0t$  values attained (see Murray *et al.*, 1979). Comparisons of the thermal stability profiles show that most of the difference results from the presence of high-stability duplexes in the leaf which are not present in the nuclear preparations. These sequences are melting very close to the native  $T_m$  in this solvent and thus they are nearly perfectly matched as would be expected for chloroplast sequences. Moreover, using a value of 11% for the fraction of chloroplast DNA in the leaf preparation (see below) we may calculate that at  $C_0t$  9.5 about 70% of the chloroplast DNA should be base-paired. Thus the differences in the thermal stability profiles are consistent with the direct quantitation of chloroplast DNA in the leaf preparation.

The melting analysis only tells us that nuclear DNA lacks a high-stability repeat component present in total leaf DNA. Since this component is present in green leaves, we suspect it consists primarily of chloroplast DNA, but we cannot rule out the contribution of mitochondrial DNA or contamination with bacterial or viral DNA. To assess directly the amount of chloroplast DNA in these preparations, we purified mung bean chloroplast DNA and radioactively labeled it *in vitro* (Murray *et al.*, 1977). By comparing the rate of reassociation of labeled chloroplast DNA by itself with the rates obtained when excess amounts of unlabeled DNAs are added,

associated DNA (8.8% and 6.8% of the denatured  $A_{260}$  nm for leaf and nuclei respectively) was compared to that of native DNA (27.5%), allowing for the 1.6% shift observed for single strands under these conditions. The fraction which was duplex was 27.8% [= (8.8 - 1.6)/(27.5 - 1.6)] for leaf DNA and 20.8% [= (6.8 - 1.6)/(27.5 - 1.6)] for nuclear DNA. Native  $T_m$  for fragments 300 nucleotide pairs long was 60.7°C.

we can directly calculate the amount of chloroplast DNA in these DNA's.

Figure 57 shows the reassociation of  $^3\text{H}$ -mung bean chloroplast DNA fragments in the presence and absence of excess unlabeled mung bean total leaf DNA. In each case the tracer reassociated to an extent of about 80%. The 16–20% tracer component that failed to reassociate probably represents molecules too short to form duplexes capable of binding to hydroxylapatite (Murray *et al.*, 1977). Purity of the chloroplast tracer is suggested by computer analysis, which fits the entire 80% reassociation reaction to one second-order kinetic component, as expected for chloroplast DNA (Kolodner and Tewari, 1975).

The percentage of chloroplast DNA in the driver DNA's was calculated in the following way. A control reaction without any added driver DNA established the absolute concentration of  $^3\text{H}$ -chloroplast tracer DNA (given a chloroplast rate constant of 5.2 as expected for a DNA of kinetic complexity  $1.45 \times 10^5$  nucleotide pairs; Kolodner and Tewari, 1975) and also the ratio of  $^3\text{H}$ -chloroplast DNA to  $^{14}\text{C}$ -*E. coli* DNA included

in the tracer preparation as a nonaccelerated internal kinetic standard. The rate of the *E. coli* reaction was used as a reference point thereafter to calculate the acceleration of the chloroplast reassociation when unlabeled plant DNA was added. For example, in the control reaction without unlabeled mung bean leaf DNA (Figure 57) the concentrations of  $^{14}\text{C}$ -*E. coli* DNA and  $^3\text{H}$ -chloroplast DNA are calculated as 197 and  $2.06 \mu\text{g/ml}$ , a ratio of 95.7. The same reaction mixture was then diluted with total mung bean leaf DNA to a final leaf DNA concentration of  $55.4 \mu\text{g/ml}$ . The *E. coli* concentration is now calculated as  $34.9 \mu\text{g/ml}$ , so that the  $^3\text{H}$ -chloroplast DNA concentration is  $34.9 \mu\text{g/ml} / 95.7 = 0.365 \mu\text{g/ml}$ . The reassociation rate of the chloroplast tracer is accelerated by a factor of 16.8 ( $k = 87.5$  with and 5.2 without leaf DNA) so that the total concentration of chloroplast DNA in the driven reaction is  $16.8 \times 0.365 = 6.13 \mu\text{g/ml}$ . Subtracting the  $0.365 \mu\text{g/ml}$  of chloroplast DNA contributed by the  $^3\text{H}$ -tracer leaves  $5.77 \mu\text{g/ml}$  chloroplast DNA in the mung bean leaf DNA. Thus, 10.4% ( $5.77 \mu\text{g/ml} / 55.4 \mu\text{g/ml} \times 100\%$ )

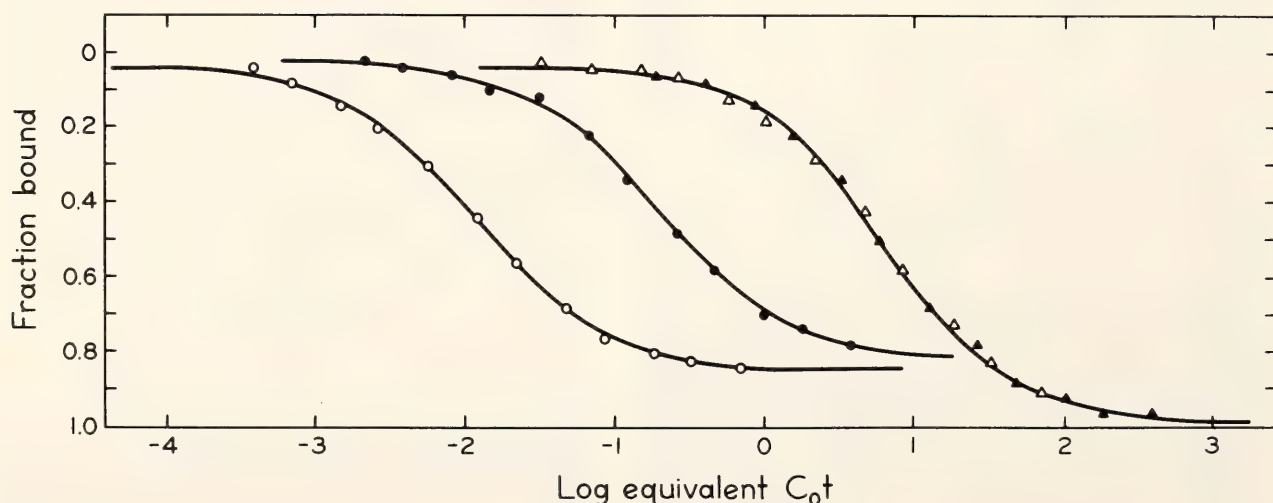


Fig. 57. Reassociation kinetics of a constant ratio of  $^3\text{H}$ -mung bean chloroplast DNA and  $^{14}\text{C}$ -*E. coli* DNA in the absence (closed symbols) and presence (open symbols) of excess unlabeled mung bean leaf DNA. The chloroplast reactions are plotted against  $^3\text{H}$ -chloroplast tracer  $C_0t$ 's ( $\circ$ ), while the *E. coli* reactions are plotted against *E. coli*  $C_0t$ 's ( $\triangle$ ). Aliquots of a mixture of  $^3\text{H}$ -mung bean chloroplast DNA and  $^{14}\text{C}$ -*E. coli* were mixed with or without driver DNA, reassociated in 0.4 M phosphate buffer at  $66^\circ\text{C}$  and fractionated on hydroxylapatite as detailed by Murray *et al.* (1978).



TABLE 21. Percent Chloroplast DNA in Mung Bean Leaf, Embryo, and Leaf Nuclear, and in Pea Leaf DNA\*

Driver DNA	% Chloroplast DNA			Haploid Nuclear Genome (pg)	Chloroplast Genomes per Haploid Nucleus
	Expt. 1	Expt. 2	Average		
Mung bean leaf	10.4	11.8	11.1	0.48	360
Mung bean embryo	4.4	6.6	5.5	0.48	180
Mung bean leaf nuclear	0.9	1.1	1.0	0.48	30
Pea leaf	2.4	...	...	4.6	750

\* Second-order rate constants for the chloroplast and *E. coli* reassociations were obtained by least-squares computer fits for a single second-order component (Murray *et al.*, 1978). Calculations of percent chloroplast DNA were done as described in the text. All tracer and driver DNA's had a modal single-strand length of 300 nucleotides.

of leaf DNA is actually chloroplast DNA. The percent of chloroplast DNA in the several DNA preparations is shown in Table 21. The reproducibility of this measurement is demonstrated by the very similar percentages calculated for each of the mung bean preparations in two separate experiments.

Thermal stability profiles of the duplexes formed during reassociation of tracer mung bean chloroplast DNA with driver pea and mung bean DNA's are shown in Figure 58. The mung bean-mung bean duplexes melt over a narrow temperature range, indicating the absence of base-pair mismatch, and at a high  $T_e$  (81°) consistent with the 37–39% GC base composition generally found in higher plant chloroplast DNA (Kung, 1977). In contrast, the pea-mung bean hybrid melts over a wider temperature range with a  $\Delta T_e$  of 3.5° compared to the mung bean-mung bean duplexes. Because such a small  $\Delta T_e$  will not appreciably affect the rate of the mung bean tracer reassociation when driven with pea DNA (Marsh and McCarthy, 1974), we made no corrections for mismatch effects on reassociation rates in determining the percentage of chloroplast DNA in pea leaves (Table 21). Some of the hybrid duplexes melt almost at native  $T_e$ , indicating very great sequence conservation, as expected for chloroplast ribosomal RNA cistrons (Thomas and

Tewari, 1974). Other hybrid duplexes melt at relatively low temperatures and thus possess considerable base-pair mismatch.

## DISCUSSION

Two different experimental approaches suggest a significant contribution of chloroplast DNA to the total DNA in mung bean leaves; quantitative estimates using a purified chloroplast probe indicate that 11% of the mung bean leaf DNA is in fact chloroplast DNA. Such large chloroplast components can seriously complicate analysis of mismatch in repeated nuclear sequences. In mung bean about a fourth of the putative nuclear repeats in the leaf preparation are actually chloroplast sequences. This problem may be more acute for small genomes or when the fraction of repeated nuclear DNA is small.

Using a purified pea chloroplast DNA probe Lamppa and Bendich (1979) recently quantitated the amount of chloroplast DNA in shoot tissue of nine different angiosperms. The percent of chloroplast DNA varied from 0.9% in broad bean to 3.3% in muskmelon. Three of these species have nuclear genomes at least twice as large as that of mung bean, and the other six are ten or more times larger, so it is not entirely surprising to find a significantly larger

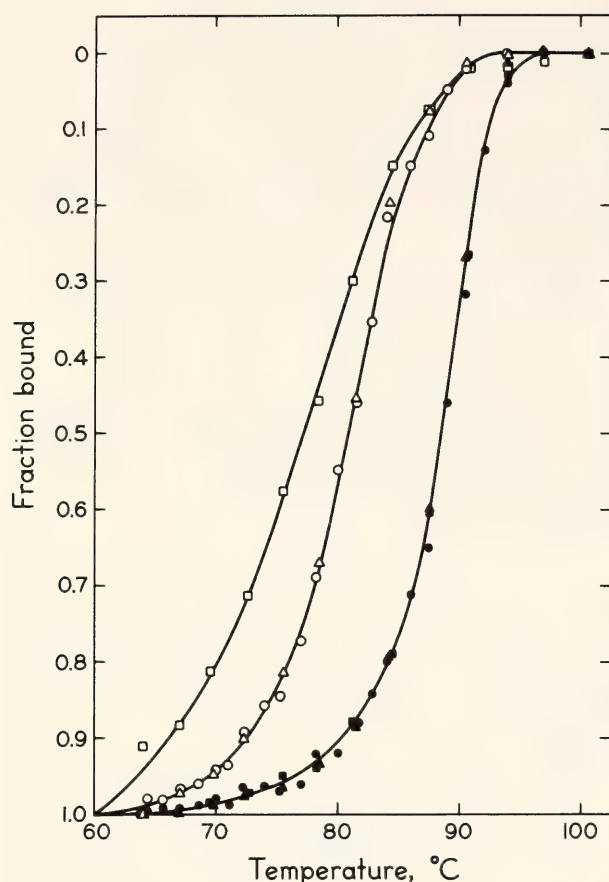


Fig. 58. Hydroxylapatite melts of duplexes formed between  $^3\text{H}$ -mung bean chloroplast tracer DNA and unlabeled mung bean nuclear DNA (○), mung bean leaf DNA (△) and pea leaf DNA (□). The ratios of driver chloroplast DNA to tracer chloroplast DNA are calculated at 6, 7, and 16, respectively. Melts of the  $^{14}\text{C}$ -*E. coli* duplexes present as internal thermal standards within the three chloroplast reaction mixtures are shown by ●, ▲, ■, respectively. Each point represents an aliquot of the reassociation mixture which was heated for 20 minutes at the indicated temperature in .12 M phosphate buffer in a twenty-five position temperature gradient melting block and then immediately fractionated into single and double strands on hydroxylapatite at 60°C. The data are normalized to 100% reassociation. The actual extent of reassociation of the  $^3\text{H}$ -chloroplast and  $^{14}\text{C}$ -*E. coli* DNA was 82% & 92%, 82% & 88%, and 66% & 82% for the mung bean nuclear, mung bean leaf, and pea leaf reactions, respectively.

chloroplast DNA fraction in mung bean leaves. Indeed, we find a much lower percentage of chloroplast DNA in pea, with ten times as much nuclear DNA, than in mung bean. However, the absolute amount of chloroplast DNA in mung

bean (360 copies per haploid genome) approximately equals that of corn and barley, both with ten times more nuclear DNA, and is at least twice the amount of chloroplast DNA in three cucurbit species with nuclear genomes at least twice as large. These findings raise the possibility that the absolute amount of chloroplast DNA varies greatly from family to family, with less variation within a family.

We find twice as much chloroplast DNA in mung bean primary leaves as in embryos, while Murray *et al.* (1979) found no more than 1–2% chloroplast DNA in root tissue by indirect analyses. We are currently extending these experiments to other tissues and developmental stages.

There is fragmentary evidence for the presence of chloroplast DNA sequences in the nucleus (Siegel, 1974; Kung, 1977). Our experiments with mung bean nuclear DNA define the upper limit of possible nuclear “chloroplast” sequences at 1%, or 30 chloroplast genomes per nucleus. The identical melting profiles obtained when chloroplast tracer is driven with leaf and nuclear DNA establish a second limitation on the kinds of chloroplast-homologous sequences that might reside in the nucleus. At least four models are compatible with our results. (1) All 30 chloroplast genomes in the nuclear preparation result from contamination with the DNA of broken chloroplasts. (2) There are up to 30 complete chloroplast genomes in the nucleus, all of which are perfectly conserved in base sequence compared to the DNA in chloroplasts. (3) There are only a few copies, or small fragments, of the chloroplast genome in the nucleus. Sequence divergence in such a small fraction would be obscured by the relatively large mass of contaminating genomes. (4) There may be any number of nuclear sequences which, although originally homologous to chloroplast DNA, are now so diverged in sequence that



they cannot form stable duplexes with chloroplast DNA under our reassociation conditions ( $T_e - 21^\circ$ ). We hope to resolve these possibilities in mung bean and other species by using very highly purified nuclear DNA and more sensitive tests designed specifically to detect only chloroplast sequences covalently associated with nuclear DNA.

## REFERENCES

- Chang, C. T., T. C. Hain, J. R. Hutton, and J. G. Wetmur, *Biopolymers*, **13**, 1847–1857, 1974.
- Cuellar, R. E., G. A. Ford, W. R. Briggs, and W. F. Thompson, *Proc. Nat. Acad. Sci. U.S.A.*, **75**, 6026–6030, 1978a.
- Cuellar, R. E., G. A. Ford, W. R. Briggs, and W. F. Thompson, *Carnegie Inst. Washington Year Book* **77**, 330–332, 1978b.
- Kolodner, R., and K. K. Tewari, *Biochim. Biophys. Acta*, **402**, 372–390, 1975.
- Kung, S., *Annu. Rev. Plant Phys.*, **28**, 401–437, 1977.
- Lamppa, G. K., and A. J. Bendich, *Plant Phys.*, **63**, 660–668, 1979.
- Manning, J. E., D. R. Wolstenholme, R. S. Ryan, J. A. Hunter, and O. C. Richards, *Proc. Nat. Acad. Sci. U.S.A.*, **68**, 1169–1173, 1971.
- Marsh, J. L., and B. J. McCarthy, *Biochemistry*, **13**, 3382–3387, 1974.
- Melchior, W. B., and P. H. Von Hippel, *Proc. Nat. Acad. Sci. U.S.A.*, **70**, 298–302, 1973.
- Murray, M. G., H. S. Belford, and W. F. Thompson, *Carnegie Inst. Washington Year Book* **76**, 262–267, 1977.
- Murray, M. G., R. E. Cuellar, and W. F. Thompson, *Biochemistry*, **17**, 5781–5790, 1978.
- Murray, M. G., R. E. Cuellar, and W. F. Thompson, submitted for publication, 1979.
- Preisler, R. S., and W. F. Thompson, *Carnegie Inst. Washington Year Book* **77**, 323–330, 1978.
- Siegel, A., in *Modification of the Information Content of Plant Cells*, pp. 15–26, R. Makkam, R. D. Davis, D. A. Hapwood, and R. W. Horne, eds., N. Holland/Elsevier, Amsterdam, 1974.
- Thomas, J. R., and K. K. Tewari, *Proc. Nat. Acad. Sci. U.S.A.*, **71**, 3147–3151, 1974.

## BIBLIOGRAPHY

- 534 Avron, M., and U. Schreiber, Properties of ATP-driven reverse electron flow in chloroplasts, *Biochim. Biophys. Acta*, **546**, 436–447, 1979.
- 646 Avron, M., and U. Schreiber, Properties of ATP-induced chlorophyll luminescence in chloroplasts, *Biochim. Biophys. Acta*, **546**, 448–454, 1979.
- 640 Armond, P. A., and L. A. Staehelin, Lateral and vertical displacement of integral membrane proteins during lipid phase transition in *Anacystis nidulans*, *Proc. Nat. Acad. Sci. U.S.A.*, **76**, 1901–1905, 1979.
- 649 Armond, P. A., M. R. Badger, and O. Björkman, Characteristics of the photosynthetic apparatus developed under different thermal growth regimes. *Proc. Inter. Symp. Chloroplast Devel.*, 857–862, 1978.
- Armond, P. A., see Björkman, O.; Raison, J. K.
- Badger, M. R., see Armond, P. A.; Björkman, O.
- Belford, H. S., see Stein, D. B.; Thompson, W. F.
- Berry, J. A., see Carey, R.; Ehleringer, J.; Pike, C. S.; Raison, J. K.
- 673 Björkman, O., The response of photosynthesis to temperature, *Proc. British Ecological Soc. Symp.*, in press, 1979.
- 672 Björkman, O., M. R. Badger, and P. A. Armond, Response and adaptation of photosynthesis to high temperature. In *Adaptations of Plants to Water*

- and *High Temperature Stress*, P. Kramer and N. Turner, eds., 1980, Wiley-Interscience, New York, in press, 1979.
- Björkman, O., see Armond, P. A.
- 642 Blatt, M. R., and W. R. Briggs, Blue light-induced cortical fiber reticulation concomitant with chloroplast aggregation in the alga *Vaucheria sessilis*, *Planta*, in press, 1979.
- 643 Blatt, M. R., N. K. Wessells, and W. R. Briggs, Actin and cortical fiber reticulation in the siphonaceous alga *Vaucheria sessilis*, *Planta*, in press, 1979.
- 665 Bowles, D. J., P. H. Quail, D. J. Morre, and G. C. Hartman, Use of markers in plant cell fractionation. In *Plant Organelles. Methodological Surveys in Biochemistry*, 9, E. Reid, ed., Ellis Horwood, Chichester, England, in press, 1979.
- Briggs, W. R., see Blatt, M. R.; Britz, S. J.; Cross, J. W.; Cuellar, R. E.; Song, P.-S.; Vanderhoef, L. N.
- 650 Britz, S. J., and W. R. Briggs, News on a blue light-absorbing photoreceptor system. In *Plant Growth and Light Perception, Proceedings, European Photomorphogenesis Meetings, Aarhus, Denmark, Aug. 14-19, 1978*, B. I. Deutsch and A. O. Gyldenholm, eds., pp. 17-24, Aarhus, Denmark, 1979.
- Brown, J. S., see Lutz, M.; van Ginkel, G.
- 587 Carey, R., and J. A. Berry, Effects of low temperature on respiration and uptake of  $Rb^+$  ions by excised barley and corn roots. *Plant Physiol.*, 61, 858-860, 1978.
- 656 Cross, J. W., and W. R. Briggs, Solubilized auxin binding protein. Subcellular localization and regulation by a soluble factor from corn coleoptile homogenates, *Planta*, 146, 263-270, 1979.
- 648 Cuellar, R. E., G. A. Ford, W. R. Briggs, and W. F. Thompson, Application of higher derivative techniques to analysis of high-resolution thermal denaturation profiles of reassociated repetitive DNA, *Proc. Nat. Acad. Sci. U.S.A.*, 75, 6026-6030, 1979.
- Cuellar, R. E., see Murray, M. G.; Thompson, W. F.
- 613 Ehleringer, J., and H. A. Mooney, Leaf hairs: effects on physiological activity and adaptive value to a desert shrub, *Oecologia*, 37, 183-200, 1978.
- 615 Ehleringer, J., H. A. Mooney, and J. Berry, Photosynthesis and microclimate of a desert winter annual. *Ecology*, in press, 1979.
- Ford, G. A., see Cuellar, R. E.
- 664 Fork, D. C., The influence of changes in the physical phase of thylakoid membrane lipids on photosynthetic activity. In *Low Temperature Stress in Crop Plants: The Role of the Membrane*, J. M. Lyons and J. K. Raison, eds., U.S.-Australia Science Seminar, Academic Press, New York, in press, 1979.
- 627 Fork, D. C., N. Murata, and N. Sato, The effect of growth temperature on lipid and fatty acid composition, and the dependence on temperature of light-induced redox reactions of cytochrome *f* and of light energy redistribution in the thermophilic blue-green alga *Synechococcus lividus*. *Plant Physiol.*, 63, 524-530, 1979.
- French, C. S., see Nielsen, N. C.
- Fugate, R. D., see Song, P.-S.
- Hartman, G. C., see Bowles, D. J.
- Henningsen, K. W., see Nielsen, N. C.
- 652 Levitt, J., Crop tolerance to suboptimal land conditions—a historical overview. In *Crop Tolerance to Suboptimal Land Conditions*. Proceedings of a symposium sponsored by the American Society of Agronomy, Crop Science Society of America and Soil Science Society of America in Houston, TX, Nov. 28-Dec. 3, 1976, pp. 161-171, American Soc. Agronomy, Madison, WI, 1978.
- 666 Levitt, J., Role of proteins in the freezing, injury, and resistance of biological material. In *Advances in Chemistry*, Amer. Chem. Soc., in press, 1979.
- 657 Levitt, J., Role of SH and SS groups in damage to biological systems at low water activities. In *Dry Biological Systems*, J. H. Crowe and J. S. Clegg, eds., pp. 245-256, Academic Press, New York, 1978.



- 653 Lutz, M., J. S. Brown, and R. Remy, Resonance Raman scatterings of chlorophyll-protein complexes. In *Proceedings of the Sixth International Conference on Raman Spectroscopy, Bangalore, India, September 4-9, 1978*, E. D. Schmid, R. S. Krishnan, W. Kiefer, and H. W. Schrotter, eds., pp. 158-159, Heyden, London, Vol. 2.
- 638 Lutz, M., J. S. Brown, and R. Remy, Resonance Raman spectroscopy of chlorophyll-protein complexes, *Ciba Foundation Symp. No. 61, Chlorophyll organization and energy transfer in photosynthesis*, pp. 105-125, Ciba Foundation, London, 1978.
- Mooney, H. A., *see* Ehleringer, J.
- Morre, D. J., *see* Bowles, D. J.
- Murata, N., *see* Ford, D.
- 630 Murray, M. G., R. E. Cuellar, and W. F. Thompson, DNA sequence organization in the pea genome. *Biochemistry*, 17, 5781-5790, 1978.
- Murray, M. G., *see* Thompson, W. F.
- 618 Nielsen, N. C., R. M. Smillie, K. W. Henningsen, D. von Wettstein, and C. S. French, Composition and function of thylakoid membranes from grana-rich and grana-deficient chloroplast mutants of barley, *Plant Physiol.*, 63, 174-182, 1979.
- 660 Pike, C. S., J. A. Berry, and J. K. Raison, Fluorescence polarization studies of membrane phospholipid separations in warm- and cool-climate plants. In *Low Temperature Stress in Crop Plants: The Role of the Membrane*, J. M. Lyons and J. K. Raison, eds., U.S.-Australia Science Seminar, Academic Press, New York, in press, 1979.
- Pike, C. S., *see* Raison, J. K.
- 670 Quail, P. H., Plant cell fractionation, *Annu. Rev. Plant Physiol.*, 30, 425-484, 1979.
- Quail, P. H., *see* Bowles, D. J.; Vanderhoef, L. N.
- 651 Raison, J. K., J. A. Berry, P. Armond, and C. S. Pike, Membrane properties in relation to adaptation of plants to high and low temperature stress. In *Adaptations of Plants to Water and High Temperature Stress*, P. Kramer and N. Turner, eds., Wiley-Interscience, New York, in press, 1978.
- Raison, J. K., *see* Pike, C. S.
- Remy, R., *see* Lutz, M.
- Sato, N., *see* Fork, D.
- Schreiber, U., *see* Avron, M.
- Smillie, R. M., *see* Nielsen, N. C.
- 637 Song, P.-S., R. D. Fugate, and W. R. Briggs, Flavin as a photoreceptor for phototropic transduction: fluorescence studies of model and corn coleoptile systems. *6th Flavin Symposium Proc.*, K. Yagi, ed., Academic Publ., in press, 1979.
- Staehelin, L. A., *see* Armond, P. A.
- 654 Stein, D. B., W. F. Thompson, and H. S. Belford, Studies on DNA sequences in the Osmundaceae, *J. Mol. Evol.*, in press, 1979.
- 611 Stemler, A., Photosystem II activity depends on membrane-bound bicarbonate, *Symposium on Photosynthetic Oxygen Evolution*, pp. 283-293, H. Metzner, ed., Tübingen, West Germany, 1979.
- 658 Thompson, W. F., and M. G. Murray, The nuclear genome: structure and function. In *Comprehensive Plant Biochemistry*, E. Conn and P. Stumpf, eds., Academic Press, New York, in press, 1979.
- 659 Thompson, W. F., M. G. Murray, H. S. Belford, and R. E. Cuellar, Patterns of DNA sequence interspersion in higher plants. In *Symposium on Emergent Techniques for the Genetic Improvement of Crops*, I. Rubenstein, ed., Univ. Minnesota Press, Minneapolis, MN, in press, 1979.
- Thompson, W. F., *see* Cuellar, R. E.; Murray, M. G.; Stein, D. B.
- 644 Vanderhoef, L. N., W. R. Briggs, and P. H. Quail, Red light-inhibited mesocotyl elongation in maize seedlings. II. Kinetic and spectral studies. *Plant Physiol.*, 63, 1062-1067, 1979.
- 629 van Ginkel, G., Photoactivity of isolated PS-1 particles upon combination with artificial lipid membranes or Triton X-100 micells. *Photochem. Photobiol.*, in press.
- 636 van Ginkel, G., and J. S. Brown, Endogenous catalase and superoxide dismutase activities in photosynthetic membranes. *FEBS Lett.*, 94, 284-286, 1978.
- von Wettstein, D., *see* Nielsen, N. C.
- Wessells, N. K., *see* Blatt, M. R.

## SPEECHES

- Armond, Paul A., Thermal acclimation of photosynthesis: Effect of growth temperature on photosynthetic characteristics, Department of Botany, Hebrew University of Jerusalem, Jerusalem, Israel, July 4, 1978.
- Armond, Paul A., Alterations in composition and stability of the photosynthetic apparatus induced by growth temperature, Department of Biochemistry, Weizmann Institute of Science, Rehovot, Israel, July 7, 1978.
- Armond, Paul A., Characteristics of the photosynthetic apparatus developed under different thermal growth regimes, International Conference on Chloroplast Development, Spetsai, Greece, July 12, 1978.
- Armond, Paul A., Thermal acclimation of photosynthesis: Effect of growth temperature on the photosynthetic apparatus, Department of EPO Biology, University of Colorado, Boulder, Colorado, October 16, 1978.
- Armond, Paul A., J. A. Berry, and O. Björkman, Acclimation and response of the photosynthetic apparatus to high temperatures, International Symposium on Biological Applications of Solar Energy, Madurai, India, December 2, 1978.
- Armond, Paul A., Fluorescence techniques for analyzing the photosynthetic apparatus, UNEP Training Course in Biofuels, Bioproductivity, and Photosynthesis, Madurai Kamaraj University, Madurai, India, December 11, 1978.
- Armond, Paul A., Chloroplast membrane morphology: structure-function relationships, UNEP Training Course in Biofuels, Bioproductivity, and Photosynthesis, Madurai Kamaraj University, Madurai, India, December 15, 1978.
- Armond, Paul A., Photosynthetic responses to temperature. III. Temperature-induced morphological alterations to membranes. Stanford-Carnegie Plant Sciences Seminar, Carnegie Institution, Stanford, California, April 4, 1979.
- Armond, Paul A., Physiological and morphological responses of photosynthetic membranes to temperature, Department of Biology, Virginia Polytechnic Institute, Blacksburg, Virginia, May 10, 1979.
- Armond, Paul A., John L. Hess, L. Andrew Staehelin, High temperature-induced disorganization of the pigment-protein complexes in chloroplast membranes of *Nerium oleander*, American Society for Photobiology, Pacific Grove, California, June 28, 1979.
- Badger, Murray, A mechanism for concentrating CO<sub>2</sub> in *Chlamydomonas reinhardtii* and *Anabaena variabilis* and its role in photosynthetic CO<sub>2</sub> fixation, Stanford-Carnegie Plant Sciences Seminar, Carnegie Institution, Stanford, California, November 1, 1978.
- Belford, Heather, Comparison of single-copy sequences within the genus *Atriplex*, Stanford-Carnegie Plant Sciences Seminar, Carnegie Institution, Stanford, California, February 14, 1979.
- Belford, Heather, Comparison of single-copy DNA sequences within the genus *Atriplex*, Yale University, New Haven, Connecticut, April 6, 1979.
- Belford, Heather, Comparison of single-copy DNA sequences among several *Atriplex* species, University of Massachusetts, Amherst, Massachusetts, April 11, 1979.
- Belford, Heather, Evolution in the genus *Atriplex*: A molecular hybridization approach, Smith College, Northampton, Massachusetts, April 13, 1979.
- Berry, Joseph A., *In vivo* studies of <sup>18</sup>O<sub>2</sub> fixation, Workshop on RuP<sub>2</sub> carboxylase-oxygenase, Australian National University, Canberra, Australia, January 25–26, 1979.
- Berry, Joseph A., Photosynthetic responses to temperature, II. High temperature limits to biochemical reactions, Stanford-Carnegie Plant Sciences Seminar, Carnegie Institution, Stanford, California, March 14, 1979.
- Berry, J. A., *see* Armond, P. A.
- Björkman, Olle, Australian–United States Workshop on Adaptation of Plants to Water and High-Temperature Stress, Adaptation of the photosynthetic system to high temperature, Carnegie Institution of Washington, Stanford, California, November 13, 1978.
- Björkman, Olle, Photosynthetic responses to temperature, I. Physiological adaptations, Stanford-Carnegie Plant Sciences Seminars,



- Carnegie Institution of Washington, Stanford, California, March 7, 1979.
- Björkman, Olle, The response of photosynthesis to temperature, British Ecological Society, University of Edinburgh, Scotland, March 29, 1979.
- Björkman, Olle, Ecological aspects of  $C_4$  photosynthesis, "The George N. Lamb Lecture," University of Nebraska, School of Life Sciences, Lincoln, Nebraska, May 3, 1979.
- Björkman, Olle, Response and adaptation in higher plants to high-temperature stress, "The George N. Lamb Lecture," University of Nebraska, Lincoln, Nebraska, May 4, 1979.
- Björkman, O., *see* Armond, P. A.
- Briggs, Winslow R., and Steven J. Britz, News on a blue light-absorbing photoreceptor, Annual European Symposium on Photomorphogenesis, Aarhus, Denmark, August 14, 1978.
- Briggs, Winslow R., The blue light photoreceptors in plants and fungi, Department of Biology, Utah State University, Logan, Utah, November 15, 1978.
- Briggs, Winslow R., Recent phytochrome investigations, Department of Biology, University of Utah, Salt Lake City, Utah, November 16, 1978.
- Briggs, Winslow R., Physiological and spectroscopic studies of a blue light photoreceptor system in higher plants and fungi, Department of Biology, University of Utah, Salt Lake City, Utah, November 16, 1978.
- Briggs, Winslow R., Blue light photoreception in higher plants and fungi, Department of Biological Sciences, University of California at Santa Barbara, Goleta, California, January 10, 1979.
- Briggs, Winslow R., Blue light photoreceptors in higher plants and fungi, Developmental Biology Group, Stanford University, Stanford, California, January 26, 1979.
- Briggs, Winslow R., Blue light photoreception in higher plants and fungi, Department of Biology, University of California at Santa Cruz, Santa Cruz, California, February 27, 1979.
- Briggs, W. R., *see* Gorton, H.; Mandoli, D. Britz, S. J., *see* Briggs, W. R.
- Brown, Jeanette S., Spectroscopic characteristics of chlorophyll proteins from *Euglena*, American Society for Photobiology, Asilomar, Pacific Grove, California, June 28, 1979.
- Collatz, G. James, Limitation on the rate of carboxylation in response to environmental factors, Botany Department, University of California, Berkeley, California, February 15, 1979.
- Collatz, G. James, Limitations on the rates of carboxylation during steady state photosynthesis, Botany Department, University of Illinois, Urbana-Champaign, Illinois, April 5, 1979.
- Collatz, G. James, Limitations on the carboxylation rate during steady state photosynthesis, Stanford-Carnegie Plant Sciences Seminar, Carnegie Institution of Washington, Stanford, California, April 11, 1979.
- Fork, David C., Role of carotenoids as photosynthetic accessory pigments, University of California, Davis, California, November 9, 1978.
- Fork, David C., The influence of changes in the physical phase of thylakoid membrane lipids on photosynthetic activity, U.S.-Australia Science Seminar: Low temperature stress in crop plants: The role of the membrane, Honolulu, Hawaii, March 28, 1979.
- Foster, J. V., and John L. Hess, Isolation of soluble proteins from cotton leaf tissue and determination of oxidative enzyme levels, Cotton Physiology Conference, Beltwide Cotton Conferences, Phoenix, Arizona, January 8, 1979.
- Gorton, Holly, and W. R. Briggs, Phytochrome responses of light-grown corn seedlings in the presence and absence of Sandoz, a chlorosis-inducing herbicide, American Society for Photobiology, Asilomar, Pacific Grove, California, June 28, 1978.
- Harvey, Geoffrey W., Seasonal photosynthetic unit size alteration in three herb layer components of a deciduous forest community, Stanford-Carnegie Plant Sciences Seminar, Carnegie Institution, Stanford, California, November 15, 1979.
- Harvey, Geoffrey W., Investigation of the mechanism of the membrane bound energy linked pyrophosphatase of *Rhodospirillum rubrum*, Laboratory of Chemical Biodynamics, University of California, Berkeley, California, April 25, 1979.
- Hess, John L., Oxygen and superoxide dismutase, Stanford-Carnegie Plant Science

- Seminar, Carnegie Institution, Stanford, California, Oct. 18, 1978.
- Hess, John L., Superoxide dismutase: A perspective with other oxidative enzymes from leaf tissue, Botany Department, University of California, Berkeley, California, April 25, 1979.
- Hess, J. C., *see* Armond, P. A.; Foster, J. V.
- Jorgensen, Richard, Gene organization in transposons Tn5 and Tn10, Molecular Genetics Seminar, Stanford University, Stanford, California, February 23, 1979.
- Jorgensen, Richard, Gene organization in transposons Tn5 and Tn10, Department of Biology, Washington University, St. Louis, Missouri, February 26, 1979.
- Jorgensen, Richard, A gene organization in transposable antibiotic resistance determinants, Stanford-Carnegie Plant Sciences Seminar, Carnegie Institution, Stanford, California, May 30, 1979.
- Levitt, Jacob, Injurious effects of lipid phase transition on plants exposed to high- or low-temperature stresses, Department of Botany, Hebrew University, Rehovot, Israel, March 9, 1979.
- Levitt, Jacob, Some recent advances in stress physiology, Department of Soils and Water, Volcani Center, Israel, March 18, 1979.
- Levitt, Jacob, Current concepts of membrane damage by environmental stress, Washington State University, Pullman, Washington, April 23, 1979.
- Levitt, Jacob, Chilling injury to plants, Washington State University, Pullman, Washington, April 23, 1979.
- Levitt, Jacob, Environmental stresses in plants, Washington State University, Prosser, Washington, April 24, 1979.
- Levitt, Jacob, General discussion of chilling and freezing injury, Washington State University, Wenatchee, Washington, April 24, 1979.
- Levitt, Jacob, Current concepts of membrane damage by environmental stress, University of Washington, Bellingham, Washington, April 26, 1979.
- Levitt, Jacob, Chilling injury to plants, University of Washington, Seattle, Washington, April 27, 1979.
- Levitt, Jacob, Chilling injury to plants, Oregon State University, Corvallis, Oregon, April 28, 1979.
- Mandoli, D. and W. R. Briggs, Growth characteristics of etiolated *Avena sativa* (cv. Lodi) in response to red and green light, American Society for Photobiology, Asilomar, Pacific Grove, California, June 26, 1979.
- Murray, Michael G., DNA sequences repetition and interspersions in higher plants, Symposium "Emergent techniques for the genetic improvement of crops," University of Minnesota, St. Paul, Minnesota, March 19, 1979.
- Murray, Michael G., DNA sequence organization in higher plants, Agronomy Department, University of California, Davis, California, May 8, 1979.
- Pike, Carl S., Does phytochrome control growth through effects on the cell membrane and the cell wall? Stanford-Carnegie Plant Science Seminar, Carnegie Institution, Stanford, California, October 25, 1979.
- Pike, Carl S., Fluorescence polarization studies of membrane phospholipid phase separations in warm and cool climate plants, U.S.-Australia Science Seminar: Low-temperature stress in crop plants: The role of the membrane, Honolulu, Hawaii, March 27, 1979.
- Quail, Peter H., ATP levels correlate with in vivo-induced phytochrome pelletability. Institut für Biologie, III, Universität Freiburg, West Germany, August 11, 1978.
- Quail, Peter H., Phytochrome pelletability: Requirement for phosphorylation energy in vivo. Annu. European Symposium on Photomorphogenesis, Aarhus, Denmark, August 15, 1978.
- Quail, Peter H., Phytochrome and its sub-cellular localization. Department of Botany, University of Wisconsin, Madison, Wisconsin, October 5, 1978.
- Quail, Peter H., Phytochrome pelletability: Requirement for phosphorylation energy in vivo. Botany Department, University of California, Davis, California, October 18, 1979.
- Raison, John, Membrane lipid fluidity—a factor in determining the temperature limits of both plants and animals, Department of Pharmacology, University of Alberta, Edmonton, Alberta, Canada, September 7, 1978.
- Raison, John, The role of membrane lipids in the adaptation of plants and animals to low and high temperature, Plant Research Laboratory, Michigan State University,



- East Lansing, Michigan, September 27, 1978.
- Raison, J., *see* van Ginkel, G.
- Staehelin, L. A., *see* Armond, P. A.
- Thompson, William F., Sequence organization in higher plant DNA, Department of Botany, University of California, Berkeley, California, October 27, 1978.
- Thompson, William F., DNA sequence organization and evolution in higher plants, Department of Botany, University of California, Davis, California, November 8, 1978.
- Thompson, William F., Comparison of sequence organization patterns in the pea and mung bean genomes, Biological Sciences Department, Stanford University, Stanford, California, November 27, 1978.
- Thompson, William F., DNA sequence organization in higher plants, Brandeis University, Waltham, Massachusetts, April 5, 1979.
- Thompson, William F., Contrasting patterns of DNA sequence organization in higher plants, Brookhaven Nat. Labs, Upton, New York, April 6, 1979.
- Thompson, William F., Contrasting patterns of DNA sequence organization in higher plants, Yale University, New Haven, Connecticut, April 10, 1979.
- Thompson, William F., Contrasting patterns of DNA sequence organization in two leguminous species, University of Massachusetts, Amherst, Massachusetts, April 12, 1979.
- Thompson, William F., DNA sequence organization in peas and mung beans, Smithsonian Radiation Biology Lab., Rockville, Maryland, April 13, 1979.
- Thompson, William F., Contrasting patterns of DNA sequence organization in higher plants, Department of Embryology, Carnegie Institution of Washington, Baltimore, Maryland, May 1, 1979.
- Thompson, William F., DNA sequence organization in two leguminous plants, University of California, Santa Cruz, California, May 29, 1979.

## PERSONNEL

### *Research Staff*

Joseph A. Berry  
 Olle Björkman  
 Winslow R. Briggs, Director  
 Jeanette S. Brown  
 David C. Fork  
 C. Stacy French, Director Emeritus  
 William M. Hiesey, Emeritus  
 Malcolm A. Nobs  
 William F. Thompson

### *Research Associate*

Michael G. Murray

### *Postdoctoral Fellows*

Roland Caubergs, NATO Fellowship, University of Antwerp, Belgium<sup>1</sup>  
 Richard A. Jorgensen, National Science Foundation Fellowship, University of Wisconsin, Madison, WI  
 Jacob Levitt, Senior Fellow, University of Minnesota, Minneapolis, MN

<sup>1</sup> To April 1, 1979.

Carl S. Pike, National Science Foundation Fellowship, Franklin and Marshall College, Lancaster, PA

### *Carnegie Institution of Washington Postdoctoral Fellows*

Paul A. Armond  
 Murray R. Badger<sup>2</sup>  
 W. J. S. Downton, Senior Fellow, CSIRO, Adelaide, Australia  
 Mary Helen Goldsmith, Senior Fellow, Yale University<sup>3</sup>  
 Geoffrey W. Harvey  
 John L. Hess, Senior Fellow, Virginia Polytechnic Institute and State University, Blacksburg, VA  
 Shmuel Malkin, Senior Fellow, Weizmann Institute of Science, Israel<sup>4</sup>  
 Anastasios Melis  
 Peter H. Quail, Senior Fellow

<sup>2</sup> To October 31, 1978.

<sup>3</sup> To June 30, 1978.

<sup>4</sup> To November 30, 1978.

John K. Raison, Senior Fellow, CSIRO,  
Canberra, Australia<sup>5</sup>  
Gijsbert van Ginkel<sup>6</sup>

### *Students*

Heather S. Belford, Graduate, University  
of Massachusetts, Amherst, MA<sup>7</sup>  
Michael R. Blatt, Graduate, Stanford Uni-  
versity, Stanford, CA  
G. James Collatz, Graduate, Stanford Uni-  
versity, Stanford, CA  
Richard Cuellar, Graduate, Stanford Uni-  
versity, Stanford, CA  
Holly Gorton, Graduate, Stanford Univer-  
sity, Stanford, CA  
Dina F. Mandoli, Graduate, Stanford Uni-  
versity, Stanford, CA  
Jeffrey Palmer, Graduate, Stanford Uni-  
versity, Stanford, CA  
Richard Preisler, Graduate, Stanford Uni-  
versity, Stanford, CA  
Jeffrey R. Seemann, Graduate, Stanford  
University, Stanford, CA

<sup>5</sup> To January 19, 1979.

<sup>6</sup> To November 30, 1978.

<sup>7</sup> To May 31, 1979.

William Williams, Graduate, Stanford Uni-  
versity, Stanford, CA

### *Clerical and Technical Staff*

Benny Catanzaro, Electronic Technician  
Dorothy Ruth Fischer, Administrative  
Assistant—Accountant  
Glenn A. Ford, Laboratory Manager  
Edward G. Gausden, Technician  
Steven M. Graff, Laboratory Technician  
Richard W. Hart, Mechanical Engineer  
James Johnson, Technician<sup>8</sup>  
Kathleen Keller, Department Secretary<sup>9</sup>  
Anne E. Kimber, Laboratory Technician<sup>10</sup>  
Fred Lakin, Technical Illustrator  
David W. Lendrum, Technician  
Nancy E. Malich, Laboratory Technician  
Frank Nicholson, Senior Technician  
Debra Peters, Laboratory Technician  
Norma J. Powell, Typist  
Pedro Pulido, Technician  
Celia M. Smith, Laboratory Technician  
Patricia Sullivan, Laboratory Technician  
Aida Wells, Department Secretary

<sup>8</sup> To December 8, 1978.

<sup>9</sup> To December 31, 1978.

<sup>10</sup> To November 30, 1978.









# *Developmental Biology Research Group*

*Pasadena, California  
and Kerckhoff Marine Laboratory,  
Corona Del Mar, California*

Roy J. Britten  
*Senior Research Fellow*

Eric H. Davidson  
*Professor, California Institute of Technology*





Contents

Introduction . . . . . 243

DNA Sequence Organization around mRNA's in the Sea Urchin . . . . . 244

Sequence Organization of Repetitive DNA Sequence Family Members . . . . . 244

Primary Structure of Repetitive Sequence Elements in Sea Urchin DNA . . . . . 245

Repetitive Sequence Transcripts in Sea Urchin Eggs and Embryos . . . . . 246

Double-stranded hnRNA from Sea Urchin Gastrula . . . . . 246

Conservation of the Pattern of Repeated DNA Transcripts in  
Sea Urchin Oocytes . . . . . 247

Initial Studies of the Evolution of Sequence Organization in Sea Urchins . . . . . 247

Polymorphism of Single Copy DNA Sequences . . . . . 248

Correlation between Intraspecies and Interspecies DNA Sequence Divergence . . . . . 249

Evolutionary Sequence Conservation of Transcribed Single Copy DNA . . . . . 249

Complexity of RNA Sequences in the Eggs of Two Species of Flies . . . . . 250

The Expression of Histone Genes in Sea Urchin Oogenesis . . . . . 251

Size Distribution of Poly(A) Tracts in Early Mouse Embryos . . . . . 251

Expression of Genes Coding for Rare Sea Urchin Embryo Messages . . . . . 252

Transcript Size of Sea Urchin Messages . . . . . 252

cDNA Clones from Eggs and Gastrulae of Sea Urchin . . . . . 253

Synthesis and Decay Rates of Structural Gene Transcripts . . . . . 253

Distinct Single Copy Sequence Sets in Sea Urchin Nuclear RNA's . . . . . 254

Gene Organization in the Sea Urchin . . . . . 254

Isolation of Cloned DNA Sequences Coding for Insulin-like mRNA's . . . . . 255

Immunoglobulin (IgA) Gene Transcripts in Nuclear RNA and mRNA . . . . . 255

Staff . . . . . 256

Publications . . . . . 256





## INTRODUCTION

The Developmental Biology Research Group continues to focus on four areas of molecular biology: the sequence organization of the genome, the evolution and variation of the DNA and its sequence organization, the regulation of gene expression, and the modulation of genetic activity during embryonic development. We work primarily with the sea urchin, although some of the work summarized below is with vertebrate or mammalian systems. A large fraction of the work with DNA uses the new powerful methods of recombinant clones, restriction mapping, and direct sequencing. DNA re-association and RNA/DNA hybridization, which originally formed the core around which much of this work developed, remain essential and, in fact, are the tools that make analysis and

interpretation of the recombinant clones possible. Again this year, only short abstracts are included, and the report is essentially identical to that in the annual report of the Biology Division of the California Institute of Technology.

The work described in the following research reports has been also supported by:

American Cancer Society  
American Cancer Society, California  
Division  
Biomedical Research Support Grant (NIH)  
Charles B. Corser Fund for Biological  
Research  
March of Dimes  
National Institutes of Health, USPHS  
National Science Foundation  
Veterans Administration  
Weizmann Fellowship

## DNA SEQUENCE ORGANIZATION AROUND mRNA's IN THE SEA URCHIN

*Terry L. Thomas and Eric H. Davidson*

We have cloned two DNA sequences, Sp34 and Sp88, which have been shown to code for rare mRNA's. These clones display a complex DNA sequence organization. Thus in each cloned fragment there exist several nonrepetitive DNA sequence elements interspersed with different repetitive DNA sequence elements. We have also shown that the number of Sp88 and Sp34 mRNA's change drastically during sea urchin development (This Report, p. 252). The length of Sp88 transcripts changes during development (This Report, p. 252).

The Sp88 and Sp34 DNA fragments contain only flanking sequences which are located 3' to the coding region. Consequently, we are now attempting to isolate longer DNA sequences containing the Sp88 and Sp34 structural genes. This is being done by screening bacteriophage  $\lambda$  libraries containing  $\sim 15$  kb sea urchin DNA inserts, with labeled DNA probes made from the codogenic regions of Sp88 and Sp34. With these  $\lambda$  recombinants, we

will determine the longer range sequence organization surrounding Sp88 and Sp34 coding regions; that is, we will define with respect to the coding region the location of repetitive sequence elements and other codogenic and noncodogenic single copy DNA sequences. We will also use these clones to examine further the interesting and probably complex relationship between the primary transcripts of Sp88 and Sp34 and their respective mRNA's. Sp88 and Sp34  $\lambda$  recombinants also will be invaluable in testing two aspects of the Britten-Davidson model of gene regulation. In particular, we can ask whether there are other structural genes adjacent to the same repetitive sequence family members as found in Sp88 or Sp34; that is, do certain repetitive sequence families define gene batteries? We can also ask about the relationship between repetitive sequences adjacent to expressed structural genes and repetitive sequence transcripts in the nuclear RNA of various developmental stages.

## SEQUENCE ORGANIZATION OF REPETITIVE DNA SEQUENCE FAMILY MEMBERS

*David M. Anderson, Richard H. Scheller, and Eric H. Davidson*

Individual members of four separate repetitive sequence families have been isolated, along with several thousand nucleotides of flanking DNA, from the sea urchin genome<sup>1</sup> cloned in the bacteriophage  $\lambda$ . Three major projects using these clones are now in progress.

(1) The DNA sequence organization around repetitive sequence elements is being analyzed with respect to repetitive and single copy sequences, and any cross-homologies in the DNA flanking different

members of the same family. We have observed both the typical interspersed pattern of sequence organization and several regions of clustered repetitive DNA. Individual members of a repetitive family frequently occur within 15,000 nucleotides of each other. Preliminary data indicate that members of one repetitive family tend to occur near each other at several locations in the genome, although not always in the same orientation.

(2) The repetitive DNA families that



were used in the initial screening of the  $\lambda$  library were selected because they exhibited embryonic stage-specific changes in their representation in nuclear RNA populations. We are now studying the transcription of single copy DNA flanking several members of a repetitive family highly represented in gastrula nuclear RNA. One of these single copy sequences is represented in gastrula nuclear RNA at 100 times the average single copy DNA transcript concentration.

(3) The relationships between individual members of a given repetitive sequence family are also being examined.

We have identified subfamilies in two of our repetitive families by determining the thermal stability of hybrids formed between individual family members and comparing the data to those obtained from hybrids formed with total genomic DNA. It now seems clear that for the repetitive families we have studied, the total number of family members in the genome has arisen through several probably independent multiplication events. Each of these multiplications appears to have generated a subfamily of closely related elements. We are now isolating one such subfamily.

## PRIMARY STRUCTURE OF REPETITIVE SEQUENCE ELEMENTS IN SEA URCHIN DNA

*James W. Posakony and Eric H. Davidson*

In order to investigate the internal organization of repetitive sequence elements, we have determined the nucleotide sequence of seven such elements cloned from sea urchin DNA (Scheller *et al.*, 1977). Each clone contains a representative of a different repetitive sequence family; these families show a wide variation in both the number and sequence divergence of their members (Klein *et al.*, 1978).

A variety of computer techniques (R. F. Murphy, unpublished) were used to search the nucleotide sequences both for internal structural features and for sequence blocks shared among different repeats. These studies revealed the statistically significant occurrence of direct and inverted repetitions of varying lengths and of alternating runs of AT and GC base pairs. Furthermore, five of the seven repeats contain a sequence matching at least seven out of eight nucleotides with the sequence TTCAGGAT; the other two contain a six out of eight match. Aside from the unlikelihood of a chance occur-

rence of this homology, the sequence is of interest because of its close similarity to a consensus sequence representing the junctions between intervening and coding sequences in several eukaryotic genes (Breathnach *et al.*, 1978). Thus, repetitive sequence elements in sea urchin DNA appear to have a highly nonrandom internal organization and, in addition, different repetitive families may be related by short sequence homologies not detectable by physical-chemical methods.

### REFERENCES

- Breathnach, R. C., C. Benoist, K. O'Hare, F. Gannon, and P. Chambon. (1978) *Proc. Nat. Acad. Sci. U.S.A.* 74: 4853-4857.
- Klein, W. H., T. L. Thomas, C. Lai, R. H. Scheller, R. J. Britten, and E. H. Davidson. (1978) *Cell* 14: 889-900.
- Scheller, R. H., T. L. Thomas, A. S. Lee, W. H. Klein, W. D. Niles, R. J. Britten, and E. H. Davidson. (1977) *Science* 196: 197-200.

## REPETITIVE SEQUENCE TRANSCRIPTS IN SEA URCHIN EGGS AND EMBRYOS

*Frank Costantini, William H. Klein, and Eric H. Davidson*

We have previously reported that the sea urchin egg contains transcripts representing most of the repetitive sequence families in the genome and in widely varying prevalence, and that most repetitive sequence transcripts (RST's) are 1000 to 2000 nucleotides or longer. Recently, we have found that many of the egg RST's are polyadenylated. We have isolated egg poly(A)-RNA, labeled it in vitro with  $^{125}\text{I}$ , and isolated those transcripts containing repetitive sequences by hybridization to mercurated total repetitive DNA and chromatography on sulfhydryl Sepharose. About 25% of the poly(A)-RNA molecules (average fragment length about 1400 NT) appear to contain a repetitive sequence. Hybridization kinetics with excess sea urchin DNA showed that these transcripts consist mostly of single copy sequence, and only about 20% of their length, on the average, is repetitive sequence. Thus most of the egg repetitive sequence transcripts are

linked to single copy transcripts. Since most of the single copy sequences in egg RNA are maternal mRNA's, these results suggest that the egg RST's may be linked to single copy maternal mRNA's.

By isolating gastrula polysomal mRNA that is only slightly degraded in length (about 1500 NT weight average length) we have observed a previously undetected fraction of polysomal mRNA consisting of covalently-linked single copy and repetitive sequences. These transcripts were detected by the same methods used for polyadenylated egg RNA, and also by hydroxyapatite chromatography. At least 20% of labeled polysomal RNA consists of such transcripts. These molecules are not contaminating nuclear transcripts, as shown by pulse-labeling experiments. The presence of repetitive sequences in gastrula polysomal RNA has also been detected by hybridization of cloned individual repetitive sequences with polysomal RNA.

## DOUBLE-STRANDED hnRNA FROM SEA URCHIN GASTRULA

*Laurence A. Lasky and Eric H. Davidson*

This project has revolved around the isolation and characterization of RNA: RNA duplex molecules from hnRNA of sea urchin gastrula stage embryos. Previous work from this laboratory has shown that interspersed repetitive sequence elements are symmetrically represented in hnRNA of gastrula. hnRNA from gastrula was labeled in vivo, isolated, and reassociated. Duplex RNA was isolated by cellulose-ethanol chromatography. The reaction showed second-order kinetics. Approximately 15% of the total

radioactivity was bound to the column after a 10 min pulse-label and incubation to Rot 2000. The isolated duplex fraction was characterized with respect to size, thermal melting behavior, and structure in the electron microscope. These results suggested that hnRNA duplexes consisted of covalently linked double- and single-stranded regions. The isolated hnRNA duplex fraction was also used to titrate a number of interspersed repeat element clones. These experiments demonstrated that the RNA transcripts for



most of the elements tested were ~70-fold more concentrated in the duplex fraction. Further experiments with the hnRNA duplex fraction will include a

characterization of the adjacent single-strand regions which are covalently linked to the duplexes.

## CONSERVATION OF THE PATTERN OF REPEATED DNA TRANSCRIPTS IN SEA URCHIN OOCYTES

Gordon P. Moore and Roy J. Britten

Previous studies with cloned repetitive DNA sequences of the sea urchin *Strongylocentrotus purpuratus* demonstrated that repetitive elements are transcribed in a specific fashion into RNA which is then stored in the mature oocyte (Costantini *et al.*, 1978). That is, some repetitive DNA transcripts are highly abundant and others less so. Another series of measurements (Scheller *et al.*, 1978) also demonstrated specific contrasting patterns of repeat transcripts in nuclear RNA of various embryonic stages of development and adult tissues.

We have initiated the study of the evolutionary stability of these specific patterns of transcripts by measuring the concentration of transcripts in a related species of sea urchin. The evolutionary lines leading to *S. purpuratus* and *S. franciscanus* diverged approximately fifteen million years ago. We have measured the concentration of RNA sequences in *S. franciscanus* oocytes complementary to the same set of cloned repetitive DNA elements of *S. purpuratus* using

kinetic and titration techniques. Costantini *et al.* (1978) isolated a fraction of the total repetitive DNA sequences of *S. purpuratus* complementary to the abundant class of repetitive oocyte transcripts. We have reacted this tracer with *S. franciscanus* oocyte RNA. Results clearly show that the pattern of transcript accumulation is conserved. That is, repetitive transcripts abundant in *S. purpuratus* are also abundant in *S. franciscanus*. Evolutionary conservation of the pattern of repeat sequence transcript accumulation lends support to the view that the specific pattern of repeat transcription is physiologically important to the development and maintenance of the organism.

### REFERENCES

- Costantini, F. D., R. H. Scheller, R. J. Britten, and E. H. Davidson. (1978) *Cell* 15: 173-187.  
Scheller, R. H., F. D. Costantini, M. R. Kozlowski, R. J. Britten, and E. H. Davidson. (1978) *Cell* 15: 189-203.

## INITIAL STUDIES OF THE EVOLUTION OF SEQUENCE ORGANIZATION IN SEA URCHINS

Gordon P. Moore and Roy J. Britten

Repetitive DNA in the sea urchin genome falls into two categories. About 65% of repeats are short relative to a structural gene and generally interspersed with single copy DNA. The remaining

35% are greater than 2000 nucleotides in length. The two classes can be separated by intermediate *C<sub>0</sub>t* reassociation, treatment with S1 nuclease and chromatography on Sepharose 2B. The long repeats

reassociate precisely to yield high thermal stability duplexes, whereas the short repeats are divergent and form low melting hybrids (Britten *et al.*, 1976; Eden *et al.*, 1977).

We have examined the sequence homologies between the long and short classes of repeat DNA and individual cloned repetitive elements, each a representative of a family of repeats. Kinetics of hybridization indicate that each repeat family is predominately contained in one class or the other. Nevertheless, each cloned element reacts to some extent with the other class of repeat. Thus the two classes are overlapping in the sense that some sequences are shared between them.

Why are the long repeats precisely matched? One possibility is that selection acts to prevent sequence divergence during evolution. Alternatively, long repeats might be the products of recent multiplication. We approached this question by preparing a high thermal stability frac-

tion of *S. purpuratus* repeats in 2.4 M tetraethyl ammonium chloride which suppresses the effect of base composition on thermal stability. We reacted this fractionated *S. purpuratus* repeat DNA with an excess of total DNA from the related urchin species *S. franciscanus* and melted the resulting duplexes. Results indicated that the high thermal stability repeats had diverged to the same extent as the average repeat. We conclude that precisely matched repeats are not more highly selected than the average repeat and that recent multiplication is a more plausible mechanism to explain their relative lack of sequence divergence.

#### REFERENCES

- Britten, R. J., D. E. Graham, F. C. Eden, D. M. Painchaud, and E. H. Davidson. (1976) *J. Mol. Evol.* 9: 1-23.  
 Eden, F. C., D. E. Graham, E. H. Davidson, and R. J. Britten. (1977) *Nucleic Acids Res.* 4: 1553-1567.

### POLYMORPHISM OF SINGLE COPY DNA SEQUENCES

Terrence J. Hall and Roy J. Britten

The 4% single copy DNA sequence polymorphism of *Strongylocentrotus purpuratus* reported last year has been confirmed and the measurements extended. New procedures, including the measurement of the length of duplexed DNA after S1 digestion, have increased the accuracy and clarity of interpretation of these measurements. Several additional pairs of individuals have been studied and the average sequence difference between individual genomes remains about 4° with an uncertainty of less than 1°. The length of the duplexed regions is very slightly shorter for reassociated inter-individual DNA compared to that from the same individual. We do not know if this is due to rearrangement events or the

digestion of short regions of high local sequence divergence.

Studies of the single copy DNA sequence polymorphism of a second species (*S. drobachensis*) have been initiated. DNA of one individual collected at Woods Hole, Massachusetts, was labeled and reassociated with that of another individual from Woods Hole and with the mixed DNA from several individuals collected near Vancouver, British Columbia. In both cases the length-corrected melting temperatures were about 1° below that observed for reassociation with driver DNA from the same individual. The earlier measurements for *S. purpuratus* show the polymorphism to be widespread. Possible homozygosity due to in-



breeding in local populations was not observed. Thus heterozygosity was large, and the average thermal stability for re-associated DNA from one individual was halfway between that of perfect duplex and that observed for interindividual re-associated DNA. If the same situation is true for *S. drobachiensis* it appears that

the single copy DNA polymorphism of this species is half of that for *S. purpuratus*, or about 2% average nucleotide sequence difference. It also appears that there is no greater sequence difference between East and West Coast individual genomes than between the two genomes of East Coast individuals.

## CORRELATION BETWEEN INTRASPECIES AND INTERSPECIES DNA SEQUENCE DIVERGENCE

John W. Grula and Roy J. Britten

Measurements of sequence divergence between the single copy DNA's of two species show a wide spectrum of degrees of sequence difference. Further, in studies of polymorphism, a majority of the DNA appears to show little sequence difference between individual genomes while a smaller fraction exhibits a large sequence difference. Is this range of divergence the result of chance or natural selection?

If the same set of single copy DNA which showed small polymorphism also displayed small interspecies divergence, it would support the natural selection alternative and indicate that these sequences are being conserved in evolution. Therefore we have isolated two fractions of labeled *Strongylocentrotus purpuratus* single copy DNA on the basis of thermal stability after reassociation with DNA of a different individual of the same species. To test the fractionation, these preparations were reassociated with mixed *S. purpuratus* DNA, giving  $T_{ms}$  of 58° and 54° (compared to 60° for perfect

duplexes of their length in the 2.4 M tetraethyl ammonium chloride system). When they were reassociated with *S. franciscanus* DNA,  $T_{ms}$  of 52° and 47°, respectively, were observed. These measurements suggest a correlation between degree of polymorphism and interspecies divergence. Complementary measurements in which the fractionation is carried out on the basis of interspecies sequence differences also suggest a correlation, but it may be somewhat weaker.

Thus it appears that a large fraction of the single copy DNA sequences of these sea urchins is under selective pressure. It is worth noting that only a much smaller fraction of the single copy DNA (6%) has been shown to be made up of structural genes, on the basis of its transcription into the complex class of maternal message in mature oocytes. The single copy sequences other than those coding for structural genes appear to be under sequence-dependent selective pressure.

## EVOLUTIONARY SEQUENCE CONSERVATION OF TRANSCRIBED SINGLE COPY DNA

Terrence J. Hall and Roy J. Britten

Comparisons have been made in sea urchins between the interspecies sequence divergence of total single copy DNA and

the fraction of the single copy DNA which is transcribed to yield nuclear RNA or mature egg RNA. Labeled single

copy DNA of *Strongylocentrotus purpuratus* was hybridized with gastrula nuclear RNA or total egg RNA and the duplexed fragments isolated on hydroxyapatite. The resulting specific tracers are termed nDNA and oDNA and consist of short fragments of single copy DNA (100–500 nucleotides) which contain regions which are transcribed. However their full length is not necessarily represented in the RNA. These tracers were reassociated with an excess of sheared DNA from *S. purpuratus* or *S. franciscanus*. The resulting duplexes were digested with S1 nuclease to remove unpaired regions and the duplex length was measured. Samples were heated to a series of temperatures, cooled, digested with S1 and the remaining duplexes assayed. Least squares methods were used to determine the  $T_m$  (temperature at which half the duplexes were melted) and the resulting values were corrected

for the length by adding  $C = (500/\text{duplex length})$ . The interspecies duplex lengths were about half of the intraspecies duplex lengths, presumably as a result of digestion of clusters of unpaired nucleotides, and the length reduction was somewhat less for the specifically transcribed tracers.

Compared to intraspecies duplexes (between different individuals), the interspecies duplexes with total single copy tracer were reduced in  $T_m$  by  $9.7^\circ$ . The same comparison for nDNA tracer yielded  $6.5^\circ$ . With the oDNA tracer, *S. franciscanus* duplexes showed a  $T_m$  only  $4.4^\circ$  below those with *S. purpuratus*. A clear conclusion can be drawn that these transcribed regions have been conserved in sequence relative to total single copy DNA during the more than 15 million years of independent evolution of *S. franciscanus* and *S. purpuratus*.

## COMPLEXITY OF RNA SEQUENCES IN THE EGGS OF TWO SPECIES OF FLIES

Barbara R. Hough-Evans, Marcelo Jacobs-Lorena,\*  
Michael R. Cummings,† and Eric H. Davidson

We have extracted RNA from the eggs of two species of flies, the housefly *Musca domestica* and the fruit fly *Drosophila melanogaster*, and measured its complexity (that is, the number of nucleotides of diverse sequence represented). *Musca* and *Drosophila* diverged in evolution at least 63 million years ago, and their genomes differ in several respects. First, *Musca* has 5 times more total DNA and  $3\frac{1}{2}$  times more single copy DNA. Second, the single copy and repetitive sequences of *Musca* DNA are arranged in

a short-period interspersal pattern like those of *Xenopus*, sea urchin, and most other eukaryotic DNA's, while *Drosophila* DNA is arranged in a long-period interspersal pattern, with both nonrepetitive and repetitive sequences of 5–10 times the length of those observed in *Musca*.

The egg RNA complexities were determined by hybridization of excess RNA with radioactively labeled nonrepetitive DNA. We found that the egg RNA of *Musca* contains twice the complexity of *Drosophila* egg RNA ( $2.4$  vs.  $1.2 \times 10^7$  nucleotides). *Musca* egg RNA is thus similar in complexity to the RNA of eggs of *Xenopus* and sea urchin, while *Drosophila* egg RNA is unusually low in complexity.

\* Case Western Reserve University School of Medicine, Cleveland, Ohio.

† Department of Biological Sciences, University of Illinois at Chicago, Chicago, Illinois.



## THE EXPRESSION OF HISTONE GENES IN SEA URCHIN OOGENESIS

*Barbara R. Hough-Evans, Alex Mauron,\* and Eric H. Davidson*

The histone genes of the sea urchin *Strongylocentrotus purpuratus* exist in the genome as a cluster of repeated genes, with the "spacer DNA" between them equally repeated. These genes and the spacer regions have been reproduced as recombinant DNA in the bacterial plasmid pBR322 in the Kedes Laboratory at Stanford. Cloned fragments containing single genes or spacers are now being prepared. The adjacent individual genes coding for histones H2B and H3, and the

\*Stanford University Medical School, Palo Alto, California.

spacer DNA between them, are to be strand-separated, labeled to high specific activity, and hybridized to mature sea urchin egg RNA and to cytoplasmic and nuclear RNA's extracted from vitellogenic oocytes and previtellogenic oocytes. The goal of the project is to determine the time of appearance, and the accumulated amounts, of stored histone mRNA's during oogenesis. We are also interested in finding out if spacer regions are transcribed, and whether the mRNA's of all five genes are produced and stored at the same rate.

## SIZE DISTRIBUTION OF POLY(A) TRACTS IN EARLY MOUSE EMBRYOS

*Lajos Pikó\* and Kerry B. Clegg\**

Previously we have shown that the unfertilized mouse egg contains about 0.7 pg of poly(A) sequences in its cytoplasm. The amount of poly(A) remains unchanged in the fertilized one-cell egg but drops sharply, to about 0.25 pg per embryo, at the two-cell stage. The poly(A) content increases progressively from the four- to eight-cell stage onward to about 1.5 pg in the early blastocyst (32 cells).

To explore the significance of the changes in poly(A) content, we have analyzed the size distribution of poly(A) tracts (defined as material resistant to RNase A and T1) in total unlabeled RNA isolated from unfertilized and fertilized one-cell eggs and two-cell embryos. The poly(A) tracts were fractionated by polyacrylamide gel electro-

phoresis, eluted from the gel slices, and assayed by hybridization with [<sup>3</sup>H]poly(U). Essentially identical patterns were obtained for the three stages, with a sharp peak of 20–30 nucleotides and a broad peak of up to 250 nucleotides (the majority ranging between 120 and 200). The number average molecular weight of poly(A) tracts varied within narrow limits, from 63 to 75. Labeling experiments with [<sup>3</sup>H]adenosine have failed to detect any significant turnover of the poly(A) sequences or synthesis of poly(A)-containing RNA in the one-cell fertilized egg, although newly synthesized poly(A)-containing RNA is clearly detected at the two-cell and later stages. These results indicate that poly(A)-containing RNA is stored in the mouse egg and that neither the amount nor the size of the poly(A) sequences changes significantly upon fertilization. Protein

\*Veterans Administration Medical Center, Sepulveda, California.

synthesis in the one-cell embryo may utilize stored messenger RNA's exclusively. The significant drop in poly(A) content at the two-cell stage cannot be accounted for by a reduction in poly(A)

length and may represent a turnover of maternally inherited mRNA. Poly(A)-containing RNA is synthesized in progressively larger amounts from the two-cell stage onward.

## EXPRESSION OF GENES CODING FOR RARE SEA URCHIN EMBRYO MESSAGES

*Ze'ev Lev, Terry L. Thomas, Amy Shiu Lee,  
Robert C. Angerer,\* and Eric H. Davidson*

Measurements are presented of the number of transcripts in sea urchin embryos and in adult intestine cells complementary to two cloned genomic single copy sequences, Sp88 and Sp34. These sequences apparently code for maternal mRNA's stored in the egg. About 1000 and 1400 transcripts are stored per egg, close to the average value for maternal mRNA's. RNA's complementary to the cloned sequences are also found in the polysomal message of early embryos. The number of polysomal transcripts

representing each cloned sequence is typical of the "complex," or "rare" class of message in sea urchin embryos. Expression of these putative complex class structural genes is regulated developmentally. Thus polysomal transcripts of both sequences essentially disappear by the pluteus stage. One sequence is again represented at a low level in adult intestine cytoplasmic RNA, while the other is absent. However, in all the developmental stages and tissues examined, the number of nuclear transcripts of the cloned sequences remains about the same as for any average single copy sequence transcript.

\*Department of Biology, University of Rochester, Rochester, New York.

## TRANSCRIPT SIZE OF SEA URCHIN MESSAGES

*Amy Shiu Lee and Eric H. Davidson*

Two sea urchin recombinant DNA clones, Sp88 and Sp34, contain sequences which code for maternal mRNA stored in the egg. RNA's complementary to the cloned sequences are also found in nuclear transcripts of all developmental stages examined, as well as polysomal message of 16-cell embryos (*Year Book* 77, pp. 373-374). The size of these transcripts as they occur in different developmental stages is being examined by DMSO gradients, as well as by RNA blotting techniques. Preliminary results indicate that in the maternal RNA population of the egg, Sp88 hybridizes to two

RNA transcript sizes, ~4000 NT and 1600 NT. These transcripts appear to be polyadenylated. In the case of Sp34, the major egg transcript size is 4000 NT. The 16-cell polysomal RNA's reacting with Sp88 are of typical message length; they are ~1800 NT long. However, at the gastrula stage when the Sp88 transcript is not represented in polysomal or cytoplasmic RNA populations, the transcripts detected in the nucleus are over 6000 NT long. Work is in progress to determine if Sp34 transcripts expressed during embryonic stages are similar in size to the Sp88 transcripts.



## cDNA CLONES FROM EGGS AND GASTRULAE OF SEA URCHIN

*Laurence A. Lasky, Jay W. Ellison, Ze'ev Lev,  
Terry L. Thomas, and Eric H. Davidson*

cDNA clones have been constructed using polyadenylated RNA from eggs and gastrulae of *Strongylocentrotus purpuratus*. These clones have been constructed using the double-stranded DNA approach in the vector pBR322. Several clones have been isolated from both stages and characterized with respect to insert size and restriction enzyme sites. One such clone from gastrula has been found to be represented at about 20 copies per cell in gastrula polysomal

RNA, but appears to be absent from blastula messenger RNA. In addition, a new library of cDNA clones is being constructed by cloning of RNA:cDNA hybrids. This library will consist of a large number of clones which can be screened with various probes. In this way, it should be possible to isolate several cDNA clones which correspond to mRNA sequences specific for given stages in early development.

## SYNTHESIS AND DECAY RATES OF STRUCTURAL GENE TRANSCRIPTS

*Jay W. Ellison and Eric H. Davidson*

A recent observation concerning transcription in sea urchins is that structural gene transcripts absent from polysomes of a given tissue are nonetheless present in the nuclear RNA of that tissue (Wold *et al.*, 1978). This finding implies that post-transcriptional events play some role in the regulation of those structural genes. Specific predictions of the nature of this level of regulation have recently been proposed (Davidson and Britten, 1979).

The present study is designed to ask questions about the extent of transcriptional control of the expression of structural genes. Specifically, we wish to determine whether mRNA's which differ in prevalence in the cytoplasm also differ in their rates of synthesis. Embryos are labeled with exogenous [<sup>3</sup>H]guanosine, and the specific activity of the GTP pool is determined as a function of labeling time. Nuclear RNA is prepared at vari-

ous times after labeling and is hybridized with an excess of a cloned DNA sequence complementary to a cytoplasmic poly(A)-containing RNA. From the GTP-specific activity measurements and the flow of radioactivity into the complementary transcript, we can derive synthesis and decay rate constants for the cDNA transcript. Comparison of these parameters for cDNA's representing mRNA's of varying abundance should shed some light on the degree of transcriptional regulation of structural gene expression.

## REFERENCES

- Davidson, E. H. and R. J. Britten. (1979) *Science* 204: 1052-1059.  
Wold, B. J., W. H. Klein, B. R. Hough-Evans, R. J. Britten, and E. H. Davidson. (1978) *Cell* 14: 941-950.

## DISTINCT SINGLE COPY SEQUENCE SETS IN SEA URCHIN NUCLEAR RNA's

*Susan G. Ernst and Eric H. Davidson*

The purpose of this study was to determine whether nuclear RNA's (nRNA) of sea urchin embryos and adult tissues contain identical or partially distinct sets of single copy sequence transcripts. A DNA tracer was prepared consisting mainly of sequences absent from gastrula nRNA; 3.6% of this tracer reacted with adult intestine nRNA but not with gastrula nRNA. The existence of a dif-

ferentially transcribed DNA fraction was verified by its partial purification and rehybridization to intestine and gastrula nRNA's. About one third of the genomic single copy sequence is represented in both nRNA's, or about  $2 \times 10^8$  nucleotides. The differentially transcribed portion of the single copy genome identified in this work includes about  $3.5 \times 10^7$  nucleotides.

## GENE ORGANIZATION IN THE SEA URCHIN

*Ze'ev Lev and Eric H. Davidson*

This project is concerned with the relation between hnRNA and mRNA in a differentiating animal cell system. The sequence complexity and transcript length of both mRNA and hnRNA have been measured in several embryonic stages and adult tissues of the sea urchin. It has been shown that the sequence complexity of nuclear RNA is 30–40% of the complexity of total single copy sequences existing in the sea urchin genome. The complexity of mRNA varies according to the tissue tested between 0.8 and 4.5% of total DNA single copy sequence complexity. It is reasonable to assume that about 10% of the whole single copy genome are mRNA sequences. Recent results suggest that most, or even all, mRNA sequences appear in hnRNA of every tissue (Wold *et al.*, 1978; also see This Report, p. 246). It is concluded that  $10\%/40\% = 25\%$  of hnRNA sequences are sequences included at some time in mRNA (Wold *et al.*, 1978). This is about the same as the ratio of sizes between the two RNA populations. The size of mRNA molecules is about 1.8 kb

and the size of hnRNA molecules is about 8.0 kb.

There are many possible explanations for this relationship. Two of the most simple possibilities are (1) each hnRNA molecule contains one mRNA sequence, which constitutes about 25% of its length, and (2) all mRNA sequences are confined to a 25% class of hnRNA's, and 75% have no mRNA sequences at all but perform other functions, possibly regulative. In the first case, where each hnRNA molecule carries one mRNA sequence, it would be predicted that at the DNA level the gene organization is such that the genes are at least 8.0 kb apart. The second alternative predicts that the genes are clustered in groups of about four genes per group.

In order to distinguish between these two possibilities, we use cDNA clones as a probe to screen the cloned library of sea urchin genomic DNA. Selected genomic clones will be purified and the positions of the sequences coding for mRNA and hnRNA prepared from a given embryonic stage or adult tissue will



be determined, using biochemical and electron microscopy techniques. If the results show clustering of genes, this will be considered as a confirmation of model (2). However, the experiment is inconclusive if only one gene is found to be expressed within a long DNA sequence. Thus, it is always possible that genes included in this sequence are expressed only at some time during the life cycle of the sea urchin other than that from

which the diagnostic mRNA was obtained. We shall try to overcome this difficulty by testing mRNA preparations made from many different tissues.

#### REFERENCE

- Wold, B. J., W. H. Klein, B. R. Hough-Evans, R. J. Britten, and E. H. Davidson. (1978) *Cell* 14: 941-950.

### ISOLATION OF CLONED DNA SEQUENCES CODING FOR INSULIN-LIKE mRNA's

*Terry L. Thomas, Argiris Efstratiadis,\* and Eric H. Davidson*

The importance of insulin in mammalian physiology is well known. Interestingly, there are a number of examples of insulin-like activities in invertebrates, including the starfish, an echinoderm. We are currently attempting to isolate insulin-like structural genes from the sea urchin. This is being done by screening our *Strongylocentrotus purpuratus*  $\lambda$  libraries with a cloned rat insulin cDNA probe. This clone was constructed by Efstratiadis *et al.* of Harvard University Medical School. At present we have iso-

lated three different  $\lambda$  recombinants sharing some homology with the rat insulin probe. We are determining the extent of this homology by hybridization methods and by direct DNA sequencing.

Our interests in the insulin clones are directed at the genome organization surrounding the insulin structural gene and in the expression of a structural gene with a known gene product in either embryonic or adult tissues. Model tests similar to those described for Sp88 and Sp34 are also of considerable interest. Efstratiadis will compare the DNA sequence of the rat insulin intervening sequences with any intervening sequences found in the sea urchin insulin gene.

\* Department of Biological Chemistry, Harvard University Medical School, Boston, Massachusetts.

### IMMUNOGLOBULIN (IgA) GENE TRANSCRIPTS IN NUCLEAR RNA AND mRNA

*Terry L. Thomas, Kathryn A. Calame,\* Leroy E. Hood,\* and Eric H. Davidson*

We are examining the expression of the IgA heavy chain, constant region structural gene in the nuclear RNA and mRNA of several myelomas and mouse tissues. This sequence has been cloned as a full-length cDNA. We have prepared strand-separated radioactively labeled

tracers of the IgA constant region sequence and have reacted these tracers with nuclear RNA and mRNA from the above sources. All transcripts are completely asymmetric. In a myeloma producing large quantities of IgA, there are  $>10^4$  mRNA transcripts loaded on polyosomes; there are  $\leq 2 \times 10^3$  transcripts per nucleus. In nuclear RNA from mouse liver and a myeloma that does not pro-

\* California Institute of Technology, Pasadena, California.

duce IgA, there are  $\sim 0.6$  and 0.2 copies per nucleus, respectively, of IgA constant region transcript. At this point we are not sure these latter observations are real because we cannot rule out contaminating lymphocytes as a source for these transcripts, although this seems unlikely for the nonproducing myeloma. We are

now making more measurements on nuclear RNA and mRNA preparations from tissues (fetal brain and adult brain) less likely to be contaminated with circulating lymphocytes. These experiments will provide a quantitative measure of the level of expression in both nuclear RNA and mRNA of the Ig genes.

## STAFF

Senior Research Associate: Roy J. Britten

Professor: Eric H. Davidson

Visiting Associates: Lajos Pikó, Ji-hou Xin

Senior Research Fellows: Barbara R. Hough-Evans, William H. Klein, Amy Shiu Lee, John W. Roberts, Terry L. Thomas

Weizmann Research Fellow: Ze'ev Lev

Research Fellows: David M. Anderson, Susan G. Ernst, John W. Grula, Terrence J. Hall, Laurence A. Lasky, Gordon P. Moore

Graduate Students: Frank Costantini, Jay

W. Ellison, James W. Posakony, Richard H. Scheller

Research Staff: Clifford Beall, Peggy R. Bierer, Margaret E. Chamberlin, Steven T. Eckmann, Susan E. Gerber, Roberta Gerson, Robert L. Kimlich, Patrick S. Leahy, Peter Sin-Yi Lu, Michael Lusby, Linda McAllister, Jean Mueller, Peter E. Nolan, Jane Rigg, Richard M. Rohan, Sydne A. Schurmeier, Douglas Tally, Steven G. Trabert, Linda Vock

Laboratory Staff: Fargo Balliett, Terrence Guigni, Edward D. Kusby, Kim MacQuarrie, George Pauls

## PUBLICATIONS

Britten, R. J., A. Cetta, and E. H. Davidson. (1978) The single copy DNA sequence polymorphism of the sea urchin *S. purpuratus*. *Cell* 15: 1175-1186.

Chamberlin, M. E., G. A. Galau, R. J. Britten, and E. H. Davidson. (1978) Studies on nucleic acid reassociation kinetics: V. Effects of disparity in tracer and driver fragment lengths. *Nucleic Acids Res.* 5: 2073-2094.

Costantini, F. D., R. H. Scheller, R. J. Britten, and E. H. Davidson. (1978) Repetitive sequence transcripts in the mature sea urchin oocyte. *Cell* 15: 173-187.

Davidson, E. H. and R. J. Britten. (1979) Regulation of gene expression: Possible role of repetitive sequences. *Science* 204: 1052-1059.

Ernst, S., R. J. Britten, and E. H. Davidson. (1979) Distinct single copy sequence set in sea urchin nuclear RNA's. *Proc. Nat. Acad. Sci. U.S.A.* 76: 2209-2212.

Hough-Evans, B. R., S. G. Ernst, R. J. Britten, and E. H. Davidson. (1979) RNA complexity in developing sea urchin oocytes. *Develop. Biol.* 69: 225-236.



- Klein, W. H., T. L. Thomas, C. Lai, R. H. Scheller, R. J. Britten, and E. H. Davidson. (1978) Characteristics of individual repetitive sequence families in the sea urchin genome studied with cloned repeats. *Cell* 14: 889-900.
- Lee, A. S., R. J. Britten, and E. H. Davidson. (1978) Short period repetitive sequence interspersions in cloned fragments of sea urchin DNA. *Cold Spring Harbor Symp. Quant. Biol.* 42: 1065-1076.
- Lev, Z., T. L. Thomas, A. S. Lee, R. C. Angerer, R. J. Britten, and E. H. Davidson. (1979) Developmental expression of two cloned sequences coding for rare sea urchin embryo messages. *Devel. Biol.*: in press.
- Moore, G. P., R. H. Scheller, E. H. Davidson, and R. J. Britten. (1978) Evolutionary change in the repetition frequency of sea urchin DNA sequences. *Cell* 15: 649-660.
- Scheller, R. H., F. D. Costantini, M. R. Kozlowski, R. J. Britten, and E. H. Davidson. (1978) Specific representation of cloned repetitive DNA sequences in sea urchin RNA's. *Cell* 15: 189-203.
- Wold, B. J., W. H. Klein, B. R. Hough-Evans, R. J. Britten, and E. H. Davidson. (1978) Sea urchin embryo mRNA sequences expressed in the nuclear RNA of adult tissues. *Cell* 14: 941-950.





*Department  
of Terrestrial Magnetism*

*Washington, District of Columbia*

George W. Wetherill

*Director*

*Carnegie Institution of Washington Year Book 78, 1978-1979*



# Contents

Introduction . . . . .	263	Diffusion of water in a granitic melt: an experimental study . . . . .	352
Physics and Chemistry of the Earth . . . . .	272	Diffusivity and solubility of helium in granitic and basaltic glasses—mechanisms of helium degassing . . . . .	355
Subduction zones and island arcs . . . . .	272	Raman spectroscopic studies of $P_2O_5$ - and $TiO_2$ -bearing mineral glasses . . . . .	359
Subduction beneath western South America: overview and the <i>ScSp</i> controversy . . . . .	272	Galaxies, Stars, and Planetary systems . . . . .	363
Subduction of the Nazca Plate beneath Peru as determined from seismic observations . . . . .	276	Galaxies and their evolution . . . . .	363
On bending of the subducting plate and double Benioff zones . . . . .	284	Dynamical properties of spiral galaxies as a function of Hubble type . . . . .	363
Toward a quantitative model of stress diffusion after large subduction zone earthquakes: applications to northern Japan . . . . .	288	The gaseous disk of the S0 galaxy NGC 4203 . . . . .	373
Isotopic studies of Cenozoic Andean calc-alkaline rocks . . . . .	298	<i>B - V</i> color profiles of luminous elliptical galaxies . . . . .	376
Nd isotopic composition of recent andesites from Indonesia . . . . .	304	Globular cluster ages . . . . .	379
Oxygen isotope research . . . . .	308	Supernova remnants in M31 . . . . .	383
The oceanic crust and lithosphere . . . . .	311	Star formation and the early history of the solar system . . . . .	383
Structure of the oceanic lithosphere from surface-wave observations: the Iceland Plateau . . . . .	311	On the role of a supernova in the formation of the solar system . . . . .	383
Stress field changes during a tectonic episode in northern Iceland . . . . .	320	The vertical distribution of young galactic objects . . . . .	388
Geochemistry of basalts from the FAMOUS area: a reexamination . . . . .	325	Numerical calculations relevant to the accumulation of the terrestrial planets . . . . .	389
Pb isotope geochemistry of the Galápagos Islands . . . . .	331	Irradiation history of Mokoia carbonaceous chondrite . . . . .	399
Trace element fractionation and the nature of the residual phases during tholeiite production in Hawaii . . . . .	335	Unusual thermal history of the Shaw chondrite . . . . .	402
Evolution of the Earth's crust and mantle . . . . .	340	Thermal history of some xenolithic ordinary chondrites . . . . .	405
Tertiary komatiites of Gorgona Island, Colombia . . . . .	340	Identification of clear taenite in meteorites as ordered FeNi . . . . .	409
Rb-Sr whole-rock studies: Virginia Piedmont . . . . .	344	Instrumentation . . . . .	414
Are ancient lead deposits chronometers of the early history of Earth? . . . . .	346	The joint CIW-IAR 21-cm receiver for high-sensitivity Southern neutral hydrogen observations . . . . .	414
Experimental studies of geochemical processes . . . . .	352	Imaging detectors . . . . .	418
		The 15-inch mass spectrometer . . . . .	419
		Bibliography . . . . .	421
		Personnel . . . . .	424





## INTRODUCTION

Some courage is required for a child to ask the question, "Where did I come from?" Parents feel they are being put to a test when it is asked. It might be thought that this mutual unease stems simply from embarrassment in putting into words the rather incredible biological "facts of life" and that it would vanish if we could outgrow our puritanical inhibitions. The discomfort may have a deeper source: The question focuses attention upon a mystery that even the older generation has not yet resolved: how the most immediate and personal fact of our experience—the consciousness of our own existence—began only a few decades ago; before that the world was very much as it is today, but we were not. Both the child and the parent have a common need to deal with the horror of nonexistence and to extend their sense of their own beginning beyond the absurdly recent barrier imposed by the dates of their conception and birth.

In our library is a book entitled *A New Era in Chemistry*, written by Harvey C. Jones, a Research Associate of the Carnegie Institution from 1903 until his death in 1916. The title reminds one that the author was writing in the living moment of the present. In our minds we can transport ourselves to his position at his desk in Baltimore, groping for the best way to explain to others the exciting new discoveries of Ostwald, Ramsay, and Rutherford, and we can understand that the experience of the present moment was the same for Jones in 1913 as it is for ourselves in 1979. With greater difficulty we can grasp the fact that this was equally true for our prehistoric human ancestors, who lived without even the warmth of a fire through the darkness of a hundred million winter nights.

Yet, however, our roots lie in a still earlier planet in which human thought was

absent, and human considerations, including national boundaries, money, and worry about the future had no meaning. The insight provided by earth scientists and astronomers gives us our only glimpse into these prehuman times, and to the billions of years during which there existed no mammals, fish, insects or worms, no organisms with more than one cell, nor even any life at all. This work reconstructs a vision of sights that were never seen, and of sounds that were never heard. Our search for "where we came from" takes us back to the supernovae in which the atoms of the chemical elements of which we are made were created, and to the watery geochemical environments in which the earliest biological chemical compounds were formed. It is there we will find the source of the chemical "hardware" still required to encode our most subtle thoughts and feelings, and without which, as far as science knows, these human attributes would not exist at all.

We live in a time when society is generous in providing the resources necessary to widen the scope and depth of this priceless understanding of the past. Throughout the world, in universities, government and industrial research institutes, as well as in more uncommon organizations like the Carnegie Institution and this Department, scientists are responding to this opportunity. This response consists of carrying out specialized and detailed observations, experiments, and theoretical calculations, which may at first sight seem unrelated but which represent the only way to make solid progress toward broader goals. Our most recent contributions to this effort are summarized in this Report.

There is in geology a fundamental half-truth named the uniformitarian doctrine which asserts that "the present is

the key to the past." With equal validity or lack thereof it can be applied to astronomy as well. By studying processes that can be observed in the Earth, Galaxy, or Universe today we can begin to understand the fundamental mechanisms which determine their evolution. The terms "the present" and "today," however, must often be used in a way which evokes a smile from those who recognize that an hour can seem a long time. The term "process" necessarily introduces the dimension of time. The characteristic time associated with processes operating today, such as the subduction of the uppermost mantle of the Earth into its interior, is often millions of years—a short time compared to the 4.5 billion years of Earth history. Much of the history of the Earth and Universe can be understood as resulting from the slow accumulation of small events over these enormous lengths of time. Yet on the other hand, real "catastrophes" do occur, in spite of the efforts of doctrinaire uniformitarianists to eradicate them from scientific inquiry. The effects of collisions of planetary bodies with one another and of galaxies with one another, and explosions of aged stars as supernovae, are of importance comparable to those resulting from more patient processes.

#### SUMMARY OF CURRENT RESEARCH

##### *Dynamical and Chemical Processes in the Earth's Mantle*

During the past decade, most earth scientists have turned their attention toward the consequences of at least the outer regions of the Earth being a great heat engine, powered by the release of nuclear energy from the radioactive disintegration of uranium, thorium, and potassium. The moving parts of the engine are several: the great 50- to 100-km-thick solid plates of the oceanic lithosphere, which migrate horizontally for thousands of kilometers before they plunge into the Earth's interior at oceanic

trenches; the more buoyant and thicker, slowly drifting rafts of continental lithosphere; the underlying plastic asthenosphere; and the deeper regions of the mantle, where the return flow from trench to ridge takes place. In a general way this mechanism is well understood: heating at depth leads to rocks having lower density, greater buoyancy, and upward motion. Cooling near the surface of the Earth has the opposite effect. The result is the complex convective system summarized by the term "plate tectonics."

These phenomena comprise a uniformitarian process par excellence. Only by the use of highly sophisticated instruments is it possible to distinguish the flow of radioactive heat to the surface of the continent from the much greater background "noise" produced by variations in sunshine. The total kinetic energy associated with global plate motion is only about  $10^5$  joules, about enough to heat the water for a cup of tea. Yet in the last 200 million years these processes have broken the Americas from Europe and Africa, and scattered once-united Australia, Africa, Antarctica, South America, and India to their present locations.

This year at DTM, considerable attention has been directed toward understanding the structure of the slab of oceanic lithospheric mantle along the western margin of South America. The collision between the oceanic and the continental lithosphere leads to the subduction of the denser and less buoyant oceanic plate into the deeper mantle of the Earth. This is the only presently available example of a tectonic environment that, over the history of the Earth, must have played a major role in mountain building, ore formation, and the evolution of continents.

For some years workers at DTM and at Cornell University have interpreted seismic data from this region in a conflicting manner. The DTM group has argued that this subduction is "normal," i.e., is very similar to that found through-



out the world in island arcs such as Japan, where the interaction is between two oceanic plates. In contrast, the Cornell group has maintained that in the regions of central Peru and central Chile the ocean-continent subduction is characteristically different: the subduction angle is very shallow, about  $10^\circ$ , in contrast with the normal subduction angle of  $30^\circ$ . Elsewhere, in the geographically intermediate region of southern Peru and northern Chile, both groups agree that the subduction angle is normal, i.e. about  $30^\circ$ . Acceptance of the shallow angle of subduction leads to the difficulty that its eastward continuation would require the South American continental lithosphere to be relatively thin, whereas our seismic data indicate it is 300–400 km thick.

This year Hasegawa and Sacks describe a detailed reinvestigation of the seismic data in this region of subduction, and are led to conclusions which appear to reconcile the previously conflicting interpretations. It seems that both interpretations were partly true and partly false, and that, as usual, the real Earth fails to conform to simple models developed to interpret limited sets of data. By making use of the finer spatial resolution available by use of the densely spaced local earthquakes, the subducted slab has been mapped in more detail. It is found that for the first 100 km of descent, the slab enters at the normal  $30^\circ$  angle. However, below this depth it is bent to a nearly horizontal angle. This horizontal slab extends eastward about 300 km, and then dips steeply below the thick lithosphere of the principal portion of the South American continent. When viewed at the earlier lower resolution, the  $10^\circ$  subduction angle represents the averaged value of the initial steeper angle and that of the horizontal region. Snoke, Sacks, and James explain how this more refined picture of the subduction geometry fits in well with several lines of evidence obtained at DTM which supported the normal  $30^\circ$  subduction angle. This evidence correctly defined the

steeply dipping initial portions of the subduction, but did not identify the horizontal portion.

Simple inspection of a map of western South America demonstrates that the downgoing slab of oceanic lithosphere has had, during the past several million years, a profound effect on the surface geology and geography of this region: it has produced the Andes mountains, the belt of active and dormant volcanoes, and the great thicknesses of volcanic deposits. It could be that these effects are primarily physical in origin, and that little new material is added to the continent by these processes. On the other hand, it is possible that the slab itself is melted, and that material derived from oceanic mantle is thereby injected into the crust of the continents, causing them to grow with time. As in most such problems, it is likely that neither of these simple pictures is really correct, but it is also likely that neither has entirely missed the truth. Definition of more detailed mechanisms for volcanism and production of igneous rocks above subduction zones is at present a lively field of research in many laboratories.

In addition to conclusions based on major element petrology, studies of trace elements and isotopic measurements are making major contributions toward the resolution of this problem. Last year James described work carried out in collaboration with Magaritz and Whitford, in which it was shown that the dominant element in the Andean volcanic rocks, oxygen, was clearly enriched in the heavy isotope  $^{18}\text{O}$ . These rocks were thereby shown to carry the isotopic signature of material from the continental crust, only a minor portion being derived from the oceanic lithosphere.

In the current Report, Tilton gives the results of measurements of lead and neodymium isotopes from southern Peru and northern and central Chile. The region in Peru is the same as that discussed by James. It also lies in the zone that seismologists agree is a "normal" subduc-



tion zone: a 30° subduction overlain by asthenospheric material, interpreted as partially melted mantle and hence a probable source of the volcanic lavas observed at the surface. Tilton's work strongly confirms James' conclusion that the continental crust has contributed to these volcanic rocks. The isotopic composition of their lead is totally unlike lead from oceanic regions, inasmuch as it is relatively depleted in  $^{206}\text{Pb}$  but not in  $^{208}\text{Pb}$ , showing that it came from a source region which has been depleted in uranium but not in thorium. The source of this lead is not oceanic and therefore must in some way be continental. The  $^{143}\text{Nd}/^{144}\text{Nd}$  data confirm this view. Tilton suggests that the most likely continental source is the lower crust. Although rocks known to be derived from the lower crust are poorly represented at the surface, those that are available provide evidence that they are the kind of rocks from which lead of this isotopic composition could be derived.

This detailed identification of the continental source region differs from that given earlier by James, who felt that the strontium isotopic compositions suggest that the continental contribution results from erosion of continental sediments into the oceanic trench at the continent-ocean boundary and subduction of these sediments along with the ocean lithosphere, followed by recycling of this continental material back to the continent by partial melting of the subducted materials. The relative contributions of these two continental sources will provide an important topic for further study.

Whitford and White describe neodymium and strontium isotope studies of oceanic subduction zones in Indonesia. One of these, the Sunda arc in Java, may be thought of as a "classical" oceanic island arc, a good candidate for comparison with the ocean-continent subduction in Peru. In this case the strontium and neodymium isotope data show evidence that only a minor component is derived from the continental crust. The isotope

ratios conform to the trends previously associated with mantle rocks, and there is little doubt that the dominant source of these rocks is in the mantle of the Earth. On the other hand, the isotope ratios are also distinct from those of the mantle source associated with the most abundant ocean volcanic rock—the mid-ocean ridge basalts. It appears that these lavas from the ridges are not simply derived by melting of the subducted oceanic lithosphere, but possibly involve the tapping of a deeper portion of the oceanic mantle that is less depleted in "crust-forming" elements with large ionic radii, e.g., K, Rb, and U. The other Indonesian arc studied by Whitford and White (the Banda arc) is anomalous in that it appears that continental crust is being subducted beneath oceanic mantle. This inference is supported by these isotopic studies, which reveal the effects expected for an admixture of material with a previous continental crustal history. A similar conclusion was reached by Magaritz, Whitford, and James two years ago using oxygen isotopic measurements. When results such as these are combined with similar work from other laboratories, one gets the feeling that the complexities of this new "mantle geology" will not prove overwhelming, and that combined application of the many tools of geochemistry and geophysics can reveal the characteristics of these rocks despite their occurrence deep within the Earth.

Within the ocean basins, far from subduction zones, large volumes of lava flow from the Earth's interior to the surface. Along the axis of the midocean ridge system, these are the near-surface expression of the generation of new oceanic lithospheric plates, about 50 km in thickness, which on time scales of  $10^7$ – $10^8$  years migrate toward the trenches and associated subduction zones where they are consumed. An account of a seismic investigation of such a spreading lithospheric plate is given by Evans and Sacks. Volcanic eruptions also occur on oceanic islands that are unrelated to the



ridge system. Over the past 20 years, isotopic and trace element investigations have clearly shown that the mantle sources of these two types of oceanic volcanism are distinct. Those from the ridges appear to be derived from a much more homogeneous mantle source which has been depleted in the elements with large ionic radii—those needed to form basalts. The sources of the oceanic island volcanic rocks are much more heterogeneous, both chemically and isotopically. Furthermore, these sources do not appear to drift with the oceanic lithosphere and asthenosphere, but remain relatively fixed in the mantle, producing chains of islands (as in Hawaii) as the oceanic lithosphere drifts by above their source. Although these things are poorly understood, the mantle sources of these oceanic islands are usually thought to lie at great depth, below the asthenosphere. From these sources, material could rise toward the surface as “plumes” or “blobs.”

The full complement of trace element and isotopic techniques are now being directed, both here and in other institutions, toward the goal of replacing the present “cartoon models” for the formation of these oceanic igneous rocks with some real understanding. Several studies of this kind are described in this Report.

Because the models for oceanic volcanism are rooted in plate tectonic theory, they tend to emphasize the global aspects of the problem. However, where studies are made of local regions (e.g., single islands), local complexities are almost always found which strongly modulate global trends. It is likely that an approach to the full understanding of these global phenomena will require considerable understanding of these local effects as well. In the Hawaiian Islands, Hofmann and Wright are carrying out a detailed study of the causes of variation over time of lavas from a single volcano, Kilauea. Their data support the view that the fundamental mantle source of these lavas is both chemically and isotopically homogeneous and uniform. As-

suming this to be the case, they then show that the observed monotonic changes in the trace element composition of the lavas erupted over a two-year period can be explained in terms of a time-varying degree of partial melting of the mantle source rocks. These variations also show that the degree of partial melting is less than previously believed, and that the minerals that contain the large ion elements required to form basalts are not completely consumed in this melting. Thus the mantle source can remain “fertile” and can continue to produce basaltic lavas in the future. White considers similar problems of local variability in the midocean ridge environment, using samples obtained from a small region of the mid-Atlantic ridge by the FAMOUS undersea expedition. Here again it appears that local chemical evolution of the magmas is superimposed upon a fundamentally uniform mantle source.

On the other hand, similar measurements made by White on young volcanic rocks from the Galápagos show that these rocks cannot be understood as the result of local magmatic evolution of lavas from a uniform source. In this case the source is heterogeneous, and some record of the previous history of the source is still preserved in the isotopic composition of the rocks. This evidence can then be used to distinguish more global models of mantle evolution that are compatible with the measurements from those that are not.

On an even more local scale, the formation of these lavas depends on the physical chemistry of the melting process, on both kinetic and equilibrium effects. For some years Hofmann has been carrying out at DTM a research program directed toward understanding these phenomena. This year, Jambon and Ryerson, their colleagues at the Geophysical Laboratory Mysen and Virgo, and Shelby at the Sandia Corporation, Livermore, California, contributed to this work. Their studies include measurements of the mobility of water in granitic melts and the



role this plays in altering the properties of the melt, investigations of the solubility properties and mobility of the geochemically important inert gas helium, and structural studies of silicate melts.

In healthy science and in a stimulating research group, it is necessary that there be lively interplay between theory, experiment, and observation. Theoretical work—applying continuum mechanics to the distribution of stress in natural rocks—is described in papers by Linde, Heinze, and Sacks. On the observational side, Stefansson, Sacks, and Linde report field observations of the actual change in the stress field in northeastern Iceland during a tectonic episode involving a wide range of phenomena: volcanic eruption, land subsidence, faulting, and earthquakes. Although the goal of accurately modeling the detailed complexity of these interacting plates and the internal stresses resulting from these interactions remains distant, it is encouraging that these effects appear amenable to theoretical discussion.

### *Isotopic Studies of Older Rocks*

When isotopic geochemical and geochronological studies were started at DTM about 30 years ago, much of the emphasis was placed on older rocks of the Earth, particularly those in the Precambrian, ranging in age from 500 m.y. to 3000 m.y. This work permitted delineation of the scope of Precambrian time and the distribution of these ancient rocks on the continents. With the advent of plate tectonics during the 1960's, attention shifted to the youngest rocks, particularly those from the oceanic regions. This shift took place because the "action"—the production and destruction of lithosphere—occurs in the young ocean basins. Although at least similar processes must also have occurred before the formation of the oldest preserved ocean basins about 200 million years ago, most of that record has now been lost. The surviving record will be found in the

vestiges of old oceanic events preserved in the continents. Now that earth scientists are beginning to understand the processes occurring in the young oceans, it can be expected that there will be renewed interest in older rocks, making use of new insights into the Earth's fundamental tectonic processes from study of more recently formed rocks.

Three geochemical investigations involving older material are given in this Report. Bugnon, Tera, and Brown report lead isotope measurements on 2640-million-year-old ores and their host rocks from the Abitibi greenstone belt in Ontario. They show that the mineralization and the formation of the country rocks were very nearly contemporaneous. However, if one uses these data to calculate the isotopic composition of the lead in these rocks at the time of their formation, it looks like lead about 2900 million years in age, according to the simplest models for evolution of the isotopic composition of lead in the Earth's mantle. The authors present some evidence that this is not a purely local phenomenon. Measurements of this kind will be used to provide information on the time scale for the evolution and early differentiation of the Earth's core and mantle.

Echeverría reports a geochemical investigation of an unusual type of magnesium-rich volcanic rock, spinifex-textured komatiite, of Tertiary (<60 m.y.) age from Colombia. These rocks have an unusually high melting point, and are almost entirely confined to the ancient Archean greenstone belts. The high mantle temperature required to form these rocks has been used as a constraint on the thermal evolution of the Earth. This work shows that very similar rocks can also be formed in relatively recent times. Investigation of such young komatiites will provide valuable data about the unusual mantle environment required to form these lavas and implications for the early history of the Earth.

In another study of older rocks, Mose has found billion-year-old Precambrian



rocks, which intrude even older gneisses, under the Virginia Piedmont. In attempting to reconstruct plate tectonic events before formation of the present ocean basins, previous workers have concluded that the Virginia Piedmont was located on a young ( $\sim 300$ -m.y.) plate which collided with the ancient North American plate during the Paleozoic. This work shows that the Piedmont rocks were also on a Precambrian plate of similar age, and may never have been separated from the North American plate.

### *Galaxies and their Evolution*

It may seem a great leap from the Earth's interior to the galaxies, and at present it must be admitted that there is little cross-fertilization between Galactic and extragalactic astronomy on the one hand, and geology on the other. Nor need there be, to justify great interest in these two areas of science. Nevertheless, it doesn't seem likely that this separation will always exist. The present situation is probably a consequence of our limited knowledge as to how galaxies form and evolve. For example, our understanding of the history of the Earth is badly in need of the type of constraint that could be provided by knowledge of its initial conditions and of the physical and chemical environment in which the Sun and planets formed. Although still rudimentary, knowledge in this area is increasing rapidly by work on meteorites, lunar rocks, and the oldest rocks of the Earth, by observations relevant to star formation, and by theoretical work on star and planet formation. Even now, our interpretation of the meteoritic isotopic data and the resulting time scale for the formation of the solar system is limited by uncertainty in the rate of heavy element formation in the Galaxy throughout its history. There is also observational evidence that the oldest stars in the disk of the Galaxy may not be significantly older than the well-established 4.5-b.y. age of the solar system. It is thus pos-

sible that the formation of the solar system is related to some unique event or environment in the history of the Galaxy, and present-day observation of star formation could lead to false inferences. Galactic events may even have been significant in more recent times. At the present time the supernova rate in the Galaxy is such that a supernova occurs within 50 light years of the Earth about once every 70 million years, a rather short time from the geological point of view. Even at this distance, unusual environmental stresses could occur for which terrestrial organisms would lack time to respond adaptively. These events could have been more frequent in early solar system history. In this Report, Herbst and Rajan evaluate the probability of supernovae actually providing a significant quantity of the mass of the solar system at the time of its formation. Other ways in which terrestrial history may be coupled to Galactic events can easily be suggested. However, these possibly important and real phenomena will continue to appear to be nothing but wild speculations until our understanding of the ways in which galaxies evolve improves.

Rubin, Ford, and Thonnard report new observations which begin to establish relationships between observable parameters of spiral galaxies, such as mass, luminosity, velocity as a function of distance from the center of the galaxy, and the morphology of the galaxy. Last year these workers discussed similar results from a small sample of large galaxies. This year the sample is extended to a larger number of smaller galaxies. The earlier work produced the surprising result that the rotation velocity continued to rise with increasing distance from the center of the galaxy. The fundamental laws of motion relate the rotation velocity at a given distance to the total mass of the galaxy within that distance from the center. Use of the laws of motion then leads to the conclusions that the luminous mass in the galaxy is but a fraction of



its total mass, and that the actual extent of a galaxy extends well beyond its optical boundaries. This year the work was extended to include 21 smaller spiral galaxies, and the same result was found. When the rotational velocity is plotted vs. distance from the galactic nucleus, all galaxies, large and small, are found to fall nearly on a single curve, except for distances very near the nucleus. The principal difference between large and small galaxies appears to be simply that in large galaxies the measurements can be made at greater nuclear distances.

In a separate report, Burstein and Krumm discuss their 21-cm radio observations of neutral hydrogen for a galaxy also studied by Rubin and Ford, but of a type intermediate between spiral and elliptical. These observations permit measurement of rotation velocity well beyond the edge of the optical boundary of the galaxy. Again, no evidence is found for a decreasing velocity, indicating that the mass is not centrally concentrated.

The work of Burstein and Krumm on this galaxy, as well as observations described in this Report by Gallagher, Faber, and Burstein on elliptical galaxies, sheds some light on various ways in which galaxies may evolve. The first case is that of a moderate-size galaxy of a type transitional between elliptical and spiral. As mentioned above, the optically visible galaxy is accompanied by an unseen disk of neutral hydrogen several times the luminous mass and of much greater spatial extent. Because there are no plausible sources for this hydrogen in the vicinity of this galaxy, it seems that this disk has been present since the galaxy was formed. In contrast, the other galaxies studied are giant elliptical galaxies and the measurements suggest that these have acquired a large amount of their mass by tidal stripping of nearby galaxies.

In our own Galaxy, Carney reports optical measurements of the age of the "population II" stars which are not concentrated in the disk of the Galaxy but

rather occur in more randomly oriented orbits—either in globular clusters or as individual stars in the "halo" of the Galaxy. These stars turn out to be very old, almost all of them between 10 and 20 billion years. These ages show that at least many of the stars in the Galaxy are much older than the solar system. However it is possible that in some sense they are "older than the Galaxy"—i.e., they predate the present spiral structure and the formation of stars with the composition of the Sun.

### *The Early History of the Solar System*

In spite of the reservations discussed above (that there may be important differences between star formation in the Galaxy 4.5 billion years ago and star formation today), observational data relating to recent formation of stars of one solar mass represents the greatest single missing piece in the puzzle of the formation of the solar system and the Earth. Some observational data on the location within the Galaxy of recent star formation is provided by Lockman in this Report.

However, there is much evidence that can be obtained from the solar system itself, evidence that has not yet been fully exploited.

One such line of evidence is provided by the residual population of small bodies, asteroids and comets, which remain after the formation of the solar system. Their abundance and orbital distribution can be observed today, and evidence regarding the past evolution of this population is provided by observation of the record of ancient impact cratering on the Moon, Earth, and planets. Theories for the formation of the solar system can be plausibly constrained by the requirement that the bodies which formed the planets evolve in a natural way to explain the observed population and impact effects of the small bodies.

One approach to solar system forma-



tion that seems very promising in this regard has been developed from qualitative beginnings into a rather quantitative theory by Safronov and his co-workers in Moscow. This involves the formation of at least the inner terrestrial planets by a continuing sweeping up of small bodies by larger ones. When worked out quantitatively, this approach requires relatively few free parameters and assumptions. This year, Wetherill reports an extension of this theory to include the fact that the accumulating bodies are not freely moving objects analogous to molecules in the kinetic theory of gases, but are constrained to move in Keplerian orbits about the Sun. The complications introduced by explicitly introducing this physically realistic requirement dictate a numerical approach to the problem, rather than the earlier analytical one. When this is done, it turns out that the predictions of the earlier theory are still valid. In addition, new effects, such as radial spread of the orbits of the accumulating bodies, are found. Although much work remains to be done, it appears that "ground rules" for this mode of planet formation can be established. For example, it should be possible to say whether or not prior formation of the very large planets, Jupiter and Saturn, is necessary to maintain the eccentric orbits in the inner solar system needed for planetary encounters and accumulation.

Another line of direct evidence regarding the early solar system is provided by detailed measurements on meteorites. Some meteorites resemble material that crystallized from a liquid state, similar to volcanic rocks on the Earth or metal in a blast furnace. However, the majority are better described by the term "regolith," which is the geologist's generalization of the more familiar concept of "soil." Regoliths are mixtures of crystalline and glassy fragments and their disintegration products, and form blankets on planetary surfaces. On the Earth, the abundant presence of water and the re-

sulting weathering and erosion produce regoliths which usually are clay mineral deposits, the end product of the disintegration and transportation of terrestrial rocks. On the other hand, an airless planetary body like the Moon has a regolith consisting almost entirely of rock fragments formed by impact cratering. Moreover, the absence of a lunar atmosphere and magnetic field leads to exposure of the lunar regolith fragments to the solar wind and energetic nuclear bombardment accompanying solar flare activity. The evidence for this exposure is preserved in the lunar regolith particles in a number of ways. For example, the penetrating nuclear bombardment produces tracks in these minerals, which can be observed in a microscope in much the same way that cosmic ray scientists record these energetic particles in photographic film.

Many meteorites are regolithic assemblages remarkably similar to the lunar regolith. Others resemble it qualitatively but not quantitatively. Still others are assemblages of fragmental material which are quite different. All these regolithic assemblages bear a record of the time and place of their formation, but the interpretation of this record is not simple.

Rajan, Kothari, and Scott are directing a variety of experimental techniques toward the goal of untangling this regolithic record and learning the time, place, and circumstances under which these regoliths were developed. In some cases, it appears quite possible that we have in these meteorites samples of surface materials formed into a regolith during geologically recent times on the surface of an asteroid, in a way very similar to the way the lunar regolith is being developed today. In other cases at least superficially similar, the regolith was more likely developed on an analogous surface but at a time more nearly contemporaneous with the formation of the solar system. Still others are probably relics of the even earlier original accumulation of the meteorite parent bodies. One of these techniques, involving electron-beam microanalysis of



the distribution of nickel in the metallic grains of stone meteorites, is used by these workers to uncover the thermal history of the astronomical body from which these meteorites were derived. In turn, this permits relating the body's thermal history to its metamorphic history, dated by radiometric and nuclear track techniques. Although this problem is obviously a complex one, such measurements are providing detailed first-hand information about the solar system

from times and distances inaccessible in any other way.

Returning to the theme introduced at the outset, all these diverse activities can be viewed as expressions of the unique need of the human mind to transcend, both in space and time, the finite boundaries that restrict us. We are grateful for the opportunity to join with our scientific colleagues throughout the world in this venture.

*George W. Wetherill*

## PHYSICS AND CHEMISTRY OF THE EARTH

### SUBDUCTION ZONES AND ISLAND ARCS

#### SUBDUCTION BENEATH WESTERN SOUTH AMERICA: OVERVIEW AND THE *ScSp* CONTROVERSY

*J. A. Snoke,\* I. S. Sacks, and D. E. James*

Two conflicting models have been proposed for subduction beneath central Peru and central Chile. One model (Isacks and Molnar, 1971; Stauder, 1975; Barazangi and Isacks, 1976, 1979) is based primarily on an analysis of the seismicity, and it postulates shallow subduction with a plate dip of about  $10^\circ$ . The other model (Snoke *et al.*, 1977; Sacks, 1977) is based primarily on an analysis of converted seismic waves (*ScSp*) and postulates normal subduction with a dip of  $\sim 30^\circ$  for the downgoing plate to a depth of at least 120 km. Recently Barazangi and Isacks (1979) have questioned the quality of the South American *ScSp* data; if their conclusions are valid, the strongest argument against the shallow-subduction model is removed. In this report, we give an overview for the two models, and we reexamine the South American *ScSp* data.

Beneath both central Peru and central

Chile the seismicity at depth is scattered with no apparent large-scale patterns. Barazangi and Isacks (1976, 1979) propose that this scatter is caused by poor locations, and that if certain selection criteria are applied a pattern emerges in the seismicity; this forms the basis for their shallow-subduction model. James (1978) countered that a detailed study of the spatial distribution of earthquakes beneath central Peru shows that the seismicity tends to be confined to small, active clusters, and he raised questions about the implications of selection criteria. However, the questions raised by James do not provide direct evidence against the shallow-subduction model. Nor does the normal-subduction model provide an alternative explanation for the differences in the seismicity patterns in the different regions.

The seismological evidence supporting the normal-subduction model is based in part on indirect evidence from anelasticity studies (Sacks and Okada, 1974; Sacks, 1977) and observations of mantle-converted *Sp* arrivals (Sacks and Snoke, 1977), which indicate a uniformly thick (300–400 km) continental lithosphere beneath at least the shield region of South America. The evidence from these studies pertains to regions to the east of the subduction zones, however, and there-

\* Virginia Polytechnic Institute and State University, Blacksburg, Virginia.



fore bears only indirectly on its geometry in that it limits the eastern extent of any possible shallow subduction.

The direct evidence supporting the normal-subduction model for these regions is based on the identification of *ScSp* arrivals on seismograms at South American stations (Snoke *et al.*, 1977). From studies of seismograms at Japanese stations (Okada, 1977; Hasegawa *et al.*, 1978) *ScSp* has been shown to be due to the conversion of *ScS* from large, nearby deep-focus earthquakes to *P* at the interface between the upper boundary of the descending plate and the overlying mantle wedge. Snoke *et al.* used the same interpretation for *ScSp* observations at South American stations in central Peru (NNA), southern Peru (ARE), and central Chile (PEL). For *ScSp* to be of sufficient amplitude to be visible on seismograms, the dip of the conversion interface must be at least  $28^\circ$  to a depth of at least 120 km. Hence the *ScSp* observations provide direct evidence for the normal-subduction model in these regions.

### *The ScSp Controversy*

Because the *ScSp* data comprise the major objection to the shallow-subduction model, Barazangi and Isacks (1979) have examined some of these data to evaluate their quality. Figure 1 (their fig. 13) shows a comparison between (traced) records of *ScS* arrivals both at NNA (in central Peru) and at Japanese stations. *ScSp* is a clear arrival in the Japanese examples shown, but it is not a clear arrival in the NNA records. They conclude that the NNA *ScSp* data are too poor to provide constraints on the subduction model.

We reject Barazangi and Isacks' dismissal of *ScSp* for three reasons:

(1) *Data selection*: Barazangi and Isacks compared highly selected Japanese data with unselected South American data. While *ScSp* is generally a stronger arrival in Japan than in South America, Fig. 2 demonstrates that there

is variability in the Japanese data as well.

(2) *Reduced tracings may not faithfully preserve information*: Fig. 3 shows photographs of *ScSp* arrivals at South American stations including two of the NNA records shown (in traced versions) in Fig. 1. The *ScSp* arrivals are quite clear in Fig. 3 although not apparent in the Barazangi and Isacks tracings.

(3) *Signal-to-noise considerations*: One would not expect to see *ScSp* on five of the eight records shown in Fig. 1. Snoke *et al.* (1979) describe in some detail the fact that if one follows a criterion for the observability of the *ScSp* based on a comparison between the (signal-generated) noise amplitude and the expected *ScSp* amplitude, *ScSp* is observed on every South American record with a low enough noise level.

Barazangi and Isacks also suggest that if *ScSp* arrivals exist at NNA, they might correspond to bottom-of-the-slab conversions for a  $10^\circ$  dipping slab. Figure 4 shows that this is not possible because the amplitudes expected for such a model are of too low an order of magnitude—the conversion-interface dip must be about  $30^\circ$ .

In the following paper, it is shown that a  $30^\circ$  subduction down to at least 100 km in central Peru satisfies the seismicity data selected by Barazangi and Isacks, even though it disagrees with their interpretation and model.

### *References*

- Barazangi, M., and B. Isacks, Spatial distribution of earthquakes and subduction of the Nazca Plate beneath South America, *Geology*, 4, 686–692, 1976.
- Barazangi, M., and B. Isacks, Subduction of the Nazca Plate beneath Peru: evidence from spatial distribution of earthquakes, *Geophys. J. Roy. Astron. Soc.*, 57, 537–555, 1979.
- Hasegawa, A., N. Umino, and A. Takagi, Double-planed deep seismic zone and

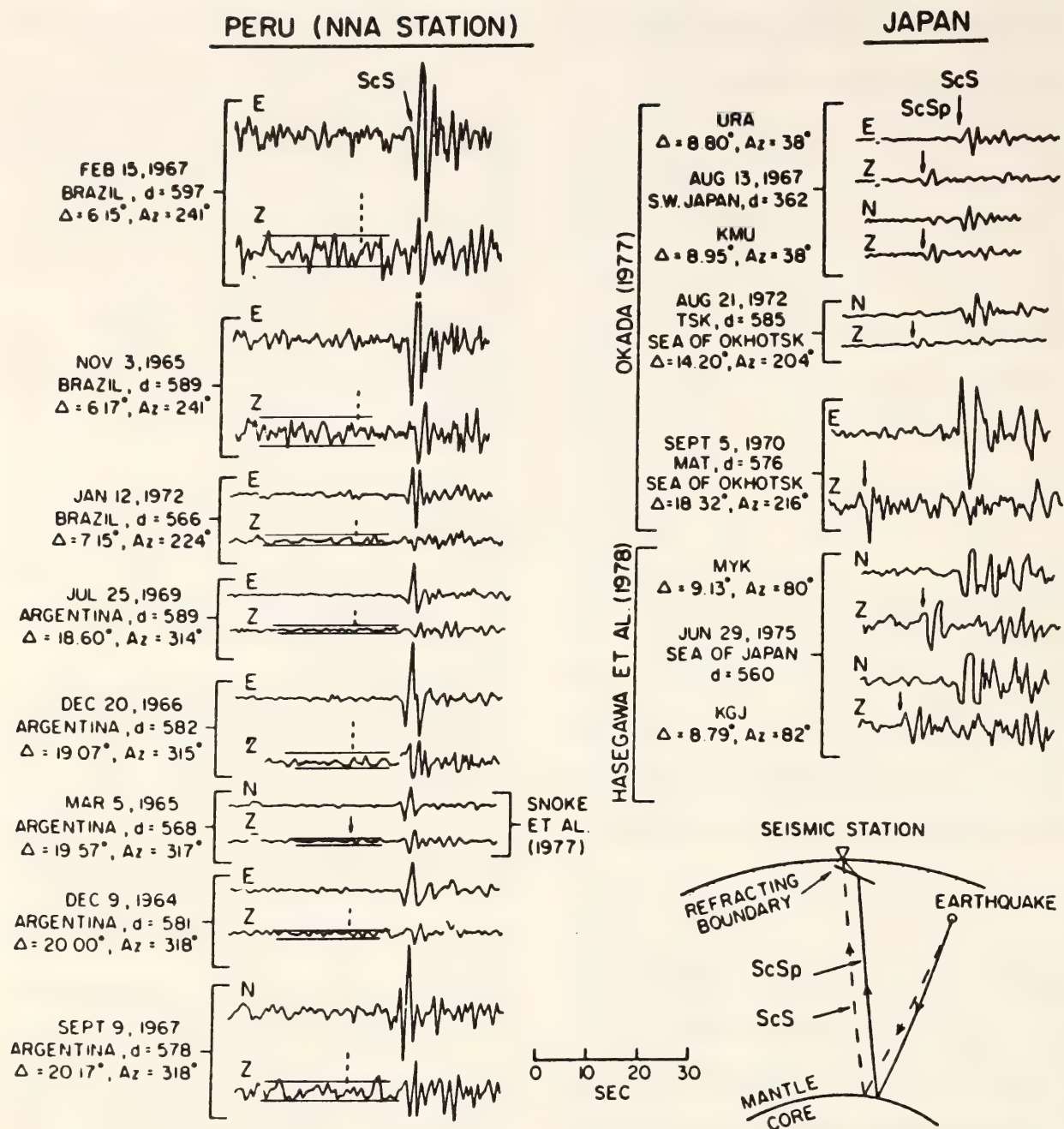


Fig. 1. Figure 13 from Barazangi and Isacks (1978), with permission. The left-hand side includes tracings of vertical-component and horizontal-component seismograms from NNA showing strong *ScS* arrivals from large, nearby deep-focus earthquakes. The dashed vertical lines on the *Z* components are the expected *ScSp* arrival times. (In fact, deviations in the *ScSp* arrivals of up to 1.5 sec are possible.) The horizontal lines on the vertical-component records (not in the original figure) indicate the expected peak-to-peak amplitude for *ScSp* (see text). The right-hand side includes an insert showing the ray geometry for *ScS* and *ScSp* and tracings of (selected) *ScS* and *ScSp* arrivals at Japanese stations.

upper mantle structure in the north-eastern Japan arc, *Geophys. J. Roy. Astron. Soc.*, 54, 281–296, 1979.

Isacks, B. L., and P. Molnar, Distribution of focal-mechanism solutions of

mantle earthquakes, *Rev. Geophys.*, 9, 103–174, 1971.

James, D., Subduction of the Nazca Plate beneath central Peru, *Geology*, 6, 174–178, 1978.



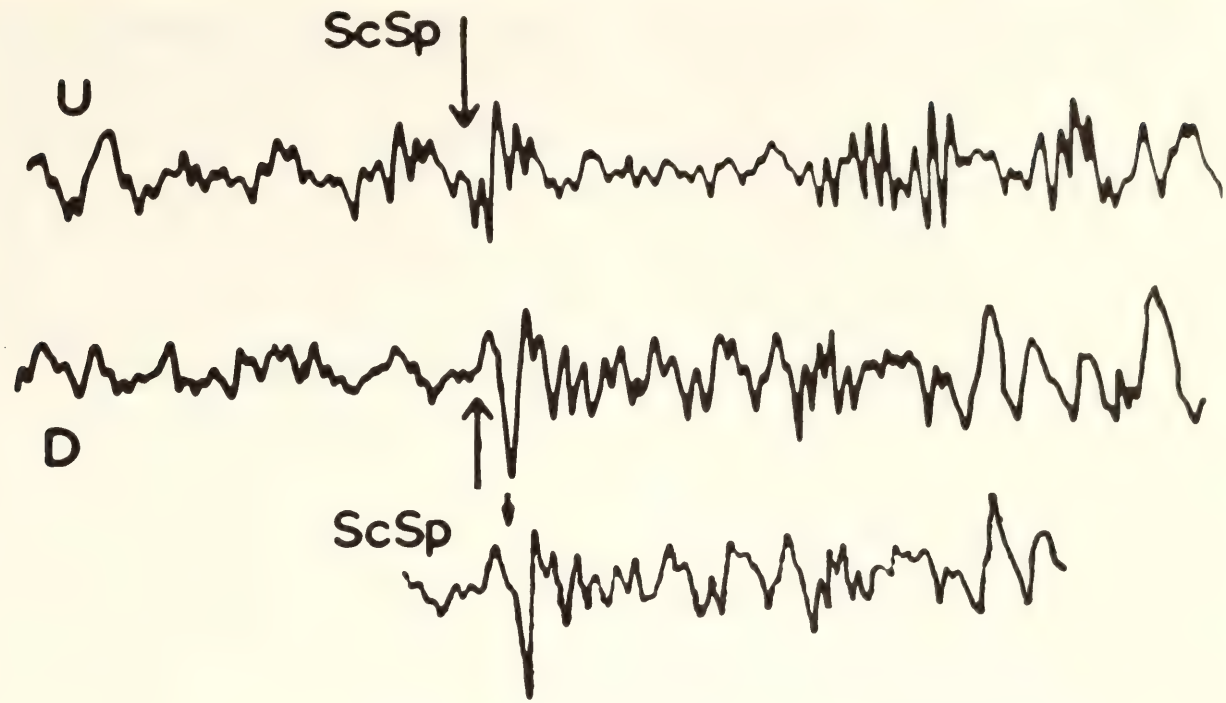


Fig. 2. Photograph of fig. 25 from Okada (1977) of seismograms from MAT in central Honshu, Japan for two events showing *ScSp* arrivals. Note that the arrival is much clearer on the second event. A tracing of the 5 September 1970 record from Barazangi and Isacks (in which they did not include the noise preceding the *ScSp* arrival) is included at the bottom.

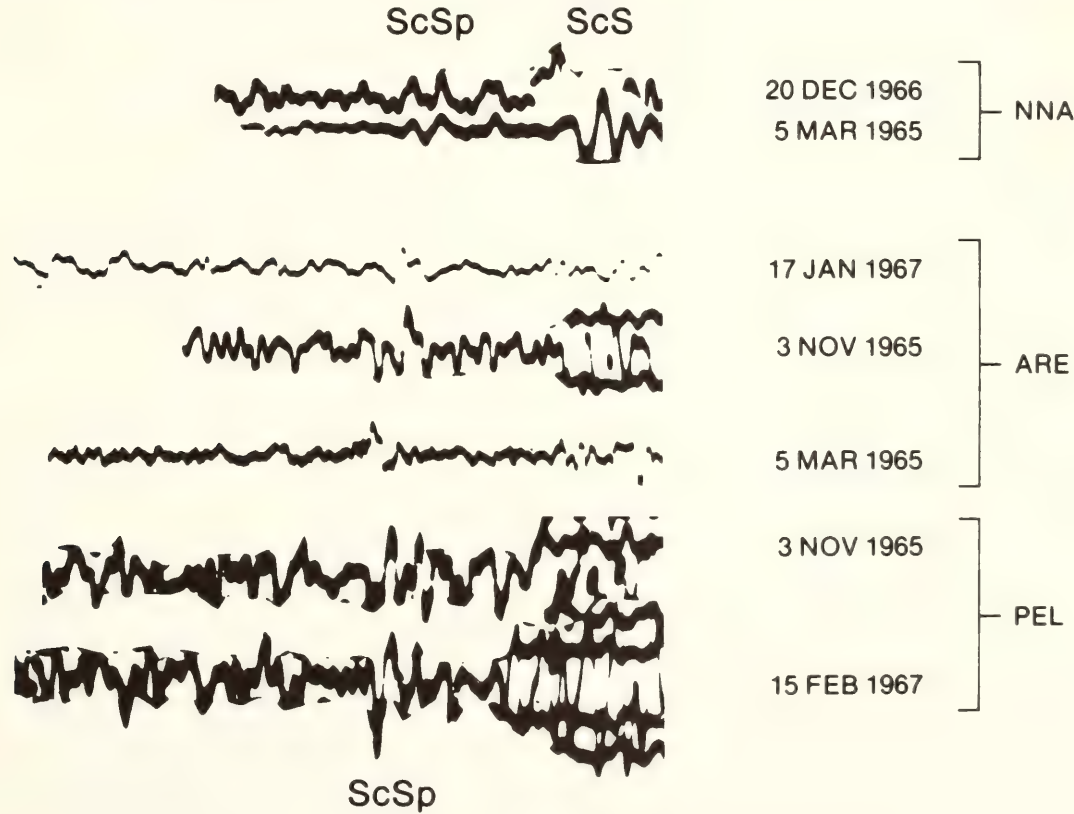


Fig. 3. Photographs of vertical-component seismograms showing *ScSp* at each of three WWSSN South American stations: NNA (central Peru), ARE (southern Peru), and PEL (central Chile). The traces are aligned at the onset of *ScS* for each station—at NNA on the vertical component with its clear onset and for the other stations on the (not shown) horizontal components. Note the similarities of the wave forms of the two NNA examples and the three ARE examples. There is a time mark just before *ScS* on the NNA record of 20 December 1966 and one during *ScSp* on the ARE record of 5 March 1965.

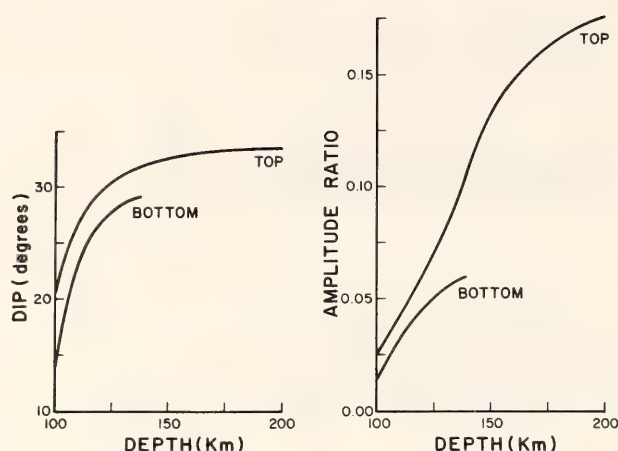


Fig. 4. (Left). Slabs dip vs. depth of  $ScS$ -to- $ScSp$  conversion for both top-boundary and bottom-boundary conversions. The plate thickness is 60 km with an enhancement of the J.-B. velocities of 5% inside the plate. The incident  $ScS$  is taken to be vertical, and the curves correspond to  $T_{scs} - T_{scsp} = 10$  sec. The bottom boundary conversion line ends because, for larger dip angles/conversion depths, the differential travel time is always greater than 10 seconds. Changing the plate thickness or the percentage enhancement has little effect on the curves. (Right).  $ScSp$ -to- $ScS$  amplitude ratio vs. conversion depth for the same plate parameters as in the left diagram. The amplitude ratios take into account geometrical spreading for  $ScSp$  measured on a vertical instrument and  $ScS$  on a radial instrument, as well as the Zoeppritz conversion efficiency. The curves are little affected by the plate thickness, but the amplitude ratios are approximately proportional to the percentage enhancement.

Okada, H., Fine structure of the upper mantle beneath Japanese island arcs as revealed from body wave analyses, Doctor of Science Thesis, Hokkaido University, Japan, 1977.

Sacks, I. S., Interrelationships between volcanism, seismicity, and anelasticity in western South America, *Tectonophysics*, 37, 131–139, 1977.

Sacks, I. S., and H. Okada, A comparison of the anelasticity structure beneath western South America and Japan, *Phys. Earth Planet. Interiors*, 9, 211–219, 1974.

Sacks, I. S., and J. A. Snoke, The use of converted phases to infer the depth of the lithosphere-asthenosphere bound-

ary beneath South America, *J. Geophys. Res.*, 82, 2011–2017, 1977.

Snoke, J. A., I. S. Sacks, and H. Okada, Determination of subducting lithosphere boundary by use of converted phases, *Bull. Seismol. Soc. Amer.*, 67, 1051–1060, 1977.

Stauder, W., Subduction of the Nazca Plate under Peru as evidenced by focal mechanism and by seismicity, *J. Geophys. Res.*, 81, 1053–1064, 1975.

#### SUBDUCTION OF THE NAZCA PLATE BENEATH PERU AS DETERMINED FROM SEISMIC OBSERVATIONS

A. Hasegawa and I. S. Sacks

Western South America is the only major subduction zone where an oceanic slab descends under a continent. Study of the subduction of the Nazca Plate beneath this region provides a knowledge of the differences and the similarities between the subduction process of the oceanic slab beneath a continent as opposed to an island arc.

While there is agreement on the geometry of the subduction process beneath southern Peru and northern Chile, two conflicting models have been proposed for the subduction beneath central Peru and central Chile. This controversy is discussed more fully in the preceding paper. One model (based mainly on the teleseismically determined seismicity; e.g., Barazangi and Isacks, 1976, 1979; Isacks and Molnar, 1971; Isacks and Barazangi, 1977; Stauder, 1975; Sykes, 1972) postulates a shallow-dipping ( $10^\circ$ ) seismic zone, whereas the other (based primarily on an analysis of  $ScSp$  waves, e.g., James, 1978; Okada, 1973; Sacks, 1977; Snoke *et al.*, 1977, 1979) postulates subduction at an angle of  $30^\circ$ .

The accuracy of hypocenter locations of the ISC and USGS in this region, especially in focal depth, is poor because of the sparse distribution of seismic stations, and this fact makes it difficult to



interpret the subduction process beneath central Peru and central Chile. Local seismic network data are essential to resolve this kind of controversy.

A local net of nine stations (see insert, Fig. 5) was operated in 1965 by San Agustín University's Characato Observatory. The data from this net is important because the area it covers includes portions of both categories of subduction zones, namely southern Peru for which no disagreement exists and central Peru for which opposing models have been proposed.

### *Spatial Distribution of Earthquakes beneath Arequipa Network*

Figure 5 shows the vertical section of the earthquakes located by more than five stations of the Arequipa network in southern Peru from January to December, 1965. The method used to locate these events is discussed in detail by James *et al.* (1969).

In both regions in Fig. 5, the trend of deep seismic zone above 100 km extends into the deeper part, with a constant dip angle of about  $30^\circ$ . There is other seismic

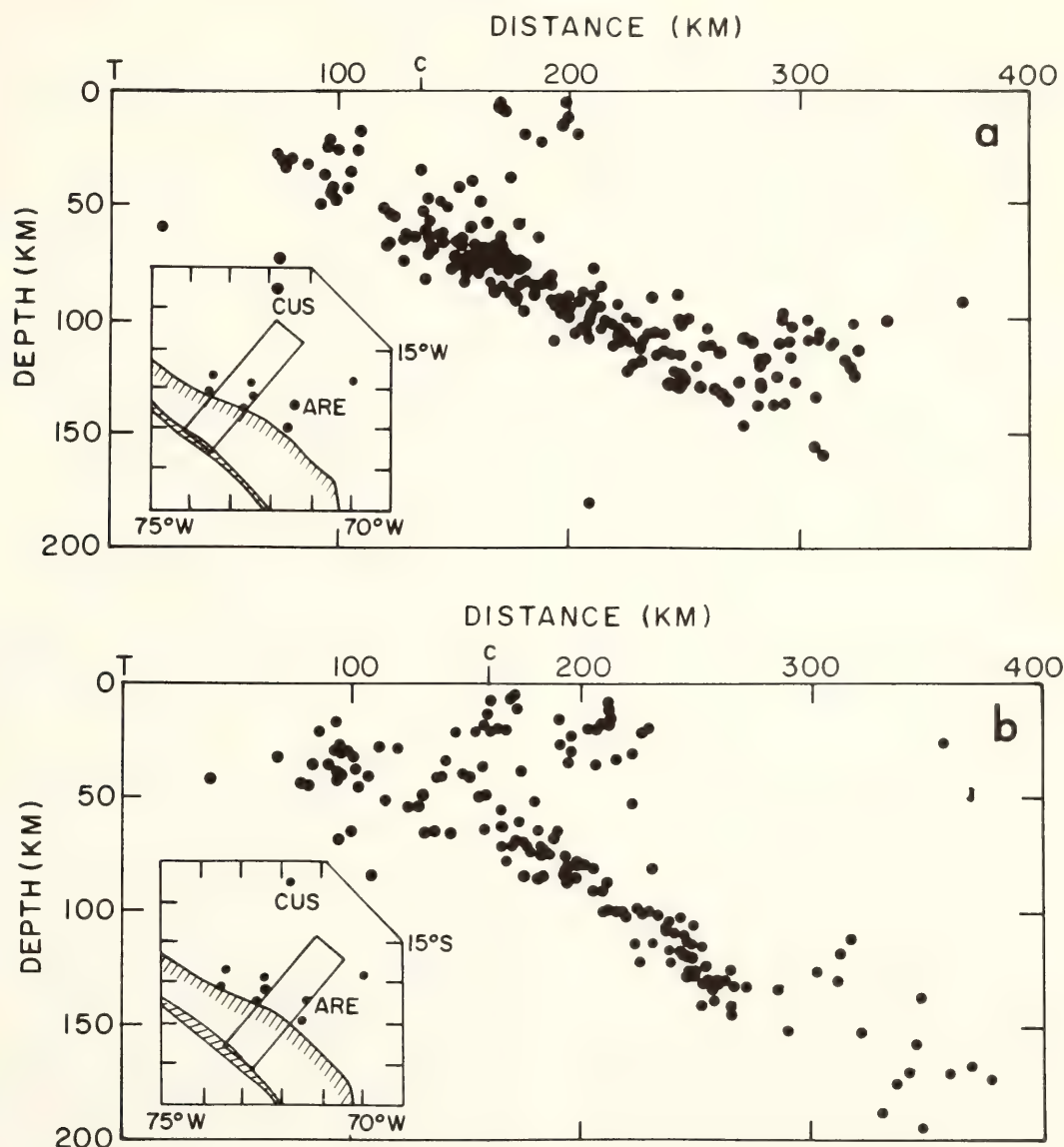


Fig. 5. Vertical cross sections of earthquakes located inside the rectangles on the inserted maps, from more than five stations of the Arequipa network in southern Peru (after James *et al.*, 1969). Locations of seismic stations of the Arequipa network are shown by solid circles in the inserted maps. *T* denotes trench axis, *C* denotes coast. The northern region (Fig. 5a) and southern region (Fig. 5b) correspond to the abnormal subduction and normal subduction areas, respectively.

activity above this seismic zone, as pointed out by James (1978). Also it may be seen in the northern region (Fig. 5a) that the deep seismic zone bends and the dip angle decreases at a depth of about 100 km, similar to the Barazangi and Isacks result (1979). Because of the scatter of the hypocenters, however, it is difficult to conclude which model this seismicity located by the local seismic network supports.

#### *Relocation of Earthquakes beneath the Arequipa Network*

We attempted to eliminate the scatter in the hypocenter locations resulting from an inhomogeneous data set. Station corrections grouped by source region were calculated in order that earthquake hypocenters could be accurately located relative to each other. The relocation procedure was as follows. First we selected the events which were observed on at least seven of the nine Arequipa Net stations. (Too few events were observed on more than eight stations to adequately estimate the source-region station corrections.) These earthquakes were carefully relocated using the usual four-parameter method, and adopted as the standard earthquakes in order to estimate the source-region station correction at each station. The number of events thus adopted as standards was 61. The source-region station corrections for *P* and *S* waves were then computed by averaging arrival time residuals of the events located in a rectangular region of  $50 \times 100$  km. By moving this rectangular region (with overlaps), we obtained the station correction for each source region. All events with focal depths greater than 50 km were relocated using these source-region station corrections.

Figure 6 shows the vertical section of the earthquakes thus relocated. We can see from this figure that the deep seismic zone beneath the northern region (Fig.

6a) dips with a normal dip angle near  $30^\circ$  above about 100-km depth and that, at this depth, it deforms and changes its dip angle to be approximately horizontal. The seismic activity along this deep seismic zone is continuous, and all the deep events which were located on the extension of the seismic zone above 100 km with a dip angle near  $30^\circ$  (Fig. 5a) are relocated on this thinner seismic zone (Fig. 6a). It seems reasonable, therefore, that all these earthquakes lie on the deep seismic zone and not in the continental lithosphere. We conclude, therefore, that the descending Nazca Plate beneath central Peru dips at an angle near  $30^\circ$  above about 100-km depth and then bends and decreases its dip angle to nearly horizontal. In southern Peru to northern Chile, however, the Nazca Plate descends with an almost constant dip angle of about  $30^\circ$  down to at least 300 km.

We should note that the apparent thickness of the deep seismic zone in Fig. 6 increases in the inland region. This is mainly due to the contortion of the deep seismic zone in that region and the wide section shown. To investigate this, the northern and southern regions (Fig. 6a and 6b) were divided into four subregions, respectively. The earthquakes located in each subregion are plotted on vertical sections in Fig. 7. The dip angle increases slightly from north to south and the deep seismic zone is not as thick as in Fig. 6. The solid curve in Fig. 7 shows the shape of the deep seismic zone inferred from the seismicity in each vertical section. For easier comparison, these subregions are superposed in Fig. 8. The change in the shape of the deep seismic zone from north to south is easily seen. The change is greatest between regions 3 and 6 but is still continuous. This contortion is considered to be due to the transition from the nearly horizontal Nazca Plate at the deeper part in the northern region to the more steeply dipping Nazca Plate in the southern region.



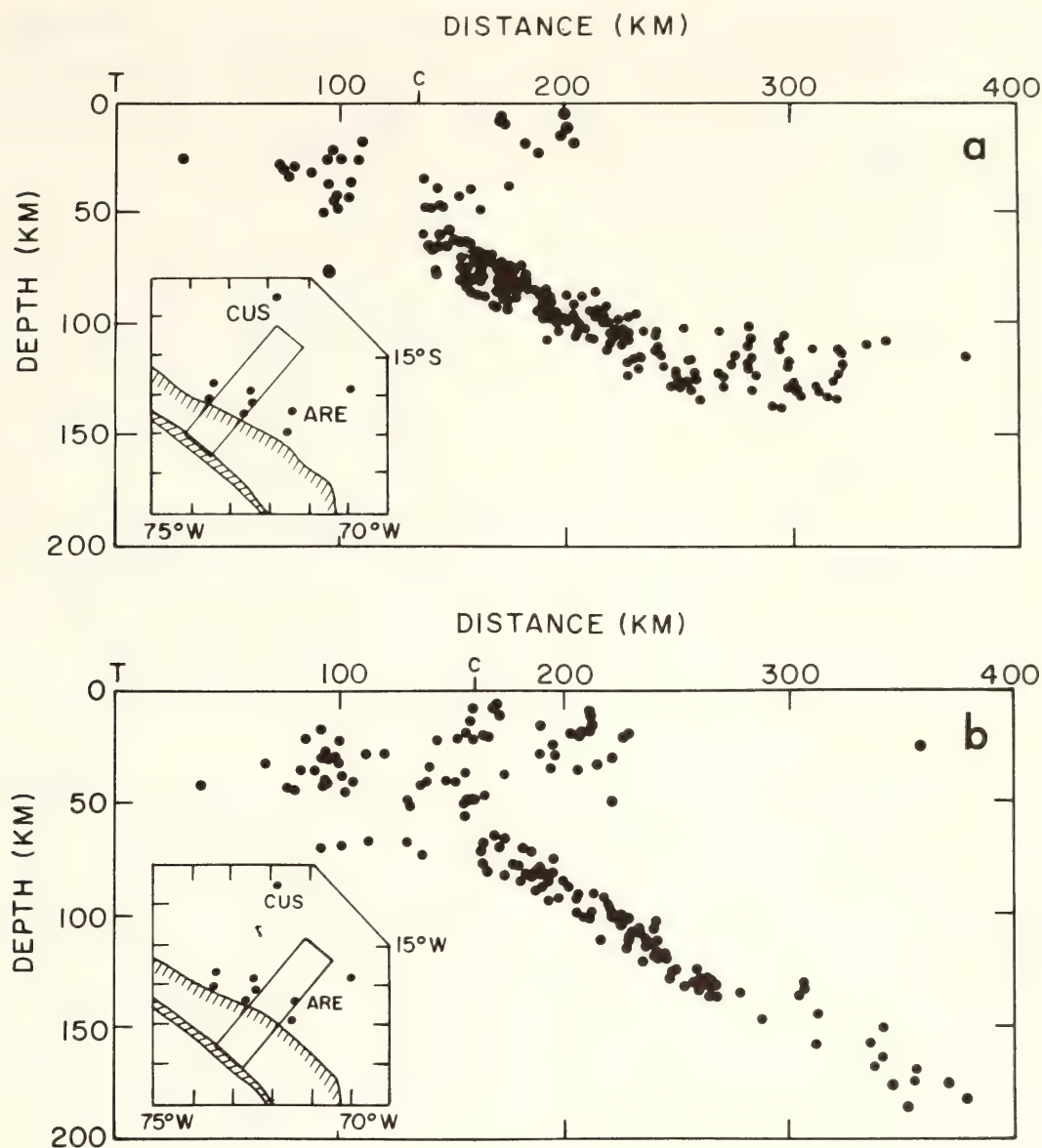


Fig. 6. Vertical cross sections of earthquakes relocated using source-region station correction. Otherwise, as in Fig. 5.

### *Focal Mechanism Solutions*

In order to understand the subduction process beneath an island arc or continent, it is essential to investigate focal mechanisms of earthquakes occurring in the subduction region. Stauder (1975) determined focal mechanisms of earthquakes beneath Peru from *P*-wave first motions and *S*-wave polarization angles. Since there are not many earthquakes for which *P*-wave and *S*-wave data are available at widely distributed stations, the few solutions determined by Stauder do not allow complete understanding of the subduction process beneath Peru. An

analysis of composite mechanism solutions of groups of small earthquakes for which individual mechanism solutions cannot be determined is therefore of great importance (e.g., Ritsema, 1955; Aki, 1966). Here the earthquake-generating stress field beneath Peru and its relation to the shape of the descending slab are investigated in detail by obtaining the composite mechanism solutions for earthquakes in this region. About 300 well-located earthquakes, which were selected by Barazangi and Isacks (1979), are analyzed. The number of *P*-wave readings for these events is about 8,000.

The seismic region is divided into seven

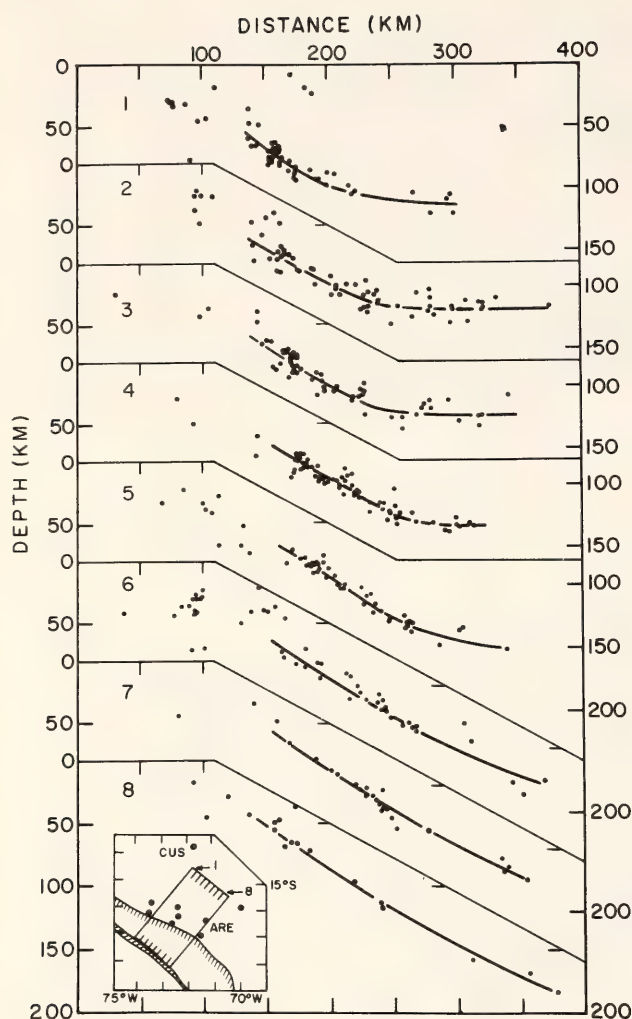


Fig. 7. Divided vertical cross sections of relocated earthquakes, located inside the rectangles from region 1 to region 8 on the inserted map. Solid curves show the shape of the deep seismic zone inferred from the seismicity in each vertical section.

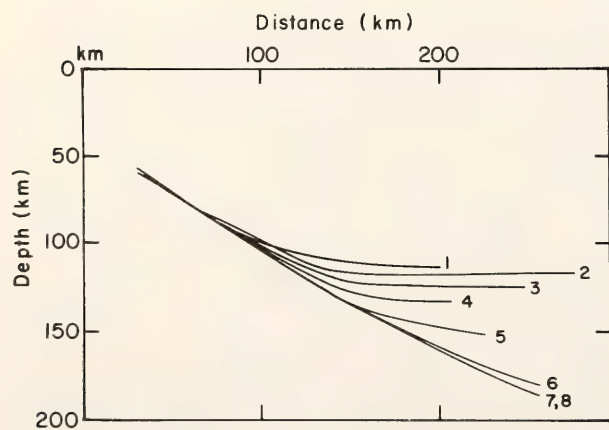


Fig. 8. Inferred shape of the deep seismic zone in each vertical section from region 1 to region 8 on the inserted map in Fig. 7, showing the change in the shape from the northern region to southern region.

subregions from *A* to *G*, as shown in Fig. 9, and the events located in each sub-region are projected onto vertical sections approximately perpendicular to the local strike of the Peru Trench. Earthquakes that are close to one another on the vertical sections and whose mechanism types are therefore presumed to be similar to each other, are taken as one group, and *P*-wave first motions of the earthquakes in the same group are superimposed on the same focal sphere. The earthquakes for which individual mechanism solutions are already determined by Stauder (1975) are excluded.

Some of the composite focal mechanisms obtained are shown on the vertical sections of earthquake hypocenters in Fig. 10. Stauder's mechanism solutions for large earthquakes are also presented in the figure. The composite mechanism solutions for intermediate-depth earthquakes in vertical section *B* (Fig. 10) indicate normal faulting or strike slip faulting, the trend of tension axis varying from the northeast to the east. The transition from shallow-focus reverse faulting to this mechanism type occurs

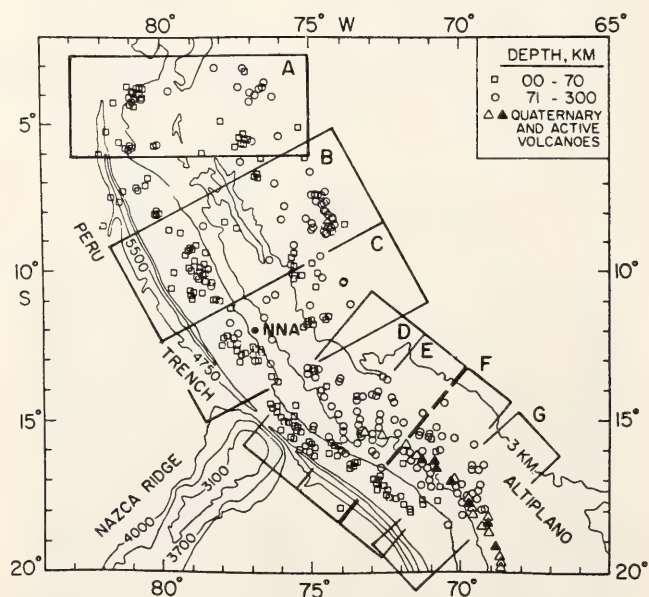


Fig. 9. Seismicity map in Peru showing events selected by Barazangi and Isacks (1979). Locations of station NNA and seismic cross sections from *A* to *G* used for the composite mechanism study are shown.



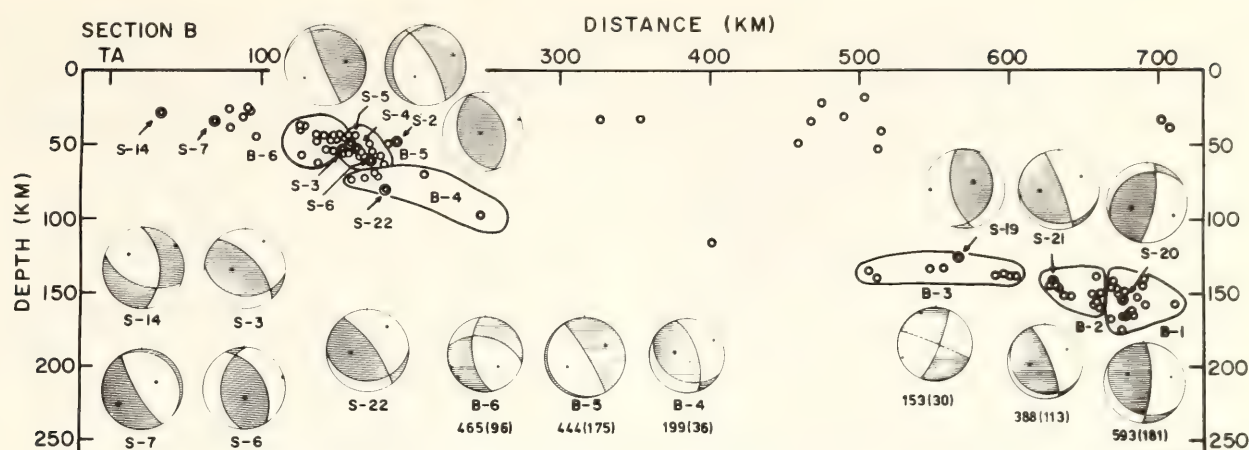


Fig. 10. Composite mechanism solutions on the vertical cross section for region *B* shown on the map in Fig. 9. Circles denote the hypocenter locations. Mechanism solutions for earthquake groups enclosed by solid curves are shown on the lower focal hemisphere by equal area projection. Shaded areas indicate quadrants of rarefaction first motion. The numeral in each solution denotes the number of *P* readings, and the numeral in parenthesis indicates the number of inconsistent stations for each mechanism solution. Mechanism solutions determined by Stauder (1975) are also included (double circles).

at about 70-km depth. Stauder classified focal mechanisms of intermediate-depth earthquakes beneath Peru into two types: shallower foci of intermediate-depth earthquakes have horizontal E-W tension axes, and the deeper foci are characterized by normal faulting with tension axes dipping about  $30^\circ$  and trending to the ENE (although there are several exceptions to this classification).

The present composite mechanism study reveals that the change in dip angle of tension axis for intermediate-depth earthquakes is closely related to the shape of the Nazca Plate. Figure 11a shows the projection of tension and compression axes of intermediate-depth earthquakes on the lower focal hemisphere. Earthquake groups in the subduction area with a plate dip of about  $30^\circ$  (vertical sections *F* and *G* in Fig. 9) have tension axes dipping about  $30^\circ$  (double circle). Beneath the shallow subduction area (vertical sections *A* to *E* in Fig. 9), earthquake groups in the coastal region, where the descending Nazca Plate dips near  $30^\circ$ , also have tension axes dipping near  $30^\circ$  (circle), and those in the inland region where the Nazca Plate

is almost horizontal tend to have near-horizontal tension axes (triangle). This implies that the tension axis is nearly parallel to the local dip of the descending Nazca Plate, although the compression axis scatters more widely. This is also the case for large earthquakes whose individual mechanism solutions are determined by Stauder (Fig. 11b). Earthquake groups B-1 and B-2, which are represented by squares, have tension axes dipping about  $30^\circ$ . These groups are located in the easternmost part of the region, and there the nearly horizontal Nazca Plate seems to bend downward again (Fig. 10). Therefore, earthquake groups B-1 and B-2 (and earthquakes 20 and 21 in Stauder's paper) are also considered to indicate down-dip extension. These mechanism solutions and the downward-bending pattern of the easternmost part of the deep seismic zone suggest the existence of an aseismic portion of the descending slab which extends to greater depth with a relatively steep dip angle, as illustrated in Fig. 12 by broken curves. Thus the descending Nazca Plate seems to behave as a stress guide even in the shallow subduction

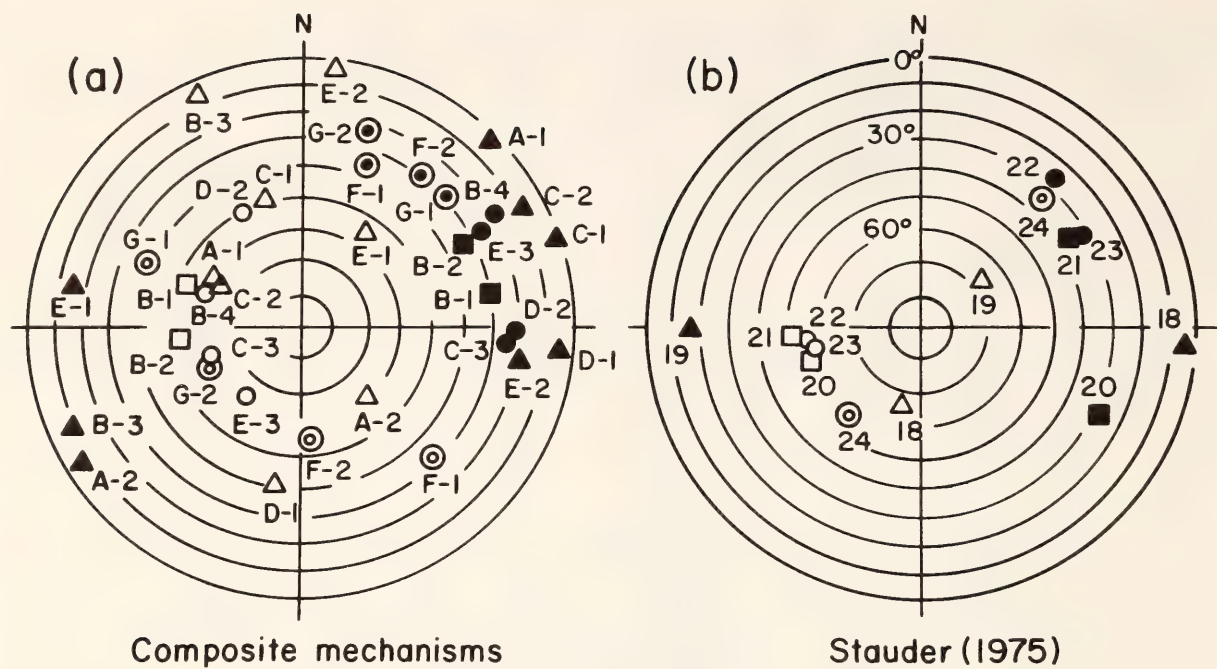


Fig. 11. Equal-area projections of compression and tension axes of intermediate-depth earthquakes, for composite mechanism solutions (a), and for those determined by Stauder (1975) (b). The compression axes are represented by open circles, triangles, squares, and double circles, and the tension axes by filled symbols.

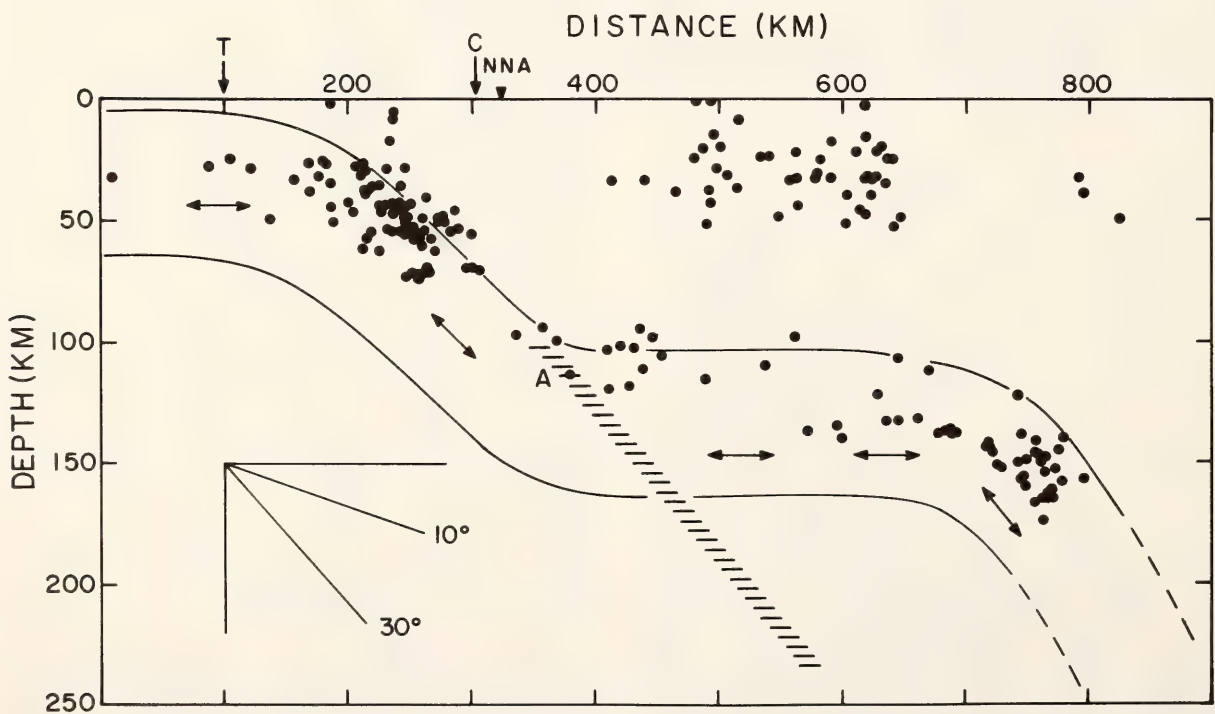


Fig. 12. Cross section showing the inferred geometry of the descending Nazca Plate beneath central Peru. Seismicity is from fig. 10 of Barazangi and Isacks (1979). This is a 1000-km-wide section and therefore assumes the deformation in the slab over this width. The hatched zone denotes the possible conversion plane of the *ScSp* arrivals at station NNA (triangle) estimated by Snoke *et al.* (1977). Tension axes, shown by arrows, for focal mechanisms of intermediate-depth earthquakes are approximately parallel to the local dip of the descending Nazca Plate.



region. The inferred earthquake-generating stress field beneath central Peru is schematically illustrated in Fig. 12 by thick arrows.

### *Comparison with Previous Models*

In order to know whether or not our revised subduction model can explain the *ScSp* observations at NNA, we reexamined the geometrical relationship between the location of the possible conversion plane for *ScSp* arrivals and that of the deep seismic zone beneath NNA. Figure 12 shows a vertical section of earthquakes which were selected in Region 2 in central Peru by Barazangi and Isacks (1979). Our model provides a good fit to this seismicity pattern. The possible conversion plane of *ScSp* arrivals at NNA (Snoke *et al.*, 1977) is projected on this vertical section as a hatched zone. Amplitude ratio considerations suggest that conversion takes place at point A. The depth and dip of the interface as determined from *ScSp* observations are consistent with the profile of the subducting plate as determined in this study. The *ScSp* data provide strong support for the initial 30° dip of the subducting slab.

We conclude that both previous models were but partially correct. The proponents of the 30°-dipping model were correct for depths less than about 100–110 km, but they erred in assuming that the dip remained at 30° for greater depths. The shallow-dipping (10°) model is a reasonable gross average for the subduction but overlooks the 30° subduction down to depths of at least 100 km.

### *Concluding Remarks*

Both the seismicity and the *ScSp* observations in central Peru are explained by our revised subduction model, which postulates that the Nazca Plate descends beneath the continent with a normal dip angle ( $\sim 30^\circ$ ) to a depth of about 100 km and then assumes an extremely shallow (near-horizontal) dip angle. The focal

mechanism study shows that intermediate-depth earthquakes ( $h \geq 70$  km) within the descending slab have tension axes nearly parallel to the local dip of the slab. This orientation of tension axes suggests that, at about 700–800 km inland of the trench, the slab again dips at 30° and an aseismic portion of the slab may extend deeper into the mantle.

Anelasticity determinations by Sacks (1969) seem to support this suggestion. His results indicate that coastal stations above the horizontal subduction area have low-frequency shear arrivals from nearby deep earthquakes and that CUZ, an inland station far from the coast, has high-frequency shear arrivals. The high-*Q* to CUZ may result from paths of low attenuation within the inland aseismic descending slab. Whether or not this aseismic portion of the descending slab is continuous down to a 600-km depth is not clear. The low-*Q* value at the coastal stations is considered to be caused by the low-*Q* path within the mantle below the descending slab. A more quantitative analysis is currently under investigation.

### *References*

- Aki, K., Earthquake generating stresses in Japan for the first motion radiation patterns, *Bull. Earthq. Res. Inst.*, 44, 447–471, 1966.
- Barazangi, M., and B. Isacks, Spatial distribution of earthquakes and subduction of the Nazca Plate beneath South America, *Geology*, 4, 686–692, 1976.
- Barazangi, M., and B. Isacks, Subduction of the Nazca Plate beneath Peru: Evidence from spatial distribution of earthquakes, *Geophys. J. Roy. Astron. Soc.*, 57, 537–555, 1979.
- Isacks, B., and P. Molnar, Distribution of stresses in the descending lithosphere from a global survey of focal mechanism solutions of mantle earthquakes, *Rev. Geophys. Space Physics*, 9, 103–174, 1971.

Isacks, B., and M. Barazangi, Geometry of Benioff zones: Lateral segmentation and downwards bending of the subducted lithosphere, in *Island Arcs, Deep Sea Trenches, and Back Arc Basins*, Ewing Series 1, pp. 99–114, M. Talwani and W. Pitman, eds., American Geophys. Union, Washington, D.C. 1977.

James, D., Subduction of the Nazca Plate beneath central Peru, *Geology*, 6, 174–178, 1978.

James, D., I. S. Sacks, E. Lazo, and P. Aparicio, On locating local earthquakes using small networks, *Bull. Seismol. Soc. Amer.*, 59, 1201–1212, 1969.

Okada, H., Converted *P* phases from the ScS phase at the inclined deep seismic zone, *Carnegie Inst. Wash. Year Book* 72, 238–245, 1973.

Ritsema, A. R., The faultplane technique and the mechanism in the focus of the Hindu Kush earthquakes, *Indian Jour. Meteor. Geophys.*, 6, 41–50, 1955.

Sacks, I. S., Distribution of absorption of shear waves in South America and its tectonic significance, *Carnegie Inst. Wash. Year Book* 67, 339–344, 1968.

Sacks, I. S., Interrelationships between volcanism, seismicity, and anelasticity in western South America, *Tectonophys.*, 37, 131–139, 1977.

Snoke, J. A., I. S. Sacks, and H. Okada, Determination of subducting lithosphere boundary by use of converted phases, *Bull. Seismol. Soc. Amer.*, 67, 1051–1060, 1977.

Snoke, J. A., I. S. Sacks, and D. James, Subduction beneath western South America: Evidence from converted phases, *Geophys. J. Roy. Astron. Soc.*, 58, in press, 1979.

Stauder, W., Subduction of the Nazca Plate under Peru as evidenced by focal mechanisms and by seismicity, *J. Geophys. Res.*, 81, 1053–1064, 1975.

Sykes, L. R., Seismicity as a guide to global tectonics and earthquake prediction, *Tectonophys.*, 13, 393–414, 1972.

## ON BENDING OF THE SUBDUCTING PLATE AND DOUBLE BENIOFF ZONES

A. T. Linde and I. S. Sacks

Oceanic lithosphere is consumed by subduction at convergent plate margins. During this process the plate undergoes large deformation and the region is characterized by seismicity often extending to depths around 600 km. The deep seismicity usually forms a plane, which is accepted as lying just inside the upper boundary of the subducting plate. Precision seismicity studies have demonstrated that, in some cases, this dipping plane of seismicity has a double-layered structure. In this report, we investigate constraints that might be placed on models for the subduction process from simple considerations of the seismicity and geometry of the subducting plate.

### *Bending of the Plate*

In order to subduct the oceanic lithosphere, bending of this plate must be initiated seaward of the trench. Since the eventual subduction angle is typically about  $30^\circ$ , this bending produces large deformation of the plate. We examine this bending and the seismicity associated with it with a view to determining the extent to which special rheology and strain storage are required by the data.

Figure 13 illustrates the geometry of the bending at subduction. Following Engdahl and Scholz (1977), we assume the elastic portion of the lithosphere to be 40 km thick and the radius of curvature to be 200 km. Thus the subduction angle of  $30^\circ$  is achieved by having a bent section of lithosphere about 100 km long. These values are consistent with the observed seismicity patterns.

We can calculate the maximum strain produced in the bending. The radius to the neutral axis is 200 km, and that to the upper edge of the slab is 220 km. This upper section has undergone extension from length  $200 \cdot \theta$  km to  $220 \cdot \theta$



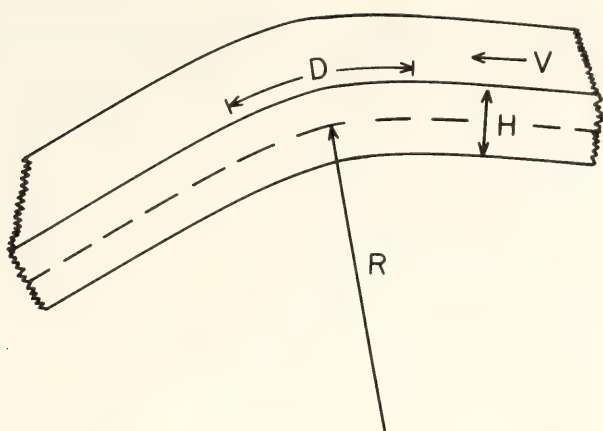


Fig. 13. Geometry of the subducting plate. The plate is curved over a distance  $D = 100$  km as it bends with radius of curvature  $R = 200$  km. We take elastic thickness  $H$  of the plate to be 40 km and the velocity of subduction  $V = 5$  cm/yr. The maximum strain produced is  $10^{-1}$ .

km where  $\theta$  is the angle of subduction (in radians). Thus the maximum strain is  $(220-200) \theta/200 \theta = 10^{-1}$ . Since most rocks are considered to be able to withstand strains less than  $10^{-4}$ , this value of  $10^{-1}$  is extremely large. This large strain has been regarded as a major rheological complication for the subduction process. However, the implications of strain rate have previously been neglected. If we consider an average subduction velocity of 5 cm/yr, then the strain rate for the bending process is about  $10^{-7}$ /yr (see Fig. 13). This is based on the assumption that the rate of bending is uniform over a distance of 50 km, half the region in which the slab is curved.

This strain rate is not unusual, being comparable to many tectonic regions where strain rates of order  $10^{-6}$ /yr are frequently encountered. In these regions the strain is released by earthquakes when it approaches  $\approx 10^{-4}$ .

The ocean floor seaward of the trench is characterized by extensive normal faulting (Hilde and Sharman, 1978), and thus we are led to ask if there is evidence that the accumulating strain is relieved by means of normal-faulting earthquakes.

If we assume that each earthquake relieves  $10^{-4}$  strain, then we need 1,000 earthquakes in each section of lithosphere as it deforms through a total strain of  $10^{-1}$ . Since we are concerned with the time scales of order  $10^6$  years, the only way we can estimate the level of seismicity is by taking global figures. We will consider only large ( $M > 8$ ) earthquakes in this discussion—this will place an upper bound on the seismicity level required to relieve the accumulated strain. If each of these large earthquakes relieves 200 km of bending lithosphere, we require (for a total trench length of 35,000 km) an average of one  $M \geq 8$  every eight years in order not to have any buildup of strain from the bending process.

The observed seismicity can be examined for evaluation of this possibility. In the last 40 years, for which we have good location data for big events, there have been two large normal-faulting events, one near San Riku, Japan, in 1933 and the other near Indonesia in 1979. If we lengthen our time window to include the last 90 years, then there are about 10 large earthquakes located seaward of the trench, although the accuracy of location is less reliable and the absence of focal mechanism solutions means that we cannot characterize them as normal-faulting events. Thus the observed large magnitude rates of occurrence are 1 in 20 years (over 40 years) or 1 in 9 years (over 90 years). These are in adequate agreement with our requirement (1 in 8 years) considering the short time sample available.

Thus, the observed seismicity for large normal-faulting events indicates that essentially all the strain caused by bending of the slab can be released by these large earthquakes. The data do not require postulation of unusual rheology to account for the large deformation; simple elasticity and fracture processes are all that are necessary. In addition, there is no requirement for large strains to be accumulated.

*Straightening of the Slab and  
Double Benioff Zones*

The descent of the plate to depths of 600 km and greater is delineated by a dipping plane of earthquakes. This zone is taken to lie near the top boundary of the subducting plate. However, there is no universally accepted model that explains how earthquakes occur at depth or what the driving mechanism is.

This problem has been complicated by the confirmation by Hasegawa *et al.* (1978) of a double Benioff zone under the Tohoku region of Japan (Fig. 14). Precise location studies in this area have shown that, in the depth range 70–170 km, the Benioff zone consists of two parallel zones separated by some 30 km. In the upper zone the earthquakes are characterized by axial compression along the dip of the plate, while those in the lower zone have axial tension in the dip direction.

This double-Benioff-zone character has been interpreted in terms of stresses produced in the slab from straightening

after subduction is initiated. Engdahl and Scholz (1977) proposed a rheologic model in which perfect elasticity applied at strains less than a yield strain and plastic flow prevailed at higher strains. We (Linde and Sacks, 1978) investigated a modified version of such a model. These studies show that stress patterns consistent with various aspects of the seismicity can be obtained from such models.

Here, rather than consider details of such possible models, we inquire whether any bending model is allowed by the level of observed seismicity and the tectonic setting for the intermediate depth range. In what follows, we will use numerical values determined for the Tohoku region, the best example of a double Benioff zone. The seismicity pattern indicates that the descending slab has been straightened before it reaches a depth of 70 km (Fig. 14) and thus, if the intermediate-depth (70–170 km) seismicity is to result from stresses produced by a straightening mechanism, we require storage of stress sufficient to produce this seismicity. We can determine this stress level by calculating, from recorded seismicity, the number of times an earthquake occurs in a given volume of material as it travels from 70 km to 170 km in depth. At the approximate subduction rate for the Tohoku region ( $\approx 10$  cm/yr) and at the observed dip of  $30^\circ$ , the corresponding time interval is 2 million years.

Figure 14 shows that the seismicity in one of the parallel dipping planes is confined to a width of 10–15 km. We consider a 200-km-wide strip of the subducting region and for intermediate depths examine the occurrence of larger ( $M > 5$ ) events over a period of 14 years (Table 1). It is apparent that the level of activity is essentially independent of depth for the range considered. In Table 2, we show the number of events in half-unit magnitude intervals and, using volume estimates derived from Wyss (1978), we calculate that,

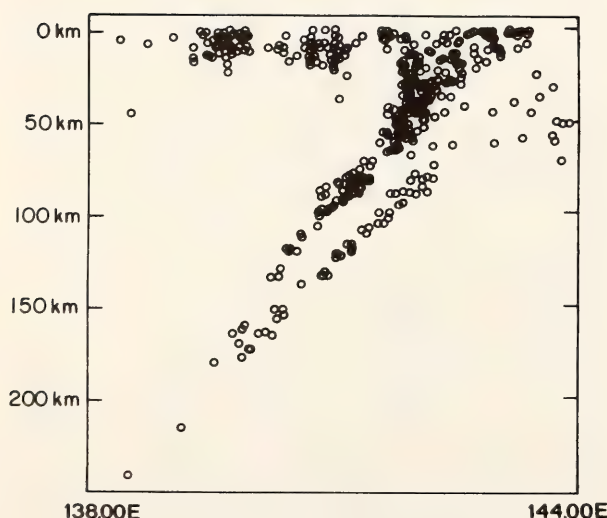


Fig. 14. Seismicity under the northeast Japan arc, from Hasegawa *et al.* (1978), showing a clear double Benioff zone. The two planes have different fault-plane solutions: the upper shows down-dip compression, the lower shows down-dip tension.



TABLE 1. Earthquakes with  $M > 5$  in Tohoku Region\*

Depth	Mag.	Date	Lat.	Long.
71	5.1	23. 6.66	38.1	141.5
78	5.5	13.11.73	38.6	142.1
81	5.8	1. 4.70	39.8	141.8
86	5.4	20. 6.69	38.6	141.8
100	5.3	26. 4.75	39.6	141.1
107	5.3	18.10.69	39.3	141.4
109	5.2	27. 1.66	39.8	140.9
110	5.1	14. 2.73	39.0	141.5
146	5.7	23. 3.70	40.1	140.2
176	6.3	20. 2.63	38.8	139.0

\* Fourteen years of data. Ordered in increasing depth.

averaged over the 14 years of seismicity, earthquakes relieve strain at the  $10^{-4}$  level in  $50\text{ km}^3$  of rock every year. The subduction rate for Tohoku is  $10\text{ cm/yr}$  and thus in the  $2 \times 10^6$  years it takes material to travel from a depth of  $70\text{ km}$  to one of  $170\text{ km}$ , earthquakes will have produced strain release in  $9.1 \times 10^7\text{ km}^3$ . Since the total volume of rock under consideration ( $200\text{ km} \times 200\text{ km} \times 12.5\text{ km}$ ) is  $5 \times 10^5\text{ km}^3$ , each unit volume of material will experience approximately 200 events. It is highly unlikely that this would occur over a period of 2 million years without some source of energy input. If we assume that each earthquake results in 100 bars of stress change, then a storage model requires an input stress of 20 kbar; this is physically unreasonable since the maximum

stress such rock can withstand is probably about 1 kbar.

In addition to this argument, the straightening situation is very similar to that for bending. We would expect that the strain is relieved continually as it accumulates but, because of the high level of seismicity caused by underthrusting in this region, it is not a simple matter to compare this with recorded seismicity.

Conclusions

By using seismicity levels to determine constraints on possible models, we are able to draw two conclusions:

(1) Strain caused by bending at initiation of subduction can be relieved by normal faulting seismicity. No unusual rheology is required to account for the large deformation, and it is not necessary to accumulate large strains.

(2) Intermediate-depth seismicity (in particular that associated with double Benioff zones) cannot be due solely to stress stored during straightening: a source of continual energy input is required.

References

Engdahl, E. R., and C. H. Scholz, A double Benioff zone beneath the Aleutians: an unbending of the lithosphere,

TABLE 2. Earthquakes of Table 1 Grouped by Magnitude Interval

Mag.	Number	Volume/ event ( $\text{km}^3$ )*	Total Volume ( $\text{km}^3$ )
5.0-5.5	7	2.3	16
5.5-6.0	2	35.0	70
6.0-6.5	1	550.0	550
			636

\* Using  $\log V = 2.38M - 12.14$  (after Wyss, 1978)

- Geophys. Res. Letters*, 4, 473–476, 1977.
- Hasegawa, A., N. Umino, and A. Takagi, Double-planed deep seismic zone and upper mantle structure in the north-eastern Japan arc, *Geophys. J. Roy. Astron. Soc.*, 54, 281–296, 1978.
- Hilde, T. W. C., and G. F. Sharman, Fault structure of the descending plate and its influence on the subduction process, *Trans. Amer. Geophys. Union*, 59, 1182, 1978.
- Linde, A. T., and I. S. Sacks, On double Benioff zones in subduction regions, *Carnegie Inst. Wash. Year Book* 77, 517–520, 1978.
- Wyss, M., Estimating expectable maximum magnitude of earthquakes from fault length, *Trans. Amer. Geophys. Union*, 59, 1125–1126, 1978.

TOWARD A QUANTITATIVE MODEL OF  
STRESS DIFFUSION AFTER LARGE  
SUBDUCTION ZONE EARTHQUAKES:  
APPLICATIONS TO NORTHERN JAPAN

W. D. Heinze and I. S. Sacks

*Introduction*

Because of interest in earthquake prediction, much work has recently focused on understanding the behavior of the transient quasi-static deformations that follow large earthquakes (Nur and Mavko, 1974; Melosh, 1976; Barker, 1976; Rundle, 1976, 1978; Rundle and Jackson, 1977a, 1977b, 1977c; Thatcher and Rundle, 1979; Rundle and Thatcher, 1979; Yang, 1979; Melosh and Raefsky, 1979; Cohen, 1979; Ikeda, 1979). Installation over the last 15 years of geodetic, strainmeter, and microearthquake seismometer networks, especially in Japan, have yielded data that now allow semi-quantitative testing of theoretical models. This paper employs a simple but adequate model to determine the main features of the stress diffusion process in the landward lithospheric plate at

thrust-type subduction zones. In addition, the viscosity of the asthenosphere beneath northern Japan is determined by comparing results from this model to direct and inferred horizontal crustal strain data in northern Japan.

Elsasser (1967) proposed that the longtime deformational behavior of a locally strained portion of lithosphere could be adequately modeled by an elastic lithosphere, a viscous low-viscosity channel (in the asthenosphere), and a rigid halfspace. We use the same model except that the low-viscosity channel is permitted viscoelastic behavior. For the time spans considered in this paper ( $< 100$  years) and for viscosities that may exist in the upper mantle ( $< 1 \times 10^{22}$  poise), the viscoelastic assumption is necessary. Both our model and Elsasser's result in diffusion-type differential equations in which the strain as a function of time at a given distance from the strain source has a pulselike appearance. Elsasser's model has been used by several workers to explain time-spatial migration of earthquakes and other features resulting from crustal deformation (Anderson, 1975; Fujii, 1978).

*Model*

The model used in this study is intended to represent approximately the behavior of the lithosphere before and after one of the large earthquakes that recur along thrust-type subduction zones. Our model is a considerable simplification of thrust-type subduction zones, but it retains the essential physics of the problem. In particular, we assume that

(1) The fault and subduction zone are two-dimensional

(2) At distances more than half a fault length away from the fault center, lithospheric flexure will not be the dominant component of lithospheric deformation (i.e., vertical displacements are ignored)

(3) The gross features of this horizontal mode of deformation can be mod-



eled by an elastic lithosphere, a viscoelastic low-viscosity channel, and a rigid halfspace

(4) At a given point along a subduction zone, large earthquakes occur at regular intervals; the time between quakes is a period of slow reloading by the oceanic slab.

The two-dimensional assumption means that we are modeling a fault that is much bigger than the natural fault. This imposes two significant limitations: at distances larger than several fault widths our model will substantially overestimate the actual strain magnitude, and the model will not give the correct response for observing stations which are more than a fault width from the line that bisects the surface projection of the fault and is perpendicular to its strike. Combined with assumption (2), above, this means that our model is applicable (for  $M > 7.3$ ) at distances from  $\sim 50$  km from the fault center out to  $\sim 300$  km, which encompasses the locations of the crustal strain observations in Japan that will be compared with the model results.

The use of only the horizontal component of the deformation, within the distance limitation mentioned in assumption (2), is supported by the finite element studies of Melosh and Raefsky (1979) and Yang (1979). Also, because viscosity is depth dependent, one expects that the time constants for flexural modes of deformation are much longer than for horizontal modes of deformation: the lowest-viscosity part of the asthenosphere almost completely controls how fast the horizontal shear stress relaxes, while flexural modes depend on viscosity over a range of depths. Our layered model is a reasonable approximation to the lithosphere-upper mantle system on the basis of its expected mechanical properties (from crustal rebound studies such as McConnell, 1968, and Peltier *et al.*, 1978; and from inferences of rock-creep properties from deformation experiments such as Stocker

and Ashby, 1973, and Ashby and Verrall, 1977). The rigid halfspace boundary condition is justified because the subducted oceanic lithosphere beneath Japan will have a much higher viscosity than the low-viscosity channel above it and thus will play no significant role in the stress relaxation in the channel.

Our choice of forcing function is based upon the observed periodic recurrence of large earthquakes in subduction zones and an assumed constant rate of subduction. The historical record of earthquakes in Japan over the last 400 years indicates that great earthquakes occur at intervals of 30 years with a standard deviation of 15 years.

Our model then (Fig. 15a) consists of an elastic lithosphere in which only horizontal strain is allowed and a viscoelastic low-viscosity channel in which only shear strain is allowed. This model is equivalent to the discrete model shown in Fig. 15b as  $dx$  approaches zero.

The equations that describe the behavior of the model are

$$\begin{aligned} H_e^2 \frac{\partial e^2}{\partial x^2} + e' - e &= 0, \\ \tau \frac{\partial e'}{\partial t} + e' - e &= 0, \end{aligned} \quad (1)$$

where  $e$  is the horizontal strain in the lithosphere,  $e'$  is the permanent shear strain that has taken place in the low-viscosity channel,  $x$  is horizontal distance ( $x = 0$  corresponds to the center of the projection of the fault plane onto the earth's surface), and  $t$  is time after the earthquake occurrence, and

$$\begin{aligned} H_e &= \left( \frac{E}{\mu} H_1 H_2 \right)^{1/2} \\ \tau &= \frac{\eta}{\mu}. \end{aligned} \quad (2)$$

For the definition of  $E$ ,  $\mu$ ,  $\eta$ ,  $H_1$ , and  $H_2$ , see Fig. 15a.

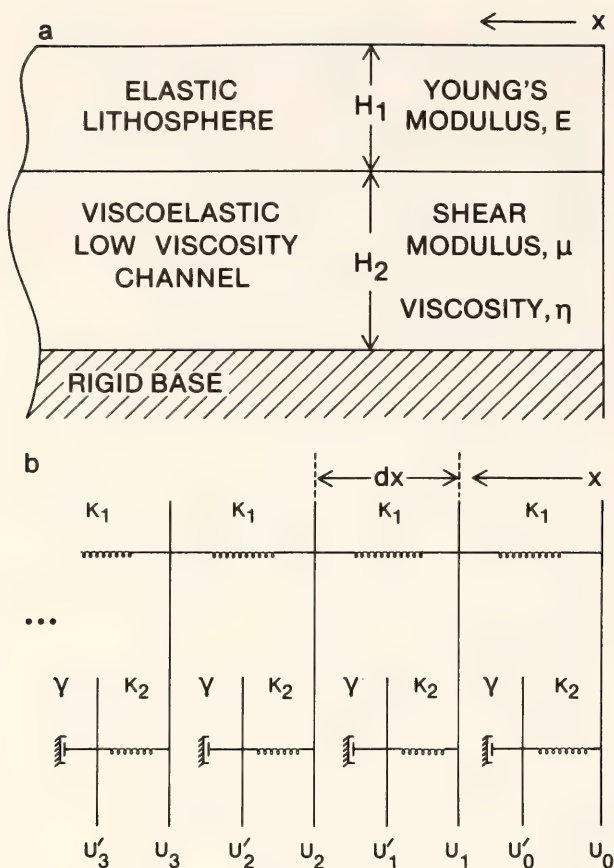


Fig. 15. Model used to simulate horizontal crustal deformation in northern Japan. (a) Continuous model: elastic lithosphere, horizontal strain only; viscoelastic low-viscosity channel, shear strain only; rigid base. (b) Discrete analogue of continuous model as  $dx \rightarrow 0$ :  $k_1 = EH_1 \frac{dy}{dx}$ ,  $k_2 = \left(\frac{\mu}{H_2}\right) dx dy$ , and  $\gamma = \left(\frac{\eta}{H_2}\right) dx dy$ , where  $dy$  is thickness in the direction perpendicular to the page.

The problem we shall solve is as follows:

Initial conditions,  $t < 0$ ,

$$\begin{aligned} e = e' &= \frac{\partial e}{\partial x} = \frac{\partial e}{\partial t} \\ &= \frac{\partial e'}{\partial x} = \frac{\partial e'}{\partial t} = 0, \end{aligned} \quad (3)$$

Boundary conditions,  $x = 0$ , ( $0 \leq t \leq T$ )

$$e = \frac{u_m}{H_e} \left(1 - \frac{t}{T}\right), \quad (4)$$

where  $u_m$  is the horizontal component of the fault offset, and  $T$  is the interval between large earthquakes.

These initial and boundary conditions represent a sudden fault offset (seismic or aseismic) followed by slow reloading over a period of time,  $T$ . In this study,  $T$  will be assumed to be 30 years, the value observed in Japan. We consider the solution for  $x > 0$ .

$$\begin{aligned} e(\tilde{x}, t) &= \\ &- \frac{2u_m}{H_e} \int_{-\infty}^{\infty} e^{i2\pi \tilde{k}_x \tilde{x}} \left[ \frac{e^{-(K^2/1+K^2)t/\tau}}{1 + K^2} \right. \\ &\left. + \frac{\tau}{T} \frac{1}{K^2} (e^{-(K^2/1+K^2)t/\tau} - 1) \right] d\tilde{k}_x, \end{aligned} \quad (5)$$

where

$$\begin{aligned} \tilde{x} &= \frac{x}{H_e}, \\ K &= 2\pi \tilde{k}_x, \\ \tilde{k}_x &= H_e k_x, \text{ and} \\ k_x &\text{ is the spatial wave} \\ &\text{number corresponding to} \\ &\text{the } x \text{ spatial coordinate.} \end{aligned} \quad (6)$$

A closed form solution could not be found, so this expression was integrated numerically using the fast Fourier transform (FFT) algorithm.

Equation 5 indicates that, formally, four parameters ( $u_m$ ,  $H_e$ ,  $\tau$ , and  $T$ ) can be uniquely determined by matching model curves to horizontal crustal strain data. For the case we are considering, however,  $u_m$  and  $T$  are well determined by independent data. The two remaining free parameters,

$$\begin{aligned} H_e &= \left(\frac{E}{\mu} H_1 H_2\right)^{1/2}, \\ \tau &= \frac{\eta}{\mu}, \end{aligned}$$

depend on five model characteristics:  $E$ ,  $\mu$ ,  $H_1$ ,  $H_2$ , and  $\eta$ , of which  $E$  and  $\mu$  are



well determined from seismic data and laboratory deformation tests on rocks. Thus, in the mathematical sense there are two free parameters: (1)  $H_e$ , which is proportional to the geometric mean of  $H_1$  and  $H_2$ , and (2)  $\eta$ , the viscosity.

It is instructive to examine the behavior of this solution (equation 5). In Fig. 16 strain as a function of  $x$  is shown for several different times. For all times, the extremum strain value occurs near the earthquake site, indicating that the true nature of this process is strain diffusion, not strain propagation. Plots of strain as a function of time at increasing distances from the fault (Fig. 17) show apparent strain pulses which propagate in space and attenuate in amplitude.

The variation of the amplitude of the pulse peak with distance (Fig. 18) illustrates several interesting features. For  $x < H_e$ , all amplitude curves are proportional to  $\exp(-x/H_e)$  (the solution for  $t = 0$ ) and no pulse appears: the maximum strain occurs at  $t = 0$  and

subsequently decreases monotonically. For  $x > H_e$  the amplitude curves exhibit two kinds of behavior. For viscosities less than  $3 \times 10^{19}$  poise the curves follow roughly a  $1/x$  dependence, while for higher viscosities the amplitude curves approach an  $\exp(-x/H_e)$ . The latter relationship is due to the fact that the postseismic unloading strain rate is so slow that the reloading from the oceanic slab predominates and thus eliminates the pulse behavior.

The amplitude curves discussed above were computed for an earthquake recurrence interval ( $T$ ) of 30 years. The viscosity for transition from pulselike to nonpulselike behavior depends on  $T$ . For an infinite recurrence interval (no reloading), pulse behavior occurs at all viscosities, and the amplitude curves for all viscosities fall on the same curve, the uppermost one in Fig. 18.

The variation of the velocity of the pulse peak with distance (Fig. 19) also undergoes a transition near  $\eta = 3 \times 10^{19}$

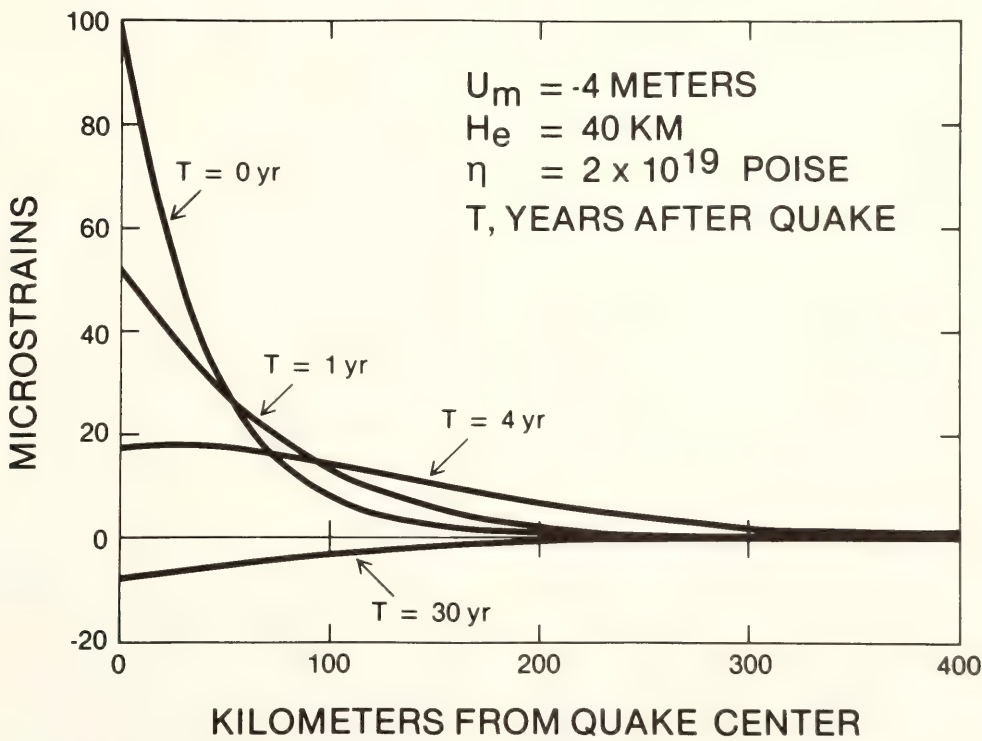


Fig. 16. Horizontal strain in the lithosphere as a function of distance from the earthquake center for various times after the quake. The extremum strain value occurs near the quake site, indicating that the true nature of this process is strain diffusion. The earthquake recurrence interval,  $T$ , is 30 years.





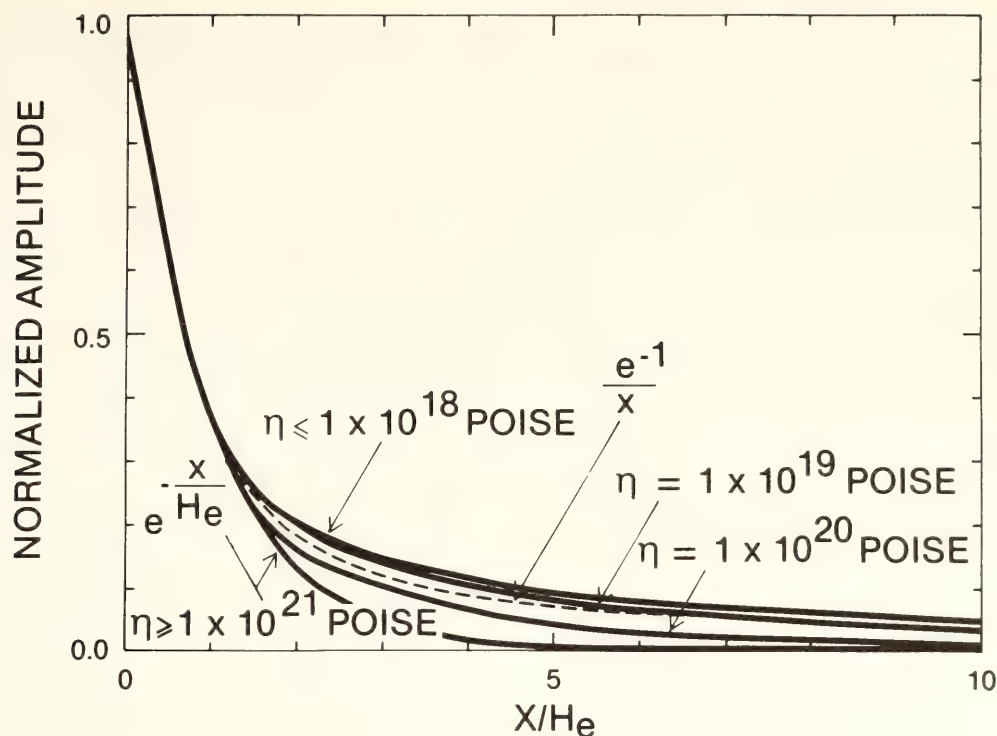


Fig. 18. The amplitude of the horizontal strain pulse normalized to the maximum horizontal strain at the earthquake site, as a function of distance normalized to the effective thickness  $H_e$  for several values of viscosity. Note that all viscosities follow the same  $\exp(-x/H_e)$  curve for  $x/H_e < 1$ . For  $\eta < 3 \times 10^{19}$  poise the curves approximately follow the analytic curve  $\exp(-1/x)$  (dashed). For  $\eta \geq 1 \times 10^{21}$  poise the curves all follow an analytic curve  $\exp(-x/H_e)$  almost exactly, and for such viscosities the strain-vs.-time curves exhibit no pulse characteristics. For  $\eta < 1 \times 10^{21}$  poise, the strain-vs.-time curves exhibit an increasing degree of pulse behavior as the viscosity decreases. The earthquake recurrence interval,  $T$ , is 30 years. For an infinite recurrence interval (no reloading), the pulse behavior occurs at all viscosities and the amplitude curves for all viscosities fall on the same curve, the uppermost one.

tends to this depth; Takagi *et al.*, 1977) and is probably no thicker than 70 km (attenuation of seismic waves increases significantly at this depth; Sacks, 1975). If the low-viscosity channel results from the temperature approaching the melting point, then the low gradients of pressure and temperature imply that the channel is no thinner than 20 km; we choose 30 km as a minimum for  $H_e$ .

The strongest constraint on the upper limit of  $H_e$  is that the top of the subducting plate under Japan serves as the effective rigid base to the lithosphere-low-viscosity channel system. Thus  $H_1 + H_2$  is limited by the average depth to the slab between the earthquake and the observation station. This average depth is almost always less than 100 km

for Japan, so that  $H_e$  is constrained to be less than 50 km.

Crustal rebound studies in several regions have yielded estimates of the average local viscosity in the upper mantle. Comparison of direct horizontal crustal strain measurements with model results should allow us to place strong constraints on the minimum local viscosity in the upper mantle and make estimates of the depth to this low-viscosity channel.

#### Comparison of Data and Model Results

*Direct Evidence.* In Hokkaido, northern Japan, accurate geodetic measurements on local grids with apertures of about 10 km allow determination of the horizontal crustal strain before and after

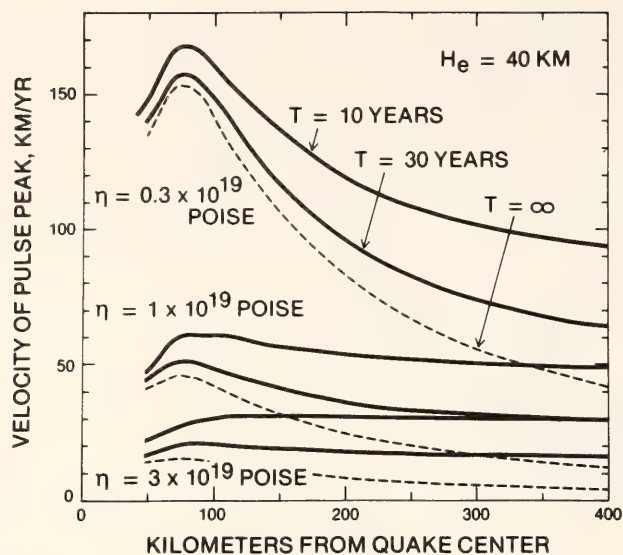


Fig. 19. The velocity of the pulse peak as a function of distance from the quake center for various values of viscosity and earthquake recurrence interval,  $T$ . These curves illustrate the same transition behavior seen in the curves of amplitude vs. distance. For  $\eta < 0.3 \times 10^{19}$  poise the strain pulse velocity exhibits a strong distance dependence. As  $\eta$  increases the velocity decreases and becomes nearly constant with distance and the strain-vs.-time curves become less pulselike in nature.

the Nemuro-oki earthquake of 1973 (Kasahara and Suzuki, 1978; Shimazaki, 1974). These measurements indicate a slow extension of the crust at 120 km from the fault plane center (station B, Fig. 21). The strain change remained extensile through 1975, when it leveled off, and by 1977 it had become compressive. Similar measurements at a station 50 km from the fault plane center (station A) started a year after the quake and indicate a rapid compression which quickly died out.

The data and model curves are compared in Fig. 21. Viscosities of  $1 \times 10^{19}$  poise and  $4 \times 10^{19}$  poise bracket the range that is consistent with the data. An insufficient time sequence of data is available to allow estimates of the noise level and so we cannot ascertain how much of the discrepancy between the data and model calculations is due to noise. We note, however, that the differences are consistent with the expected

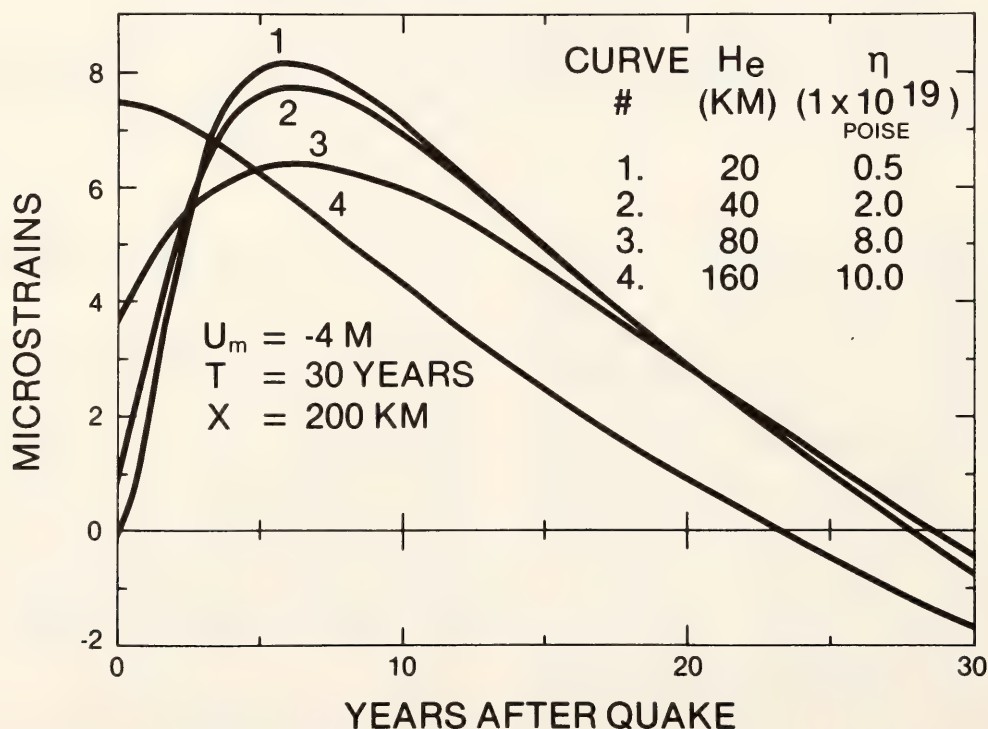


Fig. 20. The nonuniqueness of obtaining  $H_e$  and  $\eta$  simultaneously from horizontal crustal deformation data is illustrated in this diagram. Several curves of horizontal strain-vs.-time are shown, all for the same distance from the quake but where  $H_e$  and  $\eta$  are changed for each new curve. For low viscosities the curves are very similar, indicating that in this viscosity range,  $H_e$  and  $\eta$  are not independent parameters. For larger viscosities the pulse shapes are significantly different, but the behavior of the curves after 10 years remains similar because it is controlled mainly by the reloading from the oceanic lithosphere.



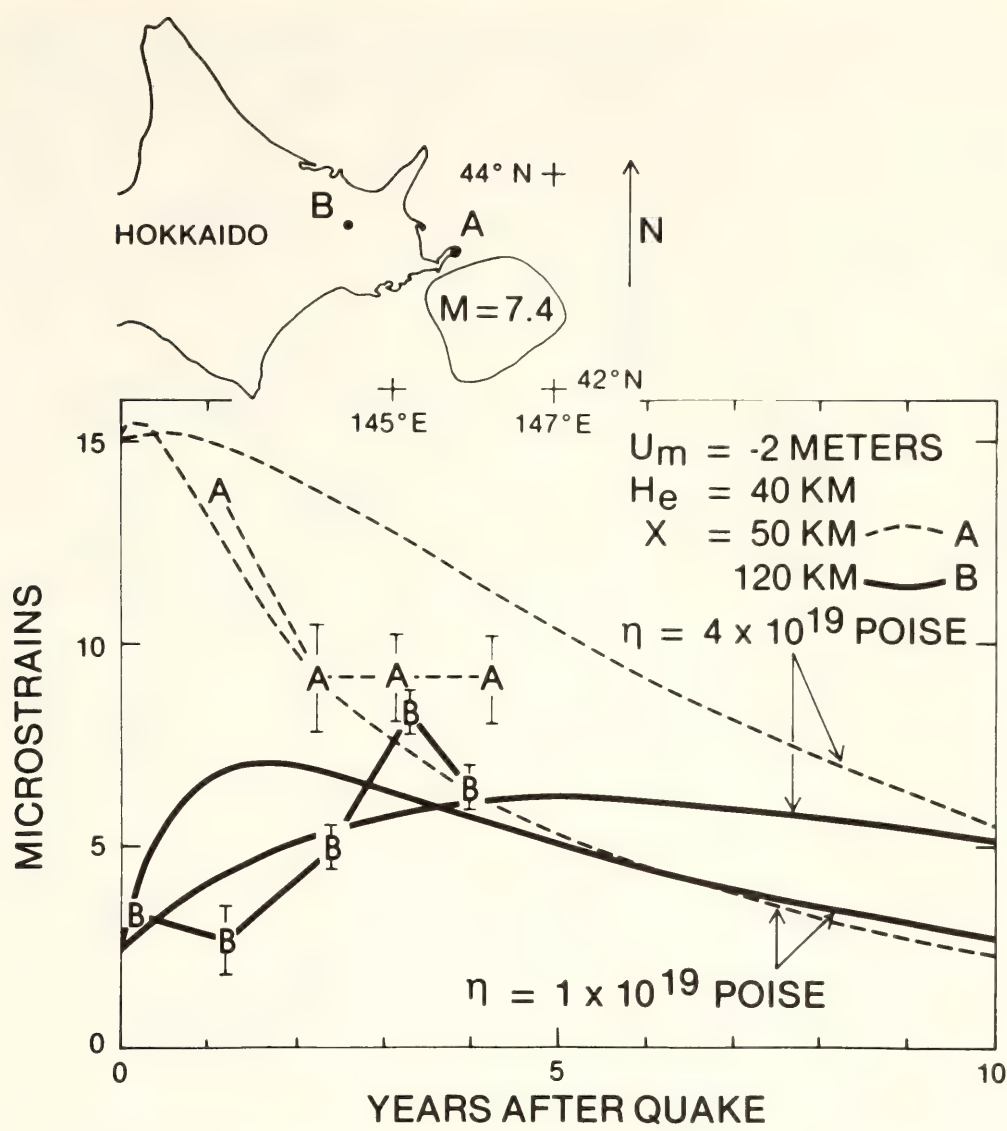


Fig. 21. Crustal strain data following the 1973 Nemuro-oki earthquake for two stations: A, 50 km from the quake center, and B, 120 km from the quake center (Kasahara and Susuki, 1978). The data were obtained by repeated geodimeter traverses over grids with apertures of about 10 km. The displacement  $u_m = -2$  meters was determined from seismic and vertical crustal deformation data (Shimazaki, 1974). The earthquake recurrence interval,  $T$ , is 30 years. The model curves shown at 50 km (dashed curves) and 120 km (solid curves) exhibit the same character as the data curves. Since virtually all the data was taken after the earthquake occurrence, the origin of the data curves is arbitrary. Therefore the first data point for each station has been plotted only to indicate the relative strain change to the second data point. Model curves are plotted for channel viscosities of  $1 \times 10^{19}$  poise and  $4 \times 10^{19}$  poise, which bracket the range that is consistent with the data.

effects of lithospheric flexure and non-linear viscous flow in the low-viscosity channel, effects which are ignored in our calculations.

*Indirect Evidence.* Tanaka (1978) has investigated the migration velocities of microearthquake swarms and other tectonic events in Tohoku (Fig. 22). Making the assumption that the migration of

these tectonic events follows the peak of the strain pulse (or the maximum strainrate point), we infer that in eastern Tohoku, about 100 km from the center of the subduction zone quakes, strain pulse velocities range from 30 to 50 km/yr, and in western Tohoku at a distance of 250 km, they range from 10 to 20 km/yr.

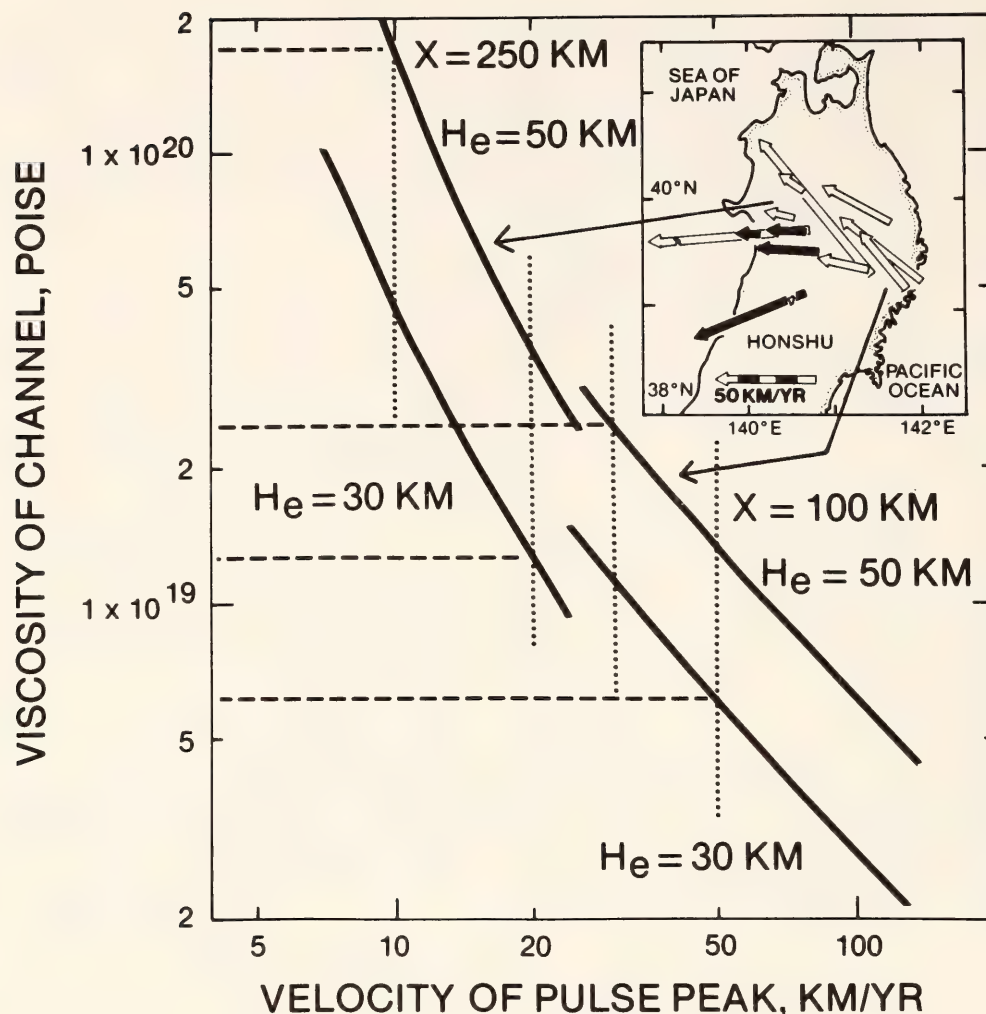


Fig. 22. From Tanaka's (1978) data we infer pulse-peak velocities of 30–50 km/yr on the east coast of Tohoku in northern Japan (100 km from the quake centers) and 10–20 km/yr on the west coast (250 km from the quake centers). At both distances ( $x = 100$  km and  $x = 250$  km), model curves of channel viscosity vs. pulse-peak velocity are shown for  $H_e = 30$  km and  $H_e = 50$  km, the lower and upper bounds of  $H_e$  inferred from other geophysical data. Comparison of the model curves with the appropriate inferred velocity range from above yields a viscosity range for the low-viscosity channel under the east coast of northern Japan of  $0.6 \times 10^{19}$  to  $2 \times 10^{19}$  poise and under the west coast of  $2 \times 10^{19}$  to  $20 \times 10^{19}$  poise. The earthquake recurrence interval,  $T$ , is 30 years.

Model curves of viscosity vs. pulse-peak velocity are compared to these velocity ranges in Fig. 17. Model curves are shown at  $x = 100$  km and  $x = 250$  km for the upper and lower bounds that were inferred above for  $H_e$  (50 km and 30 km). Since the average depth to the top of the subducting slab increases with distance from the trench, we expect the value of the  $H_e$  at  $x = 100$  km to be closer to the lower bound and at  $x = 250$  km to be closer to the upper bound. Thus at  $x = 100$  km the velocity range

implies a viscosity range of  $0.6 \times 10^{19}$  to  $2 \times 10^{19}$  poise and at  $x = 250$  km a viscosity range of  $2 \times 10^{19}$  to  $20 \times 10^{19}$  poise. The migration velocity data suggest that the velocities are from two to three times higher on the east coast of Tohoku, near the quakes, than on the west coast. Examining the curves in Fig. 19 for  $T = 30$  years, we find that for the whole range of viscosities inferred above ( $0.6 \times 10^{19}$  to  $20 \times 10^{19}$  poise) the velocity changes by less than a factor of two between 100 km and 250



km. This suggests that the inferred viscosity increase from the 100-km distance to the 250-km distance may be real. Such a viscosity increase would be consistent with nonlinear viscous behavior in the channel because the stresses are much lower at 250 km from the epicenters than at 100 km.

The inferred observation of nonlinear viscous behavior in the channel is consistent with Melosh's (1976) analysis of aftershock migration following the 1965 Rat Island earthquake in the Aleutians. Using a model identical to Elsasser's (1967) except that the viscosity in the channel was nonlinearly dependent on stress, he concluded that the data required that the channel exhibit nonlinear rather than linear behavior. Brittle yielding in a model lithosphere (by mechanisms such as microseismicity and small-scale aseismic slip) can result in much the same crustal deformation as nonlinear viscous behavior in the low-viscosity channel of a model. Future attempts to model strain diffusion in the lithosphere, especially near the fault, should probably include both nonlinear viscous behavior in the channel and yielding in the lithosphere.

### Conclusions

A simple model of the deformation processes taking place at subduction zones predicts that rapid displacement offsets along the top of the downgoing slab near the trench result in strain concentrations near the fault. These concentrations broaden with time by strain diffusion. The calculated horizontal strain as a function of time at a given distance from the fault is pulslike in nature and exhibits a velocity, shape, and amplitude which, when compared to observations, provide strong constraints on the viscosity of the low-viscosity channel and, to a lesser extent, constrain the thicknesses of the lithosphere and channel. At distances greater than half a fault length from the fault center,

the dominant deformation phenomenon should be a diffusing horizontal strain pulse accompanied by secondary tilts and vertical movements.

Direct and inferred horizontal crustal strain data indicate that the strain diffusion process in northern Japan is associated with strain pulses. The presence of strain pulses in crustal deformation data requires that the viscosity increase rapidly below the low-viscosity channel. Direct and inferred observations of crustal strain in northern Japan reflect the same character as the model curves and indicate a viscosity for the low-viscosity channel of  $0.6 \times 10^{19}$  to  $4 \times 10^{19}$  poise on the east coast, near the quakes, and  $2 \times 10^{19}$  to  $20 \times 10^{19}$  poise on the west coast.

### References

- Anderson, D. L., Accelerated plate tectonics, *Science*, **187**, 1077–1079, 1975.
- Ashby, M. F., and R. A. Verrall, Micro-mechanisms of flow and fracture, and their relevance to the rheology of the upper mantle, *Phil. Trans. Roy. Soc. London, Ser. A.*, **288**, 59–95, 1977.
- Barker, T. G., Quasi-static motions near the San Andreas Fault zone, *Geophys. J. Roy. Astron. Soc.*, **45**, 689–705, 1976.
- Cohen, S. C., Viscoelasticity and Post-seismic crustal deformations (abstract), *EOS, Trans. Amer. Geophys. U.*, **60**, 316, 1979.
- Elsasser, W. M., Convection and stress propagation in the upper mantle, in *The Application of Modern Physics to the Planetary Interiors*, pp. 223–246, S. K. Runcorn, ed., John Wiley, New York, 1967.
- Fujii, N., Propagating crustal deformation and stress diffusion (in Japanese), *Programme and Abstracts*, Seis. Soc. of Japan, no. 1, 117, 1978.
- Ikeda, K., Three dimensional geodetic inversion method for stress modelling in the lithosphere (abstract), *EOS, Trans. Amer. Geophys. U.*, **60**, 316, 1979.

- Kasahara, M., and S. Suzuki, Horizontal strain accumulation observed by the optical-electro means in the eastern part of Hokkaido (Teshikaga and Nemuro) (in Japanese), *Report of Coordinating Committee for Earthquake Prediction*, 19, 4-6, 1978.
- McConnell, R. K., Viscosity of the mantle from relaxation time spectra of isostatic adjustment, *J. Geophys. Res.*, 73, 7089-7105, 1968.
- Melosh, H. J., Nonlinear stress propagation in the earth's upper mantle, *J. Geophys. Res.*, 81, 5621-5632, 1976.
- Melosh, H. J., and A. Raefsky, Surface deformation due to vertical dip-slip faulting in a non-newtonian earth (abstract), *EOS, Trans. Amer. Geophys. U.*, 60, 316, 1979.
- Nur, A., and G. Mavko, Post-seismic viscoelastic rebound, *Science*, 183, 204-206, 1974.
- Peltier, W. R., W. F. Farrell, and J. A. Clark, Glacial isostasy and relative sea level: a global finite element model, in: *Numerical Modeling in Geodynamics, Tectonophys.*, 50, pp. 81-110, M. N. Toksoz, ed., 1978.
- Rundle, J. B., Anelastic processes in strike slip faulting: application to the San Francisco earthquake of 1906, Ph. D. dissertation, Univ. of Calif. at Los Angeles, Los Angeles, 1976.
- Rundle, J. B., Viscoelastic crustal deformation by finite quasi-static sources, *J. Geophys. Res.*, 83, 5937-5945, 1978.
- Rundle, J. B., and D. D. Jackson, A viscoelastic relaxation model for post-seismic deformation from the San Francisco earthquake of 1906, *Pure Appl. Geophys.*, 115, 401-411, 1977a.
- Rundle, J. B., and D. D. Jackson, A three-dimensional viscoelastic model of a strike slip fault, *Geophys. J. Roy. Astron. Soc.*, 49, 575-591, 1977b.
- Rundle, J. B., and D. D. Jackson, a kinematic viscoelastic model of the San Francisco earthquake of 1906, *Geophys. J. Roy. Astron. Soc.*, 50, 441-458, 1977c.
- Rundle, J. B., and W. Thatcher, A stress relaxation model for southern California uplift (abstract), *EOS, Trans. Amer. Geophys. U.*, 60, 321, 1979.
- Sacks, I. S., Anomalous island arc asthenosphere and continental growth, in *Carnegie Inst. Wash. Year Book* 74, pp. 256-266, 1975.
- Stocker, R. L., and M. F. Ashby, On the rheology of the upper mantle, *Rev. Geophys. and Space Phys.*, 11, 391-426, 1973.
- Shimazaki, K., Nemuro-oki earthquake of June 17, 1973: a lithospheric rebound at the upper half of the interface, *Phys. Earth Planet. Interiors*, 9, 314-327, 1974.
- Takagi, A., A. Hasegawa, and N. Umino, Seismic activity in the northeastern Japan arc, *J. Phys. Earth*, 25 (suppl.), S95-S104, 1977.
- Tanaka, K., Propagation characteristics of earthquake and volcanic activity (in Japanese), *Programme and Abstracts*, Seis. Soc. of Japan, no. 1, 81, 1978.
- Thatcher, W., and J. B. Rundle, A model for the earthquake cycle in under-thrust zones (abstract), *EOS, Trans. Amer. Geophys. U.*, 60, 321, 1979.
- Yang, M., Time dependent tectonic deformation and stress of lithosphere after earthquakes (abstract), *EOS, Trans. Amer. Geophys. U.*, 60, 316, 1979.

#### ISOTOPIC STUDIES OF CENOZOIC ANDEAN CALC-ALKALINE ROCKS

G. R. Tilton

In previous reports, James and his colleagues outlined extensive petrogenetic studies of Cenozoic calc-alkaline lavas from southern Peru. A complete summary of the results was given in the last Report (James, 1978). From a geochemical standpoint the observations include



data on selected major elements, large ion lithophile (LIL) elements, nickel, and isotopic measurements on strontium and oxygen. James originally explained the origin of the lavas in terms of a disequilibrium partial melting of mantle source material. Such an explanation best fit the observations that the lavas contain highly radiogenic strontium with  $^{87}\text{Sr}/^{86}\text{Sr}$  ratios of 0.7053–0.7079, and that the Rb-Sr data define “pseudo isochrons” yielding ages of 400 m.y. but with different apparent initial  $^{87}\text{Sr}/^{86}\text{Sr}$  ratios. Nevertheless, subsequent oxygen isotope work (Magaritz *et al.*, 1978) showed that the lavas contain a small but significant component of crustal material, based on the observation that the  $^{18}\text{O}/^{16}\text{O}$  ratios in the lavas are measurably higher than in similar lavas from oceanic island arcs where the source is predominantly or entirely in the mantle. This led James to propose that the crustal component consists of subducted greywacke sediments that originated from the continental crust in southern Peru, which is known to contain Precambrian rocks. The present investigations apply lead and some neodymium isotope data as additional tracers to study the problem of the origin of the lavas. Other data from northern and central Chile are compared with the Peruvian results.

### Geological Settings

The setting of the Peruvian lavas is uniquely different from that of most volcanic lavas, especially those from ocean basins, in two important ways: (1) in Peru the lavas were extruded in areas of known outcrops of Precambrian sialic rocks, and (2) the crust in southern Peru attains exceptionally great thickness, over 70 km in places (James, 1971). Perhaps of equal importance is the great width of the belt of thick (over 60 km) crust, about 200 km in southern Peru. The locations of the Arequipa and Barroso volcanic areas are designated by the symbols A and B in Fig. 23. Area C

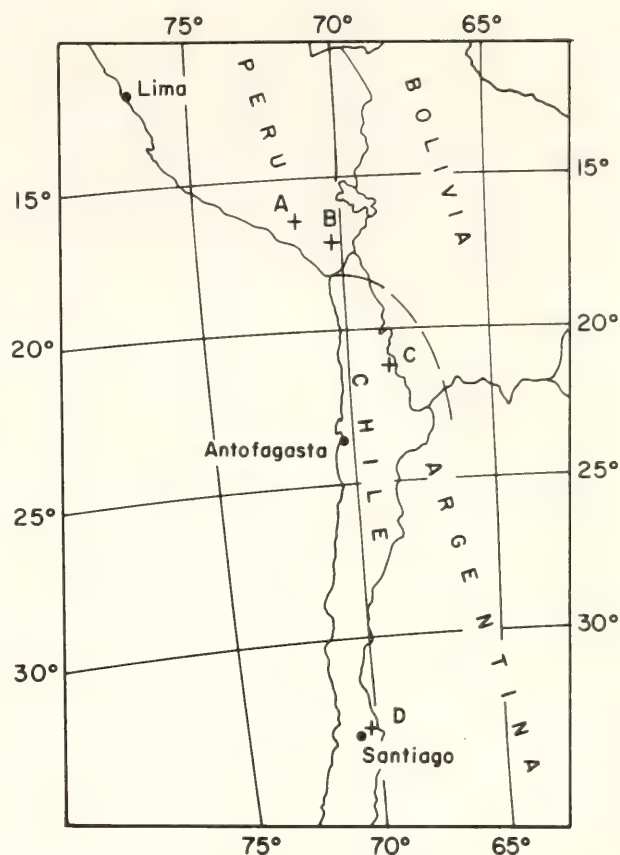


Fig. 23. Locations of samples. A: Arequipa Volcanics; B: Barroso Volcanics; C: Ascotan-Ollague Area, Chile; D: Disputada Mine Area, Chile. Dashed line is approximate southern limit of observed Precambrian basement complex in northern Chile and southern Bolivia.

is situated in northern Chile beyond the limit of known Precambrian basement rocks but still within the belt of thick crust, but the width of the belt has thinned to about 50 km here. At C the  $^{87}\text{Sr}/^{86}\text{Sr}$  ratios (Pichler and Zeil, 1972; analyses by C. E. Hedge) vary between 0.7051 and 0.7071 and, as in southern Peru, the Rb-Sr data plot approximately along a 500-m.y. “pseudo isochron.” Area D is in the high Andes east of Santiago near the Disputada copper mine. The maximum crustal thickness in this area is estimated at 50–60 km, but such depths are attained only locally under the crest of the Andes. Significantly, the  $^{87}\text{Sr}/^{86}\text{Sr}$  ratios of the volcanic rocks here are 0.704 for all values of the Rb/Sr ratio (Drake, 1979).

Ages

All rocks are geologically very young. The Arequipa and Barroso volcanics are of Pliocene-Quaternary age. The northern Chile andesites (*C* in Fig. 23) are Quaternary, and the central Chile samples are Miocene or younger.

Results and Discussions

The lead isotope ratios from localities *A*, *B*, and *D* are given in Table 3 and plotted in correlation diagrams in Fig. 24. The Nd isotope data are listed in Table 4, together with relevant data from additional samples obtained from other laboratories.

One of the most remarkable features of the lead data are the low values of the <sup>206</sup>Pb/<sup>204</sup>Pb ratios in the Arequipa and Barroso volcanics. The ratio for PE 24 is one of the lowest found in any young volcanic rock. Inspection of Fig. 24 shows

immediately that the lead in the Arequipa and Barroso volcanics cannot be accounted for by the kinds of lead found in oceanic volcanic rocks (which plot along regression line *ORL*) or by lead in pelagic sediments from the southern Pacific Ocean basin. DePaolo and Wasserburg (1977) reached a similar conclusion from Nd isotope data on lavas of the El Misti volcano near Arequipa (Table 4). The <sup>143</sup>Nd/<sup>144</sup>Nd ratios in andesite and rhyolite are lower than the ratios for either ocean ridge basalt or pelagic sediments from DSDP leg V. The Nd data obtained in the present study on PE 82 and PE 129 lead to the same conclusions as those reached by DePaolo and Wasserburg. The Pb and Nd data thus support the conclusion reached by James (1978) and by Magaritz *et al.* (1978) that these volcanic rocks contain a component of crustal origin.

Comparison of Pb and Nd data from areas *A* and *B* with those from *D*

TABLE 3. Isotopic Composition and Concentration of Lead in Andean Igneous Rocks

	<sup>206</sup> Pb/ <sup>204</sup> Pb	<sup>207</sup> Pb/ <sup>204</sup> Pb	<sup>208</sup> Pb/ <sup>204</sup> Pb	Concentration PPM
Arequipa Volcanics: ( <i>A</i> in Fig. 23)				
PE 24	17.794	15.623	38.784	12.47
PE 26	18.019	15.626	38.737	12.20
PE 47	17.845	15.612	38.724	11.35
PE 49	17.844	15.610	38.643	16.40
PE 82	17.984	15.592	38.603	13.38
PE 83	17.948	15.603	38.657	16.17
Barroso Volcanics: ( <i>B</i> in Fig. 23)				
PE 129	18.277	15.597	38.527	22.11
PE 130	18.291	15.589	38.471	10.66
PE 131	18.246	15.584	38.467	15.67
PE 144	18.157	15.581	38.540	15.90
PE 145	18.166	15.588	38.708	16.46
Central Chile: ( <i>D</i> in Fig. 23)				
D-8D Andesite	18.624	15.615	38.542	7.01
D-5C Rhyolite	18.612	15.608	38.527	11.26
D-16B Quartz Diorite	18.600	15.624	38.545	15.48
D-22 Quartz Diorite	18.636	15.617	...*	7.60
Pyrite, Disputada Mine	18.611	15.615	38.510	0.28

\* Unspiked mass spectrometer run failed. Concentration calculated by assuming <sup>208</sup>Pb/<sup>206</sup>Pb equal to that in sample D-8D.



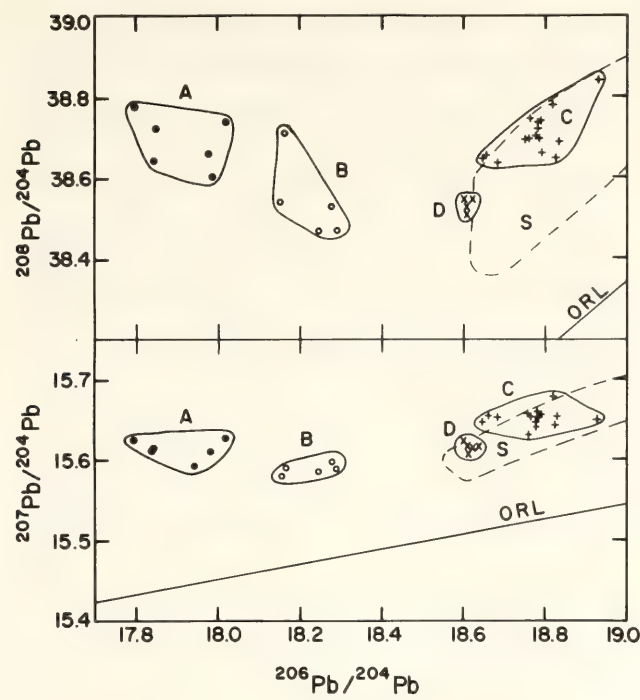


Fig. 24. Lead isotope correlation diagram for Andean samples. Letters refer to localities given in Fig. 23. Data for area C are unpublished analyses by S. E. Church. ORL = regression line for ocean basin tholeiites and alkali basalts. Dashed field labeled S = pelagic sediments and manganese nodules from the south Pacific Ocean Basin, analyses taken from the literature.

strengthens this conclusion. Differences in Nd isotope ratios between lavas from the Marianas arc and South America (Table 4) show quite clearly that the

geochemical conditions are more “oceanic” at locality D than in southern Peru. The same conclusion was reached by Klerkx *et al.* (1977) in a comprehensive summary of Sr isotope data from the central and southern Andes. The  $^{206}\text{Pb}/^{204}\text{Pb}$  ratios at D are higher than those at A and B, and in that sense are more similar to the ratios in calc-alkaline rocks from oceanic arcs such as the Marianas Islands (Meijer, 1976) or Aleutian Islands (Kay *et al.*, 1978). The  $^{207}\text{Pb}/^{204}\text{Pb}$  ratios from volcanic rocks at D are higher than those from the Marianas (Meijer, 1976) and Tonga (Sinha and Hart, 1972) arcs, which plot along ORL in Fig. 24. The Pb ratios at D could be strongly controlled by lead from pelagic sediments of the Pacific Ocean basin according to the fields shown in Fig. 24. Since there is clear evidence that pelagic-sediment Pb does not control the isotopic composition of Pb in the Marianas and Tonga arcs and in the Arequipa and Barroso volcanics, the general agreement in isotope ratios from C and D with ratios from the sediments may well be fortuitous. The ratios at C and D are, in fact, very similar to those found in the Cascade volcanics of the northwestern U.S., for which Church (1976) has given strong evidence that

TABLE 4. Isotopic Composition of Neodymium

Sample	$^{143}\text{Nd}/^{144}\text{Nd}^*$	$\epsilon_{\text{Nd}}^{\dagger}$	Reference $^{\ddagger}$
Chile Andesite, D-8D	$0.512860 \pm 19$	+4.1	
Chile Quartz Diorite, D-16B	$0.512890 \pm 19$	+4.7	
Arequipa Volcanic, PE 82	$0.512291 \pm 13$	-7.0	
Barroso Volcanic, PE 129	$0.512514 \pm 19$	-2.6	
Peru Andesite, El Misti		-8.9	DPW
Peru Rhyolite, El Misti		-12.7	DPW
Andesite, Marianas Arc		+6.8	DPW
Mean Ocean Ridge Basalt		+10	DPW
Pelagic Sediment, DSDP Leg V, Hole 37		-3.3	MCW

\*  $^{143}\text{Nd}/^{144}\text{Nd}$  ratios normalized to  $^{146}\text{Nd}/^{144}\text{Nd} = 0.72190$ . Values after  $\pm$  are standard deviations.  
 $\dagger \epsilon = (R_s/R_f - 1)10^4$ , where  $R_s = ^{143}\text{Nd}/^{144}\text{Nd}$  of sample,  $R_f = ^{143}\text{Nd}/^{144}\text{Nd}$  of chondritic meteorites ( $= 0.51265$  for the conditions used in this work).  
 $\ddagger$  DPW: De Paolo and Wasserburg (1977); MCW: McCulloch and Wasserburg (1978).

the component of lead responsible for the high  $^{207}\text{Pb}/^{204}\text{Pb}$  ratios is derived from continental sources rather than from pelagic sediments of the NE Pacific Ocean basin. For these reasons, the agreement in lead ratios between volcanic rocks of areas *C* and *D* and the pelagic sediments of the southern Pacific Ocean cannot be taken as proof that the lead in the rocks is due to lead from the sediments.

There are three general ways in which crustal material might be added to the magmas of the Arequipa and Barroso volcanics. One is through subduction of continent-derived sediments, as proposed by James (1978) and by Klerkx *et al.* (1977). Other more direct mechanisms would involve contamination at upper or lower crustal levels. We consider each of these mechanisms in turn.

James (1978) suggested that subduction of greywacke sediments best fit the Sr and other trace element data from the two volcanic series. In particular, greywacke is sufficiently close to the calc-alkaline rocks in bulk composition so that rather substantial fractions of it can be added to mantle-derived material to raise the  $^{87}\text{Sr}/^{86}\text{Sr}$  ratios to 0.706–0.707 without seriously affecting the bulk chemistry of the resulting lava. Greywacke is rare in the sediments along the coast of South America, and we have no knowledge of the isotopic composition of Pb expected in such a component. We can, however, make a comparison with Pb data from greywacke sediments in the western U.S. Data from the Franciscan assemblage of California (Sinha and Davis, 1971) and the Tyee Formation of northwestern Oregon (Church, 1976) show generally higher  $^{206}\text{Pb}/^{204}\text{Pb}$  and  $^{208}\text{Pb}/^{204}\text{Pb}$  ratios than those in the Arequipa and Barroso volcanics. For example, in Oregon the  $^{206}\text{Pb}/^{204}\text{Pb}$  ratios are all greater than 19.0, the  $^{208}\text{Pb}/^{204}\text{Pb}$  ratios greater than 38.95. In California the  $^{206}\text{Pb}/^{204}\text{Pb}$  ratios range from 18.44 to 19.33, averaging 18.78. The average  $^{208}\text{Pb}/^{204}\text{Pb}$  ratio is 38.59. The tectonic settings in California and Oregon are

similar to that of any presumed greywacke source in southern Peru in that all three areas are located along continental margins that border on Precambrian cratons containing rocks that are about 2000 m.y. old. The Pb data, as best they can now be evaluated, do not lend support to the greywacke subduction process as a mechanism for adding continental lead to the Arequipa and Barroso lavas.

We next consider the possibility of contamination with material in an upper crustal environment, or alternatively the addition of granitic material from the upper crust to the magmas through subduction thereby contaminating the magmas, as favored by Klerkx *et al.* (1977). To explain the Pb and Sr data, the contamination would have to be very selective. Potassium feldspar from a Precambrian terrane is the most likely mineral to dominate the contamination because it would contain highly radiogenic Sr and relatively nonradiogenic Pb and because it is one of the minerals most easily attacked in hydrothermal processes. The  $^{208}\text{Pb}/^{204}\text{Pb}$  ratios argue against this mechanism. If the low  $^{206}\text{Pb}/^{204}\text{Pb}$  ratios are the result of potassium feldspar contamination, the  $^{208}\text{Pb}/^{204}\text{Pb}$  ratios should also be anomalously low because potassium feldspars are strongly depleted in both U and Th with respect to Pb. However the  $^{208}\text{Pb}/^{204}\text{Pb}$  ratios for localities *A*, *B*, *C*, and *D* are all nearly equal (Fig. 24). Values of about 37.9 and 38.2 would be expected for the  $^{208}\text{Pb}/^{204}\text{Pb}$  ratios of the Arequipa and Barroso volcanics for the feldspar contamination process. The mechanism must selectively decrease the U/Pb ratio in the contaminant phase without reducing the Th/Pb ratio appreciably.

Granulitic rocks, which are probably constituents of the lower crust, qualitatively meet the requirement for U-Th differentiation. Since granulites form under high pressure conditions, LIL elements, including U, Th, and Pb tend to be excluded. It is well known that U/Pb



ratios in such rocks tend to be lower than those in most other igneous rocks (e.g., Montgomery and Hurley, 1978). It is also known, both from direct measurements of U and Th concentrations in granulites (e.g., Heier and Thoresen, 1971) and from calculated Th/U ratios based on accumulation of radiogenic  $^{206}\text{Pb}$  and  $^{208}\text{Pb}$  in Precambrian granulite (Montgomery and Hurley, 1978), that U is generally excluded more strongly than Th from granulitic rocks. Depending on the age and metamorphic history of the granulite, it is also possible to generate high  $^{207}\text{Pb}/^{204}\text{Pb}$  ratios.

Montgomery and Hurley (1978) give Sr and Pb isotopic analyses from granulite of the Guayana shield of southern Venezuela that illustrate the kind of contamination required to explain the Arequipa and Barroso volcanic Pb and Sr data. Different whole-rock specimens of the granulite establish an age of  $2022 \pm 67$  m.y. by the Rb-Sr method. The mean  $^{87}\text{Sr}/^{86}\text{Sr}$  ratio of the samples is 0.80 with a standard deviation of 0.02, providing a source of radiogenic Sr. The mean Sr concentration is 105 ppm.

The lead data of the granulite also qualitatively fit the requirements of the model. In 11 samples of granulite the mean isotope ratios are  $^{206}\text{Pb}/^{204}\text{Pb} = 18.30$ ;  $^{207}\text{Pb}/^{204}\text{Pb} = 16.50$ ;  $^{208}\text{Pb}/^{204}\text{Pb} = 43.01$ . Taking the ratios for the samples of area D as "normal," the  $^{206}\text{Pb}/^{204}\text{Pb}$  ratio is low in the granulite, while the  $^{207}\text{Pb}/^{204}\text{Pb}$  and  $^{208}\text{Pb}/^{204}\text{Pb}$  ratios are high. Qualitatively, this is the trend described by the Arequipa and Barroso volcanic leads. It is not possible to derive a quantitative mixing model using the granulite leads and a reasonable mantle lead as the sources of the Arequipa and Barroso volcanic leads, but there is no particular reason to expect an exact fit from these data, which involve a small number of samples from a broad area. Granulites from the basement complex of southern Peru will provide a better evaluation of this mixing model.

From Nd and Sr isotopic studies of Tertiary volcanic lavas in northwest Scotland, Carter *et al.* (1978) conclude that some of the magmas have been contaminated by the Lewisian granulite and amphibolite facies basement through which they were erupted. Significantly, the Scottish lavas do not occur in a subduction zone environment, showing that a subduction process is not essential to the production of the kinds of isotope patterns observed in southern Peru.

### Summary

(1) The lead and neodymium isotope data support the conclusion that material from the Precambrian sialic crust is involved in the production of calc-alkaline lavas of the Arequipa and Barroso volcanic rocks in southern Peru. (2) The involvement of crustal material may be aided by the presence of a wide belt of thick crust, more than 60 km deep, in the area where the volcanic rocks occur. (3) The mechanism of the contamination is not clearly established, but may involve contamination with lower crustal (granulitic or amphibolitic) material. (4) Lead, neodymium, and strontium isotopic ratios in calc-alkaline rocks of the Disputada Mine district of central Chile more closely match the ratios of oceanic lavas from the Marianas and Tonga arcs than those of the Arequipa and Barroso volcanics. Any continentally derived contamination in the central Chile rocks apparently consists of geologically young material with a large oceanic component.

### References

- Carter, S. R., N. M. Evenson, P. J. Hamilton, and R. K. O'Nions, *Science*, **202**, 743-746, 1978.
- Church, S. E., The Cascade Mountains revisited: A reevaluation in the light of new lead isotopic data, *Earth Planet. Sci. Lett.*, **29**, 175-188, 1976.

- DePaolo, D. J., and G. J. Wasserburg, The sources of island arcs as indicated by Nd and Sr isotopic studies, *Geophys. Res. Lett.*, 4, 466–468, 1977.
- Drake, Robert E., personal communication, 1979.
- Heier, K. S., and K. Thoresen, Geochemistry of high grade metamorphic rocks, Lofoten-Vesteralen, North Norway, *Geochim. Cosmochim. Acta*, 35, 89–99, 1971.
- James, David E., Andean crustal and upper mantle structure, *J. Geophys. Res.*, 76, 3246–3271, 1971.
- James, David E., On the origin of the calc-alkaline volcanics of the central Andes: A revised interpretation, *Carnegie Inst. Wash. Year Book* 77, 562–590, 1978.
- Kay, R. W., S.-S. Sun, and C.-N. Lee-Hu, Pb and Sr isotopes in volcanic rocks from the Aleutian Islands and Pribilof Islands, Alaska, *Geochim. Cosmochim. Acta*, 42, 263–273, 1978.
- Klerkx, J., S. Deutsch, H. Pichler, and W. Zeil, Strontium isotopic composition and trace element data bearing on the origin of Cenozoic volcanic rocks of the central and southern Andes, *J. Volcanology and Geothermal Research*, 2, 49–71, 1977.
- Magaritz, M., D. J. Whitford, and D. E. James, Oxygen isotopes and the origin of high  $^{87}\text{Sr}/^{86}\text{Sr}$  andesites, *Earth Planet. Sci. Lett.*, 40, 220–230, 1978.
- McCulloch, M. T., and G. J. Wasserburg, Sm-Nd and Rb-Sr chronology of continental crust formation, *Science*, 200, 1003–1011, 1978.
- Meijer, Arend, Pb and Sr isotopic data bearing on the origin of volcanic rocks from the Mariana island-arc system, *Bull. Geol. Soc. Amer.*, 87, 1358–1369, 1976.
- Montgomery, C. W., and P. M. Hurley, Total-rock U-Pb and Rb-Sr systematics in the Imataca series, Guayana shield, Venezuela, *Earth Planet. Sci. Lett.*, 39, 281–290, 1978.
- Pichler, W., and W. Zeil, The Cenozoic rhyolite-andesite association of the Chilean Andes, *Bull. Volcanol.*, 35, 424–452, 1972.
- Sinha, A. K., and T. E. Davis, Geochemistry of Franciscan volcanic and sedimentary rocks from California, *Carnegie Inst. Wash. Year Book* 69, 394–400, 1971.
- Sinha, A. K., and S. R. Hart, A geochemical test of the subduction hypothesis for the generation of island arc magmas, *Carnegie Inst. Wash. Year Book* 71, 309–312, 1972.

#### ND ISOTOPIC COMPOSITION OF RECENT ANDESITES FROM INDONESIA

D. J. Whitford,\* W. M. White,  
P. A. Jezek,† and I. A. Nicholls‡

#### Introduction

Neodymium isotopes have been used in several recent studies of lavas from both island arcs and active continental margins in an attempt to resolve some of the long-standing problems surrounding the origin of this group of rocks (DePaolo and Wasserburg, 1977; Hawkesworth *et al.*, 1977, 1979). Andesitic rocks from the island arcs of the Marianas, New Britain, and the South Sandwich Islands are characterized by relatively high  $^{143}\text{Nd}/^{144}\text{Nd}$  ratios (0.5129–0.5131). Andesites from the Andes are characterized by a much broader range of compositions from 0.5130 (Ecuador) to 0.5120 (Peru), which suggests a greater variability in their sources and, for the Peruvian lavas, possible assimilation of old continental crust (De Paolo and Wasserburg, 1977; Hawkesworth *et al.*, 1979).

Perhaps of greater importance is the relationship between  $^{143}\text{Nd}/^{144}\text{Nd}$  and  $^{87}\text{Sr}/^{86}\text{Sr}$ . Oceanic basalts with  $^{87}\text{Sr}/^{86}\text{Sr}$  ratios of 0.7025–0.7055, exhibit a well-defined inverse correlation that is gen-

\* University of British Columbia, Vancouver, British Columbia.

† Smithsonian Institution, Washington, D.C.

‡ Department of Earth Sciences, Monash University, Clayton, Victoria, Australia.



erally assumed to reflect the isotopic heterogeneity of the mantle (DePaolo and Wasserburg, 1976; Richard *et al.*, 1976; O'Nions *et al.*, 1977). The isotopic compositions of many andesitic rocks are displaced from this mantle array toward higher  $^{87}\text{Sr}/^{86}\text{Sr}$  ratios. This phenomenon has been interpreted to result from interaction of oceanic crust with seawater ( $^{87}\text{Sr}/^{86}\text{Sr} = 0.709$ ) and from the subsequent incorporation of subducted crust into the parental magmas of the erupted lavas.

It is the purpose of this study to further investigate island arc petrogenetic processes using the isotopic composition of Nd in Quaternary lavas from two arcs of Indonesia—the Sunda arc in Java and the Banda arc of eastern Indonesia.

#### *Quaternary Lavas from Indonesia*

The Pleistocene and recent lavas from the Sunda arc are typical of rocks from a mature island arc. Those showing affinities with island arc tholeiites lie 100–150 km above the seismically active Benioff zone, whereas those with compositions ranging from calc-alkaline to high-K calc-alkaline occur 200–250 km above the seismic zone. More distant from the trench, where the depth to the Benioff zone is approximately 400 km, high-K alkaline lavas have been erupted from the Pleistocene volcano, Muriah.

$^{87}\text{Sr}/^{86}\text{Sr}$  ratios range from 0.704 to 0.706, with most rocks between 0.704 and 0.705 (Whitford, 1975a). The few scattered ratios between 0.7052 and 0.7060 were interpreted to result from crustal contamination, either during ascent of the magma or in the case of the volcano Papandajan, from subduction and subsequent melting of continental-derived sediments.

By contrast, the geochemistry of the Recent lavas from the Banda arc appears to reflect their unusual tectonic setting, where subduction of continental material is taking place beneath a volcanic arc that is underlain by Mesozoic

oceanic crust. In terms of their major and trace element abundances these rocks are typical island arc lavas. On the other hand, they are characterized by a range of unusually high  $^{87}\text{Sr}/^{86}\text{Sr}$  ratios, up to 0.7095 (Whitford and Jezek, 1977). Furthermore, the rocks show an enrichment in  $\delta^{18}\text{O}$  (up to 9.2‰ relative to SMOW) that correlates with  $^{87}\text{Sr}/^{86}\text{Sr}$ ; this is interpreted as a result of subduction and subsequent melting of sialic material derived from the Australian continental margin (Magaritz *et al.*, 1978; Whitford and Jezek, 1977).

#### *Results*

$^{143}\text{Nd}/^{144}\text{Nd}$  ratios are listed in Table 5 together with  $^{87}\text{Sr}/^{86}\text{Sr}$  ratios and the concentrations of  $\text{SiO}_2$  and  $\text{K}_2\text{O}$ .  $^{143}\text{Nd}/^{144}\text{Nd}$  ratios range from 0.51286 to 0.51248 and exhibit no correlation with either  $\text{K}_2\text{O}$  or  $\text{SiO}_2$ . There is a poorly defined overall inverse correlation between  $^{87}\text{Sr}/^{86}\text{Sr}$  and  $^{143}\text{Nd}/^{144}\text{Nd}$  (Fig. 25). The measured Nd ratios lie well within the range defined by analyzed lavas from other island arcs and active continental margins (Fig. 25), although the high  $^{87}\text{Sr}/^{86}\text{Sr}$  ratios clearly distinguish the lavas from the Banda arc.

#### *Discussion*

Most of the lavas from the Sunda arc in Java plot within or close to the mantle array (Fig. 25). That they plot toward the high  $^{87}\text{Sr}/^{86}\text{Sr}$  side of the array suggests that mantle-type isotopic compositions may have been modified by the addition of a high  $^{87}\text{Sr}/^{86}\text{Sr}$  component, either altered oceanic crust, or perhaps subducted sediments, possibly derived from Australia.

The anomalous calc-alkaline sample 71-991 is characterized by a relatively high  $^{87}\text{Sr}/^{86}\text{Sr}$  ratio together with an anomalous enrichment in LIL elements, particularly in relation to the depth to the underlying Benioff zone (Whitford, 1975a; Whitford and Nicholls, 1976).

TABLE 5. Nd and Sr Isotopic Composition of Quaternary Lavas from Indonesia

Sample	Suite‡	SiO <sub>2</sub> †	K <sub>2</sub> O†	<sup>87</sup> Sr/ <sup>86</sup> Sr†	<sup>143</sup> Nd/ <sup>144</sup> Nd ± 2σ Mean*
<i>Sunda arc</i>					
71-1026	CA	50.7	1.08	0.70476	0.51283 ± 3
72-1142	CA	56.2	2.24	0.70476	0.51283 ± 3
72-1076	CA	52.9	1.63	0.70498	0.51286 ± 3
71-991	ACA	58.8	1.32	0.70565	0.51262 ± 4
71-980	HKCA	56.8	2.64	0.70488	0.51269 ± 5
71-982	HKCA	48.1	1.61	0.70472	0.51274 ± 3
72-940	A	54.4	8.0	0.70424	0.51276 ± 3
					0.51276 ± 2
<i>Banda arc</i>					
T7	CA	55.9	0.96	0.70842	0.51258 ± 3
T8	CA	59.4	1.17	0.70947	0.51248 ± 3
CH23	HKCA	57.0	2.52	0.70651	0.51265 ± 3
CH29	HKCA	58.4	2.07	0.70767	0.51258 ± 3

\* <sup>143</sup>Nd/<sup>144</sup>Nd ratios have been normalized to <sup>146</sup>Nd/<sup>144</sup>Nd = 0.7219. BCR-1, <sup>143</sup>Nd/<sup>144</sup>Nd = 0.51270 ± 3. UCSD Nd, <sup>143</sup>Nd/<sup>144</sup>Nd = 0.51197 ± 2.  
† Sr isotopic compositions as well as SiO<sub>2</sub> and K<sub>2</sub>O concentrations from Whitford (1975) and Whitford and Jezek (*Year Book* 76, 845–855). <sup>87</sup>Sr/<sup>86</sup>Sr ratios have been normalized to <sup>88</sup>Sr/<sup>86</sup>Sr = 0.1194 and are reported relative to E + A Sr <sup>87</sup>Sr/<sup>86</sup>Sr = 0.70800 (Banda arc) and NBS SRM 982 Sr <sup>87</sup>Sr/<sup>86</sup>Sr = 0.71022 (Sunda arc).  
‡ Suites: CA—calc-alkaline; ACA—anomalous calc-alkaline; HKCA—high-K calc-alkaline; A—alkaline (high-K).

High <sup>207</sup>Pb/<sup>204</sup>Pb ratios (up to 15.77 at <sup>206</sup>Pb/<sup>204</sup>Pb = 18.98) in lavas from this volcano suggested the involvement of an old crustal component in their generation, the most likely source being from subducted sediments (Whitford, 1975b). Sample 71-991 plots close to the mantle array in Fig. 25, although it is clearly enriched in <sup>87</sup>Sr/<sup>86</sup>Sr. The relatively low <sup>143</sup>Nd/<sup>144</sup>Nd ratio is compatible with the view that the source of this lava has been contaminated with a crustal component characterized by radiogenic Sr and non-radiogenic Nd.

The high-K trachyte 72-940 is from the alkaline volcano Muriah. It plots well within the mantle array (Fig. 25), which reinforces the argument that despite the enrichment in K and related elements, these rocks are mantle derived and do not manifest crustal contamination. In addition, the <sup>143</sup>Nd/<sup>144</sup>Nd and <sup>87</sup>Sr/<sup>86</sup>Sr ratios are close to those predicted for single-stage mantle evolution (e.g., O’Nions *et al.*, 1977), a result which

implies that the extreme large ion lithophile element enrichment in the source regions of these lavas (Whitford, 1975b) must have occurred only shortly before their formation. Any long-term enrichment for periods greater than a few hundred million years would have resulted in relatively lower <sup>143</sup>Nd/<sup>144</sup>Nd ratios and substantially higher <sup>87</sup>Sr/<sup>86</sup>Sr ratios.

The four analyzed lavas from the Banda arc plot in a linear field from the mantle array toward the average upper crustal composition (DePaolo and Wasserburg, 1979). The Banda arc array projects back toward the field defined by the samples from the Sunda arc which may therefore model the uncontaminated end member in the mixing process. By themselves, the Nd results do not provide conclusive evidence for the mixing model, but it should be noted that they are consistent with the sediment subduction and melting model. It may also be significant that the maximum proportion of sialic material involved is about 25–30%, very



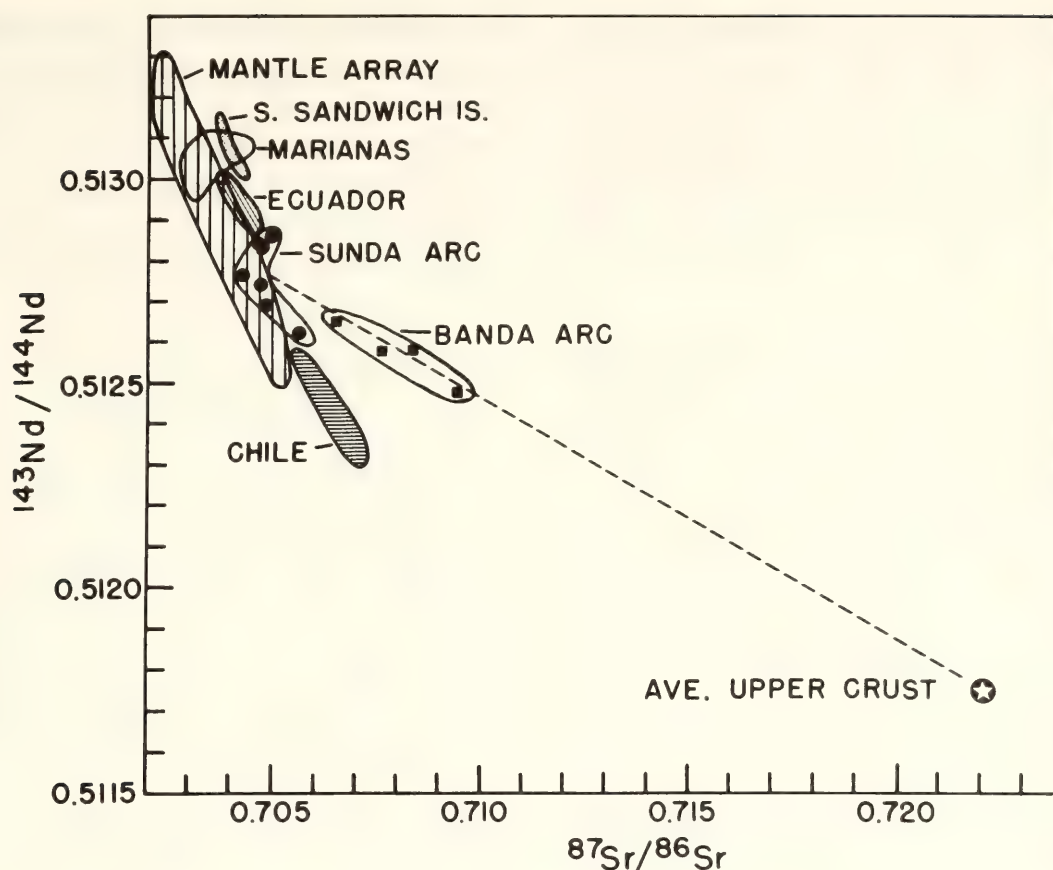


Fig. 25.  $^{143}\text{Nd}/^{144}\text{Nd}$  vs.  $^{87}\text{Sr}/^{86}\text{Sr}$  for Quaternary lavas from the Sunda and Banda arcs of Indonesia. Also plotted are fields of lavas from other island arcs and the active continental margin of South America (De Paolo and Wasserburg, 1977; Hawkesworth *et al.*, 1977, 1979), the mantle array defined by oceanic basalts (O'Nions *et al.*, 1977; Richard *et al.*, 1976; White and Hofmann, *Year Book 77*, pp. 596–606, and unpublished), and De Paolo and Wasserburg's (1979) estimate of the average upper crust. The lavas of the Banda arc appear to lie on a mixing line between the mantle array and the upper crust.

close to that determined by Magaritz *et al.* (1978) on the basis of relationships between  $\delta^{18}\text{O}$  and  $^{87}\text{Sr}/^{86}\text{Sr}$ .

### References

- DePaolo, D. J., and G. J. Wasserburg, Nd isotopic variations and petrogenetic models, *Geophys. Res. Lett.*, **3**, 249–252, 1976.
- DePaolo, D. J., and G. J. Wasserburg, The sources of island arcs as indicated by Nd and Sr isotopic studies, *Geophys. Res. Lett.*, **4**, 465–468, 1977.
- DePaolo, D. J., and G. J. Wasserburg, Petrogenetic mixing models and Nd-Sr isotopic patterns, *Geochim. Cosmochim. Acta*, **43**, 615–627, 1979.
- Hawkesworth, C. J., R. K. O'Nions, R. J. Pankhurst, P. J. Hamilton, and N. M. Evensen, A geochemical study of island-arc and back-arc tholeiites from the Scotia Sea, *Earth Planet. Sci. Lett.*, **36**, 253–262, 1977.
- Hawkesworth, C. J., M. J. Norry, J. C. Roddick, P. E. Baker, P. W. Francis, and R. S. Thorpe,  $^{143}\text{Nd}/^{144}\text{Nd}$ ,  $^{87}\text{Sr}/^{86}\text{Sr}$ , and incompatible element variations in calc-alkaline andesites and plateau lavas from South America, *Earth Planet. Sci. Lett.*, **42**, 45–57, 1979.
- Magaritz, M., D. J. Whitford, and D. E. James, Oxygen isotopes and the origin of high- $^{87}\text{Sr}/^{86}\text{Sr}$  andesites, *Earth Planet. Sci. Lett.*, **40**, 220–230, 1978.
- O'Nions, R. K., P. J. Hamilton, and N. M. Evensen, Variations in  $^{143}\text{Nd}/^{144}\text{Nd}$

- and  $^{87}\text{Sr}/^{86}\text{Sr}$  ratios in oceanic basalts, *Earth Planet. Sci. Lett.*, **34**, 13–22, 1977.
- Richard, P., N. Shimizu, and C. J. Al-  
lègre,  $^{143}\text{Nd}/^{146}\text{Nd}$ , a natural tracer:  
an application to oceanic basalts,  
*Earth Planet. Sci. Lett.*, **31**, 269–278,  
1976.
- Whitford, D. J., Strontium isotopic stud-  
ies of the volcanic rocks of the Sunda  
arc, Indonesia, and their petrogenetic  
implications, *Geochim. Cosmochim.*  
*Acta*, **39**, 1287–1302, 1975a.
- Whitford, D. J., Geochemistry and pe-  
trology of volcanic rocks from the  
Sunda arc, Indonesia, Unpubl. Ph.D.  
thesis, Australia National University,  
1975b.
- Whitford, D. J., and P. A. Jezek, Geo-  
chemistry of Cenozoic and Recent  
lavas from the Banda arc, Indonesia,  
*Carnegie Inst. Wash. Year Book* **76**,  
845–855, 1977.
- Whitford, D. J., and I. A. Nicholls, Po-  
tassium variation in lavas across the  
Sunda arc in Java and Bali, in *Vol-  
canism in Australia*, pp. 63–75, R. W.  
Johnson, ed., Elsevier, Amsterdam,  
1976.

## OXYGEN ISOTOPE RESEARCH

David E. James

### Introduction

One of the more contentious issues in petrology and geochemistry today concerns the role of crustal contamination in modifying the isotopic and trace element character of continental igneous rocks. Involved are such questions as degree and age of mantle heterogeneity, the long-term integrity (or even existence) of thick continental lithosphere, and, ultimately, the origin (crustal or mantle) of magmas of intermediate composition.

These questions arise because of the highly variable composition of Sr, Nd, and Pb isotopes in continental lavas. The

isotopic composition of continental igneous rocks commonly lies in a range that could include “enriched” mantle, slightly “depleted” crust, or crustal contamination of “normal” mantle-derived magmas. The radiogenic isotopes cannot be used directly to distinguish between these alternatives.

The ambiguities inherent in the interpretation of radiogenic isotopes led us two years ago to undertake a study of stable oxygen isotopes. Oxygen isotopes are useful, in that mantle oxygen varies over the narrow range  $\delta^{18}\text{O} = +5.5$  to  $+6.5\text{‰}$ , whereas upper crustal rocks typically have  $\delta^{18}\text{O}$  values that are greater than  $9\text{‰}$  and commonly much higher than that.\* Thus if the radiogenic isotopic composition of continental igneous rocks is due to crustal contamination of mantle-derived magmas, the oxygen isotope composition of the hybrid melt should show relative enrichment in  $^{18}\text{O}$ . It may be, of course, that material in the lower crust does not differ significantly in  $\delta^{18}\text{O}$  from normal mantle, in which case lower crustal contamination will not be reflected in  $^{18}\text{O}$  enrichment. The work described below on deep crustal xenoliths brought up in Kilbourne Hole maar, New Mexico, is designed to answer in part the question of the isotopic composition of the lower crust.

In previous studies (see *Year Book* **76** and **77**) we were able to show that some island arc and continental arc andesites with unusually high  $^{87}\text{Sr}/^{86}\text{Sr}$  ratios are also enriched in  $^{18}\text{O}$ . In the case of the Banda arc volcanics,  $\delta^{18}\text{O}$  increases systematically with increasing  $^{87}\text{Sr}/^{86}\text{Sr}$  (Magaritz *et al.*, 1978). Magaritz *et al.* concluded that the high  $\delta^{18}\text{O}$  was inherited from continentally derived sedimentary material that was swept down the subduction zone and subsequently involved

\*  $\delta^{18}\text{O} =$

$$\left( \frac{(^{18}\text{O}/^{16}\text{O})_{\text{std}} - (^{18}\text{O}/^{16}\text{O})_{\text{sample}}}{^{18}\text{O}/^{16}\text{O}_{\text{std}}} \right) \times 1000,$$

where std refers to standard mean ocean water (SMOW).



in melting and andesite petrogenesis. The results of that study suggested that oxygen might be used as a general isotopic tracer to measure the degree of involvement of crustal materials in magma genesis. This report describes very preliminary efforts to study that problem in detail.

### *Instrumentation*

Oxygen isotope analyses described in previous Reports were done using facilities maintained by Drs. Hoering and Rumble at the Geophysical Laboratory. With the decision to undertake a more ambitious program of oxygen isotope analysis it became clear that a new oxygen-extraction line would have to be constructed at DTM to relieve the overburdened facilities of the Geophysical Laboratory. The new system, built during the fall and winter of this past year, follows the basic design described by Clayton and Mayeda (1963).  $\text{BrF}_5$  reagent is used to dissolve the silicate samples and release oxygen. Reaction vessels and metal tubing of the extraction line are nickel, and all other components including valves, seals, and traps are of monel, Teflon, or Kel-F, all of which are inert to the highly reactive  $\text{BrF}_5$  reagent. The extraction system uses molecular sieve vacuum pumps in place of mercury-diffusion pumps. The  $\text{CO}_2$  gas, obtained by burning a carbon rod in the presence of the  $\text{O}_2$  released from the sample, is measured in a gas mass spectrometer which is maintained and generously made available by Dr. Hoering of the Geophysical Laboratory.

### *Data*

Reliable determinations of  $\delta^{18}\text{O}$  in samples collected from the new extraction line have only been possible in the several weeks prior to the writing of this report. The quantity of data is accordingly rather limited, but the few  $\delta^{18}\text{O}$  values that have been obtained are ac-

curate to within about  $\pm 0.1\%$ . All  $\delta^{18}\text{O}$  values are normalized to the CIT rose quartz standard with an assumed value of  $8.45\%$ . Using this value for rose quartz, NBS #28 quartz sand yields  $\delta^{18}\text{O} \simeq 9.55\%$ .

### *Results*

Preliminary analyses have been completed for three groups of rocks.

(1) Precambrian gneiss complex of southern Peru. The ancient gneisses of this complex have been considered a possible contaminant responsible for high  $^{87}\text{Sr}/^{86}\text{Sr}$  and low  $^{206}\text{Pb}/^{204}\text{Pb}$  ratios observed in late Cenozoic volcanics of southern Peru (see Tilton, this Report).

(2) Late Mesozoic/Early Tertiary intrusive rocks of the Andean batholith near Arequipa, Peru.

(3) Lower crustal xenoliths from Kilbourne Hole maar, New Mexico. These samples are being studied as part of a joint investigation undertaken with Drs. E. Padovani and S. R. Hart of MIT to determine the isotopic composition of the lower crust. Sr and Nd isotopes are being analyzed by Drs. Padovani and Hart, and O isotopes on the same samples are being analyzed at the DTM.

*Precambrian gneiss.* The Arequipa Massif is a large coherent block approximately  $800 \times 100$  km in extent, which has remained virtually undeformed during the development of the present Andean arc (Shackleton *et al.*, 1979). The basement complex of the Massif consists of gneisses, schists, and related metamorphic and igneous rocks. The metamorphic complex has been considered by some an extension of the Brazilian shield, and paleomagnetic work by Shackleton *et al.* (1979) appears to support the conclusion that the Massif is an integral part of the American plate. On that basis, it is reasonable to assume that much of the central Andean chain may be underlain by a Precambrian complex. Such a complex would be an obvious source for high  $^{87}\text{Sr}/^{86}\text{Sr}$  and low  $^{206}\text{Pb}/$

$^{204}\text{Pb}$  material that is required if the anomalous isotopic compositions of the late Cenozoic volcanics are the result of crustal contamination.

Four Precambrian samples were analyzed, two from the Mollendo gneiss of coastal Peru and two from the Charcani gneiss near Arequipa (the most easterly extent of the Massif). The Mollendo gneiss, with  $^{87}\text{Sr}/^{86}\text{Sr}$  ratios of 0.75–0.77, has  $\delta^{18}\text{O} = 11.5\text{--}12.5\text{‰}$ ; the Charcani gneiss, with  $^{87}\text{Sr}/^{86}\text{Sr}$  ratios of 0.73–0.75, has  $\delta^{18}\text{O} = 7.3\text{--}9.7\text{‰}$ . From previous calculations (see James, 1978), trace element and radiogenic isotopic compositions require that if the anomalous isotopic ratios of the central Andean volcanics are due to crustal contamination the ratio of contaminant to parent must be  $\sim 1:1$ . The  $\delta^{18}\text{O}$  values of the late Cenozoic volcanics near Arequipa are  $\sim 7.0\text{‰}$ . The contaminant cannot, therefore, be of the oxygen isotope composition of the Mollendo gneiss. The oxygen data alone are not sufficient to exclude the Charcani gneiss as a contaminant,

although it would be difficult to reconcile other trace element data with such contamination.

*Andean batholith.* The rocks of the Andean batholith, emplaced during late Cretaceous/early Tertiary time into the general region of the Arequipa Massif, exhibit  $\delta^{18}\text{O}$  values that appear to vary systematically along a transect of the pluton (see Fig. 26). In detail, however, the correlation is with degree of alteration of the rock. Samples 16, 87, 88, and 89 show extensive plagioclase sericitization and other evidence of alteration. The remaining samples, diorite to granodiorite in composition, show slight evidence of alteration, primarily minor sericitization of plagioclase, but are not notably different from one another. Among these latter samples,  $\delta^{18}\text{O}$  varies between about 6.0 and 7.5‰, averaging 6.7‰ ( $^{87}\text{Sr}/^{86}\text{Sr}$ )<sub>i</sub> ratios for these same samples average 0.7052, based on an assumed age of 80 m.y.

From the data collected, there is no evidence that any of the rocks in this

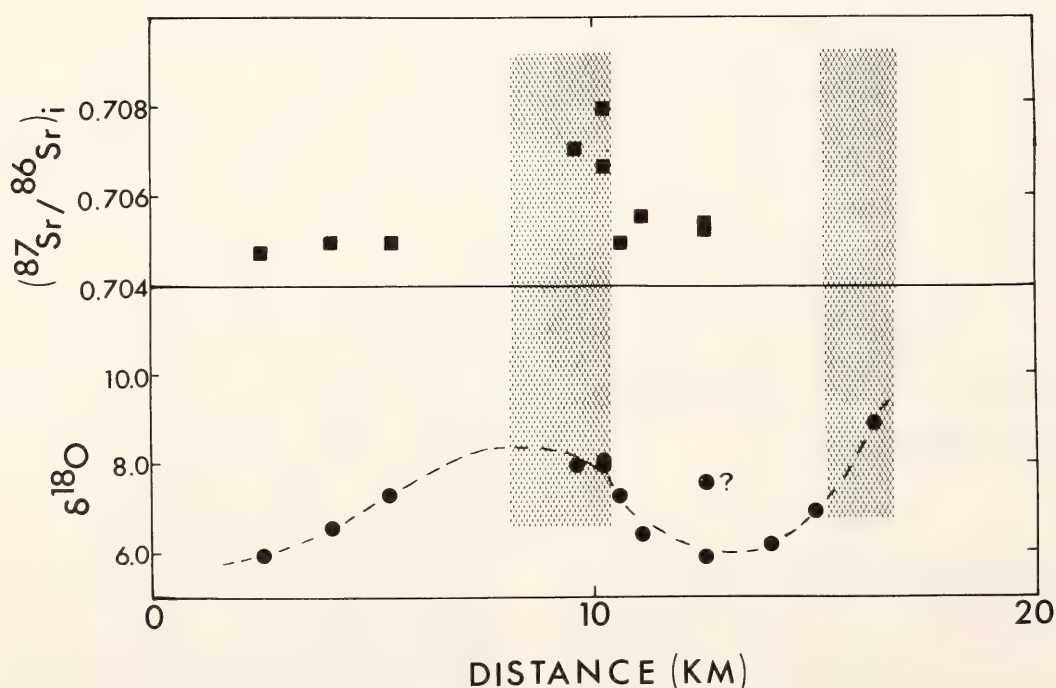


Fig. 26.  $\delta^{18}\text{O}$  and  $^{87}\text{Sr}/^{86}\text{Sr}$  ratios for intrusive rocks of the Arequipa batholith are plotted vs. distance along the Pan-American Highway between La Repartition and Arequipa, Peru. Low-temperature alteration is confined to zones characterized by high  $\delta^{18}\text{O}$  and high  $^{87}\text{Sr}/^{86}\text{Sr}$ .  $^{87}\text{Sr}/^{86}\text{Sr}$  initial ratios have been calculated assuming an average of 80 m.y. for the batholith.



part of the Arequipa batholith have been affected by hydrothermal alteration, a process that tends to produce much lower  $\delta^{18}\text{O}$  values. All samples that show evidence of alteration have high  $\delta^{18}\text{O}$ , indicative of low-temperature processes. The  $\delta^{18}\text{O}$  values of comparatively unaltered samples are within the range of mantle values or are very slightly higher. They are lower than  $\delta^{18}\text{O}$  measured in the late Cenozoic andesites ( $\sim 7.0\%$ ). The  $\delta^{18}\text{O}$  of the plutonic rocks suggests that they are predominantly of mantle origin and little contaminated by rocks of the Precambrian complex which they intrude.

*Kilbourne Hole xenoliths.* Oxygen isotopes have been measured for a Kilbourne Hole garnet granulite of deep crustal origin (20–25 km depth). The sample has been cut in seven slabs corresponding to different layers, and each slice has been analyzed. Preliminary Sr and Nd isotopic results show the layers to be in isotopic disequilibrium, with no internal isochron. Oxygen isotopes, on the other hand, are equilibrated throughout the rock, giving a consistent  $\delta^{18}\text{O}$  across the sample of  $8.77 \pm .05\%$ . The high  $\delta^{18}\text{O}$  shows, however, that the xenolith is greatly out of equilibrium with the mantle and that at least some rocks of the lower crust are comparatively rich in  $^{18}\text{O}$ .

### References

- Clayton, R. N., and T. K. Mayeda, The use of bromine pentafluoride in the extraction of oxygen from oxides and silicates for isotopic analysis, *Geochim. Cosmochim. Acta.*, 27, 43–52, 1963.
- James, D. E., On the origin of the calc-alkaline volcanic of the central Andes: a revised interpretation, *Carnegie Inst. Wash. Year Book* 77, 562–590, 1978.
- Magaritz, M., D. J. Whitford, and D. E. James, Oxygen isotopes and the origin of high  $^{87}\text{Sr}/^{86}\text{Sr}$  andesites, *Earth Planet. Sci. Lett.*, 40, 220–230, 1978.
- Shackleton, R. M., A. C. Ries, M. P. Coward, and P. R. Cobbold, Structure, metamorphism and geochronology of the Arequipa Massif of coastal Peru, *J. Geol. Soc. Lond.*, 136, 195–214, 1979.

## THE OCEANIC CRUST AND LITHOSPHERE

### STRUCTURE OF THE OCEANIC LITHOSPHERE FROM SURFACE-WAVE OBSERVATIONS: THE ICELAND PLATEAU

*J. R. Evans\* and I. S. Sacks*

#### *Introduction*

The region immediately north of Iceland is known as the Iceland Plateau, since the bathymetry of the area is relatively shallow (about 1500–2000 m) and flat. The western margin is marked by the northward extension of the Mid-Atlantic Ridge, known as the Kolbeinsey Ridge or Iceland–Jan Mayen Ridge. This is classified an elevated spreading center, its crest lying at a depth of only 1000 m. The southern and northern boundaries are marked by transform faults—the Tjornes fracture zone in the south and the Jan Mayen fracture zone in the north. The eastern boundary is (less clearly) defined by a broad rise known as the Jan Mayen Ridge. From observations of magnetic lineations, Talwani and Eldholm (1977) have shown that the crust of the Iceland Plateau was formed by seafloor spreading. The major features of the region are shown in Fig. 27.

We have examined records of surface wavetrains generated by earthquakes on the Jan Mayen fracture zone which have crossed the Iceland Plateau to the Carnegie DTM broadband seismograph station at Akureyri, Iceland (AKU). From the dispersion of these wavetrains, we have constructed models of shear-wave velocity structure beneath the region to depths of up to 100 km. The models are

\* Institute of Geological Sciences, Edinburgh, United Kingdom.

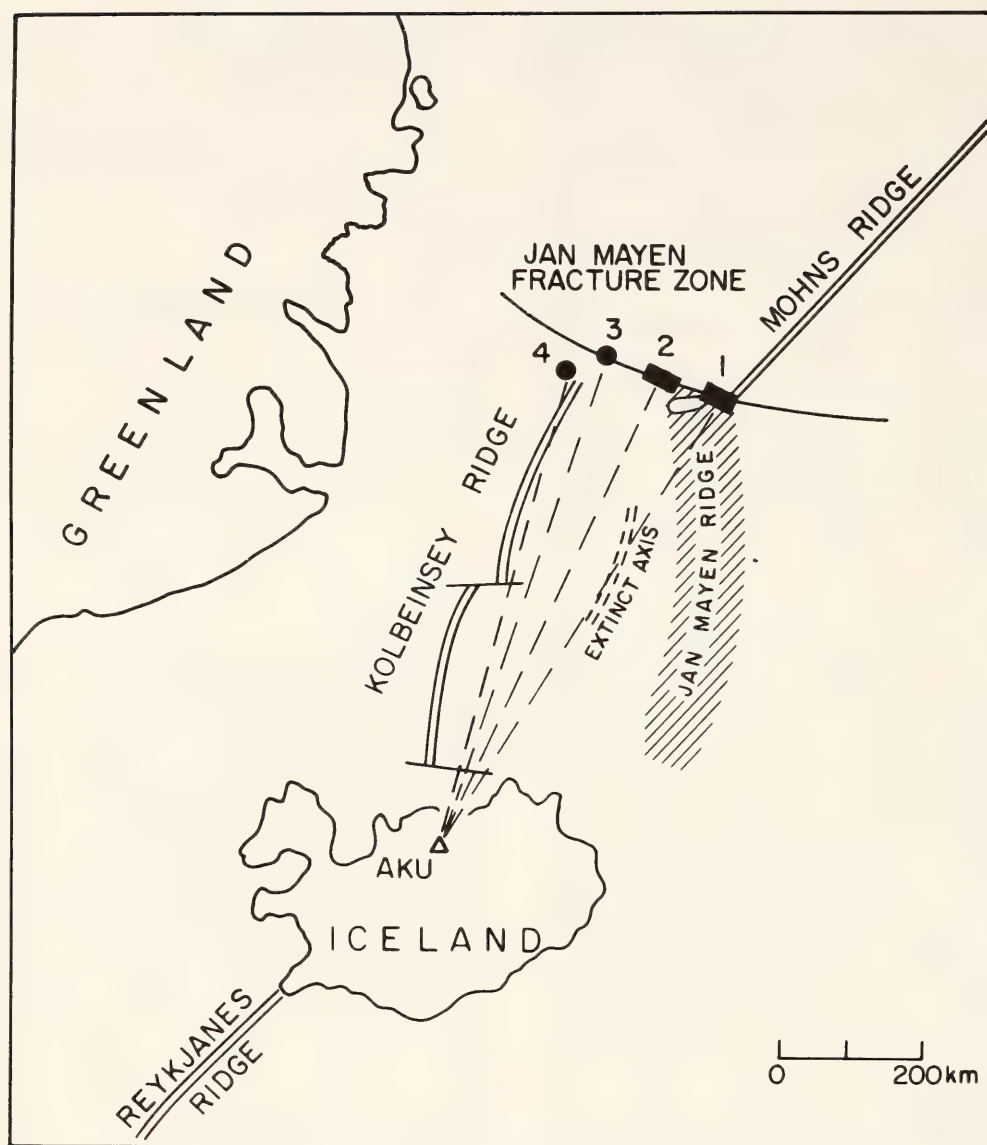


Fig. 27. Map of the Iceland region showing the principal features of the Iceland Plateau and the paths traversed by the wavetrains studied. The Iceland Plateau itself is the area north of Iceland lying between the Kolbeinsey and Jan Mayen Ridges. The eastern part of the Plateau was formed from an (extinct) spreading axis, within the present Plateau boundaries, active between 24 m.y. and 18 m.y. ago. The western part was formed from the Kolbeinsey Ridge, active since 13 m.y. ago. The Jan Mayen Ridge is identified with a magnetic quiet zone. This and other evidence suggests that it is a continental fragment.

Earthquakes on the Jan Mayen fracture zone generate surface wavetrains which travel across the Plateau, and the group velocity dispersion of these wavetrains may be inverted to give models of shear-wave structure beneath the Plateau. The broken lines indicate the surface-wave paths studied and the numbers identify the earthquake groups. (Azimuthal Equidistant projection centered on AKU).

characterized by a crust of about 20-km thickness—much greater than the 6–8 km typical of oceanic areas. The lithosphere is about 50 km thick throughout the region, and this value is consistent with other determinations of the thickness of young oceanic lithosphere.

### *Method*

The Carnegie broadband seismograph at Akureyri, Iceland, has operated since July 1972. Earthquake records analyzed are listed in Table 6. The earthquakes are all shallow and associated with the



TABLE 6. Earthquakes Used in This Study

No.	Date	Time	Lat.	Long.	mb	Dist. to AKU, degrees
1a	72Oct25	18:25:54	70.9N	7.0W	5.3	6.7
1b	72Nov14	4:31:42	71.0N	7.9W	5.1	6.6
1c	73Jan 2	23:20:15	71.3N	7.5W	4.7	6.7
1d	73Jan 4	8:03:51	71.1N	7.7W	5.1	6.7
2a	75Apr16	1:27:18	71.5N	10.4W	6.1	6.5
2b	76Jun12	10:34:48	71.4N	8.6W	4.8	6.7
3a	73Sep27	12:29:03	71.5N	12.1W	5.1	6.5
3b	76May25	12:45:27	71.6N	12.4W	4.6	6.3
3c	76May25	14:04:51	71.6N	12.2W	4.6	6.3
4a	77Feb13	15:08:30	70.8N	14.0W	4.5	5.4

Jan Mayen fracture zone. The magnetic tape records were digitized and then analyzed using the multiple-filtering procedure (Landisman *et al.*, 1969) modified according to Nyman and Landisman's (1977) suggestion for optimizing resolution in the frequency-time diagram. Theoretical dispersion curves were calculated using the algorithms published by Schwab and Knopoff (1972), with minor modification. The models were fitted to the data by inspection, and by the use of a single-iteration least-square inversion. Our procedure has been described in detail in Evans and Sacks (1979). Neither the quantity nor the quality of the data required the use of a formal inversion technique.

We obtained one useful constraint on the surface-wave inversion from observation of body-wave phases. Most of the larger earthquakes that we have studied gave rise to a high-frequency (5 Hz) precursor to  $S$ , which we refer to as  $S_n$  (see Fig. 28). Similar arrivals are observed elsewhere in oceanic structure (e.g., Hart and Press, 1973), and Mantovani *et al.* (1977) have shown that they may be regarded as stationary phases of higher-mode surface waves. Mantovani *et al.* also showed that for structures containing an oceanic low-

velocity zone most of the energy associated with the onset of  $S_n$  travels in the lid over the low-velocity zone, and that the group velocity of the onset approaches the shear-wave velocity of the lid. In the present study, we find that the velocity between the Jan Mayen fracture zone and AKU is about 4.55 km/sec. Therefore, in our analysis of surface-wave observations we favor structures in which the lid velocity reaches 4.55–4.6 km/sec.

#### Surface-Wave Observations

For the purposes of analysis, we divide the epicenters studied into four groups on the basis of similarity of the dispersion curves obtained and of geographic proximity (see Table 6).

*Group 1.* This group of epicenters lies at the eastern end of the seismically active section of the Jan Mayen fracture zone. The path crossed by the wavetrains is mostly within the Iceland Plateau, much of it lying along the extinct spreading axis which forms the eastern part of the plateau. About 15% of the path length passes over the Jan Mayen Ridge, so the dispersion of this group of wavetrains may be slightly affected by this (assumed) continental fragment.

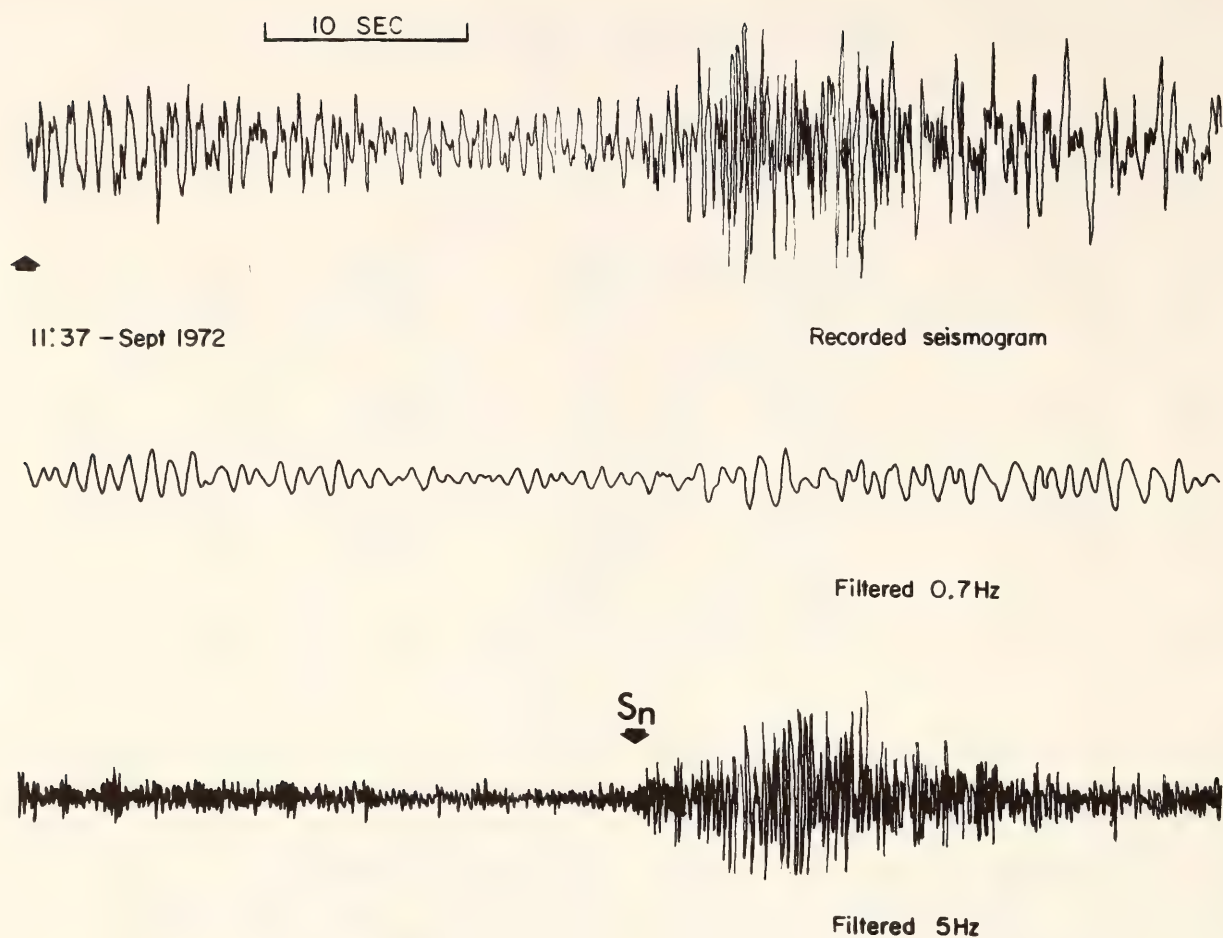


Fig. 28. Short-period record at AKU for earthquake of 8 September 1972, and records derived from it by narrow-band filtering at 0.7 Hz and 5 Hz. The high-frequency precursor to  $S$ , identified as  $S_n$ , is most apparent when filtered at about 5 Hz and is therefore assigned this frequency.

Figure 30 shows the dispersion data obtained and illustrates many of the features of the data and models that we examined in this study. The Rayleigh-wave dispersion is fairly typical of oceanic structures, but the Love-wave dispersion is not. In normal oceanic structures, the Love-wave velocity increases rapidly with period in the period range 5–10 sec, and then remains roughly constant between 15 and 100 sec (for an example, see Fig. 29). In contrast, the Love-wave dispersion curve shown in Fig. 30 has a shallow slope more typical of continental regions. Because the shorter-period Rayleigh-wave velocities are dominated by the water layer and are therefore not sensitive to crustal structure, the Love-wave data are more

useful in determining crustal thickness. The Love-wave data of Fig. 30 suggest that the structure may involve a thick crust overlying a normal oceanic mantle.

We find that such structures do indeed provide a reasonable fit to the data. Figure 30 shows two models of this kind. In both cases, we find that the Love-wave dispersion is due to a gradient structure in the crust. In such models, it is difficult to assign a particular depth to the crust-mantle boundary. The criterion that we have adopted is to assign the position of the crust-mantle boundary in a given model to the shallowest depth for which the shear velocity exceeds 4.35 km/sec. By examining a series of models we estimate the range of depths possible for this crust-mantle



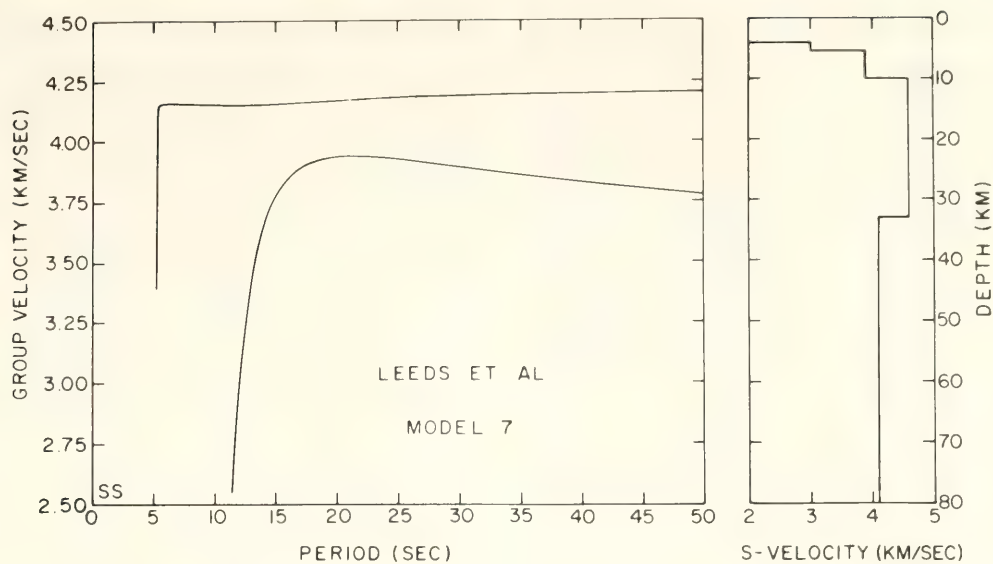


Fig. 29. Theoretical group velocity dispersion curves for a typical model of young oceanic structure (model 7 of Leeds *et al.*, 1974). Note particularly the steep rise in the upper (Love-wave) group velocities between 5 and 8 sec period, which is determined by sediment and crustal structure, and the rounded 'knee' of the Rayleigh-wave dispersion curve at about 12 sec period, also strongly influenced by crustal structure.

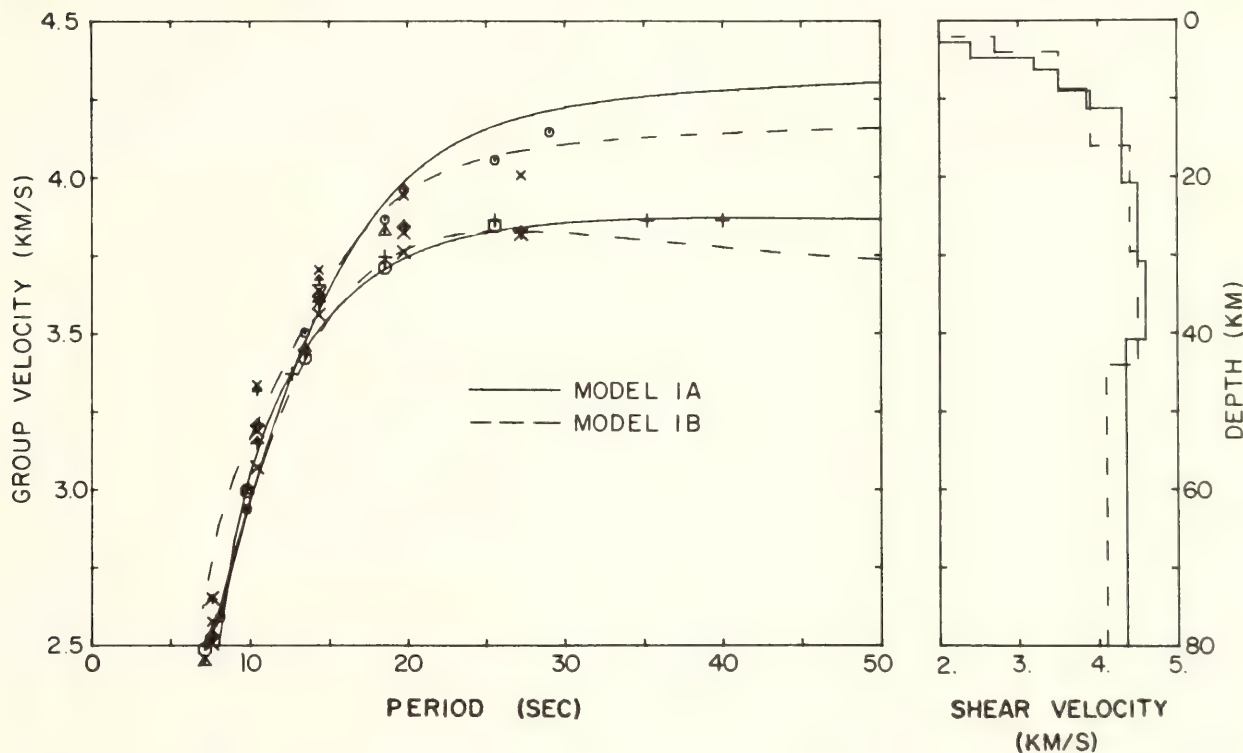


Fig. 30. Observed and theoretical dispersion curves for group 1 earthquakes (see Fig. 27 for position of earthquakes and paths). Here and in Figs. 31, 32, and 33, observed dispersion is indicated by the symbols in the left-hand section. Small symbols represent the dispersion observed on the east-west component (interpreted as Love waves) and large symbols that observed on the vertical component (interpreted as Rayleigh waves). Large and small symbols of the same type are derived from the same earthquake. The right-hand sections show representative velocity-depth curves; solid and dashed lines corresponding to the solid and dashed dispersion curves in the left-hand sections of the figures. In each case the upper pair of lines is Love-wave dispersion (compare with small symbols) and the lower pair Rayleigh-wave dispersion (compare with large symbols). Note the large crustal thickness (about 16–20 km) in both model 1A and 1B. Models with a crust typical of oceanic structures fail to fit the Love-wave dispersion data.

boundary, and we find that the data in Fig. 31 imply a crustal thickness of 15–20 km. Very little of this thickness can be ascribed to the 15% of the path that crosses the Jan Mayen Ridge. To produce the observed dispersion, a crustal component of this thickness or greater must be present over a large part of the path length. Moreover, this interpretation is consistent with the results for group 2 paths, which do not cross the Jan Mayen Ridge. The depth to the top of the channel is found to be 40–50 km. The maximum velocity attained in the lid is 4.5–4.6 km/sec, in reasonable agreement with the  $S_n$  observations. The data do not provide a good estimate of channel velocity. The channel shear-wave velocity influences the group velocity of Love waves in the range 30–50 sec strongly, but these periods were not observed for the group 1 earthquakes. In their absence the channel shear-wave velocity is determined by the Rayleigh-wave observations at 40 sec and the

Love-wave observations at 30 sec. These tend to conflict, and neither is particularly reliable since both lie at the limit of resolution of the data. Thus either of the models shown may be regarded as a reasonable fit to the surface-wave data. The models suggest that the channel shear-wave velocity may be lower for this path than for groups 2 and 3 below. This low velocity may be associated with the extinct spreading axis at the east of the Plateau.

*Group 2.* The second group of epicenters lies near the middle of the seismically active portion of the Jan Mayen fracture zone. The surface waves generated travel across the middle of the Plateau, an area formed from both the eastern (extinct) and western spreading centers. Figure 31 shows the data obtained from these earthquakes. The model shown gives an excellent fit to the data from earthquake 2a (at  $M_b = 6.1$ , the largest event) and a good fit to the remainder. Both data and model show

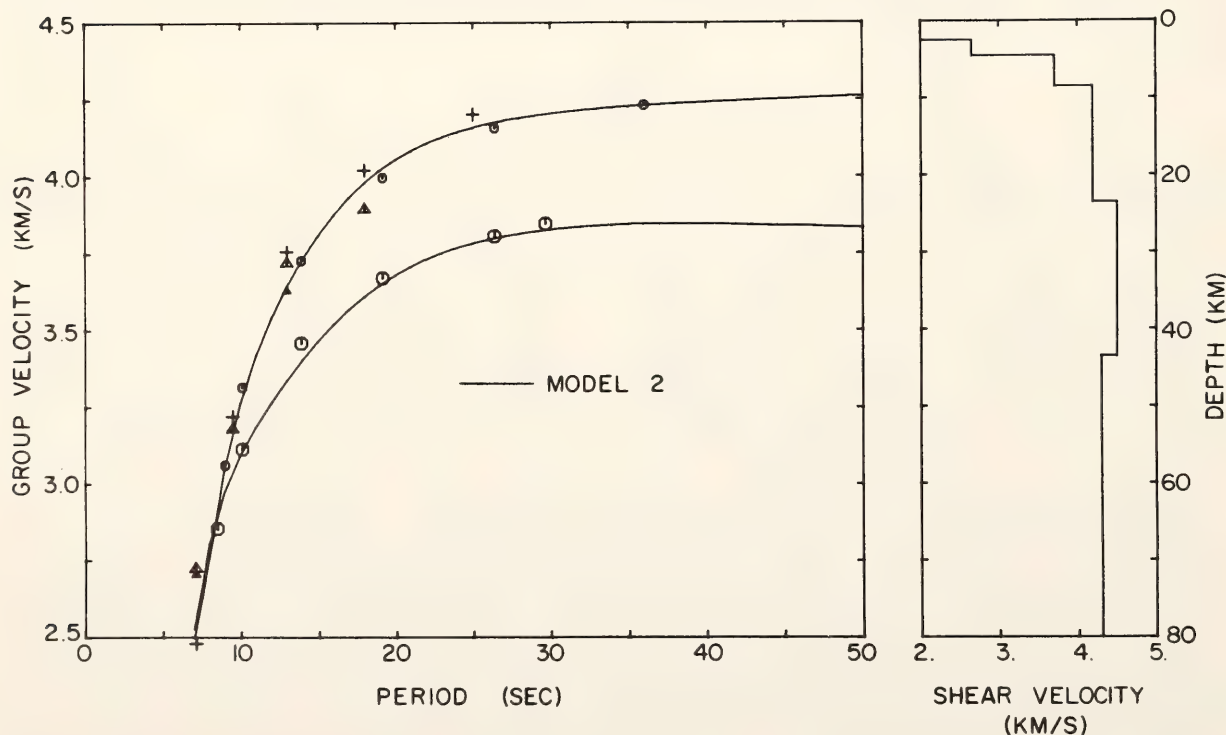


Fig. 31. Observed and theoretical dispersion curves for group 2 earthquakes. See Fig. 27 for location of earthquakes and paths; see text of Fig. 27 for a detailed explanation of the figure. Note the large crustal thickness (over 20 km) in model 2 (see model 1).



features similar to those of group 1 earthquakes. We find a crustal thickness of about 20 km, a total lithospheric thickness of 40 km, and a lid velocity of about 4.6 km/sec (in agreement with the  $S_n$  velocity). In this case, good Love-wave data to 40 sec were obtained, and the channel velocity is determined at 4.3 km/sec.

*Group 3.* The third group of epicenters lies at the western end of the Jan Mayen fracture zone. The path taken by the wavetrains crosses the younger western margin of the Plateau. We see that the slope of the Love-wave data shown in Fig. 32 is greater than that of the data from the paths in the older sea floor. This is reflected in the models that we constructed. They show a crustal thickness of about 12–18 km and a total lithospheric thickness of about 40–50 km. The channel shear-wave velocity in the model is about 4.3 km/sec but is not well determined by the available data.

*Group 4.* This group contains only one

event, directly on the axis of the Kolbeinsey Ridge. The wavetrains traveled close to the ridge axis across the northern part of the path and across young crustal material south of the Spar fracture zone. Although some vertically polarized energy was found in the period range 5–15 sec, the observed surface wavetrain was largely horizontally polarized. We conclude that this energy propagated as Love waves, even though the dispersion is surprisingly similar to that of the Rayleigh waves of group 3 earthquakes. However, if the energy observed from the group 4 earthquakes has been propagated as Rayleigh waves, it must have suffered a strong conversion to Love waves near AKU in order to be horizontally polarized at AKU. Since we can find no evidence for such conversion on records from the larger group 3 events, we reject this possibility. We model the observations using structures such as that shown in Fig. 33. They imply a crustal thickness of 15 km and a

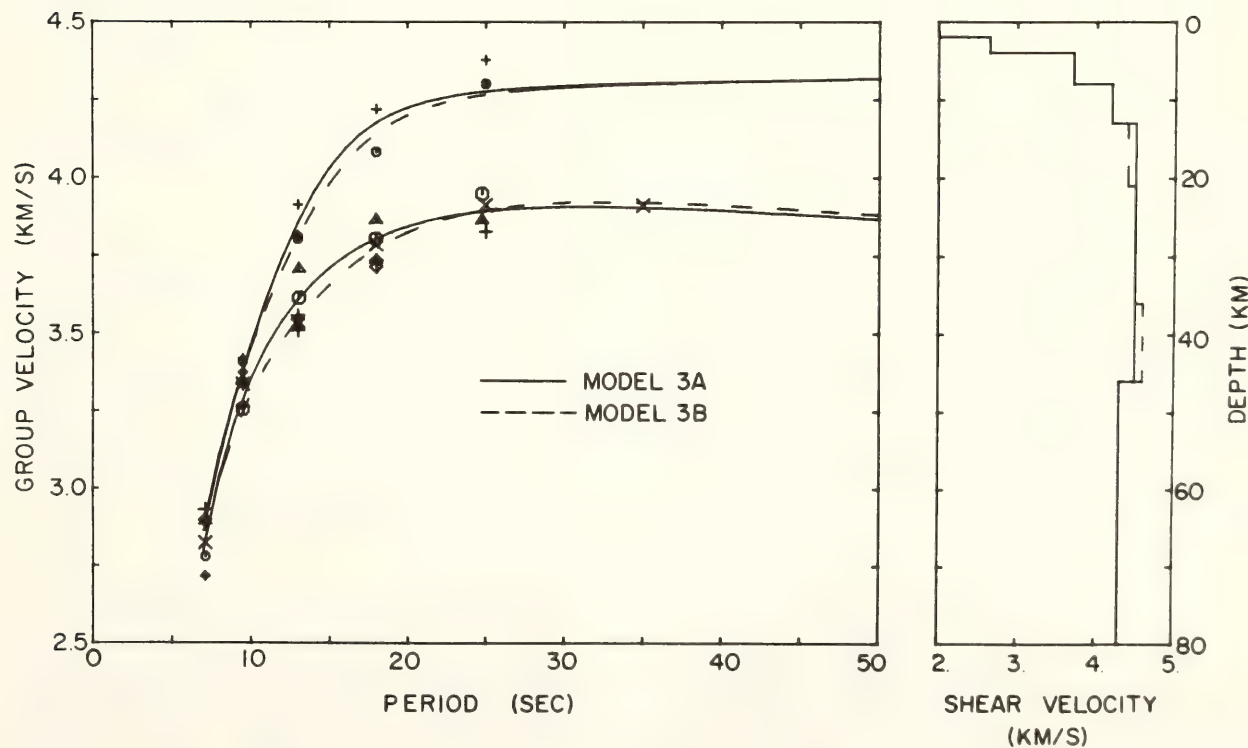


Fig. 32. Observed and theoretical dispersion curves for group 3 earthquakes. Fig. 27 shows the location of earthquakes and paths, and the text of Fig. 30 gives a detailed explanation of the figure. Note the large crustal thickness (15–20 km) in model 3 (see models 1 and 2).

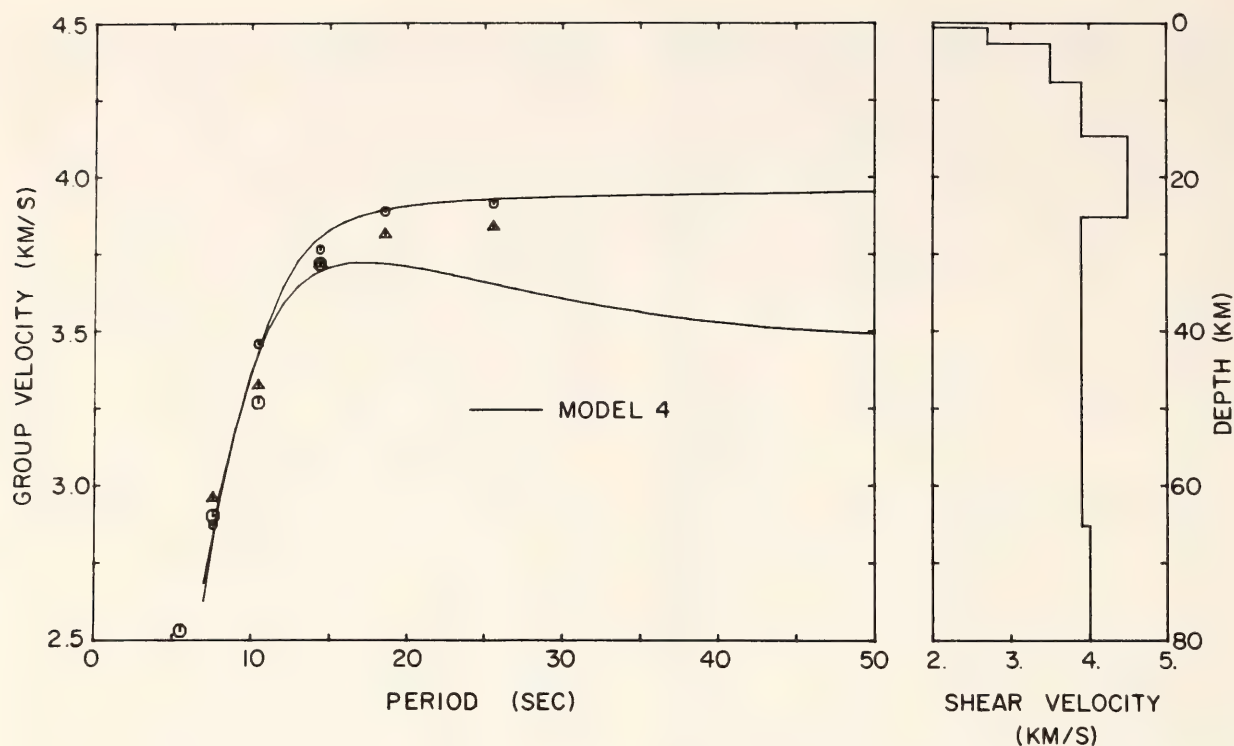


Fig. 33. Observed and theoretical dispersion curves for group 4 earthquakes. Fig. 27 shows the location of earthquakes and paths, and the text of Fig. 30 gives a detailed explanation of the figure. Note that at the (elevated) ridge the crustal thickness ( $\approx 15$  km) in model 4 is substantial (see models 1, 2, and 3).

total lithospheric thickness of about 25 km, underlain by a layer of low shear-wave velocity ( $\sim 3.9$  km/sec).

*Summary.* Each of the models that we have constructed to fit these observations has a crust of unusual thickness—about 20 km at the eastern edge of the Plateau and somewhat less in the west. The total lithospheric thickness is consistently found to be about 30–50 km, except near the axis of the Kolbeinsey Ridge where it is only 25 km. The channel velocity beneath the region appears to be about 4.3 km/sec, except again at the ridge axis where it is found to be extremely low. The structure is shown in Fig. 34.

### Gravity Data

Cochran and Talwani (1978) have discussed the gravity field of the North Atlantic in detail. They attribute the large-scale positive anomaly present over much of the North Atlantic to a mass deficiency at a depth of several hundred

kilometers. Gravity measurements over the Iceland Plateau show a positive anomaly of about 50 mgal over most of the region. After subtracting the field due

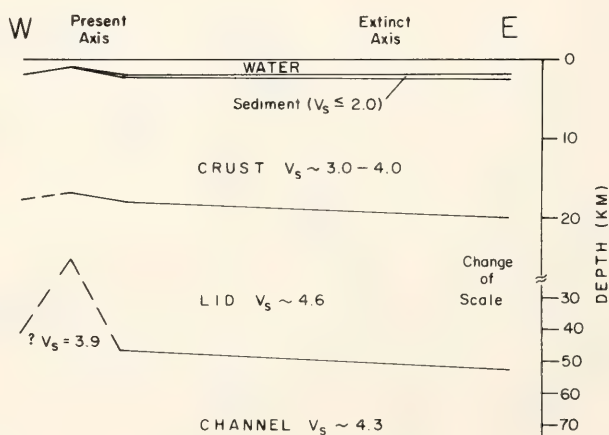


Fig. 34. Sketch showing east-west section through the Iceland Plateau, as determined from the surface-wave study (note change in vertical scale at 30-km depth). The total lithospheric thickness is about 50 km throughout the Plateau region. The crust, although everywhere thick, is thinner to the west near the present spreading axis (Kolbeinsey Ridge) than to the east near the extinct spreading center.



to the deep deficiency, we find that the net free-air anomaly over the Iceland Plateau is small, which suggests that the Plateau itself is in isostatic equilibrium. This implies that the extra mass associated with the excess elevation of the seafloor must be compensated by a mass deficiency elsewhere in the crust or upper mantle. The model that we have derived in the preceding sections accounts for this.

The excess elevation of the seafloor over that of ocean basins of similar age is about 2000 m, a little less near the Kolbeinsey Ridge, and a little greater in the eastern part of the basin. The hydrostatic load resulting from this excess is given by  $h\rho g$ , where  $\rho$ , the effective density, is the difference of the density of the excess crustal material and the seawater it displaces,  $h$  is the excess elevation of the seafloor, and  $g$  the acceleration due to gravity.  $\rho$  is of order 1.0–1.5 g/cc. The difference in density between the lower crustal material and that of the lithospheric lid is only about 0.2–0.3 g/cc. Thus if this hydrostatic load due to the elevation is offset by a buoyancy resulting from the presence of excess crustal material at depth, then the amount of the material at depth must be of order  $5\times$  greater than that displacing seawater. Thus, every kilometer of excess in crustal elevation implies about  $(5 + 1)$  km excess in total crustal thickness. The 2000-m elevation of the Iceland Plateau, then, implies 12 km due to the excess elevation, plus 7 of normal oceanic crust, giving a total thickness of about 19 km, similar to the value derived from the surface-wave studies. The normal and Plateau structures are compared in Fig. 35.

### Conclusions

We have investigated the dispersion of surface waves across the Iceland Plateau, and find that the region is characterized by a crust of about 20-km thickness. Isostatic compensation for this

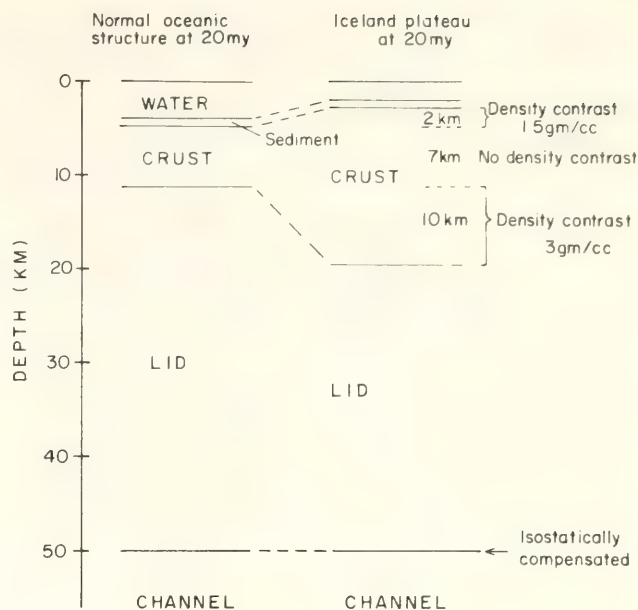


Fig. 35. Isostatic compensation for a thick crust. The excess elevation of the sea floor is offset by depressing the base of the crust such that the weight of each column is the same. Since the density contrast between the upper crustal layers and sea water (1.5 gm/cc) is much greater than that between the lower crust and the lithosphere (0.3 gm/cc), only a sixth of the excess crustal thickness is manifested as elevation of the sea floor. The Iceland Plateau is elevated by 2000 m relative to other young ocean floors; this may be accounted for as isostatic compensation for a crust of 20-km thickness.

excess thickness causes the region to be elevated relative to ocean basins of similar crustal age. Our analyses suggest that the crustal thickness may be greater on the eastern margin than on the west. The younger western part is less elevated than the older eastern part, accounting for the flat bathymetry of the Plateau.

We find that the total lithospheric thickness over most of the Plateau is about 40–50 km. Since the age of the crust in this region is typically less than 20 m.y. and nowhere greater than 25 m.y., this figure is in good agreement with estimates of the thickness of young oceanic lithosphere given for the Pacific (Forsyth, 1977; Leeds *et al.*, 1974) and the North Atlantic (Evans and Sacks, 1978). It appears, therefore, that in this region a thicker crust is produced at the

ridge but that the lithosphere thickens with age (presumably due to underplating) at a similar rate to other oceanic regions. Our model of structure near the axis of the Kolbeinsey Ridge shows a considerable crustal thickness (12–15 km) and a total lithospheric thickness of about 30 km. This total thickness is similar to that found in studies of structure near the axis of the Reykjanes Ridge (Keen *et al.*, 1979; Evans and Sacks, 1979). The shear-wave velocity in the low-velocity zone beneath the ridge axis appears to be very low (about 3.9 km/sec) whereas throughout the rest of the region the channel velocity is about 4.3 km/sec, similar to that of "average" models of oceanic shear-wave velocity structure (Dorman *et al.*, 1960).

### References

- Cochran, J. R., and M. Talwani, Gravity anomalies, regional elevation and the deep structure of the North Atlantic, *J. Geophys. Res.*, **83**, 4907–4924, 1978.
- Dorman, J., M. Ewing, and J. Oliver, A study of shear velocity distribution in the upper mantle by mantle Rayleigh waves. *Bull. Seismol. Soc. Amer.*, **50**, 87, 1960.
- Evans, J. R., and I. S. Sacks, Structure of the oceanic lithosphere from surface wave observations: North Atlantic, *Carnegie Inst. Wash. Year Book* **77**, 527, 1978.
- Evans, J. R., and I. S. Sacks, Lithospheric structure in the North Atlantic from observations of Love and Rayleigh waves, submitted to *J. Geophys. Res.*, 1979.
- Forsyth, D. W., The evolution of the upper mantle beneath mid-ocean ridges, *Tectonophysics*, **38**, 89–118, 1977.
- Hart, R. S., and F. Press,  $S_n$  velocities and the composition of the lithosphere in the regional Atlantic, *J. Geophys. Res.*, **78**, 407–411, 1973.
- Keen, C. E., A. Fricker, M. J. Keen, and L. Blinn, A study of the Reykjanes Ridge by surface waves using an earthquake-pair technique, in *Current Research*, Pt. A, Canada Geological Survey Paper **79-1A**, 273–279, 1979.
- Landisman, M., A. Dziewonski, and Y. Sato, Recent improvements in the analysis of surface wave observations, *Geophys. J. Roy. Astron. Soc.*, **17**, 369–403, 1969.
- Leeds, A. R., L. Knopoff, and E. G. Kausel, Variations of upper mantle structure under the Pacific Ocean, *Science*, **186**, 141–143, 1974.
- Mantovani, E., F. Schwab, H. Liao, and L. Knopoff, Teleseismic  $S_n$ : a guided wave in the mantle. *Geophys. J. Roy. Astron. Soc.*, **51**, 709–726, 1977.
- Nyman, D. C., and M. Landisman, The display equalized filter for frequency-time analysis, *Bull. Seismol. Soc. Amer.*, **67**, 393–404, 1977.
- Schwab, F. A., and L. Knopoff, Fast surface wave and free mode computations, *Methods in Computational Physics*, **11**, p. 87, Academic Press, New York, N.Y., 1972.
- Talwani, M., and O. Eldholm, Evolution of the Norwegian-Greenland Sea, *Geol. Soc. Amer. Bull.*, **88**, 969–999, 1977.

### STRESS FIELD CHANGES DURING A TECTONIC EPISODE IN NORTHERN ICELAND

R. Stefánsson,\* I. S. Sacks, and A. T. Linde

#### *Tectonic Setting*

Iceland straddles the North Atlantic Ridge and thus provides opportunities to study the spreading and rifting process in some detail.

In late 1975, a series of tectonic events started in northeastern Iceland. A minor volcanic eruption within the Krafla caldera (Fig. 36) was followed by a subsidence of land which far exceeded the erupted volume. In the Krafla area, vertical and horizontal fault movements

\* The Icelandic Meteorological Office, Reykjavik, Iceland.



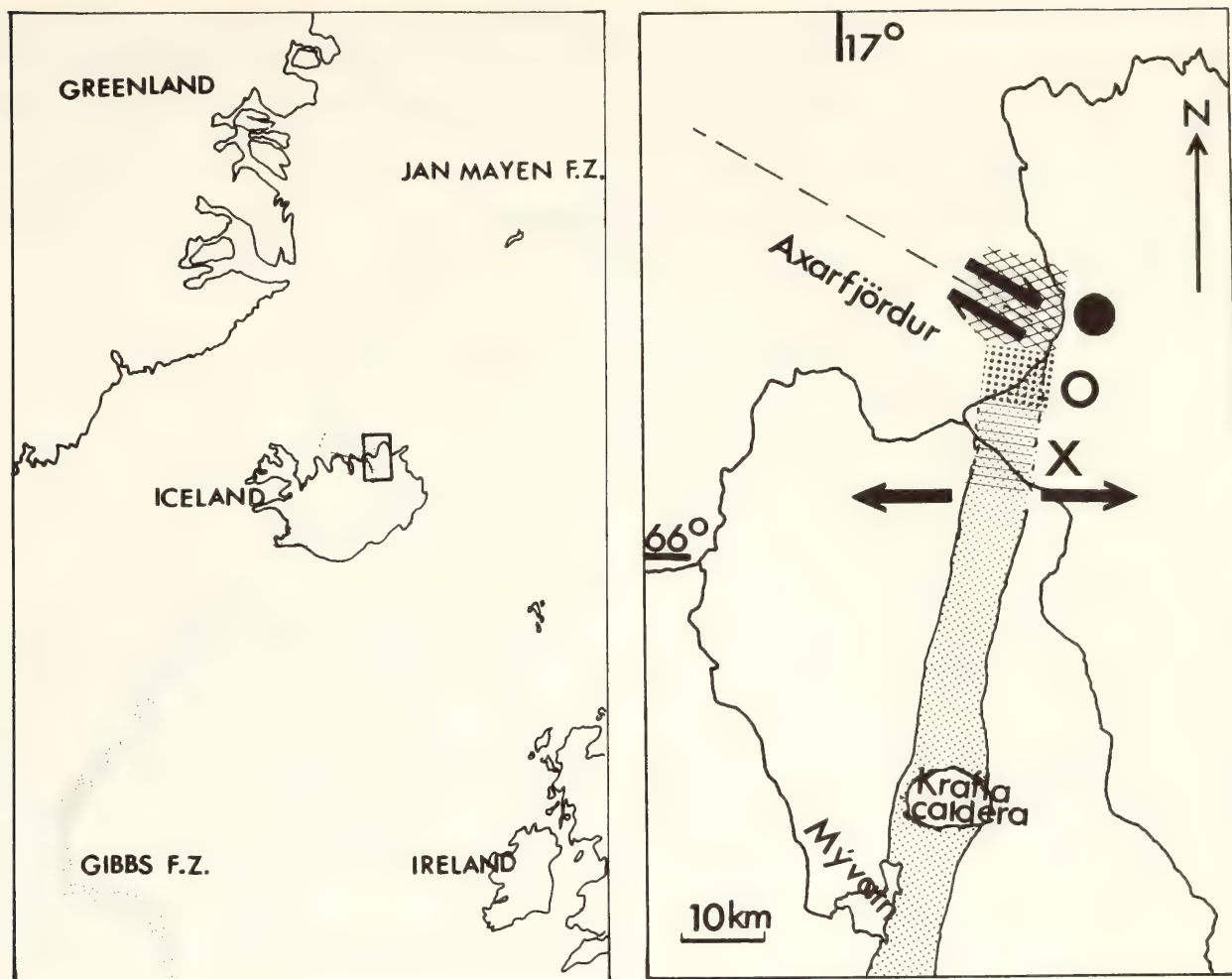


Fig. 36. (Left) The currently active zone of the Mid-Atlantic Ridge through Iceland in relation to other parts of the ridge (stippled), as seismically defined. (Right) Enlargement of the northeastern Iceland area within the rectangle shown in left diagram. The shaded area is the fault swarm within which widening cracks have been observed. Seismic activity started near the Krafla caldera, spread after one day northward to the region marked X. After five days, activity started in the region marked O; earthquakes followed on the transform fault (●) through Axarfjörður.

were of order 1 meter. A day later an intense earthquake swarm began about 30 km north of the caldera, accompanied by widening of rifts and subsidence within the fault swarm; the apparent widening and subsidence were of the order of 1–2 meters. The activity migrated to the north, toward the junction of the currently active spreading zone and a northwest-trending transform fault. On January 13, 1976 a major earthquake took place on the transform fault near its junction with the ridge, and its focal mechanism corresponded to right lateral strike slip, as indicated in Fig. 36. The migration of seismic activity into previously inactive regions allowed us to

assess the changes in stress as these activities developed.

### Data

The earthquakes were located by the Iceland weather bureau using local station readings. The data analyzed came from the Carnegie broad band, tape-recording seismograph operating at Akureyri in northern Iceland. The seismograph is about 50–100 km from the active zones (Fig. 36). The zones are fairly small, of order 10 km, so that the geometry of the ray paths is essentially unchanged in the comparison of events in the various zones.

In order to have as homogeneous a data set as possible, events having approximately the same magnitude were studied. This was done to exclude the complication of stress drop as a function of magnitude, though this relationship is not suspected. Magnitudes ( $M$ ) in the range  $3\frac{1}{2}$ – $4\frac{1}{2}$  were chosen. These gave good signal-to-noise ratios, from 10 Hz down to a few tenths of a Hertz, and were sufficiently numerous to allow an assessment of the scatter of the process.

The clear temporal and spatial migration of the seismic activity made it easy to determine the onset in each region. Krafla activities started on 20 December 1975, the southern group (X in Fig. 36) on 21 December, and the northern spreading region (O in Fig. 36) on 25 December. Transform fault events (● in Fig. 36) were recorded from 6 January 1976, and the main shock ( $M = 6.4$ ) occurred on 13 January.

### Analysis

Stress drops are usually calculated from determination of the low-frequency asymptote (proportional to seismic moment  $M_0$ ) and a corner frequency. This corner frequency is usually determined by the intersection of the high-frequency and low-frequency straight-line envelopes on a plot of log displacement amplitude vs. log frequency (see Fig. 37).

It has been shown, however, that if rupture propagation is uneven, the corner is deformed (Linde *et al.*, 1975). We believe that much of the scatter in stress drops reported in the literature (e.g., Tucker and Brune, 1973) may be due to unstable determination of the frequency corner. Another rather common form of the displacement spectrum is shown on the right-hand side of Fig. 37. Here the radiated spectrum can be characterized by three straight-line segments with two corners. The lowest frequencies have constant amplitude; at some frequency, amplitude decreases as  $f^{-1}$ ; and at the highest frequencies, amplitude de-

creases at least as  $f^{-2}$ . Examples of the two types of radiated spectra described above and in Fig. 37 are shown in Figs. 38 and 39.

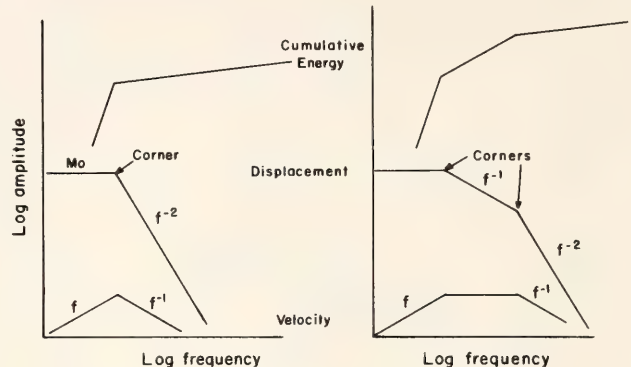


Fig. 37. Schematic showing radiated spectra. (Left) A "simple" earthquake may be characterized by a two-segment displacement spectrum. Most of the energy is in the vicinity of the corner. The frequency at the corner is inversely proportional to the length of the rupture. (Right) Radiation due to uneven rupture propagation or heterogeneous stress distribution. Most of the energy may be associated with the  $f^{-1}$  segment of the three-segmented displacement spectrum. Neither of the two corners is simply related to the rupture size.

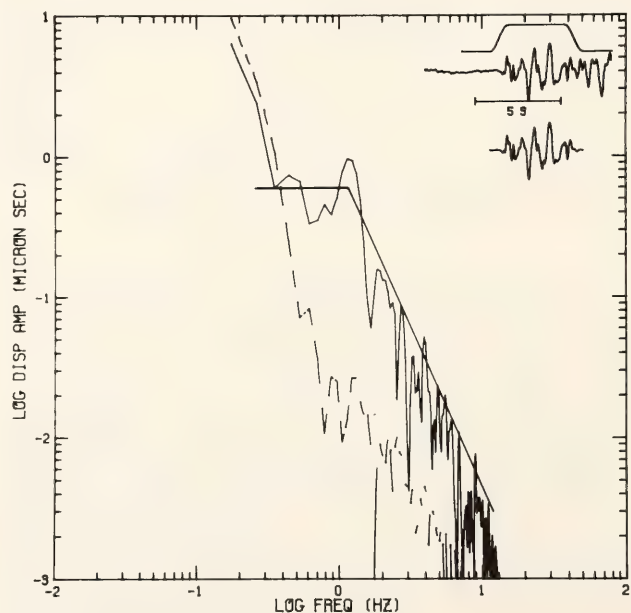


Fig. 38. Displacement spectrum of magnitude 3.9 "simple" event near Krafla. The signal analysed and window used are shown at upper right. The broken line is the noise determined from a similar window preceding the arrival. The straight lines represent the type of displacement spectrum (Fig. 37) used to estimate source parameters.



We use an alternate method for determining stress drop which is fundamentally more stable. It is based on the stress drop  $\sigma = \mu E/Mo$  where  $\mu$  is the rigidity,  $Mo$  is the seismic moment, and  $E$  is the total radiated energy. This total radiated energy is proportional to  $\int_0^\infty V^2 df$  where  $V$  is the velocity of the ground motion. ( $Mo$  and  $V$  are of course to be corrected for all geometric, distance, and attenuation effects.) We can determine the range of frequency over which we must integrate to include most of the energy by observing when  $\int_0^f V^2 df$  no longer increases substantially with increasing  $f$ . Figure 37 shows the process schematically. Figure 40 shows the results from a "simple" earthquake (Fig. 37, left) where most of the energy is in the vicinity of the corner. Figure 41 shows the results from the radiated spectrum of Fig. 39; in this case there is substantial energy between the two corners. Note

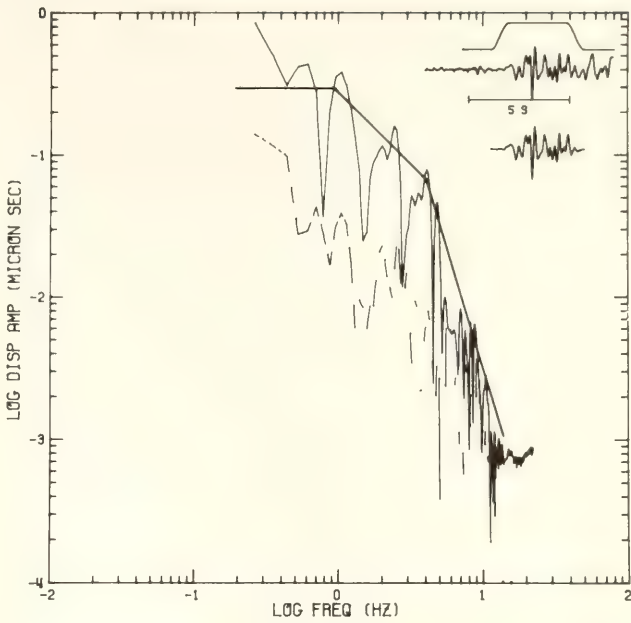


Fig. 39. Displacement spectrum of magnitude 3.8 event near Krafla. The rupture process was uneven and the radiated spectrum is more complex than that in Fig. 38. See Fig. 38 for further details.

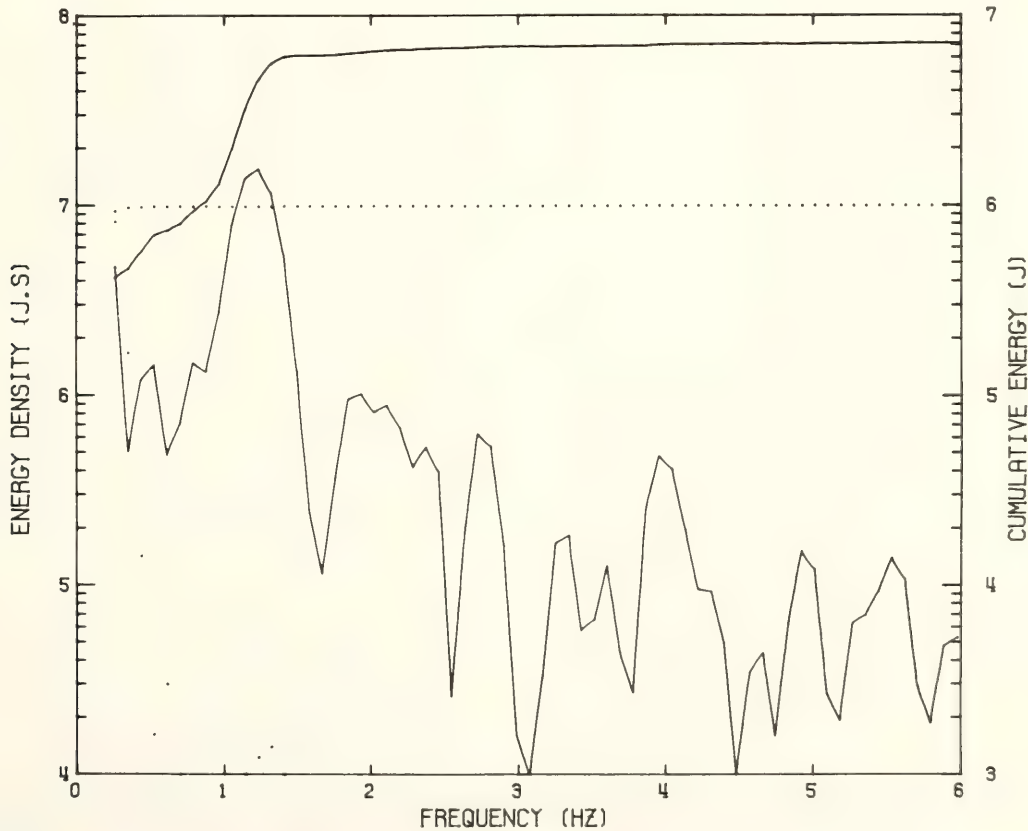


Fig. 40. Cumulative energy (upper curve) and energy density vs. frequency from the spectrum shown in Fig. 38. Most of the energy is radiated in the range 1–1.5 Hz, which includes the corner frequency. Dots indicate the noise level.

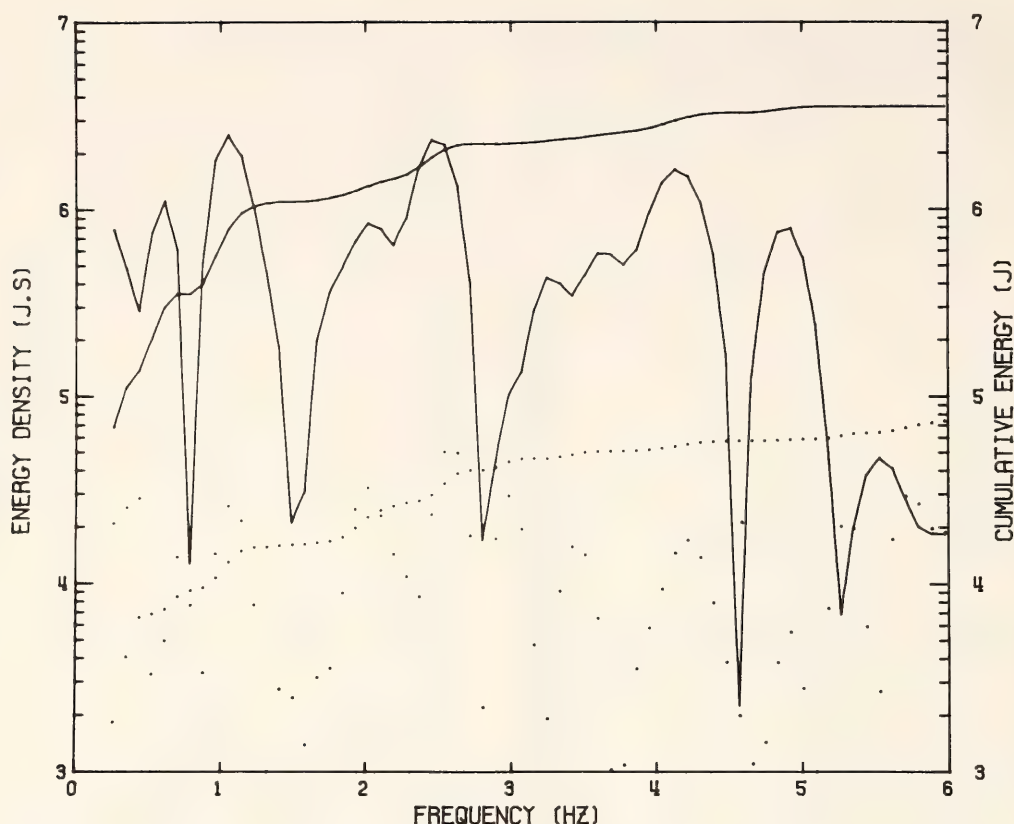


Fig. 41. Cumulative energy (upper curve) and energy density vs. frequency from the spectrum shown in Fig. 39. The energy density remains high up to 4 Hz. In both examples the cumulative energy approaches a limit which can be easily determined.

that in both cases, despite the complexity of the radiated spectrum, the total cumulative energy can be reliably determined.

in relatively unfractured rock which is much stronger, or (2) stress in the region is relieved by the first few earthquakes.

If this behavior is found in other ac-

### Results

The stress-drop data is shown as a function of time in Fig. 42. The general trend of stress drop in each region is to decrease with time after the onset. The effect is clearer in Fig. 43, where the first five days of data after the onset are plotted. In the case of the transform fault event, the main shock is plotted as the onset. The initial stress drop for the three regions shown are 3–6 bars. This decreases to about 1 bar after three days.

### Discussion

There are two possible causes for the decrease in stress drop after onset of activity: (1) the first earthquakes are

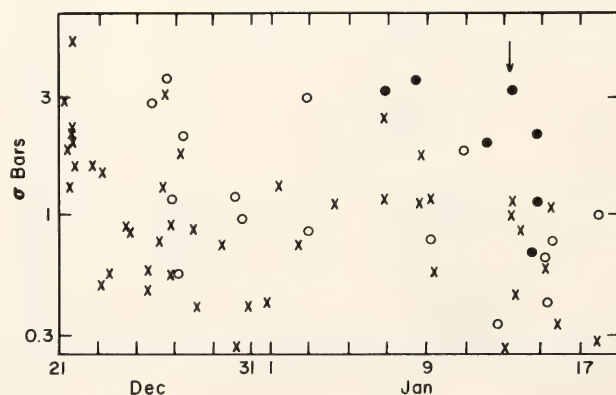


Fig. 42. Stress drop vs. date for events in the three groups as marked in Fig. 36 (Right). The arrow indicates the main event ( $M = 6.4$ ) on the transform fault. Group  $\times$  starts on 21 December, group  $\circ$  on 25 December, group  $\bullet$  on 6 January. In each case the stress drops are higher on these days than on succeeding days. See Fig. 43 for expanded plot.



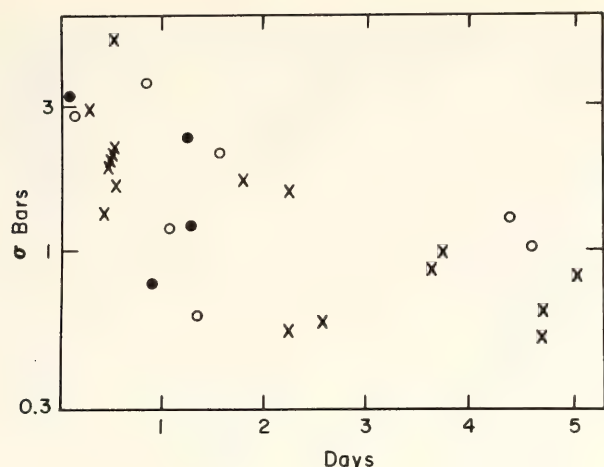


Fig. 43. Stress drop vs. time for the three regions marked in Fig. 36. Stress changes are plotted as a function of time for the five days following the onset of seismic activity in each region.

tive regions of the earth, the technique described here may be valuable in determining whether particular regions are in a state of high stress and therefore "ready" for a large earthquake.

### References

- Linde, A. T., I. S. Sacks, and J. A. Snoke, Multiple rupture earthquakes and the determination of source parameters, *Carnegie Inst. Wash. Year Book* 74, 281, 1975.
- Tucker, B. E., and J. N. Brune, Seismograms, S-wave spectra, and source parameters for aftershocks of San Fernando, California, earthquake of February 9, 1971, in *Geological and Geophysical Studies, III*, pp. 69-121, U.S. Dept. of Commerce, 1973.

### GEOCHEMISTRY OF BASALTS FROM THE FAMOUS AREA: A REEXAMINATION

William M. White

The FAMOUS (French-American Mid-Ocean Undersea Study) project was an intensive geophysical and geological study of a small area of the Mid-

Atlantic Ridge near 37°N. Its purpose was to generate a detailed picture of the manner in which new ocean floor is created. This is important not only intrinsically but also because the geochemistry of basalts is often used to make inferences about the mantle from which the basalts are derived. This requires a knowledge of the processes that have affected the basalts during their generation and evolution.

Bryan and Moore (1977) were able to demonstrate the existence of regular compositional and petrographic variations within the rift valley in the FAMOUS area: the most primitive lavas occur in the center and the more differentiated ones on the flanks. Bryan and Moore suggested that this zonation resulted from fractional crystallization in a crustal magma chamber. An isotopic and trace element study of FAMOUS basalts by White and Bryan (1977) revealed that the lavas had a uniform Sr isotopic composition, but variations in large ion lithophile (LIL) elements were too great to result from fractional crystallization alone. White and Bryan suggested that LIL-element variation resulted from variations in the extent of melting.

A subsequent study of rare earths in FAMOUS basalts by Langmuir *et al.* (1977) revealed a variation in rare earth patterns, including some basalts depleted in light rare earth (LRE) elements, much greater than found by White and Bryan. Citing the Sr isotopic evidence for source homogeneity, Langmuir *et al.* suggested a complex partial melting model, dynamic melting, to explain the rare earth variations.

Since White and Bryan (1977) and Langmuir *et al.* (1977) analyzed different sample sets, and in view of the large variation in rare earth patterns, it seemed advisable to check the assumption of source homogeneity with additional Sr isotopic analyses and, more importantly, with Nd isotopic analyses. The latter seemed particularly important in view of a recent study by Zindler *et al.* (1978)

of basalts from the Reykjanes Peninsula in Iceland. These basalts have a uniform Sr isotopic composition but variable rare earth patterns and Nd isotope ratios. An additional objective of this study was to determine the extent that trace element abundances reflect the compositional zonation observed by Bryan and Moore (1977) and to try to determine the cause of this zonation.

### Results

Samples were analyzed for K, Rb, Cs, Sr, Ba, and rare earths and for  $^{87}\text{Sr}/^{86}\text{Sr}$  and  $^{143}\text{Nd}/^{144}\text{Nd}$  ratios by mass spectrometry. These data are added to the data of White and Bryan (1977) and Langmuir *et al.* (1977).

A summary of analytical results is given in Table 7. Sr isotope ratios range from 0.70286 to 0.70299, and with one exception Nd isotope ratios vary only from 0.513150 to 0.513192. These ranges are similar to those expected from analytical error. Nd and Sr isotope ratios of FAMOUS basalts reported here are essentially identical to those reported from Leg 37 basalts by O'Nions *et al.* (1977) when differences in the analyzed values of the interlaboratory standards are considered. Thus, basalts erupted in the FAMOUS region have been isotopically uniform for the past 3 m.y.

The geographic distribution of Rb and Yb abundances are shown in Fig. 44. Lavas in the central part of the rift valley tend to be poorest in LIL ele-

TABLE 7. Summary of Isotopic and Trace Element Analytical Results

Sample*	$^{87}\text{Sr}/^{86}\text{Sr}^\dagger$	Rb/Sr	$^{143}\text{Nd}/^{144}\text{Nd}^\ddagger$	Sm/Nd
519-4	$0.70299 \pm 4$		$0.513150 \pm 35$	0.320
521-16	$0.70286 \pm 5$		$0.513183 \pm 25$	0.294
521-4-3	$0.70297 \pm 6\%$	0.045§	$0.513172 \pm 20$	0.287
523-1	$0.70289 \pm 3$	0.044	$0.513093 \pm 35$	0.277
523-2			$0.513192 \pm 40$	0.267
524-4	$0.70289 \pm 6$		$0.513192 \pm 25$	0.329
525-2				0.294
525-5-2	$0.70298 \pm 4$	0.037	$0.513187 \pm 35$	0.303
525-5-3	$0.70296 \pm 6\%$	0.034§	$0.513178 \pm 30$	0.327
526-3				0.297
526-5	$0.70297 \pm 4$	0.053	$0.513161 \pm 20$	0.281
526-6	$0.70288 \pm 5$	0.029	$0.513195 \pm 25$	0.302
521-1-1	$0.70289 \pm 6$	0.024	$0.513186 \pm 20$	0.337
527-4				0.300
527-6-1	$0.70294 \pm 7\%$	0.063§	$0.513166 \pm 25$	0.290
528-4	$0.70289 \pm 5$	0.025	$0.513167 \pm 40$	0.327
529-4	$0.70296 \pm 5$	0.035	$0.513174 \pm 25$	0.303
534-2	$0.70291 \pm 6$	0.034	$0.513174 \pm 30$	0.318
534-3	$0.70288 \pm 6\%$	0.034§		0.303
528-3		0.030		0.324
529-3-2a	$0.70287 \pm 6$		$0.513147 \pm 35$	0.296

\* See Bryan and Moore (1977) for sample locations and descriptions.

†  $^{87}\text{Sr}/^{86}\text{Sr}$  normalized to  $^{86}\text{Sr}/^{88}\text{Sr} = 0.11940$  and relative to 0.70800 for E & A standard.

‡  $^{143}\text{Nd}/^{144}\text{Nd}$  normalized to  $^{146}\text{Nd}/^{144}\text{Nd} = 0.7219$  and relative to 0.512708 for BCR-1 standard.

§  $^{87}\text{Sr}/^{86}\text{Sr}$  and Rb/Sr from White and Bryan (1977).

|| Sm/Nd from Langmuir *et al.* (1977).



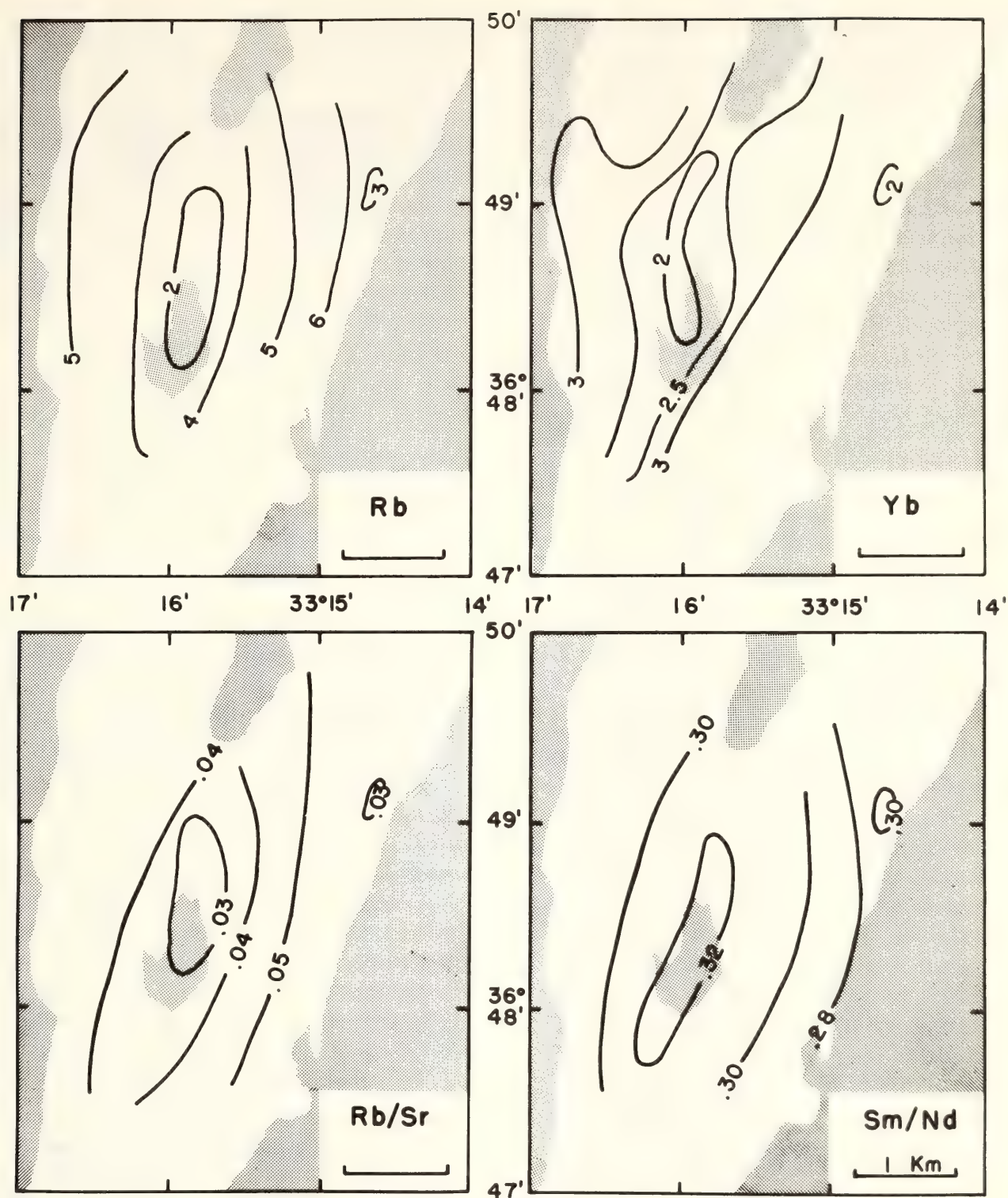


Fig. 44. Geographic zonation in LIL-element contents of rift valley lavas in the FAMOUS area. Clockwise from top left: Rb (ppm), Yb (ppm), Sm/Nd, Rb/Sr. Rift valley walls and central volcanic highs are shaded. Compare figs. 12 and 13 of Bryan and Moore (1977).

ments, with concentrations increasing systematically outward. The total ranges are 1.40–6.7 ppm in Rb and 1.38–3.92 ppm in Yb. Geographic patterns of other LIL-element abundances are similar to

those of Rb and Yb. Figure 44 also shows the geographic variation in Rb/Sr and Sm/Nd. There is a systematic increase in Rb/Sr and decrease in Sm/Nd outward from the center of the rift valley.



The total ranges are 0.024–0.063 in Rb/Sr and 0.267–0.337 in Sm/Nd. Variations of other LIL-element ratios, such as K/Rb and Ba/K, are similar to that of Sm/Nd.

### Discussion

The small range in both Sr and Nd isotope ratios confirms the inference of White and Bryan (1977) that the mantle source of FAMOUS basalts is essentially isotopically uniform, in contrast with the large variation in  $^{87}\text{Sr}/^{86}\text{Sr}$  ratios observed by White *et al.* (1976) between 32°N and 39°N along the Mid-Atlantic Ridge. The Sr and Nd isotopic uniformity implies either that the source is uniform in its Rb/Sr and Sm/Nd ratios or that heterogeneities in these ratios are relatively young (i.e., less than about 80 m.y. old). It is not possible to distinguish between these alternatives, but the former interpretation is accepted here if only because the latter seems *ad hoc*.

To explain the geographic zonation in the chemical and petrographic characteristics of FAMOUS basalts, Bryan and Moore (1977) suggested that a large, zoned magma chamber existed in the crust beneath the valley. They suggested that the hottest and most primitive magma is located at the center of the chamber, while cooler, differentiated magma occurs on the flanks. Chemical zonation resulted principally from fractional crystallization, although some diffusive volatile transport seemed necessary to account for variations in  $\text{K}_2\text{O}$ ,  $\text{H}_2\text{O}$ , and  $\text{TiO}_2$ . In their view, geographic zonation in the rift valley simply mirrors zonation in the magma chamber below.

There are a number of serious difficulties with the magma chamber model. First, fractional crystallization alone cannot account for the range of trace element abundances and ratios observed, even if the model is modified to include periodic partial refilling and magma mixing, as suggested by O'Hara (1977). Conceivably, this difficulty could be overcome by volatile transport, as suggested

by Bryan and Moore, but this is a rather *ad hoc* hypothesis for which there is no independent evidence. An alternative model proposed by Nisbet and Fowler (1978) also relies on fractional crystallization to produce rift valley zonation and hence is unsatisfactory. Second, any magma chamber of the dimensions considered by Bryan and Moore should be convectively unstable. Any basaltic magma body thicker than a few meters will have a Rayleigh Number which exceeds the critical value for convective flow, about  $10^3$ . For a 1-km-thick chamber, Shaw (1974) calculates a Rayleigh Number of  $5 \times 10^{14}$  and a velocity of 500 km/yr. This corresponds to a turnover time of several days. Since the boundary layer will be no more than a meter or so (Shaw, 1974), such a chamber will be well mixed and could not be zoned. Third, thermal models suggest that the maximum width of a steady state magma chamber is only 1–2 km for ridges with a half spreading rate of 1 cm/yr, as is the case in the FAMOUS regions (Nisbet and Fowler, 1978). Finally, shear-wave data suggest there is presently no crustal magma chamber in the FAMOUS region (Nisbet and Fowler, 1978). Thus, some other cause must be found for the LIL-element variations and chemical zonation in the FAMOUS rift valley.

Langmuir *et al.* (1977) suggested a magma generation model which they termed dynamic melting. They noted that the mantle beneath the ridge should be zoned with respect to degree of melting (Fig. 45). In their model, melt can be tapped from any of these zones, leaving some residual melt. As asthenosphere continues to rise, further melting occurs and the new melt created mixes with that remaining. They found that this process along with fractional crystallization can at least qualitatively account for the variety of rare earth patterns observed in FAMOUS basalts. While no attempt has been made here to determine if dynamic melting can explain the variation



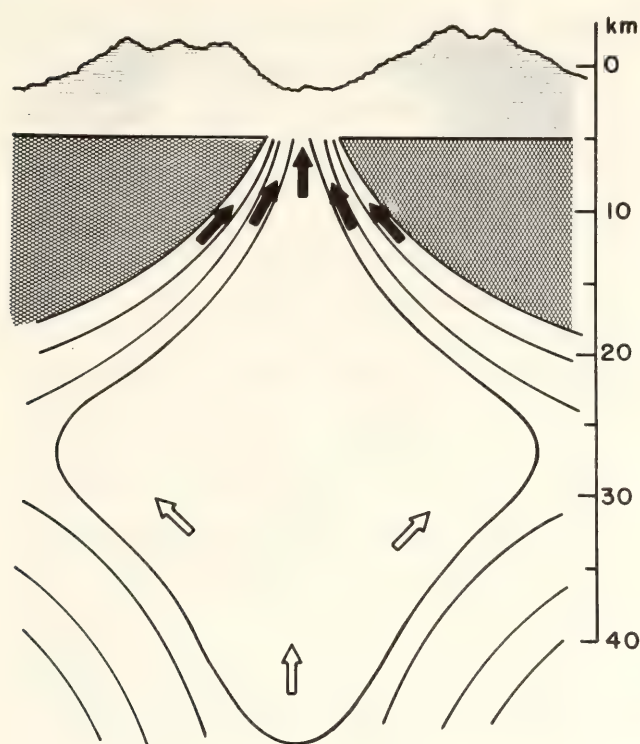


Fig. 45. Schematic cross section of the mantle beneath the FAMOUS area (after Langmuir *et al.*, 1977). Contours are degree of melting. Solid arrows indicate possible flow of melt into the rift valley. Open arrows indicate flow of mantle.

in K, Rb, Cs, Sr, and Ba, as well as rare earths, it seems likely that it can; dynamic melting is therefore accepted as the cause of the observed variation in LIL elements.

While dynamic melting may explain the variation in LIL-element abundances, it does not account for their geographic distribution in the rift valley; Langmuir *et al.* made no attempt to address this problem. One possible explanation for the zonation is consistent with the dynamic melting hypothesis and is suggested by Fig. 45. Perhaps zoning in the rift valley simply reflects zoning with respect to degree of melting in the mantle below. Melt may be channelled parallel to the degree-of-melting contours through a sort of inverted funnel, reproducing the zonation of the mantle in the rift valley on a much smaller scale. This zonation would be enhanced by fractional crystallization, as the flank lavas would

pass through the crust more slowly than the central ones (Nisbet and Fowler, 1978). If this "inverted funnelling" actually occurs, it should occur almost universally beneath midocean ridges, and chemical zonation in the rift valley should be common except perhaps on fast-spreading ridges where large magma chambers develop.

Finally, the possibility that the rift valley zonation is a transient phenomenon must be considered. Bryan and Moore (1977) divided the basalts into four age groups on the basis of palagonitization and manganese crust thickness. While absolute ages could not be assigned, several lines of evidence suggested that the oldest lavas are no older than a few tens of thousands of years (Bryan and Moore, 1977). Flank lavas are generally older than central lavas, but they are considerably younger than the inferred spreading age of the crust on which they occur. The depleted basalts almost all fall in Bryan and Moore's (1977) age group 1 (youngest) whereas the LIL-element-enriched basalts typically fall in age groups 2 and 3. (It should be noted that the second most-LRE-enriched sample, 523-1, falls in age group 1 and hence is apparently younger than the most-LRE-depleted basalt, 527-1-1, which is of age group 2.) This suggests that the LIL-element-depleted lavas represent the latest magma batch to arrive beneath the rift valley, and the LIL-element-enriched flank lavas are derived from an older magma batch. The overlap in ages of the flank and central types requires that several magma types must supply magma to the surface simultaneously. New magma is presumably preferentially channelled through zones of weakness beneath the center of the valley (Nisbet and Fowler, 1978). It is suggested that the central lavas are derived either directly from the mantle or from a young magma pocket or small chamber beneath the central volcanic axis. The flank lavas are derived from older residual magma pockets which become increasingly iso-

lated from resupply from the mantle, although new magma may occasionally reach these pockets and mix with the old magma. The zoning in the rift valley would thus result from the overprint of two factors. First, the character of the magma-supplying volcanism in the valley is gradually changing (becoming more LRE depleted and decreasing in Rb/Sr) because of variation in partial melting parameters. This variation seems to be taking place on a time scale of a few tens of thousands of years and may perhaps be cyclical (White and Bryan, 1977). Second, flank lavas are derived from old magma that has had time to fractionate. This fractional crystallization produces the variation in MgO/FeO and the petrographic features observed by Bryan and Moore (1977). This model differs from that of Nisbet and Fowler (1978) and from Byerly and Wright's (1978) model for the genesis of Leg 37 basalts only in that it requires a change with time in the character of the parental magma being supplied from the mantle. It accommodates the dynamic melting model of Langmuir *et al.* (1977) as the principal factor producing LIL variation in FAMOUS basalts, but requires a systematic variation with time in the dynamic melting product.

### Summary

Basalts from the FAMOUS region have uniform Sr and Nd isotopic compositions, with average  $^{87}\text{Sr}/^{86}\text{Sr}$  of 0.70292 and  $^{143}\text{Nd}/^{144}\text{Nd}$  of 0.51317. This isotopic homogeneity requires that the source region be homogeneous in Rb/Sr and Sm/Nd, or that heterogeneities in these ratios be younger than about 80 m.y.

LIL-element abundances in FAMOUS basalts show a systematic geographic distribution. Lavas from the central axis of the rift valley are the most depleted in LIL elements and have the lowest Rb/Sr and highest Sm/Nd, K/Rb, and K/Ba

ratios. There is a gradual increase in LIL-element abundances and Rb/Sr ratios and decrease in Sm/Nd, K/Rb, and K/Ba outward toward the flanks.

The observed variation in LIL-element abundances and ratios are too great to have resulted from fractional crystallization alone. For this reason and others, models by Bryan and Moore (1977) and Nisbet and Fowler (1978), constructed to explain chemical zonation in the rift valley, are found inadequate. LIL-element variation in FAMOUS basalts most likely result from processes in the mantle similar to those encompassed in the dynamic melting model of Langmuir *et al.* (1977).

Two possible origins of the rift valley zonation are proposed. In the first, zonation in the rift valley reflects degree of melting zonation on a much larger scale in the mantle. In this case, rift valley zonation should be a steady state feature and should be common to all ridges where large crustal magma chambers do not develop. In the second model, there is a systematic change with time in the parental magma-feeding volcanism in the valley, with melts becoming progressively more depleted in LIL elements as a result of changing melting parameters. In both models, central lavas experience less fractional crystallization because the residence time of magma in the crust increases with distance from the central axis. In order to choose between these two possible models, at least one additional intensive study of a midocean ridge segment will have to be made. A failure to find the chemical zonation observed in the FAMOUS area would favor the second model.

### References

- Bryan, W. B., and J. G. Moore, Compositional variations of young basalts in the Mid-Atlantic Ridge rift valley near lat  $36^{\circ}49'N$ , *Geol. Soc. Amer. Bull.*, 88, 556–570, 1977.



- Byerly, G. R., and T. L. Wright, Origin of major element chemical trends in DSDP Leg 37 basalts, Mid-Atlantic Ridge, *J. Volcanol. Geotherm. Res.*, **3**, 229–279, 1978.
- Langmuir, C. H., J. F. Bender, A. E. Bence, G. N. Hanson, and S. R. Taylor, Petrogenesis of basalts from the FAMOUS area: Mid-Atlantic Ridge, *Earth Planet. Sci. Lett.*, **36**, 133–156, 1977.
- Nisbet, E. G., and C. M. R. Fowler, The Mid-Atlantic Ridge at 37 and 45°N: some geophysical and petrological constraints, *Geophys. J. Roy. Astron. Soc.*, **54**, 631–660, 1978.
- O'Hara, M. S., Geochemical evolution during fractional crystallization of a periodically refilled magma chamber, *Nature*, **266**, 503–507, 1977.
- O'Nions, R. K., P. J. Hamilton, and N. M. Evensen, Variation in  $^{143}\text{Nd}/^{144}\text{Nd}$  and  $^{87}\text{Sr}/^{86}\text{Sr}$  ratios in oceanic basalts, *Earth Planet. Sci. Lett.*, **34**, 13–22, 1977.
- Shaw, H. R., Diffusion of  $\text{H}_2\text{O}$  in Granitic Liquids, in *Geochemical Transport and Kinetics*, pp. 139–170, A. W. Hofmann, B. J. Giletti, H. S. Yoder, and R. A. Yund, eds., Carnegie Institution of Washington, Washington, D.C., 1974.
- White, W. M., and W. B. Bryan, Strontium isotope, K, Rb, Cs, Sr, Ba and rare earth geochemistry of basalts from the FAMOUS area, *Geol. Soc. Amer. Bull.*, **88**, 571–576, 1977.
- White, W. M., J.-G. Schilling, and S. R. Hart, Evidence for the Azores mantle plume from strontium isotope geochemistry of the Central North Atlantic, *Nature*, **263**, 659–663, 1976.
- Zindler, A., S. R. Hart, F. Frey, and S. P. Jakobsson, Nd and Sr isotope compositions and REE abundances in Reykjanes Peninsula basalts: evidence for mantle heterogeneity, *EOS: Trans. Amer. Geophys. U.*, **59**, 410, 1978.

# PB ISOTOPE GEOCHEMISTRY OF THE GALÁPAGOS ISLANDS

William M. White

Sun and Hanson (1975) and Brooks *et al.* (1976) have shown that Pb and Sr isotope ratios of young oceanic basalts scatter about isochrons having ages of about 1.8 b.y. These “mantle isochrons” clearly indicate the antiquity of mantle heterogeneity but their further interpretation is a subject of current debate. In last year's Report, White and Hofmann (1978) reported on Sr and Nd isotope geochemistry of basalts from the Galápagos Islands. They found that the average  $^{87}\text{Sr}/^{86}\text{Sr}$  and Rb/Sr ratios of Galápagos tholeiites fell on the 1.6-b.y. oceanic mantle isochron of Brooks *et al.* (1976). In addition, they found that average  $^{87}\text{Sr}/^{86}\text{Sr}$  and Rb/Sr ratios of tholeiites from each island define a younger mantle isochron having an age of about 600 m.y.

Construction of Rb/Sr mantle isochrons requires the implicit assumption that  $^{87}\text{Sr}/^{86}\text{Sr}$  and Rb/Sr ratios are representative of their mantle sources. While isotope ratios of basalts may be justifiably taken as representative of their sources, this may not be the case for Rb/Sr ratios (see Hofmann and Wright, this Report). Because two U isotopes decay to two Pb isotopes, time information may be derived directly from the Pb isotope ratios without consideration of U/Pb ratios. For this reason, and as a test of oceanic mantle isochrons and the Galápagos Rb/Sr mantle isochron of White and Hofmann, a Pb isotope study of basalts from the Galápagos Islands was undertaken. The preliminary results of this study are reported here.

Results are reported in Table 8. Pb isotope ratios show a remarkable range, with  $^{206}\text{Pb}/^{204}\text{Pb}$  varying from 18.26 to 20.11. This covers a large part of the range of all oceanic basalts. The lowest ratios fall within the field of midocean ridge basalts. U and Pb concentrations vary within 0.065–0.455 ppm and 0.330–

TABLE 8. U and Pb Concentrations and Pb Isotope Ratios of Galápagos Basalts

Island	Sample	$^{206}\text{Pb}/^{204}\text{Pb}$	$^{207}\text{Pb}/^{204}\text{Pb}$	$^{208}\text{Pb}/^{204}\text{Pb}$	$\mu$
Floreana	FL-3	19.879	15.632	39.559	7.51
	FL-26	19.535	15.583	39.114	11.95
Santa Cruz	E-1	18.526	15.487	37.961	8.16
	SC-78	18.506	15.498	37.943	
	SC-100	18.442	15.453	37.853	14.37
	SC-163	18.555	15.508	38.016	
Isabela	E-134	18.263	15.524	37.956	14.93
	E-63	18.744	15.545	38.308	
Santiago (San Salvador)	E-76	18.881	15.533	38.390	26.64
San Cristobal	E-103	18.838	15.536	38.386	25.61
Española	H334	18.978	15.557	38.429	
Marchena	E-15	18.840	15.526	39.399	18.42
Pinta	E-8	19.124	15.566	38.927	
Fernandina	E-42	19.068	15.526	38.607	34.19
Darwin	E-35	20.114	15.730	39.947	9.18

2.42 ppm, respectively.  $^{238}\text{U}/^{204}\text{Pb}$  ( $\mu$ ) ranges from 7.51 to 34.19. There is no correlation between Pb isotope ratios and  $\mu$ .

Alkali basalts and tholeiites from the island of Santa Cruz, which have indistinguishable Sr and Nd isotope ratios (White and Hofmann, 1978), also have virtually indistinguishable Pb isotope ratios. This strongly suggests that these basalts are derived from a single source. This source has  $^{87}\text{Sr}/^{86}\text{Sr} \sim 0.70265$ ,  $^{143}\text{Nd}/^{144}\text{Nd} \sim 0.51315$ , and  $^{206}\text{Pb}/^{204}\text{Pb} \sim 18.50$ , values which are typical of midocean ridge basalts. Thus far, only one tholeiite and one alkali basalt have been analyzed for U and Pb concentrations. The alkali basalt has higher U and Pb concentrations but lower  $\mu$  than the tholeiite.

The Pb isotope data are plotted in Fig. 46, with fields of midocean ridge basalts and other oceanic islands shown for comparison (data from a compilation of

Sun, in press). The data fall along the trend of other oceanic basalt data which have  $\Delta(^{207}\text{Pb}/^{204}\text{Pb})/\Delta(^{206}\text{Pb}/^{204}\text{Pb}) \sim 0.1$  (Sun, in press). As do all oceanic basalts, Galápagos basalts have Pb isotope ratios which fall considerably to the right of the geochron, implying that their source has experienced an increase in its U/Pb ratio at some point in the past.

A regression line through the Galápagos data has a slope of 0.1105, indistinguishable from the slope of all oceanic data. If this line is interpreted as an isochron, the age is  $1.81 \pm 0.12$  b.y. Assuming that this interpretation is valid, a simple two-stage model can be constructed to account for Pb isotope evolution of the source of Galápagos basalts. In the first stage, from 4.55 to 1.81 b.y. ago, the mantle had a uniform  $\mu$  value, and  $^{206}\text{Pb}/^{204}\text{Pb}$  and  $^{207}\text{Pb}/^{204}\text{Pb}$  grew uniformly from primordial values (Tatsumoto *et al.*, 1973) to 14.633 and



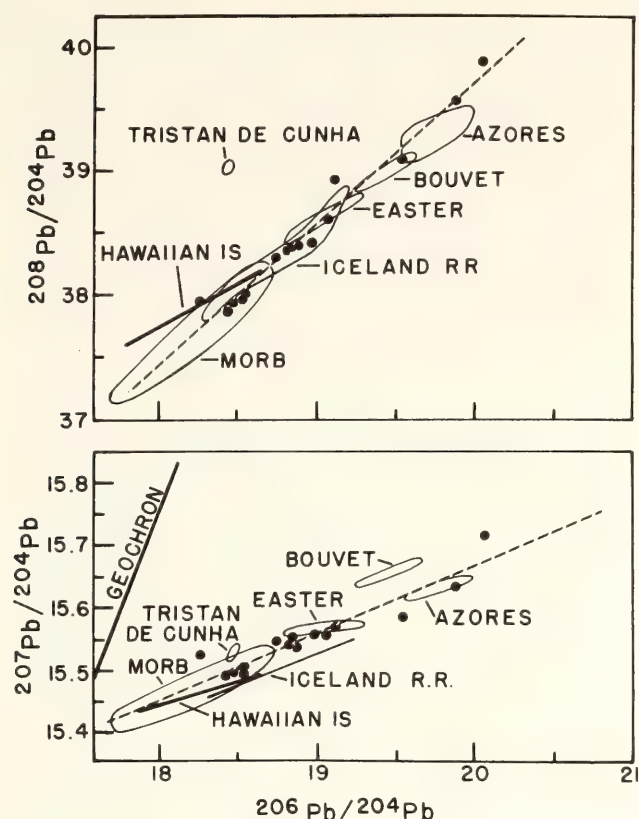


Fig. 46. Variation of lead isotope ratios in Galápagos basalts. Data from other oceanic regions (from Sun, in press) is shown for comparison. Lines are  $2\sigma$  error regression lines through Galápagos data.

15.068, respectively. The apparent value of  $\mu$  for this stage is 7.60. At 1.81 b.y. ago, this reservoir was differentiated to produce values ranging from 11.2 to 16.9 and averaging 13.3, accounting for the range in Pb isotope ratios in Galápagos basalts. To account for the scatter about the 1.81-b.y. isochron, the model must be made slightly more complex, either by postulating that  $\mu$  was not totally uniform in the first stage or that differentiation took place over a finite period of time. To account for the  $^{208}\text{Pb}/^{204}\text{Pb}$  ratios and their correlation with  $^{206}\text{Pb}/^{204}\text{Pb}$ , the  $^{232}\text{Th}/^{238}\text{U}$  ( $\kappa$ ) ratio in the first stage is 3.40, increasing to 3.95 at 1.81 b.y. The calculated value for  $\mu$  in the first stage falls within the range of values estimated for the bulk earth (crust + mantle), 7.5–9.5, but the Th/U ratio in the first stage seems somewhat low. The implied  $\mu$ 's of the second stage

are within the range observed in the basalts.

The above solutions for a two-stage model are unique. To the extent that data from other oceanic islands and ridges fall along the same trend as the Galápagos data, the model is generally applicable to the oceanic mantle. Unfortunately, there is no constraint on the type of model to be fit to the data, and any number of equally satisfactory 2+n stage or continuous-evolution models could be constructed.

While the above model does not necessarily reflect reality, it is useful to compare its implications with the implications of the Sr and Nd isotope data of Galápagos and other oceanic basalts. Galápagos basalts, like most oceanic basalts, have  $^{87}\text{Sr}/^{86}\text{Sr}$  and  $^{143}\text{Nd}/^{144}\text{Nd}$  ratios which require that the time-averaged Rb/Sr and Sm/Nd ratios of their sources be lower and higher, respectively, than that estimated for the bulk earth (White and Hofmann, 1978). This feature has been generally interpreted as indicating that the suboceanic mantle has experienced a general depletion in large ion lithophile elements (Tatsumoto *et al.*, 1965; O'Nions *et al.*, 1977), perhaps because of extraction of a partial melt. A partial melting event would leave a residual mantle with higher Th/U ratio consistent with the two-stage model above, but with a lower U/Pb ratio (Tatsumoto, 1978). The latter is opposite to the change required by the Pb isotope data. Thus, if the present understanding of U-Pb partitioning is correct, the Pb isotope data cannot be accounted for by a simple partial melting event. Possible explanations for this discrepancy include separation and downward migration of a sulfide phase which extracts Pb from the mantle (Vidal and Dosso, 1978; Sun, in press) and continuous crust-mantle mixing (Russell and Birnie, 1974; Evensen *et al.*, 1979), but further work is clearly needed to resolve this problem.

The "age" implied by the trend of the

Galápagos Pb isotope data is not significantly different from mantle isochron "ages" based on Pb-Pb and Rb-Sr data of all oceanic basalts (Sun and Hanson, 1975; Brooks *et al.*, 1976), but is greatly different from the Rb-Sr mantle isochron age of Galápagos tholeiites (White and Hofmann, 1978). One possible explanation of this discrepancy is that some event or process in the source has affected the Rb-Sr system but not the Pb-Pb system (Brooks *et al.*, 1976). Another possibility is fractionation of Rb and Sr during magma generation and evolution. Rb-Sr mantle isochrons based on "fractionated" Rb/Sr ratios would underestimate any true age (see Hofmann and Wright, this Report). However, the opposite would be true of Sm-Nd isochrons; i.e., isochrons based on "fractionated" Sm/Nd ratios would overestimate a true age. Average  $^{143}\text{Nd}/^{144}\text{Nd}$  and Sm/Nd of tholeiites from each Galápagos island scatter about a line having a slope of 0.0018, implying an age of  $450 \pm 115$  m.y. (White and Hofmann, unpublished data). This is not significantly different from the age of the Rb-Sr mantle isochron of White and Hofmann (1978). Thus the discrepancy between ages based on Rb-Sr and Sm-Nd on the one hand and Pb-Pb data on the other is apparently not due to fractionation of Rb/Sr and Sm/Nd.

An alternative explanation of Pb-Pb, Rb-Sr, and Sm-Nd mantle isochrons is that they are not isochrons but mixing lines. In this case, the apparent "age" of the  $^{207}\text{Pb}/^{204}\text{Pb}$  vs.  $^{206}\text{Pb}/^{204}\text{Pb}$  slope is the *minimum* time since complete isotopic equilibration of the end-member reservoirs. A test of two-component mixing can be made by plotting different isotope ratios against one another. On such plots, the data should lie along a smooth curve connecting the end members. White and Hofmann (1978) found that Sr and Nd isotope data do indeed scatter about an approximately straight

line. Much of this scatter was subsequently found to be a result of weathering effects on  $^{87}\text{Sr}/^{86}\text{Sr}$  ratios (White and Hofmann, unpublished data). Plots of  $^{206}\text{Pb}/^{204}\text{Pb}$  against  $^{143}\text{Nd}/^{144}\text{Nd}$  are shown in Fig. 47. In general, the Pb and Sr data are rather well correlated. The correlation between Nd and Pb isotope ratios is somewhat poorer. Scatter on these plots rules out simple two-component mixing unless it is postulated that one or both of the end-member reservoirs was somewhat heterogeneous. This is not an unreasonable supposition, as the principal candidate for the depleted end member, the source of midocean ridge basalts, has limited but real variability in its isotope composition. It should be pointed out that the correlation between various isotope ratios of Galápagos basalts is considerably better than that of all oceanic basalts (e.g., Sun, in press).

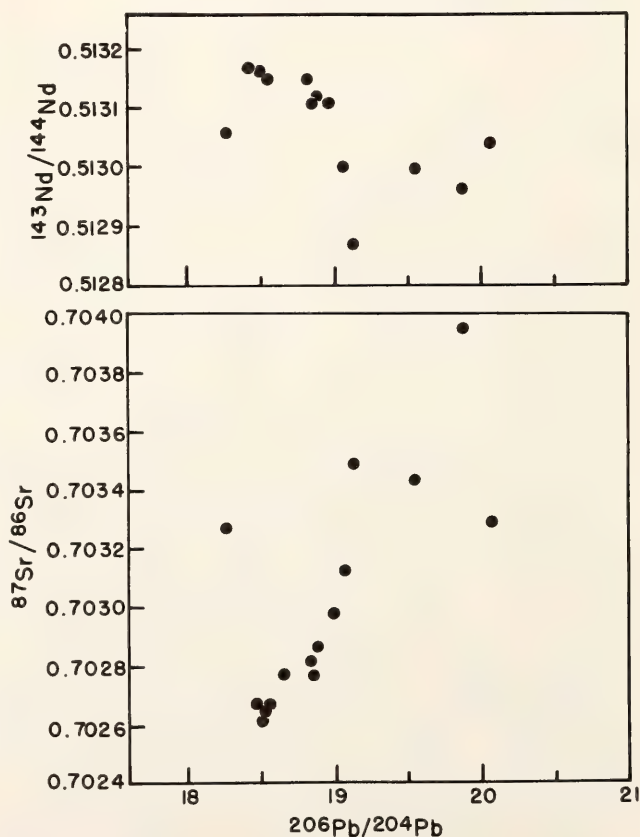


Fig. 47. Variation of  $^{143}\text{Nd}/^{144}\text{Nd}$  and  $^{87}\text{Sr}/^{86}\text{Sr}$  with  $^{206}\text{Pb}/^{204}\text{Pb}$ .



### Summary

(1) Lead isotope ratios in Galápagos basalts fall along the oceanic basalt trend and cover a remarkably large part of this range. The lowest ratios fall within the field of midocean ridge basalts.

(2) U and Pb concentrations range from 0.065–0.455 ppm and 0.330–2.42 ppm, respectively.  $\mu$  ranges from 7.51–34.19.

(3) A regression line fit to the  $^{207}\text{Pb}/^{204}\text{Pb}$  vs.  $^{206}\text{Pb}/^{204}\text{Pb}$  data has a slope of 0.1105, corresponding to an age of 1.81 b.y. This age is similar to that derived from all oceanic lead data. A two-stage model constructed to account for the data has a first stage with  $\mu = 7.60$  and  $\kappa = 3.40$ . At 1.81 b.y.,  $\kappa$  increases to 3.95 and  $\mu$  increases to 11.2–16.9. Extraction of melt from the mantle, postulated to explain Sr and Nd isotope ratios, does not explain the increase in  $\mu$ .

(4) The 1.81-b.y. age derived from the lead data contrasts with the approximate 500-m.y. age of Rb-Sr and Sm-Nd mantle isochrons of Galápagos basalts. No entirely satisfactory explanation of this discrepancy can be given at present.

Points (3) and (4) above illustrate the complexity of the earth's evolution and the failure of simple models. Clearly, further effort is required before the chemical evolution of the earth is understood.

### References

- Brooks, C., S. R. Hart, A. Hofmann, and D. E. James, Rb-Sr mantle isochrons from oceanic regions, *Earth Planet. Sci. Lett.*, **32**, 51–61, 1976.
- Evensen, N. M., P. J. Hamilton, and R. K. O'Nions, Lead isotopes crustal evolution and mantle mixing: a model, *EOS: Trans. Amer. Geophys. U.*, **60**, 406, 1979.
- O'Nions, R. K., P. J. Hamilton, and N. M. Evensen, Variations in  $^{143}\text{Nd}/^{144}\text{Nd}$  and  $^{87}\text{Sr}/^{86}\text{Sr}$  ratios in oceanic basalts, *Earth Planet. Sci. Lett.*, **34**, 13–22, 1977.
- Russell, R. D., and D. J. Birnie, A bi-directional mixing model for lead isotope evolution, *Phys. Earth Planet. Interiors*, **8**, 158–166, 1974.
- Sun, S.-S., Lead isotopic study of young volcanic rocks from mid-ocean ridges, ocean islands and island arcs, *Phil. Trans. Roy. Soc. London Ser. A.*, in press.
- Sun, S.-S., and G. N. Hanson, Evolution of the mantle: geochemical evidence from alkali basalt, *Geology*, **3**, 297–302, 1975.
- Tatsumoto, M., Isotopic composition of lead in oceanic basalt and its implication to mantle evolution, *Earth Planet. Sci. Lett.*, **38**, 63–87, 1978.
- Tatsumoto, M., C. E. Hedge, and A. E. J. Engel, Potassium, rubidium, strontium, thorium, uranium, and the ratio of strontium-87 to strontium-86 in oceanic tholeiitic basalt, *Science*, **150**, 886–888, 1965.
- Tatsumoto, M., R. J. Knight, and C. J. Allègre, Time differences in the formation of meteorites as determined from the ratio of lead-207 to lead-206, *Science*, **180**, 1279–1283, 1973.
- Vidal, P., and L. Dosso, Core formation: catastrophic or continuous? Sr and Pb isotope constraints, *Geophys. Res. Lett.*, **5**, 169–172, 1978.
- White, W. M., and A. W. Hofmann, Geochemistry of the Galápagos Islands: implications for mantle dynamics and evolution, *Carnegie Inst. Wash. Year Book* **77**, 596–606, 1978.

### TRACE ELEMENT FRACTIONATION AND THE NATURE OF THE RESIDUAL PHASES DURING THOLEIITE PRODUCTION IN HAWAII

A. W. Hofmann and T. L. Wright\*

Tholeiitic volcanism is volumetrically by far the most important form of magma production derived from the mantle. It is widely believed that tholei-

\* U.S. Geological Survey, Reston, Virginia.

ites (or their precursors) are formed by relatively large degrees of melting in the mantle, and melt fractions of from 10 to 30 percent are often quoted (e.g., Green and Ringwood, 1967; Gast, 1968; Scarfe *et al.*, 1979). Extraction of a basaltic melt removes from the mantle the "eclogite components" garnet and clinopyroxene. The question arises whether one or both of these phases are completely consumed by tholeiite production. If they are, the residual assemblage will consist essentially of olivine and orthopyroxene and will never again yield a melt of basaltic composition. In this case, the mantle must be expected to contain large volumes of "barren" material. If garnet and clinopyroxene do stay behind, the residual mantle will remain fertile to produce more basalt in a later episode of melting. Furthermore, this residual mantle will preferentially lose its light rare earth elements and will then resemble the typical "depleted" mantle found at midocean ridges.

In this report we present what we believe to be the strongest and most detailed evidence yet recorded to demonstrate the persistence of both garnet and clinopyroxene in one source region of tholeiitic melts, that beneath Kilauea volcano. Our line of reasoning is as follows. First, we show that the major element, trace element, and isotopic abundances of the sequence of lavas that erupted over a period of two years on the east rift of Kilauea (Mauna Ulu eruption) are consistent with a chemically and isotopically uniform source composition. Then, assuming that the source is indeed uniform, we show that the monotonically decreasing abundances of incompatible elements are the result of a gradually increasing degree of melting in the source. Finally, by comparing the behavior of Sr and the REE with that of the incompatible elements Ba, K, and Rb, we show that both clinopyroxene and garnet must remain in the mantle residue of all the lavas.

### Results

Abundances of K, Rb, Cs, Sr, Ba, and  $^{87}\text{Sr}/^{86}\text{Sr}$  ratios were reported last year (Hofmann *et al.*, 1978). New REE concentrations, corrected for "olivine control" (see Wright *et al.*, 1975) are shown on Fig. 48. This plot shows a fan-shaped pattern with nearly constant Yb values of about 9 and Ce values ranging from 35 to 42 relative to chondritic abundances. The variation of concentrations with date of eruption is shown on Fig. 49. Here, the results are plotted in percent deviation from the mean, because this representation illustrates the relative magnitude of the abundance variations. The plots are arranged in the order of decreasing negative slope. The behavior of Ce is similar to that of K, Rb,

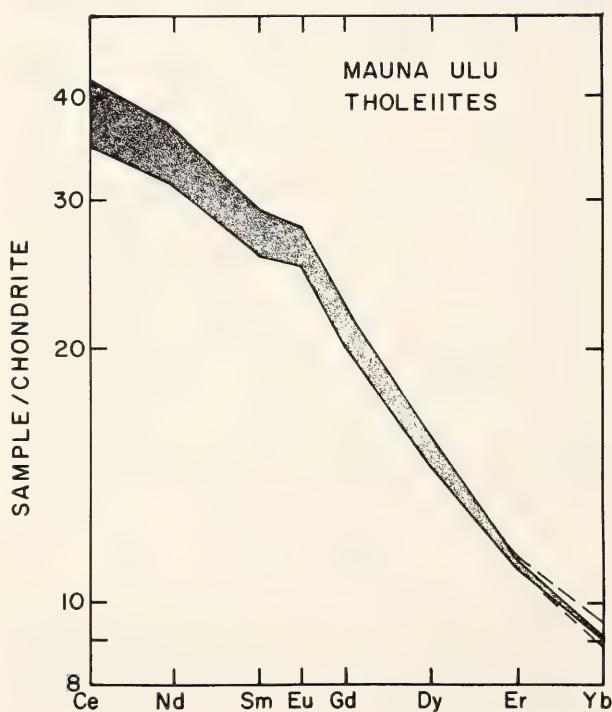


Fig. 48. Rare earth concentrations of 12 Mauna Ulu tholeiites. The shaded region represents the range of all 12 samples except for the Yb concentrations of two samples which deviate from the Yb mean value by more than 2%. These are indicated by dashed lines. All concentrations are divided by the chondritic abundances and corrected for olivine fractionation or accumulation by normalizing to an MgO concentration of 7.0% (for details, see Wright *et al.*, 1975).



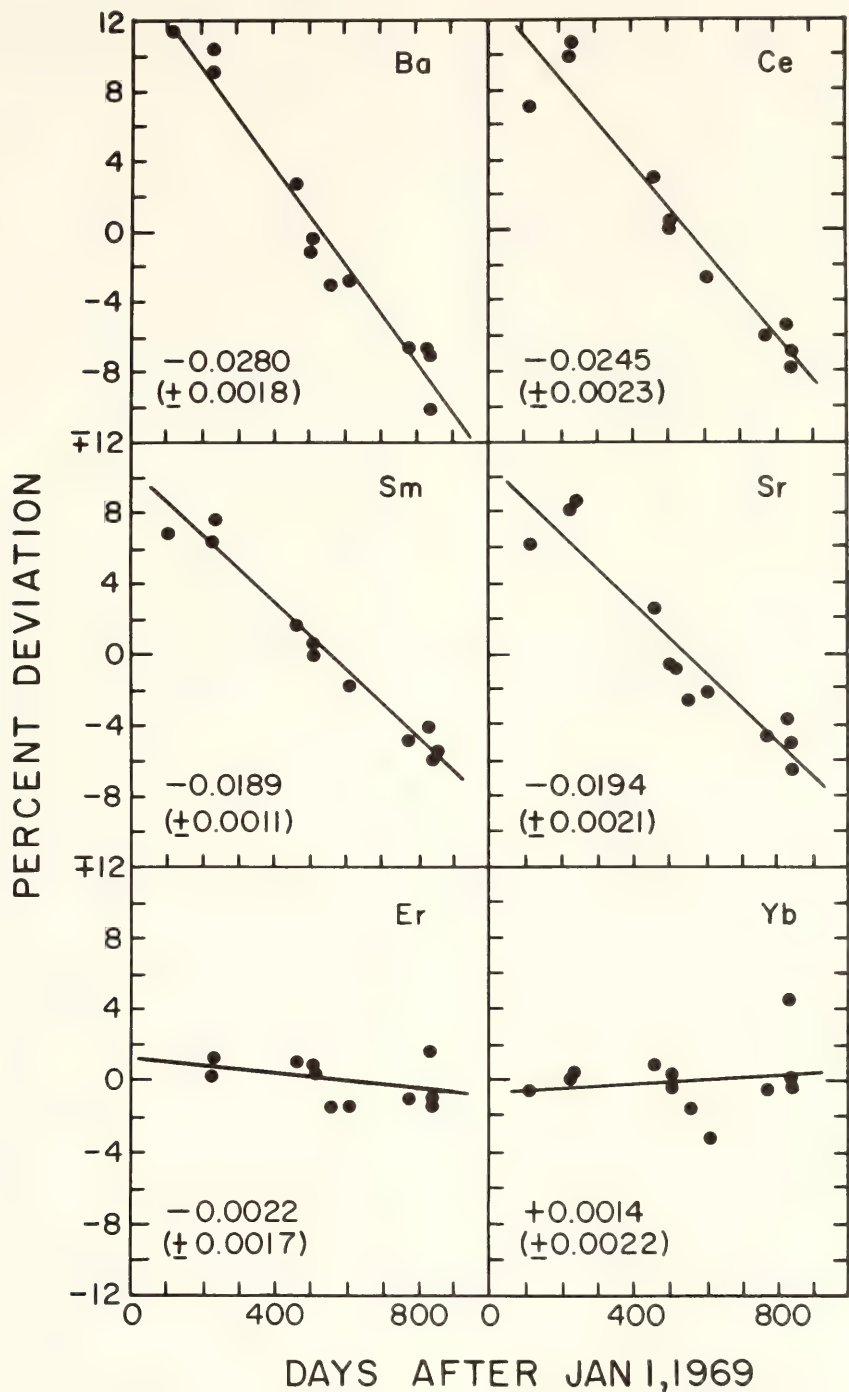


Fig. 49. Examples of concentration dependence on date of eruption. Concentrations are corrected for olivine control as in Fig. 48. The normalized values are plotted as percent deviation from the mean of each set. The date of eruption is given in days after Jan. 1, 1969. The slope and its standard error is given for each regression line.

and Ba (only Ba shown), Sr is similar to Sm and Eu, and Yb does not change systematically with time and is similar to all the major element abundances previously described by Wright *et al.* (1975). In most cases the deviations from the regression lines, drawn for reference, are within  $\pm 1$  percent, the estimated ana-

lytical error. Somewhat greater analytical errors may be introduced by two factors: (1) the normalization procedure that removes the effect of olivine fractionation or accumulation may be oversimplified by the use of a single olivine composition ( $Fo_{86.2}$ , see Wright *et al.*, 1975) and is also affected by possible

inhomogeneities in the olivine phenocryst content, and (2) during mass spectrometric analysis, some of the REE abundances (e.g., Ce, Eu, and Dy, but not Nd and Sm) can be affected by insufficiently monitored interferences of metal or oxide species of other elements. Even so, at least 9 of the 12 Ce, Nd, Sm, Eu, Dy, and Yb values lie within  $\pm 1$  percent of their respective regression line. Replicate analyses are in progress to check for significant deviations.

### Discussion

*Source Composition.* All the chemical and isotopic data gathered so far are consistent with the assumption that the source is uniform in composition, that it contains the phases olivine, orthopyroxene, clinopyroxene, and garnet, and that it undergoes quasi-eutectic melting with varying melt fractions. The critical results in this respect are the (olivine normalized) constant major element concentrations (Wright *et al.*, 1975), the constant ratios between those trace elements that have effective bulk partition coefficients of zero between solid and melt, namely K, Rb, Cs, and Ba, and the constant  $^{87}\text{Sr}/^{86}\text{Sr}$  ratios (Hofmann *et al.*, 1978). These observations do not unequivocally prove the uniformity of the source, but nevertheless lend much stronger support to this assumption than can be found in other cases of less systematically sampled and analyzed sequences of lavas. We therefore continue this discussion under the assumption that the source of all the lavas is uniform in composition.

### Degree of Melting

Detailed model calculations for partial melting have not yet been completed. However, it is immediately clear from Fig. 48 that the degree of melting is on the order of 5–10 percent if the source has a flat REE pattern that is 2–4 times enriched over chondritic abundances.

This conclusion follows from the fact that Ce is about 40 times enriched and is nearly as incompatible as Ba (see Fig. 49). For a perfectly incompatible element (having a bulk partition coefficient of zero) the melt fraction  $F$  is given by  $F = C_o^i/C_t^i$  where  $C_o^i$  is the initial concentration of the element in the solid (before melting) and  $C_t^i$  is the concentration in the melt. The calculation of the absolute melt fraction is not well constrained because of the uncertainty in the source composition. A much firmer conclusion can be reached about the relative degrees of melting: The K, Rb, and Ba abundances decrease by about 20 percent (Fig. 49) during the course of eruption, and this corresponds to an increase in the degree of melting of 20 percent. This change in the degree of melting is important, because it leads to a differential release of other trace elements with bulk partition coefficients  $D_o > 0$ . This in turn can be used to determine the residual mineral phases in the mantle, at least to the extent that their partition coefficients are approximately known.

### Residual Phases

The upper mantle is generally believed to consist of the major phases olivine, orthopyroxene, clinopyroxene, and garnet (or spinel at shallow depths). Of these, olivine and orthopyroxene have extremely low partition coefficients for all the trace elements analyzed, and any addition of these phase compositions to the melt merely dilutes the concentrations. Clinopyroxene is a significant host to Sr and REE, but not to K, Rb, and Ba. Garnet is a host phase to the REE but not to Sr, K, Rb, and Ba. Irving (1978) has reviewed the experimental determinations of some of the relevant partition coefficients  $K_D$ . Important are, for example,  $K_D$  (Sr, cpx-liq) = 0.1 to 0.3,  $K_D$  (Ce, clinopyroxene-liquid) = 0.1 to 0.2,  $K_D$  (Yb, garnet-liquid) = 4. Garnet is the only known mineral that dis-



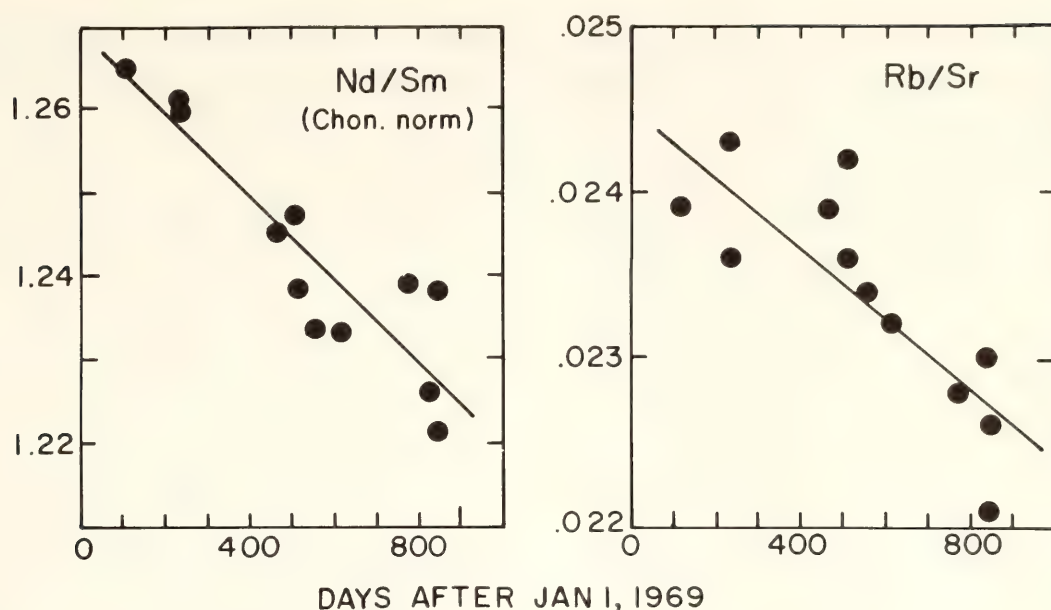


Fig. 50. Variation of Nd/Sm (chondrite normalized) and Rb/Sr with date of eruption. The fractionation of these trace element ratios in the mantle will ultimately result in isotopic heterogeneity of Nd and Sr.

criminate strongly against the light REE and in favor of Yb. In the Mauna Ulu lavas, the Ce concentration decreases as the degree of melting increases, but the Yb concentration remains constant. Within the framework of our assumption of constant initial composition of the source and equilibrium partial melting, these observations demonstrate conclusively that garnet remains as a residual phase in the mantle. This is contrary to the widely held belief that garnet is completely consumed during the generation of tholeiitic melts.

In addition to garnet, clinopyroxene must also be a residual phase. This point was argued in last year's report (Hofmann *et al.*, 1978) on the basis of the only partially incompatible behavior of Sr, as shown for example by the increasing Sr/Ba ratios.

The presence of residual garnet and clinopyroxene has important consequences for the isotopic evolution of the mantle. Our results demonstrate that both Rb/Sr and Nd/Sm are fractionated during tholeiite production beneath Kilauea (see Fig. 50). This volcanism therefore generates a significant volume

of partially depleted but not completely barren mantle, in which the Rb/Sr and Nd/Sm ratios have been lowered by the withdrawal of tholeiitic melt. The trace element variations observed by White (this Report) in the FAMOUS area can be interpreted in the same way.

The fractionation of Rb/Sr and Nd/Sm ratio in ocean island tholeiites is also important to the interpretation of the so-called mantle isochrons (Brooks *et al.*, 1976). In the case of the Mauna Ulu tholeiites, the melts have on the average higher Rb/Sr and lower Sm/Nd ratios than the source mantle. If this should turn out to be generally true for ocean island tholeiites, the model ages based on average isotopic ratios and average Rb/Sr and Sm/Nd ratios of oceanic island tholeiites will be biased on the young side in the case of Rb-Sr, and on the old side in the case of Sm-Nd.

#### References

- Brooks, C., S. R. Hart, A. W. Hofmann, and D. E. James, Rb-Sr mantle isochrons from oceanic regions, *Earth Planet. Sci. Lett.*, **32**, 51-61, 1976.

Gast, P. W., Trace element fractionation and the origin of tholeiitic and alkaline magma types, *Geochim. Cosmochim. Acta*, 32, 1057–1086, 1968.

Green, D. H., and A. E. Ringwood, The genesis of basaltic magma, *Contrib. Mineral Petrol.*, 15, 103–190, 1967.

Hofmann, A. W., J. L. Wright, and M. Feigenson, Trace element and Sr isotope abundances in recent lavas from Kilauea, Hawaii, *Carnegie Inst. Wash. Year Book* 77, 590–596, 1978.

Irving, A. J., A review of experimental studies of crystal/liquid trace element partitioning, *Geochim. Cosmochim. Acta*, 42, 743–770, 1978.

Scarfe, C. M., B. O. Mysen, and C. S. Rai, Invariant melting behavior of mantle material: partial melting of two lherzolite nodules, *EOS, Trans. Amer. Geophys. U.*, 60, 401, 1979.

Wright, T. L., D. A. Swanson, and W. A. Duffield, Chemical compositions of Kilauea east-rift lava, 1968–1971, *J. Petrology*, 16, 110–133, 1975.

## EVOLUTION OF THE EARTH'S CRUST AND MANTLE

### TERTIARY KOMATIITES OF GORGONA ISLAND, COLOMBIA

*Lina M. Echeverría*

#### *Introduction*

Komatiites are a class of exotic volcanic rocks of ultrabasic composition. Because of their exceptionally high melting temperatures (1600°C at 10 kb pressure; Arndt, 1976), they are indicative of anomalously high temperatures in their source regions. Except for two Paleozoic occurrences (Upadhyay, 1978; Stephenson, 1974; Arndt *et al.*, 1977), all previously discovered komatiites are restricted to Precambrian terranes. Detailed field work on Gorgona Island (78°12'W, 2°58'N), Colombia, shows the existence of spinifex-textured komatiites within an unmetamorphosed Tertiary

sequence of ultrabasic and basic rocks. The island represents a southward extension of the Baudó Range of upper Cretaceous to lower Tertiary age. The coastal Baudó Range is the youngest of a series of basic-ultrabasic belts whose age decreases eastwardly. The presence of spinifex-textured komatiites within this Tertiary belt represents a unique occurrence. The geology of Gorgona had been

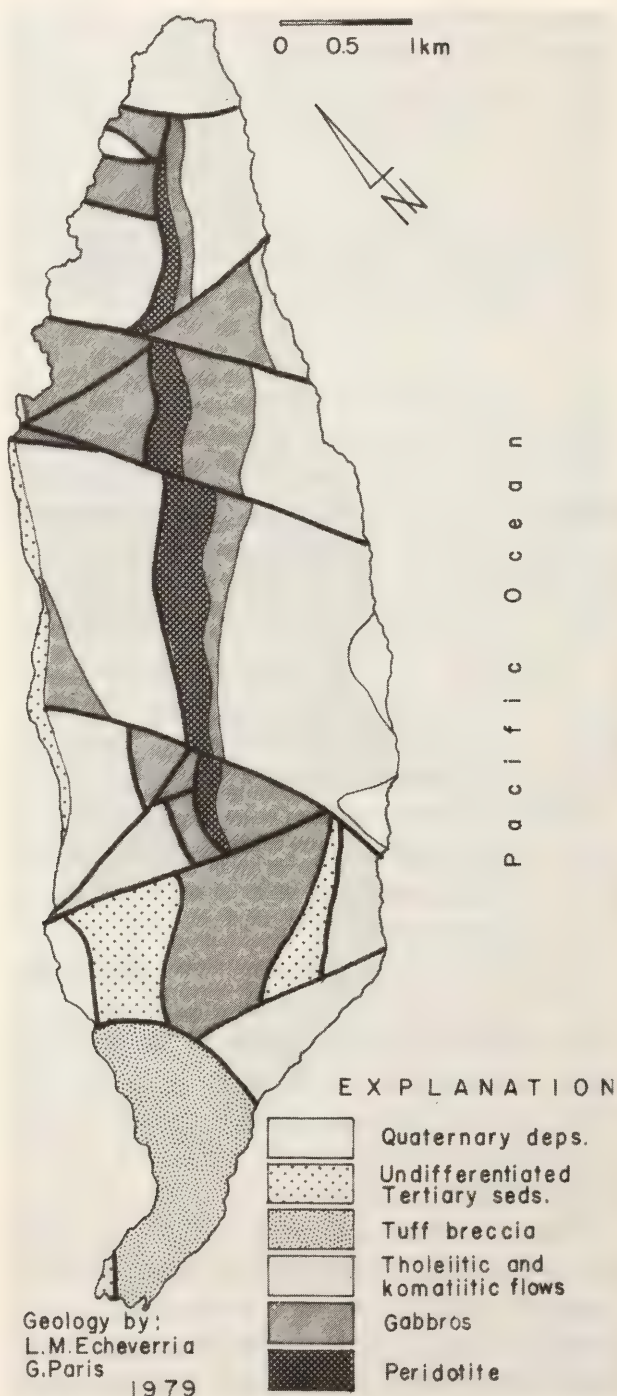


Fig. 51. Generalized geologic map of Gorgona Island, Colombia.



described by Gansser (1950), but no komatiites were identified, as these rocks had not yet been recognized.

### *Summary of Field Relations and Petrography*

The komatiitic flows of Gorgona Island are found within the volcanic sequence of the basic complex (Fig. 51). The exposed base of the complex is made up by peridotite, which in turn is overlain by coarse-grained poikilitic gabbro. Absence of layering is characteristic of the gabbro section. Grain size in the gabbros decreases upwards in the section, and the pyroxene oikocrysts disappear. The volcanic sequence overlies the gabbro section. The bulk of the volcanics is represented by basaltic flows displaying large-scale pillow structure. The komatiitic flows are found within the basaltic

section; structures typical of Archean komatiitic flows (Pyke *et al.*, 1973; Arndt *et al.*, 1977) are displayed by a 1.5-m-thick flow in one locality (Echeverría, in preparation). The Gorgona komatiites are unaltered and unmetamorphosed rocks with spinifex texture defined by olivine blades (Fig. 52). The best-developed spinifex textures exhibit sheafs of olivine blades approximately 7–10 cm long, and blades 3–5 cm long are commonly found. The interblade filling consists of sheafs of well-developed skeletal clinopyroxene crystals and unaltered glassy material. Plagioclase may also be present as an interblade material; it occurs as laths intergrown with clinopyroxene. Microspinifex textures with olivine grains 0.5–1.0 cm long developed in a flow with “popcorn” pillow structure (pillows on the order of 10 cm in diameter).

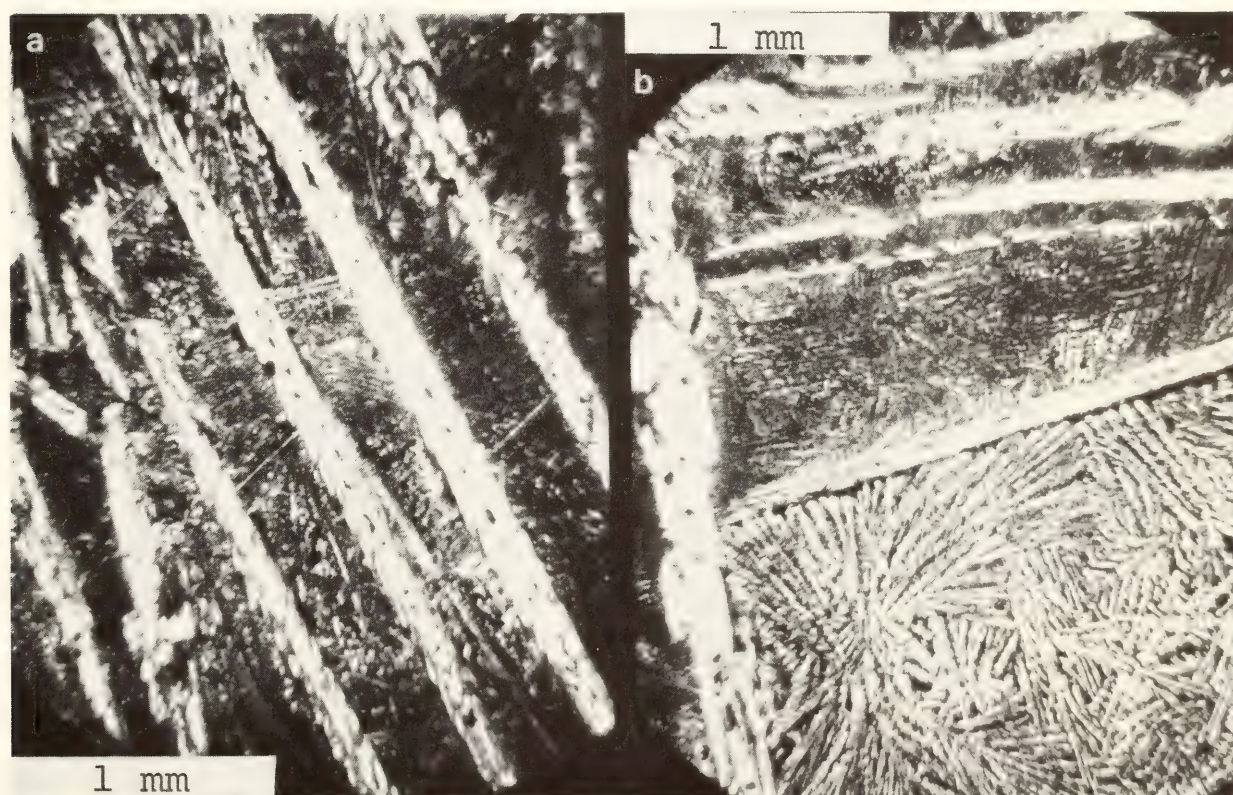


Fig. 52. (a) Photomicrograph of spinifex-textured komatiitic flow from Gorgona Island. Clinopyroxene needles and glass constitute the groundmass for large blades of olivine; trains of spinel grains are included in the olivine. Uncrossed polars. Sample GOR-71. (b) Detail of spinifex texture from Gorgona. Rays of clinopyroxene needles and coarser olivine. Uncrossed polars. Sample GOR-71.



Geochemistry

Major element analyses have been performed on six samples of komatiites and three basalts from Gorgona Island (Table 9). The komatiites are characterized by MgO (anhyd.) contents ranging from 15% wt to 17% wt,  $\text{TiO}_2 \leq 0.72\%$  wt, and CaO/Al<sub>2</sub>O<sub>3</sub> ratios on the order of 0.85. The basalts have lower MgO values (5.3–9.2% wt), higher TiO<sub>2</sub> (1.2–1.8% wt), and lower CaO/Al<sub>2</sub>O<sub>3</sub> ratios (0.78) than the associated komatiites. Comparison between the major element chemistry of Gorgona komatiites and Archean komatiites is shown on Fig. 53. In the  $\text{FeO}^*/(\text{FeO}^* + \text{MgO})$  vs. Al<sub>2</sub>O<sub>3</sub> plot, the Gorgona komatiites fall on the komatiite field and closely resemble pyroxenitic komatiites from Munro Twp.; this is also true for MgO vs. TiO<sub>2</sub> and for SiO<sub>2</sub> vs. TiO<sub>2</sub> plots. One of the basalts falls on the field of basaltic komatiites, whereas the remaining two samples plot on the field of tholeiitic basalts. Five samples were analyzed for their rare earth element contents by isotope dilution mass spectrometric methods.

Fig. 54 shows the chondrite-normalized rare earth patterns for the Gorgona komatiites and basalts. All samples are low in total rare earth element abundance. The pyroxenitic and basaltic komatiites are strongly depleted in light rare earth elements with  $(\text{Ce}/\text{Sm})_N = 0.34$  (ave.), where  $(\text{Ce}/\text{Sm})_N$  denotes the chondrite-normalized ratio of Ce to Sm. The tholeiitic basalts have higher REE abundances and show patterns which are nearly flat to slightly enriched in light rare earth elements with  $(\text{Ce}/\text{Sm})_N = 1.15$  (ave.). With the exception of sample 6A, there is a negative correlation between MgO content and REE abundances. Furthermore, all samples show a depletion of Er and Yb relative to Gd and Dy. These features have been reported for Archean komatiites (Whitford and Arndt, 1978; Arth *et al.*, 1977). The REE patterns suggest that the komatiites may have been generated by increased melting of the source region which had previously yielded the tholeiitic basalts. However, it is also possible that the source region had been depleted during a previous melting episode.

TABLE 9. Major Element Analyses of Gorgona Komatiites and Basalts

	Komatiites						Basalts		
							Komatiitic	Tholeiitic	
	6	38	47	71	72	73	6A	23A	70
SiO <sub>2</sub>	46.93	46.19	47.34	46.46	46.00	46.33	48.69	49.95	52.67
TiO <sub>2</sub>	0.72	0.65	0.41	0.67	0.71	0.71	1.15	1.41	1.83
Al <sub>2</sub> O <sub>3</sub>	12.71	13.04	12.34	12.27	12.59	12.98	14.09	13.77	12.78
FeO*	11.25	11.45	10.06	11.30	11.40	11.33	13.06	10.50	13.39
MgO	15.77	15.03	17.05	17.05	16.16	15.54	7.41	9.16	5.25
CaO	10.88	10.96	1.08	10.48	10.83	10.93	11.66	10.89	9.13
Na <sub>2</sub> O	1.13	1.20	1.22	1.33	1.19	1.26	3.07	2.88	2.61
K <sub>2</sub> O	0.05	0.04	0.02	0.02	0.02	0.03	0.03	0.45	0.14
MnO	0.20	0.19	0.16	0.18	0.21	0.21	0.25	0.20	0.21
Total	99.65	98.93	99.68	99.77	99.11	99.32	99.41	99.20	98.02
$\frac{\text{FeO}^*}{\text{FeO}^* + \text{MgO}}$	0.42	0.43	0.37	0.40	0.41	0.42	0.64	0.53	0.72
CaO/Al <sub>2</sub> O <sub>3</sub>	0.86	0.84	0.90	0.85	0.86	0.84	0.83	0.79	0.71



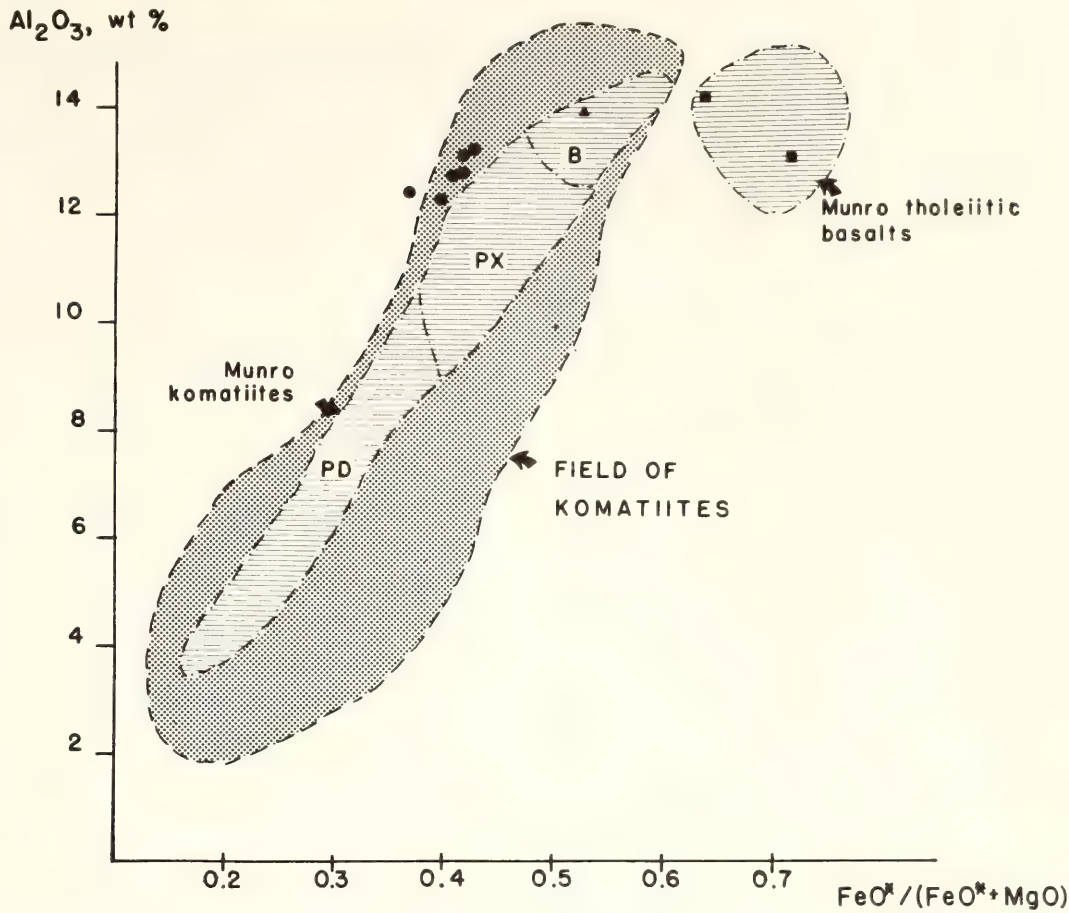


Fig. 53.  $\text{FeO}^*/(\text{FeO}^*+\text{MgO})$  vs.  $\text{Al}_2\text{O}_3$  wt % diagram for Gorgona komatiites and basalts and comparison with Archean komatiites. Circles are pyroxenitic komatiites; triangle, basaltic komatiite; squares, tholeiitic basalts. Fields of komatiites and Munro komatiites are after Arndt *et al.* (1977). B: basaltic komatiites; PX: pyroxenitic komatiites; PD: peridotitic komatiites.

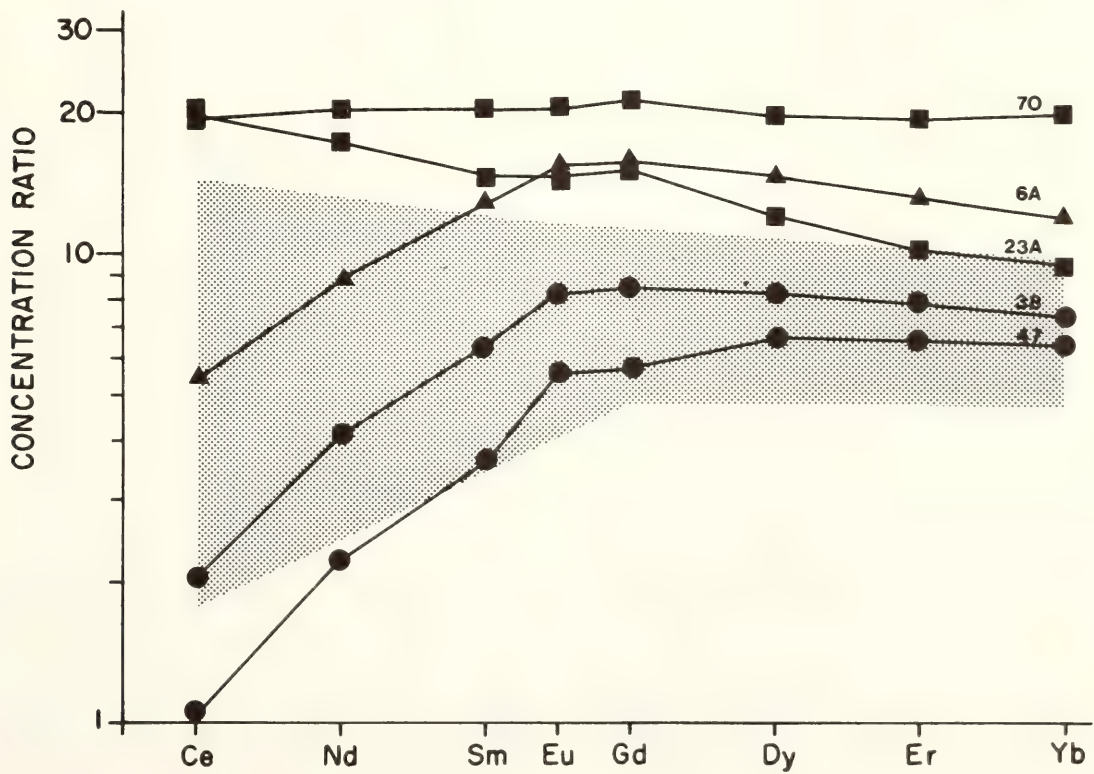


Fig. 54. Chondrite-normalized REE abundance patterns for Gorgona komatiites and basalts. Symbols as in Fig. 53. Shaded area represents field for komatiites, after Arth *et al.* (1977).

### Significance

The presence of well-developed spinifex textures, together with the major and trace element features, clearly characterizes the Gorgona ultrabasic flows as komatiites. The existence of Phanerozoic komatiites associated with tholeiitic basalts raises an important question in the generation of ultrabasic lavas: It suggests that the unique geotectonic conditions regarded by some authors (Brooks and Hart, 1972; Anhaeusser *et al.*, 1969) as essential to the generation of Archean komatiites may indeed not be required for the production of ultrabasic lava. Although the process responsible for these lavas requires further investigation, it is clear that it involves high-degree melting of the mantle (Arndt, 1977) during one or several episodes. Furthermore, it is apparent that such high degree of fractional melting was possible during Tertiary times, apparently as an end product of the generation of tholeiitic basalts.

### References

- Anhaeusser, R., M. Mason, J. Viljoen, and R. P. Viljoen, A reappraisal of some aspects of Precambrian shield geology, *Geol. Soc. Amer. Bull.*, 80, 2175–2200, 1969.
- Arndt, N. T., Melting relations of ultramafic lavas (komatiites) at 1 atm. and high pressure, *Carnegie Inst. Wash. Year Book* 75, 555–562, 1976.
- Arndt, N. T., Ultrabasic magmas and high-degree melting of the mantle, *Contrib. Mineral. Petrol.*, 64, 205–221, 1977.
- Arndt, N. T., A. J. Naldrett, and D. R. Pyke, Komatiitic and iron-rich tholeiitic lavas of Munro Township, Northeast Ontario, *J. Petrol.*, 18, 319–369, 1977.
- Arth, J. G., N. T. Arndt, and A. J. Naldrett, Genesis of Archean komatiites from Munro Township, Ontario: trace-element evidence, *Geology*, 5, 590–594, 1977.
- Brooks, C., and S. R. Hart, An extrusive basaltic komatiite from a Canadian Archean metavolcanic belt, *Can. J. Earth Sci.*, 9, 1250–1253, 1972.
- Gansser, A., Geological and petrological notes on Gorgona Island in relation to North-Western S. America, *Schweiz. Mineral. Petrogr. Mitt.*, 30, 219–237, 1950.
- Pyke, D. R., A. J. Naldrett, and A. R. Eckstrand, Archean ultramafic flows in Munro Township, Ontario, *Geol. Soc. Amer. Bull.*, 84, 955–978, 1973.
- Stephenson, J. F., Geology of the Oswagau Lake (East Half) Area, Manitoba Mines Branch, Publ. 74-1, 1974.
- Upadhyay, H. D., Phanerozoic peridotitic and pyroxenitic komatiites from Newfoundland, *Science*, 202, 1192–1195, 1978.
- Whitford, D. J., and N. T. Arndt, Rare earth element abundances in a thick, layered komatiite lava flow from Ontario, Canada, *Earth Planet. Sci. Lett.*, 41, 188–196, 1978.

### RB-SR WHOLE-ROCK STUDIES: VIRGINIA PIEDMONT

Douglas G. Mose\*

The Virginia Piedmont has long remained an area in which the plutonic, volcanic, and tectonic history is poorly understood. However, in 1974 L. Glover and his associates at Virginia Polytechnic Institute and State University began studies to produce a 1:24,000-scale map traverse through the Virginia Piedmont along the east-west James River from the Triassic basin at Richmond to the Columbia syncline at Columbia.

The map project by Glover and his associates has delineated a sequence of high-grade metamorphic rocks that belong to the Raleigh and Charlotte belts. The oldest unit in the James River area appears to be the State Farm Gneiss, a probable meta-arkose. This unit is over-

\* George Mason University, Fairfax, Virginia.



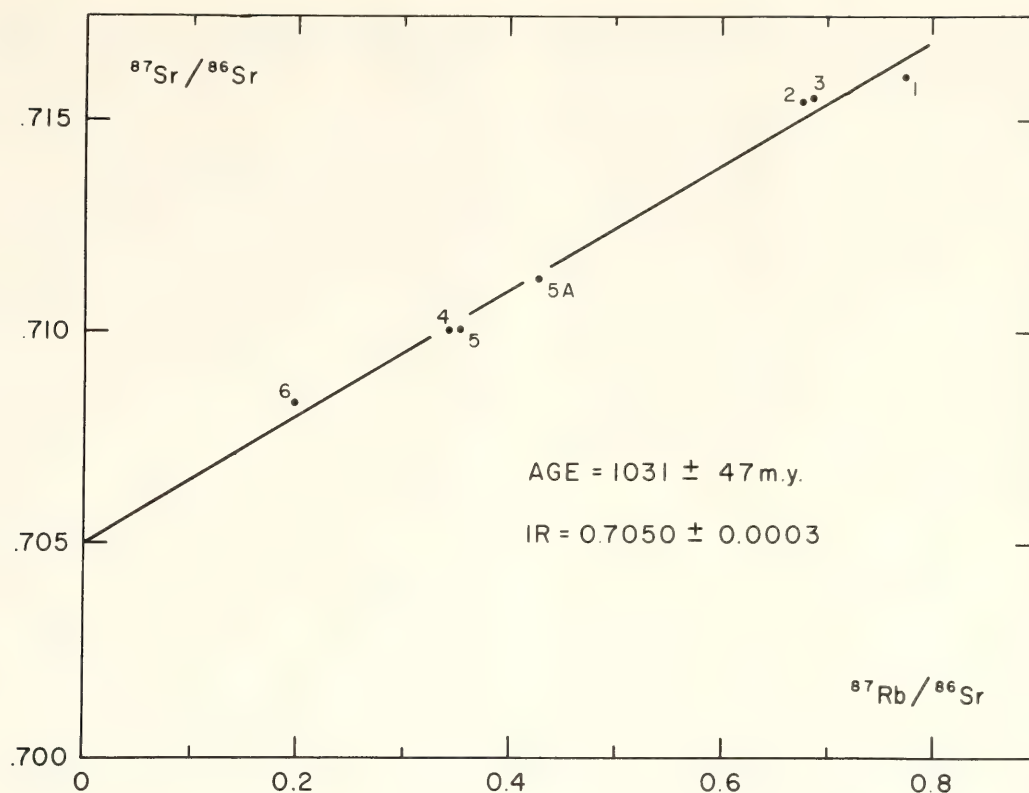


Fig. 55. Isochron diagram for the State Farm Pluton.

lain by the Sabot Amphibolite, probably a metamorphosed basaltic lava sequence, which in turn is overlain by the Maiden's Gneiss, a probable metagraywacke which is modally similar to the upper Glenarm metagraywacke reported by Hopson (1964) from the Maryland Piedmont.

Prior to the Rb-Sr work discussed below, these rock units along the James River were only known to be more than about 330 m.y., the age of the Petersburg Granite which intruded into the eastern end of the James River map traverse area (Wright *et al.*, 1975). An examination of the units revealed that all three units were not suitable for Rb-Sr whole-rock isochron study. However, the State Farm Gneiss was intruded by a granodiorite pluton (State Farm Pluton) which was sampled for Rb-Sr study.

Seven samples, each of approximately 10 kg, from the State Farm Pluton were analyzed for Rb and Sr using standard techniques. The Sr isotopic analyses were made at DTM, the Rb isotopic

analyses at Florida State University. The Rb-Sr age and initial  $^{87}\text{Sr}/^{86}\text{Sr}$  ratio shown on the isochron diagram (Fig. 55) were calculated using York Model I regression treatment described by Brooks *et al.*, 1972. The errors associated with the age and initial  $^{87}\text{Sr}/^{86}\text{Sr}$  ratio on the isochron diagram are given at the 68 percent confidence level.

Rb-Sr whole-rock data indicate that the State Farm Pluton is  $1031 \pm 47$  m.y. old. The State Farm Gneiss which is intruded by this pluton is therefore older and probably similar in age to the Baltimore Gneiss and the Grenville rocks of the western Appalachian basement. No unconformity has been found between the State Farm Gneiss and the overlying Sabot Amphibolite, or between the Sabot and the Maiden's Gneiss, suggesting that the units all constitute a sequence of billion-year-old rocks (L. Glover, personal communication, 1979).

Plate tectonic models proposed since 1972 (Rodgers, 1972; Rankin, 1975) have assumed that the Piedmont Prov-

ince was located on a plate composed of post-Grenville rocks which collided with the North American Plate in Paleozoic time. However, the Rb-Sr study reported here shows that Grenville basement rocks are located in the Piedmont, east of the suture zone proposed by the above authors. It now seems likely that the Piedmont has never been much separated from the North American Plate, and that a common Grenville basement underlies both the Grenville Blue Ridge and the Piedmont Province.

### References

- Brooks, C., Hart, S. R., and I. Wendt, On the realistic use of two-error regression treatments as applied to Rb-Sr data, *Rev. Geophys. and Space Sciences*, 10, 551, 1972.
- Hopson, C. A., The crystalline rocks of Howard and Montgomery Counties, in *The Geology of Howard and Montgomery Counties*, Maryland Geological Survey, 27, 1964.
- Rankin, D. W., The continental margin of eastern North America in the southern Appalachians: The opening and closing of the Proto-Atlantic ocean, *Amer. Jour. Sci.*, 275-a, 298, 1975.
- Rodgers, J., Latest Precambrian (post-Grenville) rocks of the Appalachian region, *Amer. Jour. Sci.*, 272, 507, 1972.
- Wright, J. E., Sinha, A. K., and L. Glover, Age of zircons from the Petersburg granite, Virginia, *Amer. Jour. Sci.*, 275, 848, 1975.

### ARE ANCIENT LEAD DEPOSITS CHRONOMETERS OF THE EARLY HISTORY OF EARTH?

*M.-F. Bugnon,\* F. Tera, and L. Brown*

The isotopic composition of lead on the Earth can vary from one place to another because lead is the product of mixing two components: (1) primordial

lead, apparently of isotopic composition identical to that found in some sulfides in old iron meteorites, and (2) radiogenic lead produced by the decay of  $^{238}\text{U}$ ,  $^{235}\text{U}$ , and  $^{232}\text{Th}$  into  $^{206}\text{Pb}$ ,  $^{207}\text{Pb}$ , and  $^{208}\text{Pb}$ , respectively. A fourth isotope,  $^{204}\text{Pb}$ , is the least abundant and is not produced by any known natural nuclear process on Earth; thus  $^{204}\text{Pb}$  is used as an index to the relative abundance of primordial Pb.

Because of the availability of nuclear, gravitational, and kinetic energy, a planet like Earth melts and differentiates to variable degrees for an extended time after accretion, which tends to obscure its early history. Occasionally the isotopic imprint of an old but extremely dominant event may be preserved to the present time. Such an example is the episode of intense bombardment of the lunar surface  $\sim 4$  billion years ago (Tera *et al.*, 1974). In the living and relentlessly dynamic Earth, such imprints are all but erased, but heterogeneities are often partly preserved because mixing and assimilation are often incomplete. One type of heterogeneity is parent-daughter fractionation resulting from partition of the parent and daughter elements between liquid and mineral phases during geological processes, such as partial melting and crystallization. In the oldest rocks, these relic heterogeneities constitute the temporal record of the early history of the planet. In this progress report, further attention is directed to the record of some of Earth's ancient history, as recorded in old lead deposits.

Ancient lead deposits  $\sim 2.7$  b.y. old are widely distributed. They have been found in Africa, Australia, Europe, India, and North America. These deposits have a unique lead isotopic composition, suggestive of a similar history prior to deposition. Lead sulfide deposits (galena) contain little or no uranium or thorium; thus, their lead isotopic composition has remained essentially unaltered since deposition. Such lead composition (of old ores of wide distribution) "sums up"

\* University of Montreal, Montreal, Quebec.



the Earth's history prior to deposition. The question is, can details of that early history be unraveled?

Our preliminary study is concerned with the isotope geology of Kidd Creek Mine, discovered in 1963, 17 miles north of the town of Timmins, Ontario, Canada. The mine is a stratiform Cu-Zn-Pb-Ag deposit of volcanogenic origin located in the west end of the Abitibi volcanic belt of the Canadian Shield. The mineralization occurs in a volcanic-sedimentary sequence at a rhyolite-basalt contact. The ores were formed at the end of the felsic cycle by precipitation of sulfides from hot hydrothermal solutions at the sea water-volcanic rock interface (Walker and Mannard, 1974). We have sampled the massive ore zone of the deposit and separated five types of sulfides: galena, pyrite, pyrrhotite, sphalerite, and chalcopyrite.

The Pb isotopic analysis of the above-mentioned sulfides, as well as that of two different country rocks, are plotted in Fig. 56 in a  $^{207}\text{Pb}/^{206}\text{Pb}$  vs.  $^{204}\text{Pb}/^{206}\text{Pb}$  correlation diagram. In this diagram, errors resulting from the least abundant isotope,  $^{204}\text{Pb}$ , are not correlated and variation in the important geochronological parameter  $^{207}\text{Pb}/^{206}\text{Pb}$  are clearly exposed. In this representation, genetically related samples (i.e., samples that were isotopically homogenized with regard to Pb at time  $\tau$  and have remained undisturbed since then) containing different U/Pb will fall on a straight line (i.e., they form an isochron). The isochron's intercept on the  $^{207}\text{Pb}/^{206}\text{Pb}$  axis,  $I_2$ , provides the composition of radiogenic  $^{207}\text{Pb}/^{206}\text{Pb}$  produced by the *in situ* decay of  $^{235}\text{U}$  and  $^{238}\text{U}$ . From the value of the intercept, the age can be calculated from the relationship:

$$I_2 = \left( \frac{^{235}\text{U}}{^{238}\text{U}} \right)_{\text{Today}} \cdot \frac{e^{\lambda_5 \tau} - 1}{e^{\lambda_8 \tau} - 1}, \quad (1)$$

where  $(^{235}\text{U}/^{238}\text{U})_{\text{Today}} = \frac{1}{137.8}$  and  $\lambda_5$ ,  $\lambda_8$  and  $\tau$  are the decay constants of

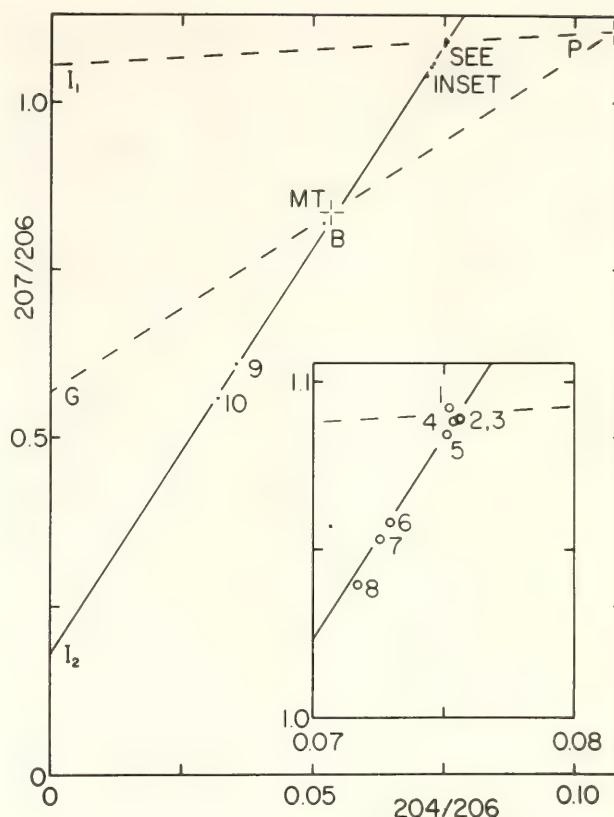


Fig. 56. Isotopic data of samples from Kidd Creek mine (Timmins) plotted on  $^{207}\text{Pb}/^{206}\text{Pb}$  vs.  $^{204}\text{Pb}/^{206}\text{Pb}$  diagram. The data define an isochron with an intercept  $I_2$  corresponding to crystallization age  $2.64 \pm 0.06$  b.y. The ten samples shown are identified by numerals: 1 and 2 are galenas; 3, pyrite; 4, sphalerite; 5, pyrrhotite; 6, chalcopyrite a; 7, leached chalcopyrite b; 8, leach of chalcopyrite b; 9 and 10 are different whole rocks.  $B$  is the composition of our blank ( $1.5 \times 10^{-9}$  g Pb/1-g sample).  $MT$  is modern terrestrial Pb as estimated by Stacey and Kramers (1975).  $P$  stands for primordial Pb. The intercept  $I_1$  is the composition of radiogenic Pb of the first stage corresponding to a time interval  $T - \tau$  where  $T$  is the age of the source and  $\tau$  is the crystallization age. A geochron ( $G$ ) giving a single-stage "age of the earth" (4.43 b.y.; ref. 1 in Table 11) is obtained from the line connecting  $P$  and  $MT$ .

$^{235}\text{U}$ , the decay constant of  $^{238}\text{U}$ , and the age of the samples, respectively. The age of samples, as obtained from the isochron in Fig. 56, is  $2.64 \pm 0.06$  b.y. This is either the crystallization age of the rocks or the date of the last dominant metamorphism. It follows from the apparent genetic relationship of the sulfides and the rocks (as demonstrated by their near-perfect alignment in a linear trend)

that this age also dates the deposition of the sulfide ores. In other words, in a first approximation, it appears that the processes of formation of the rocks and deposition of the ores took place simultaneously.

The 2.64-b.y. age obtained falls within the spectrum of ages established for samples from that region. Tilton and Steiger (1969) obtained a U-Pb age of  $2.700 \pm 0.050$  b.y. for zircons from granitic rocks at Manitouwadge, Ontario, which is located  $\sim 300$  km northwest of Timmins. Nunes *et al.* (1978) obtained two U-Pb ages of 2.710 and 2.725 b.y. for zircons from acid volcanic rocks in the region south of Timmins. Other U-Pb ages on zircons from Abitibi belt range from 2.65 to 2.74 b.y. (Krogh and Davis, 1971; Steiger and Wasserburg, 1969) for volcanic rocks and associated plutons. The 2.7-b.y. age is characteristic of a number of shield areas: southern Rhodesia (Holmes and Cahen, 1957), western Australia (Wilson *et al.*, 1960), eastern Finland (Wetherill *et al.*, 1962), Mysore district of India (Murthy and Sadashivaiah, 1966), and the Canadian Shield (Tilton and Steiger, 1969). Lead isotopic data for galenas from these shields are

shown in Table 10, as summarized by Tilton and Steiger (1969). We have added to Table 10 our values for Kidd Creek galena. The consistency of the isotopic values is remarkable, and its simplest explanation (taking Fig. 56 into account) is that these sulfide ores were deposited on a global scale within a narrow time interval around 2.64 billion years ago. Barring complications arising from superimposed metamorphism, if this conjecture is valid then isochrons of samples (rocks and associated deposits) from these regions should yield ages clustering around 2.6 b.y. Further investigations are under way to examine this point.

If we assume that the galena's lead evolved, prior to final deposition, in a single stage for a time interval  $T - \tau$  where  $T$  is the age of the source, then it is possible to calculate the age of the source from the relationship

$$I_1 = \left( \frac{^{235}\text{U}}{^{238}\text{U}} \right)_{\text{Today}} \cdot \frac{e^{\lambda_5 T} - e^{\lambda_5 \tau}}{e^{\lambda_8 T} - e^{\lambda_8 \tau}}, \quad (2)$$

where  $I_1$  is the so-called radiogenic initial  $^{207}\text{Pb}/^{206}\text{Pb}$ . It is the lead produced in the source through uranium decay for the

TABLE 10. Isotopic Composition of Lead from Galenas in Shield Areas Containing Minerals with Ages of 2700 m.y.\*

Locality	Pb <sup>206</sup> /Pb <sup>204</sup>	Pb <sup>207</sup> /Pb <sup>204</sup>	Pb <sup>208</sup> /Pb <sup>204</sup>	Pb <sup>207</sup> /Pb <sup>206</sup>
Southern Rhodesia†	13.68	14.95	33.53	1.0928‡
Kalgoorlie, W. Australia	13.82	15.00	33.67	1.0854‡
	13.81	15.03	33.87	1.0879§
Mysore, India	14.01	14.57	33.43	1.0399‡
	13.605	14.76	33.71	1.0850§
Suomussalmi, Finland	13.61	14.85	33.49	1.0910
Manitouwadge, Ontario	13.30	14.52	33.58	1.0921¶
Timmins, Ontario	13.22	14.41	33.18	1.0912**

\* From Tilton and Steiger (1969), except Timmins values.  
† Average of eight analyses.  
‡ Russell and Farquhar (1960).  
§ Tilton and Steiger (1969).  
|| O. Kouvo (personal communication).  
¶ Tilton and Steiger (1965).  
\*\* This work.



span of time  $T - \tau$  and its composition value is obtained from

$$I_1 = \frac{\left(\frac{^{207}\text{Pb}}{^{204}\text{Pb}}\right)_{\text{Ga}} - \left(\frac{^{207}\text{Pb}}{^{204}\text{Pb}}\right)_{\text{prim}}}{\left(\frac{^{206}\text{Pb}}{^{204}\text{Pb}}\right)_{\text{Ga}} - \left(\frac{^{206}\text{Pb}}{^{204}\text{Pb}}\right)_{\text{prim}}} \quad (3)$$

Ga stands for galena and prim for primordial Pb, as was first determined by Patterson *et al.* (1953) and later by Tatsumoto *et al.* (1973). From Equation 2 we obtain  $T = 4.56 \pm 0.03$  b.y. for the age of the source. This is almost exactly the age of the oldest known meteorites (e.g., the age of Angra Dos Reis by U-Pb, Th-Pb, and Pb-Pb methods is 4.55 b.y.; Wasserburg *et al.*, 1977). Assuming the validity of the single-stage model, the 4.56-b.y. age would represent the time at which the U/Pb ratio of the material that forms the Earth increased from the very low ratio characteristic of average solar system material. If one further assumes this fractionation was associated with the formation of the Earth (e.g., extraction of Pb into the core during accretion), then this 4.56-b.y. age would be the age of the Earth. We summarize in Table 11 the results of other single-stage model calculations of the age of the Earth. All the ages shown are based on the more recent values for the decay constants (Jaffey *et al.*, 1971) and primordial Pb (Tatsumoto *et al.*, 1973).

The isochron in Fig. 56 can be looked upon as a mixing line of two end members. One end point is the galena datum showing the composition of lead 2.64 b.y. ago when the galena was completely separated from U and Th. If we define a fractionation factor  $F \equiv \mu_2/\mu_1$  where  $\mu = (^{238}\text{U}/^{204}\text{Pb})_{\text{Today}}$  and the subscripts 2 and 1 refer to the sample (i.e., second stage) and the source from which it was derived (first stage) respectively, then for galena,  $F = 0$ . The other end member of the isochron in Fig. 56 is at the

TABLE 11. Summary of "Age of the Earth" Calculations

Age of Earth in b.y.	Reference*	Basis of Calculation†
4.43	1	Modern sediments of zero age.‡
4.53	2	Initial Pb in feldspar and 2.70-b.y. zircon age for the rocks.
4.47§	3	Initial Pb in feldspar and 3.6-b.y. zircon age for the rocks.
4.53§	3	Assuming that Pb in the 3.6-b.y. feldspar was modified by a well-documented (3) metamorphism at 2.7 b.y.
4.56	4	Galena, other sulfides, and whole rocks Pb-Pb isochron of 2.64 b.y.

\* 1. Patterson (1956); 2. Tilton and Steiger (1969); 3. Gancarz and Wasserburg (1977); 4. this work.

† Recent values for decay constants (Jaffey et al., 1971) and primordial Pb (Tatsumoto et al., 1973) were used.

‡ The above footnote applies. In addition, the M.T. values of Stacey and Kramers (1975) are used in the calculation.

§ 4.47 b.y. is preferred by the authors.

intercept  $I_2$  corresponding to a hypothetical mineral phase that lost all its Pb when the rocks last crystallized (or metamorphosed). For such a phase, if it existed,  $F$  would be infinite. The spread of samples between the two end members is a reflection of the range of U-Pb fractionation during metamorphism. We have not yet measured the U concentration in the rocks, but the U/Pb ratio is calculable from the relationship

$$\left(\frac{^{206}\text{Pb}}{^{204}\text{Pb}}\right)_{\text{rock}} = \left(\frac{^{206}\text{Pb}}{^{204}\text{Pb}}\right)_{\text{Ga}} + \mu_2(e^{\lambda_2\tau} - 1). \quad (4)$$

For whole rocks 9 and 10,  $\mu_2$  is 29.7 and 36.2, respectively. Similarly, we can cal-

culate U/Pb for the source from the relationship

$$\left(\frac{^{206}\text{Pb}}{^{204}\text{Pb}}\right)_{\text{Ga}} = \left(\frac{^{206}\text{Pb}}{^{204}\text{Pb}}\right)_{\text{prim}} + \mu_1(e^{\lambda_8 T} - e^{\lambda_8 \tau}). \quad (5)$$

We calculate from Equation 5,  $\mu_1 = 7.49$ . This is to be compared with an estimated  $\mu \sim 9$  for the Earth. If this single-stage model is correct, it appears that during the time span 4.56–2.64 b.y. ago there existed magma sources with low  $\mu$  from which rocks and sulfide ore deposits were derived. Alternatively, multiple heterogeneous sources may have existed which were subsequently homogenized by thorough mixing at 2.64 b.y. In such case,  $\mu_1 = 7.5$  is an average for higher and lower values in pre-existing sources.

From the definition of  $F \equiv \mu_2/\mu_1$  we calculate  $F$  to be 4.0 and 4.8 for whole rocks 9 and 10, respectively. Thus, the extruded magma from which the rocks were formed was, on the average, enriched in uranium relative to lead by a factor of  $\sim 5$  as compared to U/Pb ratio in the source.

We also show the Pb isotopic data on a  $^{208}\text{Pb}/^{206}\text{Pb}$  vs.  $^{204}\text{Pb}/^{208}\text{Pb}$  correlation diagram (Figure 57). The sulfide ores and WR10 define a tight linear trend but WR9 falls off the line. This does not necessarily indicate a disturbed system. As in the case of Fig. 56, the intercept of the isochron yields the value of radiogenic Pb, and the age is obtained from the relationship

$$I_2 = \frac{^{232}\text{Th}}{^{238}\text{U}} \cdot \frac{e^{\lambda_2 \tau} - 1}{e^{\lambda_8 \tau} - 1}, \quad (6)$$

where  $\lambda_2$  is the decay constant of  $^{232}\text{Th}$ . Thus samples of the same age,  $\tau$ , can have different intercepts  $I_2$  because of different Th/U. The data shown in Fig. 57 are consistent with two 2.64-b.y.-old systems derived from the same source

but which fractionated Th/U differently. The specific Th/U of the source is obtained from

$$I_1 = \frac{^{232}\text{Th}}{^{238}\text{U}} \cdot \frac{e^{\lambda_2 T} - e^{\lambda_2 \tau}}{e^{\lambda_8 T} - e^{\lambda_8 \tau}}, \quad (7)$$

where

$$I_1 = \frac{\left(\frac{^{208}\text{Pb}}{^{204}\text{Pb}}\right)_{\text{Ga}} - \left(\frac{^{208}\text{Pb}}{^{204}\text{Pb}}\right)_{\text{prim}}}{\left(\frac{^{206}\text{Pb}}{^{204}\text{Pb}}\right)_{\text{Ga}} - \left(\frac{^{206}\text{Pb}}{^{204}\text{Pb}}\right)_{\text{prim}}}. \quad (8)$$

Using the numerical values for  $\tau$  and  $T$  as obtained from Equations 1 and 2, we calculate  $^{232}\text{Th}/^{238}\text{U} = 4.091$  (or  $^{232}\text{Th}/\text{U} = 4.06$ ) for the source. This is slightly higher than the value of  $\sim 3.8$  for the most primitive meteorites. The reversed position of  $I_1$  relative to  $I_2$  in Fig. 57 as compared with Fig. 56 is a natural consequence of the fact that  $\lambda_5 > \lambda_8 > \lambda_2$ .

Although the data presented are of a limited scope, they raise a number of questions which we hope to address in the near future. Some of these questions are outlined below. (1) How do the rock formations in old shields relate in time to the deposition of presently associated ores? The data on Timmins' samples suggest that the two processes were essentially simultaneous in this region and that a straightforward isotopic correlation may survive in spite of subsequent metamorphism. In each such case the Pb of the galena represents the initial Pb,  $I_1$  of the system (see Fig. 56). (2) From  $I_1$  an "age of the Earth" can be calculated using Equation 2. What is the range of values obtained for the age of the Earth from different initial leads, and what is the meaning of such a range in terms of the history of the early evolution of the Earth? (3) What are the U/Pb ratios and Th/U ratios of the sources from which the rocks were derived, and how similar or dissimilar were the sources with regard to these elements?



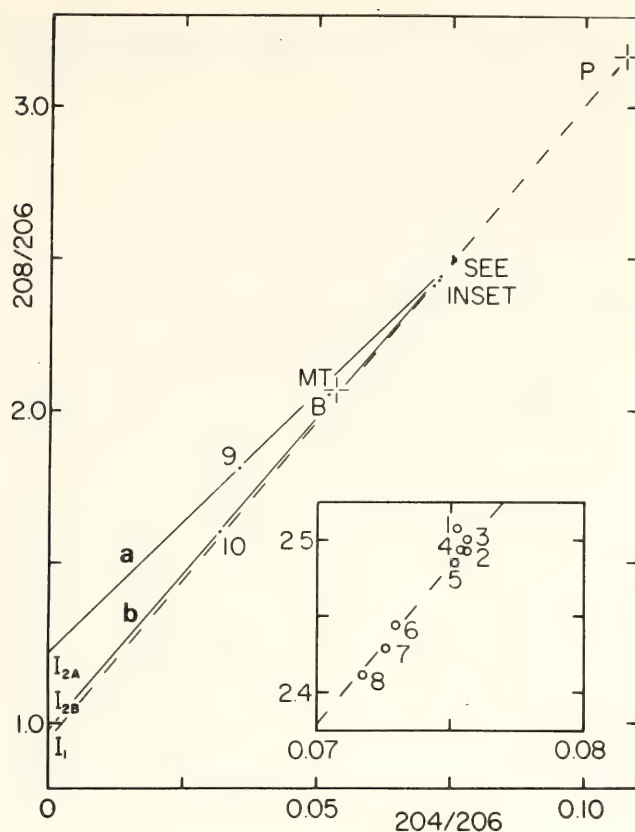


Fig. 57. Isotopic data of samples from Kidd Creek mine plotted on  $^{208}\text{Pb}/^{206}\text{Pb}$  vs.  $^{204}\text{Pb}/^{206}\text{Pb}$  diagram. Numerals and symbols are the same as in Fig. 56. The data are consistent with two 2.64 b.y. systems, lines *a* and *b*, where samples on line *a* are characterized by higher Th/U than those on line *b*. Because  $^{238}\text{Th} > ^{232}\text{Th}$ , intercept  $I_1$  (the composition of radiogenic Pb of the first stage) may plot below  $I_2$  (the composition of radiogenic Pb of the second stage). The relative positions of the two intercepts, however, are dependent also on the relative values of Th/U in the two stages. Decrease in Th/U in the second stage as compared with the first effects a shift in a direction opposite to that caused by the difference in the decay constants.

### References

- Gancarz, A. J., and G. J. Wasserburg, Initial Pb of the Amîtsoq gneiss, West Greenland and implication for the age of the earth, *Geochim. Cosmochim. Acta*, **41**, 1283–1301, 1977.
- Holmes, H. H., and L. Cahen, Geochronologie Africaine, *Mem. Acad. Roy. Sci. Coloniales*, **169**, 1957.
- Jaffey, A. H., K. F. Flynn, L. E. Glendenin, W. C. Bentley, and A. M. Essling, Precision measurement of half-lives and specific activities of  $^{235}\text{U}$  and  $^{238}\text{U}$ , *Phys. Rev. C*, **4**, 1889, 1971.
- Krogh, T. E., and G. L. Davis, Zircon U-Pb ages of archaean metavolcanic rocks in the Canadian Shield, *Carnegie Inst. Wash. Year Book* **70**, 241–242, 1971.
- Murthy, V. R., and M. S. Sadashivaiah, Rb-Sr ages of the Precambrian crystalline complex, Mysore, India, *Trans. Amer. Geophys. U.*, **47**, 207, 1966.
- Nunes, P. D., D. R. Pyke, and L. S. Jensen, Towards an absolute age stratigraphy for Abitibi Greenstone belt, Eastern Ontario—Zircon ages from the Timmins and Kirkland lake area; 1978 meeting of GAC-AGS-MAC (abstract), 1978.
- Patterson, C., Age of meteorites and the earth, *Geochim. Cosmochim. Acta*, **10**, 230–237, 1956.
- Patterson, C., H. Brown, G. R. Tilton, and M. G. Inghram, Concentration of U and Pb and the isotopic composition of lead in meteoritic material, *Phys. Rev.*, **92**, No. 5, 1234, 1953.
- Russell, R. D., and R. M. Farquhar, *Lead Isotopes in Geology*, Interscience Publishers, Inc., New York, 243 pp., 1960.
- Stacey, J. S., and J. D. Kramers, Approximation of terrestrial lead isotope evolution by a two-stage model, *Earth Planet. Sci. Lett.*, **26**, 207–221, 1975.
- Steiger, R. H., and G. J. Wasserburg, Comparative U-Th-Pb systematics in  $2.7 \times 10^9$  yr plutons of different geologic histories, *Geochim. Cosmochim. Acta*, **33**, 1213–1232, 1969.
- Tatsumoto, M., R. J. Knight, and C. J. Allègre, Time differences in the formation of meteorites as determined from the ratio of lead-207 to lead-206, *Science*, **180**, 1279, 1973.
- Tera, F., D. A. Papanastassiou, and G. J. Wasserburg, Isotopic evidence for a terminal lunar cataclysm, *Earth Planet. Sci. Lett.*, **22**, 1–21, 1974.
- Tilton, G. R., and R. H. Steiger, Lead

isotopes and the age of the earth, *Science*, 150, 1805, 1965.

Tilton, G. R., and R. H. Steiger, Mineral ages and isotopic composition of primary lead at Manitouwadge, Ontario, *J. Geophys. Res.*, 74, 2118–2132, 1969.

Walker, R. R., and G. W. Mannard, Geology of the Kidd Creek mine—a progress report, CIMM Bulletin, 41–57, December, 1974.

Wasserburg, G. J., F. Tera, D. A. Papanastassiou, and J. C. Huneke, Isotopic and chemical investigations of Angra Dos Reis, *Earth Planet. Sci. Lett.*, 35, 294, 1977.

Wetherill, G. W., O. Kouvo, G. R. Tilton, and P. W. Gast, Age measurements on rocks from the Finnish precambrian, *J. Geol.*, 70, 74, 1962.

Wilson, A. F., W. Compston, P. M. Jeffrey, and G. H. Riley, Radioactive ages from the precambrian rocks in Australia, *J. Geol. Soc. Australia*, 6, 179, 1960.

#### EXPERIMENTAL STUDIES OF GEOCHEMICAL PROCESSES

##### DIFFUSION OF WATER IN A GRANITIC MELT: AN EXPERIMENTAL STUDY

A. Jambon

##### Introduction

The mobility of water in granitic melts is important to the understanding of magmatic processes because of the drastic effect of water on the properties of the melt, such as viscosity, density, melting point and crystallization behavior. Very few measurements of the diffusivity of water have been made at temperatures in excess of 500°C (Fig. 58). The scatter in these results may be caused by the experimental difficulties and perhaps by the dependence of diffusivity upon water concentration. Such a concentration dependence was inferred by Shaw (1974) on the basis of water sorption experiments in obsidian, but this interpretation

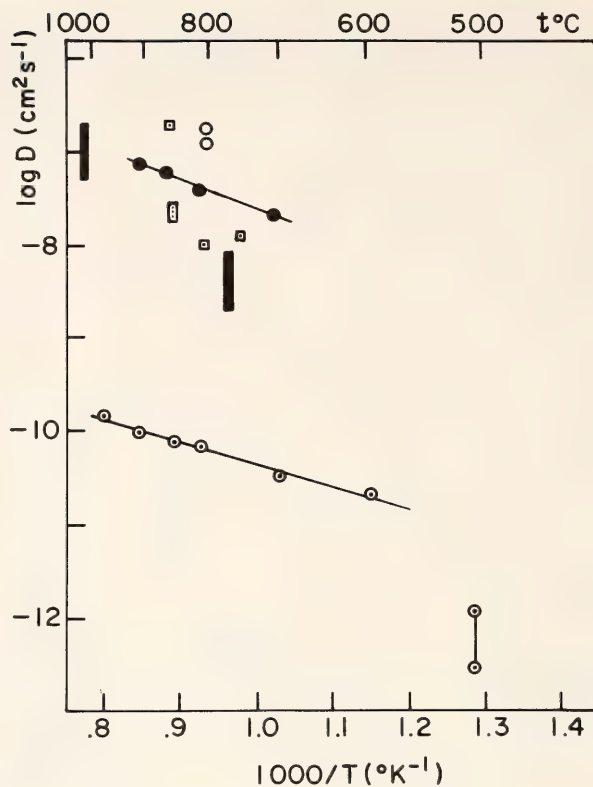


Fig. 58. Results for diffusion of water in granitic melts: bars = Arzi (1978), square = Shaw (1974), full circles = Jambon *et al.* (1978), empty and dotted circles = this study. Most of the scatter in the results is probably due to different experimental conditions, as discussed in the text.

was rejected by Arzi (1978), who determined diffusivities from the kinetics of melting of granite. Neither of these experiments was specifically designed to measure the concentration dependence of the diffusivity, and so far the problem has remained unresolved. Recent results on the diffusivity of Cs in hydrated melts (Jambon *et al.*, 1978; Watson, 1979) have shown a difference of three orders of magnitude between dry and hydrated melts. It is therefore clear that meaningful applications of the diffusion data to real magmas is not possible until the effect of water concentration on the mobility of water and other species has been determined.

We have started two kinds of experiments: (1) dehydration of natural obsidian (0.4 wt % H<sub>2</sub>O), and (2) hydration of initially dry obsidian under water



pressure in the range 800–900°C and 1 kbar.

### *Experimental Techniques*

*Dehydration Runs.* The obsidian specimen is from Valles Caldera (New Mexico). It was previously studied for the diffusion of cations (Magaritz and Hofmann, 1978) and water (Shaw, 1974). Samples were cut as wafers 1–4 cm<sup>2</sup>, 0.5–3 mm thick, and polished. Water loss in air was measured by successive weighing of a sample annealed at a constant temperature in the range 500–980°C. The diffusion coefficient was then calculated from the weight loss (= water loss) of the sample, using the diffusion equation for a semi-infinite medium (Crank, 1975, p. 32), which is also valid for slabs of finite thickness at sufficiently small water loss.

*Hydration Runs.* Platinum tubing of 2-mm diameter was filled with dehydrated obsidian at a temperature of about 1550°C, cut to lengths of 1–3 cm, and reannealed at 1300°C. The cylinder was then sealed with an aqueous solution inside a platinum capsule and run in a cold seal pressure vessel at 1 kbar, in the range 800–900°C. The melting point under these conditions is about 750°C. We used two different solutions: (1) distilled water, and (2) distilled water with very finely crushed obsidian powder. It is desirable to adjust the composition of the hydrothermal solution so that it is in cationic equilibrium with the obsidian in order to minimize compositional changes other than variation of water content. The use of powder is a relatively crude approach to the problem but it is hoped to bring about a relatively rapid approach to cation equilibrium between obsidian and solution. After the diffusion run (up to 10 days), the quenched glass cylinder was cut with a diamond-blade saw into slices about 0.3 mm thick ( $\approx 2$  mg), cleaned, carefully weighed on a microbalance, and measured with an accuracy of  $2 \times 10^{-6}$  g and  $2 \times 10^{-3}$  mm. The

samples were then heated progressively to 1200°C overnight, and the weight loss was then considered to be equal to the water content of the initial slice. Weight loss of a dry sample under the same conditions was found to be zero within the accuracy of the measurement. The overall accuracy in the water concentration was 0.3–0.5% H<sub>2</sub>O. This technique yields penetration curves and is the only one feasible to determine the diffusivity as a function of the water concentration for very small samples. Given the concentration gradient, it is theoretically possible to derive a diffusion coefficient for each concentration (Crank, 1975, p. 231).

### *Experimental Results*

The results of the dehydration runs of obsidian with an initial water concentration of 0.4 percent are shown on Fig. 58. With the exception of the two runs at 510°C, all the results fit an Arrhenius law:

$$D = 1.5 \times 10^{-8} \exp - 11.250/RT,$$

with  $D$  in cm<sup>2</sup> sec<sup>-1</sup> and activation energy in kcal/mole (Fig. 58). The 510°C data (two measurements) are significantly below this line, even though the accuracy at this temperature is comparatively low. All other diffusivities fall in the range  $10^{-10}$  to  $10^{-11}$  cm<sup>2</sup> sec<sup>-1</sup>.

The hydration results are preliminary but nevertheless permit some general conclusions. The mean diffusion coefficient (calculated for  $C/C(0) = 0.5$ ) is about the same for water + powder and water runs. An anomalous downward curvature is observed in the upper part of the concentration profile of pure water runs (Fig. 59, dashed line), as would be expected if diffusivity is strongly concentration dependent. The anomalous curvature may be interpreted in the following way: interdiffusion of alkalis and hydrogen ions has a strong effect on the total flux of water. If alkalis are moving from the melt into the solution, then the ap-

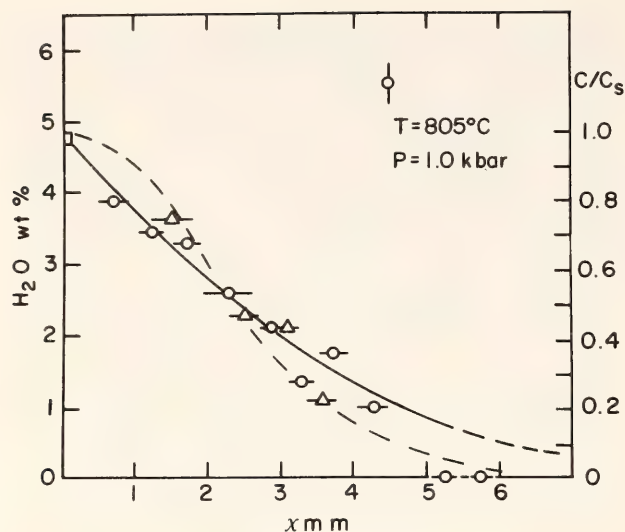


Fig. 59. Concentration gradient of water in obsidian: water + powder. Different symbols are for two runs of the same duration. The curve through the points is an error function complement of  $x/2\sqrt{Dt}$  for a diffusion coefficient of  $1.7 \times 10^{-7} \text{ cm}^2 \text{ sec}^{-1}$ . This line is closely fitted between 4.8 and 1 percent water. Sharp decrease below this value is believed to be real and corresponds to a substantial decrease in  $D$  at low water concentration. The dashed line is an approximate fit to the concentrations measured in two runs containing pure water under similar conditions.

parent diffusivity is increased especially at the surface (Lanford *et al.*, 1979). The runs containing obsidian powder yield gradients conformable to an error function profile (Fig. 59) as expected for a constant diffusivity, except in the low-concentration range (below 1%) where the concentration drops abruptly to zero. The shape of the curve at low concentration is poorly determined. However, there appears to be a significant decrease in  $D$  values at  $C/C_s \leq 0.2$ . Although this result cannot be demonstrated from the hydration curves alone, it is the only interpretation that is also compatible with the dehydration results. The diffusivity, assumed to be constant in the range  $1 \leq C/C_s \leq 0.2$ , at  $800^\circ\text{C}$  1 kbar is  $1.7 \times 10^{-7} \text{ cm}^2 \text{ sec}^{-1}$ . This is about one order of magnitude faster than the diffusivity given by Shaw (1974) from hydration runs at the same temperature; however it is similar to Shaw's results obtained on a partially prehydrated

specimen. A more detailed comparison with Shaw's results is not possible because Shaw did not determine concentration profiles.

### Discussion

The hydration runs yield mean diffusivities within the range ( $10^{-7}$ – $10^{-8} \text{ cm}^2 \text{ sec}^{-1}$ ) of previously published results (Fig. 58). The difference between the low-concentration diffusivity ( $C < 0.4\%$   $\text{H}_2\text{O}$ ) obtained in the dehydration experiments and the higher concentration results (1–5%  $\text{H}_2\text{O}$ ) is striking. There are three orders of magnitude difference between the two sets of results. The difference is probably not due to different mechanisms in sorption and desorption behavior, because Jambon *et al.* (1978) reported diffusivities from dehydration of obsidian (5.5%  $\text{H}_2\text{O}$ ) that were in the same range as the present hydration results. The most likely explanation is that there is a sharp decrease in diffusivity probably at about 0.5–1% water concentration. More experiments are required to find out the correct relationship between  $D$  and  $C$ , especially in the range 0–1% water concentration.

It is interesting to note that all natural obsidians have a water content of 0.1–0.5%. On the basis of our results this may be explained in the following way: in the high-concentration range water mobility is such that obsidians can easily lose their water to the surroundings. When the water content drops below 0.5%, the diffusivity becomes so low that further loss is insignificant. This diffusive effect will be enhanced by the great increase in viscosity, hindering efficient convection. For the same reasons it seems very difficult to contaminate a dry granitic magma with water. Convection and diffusion transfer will be so slow that they cannot have a significant effect on magmatic bodies. On the other hand, hydrated melts because of their lower viscosity and higher diffusivity will be able to exchange water rapidly with the



surrounding rocks. This could lead to isotopic exchange for oxygen and hydrogen in a very efficient way.

The strong concentration dependence of the water diffusivity may also provide an explanation for the apparently extreme resistance to hydration and weathering of tektite glasses (J. A. O'Keefe, personal communication, 1979). If the difference in diffusivity between "wet" and "dry" glasses observed in this study is applicable to lower temperatures, a granitic glass, once dehydrated, should show this resistance to rehydration (except in an environment of very high water pressure).

It is tempting to relate the compositional effects to the structure of melts. It is generally accepted that the addition of water to a granitic melt results in a depolymerization of the structure. This effect is particularly well reflected by the viscosity variations of these melts with the water content, as well as with the general chemical composition (e.g., granite, basalt). Thus, the degree of polymerization may be lowered not only by the addition of water but also by the addition of alkalis, alkaline earths, or transition metals. The diffusivity of water appears to increase sharply in the range 0–1% H<sub>2</sub>O, as does probably the diffusivity of Cs (Jambon *et al.*, 1978; Watson, 1979). On the other hand, the diffusivity of Cs is very similar in granitic and basaltic glasses. Therefore it appears unlikely that the enhancement of diffusivity by increased water concentration is simply the result of depolymerization of the melt. We do not have a good explanation for this phenomenon, and we note only that current models of silicate melt structure cannot account for observed differences in mobility.

### References

- Arzi, A. A., Fusion kinetics, water pressure, water diffusion and electrical conductivity in melting rock interrelated, *J. Petrol.*, 19, 153–169, 1978.
- Crank, J., *The Mathematics of Diffusion*, 2nd ed., Oxford Univ. Press, 1975.
- Jambon, A., J. P. Carron, F. Delbove, Données préliminaires sur la diffusion dans les magmas hydratés: le césium dans un liquide granitique à 3 kbar, *C. R. Acad. Sci.*, D287, 403–406, 1978.
- Lanford, W. A., K. David, P. La Marche, T. Laursen, R. Groleau, Hydration of soda lime glass, *J. Non Cryst. Solids*, in press, 1979.
- Magaritz, M., and A. W. Hofmann, Diffusion of Sr, Ba and Na in obsidian, *Geochim. Cosmochim. Acta*, 42, 595–605, 1978.
- Shaw, H. R., Diffusion of H<sub>2</sub>O in granitic liquids, part I, experimental data; part II, mass transfer in magma chambers, in *Geochemical Transport and Kinetics*, A. W. Hofmann, B. J. Giletti, H. S. Yoder, Jr., R. A. Yund, eds. Carnegie Institution Publication 634, 139–170, 1974.
- Watson, E. B., The effect of dissolved water on cesium diffusion in molten granite, *Abstr. Trans. Amer. Geophys. U.*, 60, 402, 1979.

### DIFFUSIVITY AND SOLUBILITY OF HELIUM IN GRANITIC AND BASALTIC GLASSES—MECHANISMS OF HELIUM DEGASSING

A. Jambon and J. E. Shelby\*

#### Introduction

The recent discovery of a primordial helium component in the mantle has increased the interest in rare gas geochemistry of volcanic rocks. To make quantitative estimates of helium abundance, distribution, and migration during the Earth's evolution, fundamental data are lacking: solubility, diffusivity, and partitioning are completely unknown in crystals as well as in melts and glasses. The present study at low temperature (200–300°C) was especially designed to understand the helium composition and

\* Sandia Laboratories, Livermore, California.

its variations in basaltic and granitic glasses.

### Experimental Procedure

The samples used in this study are two obsidians and one basaltic glass. The obsidians are from Iceland and Valles Caldera (New Mexico). Both glasses have been the subject of extensive study on cationic diffusion (Carron, 1968; Jambon and Carron, 1973; Jambon and Semet, 1978; Jambon *et al.*, 1978; Magaritz and Hofmann, 1978). Analyses of the glasses can be found in Magaritz and Hofmann (1978). The basaltic glass has been remelted from a Kilauea basalt studied by Hofmann and Magaritz (1977) for cation diffusion at high temperatures. The specimens are prepared as thin disks 1.5 cm in diameter and 0.3 mm thick. By monitoring the permeation of He through this disk it is possible to determine both diffusivity and solubility. The technique has been described in detail by Shelby (1972) and has been applied to the study of many synthetic glasses. The limitations of the technique are (1) the temperature is limited to below 300°C, and (2) He is the only species measurable for these specimens. Attempts to study both Ne and D<sub>2</sub> failed because of low permeabilities.

The steady state flux of helium through the specimen,  $J_{ss}$ , is related to permeability  $k$ , by:  $J_{ss} = k PA/L$  where  $P$  is the pressure gradient through the specimen of area  $A$  and thickness  $L$ .  $J_{ss}$  is measured with a mass spectrometer by comparison with a helium flow standard. After the He flow through the disk has reached steady state, the He supply is shut off and the transient flux,  $J$ , is measured as a function of time,  $t$ . From this, the diffusivity  $D$  is calculated using the equation:

$$J = -2J_{ss} \sum_{n=1}^{\infty} (-1)^n \exp - (n^2 \pi^2 D t / L^2).$$

Finally, the solubility  $S$  is given by:  $S = k/D$ .

### Results and Discussion

**Obsidians.** The temperature dependence of  $D$  and  $S$  is shown in Figs. 60 and 61.  $D$  exhibits a typical Arrhenius dependence:

$$D_I = 7.7 \times 10^{-4} \exp - 8.010/RT \quad \text{cm}^2 \text{ sec}^{-1}$$

$$D_{Vc} = 1.6 \times 10^{-3} \exp - 8.590/RT \quad \text{cm}^2 \text{ sec}^{-1}$$

for Icelandic and Valles Caldera obsidians, respectively (the activation energy in kcal/mole). The solubilities are:

$$S_I = 5.3 \times 10^{-3} \exp - 0.815/RT \quad \text{cm}^3/\text{g atm STP}$$

$$S_{Vc} = 1.5 \times 10^{-3} \exp + 0.880/RT \quad \text{cm}^3/\text{g atm STP}.$$

These values for the two obsidians are very similar. The small but significant differences can be probably explained by the difference in chemical composition ( $\text{SiO}_2 = 76.87\%$  for Valles Caldera and  $72.20\%$  for Iceland). These are the highest diffusivities ever measured for any species in these glasses—at 300°C  $D_{\text{He}}/D_{\text{Na}} \simeq 10^4$ . This confirms that, in a given matrix, diffusivities depend mainly on radius and charge of diffusing species. Thus both Ne (same charge and greater radius) and Na (greater charge and approximately same radius) have diffusivities several orders of magnitude below that of He in this temperature range. At a temperature of 300°C, He is as mobile as many cations at temperatures exceeding 900°C.

The diffusivities can be compared to those measured in silica and albite glasses (Shelby, 1972; Shelby and Eagan, 1976). The albite glass displays a very similar behavior. This is not surprising, because albite has a framework silicate stoichiometry and a silica content very close to that of our obsidians. The solubility is relatively insensitive to temperature. It is comparable to the solubility of He in melts at high temperature:  $S =$



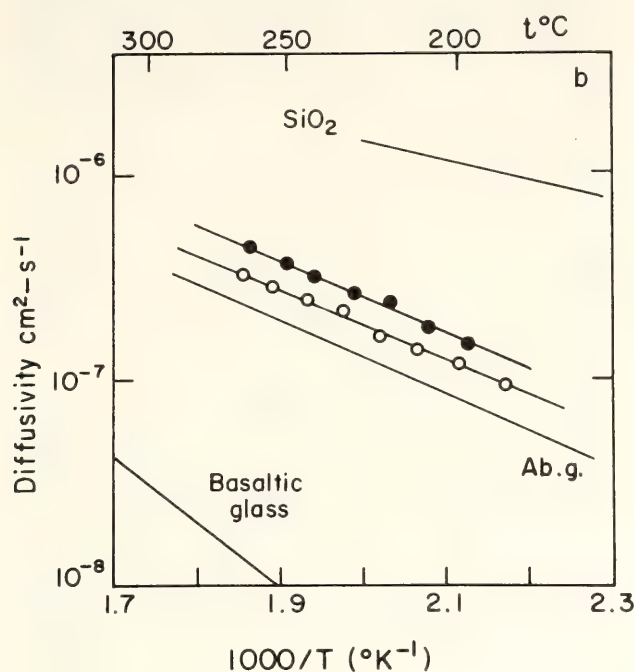


Fig. 60. Arrhenius plot of the He diffusivities measured: full circles, Valles Caldera; empty circles, Icelandic obsidian. Estimated value from permeability measurement is shown for basaltic glass as well as for silica and albite glasses. The increase of diffusivity with silica content is evident.

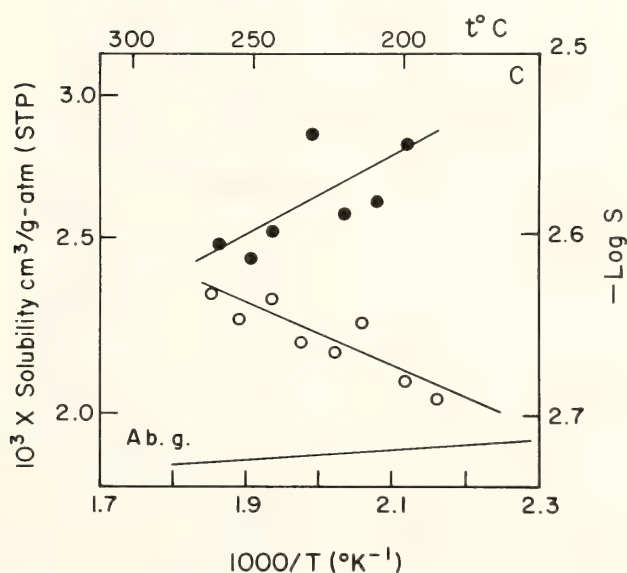


Fig. 61. Arrhenius plot for solubilities. Empty and full circles are for Icelandic and Valles Caldera obsidians, respectively. The scatter is mainly due to scale; the variation of solubility in this temperature range is almost negligible. Solubility in albite glass is shown for comparison.

$1.2 \times 10^{-4}$  for enstatite melt at  $1500^{\circ}\text{C}$  (Kirsten, 1968) and  $2.7 \times 10^{-3}$  at  $1300^{\circ}\text{C}$  for a gabbro-diabase melt (Gerling, 1940). As Shelby *et al.* (1976) experimentally showed, Henry's law is obeyed in the range 0–100 bar He pressure for silica glass. We therefore believe that the solubilities determined in this study can be applied to all the geological settings.

**Basaltic Glass.** The permeability of basaltic glass is about two orders of magnitude lower at  $250^{\circ}\text{C}$ , with an activation energy about twice that of obsidians. This hindered measurements of the diffusivity and hence solubility. From the measurements of Shelby and Eagan (1976) we can estimate a diffusivity for basaltic glass of about  $7 \times 10^{-3} \exp - 14.0/RT$ , that is  $10^{-8} \text{ cm}^2 \text{ sec}^{-1}$  at  $250^{\circ}\text{C}$ . This is derived from the strong correlation between diffusivity and silica content of glasses. Using this estimate and the measured permeability, one obtains an estimate for the solubility,  $S_b = 3 \times 10^{-3} \exp - 2.0/RT$  (e.g.,  $4 \times 10^4 \text{ cm}^3/\text{g STP}$ , at  $250^{\circ}\text{C}$ ). Whatever the accuracy of this extrapolation, it shows that both solubility and diffusivity in this melt are significantly lower than in obsidians. On this basis we can compute a partition coefficient  $K_{b/w}$  between basalt glass and seawater as the ratio of the volumes (STP) in one gram of each phase per atm He pressure. Using the solubility of He in seawater (Weiss, 1970), one finds  $K_{b/w} = 1.4 \times 10^{-2}$  in the range 0– $100^{\circ}\text{C}$ . We can make the same calculation for the equilibrium  $\text{CO}_2$  (ideal gas) and glass and find  $K_{b/g} = 2 \times 10^{-7}$ . This means that He is strongly partitioned into water and even more into a gas phase.

### Geochemical Implications

Measurement of the rare gas concentration and isotopic composition in the glassy margin of oceanic basalt pillows has been used to derive the composition and abundance of the gas component in

the mantle. He is particularly interesting in that it exhibits isotopic variations, the mantle component having a  $^3\text{He}/^4\text{He}$  ratio about ten times the atmospheric ratio. He diffusivity in glasses is so high that quantitative retention in naturally quenched glasses is unlikely for any geologically significant length of time.

Consider first the glasses analyzed by Craig and Lupton (1976) from DSDP leg 34. They have a comparatively low He content correlated with a low  $^3\text{He}/^4\text{He}$  ratio,  $R \simeq 4 \times 10^{-6}$ . From a simple diffusion-loss model assuming  $D(^3\text{He})/D(^4\text{He}) = 1.15$  (see Craig and Lupton, 1976), we find that these samples underwent about 95% loss, assuming an initial ratio of  $1.4 \times 10^{-5}$  similar to that of young tholeiites. If we assume the age of sample (30 m.y.) to be equal to the duration of loss, the model requires a diffusivity of  $10^{-15} \text{ cm}^2 \text{ sec}^{-1}$ . From our data, the diffusivity at  $0^\circ\text{C}$  is estimated to  $4 \times 10^{-14} \text{ cm}^2 \text{ sec}^{-1}$ . The discrepancy can be reconciled in view of the uncertainty of the extrapolation and the

trapping effect of vesicles. It can be shown that when a small amount of vesicles is present the effective diffusion coefficient reduces to  $D'$ , given by:

$$D/D' = 1 + f/K (1-f)$$

where  $f$  is the fraction of vesicles and  $K$  the partition coefficient between basaltic glass and gas in vesicles. This ratio may be as high as  $10^2$ – $10^4$  because of the low value of  $K$ .

If we look now at He abundance for oceanic tholeiite glasses, as plotted in Fig. 62, all the recent tholeiites have approximately constant  $^3\text{He}/^4\text{He}$  with the He abundance varying by more than two orders of magnitude. The loss of helium by vesiculation at high temperature (escaping of bubbles) as well as enrichment of volatiles (bubbles upwelling) can occur depending on the dynamics of magmatism. No significant fractionation is expected to occur at high temperature. These processes can account fairly well for the variations observed in recent oceanic tholeiites. Moreover, alteration

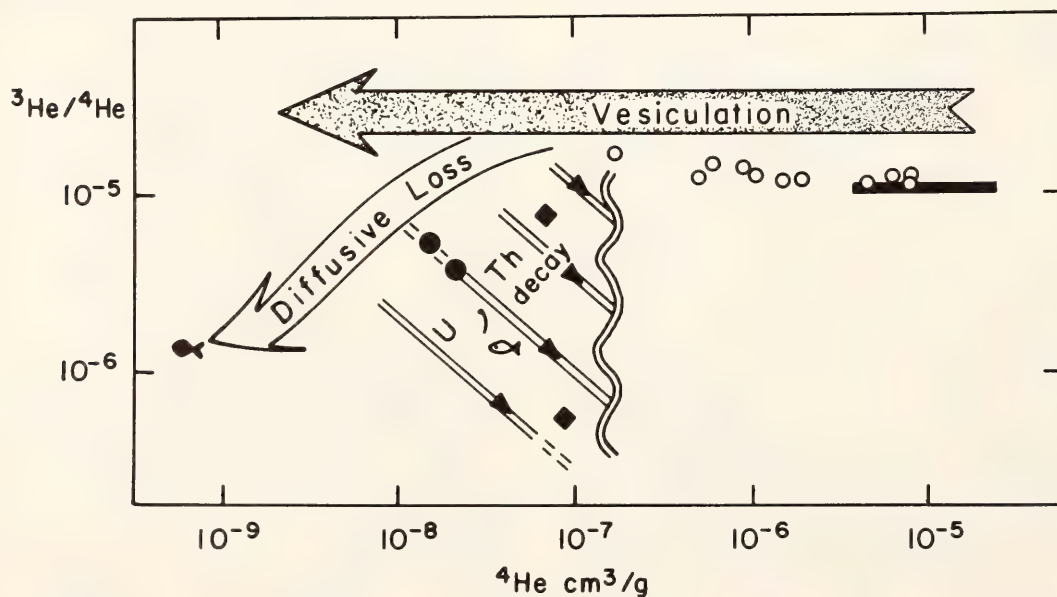


Fig. 62. Variations of isotopic ratio with He abundance. Full circles, DSDP tholeiites; full squares, alkali basalts; empty circles, midoceanic tholeiite glasses (Lupton and Craig, 1975; Craig and Lupton, 1976). The bar represents the range of measurements reported by Kurz *et al.* (1979) for MORB glasses. Empty fish, seawater; full fish, basaltic glass in equilibrium with seawater. Vesiculation can account for abundance variations in recent tholeiites; additional diffusive loss is required for old tholeiite. U, Th decay plays a significant role for alkali basalts.



of the glass may liberate part of the gas trapped in these vesicles, accounting for a more significant loss for comparatively older pillows.

### Conclusions

The diffusivity of He in natural glasses has been shown to be very high relative to cationic diffusion. The diffusion and solubility data have been used to estimate the migration rate and mechanism of He in oceanic basalts, as follows: (1) none of these basalt glasses is equilibrated with seawater, (2) vesiculation can explain all the variations of He abundance in glass margins of pillows for recent tholeiites, and (3) for older tholeiites, diffusive loss over several tenths of m.y. can account for the concomitant variation of isotopic ratio and abundance.

### References

- Carron, J. P., Autodiffusion du sodium et conductivité électrique des obsidiennes granitiques, *C. R. Acad. Sci.*, 266D, 854–857, 1968.
- Craig, H., and J. E. Lupton, Primordial neon, helium and hydrogen in oceanic basalts, *Earth Planet. Sci. Lett.*, 31, 369–385, 1976.
- Gerling, E. K., On the solubility of helium in melts, *C. R. Dokl. Acad. Sci. URSS*, 37, 22–23, 1940.
- Hofmann, A. W., and M. Magaritz, Diffusion of Ca, Sr, Ba and Co in a basalt melt: implications for the geochemistry of the mantle, *J. Geophys. Res.*, 82, 5432–5440, 1977.
- Jambon, A., and J. P. Carron, Etude expérimentale de la diffusion des éléments alcalins K, Rb, Cs dans une obsidienne granitique, *C. R. Acad. Sci.*, 276D, 3069–3072, 1973.
- Jambon, A., J. P. Carron, and F. Delbove, Données préliminaires sur la diffusion dans les magmas hydratés: le césium dans un liquide granitique à 3 k bar, *C. R. Acad. Sci.*, 287D, 403–407, 1978.
- Jambon, A., and M. Semet, Lithium diffusion in silicate glasses of albite, orthoclase and obsidian composition: an ion microprobe determination, *Earth Planet. Sci. Lett.*, 37, 445–450, 1978.
- Kirsten, T., Incorporation of rare gases in solidifying enstatite melts, *J. Geophys. Res.*, 73, 2807–2810, 1968.
- Kurz, M. D., T. L. Torgersen, and W. J. Jenkins, Helium in oceanic basalt glasses, *EOS: Trans. Amer. Geophys. U.*, 60, 408, 1979.
- Lupton, J. E., and H. Craig, Excess  $^3\text{He}$  in oceanic basalts: evidence for terrestrial primordial helium, *Earth Planet. Sci. Lett.*, 26, 133–139, 1975.
- Magaritz, M., and A. W. Hofmann, Diffusion of Sr, Ba and Na in obsidian, *Geochim. Cosmochim. Acta*, 42, 595–605, 1978.
- Shelby, J. E., He migration in glass-forming oxides, *J. Appl. Phys.*, 43, 3068–3072, 1972.
- Shelby, J. E., and R. J. Eagan, He migration in sodium aluminosilicate glasses, *J. Amer. Ceram. Soc.*, 59, 420–425, 1976.
- Shelby, J. E., S. C. Keeton, and J. J. Ianucci, Effect of gas composition on the pressure dependence of helium solubility in vitreous silica, *J. Appl. Phys.*, 47, 3952–3955, 1976.
- Weiss, R. F., Helium isotope effect in solution in water and seawater, *Science*, 168, 247–248, 1970.

### RAMAN SPECTROSCOPIC STUDIES OF $\text{P}_2\text{O}_5$ -AND $\text{TiO}_2$ -BEARING MINERAL GLASSES

F. J. Ryerson, Bjorn O. Mysen,\*  
and David Virgo\*

#### Introduction

Important igneous processes, such as diffusion, nucleation, crystal growth,

\*Geophysical Laboratory, Carnegie Institution of Washington, Washington, D. C.

major and trace element partitioning, and silicate liquid immiscibility, depend on the thermodynamic and physical properties of silicate melts. In order to better understand such processes, a more detailed knowledge of silicate melt structure is required. A major obstacle of such quantification involves the role of amphoteric cations such as  $\text{Al}^{+3}$ ,  $\text{Fe}^{+3}$ ,  $\text{Ti}^{+4}$  and  $\text{P}^{+5}$ . These cations have small ionic radii, and the possibility of their copolymerization in silicate anions exists: i.e., they may act as network formers. However, mineral analogies also indicate their existence in octahedral sites, i.e., as network-modifying cations. Hence, such cations may be distributed between two distinctly different sites, and this distribution may be a function of composition and external parameters. In order to understand their behavior, the effect of  $\text{P}_2\text{O}_5$  and  $\text{TiO}_2$  on quenched melts of various structural types has been investigated with the aid of Raman spectroscopy. The experimental techniques are identical to those of Sharma *et al.* (1978).

### Raman Spectra

$\text{Na}_2\text{SiO}_3$ . The vibrational bands most diagnostic of the anionic constitution of  $\text{Na}_2\text{SiO}_3$  glass (henceforth referred to as NMS) occur at  $610\text{ cm}^{-1}$  and in the range  $800\text{--}1100\text{ cm}^{-1}$  (Fig. 63a). The high-frequency envelope is composed of three bands with peaks at  $851\text{ cm}^{-1}$  and  $973\text{ cm}^{-1}$ , and a well-developed shoulder at  $1060\text{ cm}^{-1}$ . These bands reflect Si-O stretching modes of a monomer ( $\text{SiO}_4$ ), chains ( $\text{Si}_2\text{O}_6$ ), and sheets ( $\text{Si}_2\text{O}_5$ ), respectively, based upon comparison with crystal spectra and dynamical models (Brawer and White, 1975). The  $610\text{-cm}^{-1}$  band is a Si-O bending mode in a chain (Etchepare, 1972).

The addition of 10 mole %  $\text{TiO}_2$  to NMS produces a dramatic decrease in the intensities of the  $610\text{-cm}^{-1}$  and  $970\text{-cm}^{-1}$  bands, while the intensity of the  $850\text{-cm}^{-1}$  band increases (Fig. 63b). These changes indicate the formation of

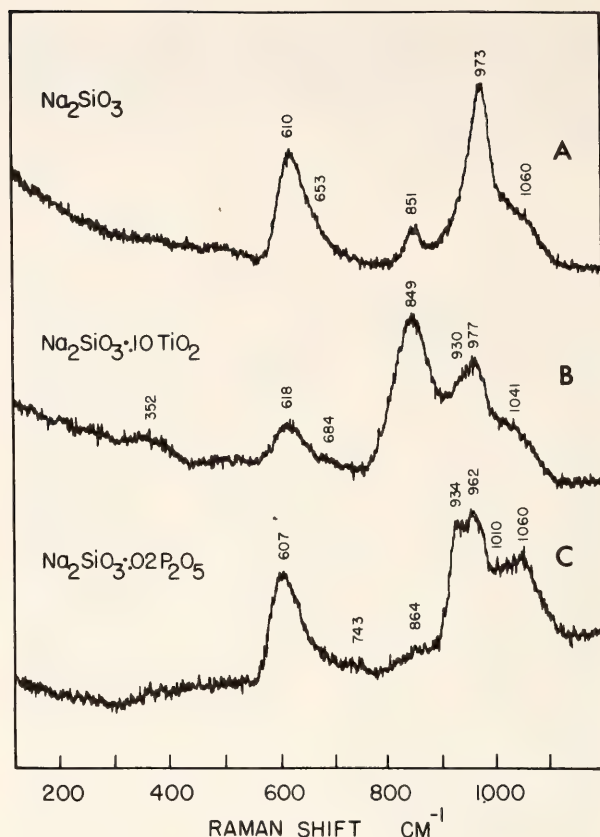


Fig. 63. Raman spectra of (A)  $\text{Na}_2\text{SiO}_3$ , (B)  $\text{Na}_2\text{SiO}_3 \cdot 0.10\text{ TiO}_2$ , and (C)  $\text{Na}_2\text{SiO}_3 \cdot 0.02\text{ P}_2\text{O}_5$  glasses.

monomers at the expense of chains, i.e., depolymerization. Also evident is the development of a  $930\text{-cm}^{-1}$  shoulder on the  $970\text{-cm}^{-1}$  band. Various workers (Tobin and Baak, 1968, among others) have observed a similar band in  $\text{TiO}_2$ -bearing glasses which has been attributed to  $\text{TiO}_4$  units. Hence, the spectra indicate that  $\text{TiO}_2$  is acting as a network-modifying component in these melts, and the presence of the  $930\text{-cm}^{-1}$  band indicates that it is doing so as a tetrahedrally coordinated cation.

The spectrum of  $\text{P}_2\text{O}_5$ -bearing NMS indicates almost total disappearance of the  $850\text{-cm}^{-1}$  monomer band, while the  $1060\text{-cm}^{-1}$  shoulder has emerged as a distinct peak (Fig. 63c). Both features indicate polymerization of silicate anions resulting from the presence of  $\text{P}_2\text{O}_5$ . The bands near  $960\text{ cm}^{-1}$  and  $1060\text{ cm}^{-1}$  also appear to be split. Investigations of  $\text{MO-P}_2\text{O}_5$  glass spectra reveal no bands in



this frequency range. The new bands may indicate decoupled Si-O and P-O stretch vibrations in chains and sheets. Through chromatographic analysis, Masson *et al.* (1974) have shown that copolymerization of  $\text{PO}_4$  and  $\text{SiO}_4$  units is possible in such anions. A weak band at  $743\text{ cm}^{-1}$  corresponds to a band in  $\text{MO-P}_2\text{O}_5$  glasses associated with P-O-P vibrations (Babovich, 1962), and may indicate clustering of  $\text{PO}_4$  units.

### 3-D Network Melts: $\text{SiO}_2$ , Ab

The spectrum of  $\text{SiO}_2 \cdot 0.05\text{ P}_2\text{O}_5$  displays marked changes in both low- and high-frequency regions compared to  $\text{SiO}_2$  (Fig. 64a, b). The low-frequency portion of the spectrum is poorly understood and will not be discussed here. The high-frequency portion of the  $\text{SiO}_2$  glass spectrum is characterized by two broad but distinct peaks, at  $1055\text{ cm}^{-1}$  and  $1188\text{ cm}^{-1}$ . These correspond to Si-O stretch modes in a network (Bates *et al.*, 1974). With the addition of  $\text{P}_2\text{O}_5$ , the two bands cannot be resolved, and a single high-frequency envelope is present between  $1000\text{--}1275\text{ cm}^{-1}$ . No bands corresponding to those in  $\text{P}_2\text{O}_5$  glass appear between  $1000\text{--}1275\text{ cm}^{-1}$  (Galeener and Mikkelsen, 1979); hence, it may be argued that this high-frequency envelope is the result of decoupled Si-O and P-O vibrations in a network. A new band is observed at  $1325\text{ cm}^{-1}$  and is attributed to the vibrations of the  $\text{P}=\text{O}$  bond. This band occurs at  $1390\text{ cm}^{-1}$  in glassy  $\text{P}_2\text{O}_5$  (Galeener and Mikkelsen, 1979), and its shift to lower frequencies may indicate a weakening of the double bond from the proximity of highly electro-negative  $\text{Si}^{+4}$ .

In summary, the spectrum of  $\text{P}_2\text{O}_5$ -doped  $\text{SiO}_2$  is consistent with a random distribution of  $\text{P}^{+5}$  in copolymerization with  $\text{SiO}_2$  in the network. No P-O-P linkages are observed, and the  $\text{P}=\text{O}$  remains intact.

The effect of  $\text{TiO}_2$  upon Ab is manifested in two features (Fig. 64c, d): (1)

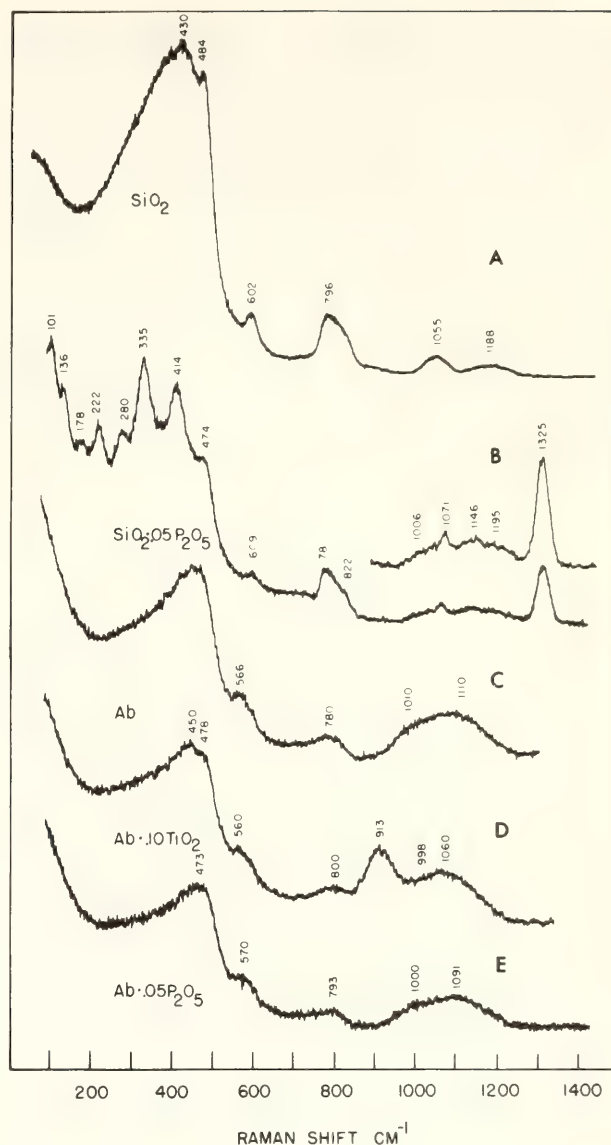


Fig. 64. Raman spectra of (A)  $\text{SiO}_2$ , (B)  $\text{SiO}_2 \cdot 0.05\text{ P}_2\text{O}_5$ , (C) Ab, (D)  $\text{Ab} \cdot 0.10\text{ TiO}_2$ , (E)  $\text{Ab} \cdot 0.05\text{ P}_2\text{O}_5$  glasses.

the downward shift of the high-frequency envelope and (2) the emergence of a new band at  $913\text{ cm}^{-1}$ . The first feature is explained by coupling of Ti-O and Si-O stretch vibrations in a network. A similar trend has been noted for the addition of alkali aluminum complexes to  $\text{SiO}_2$  melts (Sharma *et al.*, 1978). The  $913\text{-cm}^{-1}$  band is attributed to the presence of  $\text{TiO}_4$  tetrahedra. Hence,  $\text{Ti}^{+4}$  exists in tetrahedral coordination within the network, and as isolated tetrahedra.

The presence of  $\text{P}_2\text{O}_5$  in albite has little effect on the spectrum (Fig. 64e). Some resolution is lost in the high-frequency

envelope, presumably because of decoupled Si-O and P-O vibrations, but otherwise no new bands appear. On this basis, it is concluded that  $P^{+5}$  is part of the network and produces no structural changes. In this regard, it is noted that the Raman spectrum of  $NaAl_2PSiO_8$  glass is identical in all major features to albite glass (Ryerson *et al.*, unpublished data, 1979). In both cases, the  $P=O$  cannot exist if infinite network structures are to be formed.

### Discussion

It is important to use the structural interpretation of the Raman spectra of  $TiO_2$ - and  $P_2O_5$ -doped glasses to explain fluctuations in mineral-melt equilibria caused by these elements. In polymerized melts,  $P^{+5}$  enters the silicate framework, and in  $SiO_2$  melts the  $P=O$  remains intact. In depolymerized melts  $P_2O_5$  has a dramatic polymerizing effect, such that the monomer is almost entirely absent in NMS. These observations support the model of Ryerson and Hess (1979) in which the rapid decrease in the activity of  $SiO_2$  in the system  $P_2O_5$ - $SiO_2$  is attributed to  $P^{+5}$  as a network-forming component. The data also support the hypothesis that the addition of  $P_2O_5$  to depolymerized melts results in clustering of  $PO_4$  groups, which in turn complex with other metal cations destroying non-bridging bonds and polymerizing the melt.

Based on phase equilibrium arguments,  $TiO_2$  is expected to act in much the same manner as  $P_2O_5$  (Kushiro, 1975). This appears to be the case for 3-D network melts where  $Ti^{+4}$  enters the network. There appears to be a concentration limit to this substitution inasmuch as isolated  $TiO_4$  groups are also recognized. The addition of  $TiO_2$  to NMS causes depolymerization. This conclusion does not agree with the increased activity of  $SiO_2$  displayed in the shift of the olivine-enstatite cotectic when  $TiO_2$  is added

(Kushiro, 1975). This disagreement may be due in part to the dilution of  $SiO_2$  by  $TiO_2$  in the composition chosen: i.e., metasilicate stoichiometry is not preserved. Further work is in progress along the joins between  $Na_2SiO_3$  and  $Na_2TiO_3$  and  $TiSi_2O_6$  in order to address this question.

### References

- Babovich, Y. S., An investigation of the structure of glassy phosphates using Raman spectra, *Opt. Spectrosc.*, **13**, 274-277, 1962.
- Bates, J. B., R. W. Hendricks, and L. B. Shaffer, Neutron irradiation effects and structure of noncrystalline  $SiO_2$ , *J. Chem. Phys.*, **61**, 4163-4176, 1974.
- Brawer, Steven A., and William B. White, Raman spectroscopic investigation of the structure of silicate glasses. I. The binary alkali silicates, *J. Chem. Phys.*, **63**, 2421-2432, 1975.
- Etchepare, J., Study by Raman spectroscopy of crystalline and glassy diopside, in *Amorphous Materials*, R. W. Douglas and B. Ellis, eds., pp. 337-346, John Wiley and Sons, Inc., New York, 1972.
- Galeener, F. L., and J. C. Mikkelsen, Jr., Raman spectra and structure of pure vitreous  $P_2O_5$ , *Solid State Comm.*, **30**, 505-510, 1979.
- Kushiro, Ikuo, On the nature of silicate melt and its significance in magma genesis: regularities in the shift of liquidus boundaries involving olivine, pyroxene, and silica minerals, *Amer. J. Sci.*, **275**, 411-431, 1975.
- Masson, C. R., W. D. Jamieson, and F. G. Mason, Ionic constitution of metallurgical slags, in *The Richardson Conference on Physical Chemistry of Process Metallurgy*, I.M.M., London, 1974.
- Ryerson, F. J., and P. C. Hess, The role of  $P_2O_5$  in silicate melts, *Geochim. Cosmochim. Acta*, in press, 1979.
- Sharma, S. K., D. Virgo, and B. Mysen,



Structure of melts along the join  $\text{SiO}_2\text{-NaAlSiO}_4$  by Raman spectroscopy, *Carnegie Inst. Wash. Year Book* 77, 682-658, 1978.

Tobin, Marvin C., and Tryggve Baak, Raman spectra of some low expansion glasses, *J. Opt. Soc. Amer.*, 58, 1459-1461, 1968.

## GALAXIES, STARS, AND PLANETARY SYSTEMS

### GALAXIES AND THEIR EVOLUTION

#### DYNAMICAL PROPERTIES OF SPIRAL GALAXIES AS A FUNCTION OF HUBBLE TYPE

*Vera C. Rubin, W. Kent Ford, Jr., and  
Norbert Thonnard*

The forms of spiral galaxies are amazingly varied, yet astronomers are able to classify them into operationally useful classes: Sa galaxies, with large nuclear bulges surrounded by tightly wound smooth arms which are barely resolved into knots; Sb galaxies, with moderate-sized bulges, arms more open, and increasingly resolved into emission regions; and Sc galaxies, with small nuclear bulges, arms well open, and composed of discrete luminous segments. During the 50 years since Hubble (1926) first recognized the regularity of these forms, there has been progress in understanding the variation of some physical parameters such as mass, color, luminosity, and rate of star formation with galaxy morphology. It would be premature, however, to conclude that the significance of the Hubble sequence is now understood. At times over the years the sequence has been assumed to be an evolutionary one, with galaxies evolving along it. However, because of the differences in masses of galaxies of different types, in recent years it was considered unlikely that galaxies altered their types. The current indications that field galaxies can merge, and that elliptical galaxies in clusters can gain mass at the expense of the outer envelopes of their less massive neighbors (Gallagher and Ostriker, 1972; Ostriker,

1977), once again reopens this question and reminds us of how rudimentary is our understanding of the evolution of galaxies.

We reported last year (Rubin *et al.*, 1978a, 1978b) on the start of a long-range program to study the dynamical properties and mass distributions within galaxies as a function of Hubble type, in order to answer the question, "What are the important dynamical parameters in determining where a galaxy is located along the Hubble sequence?" The availability of large optical telescopes, high-resolution spectrographs, and efficient image tubes makes it possible to detect emission across much of the optical image of a spiral galaxy and to deduce accurate rotational velocities as a function of position within the galaxy. Thus, an observational program which could not have been undertaken a few years ago can now obtain dynamical information of high accuracy for a significant sample of galaxies.

Our initial observations were directed to a small sample of large, high-luminosity spirals, of classes Sa, Sb, and Sc, and were discussed in our report of last year. We repeat several of the major conclusions here, so that we can compare these with our present studies.

(1) Circular velocities are approximately constant (i.e., rotation curves are flat) across the optical image of the galaxy to large distances from the nucleus. This indicates that there is significant mass at the outer regions of the optical galaxy. The lack of an (expected) decrease in rotational velocities with increasing nuclear distances indicates that

the mass in a high-luminosity spiral is not centrally condensed, as it is, for example, in the solar system, where almost all the mass is located in the Sun. The emission regions we observe respond to the total mass of the galaxy; hence our conclusions refer to the total dynamical mass, both luminous and nonluminous matter.

(2) There is a decrease in circular velocity from types Sa through Sc; circular velocities are near  $V \sim 320$  km/sec for Sa galaxies, and decrease to  $V \sim 200$  km/sec for Sc galaxies. Hence mass density ( $V^2/R^2$ ) at any  $R$  decreases along the Hubble sequence. This might reflect a higher density in the primordial mass distribution from which the early-type (large-bulge) galaxies condensed.

(3) Often, velocity gradients are observed across spiral arms; line-of-sight velocities are lower on the inner edge than on the outer edge. This observation, a prediction of the density-wave theory, will be relevant for any model that attempts to explain how spiral arms are formed and maintained during the lifetime of a galaxy.

(4) Spiral structure is well defined, and star formation is taking place, at nuclear distances in excess of 50 kpc. This result has implications for theories of star formation, for galactic structure and evolution, for cosmology, and for our own Galaxy. If our Galaxy resembles the high-luminosity galaxies that we have studied, then it is unlikely that it is as small as 15 kpc. It is also unlikely that the Sun, located at 10 kpc from the center, resides at about the limit of active star formation in the Galaxy, and that the rotational velocities decrease for nuclear distances greater than 10 kpc. Instead, it appears likely that the radius and the mass of the Galaxy are substantially greater than generally assumed, and that the solar location is not a suburban one on the outskirts of the bulk of the Galaxy.

From these conclusions, there is now no doubt that the integrated mass in a

high-luminosity spiral increases linearly with nuclear distance and is not approaching a limiting mass at the edge of the optical image (Rubin, 1979). Because it is unlikely that the mass distribution drops precipitously to zero at the edge of the optical image, this result suggests that high-luminosity galaxies contain a component of nonluminous matter which is distributed to an even larger radius than is the luminous mass. Massive halos around galaxies have been postulated earlier for stability reasons (Ostriker *et al.*, 1974; Einasto *et al.*, 1974). Our results strengthen the view that the optical galaxy is just a luminous disk within a more massive agglomeration. Additional support for this view comes from 21-cm observations of spirals, which show that the neutral-hydrogen distribution often extends beyond the optical image (Roberts 1975; Krumm and Salpeter 1979; Bosma, 1978; Salpeter, 1978). This result is so fundamental to an understanding of mass distributions in galaxies that we have extended our observations this year to galaxies of lower luminosity. Our principal aim is to learn if hidden mass is also a significant component for galaxies of lower luminosity.

Notable variations exist among the galaxies within a single Hubble class. Sc galaxies range from small, low-luminosity, low-mass objects, to galaxies of gigantic dimensions and enormous luminosities. Luminosity differences among Sc's have been well studied in an attempt to establish a "standard candle" for cosmological use. Differences in diameters, masses, and rotational velocities are only now being investigated. From our observing program, designed to exploit this range in Sc properties, we hope to learn how the variation in the dynamical properties within a single Hubble type compares to the range in dynamical properties among high-luminosity galaxies of all Hubble types.

We have now obtained rotational velocities as a function of nuclear dis-



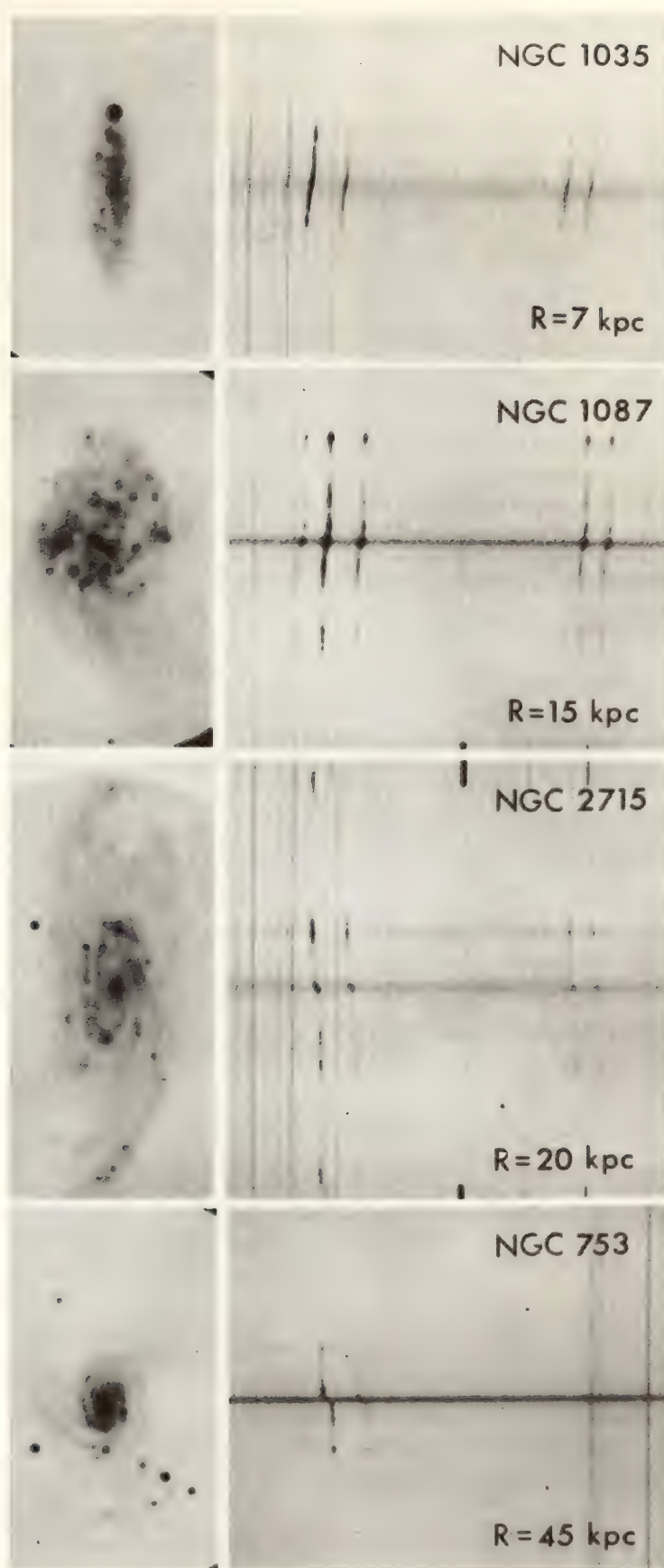


Fig. 65. Image-tube direct plates and major-axis spectra for 4 Sc galaxies with radii which range from 7 to 45 kpc. The strongest emission line is  $H\alpha$ , flanked by two [NII] lines; the doublet lines are both [SII]. The displacement of the lines indicates the line-of-sight velocity of the emitting gas. The direct plates were taken at the 72-inch telescope at Lowell Observatory; the spectra were obtained at the Kitt Peak National Observatory 4-m telescope.

tances for 21 Sc galaxies, with luminosities ranging from  $3 \times 10^9$  to  $2 \times 10^{11} L_{\odot}$ , masses from  $10^{10}$  to  $2 \times 10^{12} M_{\odot}$ , and radii from 4 to 122 kpc. The galaxies were observed with the 4-meter telescopes of the Kitt Peak National Observatory and the Cerro Tololo Inter-American Observatory, with a spectrograph incorporating a Carnegie image tube. The plates are at high velocity scale (25Å/mm) and high spatial scale (25"/mm), and in general emission is

recorded over more than 80% of the optical image. Some spectra are illustrated in Fig. 65. Figure 65 also reproduces direct photographs of a few of the galaxies; these come from image-tube photographs made with the 72-inch Perkins telescope of the Ohio State and Ohio Wesleyan Universities at Lowell Observatory. Plots of the rotational velocities as a function of nuclear distances are shown for all 21 galaxies in Fig. 66; the galaxies are ordered by increasing

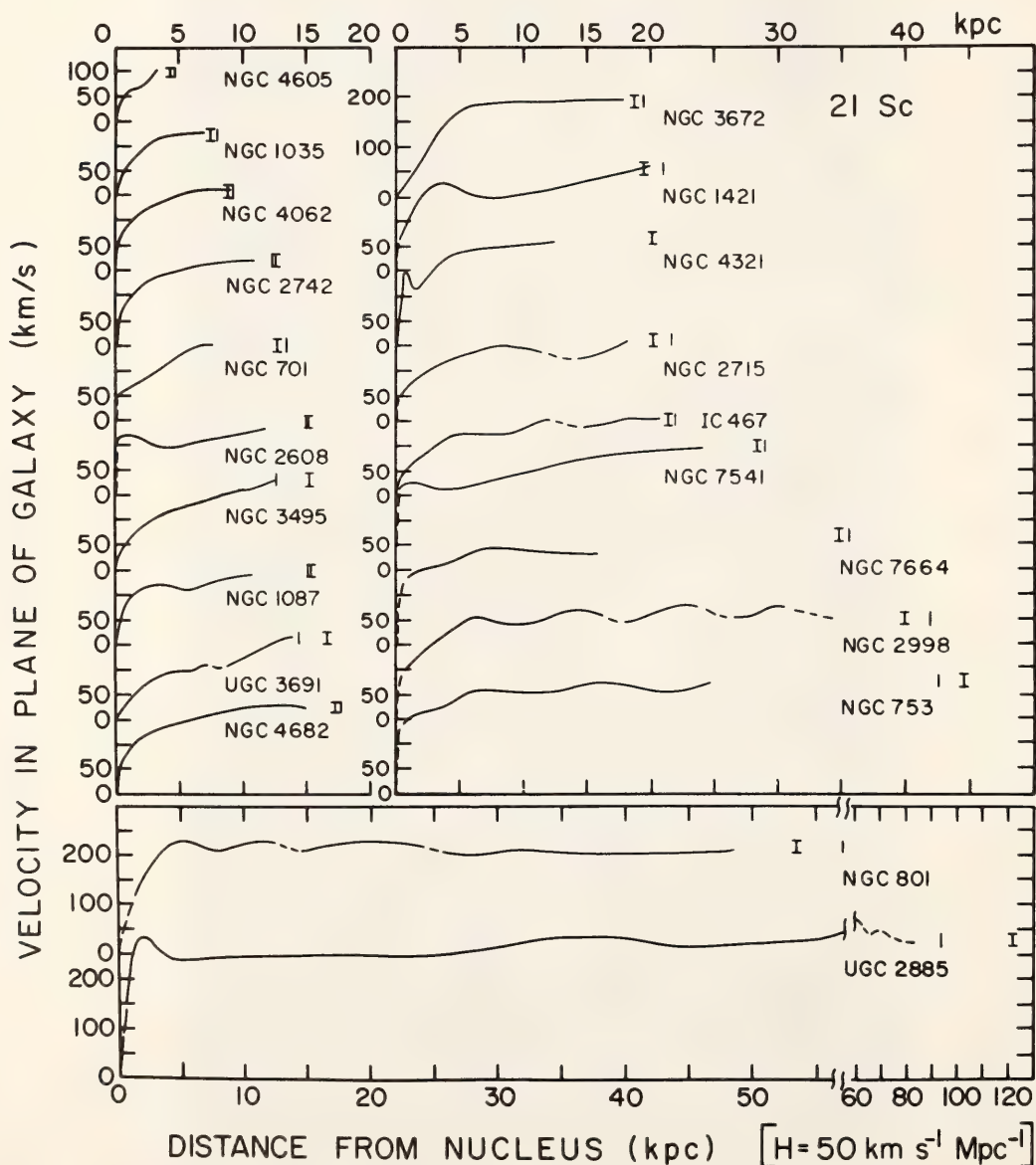


Fig. 66. Velocities in the plane of the galaxy as a function of distance from the nucleus for 21 Sc galaxies. The short vertical line marks the deVaucouleurs radius of each galaxy; the line with bars shows the radius corrected for extinction in our Galaxy and for projection effects. Dashed lines near the nucleus indicate regions with no measured velocities. At larger radial distances, dashed lines indicate regions where the velocity decrease is faster than Keplerian.



size. For each galaxy, a bar is drawn to indicate the edge of the optical image (the 25 mag/□ isophote). Five of these galaxies were observed earlier in the high-luminosity study. The major features of these velocities are described below.

(1) Almost all spectra show *rising* velocities as a function of distance from the nucleus; only the largest galaxies have flat rotation curves. The smallest Sc's exhibit the same unexpected mass distribution as do the high-luminosity galaxies. Integrated masses are increasing at the outer regions of the optical galaxies. Thus it is likely that non-luminous mass exists beyond the optical disk for these galaxies also. The distribution of this mass, whether in a disk or in a spheroid, is unrestricted by our observations.

(2) Within a few kiloparsecs of the nucleus, the galaxies exhibit great velocity individuality, which is only weakly correlated with diameter. In some galaxies, rotational velocities are already high at the first measured point beyond the nucleus (NGC 701, 2608, 7541, 7664, 753, and UGC 2885); in others, there is a very gentle increase in velocity with radius (NGC 1035, 4062, 3495, 3672, IC 467). High velocities just off the nucleus are an indication of a massive nucleus; for most of these galaxies this indication is accompanied by a stellarlike point nucleus on the available photographs. Moreover, all galaxies with massive nuclei that were observed by Dressel and Condon (1978) also are continuum radio sources. Thus the radio nuclear properties, the optical nuclear properties, and the dynamical nuclear properties of the galaxies with high circular velocities just off the nucleus all give evidence for an energetic massive nuclear source.

(3) Beyond the nucleus, the velocities are unexpectedly similar. Velocities rise rapidly to about 5 kpc, and more slowly thereafter. Excluding the two largest galaxies, velocities for the remaining 19 can be superimposed to form a single com-

posite curve; the spread in velocity  $V$  about this mean curve is only  $\pm 50$  km/sec at any nuclear distance  $R$ . It is more instructive, however, to examine the velocities in two groups, those for the smallest and those for the largest galaxies. In Fig. 67, we show the region in the  $V, R$  plane occupied by the rotation curves for the 10 smallest galaxies. A mean curve rises to about  $V = 100$  km/sec at  $R = 2.5$  kpc and then rises more slowly to  $V_{\max} = 160$  km/sec at  $R = 15$  kpc. One reason that very small galaxies have low maximum velocities is because they do not have the large radii associated with the largest velocities. The total scatter about the mean curve is  $\pm 32$  km/sec; this indicates a total range of density at any  $R$  less than a factor of three.

When the velocities for the nine largest galaxies (excluding NGC 801 and UGC 2885) are superposed, they cover the region indicated in Fig. 67. Here the total spread about the mean curve is  $\pm 50$  km/sec; here too the variation in density is less than a factor of three at any  $R$ . The mean curve for the largest galaxies rises more steeply, and the final velocity is higher than that for the small galaxies. This surprising resemblance of all Sc rotation curves suggests that Sc galaxies sit in similar gravitational potentials only weakly dependent on the size of their luminous image.

For almost every galaxy, the final velocity is the highest rotational velocity,  $V_{\max}$ . If we could observe beyond the optical image, would the velocities continue to rise, or is the mass there decreasing rapidly enough so that decreasing velocities would finally be observed? Radio observations of neutral hydrogen may enable us to answer these questions. Extended 21-cm velocities for a few galaxies (Krumm and Salpeter, 1979; Burstein and Krumm, 1979) apparently show little decrease in velocity. However, for galaxies with radii as large as 50 kpc, the difference between a flat rotation curve and one falling as  $1/\sqrt{R}$  beyond

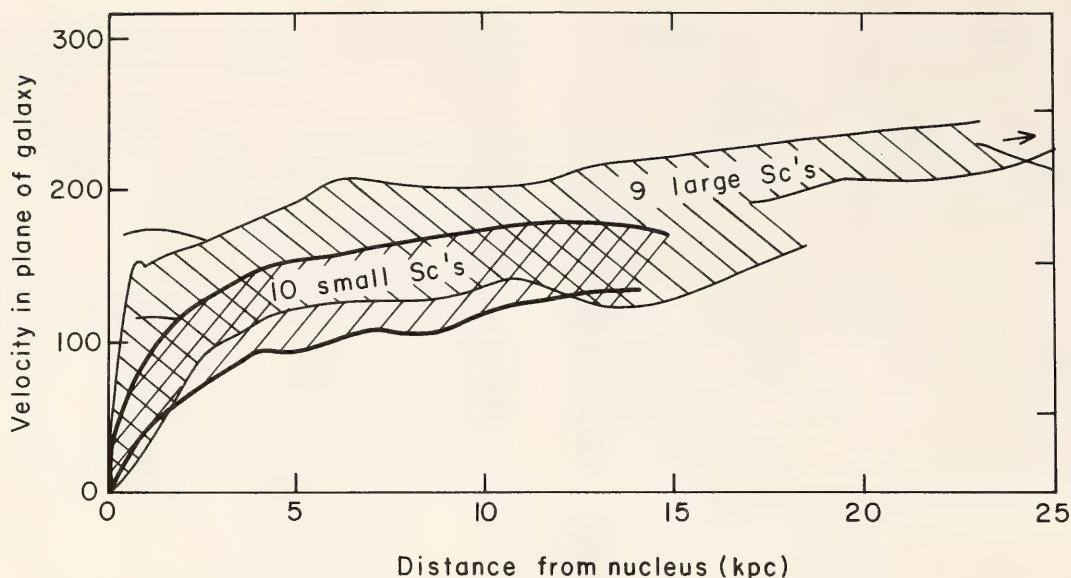


Fig. 67. The superposition of rotation curves for 19 Sc galaxies. The two largest galaxies have been omitted. Small galaxies generally have a smaller maximum velocity than do large galaxies.

$R = 50$  kpc (i.e., Keplerian, no mass beyond 50 kpc) is not large; velocities would only decrease from  $V = 250$  km/sec at  $R = 50$  kpc to  $V = 210$  km/sec at  $R = 70$  kpc. Detailed velocity mapping at 21-cm, beyond the optical image for some of the galaxies, will be critical in answering this question.

The correlation of the maximum rotational velocity with the radius of the galaxy has been discussed by Tully and

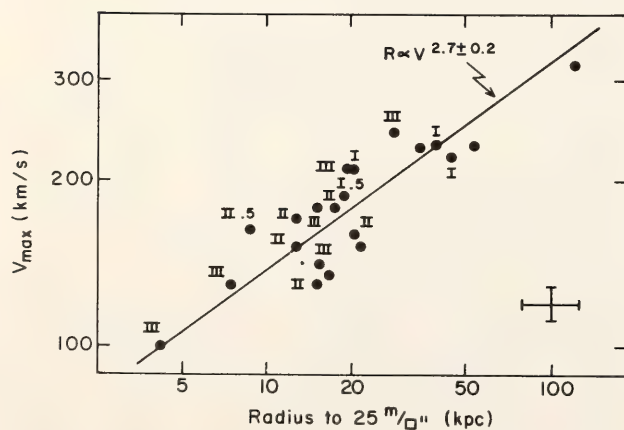


Fig. 68. The maximum rotational velocity as a function of radius for 21 Sc galaxies. The line is the mean of the two least-squares regression lines. Galaxies of high luminosity (class I) tend to have higher  $V_{\max}$  and larger  $R$ .

Fisher (1977) and shown to be linear on a  $\log V_{\max}$ ,  $\log R$  plot. In Fig. 68 we plot the relation of  $V_{\max}$  to  $R$  for the 21 Sc galaxies. An intuitive understanding of this relation can be had in terms of the individual rotation curves and their superposition. Given a continuously rising rotation curve, small galaxies have low velocities because they do not extend into the domain where velocities become high, and also because the scatter about the mean curve is correlated with radius. Within the range shown in Fig. 67, large galaxies tend to have the highest velocities. If all Sc galaxies shared parts of a common rising rotation curve with no scatter (i.e., small galaxies just the initial rising part, larger galaxies a more extended portion), there would be a one-to-one relation between  $V_{\max}$  and  $R$ ;  $V_{\max}$  would be specified as soon as  $R$  was given. From Fig. 67, it is clear that a mean curve would be continuously rising, and would approximate a straight line on a  $\log V_{\max}$ ,  $\log R$  plot. Thus for Sc galaxies, at all except the very highest luminosities, the correlation of  $V_{\max}$  with  $R$  (and its form) is a consequence of the small scatter about a mean rotation curve which is almost a straight line in



the  $\log V_{\max}$ ,  $\log R$  plane. Note that at the very highest luminosities, this linearity breaks down, for  $V$  is constant as  $R$  increases at very large  $R$ .

(4) There are significant correlations between the rotational velocity of a galaxy and some of its physical parameters, such as mass and luminosity. These relations are easily understood in terms of the mean rotational properties. For any galaxy, the integral mass out to its farthest observed point  $R_f$ , is given by  $M \propto V^2 R_f$ . Because of the relation between  $V$  and  $R$  discussed above, the mass is thus correlated with  $V$  and with  $R$ . But there is also a fairly strict relation between radius and luminosity for galaxies. Small galaxies are of low luminosity, large galaxies are of high luminosity. Thus correlations with  $R$  are equally correlations with optical luminosity. The details of these relations will be discussed elsewhere. We mention only a few here.

For all the Sc galaxies that we have observed, magnitudes are available from the literature. Although many are of low accuracy, there is still a strict relation between  $V_{\max}$  and blue optical luminosity ( $L \propto V_{\max}^{4.6 \pm 0.5}$ ;  $r = 0.83$ ), radius and luminosity ( $L \propto R^{1.74 \pm 0.09}$ ;  $r = 0.96$ ), and mass and luminosity ( $L \propto M^{1.04 \pm 0.08}$ ;  $r = 0.92$ ). Of particular interest is the ratio of total dynamical mass out to the edge of the optical galaxy,  $M$ , to the total blue luminosity of the galaxy  $L$ . For 20 Sc's (we lack a suitable magnitude for UGC 2885), this ratio is not a function of galaxy mass for a range of 100 in mass, and is given by  $M/L = 3.8 \pm 0.3$ , where mass and luminosity are expressed in solar units. Thus, for every "unit" of solar luminosity there are four "units" of solar mass comprising these galaxies. These are average values integrated across the entire galaxy. We know that the mass of a galaxy is decreasing slowly as a function of radius while the luminosity is decreasing rapidly. Thus, the local values of mass-to-luminosity are increasing with increas-

ing radius; the stellar mix near the nucleus has lower mass per unit luminosity than the mix at large  $R$ . It is therefore curious that, integrated over an entire galaxy, the value is the same for small galaxies as for large. This requires that small galaxies vary their stellar properties over very small distance scales, if they are to mimic the large galaxies in their integrated properties. Alternatively, the stellar populations may be entirely different, suggesting a different evolutionary history. We will have to await luminosity profiles for both the large and the small Sc's before we can clarify these questions.

(5) The detailed morphology of a galaxy is probably related to its size. To illustrate this, another view of the relation between  $V_{\max}$ , galaxy radius, and luminosity is shown by a plot of  $V_{\max}$  against Hubble type, Fig. 69. The high-luminosity galaxies we studied earlier are shown as squares; they illustrate clearly the decrease in  $V_{\max}$  with later Hubble types. The range in  $V_{\max}$  for our present sample is shown by the vertical spread at Sc.

Most of the galaxies that we have observed have morphological luminosity classifications from the revised Shapley-Ames catalogue in preparation by Sandage and Tammann. This luminosity classification, introduced by van den Bergh (1960), assigns to each spiral an estimate of its intrinsic luminosity (I the highest, III the lowest here), based solely on an established correlation between prominence of the spiral structure and the observed intrinsic luminosity. Because the morphological luminosity classification does not require a knowledge of the distance to the galaxy, it can serve as a distance indicator by identifying galaxies of high luminosity just from their appearance. We show in Fig. 69 the assigned luminosity class for each galaxy. In Table 12, we present the mean properties of the Sc galaxies as a function of assigned luminosity class. From our sample we conclude that the morphological

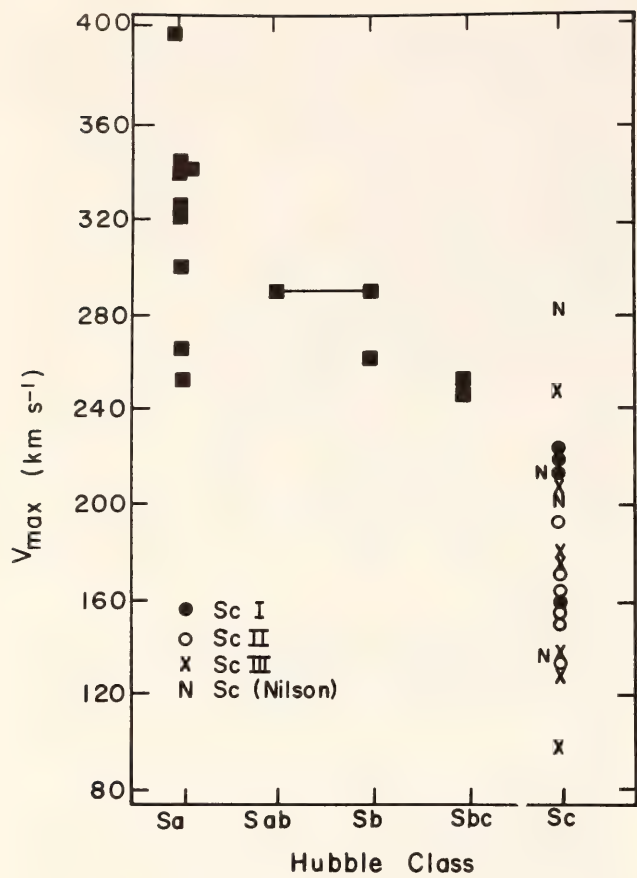


Fig. 69. The maximum rotational velocity as a function of Hubble class for 9 Sa galaxies, 4 Sab-Sbc high-luminosity galaxies, and 21 Sc galaxies of all luminosities. For the Sc galaxy the correlation between  $V_{\max}$  and luminosity class is apparent.

luminosity classification has been able to identify Sc I galaxies, those Sc spirals of highest luminosity. However, it has generally failed to separate those of lower luminosities into subclasses. Even this limited success, however, is of value for statistical studies.

Reasons for even this moderate success of the van den Bergh luminosity

scheme can be drawn from the dynamics of the Sc galaxies, which relates their morphology to their sizes. In effect, the van den Bergh luminosity criteria attempt to tell, from the appearance of the galaxy, whether it is intrinsically large or small (i.e., of high or low luminosity). So the question naturally arises, "What are the morphological differences between large and small Sc galaxies?" From our sample we note that, in general, the small low-luminosity Sc's have ill-defined tightly wound spiral arms; the large high-luminosity Sc's have better-defined, often more open arms. This morphology is consistent with the observed mean rotation curve for Sc's. In the inner rising portion, the gradient of  $V/R$  is large and there is a large differential rotation (a shear). Thus, small galaxies (and the inner parts of large ones) have undergone many differential rotations which will distort and wind up the spiral structure. In the outer, almost flat portion of the rotation curve,  $V/R$  changes only slowly with  $R$ , and the differential effect is slight. The outer parts of large galaxies undergo fewer and smaller differential rotations. Thus the persistence of spiral structure is less of a problem for the larger Sc's. A simple gravitational model may account for the moderate success of the van den Bergh luminosity classification by relating the morphology to the linear size and the form of the rotation curve. It is not yet apparent how a more complicated theory of spiral structure (such as the density-wave theory) relates to these results.

TABLE 12. Properties of Sc Galaxies Arranged by Morphological Luminosity Class

Luminosity Class	Number	$\langle V_{\max} \rangle$ (km/sec)	$\langle \text{Radius} \rangle$ (kpc)	$\langle \text{Luminosity} \rangle$ ( $10^{11} L_{\odot}$ )	$\langle \text{Absolute Magnitude} \rangle$	$\langle \text{Mass} \rangle$ ( $10^{11} M_{\odot}$ )	$f M/L$
I	4	$209 \pm 6$	$31 \pm 7$	$1.0 \pm 0.3$	$-21.9 \pm 0.3$	$3.3 \pm 0.8$	$3.2 \pm 0.2$
II	6	$157 \pm 6$	$14 \pm 2$	$0.21 \pm 0.03$	$-20.2 \pm 0.2$	$0.84 \pm 0.1$	$4.4 \pm 0.8$
III	6	$167 \pm 22$	$15 \pm 4$	$0.39 \pm 0.15$	$-20.4 \pm 0.6$	$1.4 \pm 0.6$	$3.7 \pm 0.6$
III*	4	$137 \pm 16$	$11 \pm 3$	$0.18 \pm 0.09$	$-19.7 \pm 0.6$	$0.56 \pm 0.2$	$3.8 \pm 0.9$

\* Luminosity Class III with two III: galaxies omitted.



Throughout this program, we have exploited the relation between linear radius and luminosity, and picked for study galaxies with a wide range of radii. We show in Table 13 the correlation between linear radius and other physical parameters. As predicted, the correlation is good. Unfortunately, a linear dimension can be determined from an angular dimension only after a distance is assumed. Hence, diameter is not an independent distance criterion and thus is of less interest than morphological luminosity criteria, which are distance independent. However, it should be worthwhile to devise statistical techniques to increase the usefulness of linear sizes as a tool for probing the universe.

(6) Extremely large galaxies can play a role in our understanding of the universe. From a survey of all galaxies with known velocities (published and unpublished), we have identified UGC 2885 as having the largest linear dimensions, with  $R = 122$  kpc. We had originally observed this galaxy in connection with a 21-cm observing program at the 300-ft NRAO transit telescope (Thonnard *et al.*, 1978). With a location near the galactic plane ( $b = 14^\circ$ ), it served as a filler in our observing program when the Milky Way was overhead. The enormity of the galaxy can be appreciated by noting that it is twice as large as any of the galaxies observed in our high-luminosity (i.e., large-galaxy) sample. In fact, we have found no other spirals with  $R > 75$  kpc. While they undoubtedly exist, spiral galaxies of this size are so rare that larger radial velocity surveys will be necessary to identify them. For UGC 2885, the rotation period is  $2 \times 10^9$  years at  $R = 122$  kpc. These outer regions have undergone fewer than 10 revolutions since the origin of the universe. (This number is independent of the choice of  $H$ , for both the age of the universe and the linear diameter of the galaxy scale inversely with the Hubble constant.) The arms are smooth and well developed, and there are no large-scale velocity irregularities.

Large-scale regularity coupled with so few revolutions puts an important constraint on models of galaxy formation and evolution.

We are expanding the observations of these galaxies by obtaining integrated 21-cm hydrogen observations, resolved 21-cm observations, and direct plates for luminosity profiles. We have also started observations of a set of Sa galaxies with a wide range of luminosities. Very preliminary results for these galaxies are also included in Fig. 69, where we have plotted  $V_{\max}$  values for nine Sa galaxies. Our ultimate aim is to observe a sample of galaxies (perhaps 100) of all Hubble types and all luminosities, specify their dynamical properties, and relate these properties to the past galactic history. We are now well on the way.

#### Acknowledgements

We thank Dr. D. Burstein and Dr. P. J. E. Peebles for valuable conversations. We also thank the Directors of Cerro Tololo Inter-American Observatory, Lowell Observatory, Kitt Peak National Observatory, and National Radio Astronomy Observatory, for making observing time available.

#### References

- van den Bergh, S., A preliminary luminosity classification of late-type galaxies, *Astrophys. J.*, **131**, 215, 1960.
- Bosma, A., The distribution and kinematics of neutral hydrogen in spiral galaxies of various morphological types, Ph.D. dissertation, Rijksuniversiteit te Groningen, Netherlands, 1978.
- Burstein, D., and N. Krumm, The gaseous disk of the SO NGC 4203, *Carnegie Inst. Wash. Year Book* **78**, pp. 373–376, 1979.
- Dressel, L. L., and J. J. Condon, The Arecibo 2380 MHz survey of bright galaxies, *Astrophys. J. Suppl.*, **36**, 1978.

TABLE 13. Properties of Sc Galaxies, Arranged by Linear Radius

Radius (kpc)	⟨Radius⟩	Number	⟨Luminosity⟩ Class	⟨V <sub>max</sub> ⟩ (km/sec)	⟨Luminosity⟩ (10 <sup>11</sup> L <sub>⊙</sub> )	⟨Absolute Magnitude⟩	⟨Mass⟩ (10 <sup>11</sup> M <sub>⊙</sub> )	∫M/L
28-122	54 ± 14	6	I.7 ± 0.7	230 ± 12	1.2 ± 0.2	-22.2 ± 0.2	7.4 ± 3.0	4.0 ± 0.5
15-21	18 ± 1	10	II.3 ± 0.3	168 ± 9	0.39 ± 0.05	-20.9 ± 0.2	1.2 ± 0.2	3.3 ± 0.9
4-13	9 ± 2	5	II.5 ± 0.2	143 ± 13	0.11 ± 0.03	-19.4 ± 0.4	0.49 ± 0.13	9.6 ± 0.8



- Einasto, J., A. Kaasik, and E. Saar, Dynamic evidence on massive coronas of galaxies, *Nature*, 250, 309, 1974.
- Gallagher, J. S., and J. P. Ostriker, A note on mass loss during collisions between galaxies and the formation of giant systems, *Astron. J.*, 77, 288, 1972.
- Hubble, E., Extra-galactic nebulae, *Astrophys. J.*, 64, 321, 1926.
- Krumm, N., and E. E. Salpeter, Neutral hydrogen distribution and velocity structure of some early-type galaxies, *Astrophys. J.*, 228, 64, 1979.
- Ostriker, J. P., On the dynamical evolution of galaxies in clusters, in *The Evolution of Galaxies and Stellar Populations*, pp. 369–393, B. M. Tinsley and R. B. Larson, eds., Yale University Observatory, 1977.
- Ostriker, J. P., P. J. E. Peebles, and A. Yahil, The size and mass of galaxies, and the mass of the universe, *Astrophys. J. Lett.*, 193, L1, 1974.
- Roberts, M. S., The rotation curves of Galaxies, in *Proceedings of IAU Symp. #69, Dynamics of Stellar Systems*, pp. 331–340, A. Hayli, ed., Dordrecht, Reidel, 1975.
- Rubin, V. C., Extended optical rotation curves of spiral galaxies, *Comments on Astrophys.*, VIII, 79, 1979.
- Rubin, V. C., W. K. Ford, Jr., and N. Thonnard, Rotational properties of spiral galaxies as a function of Hubble type, *Carnegie Inst. Wash. Year Book* 77, pp. 428–440, 1978a.
- Rubin, V. C., W. K. Ford, Jr., and N. Thonnard, Extended rotation curves of high-luminosity spiral galaxies. IV. Systematic dynamical properties, *Sa*→*Sc*, *Astrophys. J. Lett.*, 225, L107, 1978b.
- Salpeter, E. E., Rotation curves in the outer parts of galaxies from HI observations, in *Proceedings of IAU Symp. #77, Structure and Properties of Nearby Galaxies*, pp. 23–26, E. M. Berkhuysen and R. Wielebinski, eds., Dordrecht, Reidel, 1978.
- Sandage, A., and G. Tammann, Revised

Shapley-Ames Catalogue, in preparation.

Thonnard, N., V. C. Rubin, W. K. Ford, Jr., and M. S. Roberts, Radial velocities of spiral galaxies determined from 21-cm neutral hydrogen observations, *Astron. J.*, 83, 1564, 1978.

Tully, R. B., and J. R. Fisher, A new method of determining distances to galaxies, *Astron. Astrophys.*, 54, 661, 1977.

### THE GASEOUS DISK OF THE S0 GALAXY NGC 4203

David Burstein and Nathan Krumm\*

Until recently, almost all elliptical and S0 galaxies with detected 21-cm emission from neutral hydrogen gas have differed from those without detectable hydrogen by being physically peculiar: i.e., having an optical outer ring tidally interacting with another galaxy, or having obvious optical evidence of ongoing star formation. However, a few S0's and ellipticals emit detectable neutral hydrogen (HI gas) but are optically indistinguishable from HI-undetected E's and S0's. The number of these "ordinary" HI-detected E's and S0's is currently about 10, compared to about 60 "peculiar" HI-detected E's and S0's and about 250 HI-undetected galaxies.

Knowledge of the spatial distribution of neutral hydrogen gas in these few "ordinary" E's and S0's is not only important in understanding the difference between HI-detected and HI-undetected E's and S0's, but it could also substantially contribute to our understanding of how and why most E's and S0's keep themselves relatively clean of neutral hydrogen gas. One of the "ordinary" HI-detected ellipticals, NGC 4278, has been mapped in HI by Knapp *et al.* (1978), who find that the gas is in a "thickened" disk, with combined rotation and ran-

\* Lick Observatory, University of California, Santa Cruz, California.

dom velocities of 235 km/sec. The rotational velocities of the HI gas in NGC 4278 imply a mass of about  $2 \times 10^{11} M_{\odot}$  and a mass-to-light ratio of about 17 at a radius of 22 kpc ( $H_0 = 50 \text{ km sec}^{-1} \text{ Mpc}^{-1}$ ) for the galaxy. For comparison, the mean mass-to-light ratio for Sc galaxies is about 4 and mass is about  $2 \times 10^{11} M_{\odot}$  at radii of 20 kpc (Rubin, Ford, and Thonnard, this Report).

We have recently mapped the "ordinary" S0 galaxy NGC 4203 in neutral hydrogen using the 305-meter radio telescope at Arecibo. NGC 4203 is an S0 with no optical peculiarities (Burstein, 1979a) or evidence of ongoing star formation. A total of 55 positions around this galaxy were observed over a seven-day period, using a flat feed with no appreciable sidelobes and a half-power beamwidth of



Fig. 70. A map of the HI distribution in and around NGC 4203; 55 individual spectra arranged in position on the sky. Description given in text.



4'. Integration times were generally 3 or 5 minutes and observations were spaced on the sky in intervals of 2' in declination and 1.7' in right ascension. A map composed of these individual spectra is shown in Fig. 70; the spectra are arranged, to scale, in position on the sky. The optical diameter of the galaxy at a surface brightness of 27th mag/sec<sup>2</sup> (B magnitude) is 4.2' (Burstein, 1979a), and this diameter is roughly outlined in Fig. 70 by a thick black line between the spectra. Relevant optical and HI data along with derived physical parameters are given in Table 14. Some of the major results from these observations follow.

(1) The HI velocity dispersions perpendicular to the plane of the optical disk in NGC 4203 can be estimated from the narrow profiles in the off-axis spectra to be 20–30 km/sec. This velocity dispersion is about a factor of 10 lower than that in ellipticals (e.g., Faber and Jackson, 1976) and about twice that in spirals (e.g., Emerson, 1976). Thus, the HI in NGC 4203 is distributed in a disk sim-

ilar to, but perhaps thicker than, the HI disks in spirals.

(2) The HI rotation curve N–S has  $\Delta V_{\text{obs}} = 140$  km/sec and is flat, within the errors, to the limits of observation. Nevertheless, this rotation curve is consistent with both a cutoff in the mass distribution at  $r \geq 30$  kpc or no cutoff in mass for  $r \geq 40$  kpc. This ambiguity results from the fact that the Keplerian falloff in rotational velocity is about 15 km/sec in  $\Delta V_{\text{obs}}$  between 30 and 40 kpc for a mass with radius 30 kpc, which is within the errors of observation. Rubin and Ford have obtained an optical rotation curve for NGC 4203 that is consistent with the HI curve. Although the optical  $\Delta V_{\text{obs}} \approx 160$  km/sec, the optical curve only extends to  $r = 20''$ , well within the resolution of 4' of the radio observations.

(3) The total mass and mass-to-light ratios in NGC 4203 and 4278 are similar at a radius of 20 kpc (compare above and Table 14). It is worth noting that both galaxies are placed in the same

TABLE 14. Observational Data, NGC 4203

<i>Optical Data</i>	
$(H_0 = 50 \text{ km sec}^{-1} \text{ Mpc}^{-1})$	
$V_0 = 1075 \pm 15 \text{ km/sec}$ (V. Rubin, private communication).	
Distance = 19 Mpc (from group velocity, de Vaucouleurs, 1975).	
$r_{27}$ (radius at $B = 27\text{th mag arc sec}^{-2}$ ) = 2.1' = 12 kpc (Burstein, 1979a).	
Position angle = 8.4° (Burstein, 1979a).	
$a/b = 1.10$ .	
Disk-to-Bulge ratio = 2.0 (Burstein, 1979b).	
$\Delta V_{\text{obs}} = 160 \text{ km/sec}$ at $r = 20''$ (V. Rubin, private communication).	
<i>Radio Data</i>	
$V_0 = 1093 \text{ km/sec}$ .	
P.A. of radio disk $\approx 30^\circ$ .	
Major axis, $a = 6'$ to $8' = 34\text{--}45 \text{ kpc}$ .	
Minor axis, $b = 5'$ to $7' = 28\text{--}40 \text{ kpc}$ .	
$\Delta V_{\text{obs}} = 100 \text{ km/sec}$ , measured at peak.	
$\Delta V_{\text{corr}}$ (corrected to the plane of the galaxy) $\geq 240 \text{ km/sec}$ ( $i \leq 25^\circ$ ).	
Average gas density = $1.1 \times 10^{20} \text{ cm}^{-2}$ .	
Estimates from radio map.	
<i>Global Data Best Estimate</i>	
At a radius of $r = 40 \text{ kpc}$ , $M = 7 \times 10^{11} M_\odot$ and $M/L = 41$ .	
At a radius of $r = 20 \text{ kpc}$ , $M = 3.5 \times 10^{11} M_\odot$ and $M/L = 20$ .	

group by de Vaucouleurs (1975), although they are separated on the sky by about  $5^\circ \approx 1.8$  Mpc at the distance of the group.

(4) While the HI map of NGC 4203 shows a distribution of gas and a rotation curve similar to that of a spiral, the average gas column density in NGC 4203 is  $n_H = 1.1 \times 10^{20} \text{ cm}^{-2}$ , which is about a factor of 10 lower than in our Galaxy (Heiles, 1976).

(5) The much larger spatial extent of the HI gas than that of the stars in NGC 4203 is compelling evidence of the presence of an unseen mass component containing most ( $\geq 80\%$ ) of the total mass of the galaxy and having a different radial mass density distribution than the optical component in the galaxy. Thus, NGC 4203 is similar to those spirals that have flat extended HI gas rotation curves (e.g., Bosma, 1978) in having a dynamically determined mass several times larger than the mass inferred from the luminous stars in the galaxy.

Not only is the column density of the gas in the disk of NGC 4203 low compared to that in a spiral, but the increased velocity dispersion perpendicular to the plane in NGC 4203 implies a thicker disk than in a spiral. Thus, the local gas density in NGC 4203 must be at least a factor of 10 less than in a spiral and may explain why there is no ongoing star formation in this disk: The gas is not dense enough to initiate star formation.

The lack of any large galaxy near NGC 4203 (there are none of comparable size within  $1^\circ = 300$  Kpc), combined with the existence of extended HI disks in both NGC 4203 and in NGC 4278, suggests that these gaseous disks were not captured by these galaxies via three-body interactions, but that these disks have been associated with these galaxies since the galaxies were formed. More detailed radio observations of the disks in NGC 4203 and NGC 4278, along with searches for HI disks in other "ordinary" E's and S0's, should provide critical ob-

servational data for current theories on how galaxies in general are formed.

### References

- Bosma, A., The distribution and kinematics of neutral hydrogen in spiral galaxies of various morphological types, Ph.D. thesis, Univ. of Groningen, Netherlands, 1978.
- Burstein, D., Structure and origin of S0 galaxies: I. Surface photometry of S0 galaxies, *Astrophys. J.*, in press, 1979a.
- Burstein, D., Structure and origin of S0 galaxies: II. Disk-to-bulge ratios for S0's, *Astrophys. J.*, in press, 1979b.
- de Vaucouleurs, G., Nearby groups of galaxies, in *Galaxies and the Universe*, A. Sandage, M. Sandage, and J. Kristian, eds., Univ. of Chicago Press, 1975.
- Emerson, D. T., High resolution observations of neutral hydrogen in M31: II. The velocity field, *Mon. Notic. Roy. Astron. Soc.*, 176, 321, 1976.
- Faber, S. M., and R. E. Jackson, Velocity dispersions and mass-to-light ratios for elliptical galaxies, *Astrophys. J.*, 204, 668, 1976.
- Heiles, C., An almost complete survey of 21-cm-line radiation for  $|b| \geq 10^\circ$ . III. The interdependence of HI, galaxy counts, reddening and galactic latitude, *Astrophys. J.*, 204, 379, 1976.
- Knapp, G. R., F. J. Kerr, and B. A. Williams, HI observations of elliptical galaxies, *Astrophys. J.*, 222, 800, 1978.

### B — V COLOR PROFILES OF LUMINOUS ELLIPTICAL GALAXIES

J. S. Gallagher,\* S. M. Faber,† and D. Burstein

The most luminous kind of galaxy among all the "normal" extragalactic systems are called cD galaxies. The cD

\* University of Illinois, Urbana, Illinois.

† Lick Observatory, University of California, Santa Cruz, California.



galaxies are giant spheroidal systems, like elliptical galaxies. They are usually found in well-populated ("rich") clusters of galaxies, and in the part of a cluster where the space density of galaxies is highest (e.g., Oemler, 1974). They are generally distinguished from other spheroidal galaxies by their enormous outer envelopes (some with radii greater than 1 Mpc; Oemler, 1976) of low surface brightness. Both the location in space and the structure of cD's have led to speculations that cD galaxies were formed as a result of dynamical interactions between galaxy members of a cluster.

The various theories for the formation of cD galaxies can be divided into three categories: (1) cD's are the result of the outright merger of the most massive cluster members, which are hypothesized to have fallen to the center of the cluster as the result of dynamical friction among cluster members (e.g., Ostriker and Tremaine, 1975; Gunn and Tinsley, 1976); (2) cD's are originally massive galaxies, sitting in the bottom of the gravitational potential well in the center of the cluster, and have accumulated an extended envelope by capturing stars which are tidally-stripped from the outer regions of other cluster members (e.g., Gallagher and Ostriker, 1972); and (3) cD's are simply the high-luminosity members of a normal luminosity distribution function for ordinary elliptical galaxies.

The predominant type of galaxies populating regions of space where the mass distribution of galaxies appears to be densest are elliptical and S0 galaxies, suggesting one possible way to distinguish among these theories. Several detailed studies have shown that the average stellar population of an elliptical or an S0 not only varies with the absolute luminosity of the galaxy (e.g., Visvanathan and Sandage, 1977), but also varies within a galaxy (e.g., Faber, 1977). The stellar population gradients are such that the more-luminous ellipticals have stars that are more metal rich than the less-

luminous ellipticals, and the stars occupying the inner part of an elliptical are more metal rich than those in the outer parts.

Since the different theories for formation of cD galaxies predict rather different origins for their extended envelopes, these theories would also appear to predict different stellar population gradients within these envelopes. If the cD's are formed from mergers of the most massive cluster members, radial mixing of stars is likely (White, 1978), which should make cD's have *flatter* population gradients than ordinary ellipticals. If cD's gain their outer envelopes by accumulating the tidal debris from other cluster members, one should expect their outer envelopes to have a stellar population significantly less metal rich than the metal-rich center of the original massive central galaxy. Thus, cD's formed by tidal accumulation of stars would have *steeper* stellar population gradients than ordinary ellipticals. Finally, if cD's are simply normal ellipticals of high luminosity, their outer envelopes should have stellar population gradients similar to those of other luminous elliptical galaxies.

The outer parts of all galaxies are at surface brightnesses fainter than that of the night sky, so that obtaining even a low-resolution (about 10 Å resolution) spectrum of the stellar populations in these regions is very time consuming. For example, such a spectrum of a single cD galaxy at a surface brightness of 10% of the night sky took about 10 hours with the 3-meter Shane telescope (Faber *et al.*, 1977). Consequently, very little accurate data is available at present for determining stellar population gradients in the outer regions of galaxies of any type.

A less time-consuming method for examining stellar populations at low surface brightnesses is to use broad-band filters to form stellar-population-sensitive colors (e.g., Strom and Strom, 1978). However, these colors average out most



details in the spectrum of a galaxy; very accurate observations are therefore required to permit useful interpretations.

Here we summarize results from an exploratory attempt to measure accurately the broad-band color profiles of a cD galaxy, NGC 6166, located in the cluster Abell 2199, and two ordinary elliptical galaxies, NGC 4472 and NGC 5846. There are a variety of problems in obtaining accurate photometric measurements at surface brightnesses below that of the night sky, including contamination by faint stars or galaxies, scattered light in the telescope, detector stability, and spatial and temporal variations in the airglow. These and other considerations led to the choice of a telescope-detector system at KPNO and Mt. Lemmon, which combines rapid (1–10 Hz) differential measurements between the object and a carefully chosen sky reference position with a pulse-counting photoelectric photometer and blue ( $B$ ) and yellow ( $V$ ) color filters (avoiding the increase in atmosphere opacity in the ultraviolet). This observing system is more fully described in Gallagher and Hudson (1976).

The color gradients thus measured in these three galaxies follow, corrected for galactic reddening and redshift,  $(B - V)^0$ . The errors are the 1-sigma errors from multiple observations of the same positions.

*NGC 4472.* Six separate positional observations ranging from the center of the galaxy to a radius of 42 kpc.  $(B - V)^0 = 1.02 \pm 0.02$  near the center ( $r \leq 2$  kpc),  $(B - V)^0 = 0.95 \pm 0.03$  outside of the center ( $r \geq 2$  kpc) of the galaxy, but there is no detectable color gradient in the outer regions ( $r$  greater than 20 kpc) within the errors.

*NGC 5846.* Three positional observations from the center to a radius of 13 kpc. No color gradient at all is detected, and  $(B - V)^0 = 1.00 \pm 0.02$  outside the very center of the galaxy, which is not resolved by these observations.

*NGC 6166.* Eight positional observations from the center of the galaxy to a radius of 80 kpc.  $(B - V)^0 = 1.01 \pm 0.02$  near the center of the galaxy, while  $(B - V)^0 = 0.91 \pm 0.03$  for radii 20–80 kpc from the center. A relatively smooth change in color is seen from the center regions to radii at 20 kpc from the center.

The differences in color and color gradients between NGC 4472 and NGC 5846 point out the cosmic scatter: NGC 4472 is about twice as luminous as NGC 5846, but both have about the same color in their outer regions; NGC 4472 has a center-outer region difference in color, while NGC 5846 does not. On the other hand, the cD galaxy NGC 6166 shows both a relatively smooth color gradient of about 0.10 mag in  $(B - V)^0$  from the center to a radius of about 70 kpc, and an outer envelope bluer by about 0.06 mag than the ordinary ellipticals. Observations of five other members of the cluster Abell 2199, in which NGC 6166 is the cD galaxy, also give an average of  $(B - V)^0 = 0.95 \pm 0.03$  for elliptical galaxies about 2.5–6.0 times less luminous than NGC 4472.

Taken at face value, these observations seem most consistent with the tidal stripping process for the origin of the outer envelopes of cD galaxies; the outer envelope of NGC 6166 is bluer (more metal poor) than might be expected from a “normal” elliptical. But in view of the small number of galaxies in this sample and the quoted accuracies, these findings can only be taken as tentative though suggestive.

However, it is not our purpose to try to draw firm conclusions from these data about the formation of cD galaxies; these observations were intended only as an exploratory attempt to see if such lines of investigation could be fruitful. Our results clearly suggest that measurements like these are a promising line of attack for understanding how cD galaxies formed. However they also make it very



clear that data of high quality on many more galaxies must be obtained before an unambiguous conclusion will emerge.

### References

- Faber, S. M., The chemical composition of old stellar populations, in *The Evolution of Galaxies and Stellar Populations*, p. 157, B. M. Tinsley and R. B. Larson, eds., Yale University Press, 1977.
- Faber, S. M., D. Burstein, and A. Dressler, Spectrum of the halo of the cD galaxy in Abell 401, *Astron. J.*, 82, 941, 1977.
- Gallagher, J. S., and H. L. Hudson, Surface photometry of the spiral galaxy IC 2233 and the existence of massive halos, *Astrophys. J.*, 209, 389, 1976.
- Gallagher, J. S., and J. P. Ostriker, A note on mass loss during collisions between galaxies and the formation of giant systems, *Astron. J.*, 77, 288, 1972.
- Gunn, J. E., and B. M. Tinsley, Dynamical friction: the Hubble diagram as a cosmological test, *Astrophys. J.*, 210, 1, 1976.
- Oemler, A., The systematic properties of clusters of galaxies. I. Photometry of 15 clusters, *Astrophys. J.*, 194, 1, 1974.
- Oemler, A., The structure of elliptical cD galaxies, *Astrophys. J.*, 209, 693, 1976.
- Ostriker, J. P., and S. D. Tremaine, Another evolutionary correction to the luminosity of giant galaxies, *Astrophys. J. Lett.*, 202, L113, 1975.
- Strom, K. M., and S. E. Strom, Surface brightness and color distributions of elliptical and S0 galaxies. I. The Coma cluster elliptical galaxies, *Astron. J.*, 83, 73, 1978.
- Visvanathan, N., and A. Sandage, The color-absolute magnitude relation for E and S0 galaxies. I. Calibration and tests for universality using Virgo and eight other nearby clusters, *Astrophys. J.*, 216, 214, 1977.
- White, S. D. M., Simulations of merging galaxies, *Mon. Notic. Roy. Astron. Soc.*, 184, 185, 1978.

### GLOBULAR CLUSTER AGES

Bruce W. Carney

Population II stars offer us an opportunity to study the early chemical and dynamical phases of the Galaxy's history. These stars are found scattered throughout the field and concentrated into globular clusters, and it is in the clusters we find the best opportunities for measuring ages. The main sequence stars in the clusters are unfortunately quite faint, so detailed studies of such types of stars focus on those in the field. The data obtained so far include *UBVRIJHK* photometry, narrow-band spectrophotometry at selected wavelengths in the Paschen continuum, and high-dispersion echelle spectroscopy. Interpretation of such data requires theoretical models, both of stellar atmospheres (calculated using R. Kurucz's atomic line-blanketed program ATLAS) and stellar evolution (specifically, the published isochrones of Ciardullo and Demarque, 1977). Theory involves luminosities, temperatures, and helium and heavy-element mass fractions, whereas observations yield broad-band fluxes, narrow-band fluxes, and line strengths.

The most important parameter is the stellar effective temperature,  $T_{\text{eff}}$ , and this may be determined by comparison of the spectrophotometric fluxes against surface fluxes calculated from the model atmospheres (see Fig. 71). The temperatures of about 90 stars of various metallicities have been determined so far, and a comparison with broad-band colors indicates  $R - I$  and  $V - K$  are composition insensitive while  $B - V$  and  $U - B$  are very composition sensitive (see Peterson and Carney, 1979).

With temperatures known, interpretation of the line strengths can proceed when combined with the model atmospheres and laboratory  $gf$  values (see Peterson and Carney, 1979; Carney, 1979b). The resultant  $[\text{Fe}/\text{H}]$  ( $\equiv \log (\text{Fe}/\text{H})_* - \log (\text{Fe}/\text{H})_\odot$ ) ratios can be used to infer heavy element mass

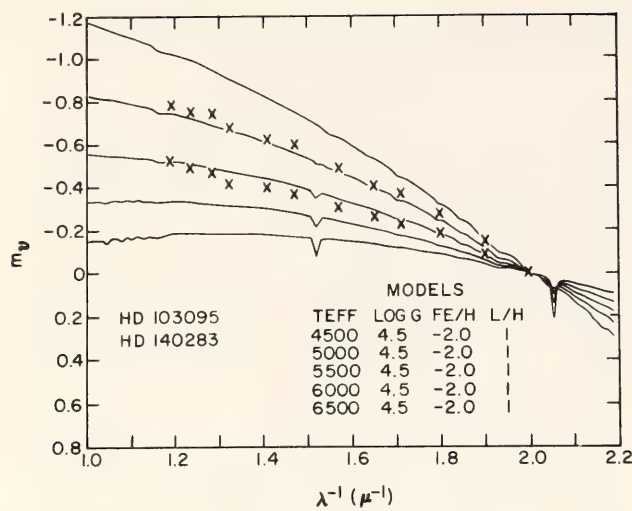


Fig. 71. Comparison of model surface flux distributions (solid lines) and spectrophotometric data for two subdwarfs. The data are monochromatic magnitudes per unit frequency, normalized to that at 5000 Å. Temperatures of about 5000° K and 5600° K are indicated for HD 103095 and HD 140283, respectively.

fractions,  $Z$ , assuming that all the elements—especially carbon, nitrogen, and oxygen—scale with iron. It also turns out that broad-band photometry can also be used to estimate  $[Fe/H]$  (see Fig. 72, taken from Carney, 1979b).

To transform  $V$  magnitudes into luminosities (bolometric magnitudes), the bolometric corrections are required. Integration over the eight broad-band fluxes, aided by the model atmosphere surface fluxes to add the 10–20% of the total flux radiated by the stars shortward of

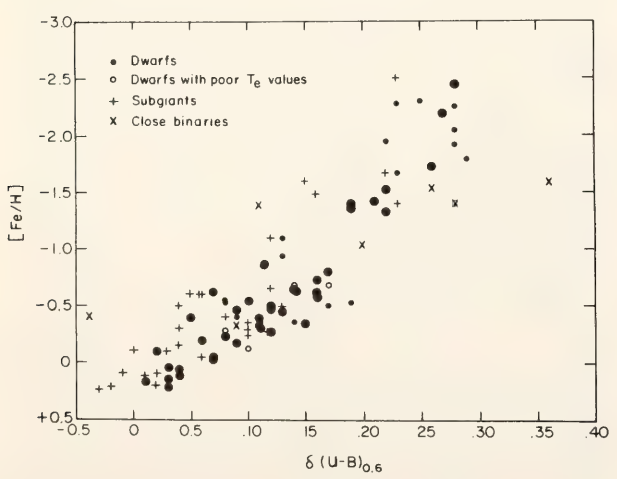


Fig. 72. The logarithmic iron-to-hydrogen abundance relative to the Sun, for dwarf stars against their normalized ultraviolet excess.

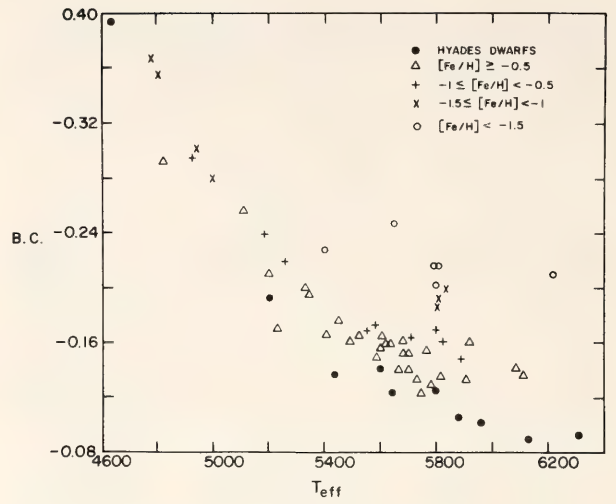


Fig. 73. Subdwarf bolometric corrections ( $B.C. = M_{bol} - M_v$ ) as a function of stellar effective temperature and metallicity.

$U$  and longward of  $K$ , yields the bolometric corrections displayed in Fig. 73 (Carney and Aaronson, 1979).

To derive the helium mass fractions, the  $M_v$  vs. color diagram of the eight subdwarfs with accurate trigonometric parallaxes was transformed to a luminosity-temperature diagram via the above techniques. The main sequence locus in this diagram is sensitive to  $Y$ , the helium mass fraction, such that a change in  $Y$  of 0.1 changes the bolometric magnitudes of the locus by 0<sup>m</sup>.25. Figure 74 shows the comparison of the eight subdwarfs and the isochrones (Carney, 1979c) at a common metallicity.  $Y =$

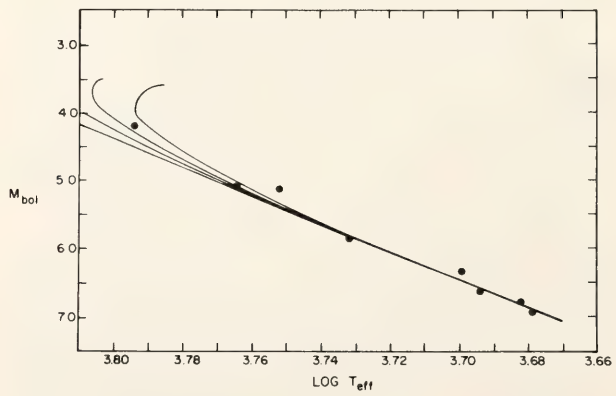


Fig. 74. Comparison of subdwarfs (dots) and model isochrones (lines) in the luminosity-temperature plane. The models have  $Y = 0.20$ ,  $Z = 0.0004$ , and ages of 7, 10, 13, and 16 billion years. If  $Y = 0.3$ , the loci drop by about 0<sup>m</sup>.25 in  $M_{bol}$ .



0.20 is indicated. The zero point of the subdwarf main sequence locus was confirmed by a statistical parallax analysis of 90 field subdwarfs (Carney, 1979c).

The only globular cluster main sequence data available are *UBV* magnitudes and colors. Transformation to luminosities and temperatures is difficult but can be done. Temperatures are derived by using deblanketing vectors, the slopes for which are  $S = \Delta(U-B)/\Delta(B-V)$ , where the changes are with respect to the solar-composition Hyades main sequence. The slopes are derived by comparing metal-poor stars to Hyades dwarfs with equal  $R-I$  and  $V-K$  colors (see Fig. 75; Carney, 1979d).

Before addressing the globular cluster stars, however, we must investigate the assumption that field stars and globular clusters belong to the same population. There are three supporting lines of evidence. First, photometrically, the field

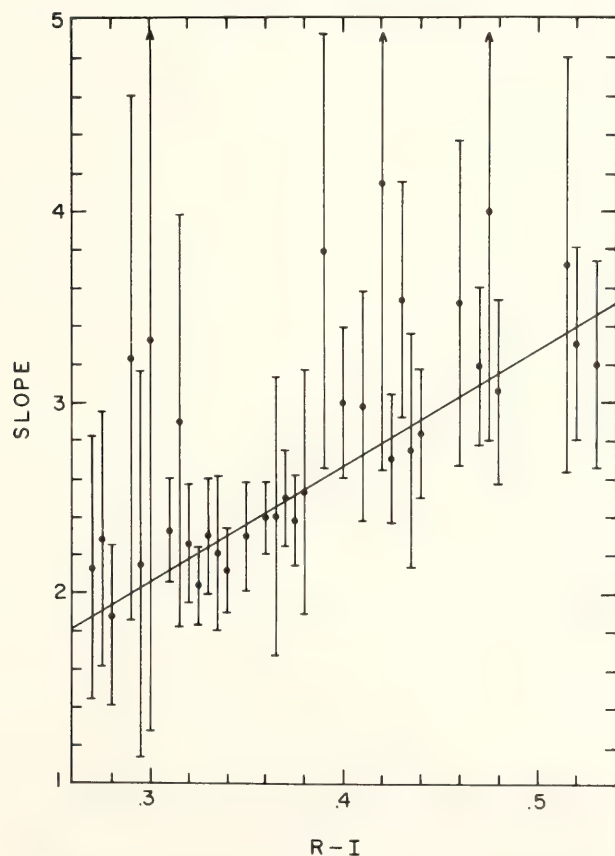


Fig. 75. Deblanketing vector [ $S = \Delta(U-B)/\Delta(B-V)$ ] slope vs. broad-band color  $R-I$  for metal-poor dwarfs. The equation of the line is  $S = 6.08(R-I) + 0.236$ .

subdwarfs and the globular cluster main sequence stars show ultraviolet excesses. Second, there is the chemical evidence, related to the first point, that both sets of stars are metal poor, by amounts up to and exceeding a factor of 100 below the solar level. Finally, there is the kinematic evidence, in that clusters and field subdwarfs are generally of high velocity, and not concentrated to the Galactic plane. In fact, both the position of the solar apex and the speed of the two systems relative to the Local Standard of Rest agree for the average of the globular clusters and the field subdwarfs (Carney, 1979c).

With temperatures derived from deblanketing,  $Z$  from independent  $[\text{Fe}/\text{H}]$  indicators, bolometric corrections from Fig. 73, and  $Y$  assumed to be 0.20, the globular cluster main sequence data were compared to the isochrones to derive distances and ages. Table 15 gives the results, with an example being given in Fig. 76 with the *UBV* data taken from Carney (1979a). Table 15 actually represents the ages derived from these fits to isochrones at an appropriate metallicity and then averaged with results from several other workers (Hartwick and Vanden Berg, 1973; Saio, 1977; Demarque and McClure, 1977), and these ages are plotted against metallicity in Fig. 77. A strong trend is indicated, fit by the expression  $t_9 = -4.9 [\text{Fe}/\text{H}] + 8.0$ , where  $t_9$  is the cluster age in billions of years. This result has important ramifications for Galactic evolution. The oldest clusters' ages also impose some limits to the Hubble constant, suggesting that  $H_0 \lesssim 60$  km/sec/Mpc. The distances derived for the clusters are only weakly related to the isochrones, since the choice of helium abundance was dictated by the parallax analyses. The distances yield a mean visual absolute magnitude for the cluster horizontal branch stars and RR Lyrae variables of about  $+0^m.7$ , with a mild dependence on metallicity (the most metal-poor cluster having the faintest horizontal branches).

TABLE 15. Globular Cluster Ages and Distances

Cluster	[Fe/H]	$t_0$	Distance (kpc)	$M_v(\text{HB/RR})$
47 Tuc	-0.5	10	4.7	0.53
M3	-1.6	18	9.2	0.80
M5	-1.1	14	7.0	0.68
M13	-1.5	17	7.0	0.69
M92	-2.1	19	6.2	1.07
NGC 6752	-1.5	15	4.1	0.56
M71	-0.2	6	...	...
M15	-2.0	17	8.0	0.99

References

Carney, B. W., The MS of the globular cluster NGC 6752, *Astron. J.*, 84, 515, 1979a.

Carney, B. W., Subdwarf ultraviolet excess and metal abundances, *Astrophys. J.*, 233, 211, 1979b.

Carney, B. W., The subdwarf helium abundances and the rotation of the galactic halo, *Astrophys. J.*, 233, 877, 1979c.

Carney, B. W., The ages and distances of eight globular clusters, *Astrophys. J. Suppl.* (March 1980 issue), 1979d.

Carney, B. W., and M. Aaronson, Subdwarf bolometric corrections, *Astron. J.*, 84, 867, 1979.

Ciardullo, R. B., and P. Demarque, Tables of Isochrones, *Trans. Yale Univ. Obs.*, 33, 1977.

Demarque, P., and R. D. McClure, Stellar populations in the disk and halo of the galaxy, in *Evolution of Galaxies and Stellar Populations*, p. 199, B. M. Tinsley and R. B. Larson, eds., Yale Univ. Observatory, 1977.

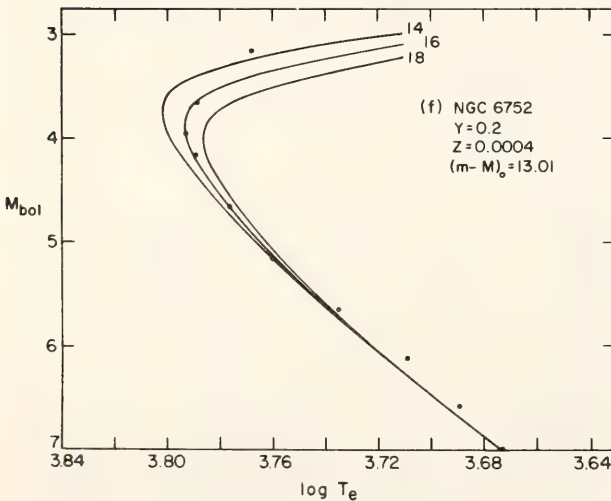


Fig. 76. The mean points of the  $V$  vs.  $B-V$  diagram for NGC 6752, taken from Carney (1979a), transformed to luminosity and temperature (dots) and model isochrones (lines) for  $Y = 0.20$ ,  $Z = 0.0004$ , and ages of 14, 16, and 18 billion years. A distance modulus of 13.01 and an age of about 16 billion years are indicated for the cluster.

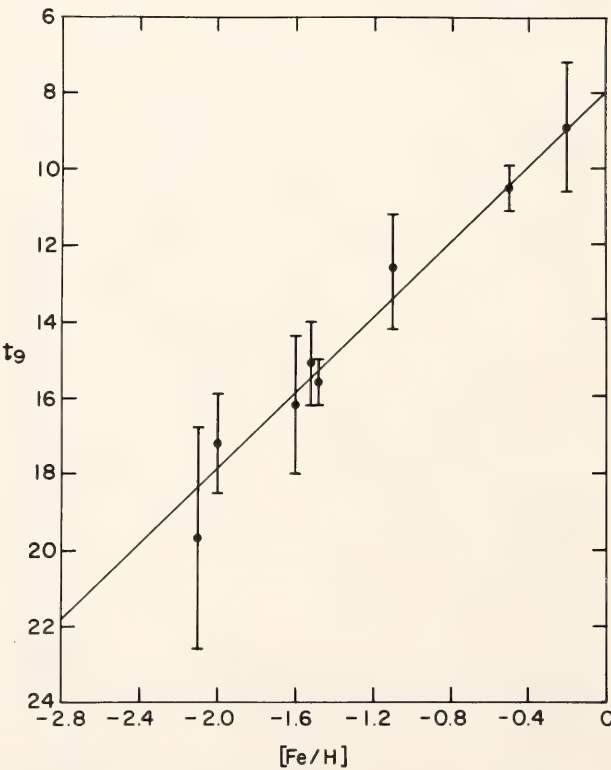


Fig. 77. Globular cluster ages in billions of years,  $t_0$ , vs. cluster metallicity  $[\text{Fe}/\text{H}]$ , with data taken from Table 15 and other work cited in the text. The line is a least-squares fit:  $t_0 = -4.9 [\text{Fe}/\text{H}] + 8.0$ .



Hartwick, F. D. A., and D. A. Vanden Berg, Theoretical isochrones for metal-rich globular clusters, *Astrophys. J.*, 185, 887, 1973.

Peterson, R. C., and B. W. Carney, Abundance analyses of metal-poor stars. II. Yellow spectra of five dwarfs, *Astrophys. J.*, 231, 762, 1979.

Saio, H., Ages of globular clusters, *Astrophys. Space Sci.*, 50, 93, 1977.

### SUPERNOVA REMNANTS IN M31

*K. C. Turner and C. Krishna Kumar\**

Kumar and Turner used the VLA in an attempt to detect radio waves from supernova remnants in M31. A 15 arc min radius field centered on  $\alpha = 0^h 36^m 14^s.5$ ,  $\delta = +40^\circ 33' 55''$  (1980) was observed at 6 cm and 21 cm for about six hours at each wavelength. The 6-cm data was useless because of thunderstorms during the observations. The 21-cm data had an rms noise of 1.6 mJy. The two optically identified SNR's (Kumar, 1976) in the field (BA 415 and 416) were marginally detected at the  $3\text{-}\sigma$  level.

### References

Kumar, C. Krishna, Supernova remnants in M31, *Publ. Astron. Soc. Pacific*, 88, 323, 1976.

### STAR FORMATION AND THE EARLY HISTORY OF THE SOLAR SYSTEM

#### ON THE ROLE OF A SUPERNOVA IN THE FORMATION OF THE SOLAR SYSTEM

*W. Herbst† and R. S. Rajan*

#### I. Introduction

Recently, isotopic anomalies have been observed in a number of elements, including O, Mg, Ne, Ca, and Ba, in high-

temperature inclusions from the carbonaceous meteorite, Allende (e.g. Clayton *et al.*, 1973). The effects are best explained in terms of an addition of a small amount of freshly synthesized material from a supernova to the protosolar nebula (Cameron and Truran, 1977; Schramm, 1978). The discovery of excess  $\text{Mg}^{26}$  and the existence of Al-Mg isochrons in certain Allende inclusions (Lee *et al.*, 1976) demonstrate that  $\text{Al}^{26}$  was present at the time of formation of the inclusions. Clayton (1977a) has advanced a picture wherein the radiogenic  $\text{Mg}^{26}$  is trapped in  $\text{Al}_2\text{O}_3$  dust grains and varying amounts of it are added to different minerals, to explain the isochron data as a mixing line. This model can be ruled out on the basis of petrology, chemistry, and recent measurements of  $\text{Mg}^{26}$  excesses in phases with low Al/Mg ratio such as mellilite; the inclusions are not simple collections of pristine interstellar dust. The possibility that the whole inclusion was condensed from supernova material elsewhere and made its transit to the parent body of Allende can also be ruled out. Since the inclusions have essentially the same cosmic ray exposure age as the rest of the meteorite (i.e., 6 m.y.), an upper limit of 2 m.y. can be deduced for the transit time of inclusions.

The large amount of  $\text{Al}^{26}$  needed to explain the observed excesses cannot be due to solar proton irradiation, since the energy needed to irradiate a substantial portion of the nebula exceeds the binding energy of the Sun. Such irradiation should also produce large anomalies in a number of other elements, which have not been observed. So the most reasonable hypothesis is that  $\text{Al}^{26}$ , which was present at the time of the formation of the inclusions, was added from a nearby supernova.

In this work we analyze four possible relationships between this supernova and the formation of the solar system: (1) the Flypaper Model (Clayton, 1977b), in which an already collapsing protosolar

\* Howard University, Washington, D.C.

† Van Vleck Observatory, Wesleyan University, Connecticut.

cloud catches the ejecta of a chance, nearby supernova; (2) the Bing Bang Model (Reeves, 1978), in which the freshly synthesized matter is attributed to the accumulated ejecta of many supernovae in an OB association; (3) the Compressed Cloud Model (Cameron and Truran, 1977; Schramm, 1978), where a supernova shock compresses a pre-existing cloud causing it to collapse while at the same time injecting the anomalous material; and (4) the Snowplow Model, which we propose, in which the solar system forms within the compressed gas shell swept up by a supernova. The last two models involve supernova-induced star formation, while the first two do not.

## II. Analysis

*A. The Flypaper Model.* We now calculate the probability ( $P$ ) as a function of supernova rate,  $N$  ( $\text{pc}^{-3} \text{yr}^{-1}$ ), that one or more chance supernovae will occur close enough to the already collapsing solar system to contribute a fraction ( $f$ ) of the final solar system's mass ( $M_{ss}$ ). Making the standard assumptions, it turns out that

$$P = N M_{ej}^{3/2} Q/f,$$

where

$$Q \equiv \frac{\pi}{6 M_{ss}^{3/2}} \int_0^{t_{ff}} r_{ss}^3 dt.$$

$r_{ss}$  = the instantaneous radius of the protosolar cloud.

$$t_{ff} = \text{free fall time} = \frac{\pi [r_{ss}(0)]^{3/2}}{8 G M_{ss}}.$$

$M_{ej}$  = mass ejected by supernova (in  $M_{\odot}$ ).

Table 16 lists the results of our calculations of the probabilities for three possible cases for the Flypaper Model. The values of  $N$ ,  $M_{ej}$  and  $f$  used are also given. The reader is referred to Herbst and Rajan (1979) for mathematical details and justification for the chosen

TABLE 16. Parameters for Three Flypaper Models

$M_{ss}$	$r_{ss}(0)$ (pc)	$t_{ff}$ (yrs)	$Q^*$	$P$
1.0	$3.6 \times 10^{-2}$	$1.13 \times 10^5$	1.52	$2.3 \times 10^{-6}$
1.5	$5.4 \times 10^{-2}$	$1.70 \times 10^5$	4.19	$6.0 \times 10^{-6}$
2.0	$7.2 \times 10^{-2}$	$2.26 \times 10^5$	8.61	$1.4 \times 10^{-5}$

\* See text for definition and units.  $N = 4 \times 10^{-13} \text{pc}^{-3} \text{yr}^{-1}$ .  $M_{ej} = 10 M_{\odot}$ .  $f = 0.004$ . See Herbst and Rajan (1979) for justification of these values.

values of  $N$ ,  $M_{ej}$  and  $f$  as well as other assumptions involved. We find values of  $P$  ranging between  $2.3 \times 10^{-6}$  and  $1.4 \times 10^{-5}$  (see Table 16). The Flypaper Model is, therefore, very unattractive, even allowing that our estimates for  $N$  and  $f$  may be off by one or two orders of magnitude.

*B. The Bing Bang Model.* We have implicitly assumed in Section IIA that the ambient level of  $\text{Al}^{26}$  in the protosolar cloud (i.e., prior to injection of "last-minute" ejecta) is negligible. This is certainly true on the average for the Galaxy (e.g., Reeves, 1972). However, since star-forming regions occupy a small volume of the Galaxy and supernovae are probably also concentrated in these regions, it is quite possible that the ambient level of freshly synthesized matter in a typical star-forming region is higher than the galactic average. Reeves (1978) has argued in this vein, and suggested that if the Sun formed in a region like Orion OB1 there would be sufficient freshly synthesized matter available to explain the isotopic anomalies whether or not a supernova triggered the solar system's formation.

It is by no means certain that the Sun did form in a region like the Orion nebula. Locating the places of formation of low-mass ( $1 M_{\odot}$  or less) stars is difficult observationally, and while it is certainly true that many low-mass stars must be forming in Orion it is impossible to say what percentage forms in OB as-



sociations as opposed to, say, T or R associations. Also, we note that OB associations are a diverse set of objects, and an analysis of the Orion OB1 situation may not have widespread applicability.

Nevertheless, we shall follow Reeves and consider the situation in Orion as it may apply to the solar system. The mass of the Orion complex in the form of gas is about  $4 \times 10^5 M_\odot$  (Kutner *et al.*, 1977). The number of supernovae within the association during the past  $10^7$  years is between 3 and 20 (Blaauw, 1964; Reeves, 1978), implying that the mean time between supernovae is approximately equal to the half-life of  $\text{Al}^{26}$  ( $7.2 \times 10^5$  yrs). The "mixing" time for this matter, measured by the time for the supernova remnant to traverse the association, is of the same order ( $\sim 10^6$  yrs), so it is somewhat meaningful to discuss an ambient level of freshly synthesized matter. An important point to note, however, is that the older subgroups of the Orion association, which supply most of the supernovae, are separated by 40 pc or more from the molecular clouds (see fig. 1 of Reeves, 1978) where the star formation is occurring. Assuming spherical ejection, then only a fraction ( $q$ ) of the total mass ejected by a supernova in Orion will be incident on the star-forming region. Since the ambient level of  $\text{Al}^{26}/\text{Al}^{27}$  will be approximately equal to that ratio in the ejecta ( $\lesssim 2 \times 10^{-3}$ ) diluted by the mass of  $\text{Al}^{27}$  in the Orion complex gas, we can write, using the notation of Section IIA

$$f = \frac{qM_{ej}}{4 \times 10^5}.$$

If we generously choose  $M_{ej} = 10M_\odot$  and  $q = 0.2$ , then

$$f = 5 \times 10^{-6},$$

a value considerably smaller than that inferred from the meteorite data (see Section IIA).

Another consideration in this analysis is that the ejecta may well have trouble penetrating the molecular cloud (Mar-

golis, 1978). This means that the typical value of  $f$  inside the cloud will be even less than that calculated above. If solar-mass stars form deep within these clouds, they are very unlikely to be contaminated with significant amounts of ejecta. However, if solar mass stars form preferentially near the edges of the cloud, then the concentration of ejecta there might be enough to raise  $f$  to the observed level. Of course, one then has the related question of why the stars should form at the edge of the cloud, and one is again very close to the supernova-induced star formation picture discussed in the next two subsections.

*C. The Compressed Cloud Model.* In this model, originally suggested by Cameron and Truran (1977) and Sehramm (1978), the supernova shock compresses the cloud to critical density while injecting the  $\text{Al}^{26}$ ,  $\text{O}^{16}$ , and other elements either as gas or grains. Hydrodynamical models of an HI cloud encountering a shock suggest that star formation is likely to occur (Woodward, 1976).

Consider a spherical, homogeneous cloud of density  $\rho$  ( $\text{cm}^{-3}$ ) and mass  $M_{ss}$  ( $M_\odot$ ), located  $d_{SN}$  (pc) from a supernova which ejects  $M_{ej}$  ( $M_\odot$ ) of freshly synthesized matter. To acquire a fraction  $f$  of the ejecta, one requires that

$$d_{SN} = 1.1 M_{ss}^{-1/6} M_{ej}^{1/2} f^{-1/2} \rho^{-1/3} \text{ pc}.$$

For a  $2M_\odot$  cloud at critical density ( $\rho \approx 2 \times 10^5 \text{ cm}^{-3}$ ), with  $f = 4 \times 10^{-4}$  and  $M_{ej} = 10M_\odot$ , we find  $d_{SN} = 2.5$  pc. This small value reemphasizes the result of Section IIA. *The solar system cannot be at its critical radius for collapse prior to the supernova event and hope to capture a sufficient amount of ejecta.* This problem is avoided when one assigns a *trigger* role to the supernova. In that case we can take a reasonable cloud density of (say)  $\rho = 100 \text{ cm}^{-3}$ , in which case we find  $d_{SN} = 30$  pc for the same values of the other parameters. This is only weakly dependent on  $\rho$  (goes as  $\rho^{-1/3}$ ), is quite representative of the size of old supernova remnants, and equals the radius of

the Canis Major R1 ring (Herbst and Assousa, 1977, 1978). We have neglected dilutions of  $\text{Al}^{26}$  both by radioactive decay and by mixing with ambient interstellar medium (density,  $n \text{ cm}^{-3}$ ) in this analysis, but neither is important until  $d_{SN} > 30 \text{ pc}$  as long as  $n \lesssim 1 \text{ cm}^{-3}$ .

A possible problem with this scenario is whether the supernova ejecta can penetrate and mix with the cloud. Margolis (1978) has pointed out the difficulties with this and suggests that the matter must be injected in the form of grains. Even so, it penetrates the cloud only with difficulty, and Margolis argues that one might even expect an anomaly gradient in the solar system.

*D. The Snowplow Model.* We suggest here an alternative to the Compressed Cloud Model which avoids the penetration problem. In the late stages of its evolution, a supernova remnant enters the "snowplow" phase in which it has pushed up an expanding compressed shell of gas (Chevalier, 1974). The density in this shell may well reach critical density for a  $2 M_{\odot}$  cloud, and the formation of stars may occur (Chevalier and Theys, 1975). Note that there was no preexisting cloud in this scenario. The cloud was both formed and brought to collapse by the supernova, and the ejecta will be within the cloud right from its beginning. All of this occurs on a time scale of the order of  $10^6$  years. In such a picture, the dilution occurs simply by mixing of ejecta with ambient matter and by any applicable radioactive decay. With the same units as before, we find

$$d_{SN} = 2.13 M_{ej}^{1/3} f^{-1/3} n^{-1/3} \text{ pc}.$$

In this case,  $d_{SN}$  represents the distance from the supernova at which the snowplow shell becomes unstable and begins forming stars. If  $M_{ej} = 1 M_{\odot}$ ,  $n = 1 \text{ cm}^{-3}$ , and  $f = 4 \times 10^{-4}$ , then  $d_{SN} = 29 \text{ pc}$ . Again, these are just about the conditions one would expect in Canis Major R1, according to Herbst and Assousa (1977, 1978).

There are observational grounds for

suspecting that both types of supernova-induced star formation are operative in Canis Major R1. The CO map of CMa OB1 (Blitz, 1979) shows a large molecular cloud to the northeast of the ring. The region of intersection between the ring and this cloud has been and probably is continuing to be a region of active star formation, as indicated by the presence of stars in reflection nebulae and CO "hot spots." However, there has also been star-formation activity along a filamentary dust cloud which extends along the emission ring well to the south of the molecular cloud. Among others, Z CMa, the well-known preserved pre-main sequence star, is found here. It is tempting to suggest that this thin, arced dust cloud is the snowplow shell of the CMaR1 supernova, which is now fragmenting into stars.

Recently, another example of star formation in an expanding shell has been discussed by Kutner *et al.* (1979). They find a thin, arced CO cloud associated with the reflection nebulae of Mon R1. This association contains several emission stars and T Tauri stars (Herbst and Warner, 1979) and has evidently been a site of recent star formation. The main difference between this region and CMaR1 is that the radius of the ring is  $\simeq 3.5 \text{ pc}$  in Mon R1. This may be understood as an effect of a higher ambient density in the presupernova region in Mon R1. With  $n \simeq 10^3 \text{ cm}^{-3}$  and  $M_{ej} = 1 M_{\odot}$ , we find that Mon R1 could serve as well as CMaR1 as a present-day example of a star-forming region where  $f \simeq 4 \times 10^{-4}$  probably applies.

### Summary

We have analyzed four possible scenarios relating the "last-minute" supernova inferred from meteorite studies to the formation of the solar system. Of these, the Flypaper Model, in which a chance supernova injects matter into an already collapsing cloud, is by far the least likely. The protosolar cloud has



far too small a cross section once collapse has begun. The ambient level of  $\text{Al}^{26}$ , even in Orion OB1, is also too low to account for the Allende inclusions unless the production of this isotope in supernovae has been greatly underestimated. This statement may not apply to the edges of molecular clouds where the ejecta may tend to accumulate. Two scenarios in which the supernova triggers the solar system's formation have been discussed. In one case, the shock wave causes the collapse of a preexisting cloud; in the other, the solar system is born in the snowplow shell of an old supernova. Each gives plausible values of  $f$  at reasonable distances ( $d_{SN} \sim 30$  pc) from the supernova, and either could be considered an appropriate picture of star formation in Canis Major R1 and for the solar system.

### References

- Blaauw, A., O associations in the solar neighborhood, *Annu. Rev. Astron. Astrophys.*, **2**, 213, 1964.
- Blitz, L., A study of the molecular complexes accompanying Mon OB1, Mon OB2 and CMa OB1, *NASA Technical Report 79708*, 1979.
- Cameron, A. G. W., and J. W. Truran, The supernova trigger for formation of the solar system, *Icarus*, **30**, 447, 1977.
- Chevalier, R. A., The evolution of supernova remnants. I. Spherically symmetric models, *Astrophys. J.*, **188**, 501, 1974.
- Chevalier, R. A., and J. C. Theys, Optically thin radiating shock waves and the formation of density inhomogeneities, *Astrophys. J.*, **195**, 53, 1975.
- Clayton, D. D., Precondensed matter: key to the early solar system, *The Moon and Planets*, **19**, 109, 1977a.
- Clayton, D. D., Solar system isotopic anomalies: supernova neighbor or pre-solar carrier?, *Icarus*, **32**, 255, 1977b.
- Clayton, R. N., L. Grossman, and T. K. Mayedov, A component of primitive nuclear composition in carbonaceous meteorites, *Science*, **182**, 485, 1973.
- Herbst, W., and G. E. Assousa, Observational evidence for supernova-induced star formation: Canis Major R1, *Astrophys. J.*, **217**, 473, 1977.
- Herbst, W., and G. E. Assousa, The role of supernovae in star formation and spiral structure, in *Protostars and Planets*, p. 368, T. Gehrels, ed., Univ. of Arizona Press, Tucson, 1978.
- Herbst, W., and R. S. Rajan, On the role of a supernova in the formation of the solar system, to be submitted to *Icarus*, 1979.
- Herbst, W., and J. Warner, R associations VI: Monoceros R1, to be submitted to *Astronom. J.*, 1979.
- Kutner, M. L., K. D. Tucher, G. Chin, and P. Thaddeus, The molecular complexes in Orion, *Astrophys. J.*, **215**, 521, 1977.
- Kutner, M. L., R. L. Dickman, K. D. Tucker, and D. E. Machnik, Ring structure in the Mon R1 molecular clouds, *Astrophys. J.*, in press, 1979.
- Lee, T., D. Papanastassiou, and G. Wasserburg,  $^{26}\text{Al}$  in the early solar system: fossil or fuel?, *Astrophys. J. Lett.*, **211**, L107, 1976.
- Margolis, S. H., Grain motions in the solar nebula, *The Moon and Planets*, **20**, 49, 1978.
- Reeves, H., Spatial inhomogeneities of nucleosynthesis, *Astron. Astrophys.*, **19**, 215, 1972.
- Reeves, H., The big bang theory of the origin of the solar system, in *Protostars and Planets*, p. 399, T. Gehrels, ed., Univ. of Arizona Press, Tucson, 1978.
- Schramm, D. N., Supernovae and the formation of the solar system, in *Protostars and Planets*, p. 384, T. Gehrels, ed., Univ. of Arizona Press, Tucson, 1978.
- Woodward, P. R., Shock-driven implosion of interstellar gas clouds and star formation, *Astrophys. J.*, **207**, 484, 1976.

# THE VERTICAL DISTRIBUTION OF YOUNG GALACTIC OBJECTS

*F. J. Lockman\**

Modern radioastronomical observations have shown that new stars are formed in relatively dense, discrete, predominantly molecular clouds of interstellar gas. Yet star formation is not occurring in all molecular clouds; a variety of arguments indicates that clouds remain stable for long periods until some mechanism, either internal or external, causes some of them to collapse, fragment, and produce a group of new stars (e.g., Kwan, 1979).

Most processes suggested as triggers of cloud collapse involve raising the external pressure on the cloud, usually by hitting it with something. Three such mechanisms are (1) collision with another cloud, (2) compression of the cloud by a shock from an exploding star (i.e., by the remnant of a supernova), and (3) compression of the cloud by a large-scale "galactic shock" induced in the low-density gas surrounding the cloud (e.g., Loren, 1976; Herbst and Assousa, 1977; Woodward, 1978). There are no theoretical objections to any of these mechanisms, and some may even have been observed in isolated instances. But it is not clear which, if any, are responsible for the large-scale pattern of star formation characteristic of our own and nearby spiral galaxies. Indeed, there is no *a priori* requirement that an external factor act on a cloud; collapse could be a natural part of every cloud's internal evolution.

Because we can never follow any single cloud for a meaningful fraction of its lifetime, it is useful instead to study the statistical properties of clouds and the spatial relationships between clouds and other objects, like young stars, throughout the Galaxy. Table 17 gives the vertical distribution, or the "thick-

TABLE 17. The Vertical Distribution of Young Objects\*

HI	Mol. clouds	Dense HII regions	Supernova remnants
120	50	30	70

\* Values: thickness ( $\sigma$  pc).

ness," of the layers of various young objects in the inner  $100^\circ$  of the Milky Way. (This is the only part of the Galaxy for which we have reliable information on the distribution of young objects, and it includes most sites of current star formation.) Besides molecular clouds, values are given for HI, dense HII regions, and supernova remnants. HI is diffuse, atomic hydrogen that is the reservoir from which molecular clouds are probably formed and into which stars pour mass at the end of their evolution. Dense HII regions are objects that result from the formation of a new, massive star in a molecular cloud; these mark sites of current star formation. Supernova remnants are the final stages in the evolution of massive stars. All of these objects lie about the plane of the Milky Way in a vertical distribution that is close to a Gaussian function; Table 17 gives the dispersion,  $\sigma$ , of the appropriate Gaussian (from Baker and Burton, 1975; Burton and Gordon, 1978; Lockman, 1977, 1979).

The data in Table 17 place rather strong constraints on the mechanism that causes collapse of molecular clouds. Note that the youngest stars (marked by the dense HII regions) are found in the thinnest layer. If a process entirely internal to a molecular cloud causes its collapse into stars, we would expect new stars to be distributed like the molecular clouds, i.e., with a  $\sigma$  of 50 pc. This is not the case, so apparently an external factor is needed to trigger cloud collapse. If the external factor is provided by shocks from supernova remnants, then young stars should have a vertical distribution

\* National Radio Astronomy Observatory, Charlottesville, Virginia.



that is the product of the SNR and the cloud distributions; this would give  $\sigma = 40$  pc for HII regions. Likewise, for star formation induced by cloud-cloud collisions we expect HII regions to have  $\sigma = 35$  pc. Neither of these dispersions is as small as the observed 30-pc dispersion of dense HII regions. In particular, the SNR-cloud interaction gives a dispersion that is much too large, so even though this mechanism might be an important local phenomenon, it is unlikely to be the major cause of star formation in the inner Galaxy.

Little is known about the vertical structure of large-scale galactic shocks, but the shocks are thought to be induced in the HI ( $\sigma = 120$  pc) by old stars ( $\sigma > 100$  pc). Both of these species have a large dispersion, so unless the strength of the galactic shock is strongly dependent on the HI density, it seems unlikely that this mechanism could produce a very narrow layer of HII regions.

These conclusions follow from the assumption of Gaussian vertical distributions for all species, and from the assumption that all species are vertically homogeneous (i.e., that the properties of molecular clouds and supernova remnants do not change with distance from the galactic plane). While both these assumptions appear to be approximately correct, further investigation is needed before more quantitative conclusions can be reached.

In summary, star formation initiated by cloud-cloud collisions comes closer to explaining the vertical distribution of HII regions than other mechanisms do. SNR-cloud interactions and large-scale galactic shocks seem less able to produce the observed narrow layer of HII regions.

### References

- Baker, P. L., and W. B. Burton, Investigation of low-latitude hydrogen emission in terms of a two-component interstellar gas model, *Astrophys. J.*, 198, 281, 1975.
- Burton, W. B., and M. A. Gordon, Carbon Monoxide in the Galaxy: III. The overall nature of its distribution in the equatorial plane, *Astron. Astrophys.*, 63, 7, 1978.
- Herbst, W., and G. E. Assousa, Observational evidence for supernova-induced star formation: CMa R1, *Astrophys. J.*, 217, 473, 1977.
- Kwan, J., The mass spectrum of interstellar clouds, *Astrophys. J.*, 229, 567, 1979.
- Lockman, F. J., Location of population I-type objects with respect to the galactic plane, *Astron. J.*, 82, 408, 1977.
- Lockman, F. J., The distribution of dense HII regions in the inner Galaxy, *Astrophys. J.*, in press, 1979.
- Loren, R. B., Colliding clouds and star formation in NGC 1333, *Astrophys. J.*, 209, 466, 1976.
- Woodward, P. R., Theoretical models of star formation, *Annu. Rev. Astron. Astrophys.*, 16, 555, 1978.

### NUMERICAL CALCULATIONS RELEVANT TO THE ACCUMULATION OF THE TERRESTRIAL PLANETS

George W. Wetherill

#### Introduction

In the past several years, there has been increasing interest in understanding the relationships between the larger and smaller bodies of the solar system and what they reveal about one another. This approach is often referred to as "comparative planetology." A result of this is that the initial state of these bodies, in other words, knowledge of the origin of the solar system, is coming to occupy a more central place in the thinking of the working scientist. Unfortunately, we are far from an adequate understanding of these initial conditions; there is much work that must be done on these problems if this situation is to be improved.

For the most part, theories of the origin

of the solar system have attempted to describe a single mechanism responsible for the formation of at least the major and terrestrial planets. Once past the initial stages, which are more properly part of the problem of star formation, these mechanisms fall into two general categories: (1) those in which planets form as a result of massive gravitational instabilities leading to large gaseous protoplanets (e.g., Kuiper, 1951; McCrea, 1960; Cameron, 1978), and (2) those in which gravitational instability plays only a minor role, if any, and the planets grow by the continuing sweeping up of smaller bodies by larger ones (e.g., Chamberlin, 1904; Safronov, 1969; Weidenschilling, 1974, 1976; Hayashi *et al.*, 1977; Greenberg *et al.*, 1978; Cox, 1978). Progress toward the goal of understanding solar system formation will require us to roll up our sleeves and make detailed quantitative studies of each of the stages of planetary growth described in these theories. It seems quite possible that this will show that fundamentally different processes were involved in the formation of the major and terrestrial planets.

Insufficient detailed work of this kind has been carried out. Insofar as it has, most attention has been given to a quantitative treatment of the gravitational accumulation of planets as a result of mutual collisions of planetesimals in the 1–1000 km range, principally assuming gas-free accumulation. Gas-free accumulation is not an attractive way to form the major planets. However, the volatile-poor composition of the terrestrial planets together with the difficulty of obtaining planet-sized gravitational instabilities at small heliocentric distances, has led a number of workers to explore more thoroughly the possibility that at least these planets formed by the sweeping-up process under conditions in which gas drag was not important.

Major contributions to the solution of this limited problem have been provided by the work of Safronov and his co-workers (Safronov, 1969; Zvyagina *et al.*,

1973; Safronov, 1978). These investigators applied the stellar dynamical techniques of Chandrasekhar (1942) to the problem of the dynamical evolution of a growing swarm of planetesimals, in which relative velocities increase by mutual gravitational perturbations and decrease by dissipative collisions and the averaging of velocities accompanying the cohesive collisions responsible for planetary growth. Subject to certain assumptions, these workers calculated that such a swarm can achieve quasi-steady states for both the velocity and the size distribution of the planetesimals.

The result for the velocity distribution is particularly significant. Most other workers have introduced the relative velocity of the planetesimals as a free parameter. If the relative velocity is too high—e.g., several times the gravitational escape velocity of the growing planet—fragmentation rather than accumulation will be dominant, and planets won't grow. On the other hand, if relative velocities are too low, the system of planetesimals will be in nearly circular concentric orbits and the collisions required for growth will not take place. Building upon earlier work of Gurevich and Lebedinskii (1950), Safronov (1962) showed that it was not necessary to avoid this problem by ad hoc introduction of a suitable relative velocity. Rather, he showed that for plausible assumptions regarding dissipation of energy in collisions and size distribution of the bodies, the mutual gravitational perturbations of the bodies caused their mean relative velocity to be only somewhat less than the escape velocity of the larger bodies. Thus, throughout the entire course of planetary growth, from 1-km planetesimals to Earth-sized planets, the system regulated itself in such a way that the larger bodies could always grow, whereas smaller objects would fragment, establishing a spectrum of sizes in the smaller planetesimal mass range.

Despite this success, as well as other important achievements, this theoretical



work has its limitations, and even its major conclusions have been questioned (Greenberg *et al.*, 1978; Levin, 1978).

One of these limitations results from the fact that the dynamical theory of Chandrasekhar, upon which Safronov's work is based, does not explicitly consider the planetesimals to be constrained to move in heliocentric Keplerian orbits. Instead, the swarm is treated in a way analogous to molecules in the kinetic theory of gases. Safronov introduced the effects of Keplerian motion by an ingenious analogy with Prandtl's semi-empirical theory of turbulence in a rotating viscous fluid. In this analogy, the shearing forces resulting from the differential circular velocities of bodies at different heliocentric distances gives rise to a partition between turbulent random motion and organized circular motion. More recently, Kaula (1980) has used Chandrasekhar's work in a somewhat different way but still in the "kinetic theory of gases" framework.

In the present work, numerical calculations are reported which explicitly involve Keplerian motion. These address two problems relevant to terrestrial planet accumulation.

(1) The orbital evolution in a gas-free medium of a swarm of equal-sized non-accreting bodies subject to mutual gravitational perturbations and collisional damping. This calculation, although far from being a simulation of real terrestrial planet formation, includes the essential physical basis of the Safronov steady state velocity distribution and permits a comparison of analytical theory with numerical calculations.

(2) The three-dimensional accumulation of a swarm of large bodies, taking into account mutual gravitational perturbations, collisional damping, and cohesion (accretion). This is a three-dimensional version of a similar problem investigated in two dimensions by Cox (1978). Cox's work, involving more precise dynamical procedures than those of the present work, led to the result that

unless initial velocities were chosen to be somewhat implausibly large, the swarm evolved into a system of  $\sim 8$ –10 small terrestrial planets rather than into the observed situation of two large bodies and two smaller bodies. In the present work, the two-dimensional results of Cox are reproduced and extended to the three-dimensional case.

### *Steady State Velocity Distribution of a Nonaccreting Swarm*

One hundred bodies of equal mass are assumed to have their initial semimajor axes distributed at random over the narrow range 0.96–1.04 A.U., and to have random initial eccentricities  $< 0.01$  and initial inclinations  $< 0.01$  radians. Because their eccentricities are not zero, many of these bodies will be in crossing orbits, permitting both collisions and gravitational perturbations by close approaches. The Öpik (1951) collision formula is used to calculate the probability of each pair undergoing a collision or close encounter. Use of the Öpik collision formula introduces the assumption that the arguments of perihelion, longitude of nodes, and position of the body in its orbit are random. The pairs that actually encounter one another during this time step are chosen at random in accordance with these Öpik probabilities. With some modifications, the procedure of Arnold (1965) for calculating orbital changes following a close encounter was adopted. The evolution of the swarm is followed through successive time steps for as long as is desired.

The evolution of the r.m.s. velocity at which a swarm of  $9 \times 10^{24}$  g (830-km-radius) bodies encounter one another is shown in Fig. 78. In three of the four cases shown, the initial r.m.s. relative velocity was very low,  $\sim 0.3$  km/sec (open circles, open and closed squares). As time increases, at first the effects of mutual perturbations dominate over collisions and the r.m.s. velocity of the swarm increases rapidly, approaching a

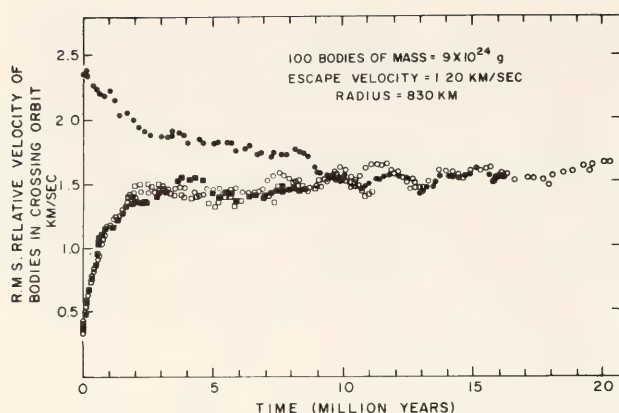


Fig. 78. Approach to the steady state distribution of r.m.s. velocity, averaged over all bodies that can encounter one another. The solid squares, open squares, and open circles represent three calculations starting from initial relative velocities of 0.3 km/sec but with different random number sequences. The solid circles correspond to an initial velocity of 2.4 km/sec. In both cases an approximately constant velocity of 1.55 km/sec is reached after a few million years.

velocity of  $\sim 1.4$  km/sec. At these higher velocities, a steady state is gradually established, wherein the increases in relative velocity caused by close encounter are on the average cancelled by decreases in relative velocity following collisions. On the time scale shown in Fig. 78, this steady state is reached after about four million years.

It is apparent from Fig. 78 that the steady state velocity achieved after about four million years is not absolutely constant but exhibits short period ( $\sim 1$  m.y.) fluctuations as well as a long-range small but monotonic increase in velocity. The short-term effects are associated with stochastic fluctuations resulting from the small number of bodies. Whether or not this effect would have a counterpart in a real solar system swarm evolving in this way depends upon the size distribution of the actual swarm. The long-term trend is a consequence of the swarm never actually reaching a final equilibrium state. Because collisions cause dissipation of energy while conserving angular momentum, the swarm will continue to spread indefinitely. However the time

scale for this effect to cause a significant increase in velocity is comparable to the full accretion times of  $\sim 10^8$  years and will not be of importance in a real solar system.

The approach to the steady state from the high-velocity side is shown by the solid circles in Fig. 78. The initial velocities of about 2.4 km/sec decrease to about 1.5 km/sec on a time scale somewhat longer than that associated with the growth from initial low velocities. This is a consequence of the lower encounter probabilities of a high-velocity swarm. However the fact that the final velocities are very similar, regardless of whether the approach is from the high-velocity or the low-velocity side, demonstrates that there is an equilibrium r.m.s. velocity toward which the swarm evolves.

For bodies of this size, this equilibrium velocity was found to be about 1.55 km/sec, slightly above the 1.20 km/sec escape velocity of the bodies. This steady state velocity is obtained by averaging over all pairs of bodies with orbits which cross one another. Another "r.m.s. velocity" of interest is obtained by averaging the velocities of bodies actually selected to encounter. This quantity approaches a steady state on the same time scale as the r.m.s. velocity plotted on Fig. 78 but is systematically smaller in value because of the increase in encounter probability with decrease in relative velocity. The r.m.s. value of this velocity was found to be  $1.23 \pm 0.5$  km/sec. Safronov (1969) described the velocity of the swarm in a third way, by referring the motion of each body to that of a hypothetical body in a circular reference orbit. The present calculations give an r.m.s. velocity defined in this way of  $0.84 \pm .02$  km/sec. Use of Safronov's equation 7.32, corresponding to a swarm of bodies of equal mass, gives a result of 1.21 km/sec. Thus the numerical and analytical theories are in fair agreement despite the differences in physical modeling introduced by Safronov's hydrodynamical analogue.



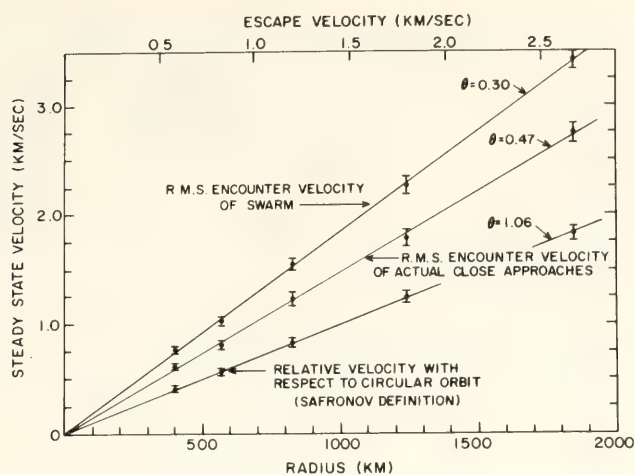


Fig. 79. Variation of steady state velocities as a function of radius (lower scale) and escape velocity (upper scale).

In addition to swarms consisting of  $9 \times 10^{24}$  g bodies, the same calculations were carried out for bodies of  $1 \times 10^{24}$  g,  $3 \times 10^{25}$  g, and  $1 \times 10^{26}$  g. In every case a steady state was achieved in a manner very similar to that shown in Fig. 78 for  $9 \times 10^{24}$  g bodies. The time scales required to reach the steady state remained at  $\sim 5$  m.y.

The calculated steady state velocities for all five assumed masses are shown in Fig. 79. For each of the three "relative velocities" discussed above, the steady state velocity is found to be a linear function of the radius and escape velocities of the body. This can be expressed in terms of the dimensionless Safronov

number  $\theta = \frac{V_e^2}{2\bar{V}^2}$  where  $V_e$  is the escape velocity and  $\bar{V}$  is a measure of the relative velocity of the swarm. For the r.m.s. encounter velocity of the pairs,  $\theta_e = 0.30$ ; for the r.m.s. encounter velocity of the pairs selected,  $\theta_a = 0.47$ ; and for Safronov's relative velocity with respect to the circular orbit,  $\theta_s = 1.06$ . The latter can be compared with Safronov's value of 0.49, when the same assumption is made about the effect of noncentral collisions on the collision cross section.

Within the accuracy of the calculations, the value of  $\theta$  is independent of the mass. This is in agreement with the

analytical theory in which  $\theta$  remains of order unity during the course of accretion.

In a real swarm, the bodies will not all have the same mass. It is planned to evaluate the effect of varying mass in subsequent work. However the essential physics of Safronov's approach is contained in the present idealized problem, and it is plausible to assume its validity will not be greatly affected by the introduction of a different mass distribution.

A typical calculated steady state distribution of eccentricity and inclination is shown in Fig. 80 for a swarm  $9 \times 10^{24}$  g bodies which had initial eccentricities and inclinations confined to the region  $e < .01$ ,  $\sin i < .01$  radians. Both the range and average value of the inclination is found to be about twice that of the eccentricity.

The distribution of the radial distribution of the bodies is shown in Fig. 81 for various elapsed times (time scaled as in Fig. 78). For the case of  $T = 6.74$  m.y. (Fig. 81c) the steady state has been reached, and it is seen that this is accompanied by a spread in the radial distribution of the bodies as well as by the spread in inclination and eccentricity shown in Fig. 80. This result has no counterpart in the analytical theory inasmuch as differences in heliocentric distance were not explicitly introduced in

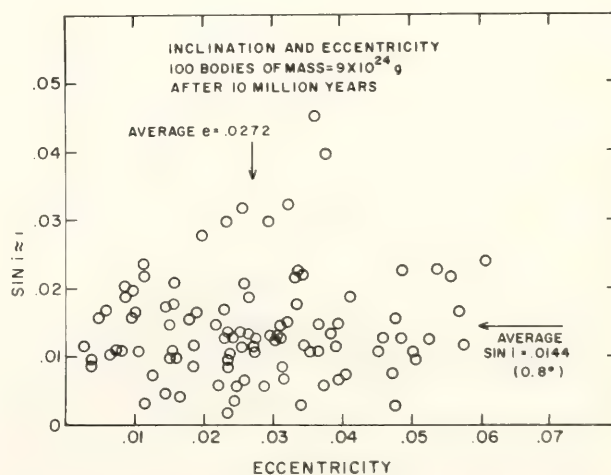


Fig. 80. Typical steady state distribution of eccentricity and inclination.

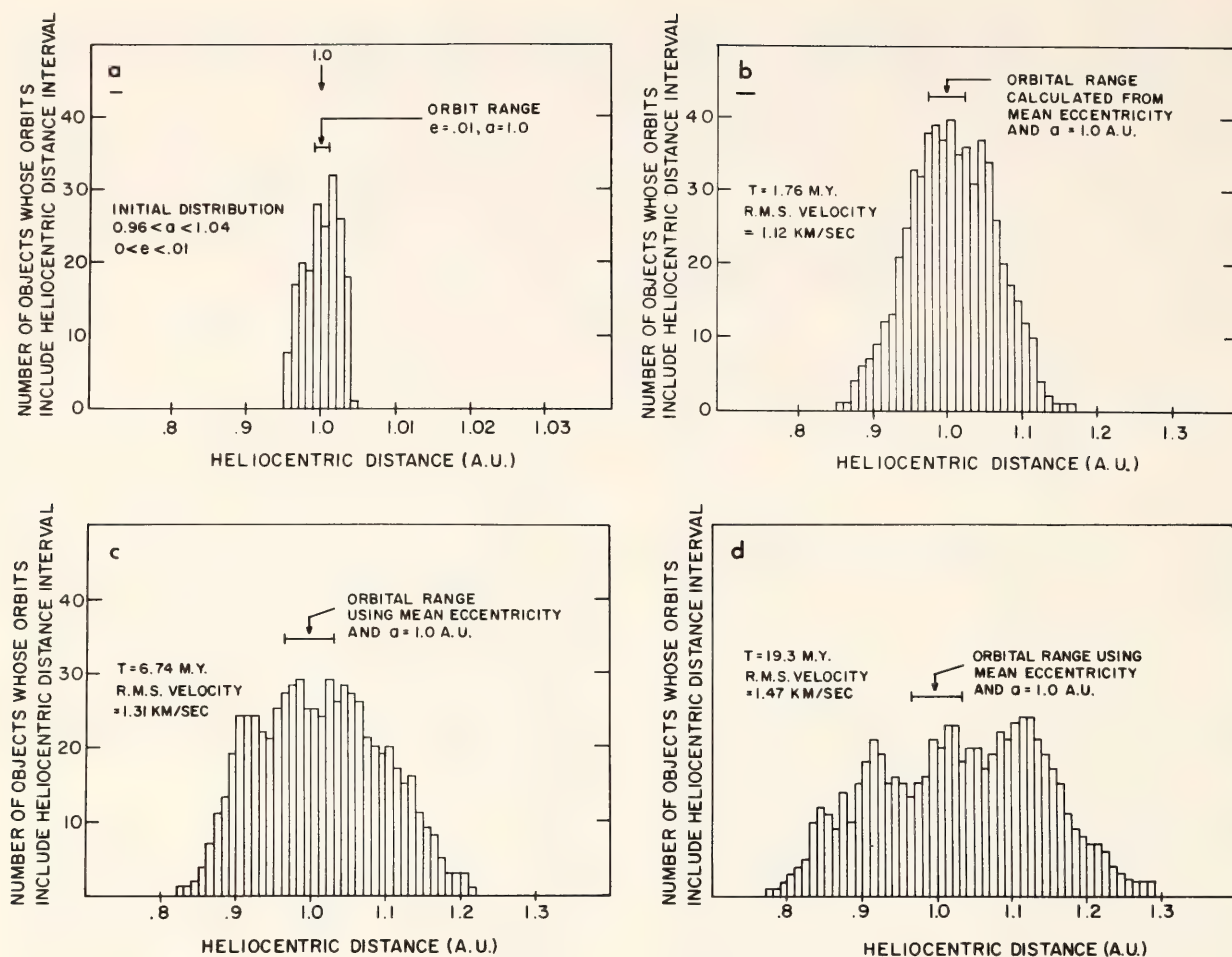


Fig. 81. Increase in radial spread of swarm as a function of time, as a consequence of collisions and gravitational perturbations. (a) Initial state; (b) after 1.8 m.y., approach to steady state; (c) 6.7 m.y., steady state approximately reached; (d) 19.3 m.y., swarm continues to spread even after reaching steady state velocity.

the earlier work. The range of heliocentric distance traversed by the bodies is considerably greater than that which would be inferred simply from the growth in eccentricity of a swarm of bodies with the same initial semimajor axis. This spread in heliocentric distance is relevant to the question of maintaining "orbital linkage" during the course of accretion (Levin, 1978; Wetherill, 1978; Greenberg *et al.*, 1978).

More details of the calculated steady state distribution of velocities are shown in Fig. 82. In analytical treatment of this problem (Chandrasekhar, 1942; Safronov, 1969; Kaula, 1980), it is assumed that the individual velocities of the bodies form a Maxwellian distribution. In Fig. 82, calculated distributions are

compared with Maxwellian distributions fitted to the peak corresponding to the most probable velocity. It may be seen that the calculated distributions resemble Maxwellian distributions but that some excess of high-velocity bodies is found.

### *Three-Dimensional Accumulation of a Swarm of Bodies of Equal Mass*

A second question to be examined is that of the consequences of treating accretion in a two-dimensional approximation. The most accurate numerical calculations involving simultaneous collision, gravitational perturbations, and planetesimal accumulation have been carried out by Cox (1978). The precision of the algorithms employed by Cox lim-



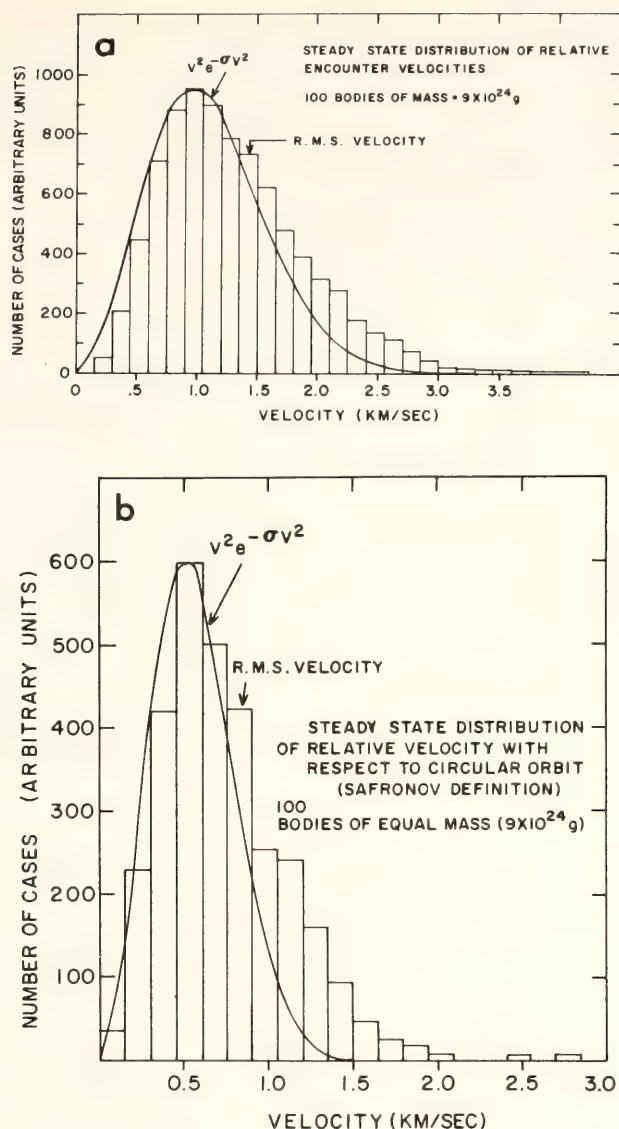


Fig. 82. Distribution of velocities after the steady state is reached. (a) relative velocities of encountering pairs (corresponds to velocities of Fig. 78 and uppermost set of points in Fig. 79). (b) relative velocity of bodies with respect to circular orbit (corresponds to lowermost set of points of Fig. 79).

ited at least his first investigation to a two-dimensional treatment of the problem (Cox *et al.*, 1978). Cox calculated the orbital evolution of a swarm of 100  $1.2 \times 10^{26} g$  bodies initially distributed over the terrestrial planet region. For initial maximum eccentricities  $\leq 0.10$ , it was found that the final state consisted of from 8 to 10 planetary bodies, rather than the four observed terrestrial planets. A result more similar to the present system of planets was found using a maximum initial eccentricity of 0.15. This eccentricity is only slightly higher than

that associated with the steady state value consistent with the Safronov numbers shown in Fig. 79.

However, for a real swarm the eccentricities would certainly be lower, because of two factors decreasing eccentricity and velocity—the prevalence of small bodies as a large fraction of the mass, and the averaging of velocities accompanying accretion. Therefore Cox's result, as discussed elsewhere (Wetherill, 1978; Greenberg *et al.*, 1978), emphasizes the fact that there is serious question as to whether or not a self-contained swarm of this kind can avoid premature orbital isolation of embryos and consequent production of too many small planets. It is also possible, as discussed in these references, that Jupiter perturbations may be important in determining whether or not this premature isolation will occur. If Jupiter is necessary, then this fact has serious implications regarding the time scale for formation of that planet and, when time-scale considerations are introduced, may require that massive gravitational instabilities have developed early in the outer solar system.

Therefore, it was thought worthwhile to investigate the extent to which Cox's result depended on his calculation being two-dimensional.

The problem with treating the accretion in three dimensions is that it is then necessary to forego the more exact numerical procedures used by Cox. This was done in the present work by calculating perturbations following close encounters in the manner developed by Öpik and Arnold, and used in the preceding discussion of the steady state velocity distribution of a nonaccreting swarm.

In order to compare these results with those of Cox, the two-dimensional case was calculated first. The results of the two-dimensional calculations for a random distribution of initial eccentricities ranging up to 0.05 are shown in Fig. 83a. Following Cox (1978), the initial semi-major axes were randomly distributed between 0.5 and 1.5 A.U. in accordance

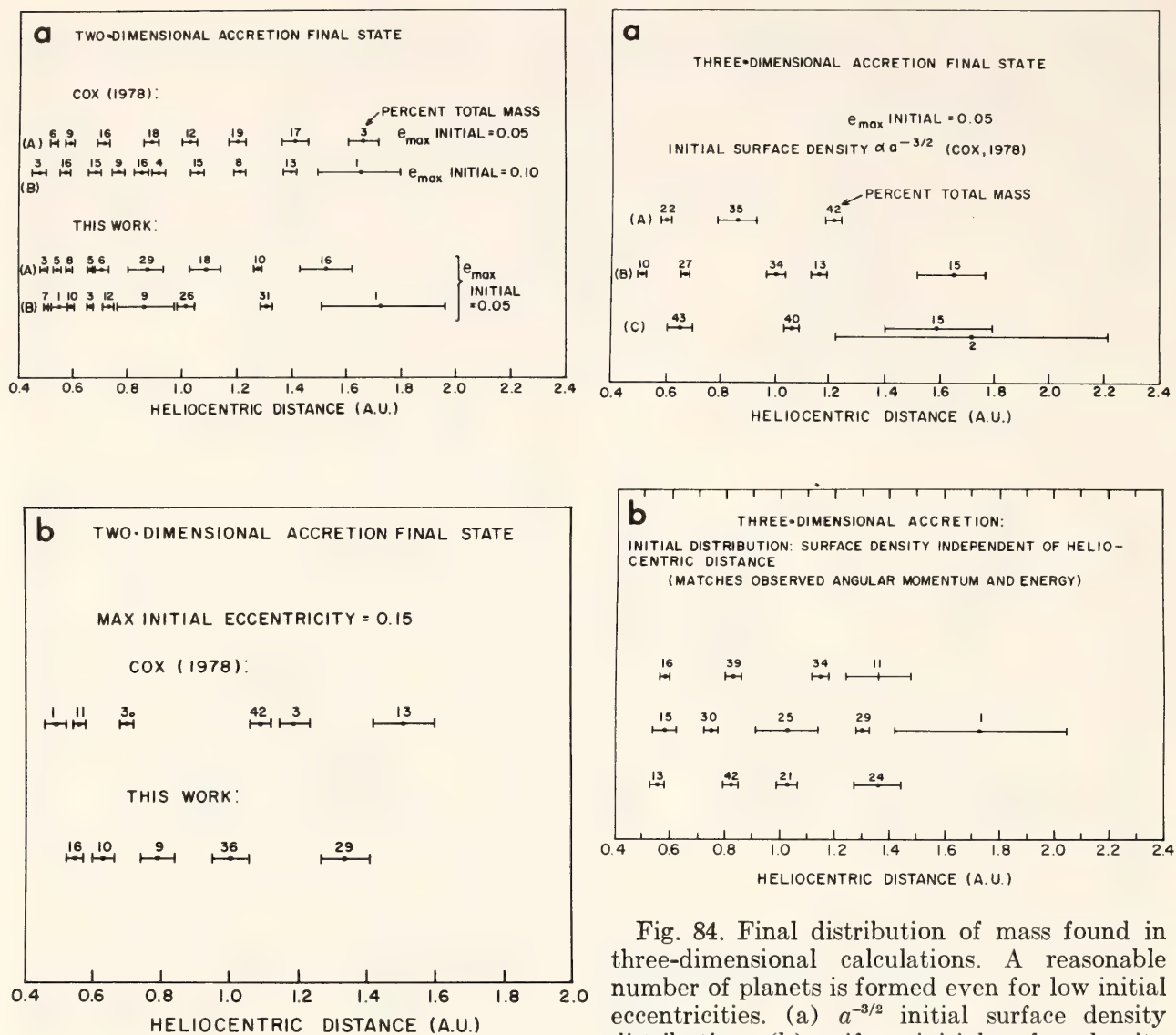


Fig. 83. Final distribution of mass found in two-dimensional calculations. With the possible exception of the highest maximum eccentricity (0.15), an excessive number of planets is formed. (a)  $e_{\max} = 0.05$  and 0.10; (b)  $e_{\max} = 0.15$ .

with a mean  $R^{-3/2}$  dependence of surface density with heliocentric distance. In agreement with Cox's result for  $e_{\max} = 0.05$  and 0.10, in the final state 8–10 bodies remain, and these tend to be concentrated at the smaller heliocentric distances. When the maximum initial eccentricity is increased to 0.15, the final number of bodies decreases to 5–6 (Fig. 83b).

When the same calculation is carried out in three dimensions, again with  $e = 0.05$ , the final number of bodies is reduced to 3–5 (Fig. 84a). This result is not strongly dependent upon the initial

Fig. 84. Final distribution of mass found in three-dimensional calculations. A reasonable number of planets is formed even for low initial eccentricities. (a)  $a^{-3/2}$  initial surface density distribution; (b) uniform initial surface density distribution.

distribution of semimajor axes, as shown by Fig. 84b. The latter results were obtained with an initial semimajor axis distribution having a mean surface density independent of heliocentric distance. As shown earlier (Wetherill, 1978), this agrees more closely with the actual total energy and angular momentum of the present terrestrial planets than does the  $R^{-3/2}$  dependence. The difference between the three-dimensional and two-dimensional result is a consequence of the lesser importance of collisions relative to gravitational perturbations in three dimensions.

This effect is seen in Fig. 85. The initial eccentricities are all low (Fig. 85a). As accumulation proceeds, many of



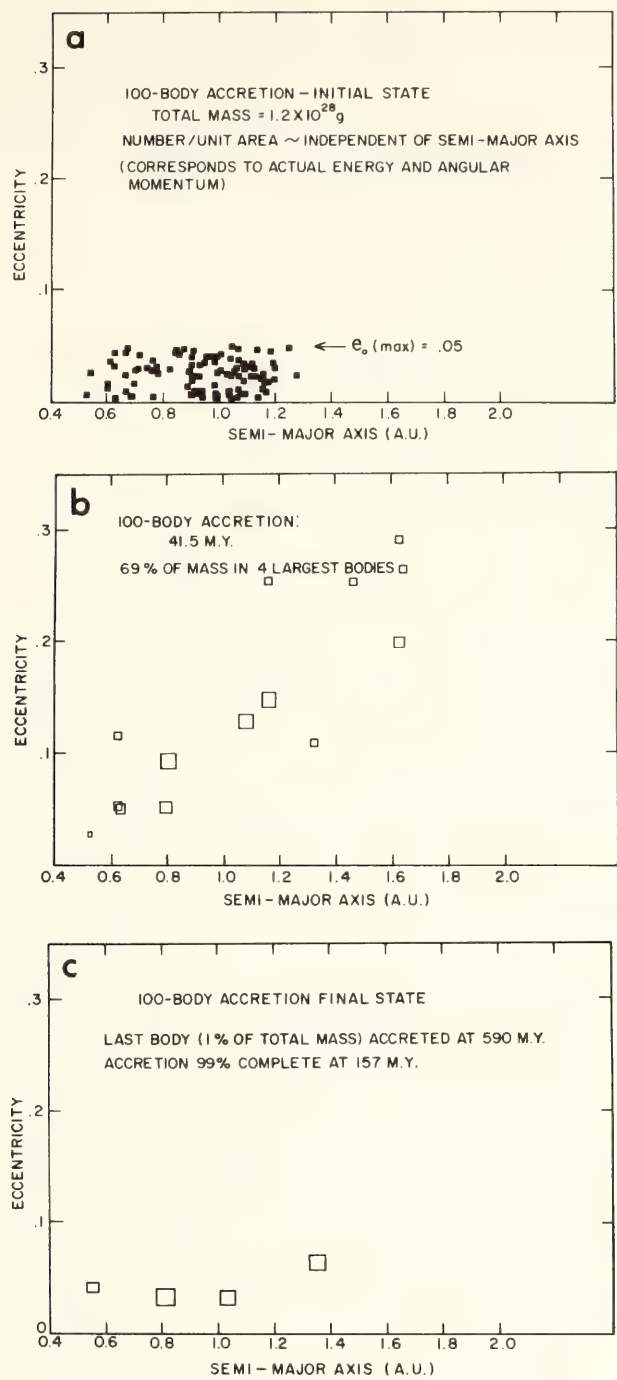


Fig. 85. Evolution of eccentricity and semi-major axis distribution, three-dimensional accumulation. (a) initial state; (b) accretion 69% complete; (c) final state.

the bodies are accelerated to more eccentric orbits and the range of semimajor axes increases (Fig. 85b). In the final state (Fig. 85c), the eccentricities are again low, as a result of the embryos' failing to cross and therefore perturb one another, the averaging of velocities of accumulating planetesimals, and the resulting circularization of the combined

orbits. The time scale for accretion is  $\sim 10^8$  years, as in characteristic of this type of accretion theory (Fig. 86).

This result should not be interpreted as confirmation that a real system of planetesimals will actually accumulate into planets as calculated. The model is still much too simple to be taken as a serious simulation of actual planetary accumulation. The result simply shows that a three-dimensional treatment goes in the direction of permitting accumulation to proceed further prior to the separation of embryos into isolated orbits. One particularly serious defect in the model, which precludes interpretation of these results as actual simulations, is the fact that all the bodies were initially assumed to be quite large,  $1.2 \times 10^{26}$  g. In a real solar system, these large bodies would be accompanied by a larger number of smaller bodies, and the effects of fragmentation would maintain a population of small bodies throughout the course of accumulation.

In comparison with the large bodies, these smaller bodies would be ineffective perturbers, but nevertheless collisions with the large numbers of small bodies would diminish relative velocities and

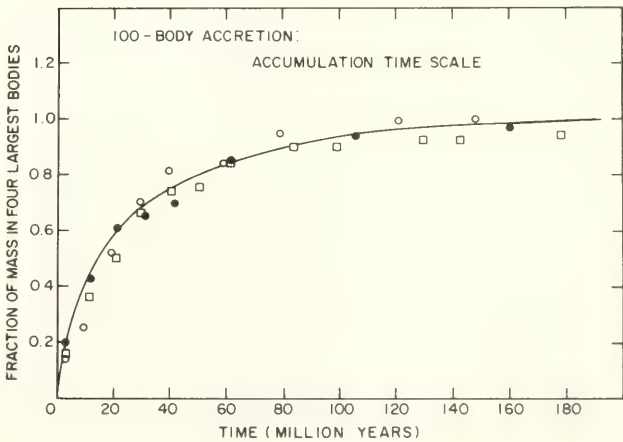


Fig. 86. Accumulation time scale. Open circles, closed circles, squares correspond to separate calculations using different random numbers. Most of the accretion occurs during the first  $\sim 20$  m.y. and is 99% complete after 150 m.y. A last "straggler" may remain for several hundred million years longer, in accordance with earlier work (Wetherill, 1977).

tend to lead to early isolation of planetary embryos. A realistic quantitative calculation of this problem is premature at this time. However, some hint of the magnitude of these effects may be obtained by making the assumption that the primary factor determining the number of isolated embryos is simply the relative importance of gravitational perturbations in comparison with collisional damping. In the numerical calculations it is possible to change artificially the effects of perturbation relative to damping by an arbitrary factor without changing the accretion rate.

The effect of increasing the importance of damping by small factors is shown in Fig. 87. A threefold increase in damping did not change the number of final embryos, whereas a fourfold increase caused the result to tend toward that found in the two-dimensional case, i.e., too many small isolated embryos. Thus, to some extent an increase in damping can be accommodated without prematurely destroying the orbital linkage of the swarm. However it is not clear at this time whether this is sufficient, or whether the introduction of long-range perturbations, possibly involving resonances with the

major planets (Greenberg *et al.*, 1978; Wetherill, 1978), can or need be invoked to form the observed number of terrestrial planets by the gas-free accumulation process.

### References

- Arnold, J. R., The origin of meteorites as small bodies, *Astrophys. J.*, 141, 1536–1556, 1965.
- Cameron, A. G. W., Physics of the primitive solar accretion disk, *The Moon and the Planets*, 18, 5–40, 1978.
- Chamberlin, T. C., Fundamental problems of geology, *Carnegie Inst. Wash. Year Book* 3, 195–258, 1904.
- Chandrasekhar, S., *Principles of Stellar Dynamics*, Univ. of Chicago Press, 1942.
- Cox, L. P., Numerical simulation of the final stages of terrestrial planet formation. Ph. D. thesis, Massachusetts Institute of Technology, 1978.
- Cox, L. P., J. S. Lewis, and M. Lecar, A model for close encounters in the planetary problem, *Icarus*, 34, 415–427, 1978.
- Greenberg, R., J. Wacker, C. R. Chapman, and W. K. Hartmann, Planetesimals to planets: a simulation of collisional evolution, *Icarus*, 35, 1–26, 1978.
- Gurevich, L. E., and A. I. Lebedinskii, Formation of the planets, *Izv. Akad. Nauk USSR, Ser. Fiz.*, 14, 765–799, 1950.
- Hayashi, C., K. Nakazawa, and I. Adachi, Long-term behavior of planetesimals and the formation of the planets, *Publ. Astron. Soc. Jap.*, 29, 163–196, 1977.
- Kaula, W. M., Equilibrium velocities of a planetesimal population, submitted to *Icarus*, 1980.
- Kuiper, G. P., On the origin of the solar system, in *Astrophysics*, Chapter 8, J. A. Hynek, ed., McGraw-Hill, New York, 1951.
- Levin, B. J., Relative velocities of planetesimals and the early accumulation of the planets, *The Moon and Planets*, 19, 289–296, 1978.

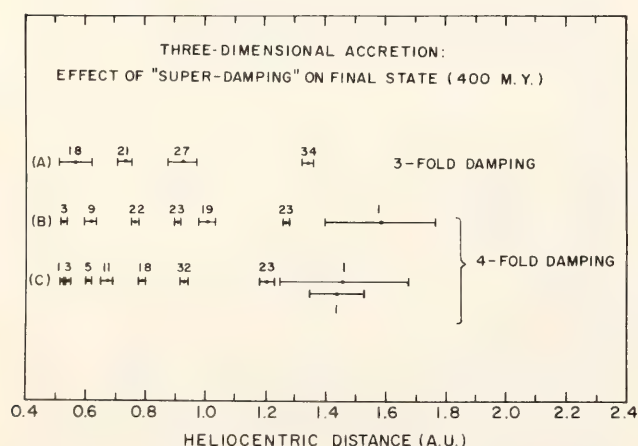


Fig. 87. Final distribution of mass when ratio of collisional damping to close encounters is artificially increased, as a rough simulation of the effect of the presence of smaller bodies in the swarm. When this ratio is increased by a factor of about four, an excessive number of planets is found.



- McCrea, W. H., The origin of the solar system, *Proc. Roy. Soc. London*, 256A, 245–266, 1960.
- Öpik, E. J., Collision probabilities with the planets and the distribution of interplanetary matter, *Proc. Roy. Irish Acad.*, 54A, 165–199, 1951.
- Safronov, V. S., Velocity dispersion in rotating systems of gravitating bodies with inelastic collisions, *Vop. Kosmogonii*, 8, 168–179, 1962.
- Safronov, V. S., *Evolution of the Proto-planetary Cloud and Formation of the Earth and Planets*, Moscow, Nauka; translated for NASA and NSF by Israel Program for Scientific Translations (1972), NASA TT F-677, 1969.
- Safronov, V. S., The heating of the earth during its formation, *Icarus*, 33, 3–12, 1978.
- Weidenschilling, S. J., A model for accretion of the terrestrial planets, *Icarus*, 22, 426–435, 1974.
- Weidenschilling, S. J., Accretion of the terrestrial planets, II, *Icarus*, 27, 161–170, 1976.
- Wetherill, G. W., Evolution of the earth's planetesimal swarm subsequent to the formation of the earth and moon, *Proc. 8th Lunar Sci. Conf.*, 1, 1–16, 1977.
- Wetherill, G. W., Accumulation of the Terrestrial Planets, in *Protostars and Planets*, pp. 565–598, T. Gehrels, ed., University of Arizona Press, Tucson, 1978.
- Zvyagina, Y. V., G. V. Pechernikova, and V. S. Safronov, A qualitative solution of the coagulation equation taking into account the fragmentation of bodies, *Astron. Zh.*, 50, 1261–1273, 1973.

#### IRRADIATION HISTORY OF MOKOIA CARBONACEOUS CHONDRITE

*B. Kothari and R. S. Rajan*

##### *Introduction*

Low energy particle tracks resulting from solar flares and which are indicative of regolithic processes have been seen in

various mineral phases in a number of gas-rich meteorites, including carbonaceous chondrites (e.g., Price *et al.*, 1975). In a stagnant regolith, track gradients are expected to be steep, since track density falls off as  $\text{depth}^{-2}$ . In contrast, in a regolith mixed by micrometeorite bombardment, gradients would be much shallower. The mean location of a grain and the extent of its shielding is indicated by the track density gradient. The distribution of track densities around the crystal surfaces can be related to its tumbling motion while on the surface.

In the present work, we report the results of detailed track measurements in the carbonaceous meteorite, Mokoia, and compare these with published data on C1 and C2 chondrites. Mokoia has been classified as a Vigarano type on the basis of its chemistry and petrography, and it has an oxygen isotopic composition transitional between C2 and C3 (Clayton, 1978).

##### *Experimental Details*

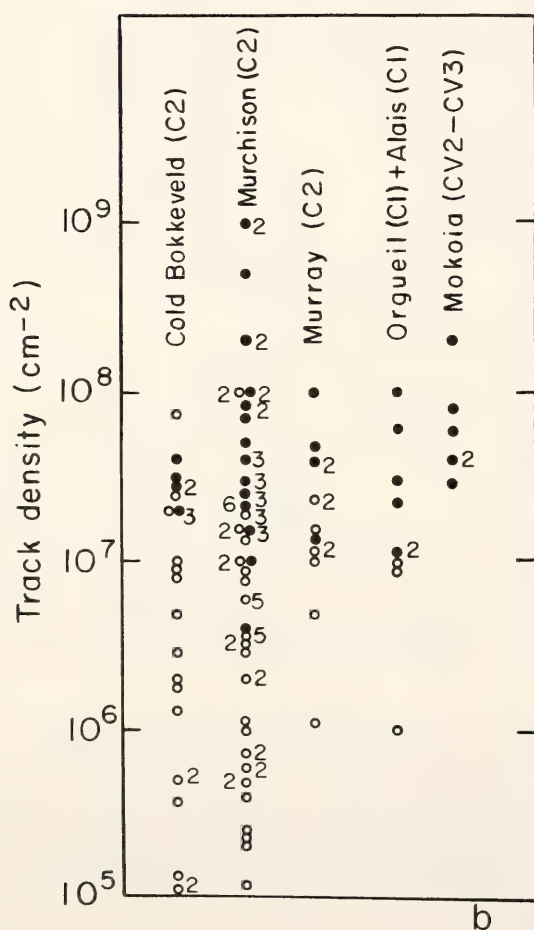
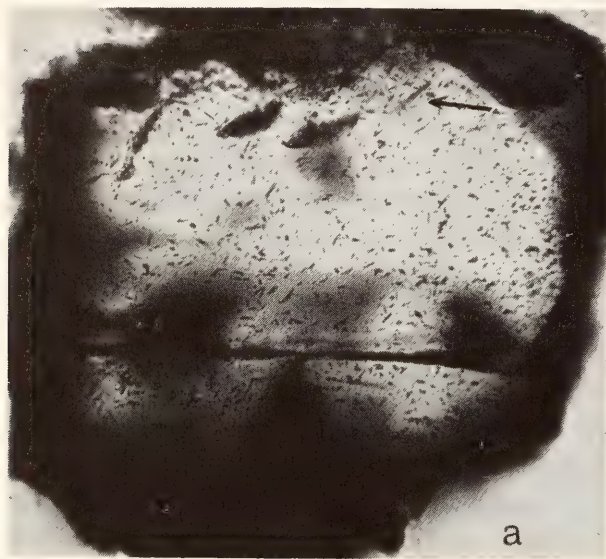
Olivine crystals were separated from the bulk sample by "freeze-thaw" technique and light crushing, and were concentrated by heavy liquids. They were mounted on epoxy buttons by hand picking, polished, and etched with WN solution (Krishnaswami *et al.*, 1971) to reveal the tracks. Initially a light etch ( $\sim 1.5$  hr) was given to avoid dissolution of high track density edges of the irradiated grains. After the irradiated grains were removed from the mount, crystals were etched further ( $\sim 3$  hr) to count cosmic ray tracks. The steepest gradients were determined by repeatedly grinding, polishing, and etching until the slope of the track profile reached a maximum.

##### *Results and Discussion*

We present our results on the irradiation features of Mokoia olivines and compare them with other carbonaceous chondrites to infer some characteristics of the

regolith dynamics of Mokoia parent body.

*Percentage of irradiated grains.* Track density measurements on olivine crystals ( $\sim 70\text{--}250\ \mu\text{m}$ ) from Mokoia fall in two regions. The peak  $\sim 2 \cdot 10^5\ \text{cm}^{-2}$  is due to cosmic ray irradiation of the meteorite. About 4% of the nearly thousand olivines



analyzed have track densities that range from  $3 \cdot 10^7\text{--}2 \cdot 10^8\ \text{cm}^{-2}$ . A typical irradiated grain is shown in Fig. 88a. The high track densities result from irradiation with solar flare particles. The percentage of irradiated crystals in Mokoia is comparable to that in other carbonaceous chondrites, where they range from 2 to 15% (Goswami *et al.*, 1976). However, the nature of irradiation differs substantially for Mokoia and is best illustrated in Fig. 88b, where track densities of the irradiated grains are plotted. The track densities of Mokoia olivines cluster tightly, within a factor of three, while other carbonaceous chondrites show a wide spread, ranging from two to four orders of magnitude. In this respect Mokoia is more similar to Kapoeta achondrite and other gas-rich chondrites (e.g., Rajan, 1974). This comparison suggests that Mokoia olivines received their irradiation in a well-stirred regolith, unlike C1 and C2 olivines which were irradiated in an essentially static regolith.

*Track density gradients.* Track density gradients were measured in all the irradiated grains. Three crystals were ground further and etched to reveal the steepest gradients. Most of the crystals analyzed show gradients,  $\rho_{\text{edge}}/\rho_{\text{inside}} \geq 2$ . These grains must have been irradiated, at least for some time, with a shielding of  $\leq 70\ \text{mg/cm}^2$ , using a revised solar flare spectrum of Hutcheon *et al.* (1974). In contrast, about half of the irradiated olivines from C1 and C2 do not show any gradients (Goswami *et al.*, 1976). This

Fig. 88. (a) A  $150\text{-}\mu\text{m}$  irradiated olivine from Mokoia carbonaceous chondrite. The track density gradient is rather shallow,  $\rho_{\text{edge}}/\rho_{\text{inside}} \sim 6$ . A long track due to a VVH ( $\geq 30$ ) nucleus is indicated by the arrow. (b) Distribution of track densities of irradiated grains from C1 and C2 meteorites (Goswami *et al.*, 1976) and Mokoia (this work). The solid circles are grains with detectable track density gradients,  $\rho_{\text{edge}}/\rho_{\text{inside}} \geq 2$ . Multiple grains having the same track density are shown by numbers. Note the tight clustering of Mokoia grains compared to other carbonaceous chondrites.



would require a well-stirred regolith during irradiation for Mokoia, unlike other carbonaceous chondrites.

In Mokoia, track density gradients are much flatter ( $\rho_{\text{edge}}/\rho_{\text{inside}} \sim 6$ ) than in Murchison and Surveyor glass, and are similar to Cold Bokkeveld results (Macdougall and Phinney, 1977). Therefore the grains must have accumulated a substantial fraction of the tracks under shielded conditions. The possibility that solar flare spectral shapes may have been different for the various meteorites is less likely.

*VVH/VH ratio.* By counting long tracks resulting from heavy nuclei ( $Z \gtrsim 30$ ), we have measured the VVH/VH ratio in the irradiated crystals. Because of the small size ( $\sim 150 \mu\text{m}$ ) of the crystals, the data have been added together to give an average value of  $\sim 7 \cdot 10^{-3}$  at an energy  $\sim 15\text{--}30 \text{ MeV/n}$ . Our value is consistent with that reported in other carbonaceous chondrites and lunar fines (Goswami and Macdougall, 1977). While the lunar data refers to irradiation over the last m.y. or so, Mokoia olivines are presumably irradiated much earlier. We are presently working on the determination of the compaction age of Mokoia, but other carbonaceous chondrites have been dated at 4.22–4.42 b.y. (Macdougall and Kothari, 1976). The measured values of the VVH/VH ratios show that the enhancement of heavy nuclei in solar flares, observed today, was also present in ancient solar flares (millions to billions of years ago) and hence must be an intrinsic property of the acceleration mechanism itself.

Based on the comparison of the rare-gas data from lunar soil and gas-rich meteorites, Anders (1975) has argued strongly in favor of a regolithic origin for all gas-rich meteorites, including carbonaceous chondrites, at distances of 2–5 A.U. from the Sun. Recently, from a study of the irradiation features such as anisotropy of irradiation, track density gradients, and spread in track densities, Goswami and Lal (1979) have concluded

that the low-energy irradiation was fairly static in nature and took place in centimeter- to meter-sized bodies which were later accreted to form the parent bodies of C1 and C2 meteorites. The limited track record of our Mokoia sample differs from other carbonaceous chondrites in many of the above features, and indicates that the irradiation of Mokoia grains took place in a well-mixed regolith. In light of the known heterogeneity of irradiation records in different fragments, we plan to study other Mokoia samples for a better characterization of its regolithic environment.

### References

- Anders, E., Do stony meteorites come from comets?, *Icarus*, 24, 363–371, 1975.
- Clayton, R. N., Meteorites and their parent bodies: evidence from oxygen isotopes, *Asteroids: An Exploration Assessment, NASA Conference Publ. 2053*, 57–75, 1978.
- Goswami, J. N., and D. Lal, A scenario for the formation of the carbonaceous chondrites based on cosmogenic clues, *Lunar and Planetary Sci.*, X, 449–451, 1979.
- Goswami, J. N., I. D. Hutcheon, and J. D. Macdougall, Microcraters and solar flare tracks in crystals from carbonaceous chondrites and lunar breccias, *Proc. 7th Lunar Sci. Conf.*, 543–562, 1976.
- Goswami, J. N., and J. D. Macdougall, Charge composition of solar flare heavy nuclei at 4 b.y. before present, *Meteoritics*, 12, 242–243, 1977.
- Hutcheon, I. D., D. Macdougall, and P. B. Price, Improved determination of the long-term average Fe spectrum from  $\sim 1$  to  $\sim 460 \text{ MeV/amu}$ , *Proc. 5th Lunar Sci. Conf.*, 2561–2575, 1974.
- Krishnaswami, S., D. Lal, N. Prabhu, and A. S. Tamhane, Olivines: revelation of tracks of charged particles, *Science*, 174, 287–291, 1971.
- Macdougall, J. D., and B. K. Kothari,

- Formation chronology for C2 meteorites, *Earth Planet. Sci. Lett.*, **33**, 36–44, 1976.
- Macdougall, J. D., and D. Phinney, Olivine separates from Murchison and Cold Bokkeveld: particle tracks and noble gases, *Proc. 8th Lunar Sci. Conf.*, 293–311, 1977.
- Price, P. B., I. D. Hutcheon, D. Braddy, and D. Macdougall, Track studies bearing on solar system regoliths, *Proc. 6th Lunar Sci. Conf.*, 3449–3469, 1975.
- Rajan, R. S., On the irradiation history and origin of gas-rich meteorites, *Geochim. Cosmochim. Acta*, **38**, 777–788, 1974.

#### UNUSUAL THERMAL HISTORY OF THE SHAW CHONDRITE

*Edward R. D. Scott and R. S. Rajan*

##### *Introduction*

The cooling rates of meteorites have been determined by two very different techniques. The first one involves the study of the major Fe-Ni minerals, kamacite (4–7% Ni) and taenite (20–45% Ni). Most taenite grains have M-shaped Ni profiles, which formed during diffusion-controlled kamacite growth and preserve a record of the cooling rates. Metallographic techniques can be used to infer cooling rates in the range of 900°–650°K by comparison with computer simulations of kamacite growth (e.g., Wood, 1967). The second technique involves counting <sup>244</sup>Pu fission tracks in phosphates and on the surfaces of various minerals in contact with phosphates (Pellas and Storzer, 1977). It is then possible to estimate the <sup>244</sup>Pu concentration in phosphate at the temperatures at which these minerals began to retain tracks. Knowing these temperatures and the <sup>244</sup>Pu half-life (82 Myr) allows measurements of cooling rates in the range 600°–300°K.

In general, the two techniques give similar results for a number of chondrites;

metallographic cooling rates of 21 chondrites range from 0.1° to 100°K Myr<sup>-1</sup> with a geometric mean of 4°K Myr<sup>-1</sup> (Wood, 1967; Taylor and Heymann, 1971), whereas fission track cooling rates for 12 chondrites give surprisingly uniform cooling rates of 0.7°–1.6°K Myr<sup>-1</sup>. The most important discrepancy is for the unique meteorite Shaw.

The uniqueness of Shaw, an L-group chondrite, is that it has experienced higher peak metamorphic temperatures of 1400°–1700°K, has coarser mineralogy and has a great scarcity of chondrules. (Fredriksson and Mason, 1967; Dodd *et al.*, 1975). These observations led Dodd *et al.* to classify it as a petrologic type 7. (For a discussion on the petrologic classification of meteorites, see Scott and Rajan, pp. 405–409, this Report.)

From metallographic studies, Berkley *et al.* (1976) derived a cooling rate of 700°K Myr<sup>-1</sup> in the temperature range of 930°–870°K. In contrast, Pellas *et al.* (1978) deduced a cooling rate of 1°K Myr<sup>-1</sup> in the range of 600°–300°K from fission track studies. Because of the gross disagreement, doubts have been cast by several authors on the validity of both techniques. There are also two conflicting models for the origin of Shaw. The first one involves partial melting at great depths (Rambaldi and Larimer, 1976), while the other suggests that Shaw has suffered impact heating and probably formed near the surface of its parent body (Berkley *et al.*, 1976; Scott and Rajan, 1979a; Taylor *et al.*, 1979). We therefore decided to reinvestigate the Shaw meteorite in order to check on the validity of both cooling rate techniques and the models for Shaw's origin.

##### *Results*

For details of the Shaw samples studied and experimental techniques, the reader is referred to Scott and Rajan (1979b). Figure 89 shows a typical etched metal grain. Shaw differs from normal slow-cooled chondrites in that the kamacite





Fig. 89. Reflected light photomicrograph of an etched metal grain enclosed by silicates in the Shaw chondrite. Virtually all the metal is composed of fine, dark plessite (*P*). Along the top right edge is a 30- $\mu\text{m}$ -wide kamacite border (*K*). Both the kamacite and silicate are separated from plessite by a clear taenite rim (*T*) which is 1–5  $\mu\text{m}$  in width. The clear taenite rim and kamacite border are narrower than in most ordinary chondrites, implying faster cooling around 750–900° K. Scale bar: 50  $\mu\text{m}$ .

borders and taenite rims are much narrower. Compositional profiles across the edges of metal grains show Ni profiles consistent with fast cooling. Figure 90 shows a Ni profile made by scanning a 2- $\mu\text{m}$ -wide electron beam in 1- $\mu\text{m}$  steps across kamacite and taenite into plessite, and from plessite through taenite to silicate. The taenite-plessite grains show the characteristic M profiles found in other meteorites, except that the maximum Ni levels detected at the outer edge of taenite, 26% Ni next to kamacite and 29% Ni adjacent to silicate, are much lower than in normal meteoritic metal (Wood, 1967). Further, the region of zoned metal is only 5–10  $\mu\text{m}$  wide compared to at least 50–100  $\mu\text{m}$  in most meteoritic metal with a comparable bulk Ni concentration. These observations and semiquantitative estimates from a

Wood plot suggest a cooling rate of  $\sim 10^3\text{--}10^4\text{ }^\circ\text{K Myr}^{-1}$ .

Kirsten *et al.* (1978) have measured aliquots of the same phosphate separates in which Pellas *et al.* (1978) counted  $^{244}\text{Pu}$  fission tracks and have deduced the concentrations of  $\text{Xe}^{136\text{f}}$  in the two phosphates whitlockite and apatite. Assuming that the highest fission track densities observed in feldspar come from adjacent whitlockite, we deduce from these data and the  $\text{Xe}^{136\text{f}}$  in whitlockite an interval of 50 Myr between 920° and 600° K. The track data of Pellas *et al.* (1978) and the deduced Xe-track time interval are plotted in Fig. 91. In this graph we plot  $\log(T - T_e)$  against time, where  $T_e$  is the black-body temperature at 2.5 A.U. (176° K). In such a plot an object cooling purely by conduction will be represented by a straight line. The

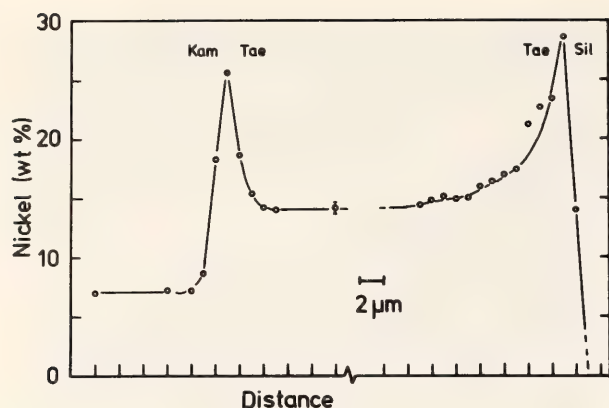


Fig. 90. Electron probe Ni profile across a metal grain in Shaw. Maximum Ni concentrations of 26–29% are found in the taenite at the kamacite or silicate interface. Except for the outer 5–10  $\mu\text{m}$ , plessite has a uniform concentration of 14% Ni. Three features of this Ni profile imply that Shaw cooled faster than normal L chondrites in the temperature interval 750–900° K: the narrow zoned region, the low Ni concentration in taenite, and the high uniform concentration in kamacite.

xenon-track time interval corresponds to a cooling rate of 6°K Myr<sup>-1</sup> between 920° and 600°K—in good agreement with

the fission track data (Pellas *et al.*, 1978). The validity of the fission track cooling rates as well as its major conflict with the metallographic cooling rates is amply confirmed.

### Discussion

Shaw's discrepant cooling rates suggest that it was reheated during a period of slow cooling. Figure 92 shows four possible thermal histories for Shaw. In models A–C, the high metamorphic temperature of around 1500°K is reached when other chondrites are being heated to lower temperatures ( $\leq 1100^\circ\text{K}$ ). But model D supposes that Shaw was reheated to  $\sim 1500^\circ\text{K}$  about 100 Myr after peak temperatures were reached in other chondrites. Models A, C, and D have reheating events lasting for  $10^4$ – $10^6$  yr (their duration is exaggerated in Fig. 92 for clarity), which produce the fast cooling rates recorded by the metal. In A and C, Shaw is a true type 7 chondrite

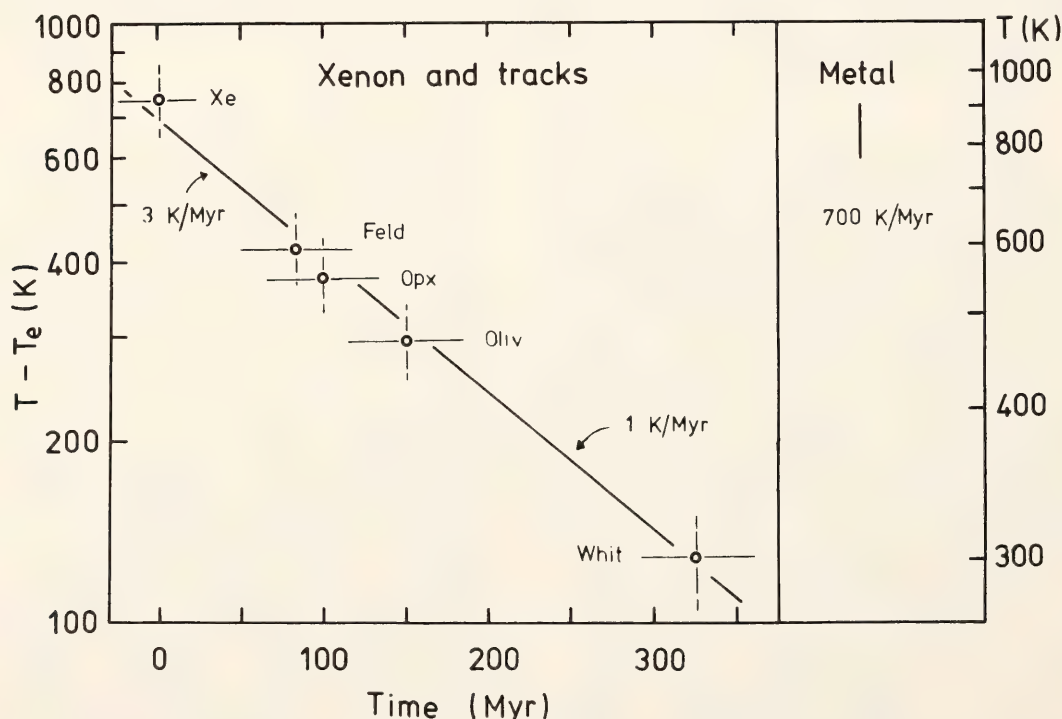


Fig. 91. Thermal history of Shaw plotted on a graph of  $\log(T - T_e)$  against time, where  $T_e$  is the surface temperature of Shaw's parent body (taken as 180° K). Data for Xe in whitlockite (Kirsten *et al.*, 1978) confirm the slow cooling rate obtained by Pellas *et al.* (1978) from fission track data in feldspar, orthopyroxene, olivine, and whitlockite. In order to reconcile the fast metal cooling rate (Berkley *et al.*, 1976; this work), we suggest that fast cooling to 750–650°K must have been followed by slow cooling at 1–3°K Myr<sup>-1</sup>.



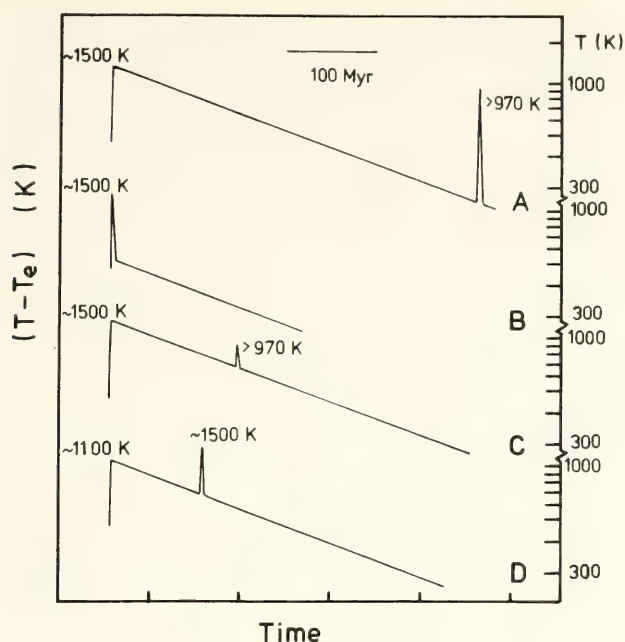


Fig. 92. Four possible models to account for Shaw's peculiar thermal history are shown. We prefer model D (See Scott and Rajan, 1979b, for a detailed discussion of the models).

that is mildly reheated, but in D, Shaw is an ordinary type 5 or 6 chondrite which experienced maximum metamorphism during the brief reheating event. From detailed considerations we conclude that model D is most likely (Scott and Rajan, 1979a, b). Even if Shaw once were a type 7 chondrite, it has experienced reheating and should not be included in comparative studies of petrologic types as a *normal* type 7 meteorite.

### References

- Berkley, J. L., R. V. Fodor, G. J. Taylor, and K. Keil, The Shaw meteorite: evidence for an igneous origin (abstract), *Meteoritics*, **11**, 249–250, 1976.
- Dodd, R. T., J. E. Groves, and G. E. Brown, Pyroxenes in the Shaw chondrite, *Geochim. Cosmochim. Acta*, **39**, 1585–1594, 1975.
- Fredriksson, K., and B. Mason, The Shaw meteorite, *Geochim. Cosmochim. Acta*, **31**, 1705–1709, 1967.
- Kirsten, T., J. Jordan, H. Richter, P. Pellas, and D. Storzer, Plutonium and uranium distribution patterns in phosphates from ten ordinary chondrites, *4th Int. Conf. Geochr. Cosmochr.* USGS Rep. 78-701, pp. 215–219, 1978.
- Pellas, P., and D. Storzer, On the early thermal history of chondritic asteroids derived from 244-plutonium fission track thermometry. In *Comets, Asteroids, Meteorites—Inter-relations, Evolution and Origins*, pp. 355–363, A. H. Delsemme, ed., Univ. of Toledo, Ohio, 1977.
- Pellas, P., M. Bourot-Denise, and D. Storzer, Shaw revisited: cooling history and U-Pu distribution in phosphates, *Lunar and Planetary Science, IX*, pp. 879–881, Lunar and Planetary Institute, Houston, Texas, 1978.
- Rambaldi, E., and J. W. Larimer, The Shaw chondrite, I. The case of the missing metal. *Earth Planet. Sci. Lett.*, **33**, 61–66, 1976.
- Scott, E. R. D., and R. S. Rajan, Thermal history of the Shaw chondrite, *Lunar and Planetary Science, X*, pp. 1095–1097, Lunar and Planetary Institute, Houston, Texas, 1979a.
- Scott, E. R. D., and R. S. Rajan, Thermal history of the Shaw chondrite, *Proc. Tenth Lunar and Planet. Sci. Conf.*, in press, 1979b.
- Taylor, G. J., and D. Heymann, The formation of clear taenite in ordinary chondrites, *Geochim. Cosmochim. Acta*, **35**, 175–188, 1971.
- Taylor, G. J., K. Keil, J. L. Berkley, D. E. Lange, R. V. Fodor, and R. M. Fruland, The Shaw meteorite: history of a chondrite consisting of impact-melted and metamorphic lithologies. *Geochim. Cosmochim. Acta*, **43**, 323–337, 1979.
- Wood, J. A., Chondrites: their metallic minerals, thermal histories, and parent planets, *Icarus*, **6**, 1–49, 1967.

### THERMAL HISTORY OF SOME XENOLITHIC ORDINARY CHONDRITES

Edward R. D. Scott and R. S. Rajan

The three ordinary chondrite groups (H, L, and LL) are each divided into



four petrologic types (3, 4, 5, and 6) according to various petrographic criteria such as the amount of glass, the degree of recrystallization of the mesostasis, and how well the chondrules are delineated (Van Schmus and Wood, 1967). Estimates of the maximum metamorphic temperatures vary but typically range from  $500^{\circ}$ – $700^{\circ}$ K for type 3 chondrites to  $1000^{\circ}$ – $1200^{\circ}$ K for type 6 (see Wasson, 1974). It is generally agreed that differing degrees of metamorphism can account for most, if not all, of the petrographic variations among ordinary chondrites, although they cannot explain the chemical differences within any of the groups.

About one quarter of the ordinary chondrites are known to contain xenoliths or foreign rock fragments ranging from several mm to cm in size (Fig. 93). Several xenolithic chondrites are rich in solar gases, solar-flare tracks, and other features characteristic of the lunar soil (e.g., Rajan, 1974), implying that they also formed in a planetary regolith. In general, xenoliths have similar bulk compositions to that of their matrix although commonly they are of different metamorphic types (Binns, 1967). It was often assumed that these meteorites had been metamorphosed after the xenoliths had been assembled or compacted to a

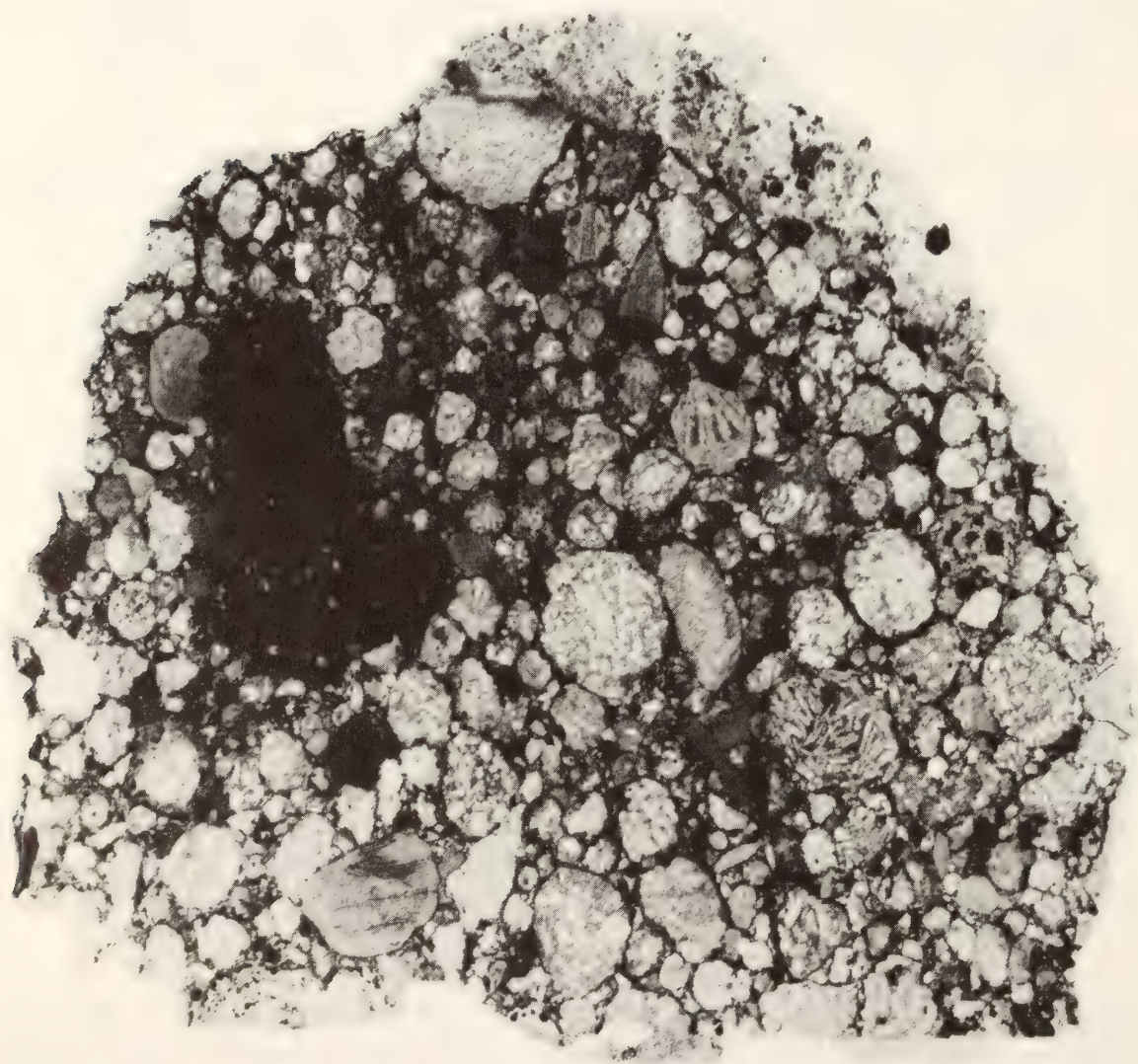


Fig. 93. Thin section of the L3 Mezö-Madaras xenolithic chondrite showing a black carbonaceous xenolith embedded in an L3 matrix rich in chondrules (mm-sized spherules). Width of section is 12 mm. (Photograph kindly supplied by W. R. Van Schmus.)



temperature appropriate to the metamorphic grade of the matrix. But the presence of solar-flare tracks and C2 carbonaceous chondrite fragments showed that St. Mesmin and Plainview, for example, had not been heated above 600°K after compaction, even though both had a matrix largely made of type 5 material (Ducatel and Poupeau, 1974; Fodor and Keil, 1976). (Quite how the rock fragments in these relatively tough rocks were welded together without baking above 600°K is not known.) However, the absence of solar-flare tracks, type 2 xenoliths, and solar gases does not necessarily mean that a xenolithic meteorite was appreciably reheated after compaction. The time of formation of xenolithic meteorites is not generally known. A few must have formed as recently as the last 1.4–3.9 Gyr (or even more recently), judging from Ar-Ar ages of their xenoliths (Schultz and Signer, 1977; Rajan *et al.*, 1979).

The metallographic techniques developed by Wood (1967) and others have been used to place constraints on the thermal history of normal chondrites (see Scott and Rajan, pp. 402–405, this Report), but they have not been used to study the metal in xenolithic chondrites. Our initial studies suggest that xenolithic chondrites may be subdivided into at least two groups, according to whether the final metallographic textures were established before or after the meteorites were compacted. We discuss below the results of our metallographic and electron probe studies on two examples, Weston and Mezö-Madaras.

In the gas-rich H chondrite Weston, which contains xenoliths ranging from type 3 to type 7 (Noonan and Nelen, 1976), most of the metal in the matrix contains normal slow-cooled taenite with cloudy borders and clear rims, and has not been reheated above 700°K since slow cooling. In addition, we found metal grains in a shocked black xenolith and several large metal-sulfide globs in the matrix with dendritic textures which

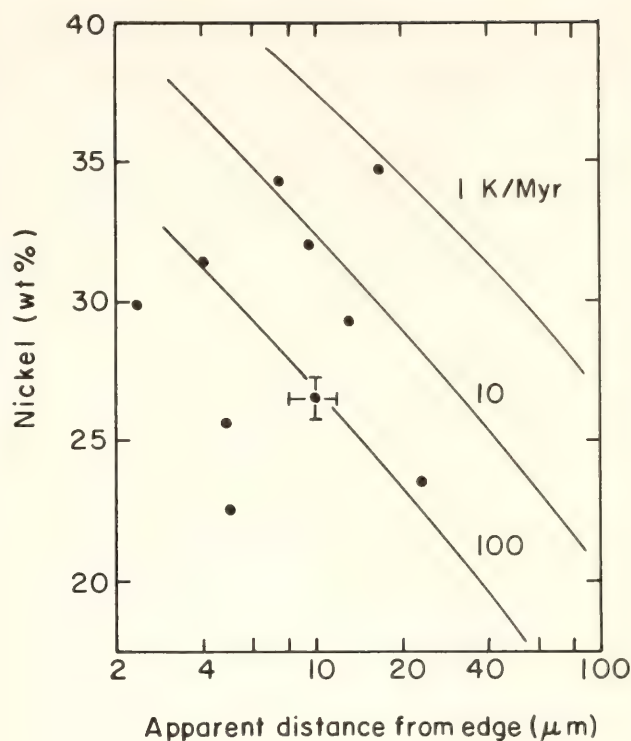


Fig. 94 Plot of Ni content at the center of taenite grains in Weston H chondrite against the apparent distances from the edge of the taenite. Metal grains for most chondrites plot parallel to the cooling curves of Wood (1967) and define a unique cooling rate. The very large spread of data in Weston implies that the metal grains cooled in different environments at  $\sim 5$ – $1000^\circ\text{K Myr}^{-1}$  before they were incorporated into the meteorite.

must have cooled much faster judging from their relatively low Ni content of their taenite grains. On a Wood diagram (Fig. 94) on which the Ni contents at the center of taenite grains are plotted against the apparent distances from the edges of the taenites, the data scatter far more than Wood (1967) found in any other single chondrite. We believe that there is a very large spread because the individual metal grains experienced cooling rates of  $5^\circ$ – $1000^\circ\text{K Myr}^{-1}$  in separate locations before compaction.

The Mezö-Madaras L3 chondrite contains L4, carbonaceous and melted xenoliths (Van Schmus, 1967). In all cases the taenite is polycrystalline and shows 1–5 μm wide rims of clear taenite enclosing cloudy taenite cores (see Fig. 96, Scott and Clarke, this Report). On Wood

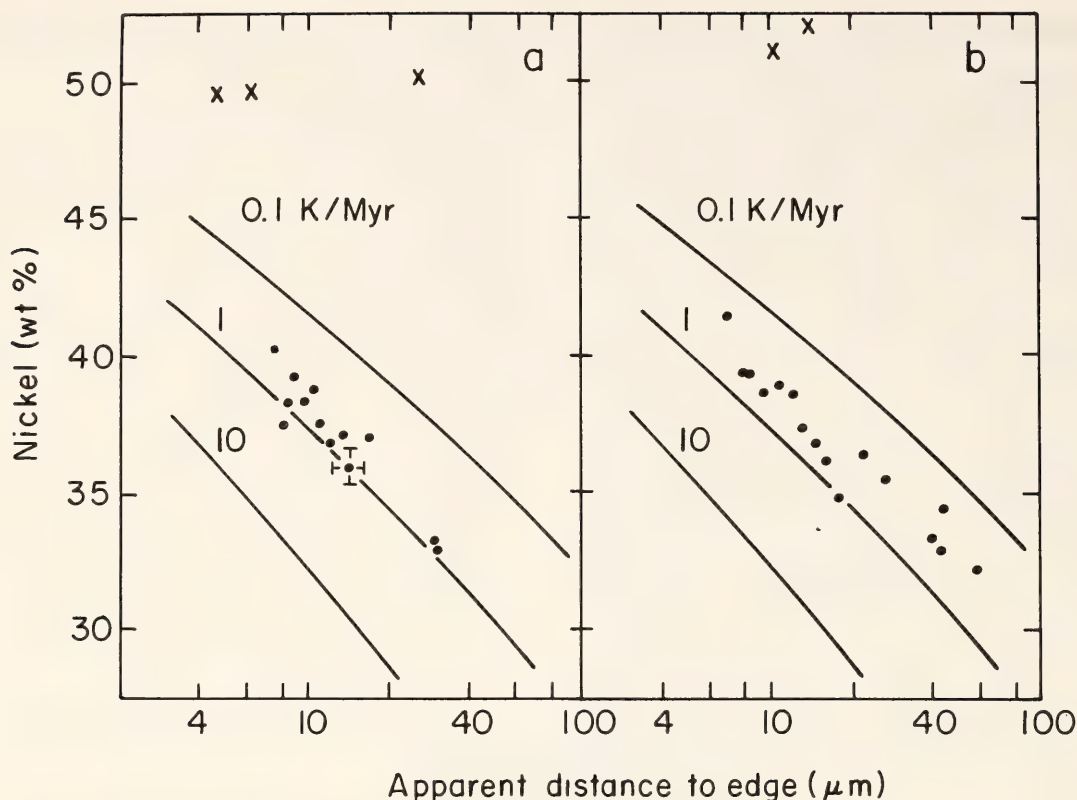


Fig. 95. Plot of central Ni content against apparent distance to edge for taenite grains in Mezö-Madaras; (a) L3 matrix; (b) L4 xenolith. Unlike Weston (Fig. 94), data for the matrix and xenolith are closely parallel to the cooling curves of Wood (1967). The cooling rate, which is given by the lower envelope of the data, is  $1^{\circ}\text{K Myr}^{-1}$  for matrix and xenolith. This implies that Mezö-Madaras cooled slowly through the range  $800\text{--}700^{\circ}\text{K}$  after compaction.

plots, data for metal grains in the matrix and an L4 xenolith (Fig. 95) lie closely parallel to Wood's cooling curves; in both cases the lower envelope of analyses defines a cooling rate of  $1^{\circ}\text{K Myr}^{-1}$ . The same value was also obtained by Wood (1967) on an unidentified sample of Mezö-Madaras. The uniformity of the cooling rates and metal textures in xenoliths of diverse metamorphic types is good evidence that Mezö-Madaras was heated to  $\sim 800^{\circ}\text{K}$  and then slowly cooled after compaction.

In summary, we feel that Mezö-Madaras material, compared to Weston, must have experienced a more complex metamorphic history. During the first stage, various metamorphic grades of the xenoliths and matrix were established. Material was subsequently broken up, recompact, and buried at great depths to account for the slow cooling rates observed in all xenoliths and matrix. The

recompaction must have occurred quite early (since the subsequent slow cooling implies that the heat source was still active) in contrast to Weston and other track-rich xenolithic meteorites.

It is interesting to note that the same sequence of metamorphism or melting, breaking up, recompaction, and subsequent burial and annealing at great depths is also required for Shaw (see Scott and Rajan, pp. 402–405, this Report), the mesosiderites, and the IC and IIE irons (see Scott, 1979), for different reasons. We conclude that the sequence of processes envisioned for Mezö-Madaras was probably widespread in many meteorite parent bodies. The requirement that meteorites be buried at great depths after recompaction implies that accretion of meteorite parent bodies continued after the maximum metamorphic temperatures had been reached. A similar model was developed for the iron



meteorites by Scott (1979), who concluded that they cooled through 800°K in large bodies that accreted from kilometer-sized bodies which were once molten (presumably because of Al<sup>26</sup>).

### References

- Binns, R. A., Structure and evolution of non-carbonaceous chondritic meteorites, *Earth Planet. Sci. Lett.*, **2**, 23–28, 1967.
- Ducatel, A., and G. Poupeau, The cosmic ray track record of the Saint Mesmin LL chondrite, *Meteoritics*, **9**, 336–337, 1974.
- Fodor, R. V., and K. Keil, Carbonaceous and non-carbonaceous lithic fragments in Plainview, Texas, chondrite: origin and history, *Geochim. Cosmochim. Acta*, **40**, 177–189, 1976.
- Noonan, A. F., and J. A. Nelen, A petrographic and mineral chemistry study of the Weston, Connecticut, chondrite, *Meteoritics*, **11**, 111–130, 1976.
- Rajan, R. S., On the irradiation history and origin of gas-rich meteorites, *Geochim. Cosmochim. Acta*, **38**, 777–788, 1974.
- Rajan, R. S., J. C. Huneke, S. P. Smith, and G. J. Wasserburg, Argon 40-Argon 39 chronology of lithic clasts from the Kapoeta howardite, *Geochim. Cosmochim. Acta*, **43**, 957–971, 1979.
- Schultz, L., and P. Signer, Noble gases in the St. Mesmin chondrite: implications to the irradiation history of a brecciated meteorite, *Earth Planet. Sci. Lett.*, **36**, 363–371, 1977.
- Scott, E. R. D., Origin of iron meteorites, in *Asteroids*, T. Gehrels, ed., Univ. of Arizona Press, in press, 1979.
- Van Schmus, W. R., Polymict structure of the Mezö-Madaras chondrite, *Geochim. Cosmochim. Acta*, **31**, 2027–2042, 1967.
- Van Schmus, W. R., and J. A. Wood, A chemical-petrologic classification for the chondritic meteorites, *Geochim. Cosmochim. Acta*, **31**, 747–765, 1967.
- Wasson, J. T., *Meteorites, classification and properties*, Springer-Verlag, New York, 1974.
- Wood, J. A., Chondrites: their metallic minerals, thermal histories and parent planets, *Icarus*, **6**, 1–49, 1967.

### IDENTIFICATION OF CLEAR TAENITE IN METEORITES AS ORDERED FeNi

Edward R. D. Scott and Roy S. Clarke, Jr.\*

Two Fe-Ni minerals are widely distributed in meteorites—body-centered cubic kamacite containing 4–7% Ni and face-centered cubic taenite, which generally contains 20–45% Ni. Most taenite grains have M-shaped Ni profiles which formed during diffusion-controlled kamacite growth and preserve a record of the cooling rates. But another variety which is more homogeneous and contains 49–57% Ni has been identified in ordinary chondrites by Taylor and Heymann (1971). It was called clear taenite to distinguish it from zoned taenite, which develops cloudy borders on etching. They deduced that clear taenite formed at low temperatures on cooling (390°–340°C) and proposed an ingenious origin—nucleation at the edge of isolated grains of kamacite due to a decrease in the equilibrium solubility of Ni in kamacite below 450°C.

During routine studies of meteoritic metal by reflected-light microscopy and electron probe analysis, we discovered that clear taenite is optically anisotropic and have found it in nearly all types of meteorite. We conclude that this mineral is the tetragonal ordered FeNi phase discovered in iron meteorites by Knudsen and co-workers using Mössbauer and x-ray diffraction techniques (Petersen *et al.*, 1977; Albertsen *et al.*, 1978a, 1978b), and that it formed from taenite, not kamacite. (Note that we use the term clear taenite as originally defined by

\* National Museum of Natural History, Smithsonian Institution, Washington, D.C.



Taylor and Heymann to include only taenite with  $\sim 48\text{--}57\%$  Ni. Except for cloudy taenite, which contains approximately  $30\text{--}40\%$  Ni and looks cloudy because it is a submicroscopic two-phase mixture (Scott, 1973), all taenite remains clear on etching.)

Optical anisotropy in clear taenite is best observed in well-polished sections using oil-immersion objectives and a powerful source of polarized light. Contrast can often be improved by slightly uncrossing the polars. Clear taenite shows a characteristic pattern of irregular grains (Fig. 96) in which subdomains are usually visible. These subdomains show flamelike or more intricate arrangements and are probably magnetic domains judging from their similarity to those seen in cohenite ( $\text{Fe}_3\text{C}$ ) under the same conditions. From the descriptions of Gooley *et al.* (1975), it is clear that the mineral

in which they found optical anisotropy was in fact Taylor and Heymann's clear taenite. Careful observations of a few large areas of clear taenite reveal three distinct orientations of grains, consistent with the symmetry change from cubic to tetragonal that occurs on ordering in FeNi. Because etching may cause apparent anisotropy, we used only unetched sections to characterize this mineral. In such sections, clear taenite is virtually identical in color to the zoned taenite which is adjacent, although their interface may sometimes be observed without crossed polars.

In addition to the  $10\text{--}60\ \mu\text{m}$  diameter grains which Taylor and Heymann (1971) identified, clear taenite also occurs in sharply defined rims of normal zoned grains. These rims, which are  $1\text{--}5\ \mu\text{m}$  wide, contain  $48\text{--}57\%$  Ni and under crossed polars show an irregular grain

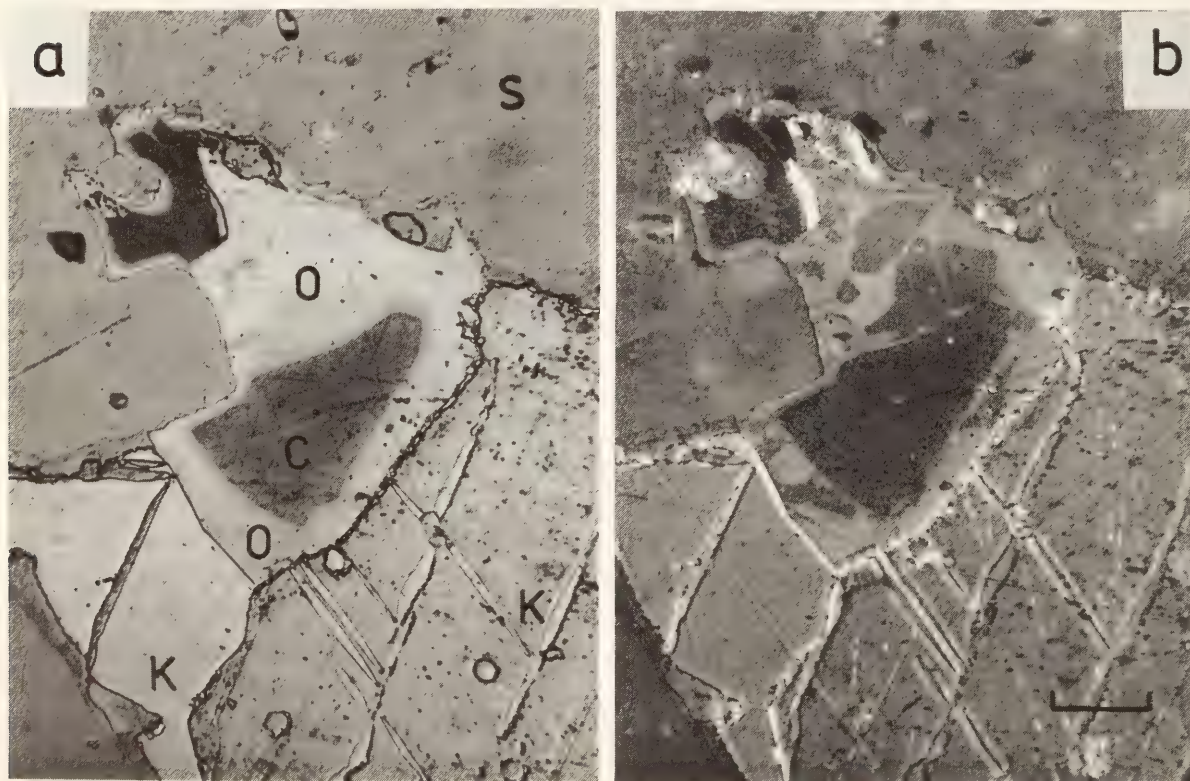


Fig. 96. Reflected light photomicrograph of metal grain in Mezö-Madaras, an L3 meteorite, etched with acid to reveal structure; (a) polarized light; (b) crossed polars. In (a) cloudy taenite (C) is surrounded by a white rim of clear taenite (O). Crossed polars show that clear taenite is optically anisotropic and reveal an irregular grain structure. Clear taenite is surrounded by kamacite (K) and silicate (S). (Polished section is carbon coated; this enhances contrast between grains in clear taenite by reducing the visibility of the subdomains.) Scale bar:  $20\ \mu\text{m}$ .



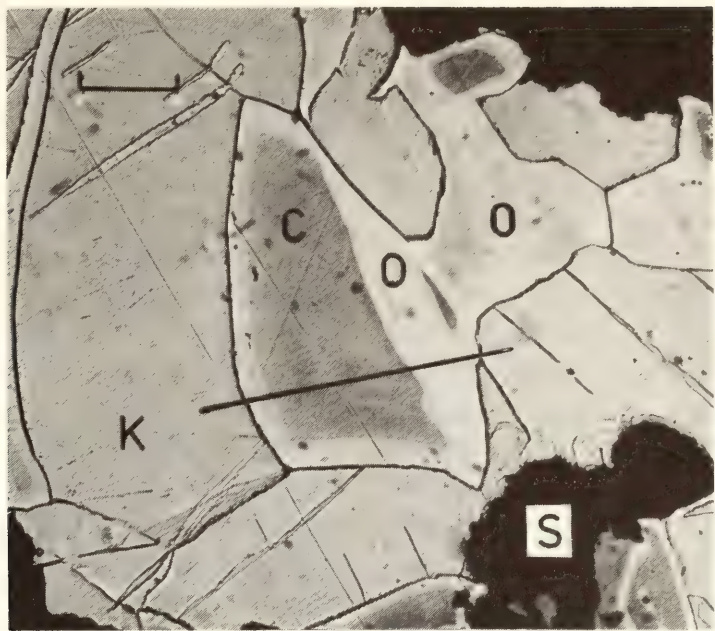


Fig. 97. Reflected light photomicrograph of metal grain in Mezö-Madaras. The line across the cloudy taenite grain (*C*) which is rimmed by ordered clear taenite (*O*) marks the location of the compositional profile shown in Fig. 98. Kamacite, *K*; silicate, *S*; scale bar: 20  $\mu\text{m}$ .

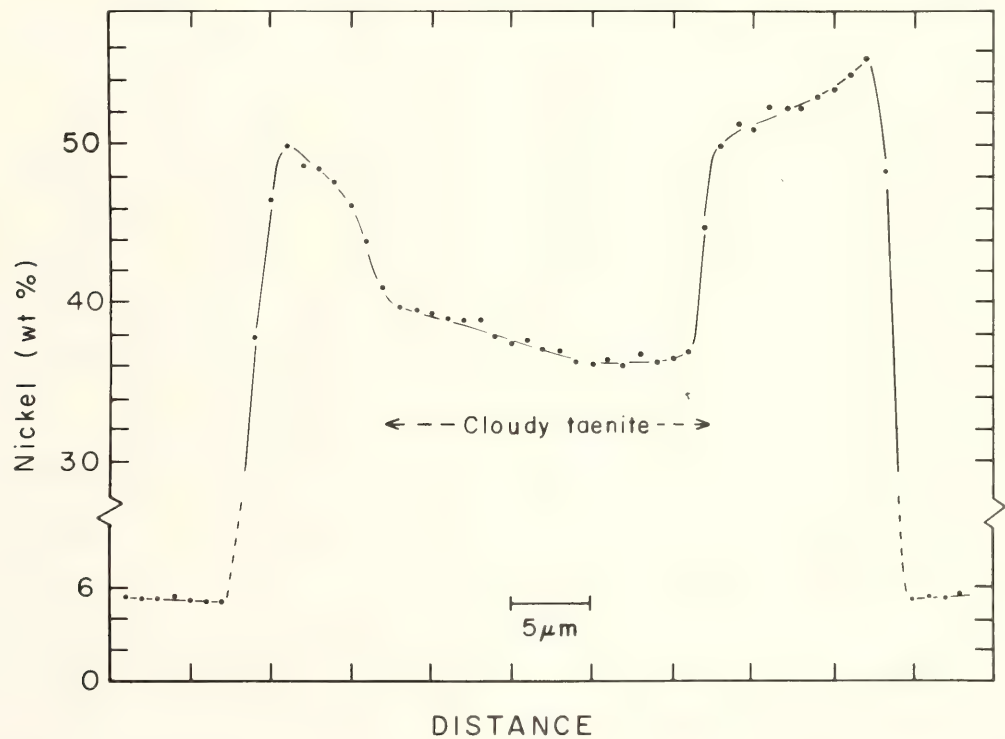


Fig. 98. Electron probe Ni profile across composite taenite grain shown in Fig. 97. The Ni profile is not smooth as other authors have found; instead there are discontinuities between the clear taenite rim which has 46–55% Ni and the cloudy taenite which has less than 40% Ni.

structure characteristic of clear taenite. On etching it can be seen that the anisotropic taenite rim corresponds precisely to the zone of clear taenite between kamacite and cloudy taenite (Fig. 96). Electron probe traverses across zoned

taenite grains with broad rims in over 10 mesosiderites and chondrites (Figs. 97 and 98) show a relatively homogeneous rim and a discontinuity at the interface between clear and cloudy taenite like that found in Estherville (Scott,

1973). These features in the M-profile were not resolved by other workers (e.g., Wood, 1964, 1967; Taylor and Heymann, 1971; Goldstein and Short, 1967) because they did not analyze small favorably located grains with broad rims.

We have found optical anisotropy in clear taenite from over 40 meteorites including H,L,LL, and CO3 chondrites, diogenites, iron meteorites, mesosiderites, and pallasites, and we conclude that all slowly cooled meteorites with zoned taenite also contain some clear, anisotropic taenite. Table 18 summarizes the compositions of clear taenite found by electron probe analysis of eight meteorites. Except in reheated meteorites and heat-affected surfaces, we have not found normal isotropic taenite with compositions in the range 45–60% Ni.

The intimate association of clear taenite with zoned taenite and its growth on grain boundaries within polycrystalline taenite show that few clear taenite grains could have formed in isolated kamacite grains as Taylor and Heymann (1971) suggested. Instead we propose that large clear taenite, which is found in ordinary chondrites and mesosiderites, formed by the inward growth of clear taenite rims at low temperatures ( $<400^{\circ}\text{C}$ ). In the mesosiderites Estherville and Emery and the L chondrite Mezö-Madaras, we have seen complete sequences of structures ranging from large clear taenite grains enclosing  $\mu\text{m}$ -sized blobs of cloudy taenite to large

zoned grains with  $\mu\text{m}$ -wide rims of clear taenite enclosing cloudy taenite. In most chondrites the intermediate stages in this sequence are less common and taenite appears to be divided into two populations. Diffusion of Ni through up to 30  $\mu\text{m}$  of clear taenite, which is required in our mechanism, may be facilitated by the numerous grain boundaries. Other processes may also play a role in the formation of clear taenite that is associated with troilite, as was suggested by Taylor and Heymann. The absence in slowly cooled iron meteorites of massive clear taenite grains and the relatively narrow rims on zoned grains may result from the relatively high metallic concentrations of P, which reduce the equilibrium concentration of Ni in taenite (Doan and Goldstein, 1970).

The anisotropic FeNi mineral that we have described is undoubtedly the ordered phase reported by Albertsen *et al.* (1978a, 1978b) in two iron meteorites. They identified it by the similarity of its Mössbauer spectrum to that of FeNi synthesized with neutron irradiation (Gros and Pauleve, 1970) and by the presence of x-ray reflections which violated the f.c.c. lattice of taenite. The only possible ordering arrangement that satisfied their data was the tetragonal L10 structure (AuCu) which can be derived from taenite by ordering Fe and Ni atoms on alternate (002) planes. From etching experiments on zoned taenite lamellae, Albertsen *et al.* deduced that FeNi was concentrated in the outer rims of these lamellae. Our observations and probe analyses of anisotropic rims are entirely consistent with their work, and taken together they characterize clear taenite containing 48–57% Ni as a new mineral.

Ordered FeNi grains several microns in size have also been reported in another iron meteorite, Santa Catharina, which contains 33% Ni, by Bowles *et al.* (1978) and Danon *et al.* (1979). Judging from the virtual absence of kamacite and normal zoned taenite in this iron, FeNi

TABLE 18. Range and Mean Composition in Wt % of Clear Taenite in Eight Meteorites\*

	Range	Mean
Fe	44–53	49
Ni	47–57	51
Co	0.01–0.8	0.03
Cu	0.11–0.38	0.24
P	$<0.01$	$<0.01$

\* Determined by electron probe analysis.



did not form by the mechanism we describe; instead local concentration of Ni by oxidation of Fe has been suggested by Bowles *et al.* but denied by Danon *et al.* Although the meteorites in which we observed clear taenite are not all entirely unaltered, the areas that we studied were free from visible oxidation.

Since the phases in cloudy taenite can only be resolved by electron microscopy, we cannot confirm the conclusion of Albertsen *et al.* (1978a, 1978b) that cloudy taenite also contains ordered FeNi. It is plausible that exsolution in the cloudy zone is triggered by ordering of FeNi, possibly through spinodal decomposition. Electron microscopy and heating experiments by Jago (1979) on submicron phases in Santa Catharina did show two taenites in a structure which might be a precursor to cloudy taenite. However, he detected extra reflections consistent with ordering in taenite (and kamacite) only after the second taenite had disappeared on heating.

Estimates of cooling rates (Goldstein and Short, 1967; Wood, 1967) ignore the existence of ordered FeNi rims and the two-phase nature of cloudy taenite. Although this is unlikely to cause large errors, a quantitative investigation of these effects would be useful. The abundances of clear and cloudy taenites provide a useful visual estimate of the cooling rate, as there are rough inverse correlations between abundances and cooling rates.

We thank R. S. Rajan for stimulating discussions, and C. G. Hadidiacos and E. Jarosewich for providing electron probe facilities at the Geophysical Laboratory and the Smithsonian Institution, respectively.

### References

- Albertsen, J. F., G. B. Jensen, and J. M. Knudsen, Structure of taenite in two meteorites, *Nature*, 273, 453–454, 1978a.
- Albertsen, J. F., M. Aydin, and J. M. Knudsen, Mössbauer effect studies of taenite lamellae of an iron meteorite, Cape York (IIIA), *Physica Scripta*, 17, 467–472, 1978b.
- Bowles, J. S., M. Hatherly, and A. S. Malin, FeNi superlattice formation by corrosion of Santa Catharina meteorite, *Nature*, 276, 168–169, 1978.
- Danon, J., R. Scorzelli, I. S. Azevedo, W. Curvello, J. F. Albertsen, and J. M. Knudsen, Iron-nickel 50–50 superstructure in the Santa Catharina meteorite, *Nature*, 277, 283–284, 1979.
- Doan, A. S., and J. I. Goldstein, The ternary phase diagram, Fe-Ni-P, *Met. Trans.*, 1, 1759–1769, 1970.
- Goldstein, J. I., and J. M. Short, Cooling rates of 27 iron and stony-iron meteorites, *Geochim. Cosmochim. Acta*, 31, 1001–1023, 1967.
- Gooley, R., R. B. Merrill, and J. R. Smyth, Anisotropic taenite in meteorites (abstract), *Meteoritics*, 10, 410, 1975.
- Gros, Y., and J. Pauleve, Etude par effet Mössbauer de l'ordre dans un alliage Fe-Ni 50–50 irradié par des neutrons ou des électrons, *J. Phys. Paris*, 31, 459–470, 1970.
- Jago, R. A., Santa Catharina and the origin of cloudy taenite in meteorites, *Nature*, 279, 413–415, 1979.
- Petersen, J. R., M. Aydin, and J. M. Knudsen, Mössbauer spectroscopy of an ordered phase (superstructure) of FeNi in an iron meteorite, *Phys. Lett.*, 62A, 192–194, 1977.
- Scott, E. R. D., The nature of dark-etching rims in meteoritic taenite, *Geochim. Cosmochim. Acta*, 37, 2283–2294, 1973.
- Taylor, G. J., and D. Heymann, The formation of clear taenite in ordinary chondrites, *Geochim. Cosmochim. Acta*, 35, 175–188, 1971.
- Wood, J. A., The cooling rates and parent planets of several iron meteorites, *Icarus*, 3, 429–459, 1964.
- Wood, J. A., Chondrites: their metallic minerals, thermal histories, and parent planets, *Icarus*, 6, 1–49, 1967.

## INSTRUMENTATION

THE JOINT CIW-IAR 21-CM RECEIVER  
FOR HIGH-SENSITIVITY SOUTHERN  
NEUTRAL HYDROGEN OBSERVATIONS*E. T. Ecklund, N. Thonnard, and  
K. C. Turner*

At the time of the writing of this report, 10 large wooden crates, weighing a total of 6,100 pounds and occupying 475 cubic feet, are on a ship en route for Buenos Aires, Argentina. This is a happy occasion for those of us at the DTM and the Instituto Argentino de Radioastronomía (IAR) who have worked for the past few years to develop a state-of-the-art 21-cm receiver for the 100' radio telescope in Argentina. The complete system was fully tested at DTM both in the lab and on the sky. By March 30, 1979, all hardware and software "bugs" had been eliminated and the system was working better than our original specifications.

*The Front End*

By the first weeks of November 1978, the 21-cm front end with all of its control circuits and interconnecting wiring was completed and tests of the entire system had begun. The system noise temperature was measured at the junction of the feed and the rest of the receiver using a room temperature and liquid nitrogen load. With the paramp gain adjusted to 19.5 dB, the system noise temperature was 60° K. The value of the calibrating noise source was also carefully measured and determined to be 5.9° K. Initial gain-stability and temperature-controller tests were run with the receiver connected to a room temperature load. This made small gain instabilities in the receiver six times more apparent in the output record because of the large (360° K) signal. This allowed us to identify and to correct the following sources of small instabilities.

(1) Because of the large line voltage variations expected in Argentina (220–190 V), the power supplies for the receiver had to be well regulated. As first tested, the receiver had a 0.05-dB gain change for a 10% change in line voltage. This instability in gain was tracked to a 10-mV change in the +15 V and +12 V supplies resulting from temperature changes in the regulators caused by large changes in power dissipation as the line voltage varied. By using two regulator stages, with the second regulator inside the temperature-controlled section of the front-end box, no change in power supply voltage nor receiver gain ( $<0.001$  dB) was detectable over a line voltage change from 240 V to 180 V.

(2) Considerable testing was required to optimize empirically the temperature controller. Because of the large thermal capacity of the heating/cooling modules, phase shifts would cause thermal oscillations when the gain was high enough for good temperature control. This was remedied by changing the gain and time constants in the power amplifier loop of the temperature controller, by selecting carefully the location of temperature-sensing thermistor, and by adding a large thermal reservoir that was well coupled to the airstream inside the front-end box. After these changes, the front-end box temperature remained within  $\pm 0.02^\circ$  C from nominal, over an ambient temperature range from 10° to 30° C. The maximum peak-to-peak oscillation was  $0.04^\circ$  C with a 1.7-min period. Even under worst-case conditions when the ambient temperature was  $-6^\circ$  C, the temperature offset from nominal was  $-0.05^\circ$  C with a  $0.1^\circ$  C peak-to-peak oscillation.

(3) As the gain of the parametric amplifier is very temperature dependent and as the maximum length of a single observation is never more than 20 minutes, we decided to stabilize the system further by



coupling a second large thermal reservoir directly to the paramp to increase to approximately one hour the thermal time constant of the paramp. This completely decoupled the paramp from any rapid, small-scale variations in temperature within the front-end box.

These changes resulted in an exquisite gain stability for the receiver. The worst gain changes occurred when the receiver was moved from a warm room to the  $-6^{\circ}\text{C}$  outdoors (a rather severe test!), but even in this case the gain changed slowly by only 0.01 dB per hour. Normally, the only changes were slow, long-term drifts of 0.04 dB over a 24-hour period, which would be undetectable during normal observations.

In early March 1979, the receiver was tested outdoors with the feed pointing to the zenith (See Fig. 99). The half-power beamwidth of the feed is  $60^{\circ}$ , so that the main beam covered a large section of sky; parts of the Derwood laboratory building and 60' antenna were within the field of view of the feed's tapered main beam. In spite of this, the total system temperature was only  $70^{\circ}\text{K}$  when the Galactic plane was below the horizon. This is probably an upper limit to the system temperature we will have at the telescope. One pleasant surprise was that the load switch contributed only  $3.5^{\circ}\text{K}$  to the system temperature. Our original expectation was that a practical switch would contribute  $10\text{--}12^{\circ}\text{K}$  to the system temperature. We therefore designed the front end so that the load switch was easily removable for observations not requiring it, but with the low loss of this switch, it can stay in the system permanently.

### *The Back End*

As has been mentioned previously (*Year Book 75*, p. 143), the data taking, receiver control, and spectrum calibration is being handled by computer. This allows considerable flexibility in data taking and observing, but also makes the



Fig. 99. The new 21-cm front end with the feed pointed to the zenith during testing at our Derwood, Maryland, laboratory. Excluding the feed, the front end box is 75 cm square by 95 cm high.

operation of the receiver vitally dependent on the computer (see Fig. 100). Two computers are used: a minicomputer for data acquisition and a microprocessor for receiver control. The minicomputer, a PDP-11/20, generates a 6-msec interrupt which is the basic timing of the receiver. This starts the sampling of the spectrum through a 112-channel multiplexer and an ADC that is interfaced with the PDP-11, and adds the digitized sample to one of four double precision arrays. At specific multiples of the basic 6-msec interrupt, the PDP-11 generates other interrupts which communicate with



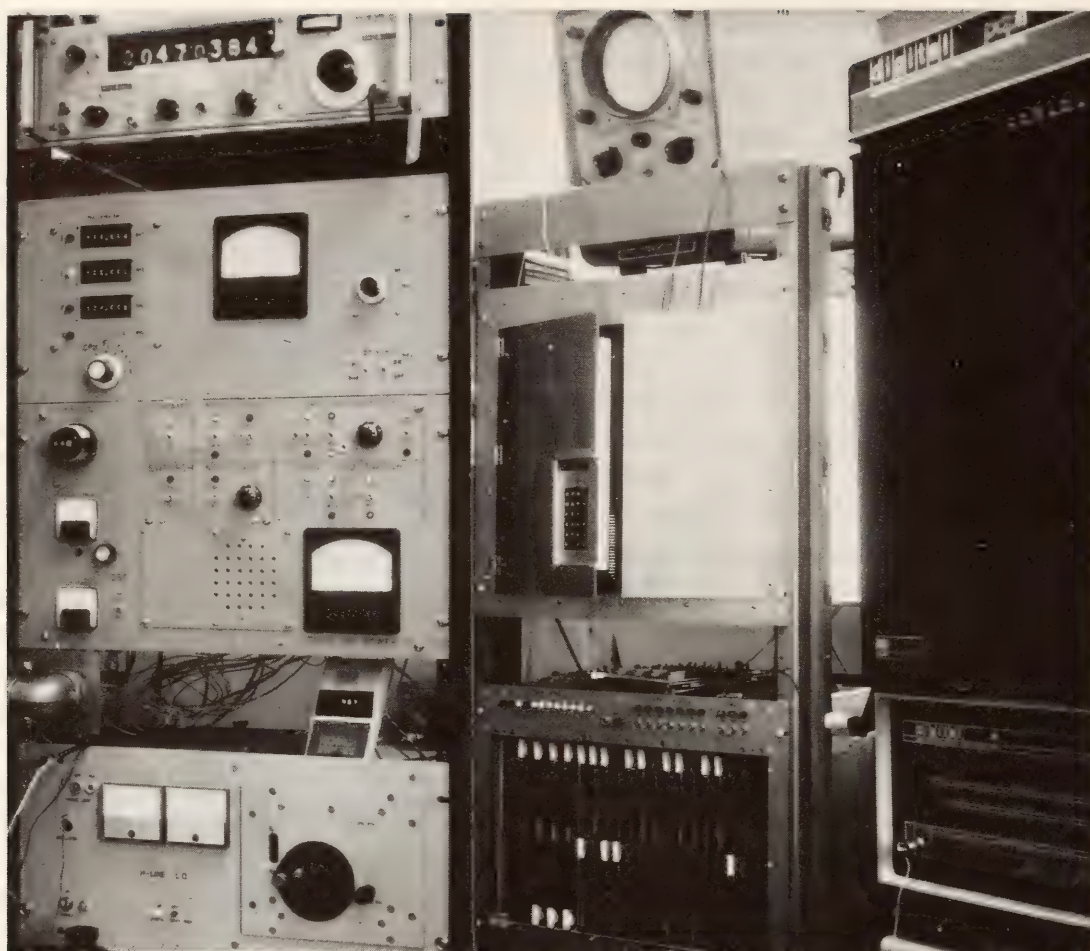


Fig. 100. The new back end for the IAR radio astronomy receiver. In the left-hand rack (from top to bottom) is the frequency counter for the first local oscillator, the second converter with its frequency-switching synthesizer, the main front-end control panel, and the reference generator for the first local oscillator. The middle rack has the oscilloscope displaying the current spectrum, the receiver control microprocessor, and the bin with the 112-channel power detectors, multiplexer, and ADC. The right-hand rack has the nine-track digital tape deck and the PDP-11 central processor. Not shown in this picture is the multi-channel filter spectrometer, third converter, temperature controller, floppy disk drives, and power supplies.

a MOSTEK KIM-1 microprocessor that both controls the receiver and gives a real-time display of the accumulating spectrum. Unfortunately, the completion of the receiver was delayed many months when in the fall of 1978, N. Thonnard, who had previously been responsible for the front end and only the analog parts of the back end, also had to finish the digital and software components of the back end.

Three observing modes are possible with the present receiver software. The programs are: TOTPWR for position-switched observations, LOADSW for

load-switched observations, and FREQ-SW for frequency-switched observations. A sample spectrum taken in the load-switched mode is shown in Fig. 101. Except for two assembler-language subroutines which transmit the data between the PDP-11 and the ADC, DAC and receiver control circuits, all other programs are coded in FORTRAN. These are stored on floppy disks, which have lots of extra space for temporary data storage. The three observing programs are self-prompting so that the observer need only know the name of the program to use it. The basic architecture of all



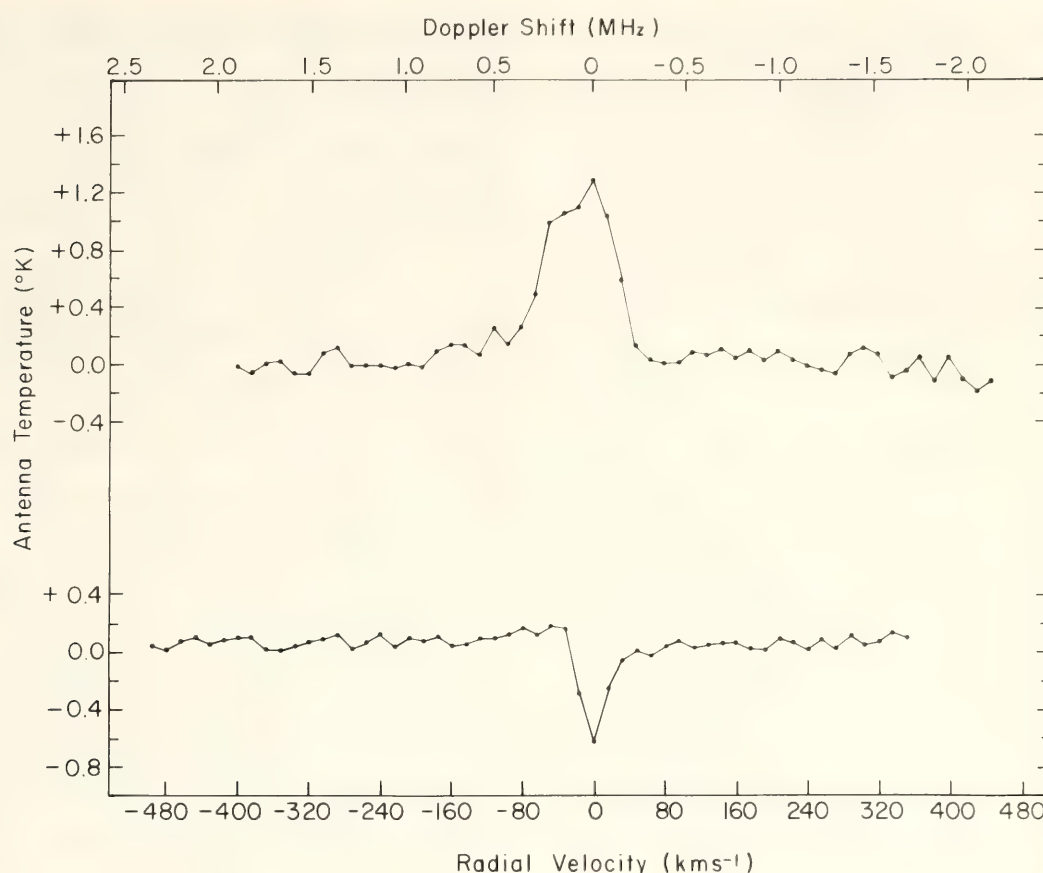


Fig. 101. The upper spectrum was taken in the load-switched observing mode for only 2 minutes with the feed (60° HPBW) centered at  $l = 183^\circ$ ,  $b = +65^\circ$ . The lower spectrum was taken in the position-switched (total power) observing mode where the displayed profile is the difference between a 2-minute observation centered at  $l = 158^\circ$ ,  $b = -10^\circ$  and a second 2-minute integration taken 10 minutes later centered at  $l = 160^\circ$ ,  $b = -12^\circ$ . Note that over the 4-MHz observing bandwidth, the baselines show very little structure.

three is very similar. The mainline program essentially communicates with the observer, asks questions as to how observations are to be conducted, and communicates with numerous subroutines to accomplish the various necessary tasks. The subroutines are also very similar for the three observing modes with only minor changes needed to accommodate the differences. With this modular structure, changes can be made easily in the observing programs to satisfy specific needs without modifying the entire system.

The programs necessary to operate the KIM-1 microprocessor are coded in machine language. These programs are stored on an audio cassette tape and need to be reloaded at the initial power-up. The power supplies for the micro-

processor system have a large time constant so that power dropouts of up to a few seconds do not erase the program. As with the PDP-11 programs, the microprocessor programs are also very modular with numerous subroutines so that they also can be changed without rewriting the entire system.

In Fig. 100 we show part of the receiver back end as it was set up at our Derwood observatory for testing. In Fig. 101 we show spectra obtained with only a 2-minute integration over a 4-MHz bandwidth. The flatness of the baseline in both the load switched and total power observations attest to the excellent impedance match and stability of the front end. Comparing this to the old system at the IAR, the RMS noise is a factor of three less, implying that the same sensi-

tivity limit can be reached in only one tenth the time. Also, since the baseline is at least one to two orders of magnitude better, very faint, extended velocity features will now be detectable. This opens up many new opportunities for us in Galactic and extragalactic neutral hydrogen research in the Southern Hemisphere.

### IMAGING DETECTORS

*W. K. Ford, Jr.*

The cascaded image intensifier systems developed by the Carnegie Institution have had widespread success in obtaining many diverse types of astronomical observations. Among the advantages of these detectors are their relatively high efficiencies compared with photographic plates and their large format compared with available digital detectors.

An improved version of the original Carnegie tube was developed with NSF support in the early 1970's. These tubes are characterized by higher gains and more uniform phosphors than the original cascaded tubes. Systems incorporating early versions of the improved tube (RCA type C33063) have been used extensively at Lowell Observatory and at Las Campanas. Other versions of this tube (RCA C33063-EP3), produced more recently, have been incorporated into systems that are heavily scheduled, for example, at Kitt Peak, Cerro Tololo, and at Las Campanas.

The image intensifiers in these systems derive their advantage over unaided photographic systems from the efficiency of photocathodes. Primary photoelectrons from the cathode are accelerated, multiplied, and focused onto a phosphor screen. The intensified image thus produced is recorded with a fast transfer lens and photographic plate. The rate at which photoelectric events from a given image are displayed by the phosphor screen depends on the conversion efficiency of the photocathode. It is the

cathode efficiency that determines in a fundamental way the performance of the system as a whole. The brightness of the photoelectron events is determined by the accelerating voltage, the efficiency of phosphor screen, and the internal electron multiplication. The two-stage tubes discussed here have sufficient gain that the random fluctuations in the intensified image can be recorded on III a-J plates with a fast transfer lens as a mottled or grainy pattern. Hence the system is quantum-noise limited (see, for example, *Year Book 74*, pp. 135-137). Low-contrast images are recorded by stopping down the transfer lens to achieve longer integrations on the photographic plate.

Since the photocathode efficiency sets the upper limit to the overall efficiency of the intensifier system, it is important for our astronomical applications to develop systems with as high quantum efficiencies as possible. Also, in applications such as direct image tube photography (rather than the more usual spectroscopic applications) it is necessary to have a uniform response across the field. During this report year we have been exploring with RCA various ways that might be used in the formation of the photocathodes to improve the sensitivity and uniformity in the cascaded tubes. It now appears that it may be possible to devise a method of cathode formation from small alkali generators located in small appendages connected to the tube envelope. This can be done without changing the basic design of the tube. Processing photocathodes from similar appendages has resulted in significant improvements in uniformity and sensitivity in other types of intensifiers. By adapting this technique to the fabrication of our cascaded tubes, it may be possible to make a significant improvement in photocathode quality.

The cascaded image intensifier systems are well suited to observing problems where relatively high resolution and only moderate photometric accuracy is required. Other systems, especially those



not requiring photographic recording of the data, are better suited for astronomical problems involving accurate spectrophotometry or sky subtraction. The detectors used in these digital systems are evolving rapidly, particularly the silicon imaging devices (Ford, 1979).

One of the interesting solid state sensors is the Reticon®, a linear array of photodiodes. The array is "self scanned"—i.e., the photodiodes are connected in turn by FET switches on the chip to a common output line to produce a video signal. These devices are inherently relatively noisy, but they have the advantage of being available with formats and pixel sizes that are useful for spectroscopy. For example, Shectman at the Hale Observatories has built a photon-counting image intensifier system for the Las Campanas Observatory that uses two rows of photodiodes to sample the spectra from sky and object apertures (see *Year Book* 77 p. 200). The photodiode array detects photoelectron scintillations displayed by a high-gain image intensifier system.

A different approach has been developed by Tull and his colleagues at the University of Texas (see Vogt *et al.*, 1978): the Reticon® is used as the prime sensor in a spectrophotometric system in order to take advantage of the high quantum efficiency of the silicon photodiodes. This method requires cooling the array to  $-100^{\circ}\text{C}$  or below to reduce thermal leakage. With the thermal leakage thus made negligible, the photogenerated charge from low-light levels can be accumulated and read out in a single scan.

In order to measure accurately surface brightnesses, we have built at DTM an experimental instrument that in its present form can best be described as a "profile meter." The basic part of this instrument is a general purpose dewar with a capacity of about 1 liter of liquid nitrogen. This dewar has an upward-looking cold surface that is suitable for cooling either a self-scanned photodiode

array or a CCD array at the Cassegrain focus of a telescope. Initially the sensor will be a Reticon 1024S, a linear array of 1024 photodiodes each  $25\ \mu \times 2500\ \mu$  in size. Using broad spectral bands and moderately fast focal ratio telescopes, we should be able to measure accurate profiles to very low limits of surface brightness.

### References

- Ford, W. Kent, Jr., Digital imaging techniques, *Annu. Rev. Astron. Astrophys.*, **17**, 189, 1979.  
 Vogt, Steven S., Robert G. Tull, and Phillip Kelton, Self-scanned photodiode array: high performance operation in high dispersion astronomical spectrophotometry, *Appl. Opt.*, **17**, 574, 1978.

### THE 15-INCH MASS SPECTROMETER

*Louis Brown*

During the 60 years of its existence, the mass spectrometer has evolved as an analytical instrument of importance for many fields of research. Its first crude form sufficed to allow the discovery of isotopes, the enumeration and later the accurate weighing of which were its early tasks. The introduction of the electrometer tube during the 1930's removed its dependence on photographic plates for beam detection and allowed the determination of the isotopic composition of the elements to accuracies of a percent. The great increase in electronic capability that physicists acquired during the Second World War initiated technical improvements that are still continuing, thereby opening new opportunities for study. Very stable power supplies for analyzing magnet and ion accelerator allowed reproducible switching of the beam. Vibrating-reed electrometers gave remarkably linear responses for currents

in the range of  $10^{-14}$  to  $10^{-10}$  A; electron multipliers extended the range downward by more than two orders of magnitude although with poorer accuracy. A variety of chemical techniques improved the probability of thermal ionization. Last, the unavoidable and deleterious effect of the fluctuation of beam intensity has been greatly reduced by converting the electrometer output to digital form and using a small computer to measure a large number of isotopic ratios, thereby averaging out the fluctuations. Application of these techniques has seen precision improve from parts per  $10^2$  in 1950 to parts per  $10^5$  at the present time. With each improvement in accuracy, a new radiological clock has become available.

The 6-inch and 9-inch spectrometers of the Department employ these techniques and have served the staff well, as examination of the past annual reports shows. Their relatively small size, indicated by the radius of the ions in the magnetic field as given in the name of each instrument, is a disadvantage in the accurate measurement of heavy masses. To circumvent this, as well as to apply useful technical improvements, a 15-inch machine has been constructed and is now taking a heavy load of research.

The basic design was by Kenneth Burrhus, who also supervised the construction and joined in the early tests. The larger radius was achieved with a magnet having a much more compact design than the two earlier machines. This involved no design compromises, as the new magnet shows flawless optics for the lightest and the heaviest ions. The ion source and accelerator are contained in an 8-inch aluminum cube, which makes for easy maintenance and reduces interfering ions by placing the chamber walls farther away from the hot filament. Where desirable, acceleration voltages of 10 kV can be applied, compared with a maximum of 5 kV for the older machines. A moderately large liquid nitrogen cold trap, capable of holding its charge for six hours without refill, greatly reduces

the partial pressure of vapors. The vacuum at the source is typically  $4 \times 10^{-8}$  Torr one hour after loading. Rough pumping is accomplished by chemical absorption rather than a rotary pump in order to minimize the presence of organic molecules in the system.

Although the basic idea of computer control is the same as used in the smaller machines, the 15-inch has a greatly improved computer, the LSI-11. It has a rapid access memory of 28K, compared with 8K and 16K for the two older machines. It also has auxiliary memory in disks that extend the total to 278K. This has the important advantage of allowing programming to be done in high-level computer language, which allows measuring techniques to be quickly adapted to the demands of the experiment at hand, a capability often used during the last few months. Owing to the difficulty of altering old or writing new programs in machine language, the older spectrometers are effectively frozen in their routines. Small programs written in high-level language and compiled on the LSI-11 have been run on the spectrometer with 16K of memory, and the input-output devices of the three machines have been adapted to allow this kind of programming in the future.

The past few months have seen extensive experimentation on effects at the beam receiver—i.e., the Faraday cup and the multiplier—that affect accuracy. One effect that does not generally seem to be appreciated and can cause error is the escape of sputter ions from the cup, which has been observed. These ions are, of course, accelerated by potentials intended to suppress electrons. Another similar effect, which is at present only suspected, results from the release of photoelectrons produced by soft x rays that are almost certainly produced by the ions striking the bottom of the cup. The results of these experiments are being incorporated in a more elaborate beam receiver, which will (1) allow the multiplier to be used with the same slit system as the Faraday



cup, (2) have a variable slit width, (3) have a second variable-slit system upstream to reject scattered ions, (4) have an adjustable lower defining edge to remove a slight slant (about  $10^{-3}$ ) in the peak tops that occasionally appears, and do this quickly without the adjustment of focus controls, which wastes time and

beam, (5) allow use of electron-suppressor magnets in a manner that is reproducible and adjustable, (6) allow the deflection and focus of the beam before it enters the multiplier, and (7) allow room for experimentation with the beam, e.g., to determine the extent to which the soft x rays may be detrimental.

## BIBLIOGRAPHY

The publications listed below can be obtained at no charge from the Department of Terrestrial Magnetism, 5241 Broad Branch Rd., N. W., Washington, D. C. 20015. When ordering, please give reprint number(s). No reprints are available for titles marked with asterisks.

- 4501 Aldrich, L. T., Radiometric age determinations of some rocks from the Arabian Shield, Sect. 1, in *Geochronologic Data for the Arabian Shield*, U. S. Geological Survey Open-File Report No. 78-75, pp. 1-9, 1978.

— Arndt, N. T., *see* Whitford, D. J.

— Assousa, G. E., *see* Herbst, W.

— Beavan, J., *see* Evans, R.

— Bilham, R., *see* Evans, R.

— Bow, C. S., *see* White, W. M.

- 4502 Brown, L., R. S. Rajan, R. B. Roberts, F. Tera, and D. J. Whitford, A new method for determining the isotopic composition of lithium, *Nucl. Instrum. Methods*, 156, 541-546, 1978.

— Brown, L., *see* Rajan, R. S.

- 4503 Brown, R. L., Lockman, F. J., and G. R. Knapp, Radio recombination lines, in *Annual Review of Astronomy and Astrophysics*, 16, pp. 445-485, Geoffrey Burbidge, D. Layzer, and J. G. Phillips, eds., Annual Reviews, Inc., Palo Alto, California, 1978.

- 4504 Burstein, D., Quantitative results from numerical surface photometry techniques, *Amer. Astron. Soc. Photo-Bulletin*, 20, 6-12, 1979.

- 4505 Burstein, D., and C. Heiles, HI galaxy counts and reddening: variation in the gas-to-dust ratio, the extinction at high galactic latitudes, and a new

method for determining galactic reddening, *Astrophys. J.*, 225, 40-55, 1978.

— Carney, B. W., *see* Peterson, R. C.

— Davies, G. F., *see* Lux, R. A.

— Duncan, R. A., *see* Whitford, D. J.

- 4506 Evans, R., J. Beavan, R. Bilham, and G. King, A survey of Earth strain tides in Great Britain, *Geophys. J. Roy. Astron. Soc.*, 57, 119-135, 1979.

— Ford, W. K., Jr., *see* Peterson, C. J., Rubin, V. C., and Thonnard, N.

— Fredriksson, K., *see* Noonan, A. F.

- 4507 Goldstein, S. J., Jr., K. C. Turner, and R. T. Rood, Fluctuations in the background radiation at 1394 MHz, *Astrophys. J.*, 229, 455-460, 1979.

— Goldstein, S. J., Jr., *see* Rood, R. T.

- 4508 Greisen, E. W., and F. J. Lockman, The kinematics and distribution of cool HI clouds towards three galactic HII regions, *Astrophys. J.*, 228, 740-747, 1979.

— Heiles, C., *see* Burstein, D.

- 4509 Herbst, W., and G. E. Assousa, The role of supernovae in star formation and spiral structure, in *Protostars and Planets*, pp. 368-383, Tom Gehrels, ed., Univ. of Arizona Press, Tucson, 1978.

- 4510 Herbst, W., and G. E. Assousa, Supernovas and star formation, *Sci. Amer.*, 241, 138-145, 1979.

- 4511 Herbst, W., R. Racine, and J. W. Warner, Optical and infrared properties of the newly formed stars in Canis Major R1, *Astrophys. J.*, 223, 471-482, 1978.

- 4512 Hofmann, A. W., Diffusion experiments in isotope geology, in *Lectures in Iso-*

- tope Geology*, pp. 189–193, E. Jäger and J. C. Hunziker, eds., Springer-Verlag, Berlin, 1979.
- 4513 Hofmann, A. W., Geochronology of the crystalline rocks of the Schwarzwald, in *Lectures in Isotope Geology*, pp. 215–221, E. Jäger and J. C. Hunziker, eds., Springer-Verlag, Berlin, 1979.
- 4514 Hofmann, A. W., Isotope and trace element geochemistry of the Earth's mantle, in *Lectures in Isotope Geology*, pp. 203–206, E. Jäger and J. C. Hunziker, eds., Springer-Verlag, Berlin, 1979.
- 4515 Hofmann, A. W., Rb-Sr dating of thin slabs: an imperfect method to determine the age of metamorphism, in *Lectures in Isotope Geology*, pp. 27–29, E. Jäger and J. C. Hunziker, eds., Springer-Verlag, Berlin, 1979.
- Hofmann, A. W., see White, W. M.
- Huneke, J. C., see Rajan, R. S.
- Husebye, E. S., see Sacks, I. S.
- \*4516 James, D. E., Origin of high  $^{87}\text{Sr}/^{86}\text{Sr}$  ratios in central Andean calc-alkaline lavas (ext. abstr.), *Short Papers of the Fourth International Conference, Geochronology, Cosmochronology, Isotope Geology 1978*, U. S. Geological Survey Open-File Report No. 78-701, pp. 199–201, Aspen, Colorado, 1978.
- James, D. E., see Magaritz, M.
- Jezek, P. A., see Whitford, D. J.
- 4517 Kelly, W. R., F. Tera, and G. J. Wasserburg, Isotopic determination of silver in picomole quantities by surface ionization mass spectrometry, *Anal. Chem.*, **50**, 1279–1286, 1978.
- King, G., see Evans, R.
- Knapp, G. R., see Brown, R. L.
- \*4518 Kothari, B. K., K. Marti, S. Niemeyer, S. Regnier, and J. R. Stephens, Noble gas trapping during condensation: a laboratory study (ext. abstr.), *Lunar and Planetary Science X*, pp. 682–863, Houston, Texas, 1979.
- Linde, A. T., see Sacks, I. S.
- 4519 Lockman, F. J., Radio studies of the distribution of ionized gas, in *Intern. Astron. Union Symp. No. 84, The Large-Scale Characteristics of the Galaxy*, pp. 73–79, W. B. Burton, ed., D. Reidel Publ. Co., Dordrecht, Holland, 1979.
- Lockman, F. J., see Brown, R. L., and Greisen, E. W.
- 4520 Lux, R. A., G. F. Davies, and J. H. Thomas, Moving lithospheric plates and mantle convection, *Geophys. J. Roy. Astron. Soc.*, **57**, 209–228, 1979.
- Lynds, C. R., see Rubin, V. C.
- 4521 Magaritz, M., D. J. Whitford, and D. E. James, Oxygen isotopes and the origin of high  $^{87}\text{Sr}/^{86}\text{Sr}$  andesites, *Earth Planet. Sci. Lett.*, **40**, 220–230, 1978.
- Marti, K., see Kothari, B. K.
- 4522 Mittlefehldt, D. W., and G. W. Wetherill, Rb-Sr studies of CI and CM chondrites, *Geochim. Cosmochim. Acta*, **43**, 201–206, 1979.
- Nelen, J. A., see Noonan, A. F.
- 4523 Nicholls, I. A., and D. J. Whitford, Geochemical zonation in the Sunda volcanic arc, and the origin of K-rich lavas, *Bull. Aust. Soc. Explor. Geophys.*, **9**, 93–98, 1978.
- Niemeyer, S., see Kothari, B. K.
- \*4524 Noonan, A. F., R. S. Rajan, J. A. Nelen, and K. Fredriksson, Petrologic and isotopic constraints on the origin of Bhola chondrite (ext. abstr.), *Short Papers of the Fourth International Conference, Geochronology, Cosmochronology, Isotope Geology 1978*, U. S. Geological Survey Open-File Report No. 78-701, pp. 311–312, Aspen, Colorado, 1978.
- 4525 Peterson, C. J., V. C. Rubin, W. K. Ford, Jr., and M. S. Roberts, Extended rotation curves of high-luminosity spiral galaxies. III. The spiral galaxy NGC 7217, *Astrophys. J.*, **226**, 770–776, 1978.
- Peterson, C. J., see Rubin, V. C.
- 4526 Peterson, R. C., and B. W. Carney, Abundance analyses of metal-poor stars. II. Yellow spectra of five dwarfs, *Astrophys. J.*, **231**, 762–780, 1979.
- Racine, R., see Herbst, W.
- \*4527 Rajan, R. S., L. Brown, D. J. Whitford, R. B. Roberts, and F. Tera, Lithium isotopic composition in some stone meteorites (ext. abstr.), *Lunar and Planetary Science IX*, pp. 925–927, Houston, Texas, 1978.
- 4528 Rajan, R. S., J. C. Huneke, S. P. Smith, and G. J. Wasserburg, Argon 40–



- Argon 39 chronology of lithic clasts from the Kapoeta howardite, *Geochim. Cosmochim. Acta*, 43, 957-971, 1979.
- Rajan, R. S., see Brown, L., Noonan, A. F., and Scott, E. R. D.
- Regnier, S., see Kothari, B. K.
- Roberts, M. S., see Peterson, C. J., Rubin, V. C., and Thonnard, N.
- Roberts, R. B., see Brown, L., Rajan, R. S.
- Rodriguez B., A., see Sacks, I. S.
- Romanishin, W., see Rubin, V. C.
- 4529 Rood, R. T., K. C. Turner, and S. J. Goldstein, Jr., Radio sources in globular cluster fields, *Astrophys. J.*, 225, 804-807, 1978.
- Rood, R. T., see Goldstein, S. J., Jr.
- 4530 Rubin, V. C., NGC 5506: An X-ray Seyfert galaxy, *Astrophys. J.*, 224, L55-L57, 1978.
- 4531 Rubin, V. C., Extended optical-rotation curves of spiral galaxies, *Comments Astrophys.*, 8, 79-88, 1979.
- 4532 Rubin, V. C., Redshifts, in *Trans. of the Intern. Astron. Union, Reports on Astronomy, Pt. 3, XVIIA*, pp. 14-19, E. A. Müller, ed., D. Reidel Publ. Co., Dordrecht, Holland, 1979.
- 4533 Rubin, V. C., Rotation curves of high luminosity spiral galaxies and the rotation curves of our Galaxy, in *Intern. Astron. Union Symp. No. 84, The Large-Scale Characteristics of the Galaxy*, pp. 211-220, W. B. Burton, ed., D. Reidel Publ. Co., Dordrecht, Holland, 1979.
- 4534 Rubin, V. C., W. K. Ford, Jr., C. J. Peterson, and C. R. Lynds, A new mapping of the velocity field of NGC 1275, *Astrophys. J. Suppl.*, 37, 235-249, 1978.
- 4535 Rubin, V. C., W. K. Ford, Jr., and M. S. Roberts, Extended rotation curves of high luminosity spiral galaxies. V. NGC 1961, the most massive spiral known, *Astrophys. J.*, 230, 35-39, 1979.
- 4536 Rubin, V. C., W. K. Ford, Jr., K. M. Strom, S. E. Strom, and W. Romanishin, Extended rotation curves of high-luminosity spiral galaxies. II. The anemic Sa galaxy NGC 4378, *Astrophys. J.*, 224, 782-795, 1978.
- 4537 Rubin, V. C., W. K. Ford, Jr., and N. Thonnard, Extended rotation curves of high-luminosity spiral galaxies. IV. Systematic dynamical properties, Sa→Sc, *Astrophys. J.*, 225, L107-L111, 1978.
- Rubin, V. C., see Peterson, C. J., and Thonnard, N.
- 4538 Sacks, I. S., Borehole strainmeters, in *Proc. of Conf. VII Stress and Strain Measurements Related to Earthquake Prediction*, U. S. Geological Survey Open-File Report No. 79-370, pp. 425-484, 1978.
- 4539 Sacks, I. S., A. T. Linde, A. Rodriguez B., and J. A. Snoke, Shallow seismicity in subduction zones, *Geophys. Res. Lett.*, 5, 901-903, 1978.
- 4540 Sacks, I. S., S. Suyehiro, A. T. Linde, and J. A. Snoke, Slow earthquakes and stress redistribution, *Nature*, 275, 599-602, 1978.
- Sacks, I. S., see Suyehiro, K.
- Schilling, J.-G., see White, W. M.
- \*4541 Scott, E. R. D., and R. S. Rajan, Thermal history of the Shaw chondrite (ext. abstr.), *Lunar and Planetary Science X*, pp. 1095-1097, Houston, Texas, 1979.
- Smith, S. P., see Rajan, R. S.
- Snoke, J. A., see Sacks, I. S.
- Stephens, J. R., see Kothari, B. K.
- Strom, K. M., see Rubin, V. C.
- Strom, S. E., see Rubin, V. C.
- 4542 Suyehiro, K., and I. S. Sacks, P- and S-wave velocity anomalies associated with the subducting lithosphere determined from travel-time residuals in the Japan region, *Bull. Seismol. Soc. Amer.*, 69, 97-114, 1979.
- Suyehiro, S., see Sacks, I. S.
- Tapia, M. D. M., see White, W. M.
- Tera, F., see Brown, L., Kelly, W. R., and Rajan, R. S.
- Thomas, J. H., see Lux, R. A.
- 4543 Thonnard, N., V. C. Rubin, W. K. Ford, Jr., and M. S. Roberts, Radial velocities of spiral galaxies determined from 21-cm neutral hydrogen observations, *Astron. J.*, 83, 1564-1565, 1978.

- Thonnard, N., *see* Rubin, V. C.
- Turner, K. C., *see* Goldstein, S. J., Jr., and Rood, R. T.
- Warner, J. W., *see* Herbst, W.
- Wasserburg, G. J., *see* Kelly, W. R., and Rajan, R. S.
- 4544 Weidenschilling, S. J., The distribution of orbits of cosmic dust particles detected by Pioneers 8 and 9, *Geophys. Res. Lett.*, **5**, 606–608, 1978.
- 4545 Weidenschilling, S. J., Iron/silicate fractionation and the origin of Mercury, *Icarus*, **35**, 99–111, 1978.
- 4546 Wetherill, G. W., Dynamical evidence regarding the relationship between asteroids and meteorites, workshop on *Asteroids: An Exploration Assessment*, NASA Conference Publ. No. 2053, pp. 17–35, 1978.
- 4547 Wetherill, G. W., Apollo objects, *Sci. Amer.*, **240**, 54–65, 1979.
- 4548 Wetherill, G. W., Steady state populations of Apollo-Amor objects, *Icarus*, **37**, 96–112, 1979.
- 4549 Wetherill, G. W., and J. G. Williams, Origin of differentiated meteorites, in *Origin and Distribution of the Elements*, Second International IAGC Conf., held in Paris, May 1977, pp. 19–31, L. H. Ahrens, ed., Pergamon Press, New York, 1979.
- Wetherill, G. W., *see* Mittlefehldt, D. W.
- \*4550 White, W. M., A. W. Hofmann, and C. S. Bow, Isotope and LIL element geochemistry of the Galápagos Islands (ext. abstr.), *Short Papers of the Fourth International Conference, Geochronology, Cosmochronology, Isotope Geology 1978*, U. S. Geological Survey Open-File Report No. 78-701, pp. 449–450, Aspen, Colorado, 1978.
- 4551 White, W. M., and Schilling, J.-G., The nature and origin of geochemical variation in Mid-Atlantic Ridge basalts from the Central North Atlantic, *Geochim. Cosmochim. Acta*, **42**, 1501–1516, 1978.
- 4552 White, W. M., Tapia, M. D. M., and Schilling, J.-G., The petrology and geochemistry of the Azores Islands, *Contrib. Mineral. Petrol.*, **69**, 201–213, 1979.
- 4553 Whitford, D. J., and N. T. Arndt, Rare earth element abundances in a thick, layered komatiite lava flow from Ontario, Canada, *Earth Planet. Sci. Lett.*, **41**, 188–196, 1978.
- \*4554 Whitford, D. J., and R. A. Duncan, Origin of the Ninetyeast Ridge—Sr isotope and trace-element evidence (ext. abstr.), *Short Papers of the Fourth International Conference, Geochronology, Cosmochronology, Isotope Geology 1978*, U. S. Geological Survey Open-File Report No. 78-701, pp. 451–453, Aspen, Colorado, 1978.
- 4555 Whitford, D. J., and P. A. Jezek, Origin of late-Cenozoic lavas from the Banda arc, Indonesia: Trace element and Sr isotope evidence, *Contrib. Mineral. Petrol.*, **68**, 141–150, 1979.
- Whitford, D. J., *see* Brown, L., Magaritz, M., Nicholls, I. A., and Rajan, R. S.
- Williams, J. G., *see* Wetherill, G. W.

## PERSONNEL

### Staff Members

L. Thomas Aldrich  
 George E. Assousa<sup>1</sup>  
 Louis Brown  
 Scott E. Forbush, *Emeritus*  
 W. Kent Ford, Jr.  
 Albrecht W. Hofmann  
 David E. James  
 Alan T. Linde

R. Sundar Rajan  
 Richard B. Roberts, *Emeritus*  
 Vera C. Rubin  
 I. Selwyn Sacks  
 Fouad Tera  
 Norbert Thonnard  
 Kenneth C. Turner<sup>2</sup>  
 George W. Wetherill, *Director*

<sup>1</sup> Leave of absence until January 15, 1980.

<sup>2</sup> Through November 30, 1978.



*Distinguished Service Member of Carnegie Institution*

Merle A. Tuve

*Research Associates (Staff)*Albert Jambon  
Rambabu P. Ranganayaki

Frederick J. Ryerson

*Research Associate (Nonresident)*Leonidas Ocola, Instituto  
Geofísico del Peru,  
Lima, Peru*Senior Fellow*

Edward R. D. Scott

*Carnegie Fellows (Postdoctoral)*David Burstein  
Bruce W. Carney  
Lina María Echeverría  
John R. Evans<sup>3</sup>  
W. Daniel Heinze  
William Herbst<sup>3</sup>Brajesh K. Kothari  
Felix J. Lockman<sup>3</sup>  
Richard A. Lux  
Douglas O. ReVelle<sup>3</sup>  
William M. White  
David J. Whitford<sup>3</sup>*Visiting Investigators*Akira Hasegawa  
Douglas G. Mose

George R. Tilton

*Student Trainee*Marie-France Bugnon<sup>4</sup>*Collaborators*M. Aaronson, Steward Observatory, University of Arizona, Tucson, Arizona  
E. Bajaja, Instituto Argentino de Radioastronomía, Villa Elisa, Argentina  
J. Bannister P., Universidad de Chile, Santiago, Chile  
C. S. Bow, Center for Volcanology, University of Oregon, Eugene, Oregon  
M. Bracamonte, Trujillo, PeruW. B. Bryan, Woods Hole Oceanographic Institution, Woods Hole, Massachusetts  
R. Cabre, S. J., Observatorio San Calixto, La Paz, Bolivia  
M. Casaverde R., Instituto Geofísico del Peru, Lima, Peru  
R. S. Clarke, Jr., National Museum of Natural History, Smithsonian Institution, Washington, D.C.  
R. Colomb, Instituto Argentino de Radioastronomía, Villa Elisa, Argentina<sup>3</sup> Through Autumn, 1978.<sup>4</sup> April 1979.

- G. L. Davis, Geophysical Laboratory, Carnegie Institution of Washington, Washington, D.C.
- D. W. Evertson, University of Texas at Austin, Texas
- S. M. Faber, Lick Observatory, University of California, Santa Cruz, California
- K. Fredriksson, National Museum of Natural History, Smithsonian Institution, Washington, D.C.
- J. S. Gallagher, University of Illinois, Urbana, Illinois
- A. A. Giesecke, Instituto Geofísico del Peru, Lima, Peru
- C. Heiles, University of California, Berkeley, California
- C. E. Helsley, University of Hawaii, Honolulu, Hawaii
- G. S. Hurst, Oak Ridge National Laboratory, Oak Ridge, Tennessee
- K. Janes, Boston University, Boston, Massachusetts
- P. A. Jezek, University of California, Santa Cruz, California
- M. J. S. Johnston, U. S. Geological Survey, Menlo Park, California
- N. Krumm, Lick Observatory, University of California, Santa Cruz, California
- C. Krishna Kumar, Howard University, Washington, D.C.
- I. Kushiro, Geophysical Laboratory, Carnegie Institution of Washington, Washington, D.C.
- W. A. Lanford, Yale University, New Haven, Connecticut
- J. Leutgert, University of Wisconsin, Madison, Wisconsin
- B. Lewis, University of Washington, Seattle, Washington
- A. Lindh, U. S. Geological Survey, Menlo Park, California
- A. McGarr, U. S. Geological Survey, Menlo Park, California
- R. P. Meyer, University of Wisconsin, Madison, Wisconsin
- T. Murase, Geophysical Laboratory, Carnegie Institution of Washington, Washington, D.C.
- B. O. Mysen, Geophysical Laboratory, Carnegie Institution of Washington, Washington, D.C.
- A. F. Noonan, National Museum of Natural History, Smithsonian Institution, Washington, D.C.
- H. Okada, Hokkaido University, Sapporo, Japan
- G. Olafsson, Akureyri, Iceland
- G. Paris Q., Instituto Nacional de Investigaciones Geológico Mineras de Colombia, Popayán, Colombia
- M. G. Payne, Oak Ridge National Laboratory, Oak Ridge, Tennessee
- C. J. Peterson, University of Missouri, Columbia, Missouri
- R. C. Peterson, Lockheed Palo Alto Research Laboratory, Palo Alto, California
- E. Pimental, Cuzco University, Cuzco, Peru
- G. Poupeau, Centre des Faibles Radioactivités, Gif-sur-Yvette, France
- J. E. Ramirez, S. J., Instituto Geofísico de los Andes Colombiano, Bogotá, Colombia
- M. S. Roberts, National Radio Astronomy Observatory, Charlottesville, Virginia
- A. Rodriguez B., Universidad Nacional de San Agustín, Arequipa, Peru
- W. Romanishin, University of Arizona, Tucson, Arizona
- J. E. Shelby, Sandia Laboratories, Livermore, California
- D. A. Simoni, Arequipa, Peru
- T. Simkin, National Museum of Natural History, Smithsonian Institution, Washington, D.C.
- J. A. Snoke, Virginia Polytechnic Institute and State University, Blacksburg, Virginia
- R. Stefansson, The Iceland Meteorological Office, Reykjavik, Iceland
- S.-S. Sun, CSIRO Division of Mineralogy, North Ryde, Australia
- K. M. Strom, Kitt Peak National Observatory, Tucson, Arizona
- S. E. Strom, Kitt Peak National Observatory, Tucson, Arizona
- K. Suyehiro, Tokyo University, Tokyo, Japan
- S. Suyehiro, Japanese Meteorological Agency, Tokyo, Japan
- D. A. Tomandl, University of Washington, Seattle, Washington
- D. Virgo, Geophysical Laboratory, Carnegie Institution of Washington, Washington, D.C.
- F. Volponi, Universidad Nacional de Cuyo, San Juan, Argentina
- J. G. Williams, Jet Propulsion Laboratory, California Institute of Technology, Pasadena, California
- T. L. Wright, U. S. Geological Survey, Reston, Virginia



*Supporting Staff*

Gary A. Bors, Maintenance Assistant  
Kenneth D. Burrhus,<sup>5</sup> Computer Systems  
Engineer

Caroline A. Busch, Fiscal Assistant  
Richard C. Carlson,<sup>6</sup> Typist  
Mary K. Coder, Editorial Assistant  
Richard J. Collins, Maintenance Assistant  
Dorothy B. Dillin, Librarian

John B. Doak, Electronics Research Specialist

Everett T. Ecklund, Design Engineer  
John A. Emler, Laboratory Technician  
Maura Fitz-Patrick, Receptionist

Esther Gordon, Research Assistant

Bennie Harris, Caretaker

Janet C. Hunt,<sup>7</sup> Secretary

Willis Kilgore, Jr., Caretaker

Niels M. Pedersen,<sup>8</sup> Fiscal Officer

Glenn R. Poe, Electronics Research Specialist

Carl M. Rinehart, Instrument Maker

Michael Seemann, Design Engineer—Mechanical

Terry L. Stahl, Fiscal Officer

Milton T. Taylor, Instrument Maker

Marjorie L. Zeff, Laboratory Technician

<sup>5</sup> Through August 31, 1978.

<sup>6</sup> From November 7, 1978.

<sup>7</sup> Through July 31, 1978.

<sup>8</sup> Through October 31, 1978.











# *Geophysical Laboratory*

*Washington, District of Columbia*

Hatten S. Yoder, Jr.

*Director*

*Carnegie Institution of Washington Year Book 78, 1978-1979*



# Contents

Summary of Studies in Progress . . .	433	the system $\text{CaO-MgO-FeO-Fe}_2\text{O}_3\text{-SiO}_2$ (Mysen, Virgo, and Seifert) . .	519
Experimental and Field Petrology . . .	450	Structural study of glasses of akermanite, diopside, and sodium melilite compositions by Raman spectroscopy (Sharma and Yoder) . . . . .	526
Density current models of tectonic processes (Irvine) . . . . .	450	Structure and solubility of carbon dioxide in silicate glasses of diopside and sodium melilite compositions at high pressures from Raman spectroscopic data (Sharma) . . . . .	532
Lithostratigraphic variations associated with the platinum-rich zone of the Stillwater complex (Todd, Schissel, and Irvine) . . . . .	461	Quenched melts of akermanite compositions with and without $\text{CO}_2$ —characterization by Raman spectroscopy and gas chromatography (Sharma, Hoering, and Yoder) . . .	537
Trioctahedral micas in melilite-bearing eruptive rocks (Velde) . . . . .	468	Influence of melt structure on element partitioning between olivine and melt and between clinopyroxene and melt at 1 atm (Mysen, Virgo, and Seifert) . . . . .	542
Composition of magnetite in subalkaline volcanic rocks (Osborn, Watson, and Rawson) . . . . .	475	Changes in viscosity and density of melts of sodium disilicate, sodium metasilicate, and diopside composition with pressure (Scarfe, Mysen, and Virgo) . . . . .	547
A comparison of two methods for classifying basalts (Chayes) . . . . .	481	Viscosity of silicate melts as a function of pressure: structural interpretation (Mysen, Virgo, and Scarfe) . .	551
A world data base for igneous petrology (Chayes) . . . . .	484	Pressure dependence of the glass transition temperature in glasses of diopside, albite, and sodium trisilicate composition (Rosenhauer, Scarfe, and Virgo) . . . . .	556
Shock metamorphic features in Pampa del Infierno chondrite (Boctor, Bell, and Mao) . . . . .	485	Compressional wave velocity in partially molten peridotite at high pressures (Murase and Kushiro) . . . . .	559
Ultramafic Nodules and Megacrysts . .	488	Element Partitioning . . . . .	562
Garnet lherzolite xenoliths from the kimberlites of East Griqualand, South Africa (Boyd and Nixon) . .	488	Partitioning of REE between garnet peridotite minerals and coexisting melts during partial melting (Harrison) . . . . .	562
Oxygen isotopic geochemistry of ultramafic nodules and basanite from San Carlos, Arizona (Rumble, Hoering, and Boctor) . . . . .	492	Preliminary results from an electron paramagnetic resonance investigation of the site occupancy of $\text{Gd}^{3+}$ in pyrope garnet (Harrison and Weeks) . . . . .	568
Oxide minerals in layered kimberlite-carbonate sills from Benfontein, South Africa (Boctor and Boyd) . .	493	Distribution of rare earth elements in perovskite from kimberlites (Boctor and Boyd) . . . . .	572
Petrology of kimberlite from the De Bruyn and Martin Mine, Bellsbank, South Africa (Boctor and Boyd) . .	496	Diffusion and Kinetics . . . . .	574
Invariant melting behavior of mantle material: partial melting of two lherzolite nodules (Scarfe, Mysen, and Rai) . . . . .	498	Self-diffusion of Ca in diopside (McCallister, Brady, and Mysen) . . . .	574
Structure and Properties of Liquids and Glasses . . . . .	502	Intergranular diffusion in quartz-periclase reaction couples (Brady)	577
Structures of quenched melts in the system $\text{NaAlSiO}_4\text{-CaMgSi}_2\text{O}_6\text{-Mg}_2\text{SiO}_4\text{-SiO}_2$ at 1 atm (Virgo, Mysen, and Seifert) . . . . .	502		
Three-dimensional network structures of glasses in the systems $\text{CaAl}_2\text{O}_4\text{-SiO}_2$ , $\text{NaAlO}_2\text{-SiO}_2$ , $\text{NaFe}_2\text{SiO}_2$ , and $\text{NaGaO}_2\text{-SiO}_2$ at 1 atm (Virgo, Seifert, and Mysen) . . . . .	506		
Melt structures and redox equilibria in the system $\text{Na}_2\text{O-FeO-Fe}_2\text{O}_3\text{-Al}_2\text{O}_3\text{-SiO}_2$ (Seifert, Virgo, and Mysen) .	511		
Melt structures and redox equilibria in			

Interdiffusion of S and Se in tiemannite (Boctor and Brady) . . . . .	580	Studies in high-pressure crystallography (Hazen and Finger) . . . . .	632
Kinetics and mechanism of the meta- cinnabar to cinnabar transition (Boctor and McCallister) . . . . .	582	Raman study of $\text{TiO}_2$ under high pres- sures at room temperature (Mammone and Sharma) . . . . .	636
Hydrothermal Solutions and Metasomatism . . . . .	586	Raman study of $\text{GeO}_2$ in crystalline and glassy states at high pressures (Mammone and Sharma) . . . . .	640
An experimental study of mineral solubilities and the thermodynamic properties of aqueous $\text{CaCl}_2$ in the system $\text{CaO-SiO}_2\text{-H}_2\text{O-HCl}$ (Popp and Frantz) . . . . .	586	Raman study of $n\text{-H}_2$ under very high pressures at room temperature (Sharma, Mao, and Bell) . . . . .	645
Electrical conductance studies of $\text{MgCl}_2\text{-}$ $\text{H}_2\text{O}$ and $\text{CaCl}_2\text{-H}_2\text{O}$ solutions (Frantz and Marshall) . . . . .	591	Biogeochemistry . . . . .	650
Alteration of calcium-magnesium sili- cates by chloride-bearing hydro- thermal fluids (Frantz and Popp) . . . . .	596	Stable hydrogen isotope fractionation during mixotrophic growth of <i>Chlorella</i> , a unicellular green alga (Estep) . . . . .	650
Solubility of hematite in chloride- bearing hydrothermal fluids (Boctor, Popp, and Frantz) . . . . .	602	The stability of organically bonded hydrogen atoms in microalgae toward isotopic exchange with water (Estep and Hoering) . . . . .	652
Solution of a new high-pressure phase in $\text{Ca(OH)}_2\text{-H}_2\text{O}$ (Baur and Van Valkenburg) . . . . .	606	New Techniques: Apparatus and Calibration . . . . .	655
Rock permeability during meta- morphism (Rumble and Hoering) . . . . .	608	A new approach to the resolution of optical isomers: use of chiral eluants in liquid chromatography (Hare and Gil-Av) . . . . .	655
Ultrahigh-Pressure Experiments . . . . .	612	A high-temperature diamond pressure cell for single-crystal studies (Hazen and Finger) . . . . .	658
Lattice parameters and specific volume for the perovskite phase of ortho- pyroxene composition, $(\text{Mg,Fe})\text{SiO}_3$ (Yagi, Mao, and Bell) . . . . .	612	Design of the diamond-window, high- pressure apparatus for cryogenic experiments (Mao and Bell) . . . . .	659
Hydrostatic compression of $\text{MgSiO}_3$ of perovskite structure (Yagi, Mao, and Bell) . . . . .	613	Raman spectroscopy at very high pressures (Sharma) . . . . .	660
Phase relations in the system $\text{MgO-}$ $\text{FeO-SiO}_2$ between 150 and 700 kbar at $1000^\circ\text{C}$ (Yagi, Bell, and Mao) . . . . .	614	Absolute pressure measurements and their comparison with the ruby fluorescence ( $R_1$ ) pressure scale to 1.5 Mbar (Bell and Mao) . . . . .	665
Iron-magnesium distribution coefficients between spinel [ $(\text{Mg,Fe})_2\text{SiO}_4$ ], magnesiowüstite [ $(\text{Mg,Fe})\text{O}$ ], and perovskite [ $(\text{Mg,Fe})\text{SiO}_3$ ] (Bell, Yagi, and Mao) . . . . .	618	Accurate characterization of the macro- scopic flow produced in diamonds at 1.7 Mbar (Dunn, Chrenko, DeVries, Bell, and Mao) . . . . .	669
Iron-magnesium fractionation model for the earth (Mao, Bell, and Yagi) . . . . .	621	A microanalytical technique for deter- mination of aluminum in aqueous solutions (Brady and Frantz) . . . . .	676
High-pressure wüstite: cell parameters and Mössbauer spectra (Simons and Seifert) . . . . .	625	Sodium loss from sodium metasilicate melts in $\text{CO}_2$ and $\text{CO}$ atmospheres (Seifert, Virgo, and Mysen) . . . . .	679
Melting of $\text{CoSiO}_3$ and its relationship to the stability of pyroxenoids (Simons) . . . . .	626	Quench furnace controller (Hadidiacos) . . . . .	679
The B1/B2 transition in $\text{CaO}$ from shock-wave and diamond-cell ex- periments (Jeanloz, Ahrens, Bell, and Mao) . . . . .	627	Staff Activities . . . . .	683
Observations of the freezing point and density of hydrogen in the pressure range from 1 bar to 0.65 Mbar at $25^\circ\text{C}$ (Mao and Bell) . . . . .	630	Workshop on heating the diamond- anvil, high-pressure cell . . . . .	683
High-Pressure Crystallography and Spectroscopy . . . . .	632	Petrologists' Club . . . . .	684
		Washington Crystal Colloquium . . . . .	685
		Seminar series . . . . .	685
		Lectures and symposia . . . . .	685
		Bibliography . . . . .	688
		References Cited . . . . .	690
		Personnel . . . . .	707



## SUMMARY OF STUDIES IN PROGRESS

The exciting discoveries of the past year vividly portray the pioneering character of basic research at the Geophysical Laboratory. Major advances in science have been produced by staff working alone or with a few colleagues. It is evident that the Carnegie tradition of supporting creative and industrious individual scientists has great merit. The following pages record some principal new directions being taken in geosciences. The growing awareness of the limited abundance of natural resources intensifies the need to understand the accessible parts of the earth's crust. It will continue to be the primary mission of the Geophysical Laboratory to foster new approaches toward an understanding of not only the crust but also the core and mantle.

Another mission of the Geophysical Laboratory is to train young scientists to think in original ways about major geological problems and to give them the opportunity to select those problems. At the Laboratory, total immersion in a professional environment, dedication to the pursuit of knowledge, association with outstanding colleagues, and freedom of problem choice often result in a dramatic metamorphosis of the student. The records of the past Fellows are ample evidence of the effectiveness of the Geophysical Laboratory in generating leaders in science.

Increased speed of publication in the appropriate technical journals has reduced the need for extensive summaries of the large amount of work completed during the year. Only brief mention is made here of those investigations that have been prepared for publication and will appear in print before or about the same time as the present Annual Report. Further reduction of the pages in the Annual Report is anticipated for economic reasons; however, the reader

should benefit from having all the data available in accelerated journal publication.

### *Experimental and Field Petrology*

The layered intrusions formed from basic magma have served as prime examples of the major igneous processes of crystal fractionation, crystal settling, and a wide array of other crystal-liquid interactions in a relatively static state. In the past few years the simple models have been increasingly replaced by dynamic models involving convection, density currents, infiltration metasomatism, flotation, repetitive magma influx, and magma mixing. One of the leaders of this revolutionary approach to layered intrusions is *Irvine*, whose papers on magmatic infiltration metasomatism in the Muskox intrusion and on magmatic density currents and cumulus processes are soon to appear. In his laboratory work on current structure, experimental currents are scaled to natural conditions in terms of density, viscosity, and size. From these results he has estimated approximate velocities for crystal-liquid suspension currents in intrusions and has outlined a mechanism whereby such currents may deposit graded layers of crystals on the floors of intrusions. The applicability of the proposed depositional mechanism is examined on the basis of relations in the Duke Island ultramafic complex, the Skaergaard, and other layered intrusions.

*Irvine* also gives consideration to the role in layered intrusions of double-diffusive convection, a phenomenon discovered in fluid dynamic research in oceanography (where it has sometimes been termed thermohaline convection). The process is remarkable in that the liquid itself initially and rapidly becomes horizontally stratified in terms of com-

position, temperature, and density. In one variant of the process, convecting layers are separated by thin interfaces through which heat and chemical transfer occur by diffusion. Irvine points out that the magmatic analogue would be expected where a dense, high-temperature liquid underlies a less dense, lower temperature melt. He argues that this relationship probably obtained in the Muskox intrusion and illustrates how the effect may have resulted in layer formation by bottom crystallization. In support of his interpretation Irvine points out that, through much of the Muskox layered series, the olivine crystals are aligned vertically as though they had grown in place. Density relations in the Skaergaard magma appear to lead to a different variant of double-diffusive convection. Irvine suggests, therefore, that the layers in this intrusion were probably formed by current deposition rather than bottom crystallization.

These experimental studies of density currents have led *Irvine* to apply his views to major earth tectonic processes. He shows that through alternative scaling considerations the experiments can be used to simulate processes of mantle convection, and on this basis he develops novel and remarkably comprehensive tectonic models that appear to provide new insight into orogenic processes. With methods of flow visualization derived from fluid dynamics, he shows that the process of subduction probably occurs by transport of lithosphere across a converging (descending) boundary between mantle convection cells, from the top of one cell into the body of the other. He notes also that rapid-flow zones in the interiors of density currents have positions that correspond to seismic low-velocity zones in present-earth orogenic arcs, and he suggests that volcanic arc magmas may be released from the tips of mantle currents where the flow within them divides or splits. In this model the oceanic trench is located along a line where the mantle current first affects

the top surface of the material into which it is moving. In an alternative model, continental crust is also transferred across the convergence boundary between convection cells, but it is not subducted because of its low density. Instead, it is first downbuckled and metamorphosed, then intruded and covered by the arc magma, and finally its basal parts are heated by the mantle current to temperatures at which they undergo extensive melting to yield granitic plutons and batholiths. These speculations also provide new perspectives on features such as geosynclines and back-arc basins, and on the anorogenic magmatism that yields carbonatite and kimberlite intrusions.

Such dynamic models of layered intrusions and of the earth also have practical applications to the understanding of some ore deposits. *Todd* and *Schissel* of the Johns-Manville Corporation, together with *Irvine*, describe some of the lithologic and mineralogic variations that occur through a 120-m stratigraphic interval containing a platinum- and palladium-rich zone in the layered rocks of the Stillwater igneous complex in Montana. The stratigraphy is complicated, involving many layers comprising different combinations of plagioclase, olivine, bronzite, and augite, but the section can be roughly divided into repeated (cyclic) units on the basis of lithology and plagioclase composition. From field relations it is known that the Pt-rich zone is associated with one particular olivine cumulate unit, but there are no striking mineralogical changes or differences in its vicinity, apart perhaps from a slight increase in the Fe content of olivine above the zone. The zone in places is several meters thick, and it has been traced for almost the entire 45-km length of the intrusion. Economically, the zone is potentially as important as the famous Merensky Reef (a similar, extensive platinum-rich zone in the comparable Bushveld igneous complex in South Africa) and constitutes one of the



major discoveries of the past ten years for the mining industry.

The origins of the melilite-bearing rocks have not yet been deciphered because of the lack of data characterizing these rocks. *D. Velde* has been studying in detail the constituent minerals of a large suite of melilite-bearing rocks consisting of over 300 specimens of worldwide distribution. Her report this year is on the micas that are a critical phase in the hydrous varieties of melilite-bearing rocks. Most of the micas can be described as members of the phlogopite-tetraferriphlogopite series. Aside from Ba-rich members, they contain more than 70% phlogopite or less than 20%; hence, a solid solution gap appears to exist between the two end members. To account for the composition of some of the rare varieties requires consideration of a silica-rich end member such as  $\text{KMg}_3(\text{Mg}_{0.5}\text{Si}_{3.5})\text{O}_{10}(\text{OH})_2$ , synthesized by Seifert and Schreyer (1971). One specimen also yielded a silica-rich mica, but its composition reflects a ternary solid solution involving taeniolite,  $\text{KMg}_2\text{LiSi}_4\text{O}_{10}\text{F}_2$ . Velde found that, as a rule, micas from melilite-bearing eruptive rocks do not contain eastonite or Al-siderophyllite components in solid solution. In brief, the Al-poor or Al-free micas are compatible with the peralkaline bulk composition of the rocks in which they occur, and in rocks of metaluminous composition the micas are rich in Ba and Ti. The latter peralkaline micas are evidence that even in metaluminous compositions, crystallization of melilite-bearing magmas leads to peralkaline residual liquids.

A single phase, magnetite, appears to be the key to the formation of another group of important rocks. *Osborn, Watson, and Rawson* determined the composition of magnetite in volcanic rocks as one part of an experimental study on the origin of subalkaline volcanic rock series. Analyses were made both of magnetite crystals occurring in the original rock specimens and of the crystals formed experimentally in equilibrium with co-

existing liquid in sealed capsules at total pressures of 10 kbar, 1 kbar, and 1 atm. They found notable differences in magnetite composition, especially in the tholeiitic series from the Galápagos Islands and Iceland. Particularly striking are the  $\text{TiO}_2$  and FeO contents, which are highest in magnetite in the original rock, intermediate in magnetite in the 10-kbar runs, and lowest in magnetite in the 1-kbar and 1-atm runs. The results suggest that pressure on the magma has a significant effect on the composition of the magnetite crystallizing from the liquid. The indication is that the magnetite now present in the rocks crystallized from basaltic liquids at depths of about 35–75 km. A similar but less pronounced trend in magnetite composition seems to exist in the high-Al basalts and basaltic andesites from Cascades localities, Parícutin volcano, and Santorini.

Basalt is the most common igneous rock in the crust of the earth, and there appears to be a plethora of varieties if nomenclature is a reliable guide. *Chayes*, a vigorous leader in sorting out the varieties on a quantitative basis, is engaged in a broad comparison of basalt partitions yielded by the MacDonald-Katsura criterion and his own *ol-hy-di* discriminant. The procedures are in a sense complementary, the second using essentially what is left of the basalt after normative equivalents of variables used by the first have been removed, so their joint behavior is of obvious interest. Initial results of the survey were so encouraging that he combined minor modifications of the two discriminants into a classification scheme for distinguishing alkaline from subalkaline basalts.

*Chayes* has also been active as chairman of Project 163 of the International Geological Correlation Program, whose mission is to design and develop a world data base for igneous petrology. Project 163 and its individual contributors and national affiliates have embarked on a systematic scanning and encoding of published petrographic data. Its coding

forms and procedures are being adopted or adapted by numerous groups concerned with maintaining petrographic data in readily accessible form. Such a world data base will facilitate rapid, inexpensive retrieval and analysis of a vast amount of information that was obtained at considerable cost over many years but is now so widely scattered in the world literature as to be largely unavailable to the scientific community.

Interest in meteorites stems in part from the belief that they are related in some way to the primordial material that accreted to form the protoearth. The Pampa del Infierno meteorite, a highly recrystallized  $L_6$  chondrite, is also of interest because it contains phases that bear on high-pressure transitions observed in the laboratory and that are believed to occur in the earth's mantle. Its chondritic texture is poorly preserved, and it was originally classified as an achondrite. *Boctor, Bell, and Mao* now confirm that this meteorite has undergone severe shock metamorphism. Their conclusion is based on (1) the occurrence of ringwoodite in black veinlets transecting the meteorite, (2) the complete transformation of plagioclase to diaplectic glass, (3) the presence of quench (spinifex-like) textured clasts that crystallized from an impact-generated ultramafic melt, (4) kinking and partial transformation of low-Ca pyroxene to glass, and (5) the formation of troilite-iron eutectic intergrowths. The shock features observed in Pampa del Infierno are suggestive of a minimum shock pressure of 150 kbar and may exceed 300 kbar. It would appear that the high-pressure phase transitions in the ferromagnesian minerals in the chondrite are equivalent to those that may take place at high static pressures in the earth's mantle.

#### *Ultramafic Nodules and Megacrysts*

Ultramafic nodules from kimberlites and alkali basalts are believed to be the

only direct samples of the mantle from depths as great as 250 km. The temperatures and depths last recorded by the minerals in arrays of these nodules give some notion of how the temperature changes with depth in the earth. The nodules and related megacrysts from kimberlites and the nodules from alkali basalts yield geochemical information on the source region of the magmas that carry them to the surface. Although some of these rocks are metasomatically altered, the nature of the alteration yields geochemical data on the metasomatizing fluid and the rocks or magmas with which it last equilibrated at even greater depths. These nodules, which retain a large measure of their previous state, and their host magma, which probably has responded rapidly to accommodate surficial conditions, are still the most direct source of petrologic information on the upper mantle of the earth.

*Boyd and Nixon* have shown that the depths of origin estimated for a suite of garnet lherzolite xenoliths from the kimberlites of East Griqualand, South Africa, are 35–40 km shallower than those estimated for suites of high-temperature ( $>1100^\circ\text{C}$ ) lherzolites erupted within the boundaries of the Kaapvaal craton. They suggest that the kimberlites were erupted from the base of the lithosphere and that this horizon is shelving from beneath the Kaapvaal craton toward the Indian Ocean. Temperature-depth points for the East Griqualand lherzolites plot in and on the edge of the graphite stability field, and this relationship correlates well with the fact that diamonds have never been found from the East Griqualand kimberlites. Thus, xenolith studies have a practical application in the worldwide search for diamondiferous kimberlites.

The layered kimberlite-carbonate sills of Benfontein, South Africa, have been commonly cited as evidence of a genetic relationship between kimberlites and carbonatites. According to *Boctor* and *Boyd*, the oxide minerals in the carbonate



layers from Benfontein are like those of the kimberlite; both are Cr bearing and do not show the Mn enrichment observed in magnetite and ilmenite from carbonatites. Coexisting ilmenite and spinel in the Benfontein layered sills have similar Mn and Mg contents. The differential partitioning of these elements between the spinel and ilmenite phases that has been observed in carbonatites is lacking at Benfontein, and a xenocrystic origin of ilmenite is suggested. The occurrence of kimberlite and carbonate rock (not sövite) at Benfontein does not necessarily support a genetic relation between kimberlites and carbonatites.

Kimberlite from De Bruyn and Martin Mine, Bellsbank, South Africa, differs from many other kimberlites in the lack of magnesian-rich ilmenite, in the spinel zoning trends, and in the remarkable abundance of REE and Nb in its perovskite. The various compositions of spinels in Bellsbank kimberlite, as in other kimberlites, describe an overall trend of enrichment in Fe and Ti, but unlike most kimberlitic spinels, they are deficient in Al and show progressive decrease in this element with progressive crystallization. The core-to-mantle compositional trend of spinels from kimberlite at De Bruyn and Martin Mine is similar to the compositional trend observed in lunar spinels from mare basalts. *Boctor* and *Boyd* note that the high REE content of perovskite (13.3–14.5 wt %) and its remarkable enrichment in light REE, parallel the high total REE content of Bellsbank kimberlite in comparison to other kimberlites and its extremely fractionated REE pattern.

A variety of geothermometers and geobarometers were tested by *Finnerty* and *Boyd* to ascertain their degree of agreement when applied to garnet lherzolite nodules from northern Lesotho. Broad agreement obtained for temperatures estimated from the diopside solvus and from Fe-Mg partitioning between clinopyroxene and garnet shows that differences in equilibration temperature

found for these lherzolites are likely to be real and are unlikely to be caused by disequilibrium. When the diopside solvus (Lindsley and Dixon, 1976) is used as a thermometer and the system  $\text{MgSiO}_3\text{-Al}_2\text{O}_3$  (MacGregor, 1974) as a barometer a plot for the Lesotho geotherm is obtained that exhibits minimum scatter of points and that is consistent with the diamond  $\rightleftharpoons$  graphite curve (Kennedy and Kennedy, 1976), the solidus for kimberlite melting in the presence of  $\text{H}_2\text{O}$  and  $\text{CO}_2$ , and the melting of phlogopite (Eggler and Wendlandt, 1979).

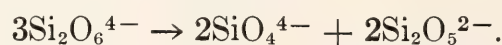
The melting behavior of two ultramafic nodules was investigated by *Scarfe*, *Mysen*, and *Rai* to determine the sequence of phases consumed, the composition of the initial melts, and the influence of the state of previous depletion of basaltic components. They used a  $^{185}\text{W}$  spike, which partitions almost entirely into the liquid, to distinguish and estimate the amount of the liquid phase. The isobaric invariant nature of the melting was confirmed at 20 and 35 kbar for a spinel-bearing nodule and at 20 kbar for a garnet-bearing nodule. At 20 kbar clinopyroxene is the first phase to be consumed on melting, whereas garnet is consumed first at 35 kbar. These observations are critical to the REE and trace element content of derivative magmas. Equilibrium is obtained within an hour, so partial melting may be a common feature in nodules in transit to the surface at longer time periods. At 20 kbar the spinel-bearing nodule gives rise initially to an olivine tholeiitic liquid; however, the more depleted garnet-bearing nodule has a higher solidus temperature, and its initial liquid is slightly richer in normative olivine. At 35 kbar the initial liquid of the less depleted spinel-bearing nodule is of alkali picrite composition. The petrologic implications of these observations are far-reaching in regard to the composition of initial magmas, their trace element content, and large volume generated within a small temperature interval.

*Structure and Properties of  
Liquids and Glasses*

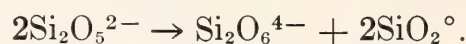
The phase equilibrium diagram has been a keystone in the understanding of the evolution of the igneous rocks. The temperature-composition surface (liquidus) representing the first appearance of crystals from liquid has been determined for hundreds of pertinent systems, yet the structures of the crystals and liquid that determine these equilibria have generally been examined only at room temperature and pressure. Structures of crystals and quenched liquid, now glass, determined at room temperature and pressure are not the same as those existing at the high temperatures and pressures on the basis of observed heat effects and changes in physical properties. Although some attention has been given to the structure of crystals at elevated temperatures (see section on High-Pressure Crystallography and Spectroscopy), the structure of the liquid has until recently been extremely difficult to characterize. In the belief that the structure of the liquid is probably as important as that of the crystals in determining phase equilibria and, in fact, the physical and chemical properties of magma, a major effort is being made to establish the principles that govern the properties of liquid and their coexisting crystals at elevated temperatures and pressures. Initially an understanding of the structure of glass is needed, then the structural changes at the transition from glass to supercooled liquid, and eventually the structure of the supercooled liquid and the liquid itself.

A consensus of the new views developed this year on the major structural units believed to be present in multi-component quenched melts has emerged. At least five structural units are recognized in silicate glasses having compositions relevant to magmas: monomers ( $\text{SiO}_4^{4-}$ ), dimers ( $\text{Si}_2\text{O}_7^{6-}$ ), chains ( $\text{Si}_2\text{O}_6^{4-}$ ), sheets ( $\text{Si}_2\text{O}_5^{2-}$ ), and three-dimensional network units ( $\text{SiO}_2^\circ$ ). When

a crystal such as a pyroxene melts the primary chains appear to disproportionate in part as follows:



A sheet structure may partially break down in the melt according to the mass-balance equation:



In a similar fashion the melting of a pyrosilicate such as melilite appears to take place in part in the following way:



The extent of these disproportionations and the relative abundance of the units can only be approximated in the absence of suitable standards. Some of the uncertainty in the interpretation of the Raman bands from which these units are deduced arises from the difficulty of resolving the envelopes of the broad bands, especially for the higher polymeric species.

The species deduced from the Raman spectra are compared by *Sharma*, *Hoering*, and *Yoder* with those obtained from the measurements on volatile trimethylsilyl (TMS) derivatives of glass using gas chromatography. The chromatograms for crystalline  $\text{Ca}_2\text{MgSi}_2\text{O}_7$  yield the expected  $\text{Si}_2\text{O}_7^{6-}$  derivative; however, the glass of equivalent composition is completely different and consists of an array of monomers to pentamers. Although there is no quantitative calibration of the TMS technique, the TMS data generally support the conclusions on types of species obtained from the Raman spectra.

In systems involving the melting of two different structures, the melt structure may or may not involve reaction of the disproportionating units. According to *Virgo*, *Mysen*, and *Seifert* no reaction takes place where  $\text{Si}_2\text{O}_6^{4-}$ ,  $\text{Si}_2\text{O}_5^{2-}$ , and  $\text{SiO}_2^\circ$  units are involved. On the other hand,  $\text{SiO}_4^{4-}$  is unstable in the presence of  $\text{SiO}_2^\circ$  units, forming either  $\text{Si}_2\text{O}_6^{4-}$  or  $\text{Si}_2\text{O}_5^{2-}$ , depending on the ratio of  $\text{SiO}_4^{4-}$  to  $\text{SiO}_2^\circ$ .



In a study of the structure of quenched melts along the simple joins  $\text{SiO}_2\text{-NaAlO}_2$ ,  $\text{SiO}_2\text{-NaGaO}_2$ ,  $\text{SiO}_2\text{-NaFeO}_2$ , and  $\text{SiO}_2\text{-CaAl}_2\text{O}_4$ , *Virgo*, *Seifert*, and *Mysen* conclude that the melt structure is probably a three-dimensional array of tetrahedrally coordinated units in which the trivalent cation is charge-balanced by the proximity in the melt structure of an alkali or an alkaline-earth cation. No evidence is found for short-range ordering of the tetrahedrally coordinated cations. They suggest that the presence of two distinct Si-O stretch bands in the Raman spectra of glasses with a three-dimensional network structure favors the view that there are two different three-dimensional complexes in the melt.

The studies on the glasses of these simple systems were undertaken to lay the foundation for understanding the changes imposed by different redox states of iron, volatiles, and especially  $\text{Al}_2\text{O}_3$  and  $\text{Fe}_2\text{O}_3$ . *Seifert*, *Virgo*, and *Mysen* used both Mössbauer and Raman spectroscopy to investigate the redox states of iron and the structure of the quenched melt in the system  $\text{NaO-FeO-Fe}_2\text{O}_3\text{-Al}_2\text{O}_3\text{-SiO}_2$  as a function of temperature and  $f_{\text{O}_2}$ . Quenched melts tend to be more polymerized under oxidizing conditions and less polymerized under reducing conditions. Using the same spectroscopic techniques *Mysen*, *Virgo*, and *Seifert* examined the quenched melts in the system  $\text{CaO-MgO-FeO-Fe}_2\text{O}_3\text{-SiO}_2$ . The proportions of the monomer and sheet components increase with increasing Ca/Mg of the melt. They also discovered that the  $\text{Fe}^{2+}/\text{Fe}^{3+}$  decreases as Ca/Mg increases. Because ferric iron does not enter the silicate network in these melts, the structure and chemical and physical properties of silicate melts with predominantly alkaline earths as network modifiers (as in basalts) may be less sensitive to changes of  $f_{\text{O}_2}$  than melts richer in alkalis (as in andesite-dacite).

*Mysen* and *Virgo* investigated the influence of  $\text{CO}_2$  on the structure of quenched melts of diopside ( $\text{CaMgSi}_2\text{O}_6$ )

and sodium melilite ( $\text{CaNaAlSi}_2\text{O}_7$ ) compositions. With increasing  $\text{CO}_2$  content the proportion of chain structures increases relative to both monomer and sheet structures. When Al is present, as in quenched melt of sodium melilite composition, it becomes a network modifier, forming  $\text{CaAl}_2\text{O}_4$  complexes, for example, in the presence of  $\text{CO}_2$ , whereas in the absence of  $\text{CO}_2$ , Al becomes a network former. In another study of  $\text{CO}_2$ -charged melts of sodium melilite and diopside compositions, *Sharma* confirms the view that  $\text{CO}_3^{2-}$  is the major carbon species in such melts. He found spectral evidence indicating that the carbonate ion has a lower symmetry in these melts, as in some crystalline carbonates. He believes that the symmetry change is the result of strong interaction of the carbonate ion with the silicate framework. This conclusion is at variance with that of *Mysen* and *Virgo* given above, wherein the carbonate complexes are stabilized with the network modifiers, i.e.,  $\text{Ca}^{2+}$ , as in crystalline carbonosilicates. According to *Sharma*, *Hoering*, and *Yoder*, the Raman bands in the  $\text{CO}_2$ -charged glasses of akermanite ( $\text{Ca}_2\text{MgSi}_2\text{O}_7$ ) composition are similar to those in glass without  $\text{CO}_2$ , and from this point of view it appears that the presence of  $\text{CO}_2$  has not brought about major changes in the silicate framework. This conclusion is at variance with those drawn on the basis of the trimethylsilyl derivatives of these glasses.

The melt structure also has an important influence on element partitioning between crystals and liquid. *Mysen*, *Virgo*, and *Seifert* determined REE and Ni partition coefficients between crystals and melts as a function of melt composition under isothermal conditions at 1 atm. For example, in the system  $\text{CaMgSi}_2\text{O}_6\text{-NaAlSiO}_4\text{-SiO}_2$ , the melts along the  $1200^\circ\text{C}$  isotherm consist of combinations of a three-dimensional network, sheets ( $\text{Si}_2\text{O}_5^{2-}$ ), and chains ( $\text{Si}_2\text{O}_6^{4-}$ ), where the proportion of the least polymerized component ( $\text{Si}_2\text{O}_6^{4-}$ ) increases with in-

creasing diopside component in the melt. The activity coefficients ( $\gamma$ ) of REE, Mn, and Ni in the melts appear to decrease as a logarithmic function of nonbridging oxygens to bridging oxygens. Careful calibration of such ratios against partition coefficients may facilitate calculation of the trace element partition coefficients between rock-forming minerals and melts.

Previous viscosity measurements made at this Laboratory on anhydrous silicate melts of geological interest have shown an isothermal decrease in viscosity with increasing pressure. All the melts investigated have highly polymerized melt structures at 1 atm. To test the general validity of the negative pressure dependence of viscosity, three melts (sodium disilicate, sodium metasilicate, and diopside) with less polymerized structures at 1 atm were studied by *Scarfe*, *Mysen*, and *Virgo*. These melts show a positive pressure dependence of the viscosity up to 20 kbar, and together with the observation that inorganic and polymer liquids commonly exhibit increasing viscosities with pressure, suggest that the results obtained for highly polymerized melts are not generally applicable. It was also observed that as a function of pressure, densities of highly polymerized melts increase at a greater rate than those of less polymerized melts, and this observation provides further evidence for the contrasting behavior of these two types of melt.

Structural information on the contrasting behavior of highly polymerized versus less polymerized melts with temperature and pressure is presented by *Mysen*, *Virgo*, and *Scarfe*. Using quenched melt of  $\text{CaMgSi}_2\text{O}_6$  composition as an example of the less polymerized melts, they found that the  $\text{SiO}_4^{4-}$  monomer becomes more abundant at higher temperature (constant pressure) and at lower pressure (constant temperature). In view of these and other data, they suggest that in melts that are less polymerized than sheets ( $\text{Si}_2\text{O}_5^{2-}$ ) the

viscosity of the melt is positively correlated with the degree of polymerization (e.g., proportions  $\text{SiO}_4^{4-}/\text{Si}_2\text{O}_6^{4-}$  and  $\text{Si}_2\text{O}_6^{4-}/\text{Si}_2\text{O}_5^{2-}$ ). Conversely, in highly polymerized silicate melts, such as albite, the viscosity decreases with increasing pressure, and no significant pressure-induced structural changes are discernible with Raman spectroscopy.

The pressure effect on the temperature of the glass transition ( $T_g$ ) should correlate with the pressure dependence of the viscosity of the melt according to *Rosenhauer*, *Scarfe*, and *Virgo*, because there are close structural similarities between a glass and its melt, particularly at temperatures near the transition from glass to supercooled liquid. The measurement of  $T_g$  by differential thermal analysis (DTA) experiments on glasses of diopside, albite, and sodium trisilicate composition to 7 kbar supports this idea. Glasses with a less polymerized structure at 1 atm, e.g., diopside, show an increase in  $T_g$  with pressure, whereas highly polymerized glasses, e.g., albite, show a decrease. This behavior parallels the contrasting pressure dependence of the viscosity of the corresponding melts.

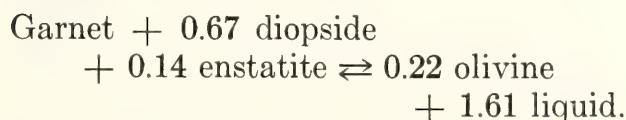
The elastic wave velocity of partially molten rocks is exceptionally important in the detection of liquid in the crust and mantle. *Murase* and *Kushiro* measured the compressional wave velocities at 5 and 10 kbar in a spinel lherzolite as a function of degree of melting. Large decreases in wave velocity and attenuation with the onset of melting were observed. They also examined the textural distribution of melt in the partially melted sample and found that 27% melting is required before the crystal grains are completely surrounded with liquid. According to *Murase* and *Kushiro*, the low-velocity zone in the mantle may have as much as 7–9% by volume anhydrous melt and a smaller amount of hydrous melt. Their study is the first successful attempt to measure the seismic properties of partially molten rocks under pressure.



*Element Partitioning*

Because of the widely held belief that trace elements in a rock should be useful in recording the geochemical properties of the source of a rock as well as its conditions of formation, a concerted effort has been made to calibrate the partitioning of elements in terms of  $P$ ,  $T$ ,  $f_{O_2}$ , bulk composition, volatile constituents, kinds and proportion of phases, site preference, and a host of other variables that appear to affect element distributions. The large number of variables affecting trace elements has dampened the initial enthusiasm for interpreting element distributions. The principles remain valid, however, and the wide range of concentration of trace elements relative to major elements is such a distinct advantage that calibration of the variables is even more desirable.

*Harrison* has investigated the partitioning behavior of rare earth elements (REE) among garnet, clinopyroxene, orthopyroxene, olivine, and liquid as a function of the degree of partial melting of a natural garnet peridotite. She found that crystal-liquid partition coefficients increase by as much as 100% as the REE content in the melt is increased from 2% to 38% and hence questions the common assumption of constant partition coefficients for REE in petrogenetic modeling. The experimentally observed REE liquid abundances can be satisfactorily modeled by an equilibrium partial melting model in which the melting reaction is



The content of light REE in even the smallest percentages of melt is, however, lower than that typical of alkalic basalts. *Harrison* concludes that the REE characteristics of such magmas may not be generated by partial melting of a garnet peridotite source unless that material is already rich in light REE.

The site occupancy of  $Gd^{3+}$  in pyrope

was investigated by *Harrison* and *Weeks* using electron paramagnetic resonance. The spectra of  $Gd^{3+}$  suggest that this ion occupies two crystallographic positions in pyrope. The crystal-field parameters of one of these sites have been identified and indicate that it is the dodecahedral site normally occupied by  $Mg^{2+}$ . Substantial lattice distortion occurs around the  $Gd^{3+}$  ion in this site. These investigators suggest that the second site may be the octahedral site normally occupied by  $Al^{3+}$ . Preliminary data indicate that some change in the relative occupancy of the two sites occurs as the  $Gd^{3+}$  content of the pyrope is changed. Thus, it is possible that multi-site substitution of REE in garnets may explain why, as noted last year, the partitioning does not follow Henry's law.

The distribution of REE in perovskite from four kimberlites that differ in their mode of emplacement and abundance of carbonate segregations was determined with the electron microprobe by *Boctor* and *Boyd*. The abundance of REE in perovskite from kimberlite varies widely from 3.1 to 13.4 wt %. Perovskite from kimberlitic dikes and sills seems to be richer in REE than perovskite from diatremes. The distribution patterns of REE in perovskite from kimberlite are suggestive of a large degree of fractionation with remarkable enrichment in the light REE (78% to 89% of total REE content) relative to the heavy REE. Thus, if perovskite is abundant in a kimberlite, its REE distribution pattern may influence the whole-rock REE pattern. The enrichment of perovskite in light REE is attributed either to the partitioning of these elements between perovskite and an immiscible carbonate liquid or to equilibration of perovskite with a  $CO_2$  vapor enriched in light REE.

Partition coefficients for nickel between olivine and an aluminous anhydrous silicate melt have been determined by *Mysen* as a function of nickel content under isothermal conditions (1300°C) at pressures between 1 atm and 20 kbar.

The partition coefficients are independent of nickel content until 1000 ppm Ni is dissolved in the forsterite; thus Henry's law is applicable to this composition. No pressure dependence of this concentration limit was observed. The partition coefficients are pressure dependent at both higher and lower nickel concentration. The pressure dependence is less pronounced in the olivine with nickel content above 1000 ppm because the activity coefficient of nickel in the coexisting liquid varies with pressure, presumably as a consequence of pressure-induced structural changes of the silicate melt.

Fractional crystallization of olivine results in a lowering of the nickel content of the magma, but the extent to which this result occurs depends on both the nickel content of the silicate magma and the confining pressure. Mysen concludes that the nickel content of magma derived from the upper mantle is commonly controlled by fractional crystallization that involves phases other than the major rock-forming minerals.

### *Diffusion and Kinetics*

Diffusion coefficients for rock-forming minerals are essential criteria for evaluating intracrystalline processes such as exsolution or homogenization of zoning. Previous attempts to obtain diffusivities for clinopyroxenes have not been successful. *McCallister*, *Brady*, and *Mysen* have measured the diffusion of  $^{45}\text{Ca}$  in diopside using a thin-film geometry and a beta-track mapping technique. Interpretation of the beta-track diffusion profiles obtained with an automated optical densitometer at the Department of Terrestrial Magnetism was complicated by the large penetration distances ( $>100\ \mu\text{m}$ ) observed for  $^{45}\text{Ca}$  beta particles in diopside. A new analysis that took into account the large beta penetrations led to a self-diffusion coefficient for Ca in diopside of  $2 \times 10^{-11}\ \text{cm}^2/\text{sec}$  at  $1300^\circ\text{C}$ . The value is the first known laboratory

determination of a diffusion coefficient in pyroxenes.

*Brady* has determined an upper bound to the possible rate of intergranular diffusion in crystalline rocks at elevated temperatures and pressures. By monitoring the rate of growth of a polycrystalline reaction rim in the presence of an aqueous solution, the measurement of intergranular diffusion was attempted. Although rim growth was too slow to detect after an initial growth spurt, the data limit the effective diffusivity of silicon and probably other major elements to values below  $10^{-9}\ \text{cm}^2/\text{sec}$ . This result places important constraints on the quantitative evaluation of material transport in crystalline rocks.

*Boctor* and *Brady* have obtained measurements of sulfur and selenium interdiffusion in the tiemannite ( $\text{HgSe}$ )-metacinnabar ( $\text{HgS}$ ) series. Electron microprobe profiles of tiemannite crystals that were packed in  $\text{HgS}$  powder and annealed in evacuated silica tubes show that the tiemannite remains compositionally binary, and a special application of the Boltzmann-Matano solution can be applied to the diffusion equation. Interdiffusion coefficients in the range  $10^{-11}$  to  $10^{-12}\ \text{cm}^2/\text{sec}$  were obtained for temperatures of  $500^\circ$ – $700^\circ\text{C}$  with an activation energy of  $105 (\pm 12)\ \text{kJ/mole}$ . The interdiffusion coefficients determined for tiemannite are larger than sulfur self-diffusion coefficients in sulfides of the same structure, such as sphalerite.

In many mercury ores metacinnabar, a high-temperature polymorph of  $\text{HgS}$  containing minor amounts of Zn, Fe, and Se in solid solution, coexists with the low-temperature polymorph cinnabar. An isothermal rate study was undertaken by *Boctor* and *McCallister* to evaluate the effect of impurities on the metacinnabar-cinnabar transition, a nucleation and growth process. Impurities as low as 0.3 to 0.5 wt %  $\text{ZnS}$  and 0.6 to 1.0 wt %  $\text{FeS}$  in solid solution in metacinnabar reduce the rate of transition significantly by increasing the barrier for nucleation



of cinnabar. The rate decreases with increase in impurity content and increases with increase in temperature. In mercury ores metacinnabar contains much higher concentrations of Zn and Fe (up to 5.0 wt % Zn and 3.0 wt % Fe) than those used in the experiments. Such high concentrations are probably responsible for the metastable coexistence of the two polymorphs through geologic time.

### *Hydrothermal Solutions and Metasomatism*

Chemical transport in many geological systems occurs by means of dissolved species in an intergranular aqueous fluid phase. For this reason it is necessary to identify the species being transported, measure their solubilities, and ascertain the compositions of fluids in equilibrium with the various mineral assemblages. Because the chloride ion is commonly found in fluid inclusions in the minerals, it is probably an important ionic species in geochemical transport and accordingly was used in the experimental studies.

*Popp* and *Frantz* completed an experimental study of speciation and free energy of aqueous  $\text{CaCl}_2$  in the system  $\text{CaO-SiO}_2\text{-H}_2\text{O-HCl}$  in the range 1–2 kbar and 425°–600°C. The Ag-AgCl buffer technique was used to determine the concentrations of total calcium and associated HCl in the fluid in equilibrium with the mineral assemblage wollastonite + quartz as a function of temperature and pressure. At 2 kbar and temperatures greater than ~550°C, associated  $\text{CaCl}_2^\circ$  is the dominant calcium species in the fluid. The data obtained at lower temperatures suggest that appreciable dissociation of  $\text{CaCl}_2^\circ$  may occur at 2 kbar and 425°C, but the data are not conclusive. Solubility constants for minerals in the system  $\text{MgO-CaO-SiO}_2\text{-H}_2\text{O-HCl-CO}$  were calculated using the data from this study and data previously obtained on aqueous  $\text{MgCl}_2$ . These data can be applied to some of the reactions taking

place in the metamorphism of a siliceous dolomite, for example.

In another approach to obtaining the character of species in solution *Frantz* and *Marshall* measured the electrical conductance of aqueous solutions containing magnesium chloride or calcium chloride from 25° to 600°C at pressures up to 4000 bars. Their efforts were directed toward determining the effect of temperature and pressure on the speciation of these salts. They found evidence that the salts remain completely dissociated at temperatures up to 400°C at densities above 0.7 g cm<sup>-3</sup>. At higher temperatures and lower densities, however, significant concentrations of ion pairs are present. These conclusions are in accord with the previous solubility experiments of *Frantz* and *Popp* and those of *Popp* and *Frantz* reported above.

The solubility constants for minerals in the system  $\text{MgO-CaO-SiO}_2\text{-HCl}$  at 500°C and 2 kbar were used by *Frantz* and *Popp* to calculate the evolution of the compositions of the fluid and the solid alteration products that result from the interaction of Ca-Mg silicate mineral (diopside) with increasing amounts of fluid containing a range of different total chloride concentrations. High total chloride (2.0 molal) in the fluid results in Si-Mg enrichment in the solids and Ca enrichment in the fluid, whereas low total chloride (0.008 molal) in the fluid results in Mg enrichment in the solids and Ca-Si enrichment in the fluid.

Solution equilibria in the system  $\text{Fe}_2\text{O}_3\text{-H}_2\text{O-H}_2\text{-HCl}$  were investigated by *Boctor*, *Popp*, and *Frantz* in the temperature range 400°–600°C at 1 and 2 kbar using a rapid quench hydrothermal technique and a modification of the Ag-AgCl buffer method. Total dissolved iron and associated HCl in equilibrium with hematite were measured, and changes in the total Fe concentration as a function of the molality of HCl were used to characterize the predominant species of iron in the fluid. In the temperature range 400°–600°C at a pressure of 1–2 kbar,

$\text{FeCl}_2$  seems to be the predominant species in the fluid. Thus, the speciation of Fe differs from that of magnesium, which is present as  $\text{MgCl}_2$  in the temperature range  $550^\circ\text{--}600^\circ\text{C}$  and 2 kbar and as both associated ( $\text{MgCl}_2$ ) and dissociated ( $\text{Mg}^+$ ) species at temperatures between  $400^\circ$  and  $550^\circ\text{C}$  and 2 kbar, as determined previously by Frantz and Popp. Free energy of formation of aqueous  $\text{FeCl}_2$  was calculated at 1 and 2 kbar over the temperature range of the experiments.

A novel approach to determining the solution of portlandite,  $\text{Ca}(\text{OH})_2$ , in water as a function of pressure was undertaken by Baur and Van Valkenburg. From visual observations in a diamond-window, high-pressure cell, they found  $\text{Ca}(\text{OH})_2$  to be very soluble at pressures above 2.8 kbar. They also observed formation of a new compound thought to be  $\text{Ca}(\text{OH})_2 \cdot n\text{H}_2\text{O}$ .

Rumble and Hoering believe that rock permeability is a factor as important in metamorphism as pressure gradient and fluid viscosity. Using the combined methods of chemical petrology and oxygen isotope geochemistry, they have established criteria for classifying rocks according to relative permeability. Rocks that attained chemical and isotopic equilibrium with a homogeneous fluid, despite premetamorphic heterogeneity, are classified as more permeable. Rocks that failed to equilibrate with a homogeneous fluid are less permeable. Calc-silicate rocks have been found to be substantially more permeable because of their capacity to expel large amounts of fluid (in this case,  $\text{CO}_2$ ) under peak metamorphic conditions. Micaceous quartzites, in contrast, are less permeable because they have a smaller amount of volatiles ( $\text{H}_2\text{O}$ ) to lose. These investigators measured in detail the  $^{18}\text{O}$ - $^{16}\text{O}$  ratios in a series of rocks metamorphosed at the same time under similar  $P$ - $T$  conditions to ascertain their variation with the amount of volatile released and hence their permeability.

### *Ultrahigh-Pressure Experiments*

On the basis of available geobarometers and geothermometers, the deepest sample from the mantle available at the surface for study is a nodule from a Lesotho kimberlite pipe, blasted out from about 250 km. The principal minerals in this sample are olivine, orthopyroxene, clinopyroxene, and garnet. To understand the structure and properties of the earth it is necessary to know the depth to which these minerals are stable and their successive breakdown products. In a systematic study of these minerals at various ultrahigh pressures, Bell and Mao and their colleagues have concentrated this year on the olivines and pyroxenes that lie primarily in the  $\text{MgO-FeO-SiO}_2$  system. Using their newly designed diamond-anvil, high-pressure cell, they examined the properties of those phases in the 150–700 kbar range at about  $1000^\circ\text{C}$ . These pressures are equivalent to depths in the mantle of approximately 600–1700 km, a region that includes most of the mantle. They discovered that at pressures above 150–200 kbar most of the minerals stable in the earth's crust and upper mantle convert to new structures dominated by spinel, a modified-type spinel (the so-called beta phase), ilmenite, stishovite, perovskite, and magnesiowüstite. Of these the perovskite structure is dominant, being denser than its component oxides. Yagi, Mao, and Bell studied the lattice parameters, compressibility, and phase relations in some detail to construct phase diagrams that apply to geochemical models of the mantle. They found that the silicate phase with perovskite structure can form with no more than 20 mole % concentration of the iron end member and that more iron-rich bulk compositions precipitated magnesiowüstite. A very important discovery in these experiments was that magnesiowüstite strongly partitions iron relative to the silicate with perovskite structure. On the basis of the differential



densities of those phases, *Mao*, *Bell*, and *Yagi* constructed a new fractionation model for the formation of the earth. Because of gravitational instability, the magnesiowüstite phase would sink toward the center and lose some of its iron to the core by chemical reduction or disproportionation. The residual, lower density magnesiowüstite would rise and become remixed with the silicate perovskite above. Reequilibration with the iron-bearing silicate with perovskite structure would again lead to sinking of the magnesiowüstite, and the process would continue to cycle. In this way the earth would become differentiated into the present earth structure deduced from seismic evidence.

Because wüstite may be an important phase in the lower mantle or even in the outer core, its crystal chemistry at high pressures is of considerable interest. *Simons* and *Seifert* determined the variation of the lattice parameter with temperature up to 1200°C and pressures up to 45 kbar for wüstite in equilibrium with metallic iron. At all temperatures the lattice parameter increases with increasing pressure because of its changing composition, and approaches a constant value of 4.323 Å, as has been previously observed. But in contrast to previous work, *Simons* and *Seifert*, utilizing Mössbauer spectroscopic and wet chemical analyses, demonstrate that wüstite, with a lattice constant of 4.323 Å, is still a nonstoichiometric phase. The  $\text{Fe}^{2+}/(\text{Fe}^{2+} + \text{Fe}^{3+})$  in wüstite in equilibrium with iron metal increases with pressure up to 31 kbar at 700°C and up to 60 kbar at around 1200°C but decreases with pressure above 200 kbar at around 1200°C (*Mao*, *Year Book* 70). *Simons* and *Seifert* consider it unlikely that stable wüstite becomes stoichiometric under any conditions of pressure and temperature.

Other oxides in addition to MgO-FeO-SiO<sub>2</sub> are important in phases stable at depths greater than 200 km, so *Jeanloz* and *Ahrens* at the California Institute of

Technology joined with *Mao* and *Bell* to study calcium oxide. A possible phase transition in CaO at approximately 650–700 kbar had been noted previously in shock-wave experiments, and visual as well as *in situ* x-ray diffraction confirmation was desired using the diamond-anvil, high-pressure cell. The transition in CaO was indeed observed in the static experiments in the predicted pressure range, and was found by x-ray diffraction to result from a change in coordination from six-fold to eight-fold. This transition could have important implications for the possible enrichment of CaO in the earth's deep mantle in a complex oxide or a silicate perovskite rather than in the simple oxide mixture assumed in the past.

For the first time at room temperature, *Mao* and *Bell* succeeded in pressurizing hydrogen until it became a solid at a pressure of 57 kbar. In the experiments with a diamond-anvil, high-pressure cell designed for operation at cryogenic as well as high temperatures, the solid hydrogen was further pressurized to 700 kbar. At 350 kbar *Mao* and *Bell* measured the density of the new solid form of hydrogen to be 0.6–0.7 g/cm<sup>3</sup>; a value of 1.0 g/cm<sup>3</sup> is thought to be necessary for hydrogen to change to the metallic state. These experiments may be important in the study of the interior of Jupiter and the outer planets, whose interiors are composed mostly of solid hydrogen. Metallic hydrogen might even be a component dissolved in the earth's core. Solid, nonconducting hydrogen could have practical uses as fuel for reactors and rockets and as an explosive. If solid hydrogen is eventually made into a metal, it is expected to be a superconductor, and may find extensive applications in the generation of electricity and in electronics.

#### *High-Pressure Crystallography and Spectroscopy*

Data on the variation of atomic arrangements with pressure provide infor-

mation about the nature and magnitude of interatomic forces and many physical properties, including density, molar volume, and compressibility. During the past year, more than 40 high-pressure crystal structures have been completed by *Hazen* and *Finger*, approximately doubling the number of materials so studied. The 15 compounds investigated—including silicate spinels, analcite, rutile and corundum-type oxides, and sodium nitrate and nitrite—were selected to resolve questions regarding the effects of compression and phase transitions in minerals. One significant result is the formulation of an empirical bulk modulus–volume relationship that may be used to predict bond compression in oxides, silicates, halides, sulfides, and many other compounds. Another achievement is the identification and characterization of an important group of reversible phase transformations called “polyhedral tilt transitions.” A third general result, based on high-pressure crystal-structure data, is that transformations of many silicates occur when the Si-O bond compresses to 1.59 Å, which may represent a minimum possible Si-O separation. The concept of a minimum stable bond distance, combined with the bulk modulus–volume relationship, has far-reaching implications for understanding the stability of polyhedral units within the earth.

The Raman spectra of  $\text{TiO}_2$  at room temperature were measured under elevated pressures in the diamond-anvil, high-pressure cell by *Mammone* and *Sharma*. In addition to being isomorphic with stishovite, a high-pressure form of  $\text{SiO}_2$ , rutile has been of considerable fundamental and applied interest because of its elastic, optical, and dielectric properties. Evidence for a high-pressure phase transition at approximately 70 kbar has been found. Factor group analysis eliminated the possibility that the high-pressure phase has a  $\text{CaCl}_2$  structure. The new phase probably has an orthorhombic  $\alpha\text{-PbO}_2$  structure, which is

2.8% denser than rutile. The pressure dependence of the phonon frequencies of  $\text{TiO}_2$  has been used to calculate the mode Grüneisen parameters and the anharmonicity in the crystal, both of which will aid in the development of a theoretical model for describing the behavior of  $\text{TiO}_2$ .

In another Raman study, *Mammone* and *Sharma* measured the spectra of crystalline and glassy  $\text{GeO}_2$  at pressures up to 80 kbar in the diamond-anvil, high-pressure cell. The principal reason for studying  $\text{GeO}_2$  is that its high-pressure forms are analogous to those of  $\text{SiO}_2$  but are stable at lower pressures and so are more amenable to study. Because glasses are typically weak Raman scatterers, it has been difficult to study their spectra under pressure. This work was the first successful study of the Raman spectrum of  $\text{GeO}_2$  glass under pressure. The pressure dependence of the phonon frequencies up to 80 kbar was measured and can now be used to obtain lattice dynamical information such as the mode Grüneisen parameters and the anharmonicity in the crystal. Raman evidence indicates to *Mammone* and *Sharma* that  $\text{GeO}_2$  glass becomes more disordered and permanently densified when compressed. No indication for a change in Ge coordination from four-fold to six-fold was found in the spectra of  $\text{GeO}_2$  glass up to 140 kbar. Crystalline  $\text{GeO}_2$  shows a tendency to transform from the hexagonal to the tetragonal (rutile) structure at  $\sim 70$  kbar, but the available thermal energy appears to be inadequate to overcome the kinetic barrier.

In a diamond-anvil, high-pressure cell specially designed for cryogenic temperatures *Sharma*, *Mao*, and *Bell* were able to confine a small volume (0.25 nl) of liquid hydrogen for subsequent compression to 650 kbar at  $25^\circ\text{C}$ . Raman spectra were measured from 9 to 626 kbar for the first time under those conditions. The rotational Raman bands, initially sharp and distinct in the fluid phase, become broad at moderate pressure and then



split at the onset of crystallization (55 kbar, 22°C). As pressure is further increased the rotational bands become diffuse and indistinguishable. Apparently, molecular rotation is greatly constrained in the disordered form of crystalline hydrogen. The vibrational band, on the other hand, is initially broad and becomes sharper. There is a significant shift of frequency, which increases gradually, levels off at about 330 kbar, and then falls as the pressure is increased to 626 kbar. These observations indicate to Sharma, Bell, and Mao that the initial rise in frequency is the direct result of compression; the leveling off means that the molecular bond is "softening," and the subsequent decrease implies that the hydrogen molecules are interacting and forming new bonds. These phenomena are consistent with the view that hydrogen is undergoing a change in bond character (possibly trending toward the metallic state) that will be terminated in a transition at a still higher pressure. The theoretical importance of these findings has generated considerable excitement in the scientific community. Because metallic hydrogen is expected to be a superconductor, its potential application to the transport of electrical energy is of exceptional interest. There is no doubt that a major discovery concerning the most fundamental element has been made.

### *Biogeochemistry*

Two principal directions of research are developing in the study of organic materials in geology. One direction involves an investigation of the chemistry of isotopes in living organisms to ascertain their expected distribution in fossil organic materials. The second direction is in determining the influence of the hydrological cycle on those isotopes distributed in the cellular organic matter in sediments. A considerable body of observations has been obtained on the carbon isotopes, but much less is known about

hydrogen isotopes. *Estep* and *Hoering* have carried out research the past two years on biological hydrogen isotope fractionation in cultures of microorganisms grown under controlled conditions. With this background information, they can now design experiments to study hydrogen isotopes in natural plant and animal populations and in the organic matter of sediments.

*Estep* continued the study of the fractionation of the stable hydrogen isotopes by cultures of microalgae. By manipulating the growth conditions of the green alga *Chlorella*, she discovered several enzymatic steps involved in hydrogen isotope fractionation. Photosynthesis is the major process involved in fractionating hydrogen isotopes, and at least two light reactions are involved. The first reaction involves light-stimulated photosynthetic electron transport, in which an isotope effect occurs during the formation of reducing power used for cell biosynthesis. A second light reaction is stimulated by red light and inhibited by blue light. Red light activates the reduction of photosynthetic products and accounts for part of the photosynthetic isotope effect. Additional fractionation occurs in the dark during the breakdown of sugars to form the precursors of fatty acids.

There is some indication that after deposition in sediments, hydrogen isotopes in organic matter will exchange with those in ground water. It is essential, therefore, to know how long the deuterium-hydrogen label in living organisms will remain intact before exchanging. Control experiments with the blue-green alga *Anacystis nidulans* were performed by *Estep* and *Hoering*. The cells are washed, disrupted in water with an enriched deuterium concentration, and then dried. Little exchange takes place over a period of 6 hr at 39°C; however, at higher temperatures (56°C) some exchange takes place in 24 hr. The equilibration of hydrogen isotopes between organically bound hydrogen and hydro-

gen in surrounding water is a very slow process. Hydrogen bonded into natural macromolecules of living cells apparently exchanges more slowly, because of rigid hydrogen bonds, steric considerations, and local environment effects on the molecules, than hydrogen bonded into free, simple organic molecules.

*New Techniques: Apparatus  
and Calibration*

A novel and surprisingly simple approach to the resolution of  $\alpha$ -amino acids measured in geochemical studies was developed by *Hare* and *Gil-Av*. The chromatographic separation of D and L amino acid isomers has been achieved using an optically active mobile phase with both ion-exchange and reverse-phase column packings. Copper and L-proline added to the mobile phase give a complex that leads to diastereomeric species by ligand exchange with the enantiomeric amino acids to be resolved. The stabilities and partitioning coefficients of these diastereomeric L-proline-copper-amino acid complexes are sufficiently different to result in the rapid resolution of most of the protein amino acids. The procedure is carried out with a simple liquid chromatographic system that analyzes underivatized amino acids and is sensitive to picomole quantities. This system greatly simplifies the analyses for D and L amino acids, which in the past involved enzyme treatments or lengthy derivatizations and often long analysis times. The approach will have an important impact on protein, peptide, and amino acid studies; more laboratories will be able to analyze for the D and L composition as well as the amino acid composition of peptides and protein. The technique should also be of particular importance to the pharmaceutical industry and for the analysis of foods and drugs.

One of the goals of the x-ray crystallographers is the study of lattice pa-

rameters and mineral structures under the conditions believed to exist in the crust and mantle of the earth. Those data can then be related directly to phase equilibria and thermodynamic measurements for developing an understanding of the properties and behavior of minerals. A major step has been taken by *Hazen* and *Finger* in the modification and application of a miniature diamond-anvil, high-pressure cell for high-temperature crystallographic studies at high pressure. A small resistance heater is placed around the diamonds, and conditions in excess of 650°C and 50 kbar have been sustained. One novel feature, previously developed by *Ohashi* and *Hadidiacos* at the Geophysical Laboratory, is the use of the thermocouple as the heater. The heater receives power during half the cycle of an alternating power source. During the other half of the cycle, the electromotive force of the thermocouple is sensed and used to control power to the furnace.

The diamond-anvil, high-pressure cell has been adapted to cryogenic conditions by *Mao* and *Bell*. With a judicious selection of special materials, they cemented the diamonds in a hardened stainless maraging steel and rigidly mounted a sample gasket onto studs in the piston supporting the lower diamond. The piston is driven into a cylinder in which the upper diamond is embedded. The piston is advanced by remotely turning spring-loaded screws that rotate in opposite directions to avoid generating torque on the system. The piston can thereby be advanced, forcing the diamonds together, when the cylinder assembly is immersed in the liquid to be loaded within a liquid helium cryostat. In this manner liquefied gases can be used as a pressure medium or the liquefied gases themselves can be studied at extreme pressures.

In still another adaptation of the diamond-anvil, high-pressure cell, *Sharma* modified the device for collecting Raman spectra at extreme pressures. The critical problems were resolved by using dia-



monds of the type IIb, which have low fluorescence with blue (488-nm) wavelength excitation, and by improving the optical coupling of the cell with the spectrometer. Because silicates are generally poor Raman scatterers, provision was made for accurate focusing of the laser beam itself and for maximizing the laser power with an ellipsoidal mirror that focused the collected scattered radiation from the sample on the slit of the monochromator. In this fashion, Raman spectra of weak scatterers under extreme pressures (e.g., 630 kbar) could be measured.

In a set of experiments with the diamond-anvil, high-pressure cell that sustained 1.7 Mbar in pressure, the highest static pressure ever produced, *Bell* and *Mao* made measurements of the force per unit area to compare with the accurate ruby-fluorescence pressure-calibration scale to 1 Mbar and to provide calibration above 1 Mbar. In these experiments ruby crystals located throughout the surface of a stainless steel sample were used with the fluorescence technique to determine the pressure distribution and the mean pressure. The force per unit-area measurements are less precise than the ruby measurements, but are considered absolute pressure measurements. The two independent calibrations were done simultaneously and yielded the same results. *Bell* and *Mao* thereby obtained confirmation of the ruby pressure scale to 1 Mbar and the first static calibration of pressure scales of any kind in the range 1–1.7 Mbar.

In the same set of experiments, one of the diamond high-pressure surfaces was observed to flow plastically. In a joint study with *Dunn*, *Chrenko*, and *DeVries* of the General Electric Research Laboratory, *Mao* and *Bell* measured the amount of plastic deformation with a

profilometer, sensitive to 125 Å. Analyses by infrared of the diamond surface that deformed and of the second surface that did not, revealed that nitrogen impurity may have enhanced the strength of one of the diamonds. The diamond that flowed is almost free of nitrogen, whereas the one that did not is saturated. It is postulated that diamond may be strengthened by the included nitrogen platelets, a property that may be important in the future selection of diamonds for high-pressure experiments.

*Brady* and *Frantz* have modified the flow-cell colorimetric technique developed by *Frantz* and *Hare* (*Year Book* 72, pp. 704–706) for measurement of millimolar concentrations of aluminum in microliter samples. The small volume of sample is injected into a flowing stream of reagent to produce a colored reaction product. The mixture is passed through an optical cell of a flow-cell colorimeter, and the observed absorption is integrated over the time interval of the sample spike. The integrated absorption is then compared with that of a standard solution. The technique is critical for the study of aluminum in aqueous solutions from hydrothermal experiments under crustal conditions. Aluminum-bearing minerals are common, and aluminum solubility is important in many metasomatic processes.

In experimental petrology, reliable temperature control is essential between 800° and 1500°C in quench furnaces. A temperature controller designed by *Hadidiacos* using the platinum heater as the temperature sensor has been developed and tested to maintain  $\pm 1^\circ\text{C}$  regulation. This controller employs phase-control techniques with current limit protection to maximize the life of the furnace. The principal advantages are its stability, low cost, and simplicity.

## EXPERIMENTAL AND FIELD PETROLOGY

DENSITY CURRENT MODELS OF  
TECTONIC PROCESSES*T. N. Irvine*

A study of density currents reported in *Year Book 77* (pp. 717–725) was directed toward understanding the mechanics of crystal sedimentation in igneous intrusions. In the course of this work, it was noted that the methods of flow visualization that were being used were also appropriate to the analysis of mantle convection, and that even the actual results were of interest in this regard. In the present study, experiments of the same type have been roughly scaled in terms of distance, time, density, and viscosity to simulate mantle events occurring over tens of millions of years. Although these experiments are extremely simple in terms of the problem, they lead to some novel concepts concerning relationships between mantle convection and many of the earth's structural and tectonic features. These concepts appear useful as bases for more rigorous theoretical and geological analyses.

*Experimental Methods and Results*

The experiments were made with the same small Plexiglas flume described in *Year Book 77* (p. 717). Its chamber measures 1×2×15 inches, and is completely enclosed except for a 3-inch length of the top at one end above a part that can be isolated as a lock behind a removable gate (Fig. 1A). In principle, the experiments differed from those described previously only in that the fluid in the lock was *less* dense than that in the rest of the chamber; consequently, when the gate was opened, the density current spread along the roof rather than the floor. The idea behind the experiment

was to simulate the upwelling and lateral spreading of low-density mantle material from depth along a mid-ocean ridge (see accompanying figures).

Two experiments representing extreme conditions can be performed with the present apparatus. In one, the flume is completely filled with the liquids so that the flow at the top is constrained by a no-slip condition along the roof. In a simple way, this experiment represents mantle flow beneath a completely rigid lithosphere. In the other experiment, the flume is only partly filled so that the flow is constrained at the top only by surface tension and the effects of gravity. In this case, one must imagine the lithospheric plates carried along by the flow without actually affecting it. Only the first experiment can be described here, but it is clearly the more realistic (and the proposed tectonic models are essentially based on it) inasmuch as coupling of the asthenosphere and lithosphere is a highly critical aspect of mantle convection and plate motion. An extra procedure in this experiment was to place a fitted lid over the lock after the gate was removed so that the roof was a smooth surface along its whole length (Fig. 1A). Irregularities of flow due to the open space were thereby avoided. The lid has two small weep-holes to allow air and extra liquid to escape.

The liquids used in the experiments were two types of silicone fluid having the same kinematic viscosities\* (1400 cs) but slightly different densities (0.97 vs. 1.01 g cm<sup>-3</sup> at 25°C). As in the previous work, the flow was photographed at short intervals (in this case, 3–5 sec) with a 35-mm camera, and the flow structure was mapped on the basis of tracers

\* Kinematic viscosity = viscosity/density.  
Units: cs = centistokes.



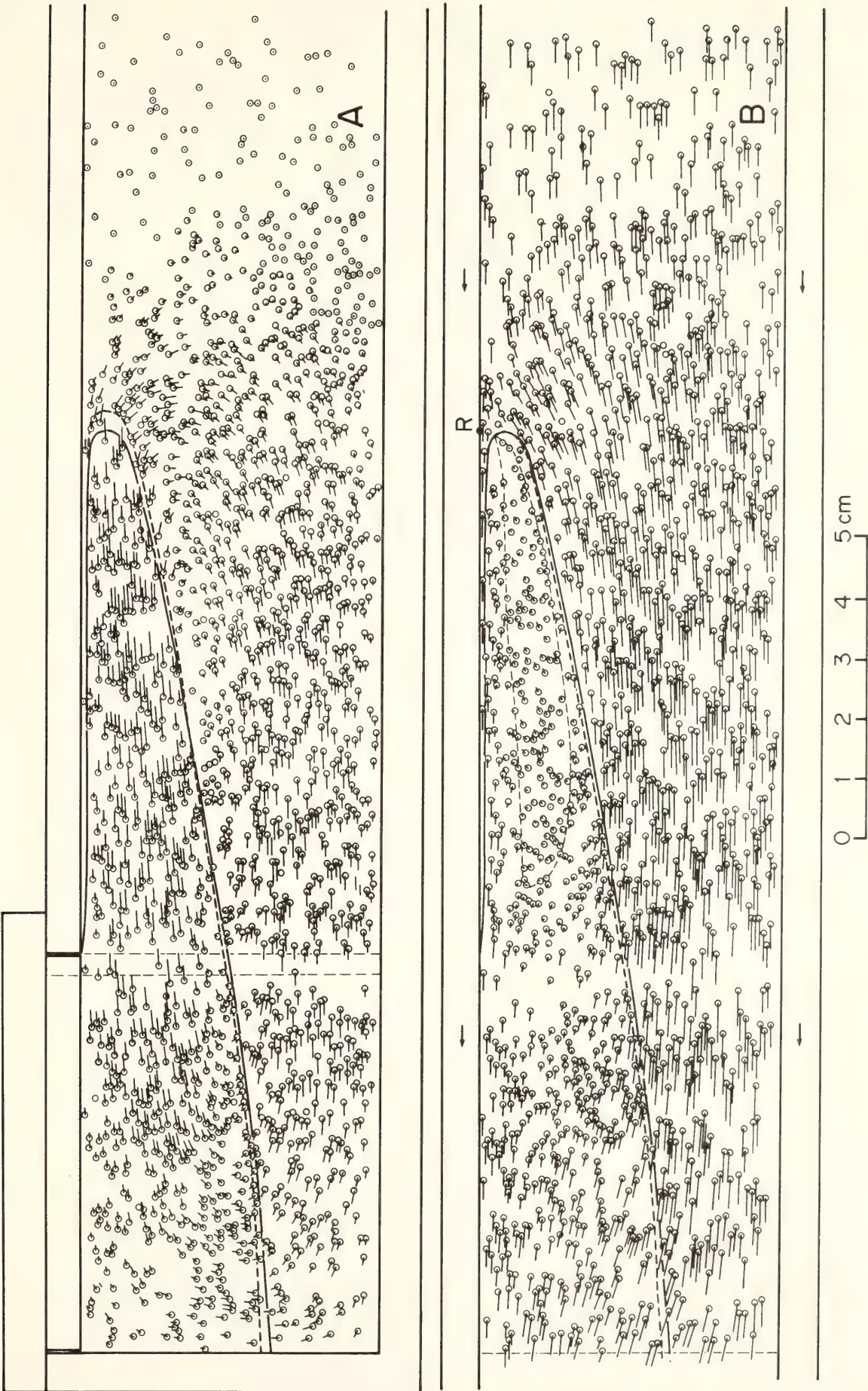


Fig. 1. Motion vectors of tracer particles during a 5.5-s flow interval while the current position changes from the solid-line profile to the dashed-line profile. In each vector, the circle indicates the initial position of the tracer and the line leads to its final position. In (A), the motion is plotted relative to the flume; in (B), it is relative to point *R*, which moves along the roof directly above the tip of the upwelling current. Diagram (A) shows the lid of the flume; the lock gate-slot is represented by the two vertical dashed lines.





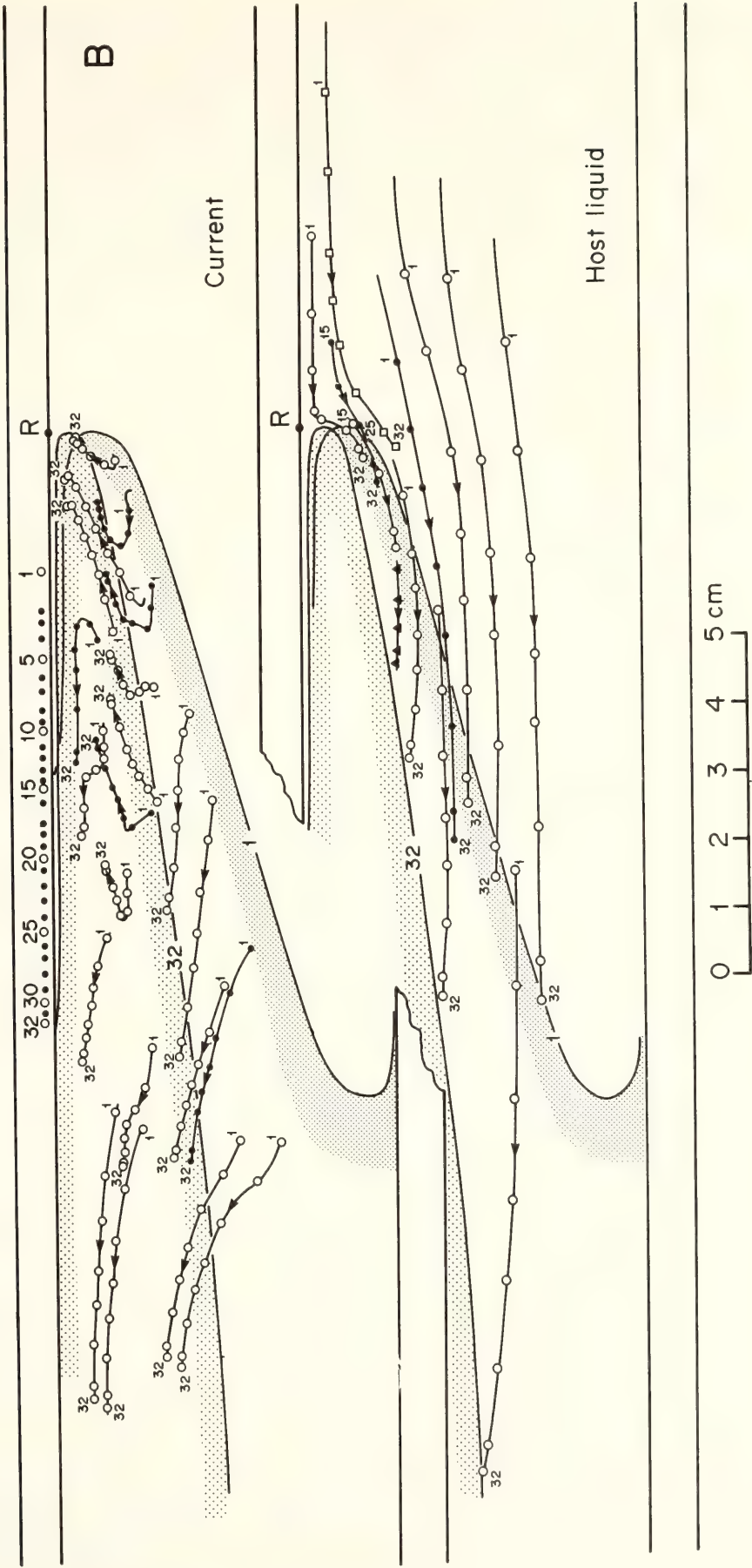


Fig. 2. Pathlines of tracer particles in the same experiment as in Fig. 1 from a series of 32 photographs representing a flow period of 98 s. Only current profiles 1 and 32 are illustrated, and the tracer positions are shown only for photos 1, 5, 10, 15, 20, 25, 30, and 32. The current and host liquid data are separated to avoid overlap. Motions are plotted as in Fig. 1. In (B), a tracer surface representing the base of the lithosphere has been defined graphically in the host liquid by joining a series of tracers that initially were in an approximately horizontal plane. The deformation of this surface was then determined by tracking the tracers. The velocity of the current ranged from  $0.167 \text{ cm s}^{-1}$  at profile 1 to  $0.045 \text{ cm s}^{-1}$  at 32; it was  $0.063 \text{ cm s}^{-1}$  at profile 18 shown in Fig. 1.

in the liquids. The tracers were polystyrene beads about 0.8 mm in diameter. The beads have virtually neutral buoyancy in the denser liquid, and for the period of the experiments (about 3 min), their tendency to settle in the less dense liquid is negligible. To avoid photographing effects of wall drag as much as possible, the tracers in the lock were introduced along its axis between two temporary baffles that were removed just before the gate was opened. In general, wall effects appear minor in the data; the indicated flow patterns are essentially two-dimensional.

Some typical experimental results are illustrated in Figs. 1 and 2; interpreted streamline patterns are shown in Fig. 3. In each case, diagram A shows motions relative to the flume; B shows them relative to the advancing front tip of the current. The latter representation is valuable because it reveals the internal circulation of the density current. A general feature of note is the marked difference between the configurations of the streamlines and the distribution of the contrasting liquids: many streamlines cross the liquid boundaries at high angles. An interesting feature in Fig. 3B is the wavelike form (inverted) of the current flow revealed by the streamlines.

Of specific tectonic significance is the way the host liquid is depressed beneath the upwelling current, especially as illustrated in Fig. 2A by the displacement of the tracer surface. The present study was initiated because of the visual similarity of this process to subduction. Note, however, that because this model "slab" lies athwart the streamlines, the process of its subduction does not appear to be the result of either "ridge push" or "slab pull." Rather, it is the result of the way the liquids circulate as they move toward gravitational stability. Note also how the tracer-defined surface doubles back on itself (beginning at current profile 10) after reaching a particular depth, and how this process produces a wavelike

irregularity in the "subduction profile." It is interesting that the doubling back did not require re-elevation of any of the host liquid that had been depressed, and did not measurably increase the length of the tracer surface (even though the latter was compressed and shortened at an earlier stage). Possibly such doubling back is a factor in determining the maximum depth of subduction zones. The end of a subducted slab should be particularly susceptible to melting, and Suyehiro and Sacks (*Year Book* 77, pp. 505-510) have defined a region of high *S*-wave attenuation ( $=$  low *Q*, a feature believed to be indicative of melting) at the bottom end of the Japan subduction zone at exactly the place where doubling back would be expected.

Also of interest with respect to tectonics is the way in which only a limited part of the current called the "rapid flow zone (RFZ)" in Fig. 3B is gaining on the front tip. In a sense, the current advances by this material being extruded forward. In this zone, the liquid is rising almost as fast as it is advancing toward the front tip. In the tectonic models presented below, rapid flow zones are portrayed in part as seismic low-velocity zones in the upper mantle, places where the mantle is generally believed to be partly melted. The postulate here is that the release of pressure associated with the rapid upwelling is the cause of the melting. If melting did occur, then because of the associated decrease in viscosity, the flow would be expected to be proportionately more rapid, and hence the rapid flow zone would probably be proportionately thinner than in the experiment, where the viscosity of the current is constant.

In Fig. 3B, point  $s_0$  is where the current first affects its host liquid just below the roof;  $s_1$  is a stagnation point where the flow splits or divides in both the current and the host liquid and the flow velocity (in a relative sense) goes to zero. Upstream from  $s_0s_1$ , host liquid



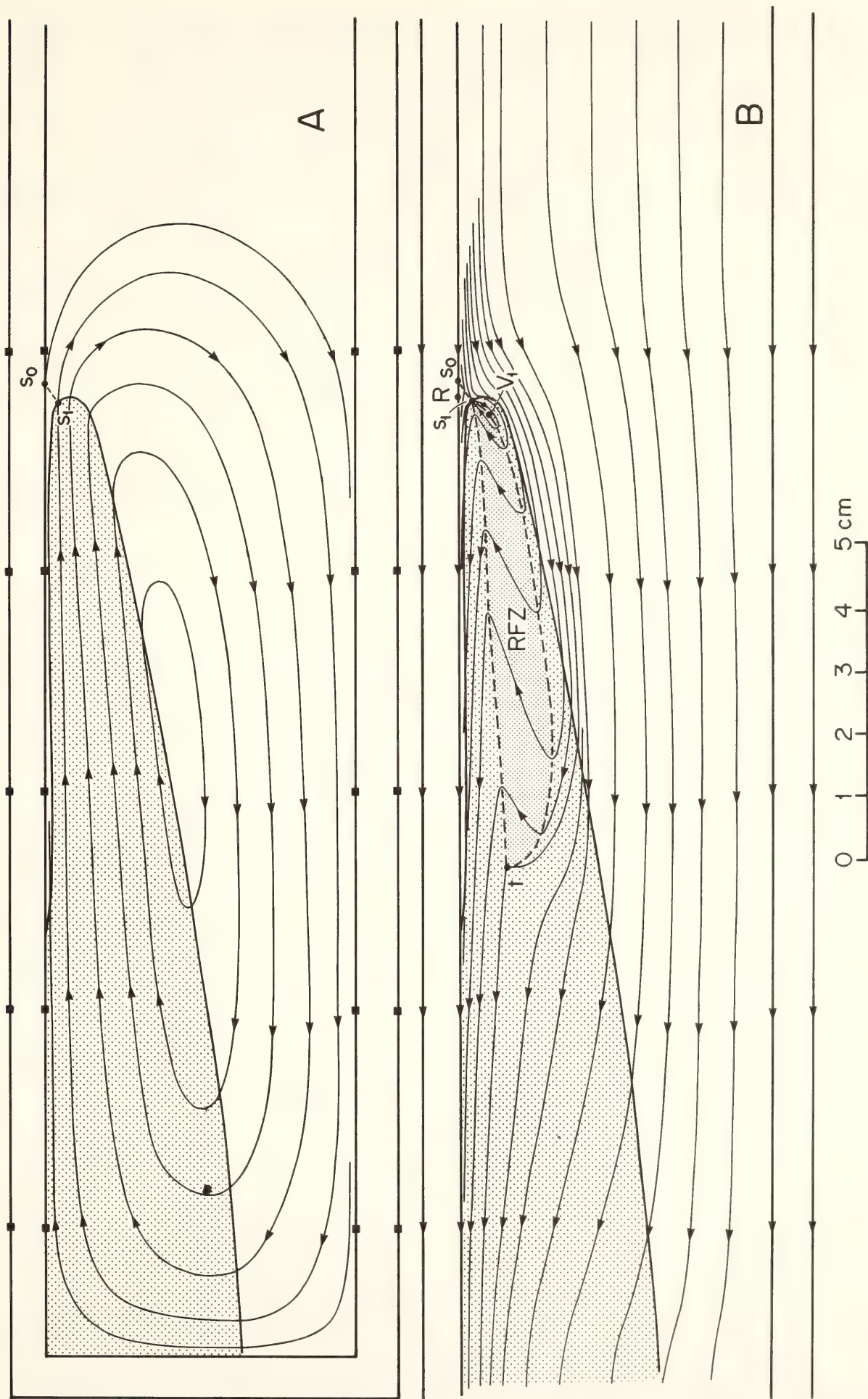


Fig. 3. Streamlines for the current in Fig. 1, plotted relative to the same reference systems. Velocity profiles in the horizontal direction are indicated by the arrowheads. Point  $s_0$  is where the upwelling current first affects the host liquid next to the roof;  $s_1$  is a stagnation point. The rapid flow zone (RFZ) is where liquid is gaining on the front tip of the current.

is being pushed upward to the roof; downstream it is being depressed beneath the upwelling current.

Scaling Considerations

In his discussion of scale models of geologic structures, Hubbert (1937) showed that a major difficulty in this type of study is designing experiments that can satisfactorily represent the very long durations of many earth processes. He suggested several ways this problem can be circumvented on theoretical grounds, and the method most appropriate here is to assume that inertial forces in the natural process were negligible in comparison with the body forces. Model ratios based on this assumption are given in Table 1, and some scaling calculations for the tectonic models appear in Table 2. According to the scaling, if the downward displacement of the host liquid by the upwelling current represents subduction of lithosphere by some 500 km, then the natural density current ostensibly simulated in the experiment would be advancing at about 1.6 cm a<sup>-1</sup>. This rate is of the same order of magnitude as the rates at which ocean floor is evidently being consumed along most currently active subduction zones. The mantle viscosity of 10<sup>22</sup> poises assumed in the scaling is based on estimates by Cathles (1975) and Peltier (1976); the assumed density of 4.5 g cm<sup>-3</sup> is an average for the mantle. Possible origins of a

TABLE 1. Scale Model Ratios for the Present Experiments\*

Length	$\lambda = l_2/l_1$
Density	$\delta = \rho_2/\rho_1$
Viscosity	$\psi = \eta_2/\eta_1$
Mass	$\mu = m_2/m_1 = \delta\lambda^3$
Time	$\tau = t_2/t_1 = \psi\tau^2/\mu^\dagger = \psi/\delta\lambda$
Velocity	$\nu = v_2/v_1 = \lambda/\tau^\dagger$

\* After Hubbert, 1937. Symbols: *t*, *l*, *m*, *ρ*, *η*, and *v*, respectively, represent time, length, mass, density, viscosity, and velocity in the original (1) and the model (2).  
† Constraint arising from the assumption that inertial forces in the natural process were negligible compared with body forces.

mantle-density contrast akin to that in the experiment are discussed in the last section of this article.

Tectonic Models

In the proposed tectonic models (Fig. 4), two upwelling density currents are shown flowing toward one another, representing the earth condition that the spreading from one mid-ocean ridge opposes that from the next. The natural process could be simulated somewhat more rigorously by using a flume with locks at both ends, but the opposing currents in the diagrams barely interfere, and in Figs. 4A and 4B the streamlines are drawn from vector sums of the tracer motions recorded in two sets of experimental data. It will be appreciated also

TABLE 2. Some Scaling Results for the Flow Experiments\*

	Original	Model	Model Ratio
Host density, g cm <sup>-3</sup>	4.5	1.01	$\delta = 0.224$
Current density, g cm <sup>-3</sup>	4.33	0.97	$\delta = 0.224$
Host viscosity, poises	10 <sup>22</sup>	14.14	$\psi = 1.414 \times 10^{-21}$
Current viscosity, poises	$9.6 \times 10^{21}$	13.58	$\psi = 1.414 \times 10^{-21}$
Distance	(Horizontal scale in Fig. 4)		$\lambda = 2.755 \times 10^{-8}$
Time			$\tau = \psi/\delta\lambda = 2.291 \times 10^{-13}$
Velocity			$\nu = \lambda/\tau = 1.203 \times 10^5$

\* Scaling equivalence for experiment in Figs. 1 and 3. Time: 1 min ≡ 8.3 Ma. Advance velocity of current: 0.063 cm sec<sup>-1</sup> ≡ 1.66 cm a<sup>-1</sup>.



that the diagrams are essentially schematic, so accuracy of detail is not of prime concern. In preparing the diagrams, it was assumed for simplicity that the distance between the mid-ocean ridges (that is, between the ends of the locks) is constant, but this is not an essential condition.

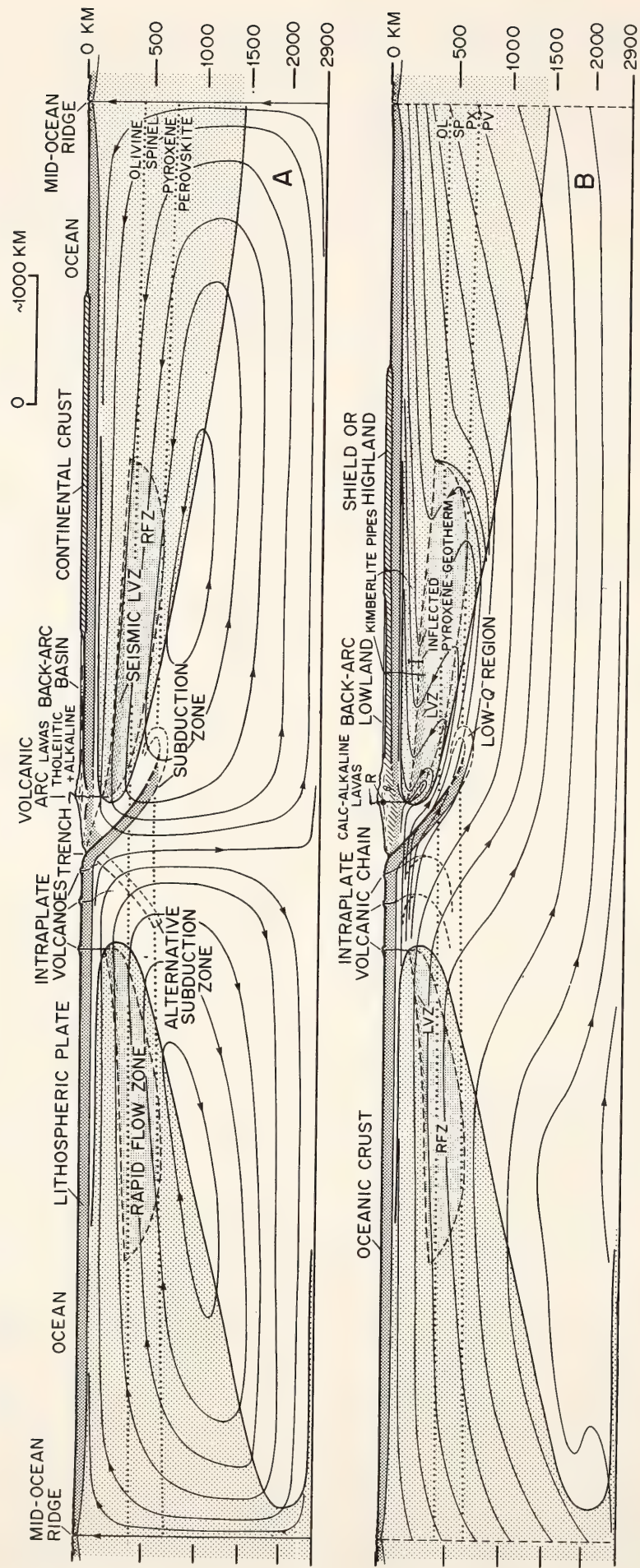
A principal feature in Figs. 4A and 4C, where the joint flow pattern is plotted relative to the mid-ocean ridges, is that the flow system appears to comprise two adjoining convection cells. It will be apparent that, if there are significant density differences between the cells along their common (descending) boundary, then material from the denser cell will tend to flow into the less dense one—or in other words, the less dense cell will grow or expand at the expense of its neighbor. Through this effect, as seen in Fig. 4A, *lithosphere is subducted by being transferred from the top of one cell into the body of the other*. The key observation here is that the subducted plate need not be parallel to streamlines (as commonly is assumed). Note also the possible alternate subduction zone. Evidently very little change is required in the convection pattern to switch or “flip” the direction or “polarity” of subduction (as apparently occurred in the New Hebrides arc).

If, however, the flow motions are plotted relative to the tip of the density current in the expanding convection cell (that is, relative to the volcanic arc), as in Figs. 4B and 4D, then the streamlines are more nearly parallel to the subduction zone, and the continent appears to be drifting because of transfer of mantle material beneath it from one ocean region to the other, the transfer occurring with a wavelike motion. Geologically in this representation, the ocean trench at the top of the subduction zone corresponds to point  $s_0$  in Fig. 3B, and the arc magma derives from the tip of the rapid flow zone at a stagnation point analogous to  $s_1$ . In the latter case, the magma is released from the partly melted rock of the

rapid flow zone as the flow divides at the stagnation point. The magma then escapes into extension fractures developing in advance of the mantle current, and these fractures lead to the volcanic pipes. If the residue of melt-depleted mantle rock at the tip of the rapid flow zone is peridotite, then it will probably have a low density compared to the adjoining host rocks (see O'Hara, 1975; Boyd and McCallister, 1976), and so it would be expected to be left behind mainly as an underplating on the base of the lithosphere. If the subduction zone is at the edge of the continent, as in Fig. 4B, then sufficient heat may be derived from the tip of the mantle current (and from the underplating) to melt some of the continental rocks. Mixing of this melt with the basic magma released from the mantle current in combination with associated metasomatic effects might then give rise to calc-alkaline magmas.

Another feature suggested in Fig. 4B is that the movement of mantle material in the rapid flow zone leads to the development of a back-arc basin or lowland. In the experiment, the flow must conform to the rigid roof of the flume, and the size of the rapid flow zone must vary accordingly. In the natural setting, however, the lithosphere can be flexed and extended, and so may tend to subside over the middle and distal parts of the rapid flow zone as the materials of this zone drain off toward the arc. This effect is likely to be enhanced if the viscosity of the rapid flow zone is lowered by partial melting. It is notable in this regard that back-arc basins characteristically overlie mantle zones of high  $S$ -wave attenuation (e.g., see Molnar and Oliver, 1969, p. 2648; Toksoz and Bird, 1977, fig. 2b).

On the oceanic side of the arc in Figs. 4A and 4B, the rapid flow zone of the weaker current is shown to be feeding intraplate volcanoes such as commonly form seamounts in front of ocean trenches. Successions of such volcanoes might develop through periodic back-





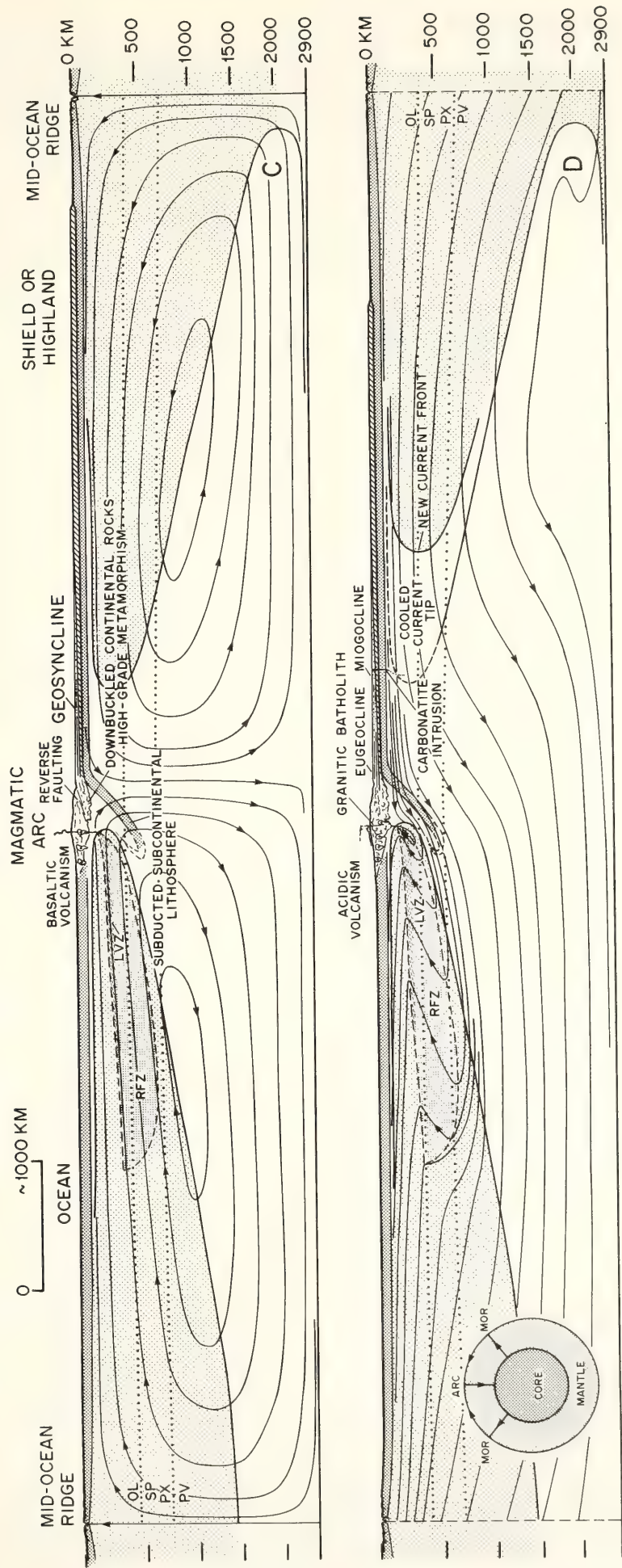


Fig. 4. Four tectonic models based on convection systems generated by graphically superimposing two sets of current streamlines. In (A) and (C), motion is plotted relative to the mid-ocean ridges; in (B) and (D), it is relative to the volcanic arc. The indicated earth scales are such that if the same volume of mantle material was rearranged in a spherical coordinate system, it would extend to the top of the core at 2900 km (see inset in (D)). The total length of each section at sea level is equal to about 100° of great-circle arc, or roughly the distance between the East Pacific Rise and the mid-Atlantic Ridge. For further discussion, see text.

stepping of the tip of the current as it is depleted of melt and cooled. In combination with roller motion parallel to the direction of flow (as commonly is observed in density currents and convecting liquids: e.g., Simpson, 1969; Richter and Parsons, 1975), this effect might also yield linear chains of the volcanoes.

The models in Figs. 4A and 4B accord with the common present-earth relationship that subduction zones dip beneath continents. The writer believes, however, that more satisfactory models of some pre-Cenozoic orogenic belts are obtained if the subduction zone is drawn to dip away from the continent as in Figs. 4C and 4D. In this case, the magmatic "arc" is fed from a current upwelling from beneath the ocean, while a geosynclinal wedge of sedimentary and volcanic rocks develops on the downwarped edge of the continent. The trench should be on the *continental* side of the arc, but it might well be occult beneath a welt of sediments and volcanic rocks. The distinctive feature of this model is that only the denser, lower lithosphere is subducted beneath the upwelling mantle current. The lighter continental rocks and geosynclinal sediments are temporarily downbuckled and may to some extent be overthrust by mantle rocks as they are transferred across the boundary between the convection cells, but ultimately they are too buoyant to be subducted. Instead, they become increasingly warmed and metamorphosed, and as they are underflowed by the tip of the mantle current they are intruded by mantle-derived magma and covered by the volcanic rocks of the arc. Finally, the basal units become so heated by the mantle current beneath that they undergo extensive melting, yielding the magma for granitic plutons and batholiths and related siliceous volcanic rocks.\* Another feature

of this model is that the continent *grows* into the ocean into which the subcontinental lithosphere is being subducted. This accords with the long-standing tenet that continents have enlarged through geologic time. A third feature is that the "basement" on which the eugeosynclinal rocks are deposited stands to be largely *destroyed* through the combined effects of subduction and partial melting. This aspect is consistent with the intense metamorphism and remobilization (and in some cases, even the apparent absence) of basement in many orogenic belts in the age range, Early Archean to latest Mesozoic.

Figures 4B, 4C, and 4D also contain suggestions concerning carbonatite and kimberlite intrusions. On the basis of their observed settings, these bodies are portrayed as being derived from mantle currents slowly upwelling beneath broad regions of "stable" continent. In addition, it is suggested that the inflections observed in the pyroxene geotherms measured in ultramafic nodules from kimberlite pipes (Boyd, 1973) represent the *tops* of rapid flow zones of mantle currents.

#### *Driving Mechanisms for the Mantle Currents*

A principal question about the modeling is whether the 4% density contrast between the liquids used in the experiments is realistic in terms of mantle relations. Certainly part of this contrast can be regarded as a thermal expansion effect relating to temperature differences such as commonly are assumed in models of mantle convection. But for the contrast to be entirely due to this cause would require an unreasonably large temperature contrast (more than 1000°C). Other factors must be invoked.

Partial melting within the current should also be a contributory factor. Indeed, in the places where this melting is expected to occur (below the mid-ocean

\* This process could be regarded as a tectonic equivalent of "zone refining," an industrial process used to remove low melting components from more refractory solids.



ridges and toward the tops of rapid flow zones), it should considerably enhance the flow. Its effects, however, are probably restricted to shallow depths.

What appears to be a more important possibility involves solid-solid phase changes, particularly the olivine-spinel transition, which occurs in mantle peridotite in the depth range 300–400 km (see Ringwood, 1975), and the pyroxene-perovskite transition, which is thought to occur at about 600–750 km.\* The olivine-spinel change entails a density increase of about 8% for olivine  $\text{Fo}_{88-93}$ , which typically makes up 65–85% of mantle peridotite. Information on the pyroxene-perovskite reactions is very limited, but they may involve a density increase of 20% or more, a possibility that is consistent with some geophysical estimates of the density increase that occurs at 600–750 km (e.g., Anderson, 1967). The pressure of the olivine-spinel transition increases with temperature (other things being equal; Akimoto and Fujisawa, 1968); therefore, the transition may be expected to be deeper near a mid-ocean ridge where hot material is rising than at points closer to a magmatic arc where cooled material is descending (see Fig. 4). Thus the average density of the lithologic column to a specific depth at or below the phase transition near a mid-ocean ridge should be less than the average density of a compositionally equivalent column extending to the same depth near the arc. In effect, the lateral density contrast due to temperature is *magnified* by the phase transition. Such lateral differences would, of course, promote convection (e.g., see Hager and O'Connell, 1979). The pressure-temperature relations of the pyroxene-perovskite transition are still unknown but probably are qualitatively the same.

\* Under mantle conditions, these transitions involve complex mineralogical reactions as well as polymorphic changes (see Ringwood, 1975, and summary in Yagi *et al.*, 1978).

# LITHOSTRATIGRAPHIC VARIATIONS ASSOCIATED WITH THE PLATINUM-RICH ZONE OF THE STILLWATER COMPLEX

*S. G. Todd,\* D. J. Schissel,\* and T. N. Irvine*

The Stillwater Igneous Complex is a well-known Precambrian stratiform-type layered intrusion of ultramafic and mafic rocks exposed with a strike-length of about 45 km along the northern edge of the Beartooth Mountains in Montana. The layered rocks have been tilted on edge since their formation, and though the topmost units have been lost through erosion (or are still concealed at depth), a thickness of almost 6 km is visible. In the past 10 years, exploration work on the complex by the Johns-Manville Corporation has resulted in the discovery and delineation of a remarkable stratigraphic zone rich in platinum and palladium. This zone is up to several meters thick and has been traced on surface and by drillhole intersections for almost the entire length of the intrusion. One section, 5.5 km in length, has an average grade of 0.65 troy ounce of Pt and Pd per short ton through a thickness of 2.1 m (Johns-Manville Corporation, 1978, p. 148) and is one of the richest known deposits of platinum-group metals (PGM) in the world.

Although there are other occurrences of PGM in the Stillwater Complex at other stratigraphic levels, none has been found that compares with the principal zone in continuity and grade. But the zone does have a counterpart in the famous Merensky Reef of the Bushveld Igneous Complex, a Precambrian intrusion in South Africa petrologically akin to the Stillwater Complex. The Merensky Reef has been the West's principal source of PGM for many years and, until the Stillwater discovery, was considered unique. Scientifically, the fact that there are two such zones is as remarkable as either zone in itself. They would seem

\* Johns-Manville Corporation, Billings, Montana.

to reflect some exceptional event (or combination of events) that happened, not just once, but twice, in two intrusions in widely separated parts of the earth's crust. But whether this event was a consequence of the way the intrusions crystallized within a few kilometers of the surface, or whether its roots go much deeper—for example, to the source regions of magmas in the mantle—is an open question.

Apart from the field studies, previous work on the Stillwater PGM zone has been principally concerned with the identification and characterization of the sulfides, native alloys, arsenides, antimonides, bismuthinides, and other minerals that contain the Pt and Pd (Cabri *et al.*, 1974, 1975, 1976). The present study deals with the compositions of the host rocks. These rocks have been examined petrographically, and their principal silicate and oxide minerals have been extensively analyzed. A principal objective was to determine if there are any distinctive lithological differences or discontinuities associated with the PGM zone that might be a clue to its origin.

### *Stratigraphic Relations*

The Stillwater Complex has been divided stratigraphically into three main parts (see Page, 1977, for history and references). The lowest is a *Basal zone* about 50 m thick composed of noritic, gabbroic, and pyroxenitic rocks, of which some are fine grained and seemingly "chilled," some highly contaminated with country rock material, and some cumulates. The Basal zone grades upward into an *Ultramafic zone*, which is generally 800–1200 m thick and consists mainly of layers of harzburgite, bronzitite, and chromitite. The Ultramafic zone is sharply overlain by a variously named section of plagioclase-rich rocks that has a maximum preserved thickness of about 4700 m. These rocks are principally norite, anorthosite, and two-pyroxene gabbro. The PGM zone occurs in this

section, about 425 m above the top of the Ultramafic zone.

Much of the published work on the complex was concentrated on the Basal and Ultramafic zones, in part because they contain conspicuous deposits of Cu-Ni sulfides and chromite. Jackson (1961, 1968, 1970) divided the Ultramafic zone into 15 roughly repetitive sequences of layers called cyclic units within which the different rocks apparently formed by gravitational accumulation of minerals in accordance with the crystallization path of the parental magma. In general, the cyclic units contain layers of olivine-rich and chromite-rich rocks overlain by bronzitite, with plagioclase and augite as interstitial phases. The indicated crystallization order is: olivine + chromite; bronzite; plagioclase; augite.

The stratigraphy of the plagioclase-rich rocks is much more diverse and has been difficult to unravel. In early work, Jones *et al.* (1960) distinguished a Banded zone and an Upper zone, whereas Hess (1960) independently defined a section comprising Norite, Lower Gabbro, Anorthosite (including five subzones), Upper Gabbro, and Hidden zones. In one of two current studies, Segerstrom and Carlson (1977, and in preparation) are attempting to map divisions similar to those of Hess over the length of the intrusion. In the other study, McCallum *et al.* (1979, and in preparation) are making a more detailed breakdown of the Hess section; they have distinguished several dozen layers and assigned them to Lower, Middle, and Upper Banded zones, and 12 subzones.

The rocks studied in the present work come mainly from a 100-m section sampled in two drillholes (denoted 7W and 18W) that overlap in the PGM zone along the Hess (1960) section line. The drillhole section spans one of the subzones defined by McCallum *et al.* (1979) and includes parts of two others; it intersects at least 28 distinguishable layers a meter or more in thickness. In general,



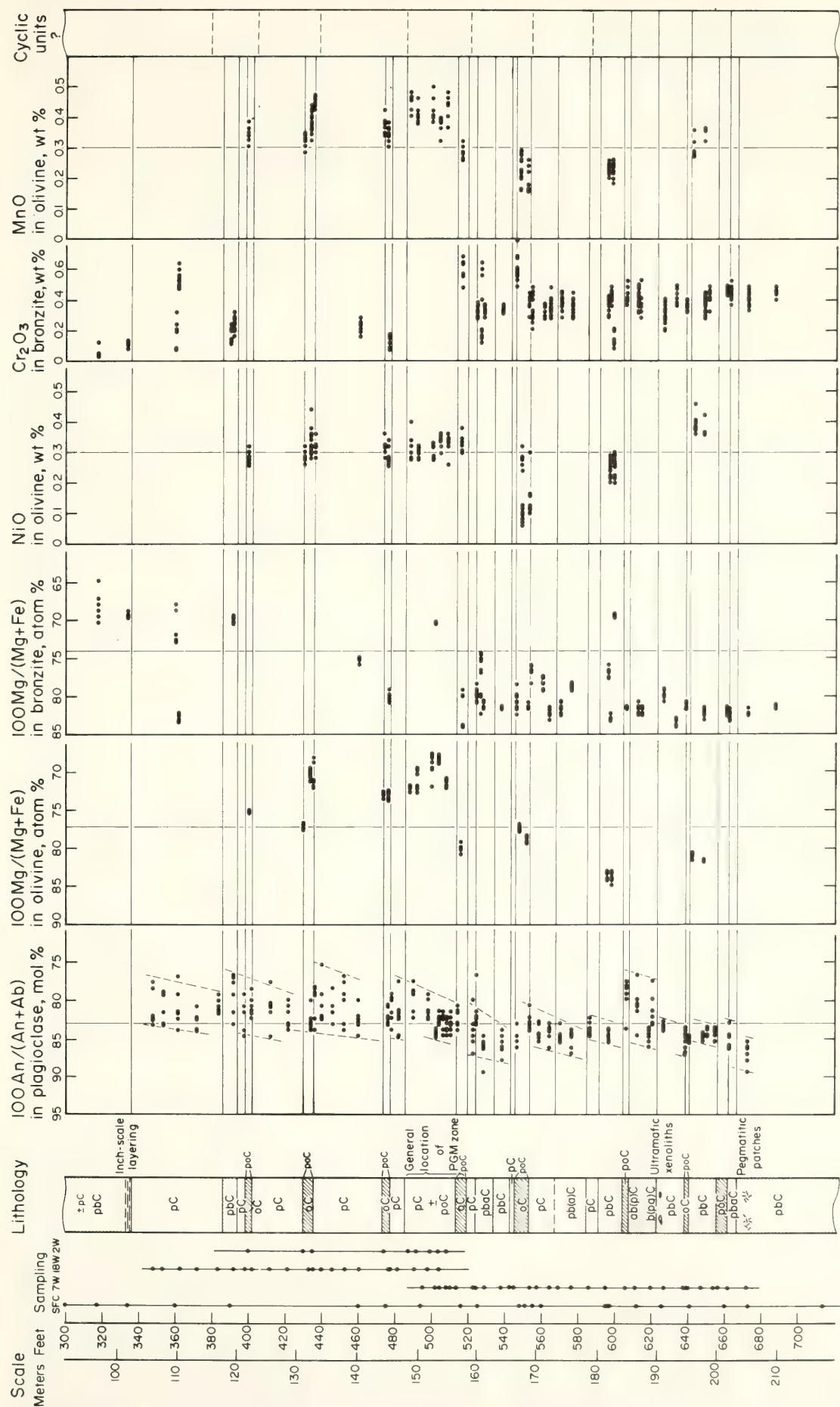


Fig. 5. Lithology and mineral variations in a 120-m section of the Stillwater Complex spanning the PGM zone. Abbreviations: *C*, cumulate; *p*, plagioclase; *o*, olivine; *b*, bronzite; *a*, augite; *SFC*, surface samples.

the rocks can be conveniently classified according to the cumulate terminology of Wager *et al.* (1960) and Jackson (1967). Regardless of whether the genetic concepts from which this terminology arose are valid or not, certain major "cumulus" minerals that commonly are subhedral to euhedral can generally be distinguished from other, less abundant "postcumulus" minerals that are either interstitial to, or reaction products of, the major phases. In day-to-day work, the terminology is used in abbreviated form—for example, plagioclase-olivine cumulate is referred to as *poC*, and plagioclase-bronzite-augite cumulate is *pbaC*. The stratigraphy of the 100-m section, with the rocks classified in this way, is shown in Fig. 5. Note in particular the olivine-bearing peridotitic (*oC*) and troctolitic (*poC*) layers, and the anorthositic (*pC*) layers. Of the eight olivine-bearing layers present in the section, the fourth through seventh from the bottom can be followed for long distances in the intrusion, and the PGM zone is usually associated with the second of these, most commonly within or just above it, but locally dropping partly below it.

In the broader picture, the crystallization relations defined by Jackson (1961, 1970) appear to hold in the first layers of plagioclase-rich rocks. Bronzite, which is the only cumulus mineral at the top of the Ultramafic zone, is joined first by plagioclase in a 275-m norite (*pbC*) layer and then by augite in a 75-m gabbro (*pbaC*) layer. A 3-m anorthosite (*pC*) layer at this level represents a minor anomaly in the crystallization sequence, but the succession immediately reverts to *pbaC* through a 10-m layer, which is followed by the layers of *pbC* and *pbaC* shown at the bottom of Fig. 5. Shortly above this level, however, the succession changes dramatically. Olivine reappears in a repetitive way, but now either in troctolitic rocks or in *oC* layers associated with anorthosite rather than with bronzitite. Augite is suppressed as

a cumulus phase for an extended stratigraphic interval, and for the next 70 m, bronzite is distinctly less abundant than it is lower in the section. Just before these changes are observed, near the pegmatitic patches indicated in Fig. 5, there is some thin layering featuring irregular, slump-like structures, and slightly above these structures are small xenoliths of ultramafic rock (highly altered but probably bronzitite) resembling material in the Ultramafic zone. A layer of melanogabbro (or feldspar-rich pyroxenite) then follows, but above it the crystallization order defined for the Ultramafic zone no longer applies. Overall, this combination of features suggests repeated influx of a new, different magma, at least some of which breached the Ultramafic zone. Although the PGM zone is not associated with either the first *oC* layer or the first *pC* layer, it does occur where these two rock types *together* first become dominant.

#### *Mineral Variations*

In addition to the samples from drill-holes 7W and 18W, some material was collected from outcrops to extend the coverage down to the top of the Ultramafic zone, and a few samples were taken from a third drillhole (2W, collared in the same section about 15 km away), to obtain olivine that was not completely altered to serpentine and other secondary minerals. The minerals were analyzed with the automated electron microprobe following current Geophysical Laboratory procedures. Many of the analyses were made on polished grain mounts, some on polished thin sections. Wherever possible, six spot analyses were made on each mineral investigated in a sample. Some 2000 analyses of this type have been obtained, most of them on plagioclase, bronzite, augite, and olivine, a few on chromite, ilmenite, sphene, clinozoisite, and other minerals encountered.

Selections of the data are shown in Figs. 5 and 6. In general, it must be said



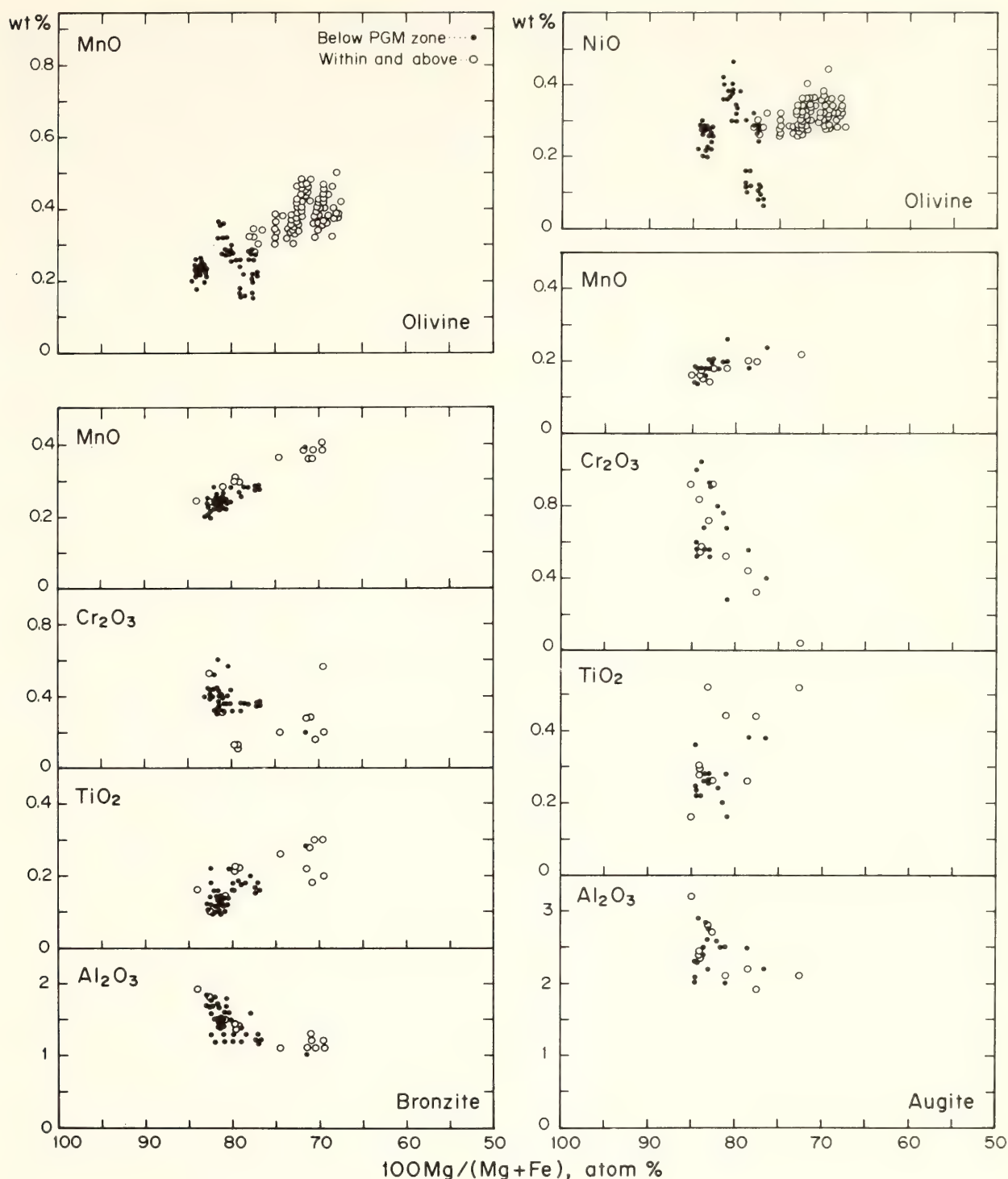


Fig. 6. Electron microprobe data on the compositions of Stillwater olivine and pyroxenes in a section including the rocks in Fig. 5 and extending down to the top of the ultramafic zone. All spot analyses obtained for olivine are plotted; only sample averages are shown for the pyroxenes.

that there are no clear differences or discontinuities associated with the PGM zone. Commonly the within-sample variation of an element in a mineral (due mainly to inconspicuous zoning) is as large as its overall variation in the sec-

tion, and although intriguing relations are suggested in several places, they are marred by seemingly erratic variations that make the relations doubtful. The one variation that does appear to be reliably indicated is that plagioclase be-

comes slightly less calcic upward through the 100-m drillhole section illustrated in Fig. 5, from  $An_{88-83}$  at the bottom to  $An_{83-77}$  at the top. This change, however, can be interpreted in at least three ways, among which a choice cannot be made. One possibility is simply that the trend is gradual; another is that there is also a small steplike decrease in An in the vicinity of the PGM zone. The third alternative is that there is a cyclic variation featuring repeated trends of upward decrease superimposed on the general trend to more sodic compositions. This last possibility is highlighted in Fig. 5 by the dashed-line envelope on the data points. The pattern obviously would not stand up to a statistical test, but essentially the same data distribution is seen in two graphs not illustrated, one in which An content was plotted on the basis of Al/Si in the plagioclase (rather than Ca/Na as in Fig. 5), the other a plot of the iron content of the plagioclase. These patterns are the only indications that have been found of a repetition in mineral variation that might be correlated with the modal repetitions that characterize the visible layering in the rocks.

The strongest indication of a mineral-composition discontinuity in association with the PGM zone comes from the olivine data. As seen in Fig. 5, the Mg/Fe of the mineral tends to be slightly higher below the PGM zone than within or above it. This stratigraphic distinction is clearer, however, in the plots of NiO and MnO vs. Mg/Fe in Fig. 6, where the analyses are seen to fall in almost completely different fields when classified on this basis. Another feature in these plots is that the Ni content of the olivine does not decrease as Mg/Fe decreases. This relationship is sufficiently unusual in rocks formed by fractional crystallization to suggest that it might be tied to the enrichment of Pt and Pd. Unfortunately, the data are too few to be convincing in either of these respects, and the stratigraphic distinction is not evident in the analytical data on the py-

roxenes. The pyroxenes below the PGM zone are mostly magnesian, both in drill-holes and surface samples, but those within and above the zone are not consistently richer in Fe (Fig. 6, C-F). The abundance of Ni in the pyroxenes is too low to be evaluated without making analyses by special trace element procedures, but the other constituents plotted in Fig. 6 show trends that are reasonably attributed simply to fractional crystallization or to variations in the ratio of cumulus crystals to trapped interstitial liquid. In particular,  $Cr_2O_3$  and  $Al_2O_3$  tend to decrease with decreasing Mg/Fe, and MnO and  $TiO_2$  to increase, all trends common to pyroxenes crystallized from tholeiitic liquids. These relationships do not necessarily refute the distinction suggested by the olivine data, but they do make it questionable. There remains a possibility, however, that if the intrusion was open to additions of fresh magma, the olivine might reflect the composition of a new, high-temperature liquid, whereas the pyroxenes perhaps were mainly derived from older or hybrid liquids.

### *Repetition of Layers*

Despite the uncertainties surrounding the petrologic relations, a suggestion can be made concerning the origin of the repetitive layering. In other stratiform intrusions (particularly the Muskox intrusion; Irvine and Smith, 1967), repetition of cyclic units appears to be essentially a consequence of repeated influx of fresh magma into the intrusion while the layers were forming. As described above, there are indications of such magma movements during formation of the Stillwater rocks under consideration. In this case, however, the layer repetition is anomalous in several respects. Ordinarily, cyclic units repeat all or part of a particular sequence of cumulates that can be identified with fractional crystallization of a single liquid. If a change of



crystallization order occurs, it is in a specific direction. To account for all the different layer successions illustrated in Fig. 5, however, alternate fractionation of liquids with at least three crystallization orders is required: (1) olivine, plagioclase, bronzite, augite; (2) plagioclase, olivine, bronzite, augite; (3) plagioclase, bronzite, augite. Note that none of these orders is the same as that given above for the Ultramafic zone, and that individually they can give either an olivine cumulate or a plagioclase cumulate *but not both*.

A possible explanation is that the observed layer sequences reflect some unknown nonequilibrium process. This interpretation, however, is not consistent with common indications that layered intrusions are differentiated in accordance with equilibrium liquidus relations (Irvine and Smith, 1967; Jackson, 1970). However, the observed layer sequences do appear to be explicable in terms of a liquid mixing process suggested by Irvine (*Year Book 74*, pp. 498–499) and illustrated in more specific form in Fig. 7. By this process, if a differentiated liquid such as  $DL_1$  crystallizing plagioclase and bronzite ( $\pm$  augite, which could be an additional phase depending on aspects of the liquid composition not shown in the diagram) were blended with a more primitive liquid located at a point such as  $PL_2$  in the olivine liquidus field, then hybrid liquids such as  $HL_1$  and  $HL_2$  could be generated that would crystallize plagioclase by itself. Thus, in terms of the Stillwater layering, by mixing liquid yielding  $pbC$  (norite) or  $pbaC$  (gabbro) with more primitive magma that could be parental to  $oC$  (peridotite), hybrid liquids can be obtained that would yield  $pC$  (anorthosite). Note also that the possible sequence of cumulates could be diverse, depending on the relative progress of the mixing and crystallization processes. Thus, when the primitive liquid is first introduced, its crystallization would probably be dominant, so the cumulate sequence might change from

$pbC$  to  $pC$  to  $oC$ . But then, as this liquid became increasingly diluted with residues of the older, fractionated liquid, crystallization might reverse along either the same or a different path, giving layer sequences, for example, from  $oC$  to  $poC$  to  $pbC$ , or from  $oC$  to  $poC$  to  $pC$  to  $pbC$ . Liquid  $PL_2$  might itself represent a transition to a third primitive melt,  $PL_3$ , that could be parental to the very thick (500+ m) anorthosite layers observed higher in the stratigraphic section.

On the basis of the layer repetition and the plagioclase composition data, a tentative subdivision of the stratigraphic section into cyclic units has been attempted along the right-hand edge of Fig. 5. Twelve units are indicated, nine containing an olivine-bearing or relatively mafic layer. The main uncertainties relate to the  $pC$  layers. In the lower part of the section, they would seem best placed at the tops of cyclic units, but in the vicinity of the PGM zone they both precede and follow  $oC$  layers, and at the top of the section they appear better placed at the bottoms of units. The philosophy, therefore, has been to assume that the  $pC$  layers represent a transitional crystallization stage (presumably associated with liquid mixing) that could have both preceded and followed the precipitation of olivine but that did not always occur. For this reason, the boundaries between cyclic units are in some cases drawn within  $pC$  layers, rather than at their top or bottom contacts.

On the basis of the above data and concepts, it is tempting to suggest that the PGM zone formed from the first major injection of the new, primitive liquid represented by  $PL_2$ —perhaps in response to a magma mixing event. Indications are that this liquid was characterized by low Mg/Fe and relatively high Ni as well as a different crystallization order. One might also speculate that this first major batch of new liquid extracted most of the low-melting sulfur, arsenic, antimony, and bismuth components (see Cabri *et al.*, 1975, fig. 7) from its source

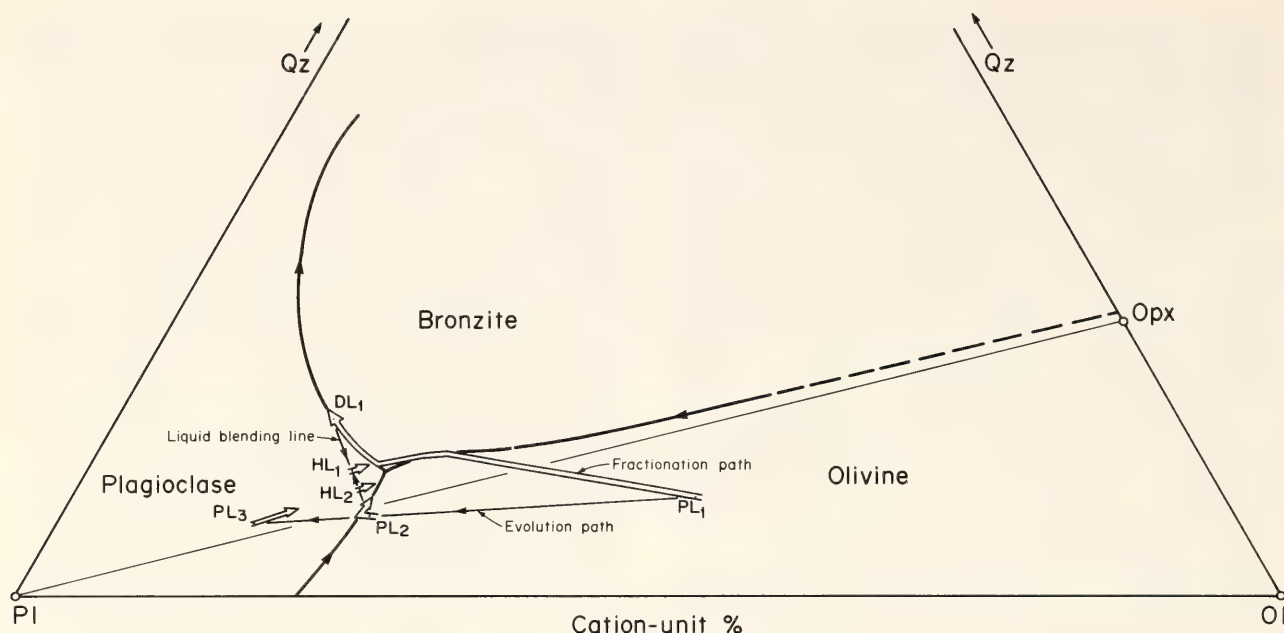


Fig. 7. Schematic diagram based on the system  $\text{Mg}_2\text{SiO}_4\text{-CaAl}_2\text{Si}_2\text{O}_6\text{-SiO}_2$  and liquidus relations deduced for tholeiitic magmas by Irvine (1979), illustrating possible effects of mixing a liquid  $DL_1$  differentiated from a primitive liquid  $PL_1$  with another primitive liquid,  $PL_2$ . Hybrid liquids  $HL_1$  and  $HL_2$  are produced. In terms of crystallization order, liquid  $PL_1$  could be parental to the ultramafic zone of the Stillwater Complex;  $PL_2$  and the hybrids, to rocks in the vicinity of the PGM zone; and  $PL_3$ , to the thick anorthosite layers that occur stratigraphically higher in the intrusion. For further discussion, see text.

region in the mantle, and in so doing scavenged most of the Pt and Pd as well. Present data are, however, no more than suggestive; the problem obviously requires (and warrants) much more research.

#### TRIOCTAHEDRAL MICAS IN MELILITE-BEARING ERUPTIVE ROCKS

*D. Velde*

Trioctahedral micas, usually described as phlogopites, are among the essential constituent minerals of melilite-bearing rocks. In alnoites, venanzites, and coppaelites, for example, phlogopite appears as phenocrysts and sometimes as a groundmass phase. In many other melilite-bearing lavas, such as melilite-olivine nephelinites, micas are found as accessory minerals in the groundmass or, infrequently, as reaction products between olivine and a residual liquid or fluid phase.

Micas in eruptive rocks are known to be variable in composition. Melilite-bearing rocks are characterized by high alkali and low silica and alumina contents compared with other basic lavas (Velde and Yoder, *Year Book* 75, pp. 574–580). The low alumina and silica totals are reflected in the chemical composition of the trioctahedral micas in which, with two known exceptions, the common eastonite–Al-siderophyllite substitution is not found. Common substitutions are  $\text{Fe}^{3+}$  and Si proxying for Al on tetrahedral sites. As shown below, an increase of Al on the tetrahedral sites accompanies substitution of Ba on interlayer sites and Ti on octahedral sites.

Micas have been analyzed in 24 melilite-bearing specimens. Reports on melilite compositions (*Year Book* 76, pp. 478–485) and nepheline solid solutions (*Year Book* 77, pp. 761–767) from the same and other (nonmica-bearing) specimens have already been published. The results discussed below are based



on 413 electron microprobe analyses. This number, however, does not reflect the relative proportions of the various types of micas in the rocks considered. The least common varieties, the silica-rich micas, are greatly overrepresented, whereas relatively few analyses were performed on specimens in which the micas showed little or no chemical variation. All structural formulas were computed on the basis of 11 oxygens; all iron was assumed to be in the ferrous state, although ferric iron is believed to be present in almost all cases.

#### *The Silica-Alumina Content of Micas*

Figure 8 shows the frequency distribution of Si, Al, and Si + Al for the 413 analyzed micas. The Si content of the micas is between 2.5 and 3.6 ions per formula unit. This range is comparable to that published by Seifert and Schreyer (1971). Even though the experimentally determined lower Si limit is 2.3 ions per formula unit (Zussman, 1979), the limit for the more complex natural systems appears to be closer to 2.5. Differences between the present results and the litera-

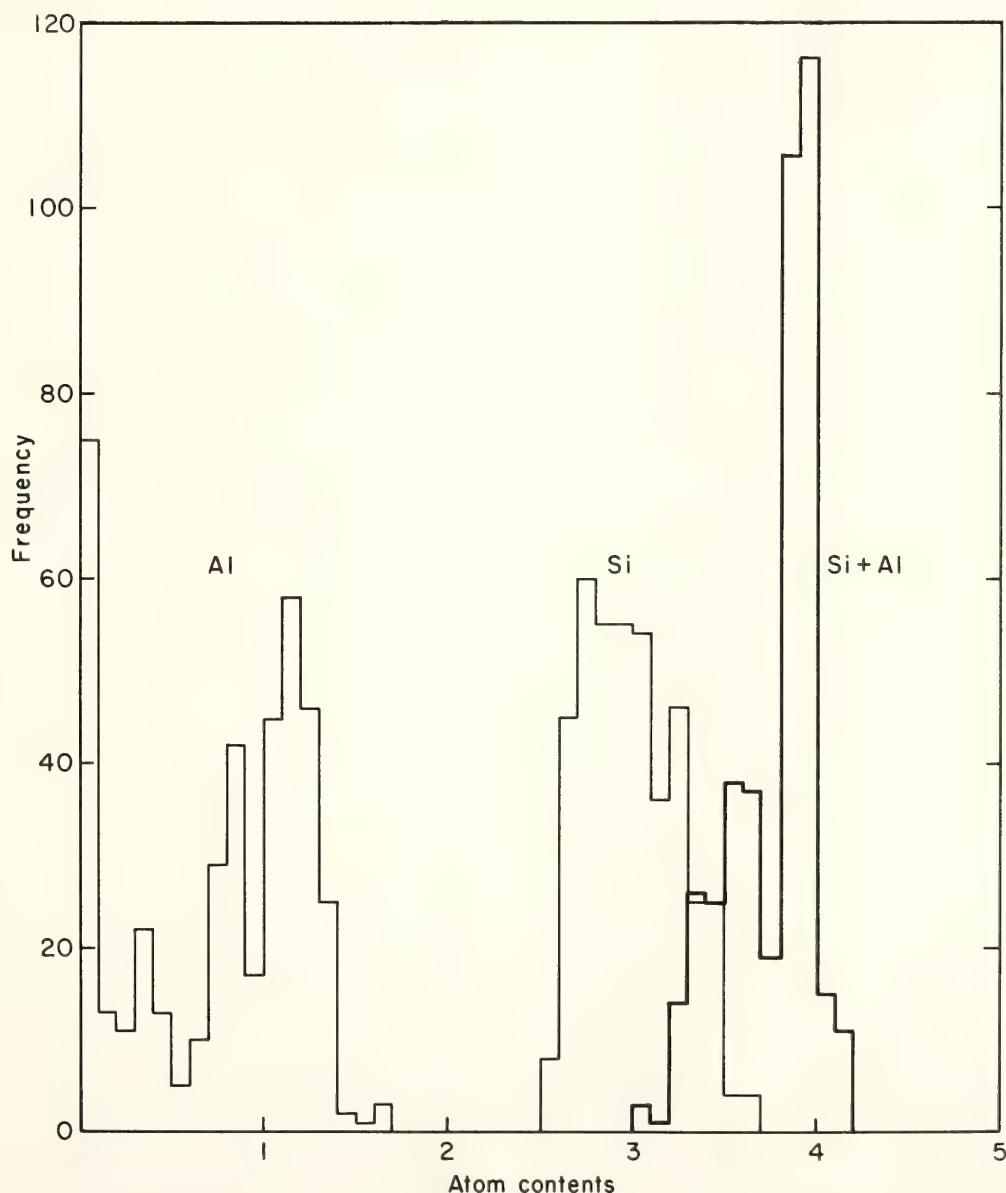


Fig. 8. Frequency distribution of Al, Si, and Si + Al (atom contents) in 413 analyzed micas from melilite-bearing eruptive rocks.

ture survey made by Seifert and Schreyer are particularly striking for the Si-rich phlogopites. These authors found 22 analyses that led to a structural formula with Si greater than 3.0 ions, and 3.2 was the upper limit. In the present study, two melilite-bearing rocks were found to contain high-silica trioctahedral micas, and they are described below.

The Si + Al content of the micas is less than 4.0 ions per formula unit in all but two cases. Some lavas contain mica xenocrysts, foreign crystals conspicuously rimmed by thick reaction zones that separate them from the enclosing rocks. These xenocrysts have a normal phlogopite composition with limited amounts of Al on octahedral sites. The second exception is a melilite-calcite-phlogopite-iron-oxide dike rock from the Oka complex, Canada (specimen Y 319); it contains micas with 0.078–0.153 Al on octahedral sites. The fact that in most micas the formula unit sum of Al + Si is less than 4.0 implies the presence of other tetrahedrally coordinated ions.

The Al content of the micas ranges from less than 0.100 atom per formula unit to 1.700. Aluminum is absent from tetraferriphlogopite, where it is totally replaced by  $\text{Fe}^{3+}$ ; it may also be absent from the silica-rich micas. There is less than 1.00 Al ion per formula unit in the micas interpreted as solid solutions between phlogopite and tetraferriphlogopite or complex solid solutions with silica-rich micas, but there is more than 1.00 Al ion per formula unit in all micas that contain high percentages of either barium or titanium, or both.

#### *Phlogopite-Tetraferriphlogopite Solid Solutions*

Ultrabasic rocks from Haystack Butte, Montana (Wendlandt, *Year Book* 76, pp. 534–539), contain micas that range from barium-rich phlogopites to low-alumina phlogopites. Three rocks from this locality were considered in the present study: one is an alnoite, in which

micas coexist with melilite (specimen Y 220); the other two are mica-bearing monticellite peridotites without melilite (specimens Y 282 and Y 283).

Figure 9 shows the compositions of analyzed micas from the three specimens in terms of Al vs. Si. Three kinds are present: barium phlogopites (Al greater than 1.0 ion per formula unit), micas intermediate between phlogopite and tetraferriphlogopite with more than 70% phlogopite, and micas close to tetraferriphlogopite with less than 20% phlogopite in solid solution. The data indicate the existence of a solid solution gap between phlogopite and tetraferriphlogopite. A similar gap has been found experimentally at 600°C (B. Velde, unpublished results).

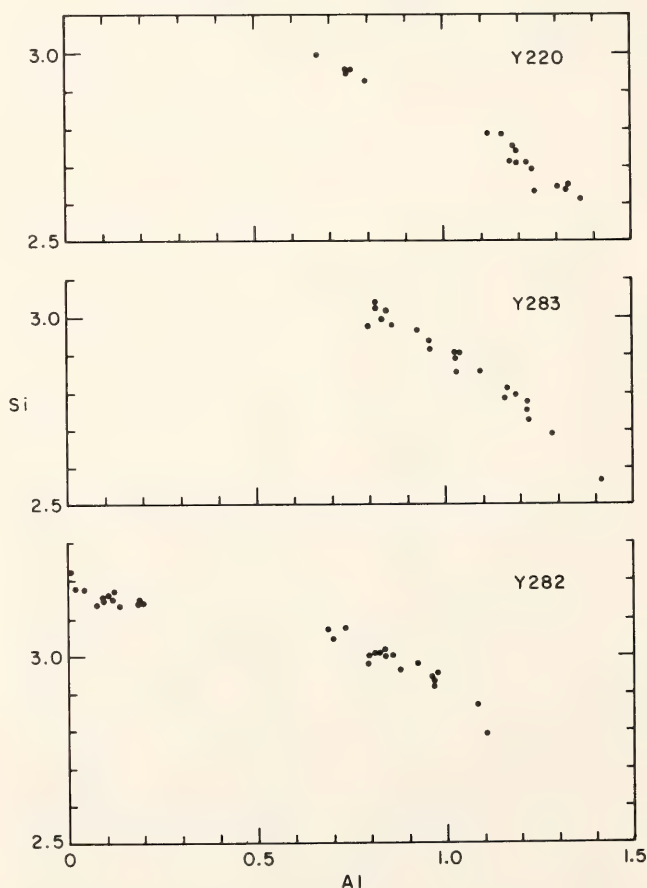


Fig. 9. Variation of Si as a function of Al (atom contents) in micas from three specimens from Haystack Butte, Montana. Micas that contain more than 1.00 ion of Al per formula unit also contain high barium. Sample Y 220 corresponds to an alnoite (melilite present); Y 282 and Y 283 are samples of monticellite peridotite.



As pointed out by R. Wendlandt, optical properties change abruptly with the entry of about 10% tetraferriphlogopite in solid solution: absorption becomes greater in the direction of the small index of refraction, and the color becomes a striking red. The absorption colors of the micas plotting close to the tetraferriphlogopite side of the diagram are of a slightly stronger vermilion red, but this difference could not be used to estimate the amount of tetraferriphlogopite in solid solution. An analysis of a tetraferriphlogopite is reported in Table 3 (No. 1).

### Silica-Rich Micas

Silica-rich micas have been found in two different specimens—a mica-bearing peridotite from Utah and the type coppaelite from Cupaello, Italy. In the Utah rock (specimen Y 127; Best *et al.*, 1968), mica coexists with melilite, olivine, and kalsilite. The compositions of the micas are represented in Fig. 10, which shows the variations of Al vs. Si. The six analyses with more than 1.00 Al ion per formula unit represent the xenocrysts with thick, complex reaction rims. All other micas contain more than 3.00 Si ions per formula unit and less than 1.00

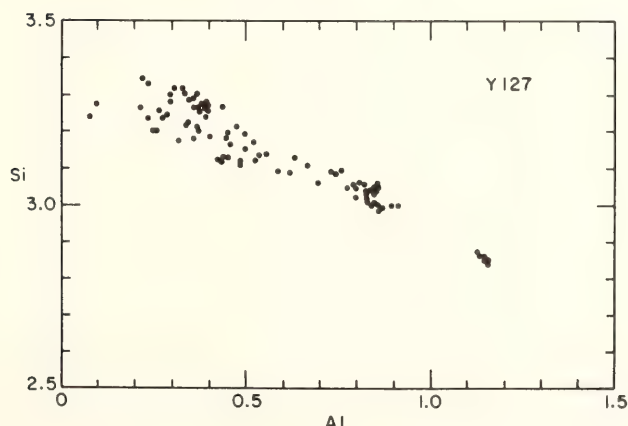


Fig. 10. Variation of Si as a function of Al (atom contents) in micas from a sample of mica-melilite-peridotite from Utah (specimen Y 127). Micas with Al contents greater than 1.00 ion per formula unit are interpreted as xenocrysts.

Al. The most silica-rich compositions correspond to micas with a slight reverse pleochroism. Little difference in the absorption color was observed between the two principal directions of vibration. Some of these micas display hour-glass zoning (Velde and Yoder, *Year Book* 76, p. 484). The weak absorption seems in-

TABLE 3. Electron Microprobe Analyses of Tetraferriphlogopite and Phlogopites||

	1	2	3	4
SiO <sub>2</sub>	40.34	44.22	44.43	34.75
Al <sub>2</sub> O <sub>3</sub>	0.40	4.18	0.47	14.18
FeO*	17.47	8.76	10.72	6.36
MgO	24.36	22.69	22.11	19.17
CaO	0.10	n.d.†	0.07	0.34
Na <sub>2</sub> O	0.09	1.63	0.84	0.05
K <sub>2</sub> O	9.54	10.04	10.18	7.50
MnO	0.13	0.08	0.09	0.11
TiO <sub>2</sub>	0.39	1.47	1.57	5.55
BaO	0.04	0.43	0.62	6.80
Cr <sub>2</sub> O <sub>3</sub>	0.06	n.d.	0.10	0.05
F‡	n.d.	5.06	n.d.	n.d.
Total	92.92	98.56	91.20	94.86
Less O ≡ F		2.13		
		96.43		
	O=22	O=22	O=22	O=22
Si	3.184	3.300	3.447	2.639
Al	0.037	0.368	0.043	1.270
Fe§	1.153	0.547	0.696	0.404
Mg	2.865	2.523	2.556	2.170
Ca	0.008	...	0.006	0.028
Na	0.014	0.236	0.126	0.007
K	0.961	0.956	1.008	0.727
Mn	0.009	0.005	0.006	0.007
Ti	0.023	0.083	...	0.317
Ba	0.001	0.013	0.019	0.202
Cr	0.004	...	0.006	0.003

\* Total Fe determined as FeO.

† Not determined.

‡ Not considered in structural formula.

§ Formula calculation based on Fe<sup>2+</sup>.

|| 1: Tetraferriphlogopite from a monticellite peridotite from Haystack Butte, Montana (Specimen Y 282). 2: Silica-rich mica from a melilite-peridotite. Head of Smith Canyon, T1S, R8E, Utah (Specimen Y 127). 3: Silica-rich mica from a coppaelite, Cupaello, Italy (Specimen Y 253; micas from this specimen appear to contain Li and F (no OH)). 4: Barium- and titanium-rich phlogopite from a melilite-olivine nephelinite from Sutherland, South Africa (Specimen Y 145).

compatible with the optical properties that characterize the phlogopite-tetraferriphlogopite substitution series, and the silica-rich micas must be considered to be different from those described in the Haystack Butte ultrabasic rocks. Furthermore, there seems to be a continuous series of compositions with no miscibility gap as in the phlogopite-tetraferriphlogopite series. These relations lead to the belief that these silica-rich micas could

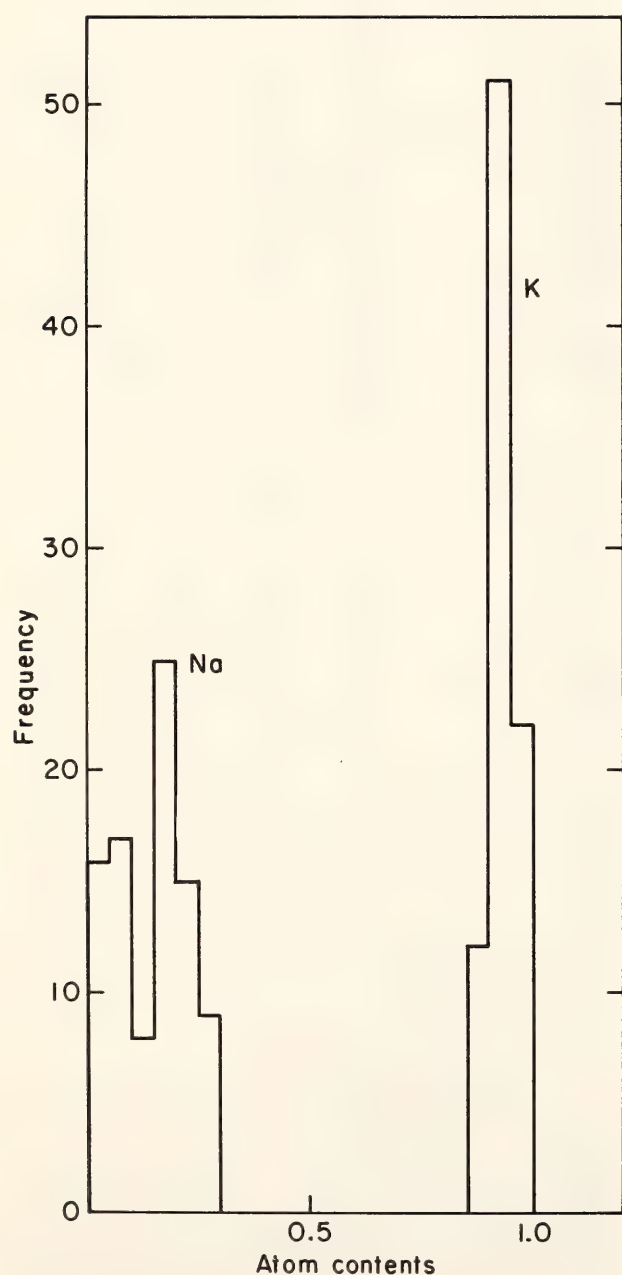


Fig. 11. Frequency distribution of Na and K (atom contents) in 88 mica analyses from a mica-melilite-peridotite from Utah (specimen Y 127).

represent at least ternary solid solution between phlogopite, tetraferriphlogopite, and a silica-rich end member. Such a composition would be similar to that of the mica synthesized by Seifert and Schreyer (1971) to which the formula  $\text{KMg}_3\text{Mg}_{0.5}\text{Si}_{3.5}\text{O}_{10}(\text{OH})_2$  was ascribed. These micas also show abnormally high alkalis, particularly Na (Fig. 11). There is an apparent correlation between Si and Na (Fig. 12), but no inverse correlation between Na and K, as would be expected if the Na entered the mica structure solely in the interlayer position. Fluorine determinations made with the electron microprobe indicate partial replacement of OH by F (Table 3, analysis 2); lithium was not analyzed.

The coppaelite from Cupaello, Italy (specimen Y 253) (Gragnani, 1972), contains large crystals of biotite and phlogopite surrounded by complex reaction rims. The crystals are interpreted as xenocrysts. Associated phenocrysts are almost pure diopside, melilite, and kalsilite. The groundmass contains small crystals of a pale mica with weak pleochroism, light reverse absorption, and commonly, hour-glass zoning. An infrared spectrum made on a separate of the groundmass crystals did not reveal OH bands. That these micas have a different substitution scheme is particularly evident in Fig. 13, and a qualitative search with the ion microprobe has revealed that they contain substantial amounts of Li. They are tentatively interpreted as ternary mixtures of tetraferriphlogopite, taeniolite ( $\text{KMg}_2\text{LiSi}_4\text{O}_{10}\text{F}_2$ ), and a silica-rich mica that could be  $\text{K}(\text{Mg},\text{Fe})_3\text{Mg}_{0.5}\text{Si}_{3.5}\text{O}_{10}\text{F}_2$ . They also contain an excess of alkali ions, and there is no apparent correlation between Na and Si, although the absence of systematic Li determinations hinders interpretation along this line.

#### *Barium and Titanium Content*

All alumina-rich micas (i.e., micas that contain more than 1.00 atom of Al per



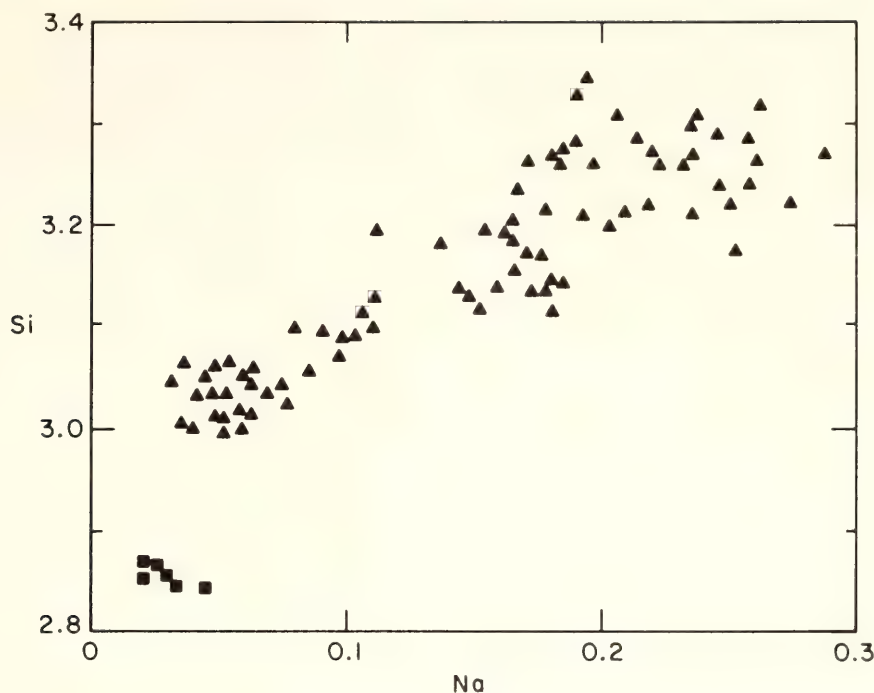


Fig. 12. Variation of Na as a function of Si (atom contents) in a mica-melilite-peridotite from Utah (specimen Y 127). Six analyses interpreted as xenocrysts are represented with a different symbol.

formula unit) contain either Ba or Ti or both. They also show a strong correlation between Al and Ba + Ti, as illustrated by Fig. 14. The results of this compilation imply that substitution of Ba on the interlayer position or of Ti on octahedral

sites is accompanied by substitution of Al for Si on tetrahedral sites.

Micas that can be interpreted as solid solutions of phlogopite and tetraferriphlogopite, even if their composition is on the phlogopite-rich side of the series,

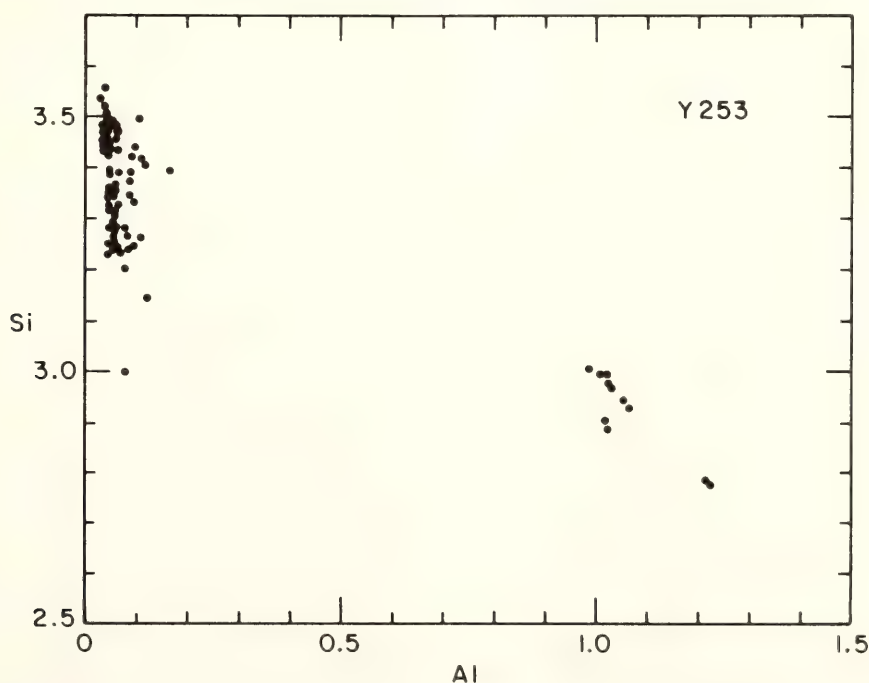


Fig. 13. Variation of Si as a function of Al (atom contents) in micas from a sample of coppaelite from Cupaello, Rieti, Italy (specimen Y 253). Micas with Al contents close to or greater than 1.00 ion per formula unit are interpreted as xenocrysts.

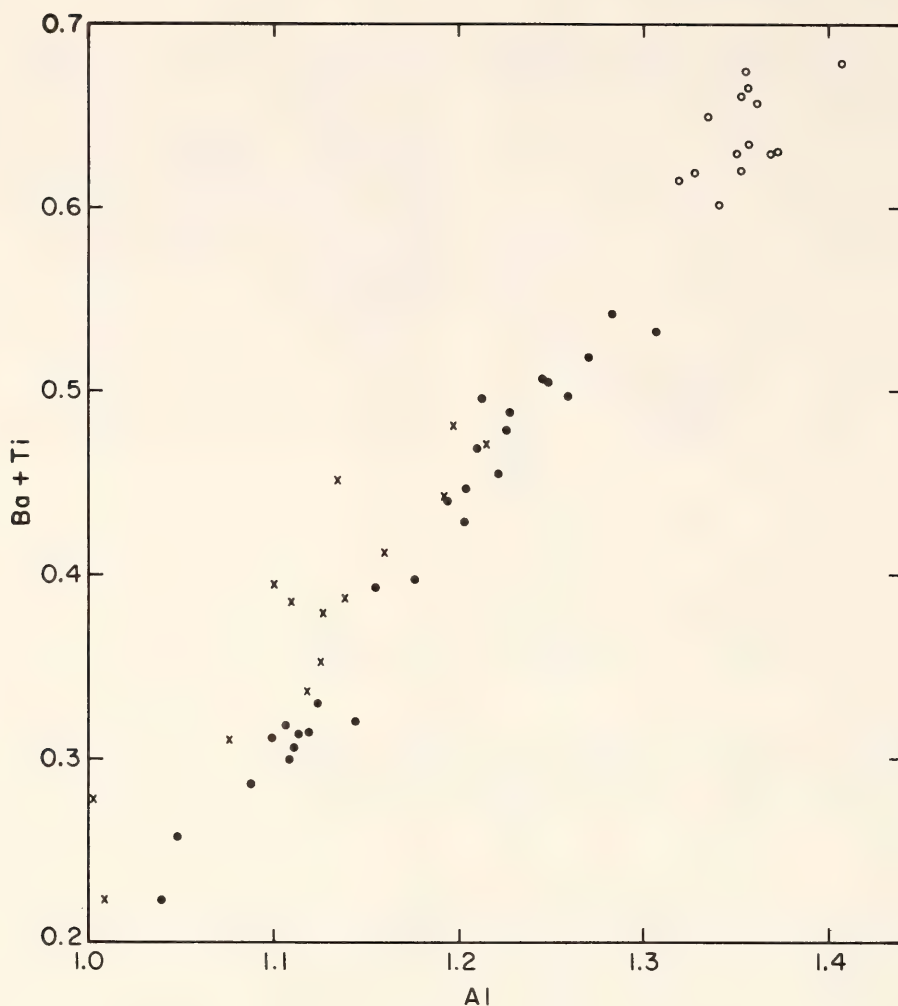


Fig. 14. Variation of Ba + Ti as a function of Al (atom contents) in micas from two specimens of meta-aluminous melilite-bearing olivine nephelinites. Solid circles, specimen Y 145 (Sutherland, South Africa); crosses, Y 186 (Modlibohov, Czechoslovakia). Open circles represent the composition of titanium-rich, barium-poor micas from a mica-bearing olivine nephelinite from Drevin, France.

contain only small amounts of either Ba or Ti. Silica-rich micas, however, even though they may contain less than 1.00 wt %  $\text{Al}_2\text{O}_3$ , show significant amounts of Ti but only small amounts of Ba. In both specimens described above, it is apparent that the substitution scheme  $2\text{Al} + \text{Ti} = 2\text{Si} + \text{Mg}$  is not applicable.

#### Conclusion

Micas found in melilite-bearing eruptive rocks do not as a rule contain any eastonite or Al-siderophyllite in solid solution. They consequently appear to be different from biotites found in eruptive rocks in general. They do not contain

enough Si + Al for total tetrahedral occupancy; hence other ions must fill some of the tetrahedral sites. The main ion is probably  $\text{Fe}^{3+}$ , at least in micas that belong to the phlogopite-tetraferriphlogopite series. Rare silica-rich micas have been found in two specimens, and in these two examples  $\text{Fe}^{3+}$  does not appear to be the only element accompanying Si on tetrahedral sites.

Some melilite-bearing lavas contain micas with Al in excess of 1.00 atom per formula unit. These micas also show high contents of Ti or Ba or both; Ti (and to a lesser extent Ba) can be found in smaller amounts in silica-rich micas, whereas these two elements are virtually



absent from tetraferriphlogopite. Satisfactory substitution schemes have not yet been worked out for the silica-rich micas containing significant amounts of Na and Li.

The reasons for the presence of these rare and complex micas relate mainly to the particular bulk composition of the melilite-bearing lavas. Although basic in composition (i.e., rich in Fe and Mg, and considerably silica-undersaturated), some of these lavas have a molar excess of alkalis over alumina (Velde and Yoder, *Year Book 75*, pp. 574–580). Trioctahedral micas are not commonly found in peralkaline chemical environments. On the other hand, the existence of Al-poor or Al-free micas may be reconciled with a peralkaline bulk composition. In melilite-bearing lavas that have a meta-aluminous bulk composition, high Ba and Ti micas are found. Micas that represent reaction products between late fluids or residual liquids and olivine typically belong to the phlogopite-tetraferriphlogopite series of composition, even though they occur in meta-aluminous lavas. This occurrence is further evidence that even in meta-aluminous bulk compositions, the crystallization of melilite, clinopyroxene, and nepheline commonly leads to peralkaline residual liquids.

#### COMPOSITION OF MAGNETITE IN SUBALKALINE VOLCANIC ROCKS

*E. F. Osborn, E. B. Watson, and  
S. A. Rawson*

As part of a continuing study of phase relations in silicate systems bearing on the origin of volcanic rocks (see Osborn and Watson, *Year Book 76*, pp. 472–478; Osborn, *Year Book 77*, pp. 784–790; Osborn, 1979), determinations have been made of the composition of magnetite occurring in the tholeiitic series of lavas from the Galápagos Islands and from Iceland, and in the calc-alkaline volcanic rocks from Cascades, Parícutin, and

Santorini localities. Analyses have been made both of magnetite crystals occurring in the original rock specimens and of the crystals formed experimentally in equilibrium with liquid in sealed capsules at total pressures of 10 kbar, 1 kbar, and 1 atm. The results suggest that for these rocks the composition of the magnetite is dependent on the pressure at which it crystallized from the liquid.

In the experimental studies, charges of powdered and dried rock were enclosed in sealed tubes of either 95Pt-5Au or 50Ag-50Pd composition, and were run at temperatures such that small-to-moderate amounts of magnetite crystals were present in the liquid-crystal mixture. In most of the runs, a charge of ~15 mg was enclosed in a tube of 1.8 mm I.D., but some of the charges, where more material was desired, were ~100 mg in tubes of 2.6 mm I.D. Runs were ordinarily 6 to 8 hr. For runs at pressures of 10 and 1 kbar, the gas-media, high-pressure apparatus of Yoder (1950) was used, in which the furnace assembly and sample capsules are fully immersed in water-pumped, purified argon. If there were trifling amounts of water in the gas, the mixture would effectively be in a Ni-NiO buffer because the tube holding the furnace assembly is pure nickel. Two runs were also made in sealed tubes at 1 atm, with air as atmosphere outside the capsule. Analyses of phases were made with an electron microprobe. Glass in samples quenched from a temperature above the liquidus was analyzed for Fe loss to the capsule in 20 runs. This Fe loss averaged 13.6% of the iron originally present, a loss affecting the FeO:Fe<sub>2</sub>O<sub>3</sub> of the mixture but having little effect on the composition of the magnetite, as discussed below.

The rock specimens\* from the Galá-

\* Sources of rock specimens were as follows: Galápagos, Mt. Jefferson and Crater Lake from A. R. McBirney; Hat Creek from I. S. E. Carmichael; Santorini from S. O. Agrell; Iceland from K. Grönvold; Parícutin from R. E. Wilcox.

pagos Islands consist of a series ranging from picrite basalt and aphyric tholeiite through ferrobalt and icelandite to siliceous trachyte. Specimens from Kerlingarfjöll, in central Iceland, consist of a fairly coarse grained olivine tholeiite and four samples of fresh, fine-grained volcanic rocks, very low in phenocrysts, and forming a series of increasing silica content, similar to the Galápagos suite. The Cascades, Parícutin, and Santorini rocks are represented by high-Al basalts, basaltic andesites, and low-silica andesites. The Cascades localities are Mount Jefferson, Crater Lake, and Mount Lassen (Hat Creek). Abundant phenocrysts are present in most of the calc-alkaline rocks, except for the Mount Lassen basalt, which contains only about 2% phenocrysts (Smith and Carmichael, 1968). On a plot of  $(\text{FeO} + \text{Fe}_2\text{O}_3)/(\text{FeO} + \text{Fe}_2\text{O}_3 + \text{MgO})$  vs.  $\text{SiO}_2$  ( $F/\text{FM}$  vs.  $\text{SiO}_2$ ) for the different rock series, distinctive curves are obtained (Fig. 15). The curves for the Galápagos and Iceland rocks have a subvertical segment with  $F/\text{FM}$  increasing until a corner is reached at an  $F/\text{FM}$  in the range 0.7–0.8 at an  $\text{SiO}_2$  content of about 50%, followed by a segment of much lower slope. The Cascades and Parícutin rock compositions have a trend (Fig. 15) of continuously increasing  $F/\text{FM}$ , without a corner. The Santorini suite forms a curve extending upward to a corner, as shown by Nicholls (1971), but at a lower slope than the corresponding curves for Galápagos and Iceland rock series. Positions on the diagram of Fig. 15 are shown for the 11 rock specimens that have been most extensively investigated in this study. In Tables 4 and 5 are listed six of the oxides (in weight percent) in these rocks, as obtained by chemical analysis, and compositional data for magnetite, as determined by the electron microprobe, with  $\text{FeO}$  and  $\text{Fe}_2\text{O}_3$  calculated assuming  $\text{R}_3\text{O}_4$  spinel stoichiometry.

Referring to Table 4, one will note that the  $\text{TiO}_2$  content of synthetic magnetites in Galápagos and Iceland

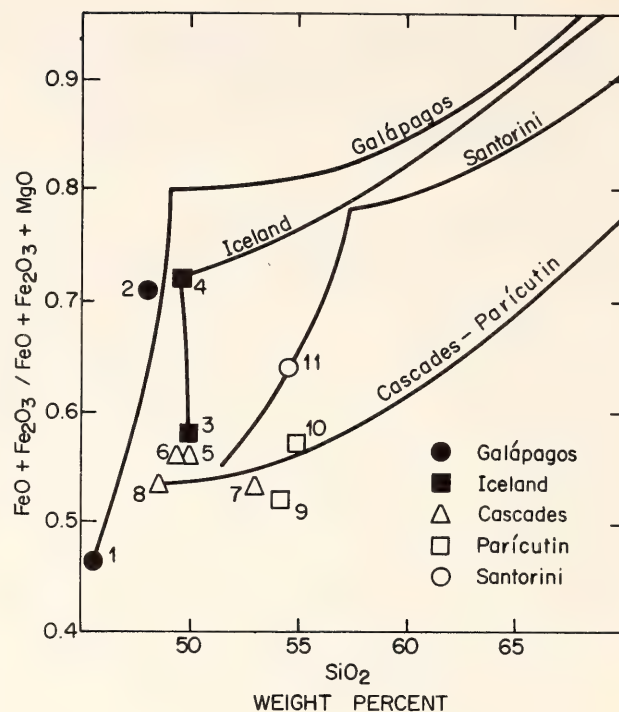


Fig. 15. Curves of  $(\text{FeO} + \text{Fe}_2\text{O}_3)/(\text{FeO} + \text{Fe}_2\text{O}_3 + \text{MgO})$  vs.  $\text{SiO}_2$ , showing general trends for rock suites from Galápagos Islands (Osborn, 1979), Iceland (plot of data from K. Grönvold, personal communication, 1977), Santorini volcano (Nicholls, 1971), Cascades-Parícutin (Osborn, 1979). The numbered points represent the 11 specimens for which data are listed in Tables 4 and 5.

specimens is much lower at 1 kbar than at 10 kbar, and the lower  $\text{TiO}_2$  content is associated with lower  $\text{FeO}$  and higher  $\text{MgO}$ ,  $\text{Fe}_2\text{O}_3$ ,  $\text{Al}_2\text{O}_3$ , and  $\text{Cr}_2\text{O}_3$ . The natural magnetites in rock specimens G-76 and I-KJ4 have compositions that extend the trends noted in progressing from 1 to 10 kbar, and apparently they crystallized at pressures significantly greater than 10 kbar and at correspondingly higher temperatures. These two rocks are the lowest in  $F/\text{FM}$  for the two series. For members of the series having a higher  $F/\text{FM}$ , G-79 and I-K245, the difference in composition of the magnetite in the rock and at 10 kbar is less pronounced, and crystallization at a pressure less than that for G-76 and I-KJ4 but greater than 10 kbar is suggested.

Data comparable to that in Table 4



TABLE 4. Composition of Magnetite in Tholeiitic Volcanic Rocks

	Composition of Rock* (partial)						Composition of Magnetite				Temp., °C	Time, hr	Phases Present†	
	TiO <sub>2</sub>	Fe <sub>2</sub> O <sub>3</sub>	FeO	MgO	Al <sub>2</sub> O <sub>3</sub>	SiO <sub>2</sub>	F/FM	TiO <sub>2</sub>	Al <sub>2</sub> O <sub>3</sub>	Cr <sub>2</sub> O <sub>3</sub>				Fe <sub>2</sub> O <sub>3</sub>
<i>Rock Specimens</i>														
(1) G-76	1.7	1.6	10.1	14.0	14.0	45.3	0.45	25	2.2	0.3	15	52	3.0	
(2) G-79	3.9	4.2	9.0	5.5	14.1	48.1	0.71	19	1.1	0.2	28	49	1.0	
(3) I-KJ4	1.4	2.0	8.7	7.7	15.4	48.9	0.58	25	1.7	0.1	16	54	0.4	
(4) K-245	2.4	3.8	10.1	5.4	13.7	48.7	0.72	24	1.3	0.1	17	54	1.2	
<i>10-kbar runs</i>														
G-76 (7)								10	5	0.4	44	33	5	8 mt + ol + py + gl
G-79 (6)								18	3	0.7	30	42	4	6 mt + ol + gl
I-KJ4 (19)								10	4	0.9	44	34	4	8 mt + ol + py + pl + gl
I-K245 (7)								18	3	0.1	32	43	3	8 mt + py + pl + gl
<i>1-kbar runs</i>														
G-76 (11)								3.2	11	11	42	21	10	8 mt + ol + pl + gl
G-79 (3)								3.9	6	1.5	53	25	9	8 mt + gl
I-KJ4 (17)								0.8	10	1.5	63	4	19	8 mt + ol + py + gl
I-K245 (6)								3.1	5.1	0.1	56	23	8.2	8 mt + pl + gl 1350 → 1160

\* Analyses of Galápagos rocks (G-76 and G-79) are from McBirney and Aoki (1966, p. 27, table 1, nos. 13 and 15); those of Iceland rocks (I-KJ4 and I-K245) are from K. Grönvold (personal communication, 1977).

† mt, magnetite; ol, olivine; py, pyroxene; pl, plagioclase; gl, glass.

TABLE 5. Composition of Magnetite in Calc-Alkaline Volcanic Rocks

	Composition of Rock* (partial)					Composition of Magnetite					Temp., °C	Time, hr	Phases Present†		
	TiO <sub>2</sub>	Fe <sub>2</sub> O <sub>3</sub>	FeO	MgO	Al <sub>2</sub> O <sub>3</sub>	SiO <sub>2</sub>	F/FM	TiO <sub>2</sub>	Al <sub>2</sub> O <sub>3</sub>	Cr <sub>2</sub> O <sub>3</sub>				Fe <sub>2</sub> O <sub>3</sub>	FeO
<i>Rock Specimens</i>															
(5) C-BX149 (M.J.)	1.5	2.6	7.5	7.7	16.1	49.7	0.56	16	1.9	0.4	34	41	2.2		
(6) C-M5331 (C.L.)	1.3	4.1	5.5	7.4	17.1	49.5	0.56	13	2.0	0.8	42	38	2.7		
(7) C-RC3 (C.L.)	1.0	2.8	4.9	6.7	16.9	52.7	0.53	15	1.7	0.9	34	39	3.4		
(8) C-C12 (H.C.)	1.1	1.8	8.0	8.6	17.4	48.5	0.53	22	3.5	0.1	20	51	1.1		
(9) P-55478	1.0	1.7	6.1	7.0	17.7	54.1	0.52	7	2.9	14	36	32	3.2		
(10) P-51W19	1.0	1.3	6.0	5.8	18.4	54.9	0.57	11	2.4	4.6	39	39	2.1		
(11) S-85	0.9	2.0	5.9	4.5	17.7	54.5	0.64	14	2.6	0.1	34	44	0.6		
<i>10-kbar runs</i>															
C-BX149 (38)								10	5	0.2	44	34	5	8	mt + ol + py + gl
C-MS331 (29)								1.3	15	0.9	53	17	12	8	mt + pl + gl
C-RC3 (31)								1.3	11	18	31	23	11	8	mt + ol + py + pl + gl
P-55478 (13)								1.6	11	14	42	19	10	8	mt + ol + py + pl + gl
P-51W19 (10)								1.7	11	14	45	20	10	8	mt + ol + py + pl + gl
S-85 (15)								1.4	6	0.2	58	22	7	8	mt + ol + py + pl + gl
<i>1-kbar runs</i>															
C-BX149 (14)								3.7	7	0.2	57	19	10	8	1350 → 1160 mt + py + pl + gl
C-MS331 (20)								1.4	12	2.1	52	17	12	8	1200 mt + pl + gl
C-RC3 (15)								0.6	13	8.0	52	5	18	8	1210 mt + ol + pl + gl
C-12 (2)								0.7	10	0.9	60	6	18	8	1180 mt + ol + gl
P-55478 (9)								1.5	9	13	45	19	11	8	1170 mt + ol + py + pl + gl
P-51W19 (5)								1.0	12	14	43	14	13	8	1190 mt + ol + pl + gl
S-85 (5)								1.1	6.3	0.1	61	18	10	8	1170 mt + pl + gl
<i>1-atm runs</i>															
C-BX149								1.2	12	1.4	57	10	16	4	1200 mt + pl + gl
C-MS331								1.4	11	2.8	53	16	12	4	1200 mt + pl + gl

\* Sources of rock analyses are as follows: Mount Jefferson (M.J.) and Crater Lake (C.L.) rocks, A. R. McBirney (personal communication, 1976); Hat Creek (H.C.) specimens, Smith and Carmichael (1968, p. 216, table 2, no. 12); Parícutin No. P-55478, *Year Book 64* (p. 264, table 5, no. 3); Parícutin No. P-51W19 is assumed to have essentially the same composition as a specimen erupted at the same time (March 1943) and listed as No. 2 by Wilcox (1954, p. 294, table 2); Santorini (S-85), Nicholls (1971, p. 83, table 3, No. 9).

† Abbreviations as in Table 4.



are shown in Table 5 for the calc-alkaline volcanic rocks from Cascades, Parícutin, and Santorini. These rocks contain magnetite of lower  $\text{TiO}_2$  and  $\text{FeO}$  contents than magnetite in the two tholeiitic series. In one of the rocks (BX 149), the magnetites formed experimentally at 10 kbar have compositions intermediate between those for 1-kbar runs and those occurring naturally in the rocks, as is the case for the rocks of Table 4. For the other five specimens—those from Crater Lake, Parícutin, and Santorini—the magnetites formed experimentally at 10 kbar are low in  $\text{TiO}_2$  and high in  $\text{Cr}_2\text{O}_3$  and  $\text{Al}_2\text{O}_3$ , closely resembling compositions at 1 kbar. Pressure in the range 1 bar–10 kbar thus seems to have little effect on the composition of the magnetites in these five rocks. In view of the fact that the  $\text{TiO}_2$  content of natural magnetite in the Crater Lake, Parícutin, and Santorini rock specimens is several times greater and the  $\text{Al}_2\text{O}_3$  content several times less than those of magnetites formed experimentally in samples of these rocks run at 10 kbar, it seems probable that the natural magnetites crystallized from magma at pressures much greater than 10 kbar.

In all the rock specimens studied, assemblages were observed to be the same in the experimental runs at 1 and 10 kbar and in the natural rocks. Whereas in the systems  $\text{Mg}_2\text{SiO}_4\text{--CaAl}_2\text{Si}_2\text{O}_8$  (Kushiro and Yoder, 1966),  $\text{Mg}_2\text{SiO}_4\text{--CaAl}_2\text{Si}_2\text{O}_8\text{--SiO}_2$  (Kushiro, *Year Book* 71, pp. 357–359), and  $\text{MgO--FeO--Fe}_2\text{O}_3\text{--CaAl}_2\text{Si}_2\text{O}_8\text{--SiO}_2$  (Osborn, 1976, olivine and anorthite cease to be compatible phases above a pressure of about 8 kbar, in the subalkaline volcanic rocks of this study olivine and plagioclase coexist at a pressure of 10 kbar as well as at 1 kbar and in the natural rocks. The higher pressure compatibility of olivine and plagioclase over that of olivine and anorthite is presumably related to partial substitution of  $\text{Na} + \text{Si}$  for  $\text{Ca} + \text{Al}$  in the anorthite structure. The difference in composition of the magnetite phase

at the different pressures is therefore not associated with a change in the general phase relations but only with a change in composition of the coexisting phases.

In the three groups of data shown in Table 4, and progressing from the original rock to the 10-kbar runs and to 1 kbar, the  $\text{TiO}_2$  and  $\text{FeO}$  in magnetite change from high to medium to low, whereas the  $\text{MgO}$ ,  $\text{Fe}_2\text{O}_3$ ,  $\text{Cr}_2\text{O}_3$ , and  $\text{Al}_2\text{O}_3$  follow a reverse sequence. These changes in composition are believed to be related largely to a shift, with change in pressure and temperature, in the position of conjugation lines joining compositions of coexisting liquid and magnetite crystals. The change in magnetite composition may, however, result to some extent from a change of  $\text{FeO}:\text{Fe}_2\text{O}_3$  brought about by two other factors. One factor is the effect of pressure on the liquid structure that may cause  $\text{FeO}:\text{Fe}_2\text{O}_3$  of the liquid to increase with pressure. The other factor is a loss of Fe to the capsule, resulting in a decrease in  $\text{FeO}:\text{Fe}_2\text{O}_3$ . To investigate the former effect, two experiments were made. In one, using a mixture in the model system  $\text{MgO--FeO--Fe}_2\text{O}_3\text{--CaAl}_2\text{Si}_2\text{O}_8\text{--SiO}_2$  having a composition close to the liquidus minimum at 10 kbar, a sample weighing 1 g was equilibrated with air at  $1330^\circ\text{C}$  in a 95Pt–5Au crucible. One half of the sample was then run at  $1330^\circ\text{C}$  at 10 kbar. In both cases the temperature of the run was above the liquidus, and the mixture was quenched to a glass. The glasses were analyzed for FeO and  $\text{Fe}_2\text{O}_3$ . It was found that no loss of Fe to the capsule occurred during the 10-kbar run, in accord with the high  $f_{\text{O}_2}$  of the liquid, but  $\text{FeO}:\text{Fe}_2\text{O}_3$  changed from 0.38 at 1 atm to 0.58 at 10 kbar. The apparent effect of an increase in pressure from 1 atm to 10 kbar was therefore a moderate increase in  $\text{FeO}:\text{Fe}_2\text{O}_3$ .

In the second experiment, a sample of Galápagos aphyric tholeiite, G-15, was used. One half of a 1-g sample of the powdered rock was analyzed for FeO and  $\text{Fe}_2\text{O}_3$ . The other half was sealed in a

95Pt-5Au capsule and run at a temperature above the liquidus ( $1250^{\circ}\text{C}$ ) at 1 kbar for 8 hr; it was then quenched to a glass and analyzed. The results show an iron loss of 10%. The  $\text{FeO}:\text{Fe}_2\text{O}_3$  was lowered from 4.0 to 1.3, but this change is accounted for precisely by the loss of metallic Fe to the capsule. The  $\text{FeO}:\text{Fe}_2\text{O}_3$  of this specimen was therefore not changed during a run at 1 kbar except through oxidation coincident with loss of Fe to the capsule.

Although oxidation of the liquid may occur during the runs because of Fe loss to the capsule, this effect is believed to be secondary with respect to causing the observed change in composition of the magnetite. This belief is based on data obtained where metallic Fe powder was added to the charge of powdered rock for a series of runs in an amount equal to 15% of the Fe present in order to approximately balance the loss of Fe that occurs during a 6–8 hr run. The metallic iron added was very pure sponge iron and was thoroughly mixed into the sample by grinding in an agate mortar. The charges, at pressures of both 1 and 10 kbar, were first held for 1 hr at a temperature  $\sim 150^{\circ}\text{C}$  above the liquidus to completely melt and to promote homogenization of the mixture. The temperature was then lowered for a 7-hr run at the desired temperature. Analyses of nine glasses, where the mixture was quenched from above the liquidus temperature, showed that on the average the Fe lost to the capsule was approximately balanced by that added to the charge. The average change in Fe content of the mixture was only  $+0.4\%$ . For two of the mixtures, however, a large unaccountable change was found:  $+10\%$  for one and  $-9\%$  for the other. For four of the mixtures there was no change in Fe content. The composition of the magnetite was obtained from runs at temperatures below the liquidus at which a small-to-moderate amount of magnetite is present in the liquid, with or without other crystals. The magnetites formed in this

series of runs do not differ materially in composition from those formed in the runs in which no Fe was added. It is concluded that the change in  $\text{FeO}:\text{Fe}_2\text{O}_3$  of a mixture during a run, because of Fe loss to the capsule, is not of major importance as a cause of the very significant changes observed in the composition of the magnetites.

Results of preliminary experiments on three calc-alkaline rocks, reported earlier (Osborn and Watson, *Year Book* 76, pp. 472–478), had suggested that high  $\text{TiO}_2$  in magnetites of volcanic rocks signifies low pressure during their crystallization. Since then, more reliable data on the composition of phases at equilibrium have been obtained in experiments in which the starting materials were ground much finer than formerly, longer run times were used, and the temperature and pressure of the runs were approached from both above and below. Furthermore, from the data obtained in studies of the Galápagos and Iceland rocks, the relation of magnetite composition to pressure is clearer. These later results, as discussed in this report, lead to the conclusion that the high- $\text{TiO}_2$  magnetites represent high-pressure ( $\geq 10$  kbar) crystallization conditions.

As explained in the previous report (Osborn and Watson, *Year Book* 76, pp. 472–478), the present experiments on magnetites are being carried out to learn more about the conditions under which magnetite coexists with liquid and the extent to which fractional crystallization paths in the model system  $\text{MgO-FeO-Fe}_2\text{O}_3\text{-SiO}_2$  would seem to be applicable to the origin of subalkaline volcanic rock series. The results confirm the applicability of phase relations in the model system in the manner originally described (Osborn, 1959), by demonstrating that magnetite is an early phase precipitating from high-Al basalts and andesites. The depth at which the magnetite crystallized appears to have been greater than  $\sim 35$  km. The study shows also that magnetite is a phase crystallizing from the tholeiitic



rocks (Galápagos and Iceland) at similar depths. The latter do not, on fractional crystallization, form a calc-alkaline series, presumably because oxygen buffering by the country rock is ineffective until the oxygen fugacity, decreasing continually during crystallization, reaches some low value. At this point, with the magma beginning to be effectively oxygen-buffered, the rate of magnetite precipitation increases, a corner occurs on the F/FM vs. SiO<sub>2</sub> curve (Fig. 15), and the curve then continues with a silica-enrichment trend at a high F/FM.

#### A COMPARISON OF TWO METHODS FOR CLASSIFYING BASALTS

*Felix Chayes*

The distinction between alkaline and subalkaline basalts is based partly on chemical composition, partly on mineral assemblage, and partly on geological association. In most published descriptions predating the days of routine electron microprobe analysis, critical information on mineral assemblages is minimal. And in many areas alkaline and subalkaline volcanic suites are intermixed, so information about geological association often is of no use in deciding the provenance of a particular specimen. Inevitably, the bulk analysis plays the major role in this respect.

The most widely used chemical criterion, the Macdonald-Katsura field boundary in the silica-total alkalis projection, is based on detailed petrographic examination of a large collection of analyzed Hawaiian lavas (Macdonald and Katsura, 1964). From the graph given in weight percent in the original description it was later assigned the value (Chayes, *Year Book* 74)

$$DM = 0.374\text{SiO}_2 - \text{Na}_2\text{O} - \text{K}_2\text{O} - 14.63,$$

a basalt being considered alkaline if and only if  $DM < 0$ . Most petrologists prefer the graphical statement and a few

(see, for instance, Kuno, 1968) have modified it slightly, though the rationale for such modifications is rarely stated.

In 1966, the writer proposed a second chemical statistic for use as a basalt discriminant, a line subparallel to the *ol-di* join in the central ternary of the Tilley-Muir projection,

$$DC = 0.134ol' + hy' - 26.94,$$

in which  $ol' = 100ol/(ol+hy+di)$  and similarly for  $hy'$ , a basalt being termed alkaline if and only if  $DC < 0$ , where  $DC = 0$  is the trace of the two-class linear discriminant function that, with data then available, best separated oceanic island basalts intimately and presumably genetically associated with nonbasaltic alkaline extrusives from those not so associated.

The complementary nature of the two statistics is evident. One was developed by a close comparison of petrography with bulk composition and relies directly on the content of silica and alkalis. The other is based primarily on geological association and utilizes only what is left of the bulk composition after extraction of the alkalis and their normative equivalent of silica (and alumina). The interest that would attach to a comparison of partitions effected by *DM* and *DC* was immediately apparent, but the amount of calculation it would require was then forbidding. Much later it was found (Chayes, *Year Book* 74) that 89.7% of a large store of Hawaiian analyses were classified similarly by the two discriminants.

Recent developments have greatly reduced the costs of such computations, and the first results of a worldwide extension of the comparison are shown in Table 6. The data are published analyses of Cenozoic nominal basalts, trachybasalts, tholeiites, and hawaiites drawn from the writer's data base. The argument of the first four columns of the table is the number of specimens from areas identified by row captions and classified as alkaline or subalkaline by

TABLE 6. Basalt Partition by *DC* and *DM* Statistics\*

	<i>DC</i>		<i>DM</i>		<i>C</i> , %
	alk	subalk	alk	subalk	
<i>Dominantly subalkaline</i>					
Brtoarctic Province	100	161	107	154	78.2
Hawaiian Islands	125	450	170	405	89.7
Japan	217	375	297	295	84.1
Mid-Atlantic Ridge	31	138	8	161	80.5
North Pacific Rim	25	218	30	213	88.9
Westernmost US	17	113	50	80	70.0
<i>Dominantly alkaline</i>					
African Rift	243	182	333	92	74.1
Canary Islands	497	26	516	7	96.4
Eastern Europe	237	56	269	24	88.4
Southern Europe	217	70	251	36	86.1
Western Europe	345	72	398	19	86.3

\* *C* is the percent of consistent classifications. For definitions of other terms and description of data, see text.

one of the discriminants. The entry in column 5 is the percentage of analyses classified similarly by the two discriminants.

Only a few of the entries in column 5 are large enough to suggest that one of the discriminants would be a satisfactory taxonomic proxy for the other, but the cell frequencies from which even the smallest has been calculated indicate a highly significant nonrandom association. The first four entries in any row of Table 6 are in fact marginal totals in a 2 × 2 contingency table. The smallest entry in column 5 is for the row titled “Westernmost US”; for the marginal totals listed in this row the expected frequency of consistent classification, on the assumption of independence, is [(17 × 50) + (113 × 80)]/130 = 76.1, or 58.5%, compared to an observed value of 91/130 or 70%.

The percentage of consistent classifications of course cannot be tested directly, but the sum of cell frequencies contributing to it can. In this case, for instance, there are 91 consistent and 39 inconsistent classifications, from which  $\chi^2$  is 22.78; the excess of consistent over inconsistent

classifications is easily significant at the 0.001 level.

As shown in Table 6, many more basalts are identified as alkaline by *DM* than by *DC*. Among the larger subsets in the table the only exception to this rule is the mid-Atlantic ridge. Of the 3915 analyses so far processed, 2054 are alkaline according to *DC*, 2429 according to *DM*. For every mismatch in which *DM* > 0, there are almost five in which *DM* < 0. Can this asymmetry be reduced by minor adjustments in the definitions of the discriminants?

The mismatch (*DM* < 0, *DC* > 0) is heavily concentrated in rocks that are either low in *ol* or actually *q*-normative, i.e., whose analyses plot close to and on either side of the join *di-hy* in the Tilley-Muir projection. The great majority of the points in question could not be reached by a minor shift of the trace of *DC* in the *di-hy-ol* ternary. Many are marginal, however, in the sense that although *DC* is a sizable positive number, *DM* is a small enough negative number that its sign might well change in response to small changes in the slope or intercept of the Macdonald-Katsura



field boundary. In fact, merely changing the  $(\text{Na}_2\text{O} + \text{K}_2\text{O})$  intercept of the Macdonald-Katsura diagram from  $-14.63$  to  $-14.0$  dramatically reduces the imbalance in several of the larger subsets, and in some this change has the further effect of materially increasing the percentage of consistent classification. In the Japanese data, for instance, it reduces the ratio of mismatches from more than 12:1 to less than 3:1 and increases the percentage of consistent classifications from 84.1 to 87.8. For the lavas of the African Rift Valley the same change of intercept reduces the mismatch ratio from 10:1 to less than 2:1 and increases the percentage of consistent classification from 74.1 to 80.2.

For the Hawaiian data the mismatch ratio falls from more than 7:1 to well under 2:1, but the improvement in percentage of consistent classification—from 89.7 to 90.6—is hardly of much moment. The distribution of data in the scatter diagram given by Macdonald and Katsura is such that a shift of intercept of this size moves several of the points on which their field boundary is based from one class to another. The desired enlargement of the subalkaline field in the high-silica region can also be obtained by a rotation of the field boundary that does not require reclassification of any of the original Macdonald-Katsura data points. Such a rotation, however, actually increases the imbalance of mismatch types without increasing overall consistency. To the extent that consistency is a reasonable goal in work of this sort, simple translation of the field boundary is preferable to rotation about its mean.

In the only example so far found—the mid-Atlantic ridge—in which mismatches with  $DM > 0$  greatly outnumber those with  $DM < 0$ , the opposite relation between the sizes of  $DM$  and  $DC$  occurs—i.e., positive values of  $DM$  are usually sizable and associated negative values of  $DC$  are very small. What seems to be called for here is a slight leftward shift

of the trace of  $DC$  in the upper portion of the central ternary of the Tilley-Muir projection. The trace of the computed discriminant connects the points ( $ol=84.4, di=0$ ) and ( $ol=0, di=73.1$ ). If the line is rotated about the first point so that the second becomes ( $ol=0, di=75$ ), the ratio of mismatches ( $DM > 0 / DM < 0$ ) in the mid-Atlantic ridge suite is reduced from 5.6:1 to 3.8:1, and the percentage of consistent classification is increased from 80.5 to 85.8.

With the indicated modifications of  $DM$  and  $DC$ , all entries in column 5 of Table 6 would be over 80% and the weighted average for the column would be 88.5% instead of the present 84.9%. There seems to be little question that these two complementary definitions of “alkalinity” in basalt are related, and it is clear from the discussion that material improvement in the consistency of their performance as taxonomic devices could be obtained by rather minor *ad hoc* modifications in their definitions.

The following procedure, part of a suggestion presented for discussion at the Padua meeting of the IUGS Subcommittee on Systematics in Petrology in 1979, serves to isolate most of what are conventionally regarded as alkaline basalts from the remainder.

### Definition

A basalt is alkaline if (I) it contains modal feldspathoid, or (II) its analysis plots above and left of both (a) the Macdonald-Katsura line, as revised here, in the alkali-silica projection, and (b) the trace of the linear discriminant, as revised here, in the Tilley-Muir projection.

### Application

If (I) is true, there is an overwhelming probability that (II) will also be true; i.e., given that (I) is true, there is really no need to test (II). The basalt is alkaline.

If (II) is true, (I) may or may not be true but is not required. The basalt is alkaline.

If (I) is false (or unknown), (II) may or may not be true. If modal or normative quartz is present or the ratio of modal olivine to rhombic + pigeonitic pyroxene is less than 4:1, there is a strong probability that (II) is false. If critical modal information is lacking, both parts of (II) are to be tested. If both parts of (II) are false or the modal criteria proposed in this paragraph are satisfied, the basalt is subalkaline.

To use (II), incidentally, it is not necessary to plot the analysis in either projection. If the quantities  $DM'$  and  $DC'$  are both negative, where, in weight percent,

$$DM' = 0.374SiO_2 - Na_2O - K_2O - 14,$$

and

$$DC' = 0.111ol' + hy' - 25,$$

conditions (II) are satisfied and the basalt is alkaline. From the survey described above the odds appear to be better than 7:1 that  $DM'$  and  $DC'$  will agree in sign in Cenozoic rocks called basalt. Work on the project continues, and further refinement and adjustment of the discriminants may somewhat improve these odds. It seems likely, however, that a sizable residue of inconsistent classifications by criteria (II) (a) and (II) (b) will persist. If such ambiguities cannot be resolved by mineralogical information—or, as new data gradually accumulate, by trace element associations—the basalts in which they occur simply should not be specifically categorized as either alkaline or subalkaline.

#### A WORLD DATA BASE FOR IGNEOUS PETROLOGY

*Felix Chayes*

The pressing need for a comprehensive and readily accessible electronic information system for igneous petrology has

been described in earlier reports (see for instance, Chayes, *Year Book* 73) and elsewhere (Chayes, 1978a). With practical examples drawn from a base of restricted coverage and limited information content it has recently been argued (Chayes, 1979c) that a facility of this type would be of immense utility in many aspects of petrological research. At the writer's suggestion, responsibility for organizing and encouraging work aimed at the development of such a facility has been centered in Project 163 of the International Geological Correlation Program.

The growth of the project as an *ad hoc* scientific club is proceeding at a satisfactory rate. Its current mailing list includes over 160 petrologists from 26 countries. During the report year it conducted a workshop designed for specialists expected to be influential in forming or managing regional centers, and sponsored a symposium and demonstration for the general geological public. More than 60 contributors, some as individuals, some in affiliation with one or other of the national groups that have been formed, have begun the task of extracting data from the world literature and encoding it in project data forms. These activities are reviewed in circulars 78-7 and 79-3 of the series maintained by the project. Copies of project circulars (Chayes, 1978b, c, d; 1979a, b; Chayes and Mutschler, 1979) are available for interested readers.

The project data form, the most recent version of which is described in circular 79-2, provides a means for conveniently recording information about the geological association, age, petrography, mineral assemblage, and chemical composition of igneous rocks of all kinds. During the report year the first processor for electronically scanning, editing, storing, and retrieving such information was put into pilot operation. Provisional, in some respects incomplete, and subject to continual revision, this prototype of the project information system is now ready for more or less routine use in processing



data submitted by contributors. It is described in project circular 78-6B. The current program requires rather substantial memory, but a version suitable for use on a minicomputer is under development.

For entry into the system, data submitted on coding forms must of course first be put in machine-readable form. The completed coding form may be used as punch copy for this purpose, cards being punched in the format described in circular 78-3D. This transfer procedure has proved very time-consuming when attempted by amateurs (like the writer), and the complexity of the form—it contains eight lists of which seven are of variable length and six optional!—makes it unsuitable copy for commercial use. Data preparation will be greatly facilitated by a recently prepared conversational program that permits essentially free-field input format and issues numerous prompts and queries. The program, KRDKON, is described in circular 79-1 and will be made available to any project contributor who wishes to use it. Experience with KRDKON in the near future is expected to provide the first firm cost estimates of what will almost certainly be the most demanding single operation in the construction of the new data base, the movement of data from hard copy to machine-readable form.

#### SHOCK METAMORPHIC FEATURES IN PAMPA DEL INFIERNO CHONDRITE

*N. Z. Boctor, P. M. Bell, and H. K. Mao*

The Pampa del Infierno meteorite was found in a ploughed field at Avia Terai, Chaco Territory, Argentina, in 1885 (Hey, 1966). It has been classified both as a basaltic achondrite (Urey and Craig, 1953; Deüser, 1968; Jerome and Goles, 1971) and as an ordinary chondrite (Mason 1963; McCarthy *et al.*, 1974). In the present study, more detailed data were obtained on the petrology and mineral chemistry of the

meteorite. It is shown to be an L6 chondrite that has undergone shock metamorphism at minimum peak pressure of about 150 kbar to a pressure greater than 300 kbar. The discovery of the high-pressure spinel form of olivine, ringwoodite, in Pampa del Infierno is of interest in relation to the nature of the olivine-spinel phase transition in the earth's mantle.

#### *Petrography and Mineral Chemistry*

Pampa del Infierno contains only a few chondrules, and their presence is generally obscured by recrystallization and shock effects. The meteorite is also characterized by veining and dark clasts, presumably of shock origin (Fig. 16). The chondrules are of the barred type and are composed of either olivine ( $\text{Fo}_{75.4}$ ) or low-Ca pyroxene ( $\text{En}_{75}\text{Wo}_{1.16}\text{Fs}_{20.84}$ ) with interstitial plagioclase glass and rare clinopyroxene. In addition to chondrules, two types of dark "clasts" can be distinguished on the basis of mineralogy and texture. One kind is composed of olivine ( $\text{Fo}_{76}$ ), low-Ca pyroxene ( $\text{En}_{77.5}\text{Wo}_{1.6}\text{Fs}_{20.9}$ ), and glass of plagioclase composition ( $\text{Ab}_{81.9}\text{Or}_{6.6}\text{An}_{11.5}$ ), plus interstitial troilite and metal. The olivine crystals have shock features such as fracturing, undulose extinction, and mosaicism. The low-Ca pyroxene shows kinking, microtwinning similar to that reported for clinoenstatite (Carter, 1976), and partial transformation to a mafic glass of much the same composition. Eutectic intergrowths of troilite and iron apparently formed by crystallization from shock melt. Discrete metal grains are also present; they are composed of a very fine intergrowth of kamacite and taenite (plessite). The other type of "clast" shows a spinifex-like texture and consists of skeletal olivine crystals of two different sizes and interstitial glass. The large olivine crystals ( $\text{Fo}_{81.4}$ ) are more magnesian than the smaller crystals ( $\text{Fo}_{69.3}$ ), and the glassy matrix encloses partly resorbed chromite crystals and



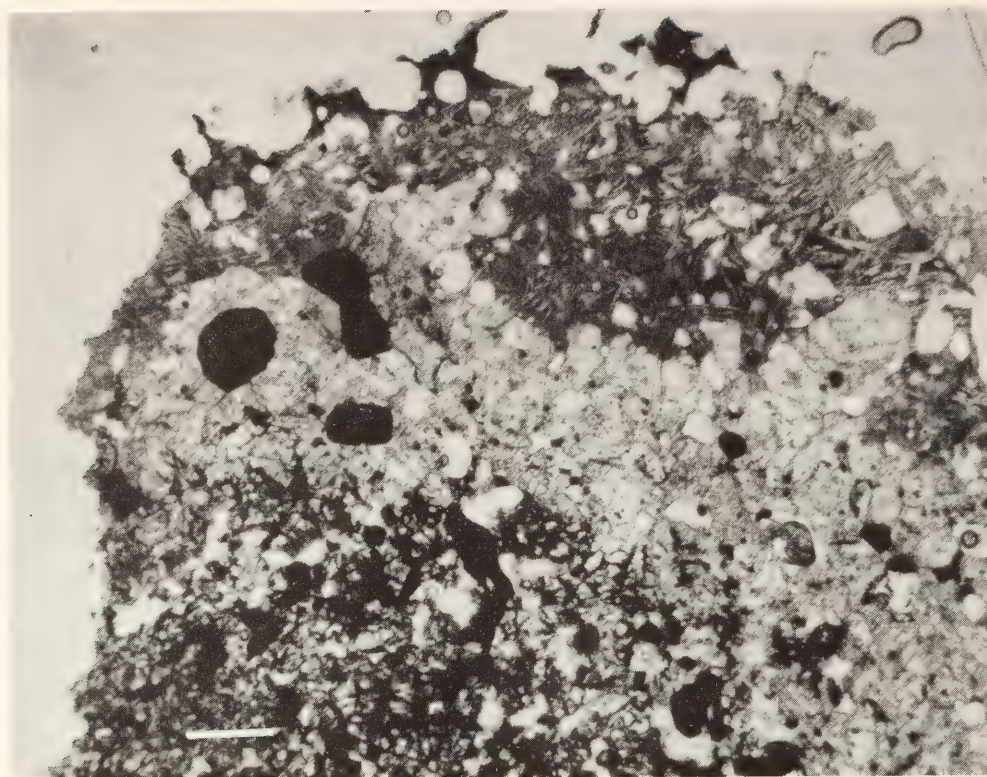


Fig. 16. General view of a thin section of Pampa del Infierno chondrite showing dark granular clasts and spinifex-textured clast; plane polarized light. Bar = 0.1 mm.

rare globules of troilite-iron-eutectic intergrowths.

The light-colored portion of the meteorite (Fig. 16) has a granular texture and is composed of olivine ( $\text{Fo}_{75.3}$ ), low-Ca pyroxene ( $\text{En}_{77.4}\text{Wo}_{1.5}\text{Fs}_{21.7}$ ), clinopyroxene ( $\text{En}_{49.9}\text{Wo}_{44.3}\text{Fs}_{8.8}$ ), and plagioclase glass ( $\text{Ab}_{83.7}\text{Or}_{6.6}\text{An}_{10.3}$ ), with minor amounts of troilite, metal, and chromite. The olivine is highly fractured and has undulatory extinction; the clinopyroxene displays polysynthetic twinning. Troilite is recrystallized, and the Fe-Ni metal assemblage is distinctly segregated into kamacite (4.2–6.4 wt % Ni) and taenite (32.4–47.4 wt % Ni) phases, but minor amounts of plessite are also present.

A black veinlet ranging in thickness between 0.5 and 1 mm transects the matrix. The vein material consists of a very fine grained, translucent brown phase enclosing abundant spheres of troilite-iron eutectic intergrowths. The vein also encloses highly fractured, angular fragments of olivine containing pale

purple inclusions of ringwoodite (Fig. 17), the identity of which was verified by x-ray diffraction. The occurrence of ringwoodite in Pampa del Infierno is very similar to that in Tenham meteorite, as described by Binns (1970) and recently confirmed through electron diffraction studies by Poirier and Madon (1979). Also present in the vein is a pale brownish phase displaying very weak birefringence and having a composition similar to that of the low-Ca pyroxene in the matrix. The structural state of this phase is under investigation to determine whether it is the same as the high-pressure, perovskite-type structure of low-Ca pyroxene recently synthesized by Yagi, Mao, and Bell (this Report).

### Discussion

The mineral chemistry of olivine, pyroxene, plagioclase glass, and chromite is similar to that reported by Van



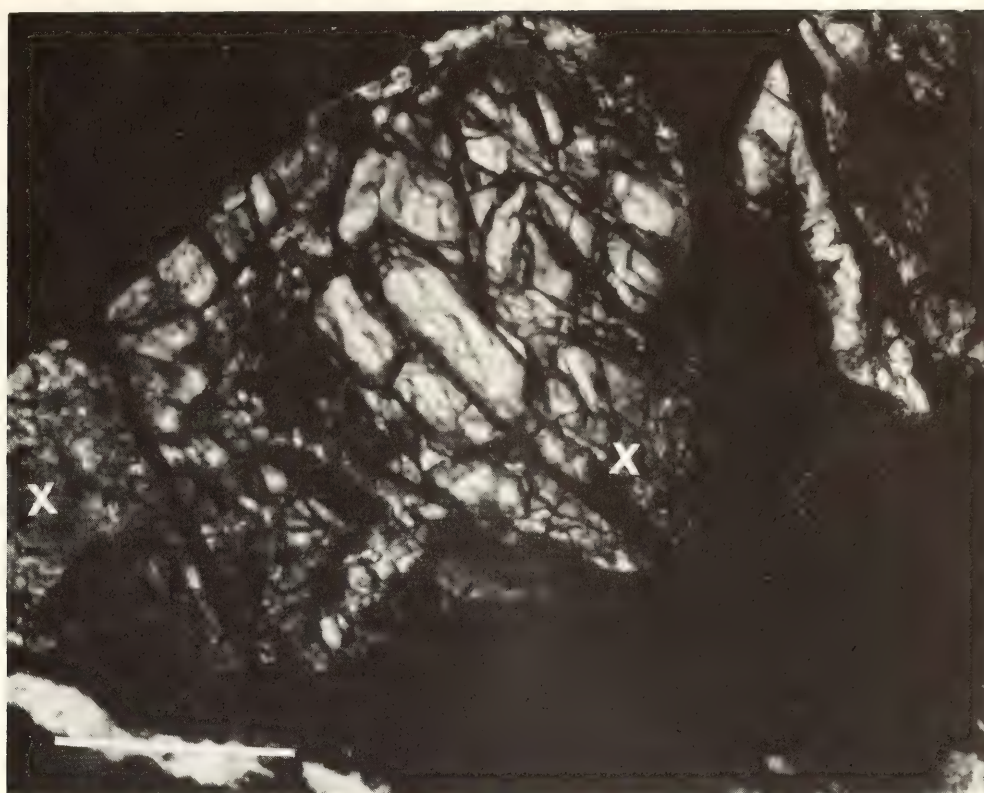


Fig. 17. Magnified portion of black vein enclosing angular fragment of olivine with inclusions of ringwoodite (X); plane polarized light. Bar = 0.025 mm.

Schmus (1969) for chondrites belonging to the L6 subgroup of Van Schmus and Wood (1967). Pampa del Infierno, however, has been metamorphosed by impact. The following features suggest the pressures reached during the impact event. The fracturing, undulatory extinction, and mosaicism observed in the olivine are indicative of shock pressures in the range from 50 to 250 kbar (Carter *et al.*, 1968; Snee and Ahrens, 1975). Olivine of the composition common to the Pampa del Infierno chondrite transforms to the spinel phase ringwoodite at pressures greater than 100 kbar, and changes to pyroxene with perovskite structure, magnesiowüstite, and stishovite at pressures greater than 225 kbar (see Yagi, Mao, and Bell, this Report). The occurrence of ringwoodite in Pampa del Infierno, therefore, indicates a minimum pressure greater than 100 kbar and less than 225 kbar. Solid-state transformation of plagioclase to glass can be initiated by shock pressures of 150 kbar (Milton and

DeCarli, 1963) and is completed at pressures greater than 300 kbar (Stöffler, 1972). Shock melting and vesiculation of plagioclase of oligoclase composition occur at 425 kbar (Stöffler, 1972). The complete transformation of plagioclase to glass in Pampa del Infierno chondrite and the lack of vesiculation and flow structures suggest peak pressures greater than 300 kbar and less than 425 kbar.

The occurrence of ultramafic clasts showing spinifex-like texture is very rare in meteorites and has been reported in only one other sample, the Eva meteorite (Fodor and Keil, 1976). The "clasts" are believed to have formed by crystallization of an impact-generated ultramafic melt similar in composition to the host meteorite. The temperature of formation of troilite-iron intergrowths varies with pressure from  $990^{\circ} \pm 5^{\circ}\text{C}$  at 30 kbar (Brett and Bell, 1969) to  $1158^{\circ} \pm 18^{\circ}\text{C}$  at  $100 \pm 6$  kbar (Usselman, 1975). Much higher temperatures must have prevailed locally in Pampa del Infierno to account

for the formation of the impact-generated ultramafic melt.

In conclusion, the shock features in Pampa del Infierno chondrite indicate a shock metamorphic event at a minimum peak pressure of 150 kbar to a pressure greater than 300 kbar. The composition

of the meteorite is close to that postulated for the earth's mantle. Therefore, the high-pressure phase transitions observed in ferromagnesian minerals in the chondrites are possible indications of the nature of similar high-pressure phase transitions in the earth's mantle.

## ULTRAMAFIC NODULES AND MEGACRYSTS

### GARNET LHERZOLITE XENOLITHS FROM THE KIMBERLITES OF EAST GRIQUALAND, SOUTH AFRICA

*F. R. Boyd and P. H. Nixon*

A cluster of kimberlite pipes and dikes in East Griqualand, South Africa (Fig. 18), along the southeastern border with Lesotho, has a tectonic setting that differs markedly from the well-known diamondiferous pipes that are within the boundaries of the Kaapvaal craton. The East Griqualand kimberlites were erupted outside the craton where the upper mantle and crust are in transition from subcon-

tinental to suboceanic structure. Zircons from the Ramatseliso pipe (Davis, 1977) and the Clarkton pipe (G. L. Davis, personal communication) have been dated at 150 and 194 m.y., respectively. These ages contrast markedly with ages of about 90 m.y. that are characteristic of most diamondiferous kimberlites within the Kaapvaal craton. Eruption of the East Griqualand kimberlites appears contemporaneous with the vast outpouring of Karroo basalts that inundated much of southern Africa during the Jurassic era (Fitch and Miller, 1971).

Estimates of the temperatures and depths of origin of the garnet lherzolite xenoliths from East Griqualand (Fig. 19) suggest that they have been erupted from depths that are 35–40 km shallower than those estimated for high-temperature ( $>1100^{\circ}\text{C}$ ) nodule suites from within the Kaapvaal craton (Boyd, 1973; Boyd and Nixon, 1978; Danchin, 1979). Kimberlite eruptions may be initiated by diapiric rise of partially molten mantle within the asthenosphere (Boyd, *Year Book* 75). The shallower depths of origin for the East Griqualand lherzolites may reflect a shelving of the top of the asthenosphere from beneath the Kaapvaal craton toward the Indian Ocean.

The temperature-depth estimates for the East Griqualand lherzolites (Fig. 19) suggest that these rocks originated within and on the edge of the graphite stability field. This relationship correlates well with the fact that there has been no production of diamonds from these kim-

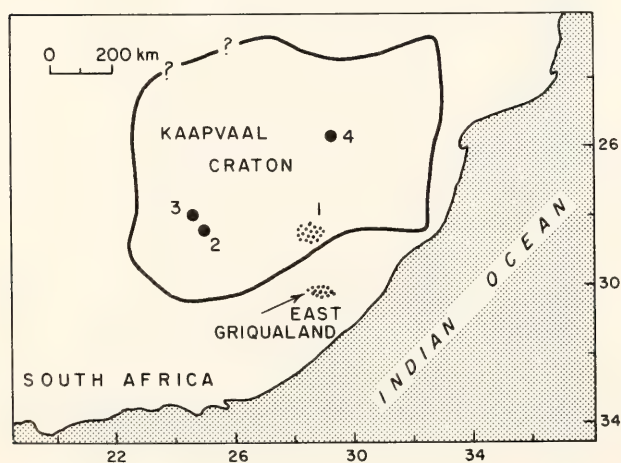


Fig. 18. Map of southern Africa showing selected kimberlite localities and the boundaries of the Kaapvaal craton. Political boundaries have been omitted for simplicity. Numbered kimberlite localities within the craton have yielded nodule suites for which paleogeotherms have been estimated. 1. Pipes of northern Lesotho and the Monastery Mine, South Africa. 2. Kimberley pipes. 3. Frank Smith Mine. 4. Premier Mine.



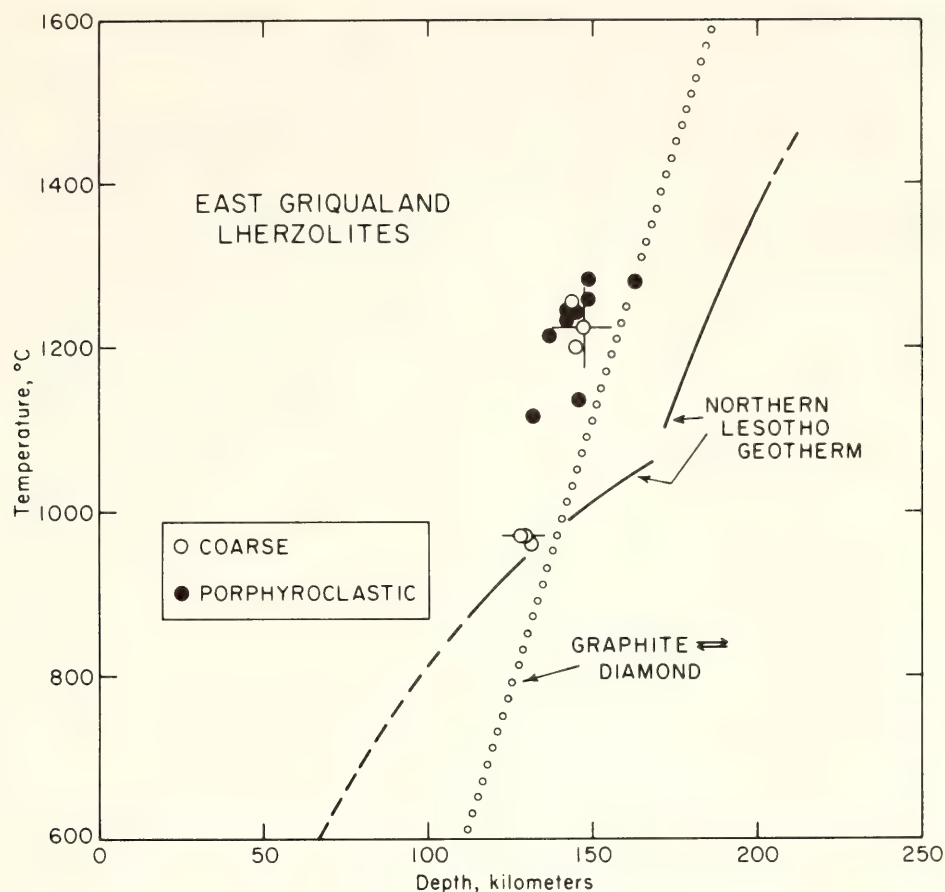


Fig. 19. Estimated temperatures and depths of origin of lherzolite xenoliths from the kimberlites of East Griqualand compared with the graphite  $\rightleftharpoons$  diamond transition (Kennedy and Kennedy, 1976) and the northern Lesotho geotherm (Boyd, 1973, fig. 7a).

berlites. The data in Fig. 19 thus illustrate a potential practical application of xenolith studies that could be of significant assistance in the worldwide search for diamondiferous kimberlites.

Lherzolites with equilibration temperatures less than 1100°C have been found at Abbotsford, Clarkton, Ramatseliso, Mzongwana, and Zeekoegat. Some of them are extensively altered to serpentine and carbonate, but even in the most altered specimens the outlines of primary grain boundaries are preserved. The textures of all these rocks are *coarse\** with olivine grains ranging up to 1 cm. Deformation has been mild; some grains of olivine and phlogopite show undulate extinction, but there is no mosaic olivine. Chromite is relatively abundant in rounded grains that are unusually coarse

(1–2 mm). Garnet and diopside are sparse, and kelyphite rims on the garnets are relatively thin (0.1–0.2 mm). Phlogopite has been found in only 3 of 11 low-temperature (<1100°C) lherzolites discovered in East Griqualand.

Five of the low-temperature lherzolites contain diopside with  $\text{Ca}/(\text{Ca} + \text{Mg})$  close to 0.500 (Fig. 20). Solid solution with enstatite is so restricted that the diopside solvus can be used only to estimate a maximum equilibration temperature. This maximum equilibration temperature cannot be much greater than 700°–800°C (solvus of Lindsley and Dixon, 1976). Garnet lherzolites with equilibration temperatures in that low range have not previously been found in nodule suites from southern Africa. These rocks have probably come from rather shallow depths (~50–100 km). Spinels from three of these lherzolites have Al/

\* The textural terminology used in this article follows the definitions of Harte (1977).

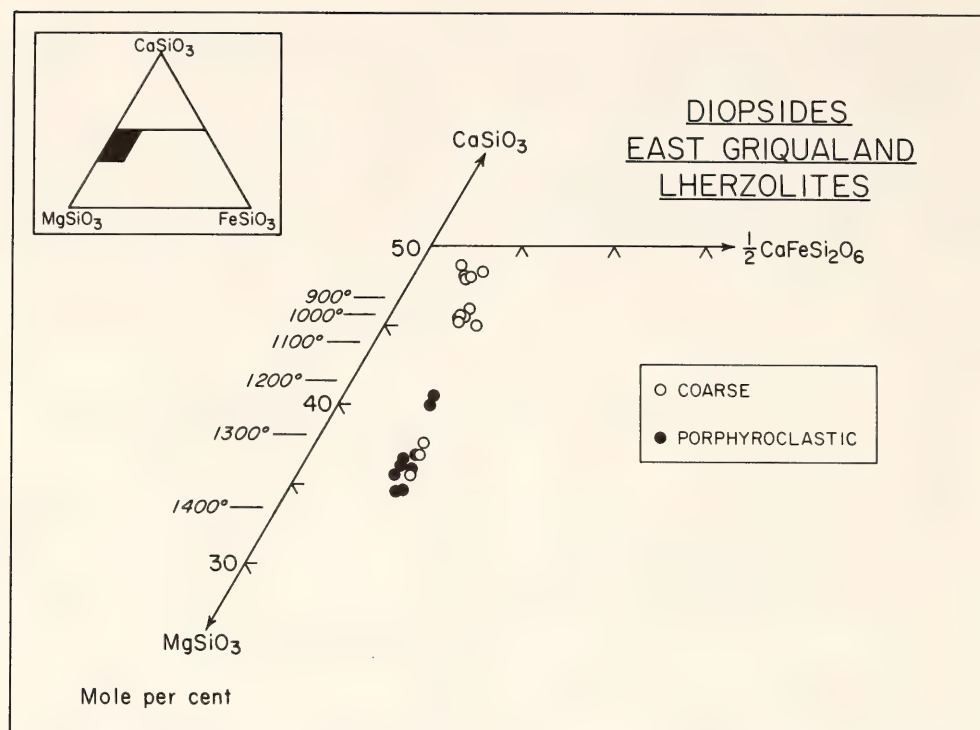


Fig. 20. Compositions of diopsides from East Griqualand lherzolites plotted in the pyroxene quadrilateral.

(Al + Cr +  $\text{Fe}^{3+}$ ) in the range 0.47–0.81. The aluminous character of the spinels also suggests a relatively shallow origin.

Three coarse lherzolites from Abbotsford with equilibration temperatures of 960°–970°C (Fig. 19) have varied and pronounced inhomogeneities. There are also lesser but significant inhomogeneities in a few of the high-temperature lherzolites. Such inhomogeneities are rare in garnet lherzolite nodules from kimberlites (Boyd and Finger, *Year Book* 74). The three Abbotsford specimens are all small nodules, with maximum dimensions of 4–5 cm, and they lack structures such as modal or textural variations. Nevertheless, there is a zone in one specimen (PHN 3021) in which the olivine and enstatite are markedly enriched in Fe. In a second specimen (PHN 3028) the margins of enstatite grains are enriched in  $\text{FeO}$ ,  $\text{TiO}_2$ , and  $\text{Al}_2\text{O}_3$  with zoning extending over an interval of 600–900  $\mu\text{m}$  from the edges. A third specimen (PHN 3020) has inhomogeneities involving the

jadeite content of the diopside and the  $\text{TiO}_2$  and  $\text{FeO}$  in the garnet.

A cause of these inhomogeneities may be metasomatism immediately prior to eruption. Preliminary study of ilmenite-bearing xenoliths from East Griqualand has provided evidence for such metasomatism. The inhomogeneities do not appreciably affect temperature estimates for these lherzolites, based on  $\text{Ca}/(\text{Ca} + \text{Mg})$  in diopside, but they do affect the depth estimates, based on  $\text{Al}_2\text{O}_3$  in enstatite. In calculating the points for the Abbotsford lherzolites (Fig. 19) it was assumed that for each specimen the more magnesian enstatite is primary or least altered.

High-temperature (> 1100°C) lherzolites have been found at Abbotsford, Ramatseliso, and Clarkton. Their textures range from *coarse* to *fluidal porphyroclastic*. In this respect they resemble the high-temperature lherzolites from the Frank Smith pipe (Boyd, *Year Book* 73) but contrast with those found in northern Lesotho (Nixon and Boyd, 1973a) in that



the latter are all deformed. The grain size of the mosaic olivine forming the groundmass of the porphyroclastic peridotites tends to be unusually coarse, ranging up to 0.5–1 mm. Strain-free tablets of olivine formed in porphyroclasts are also coarse, ranging up to 2 mm. In some cases neoblasts appear to have largely or completely consumed their porphyroclastic hosts.

Marked differences in deformation are exhibited by peridotites from different localities in East Griqualand, and there are even differences between peridotites from different kimberlites at the same locality. The most severely deformed specimens are from Ramatseliso. Enstatite porphyroclasts in peridotites from this pipe are commonly fluidized. The range in mosaic olivine grain size in individual specimens is unusually large, 0.05–0.5 mm.

Deformation of high-temperature lherzolites from the Clarkton pipe is much less severe. Two of the high-temperature lherzolites from Clarkton have *coarse* texture (Fig. 19) and in the others recrystallization to mosaic olivine is minimal. Nodules in the Clarkton kimberlite tend to be severely altered to serpentine and carbonate. It is difficult to estimate the original grain size of mosaic olivine in these altered nodules, but it appears to have a large range of 0.05–0.3 mm. One specimen from the southeast blow at Abbotsford has rather fine mosaic olivine ( $\sim 0.1$  mm), whereas in others from the east dike and northwest blow, the mosaic olivine ranges up to 0.5 mm.

These deformation textures are believed to result from conduit formation (Mercier, 1979) and are functions of the magnitude of the stresses that developed prior to eruption.

The small size and altered nature of many of the East Griqualand xenoliths preclude the making of meaningful bulk chemical or modal analyses. Nevertheless, the mineral analyses provide some insights into the origins of these rocks, and these analyses show consistent dif-

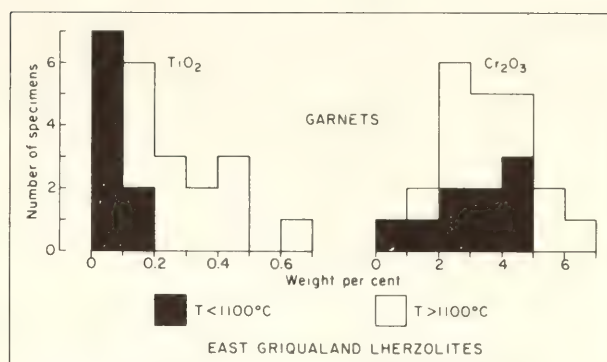


Fig. 21. Variation of  $\text{TiO}_2$  and  $\text{Cr}_2\text{O}_3$  in garnets from East Griqualand lherzolites.

ferences between the high-temperature, mainly deformed lherzolites and the low-temperature, coarse suite. Olivines in the high-temperature lherzolites have an average  $\text{Mg}/(\text{Mg} + \text{Fe})$  of 0.919, whereas for olivines in the low-temperature suite this ratio is 0.910 (standard error for both is 0.003–0.004). Olivines in the high-temperature suite contain significant  $\text{Al}_2\text{O}_3$  (0.05 wt %),  $\text{CaO}$  (0.11 wt %), and  $\text{Cr}_2\text{O}_3$  (0.06 wt %). These elements were not detected ( $< 0.03$  wt %) in the low-temperature suite.

Garnets from the two suites do not differ in  $\text{Cr}_2\text{O}_3$  content, but the high-temperature garnets contain markedly more  $\text{TiO}_2$  (Fig. 21). These chemical relations closely resemble those found for the lherzolites from the Frank Smith Mine (Boyd, *Year Book* 73) and the Premier Mine (Danchin, 1979). They somewhat resemble chemical variations found for the lherzolites from northern Lesotho pipes (Nixon and Boyd, 1973a), but in the latter suite the garnets in the low-temperature, coarse lherzolites are richer in  $\text{Cr}_2\text{O}_3$ . If variable depletion by partial fusion and removal of liquid were the only process affecting the mineral chemistry of these rocks, enrichment of  $\text{Cr}_2\text{O}_3$  would be expected to accompany depletion of  $\text{TiO}_2$  and  $\text{FeO}$ . The fact that  $\text{Cr}_2\text{O}_3$  in the garnets is relatively constant, whereas  $\text{TiO}_2$  is richer in the garnets and  $\text{FeO}$  is richer in the olivines of the high-temperature Frank Smith

lherzolites, led Boyd (*Year Book 73*) to speculate that metasomatism might have affected the mineral chemistry of these high-temperature rocks. Chemical variations found for the East Griqualand lherzolites suggest the same possibility.

Boyd (*Year Book 75*) noted that the depths to the points of inflection are approximately the same for a number of geotherms constructed for different nodule suites erupted within the Kaapvaal craton. One possible interpretation for these points of inflection is that they mark the tops of diapirs, and Boyd (*Year Book 75*) speculated that the constancy in depth might be caused by diapirs impinging on the base of a rigid lithosphere. Nixon and Boyd (1979) found evidence for a shallower point of inflection for an oceanic (Malaita) nodule suite, and this finding is consistent with a model in which there is a well-defined lithosphere-asthenosphere boundary. Preferred estimates (A. A. Finnerty and Boyd, in preparation) suggest a depth near 170 km for inflections within the Kaapvaal craton and approximately 110 km for Malaita. Data for the high-temperature lherzolites from East Griqualand (Fig. 19) suggest that they were erupted from a depth near 130 km. These relations are consistent with a model in which the base of the lithosphere shelves from beneath the Kaapvaal craton toward the Indian Ocean, although such an interpretation is difficult to reconcile with recent conflicting geophysical studies (e.g., Jordan, 1979; Anderson, 1979).

#### OXYGEN ISOTOPIC GEOCHEMISTRY OF ULTRAMAFIC NODULES AND BASANITE FROM SAN CARLOS, ARIZONA

*D. Rumble III, T. C. Hoering, and  
N. Boctor*

Oxygen isotopic analyses of mafic and ultramafic rocks provide direct evidence on the isotopic composition of magma source regions because of the very small isotopic fractionations between minerals

and magma at high temperature. It has been shown that unaltered basalts, gabbros, intrusive ultramafic rocks, and ultramafic nodules in basalt are remarkably homogeneous in their  $^{18}\text{O}$  content, relative to the range of some 50‰ observed for all other rock types. Fresh basalts range in  $\delta^{18}\text{O}$  values between 5.5 and 5.9‰ (Muehlenbachs and Clayton, 1972; Taylor, 1968). Ultramafic rocks vary from 5.4 to 5.8‰ (Taylor, 1968). Pyroxenes from ultramafic rocks lie in the range 5.4–6.4‰ (Taylor, 1968; Garlick *et al.*, 1971), and phlogopites and amphiboles average  $5.6 \pm 0.2\%$  (Boettcher *et al.*, 1979). The uniformity of these values is taken as evidence that the mantle is the same throughout in its oxygen isotopic composition.

The isotopic composition of oxygen in igneous rocks is sensitive to alteration by various secondary processes. Oxygen isotopic analyses have been used to detect the operation of processes such as ocean floor weathering (Muehlenbachs and Clayton, 1972), crustal assimilation and contamination (Taylor and Turi, 1976), and hydrothermal alteration by heated meteoric water (Taylor and Forester, 1971).

The ultramafic nodules at San Carlos occur within a 3–6 m thick Tertiary or Quaternary basanite flow that caps Peridot Mesa. The nodules have been classified into two groups (Frey and Prinz, 1978); Group I is Cr- and Mg-rich, and Group II is Fe-, Al-, and Ti-rich. In the present study, isotopic analyses were made of minerals separated from Group I spinel lherzolites, Group II spinel pyroxenites, and vesicular and nonvesicular basanites (Table 7). Spinel lherzolites and spinel pyroxenites, respectively, are the predominant nodule types in Group I and Group II. Olivine mineral separates and olivine-rich rocks were not analyzed because of the difficulty of obtaining quantitative oxygen yields with  $\text{BrF}_5$  as the fluorinating agent.

The analytical results (Table 7) show



TABLE 7.  $\delta^{18}\text{O}$  Values of Basanite and Ultramafic Nodules

	$\delta^{18}\text{O}_{\text{smow}}, \%$
<i>Basanite</i> (whole-rock analyses)	
nonvesicular	$+5.6 \pm 0.3^*$ (3 samples)
vesicular	$+6.4 \pm 0.1$ (2 samples)
<i>Ultramafic nodules</i>	
Group I (minerals separated from spinel lherzolite)	
Cr-diopside ( $\text{En}_{51.2}\text{Fs}_{4.7}\text{Wo}_{44.1}$ )	$+6.1 \pm 0.1$ (2 analyses)
Orthopyroxene ( $\text{En}_{89.5}\text{Fs}_{8.3}\text{Wo}_{2.2}$ )	$+6.2 \pm 0.1$ (2 analyses)
Group II (whole-rock analyses)	
Spinel pyroxenite	$+5.7 \pm 0.2$ (4 samples)

\* The reported uncertainty is equal to one standard deviation of the mean.

that the nodules, minerals, and basanite are all very similar in their oxygen isotopic composition with  $\delta^{18}\text{O}$  values close to those reported by other workers for fresh basalts and ultramafic rocks, as discussed above. Only the values for vesicular basanite ( $+6.4\%$ ) appear slightly high, a feature that may indicate secondary alteration.

Analyses of the San Carlos nodules and basanite support the inference that the mantle is uniform in its oxygen isotopic composition.

OXIDE MINERALS IN LAYERED  
KIMBERLITE-CARBONATE SILLS FROM  
BENFONTEIN, SOUTH AFRICA

*N. Z. Boctor and F. R. Boyd*

The Benfontein layered kimberlite-carbonate sills are commonly cited as evidence of a genetic relationship between kimberlite and carbonatite (e.g., Dawson and Hawthorne, 1973; Basu, 1978). It has been shown that carbonatites have a characteristic assemblage of iron-titanium oxide minerals that differs from that observed in kimberlite (Boctor and Svisero, *Year Book* 77, pp. 876–880; Mitchell, 1978*b*; McMahon and Haggerty, 1979). The oxide minerals in the carbonate layers at Benfontein are found to be kimberlitic and to differ from

oxides in carbonatite from alkaline igneous complexes.

The samples investigated from the Benfontein sills are (1) kimberlite composed of olivine phenocrysts, rare phlogopite, ilmenite xenocrysts, spinel, and perovskite in a matrix of calcite; and (2) oxide-carbonate layers containing 80–30% by volume cumulate spinel and perovskite. Some of the specimens show “graded bedding,” owing to an upward decrease in cumulate oxides, with oxide-free carbonate layers in which miniature diapirs of calcite, described by Dawson and Hawthorne (1973), occur near the top.

*Spinel*s

In the kimberlite, spinels occur as idiomorphic crystals in the carbonate groundmass and as clusters of crystals that mantle ilmenite xenocrysts. When the electron microprobe analyses of the spinels (Table 8) are plotted in the spinel prism (Fig. 22), they fall within the front rectangular face bounded by the  $\text{Mg}_2\text{TiO}_4$ ,  $\text{Fe}_2\text{TiO}_4$ ,  $\text{MgAl}_2\text{O}_4$ , and  $\text{FeAl}_2\text{O}_4$  end members. In this respect they are similar to late-stage spinels observed in other kimberlites (Haggerty, 1973; Boctor and Boyd, *Year Book* 77, pp. 870–876; Boctor and Meyer, 1979). The spinels in the oxide-carbonate layers

TABLE 8. Representative Electron Microprobe Analyses of Spinel and Ilmenite in the Layered Kimberlite-Carbonate Sills at Benfontein\*

	1	2	3	4	5	6	7
SiO <sub>2</sub>	0.13	0.14	0.16	0.14	0.13	0.14	0.16
TiO <sub>2</sub>	13.21	20.31	20.37	21.99	52.72	54.02	52.36
Al <sub>2</sub> O <sub>3</sub>	8.28	8.61	8.89	8.36	0.37	0.40	0.58
Cr <sub>2</sub> O <sub>3</sub>	21.08	1.84	0.28	0.37	1.82	1.30	2.27
Fe <sub>2</sub> O <sub>3</sub>	10.34	13.42	14.29	12.70	3.85	4.28	5.65
FeO	32.63	38.47	39.50	39.30	26.57	23.13	20.44
MnO	0.33	0.54	0.62	0.50	0.48	0.61	0.28
NiO	<0.01	0.09	0.01	0.06	0.02	0.06	<0.01
MgO	14.23	15.92	15.98	16.21	13.54	16.64	17.38
CaO	0.13	0.33	0.30	<0.01	<0.01	<0.01	<0.01
Totals	100.35	99.67	100.16	99.63	99.49	100.51	99.12

\* 1-2: Core and rim of zoned spinel in carbonate. 3: Unzoned spinel in carbonate. 4: Spinel in kimberlite. 5-6: Ilmenite in kimberlite. 7: Ilmenite in carbonate.

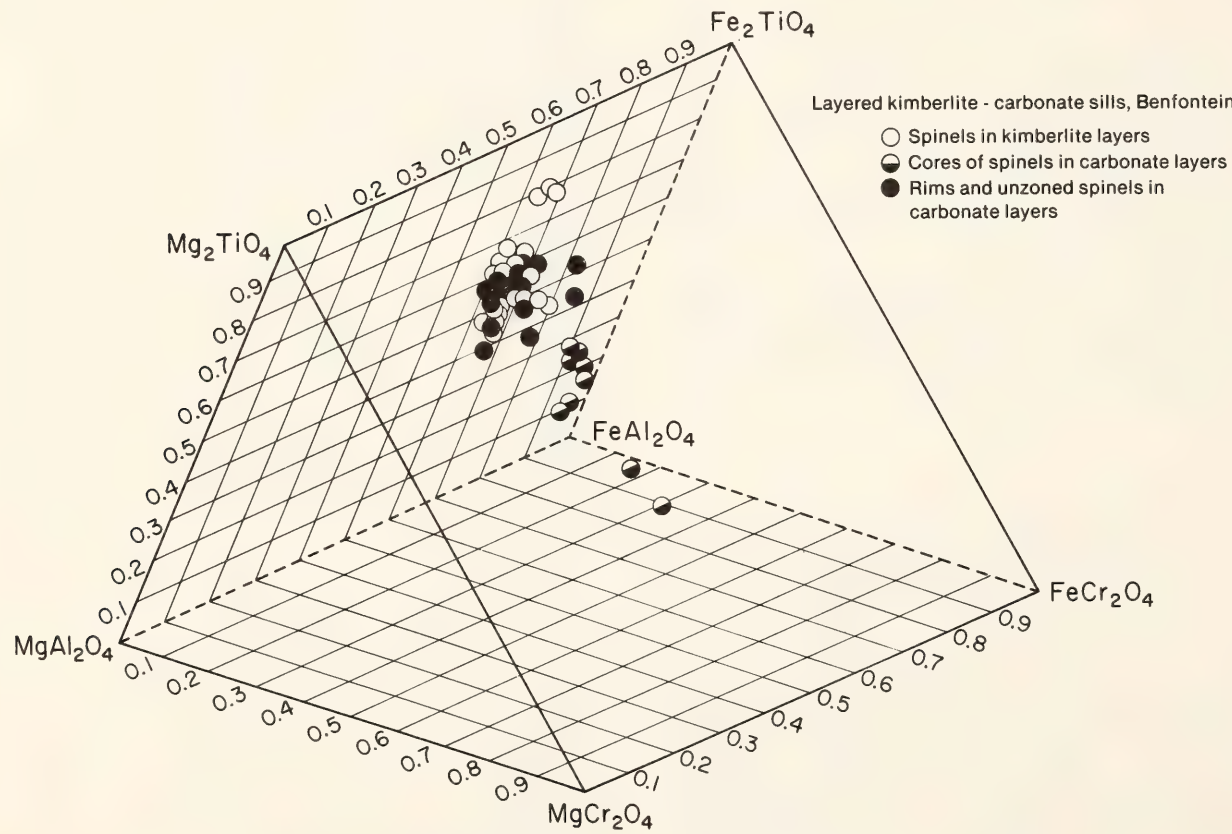


Fig. 22. The composition of spinels in the kimberlite and carbonate layers, Benfontein, plotted in the spinel prism.

occur as idiomorphic crystals that are commonly rimmed by thin mantles of perovskite. In a few of these crystals an intervening layer of carbonate separates the two phases. Most of the spinels in the carbonate layers are unzoned and

have a composition similar to that of spinels in the kimberlite. A few are zoned, however, displaying cores of a Cr-bearing spinel and rims that are similar in composition to the unzoned spinels (Table 8; Fig. 22).



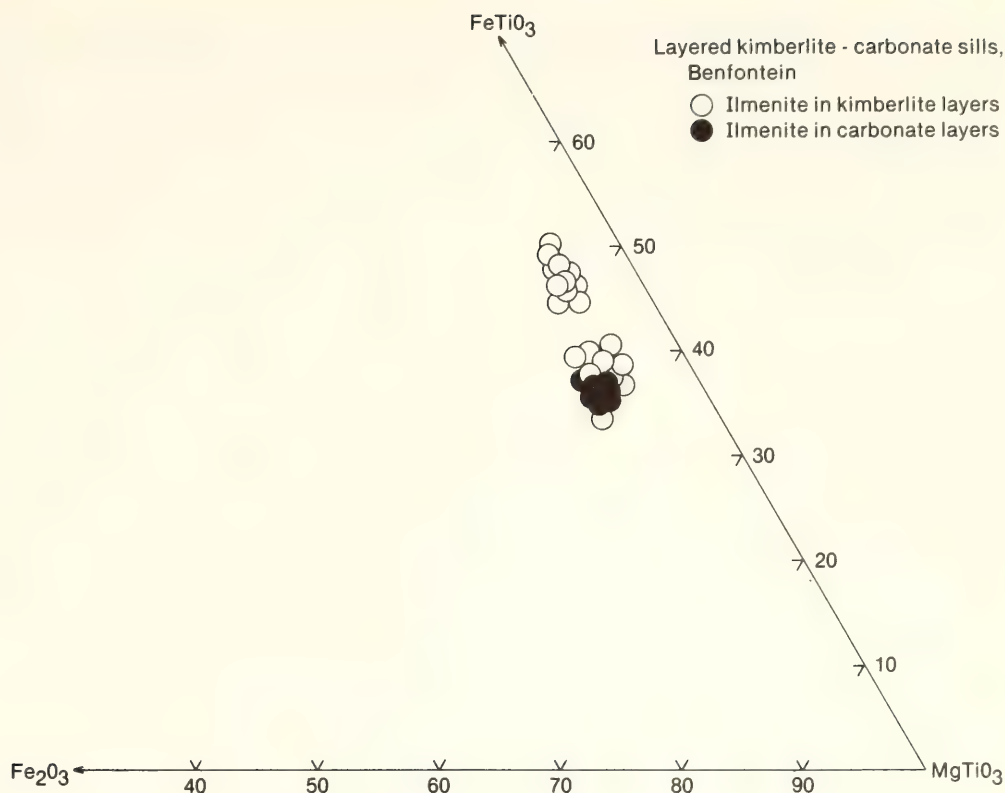


Fig. 23. The composition of ilmenite in the kimberlite and carbonate layers, Benfontein, in terms of their  $\text{MgTiO}_3$ ,  $\text{FeTiO}_3$ , and  $\text{Fe}_2\text{O}_3$  content.

### Ilmenite

The ilmenite xenocrysts are similar in composition ( $\text{MgO}$  13.5–18.1 wt %,  $\text{Cr}_2\text{O}_3$  1.0–1.9 wt %) to ilmenite nodules in many kimberlites (Fig. 23). Irregular islands of ilmenite occur as inclusions in spinels, in both the kimberlite and carbonate layers. Their composition is similar to that of ilmenite xenocrysts. In the carbonate layers no Mn enrichment was observed in ilmenite, like that observed by Haggerty *et al.* (1979) in ilmenite associated with immiscible carbonate liquid in Monastery diatreme.

### Discussion

The characteristic iron–titanium oxide minerals of carbonatites from alkaline complexes are titaniferous magnetite and ilmenite. Ilmenite occurs as lamellar intergrowths in magnetite or as a discrete phase. The magnetite-ilmenite intergrowths apparently formed by exsolu-

tion by the mechanism suggested by Buddington and Lindsley (1964). Manganese and magnesium concentrate in ilmenite relative to coexisting magnetite, in agreement with the experimental data of Mazzullo *et al.* (1975) and Pinckney and Lindsley (1976). The magnetite is generally Ti-poor and when not exsolved may be rich in Mn as in Oka carbonatite (McMahon and Haggerty, 1979). Ilmenite is remarkably enriched in Mn and is virtually Cr-free relative to kimberlitic ilmenite, although its Mg content may overlap with that of kimberlite (Boctor and Svisero, *Year Book* 77, pp. 876–880; Mitchell, 1978b).

At Benfontein the spinels and ilmenite in the carbonate-rich layers are typically kimberlitic. They are Cr-bearing and do not show the Mn enrichment observed in magnetite and ilmenite from carbonatites associated with alkaline rocks. The coexisting ilmenite and spinels at Benfontein have similar Mg and Mn contents. The partitioning of these ele-

ments between spinel and ilmenite observed in carbonatites from alkaline rock associations is lacking at Benfontein. Therefore, the spinel and ilmenite at Benfontein are not in equilibrium, and this nonequilibrium is consistent with a xenocrystic origin of ilmenite. The irregular inclusions of ilmenite in the spinels are probably remnants of ilmenite xenocrysts resorbed by the liquid from which the spinels crystallized.

In conclusion, iron-titanium oxide minerals in carbonate-oxide layers at Benfontein are typically kimberlitic and differ from those observed in sövite from alkaline complexes. The occurrence of layered carbonate rocks with kimberlite at Benfontein does not necessarily imply a genetic relationship between kimberlites and carbonatites of alkaline rock associations.

PETROLOGY OF KIMBERLITE FROM THE  
DE BRUYN AND MARTIN MINE,  
BELLSBANK, SOUTH AFRICA

*N. Z. Boctor and F. R. Boyd*

The micaceous kimberlite at Bellsbank, South Africa, is characterized by high concentrations of incompatible elements (REE, Nb, Zr, Hf, and Ta) relative to other South African kimberlites (Fesq *et al.*, 1975; Kable *et al.*, 1975). Incompatible elements tend to concentrate in the residual liquid during crystallization of kimberlitic magma. Therefore, a study of the mineral composition of groundmass minerals in Bellsbank kimberlite may provide clues to the behavior of these elements during the final stages of crystallization of kimberlitic magma. Perovskite, a groundmass mineral, in kimberlite from De Bruyn and Martin Mine, Bellsbank, was found to be remarkably enriched in rare earth elements relative to other South African kimberlites. Moreover, the kimberlite from De Bruyn and Martin Mine differs from most kimberlites in its lack of Mg-rich ilmenite and in the compositional trend of its spinel.

The kimberlite from the De Bruyn and Martin Mine is composed mainly of serpentized olivine and phlogopite in a fine-grained groundmass of calcite, serpentine, spinel, and perovskite. Olivine (Fo 89.5–92.5) occurs mostly as large xenocrysts with serpentized margins and shows a slight increase in fayalite content toward the margins. A few small euhedral crystals of olivine also occur in the groundmass; their composition, however, is similar to that of the large xenocrysts. The olivine xenocrysts are similar in composition to the large, rounded olivines from the Liqhobong pipe, which were interpreted as the product of disaggregated ultrabasic nodules (Nixon and Boyd, 1973b). The euhedral nature of the olivine phenocrysts in the groundmass suggests that they crystallized from the kimberlitic magma. The olivine contains minor amounts of Ni in solid solution (0.1–0.5 wt % NiO), and heazlewoodite occurs as a secondary sulfide in the serpentized portions.

Spinel occurs both as zoned and unzoned crystals. The zoned crystals are mostly idiomorphic, displaying cores of Mg-Al chromite, intermediate zones of titaniferous magnesian chromite, and rims of titaniferous magnetite. The Mg-Al chromite is generally uncommon; many of the zoned spinel crystals display cores of titaniferous magnesian chromite and rims of titaniferous magnetite. In a few of the zoned crystals, a thin intervening zone of dolomite or serpentine occurs between the titaniferous magnesian chromite cores and the magnetite rims. Idiomorphic unzoned crystals of titaniferous magnetite occur in the groundmass and are similar in composition to the magnetite in the outermost rims of the zoned crystals.

From core to mantle the compositional trend in the spinels is toward decrease in Al and increase in Fe and Ti (Table 9; Fig. 24). The zoning trends of early formed, primary spinels in kimberlites (Haggerty, 1975) are consistently from the join  $\text{MgCr}_2\text{O}_4\text{-FeCr}_2\text{O}_4$  to the join



TABLE 9. Representative Electron Microprobe Analyses of Spinels from De Bruyn and Martin Mine, Bellsbank\*

	1	2	3	4	5	6	7	8
SiO <sub>2</sub>	0.17	0.12	0.12	0.20	0.16	0.16	0.29	0.15
TiO <sub>2</sub>	0.75	0.76	0.86	3.07	3.55	1.91	9.30	7.18
Al <sub>2</sub> O <sub>3</sub>	7.20	7.14	7.26	1.40	1.11	1.33	0.14	0.05
Cr <sub>2</sub> O <sub>3</sub>	56.89	57.43	57.12	56.18	54.79	58.50	1.16	0.28
Fe <sub>2</sub> O <sub>3</sub>	3.21	3.27	3.85	4.97	5.27	4.90	26.92	29.14
FeO	18.61	18.06	18.71	22.55	23.33	21.09	55.18	55.35
MnO	1.03	0.95	1.28	1.22	0.94	1.11	1.43	1.22
MgO	11.09	11.55	11.61	10.45	10.46	10.61	5.46	5.13
CaO	0.05	0.04	0.01	0.20	0.08	0.11	0.06	0.12
Totals	99.01	99.27	100.82	99.85	99.69	99.67	99.95	98.63

\* Analyses 1-3: Mg-Al chromite. Analyses 4-6: titaniferous magnesian chromite. Analyses 7-8: titaniferous magnetite.

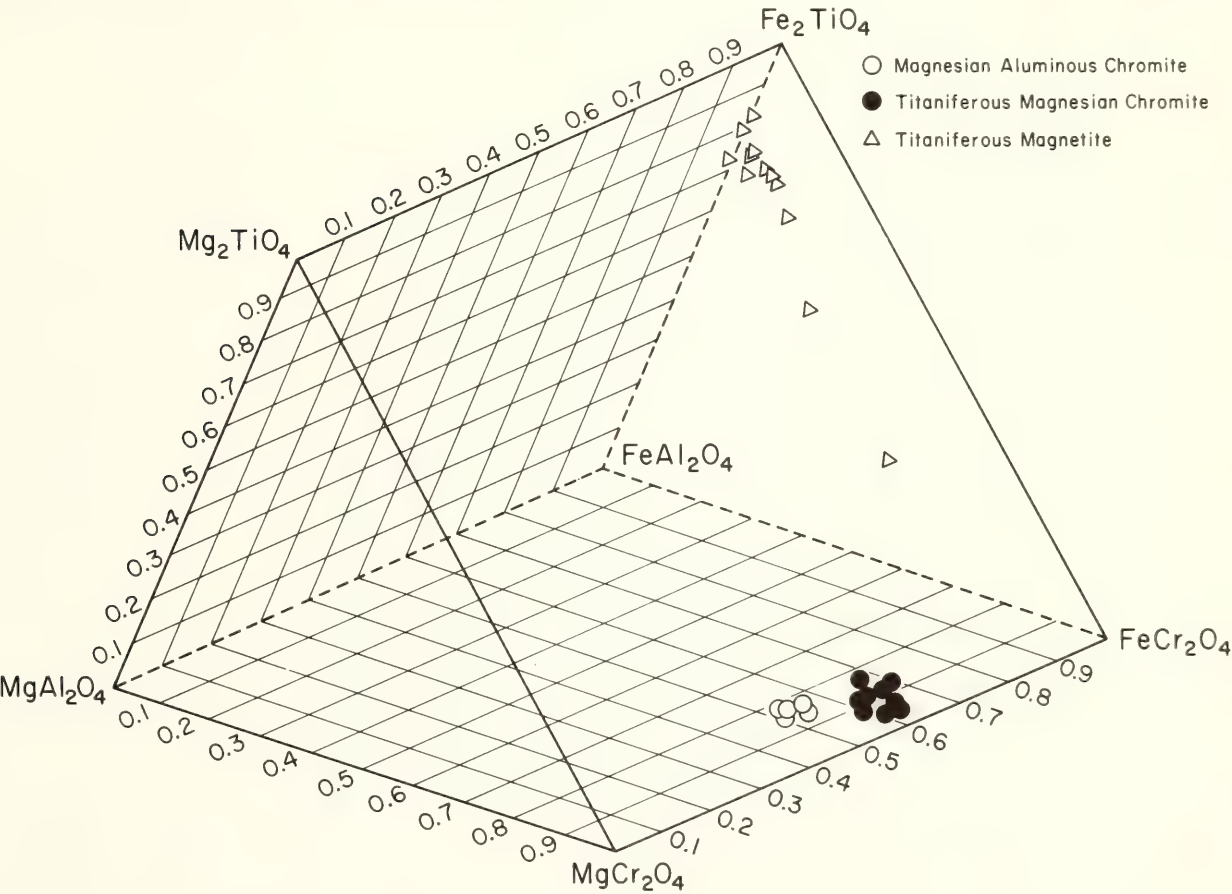


Fig. 24. Composition of the spinels from De Bruyn and Martin Mine, Bellsbank, plotted in the spinel prism.

MgAl<sub>2</sub>O<sub>4</sub>-FeAl<sub>2</sub>O<sub>4</sub>, with subsequent enrichment in Fe and Ti. Spinels in kimberlite from the De Bruyn and Martin Mine share with other kimberlitic spinels the overall trend of enrichment in Fe and Ti (Haggerty, 1975; Mitchell and Clark,

1976), but are generally poor in Al in comparison and show progressive decrease in this element with progressive crystallization. The only other known kimberlitic spinels that show similar depletion in Al<sub>2</sub>O<sub>3</sub> are those of micaceous

kimberlites from Kirkland Lake (Mitchell, 1978a) and from Tunraq, Canada (Mitchell, 1979). The depletion of Al seems to be characteristic of spinels in micaceous kimberlites and may be attributed to early crystallization of abundant phlogopite that depleted the liquid from which the spinel crystallized in aluminum. The compositional trend of spinels from kimberlite at De Bruyn and Martin Mine is also similar to the trend observed in some lunar spinels from mare basalts (Haggerty, 1972).

Perovskite in kimberlite from the De Bruyn and Martin Mine is Cr- and Nb-bearing and is characterized by the highest concentration of REE known for perovskite from South African kimberlite. The light REE are preferentially concentrated in perovskite and account for ~89% of its total REE content. The possible mechanisms that led to such enrichment are discussed by Boctor and Boyd (this Report).

#### INVARIANT MELTING BEHAVIOR OF MANTLE MATERIAL: PARTIAL MELTING OF TWO LHERZOLITE NODULES

*C. M. Scarfe, B. O. Mysen, and C. S. Rai\**

Geochemical and geophysical evidence suggests that basalts are derived from partial melting of peridotite in the upper mantle; yet experimental data on the degree of fusion and the composition of liquids are limited. To fulfill this important need, the  $\beta$ -track mapping technique has been used by Mysen and Kushiro (1977) to investigate both dry and wet melting of peridotite to 35 kbar and by Wendlandt and Mysen (*Year Book 77*, pp. 756–761) to determine melting in the presence of CO<sub>2</sub> to 30 kbar. Melting at temperatures just above the solidus was interpreted in all cases to be isobarically invariant, resembling melting relation-

ships found in the synthetic system CaO-MgO-Al<sub>2</sub>O<sub>3</sub>-SiO<sub>2</sub> (Yoder, 1976).

The present study, also using  $\beta$ -track mapping techniques, extends the dry melting experiments of Mysen and Kushiro (1977) and emphasizes the importance of invariant melting behavior at low degrees of partial melting in the upper mantle. To test the effect of variations in bulk composition and mineralogy on the melting of peridotite, two nodules were studied. Spinel lherzolite 66PAL-3, from the Honolulu Volcanic Series, Hawaii, is relatively undepleted in its basaltic components, whereas garnet lherzolite GP11858 is a more depleted nodule from the Wesselton kimberlite pipe, Kimberley, South Africa (Table 10).

#### *Experimental Methods*

Powdered samples (<5- $\mu$ m grain size) were dried at 600°C for 22 hr to decompose secondary minerals. Approximately 15 ppb radioactive tungsten-185 in ammonium hydroxide solution was added to the powders before they were reground for 1 hr in an agate mortar. Because the liquid-crystal and liquid-vapor partition coefficients for <sup>185</sup>W exceed 50, practically all the tungsten enters the melt phase (Wendlandt and Mysen, *Year Book 77*). Thus, the degree of melting of the rock can be determined by comparing the concentration of <sup>185</sup>W in a partially melted sample to that in a completely melted charge (Mysen and Kushiro, 1977). The  $\beta$  activities of the standards and unknowns were recorded on Ilford K-5 nuclear emulsions using the technique of Mysen and Seitz (1975).

Melting experiments were carried out in a solid-media, high-pressure apparatus (Boyd and England, 1960). The piston-out technique was used with a -4% correction for friction. Pressures have an uncertainty of  $\pm 0.5$  kbar, and temperatures measured with Pt-Pt90Rh10 thermocouples have an uncertainty of  $\pm 10^\circ\text{C}$ . Because previous workers have

\*Hawaii Institute of Geophysics, University of Hawaii, Honolulu, Hawaii 96822.



TABLE 10. Chemical Composition and Norms of Nodules\*

	GP11858†	66PAL-3‡
SiO <sub>2</sub>	43.68	45.10
TiO <sub>2</sub>	0.27	0.13
Al <sub>2</sub> O <sub>3</sub>	2.12	3.92
Cr <sub>2</sub> O <sub>3</sub>	0.42	0.31
Fe <sub>2</sub> O <sub>3</sub>	2.37	1.00
FeO	4.91	7.29
MnO	0.06	0.14
NiO	0.27	0.25
MgO	41.90	38.81
CaO	1.96	2.66
Na <sub>2</sub> O	0.17	0.27
K <sub>2</sub> O	0.06	0.02
H <sub>2</sub> O <sup>+</sup>	2.35	0.07
H <sub>2</sub> O <sup>-</sup>	0.12	0.12
Totals	100.66	100.10
MgO/(MgO+FeO+0.9Fe <sub>2</sub> O <sub>3</sub> )	0.91	0.89
Na <sub>2</sub> O+K <sub>2</sub> O	0.23	0.29
CaO/Al <sub>2</sub> O <sub>3</sub>	0.92	0.68
Or	0.35	0.12
Ab	1.44	2.28
An	4.84	9.43
Di	3.84	2.98
Hy	16.39	20.23
Ol	69.68	63.82
Cr	0.62	0.46
Il	0.51	0.25

\* For norm calculation all Fe converted to FeO to facilitate comparison with norms in Table 11.

† Scarfe *et al.* (1972) ; contains 3% modal garnet and some serpentine.

‡ Jackson and Wright (1970) ; contains 1% modal spinel.

noted loss of iron from the charge to the capsule and the adverse effect this has on melting relationships, starting materials were placed in graphite containers that were sealed inside 3-mm O.D. platinum capsules. The graphite containers prevented iron loss to the platinum capsule and maintained a relatively low  $f_{O_2}$  at the graphite-CO-CO<sub>2</sub> buffer. A Pyrex glass sleeve around the heating element inhibited water access to the sample region and minimized hydrogen diffusion into the capsule. Most runs were of 1 hr duration. That no change occurred in the proportion of melt produced in experiments at 1 and 10 hr was taken to indicate that equilibrium was achieved in the shorter runs.

Results

The melting relations of 66PAL-3 and GP11858 are summarized in Figs. 25 and 26 as a function of temperature and degree of melting. The size of the data points indicates uncertainties in temperature ( $\pm 10^\circ\text{C}$ ) and percentage of melt ( $\pm 1\sigma$ ). Preliminary data on the compositions of selected partial melts are shown in Table 11.

At 20 kbar the solidus of 66PAL-3 lies at 1420°C. Using the classification of Irvine and Baragar (1971), the initial liquid is olivine tholeiitic in composition up to 23% melting, and it coexists with olivine, orthopyroxene, clinopyroxene, and a trace of spinel. At 1440°C clino-

TABLE 11. Selected Melt Compositions†

	66PAL-3 20 kbar 1425°C	66PAL-3 20 kbar 1475°C	GP11858 20 kbar 1475°C	66PAL-3 35 kbar 1530°C
SiO <sub>2</sub>	46.62	45.66	45.71	43.65
TiO <sub>2</sub>	0.67	0.52	0.48	0.67
Al <sub>2</sub> O <sub>3</sub>	13.40	10.80	12.42	9.00
FeO*	7.45	7.63	8.31	9.26
MnO	0.28	0.25	0.33	0.26
MgO	14.97	21.56	15.81	23.58
CaO	13.21	9.22	10.08	8.13
Na <sub>2</sub> O	0.90	0.46	1.16	0.68
K <sub>2</sub> O	0.12	0.04	0.38	0.06
<i>Cation Norm</i>				
Or	0.71	0.24	2.31	0.35
Ab	8.10	4.12	10.71	6.10
An	32.24	27.20	28.34	21.33
Cpx	26.75	14.72	18.46	15.21
Opx	7.73	21.78	11.86	10.35
Ol	23.53	31.22	27.64	45.72
Il	0.94	0.72	0.69	0.93

† Electron microprobe analyses of glass using a beam current of 0.01  $\mu$ A.  
\* Total Fe as FeO.

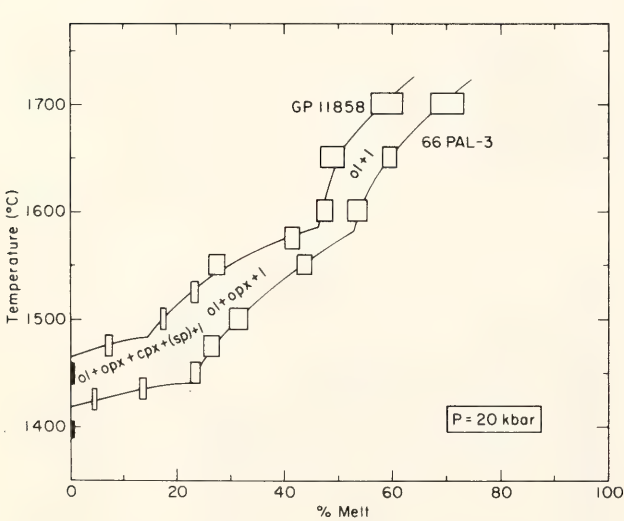


Fig. 25. Melting curves for 66PAL-3 and GP11858 at 20 kbar. Abbreviations: ol, olivine; opx, orthopyroxene; cpx, clinopyroxene; sp, spinel; l, liquid. Filled data points indicate the absence of liquid.

pyroxene and spinel are completely melted, and between 1440°C and 1580°C liquids of tholeiitic picrite composition coexist with olivine and orthopyroxene.

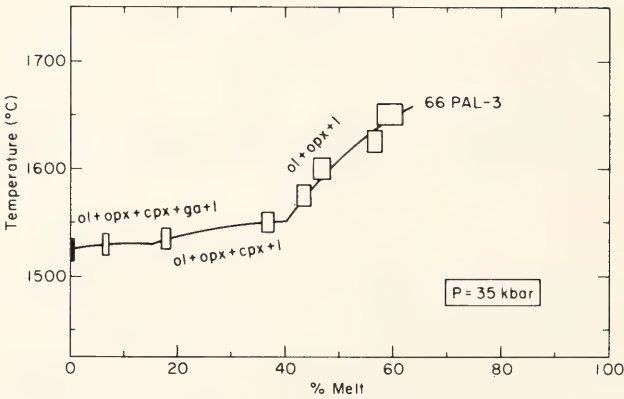


Fig. 26. Melting curve for 66PAL-3 at 35 kbar. Abbreviations as in Fig. 25; ga, garnet. Filled data point indicates the absence of liquid.

Above 1580°C, liquids calculated from known proportions of liquid and coexisting olivine are peridotitic komatiite in composition. Similar trends were observed for GP11858; however, its fusion curve is displaced to higher temperatures. The solidus temperature is 1465°C and only 15% initial melt is produced before clino-



pyroxene is lost at 1485°C. Liquid compositions are slightly more olivine-normative than those described for 66PAL-3. Because GP11858 is not in its stability field at 20 kbar, residual garnet could be present in the initial melting interval; however, no residual garnet was identified.

At 35 kbar the solidus of 66PAL-3 lies at 1525°C and the initial liquid is in equilibrium with olivine, orthopyroxene, clinopyroxene, and garnet. No residual spinel was observed. Because of interference from quench phases, the composition of liquids at 35 kbar was difficult to determine; however, the more reliable analyses indicate an alkali picrite composition for the initial liquid. At 1535°C, garnet is lost, and olivine, orthopyroxene, and clinopyroxene coexist with a liquid of increasing olivine-normative content to 1550°C and 40% melting.

Variation in the composition of the coexisting solid phases correlates well with the melting relationships. For example, the  $Mg/(Mg + \Sigma Fe)$  content of olivine and orthopyroxene at both 20 and 35 kbar varies only slightly in the initial melting interval, but shows larger increases where a phase is lost and an inflection occurs in the melting curve. Materials balance calculations show that as fusion proceeds liquids coexist with residual solid assemblages of increasing harzburgitic character.

### *Discussion*

Initial melting of spinel lherzolite 66PAL-3 produces liquid of olivine tholeiite composition at 20 kbar and alkali picrite composition at 35 kbar. These

results are in general agreement with the melting studies of Mysen and Kushiro (1977) on undepleted garnet lherzolite PHN1611. Because of the chemically depleted or refractory nature of garnet lherzolite GP11858, its melting curve at 20 kbar is displaced to higher temperatures and the amount of initial melt is reduced. The composition of the initial melt is slightly more olivine-normative than that of the corresponding melt for 66PAL-3 at 20 kbar.

The flat slope of the melting curves at temperatures just above the solidus (Figs. 25 and 26) and the almost constant composition of liquids and coexisting solid phases in this interval suggest that melting approximates isobaric invariant behavior. At 20 kbar in the spinel peridotite stability field, olivine, orthopyroxene, clinopyroxene, and spinel participate in melting until clinopyroxene and spinel are consumed. At 35 kbar in the garnet peridotite stability field, olivine, orthopyroxene, clinopyroxene, and garnet coexist with liquid until garnet is lost. As soon as clinopyroxene or garnet disappears, a distinct change of slope is observed in the fusion curves, and melting is no longer isobarically invariant.

The petrological applications of the principle of invariant melting have been extensively reviewed by Yoder (1976). It is worth emphasizing, however, that the results of this and previous melting studies on synthetic and natural systems indicate that during initial melting of mantle material large amounts of basaltic (at 20 kbar) or picritic (at 35 kbar) liquid of essentially constant composition are produced irrespective of the proportions of the solid phases in the parental lherzolite.

## STRUCTURE AND PROPERTIES OF LIQUIDS AND GLASSES

### STRUCTURES OF QUENCHED MELTS IN THE SYSTEM $\text{NaAlSi}_3\text{O}_8$ - $\text{CaMgSi}_2\text{O}_6$ - $\text{Mg}_2\text{SiO}_4$ - $\text{SiO}_2$ AT 1 ATM

*D. Virgo, B. O. Mysen, and F. Seifert*

The structures of quenched melts of most of the geologically important end-member mineral compositions and of relevant binary and ternary joins at 1 atm have now been completed. With these results it is possible to delineate the anticipated structural species present in melts with compositions corresponding to those of major igneous rocks. By integrating studies of silicate melt structure with measurements of physical and chemical properties of melts, a fuller understanding of the processes of magma formation and evolution can be obtained.

The bulk compositions of the major igneous rocks can be considered to a first approximation in terms of the compositional variations in the basalt tetrahedron,  $\text{CaMgSi}_2\text{O}_6$ - $\text{Mg}_2\text{SiO}_4$ - $\text{NaAlSi}_3\text{O}_8$ - $\text{SiO}_2$  (Di-Fo-Ne-SiO<sub>2</sub>), of Yoder and Tilley (1962). The structures of 1-atm melts relevant to this system and reported elsewhere are  $\text{SiO}_2$ - $\text{CaAl}_2\text{O}_4$  (Virgo, Seifert, and Mysen, this Report);  $\text{SiO}_2$ - $\text{NaAlSi}_3\text{O}_8$ - $\text{CaMgSi}_2\text{O}_6$ ,  $\text{MgSiO}_3$ - $\text{CaSiO}_3$ , and  $\text{Mg}_2\text{SiO}_4$ - $\text{NaAlSi}_3\text{O}_8$ - $\text{CaAl}_2\text{Si}_2\text{O}_8$  (Mysen, Virgo, and Seifert, this Report). The structures of 1-atm melts in the systems  $\text{CaMgSi}_2\text{O}_6$ - $\text{NaAlSi}_3\text{O}_8$ - $\text{CaAl}_2\text{Si}_2\text{O}_8$  and  $\text{CaMgSi}_2\text{O}_6$ - $\text{Mg}_2\text{SiO}_4$  described herein and all the above data are used to discuss the distinct structural types for bulk compositions within the basalt tetrahedron.

Starting materials for the preparation of glasses at 1 atm were combinations of spectrographically pure  $\text{CaCO}_3$ ,  $\text{Na}_2\text{CO}_3$ ,  $\text{MgO}$ ,  $\text{Al}_2\text{O}_3$ , and  $\text{SiO}_2$ . Glasses were prepared with the same procedures described by Virgo, Seifert, and Mysen

(this Report). Raman spectra were measured on small fragments of glass using techniques described by Sharma *et al.* (Year Book 77, pp. 652-658). Raman spectra of 1-atm glasses in the systems  $\text{CaMgSi}_2\text{O}_6$ - $\text{NaAlSi}_3\text{O}_8$ - $\text{CaAl}_2\text{Si}_2\text{O}_8$  and  $\text{CaMgSi}_2\text{O}_6$ - $\text{Mg}_2\text{SiO}_4$  are given in Figs. 27-30. The measured peak positions are given in Table 12.

### Discussion

*$\text{CaMgSi}_2\text{O}_6$ - $\text{NaAlSi}_3\text{O}_8$ - $\text{CaAl}_2\text{Si}_2\text{O}_8$  System.* The structures of the glasses of the end-member mineral compositions are discussed elsewhere ( $\text{CaMgSi}_2\text{O}_6$ , Mysen, Virgo, and Scarfe, this Report;  $\text{NaAlSi}_3\text{O}_8$ , Sharma, Virgo, and Mysen, Year Book 77, pp. 652-658;  $\text{CaAl}_2\text{Si}_2\text{O}_8$ , Virgo, Seifert, and Mysen, this Report). The Raman spectrum of the glass of  $\text{Ab}_{50}\text{An}_{50}$  (mole %, Fig. 27) composition is similar to those of the end-member glasses along this join, and the prominent features are a strong band at  $484\text{ cm}^{-1}$ , a high-frequency shoulder at  $572\text{ cm}^{-1}$ ,

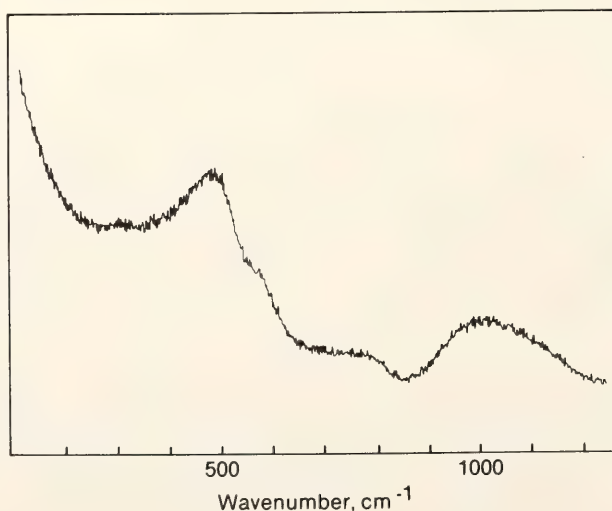


Fig. 27. Unpolarized ( $I_{||} + I_{\perp}$ ) Raman spectrum of  $\text{Ab}_{50}\text{An}_{50}$  glass (mole %) (laser  $488.0\text{ nm Ar}^+$  ion,  $300\text{ mW}$ ).



TABLE 12. Raman Frequencies of Glasses in the Systems Ab-An-Di and Di-Fo at 1 atm

Composition wt %	T, °C	Wave Number, cm <sup>-1</sup>									
		484s,p*	572Sh,p	570Sh,p	588Sh,p	611s,p	773w	878Sh,p	967s,p	978w,p	1005Sh,p
Ab <sub>50</sub> An <sub>50</sub>	1550	472s,p	570Sh,p	588Sh,p	611s,p	773w	878Sh,p	967s,p	978w,p	1005Sh,p	1120w,p
Ab <sub>75</sub> Di <sub>25</sub>	1550	466s,p	570Sh,p	588Sh,p	611s,p	776w	878Sh,p	967s,p	978w,p	1005Sh,p	1044w,p
Ab <sub>50</sub> Di <sub>50</sub>	1550	...	570Sh,p	588Sh,p	611s,p	763w	878Sh,p	967s,p	978w,p	1005Sh,p	1030w,p
Ab <sub>25</sub> Di <sub>75</sub>	1550	...	570Sh,p	588Sh,p	611s,p	764w	878Sh,p	967s,p	978w,p	1005Sh,p	1033s,p
An <sub>75</sub> Di <sub>25</sub>	1550	...	570Sh,p	588Sh,p	611s,p	749w	878Sh,p	967s,p	978w,p	1005Sh,p	...
An <sub>50</sub> Di <sub>50</sub>	1550	...	570Sh,p	588Sh,p	611s,p	...	878Sh,p	967s,p	978w,p	1005Sh,p	...
An <sub>25</sub> Di <sub>75</sub>	1550	...	570Sh,p	588Sh,p	611s,p	...	878Sh,p	967s,p	978w,p	1005Sh,p	...
Di <sub>100</sub> Fo <sub>10</sub>	1575	...	570Sh,p	588Sh,p	611s,p	...	878Sh,p	967s,p	978w,p	1005Sh,p	...
Di <sub>150</sub> Fo <sub>20</sub>	1575	...	570Sh,p	588Sh,p	611s,p	...	878Sh,p	967s,p	978w,p	1005Sh,p	...
Di <sub>170</sub> Fo <sub>30</sub>	1575	...	570Sh,p	588Sh,p	611s,p	...	878Sh,p	967s,p	978w,p	1005Sh,p	...

\* s, strong; w, weak; p, polarized; Sh, shoulder.  
† Not determined.

and a weak, broad envelope in the range 900–1200  $\text{cm}^{-1}$ . The high-frequency band is asymmetric in shape, however, and the presence of at least two overlapping bands at  $\sim 1004$  and  $1120 \text{ cm}^{-1}$  is implied. These latter values are to be compared with the positions of the Si(Al)-O stretch bands in  $\text{NaAlSi}_3\text{O}_8$  and  $\text{CaAl}_2\text{Si}_2\text{O}_8$  glass (1012 and 1108, and 978  $\text{cm}^{-1}$ , respectively; Virgo, Seifert, and Mysen, this Report; Table 12). It is suggested, therefore, that the structure of  $\text{Ab}_{50}\text{An}_{50}$  glass closely resembles those of the end-member of Ab and An glasses.

The ordering of end-member glass structures into domains with structures similar to those of the end-member glass compositions is clearly evident in the Raman spectra of the glasses with compositions along the Ab-Di and An-Di joins. For glasses with compositions along the Ab-Di join, the strong, low-frequency

band at  $\sim 630 \text{ cm}^{-1}$  in  $\text{CaMgSi}_2\text{O}_6$  glass occurs as a strong band in the  $\text{Ab}_{25}\text{Di}_{75}$  composition and as a weaker shoulder in both the  $\text{Ab}_{50}\text{Di}_{50}$  and  $\text{Ab}_{75}\text{Di}_{25}$  glasses (Fig. 28). Similarly, the low-frequency rocking band at  $472 \text{ cm}^{-1}$ , characteristic of  $\text{NaAlSi}_3\text{O}_8$  glass, occurs as a strong, well-resolved band in both the  $\text{Ab}_{75}\text{Di}_{25}$  and  $\text{Ab}_{50}\text{Di}_{50}$  glasses (Fig. 28). The strong, low-frequency band at  $\sim 630 \text{ cm}^{-1}$  in  $\text{CaMgSi}_2\text{O}_6$  glass is clearly evident in the  $\text{An}_{25}\text{Di}_{75}$  and  $\text{An}_{50}\text{Di}_{50}$  glasses, and those at  $\sim 500$  and  $550 \text{ cm}^{-1}$  are clearly evident in the  $\text{An}_{75}\text{Di}_{25}$  and  $\text{An}_{50}\text{Di}_{50}$  glasses (Fig. 29). There are features in the Raman spectra of glasses along the Ab-Di and An-Di joins, however, that indicate that the structures of the binary glasses are not entirely represented by an ordered arrangement of the end-member glass structures. Note the reduced intensity of the band at  $\sim 870 \text{ cm}^{-1}$ , which is attributed to  $\text{SiO}_4^{4-}$  spe-

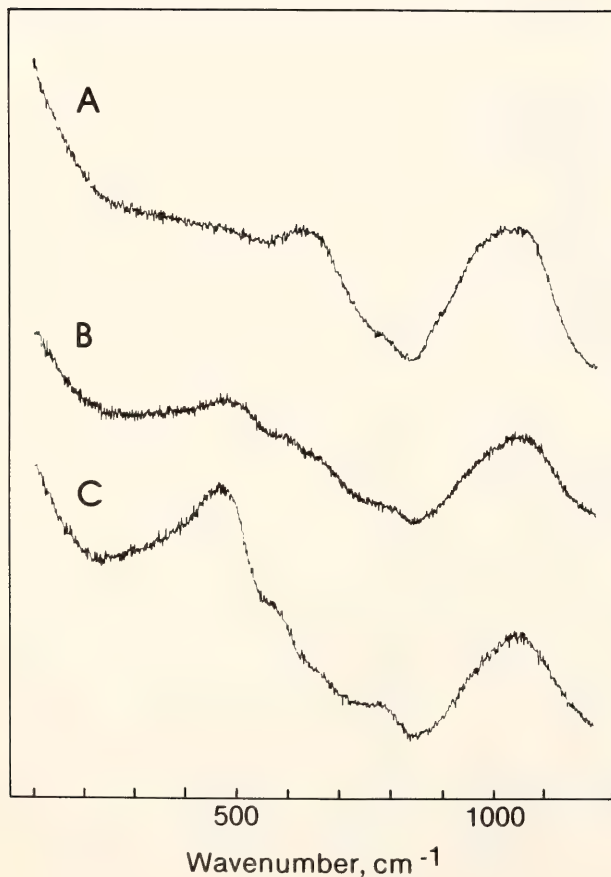


Fig. 28. Unpolarized ( $I_{\parallel} + I_{\perp}$ ) Raman spectra of (A)  $\text{Ab}_{25}\text{Di}_{75}$ , (B)  $\text{Ab}_{50}\text{Di}_{50}$ , and (C)  $\text{Ab}_{75}\text{Di}_{25}$  glasses (mole %) (laser 488.0 nm  $\text{Ar}^+$  ion, 300 mW).

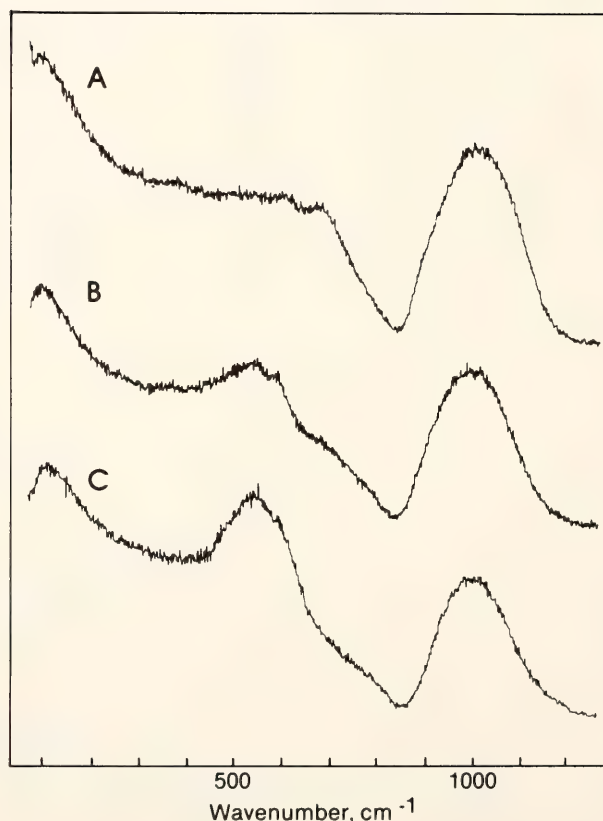


Fig. 29. Unpolarized ( $I_{\parallel} + I_{\perp}$ ) Raman spectra of (A)  $\text{An}_{25}\text{Di}_{75}$ , (B)  $\text{An}_{50}\text{Di}_{50}$ , and (C)  $\text{An}_{75}\text{Di}_{25}$  glasses (mole %) (laser 488.0 nm  $\text{Ar}^+$  ion, 300 mW).



cies (Mysen, Virgo, and Scarfe, this Report). The Si-O stretch band for the monomer species is observed as a weak shoulder in the diopside-rich samples of both binary joins, but it is clearly of reduced intensity compared with this band in the end-member  $\text{CaMgSi}_2\text{O}_6$  glass (Mysen, Virgo, and Scarfe, this Report).

*CaMgSi<sub>2</sub>O<sub>6</sub>-Mg<sub>2</sub>SiO<sub>4</sub> System.* The Raman spectra of glasses of diopside composition containing 10, 20, and 30 wt %  $\text{Mg}_2\text{SiO}_4$  component resemble those of the end-member  $\text{CaMgSi}_2\text{O}_6$  glass (Fig. 30; Mysen, Virgo, and Scarfe, this Report). In general, the spectra are composed of a strong, polarized band at  $\sim 650\text{ cm}^{-1}$  and a high-frequency envelope in the range  $800\text{--}1150\text{ cm}^{-1}$ , composed of a partially resolved band at  $\sim 800\text{ cm}^{-1}$ , a strong band at  $\sim 950\text{--}980\text{ cm}^{-1}$ , and a high-frequency shoulder at  $\sim 1005\text{ cm}^{-1}$ , which is also observed in the  $\text{Di}_{90}\text{Fo}_{10}$  (wt %) glass. These last three bands are assigned to the stretch frequencies of  $\text{SiO}_4$  tetrahedra containing 4, 2, and 1 non-bridging oxygen atoms, respectively (Brawer and White, 1975). In comparison with the spectrum of  $\text{CaMgSi}_2\text{O}_6$  glass, it can be shown that with increasing  $\text{Mg}_2\text{SiO}_4$ , there is a systematic in-

crease in the intensity of the bands at  $\sim 880$  and  $\sim 950\text{--}980\text{ cm}^{-1}$  and a decrease in the intensity of the band at  $\sim 1005\text{ cm}^{-1}$ . In fact the shoulder at  $\sim 1005\text{ cm}^{-1}$  in the spectrum of the  $\text{Di}_{90}\text{Fo}_{10}$  glass is no longer visible in the spectra of the  $\text{Di}_{80}\text{Fo}_{20}$  and  $\text{Di}_{70}\text{Fo}_{30}$  glasses. These spectral changes are interpreted in terms of an increase in the  $\text{SiO}_4^{4-}$  monomer and the  $\text{Si}_2\text{O}_6^{4-}$  chain units and a decrease in the  $\text{Si}_2\text{O}_5$  sheet component with increasing  $\text{Mg}_2\text{SiO}_4$  content.

*Structural Species in 1-atm Melts in the System Di-Fo-Ne-SiO<sub>2</sub>.* On the basis of the structural studies discussed above it is possible to define the major characteristics of multicomponent systems at 1 atm with compositions in the Di-Fo-Ne-SiO<sub>2</sub> system. In general, there are only three groups of distinct structural types that need to be considered: (1) completely polymerized structures consisting of a three-dimensional array of  $\text{TO}_2$  (where  $T$  is Si, Al); (2) depolymerized melt structures consisting principally of different proportions of chain, sheet, and monomer species; and (3) structures that are to a large extent composed of mixtures of (1) and (2).

Melts with a predominantly three-dimensional network structure (group 1) are exemplified by melts along the  $\text{SiO}_2\text{-NaAlO}_2$  and  $\text{SiO}_2\text{-CaAl}_2\text{O}_4$  joins (Sharma, Virgo, and Mysen, *Year Book* 77, pp. 652-658; Virgo, Seifert, and Mysen, this Report). For these glasses, it has been suggested that the network structure is comprised of at least two structural units, each having distinct Si/Al, but in each unit there is a random array of  $\text{SiO}_4$  and  $\text{AlO}_4$  tetrahedra. In such melt structures the alkali or alkaline-earth cation provides the necessary balance for the trivalent cation in tetrahedral coordination with the formation of  $\text{NaAlO}_2$  and  $\text{CaAl}_2\text{O}_4$  complexes. New structural data for melts along the Ab-An join, however, indicate that in multicomponent systems there may be ordered domains of  $\text{NaAlO}_2$  and  $\text{CaAl}_2\text{O}_4$  complexes.

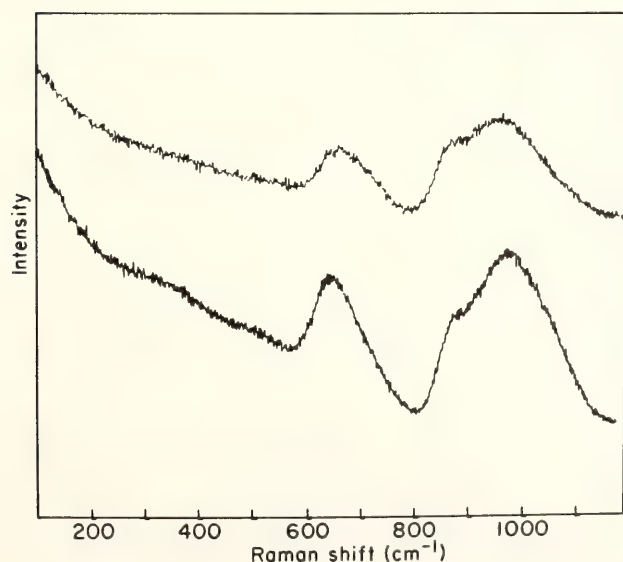
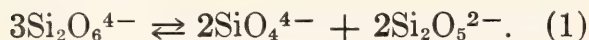


Fig. 30. Unpolarized ( $I_{\parallel} + I_{\perp}$ ) Raman spectra of (upper)  $\text{Fo}_{30}\text{Di}_{70}$  and (lower)  $\text{Fo}_{10}\text{Di}_{90}$  glasses (mole %) (laser  $488.0\text{ Ar}^+$  ion,  $300\text{ mW}$ ).

The second structural group is typified by melts with compositions in the system Fo-Di-En. The anionic species in melts of this system can be represented in principle by the disproportionation reaction



It is evident from structural data along the join  $\text{MgSiO}_3\text{-CaSiO}_3$  (Mysen, Virgo, and Seifert, this Report) that the  $\text{SiO}_4^{4-}$  species increases with increasing CaO, and it is implied from Equation 1, above, that there will be a corresponding increase in the  $\text{Si}_2\text{O}_5^{2-}$  chain component. For melt structures more depolymerized than the metasilicate composition, there is a significant increase in the  $\text{SiO}_4^{4-}$  monomer and the  $\text{Si}_2\text{O}_6^{4-}$  chain components with increasing  $\text{MgO/SiO}_2$ .

The third major structural type for compositions in the Di-Fo-Ne- $\text{SiO}_2$  tetrahedron is represented by mixtures of the two major structural groups discussed above. On the basis of the structures of glasses in the systems Ne-Di- $\text{SiO}_2$ , Fo-Ab-An (Mysen, Virgo, and Seifert, this Report), and Di-Ab-An (this report), it is evident that the melt structure will consist of domains with a three-dimensional network structure, similar to the structures of melts along the  $\text{SiO}_2\text{-NaAlO}_2$  and  $\text{SiO}_2\text{-CaAl}_2\text{O}_4$  joins, and of domains with a more depolymerized network structure, consisting principally of chains, sheets, and monomers. Significantly, however, on the basis of the structures of melts in the Fo-Ab-An and Di-Ab-An systems, distinct  $\text{SiO}_4^{4-}$  species are less stable than in the depolymerized end-member glass compositions. It is suggested that the decrease in  $\text{SiO}_4^{4-}$  species stems from a reaction with the more polymerized components of the structure. As a result of this latter reaction it can be expected that the three-dimensional network structure will be less Si(Al)-rich. This effect is not readily seen in the Raman spectra of the quenched melts except in the Fo-An glass, for which the effect of Al substitution in the residual chain and sheet components

is observed (Mysen, Virgo, and Seifert, this Report).

In summary, a comparatively simple picture is envisaged of the 1-atm structure of multicomponent melts for bulk compositions approximating major igneous rocks. The major anionic species are  $\text{TO}_2$ ,  $\text{T}_2\text{O}_5^{2-}$ ,  $\text{T}_2\text{O}_6^{4-}$ , and  $\text{TO}_4^{4-}$ , where T refers to Si(Al). The proportions of these anionic species will be determined principally by mixing melts with three-dimensional network structures with those melts that are more depolymerized and consist principally of  $\text{T}_2\text{O}_5^{2-}$ ,  $\text{T}_2\text{O}_6^{4-}$ , and  $\text{TO}_4^{4-}$  units. It is evident, however, that for bulk compositions with the non-bridging oxygen/Si(Al)  $< 2.0$ , the  $\text{TO}_4^{4-}$  monomer is unstable and reacts with  $\text{TO}_2$  units, probably to form chains.

### THREE-DIMENSIONAL NETWORK STRUCTURES OF GLASSES IN THE SYSTEMS $\text{CaAl}_2\text{O}_4\text{-SiO}_2$ , $\text{NaAlO}_2\text{-SiO}_2$ , $\text{NaFe}_2\text{SiO}_2$ , AND $\text{NaGaO}_2\text{-SiO}_2$ AT 1 ATM

*D. Virgo, F. Seifert, and B. O. Mysen*

In silicate melts with a predominantly three-dimensional network structure the presence of trivalent cations necessitates the formation of complexes of the type  $\text{NaAlO}_2$  and  $\text{CaAl}_2\text{O}_4$ , for example, because of charge-balance requirements. Furthermore, in such melts there is the possibility of short-range ordering of  $\text{SiO}_4$  and  $\text{T}^{3+}\text{O}_4$  when  $\text{T}^{3+} = \text{Al}^{3+}$ ,  $\text{Fe}^{3+}$ ,  $\text{Ga}^{3+}$ , which would lead to clustering of the alkali or alkaline-earth complexes. Such structural effects would have important consequences for modeling crystallization processes in silicate melts and physical properties such as viscosity and density.

The stability of alkali and alkaline-earth complexes of the type mentioned above has been determined at 1 atm in quenched melts with compositions along the binary joins  $\text{SiO}_2\text{-NaAlO}_2$ ,  $\text{SiO}_2\text{-NaGaO}_2$ ,  $\text{SiO}_2\text{-NaFeO}_2$ , and  $\text{SiO}_2\text{-CaAl}_2\text{O}_4$  using Raman spectroscopic techniques. Starting materials for the preparation of



the glasses at 1 atm were combinations of spectroscopically pure  $\text{CaCO}_3$ ,  $\text{Na}_2\text{CO}_3$ ,  $\text{Al}_2\text{O}_3$ ,  $\text{Fe}_2\text{O}_3$ ,  $\text{Ga}_2\text{O}_3$ , and  $\text{SiO}_2$ . Aliquots of the iron-free mixes, previously decarbonated, were contained in crimped  $\text{Pt}_{95}\text{Au}_5$  capsules and melted; then the charges were quenched in a Pt crucible standing in liquid nitrogen. The iron-bearing mixtures were melted by suspending a sintered disk of the sample on the end of a thin Pt wire and subsequently quenching the melt as described above. Raman spectra were measured on small chips of glass.

The Raman spectra of the iron-free glasses were recorded using the techniques described by Sharma *et al.* (*Year Book* 77, pp. 652–658). The iron-bearing glasses were excited with the 647.1-nm line of a  $\text{Kr}^+$  ion laser using a laser power of  $\sim 300$  mW at the sample.

### Results

The Raman spectrum of the 1-atm glass of  $\text{NaGaSi}_2\text{O}_6$  composition is given in Fig. 31, and the spectrum of the  $\text{NaFeSi}_2\text{O}_6$  glass is given by Seifert, Virgo, and Mysen (this Report). The Raman spectra for  $\text{CaAl}_2\text{Si}_2\text{O}_8$  and  $\text{CaAl}_2\text{SiO}_6$  glasses are given in Fig. 32. Measured peak positions of the Raman bands for all glasses used in this study are listed in Table 13.

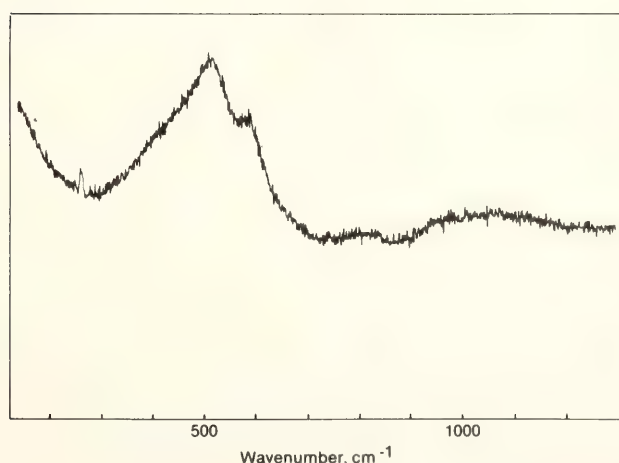


Fig. 31. Unpolarized Raman spectrum of  $\text{NaGaSi}_2\text{O}_6$  glasses (laser 488.0 nm  $\text{Ar}^+$  ion, 500 mW).

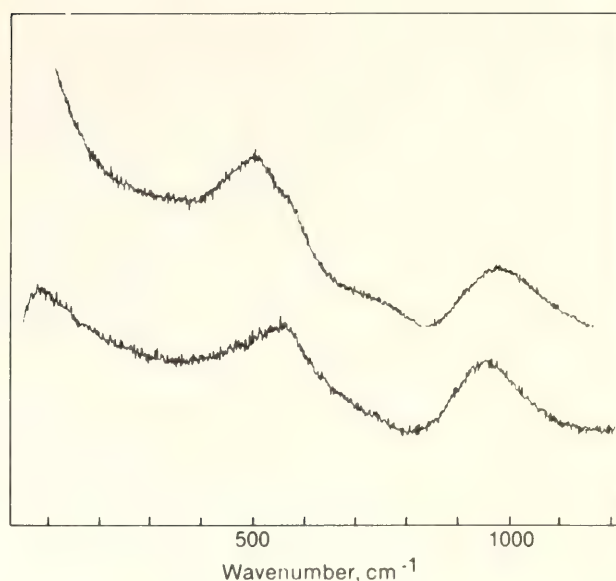


Fig. 32. Unpolarized Raman spectra of (upper)  $\text{CaAl}_2\text{Si}_2\text{O}_8$  and (lower)  $\text{CaAl}_2\text{SiO}_6$  glasses (laser 488.0 nm  $\text{Ar}^+$  ion, 500 mW).

Raman spectroscopic investigation of glasses along the join  $\text{SiO}_2$ - $\text{NaAlO}_2$  has been previously reported (Sharma, Virgo, and Mysen, *Year Book* 77, fig. 4). In this investigation an additional composition,  $\text{NaAlSi}_7\text{O}_{16}$ , was prepared to study the effect on the melt structure resulting from the substitution  $\text{Na} + \text{Al}$  for  $\text{Si}$  in a bulk composition close to  $\text{SiO}_2$  composition. The prominent spectral features of this glass are similar to those of  $\text{SiO}_2$  glass except that the high-frequency Si-O stretch bands at 1055 and 1157  $\text{cm}^{-1}$  both are lowered in frequency compared with the stretch bands in  $\text{SiO}_2$  glass (Table 13). By recording the Raman spectra of the  $\text{NaAlSiO}_4$  glass at a high sensitivity, two partially resolved bands in the high-frequency envelope between 900 and 1200  $\text{cm}^{-1}$  have been resolved (Table 13).

The Raman spectra of the  $\text{NaGaSi}_2\text{O}_6$  and  $\text{NaGaSiO}_4$  glasses are in general similar to the spectra of the aluminosilicate analogues (Table 13; Fig. 31). The Raman spectra of the  $\text{CaAl}_2\text{Si}_2\text{O}_8$  and  $\text{CaAl}_2\text{SiO}_6$  glasses are distinguished from those of the other glasses examined in this study and elsewhere (Sharma *et al.*, *Year Book* 77, pp. 652–658) in that in the high-

TABLE 13. Raman Frequencies of Glasses at 1 atm

Composition	$T, ^\circ\text{C}$	Wave Number, $\text{cm}^{-1}$									
$\text{SiO}_2^\dagger$	...	60b,s,dp*	...	490s,p	...	600w,p	...	806w,p	1065w,dp	1200w,dp	
$\text{NaAlSi}_7\text{O}_{16}$	1550	n.d.	...	493sh,p	...	601w,p	...	806w,p	1055w,wp	1157w,wp	
$\text{NaAlSi}_3\text{O}_8$	1450	...	...	472b,p	572sh,p	...	...	800w,dp	1012w,wp	1108w,wp	
$\text{NaAlSi}_2\text{O}_6$	1450	...	300w,p	472b,p	568sh,p	...	...	744w,dp	1000w,wp	1080w,wp	
$\text{NaAlSiO}_4$	1550	...	300w,p	480b,p	572sh,p	...	...	736wp	990w,p	1025w,p	
$\text{NaGaSi}_2\text{O}_6$	1450	62b,s,p	...	483b,s,p	550b,p	...	...	~767w,dp	974w,p	1080w,p	
$\text{NaGaSiO}_4$	1550	...	380sh,p	517b,s,p	...	634w,p	715w,p	...	909w,p	1007w,p	
$\text{NaFeSi}_5\text{O}_{12}$	1500	...	...	~419b,s,p	...	...	...	...	957m,p	1097w,p	
$\text{NaFeSi}_3\text{O}_8$	1400	...	351b,s,p	455b,sp	...	...	...	...	939m,p	~1067w,p	
$\text{NaFeSi}_2\text{O}_6$	1400	...	383b,s,p	451b,sp	...	...	...	739w,p	925s,p	1047w,p	
$\text{CaAl}_2\text{Si}_2\text{O}_8$	1575	...	...	506b,p	570sh,p	...	...	~749w,p	978m,p	...	
$\text{CaAl}_2\text{SiO}_6$	1575	89	...	551b,p	...	...	...	~700b,w,p	953s,p	...	

\* Abbreviations: s, strong; m, medium; w, weak; p, polarized; dp, depolarized; wp, weakly polarized; sh, shoulder; b, broad; n.d., not determined. Uncertainties ( $\text{cm}^{-1}$ ): s, 3-4; ms, 4-5; m, 5-6; mw, 7; w, 10; vw, 1-15.

$^\dagger$  Hass, 1971.



frequency region, there appears to be only a single symmetric band at  $\sim 950$ – $975\text{ cm}^{-1}$ .

The major feature of quenched melts on the join  $\text{SiO}_2$ – $\text{NaFeO}_2$  is a sharp band at  $\sim 950\text{ cm}^{-1}$  and a weaker, higher frequency shoulder at  $\sim 1050$ – $1100\text{ cm}^{-1}$ . Both high-frequency bands are polarized. The intensity of the band at  $\sim 950\text{ cm}^{-1}$  increases with increasing  $\text{NaFeO}_2$  content.

### Discussion

From the Raman spectrum of  $\text{SiO}_2$  glass as a type example of the spectra of a three-dimensional network structure (e.g., Hass, 1970; Table 13), one may conclude that the presence of the strong, polarized band at  $470$ – $500\text{ cm}^{-1}$  and the very weak, broad bands in the  $900$ – $1200\text{ cm}^{-1}$  region in glasses along the  $\text{SiO}_2$ – $\text{NaAlO}_2$  and  $\text{SiO}_2$ – $\text{NaGaO}_2$  joins is indicative of a three-dimensional array of tetrahedrally coordinated units in which most of the oxygen atoms are shared. In this interpretation, the shoulder at  $550\text{ cm}^{-1}$  is deemed analogous to the  $600\text{ cm}^{-1}$  band in the Raman spectrum of  $\text{SiO}_2$  glass and is associated with a random defect structure. The lowering of the high-frequency stretch bands in the  $\text{SiO}_2$ – $\text{NaAlO}_2$  glasses compared with those in the Raman spectrum of  $\text{SiO}_2$  is attributed to  $\text{Si(Al)}$  coupled modes (Sharma, Virgo, and Mysen, *Year Book* 77, pp. 652–658). A similar explanation is proposed for the stretch bands in  $\text{SiO}_2$ – $\text{NaGaO}_2$  glasses.

The diagnostic spectral features in the Raman spectra of a three-dimensional glass structure are also observed in the spectrum of  $\text{CaAl}_2\text{Si}_2\text{O}_8$  glass (Fig. 32). In support of the three-dimensional structure of  $\text{CaAl}_2\text{Si}_2\text{O}_8$  glass are the RDF data of Taylor and Brown (1979), who concluded that the structure of  $\text{CaAl}_2\text{Si}_2\text{O}_8$  glass consists predominantly of four-membered rings of  $\text{SiO}_4$  and  $\text{AlO}_4$  tetrahedra in which the Ca atoms occupy interstices formed from the interconnected rings.

The Raman spectrum of  $\text{CaAl}_2\text{SiO}_6$  glass is significantly different from the spectra of glasses of Al-free chain silicates (Mysen, Virgo, and Seifert, this Report; Brawer and White, 1977). Specifically, the low-frequency rocking band is at  $550\text{ cm}^{-1}$  compared with  $\sim 620\text{ cm}^{-1}$ , for example, in diopside and sodium metasilicate glasses. In addition, the high-frequency bands at  $\sim 890$ ,  $980$ , and  $1040\text{ cm}^{-1}$ , corresponding to the stretch frequencies of  $\text{SiO}_4$  tetrahedra that contain on the average 4, 2, and 1 nonbridging oxygen atoms in quenched melt of  $\text{CaMgSi}_2\text{O}_6$  composition, are not present in the high-frequency envelope of  $\text{CaAl}_2\text{SiO}_6$  glass. Instead, there is a single, symmetrically shaped band centered at  $\sim 953\text{ cm}^{-1}$ . In light of the above interpretation of the Raman spectra of other alumino-silicate glasses, it seems reasonable to conclude that the high-frequency stretch band in  $\text{CaAl}_2\text{SiO}_6$  glass is an  $\text{Si(Al)}$  coupled mode and that most of the  $\text{Al}^{3+}$  is in tetrahedral coordination.

The spectral features that were used above to characterize a three-dimensional network of Si and Al tetrahedra are not immediately obvious in the Raman spectra of Fe-bearing glasses (Seifert, Virgo, and Mysen, this Report). For example, the high-frequency envelope in the Raman spectrum of  $\text{NaFeSi}_2\text{O}_6$  glass consists of a strong band at  $\sim 950\text{ cm}^{-1}$  with a weak shoulder at  $1050\text{ cm}^{-1}$ , and furthermore, the intensity of the band at  $\sim 950\text{ cm}^{-1}$  increases with increasing Fe content for glasses along the join  $\text{SiO}_2$ – $\text{NaFeO}_2$ . It is known, for example, that in glasses with compositions along the join  $\text{Na}_2\text{O}$ – $\text{SiO}_2$ , the high-frequency bands at  $\sim 950\text{ cm}^{-1}$  and  $\sim 1100\text{ cm}^{-1}$  are assigned to the stretch frequencies of  $\text{SiO}_4$  tetrahedra containing on the average 2 and 1 nonbridging oxygen atoms, respectively (Brawer and White, 1977). In view of the latter interpretation, it might be concluded that  $\text{Fe}^{3+}$  in glasses along the join  $\text{SiO}_2$ – $\text{NaFeO}_2$  is predominantly present as a network modifying cation. Two

additional sets of data, however, preclude this interpretation. In the first instance, the  $^{57}\text{Fe}$  Mössbauer spectra of glasses of  $\text{NaFeSi}_5\text{O}_{12}$ ,  $\text{NaFeSi}_3\text{O}_8$ , and  $\text{NaFeSi}_2\text{O}_6$  compositions prepared in air at 1 atm consist of a single absorption doublet that is assigned unequivocally to ferric iron (Seifert, Virgo, and Mysen, this Report). Significantly, the calculated isomer shift is less than 0.2 mm/sec and can be compared with the value of 0.39 mm/sec for crystalline  $\text{NaFeSi}_2\text{O}_6$  where  $\text{Fe}^{3+}$  is known to be in octahedral coordination. These latter results strongly imply that ferric iron is predominantly in tetrahedral coordination in the glasses along the join  $\text{SiO}_2\text{-NaFeO}_2$ . In addition, it has been recently shown from EXAFS and RDF data (Brown *et al.*, 1978; G. E. Brown, personal communication) that  $\text{Fe}^{3+}$  is tetrahedrally coordinated in glass of  $\text{NaFeSi}_2\text{O}_6$  composition. Thus, it can be concluded that the network structure of the  $\text{SiO}_2\text{-NaFeO}_2$  glasses is a three-dimensional array of tetrahedrally coordinated polyhedra. It is necessary, therefore, to consider the assignment of the high-frequency stretch bands in the region 900–1050  $\text{cm}^{-1}$  in the Raman spectra of the  $\text{SiO}_2\text{-NaFeO}_2$  glasses to Si(Fe)-O coupled modes.

A common feature of the three-dimensional network structures discussed above has been the inference that the high-frequency stretch modes in these glasses are actually  $\text{Si}(T^{3+})$  coupled modes. Further discussion of this interpretation of the spectra is relevant in view of the possibility of local ordering of the different tetrahedrally coordinated species. This aspect of three-dimensional melt structures is examined with the aid of Fig. 33 in which the frequencies of the stretch vibrations of the glasses studied in this report are plotted as a function of  $T^{3+}/(\text{Si} + T^{3+})$ . It is evident from the data plotted in Fig. 33 that the high-frequency stretch bands involve  $\text{Si}(T^{3+})$  coupling inasmuch as the bands are lower in frequency compared with the Si-O stretch bands in  $\text{SiO}_2$  glass. The degree

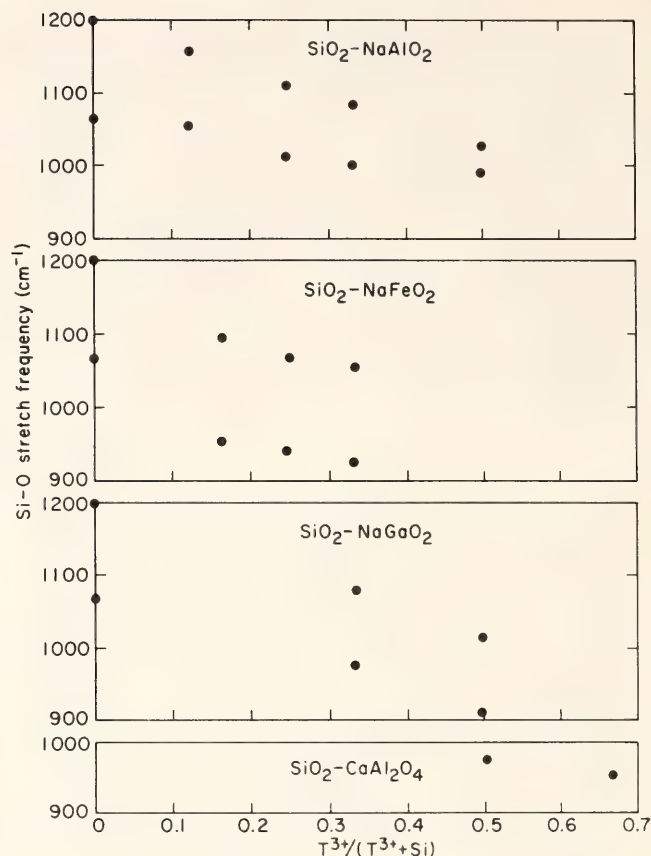


Fig. 33. Variation of the band positions of the Si-O (bridging) stretch modes for glasses along the joins  $\text{SiO}_2\text{-NaAlO}_2$ ,  $\text{SiO}_2\text{-NaFeO}_2$ ,  $\text{SiO}_2\text{-NaGaO}_2$ , and  $\text{SiO}_2\text{-CaAl}_2\text{O}_4$ , as a function of  $T^{3+}/(T^{3+} + R^{3+})$ , where  $T^{3+}$  is, respectively,  $\text{Al}^{3+}$ ,  $\text{Fe}^{3+}$ ,  $\text{Ga}^{3+}$ , and  $\text{Al}^{3+}$ .

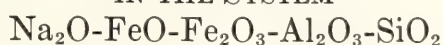
of coupling in those samples, which show two high-frequency stretch bands, may be different, as evidenced from the differential decrease of the frequencies of both bands. For glasses in the  $\text{SiO}_2\text{-NaAlO}_2$  and  $\text{SiO}_2\text{-NaGaO}_2$  systems, there is no obvious correlation between the relative intensities of the stretch bands and  $T^{3+}/(\text{Si} + T^{3+})$ ; thus, it is likely that neither of the high-frequency bands can be assigned to different nearest-neighbor configurations of  $\text{SiO}_4$  and  $\text{AlO}_4$  tetrahedra, of which there are at least five distinct possibilities. Alternatively, it is suggested that the presence of two resolved high-frequency stretch bands in these latter systems may reflect the presence of at least two distinct structural entities with different average  $T^{3+}/(\text{Si} + T^{3+})$  but in which Si and  $T^{3+}$  are randomly disordered. In terms of the above interpre-



tation, it is suggested that the high-frequency bands at 978 and 953  $\text{cm}^{-1}$  in  $\text{CaAl}_2\text{Si}_2\text{O}_8$  and  $\text{CaAl}_2\text{SiO}_6$  glasses, respectively, may result from the superposition of two Raman bands (see Fig. 33). This latter suggestion would be in agreement with the increased intensity of the stretch bands in the glasses containing  $\text{CaAl}_2\text{O}_4$  units compared with alkali-aluminosilicate glasses (e.g., Sharma, Virgo, and Mysen, *Year Book* 77, fig. 4). For glasses along the  $\text{SiO}_2$ - $\text{NaFeO}_2$  join, the frequencies of both stretch bands decrease with increasing  $\text{Fe}^{3+}/(\text{Si} + \text{Fe}^{3+})$ , and this decrease implies Si(Fe) coupling for both bands. The intensity of the low-frequency band varies in proportion to the Fe content for samples along the join, and this spectral feature may reflect different proportions of the two distinct structural units compared with the glasses containing  $\text{Al}^{3+}$  and  $\text{Ga}^{3+}$ .

In conclusion, it has been shown that the Raman spectra of 1-atm glasses in the systems  $\text{CaAl}_2\text{O}_4$ - $\text{SiO}_2$ ,  $\text{NaAlO}_2$ - $\text{SiO}_2$ ,  $\text{NaFeO}_2$ - $\text{SiO}_2$ , and  $\text{NaGaO}_2$ - $\text{SiO}_2$  are consistent with a predominantly three-dimensional array of tetrahedrally coordinated polyhedra. It is suggested, however, that there are at least two distinct structural entities in most of these glasses, each structural unit being characterized by different  $T^{3+}/\text{Si}$  where the proportions of these units may be different in distinct chemical systems. Finally, the existence of complexes of the type  $\text{NaAlO}_2$ ,  $\text{NaFeO}_2$ ,  $\text{NaGaO}_2$ , and  $\text{CaAl}_2\text{O}_4$  in the specific systems studied is necessarily inferred because of charge balance, which results from the presence of trivalent cations in tetrahedral coordinations.

#### MELT STRUCTURES AND REDOX EQUILIBRIA IN THE SYSTEM



*F. Seifert, D. Virgo, and B. O. Mysen*

An iron oxide component in a melt can play a dual role because Fe can enter both tetrahedral and octahedral sites,

i.e., act as either a network-forming or a network-modifying cation. As a result, iron in silicate melts can affect the physical and chemical properties of a melt in different ways. The structural role of Fe in a melt is presumed to be controlled by a complex interrelationship between the degree of polymerization of the host melt, the amount of Fe present, and its oxidation state.

In an attempt to determine these interrelationships, the system sodium metasilicate-acmite has been investigated in addition to the join acmite- $\text{SiO}_2$  (Virgo, Seifert, and Mysen, this Report). Some information on the local structures of the end-member quenched melts of the systems is available from Raman studies on sodium silicate (Brawer and White, 1975; Sharma *et al.*, *Year Book* 78, pp. 649-652) and jadeite (Sharma *et al.*, *Year Book* 78, pp. 652-658) and an EXAFS study (Brown *et al.*, 1978) on acmite quenched melts.

#### *Experimental*

Starting materials for the preparation of samples were spectroscopically pure  $\text{Na}_2\text{O} \cdot \text{SiO}_2$  quenched melt, spectroscopically pure  $\text{Fe}_2\text{O}_3$  or—in compositions with less than 5 wt %  $\text{Fe}_2\text{O}_3$ — $^{57}\text{Fe}_2\text{O}_3$ , and spectroscopically pure  $\text{SiO}_2$  and  $\text{Al}_2\text{O}_3$ . The mixtures were held in air or mixed gases at 1400°C as beads on Pt wire loops in a furnace for 1 hr and subsequently quenched in air, mercury, or liquid  $\text{N}_2$  to produce glasses of appropriate compositions.

The Mössbauer spectroscopic techniques applied were identical with those reported by Mysen and Virgo (1978). Except for the magnetic spectra (see below), a maximum of three absorption peaks were visually resolved when both ferrous and ferric iron were present, and no more than three Lorentzian lines were fitted (Virgo and Mysen, *Year Book* 76, pp. 400-407). The absence of any splitting or even significant broadening of the low-velocity line indicates that the posi-

TABLE 14. Hyperfine Parameters of Glasses and Crystals in the System Sodium Metasilicate-Acmite, Prepared in Air

Composition, mole % acmite	IS*	QS†	FWHH <sub>L</sub> ‡	FWHH <sub>H</sub> ‡
<i>Glasses</i>				
15	0.264	0.847	0.697	0.603
25	0.232	0.832	0.622	0.727
50	0.227	0.732	0.436	0.480
75	0.249	0.906	0.572	0.601
100	0.249	0.971	0.502	0.560
<i>Crystals</i>				
50 (Na <sub>5</sub> FeSi <sub>4</sub> O <sub>12</sub> )	0.377	0.0	0.448	
100 (NaFeSi <sub>2</sub> O <sub>6</sub> )	0.399	0.301	0.353	0.415

\* Isomer shift in mm/sec, relative to metallic iron.

† Quadrupole splitting, in mm/sec.

‡ Full width at half height; H and L indicate high- and low-velocity component peaks.

tion of the low-velocity component of the ferric doublet closely matches that of the low-velocity component of the ferrous doublet, so that the sum of these two lines can be handled numerically as a single line. Further justification for this procedure can be derived from the position of the low-velocity line in largely ferrous and completely ferric samples. For instance, in quenched melt of acmite composition the velocity changes from  $-0.132$  mm/sec (relative to metallic iron) in the reduced sample to  $-0.237$  mm/sec in the oxidized sample, which is a small change compared with the half-width of these absorption lines (about  $0.60$  mm/sec).

The  $\text{Fe}^{2+}/\Sigma\text{Fe}$  values have been calculated from the ratio of the areas of the ferrous and ferric absorption doublets. When only two lines (due to the ferrous doublet) can be observed, any deviation of the  $\text{Fe}^{2+}/\Sigma\text{Fe}$  value from 1 will be reflected in the inequality of peak areas, and the  $\text{Fe}^{2+}/\Sigma\text{Fe}$  is calculated from the difference in the peak areas.

The Raman spectra were recorded on small chips ( $\sim 1 \times 0.5 \times 0.5$  mm) of quenched melts using a double monochromator optical system and photon-counting detector (Sharma, *Year Book* 77, pp. 902–904) with the  $6471\text{-}\text{\AA}$  line of

a krypton laser operated at 200–400 mW and  $90^\circ$  with scattering geometry. In the reduced samples, oxidation of the sample surface due to excessive heating or photo-oxidation occurred, and the Raman spectra of these samples are not considered in this report.

### Results

*The System Sodium Metasilicate-Acmite under Oxidizing Conditions.* The Mössbauer spectra of samples with more than 6 mole % acmite component held in air exhibited one visually resolved doublet (Table 14; Fig. 34A) with isomer shifts ranging from  $0.23$  to  $0.26$  mm/sec and quadrupole splitting from  $0.79$  to  $0.97$  mm/sec. The Fe-bearing crystalline phases in this system,  $\text{Na}_5\text{Fe}^{3+}\text{Si}_4\text{O}_{12}$  (Bowen *et al.*, 1930) and acmite, respectively, show isomer shifts of  $0.38$  and  $0.40$  mm/sec and very small quadrupole splitting (*cf.* Fig. 34B).

The absence of any absorption peak at about  $1.8$  mm/sec and the equal intensity and half-width of the two-component peaks of the doublet indicate that more than 95% of the iron is in the ferric state in all glasses prepared in air. In glass samples with 6 mole % acmite component or less, an additional line is ob-



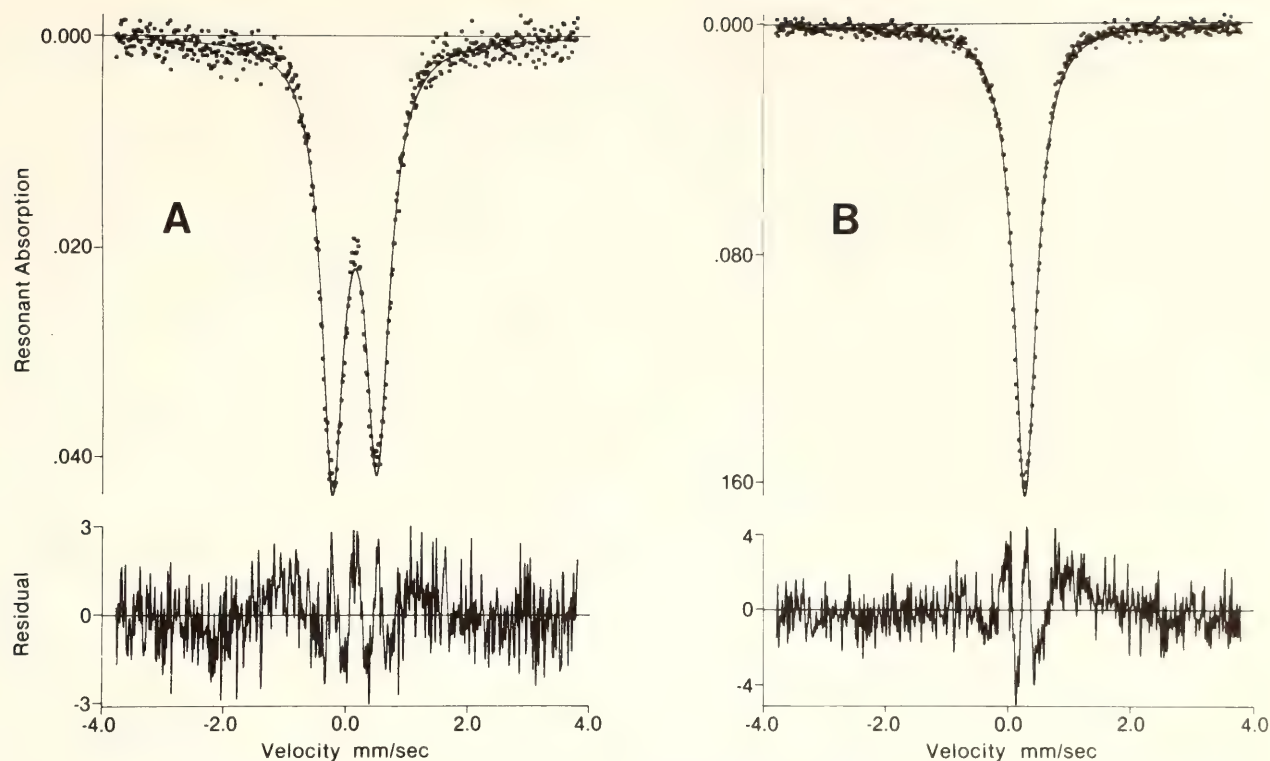


Fig. 34.  $^{57}\text{Fe}$  Mössbauer spectra of composition NFS518 (50 mole %  $\text{Na}_2\text{SiO}_3$ -50 mole %  $\text{NaFe}^{3+}\text{Si}_2\text{O}_6$ ) in air. (A) quenched melt; (B) crystalline.

served at about 1.5 mm/sec (Fig. 35), and the tail region of the envelope extends to at least  $\pm 7.5$  mm/sec. In spectra taken at 77 K (Fig. 35B) additional lines that constitute part of a broadened magnetic sextet pattern are observed, superimposed on the  $\text{Fe}^{3+}$  absorption doublet.

The Raman spectra of the glasses with

compositions along the  $\text{Na}_2\text{SiO}_3$ - $\text{NaFe}^{3+}\text{Si}_2\text{O}_6$  join are shown in Fig. 36, and the measured peak positions and band assignments of the high-frequency stretch vibrations are given in Table 15.

In the high-frequency region, the sodium metasilicate end member is characterized by a strong band at  $970\text{ cm}^{-1}$  and two weaker modes at 847 and  $1070\text{ cm}^{-1}$ .

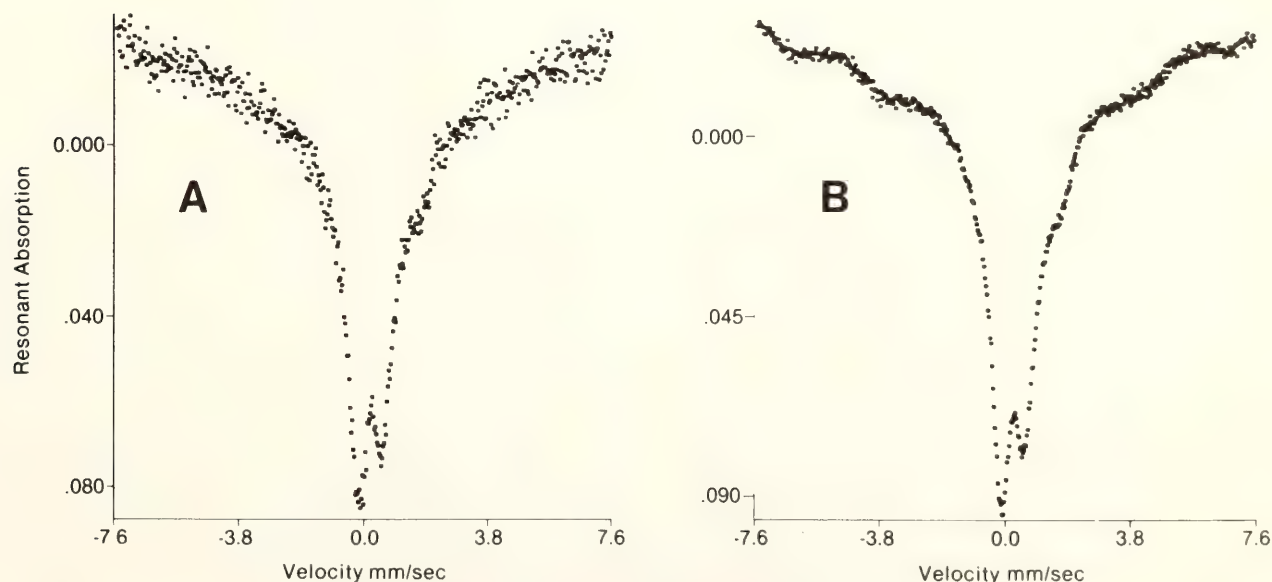


Fig. 35.  $^{57}\text{Fe}$  Mössbauer spectra of quenched melt of  $\text{Na}_2\text{SiO}_3$  composition with 1 mole %  $\text{NaFe}^{3+}\text{Si}_2\text{O}_6$ . (A)  $298^\circ\text{K}$ ; (B)  $77^\circ\text{K}$ .

TABLE 15. Vibrational Frequencies (cm<sup>-1</sup>) of Glasses on the Join Sodium Metasilicate-Acmite

0*	Mole % Acmite					Band Assignment
	6	15	25	50	75	100
360vw†	...	...	...	...	...	383w
580vw	...	...	...	...	...	...
619s	591s	577s	551m	540s	477s	451m
...	...	...	590s	605Sh	540Sh	541Sh
732vw	...	...	...	...	...	739vw
847w	847w	...	...	...	...	...
...	...	887m	877m	882s	897m	...
...	...	928m	940m	931m	...	...
970s	962s	978m	...	...	...	925s
1070Sh	1032Sh	1065m	1052m	1053s	1047m	1047m

\* Data taken from Sharma *et al.* (*Year Book* 77, pp. 649-652).  
 † s, strong; m, medium; w, weak; vw, very weak; Sh, shoulder.  
 ‡ High-frequency band assignments: Si-O<sup>2-</sup> designates vibrations in an isolated tetrahedron; -O-Fe(Si)-O<sup>-</sup>, -O-Si(Fe)-O<sup>-</sup>, and -O-Fe(Si)-O<sup>-</sup>, -O-Si(Fe)-O<sup>-</sup> designate Si, Fe-O<sup>-</sup> vibrations in tetrahedra containing, respectively, two and one nonbridging oxygen. The notations Fe(Si) and Si(Fe) imply Fe-rich and Si-rich coupled vibrations.



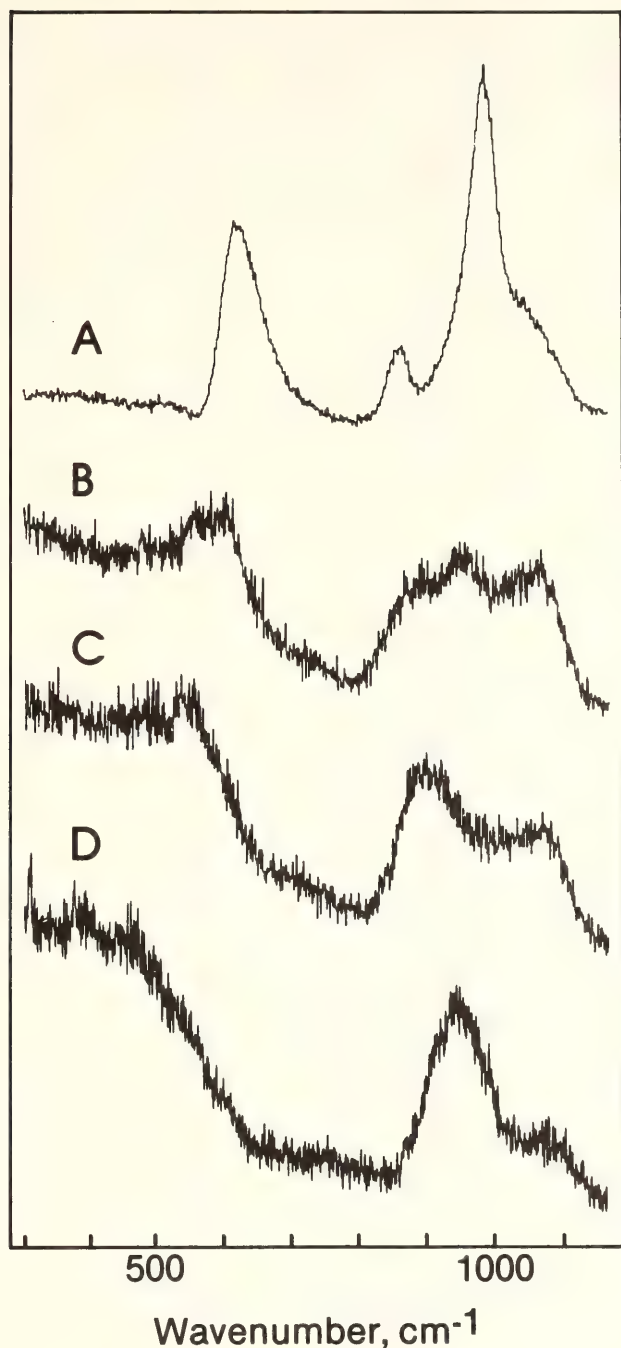


Fig. 36. Unpolarized Raman spectra of quenched melts of compositions on the join  $\text{Na}_2\text{SiO}_3\text{-NaFe}^{3+}\text{Si}_2\text{O}_6$  in air ( $1400^\circ\text{C}$ ). (A)  $\text{Na}_2\text{SiO}_3$ ; (B) 6 mole %  $\text{Na}_2\text{SiO}_3$ -94 mole %  $\text{NaFe}^{3+}\text{Si}_2\text{O}_6$ ; (C) 85 mole %  $\text{Na}_2\text{SiO}_3$ -15 mole %  $\text{NaFe}^{3+}\text{Si}_2\text{O}_6$ ; (D) 75 mole %  $\text{Na}_2\text{SiO}_3$ -25 mole %  $\text{NaFe}^{3+}\text{Si}_2\text{O}_6$ ; (E) 50 mole %  $\text{Na}_2\text{SiO}_3$ -50 mole %  $\text{NaFe}^{3+}\text{Si}_2\text{O}_6$ ; (F)  $\text{NaFe}^{3+}\text{Si}_2\text{O}_6$  ( $\text{Kr}^+$  ion laser, 200-400 mW excitation potential).

$\text{cm}^{-1}$ , whereas the acmite glass shows a strong band at  $925\text{ cm}^{-1}$  and a weaker, broadened band at  $1047\text{ cm}^{-1}$ . The spectrum of the glass containing 6 mole % acmite closely resembles that of  $\text{Na}_2\text{SiO}_3$  glass and differs substantially from the

spectra of the more Fe-rich compositions. There are, however, systematic frequency shifts for the low-iron bearing glass (Table 15), and the intensities of the bands at  $847$  and  $962\text{ cm}^{-1}$  are reduced compared with the intensity of the band at  $1032\text{ cm}^{-1}$  (Fig. 36). For more iron-rich glasses, two additional bands appear in the Raman spectra (e.g., at  $887$  and  $928\text{ cm}^{-1}$  in the glass containing 15 mole % acmite), which are assigned to the  $\text{Fe}(\text{Si})$  stretch vibrations in tetrahedra containing 2 and 1 nonbridging oxygens, respectively. For glasses in the range  $\sim 15$ -50 mole % acmite, the relative intensities of the bands assigned to  $-\text{O}-\text{Fe}(\text{Si})-\text{O}^\circ$  and  $-\text{O}-\text{Si}(\text{Fe})-\text{O}^\circ$  increase relative to the intensity of the bands assigned to  $-\text{O}-\text{Fe}(\text{Si})-\text{O}^-$  and  $-\text{O}-\text{Si}(\text{Fe})-\text{O}^-$  (Table 15; Fig. 36). With a further increase in iron content, the Raman spectra are composed of additional bands characteristic of the end-member acmite glass.

*The System Sodium Metasilicate-Acmite- $\text{Na}_2\text{O} \cdot 2\text{FeO} \cdot 4\text{SiO}_2$  under Reducing Conditions.* Compositions with only small amounts of sodium metasilicate have been investigated at low oxygen fugacities because of excessive sodium loss from the depolymerized melts close to the sodium metasilicate composition (Seifert, Virgo, and Mysen, this Report). Even in the more Si- and Fe-rich compositions, some loss of sodium to the  $\text{CO}_2/\text{CO}$  vapor phase of the furnace must be considered likely; as a result the compositions investigated may not lie exactly on the join.

As the oxygen fugacity is lowered, the ferric doublet in the Mössbauer spectra becomes asymmetric, and eventually a new line at  $\sim 1.8\text{ mm/sec}$  is observed which has increasing intensity as the oxygen fugacity decreases further (Fig. 37A, B). Concomitantly, the intensity of the high-velocity component of the ferric doublet decreases until only two lines of nearly equal area are observed (Table 16). The low-velocity component of this doublet is more intense and has a smaller

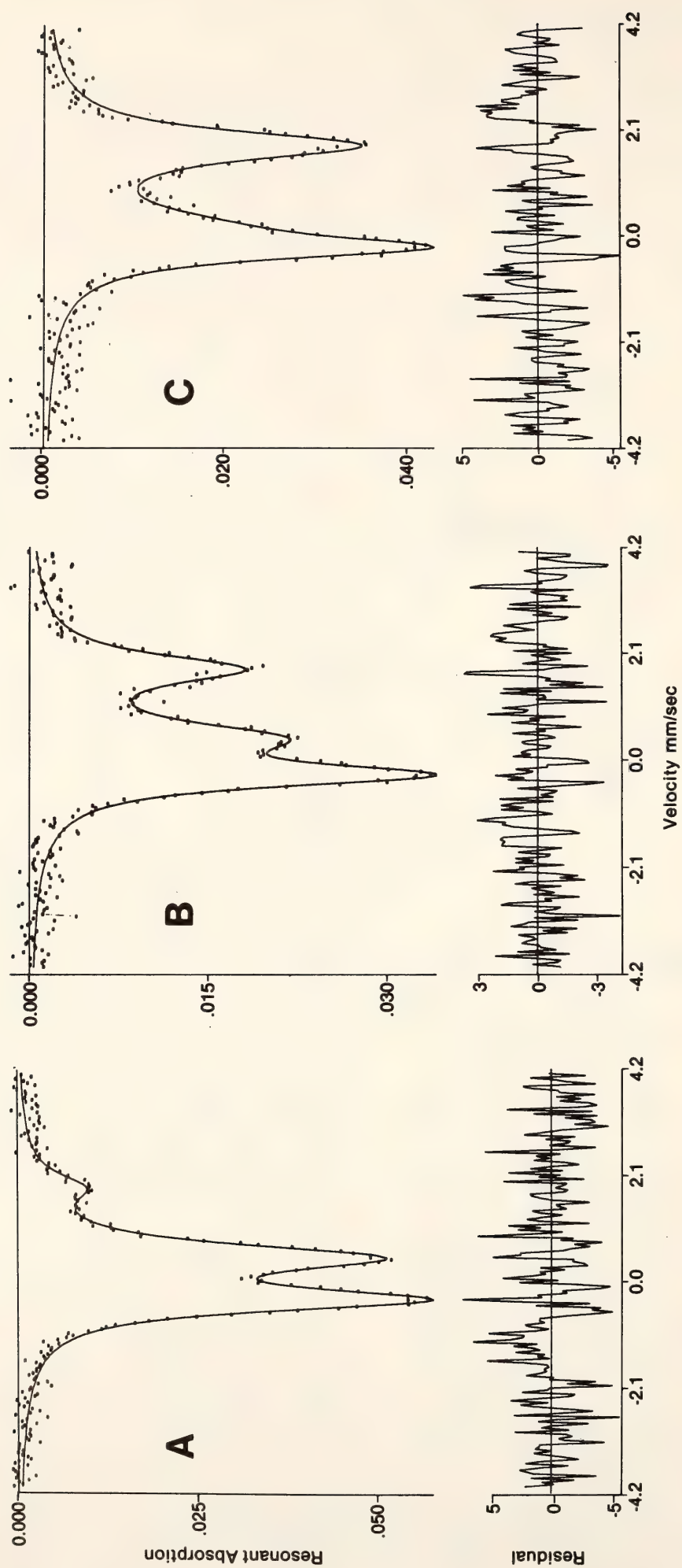


Fig. 37.  $^{57}\text{Fe}$  Mössbauer spectra of quenched melts of composition NFS518 (see Fig. 34) as a function of  $f_{\text{O}_2}$  at  $1400^\circ\text{C}$ . (A)  $f_{\text{O}_2} = 10^{-6}$  atm; (B)  $f_{\text{O}_2} = 10^{-8}$  atm; (C)  $f_{\text{O}_2} = 10^{-4}$  atm.



TABLE 16. Hyperfine Parameters and Area Ratios of Glasses in the System Sodium Metasilicate-Acmite-Na<sub>2</sub>O·2FeO·4SiO<sub>2</sub> under Reducing Conditions\*

Composition, mole % acmite	log <i>f</i> <sub>O<sub>2</sub></sub> , atm	Fe <sup>3+</sup>				Fe <sup>2+</sup>			
		IS	QS	FWHH <sub>L</sub>	FWHH <sub>H</sub>	IS	QS	FWHH <sub>L</sub>	FWHH <sub>H</sub>
50	−4	0.253	0.833	0.556	0.603	0.938	2.194	...	0.539
	−6	0.264	0.744	0.568	0.732	0.938	2.091	...	0.628
	−8	0.182	0.468	0.534	0.898	0.956	2.044	...	0.699
75	−4	0.260	0.879	0.583	0.591	0.925	2.209	...	0.592
	−6	0.283	0.759	0.609	0.720	0.940	2.060	...	0.696
	−8	...	...	...	...	0.991	1.955	0.755	0.754
100	−10	...	...	...	...	0.993	1.943	0.681	0.746
	−4	0.249	0.884	0.593	0.611	0.888	2.148	...	0.811
	−6	0.302	0.691	0.618	0.699	0.956	2.033	...	0.722
	−8	...	...	...	...	0.937	1.937	0.682	0.787

\* The compositions are given in terms of the oxidized system. Abbreviations as in Table 14.

line width than the high-velocity component. The isomer shift of the latter doublet ( $\sim 0.95$  mm/sec) is typical of ferrous iron, and the  $\text{Fe}^{2+}/\Sigma\text{Fe}$  values could be determined as described in the section on experimental techniques. The  $\text{Fe}^{2+}/\Sigma\text{Fe}$  values thus derived show systematic relationships to both bulk composition and oxygen fugacity (Fig. 38). At any constant oxygen fugacity the ratio  $\text{Fe}^{2+}/\Sigma\text{Fe}$  increases as the acmite content is increased from the 50 mole % acmite composition toward acmite, and at constant bulk composition it increases with decreasing oxygen fugacity.

### Discussion

*Coordination of Fe.* The structural role of Fe in the quenched melt can be determined to a large extent from its coordination to oxygen, which is reflected by the hyperfine parameters of the Mössbauer spectra. Tetrahedral and octahedral  $\text{Fe}^{3+}$  define well-separated ranges of isomer shifts in crystalline phases (0.19–0.30 mm/sec and 0.36–0.50 mm/sec, respectively: Annersten and Hålenius, 1976; Annersten and Olesch, 1978). The isomer shifts observed for  $\text{Fe}^{3+}$  in the quenched melts on the join sodium metasilicate-acmite and those observed by Mysen and

Virgo (1978) along the join jadeite-acmite, namely  $\sim 0.25$  mm/sec, are thus typical of  $\text{Fe}^{3+}$  in tetrahedral coordination. In addition, the rather sharp lines and the absence of any distinct asymmetry preclude the existence of significant amounts of octahedral  $\text{Fe}^{3+}$ . The magnetic splitting observed in oxidized samples close to sodium metasilicate composition supposedly arises from long relaxation times of spin-spin interactions of  $\text{Fe}^{3+}$  at these low iron concentrations (Bhargava *et al.*, 1979). The coordination of  $\text{Fe}^{3+}$  in the Fe-bearing crystalline phases of the join sodium metasilicate-acmite sharply contrasts to that in the glasses. It is known for acmite crystals, and inferred in this study from the isomer shift for the compound  $\text{Na}_5\text{FeSi}_4\text{O}_{12}$ , that  $\text{Fe}^{3+}$  occupies a slightly distorted octahedral position.

The isomer shift of ferrous iron is intermediate to that of octahedral (generally above 1.10 mm/sec) and tetrahedral ( $\sim 0.90$  mm/sec) ferrous iron in crystalline compounds. Octahedral ferrous iron seems to exhibit systematically lower isomer shifts in quenched melts compared with crystals, however, as exemplified by the isomer shift of  $\text{Fe}^{2+}$  in synthetic quenched melts (1.04–1.07 mm/sec) where  $\text{Fe}^{2+}$  is known to occupy octahedral positions from optical absorption studies (Mao, Virgo, and Bell, *Year Book* 72, pp. 631–638; Bell and Mao, *Year Book* 73, pp. 496–497). These low values might be related to the decrease of the isomer shift with increasing distortion of an octahedron (Seifert and Olesch, 1977). The quadrupole splitting also indicates distorted sites. It is concluded, therefore, that at least a major fraction of  $\text{Fe}^{2+}$  in the quenched melts studied here is incorporated into octahedral positions.

### Melt Structures from Raman Studies.

In general, the Raman bands present in the end-member quenched melts are present in the system sodium metasilicate-acmite. For  $\text{Na}_2\text{SiO}_3$  glass, the bands at

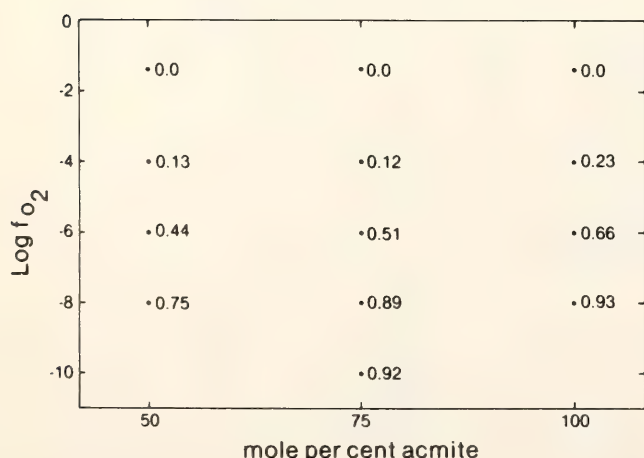


Fig. 38.  $\text{Fe}^{2+}/\Sigma\text{Fe}$  of melts on the join  $\text{Na}_2\text{SiO}_3\text{--NaFe}^{3+}\text{Si}_2\text{O}_6$  at  $1400^\circ\text{C}$  as a function of  $f_{\text{O}_2}$  and acmite component.



847, 970, and 1070  $\text{cm}^{-1}$ , respectively, are assigned to Si-O<sup>-</sup> stretches for tetrahedra containing, on the average, 4, 2, and 1 nonbridging oxygens. These stretch bands are therefore related to monomer, chain, and sheet units, respectively (Brawer and White, 1975). The bands at 925 and 1047  $\text{cm}^{-1}$  in  $\text{NaFeSi}_2\text{O}_6$  glass are attributed to Fe(Si)-O<sup>o</sup> and Si(Fe)-O<sup>o</sup> stretch vibrations, respectively, in a predominantly three-dimensional network structure (Virgo, Seifert, and Mysen, this Report). In glasses of intermediate composition along the join  $\text{Na}_2\text{SiO}_3$ - $\text{NaFeSi}_2\text{O}_6$ , two-mode behavior is exhibited in the Raman spectra in that the stretch vibrations for the sheet and chain units, characteristic of  $\text{Na}_2\text{SiO}_3$  glass, are distinct for Si and  $\text{Fe}^{3+}$ .

In view of the above interpretation, the major structural change along the join with increasing acmite is that the  $\text{SiO}_4^{4-}$  monomer unit diminishes and then disappears at acmite concentrations in excess of 6 mole %. Also, over the compositional range 0–50 mole % acmite, there is a decrease in the  $(\text{SiFe})_2\text{O}_6^{4-}$  chain units and an increase in the  $(\text{SiFe})_2\text{O}_5^{2-}$  sheet components. With a further increase in the acmite content, structural units characteristic of the three-dimensional network structure of acmite become increasingly abundant.

In summary, the Raman spectra in the system  $\text{Na}_2\text{SiO}_3$ - $\text{NaFe}^{3+}\text{Si}_2\text{O}_6$  are consistent with the concept of a local anionic structure of quenched melts varying continuously from a depolymerized melt to a three-dimensional network structure. In the systems  $\text{SiO}_2$ - $\text{NaFeSi}_2\text{O}_6$  (Virgo, Seifert, and Mysen, this Report) and jadeite-acmite (unpublished data), on the other hand, the Raman spectra in conjunction with the Mössbauer results indicate that the three-dimensional network structure of the end-member quenched melts is preserved at all intermediate compositions. The system exhibits one-mode behavior—i.e., the modes present in the end members shift continuously with composition.

## MELT STRUCTURES AND REDOX EQUILIBRIA IN THE SYSTEM

### $\text{CaO-MgO-FeO-Fe}_2\text{O}_3\text{-SiO}_2$

*B. O. Mysen, D. Virgo, and F. Seifert*

Redox ratios of geochemically important elements such as Fe and Eu have been suggested as petrogenetic indicators (Fudali, 1965; Drake, 1975). Recent studies have shown, however, that such redox ratios depend not only on the oxygen fugacity but also on the bulk composition of the melt (Lauer and Morris, 1977; Mysen and Virgo, 1978; Schreiber *et al.*, 1978). Inasmuch as both  $\text{Fe}^{2+}/\Sigma\text{Fe}$  and bulk composition affect melt structures, the determination of the local anionic structure of Fe-bearing melts is necessary to an understanding of redox equilibria in magmas. A combination of Mössbauer and Raman spectroscopic techniques is used to elucidate the relationship between redox states and the structure of melts.

Three bulk compositions— $\text{CaSiO}_3$  (Wo),  $\text{MgSiO}_3$  (En), and  $\text{CaMgSi}_2\text{O}_6$  (Di)—with varying amounts of  $\text{FeSiO}_3$  (Fs) in solution were studied. These compositions were chosen partly because their melts are not expected to have three-dimensional network structure (Etchepare, 1972), for which some data are already available (Mysen and Virgo, 1978), and partly because the modifying cations are alkaline earths, whereas in past studies the modifying cation was  $\text{Na}^+$ . Despite the importance of Ca, Fe, and Mg in magmatic rocks, the role of alkaline earth elements in silicate melts is essentially unknown.

The quenched melts were prepared from spectroscopically pure (Johnson Matthey)  $\text{MgO}$ ,  $\text{CaCO}_3$ ,  $\text{Fe}_2\text{O}_3$ , and  $\text{SiO}_2$ . All samples were prepared in a vertical quench furnace, using a 0.1-mm Pt loop as a sample holder. The samples were run in air or  $\text{O}_2$  and then quenched in Hg or liquid  $\text{N}_2$ . Run durations ranged from 4–6 hr at 1425°C to 30 min at 1585°C. These run durations are suffi-

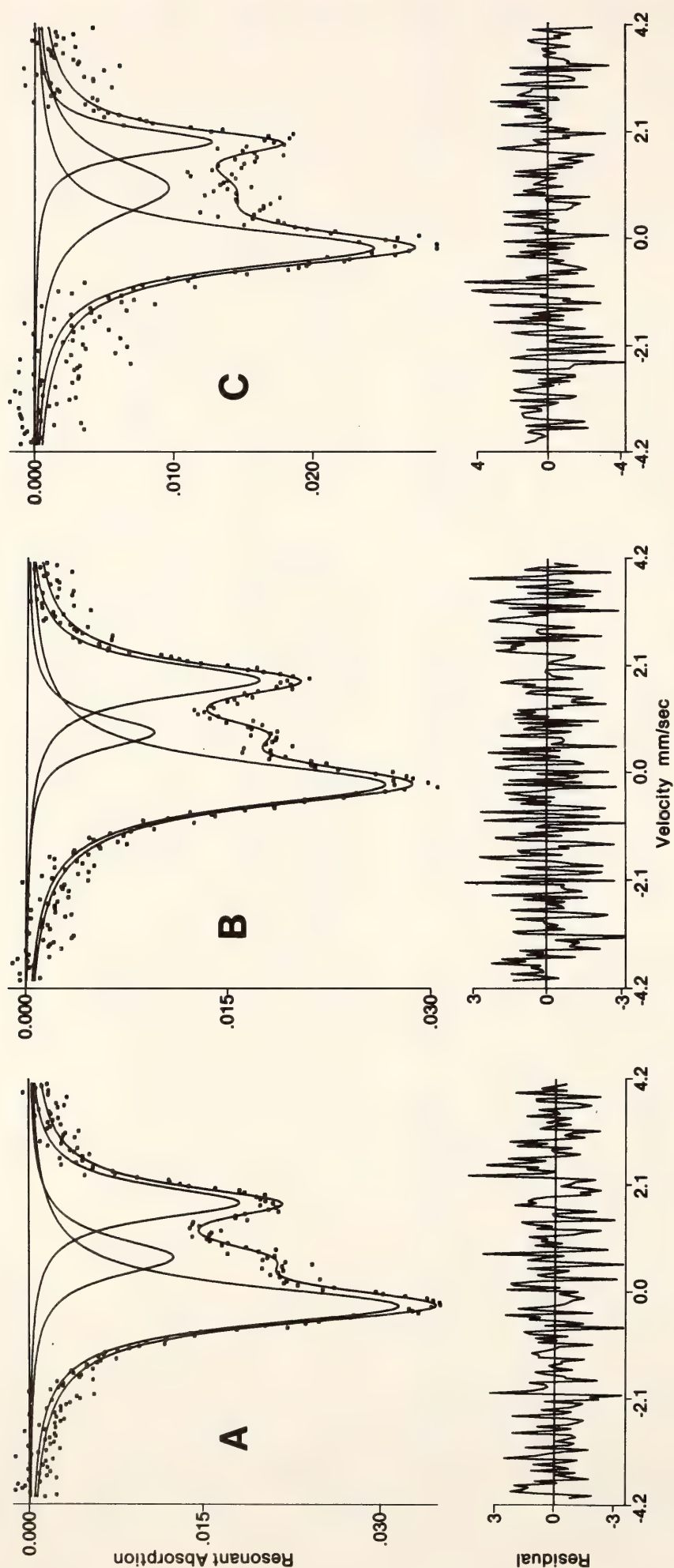


Fig. 39.  $^{57}\text{Fe}$  Mössbauer spectra of quenched melts on the join  $\text{CaSiO}_3\text{-MgSiO}_3$  with 5 mole %  $\text{FeSiO}_3$  component at  $1585^\circ\text{C}$  and 1 atm in air. (A)  $\text{CaSiO}_3$ ; (B)  $\text{CaMgSi}_2\text{O}_6$ ; (C)  $\text{MgSiO}_3$ .



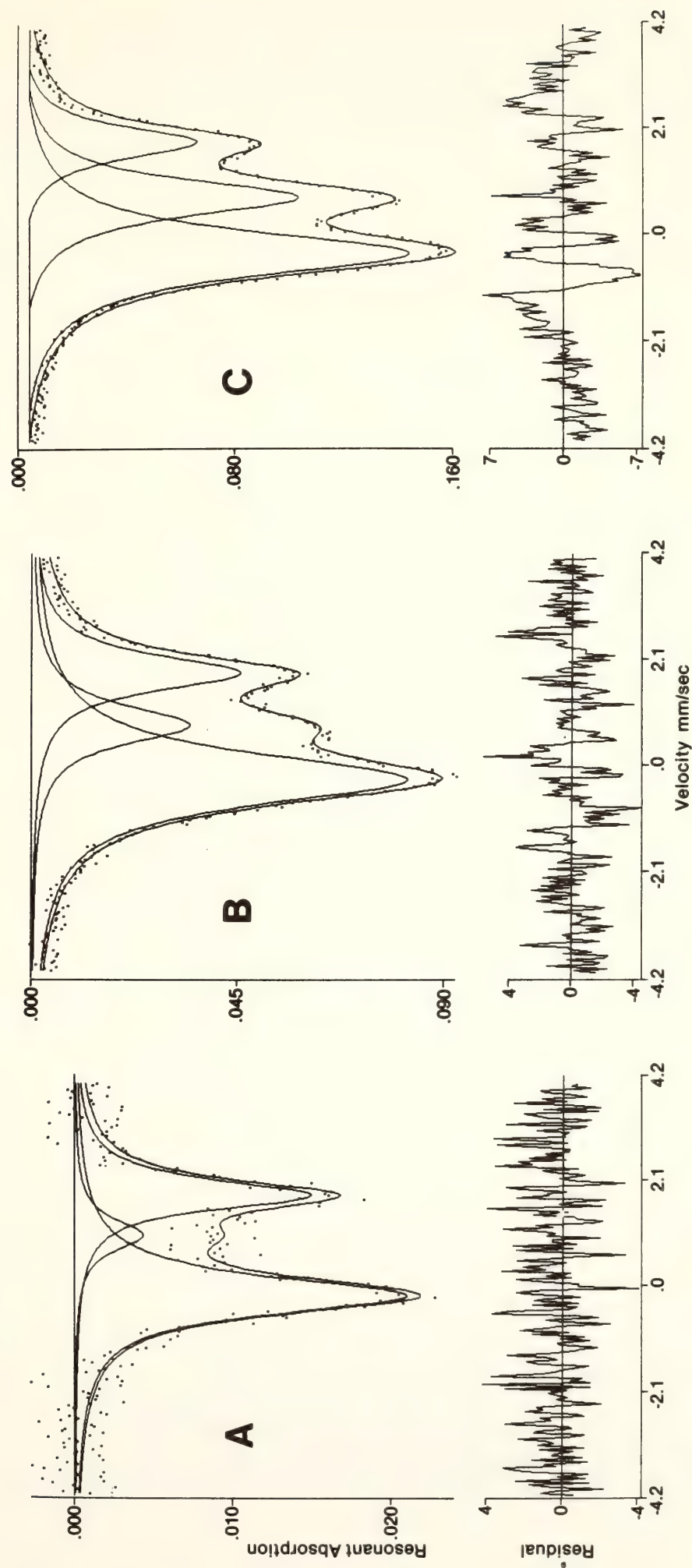


Fig. 40. <sup>57</sup>Fe Mössbauer spectra of quenched melts on the join CaMgSi<sub>2</sub>O<sub>6</sub>-FeSiO<sub>3</sub> at 1425°C and 1 atm in air. (A) 1 mole % FeSiO<sub>3</sub>; (B) 5 mole % FeSiO<sub>3</sub>; (C) 10 mole % FeSiO<sub>3</sub>.

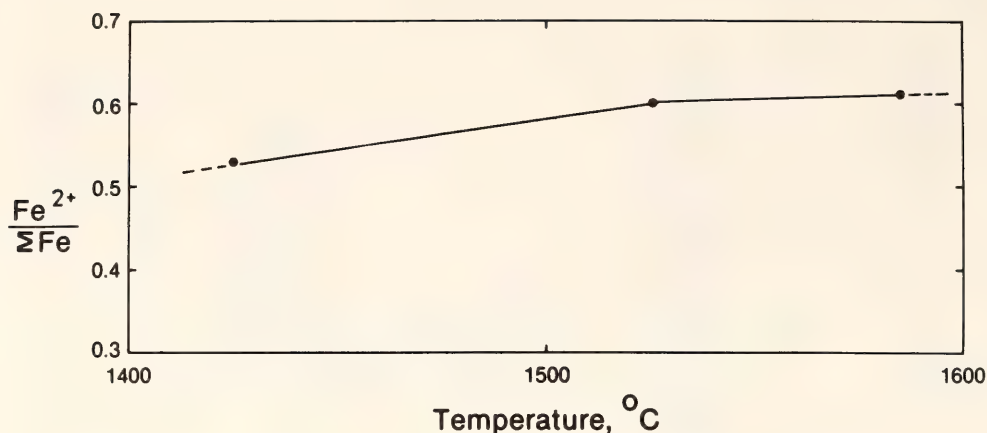


Fig. 41. Ferrous iron content of  $\text{CaMgSi}_2\text{O}_6 + 5$  mole %  $\text{FeSiO}_3$  as a function of temperature at 1 atm in air.

cient to attain equilibrium redox ratios in these melts (Mysen and Virgo, 1978).

Mössbauer spectroscopic techniques are identical with those described by Mysen and Virgo (1978) and Seifert, Virgo, and Mysen (this Report). Details about the fitting procedures are given by Seifert, Virgo, and Mysen (this Report).

Raman spectroscopy was conducted with small chips of quenched melt ( $0.5 \times 0.5 \times 1.0$  mm) using a Jobin-Yvon Raman spectrometer described by Sharma (*Year Book* 77, pp. 902–904). A  $\text{Kr}^+$  laser (excitation line 6471 Å) was used to excite Fe-bearing samples (green, or green to brown), and an  $\text{Ar}^+$  laser (excitation line 4880 Å) was used for the colorless samples. In both cases,  $90^\circ$  scattering geometry was employed.

### Results

The  $\text{Fe}^{2+}/\Sigma\text{Fe}$  of quenched melts near the join  $\text{CaSiO}_3$ - $\text{MgSiO}_3$  range between 0.35 and 0.82. The redox ratio increases with increasing Fs component at constant temperature,  $\text{Ca}/(\text{Ca} + \text{Mg})$ , and  $f_{\text{O}_2}$  (air); with increasing  $\text{Ca}/(\text{Ca} + \text{Mg})$  at constant temperature and Fs content; and with decreasing temperature at constant bulk composition and fixed amount of  $\text{FeSiO}_3$  component (Figs. 39–41; see Table 17). The  $\text{Fe}^{2+}/\Sigma\text{Fe}$  of

quenched melt of  $\text{CaMgSi}_2\text{O}_6$  composition with 5 mole % Fs component in solution quenched from  $1425^\circ\text{C}$  in air is near 0.5. This redox ratio contrasts with the  $\text{Fe}^{2+}/\Sigma\text{Fe}$  of  $\text{Na}_2\text{SiO}_3$  quenched melt with similar amounts of iron and at  $1400^\circ\text{C}$ , where  $\text{Fe}^{2+}$  was not detected (Seifert, Virgo, and Mysen, this Report). In fact, in the latter system the  $\text{Fe}^{2+}/\Sigma\text{Fe}$  remained constant over the range 6–100 mole %  $\text{NaFe}^{3+}\text{Si}_2\text{O}_6$  (Ac) component when quenched in air. An increase of the  $f_{\text{O}_2}$  from that of air to that of pure  $\text{O}_2$  does not change  $\text{Fe}^{2+}/\Sigma\text{Fe}$  appreciably. In the Mössbauer spectra of these samples, the isomer shift of ferric iron,  $\text{IS}_{\text{Fe}^{3+}}$ , is usually greater than 0.38 mm/sec, a value significantly higher than those found for quenched melts in systems such as  $\text{Na}_2\text{SiO}_3$ - $\text{NaFeSi}_2\text{O}_6$  and  $\text{NaAlSi}_2\text{O}_6$ - $\text{NaFeSi}_2\text{O}_6$ , where  $\text{IS}_{\text{Fe}^{3+}}$  generally is below 0.25 mm/sec (Mysen and Virgo, 1978; Seifert, Virgo, and Mysen, this Report). The  $\text{IS}_{\text{Fe}^{2+}}$  is near 1.00 mm/sec and does not vary significantly with bulk composition and temperature ( $1425^\circ$ – $1585^\circ\text{C}$ ) in any of these systems. The  $\text{IS}_{\text{Fe}^{2+}}$  is similar to that found in other quenched melts with  $\text{Fe}^{2+}$  in octahedral coordination (Mysen and Virgo, 1978; Seifert, Virgo, and Mysen, this Report).

The Raman spectra for the three samples on the join Wo-En are shown



TABLE 17. Mössbauer Spectroscopic Data (1 atm pressure, air)\*

Starting Composition	T, °C	QS(Fe <sup>2+</sup> ), mm/sec	IS(Fe <sup>2+</sup> ), mm/sec	QS(Fe <sup>3+</sup> ), mm/sec	IS(Fe <sup>3+</sup> ), mm/sec	Fe <sup>2+</sup> /ΣFe
CaMgSi <sub>2</sub> O <sub>6</sub> + 1 mole % FeSiO <sub>3</sub>	1425	1.918	1.014	...	...	0.82
CaMgSi <sub>2</sub> O <sub>6</sub> + 5 mole % FeSiO <sub>3</sub>	1425	2.083	0.966	1.077	0.376	0.53
CaMgSi <sub>2</sub> O <sub>6</sub> + 10 mole % FeSiO <sub>3</sub>	1425	2.214	0.921	1.114	0.372	0.36
CaMgSi <sub>2</sub> O <sub>6</sub> + 5 mole % FeSiO <sub>3</sub>	1525	2.048	0.984	1.060	0.312	0.61
CaMgSi <sub>2</sub> O <sub>6</sub> + 5 mole % FeSiO <sub>3</sub>	1585	2.046	1.024	1.024	0.335	0.60
MgSiO <sub>3</sub> + 5 mole % FeSiO <sub>3</sub>	1585	1.835	0.923	...	...	0.78
CaSiO <sub>3</sub> + 5 mole % FeSiO <sub>3</sub>	1585	2.044	0.961	0.965	0.422	0.51
CaSiO <sub>3</sub> + 10 mole % FeSiO <sub>3</sub>	1585	2.162	1.048	0.939	0.382	0.35

\* Symbols: QS(Fe<sup>2+</sup>), quadrupole splitting of Fe<sup>2+</sup>; IS(Fe<sup>2+</sup>), isomer shift of Fe<sup>2+</sup> relative to metallic Fe; QS(Fe<sup>3+</sup>), quadrupole splitting of Fe<sup>3+</sup>; IS(Fe<sup>3+</sup>), isomer shift of Fe<sup>3+</sup> relative to metallic Fe.

in Fig. 42. The high-frequency envelope (800–1100  $\text{cm}^{-1}$ ) consists of at least three Si-O stretch modes (870, 950, and 1050  $\text{cm}^{-1}$ ) where the resolution of the three bands increases with increasing CaO content of the glass. The other region of interest is the strong band at 640  $\text{cm}^{-1}$ .

Although the spectra indicate close local anionic structural similarity between quenched melts of Wo, Di, and En composition, intensity ratios of bands having wave numbers such as 650/870, 870/950, and 950/1050 may be used to discern different proportions of anionic constituents of the melts (Brawer and White, 1975, 1977; Furukawa *et al.*, 1978). Of these ratios, only that of wave numbers 870/950 shifts significantly with composition in that it increases with increasing Wo content of the glass (Fig. 42).

Etchepare (1972) ascribed bands near 870 and 1000  $\text{cm}^{-1}$  in quenched diopside melt to stretch vibrations of Si-O bands and the 650- $\text{cm}^{-1}$  band to deformations of the O-Si-O angle. This conclusion was

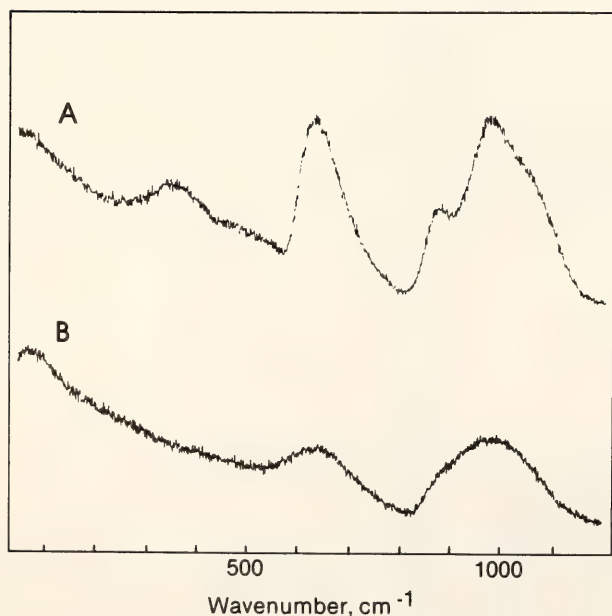
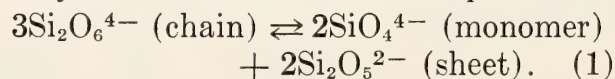


Fig. 42. Raman spectra of melts of (A)  $\text{CaSiO}_3$  and (B)  $\text{MgSiO}_3$  composition quenched from 1585°C at 1 atm in air (laser: 4880 Å  $\text{Ar}^+$ ; 200 mW). See Mysen, Virgo, and Scarfe (this Report) for the spectrum of quenched  $\text{CaMgSi}_2\text{O}_6$  melt.

based on a comparison of the Raman spectra of glassy and crystalline diopside. In a quenched melt of  $\text{Na}_2\text{SiO}_3$  composition Brawer and White (1975) ascribed the 870- $\text{cm}^{-1}$  band to Si-O stretch vibrations in isolated  $\text{SiO}_4^{4-}$  units. Furukawa *et al.* (1978) and Verweij and Konijnendijk (1976) also observed this band in quenched melt in the system  $\text{PbO-SiO}_2$  with  $\text{PbO} > \text{SiO}_2$  (molar). The authors also ascribed the 870- $\text{cm}^{-1}$  band to Si-O stretch vibrations in  $\text{SiO}_4$  monomers. The existence of a distinct band at 870–880  $\text{cm}^{-1}$  in quenched melts of alkaline earth metasilicate composition suggests that  $\text{SiO}_4$  monomers occur in these melts. The two high-frequency bands in the 800–1100  $\text{cm}^{-1}$  envelope arise from Si-O vibrations in tetrahedrally coordinated polymers with  $\text{NBO}/Z^* < 4$ . The band at 970–980  $\text{cm}^{-1}$  is characteristic of the stretch mode of NBO in a chain (Brawer and White, 1975, 1977; Furukawa and White, 1979). The band at about 1050  $\text{cm}^{-1}$  stems from Si-O stretch of bridging oxygen (BO) or that of a NBO in a sheet (Furukawa and White, 1979). Brawer and White (1975) calibrated the intensity ratio of wave numbers 970/1100 against  $\text{NBO}/Z$  of the interconnected network in the systems  $\text{Li}_2\text{O-SiO}_2$ ,  $\text{Na}_2\text{O-SiO}_2$ , and  $\text{K}_2\text{O-SiO}_2$ . In quenched melts of  $\text{CaSiO}_3$  composition  $\text{NBO}/Z \approx 1.2\text{--}1.4$  suggests that the interconnected network is more polymerized than  $(\text{Si}_2\text{O}_6^{4-})_n$  chains.

The Raman spectra, therefore, are consistent with the conclusion that in quenched melts on the join  $\text{CaSiO}_3\text{--MgSiO}_3$ , the  $(\text{Si}_2\text{O}_6^{4-})_n$  chains found in crystalline pyroxenes and pyroxenoids have been partially disproportionated into  $\text{SiO}_4^{4-}$  monomers and a complex of chains and sheets. The disproportionation to monomers, chains, and sheets may be illustrated with the expression



\* NBO denotes nonbridging oxygen; Z denotes all cations in tetrahedral coordination.



With  $NBO/Z \simeq 1.2-1.4$ , as observed in quenched melt of  $CaSiO_3$  composition, one solution for Equation 1 is that the quenched melt consists of approximately 50%  $SiO_4^{4-}$  monomers, 30% chains, and 20% sheets. The intensity ratio of wave numbers 880/980 decreases by about 20% between quenched melts of Wo and En composition. Consequently, the proportion of  $SiO_4^{4-}$  monomers decreases with increasing  $Mg/(Mg + Ca)$  of the melt. As a result, Equation 1 is shifted to the left.

### *Redox Equilibria*

The silicate polymers in quenched melts of  $Na_2SiO_3$  and metasilicates of alkaline earths appear similar when the Raman spectra in Fig. 42 are compared with those of Brawer and White (1975). Despite this similarity,  $Fe^{3+}$  in the quenched melts on the En-Wo join is in six-fold coordination, whereas  $Fe^{3+}$  is part of the network in sodium metasilicate-acmite melts. In fact, in all rock-forming silicate quenched melts where  $Na^+/Fe^{3+} \geq 1$ , ferric iron is in four-fold coordination (Mysen and Virgo, 1978; Seifert, Virgo, and Mysen, this Report). It is suggested that because of local charge-balance constraints,  $Ca^{2+}$  cannot charge-balance two  $Fe^{3+}$  in tetrahedral coordination. The ferric iron becomes a chain modifier instead. Although  $(Ca + Al) \rightleftharpoons Si$  substitution to form  $CaAl_2O_4$  complexes occurs in melts (Brawer and White, 1977; Virgo, Seifert, and Mysen, this Report), Brawer and White (1977) pointed out that the  $CaAl_2O_4$  complexes are less stable than  $NaAlO_2$  complexes.

Disproportionation reactions involving Equation 1 and  $Fe^{2+}$  and  $Fe^{3+}$  can be written. From equilibrium constants for such reactions it can be predicted that in quenched melts of alkaline earth metasilicates with increasing degree of disproportionation (Equation 1) at constant  $f_{O_2}$ ,  $Fe^{2+}/\Sigma Fe$  will decrease, in accordance with observations.

It was noted by Seifert, Virgo, and Mysen (this Report) that at fixed  $f_{O_2}$ ,  $Fe^{2+}/\Sigma Fe$  increases with increasing acmite component on the join  $Na_2SiO_3$ - $NaFeSi_2O_6$ . The acmite component is a more polymerized component than that of  $Na_2SiO_3$ . Because the activity coefficients of the components in this system remain constant in the mixing range,  $Fe^{2+}/\Sigma Fe$  must increase with increasing acmite component. Changes in the oxidation state of iron in systems with and without alkalis can also be understood by considering Equation 1. First, for a fixed  $Fe^{2+}/\Sigma Fe$  and constant  $f_{O_2}$ , a quenched melt with alkali metals as modifier will be more disproportioned (the proportion of  $SiO_4^{4-}$  is greater) than with alkaline quenched melt. Second, with a constant degree of disproportionation and  $f_{O_2}$ , a quenched melt with  $Fe^{3+}$  in six-coordination will be more reduced than one with  $Fe^{3+}$  in tetrahedral coordination, in accord with observation. Third, the dependence of  $Fe^{2+}/\Sigma Fe$  on  $f_{O_2}$  is similar for a fixed degree of disproportionation.

Riebling (1968) and Sharma *et al.* (Year Book 77, pp. 649-652) showed that the local anionic structures of silicate melts and their quenched analogues are similar. Because the results in this report were obtained on quenched melts, it is likely that the present data are also applicable to rock-forming silicate melts.

It is clear from the above summary that changes of extensive and intensive variables affect physical and chemical properties of iron-bearing, rock-forming silicate melts because of the complex structural role of iron in the melts. Acidic melts such as andesite, dacite, and granite (rhyolite) will have a large excess of  $M^+$  over  $M^{2+}$  melt modifiers. As a result, variations of redox ratios of iron will alter the degree of polymerization of the melt and, therefore, the viscosity and cation diffusion coefficients of the melt. It is expected, for example, that increasing  $f_{O_2}$  will result in increasing viscosity of the melt. Cation diffusion

coefficients in acidic, iron-bearing melt will most likely decrease with increasing oxygen fugacity. The experimental data indicate that the activity coefficients of the  $\text{Fe}^{3+}$  and  $\text{Fe}^{2+}$  complexes do not change with oxygen fugacity. As a result, partition coefficients of ferrous and ferric iron between acidic melts and minerals in equilibrium with the melt will not be affected by the oxygen fugacity.

Physical properties of basaltic melts will be affected less by changing redox ratio of iron than acidic melts because alteration of redox states results in smaller changes of NBO/BO. As a result of fractional crystallization of a basaltic melt to more acidic compositions, however, the physical properties of the magma will change gradually as the influence of redox ratios of iron on the degree of polymerization of the melt increases with increasing  $\text{M}^+/\text{M}^{2+}$ .

STRUCTURAL STUDY OF GLASSES OF  
AKERMANITE, DIOPSIDE, AND SODIUM  
MELILITE COMPOSITIONS BY  
RAMAN SPECTROSCOPY

*S. K. Sharma and H. S. Yoder, Jr.*

The melilites are major constituents of basic alkaline igneous rocks such as melilite nephelinite, olivine melilitite, and katungite; some hydrous rocks such as alnoite, turjaite, and venanzite; and some contact metamorphic rocks (Yoder, 1973). Most experimental studies have been carried out to understand the phase relations in akermanite-diopside and related melilite-bearing assemblages; however, little is known about the structure of their melts. Pisárčík *et al.* (1976) have studied the infrared spectra of the akermanite-diopside system and have proposed the presence of "shorter ( $n < 2$ ) chains of  $\text{SiO}_4$  tetrahedrons." Etchepare (1972) studied the Raman spectra of diopside glass and crystal and has suggested that the structure of diopside glass closely resembles that of diopside crystals. Sharma, Virgo, and Mysen

(1979) have reported, however, that the Raman spectrum of diopside glass shows bands in the Si-O stretching regions in addition to those reported by Etchepare (1972). A new study was undertaken, therefore, in an attempt to resolve the reported discrepancies. The structures of glasses and crystals of akermanite (Ak) ( $\text{Ca}_2\text{MgSi}_2\text{O}_7$ ) and sodium melilite (Sm) ( $\text{NaCaAlSi}_2\text{O}_6$ ) and glasses of  $\text{Di}_{50}\text{Ak}_{50}$  (mole %) and diopside (Di) ( $\text{CaMgSi}_2\text{O}_6$ ) obtained by Raman spectroscopy are reported herein.

*Sample Preparation, Apparatus,  
and Spectra*

Glasses of  $\text{Ca}_2\text{MgSi}_2\text{O}_7$  and  $\text{NaCaAlSi}_2\text{O}_6$  were made by the late Dr. J. F. Schairer. The glasses of compositions Di and  $\text{Ca}_{1.5}\text{MgSi}_2\text{O}_{6.5}$  ( $\text{Di}_{50}\text{Ak}_{50}$ , mole %) were prepared using the appropriate oxides and carbonates of high purity. The mixtures were run for several hours at  $1450^\circ\text{C}$  and subsequently quenched in Hg. The crystalline sample of akermanite was prepared at 1 atm by the Czochralski method at the Oak Ridge National Laboratory (Finch *et al.*, 1974), and crystalline sodium melilite was prepared from glass at  $1150^\circ\text{C}$  and 10 kbar (Yoder, 1973).

The Raman spectra were recorded with a Jobin-Yvon optical system Ramanor (HG.2S) Raman spectrometer (for details see Sharma, *Year Book* 77, pp. 902–904). The sample was excited with the 488.0-nm blue line of an  $\text{Ar}^+$  ion laser with laser power of  $\sim 300$  mW at the sample and  $90^\circ$  scattering geometry.

The Raman spectra of crystalline Ak and glass of Ak composition are shown in Fig. 43. The Raman spectra of glasses of Di,  $\text{Di}_{50}\text{Ak}_{50}$  (mole %), and Ak are depicted in Fig. 44. Figure 45 shows the Raman spectra of crystalline Sm and glass of Sm composition. The frequencies of Raman bands and their observed spectral characteristics are summarized in Table 18.



TABLE 18. Raman Frequencies,\* cm<sup>-1</sup>

Ca <sub>2</sub> MgSi <sub>2</sub> O <sub>7</sub> (Ak) Crystalline	CaNaAlSi <sub>2</sub> O <sub>7</sub> (Sm) Crystalline	Tentative Assignment†	Ak Glass	Di <sub>60</sub> Ak <sub>50</sub> Glass	CaMgSi <sub>2</sub> O <sub>6</sub> (Di) Glass	Sm Glass	Approximate Description of Bands in Glasses‡
...	76w‡	{ lattice modes τ(SiO <sub>3</sub> ) + ν(NaO <sub>3</sub> ) τ(SiO <sub>3</sub> ) ν <sub>s</sub> (Ca-O) δ(SiO <sub>3</sub> )	...	...	...	66s,bd	{ Disorder induced phonon density of states ν <sub>s</sub> (Ca-O) + τ(SiO <sub>4</sub> <sup>4-</sup> ) ...
91w	...		90s,bd	...	...	...	
...	144vw,bd		...	...	92s,bd	...	
208w	221(sh)		...	...	...	...	
...	248m		...	...	...	...	
308w	306m	{ ν <sub>s</sub> (Al-O-Si) ν <sub>s</sub> (Mg <sup>IV</sup> -O) ν <sub>s</sub> [Si-O-Si(Al)] ν <sub>s</sub> (Si-O-Si) ν <sub>s</sub> (Al <sup>IV</sup> -O)	...	...	...	...	{ ν <sub>s</sub> (Mg <sup>IV</sup> -O) + δ(SiO <sub>4</sub> <sup>4-</sup> ) ν <sub>s</sub> [Si-O-Si(Al)] network¶ ν <sub>s</sub> (Mg <sup>IV</sup> -O) ν <sub>s</sub> [Si-O-Si(Al)] modes of (AlSi <sub>2</sub> O <sub>7</sub> <sup>3-</sup> ) groups ν <sub>s</sub> (Si-O-Si) ...
350w(sh)	412vw,bd		358w,bd,p	~352w,bd,p	~340vw,bd,p	...	
447w	...		...	...	...	...	
477w,bd	460w		...	...	...	...	
...	485w		...	...	...	...	
...	512vw	{ ν <sub>s</sub> (Al-O-Si) ν <sub>s</sub> (Mg <sup>IV</sup> -O) ν <sub>s</sub> [Si-O-Si(Al)] ν <sub>s</sub> (Si-O-Si) ν <sub>s</sub> (Al <sup>IV</sup> -O)	...	478vw,(sh)	~490vw,bd	...	{ ν <sub>s</sub> (Mg <sup>IV</sup> -O) ν <sub>s</sub> [Si-O-Si(Al)] network¶ ν <sub>s</sub> (Mg <sup>IV</sup> -O) ν <sub>s</sub> [Si-O-Si(Al)] modes of (AlSi <sub>2</sub> O <sub>7</sub> <sup>3-</sup> ) groups ν <sub>s</sub> (Si-O-Si) ...
...	539m		~533w,bd,p	...	...	490s,bd,p	
598w	...		...	...	...	...	
...	648s		...	...	...	562(sh),p	
661m	...		683m,p	650m,p	638m,p	648(sh),p	
...	665(sh)	{ ν <sub>s</sub> (Al-O-Si) ν <sub>s</sub> [Si(Al)-O <sup>-</sup> ] mode of (AlSi <sub>2</sub> O <sub>7</sub> <sup>3-</sup> ) ν <sub>s</sub> (Si-O <sup>-</sup> ) mode of (Si <sub>2</sub> O <sub>7</sub> <sup>6-</sup> ) ν <sub>s</sub> [Si(Al)-O <sup>-</sup> ] mode of (AlSi <sub>2</sub> O <sub>7</sub> <sup>3-</sup> )	...	...	...	...	{ ν <sub>s</sub> (Si-O <sup>-</sup> ) mode of (Si <sub>2</sub> O <sub>7</sub> <sup>6-</sup> ) ν <sub>s</sub> (Si-O <sup>-</sup> ) mode of (Si <sub>2</sub> O <sub>6</sub> ) <sub>n</sub> ν <sub>s</sub> [Si(Al)-O <sup>-</sup> ] network¶ ν <sub>s</sub> (Si-O <sup>-</sup> ) modes of higher polymers¶ ...
...	724(sh),m		...	...	...	...	
...	...		~858(sh),p	~872(sh),p	~885(sh),p	...	
...	894(sh),vw		...	...	...	...	
904s	...		914s,p	...	...	...	
...	930m	{ ν <sub>as</sub> (O-Si-O)	...	968s,p	980s,p	...	{ ν <sub>as</sub> (Si-O <sup>-</sup> ) mode of (Si <sub>2</sub> O <sub>6</sub> ) <sub>n</sub> ν <sub>s</sub> [Si(Al)-O <sup>-</sup> ] network¶ ν <sub>s</sub> (Si-O <sup>-</sup> ) modes of higher polymers¶ ...
986w	972(sh)		...	...	...	980m,p	
1023vw	1023m		...	...	~1008(sh),p	...	
...	...		...	...	...	...	
1067vw	...		...	...	...	...	

\* Measurement accuracy: in the spectra of crystalline material, ± 2 cm<sup>-1</sup>; in the spectra of glasses, ± 4 cm<sup>-1</sup> for sharp and strong bands and ± 10 cm<sup>-1</sup> for broad and weak bands.

† ν<sub>as</sub>, symmetric stretch; ν<sub>as</sub>, asymmetric stretch; δ, deformation; τ, torsional modes.

‡ Abbreviations: w, weak; s, strong; bd, broad; p, polarized; dp, depolarized; sh, shoulder.

§ The spectral region in glasses where strong Rayleigh tail was observed owing to disorder-induced phonon density of states.

|| Observed in oriented single crystal of Ak (Sharma, unpublished data).

¶ See text.

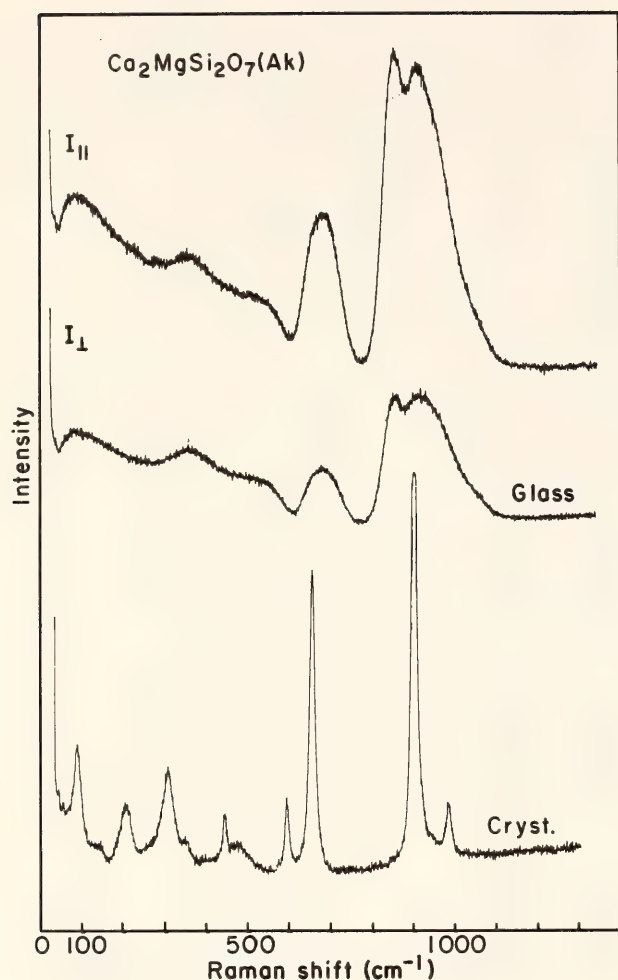


Fig. 43. Raman spectra of crystalline  $\text{Ca}_2\text{MgSi}_2\text{O}_7$  (Ak) and of glass of  $\text{Ca}_2\text{MgSi}_2\text{O}_7$  (Ak) composition.  $I_{||}$  and  $I_{\perp}$  on the glass spectra, respectively, refer to measurements with the electric vector of scattered light parallel to and perpendicular to the electric vector of the exciting laser beam (slit  $8\text{ cm}^{-1}$ , laser  $488.0\text{ nm}$ ,  $300\text{ mW}$  at the sample).

### Discussion

*Crystalline Ak and Sm.* In the Raman spectra of powdered crystalline Ak only 12 bands of 45 predicted Raman active modes are detected. The absence of other expected bands in the Raman spectra of powdered Ak crystals may be attributed to accidental degeneracy of modes, low intensities, or both.

The crystal structure of synthetic sodium melilite, a portion of the sample used in the present work, was determined by Louisnathan (1970) and was found to be isostructural with naturally occurring melilites. In addition, Louisnathan

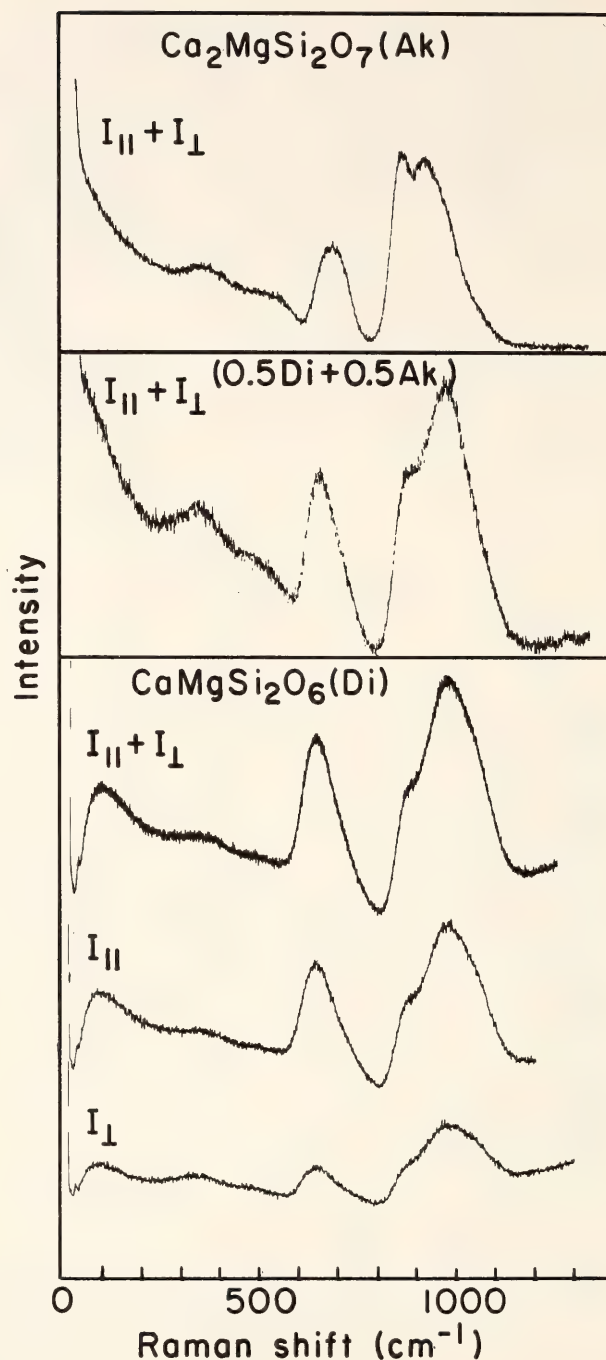


Fig. 44. Raman spectra of glasses of diopside, 0.5 diopside–0.5 akermanite (mole %), and akermanite compositions. ( $I_{||}$  and  $I_{\perp}$  refer to polarized spectra, whereas  $I_{||} + I_{\perp}$  refers to unpolarized spectrum (slit  $10\text{ cm}^{-1}$ , laser  $488.0\text{ nm}$ ,  $300\text{ mW}$  at the sample).)

suggested that Al and Si, which are four-fold coordinated, are ordered, whereas Ca and Na, in eight-fold coordination, are disordered. If distinctions between Ca and Na in the Sm crystal are ignored, the optic modes of vibration will have the same activities as in the Ak crystals.



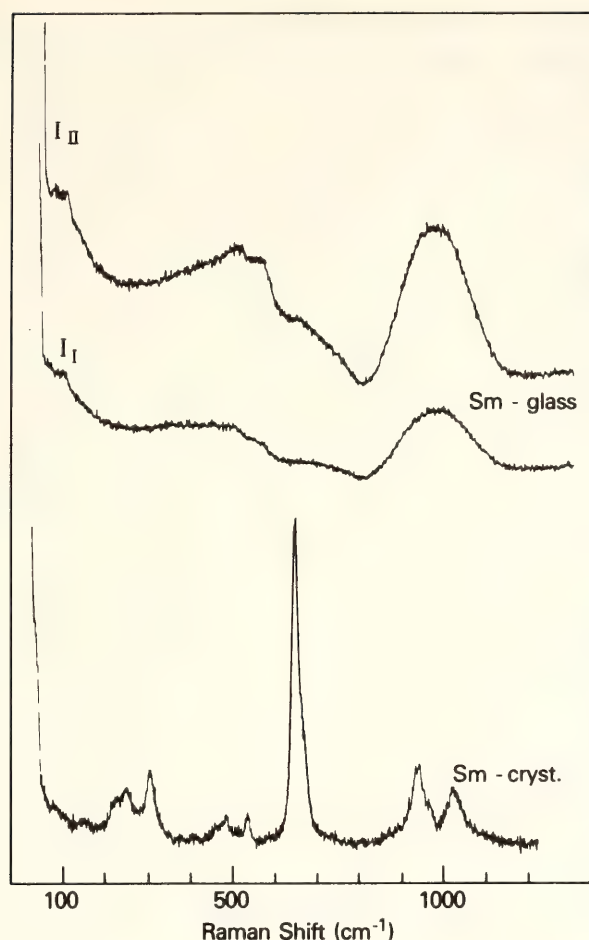


Fig. 45. Raman spectra of crystalline  $\text{NaCaAlSi}_2\text{O}_7$  (Sm) and of glass of  $\text{NaCaAlSi}_2\text{O}_7$  composition. (For notations and experimental conditions, refer to Fig. 43.)

Because Ca and Na have atomic weights that differ significantly, more than 45 Raman active modes would be expected in the spectrum of crystalline Sm, whereas only 17 bands are observed. The Ca-Na disorder and the strong ionic character of metal-oxygen bonds are expected to result in low intensity for some of the bands corresponding to  $\text{CaO}_8$  and  $\text{NaO}_8$  polyhedra. It is not possible at present to make definite assignments of all the bands in the Raman spectra of polycrystalline Ak and Sm; however, tentative assignment of the bands can be made by comparison with the spectra of other pyrosilicates. Lazarev (1972) calculated the vibrational frequencies of the  $(\text{Si}_2\text{O}_7)^{6-}$  anion with different Si-O-Si angles. Tarte *et al.* (1973) studied the infrared and Raman spectra of pyro-

silicate and germanate containing linear  $(\text{X}_2\text{O}_7)^{6-}$  anions. By comparing the present data with the data of Lazarev (1972) and Tarte *et al.* (1973), tentative assignment of the various Raman bands is made (see Table 18).

Comparison of the spectra of Ak and Sm powders (Figs. 43 and 45; Table 18) in the region of the Si(Al)-O stretching mode ( $900\text{--}1200\text{ cm}^{-1}$ ) reveals that in the spectrum of crystalline Sm, bands are relatively weaker in intensity than the corresponding bands in the spectrum of crystalline Ak. The weak intensity of the bands in the spectrum of crystalline Sm probably indicates the possibility of some disorder at Si and Al sites and strong coupling between  $\text{AlO}_4$  and  $\text{Si}_2\text{O}_7$  groups in the Sm crystal. Louisnathan (1972) has also suggested that one should consider  $(\text{AlSi}_2\text{O}_7)^{3-}$  rather than  $(\text{Si}_2\text{O}_7)^{6-}$  groups in the Sm crystals, but ruled out the possibility of disorder at the Si site. The possibility of disorder at the Si site in the Sm crystal will be explored further with infrared spectroscopy. The shoulder at  $655\text{ cm}^{-1}$  and very weak bands at  $\sim 724\text{ cm}^{-1}$  in the Sm spectra (see Table 18) do not have their counterparts in the spectrum of crystalline Ak or hardystonite ( $\text{Ca}_2\text{ZnSi}_2\text{O}_7$ ) (Sharma, unpublished data). In the spectrum of crystalline gehlenite ( $\text{Ca}_2\text{Al}_2\text{SiO}_7$ ) a shoulder of medium intensity is observed at  $655\text{ cm}^{-1}$  (Sharma, unpublished data). The bands at  $665$  and  $\sim 724\text{ cm}^{-1}$  are therefore assigned to the vibration of  $\text{AlO}_4$  tetrahedra. The  $\text{CaO}_8$  and  $\text{NaO}_8$  polyhedra, respectively, give rise to metal-oxygen stretching modes at  $\sim 380$  and  $\sim 270\text{ cm}^{-1}$  (Stern, 1974). The rocking and torsional modes of  $\text{Si(Al)O}_3$  terminal groups also appear in the region  $300\text{--}500\text{ cm}^{-1}$ . In the low-frequency region ( $50\text{--}500\text{ cm}^{-1}$ ) considerable mixing of lattice modes and the deformation and torsional modes of silicate anions may take place.

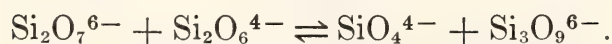
*Glasses of Ak,  $\text{Di}_{50}\text{Ak}_{50}$ , and Di compositions.* The positions and intensities of the Raman bands in the spectrum of

glass of Ak are closely related to the positions and intensities of most prominent bands observed in the spectrum of crystalline akermanite (Fig. 43; Table 18). There is, however, a strong, polarized shoulder at  $\sim 858\text{ cm}^{-1}$  in the Ak-glass spectrum, and the bands in the glass spectrum are much broader than their counterparts in the spectrum of the Ak crystal. The broadening of the Raman bands and the presence of a strong Rayleigh tail in the spectrum of the glass are the direct result of the breakdown of  $k = 0$  (where  $k$  is the wave-vector) selection rule due to disorder.

The close resemblance in the positions and relative intensities of the strong Raman bands in the spectrum of glass of Ak composition with their counterparts in the spectrum of the Ak crystal indicates that the major species in glass of Ak composition are  $\text{Si}_2\text{O}_7^{6-}$  anions, and the structure of glass resembles to a large extent that of crystalline Ak. Because the symmetrical stretching mode of  $\text{SiO}_4^{4-}$  appears at low frequency, the presence of the  $858\text{-cm}^{-1}$  band in the spectrum of glass of Ak composition indicates the presence of  $\text{SiO}_4^{4-}$  groups in the glass. It seems that some of the  $\text{Si}_2\text{O}_7^{6-}$  groups on melting of Ak crystals break down according to the following equation:



similarly,



The higher polymeric species,  $\text{Si}_2\text{O}_6^{4-}$  and  $\text{Si}_3\text{O}_9^{6-}$ , contributing to the broad asymmetric envelope at about  $914\text{ cm}^{-1}$ , cannot be resolved.

The  $\text{SiO}_4^{4-}$  groups are expected to be randomly oriented in the Ak glass and may be present at a site of lower symmetry than tetrahedral (Td) symmetry. The  $E(\nu_2)$  and  $F_2(\nu_4)$  modes of  $\text{SiO}_4^{4-}$ , which appear at  $340$  and  $527\text{ cm}^{-1}$ , respectively, in the isolated monomer, will become nondegenerate in the Ak glass, and may be contributing partially to the

bands at  $\sim 358$  and  $533\text{ cm}^{-1}$  (Tarte, 1965). The presence of the  $\text{SiO}_4^{4-}$  monomer and higher polymer species other than  $\text{Si}_2\text{O}_7^{6-}$  in the Ak glass is also confirmed by the gas chromatographic study of trimethylsilyl derivatives obtained from the Ak glass (Sharma, Hoering, and Yoder, this Report).

The observed higher density ( $d = 2.955$ ) and higher index of refraction ( $n = 1.641$ ) of the Ak glass compared with the Ak crystal ( $\rho = 2.944$ ,  $\omega = 1.632$ ,  $\epsilon = 1.639$ ; Yoder, 1973) can be explained in part as due to the presence of  $\text{SiO}_4^{4-}$  groups in the Ak glass.

The approximate descriptions of the nature of vibrations that give rise to Raman bands in the spectrum of glass of different compositions are given in Table 18. The assignments are made by comparing the glass spectrum with the spectrum of the corresponding crystal and by keeping in view the strong and polarized bands belonging to symmetrical stretching modes in the spectra of glasses.

Addition of diopside to akermanite melt results in shifting the  $\nu_s(\text{Si-O}^-)$  stretching band toward higher frequency (Table 18), and the intensity of the shoulder attributed to the  $\text{SiO}_4^{4-}$  group decreases (Fig. 44). The  $\nu_s(\text{Si-O-Si})$  band shifts toward lower frequencies and appears at  $650\text{ cm}^{-1}$  in the spectrum of the  $\text{Di}_{50}\text{Ak}_{50}$  (mole %) glass and at  $638\text{ cm}^{-1}$  in the spectrum of the glass of diopside composition. The similar behavior of the  $\nu(\text{Si-O}^-)$  and  $\nu(\text{Si-O-Si})$  stretching modes is observed on comparing the spectrum of sodium metasilicate glass to that of sodium trisilicate glass. Thus, in the melt formed from  $\text{Di}_{50}\text{Ak}_{50}$  the degree of polymerization of the silicate network increases relative to that of Ak melt. The presence of a weak shoulder at  $\sim 885\text{ cm}^{-1}$  in the glass of Di composition is significant and indicates the presence of at least some  $\text{SiO}_4^{4-}$  groups in the glass network. Because other major silicate bands in the glass of Di composition closely resemble in position and relative intensity their counter-



parts in the spectrum of crystalline Di, it can be concluded that the diopside glass does have  $(\text{Si}_2\text{O}_6)_n^{4-}$  pyroxene chains as a major species. The presence of a shoulder at  $\sim 1008\text{ cm}^{-1}$  probably indicates the presence of a small concentration of more complex polymerized species such as  $\text{Si}_2\text{O}_5^{2-}$  and  $\text{Si}_3\text{O}_9^{6-}$ .

Another important question is the coordination of Mg in the glasses of Ak and Di composition. By comparing the molar refraction and density of akermanite and diopside crystals, respectively, with the glasses of Ak and Di composition, Roy (1950) concluded that Mg is four-fold coordinated in glasses of both Ak and Di composition. In the case of glass of Ak composition the close resemblance of the major features of the Raman spectra of the glassy and crystalline phases suggests that in the glass most  $\text{Mg}^{2+}$  ions are present in four-fold coordination.

If all  $\text{Mg}^{2+}$  ions are present in four-fold coordination in glass of Di composition, the  $\text{Ca}^{2+}$  ion compensates the charge and will be present in the cavities of a three-dimensional network formed by  $[\text{CaMgO}_4]$  and  $\text{SiO}_4$  shared tetrahedra. If this is the case, the Raman spectrum of the glass of  $\text{CaMgSi}_2\text{O}_6$  composition will be expected to resemble that of  $\text{SiO}_2$  glass or the glass of jadeite composition (Sharma, Virgo, and Mysen, *Year Book* 77, p. 658), which has a three-dimensional network structure. The glasses having a three-dimensional silicate network structure give characteristic spectra that are composed of a strong polarized band in the region  $400\text{--}500\text{ cm}^{-1}$  accompanied by broad and weak bands in the region  $900\text{--}1200\text{ cm}^{-1}$  due to the Si-O (bridging) stretching mode. Because the Raman spectrum of glass of Di composition does not show the features of a three-dimensional silicate network, it may be concluded that most of the  $\text{Mg}^{2+}$  is in six-fold coordination in the glass. The above conclusion is also supported by the fact that the band at  $\sim 533\text{ cm}^{-1}$ , attributed partially to

$\text{MgO}_4$  tetrahedra in glass of Ak composition, appears at  $\sim 490\text{ cm}^{-1}$  in the spectrum of the Di glass. The decrease in the frequency of this mode can be attributed to the increase in the coordination of Mg from four-fold to six-fold in the glass of Di composition. The present study, however, does not rule out the possibility of a few percent of Mg present in four-fold coordination in the Di glass.

In the glass having  $\text{Di}_{50}\text{Ak}_{50}$  composition, the coordination of  $\text{Mg}^{2+}$  ions is less clear. It is possible that in this glass  $\text{Mg}^{2+}$  ions are present in four-, five-, and six-fold coordinations, as indicated by the presence of a very weak and broad band, attributed to  $\nu_s(\text{Mg-O})$ , at  $\sim 478\text{ cm}^{-1}$  (Table 18).

*Glass of Sm composition.* The Raman spectrum of glass of Sm composition (Fig. 45) does not resemble the spectrum of crystalline Sm. The strong bands at  $490$  and  $980\text{ cm}^{-1}$  are characteristic of a three-dimensional network having less than one nonbridging oxygen per silica. In fact the spectrum of Sm glass closely resembles that of glass of sodium trisilicate composition except that bands in the Si-O stretching region are broad and at lower frequency. Sharma *et al.* (*Year Book* 77, pp. 652–658) pointed out that the substitution of  $\text{Na}^+\text{Al}^{3+}$  for  $\text{Si}^{4+}$  in a three-dimensional network results in a lowering of the frequency of the Si-O stretching mode. It seems that in glass of Sm composition,  $\text{Al}^{3+}$  is four-fold coordinated and Na ions are present in cavities. The  $(\text{NaAlSi}_2\text{O}_7)$  groups form a three-dimensional network in that there are nonbridging oxygens to balance the electric charge on the  $\text{Ca}^{2+}$  ion. The presence of a small concentration of  $(\text{AlSi}_2\text{O}_7)^{3-}$  sheets in this network is indicated by the presence of a shoulder at  $\sim 648\text{ cm}^{-1}$  that appears at the position of the strongest Raman peak in the spectrum of crystalline Sm.

From the present work it may be concluded that the structures of the glasses of Ak and Di composition resemble those of the crystalline Ak and Di. In addition,

both glasses have monomeric  $\text{SiO}_4^{4-}$  and other higher polymeric species that are not found in their crystals. Most of the  $\text{Mg}^{2+}$  ions in the glass of Ak composition are present in four-fold coordination, whereas most of the  $\text{Mg}^{2+}$  ions in the glass of Di composition are present in six-fold coordination. The glass of Sm composition has a three-dimensional network with  $\sim 0.33$   $\text{O}^-$  ion per network-forming cation  $\text{Si}(\text{Al})$ . The  $\text{Al}^{3+}$  acts as a network former, and most of the  $\text{Na}^+$  is present in the cavities to balance the charge. Also a very small concentration of  $(\text{AlSi}_2\text{O}_7)^{3-}$  groups that are constituents of the Sm crystal is in the network structure of the glass of Sm composition.

STRUCTURE AND SOLUBILITY OF CARBON  
DIOXIDE IN SILICATE GLASSES OF  
DIOPSIDE AND SODIUM MELILITE  
COMPOSITIONS AT HIGH PRESSURES  
FROM RAMAN SPECTROSCOPIC DATA

*S. K. Sharma*

Raman spectroscopy has been used to characterize  $\text{CO}_2$ -charged glasses of diopside (Di) and sodium melilite (Sm) compositions, prepared by quenching  $\text{CO}_2$ -saturated silicate melts of Di and Sm compositions under various  $P$ - $T$  conditions. Verweij *et al.* (1977, 1978) employed Raman spectroscopy to study the types of carbon species present in the  $\text{K}_2\text{CO}_3$ - $\text{SiO}_2$  glass-forming system. In this study  $\text{CO}_2$ -charged glasses of Di and Sm compositions were selected because these glasses have different structures, Sm glass being more polymerized than Di glass (Sharma and Yoder, this Report), and because the spectral characteristics of these glasses are known. By analyzing the Raman spectra of  $\text{CO}_2$ -charged glasses of Di and Sm compositions, information is obtained about the existing carbon species, the pressure and temperature dependence of the relative concentration of carbon species, and the

effect of dissolving carbon dioxide on the glass structure.

*Experimental*

The  $\text{CO}_2$ -charged glasses were prepared by using a finely ground mixture of high-purity oxides and carbonates. For Di glasses  $\sim 10$ -mg amounts of prepared mixtures of  $\text{CaCO}_3 \cdot \text{MgO} \cdot 2\text{SiO}_2$  compositions were loaded in Pt capsules and sealed by welding. All experiments were conducted in solid-media, high-pressure apparatus (Boyd and England, 1960), using the piston-out technique. The melts were equilibrated for 5 min under various  $P$ - $T$  conditions before quenching. Similarly, the  $\text{CO}_2$ -charged Sm glasses were prepared by using a mixture of  $2\text{CaCO}_3 \cdot \text{Na}_2\text{CO}_3 \cdot \text{Al}_2\text{O}_3 \cdot 4\text{SiO}_2$  equivalent to  $(2\text{CaNaAlSi}_2\text{O}_7 + 3\text{CO}_2)$ .

The Raman spectra were recorded with a Jobin-Yvon double monochromator. The samples were excited with the 488.0-nm line of an  $\text{Ar}^+$  ion laser using a laser power of 300–400 mW at the sample and  $90^\circ$  scattering geometry. The polarization character of the Raman bands was obtained by recording separately the components of scattered radiation, which had the electric vector, respectively, parallel to and perpendicular to the electric vector of the exciting laser beam (for details see Sharma, *Year Book* 77, pp. 902–904).

*Results*

Typical Raman spectra of  $\text{CO}_2$ -charged Di glasses quenched from a liquid of  $(\text{CaMgSi}_2\text{O}_6 \cdot \text{CO}_2)$  composition under different pressures are shown in Fig. 46. The Raman spectra of a glass of Sm composition and of  $\text{CO}_2$ -charged Sm glasses quenched from a liquid of  $\text{CaNaAlSi}_2\text{O}_7 \cdot 1.5\text{CO}_2$  composition under 10 and 20 kbar pressure at  $1460^\circ\text{C}$  are presented in Fig. 47. The characteristics of the Raman bands in the spectra of all the analyzed glasses of Di and  $\text{CO}_2$ -charged Di compositions, and glasses of



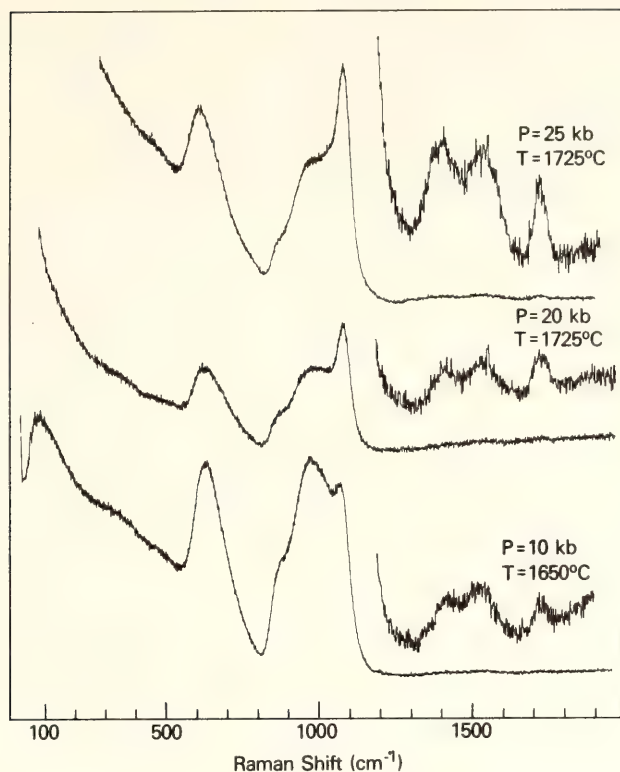


Fig. 46. Raman spectra of  $\text{CO}_2$ -charged diopside glasses, prepared by quenching melts of  $\text{CaCO}_3\cdot\text{MgO}\cdot 2\text{SiO}_2$  compositions at different pressures and temperatures. The Raman spectra in the range  $1200\text{--}1800\text{ cm}^{-1}$  were recorded with a sensitivity of  $\times 20$  for the 10-kbar glass and  $\times 22$  for the 20- and 25-kbar glasses.

Sm and  $\text{CO}_2$ -charged Sm compositions, respectively, are given in Tables 19 and 20. In some  $\text{CO}_2$ -charged glass samples that were either very small ( $<1\text{ mm}^3$ ) or highly strained, it was not possible to measure the polarization characteristics of the bands. Because of high fluorescence background at frequencies greater than in the  $1200\text{-cm}^{-1}$  region, it was difficult to record the spectra of these samples in the region  $1200\text{--}1800\text{ cm}^{-1}$ .

A strong additional band appears at  $1075 \pm 5\text{ cm}^{-1}$  and overlaps with the Si-O stretching band in the spectra of both the  $\text{CO}_2$ -charged Di and the Sm glasses. This band was resolved from the silicate band by using a graphical method (Young *et al.*, 1959). The relative intensity of the  $1075 \pm 5\text{ cm}^{-1}$  band in the spectra of  $\text{CO}_2$ -charged Di glasses quenched from various  $P$ - $T$  conditions was measured with respect to the

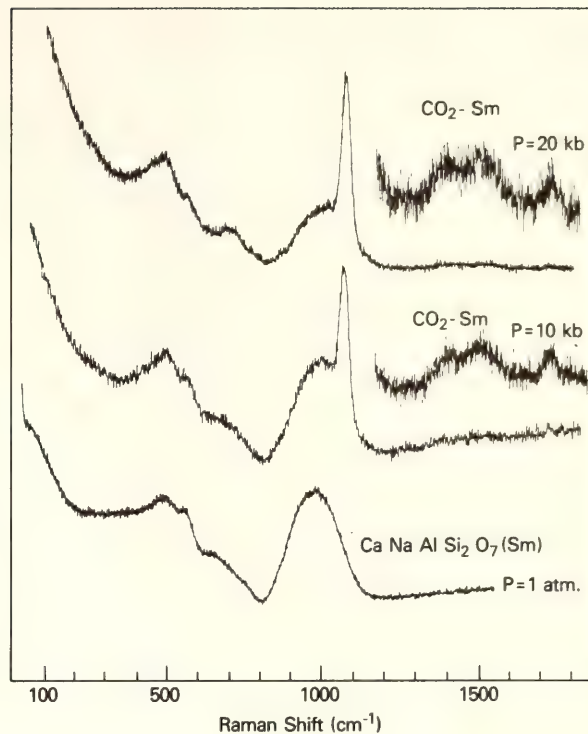


Fig. 47. Raman spectra of sodium melilite and  $\text{CO}_2$ -charged sodium melilite glasses, prepared by quenching melts of  $2\text{ CaCO}_3\cdot\text{Na}_2\text{CO}_3\cdot 4\text{SiO}_2$  composition at different pressures at  $1460^\circ\text{C}$ . The bands in the region  $1200\text{--}1800\text{ cm}^{-1}$  in  $\text{CO}_2$ -charged sodium melilite glasses were recorded with a sensitivity of  $\times 11$  for the 10-kbar glass and  $\times 3$  for the 20-kbar glass.

$\nu_s(\text{Si-O-Si})$  band and the high-frequency  $\nu_s(\text{Si-O}^-)$  band envelope. Similarly, the relative intensity of this band in  $\text{CO}_2$ -charged Sm glasses was determined with respect to both the low-frequency envelope due to the  $\nu_s[\text{Si-O-Si(Al)}]$  mode and the high-frequency band due to  $\nu_s[\text{Si(Al)-O}]$  stretch. Because the bands overlap, the accuracy of estimation of the relative concentration of the species responsible for the strong band is estimated to be  $\pm 10\%$ . The results of these estimations are presented in Fig. 48 for  $\text{CO}_2$ -charged Di glasses and in Fig. 49 for  $\text{CO}_2$ -charged Sm glasses.

### Discussion

The strong band at  $1072\text{ cm}^{-1}$ , the weak and broad doublet consisting of bands at  $1422$  and  $1530\text{ cm}^{-1}$ , and a weak, broad band at  $1730\text{ cm}^{-1}$  in the

TABLE 19. Raman Frequencies of Diopside and CO<sub>2</sub>-Saturated Diopside Glasses\*

Sample	P, kbar	T, °C	Frequency, cm <sup>-1</sup>									
CaMgSi <sub>2</sub> O <sub>6</sub> (Di)	0.001	1500	92s†	~340vw,bd	490vw,bd	638s,p	~890(sh),p	980s,p ~1008(sh),p(?)	...	...	...	...
CO <sub>2</sub> -saturated Di	10 ± 1.5	1550	~88s	~349w,bd	~480vw,bd	634s	~870m,(sh)	984s	1070m,(sh),p	...	...	...
CO <sub>2</sub> -saturated Di	10 ± 1.5	1600	~80s	~346w,bd	~486vw,bd	630	~880m,s	978	1071m,(sh),p	...	...	...
CO <sub>2</sub> -saturated Di	10 ± 1.5	1650	~86s	~346w,bd	~480vw,bd	634s,p	~882m,s	978s,p	~1422vw,bd,p	1530vw,bd,p	1730vw,bd,p	...
CO <sub>2</sub> -saturated Di	10 ± 1.5	1725	~81s	~342w,bd	490vw,bd	635s	~872m,(sh)	982s	1072m,(sh)	...	...	...
CO <sub>2</sub> -saturated Di	20 ± 1.5	1580	...	...	...	610s	~880m,(sh)	990s	1078s,p	...	...	...
CO <sub>2</sub> -saturated Di	20 ± 1.5	1650	...	...	...	626s	~878m,(sh)	978s	1079s,p	...	...	...
CO <sub>2</sub> -saturated Di	20 ± 1.5	1685	88s	...	...	628s	~876m,(sh)	980s	1078s	...	...	...
CO <sub>2</sub> -saturated Di	20 ± 1.5	1725	...	~350vw,bd	~442vw,bd	628s,p	~876m,(sh)	990s,p	~1411vw,bd	~1532vw,bd	1728vw	...
CO <sub>2</sub> -saturated Di	25 ± 1.5	1725	...	...	...	614s,p	~876m,(sh)	994s,p	~1400vw,bd	~1532vw,bd	1720vw,p	...
Tentative assignment			Disorder induced	$\nu_s(\text{Ca-O}) + \tau(\text{SiO}_4^{4-})$	$\nu_s(\text{Mg-O}) + \delta(\text{SiO}_4^{4-})$	$\nu_s(\text{Si-O-Si})$	$\nu_s(\text{Si-O}^-)$ of $\text{SiO}_4^{4-}$	$\nu_s(\text{Si-O}^-)$ mode of $[\text{Si}_2\text{O}_6]_n$	$\nu_s(\text{CO}_3^{2-})$	$\nu_{as}(\text{CO}_3^{2-})$	$\nu_{as}(\text{CO}_3^{2-})$	Overtone ( $2\nu_2$ )

\* Measurement accuracy is ±10 cm<sup>-1</sup> for weak and broad bands, ±4 cm<sup>-1</sup> for sharp and strong bands.

† Abbreviations: s, strong; w, weak; vw, very weak; m, medium; bd, broad; p, polarized; dp, depolarized; sh, shoulder.

‡ Raman bands could not be measured because of fluorescence or low intensities (see text).

§ Spectral region showing strong Rayleigh tail due to disorder-induced phonon density of states.

||  $\nu_s$ , symmetric stretch;  $\nu_{as}$ , asymmetric stretch;  $\delta$ , deformation;  $\tau$ , torsional modes.

TABLE 20. Raman Frequencies of Sodium Melilite and CO<sub>2</sub>-Saturated Sodium Melilite Glasses\*

Sample	P, kbar	T, °C	Frequency, cm <sup>-1</sup>									
CaNaAlSi <sub>2</sub> O <sub>7</sub> (Sm)	0.001	~1300	~66s,(sh)	494s,p	562(sh),p	648(sh),p	712w,bd	980s,p	...	...	...	...
CO <sub>2</sub> -saturated Sm	10 ± 1.5	1275	...	494s,p	566(sh),p	...	~714w,bd	996s,p	1074s,p (w=32cm <sup>-1</sup> )	1418w,bd	1514w,bd	~1742w
CO <sub>2</sub> -saturated Sm	10 ± 1.5	1460	...	498s,p	564(sh),p	...	~714w,bd	983s,p	1070s,p (w=34cm <sup>-1</sup> )	~1418w,bd	~1514w,bd	~1742w
CO <sub>2</sub> -saturated Sm	10 ± 1.5	1550	...	486s,p	...	...	~704w,bd	986s	1070s,p (w=32cm <sup>-1</sup> )	...	...	...
CO <sub>2</sub> -saturated Sm	20 ± 1.5	1460	...	490s	566(sh)	...	~713w	988s	1074s,p	1410w,bd	1512w,bd	1738w
CO <sub>2</sub> -saturated Sm	20 ± 1.5	1550	...	490s	570w,(sh)	...	~710w	1002s	1074s,p	...	...	...
Tentative assignment			Disorder induced	$\nu_s(\text{Si-O-Si})$ network	$\nu_s[\text{Si-O-Si(Al)}]$ modes of $(\text{AlSi}_2\text{O}_7)^-$ group	$\delta(\text{CO}_3^{2-})$	$\nu_s(\text{Si-O}^-)$	$\nu_s[\text{Si(Al)-O}^-]$ network	$\nu_s(\text{CO}_3^{2-})$	$\nu_{as}(\text{CO}_3^{2-})$	$\nu_{as}(\text{CO}_3^{2-})$	Overtone ( $2\nu_2$ )

\* Measurement accuracy, abbreviations, and symbols as in Table 19.

† Spectral region showing strong Rayleigh tail due to disorder-induced phonon density of states.

‡ Raman bands could not be measured because of fluorescence or weak intensities.



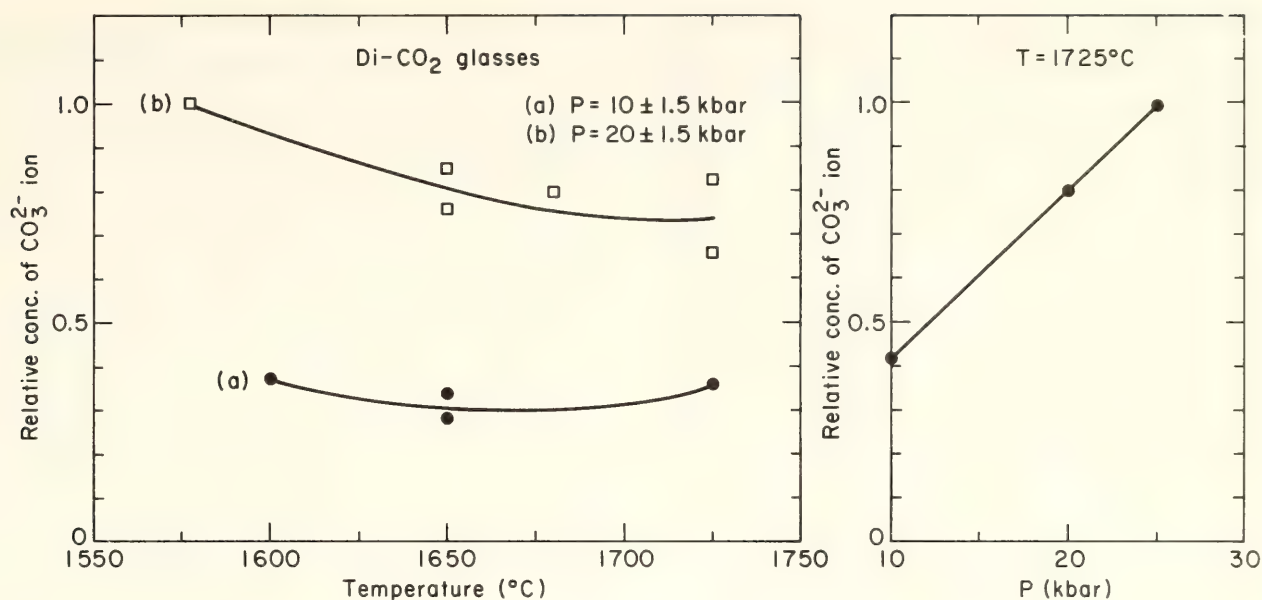


Fig. 48. Temperature and pressure dependence of the carbonate ion in CO<sub>2</sub>-charged glasses of Di composition.

spectrum of CO<sub>2</sub>-charged glasses prepared at 10 kbar are characteristic of CO<sub>3</sub><sup>2-</sup> ions (Table 19; Fig. 46). Similar features that are characteristic of CO<sub>3</sub><sup>2-</sup> ions are apparent in the spectra of all the CO<sub>2</sub>-charged Di glasses (Fig. 46; Table 19). These characteristic bands of CO<sub>3</sub><sup>2-</sup> ions are also present in the spectra of CO<sub>2</sub>-charged Sm glasses. Because these bands due to the carbonate ion show polarization characteristics not seen for crystalline powders, it can be concluded that the carbonate ions in these glasses

are not part of a carbonate mineral inclusion but rather are equivalent to CO<sub>3</sub><sup>2-</sup> ions in a fluid.

According to group theory, a free CO<sub>3</sub><sup>2-</sup> ion belonging to the  $D_{3h}$  point group should give rise to six fundamental modes of vibration [ $A'_1(R) + A''(IR) + 2 E'(R, IR)$ ] (Herzberg, 1945). The  $E'$  modes are doubly degenerate and are active in both Raman and infrared. The first overtone of the infrared active mode  $\nu_2(A''_2)$  is Raman active and appears at  $\sim 1760$  cm<sup>-1</sup>. If the carbonate ions are

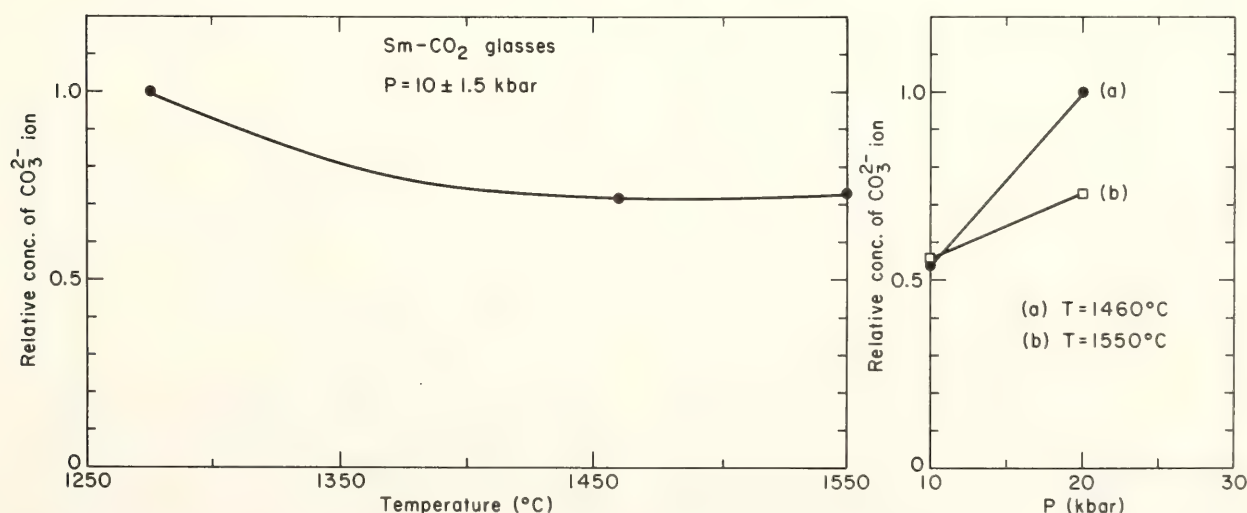


Fig. 49. Temperature and pressure dependence of the carbonate ion in CO<sub>2</sub>-charged glasses of Sm composition.

present at a site of lower symmetry, which does not have a three-fold axis, the degeneracies of the  $\nu_3(E')$  and  $\nu_4(E')$  modes are lifted. In the spectra of  $\text{CO}_2$ -charged Di glasses the presence of a doublet in the region  $1200\text{--}1500\text{ cm}^{-1}$  indicates that the symmetry of the  $\text{CO}_3^{2-}$  ion is lower ( $C_{2v}$  or  $c_s$ ) than  $D_{3h}$ . In the spectrum of  $\text{CO}_2$ -charged Di glass prepared at 25 kbar the components of  $\nu_3$  appear at  $\sim 1400$  and  $1532\text{ cm}^{-1}$  (Fig. 46; Table 19). Even at 10 kbar the  $\nu_3$  split by  $108\text{ cm}^{-1}$  (Table 19). The Raman bands due to the  $\nu_4(E)$  mode of  $\text{CO}_3^{2-}$  are usually weak, and these bands may be masked by the silicate bands.

In the spectra of  $\text{CO}_2$ -charged Sm glasses the bands due to  $\text{CO}_3^{2-}$  ions (Fig. 48; Table 20) show close resemblance to the carbonate bands observed in the spectra of  $\text{CO}_2$ -charged Di glasses. The  $\nu_3(\text{CO}_3^{2-})$  band in the spectra of Sm glasses shows a large ( $90 \pm 3\text{ cm}^{-1}$ ) splitting. A broad, weak band at  $\sim 714\text{ cm}^{-1}$  observed in the spectra of  $\text{CO}_2$ -charged Sm glass at 10 kbar  $\text{CO}_2$  pressure shows a small decrease in width and a small increase in intensity with respect to the low-frequency band due to the Si(Al)-O-Si stretch mode in the  $\text{CO}_2$ -charged Sm glass prepared at 20 kbar total pressure (Fig. 48). The  $\nu_4(E)$  deformation mode of  $\text{CO}_3^{2-}$ , which appears at  $680\text{ cm}^{-1}$  for the free  $\text{CO}_3^{2-}$  ion, probably contributes to this band. The tentative assignment of various bands in the spectra of Sm glasses is given in Table 20. The assignment of the silicate bands in the spectra of glasses of Di and Sm compositions is discussed in detail by Sharma and Yoder (this Report).

When  $\text{CO}_2$  dissolves in the melts of Di and Sm composition the structures of the melts are affected, as indicated by an increase in the frequency of the  $\nu_s(\text{Si-O}^-)$  stretching mode and a decrease in the frequency of the  $\nu_s(\text{Si-O-Si})$  mode, which appears at  $638\text{ cm}^{-1}$  in the glass of Di composition. In the  $\text{CO}_2$ -charged Di glass prepared at 25 kbar total pressure of  $\text{CO}_2$  (Table 19), this band ap-

pears at  $614\text{ cm}^{-1}$ . Further, the intensity of the shoulder at  $\sim 890\text{ cm}^{-1}$ , attributed to  $\text{SiO}_4^{4-}$  groups, decreases with increasing  $\text{CO}_2$  pressure (Fig. 46). These observations suggest that the number of nonbridging oxygens per silica decreases in the  $\text{CO}_2$ -charged melt (see Simon, 1960). In  $\text{CO}_2$ -charged glasses, with increasing  $\text{CO}_2$  pressure the terminal Si-O stretching mode ( $980\text{ cm}^{-1}$  in the glass of Sm composition) shows a small increase in frequency, and the band at  $494\text{ cm}^{-1}$ , due to the  $\nu_s[\text{Si-O-Si(Al)}]$  stretching mode, shifts to lower frequencies (Table 20). The intensity of the shoulder at  $\sim 648\text{ cm}^{-1}$  attributed to the  $(\text{AlSi}_2\text{O}_7)^{3-}$  group decreases with increasing concentration of  $\text{CO}_3^{2-}$  ions in the spectra of the  $\text{CO}_2$ -charged Sm glasses. It is suggested, therefore, that when  $\text{CO}_2$  is dissolved in the Sm glass the number of nonbridging oxygens in the melt is reduced.

The glasses of both Di and Sm compositions have  $\text{Ca}^{2+}$  cations. In view of the close resemblance of the bands due to carbonate ions in the spectra of  $\text{CO}_2$ -charged glasses of Di and Sm compositions, it seems appropriate to postulate that the majority of  $\text{CO}_3^{2-}$  ions are associated with  $\text{Ca}^{2+}$  ions in these glasses. The decrease in the number of nonbridging oxygens in the  $\text{CO}_2$ -saturated melts can thereby be explained. On the basis of this hypothesis, however, it is difficult to account for the observed large splitting of the  $\nu_3$  band of the carbonate ion in the spectra of the  $\text{CO}_2$ -charged glasses of both Di and Sm compositions. The large splitting of the  $\nu_3$  band in the spectra of  $\text{CO}_2$ -charged glasses of Di and Sm compositions probably indicates a strong interaction between the  $\text{CO}_3^{2-}$  ion and the silicate network.

In the  $\text{CO}_2$ -charged glasses of both Di and Sm compositions, the intensity of the Rayleigh wing increases with increasing  $\text{CO}_2$ , as does the intensity of the  $\nu_s(\text{CO}_3^{2-})$  band relative to the  $\nu_s(\text{Si-O-Si})$  band, and this indicates that with an increase in the concentration of  $\text{CO}_3^{2-}$



in these glasses the glass structure becomes more disordered.

It can be seen from Figs. 48 and 49 that the concentration of the carbonate ion in the  $\text{CO}_2$ -charged glasses of Di and Sm compositions increases with pressure. The effect of increasing temperature of quenching on the concentration of the  $\text{CO}_3^{2-}$  ion in these melts (Figs. 48 and 49) is relatively small compared with the effect of pressure. In the glasses prepared at 10 kbar the  $\text{CO}_3^{2-}$  concentration apparently shows a small increase with increasing quenching temperature. In the glasses prepared at 20 kbar, however, the  $\text{CO}_3^{2-}$  concentration decreases with increasing quenching temperature (Figs. 48 and 49).

The results of the present study indicate that most of the  $\text{CO}_2$  present in  $\text{CO}_2$ -charged Di and Sm glasses exists as  $\text{CO}_3^{2-}$  ions. There is a close similarity in the Raman bands due to  $\text{CO}_3^{2-}$  ions in the spectra of  $\text{CO}_2$ -charged glasses of Di and Sm compositions as well as in the spectra of  $\text{CO}_2$ -charged glasses of Ak composition (Sharma, Hoering, and Yoder, this Report). These three glasses have different structures (Sharma and Yoder, this Report), and the similarity in the spectra of the carbonate ions, especially the large ( $>90\text{ cm}^{-1}$ ) splitting of the  $\nu_3$  band, suggests that the  $\text{CO}_3^{2-}$  ions have a strong covalent interaction with silicate glasses of Di and Sm compositions.

QUENCHED MELTS OF AKERMANITE  
COMPOSITIONS WITH AND WITHOUT  $\text{CO}_2$ —  
CHARACTERIZATION BY RAMAN  
SPECTROSCOPY AND GAS CHROMATOGRAPHY

*S. K. Sharma, T. C. Hoering, and  
H. S. Yoder, Jr.*

Raman spectroscopy and gas chromatography have been used to characterize quenched melts of akermanite (Ak) composition with and without  $\text{CO}_2$ . The Ak- $\text{CO}_2$  system was chosen because both crystalline and quenched materials can

be converted readily into trimethylsilyl (TMS) derivatives that are amenable to analysis by gas chromatography for the determination of anionic constitution. Raman spectroscopy is particularly suited for identifying carbon-oxygen-containing species in silicates because silicates are relatively weak Raman scatterers, whereas carbon monoxide, carbon dioxide, and carbonate ions scatter strongly, and each has characteristic bands. Results obtained by the spectral and chromatographic methods are complementary.

A mixture of the composition  $2\text{CaO}:\text{MgO}:2\text{SiO}_2:\text{CO}_2$  was made from purified samples of a natural diopside (Twin Lakes, California), almost of end-member composition, and reagent-grade  $\text{CaCO}_3$ . The mixture is equivalent to Ak +  $\text{CO}_2$  and contains 13.9 wt % carbon dioxide. Melts of this composition were prepared in a gas-media, high-pressure apparatus (Yoder, 1950) at total pressures up to 10 kbar and temperatures of  $1375^\circ\text{--}1475^\circ\text{C}$ , and then quenched as rapidly as possible.

The concentration of carbon dioxide, existing in the quenched melts either as a neutral molecule or as a carbonate ion, was determined by thermal decomposition in an F and M Model 185 carbon-hydrogen-nitrogen analyzer. The instrument was modified to operate at  $1250^\circ\text{C}$  by installing a platinum furnace element. The response of the analyzer was calibrated by the thermal breakdown of reagent-grade calcium carbonate.

The concentrations of carbon dioxide in three charged, quenched melts of akermanite composition are 7.02, 9.51, and 10.63 wt %, respectively, for material quenched from  $1450^\circ\text{C}$  and 7.5 kbar,  $1425^\circ\text{C}$  and 7.5 kbar, and  $1375^\circ\text{C}$  and 6.5 kbar. These concentrations correspond to a range in the molar ratio of  $\text{CO}_2$  to Ak of 0.46–0.80, but do not necessarily represent the equilibrium contents under the conditions from which they were quenched. The carbon dioxide is bonded strongly, as the quenched

melts must be heated above 900°C before all the carbon dioxide is released rapidly. The residue, after thermal decomposition, was partially crystalline.

The TMS derivatives of crystalline Ak and quenched melts of the same composition were prepared and analyzed as described by Hoering and Sharma (*Year Book* 77, pp. 662–665). The gas chromatographic analyses are reported in terms of the relative proportions of silicate anions (e.g., monomer, dimer, trimer). Pure, standard TMS derivatives of silicate anions are not available for calibrating the response of the gas chromatograph. Peak heights from gas chromatograms were converted, therefore, to relative concentrations by assuming that the response of the hydrogen flame detector is proportional to the number of carbon-to-hydrogen bonds in a molecule of the TMS derivative. The atoms forming silicon-to-oxygen or silicon-to-carbon bonds are not ionized and do not contribute to the current in such a detector. The results of the gas chromatographic analyses are shown in Table 21.

Crystalline akermanite yields, as expected, primarily the dimeric derivative. About 5% of other species is present and probably represents artifacts of the derivatization procedure. The chromatograms of the quenched melts of Ak composition, synthesized with and without carbon dioxide, are completely different from that formed from the crystalline

material, and consist of a range of linear silicate anions from the monomer to the pentamer. Only small amounts of material with a cyclic structure are present. There is a slight trend toward an increasing degree of silicate polymerization with increasing carbon dioxide concentration, but it is surprising that the high concentration of carbon dioxide has so little effect on the anionic constitution.

A measure of the internal consistency of the chromatographic analyses can be obtained by noting the balance of negative charge from the anions against the positive charge from the cations ( $Mg^{2+}$  and  $2Ca^{2+}$ ). The total negative charge should be  $-6$  to counter the  $+6$  from the cations. The last column in Table 21 shows the range of deviation from the expected value. The results are sensitive to estimates of the tetramer and pentamer because these anions, respectively, have charges of  $-10$  and  $-12$ . Definitive analyses will be possible when standard compounds become available for calibrating the gas chromatograph.

The Raman spectra of the quenched melts were recorded with a Jobin-Yvon optical system Ramanor (HG.2S) spectrometer. The samples were excited with the 488.0-nm line of an  $Ar^+$  laser with a power of 200–300 mW at the sample and 90° scattering geometry. The Raman spectra of  $CO_2$ -charged, quenched melts of Ak composition are depicted in Fig. 50. The bands and their spectral characteristics are summarized in Table 22.

TABLE 21. Relative Abundance of Silicate Anions

Sample	P, kbar	T, °C	Monomer	Dimer	Trimer	Tetramer	Pentamer	Total Anion Charge
1. Ak crystal*	0.001	1520	~0.05	~0.95	vs†	vs	...	~5.7
2. Ak glass	0.001	1500	0.39	0.34	0.178	0.07	0.02	5.95
3. Ak glass	10	1650	0.36	0.40	0.22	0.02	0.0	5.80
4. Ak-CO <sub>2</sub> glass	5	1425	0.30	0.35	0.21	0.10	0.04	6.28
5. Ak-CO <sub>2</sub> glass	10	1450	0.27	0.34	0.22	0.11	0.05	6.68

\* Crystal from Finch *et al.* (1974).  
† vs, very small.



The bands assigned to the silicate portion of the CO<sub>2</sub>-charged, quenched melts are similar in intensity to those obtained on material synthesized without CO<sub>2</sub> but appear at different positions. Apparently the presence of high CO<sub>2</sub> concentrations has made some changes in the silicate framework. New bands appear at 1078 (s, p), about 700 (sh, p), 1448 (vw, bd), 1528 (vw, bd), and 1742 cm<sup>-1</sup> (vw, bd). The bands in the region 1300–1800 cm<sup>-1</sup> are very weak but distinctive, and it is difficult to measure accurately the polarization character and position of these bands because of the strong fluorescence background. The low-frequency component of the doublet in the region 1300–1600 cm<sup>-1</sup> appears polarized.

The most strongly polarized band at 1078 cm<sup>-1</sup> increases in intensity with the pressure at which the melts were quenched. This band is undoubtedly due to a carbon-bearing species. The new bands in the CO<sub>2</sub>-charged, quenched melts do not correspond to Raman-active modes of CO or CO<sub>2</sub>; hence, they are

assigned to carbonate ions (Herzberg, 1945; Colthup *et al.*, 1975).

The positions of Raman and infrared active modes for various alkaline earth carbonates are shown in Table 23. There is a striking correlation between these modes and those observed in the quenched melts, with the exception of the large splitting of the  $\nu_3$  mode.

The  $90 \pm 10$  cm<sup>-1</sup> splitting of the carbonate ions of the  $\nu_3$  band in the CO<sub>2</sub>-charged material is large. The  $\nu_3$  mode is doubly degenerate, and splitting can occur either if (1) the carbonate ion is present in a site without a three-fold axis or if (2) it is complexed covalently. In aragonite, where it is in a site of lower symmetry without a three-fold axis ( $C_s$ ), the bands are only 2 cm<sup>-1</sup> apart (White, 1974). Even in the spectra of calcite II and III at high pressures, the bands differ by only 26 cm<sup>-1</sup> (Fong and Nicol, 1971). Furthermore, in the spectra of glasses prepared at 1 atm pressure and having the composition  $(1 - X)\text{K}_2\text{CO}_3 : X\text{SiO}_2$ , where  $0.4 \leq X \leq 0.7$ , the  $\nu_3$  band of the carbonate ion is a singlet (Verweij *et al.*, 1977, 1978). This observation indicates that the silicate network can accommodate undistorted carbonate ions. In metallo-carbonate complex ions, where the carbonate ion is bonded covalently with a  $C_s$  symmetry, the  $\nu_3$  band of a carbonate ion undergoes large splitting. Splittings of as much as 80 cm<sup>-1</sup> have been observed (Nakomoto, 1978).

The experimental results described above are summarized as follows: (1) Quenched melts of akermanite composition bind CO<sub>2</sub> strongly at high concentrations. (2) The Raman spectra have bands that can be assigned to a carbonate ion. (3) There is a splitting of the  $\nu_3$  mode of the carbonate ion that correlates with covalently bonded carbonate ions. (4) Crystalline and quenched material form a high yield of TMS derivatives. The anionic constitution of the quenched melts does not change appreciably when carbonate ions are present. (5) In the

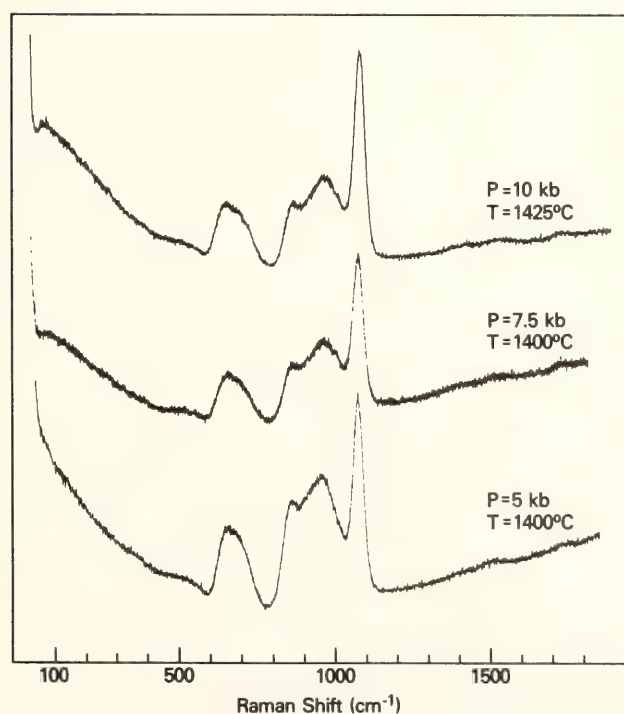


Fig. 50. Raman spectra of CO<sub>2</sub>-charged glasses of akermanite (Ca<sub>2</sub>MgSi<sub>2</sub>O<sub>7</sub>) composition.

TABLE 22. Positions of Raman Bands in the Spectra of Quenched Melts of Akermanite ( $\text{Ca}_2\text{MgSi}_2\text{O}_7$ ) Composition with and without  $\text{CO}_2$

Sample	P, kbar	T, °C	Frequencies,* $\text{cm}^{-1}$									
Ak (no $\text{CO}_2$ )	0.001	1500	...	...	...	...	...	...	...	...	...	...
$\text{CO}_2$ -Ak	5.0	1400	...	...	...	...	...	...	...	...	...	...
			~78s†	~700(sh), p	682m, p	~538vw, bd	360w, bd	...	858s, (sh), p	914s, bd, p	1078s, p	~1448vw, bd
			...	...	664m, p	~512vw, bd	...	...	868(sh), p	962s, bd, p	1078s, p	~1528vw, bd
$\text{CO}_2$ -Ak	6.5	1375	...	...	662m, p	~514vw, bd	...	...	868(sh), p	962s, bd, p	1074s, p	~1426vw, bd
			~70s	~702(sh), p	...	...	...	...	870(sh), p	966s, bd, p	1078s, p	~1524vw, bd
$\text{CO}_2$ -Ak	7.5	1400	...	...	664m, p	~514vw, bd	...	...	872(sh), p	970s, bd, p	1080s, p	~1430vw, bd
			~74s	~696(sh), p	...	...	...	...	872(sh), p	962s, bd, p	1077s, p	~1538vw, bd
$\text{CO}_2$ -Ak	7.5	1425	...	...	662m, p	~522vw, bd	...	...	870(sh), p	968s, bd, p	1082s, p	~1426vw, bd
			...	...	662m, p	~514vw, bd	...	...	872(sh), p	972s, bd, p	1080s, p	~1535vw, bd
$\text{CO}_2$ -Ak	7.5	1450	...	...	662m, p	~514vw, bd	...	...	870(sh), p	972s, bd, p	1080s, p	~1424vw, bd
			...	...	658m, p	~510vw, bd	...	...	872(sh), p	972s, bd, p	1080s, p	~1532vw, bd
$\text{CO}_2$ -Ak	10.0	1425	...	...	658m, p	~512vw, bd	...	...	872(sh), p	972s, bd, p	1080s, p	...
			~70s	~696(sh), p	...	...	...	...	872(sh), p	972s, bd, p	1080s, p	~1726vw, bd
$\text{CO}_2$ -Ak	10.0	1450	...	...	658m, p	~512vw, bd	...	...	872(sh), p	972s, bd, p	1080s, p	~1730vw, bd
			...	...	658m, p	~512vw, bd	...	...	872(sh), p	972s, bd, p	1080s, p	~1730vw, bd
Tentative band assignments§			disorder induced	$\nu_s(\text{Ca-O}) + \tau(\text{Si-O}_4^{4-})$	$\nu_s(\text{Si-O-Si})$	$\nu_s(\text{Mg-O}) + \delta(\text{Si-O}_4^{4-})$	$\nu_s(\text{Si-O}_4^{4-})$	$\delta(\text{CO}_3^{2-}) + \nu_s(\text{Si-O-C})?$	$\nu_s(\text{SiO}_4^{4-})$	$\nu_s(\text{Si-O}^-)$	$\nu_s(\text{CO}_3^{2-})$	$\nu_{as}(\text{CO}_3^{2-})$

\* Measurement accuracy is  $\pm 10 \text{ cm}^{-1}$  for weak and broad bands and  $\pm 4 \text{ cm}^{-1}$  for strong and sharp bands.

† Spectral region where strong Rayleigh tail was observed due to disorder-induced density of states.

‡ Abbreviations: w, weak; s, strong; bd, broad; p, polarized; dp, depolarized; sh, shoulder.

§  $\nu_s$ , symmetric stretch;  $\nu_{as}$ , asymmetric stretch;  $\delta$ , deformation;  $\tau$ , torsional modes.



TABLE 23. Frequencies of Raman and Infrared Active Internal Modes of  
Vibration of Alkali Earth Carbonates

Compound	$\nu_1(A_1')$		$\nu_2(A_2'')$		$\nu_3(E')$		$\nu_4(E')$		$A_2'' \times A_2''$ $2\nu_2(A_1')$		Ref.*
	Raman	I.R.	I.R.	Raman	I.R.	Raman	Raman	I.R.	Raman		
CaCO <sub>3</sub> (calcite)	1085s†	...	875m	1435w	1450s	711m	715w	715w	1748w		1
CaCO <sub>3</sub> (aragonite)	1087s	1085w	875, 870m	1464w 1466w	1490s	708 } m 712 }	699 } m 712 }		...		2,3
MgCO <sub>3</sub>	1084s	...	867m	1445w	1450s	739m	748m		1763		1,2
CaMg(CO <sub>3</sub> ) <sub>2</sub>	1099	...	879m	1448w	1437s	725w	727m		...		4
Description	C-O symmetric stretch	C-O symmetric stretch	CO <sub>3</sub> out of plane deformation	C-O asymmetric stretch	C-O asymmetric stretch	in plane deformation	in plane deformation	overtone			

\* 1: Rutt and Nicola (1974). 2: Huang and Kerr (1960). 3: Griffith (1969). 4: White (1974).  
† Abbreviations as in Table 22.

Raman spectra of  $\text{CO}_2$ -charged Ak glasses the bands assigned to silicate anions show changes that are consistent with a decrease in the number of non-bridging oxygens in the melt with increasing carbonate concentration.

Mysen (1977a,b) has postulated that the addition of carbon dioxide to silicate melts results in an increased degree of polymerization of the silicate network. Carbon dioxide captures an oxide ion to become a carbonate ion, and there is necessarily a condensation to give longer silicate chains. The observed increase in the frequency of  $\text{Si-O}^-$  symmetric stretch and decrease in the  $\text{Si-O-Si}$  symmetric stretch (Table 22) in the spectra of  $\text{CO}_2$ -saturated Ak glasses do indicate that the number of nonbridging oxygens decreases in the  $\text{CO}_2$ -saturated melt. The TMS derivatives, on the other hand, reveal that there are no major changes in the silicate anionic distribution when a high concentration of the carbonate ion is present in the melt of Ak composition.

It is not certain from the present observations whether the decrease in the number of nonbridging oxygens in the  $\text{CO}_2$ -charged glasses is a result of association of the  $\text{CO}_3^{2-}$  ion with silicon through a nonbridging oxygen or is due to the association of the  $\text{CO}_3^{2-}$  ion with cation polyhedra.

#### INFLUENCE OF MELT STRUCTURE ON ELEMENT PARTITIONING BETWEEN OLIVINE AND MELT AND BETWEEN CLINOPYROXENE AND MELT AT 1 ATM

*B. O. Mysen, D. Virgo, and F. Seifert*

Trace element abundances and abundance ratios in igneous rocks are considered valuable tools in deducing their petrogenetic history (e.g., Gast, 1968). Recent experimental data have shown, however, that the trace element partition coefficients also depend strongly on pressure, temperature, and bulk composition (Leeman, 1974; Watson, 1976, 1977;

Mysen, 1978b; Mysen and Kushiro, 1979; Hart and Davis, 1978; Irving and Frey, 1978). The single most important parameter may be the bulk composition of the melt in equilibrium with a particular mineral assemblage (Irving and Frey, 1978). Variations in bulk composition of silicate melts result in structural changes in the melts. Direct structural determination of the melts is necessary, therefore, to understand the behavior of trace elements during petrogenesis of igneous rocks.

Two crystal-liquid pairs were studied. Forsterite coexists with melt of broad compositional variation under isothermal conditions in the system  $\text{NaAlSi}_3\text{O}_8\text{-CaAl}_2\text{Si}_2\text{O}_8\text{-Mg}_2\text{SiO}_4$  (Schairer and Yoder, *Year Book 65*, pp. 204-209). Clinopyroxene coexists with a wide range of melt compositions under isothermal conditions in the system  $\text{NaAlSiO}_4\text{-CaMgSi}_2\text{O}_6\text{-SiO}_2$  (Schairer and Yoder, 1960) so that the influence of nonbridging oxygen/bridging oxygen (NBO/BO) on  $K_i^{\text{crystal-liq}}$  can be determined. The melt compositions (see Table 24) were prepared in sealed Pt containers from spectroscopically pure  $\text{SiO}_2$ ,  $\text{Al}_2\text{O}_3$ ,  $\text{MgO}$ ,  $\text{CaCO}_3$ , and reagent-grade  $\text{Na}_2\text{CO}_3$  in a vertical quench furnace and quenched in air.

Nickel and rare earth element (REE) partition coefficients were determined in the system  $\text{Ne-Di-SiO}_2$  at  $1200^\circ\text{C}$  with run durations of four days. This run length was necessary to achieve equilibrium on the basis of selected reversal experiments. The experiments were conducted with less than 10 ppm REE and less than 500 ppm Ni in the diopside. Published  $K_{\text{Ni}}^{\text{ol-liq}}$  values (Hart and Davis, 1978) were determined with about 1 wt % Ni in olivine. The analysis was carried out with beta-track mapping (Mysen and Seitz, 1975) using  $^{63}\text{Ni}$ ,  $^{141}\text{Ce}$ ,  $^{151}\text{Sm}$ , and  $^{171}\text{Tm}$  as sources of beta activity.

The Raman spectra were measured with a Jobin-Yvon double-grating spectrometer using an  $\text{Ar}^+$  ion laser and 200-400 mW power. The scattered radia-



TABLE 24. Bulk Compositions of Melts Coexisting with Crystals for which  $K_i^{x_{tal}-liq}$  are Known\*

	DNS1	DNS2	DNS3	AAF1	AAF2	AAF3
SiO <sub>2</sub>	74.60	63.53	54.24	58.58	42.96	50.12
Al <sub>2</sub> O <sub>3</sub>	12.20	16.87	17.95	11.86	19.42	15.34
CaO	3.37	5.44	9.84	...	10.68	5.44
MgO	2.42	3.91	7.07	22.35	26.93	25.79
Na <sub>2</sub> O	7.42	10.47	10.91	7.21	...	3.31

\*  $i$  = Ni, REE.

tion was detected with a photon-counting detection system.

It can be seen from the data in Fig. 51 that  $K_{Ni}^{cpx-liq}$  and  $K_{REE}^{cpx-liq}$  decrease as the melt becomes enriched in CaMgSi<sub>2</sub>O<sub>6</sub> component and depleted in NaAlSi<sub>3</sub>O<sub>8</sub> + SiO<sub>2</sub>.

Nickel and manganese partition coefficients between forsterite and melt as a function of bulk composition of melt in the system An-Ab-Fo have been determined by Watson (1977) and by Hart

and Davis (1978). Because the isotherms of the forsterite liquidus surface in the relevant portion of that system are almost parallel with the An-Ab join, the forsterite content of the melts does not change appreciably across the 1500°C isotherm studied here. Relevant partition coefficients from the work of Watson (1977) and Hart and Davis (1978) are listed in Table 25. Both  $K_{Mn}^{Fo-liq}$  and  $K_{Ni}^{Fo-liq}$  increase with increasing Ab content of the melt (Table 25). The rate of increase is more rapid between Ab<sub>50</sub> and Ab<sub>100</sub> than between Ab<sub>0</sub> and Ab<sub>50</sub> (Fo content ignored in this notation).

Raman spectra of quenched melts of compositions DNS1, DNS2, and DNS3 (Table 24) show a broad, high-frequency envelope between 850 and 1200 cm<sup>-1</sup> (Fig. 52). In composition DNS1 this envelope consists of two bands near 970 and 1050 cm<sup>-1</sup>. The shoulder at 970 cm<sup>-1</sup> in DNS1 composition is near 950 cm<sup>-1</sup> in DNS2 composition. In composition DNS3, a broad band, symmetric at 1020 cm<sup>-1</sup>, constitutes the entire high-frequency envelope.

The  $I(950)/I(1020)$  is 30–40% greater in DNS1 than in DNS2. The band near 800 cm<sup>-1</sup> is barely discernible in composition DNS3 and becomes stronger as the Ne + SiO<sub>2</sub> content of the melt increases. There is a distinct band near 660 cm<sup>-1</sup> in DNS3 melt. This band is very weak in DNS2 melt and is totally absent in melt of DNS1 composition. Finally, it is noted that the strong band slightly below 500 cm<sup>-1</sup> shifts systemati-

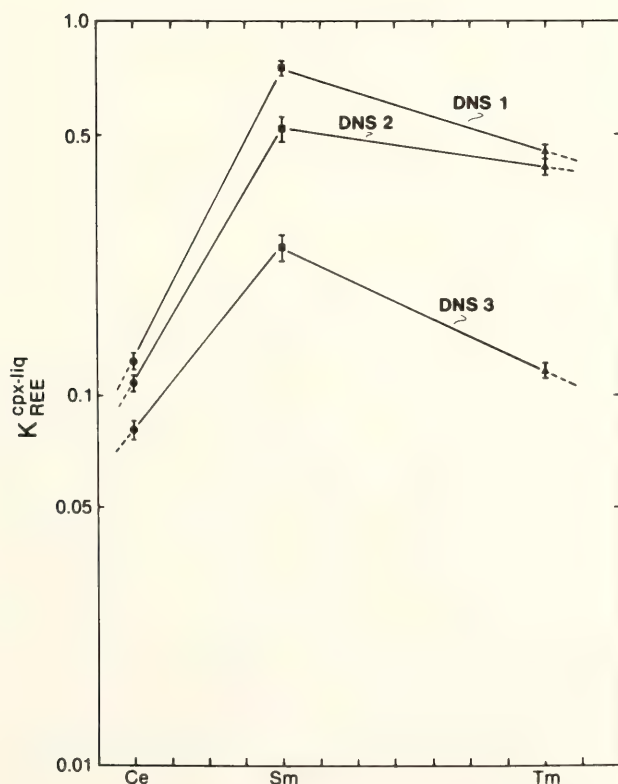


Fig. 51. Nickel and REE partition coefficients between diopside (cpx) and liquid (liq) as a function of bulk liquid composition at 1200°C in air. (A)  $K_{REE}^{cpx-liq}$ . (B)  $K_{Ni}^{cpx-liq}$ .

TABLE 25. Nickel and Manganese Partition Coefficients between Forsterite and Melt\*

	$K_{Ni}^{ol-llq}$ (Hart and Davis, 1978)	$K_{Mn}^{ol-llq}$ (Watson, 1977)
AAF1†	$6.9 \pm 0.4$	$0.82 \pm 0.02$
AAF2	$4.4 \pm 0.2$	$0.63 \pm 0.04$
AAF3	$5.04 \pm 0.06$	$0.63 \pm 0.4$

\* The data were acquired at 1450°C with liquid compositions lying close to the extensions of the tie line between the Fo corner and compositions AAF1, AAF2, and AAF3.  
† These notations refer to the compositions of the liquids of Hart and Davis (1978) and Watson (1977) that are the closest to those studied with Raman spectroscopy (1450°C liquidus compared with 1500°C for compositions used in Raman spectroscopy).

cally to higher frequency as the melt becomes enriched in Di component.

The Raman bands at 450, 800, and 1050  $cm^{-1}$  are characteristic of those found in three-dimensional melts on the join Ne-SiO<sub>2</sub> (Virgo, Seifert, and Mysen, this Report). The 1050- $cm^{-1}$  band reflects (Si,Al)-O°\* stretching, the 800- $cm^{-1}$  band is an Si-O° bending mode, and the 450- $cm^{-1}$  band is an Si-O° rocking mode. Bands at 500, 650, 950, and 1050  $cm^{-1}$  are characteristic in metasilicate melts (Brawer and White, 1975, 1977; Furukawa *et al.*, 1978; Mysen, Virgo, and Seifert, this Report). The bands at the two highest frequencies are stretching modes of (Si,Al)-O° (1050  $cm^{-1}$ ) and (Si,Al)-O- (950  $cm^{-1}$ ) in depolymerized melts [the ratio of nonbridging oxygens per silicon (NBO/Si) is greater than 0]. The bands at 650 and 500  $cm^{-1}$ , respectively, are Si-O° bending and Si-O° rocking modes. In the system Ne-Di-SiO<sub>2</sub> quenched melts show combinations of all these modes, and the intensities of individual bands are posi-

\* The notations Si-O° and Si-O-, respectively, denote vibrations across an Si-O-Si bridge and to a nonbridging oxygen. The notations (Si, Al)-O° and (Si,Al)-O- denote (Si,Al) coupling.

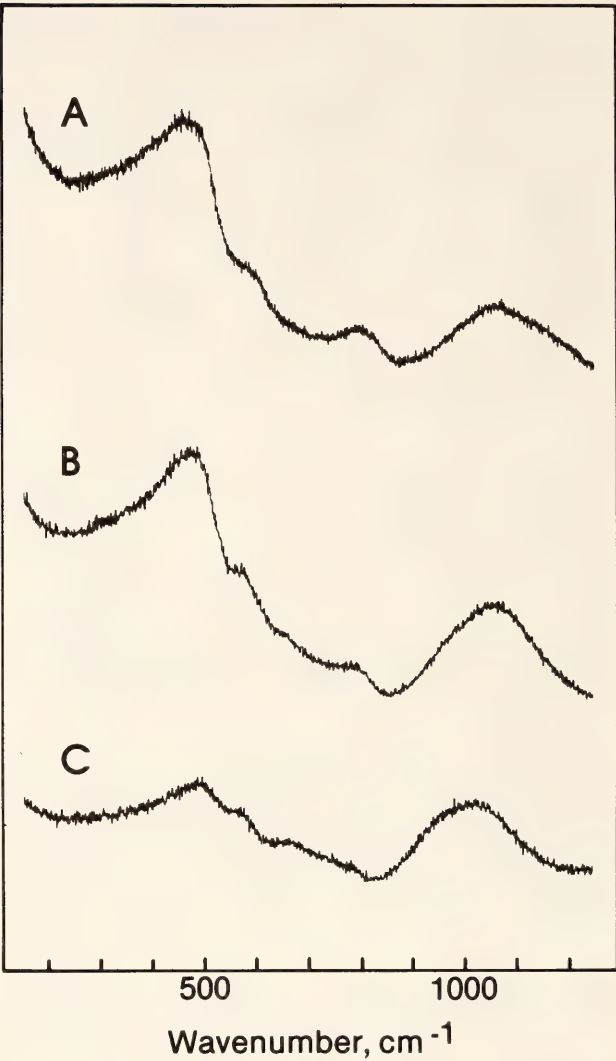


Fig. 52. Raman spectra of quenched melts. (A) DNS1, (B) DNS2, (C) DNS3. (Ar<sup>+</sup> ion source with 200–400 mW laser power.)

tively correlated with the proportions of metasilicate and three-dimensional network components. Metasilicate melts of alkaline earths (pyroxene melts) also have a medium-to-weak band at 880  $cm^{-1}$  (Mysen, Virgo, and Seifert, this Report), reflecting Si-O<sup>2-</sup> stretching in isolated SiO<sub>4</sub><sup>4-</sup> tetrahedra. The absence of this band in even the most Di-rich composition (DNS3 with 38 wt % Di component) may indicate that no separate tetrahedra exist or that the intensity of this band is so weak in the present melts that it cannot be detected beneath the low-frequency limb of the 950- $cm^{-1}$  band.

The Raman spectra of the melts in the



system Ne-Di-SiO<sub>2</sub> may be interpreted, therefore, as a mixture of metasilicate and three-dimensional network components. There is no evidence for interaction between the units to make new structural units.

The Raman spectra of quenched melts along the 1500°C isotherm of the forsterite-liquidus surface in the system NaAlSi<sub>3</sub>O<sub>8</sub>-CaAl<sub>2</sub>Si<sub>2</sub>O<sub>8</sub>-Mg<sub>2</sub>SiO<sub>4</sub> show a high-frequency envelope of stretch bands between 800 and 1150 cm<sup>-1</sup> (Fig. 53). In AAF1 melt, the low-frequency limb of this envelope shows asymmetry, whereas in AAF2 and AAF3 melts the high-frequency limb shows asymmetry. The maximum of the high-frequency envelope shifts to lower frequency with increasing An content of the melt. All spectra show a distinct band near 660–700 cm<sup>-1</sup>, which shifts to higher frequency with increasing An content of the melt. The An-free melt (AAF1) shows a broad band near 460 cm<sup>-1</sup>.

In analogy with the spectra of melts on the joins Ne-SiO<sub>2</sub> and CATS-SiO<sub>2</sub> (Virgo, Seifert, and Mysen, this Report), the 460–500 cm<sup>-1</sup> band found in all melts is ascribed to Si-O° rocking in a three-dimensional network. A large proportion of bridging oxygens (BO) in these melts is also indicated by the strong band near 1000 cm<sup>-1</sup>. This band is ascribed to (Si,Al)-O° stretching in a structure with a three-dimensional network. The lower frequency of this band compared with Al-free compositions is ascribed to extensive (Si,Al) coupling (Virgo, Seifert, and Mysen, this Report). This interpretation is further substantiated by the shift of the band to lower frequency with increasing An content of the melt. The band near 900 cm<sup>-1</sup> is tentatively ascribed to (Si,Al)-O- stretching. The band occurs near 950 cm<sup>-1</sup> in Al-free quenched metasilicate melts. As Al enters tetrahedral coordination, this band will shift to lower frequency, as also shown by Brawer and White (1977). On the basis of this interpretation of the bands at 900 and 1000 cm<sup>-1</sup>, the NBO/Si in-

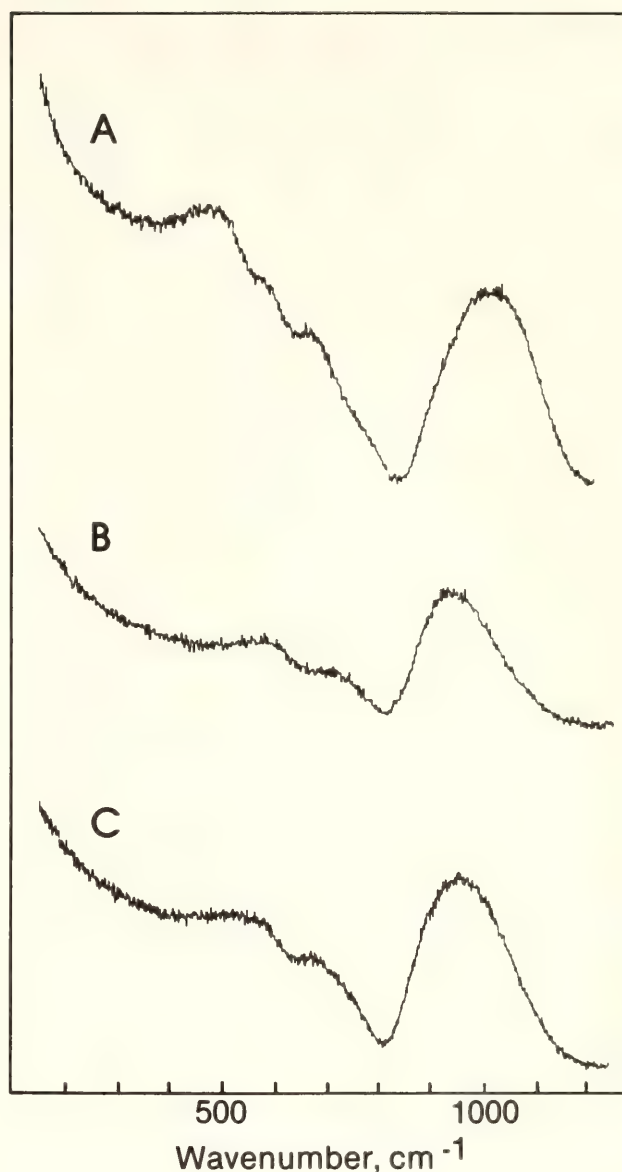


Fig. 53. Raman spectra of quenched melts. (A) AAF1, (B) AAF2, (C) AAF3. (Ar<sup>+</sup> ion source with 200–400 mW laser power.)

creases as the melts become more An-rich (at nearly constant Fo content). The presence of a significant proportion of nonbridging oxygen in these melts is also indicated by the presence of a distinct band near 650 cm<sup>-1</sup>. This band is considered diagnostic of the presence of metasilicate components in silicate melts (Brawer and White, 1975; Mysen, Virgo, and Seifert, this Report). The intensity ratio  $I(650)/I(990)$  is near 0.1 in the present melts, whereas it is between 0.6 and 0.7 in metasilicate melts. This difference indicates that the AAF1, AAF2, and AAF3 quenched melts may be a

mixture of chains and more polymerized units. Some of the more polymerized units have a three-dimensional network. There are no bands indicative of  $\text{SiO}_4^{4-}$  tetrahedra in these melts despite the large proportion of Fo component (40 wt %).

In summary, mixtures of orthosilicate and three-dimensional network components result in formation of anionic structural units of intermediate degree of polymerization. In the compositions studied here, these units have NBO/Si between 2 (chain) and 0 (three-dimensional network).

Spectroscopic studies of the structural role of divalent transition metals in silicate melts indicate that such cations are octahedrally coordinated (Mao, Virgo, and Bell, *Year Book* 72, pp. 631–638; Bell and Mao, *Year Book* 73, pp. 496–497; Seifert, Virgo, and Mysen, this Report; Boon and Fyfe, 1972). Fluorescence spectroscopy of REE in silicate

melts has suggested that oxygen coordination is between six and nine (Kurkjian *et al.*, 1963; Mockovciak *et al.*, 1965; Robinson, 1974a,b). Several different types of octahedra, depending on NBO/Si, have been suggested (Robinson, 1974b).

Inasmuch as the bulk composition and trace element content of crystals in equilibrium with the melt and the trace element content of the melt remain nearly constant in the present experimental systems, any variation of the partition coefficient must result from variation of the activity coefficient of the trace element in the melt. The partition coefficient may be expressed as:

$$K_i^{\text{xtal-liq}} = (a_i^{\text{xtal}}/a_i^{\text{liq}}) (\gamma_i^{\text{liq}}/\gamma_i^{\text{xtal}}), \quad (1)$$

or under the conditions studied here,

$$\gamma_i^{\text{liq}} \sim CK_i^{\text{xtal-liq}}, \quad (2)$$

where  $a_i^{\text{xtal}}$  and  $a_i^{\text{liq}}$ , respectively, are

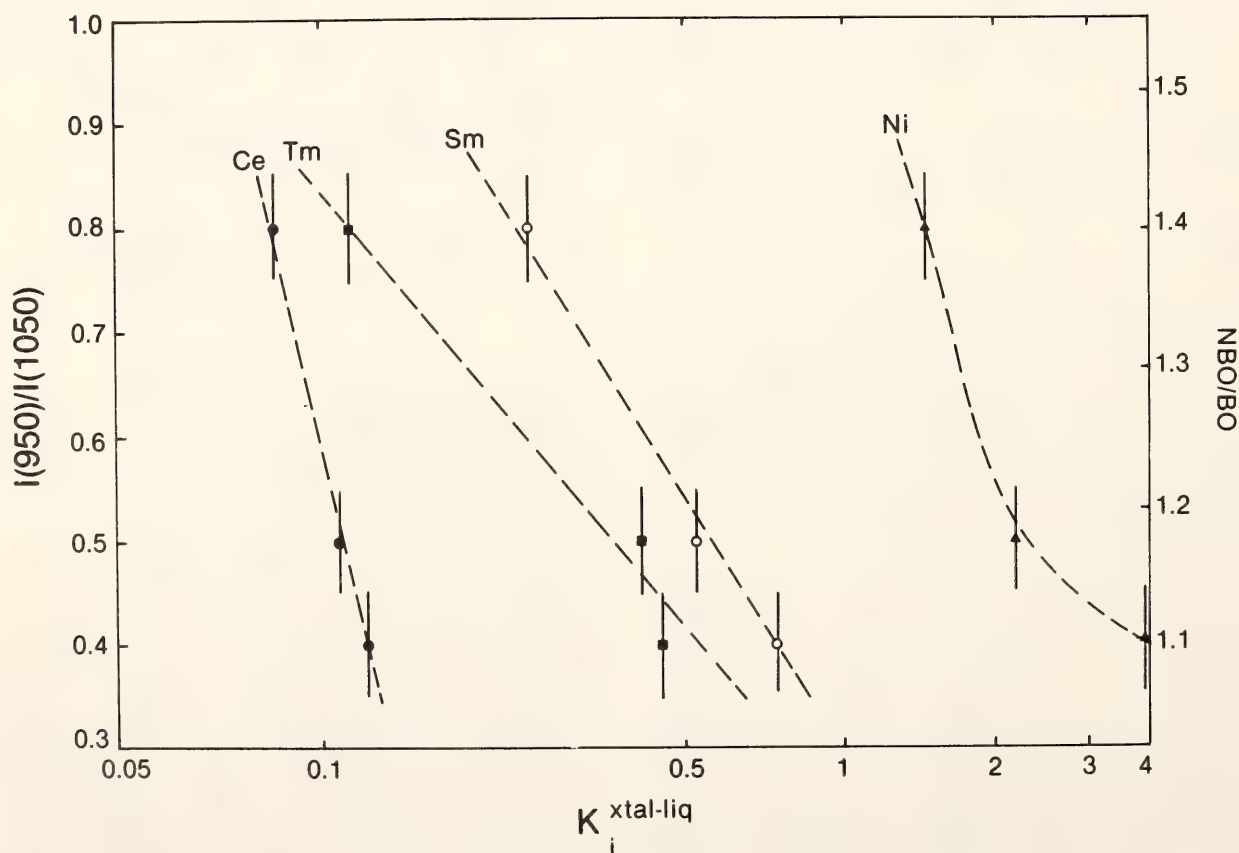


Fig. 54. Intensity ratio of wave numbers  $I(950)/I(1050)$  vs.  $K_i^{\text{xtal-liq}} = \gamma_{\text{Ni}}^{\text{liq}}$  of quenched melts in the system  $\text{CaMgSi}_2\text{O}_6\text{-NaAlSi}_3\text{O}_8\text{-SiO}_2$ .



activities of element  $i$  in crystal and melt, and  $\gamma_i^{\text{xtal}}$  and  $\gamma_i^{\text{liq}}$  are activity coefficients. The symbol  $C$  is a constant. In Fig. 54,  $K_i^{\text{xtal-liq}}$  is plotted against the intensity ratio  $I(950)-I(1050)$  and NBO/BO (calibrated after Brawer and White, 1975). The activity coefficients of the REE in the melt (Fig. 54) increase as a logarithmic function of decreasing NBO/BO, within experimental uncertainty. The activity coefficient of Ni in the melt also increases rapidly with decreasing NBO/BO.

Thus, the NBO/BO of silicate melts is closely related to the activity coefficients of trace elements when the element is a network modifier. Until detailed structural data on the role of trace elements in melts become available, the data cannot be fully interpreted. It is clear that as more experimental results on melt structure and the structural role of trace elements in silicate melts become available, the NBO/BO may become a useful parameter to calculate partition coefficients between rock-forming crystals and melt for divalent transition metals and rare earth elements.

#### CHANGES IN VISCOSITY AND DENSITY OF MELTS OF SODIUM DISILICATE, SODIUM METASILICATE, AND DIOPSIDE COMPOSITION WITH PRESSURE

*C. M. Scarfe, B. O. Mysen, and D. Virgo*

The viscosity of silicate melts is an important parameter in problems related to the generation, evolution, and emplacement of igneous rocks. Although viscosities of many melt compositions are reasonably well known at 1 atm, knowledge of the effect of pressure on melt viscosity is more limited.

All measurements on anhydrous melt compositions of geological interest have shown an isothermal decrease in viscosity with increasing pressure (Fig. 55). All the melts depicted in Fig. 55, however, have highly polymerized melt structures at 1 atm, as shown by the ratio of nonbridg-

ing oxygens to tetrahedrally coordinated cations (NBO/T) present in the melts (Table 26). In order to test the general validity of the negative pressure dependence of viscosity, three compositions were selected: sodium disilicate ( $\text{Na}_2\text{O} \cdot 2\text{SiO}_2$ ), sodium metasilicate ( $\text{Na}_2\text{O} \cdot \text{SiO}_2$ ), and diopside ( $\text{CaMgSi}_2\text{O}_6$ ). All these compositions are relatively depolymerized melts at 1 atm with  $\text{NBO/T} \geq 1$  (Table 26). Sodium disilicate and metasilicate were selected because of their chemical simplicity and low melting temperatures, and because data are available on the properties of their melts at 1 atm. Diopside was chosen because it is a major component of melts of geological interest.

#### *Experimental Methods*

Except for a single data point for  $\text{Na}_2\text{O} \cdot \text{SiO}_2$  that was measured by falling-sphere viscometry, 1-atm viscosities were measured using a concentric-cylinder viscometer (Scarfe, 1973, 1977a). Viscosities and temperatures, respectively, have uncertainties of  $\pm 5\%$  and  $\pm 5^\circ\text{C}$ .

High-pressure viscosities were measured in a solid-media, high-pressure apparatus (Boyd and England, 1960) with a furnace assembly of 0.75-inch diameter incorporating a graphite heater with a  $3^\circ$  tapered inner wall, which reduces the temperature gradient along the sample to  $10^\circ\text{C}$  (Kushiro, 1976). Sealed platinum capsules, 5 mm in diameter and 10 mm long, were used to contain the sample in all experiments. The piston-out technique was used with a  $-4\%$  correction for friction. Pressures have an uncertainty of  $\pm 0.5$  kbar, and temperatures, measured with Pt-Pt90Rh10 thermocouples, have an uncertainty of  $\pm 10^\circ\text{C}$ . Quench rates were approximately  $125^\circ/\text{sec}$ , and rapid approach to the desired experimental temperatures was facilitated by a new programmable controller (Hadidiacos, *Year Book* 76, pp. 664-668).

Crystalline starting materials were

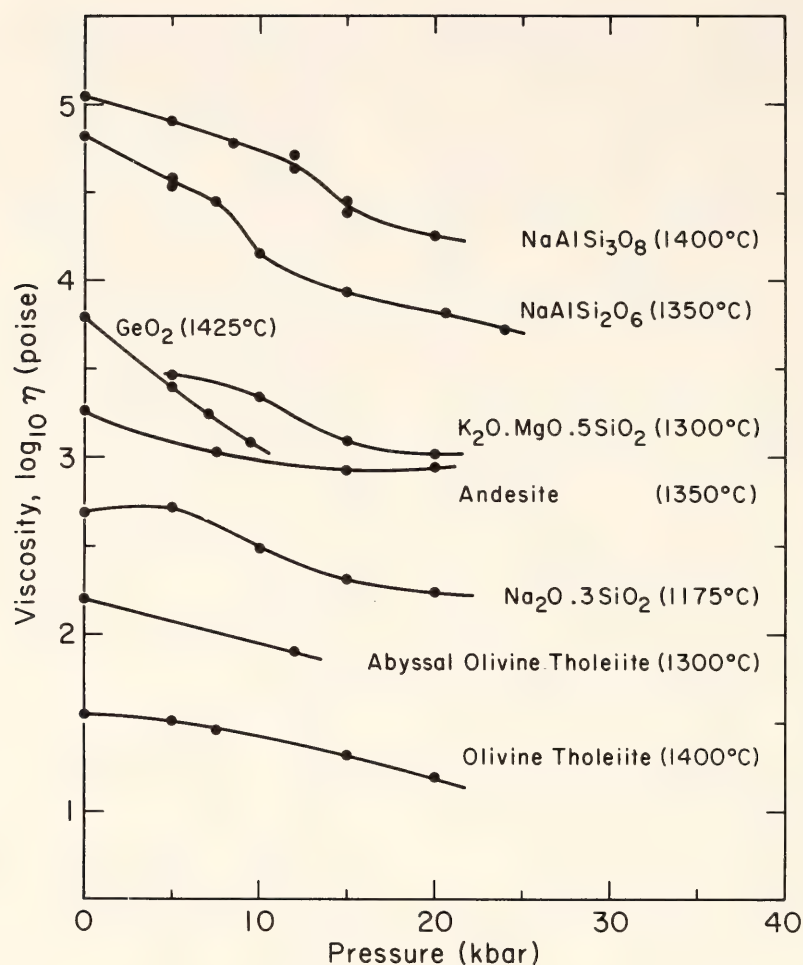


Fig. 55. Viscosity as a function of pressure for melts that have a highly polymerized structure at 1 atm (see text). All measurements were made isothermally at the temperatures shown. References are given in Table 26.

prepared from mixtures of reagent-grade  $\text{Na}_2\text{CO}_3$ ,  $\text{CaCO}_3$ ,  $\text{MgO}$ , and  $\text{SiO}_2$  at 1 atm. Glasses were not used because they soften and deform at temperatures above the glass transition. A variety of spheres of different densities (chrome diopside, forsterite, calcic plagioclase,  $\text{ZrO}_2$ , BN, and Au-Pd alloy) with diameters generally  $<1$  mm were used. Mineral and refractory spheres were made using the sphere-making device designed by Bond (1951).

Under each set of temperature-pressure conditions, two or more runs of different duration were made to determine the sinking or floating velocity of spheres of two different densities. After the charge was quenched and sectioned, the melt viscosity was calculated from the velocity and density of the spheres using

Stokes's equation combined with the Faxen correction for wall effects (Shaw, 1963). Viscosities have maximum uncertainties of  $\pm 20\%$ .

Melt densities were determined for each data point after the method of Fujii and Kushiro (*Year Book* 76, pp. 419–424). Densities of glasses were measured with a Berman balance.

### Results

Measurements at 1 atm on melts of sodium disilicate, sodium metasilicate, and diopside composition are shown in Fig. 56. A linear relationship exists between the logarithm of the viscosity and reciprocal temperature. The temperature dependence of the viscosity can be described by an Arrhenius relationship of



TABLE 26. Change in Viscosity and Density between 1 atm and 20 kbar\*

Melt Composition	NBO/T	Density, % Change		Reference
		Glass	Melt	
CaMgSi <sub>2</sub> O <sub>6</sub>	2		8.3† (15 kbar)	This report
Na <sub>2</sub> O·SiO <sub>2</sub>	2		6.7	This report
Na <sub>2</sub> O·2SiO <sub>2</sub>	1		6.3†	This report
K <sub>2</sub> O·MgO·5SiO <sub>2</sub>	0.80			Kushiro, 1977
Na <sub>2</sub> O·3SiO <sub>2</sub>	0.67			Kushiro, 1976
NaAlSi <sub>2</sub> O <sub>6</sub>	0	6.8		Kushiro, 1976
NaAlSi <sub>3</sub> O <sub>8</sub>	0	5.7		Kushiro, 1978
GeO <sub>2</sub>	0			Kushiro, <i>Year Book 77</i>
Abyssal tholeiite	<1	9.1 (18 kbar)	7.1 (12 kbar)	Fujii and Kushiro, <i>Year Book 76</i>
Olivine tholeiite	<1	3.9	12.2	Fujii and Kushiro, <i>Year Book 76</i>
Andesite	<1	4.7 (7.5–20 kbar)		Kushiro <i>et al.</i> , 1976

\*Measurements made isothermally at temperatures listed in Figs. 55, 57, 58. Pressure in parentheses indicates that measurements were performed to that pressure (e.g. 15 kbar) or over that pressure range (e.g. 10–20 kbar). Plus sign indicates increase; minus sign, decrease; all density changes are positive. NBO/T is the theoretical ratio of nonbridging oxygens to tetrahedrally coordinated cations in the melt as deduced from the chemical composition (Bottinga and Weill, 1972; Scarfe, 1973).

† Melt density at 1 atm obtained by extrapolation (Fig. 58).

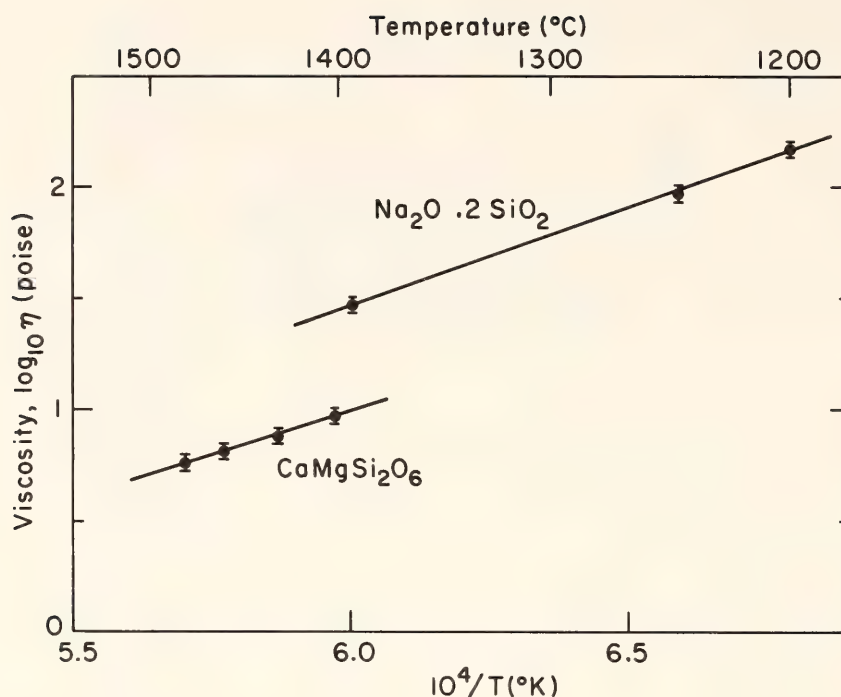


Fig. 56. Viscosity vs. reciprocal temperature for melts of  $\text{Na}_2\text{O} \cdot 2\text{SiO}_2$  and  $\text{CaMgSi}_2\text{O}_6$  composition.

the form  $\eta = \eta_0 \exp (E_\eta/RT)$ , where  $\eta_0$  is a constant and  $E_\eta$  is the activation energy for viscous flow. Activation energies for  $\text{Na}_2\text{O} \cdot 2\text{SiO}_2$  and  $\text{CaMgSi}_2\text{O}_6$ , respectively, were calculated as 41 and  $37 \pm 3$  kcal/mole. Measurements on sodium disilicate agree with the results of Shartsis *et al.* (1952), and the viscosity at  $1200^\circ\text{C}$ , the temperature at which the high-pressure experiments were made, was taken as 151 poises. Measurements on diopside are in accord with data published by Kirkpatrick (1974), and the viscosity at  $1640^\circ\text{C}$ , which was obtained by linear extrapolation, was 3 poises.

Measurements as a function of pressure were made isothermally at temperatures above the liquidus. Run durations ranged between 1 min and 1 hr. Under each set of temperature-pressure conditions, at least two runs of different duration were made to determine the sphere velocity. All time-distance curves were straight lines, most of them intersecting the time axis rather than passing through the origin (Kushiro, 1976; Kushiro *et al.*, 1976). For all compositions, viscosities increase with increasing pressure (Fig.

57); above 15 kbar, however, the viscosity of a melt of  $\text{Na}_2\text{O} \cdot 2\text{SiO}_2$  composition decreased. Changes in viscosity as a function of pressure are shown in Table 26.

In the same pressure range the density of melts and glasses increases (Fig. 58). The percentage increases are shown in Table 26. In the pressure range up to 15 kbar, glasses formed from melts exhibit smaller density changes than the melts themselves. Melt densities were used exclusively in the calculation of melt viscosities.

### Discussion

The positive pressure dependence of the viscosity of melts of  $\text{Na}_2\text{O} \cdot \text{SiO}_2$ ,  $\text{Na}_2\text{O} \cdot 2\text{SiO}_2$ , and  $\text{CaMgSi}_2\text{O}_6$  composition contrasts strongly with the negative pressure dependence of the viscosity of compositions having a polymerized three-dimensional anionic network at 1 atm. Many inorganic and polymer liquids exhibit increasing viscosities with pressure (Bridgman, 1931; O'Reilly, 1964; Sakka and MacKenzie, 1969); hence, the re-



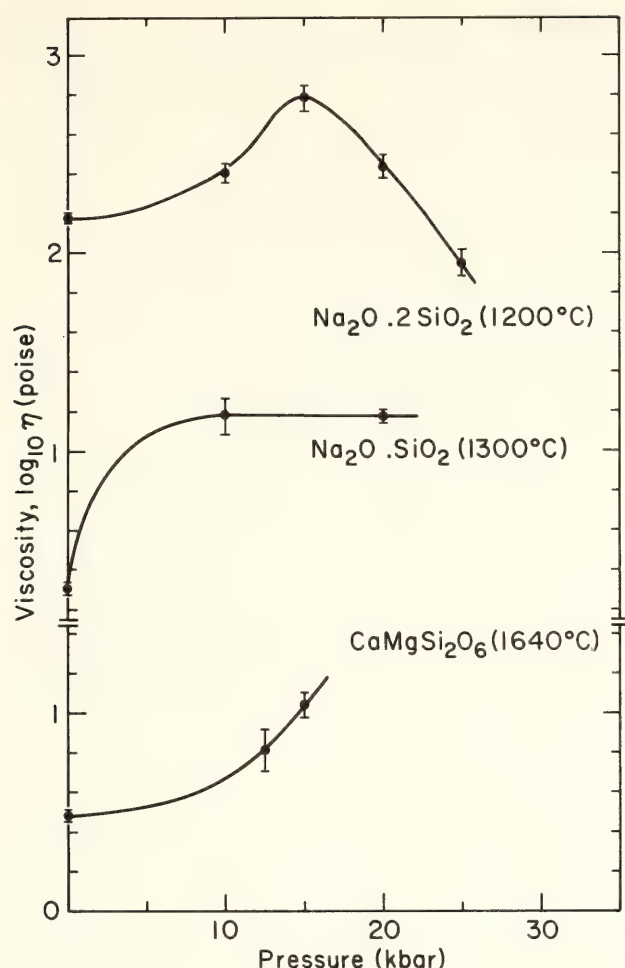


Fig. 57. Viscosity as a function of pressure for melts of  $\text{Na}_2\text{O} \cdot \text{SiO}_2$ ,  $\text{Na}_2\text{O} \cdot 2\text{SiO}_2$ , and  $\text{CaMgSi}_2\text{O}_6$  composition. All measurements were made isothermally at the temperatures shown.

sults obtained on polymerized melts ( $\text{NBO}/\text{T} < 1$ ) indicate a fundamental difference in behavior under compression of highly polymerized vs. depolymerized melts. Raman spectroscopic studies of glass of jadeite composition suggest that these highly polymerized melts undergo network collapse and weakening with pressure (Sharma, Virgo, and Mysen, *Year Book* 77, pp. 658–662). Conversely, similar detailed structural studies on melts of diopside composition demonstrate that there is a significant increase in  $\text{Si}_2\text{O}_6^{4-}$  in the melt at the expense of  $\text{SiO}_4^{4-}$  and  $\text{Si}_2\text{O}_5^{2-}$  as a function of pressure, and this result provides an explanation for the positive pressure dependence of viscosity (Mysen, Virgo, and Scarfe, this Report).

The decrease in the viscosity of melts

of sodium disilicate composition above 15 kbar, although unexpected, can be explained in the context of polymerization under compression up to 15 kbar and a collapse and weakening of the structure between 15 and 25 kbar. Support for this interpretation comes from the small density increase between 1 atm and 15 kbar and the larger density change thereafter. This observation raises the question as to whether at sufficiently high pressures other melts might exhibit similar reversals in viscosity behavior.

Although density data on all glasses and melts studied so far are not available (Fig. 58; Table 26), sodium disilicate, sodium metasilicate, and diopside melts appear to have smaller density changes than polymerized melts as a function of pressure. This observation is in accord with earlier work on alkali silicate glasses and melts (Bridgman and Simon, 1953; Bockris and Kojonen, 1960).

Finally, the 1-atm viscosity data may be used to infer that melts depolymerize as a function of temperature. This observation is supported by Raman spectroscopic evidence (Mysen, Virgo, and Scarfe, this Report).

#### VISCOSITY OF SILICATE MELTS AS A FUNCTION OF PRESSURE: STRUCTURAL INTERPRETATION

*B. O. Mysen, D. Virgo, and C. M. Scarfe*

The viscosity of rock-forming silicate melts is an important characteristic in understanding processes of magma aggregation and ascent to the surface from sites of melting, the rheology of crystal-liquid suspensions, and distribution of minerals in magma chambers during their crystallization. It has been observed (Kushiro, *Year Book* 75, pp. 611–614; Kushiro, 1978) that the viscosity of melts with a three-dimensional network structure decreases with increasing pressure to at least 24 kbar (see Scarfe, Mysen, and Virgo, this Report).

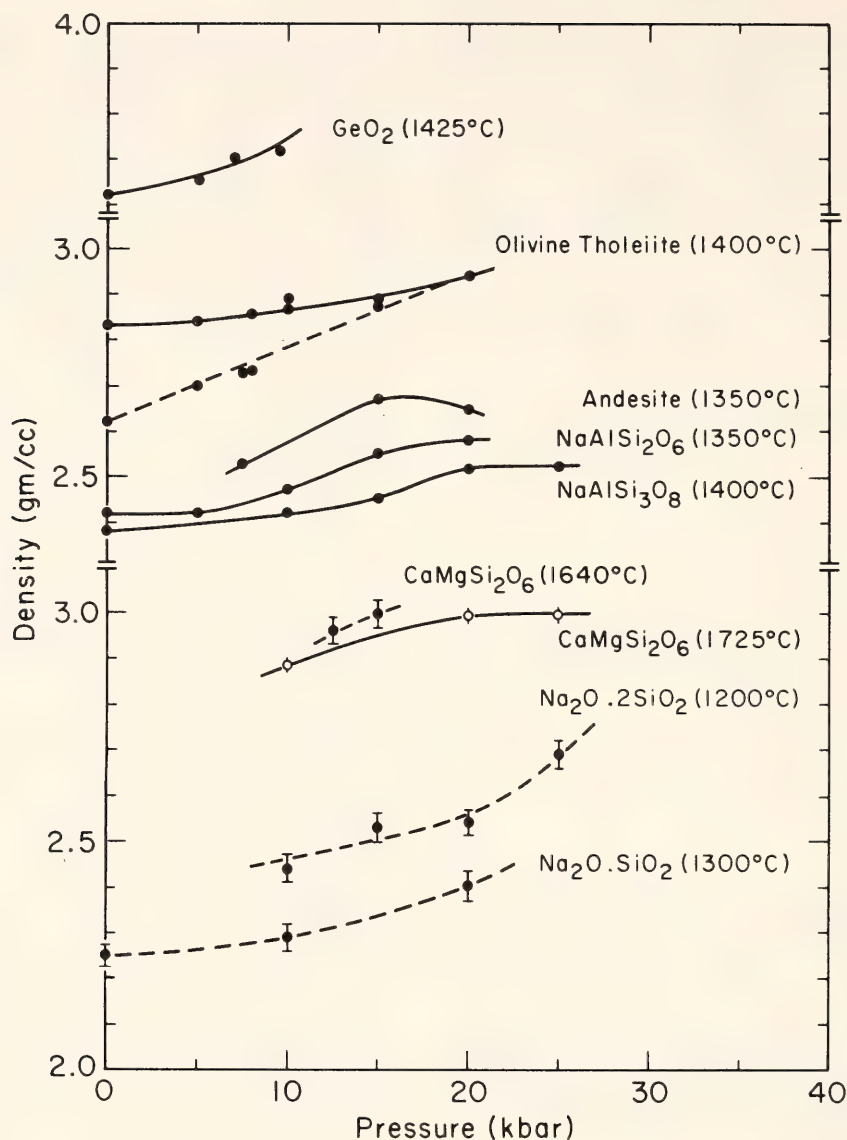


Fig. 58. Density of glasses and melts as a function of pressure. Glasses are shown as solid lines; melts, as broken lines. All measurements were made on melts and glasses prepared at the temperatures shown. References are given in Table 26.

Kushiro (*Year Book* 77, pp. 675–677) noted that this negative pressure dependence may not be a general rule for all silicate melts. He found that the viscosity of hydrous andesite melt increased between 5 and 15 kbar. The melts contained about 4 wt %  $\text{H}_2\text{O}$ . This amount of water in solution corresponds to about 2.5 bridging oxygens per silicon ( $\text{BO}/\text{Z}^* = 2.5$ ) with an albite melt as the model for andesite (e.g., Burnham, 1975). This value compares with  $\text{BO}/\text{Z} = 4$  for a

\* Z denotes tetrahedrally coordinated cation, most likely Si, Al, Ti,  $\text{Fe}^{3+}$ , or P.

three-dimensional network structure. Scarfe, Mysen, and Virgo (this Report) found that the viscosities of  $\text{CaMgSi}_2\text{O}_6$  (Di),  $\text{Na}_2\text{Si}_2\text{O}_5$  (NS2), and  $\text{Na}_2\text{SiO}_3$  (NS) melts all increase with increasing pressure under isothermal conditions. In these melts  $\text{BO}/\text{Z}$  is less than 3.

All investigated melts that show a negative pressure dependence of viscosity have a melt structure that has a large proportion of a three-dimensional network unit, at least at 1 atm pressure (Brawer and White, 1975, 1977; Virgo, Seifert, and Mysen, this Report). Results of Raman spectroscopic determination



of the structure of quenched melt of  $\text{NaAlSi}_2\text{O}_6$  composition indicate that it retains its three-dimensional network structure to at least 40 kbar (Sharma, Virgo, and Mysen, *Year Book* 77, pp. 658–662). The melts that show an increase in viscosity have a less polymerized structure at 1 atm (Etchepare, 1972; Bates *et al.*, 1974; Brawer and White, 1975; Mysen, Virgo, and Seifert, this Report). The effect of pressure on these melts is largely unknown.

To further the understanding of the effect of pressure on structures and derivative properties of silicate melts, a Raman spectroscopic investigation has been carried out with melts on the join  $\text{Na}_2\text{O}-\text{SiO}_2$  and  $\text{CaMgSi}_2\text{O}_6$  composition quenched from different temperatures and pressures. The temperatures and pressures chosen were those at which the viscosity was determined (Scarfe, Mysen, and Virgo, this Report).

The quenched melts were prepared from spectroscopically pure (Johnson and Matthey)  $\text{SiO}_2$ ,  $\text{MgO}$ ,  $\text{CaCO}_3$ , and reagent-grade  $\text{Na}_2\text{CO}_3$ . Experiments at 1 atm were conducted in a vertical quenching furnace. The charges were quenched in Hg at rates exceeding  $500^\circ\text{C}/\text{sec}$ . High-pressure experiments were carried out in a solid-media, high-pressure apparatus (Boyd and England, 1960) with quenching rates near  $250^\circ\text{C}/\text{sec}$ .

Raman spectroscopy was conducted with a Jobin-Yvon, double-grating spectrometer with a  $90^\circ$  scattering geometry and a photon-counting detection system. The excitation radiation was the 4880-Å line from an  $\text{Ar}^+$  ion laser operating with 200–400 mW power.

Melt of  $\text{CaMgSi}_2\text{O}_6$  composition was chosen for a detailed study of the influence of pressure and temperature on the structure of a relatively depolymerized melt. Its anionic structure closely resembles that of NS melt at 1 atm (Brawer and White, 1975; Mysen, Virgo, and Seifert, this Report) in that both melts consist of separate tetrahedra,

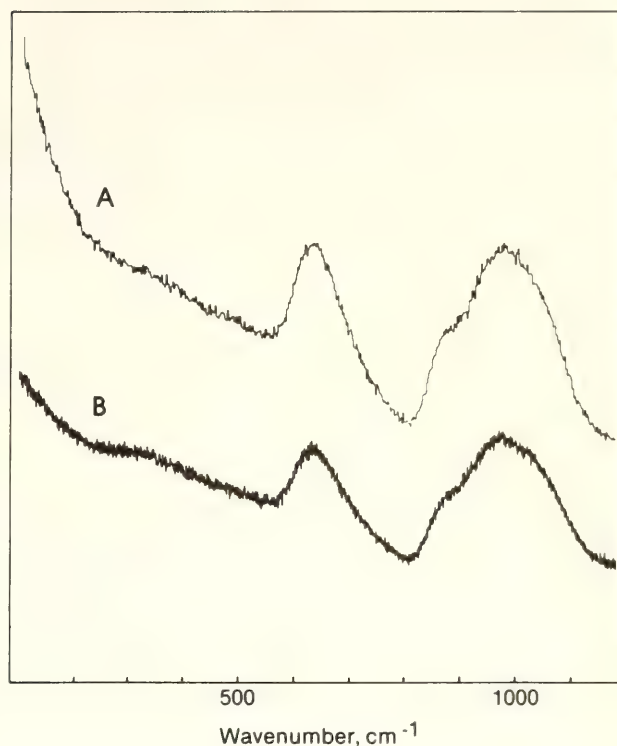


Fig. 59. Raman spectra of quenched melt of  $\text{CaMgSi}_2\text{O}_6$  composition at 1 atm as a function of quenching temperature.

chains, and probably sheets. The Di melt has a greater proportion of separate  $\text{SiO}_4^{4-}$  units than NS melt (respectively, 15–20% and less than 10%). Inasmuch as the intensity of Raman signals is more sensitive to depolymerized structural units (Brawer and White, 1975), any influence of pressure and temperature on the silicate network is more likely to be resolved in Di melt than in NS melt.

Raman spectra of Di melt at 1 atm quenched from  $1400^\circ$  and  $1550^\circ\text{C}$  are shown in Fig. 59. The band assignments are the same as those of Mysen, Virgo, and Seifert (this Report) and are summarized in Table 27. The intensity ratio reflecting the proportion of nonbridging to bridging oxygens ( $\text{NBO}/\text{BO}$ ) [ $I(980)/I(1060)$ ] increases by nearly 30% between  $1400^\circ$  and  $1550^\circ\text{C}$ . The intensity ratio reflecting the proportion of free  $\text{SiO}_4^{4-}$  tetrahedra [ $I(880)/I(980)$ ] also increases with increasing temperature (by about 15% between  $1400^\circ$  and  $1550^\circ\text{C}$ ).

Raman spectra of Di melts in the

TABLE 27. Band Assignments of Raman Spectra\*

Composition	T, °C	P, kbar	Wave Number, cm <sup>-1</sup>					
CaMgSi <sub>2</sub> O <sub>6</sub>	1400	0.001	...	631,s,p	...	864,m,p,(sh)	980,s,p	1034,s,p,(sh)
CaMgSi <sub>2</sub> O <sub>6</sub>	1550	0.001	...	640,s,p	...	877,m,p	983,s,p	1053,m,p,(sh)
CaMgSi <sub>2</sub> O <sub>6</sub>	1550	10	...	638,s,p	...	864,m,p,(sh)	974,s,p	1041,s,p,(sh)
CaMgSi <sub>2</sub> O <sub>6</sub>	1650	10	...	640,s,p	...	880,m,p,(sh)	984,s,p	1053,m,p,(sh)
CaMgSi <sub>2</sub> O <sub>6</sub>	1685	20	...	653,s,p	...	887,m,p,(sh)	973,s,p	1050,m,p,(sh)
Na <sub>2</sub> Si <sub>3</sub> O <sub>7</sub>	1200	0.001	535,s,p	587,m,p,(sh)	780,w,p	...	945,w,p	1098,s,p
Na <sub>2</sub> Si <sub>3</sub> O <sub>7</sub>	1200	15	540,s,p	590,w,p,(sh)	770,w,p	...	950,w,p	1098,s,p
Na <sub>2</sub> Si <sub>3</sub> O <sub>7</sub>	1200	25	540,s,p	...	769,w,p	...	928,w,p	1098,s,p
Na <sub>2</sub> Si <sub>2</sub> O <sub>5</sub>	1200	10	567,s,p	593,m,p,(sh)	760,w,p	...	944,m,p	1093,s,p
Na <sub>2</sub> Si <sub>2</sub> O <sub>5</sub>	1200	15	564,s,p	600,m,p,(sh)	758,w,p	...	942,m,p	1094,s,p
Na <sub>2</sub> Si <sub>2</sub> O <sub>5</sub>	1200	20	570,s,p	590,w,p,(sh)	753,w,p	...	944,m,p	1096,s,p
Na <sub>2</sub> Si <sub>2</sub> O <sub>5</sub>	1200	25	573,s,p	...	763,w,p	...	944,m,p	1096,s,p

\* Symbols: s, strong (uncertainty 3–4 cm<sup>-1</sup>); m, medium (uncertainty 5–6 cm<sup>-1</sup>); w, weak (uncertainty 10 cm<sup>-1</sup>); p, polarized; (sh), shoulder (add 100% to uncertainty).



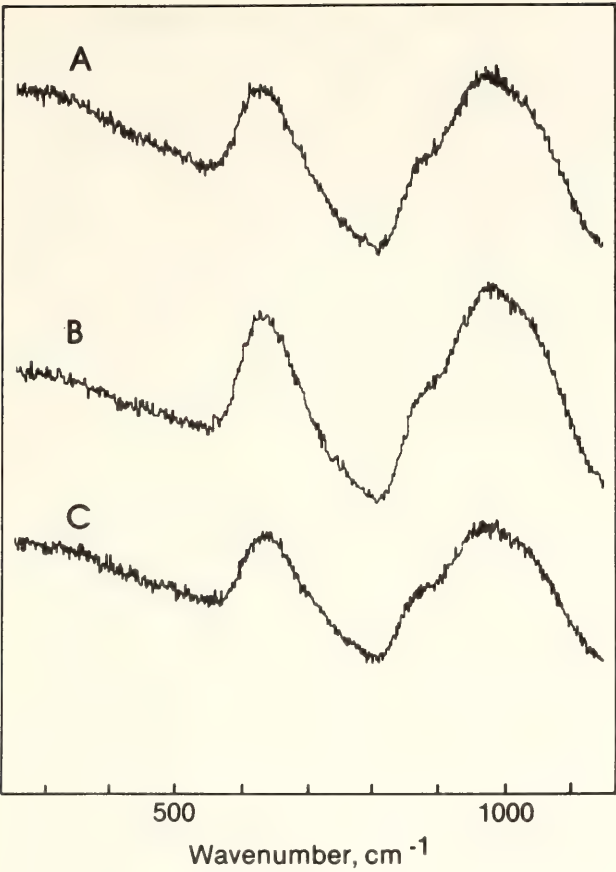


Fig. 60. Raman spectra of quenched melt of  $\text{CaMgSi}_2\text{O}_6$  composition as a function of quenching temperature and pressure.

pressure range from 1 atm to 20 kbar and at temperatures to  $1685^\circ\text{C}$  are shown in Fig. 60, and the band assignments are given in Table 27. It can be seen from these data that NBO/BO of the polymeric units decreases and the proportion of  $\text{SiO}_4^{4-}$  decreases with increasing pressure. The influence of decrease of temperature is less pronounced at high pressure than at 1 atm. It should be emphasized that because the data are from quenched melts, some back-reaction may have occurred during the quenching. The extent of this problem cannot be assessed with the present data, but it is clear that the degree of polymerization of melt of Di composition shows structural changes with variations of temperature and pressure.

The equilibrium between the anionic species in metasilicate melts may be expressed as a combination of  $\text{SiO}_4^{4-}$ ,

TABLE 28. Proportions of  $\text{SiO}_4^{4-}$ ,  $\text{Si}_2\text{O}_6^{4-}$ , and  $\text{Si}_2\text{O}_5^{2-}$  in Di Melt as a Function of Pressure and Temperature

<i>P</i> and <i>T</i>	$\text{SiO}_4^{4-}$	$\text{Si}_2\text{O}_6^{4-}$	$\text{Si}_2\text{O}_5^{2-}$
1 atm, $1400^\circ\text{C}$	23	31	46
1 atm, $1550^\circ\text{C}$	20	40	40
10 kbar, $1550^\circ\text{C}$	21	38	41
10 kbar, $1650^\circ\text{C}$	21	38	41
20 kbar, $1685^\circ\text{C}$	22	34	44

$\text{Si}_2\text{O}_6^{4-}$ , and  $\text{Si}_2\text{O}_5^{2-}$  units. Mysen, Virgo, and Seifert (this Report) discussed methods for estimating the proportions of these units from the Raman spectra. Results for quenched Di melt are shown in Table 28.

Melts of  $\text{Na}_2\text{Si}_3\text{O}_7$  composition show a decrease in viscosity with increasing pressure under isothermal conditions (Kushiro, *Year Book* 75, pp. 611–614). Band assignments of Raman spectra of quenched NS3 melt under the same conditions as studied by Kushiro are shown in Table 27. The spectra are similar in most respects within experimental resolution and also agree with those of Brawer and White (1975). The structure of quenched NS3 melt is a combination of a three-dimensional network and a somewhat more depolymerized unit (e.g., sheet) under all conditions studied. The existence of a band near  $950\text{ cm}^{-1}$  is diagnostic of the depolymerized component.

Two pressure-dependent features are discernible in the spectra. The intensity ratio  $I(490)\text{--}I(600)$  increases with increasing pressure so that the high-frequency band is not seen at the highest pressures. The intensity ratio  $I(950)\text{--}I(1100)$  shows a slight increase with increasing pressure between 15 and 25 kbar, indicating that the proportion of nonbridging oxygens may increase very slightly with increasing pressure.

Melts of  $\text{Na}_2\text{Si}_2\text{O}_5$  composition show an initial increase in viscosity with pressure (to about 15 kbar) before the vis-

cosity begins to decrease. The density of this melt increases more rapidly in the pressure regime above 15 kbar than below 15 kbar (Scarfe, Mysen, and Virgo, this Report). Band assignments of Raman spectra of the quenched NS2 melt in the same pressure and temperature range as the viscosity and density measurements are given in Table 27. This melt has an anionic structure similar to that of sheets at 1 atm (Brawer and White, 1975). According to the data (Table 27), it retains this structure to at least 25 kbar. The only pressure-dependent feature observed in the spectra is the increase in  $I(570)/I(600)$  with increasing pressure.

The generally contrasting pressure dependence of the viscosity of silicate melts is primarily related to the gross difference in the polymerization of the network structure. The viscosity of melts is positively correlated with NBO/BO. This ratio decreases with increasing pressure and with decreasing temperature in melts with NBO/Z greater than 1, as exemplified by melt of Di composition in the present report. The flow units in such melts may be depolymerized silicate components, a modifying cation, or both (Bockris *et al.*, 1955). As the pressure is increased, the size of such units may increase, resulting in greater viscosity.

In melts that are more polymerized than sheets, it is likely that bonds in the network must be broken during viscous flow (e.g., Taylor and Rindone, 1970). The structure of the silicate framework in melts with NBO/Z less than 1 does not seem to change as a function of pressure, yet the viscosity of these melts decreases significantly (Scarfe, Mysen, and Virgo, this Report). The strength of bonds [such as (Si,Al)-O-(Si,Al)] depends both on the bond length and on the presence of modifying cations. It has been found that highly polymerized silicate melts are more compressible than depolymerized melts (Bridgman and Simon, 1953; Bockris and Kojonen, 1960; Kushiro, 1976, 1978; Scarfe, Mysen, and

Virgo, this Report). A consequence of this compressibility is a compaction of the alkali and alkaline earth polyhedra. As a result, the (Si,Al)-O-(Si,Al) bonds become more polarized and hence weakened (e.g., Hess, 1977). This weakening results in decreasing viscosity (Bottinga and Weill, 1972; Hess, 1977) and is probably responsible for the lowering of the viscosity of highly polymerized melts with increasing pressure.

#### PRESSURE DEPENDENCE OF THE GLASS TRANSITION TEMPERATURE IN GLASSES OF DIOPSIDE, ALBITE, AND SODIUM TRISILICATE COMPOSITION

*M. Rosenhauer, C. M. Scarfe, and D. Virgo*

Contrasting isothermal pressure dependence of the viscosity of highly polymerized vs. depolymerized silicate melts has been reported by Scarfe, Mysen, and Virgo (this Report). Melts such as  $\text{NaAlSi}_3\text{O}_8$ ,  $\text{NaAlSi}_2\text{O}_6$ , and  $\text{Na}_2\text{Si}_3\text{O}_7$  (Kushiro, 1976, 1978) show a negative pressure dependence, whereas  $\text{Na}_2\text{Si}_2\text{O}_5$ ,  $\text{Na}_2\text{SiO}_3$ , and  $\text{CaMgSi}_2\text{O}_6$  show a positive pressure dependence. Because there are structural similarities between a glass and its melt, particularly close to the temperature of the glass transition (Riebling, 1968), the pressure effect on the temperature of the glass transition should correlate with the pressure dependence of the viscosity of the melt. Three compositions (diopside, albite, and sodium trisilicate) were selected to test this hypothesis.

#### *Experimental Methods*

At 1 atm, glass transition temperatures ( $T_g$ ) were determined by viscosity, thermal expansion, and DTA methods. Viscosities were measured using a fiber-extension viscometer; linear thermal expansion measurements were made relative to fused silica on glass rods 10 cm long at a heating rate of 4°C/min; and DTA scans were performed using an



$\text{Al}_2\text{O}_3$  standard and a heating rate of  $10^\circ\text{C}/\text{min}$  (Scarfe, 1977b and unpublished data). At high pressures, DTA experiments (Eggler and Rosenhauer, 1978) were performed in an internally heated, gas-media pressure vessel. To ensure contact between the sample and thermocouple, the starting materials were fused around the thermocouple tip and subsequently quenched to a glass. Heating and cooling rates were controlled between  $22^\circ$  and  $28^\circ\text{C}/\text{min}$ . The DTA signals were monitored on a strip-chart recorder having a sensitivity of  $5\ \mu\text{V}/\text{in}$ . Because cooling paths affect the glass transition temperature (Moynihan *et al.*, 1976a), identical procedures were used for all measurements; however, no detailed study of the influence of  $P$ - $T$  path on  $T_g$  was undertaken.

### Results and Discussion

At 1 atm the glass transition, defined by the temperature where the glass has a viscosity of  $10^{13}$  poises, is lower than  $T_g$  determined by thermal expansion or DTA methods (Table 29). These differences are a function of structural relaxation in the glass and consequently depend on the time scale of the experiment. If measurements are performed slowly over several minutes, as in the viscosity experiments, property changes are observed to commence at significantly lower temperatures than if the measurements are performed more rapidly, as in the DTA experiments (Wong and Angell, 1976).

At high pressures the compositions that have highly polymerized network structures at 1 atm have glass transition temperatures that remain essentially unchanged, as in sodium trisilicate, or exhibit a negative pressure dependence, as in albite. Diopside, conversely, has a less polymerized melt structure at 1 atm and shows a positive pressure dependence of  $T_g$  (Table 29 and Fig. 61).

High-pressure DTA also provides indirect information on the pressure de-

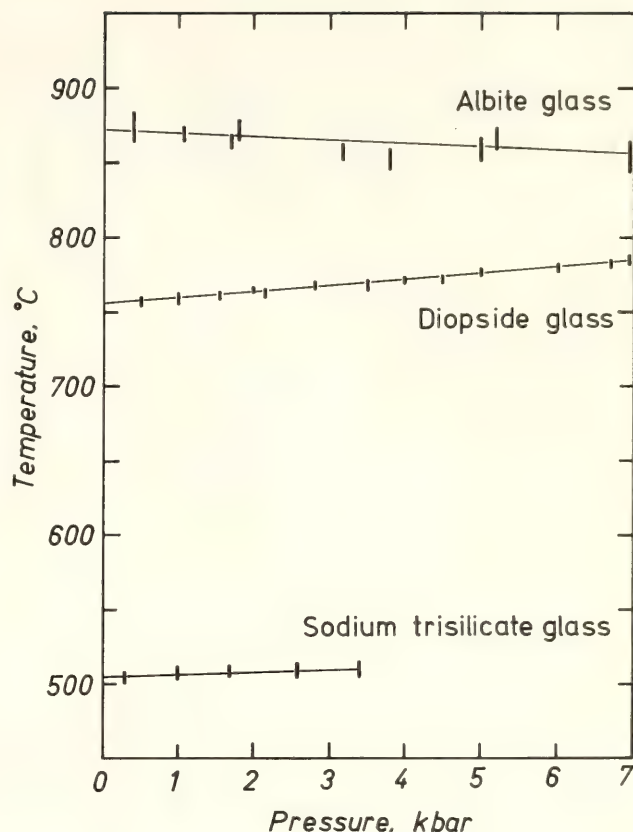


Fig. 61. Differential thermal analysis measurements of  $T_g$  as a function of pressure.

pendence of the enthalpy at  $T_g$ . The glass transition temperature is defined on an enthalpy-temperature plot as the intersection between the supercooled liquid and glass curves (Fig. 62). At temperatures above the glass transition the rate of structural relaxation is rapid, whereas at temperatures below the transition, relaxation has effectively ceased on the time scale of the experiment. The rate at which these rearrangements take place should be closely related to the viscosity of the supercooled liquid or glass. It is assumed, therefore, that similar structural rearrangements are involved in viscous flow and in enthalpy-related structural relaxation at  $T_g$  (Moynihan *et al.*, 1976b; Wong and Angell, 1976). Only the time scales for the two types of response are different. Thus, for the positive  $dT_g/dP$  shown by  $\text{CaMgSi}_2\text{O}_6$ , structural relaxation is arrested at higher temperatures than at 1 atm, and this result implies an increase in viscosity.

TABLE 29. Properties of Glasses and Melts

Composition	$T_g(^{\circ}\text{C})$ at 1 atm			$dT_g/dP$ , $^{\circ}\text{C}/\text{kbar}$	Melt Viscosity, $d\eta/dP^*$
	Viscosity at $10^{13}$ poises	Thermal Expansion	DTA		
Diopside, synthetic	$703 \pm 15$	$730 \pm 5$	755§	$3.7 \pm 0.3$	3.7 (1640°C)
Diopside, Twin Lakes, Ca.†			$755 \pm 10\dagger$ $725 \pm 10\dagger$		
Albite, synthetic	$794 \pm 15$	763	$865 \pm 20$	$-2.5 \pm 1.0$	-4.7 (1400°C)
Albite, Amelia, Va.†		815¶	$820 \pm 20$		
Sodium trisilicate	478**	$508\dagger\dagger$	$505 \pm 10\dagger$ $480 \pm 10\dagger$	$1.0 \pm 1.0$	-2.3 (1175°C)

\* Factor increase or decrease between 1 atm and 15 kbar. Experiments performed isothermally at temperatures shown (Scarfe, Mysen, and Virgo, this Report).

† Samples of natural diopside and albite were kindly provided by Drs. H. S. Yoder, Jr., and R. H. McCallister.

‡ Derived by both peak and tangent methods.

§ Briggs, 1975.

|| Arndt and Häberle, 1973.

¶ Vergano *et al.*, 1967.

\*\* English, 1923.

†† Turner and Winks, 1930.



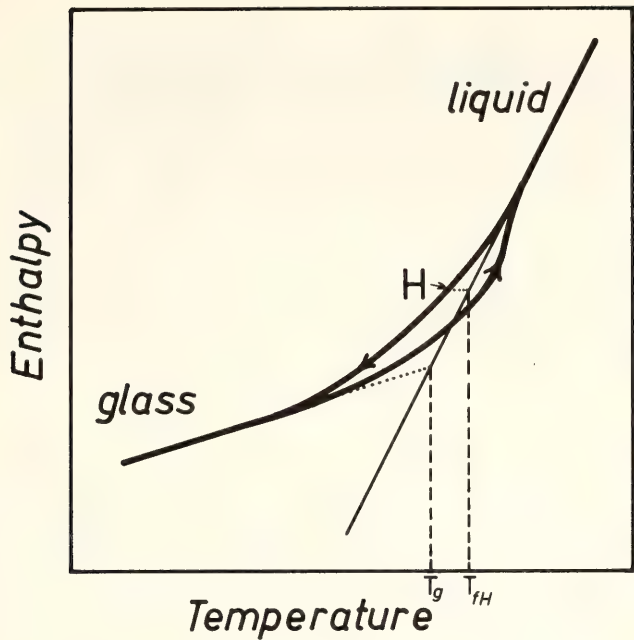


Fig. 62. Variation of enthalpy with temperature during cooling and subsequent reheating through the glass transition region (after Moynihan *et al.*, 1976a).  $T_g$ , glass transition temperature;  $T_{fH}$ , fictive temperature for enthalpy  $H$ . On cooling to low temperatures,  $T_{fH}$  reaches a constant limiting value,  $T_g$ .

For the negative  $dT_g/dP$  shown by  $\text{NaAlSi}_3\text{O}_8$ , the converse is true.

A comparison with melt viscosities (Table 29) shows that the change in the temperature of the glass transition with pressure exhibits the same general trend as the isothermal pressure dependence of melt viscosity. Less polymerized melts show an increase, and highly polymerized melts a decrease, in  $T_g$  and viscosity with pressure.

COMPRESSIONAL WAVE VELOCITY IN  
PARTIALLY MOLTEN PERIDOTITE AT  
HIGH PRESSURES

*T. Murase and I. Kushiro*

Direct measurements of elastic wave velocities in partially molten mantle minerals are needed for understanding the nature of the seismic low-velocity zone (LVZ) in the earth. Murase *et al.* (*Year Book 76*, pp. 414–416) reported the compressional wave velocity ( $V_p$ ) of

a partly melted peridotite at 1 atm. These results, however, cannot be directly applied to the LVZ because 1 atm pressure is not sufficient to eliminate porosity. In the present studies,  $V_p$  was measured at 5 kbar through the melting range of the peridotite. Preliminary measurements were also made at 10 kbar. Because of their importance to magma aggregation and seismic identification, the degree of melting and the textural distribution of the melt were also measured.

*Experimental*

The starting material was a spinel lherzolite inclusion (BCP) from a Cenozoic alkali basalt eruption in British Columbia, collected by T. N. Irvine. The lherzolite consists of olivine, orthopyroxene, clinopyroxene, and a small amount of spinel. The bulk chemical composition determined by the conventional wet chemical analysis method is given in Table 30. The  $\text{MgO/FeO}$  is 4.61, which is close to the median value given by Kuno and Aoki (1970) for 65 spinel lherzolite inclusions from around the world.

The spinel lherzolite sample was ground to 100–500  $\mu\text{m}$  grain size, dried, and packed into Pt containers 0.8 cm in

TABLE 30. Chemical Composition of  
Spinel Lherzolite Used for  
Velocity Measurements\*

$\text{SiO}_2$	45.80
$\text{TiO}_2$	0.17
$\text{Al}_2\text{O}_3$	1.34
$\text{Fe}_2\text{O}_3$	1.98
$\text{FeO}$	6.46
$\text{MnO}$	0.15
$\text{MgO}$	38.02
$\text{CaO}$	4.30
$\text{Na}_2\text{O}$	0.24
$\text{K}_2\text{O}$	0.02
$\text{P}_2\text{O}_5$	0.02
$\text{NiO}$	0.25
$\text{Cr}_2\text{O}_3$	0.53
Total	99.28

\* Analyst, H. Haramura.

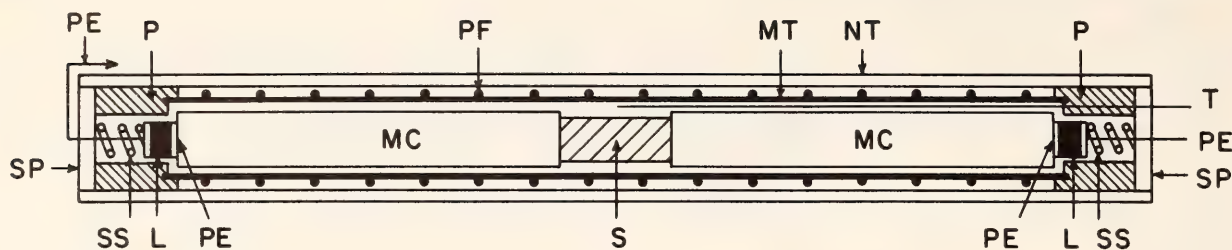


Fig. 63. Schematic diagram of the furnace. *S*, specimen; *MC*, mullite cylinder; *MT*, mullite tube; *PF*, platinum-wound furnace; *NT*, nickel tube; *PE*, platinum electrode; *L*, lithium niobate transducer; *SS*, stainless steel spring; *SP*, stainless steel plate; *P*, pyrophyllite; *T*, thermocouple.

diameter and 2 cm long. The containers were sealed by welding so that argon gas could not enter cracks or grain boundaries in the charge during the measurements. Before the charge and the transducer were assembled, the sealed charge was compressed at 5 kbar in a gas-media, high-pressure apparatus to avoid extensive deformation during the velocity measurements. The compressed charge was then placed between mullite rods, 1.0 cm in diameter and 7.0 cm long, that served as buffer rods. Lithium niobate transducers of 1-MHz natural frequency were cemented to the ends of mullite rods, as shown in Fig. 63. Sauereisen No. 8 cement was used as an adhesive to establish acoustic contact between the surface of the charge and rods. The cement was heated with the charge and rods for 5 hr at about 1100°C in air. The thickness of the cement layer was less than 0.02 cm. A stainless steel spring was placed between the other side of the transducer and the side wall of the nickel shell. All free space in and around the furnace assembly was filled with alundum powder to prevent convection of argon gas arising from the large temperature gradient in the furnace. The temperature variation within the space occupied by the charge was within 5° at 1000°C and 5 kbar; the temperature around the transducer was below 100°C.

The velocity measurements were made in the gas-media, high-pressure apparatus designed by Yoder (1950). The method used for the measurements was a modified pulse transmission technique

(Murase and McBirney, 1973). The delay time of the buffer rod assembly set up without a charge was measured at high temperature and pressure after the velocity measurements had been made on the sample. Possible error of the velocity measurements, due mostly to uncertainty in determining the first arrival of the compressional wave, is  $\pm 0.2$  km/sec or about 3%.

The degree of partial melting of the sample was measured independently by the method developed by Mysen and Kushiro (1977), where  $^{185}\text{W}$  is used as a radioactive tracer. The lherzolite sample was spiked as described by Wendlandt and Mysen (*Year Book* 77, pp. 756–761). Two samples of different grain size were prepared. One was the same as the material used for the velocity measurements; the other was finer grained (mostly 10–50  $\mu\text{m}$  in diameter). Both samples were packed in small graphite capsules, 2 mm in diameter and 4 mm long, which were then sealed in Pt capsules. Charges were run in the gas-media, high-pressure apparatus for 3 hr under 5 kbar pressure at temperatures of 1210°, 1225°, 1240°, 1250°, and 1260°C. The lengths of these runs were close to those of the velocity measurements. After quenching, the charges were polished, and  $\beta$  activities of  $^{185}\text{W}$  in the quenched melt (glass) were recorded on nuclear emulsions. The degree of melting was determined by counting the  $\beta$  tracks from the glass and comparing this frequency with that from a completely melted charge; these analyses were



kindly made by B. O. Mysen. The error of measurements is less than 10% relative. The degree of melting of the fine-grained sample is indicated to be 1–2% greater than that of the coarse-grained sample, but this difference is not significant.

Results and Discussion

Values of  $V_p$  in the peridotite at 5 and 10 kbar and the degree of melting at 5 kbar are illustrated as functions of temperature in Fig. 64. The variation of  $V_p$  in an olivine aggregate of zero porosity determined by Birch (1969) is shown

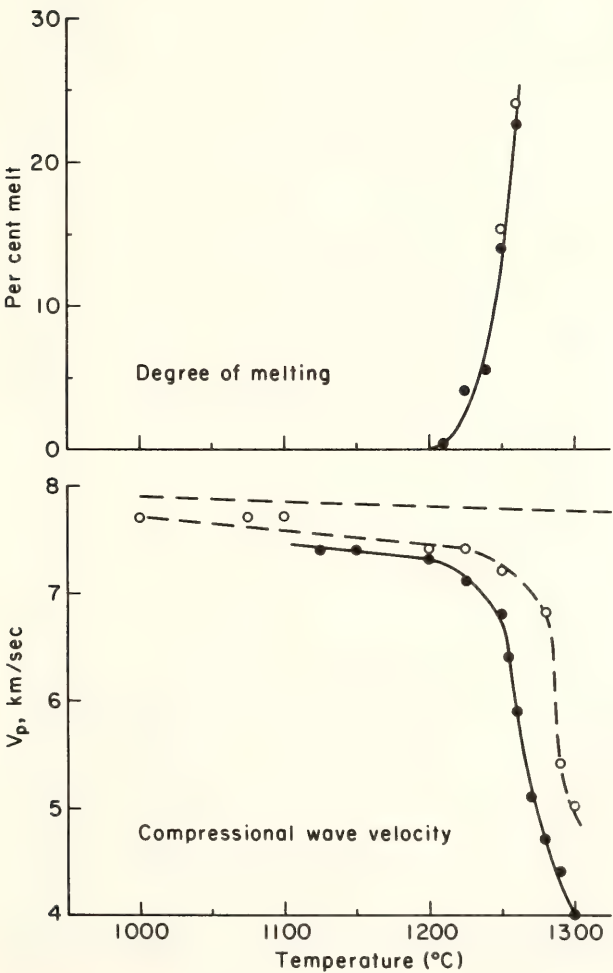


Fig. 64. (lower diagram) Compressional wave velocities vs. temperature for spinel lherzolite at 5 kbar (solid circles) and 10 kbar (open circles), and olivine aggregate of zero porosity (dashed line; Birch, 1969). (upper diagram) Percentage of melt vs. temperature for BCP at 5 kbar.

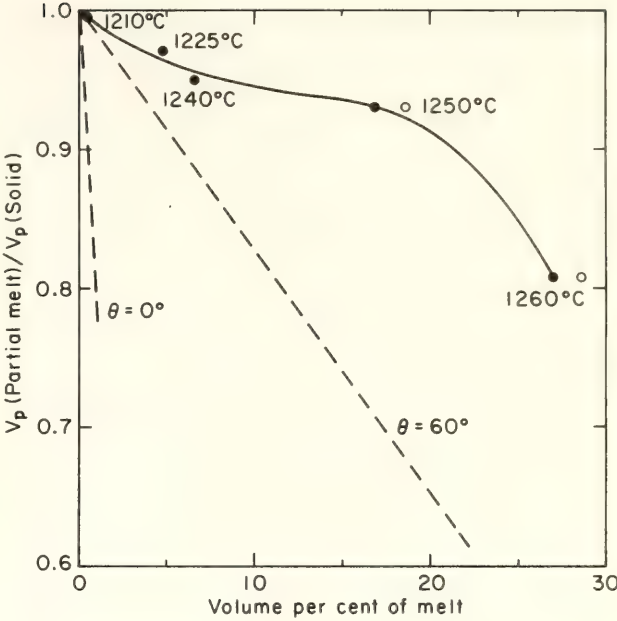


Fig. 65. Normalized compressional wave velocities in partial melts vs. volume percentage of melt for spinel lherzolite at 5 kbar (solid circles, coarse-grained sample; open circles, fine-grained sample). Dashed lines are for Cu-Pb ( $\theta = 60^\circ$ ) and Cu-Ag ( $\theta = 0^\circ$ );  $\theta$  is the dihedral angle (Stocker and Gordon, 1975).

for comparison. In the peridotite,  $V_p$  decreases with increasing temperature at a rate slightly greater than in the olivine aggregate; then at 1200° or 1230° (depending on pressure) it begins to decrease rapidly as melting begins, and at temperatures 20° higher, it drops sharply.

In Fig. 65 the velocities are normalized to the velocity of the unmelted sample at its solidus temperature (1200°C at 5 kbar) for comparison with data on other partially melted materials. The velocities show a relatively small rate of decrease with melting to about 18% melt, then the rate increases. If the relationship is applicable to the mantle, a 5% decrease in  $V_p$ , as observed for the LVZ (for example, by Nur, 1974), implies about 6–8 wt % or 7–9 vol % melting.

Values of  $V_p$  in polycrystalline material for given degrees of melting depend strongly on the textural distribution of the melt. Birch (1969) found that the observed decrease in velocity for the LVZ could be explained by 6 vol % of

spherical droplets of basaltic glass in an aggregate of olivine. Anderson and Spetzler (1970) calculated the influence of the aspect ratio of the melt droplets on  $V_p$  and showed that, if the initial melting occurs in thin intergranular films, the LVZ could be explained by as little as 0.1% and 1.0% melting, respectively, at aspect ratios of  $10^{-2}$  and  $10^{-3}$ . Stocker and Gordon (1975) measured the velocity of a series of partially molten alloys having different volume fractions of fluid and different dihedral angles. From their results, as shown in Fig. 65, it is evident that, if the dihedral angle of the melt in the LVZ is zero, only a few tenths of 1 vol % of fluid would be indicated. For a dihedral angle of  $60^\circ$ , almost 5% melting is implied.

The distribution of melt of the present samples was examined in the polished charges used for measuring degree of melting. In all charges at 5 kbar, the melt is along grain boundaries. At 4% melting ( $1225^\circ\text{C}$ ) it occurs only near grain-boundary triple junctions. With greater melting it tends to wet the grains, but the melt regions are still discontinuous at 17% melting ( $1250^\circ\text{C}$ ), and not until 27% melting ( $1260^\circ\text{C}$ ) are

most grains completely wetted. These observations suggest that melt regions in the LVZ probably have very complex geometry. The relationship between the normalized velocities and dihedral angle, however, appears to agree qualitatively with the relationship in alloys. At less than 17% melting, dihedral angles in the peridotite are relatively large, and  $V_p$  decreases more slowly than at a greater degree of melting when the angle is smaller. It is suggested, therefore, that about 7–9 vol % melting is probably an upper limit for the LVZ. It should be noted, however, that this estimate is based on measurements made under anhydrous conditions. If a small amount of  $\text{H}_2\text{O}$  is present, the melt would have a lower viscosity and so would probably wet crystals more efficiently and thus have a smaller dihedral angle. In this case, a smaller degree of melting ( $<7$  vol %) would be indicated for the LVZ.

The amplitude of the compressional waves decreases rapidly above  $1200^\circ\text{C}$  at 5 kbar. If it is assumed that the attenuation for the buffer can be neglected,  $Q$  at  $1250^\circ$  and  $1300^\circ\text{C}$  is about 10, or about the same as in completely molten rocks (Murase and McBirney, 1973).

## ELEMENT PARTITIONING

### PARTITIONING OF REE BETWEEN GARNET PERIDOTITE MINERALS AND COEXISTING MELTS DURING PARTIAL MELTING

*Wendy J. Harrison\**

The enrichment of large ion lithophile (LIL) and light rare earth elements (LREE) in alkalic basalts may be derived by small percentages of partial melting of a source material, such as garnet peridotite, having a chondritic

REE pattern (Gast, 1968; Kay and Gast, 1973; Shimizu and Arculus, 1975). The REE characteristics of the calculated abundance patterns are determined primarily by the abundances of garnet and clinopyroxene in the source, by the degree of melting, and by the magnitude of the crystal-liquid partition coefficients for the REE's. In the absence of a definitive set of partition coefficients for natural garnet peridotite minerals and coexisting melts, data have been extrapolated from other systems, for example, experimentally determined values in simple and complex synthetic systems

\* Work carried out under a cooperative predoctoral fellowship program of the Geophysical Laboratory and the University of Manchester, England.



(Mysen, 1978a; Shimizu and Kushiro, 1975). It is known, however, that garnet-liquid partition coefficients and, to a lesser degree, clinopyroxene-liquid partition coefficients vary substantially as a function of pressure, temperature, phase composition, and trace element concentration (e.g., Wood, *Year Book* 75, pp. 659–662; Harrison, *Year Book* 77, pp. 682–689; Irving, 1978; Irving and Frey, 1978; Mysen, 1978a), and thus substantial uncertainties necessarily accrue. To assess the magnitude of variation of partition coefficients during a partial melting event and the possibility that REE characteristics of alkalic basalts may be generated by small degrees of partial melting of a garnet peridotite, partition coefficients for Ce, Sm, and Tm between garnet, clinopyroxene, orthopyroxene, olivine, and melts have been determined at 2.3%, 8%, 20%, and 37.7% melting of a garnet lherzolite at 35 kbar.

### *Experimental Methods*

The starting material was a sheared garnet lherzolite nodule, PHN 1611, described by Nixon and Boyd (1973a). This nodule was chosen because its major and minor element composition is considered representative of relatively undepleted upper mantle material and its REE pattern is essentially chondritic (Shimizu, 1975).

If selected percentages of melt coexisting with known mineral assemblages are to be obtained, the melting relations of PHN 1611 are required. Previous determinations of these relations were affected by loss of iron to the sample containers (Mysen and Kushiro, 1977; Wendlandt and Mysen, *Year Book* 77, pp. 756–761). Therefore, a redetermination of the melting relations has been made using graphite capsules, the element  $^{185}\text{W}$  (as an indicator of the amount of liquid), and the technique of Wendlandt and Mysen (*Year Book* 77, pp. 756–761).

Rare earth element analysis was per-

formed by autoradiography (Mysen and Seitz, 1975; Mysen, 1978a). The isotopes cerium-141, samarium-151, and thulium-171 were added in dilute acidic solutions (1.716 ppm  $^{141}\text{Ce}$ , 1.277 ppm  $^{151}\text{Sm}$ , and 0.0536 ppm  $^{171}\text{Tm}$ ) to three samples of PHN 1611. Partition coefficients,  $D^{a/b} = (\text{concentration of element } i \text{ in phase } a) / (\text{concentration of element } i \text{ in phase } b)$ , were determined. The chondrite-normalized REE patterns for the melts were also calculated (Mysen and Holloway, 1977).

All experiments were conducted in a solid-media, high-pressure apparatus (Boyd and England, 1960) using a piston-out technique. No corrections have been applied for pressure loss due to friction, and the nominal pressures quoted are precise to  $\pm 0.5$  kbar. Temperatures were measured with  $\text{Pt}_{100}\text{-Pt}_{90}\text{Rh}_{10}$  thermocouples and were automatically controlled to  $\pm 1^\circ\text{C}$  (Hadidiacos, *Year Book* 71, pp. 620–622). No corrections were made for the effect of pressure on the electromotive force of the thermocouples. The precision of temperature measurements is probably about  $3^\circ\text{C}$ . All runs were made at 35 kbar for a duration of 1 hr.

### *Results*

The redetermined anhydrous melting relations of nodule PHN 1611 as a function of the weight percentage of melting are shown in Fig. 66. On the basis of the new data, four melts were selected for REE studies: 2.3% melt ( $1580^\circ\text{C}$ ), 8.00% melt ( $1585^\circ\text{C}$ ), 20% melt ( $1620^\circ\text{C}$ ), and 37.7% melt ( $1635^\circ\text{C}$ ). The first two melts coexist with the mineral assemblage olivine + orthopyroxene + clinopyroxene + garnet, the melting reaction for which is approximately isobarically invariant (Mysen and Kushiro, 1977). To a first approximation, therefore, partitioning behavior may be examined independently of pressure (35 kbar), temperature ( $1580^\circ\text{C}$ –

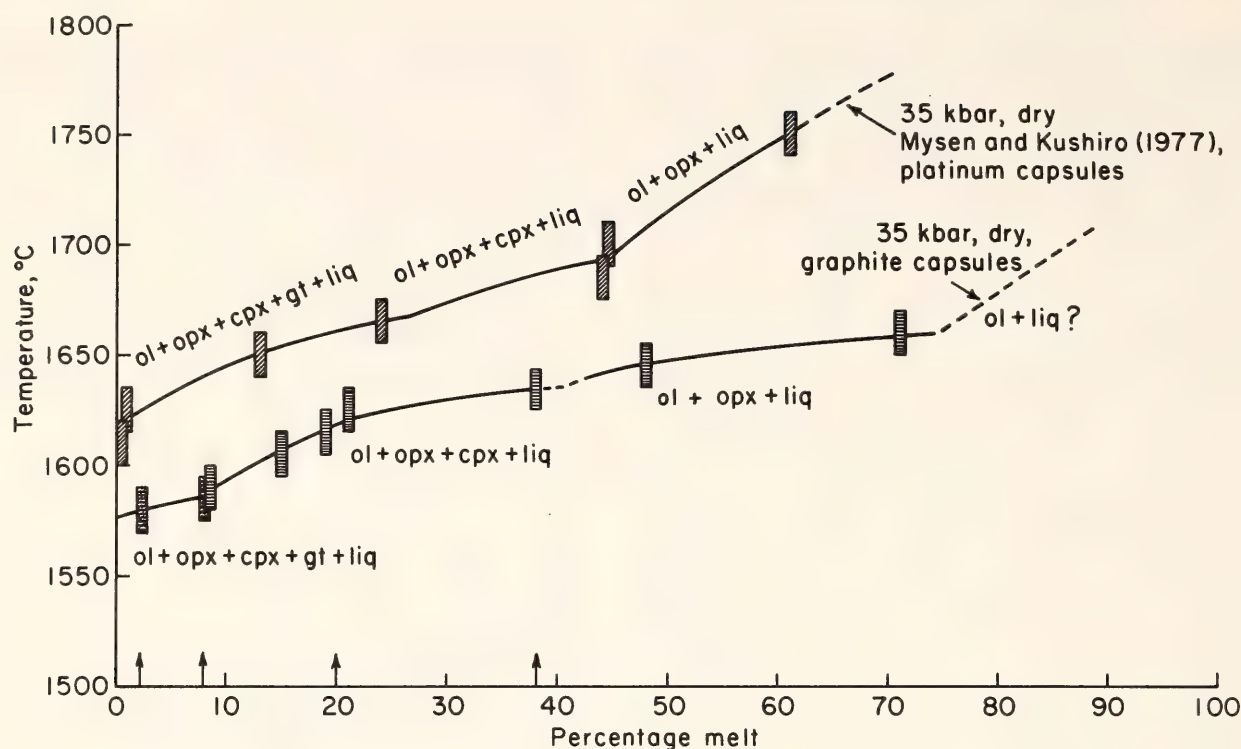


Fig. 66. Melting curves of nodule PHN 1611 at 35 kbar pressure (anhydrous). Upper curve determined by Mysen and Kushiro (1977) with no control on iron loss to noble-metal capsules. Lower curve determined in this investigation using graphite capsules. Size of symbols includes uncertainties in temperature ( $\pm 10^\circ\text{C}$ ) and determination of percentage of liquid ( $\pm 1\sigma$ ). Arrows indicate melt percentages selected for REE partitioning experiments.

1585°C), and melt composition, that is, as a function only of the trace element concentration in the melt or crystal.

The second two melts (20% and 37.7%) coexist with the assemblage olivine + orthopyroxene + clinopyroxene. Because this assemblage melts in an approximately isobaric, univariant fashion, partitioning of the REE may not be evaluated independently of temperature and compositional variables. The temperature difference between 20% and 37.7% melt is only 15°C, however, and can realistically be ignored.

#### REE Partition Coefficients

The partition coefficients determined in this work for three REE between garnet (Fig. 67), clinopyroxene (Fig. 68), orthopyroxene (Fig. 69), olivine (Fig. 70), and various amounts of melt at high pressure and temperature provide a coherent set of data that is complementary

to the studies in synthetic systems by Mysen (1978a). Values of  $D_{\text{REE}}$  are, in general, close to those determined at similar pressures and temperatures in synthetic systems and fall within the much broader range of values defined from analyses of natural systems (for reviews of data see Cullers *et al.*, 1973; Irving, 1978; Irving and Frey, 1978).

In the range 2–8% melt both temperature (1580°–1585°C) and melt composition are essentially constant; however,  $D_{\text{REE}}^{\text{mineral-liquid}}$  may vary. This variation must be a consequence of the changing REE concentrations in the minerals, that is, Henry's law is not obeyed (Mysen, 1978a,c; Harrison, *Year Book* 77, pp. 682–689).

Partition coefficients for cerium between clinopyroxene, orthopyroxene, olivine, and liquids increase systematically from 2% to 8% partial melt. This increase is predicted if Henry's law is not obeyed, as the minerals coexisting with



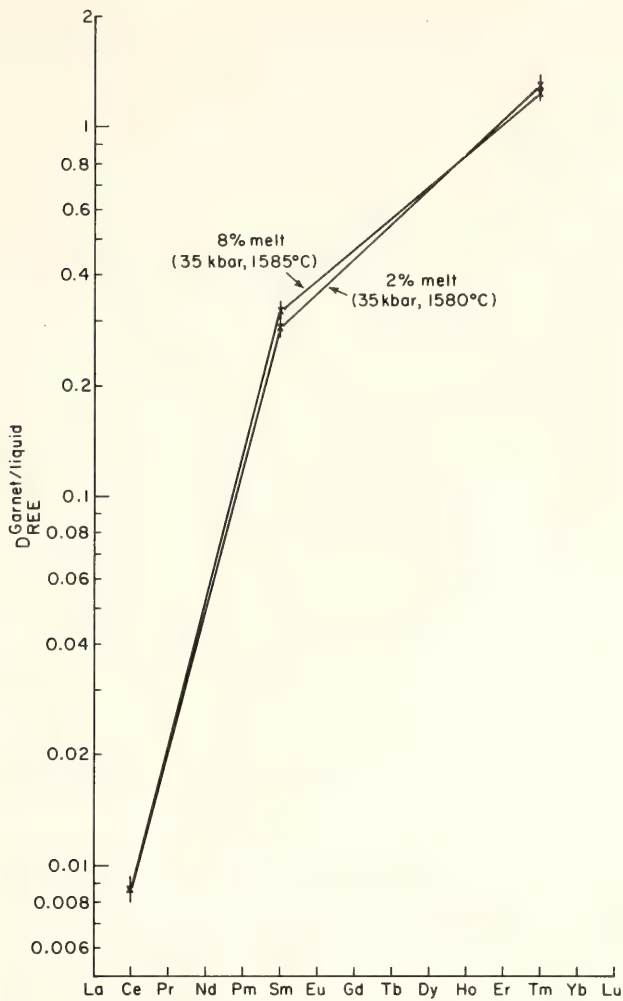


Fig. 67. Partition coefficients for Ce, Sm, and Tm between garnet and melt produced by 2.3% and 8% partial melt of PHN 1611. Error bars  $\pm 1\sigma$ .

8% melt have lower cerium concentrations than those at 2.3% melt (e.g., clinopyroxene contains 11.34 ppm Ce at 2.3% melt and 4.705 ppm Ce at 8% melt). Clinopyroxene, orthopyroxene, and olivine have cerium concentrations (respectively, 11.34, 2.79, and 1.5 ppm at 2.3% melt) greater than the concentration range of Henry's law behavior suggested by Mysen (1978a) for samarium. The larger ionic radius of cerium relative to samarium would suggest that these limits for Sm (1 ppm in Opx, 0.5 ppm in olivine) would be lower for Ce; thus it is very probable that variation in  $D_{\text{Ce}}^{\text{Cpx/liquid}}$ ,  $D_{\text{Ce}}^{\text{Opx/liquid}}$ , and olivine/liquid can be ascribed to non-Henry's law behavior in the crystals. The garnet

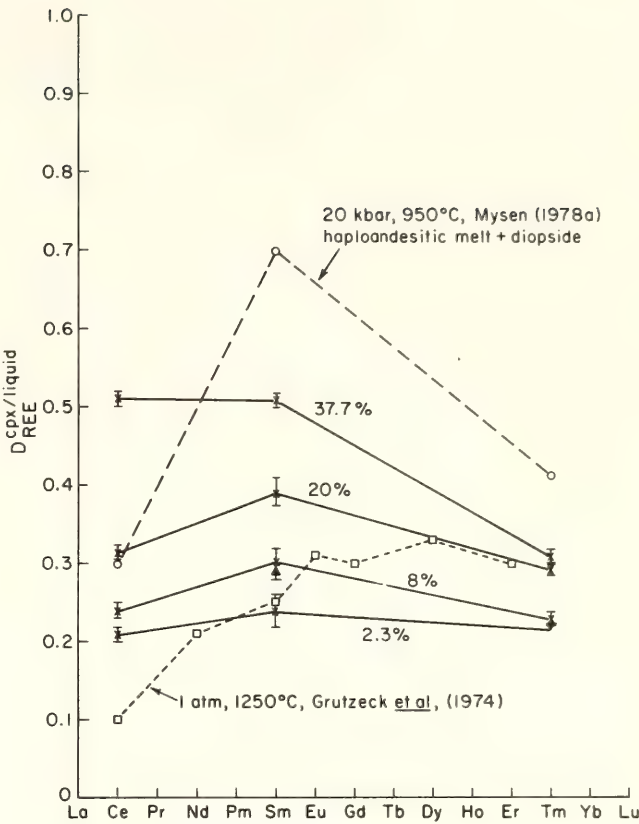


Fig. 68. Partition coefficients for Ce, Sm, and Tm between clinopyroxene and melts produced by 2.3%, 8%, 20%, and 37.7% partial melting. Error bars are  $\pm 1\sigma$ . Some data points have been displaced for clarity of presentation. Also shown are the data of Grutzeck *et al.* (1974) at 1 atm and 1250°C for diopside coexisting with a liquid in the system Ab-An-Di, and the data of Mysen (1978a) at 20 kbar and 950°C for diopside coexisting with a haploandesitic melt. The triangle denotes a value for  $D_{\text{Sm}}$  at 15 kbar, 1450°C, for diopside coexisting with a basaltic melt determined by Mysen.

partition coefficients, however, do not vary between 2% and 8% melt. Partition coefficients for *samarium* are likewise variable, and it is suggested that Henry's law is not obeyed for Sm in any of the minerals. With the exception of  $D_{\text{Tm}}^{\text{garnet/melt}}$  where the garnets contain 1.8 ppm Tm at 2% melt and 1.6 ppm Tm at 8% melt, the *thulium* partition coefficients are essentially constant. It is suggested that Henry's law behavior is obtained for thulium in olivine, orthopyroxene, and clinopyroxene as a consequence of the low concentrations of thulium in these minerals (respectively, 0.296, 0.068, and 0.050 ppm at 2.2%

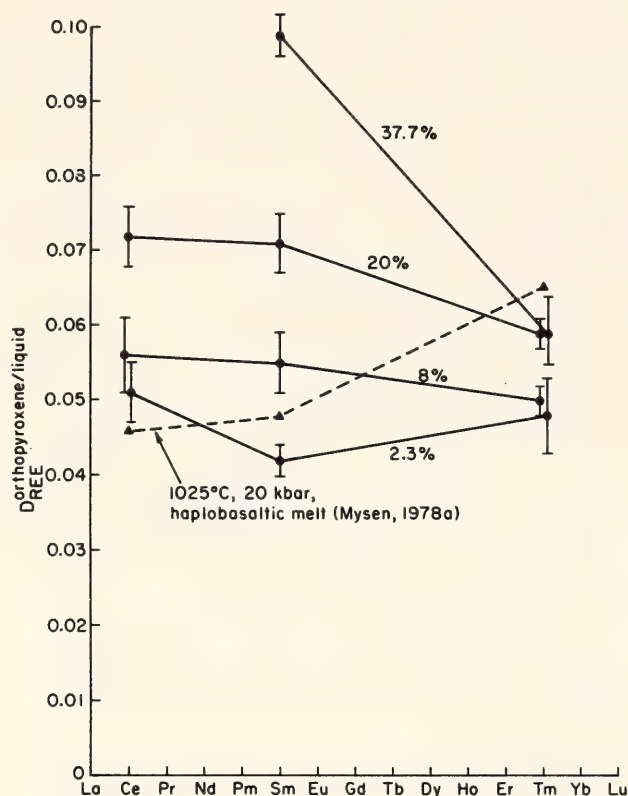


Fig. 69. Orthopyroxene/liquid partition coefficients for Ce, Sm, and Tm determined at 2.3%, 8%, 20%, and 37.7% partial melting. Error bars are  $\pm 1\sigma$ . Also shown are data of Mysen (1978a) at 20 kbar and 1025°C in the system plagioclase<sub>82</sub>-forsterite<sub>16</sub>-silica<sub>2</sub>. Some data points have been displaced for clarity of presentation.

melt, decreasing to 0.289, 0.061, and 0.045 ppm at 8% melt). Because garnet is important in controlling the LREE/HREE pattern in a partial melt, it is essential to have a well-defined value of  $D_{\text{garnet/liquid}}$  especially for heavy REE. The assumption of Henry's law behavior during an evolutionary process involving garnet is likely to lead to substantial uncertainty.

Values of  $D_{\text{REE}^{\text{crystal/liquid}}}$  vary much more between 20% and 37.7% melt than at the low percentages of melt. Unlike the first melting interval, the variation in melt composition and, to a lesser extent, temperature (1620°–1635°C) is significant, so the variation in partition coefficients cannot be ascribed solely to non-Henry's law behavior.

It is important to note that an increase in  $D_{\text{REE}^{\text{crystal/liquid}}}$  of up to 100% may

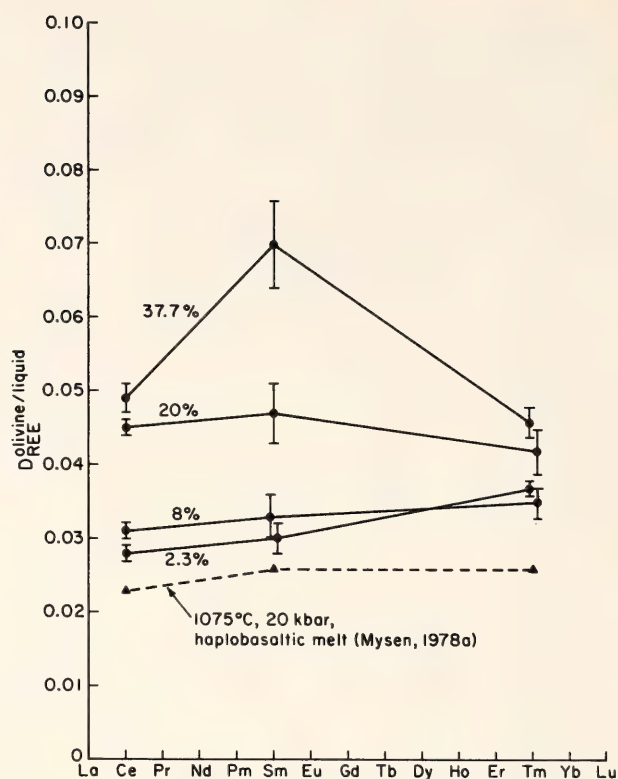


Fig. 70. Olivine/liquid partition coefficients for Ce, Sm, and Tm as a function of degree of partial melting. Also shown for comparison are the data of Mysen (1978a) at 20 kbar and 1075°C for forsterite coexisting with a haplobasaltic, hydrous melt. Some data points have been displaced for clarity of presentation.

result from increasing the percentage of melt in the system from 2% to 38%. Whether this increase reflects changes in temperature (1580°–1635°C), composition of melts and minerals, or trace element substitution behavior cannot be evaluated; this increase does, however, have important consequences for evolutionary models based on REE abundances.

#### REE Enrichment in Melts

In Fig. 71, the enrichment of radioactive Ce, Sm, and Tm in the melts relative to the initial spike is depicted. The enrichment factor, in these experiments, is identical with the chondrite-normalized REE pattern that could be derived from partial melts of this nodule (Mysen and Holloway, 1977).

It is possible to calculate the theo-



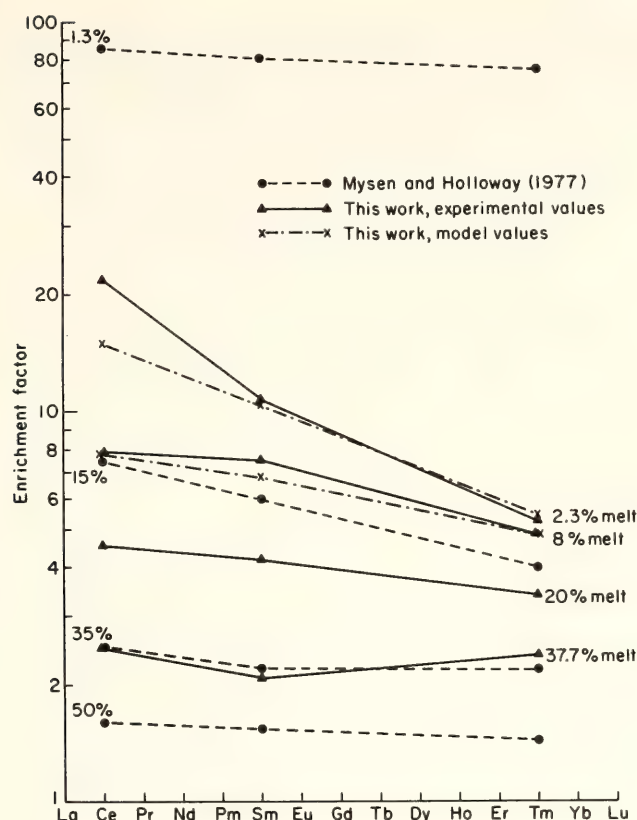
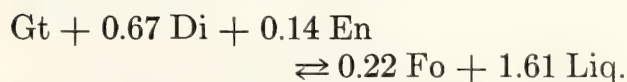


Fig. 71. Enrichment factors of Ce, Sm, and Tm in liquids produced by 2.3%, 8%, 20%, and 37.7% partial melting of PHN 1611 at 35 kbar denoted by triangles. Also shown are the enrichment factors for 2.3% and 8% partial melts calculated for equilibrium partial melting using the equations of Shaw (1970), denoted by crosses (see text). Enrichment factors for 1.3%, 15%, 35%, and 50% partial melts at 20 kbar for PHN 1611 are shown (Mysen and Holloway, 1977).

retical enrichment factors of REE in partial melts using the equations of Shaw (1970) and Mysen (*Year Book* 76, pp. 541–545) for equilibrium partial melting, which is the case defined by these experiments. The phase proportions contributing to the melt are unknown, but as a first approximation the reaction stoichiometry for invariant melting in the system CaO-MgO-Al<sub>2</sub>O<sub>3</sub>-SiO<sub>2</sub> derived by Kushiro and Yoder (*Year Book* 73, pp. 266–269) and Mysen (*Year Book* 76, pp. 557–563) may be used:



The initial modal composition of the starting mix was that determined by

Nixon and Boyd (1973a) for the nodule PHN 1611 (10% garnet, 10% Cpx, 20% Opx, 60% olivine). Partition coefficients used in the calculations were those determined at 2% and 8% melt.

The calculated enrichment factors of Ce, Sm, and Tm in the 2% melt are, respectively, 15, 10.5, and 5.5. Compared with the experimentally determined enrichment factors at 2% melt, cerium is lower (Ce = 22 experimentally) and samarium and thulium are essentially the same (Sm = 10.7, Tm = 5.3).

The lower value for cerium obtained using the reaction stoichiometry of the iron-free synthetic system implies that more garnet must be entering the melt relative to clinopyroxene in the natural system; i.e., the presence of Fe has a greater effect in reducing the stability of garnet than it does in reducing the stability of clinopyroxene.

As for 2% melt, the calculated REE enrichment in an 8% partial melt is in excellent agreement with the experimentally determined pattern. It is to be expected that the greatest deviation from the ideal behavior predicted from the CaO-MgO-SiO<sub>2</sub>-Al<sub>2</sub>O<sub>3</sub> reaction stoichiometry would obtain at the lowest percentages of melt. Initial melts will be very iron rich; thus the effect of Fe on mineral stabilities will be greater at smaller amounts of melt than at larger amounts of melt when the Fe content is diluted. No theoretical calculations of REE enrichment are possible at 20% and 38% melt because the melting reaction is unknown.

When the experimental results are compared with REE data from those alkali basalts considered to have originated by partial melting of garnet lherzolite (Ce/Tm 2–15 and Ce enrichment of 40–200; Kay and Gast, 1973; Frey *et al.*, 1978; Shimizu and Arculus, 1975), it is evident that these basalts are much too enriched in LREE to have been generated from such a source by even very small degrees of anhydrous partial melting unless the source had

been previously enriched, for example, by a metasomatic event (Mysen, 1979; Wendlandt and Harrison, 1979).

PRELIMINARY RESULTS FROM AN  
ELECTRON PARAMAGNETIC RESONANCE  
INVESTIGATION OF THE SITE OCCUPANCY  
OF  $Gd^{3+}$  IN PYROPE GARNET

W. J. Harrison\* and R. A. Weeks†

Recent trace element partitioning experiments have indicated that deviations from dilute solution behavior (Henry's law) occur in many minerals over concentration ranges of geological interest (Harrison, *Year Book 77*, pp. 682–689; Mysen, 1978a,b,c; Wood, *Year Book 75*, pp. 659–662). It was reported last year (Harrison, *Year Book 77*, pp. 682–689) that garnet-liquid partition coefficients for rare earth elements (REE), for example, may change by up to a factor of five times as the rare earth concentration in the garnet changes over a few tens of parts per million, and it was suggested that substitution may be occurring on more than one site in the garnets.

Garnet is an important mineral in controlling the REE abundance patterns in alkalic basalts (Kay and Gast, 1973; Shimizu and Arculus, 1975), and thus it is essential that the mechanism of REE substitution be evaluated before reliable values of REE partition coefficients may be obtained.

If substitution does occur on more than one site in the garnet, then the lower free-energy site, preferentially occupied at low rare earth concentrations, may accept only a few parts per million of REE. Higher concentrations are accommodated on an additional site in the structure.

The technique of electron paramag-

netic resonance (EPR) is sensitive to low concentrations of REE and was thus selected for evaluation of the site occupancy of a REE,  $Gd^{3+}$ , in pyrope garnet.

*Experimental Methods*

Single crystals of  $Gd^{3+}$ -spiked pyrope were grown from spectroscopically pure oxide mixes of  $MgO$ ,  $Al_2O_3$ , and  $SiO_2$ . Gadolinium was added to the oxide mixes as a chloride in 0.5N HCl solution (also high purity), and the oxide mix was fired at 1500°C and 1 atm to decompose the chloride. Mixes were prepared for garnets containing two different Gd concentrations, 60 and 200 ppm. Mixes with about 20 wt %  $H_2O$  were contained in Pt capsules of 5 mm diameter. Garnets were synthesized in a solid-media, high-pressure apparatus (Boyd and England, 1960) by holding the mixture at 30 kbar and 1200°C for 15–20 min. Under these conditions, most of the sample is melted and a few nuclei form. The temperature was then reduced at a rate of 30°C/min to a subsolidus temperature of 900°C, and the sample was held at this temperature for 1 hr. Crystal growth occurs during the cooling period, and typically four to five crystals of 1 mm diameter are formed. Some aluminous, quench pyroxene crystals also form in the melt during the cooling period, but these are readily separated from the garnets in an ultrasonic bath.

Garnets containing samarium-151 were also grown in the manner described above. Autoradiographs (Mysen and Seitz, 1975) prepared from these garnets verify homogeneous trace element distribution in the crystals grown in this way.

The crystals used for EPR spectra were ground to less than 5- $\mu$ m grain size for powder spectra. Large single crystals were mounted in known orientations on Teflon rods for single-crystal spectra.

Electron paramagnetic resonance spectra were observed using a 35-GHz spectrometer at temperatures of about 78°

\* Work carried out under a cooperative predoctoral fellowship program between the Geophysical Laboratory and the University of Manchester, England.

† Oak Ridge National Laboratory, Oak Ridge, Tennessee.



and about 300°K. Powder samples were vacuum-sealed in high-purity silica tubes that were positioned along the axis of a cylindrical cavity resonating in the  $TF_{101}$  mode. The spectra of garnets grown without gadolinium were also measured. No spectral components were detected in these samples, and it is, therefore, assumed that all the components shown in Figs. 72 and 73 are due to  $Gd^{3+}$ .

### Discussion

The analysis of the spectra shown in Figs. 72 and 73 consists of associating the peaks in the spectrum with singularities in the spin Hamiltonian and is based on the assumptions of Low and Offenhacher (1965), Reynolds *et al.* (1972), and Morris (1975). The separation of these peaks is then used to calculate the significant crystal-field parameters. If the values thus found are inconsistent (e.g.,  $b_2^2 > b_2^0$  and  $b_4^0 \geq b_2^0$ ), then new assignments are made. A consistent set of singularities in Fig. 72, marked by the symbols  $a_x, a_y, a_z, b_x, b_y, b_z, c_x, c_y, c_z, e_x, e_y, e_z, f_x, f_y, f_z, g_x, g_y, g_z$ , has been identified.\*

If the set of singularities identified in Fig. 72 is assigned to gadolinium in a particular structural site, referred to as site A, then there are a number of additional features, also identified in Figs. 72 and 73, that may be attributed to gadolinium in a distinctly different structural site (site B). A consistent set of crystal-field parameters has not yet been calculated for site B. A first approximation based on the two most prominent singularities of this second set indicates that the outermost peaks, those corresponding to  $a_z$  and  $g_z$  in site A, will be

\* The crystal-field parameters calculated from this assignment are  $b_2^0 = +630$  G,  $b_2^2 = +416$  G,  $b_4^0 = +4.4$  G,  $b_4^4 = -9$  G,  $b_6^0 = +0.7$  G. The ratio  $b_2^2/3b_2^0 = 0.22$ , and thus the structure of the transition  $M_s = 1/2 \leftrightarrow M_s = -1/2$  is determined by the condition  $1/9 < b_2^2/3b_2^0 \leq 1/3$ . The structure expected for this condition is indicated by the symbol *d* in Fig. 73.

at lower and higher magnetic fields than are covered in Fig. 72. The sensitivity of the spectrometer used was not adequate to resolve these singularities.

It is concluded that there are two sites for  $Gd^{3+}$  substitution in  $Mg_3Al_2Si_3O_{12}$  garnet; however, it is not possible to equate unequivocally sites A and B with structural sites in pyrope. There are three cation sites in pyrope onto which REE could substitute: the dodecahedral site, the octahedral site, and the tetrahedral site, respectively, normally occupied by  $Mg^{2+}$ ,  $Al^{3+}$ , and  $Si^{4+}$  (e.g., Geller, 1967).

Simple considerations of ionic radius indicate that the dodecahedral site is the most likely to accept REE and that the tetrahedral site is probably too small (ionic radii are  $Mg^{2+}$  VIII = 0.98 Å,  $Al^{3+}$  VI = 0.61 Å,  $Si^{4+}$  IV = 0.34 Å,  $Gd^{3+}$  VIII = 1.14 Å, and  $Gd^{3+}$  VI = 1.06 Å; Whittaker and Muntus, 1970).

The crystal-field parameters of site A do not, however, describe either a regular cubic or an octahedral symmetry. This result implies that there is substantial lattice distortion by  $Gd^{3+}$  substitution.

On the basis of the crystal chemistry of REE garnets (Keith and Roy, 1954; Schneider *et al.*, 1961; Geller, 1967), site A has tentatively been assigned to the dodecahedral site. The second site (site B) has not yet been fully characterized, but may be the octahedral site (Schneider *et al.*, 1961).

Whether the deviations from Henry's law behavior may be explained by multiple site substitution cannot be established without data on the change of the relative abundances of  $Gd^{3+}$  in each site as the  $Gd^{3+}$  concentration in the crystal decreases. From the relative intensities of the singularities for the two sites in the spectrum of the sample doped with 200 ppm Gd, it is suggested that at this total Gd concentration the two sites are occupied by approximately equal concentrations of Gd. Some singularities do have different intensities in the 60-ppm sample, however, and this observation suggests that the sites may be differently occu-

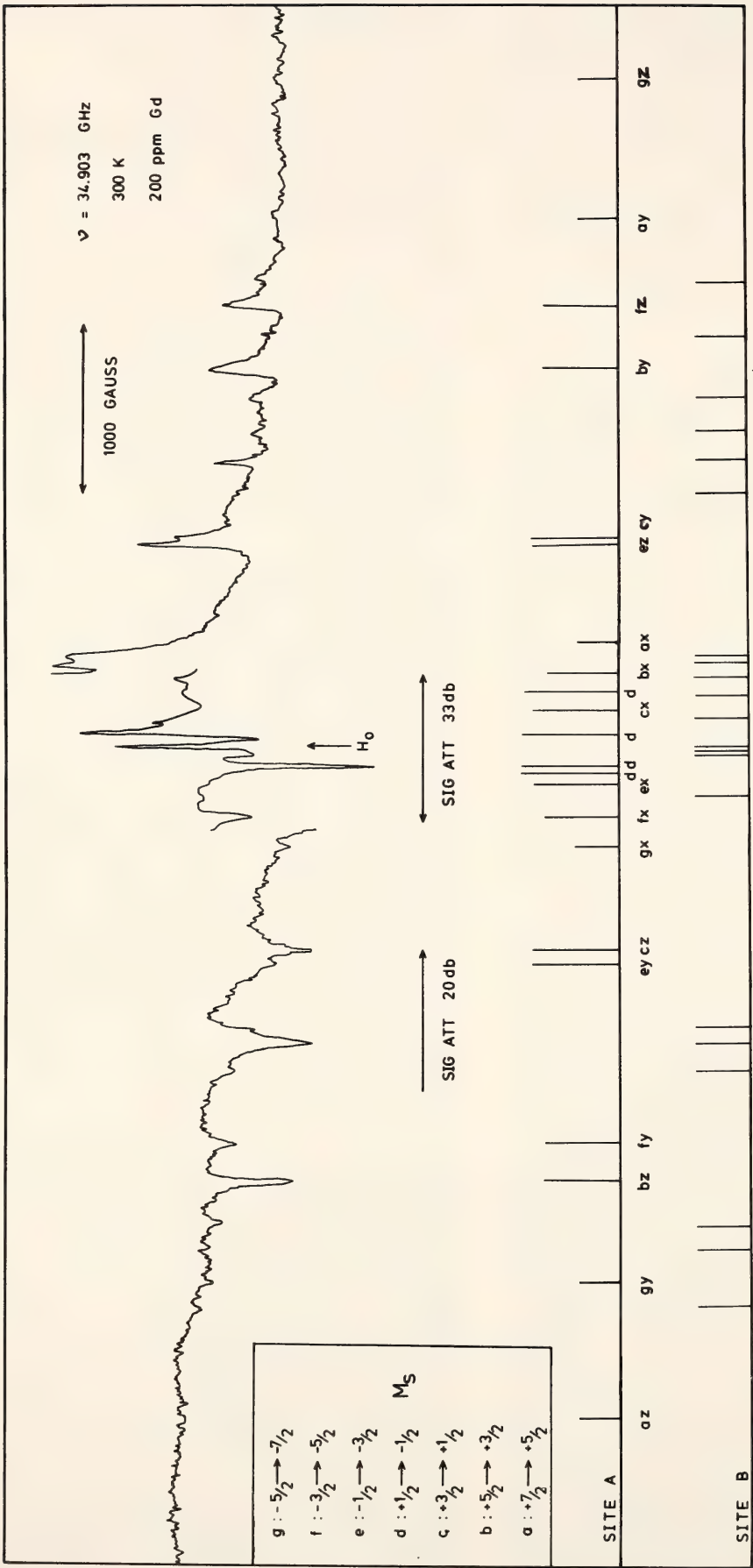


Fig. 72. Electron paramagnetic resonance spectrum, recorded at 300°K, of 200 ppm Gd<sup>3+</sup> in polycrystalline Mg<sub>3</sub>Al<sub>2</sub>Si<sub>3</sub>O<sub>12</sub> for a 10-kG sweep of the magnetic field. Observed derivative at 35 GHz is shown in the upper part of the figure. The central part of the spectrum has been recorded at reduced gain.  $H_0 = 12,516$  G. Positions of the absorption singularities for  $M_s \rightarrow M_s - 1$  transitions are indicated in the lower part of the figure. The transitions are designated by letter according to the code shown at the left of the figure and by a cartesian coordinate. The signs assigned to the transitions have not been verified by low-temperature measurements. Only site A has been characterized. Site B comprises singularities that are not accounted for by site A (see text).





Fig. 73. Electron paramagnetic resonance spectra, recorded at 300°K, of polycrystalline  $\text{Mg}_3\text{Al}_2\text{Si}_3\text{O}_{12}$  garnet containing 200 and 60 ppm  $\text{Gd}^{3+}$  for a 1-kG sweep of the magnetic field. The center spectrum was recorded at higher gain. These spectra show the  $+\frac{1}{2} \rightarrow -\frac{1}{2}$  singularities (calculated from the spin Hamiltonian constants) which are designated  $d_1$ – $d_4$ , according to the code at the left-hand side of the figure. The stick diagram for site A shows the positions of these singularities at 200 ppm  $\text{Gd}^{3+}$ . The singularities not accounted for in site A are shown below the 60 ppm  $\text{Gd}^{3+}$  spectrum and are assigned to site B. It can be seen that some changes in peak intensities occur in the spectra at 60 ppm  $\text{Gd}^{3+}$  and at 200 ppm  $\text{Gd}^{3+}$ . These changes indicate that there is probably a change in the site occupancy of Gd. The 200 and 60 ppm  $\text{Gd}^{3+}$  spectra have been aligned with respect to  $b_x$ ,  $d_1$ , and  $H_0$ . The shift of all other singularities to lower fields in the 60-ppm spectrum is unexplained.

pied at lower Gd concentrations. More careful characterization of the spectra at lower REE concentrations is required before a quantitative statement of site occupancy can be made.

The preliminary data reported here indicate that a model of multiple site substitution of REE in garnets may explain non-Henry's law behavior observed in crystal-liquid partitioning studies.

#### DISTRIBUTION OF RARE EARTH ELEMENTS IN PEROVSKITE FROM KIMBERLITES

*N. Z. Boctor and F. R. Boyd*

Kimberlites are known to be remarkably enriched in rare earth elements (REE) relative to ultramafic and other mantle-derived rocks (Haskin *et al.*, 1966; Frey *et al.*, 1971; Philpotts *et al.*, 1972; Mitchell *et al.*, 1973; Fesq *et al.*, 1975). Perovskite, a common groundmass mineral in kimberlites, is known for its capacity to concentrate REE and other incompatible elements. Perovskite is known to form in the final stages of crystallization of kimberlitic magma, as demonstrated by its occurrences as a groundmass mineral and as a component in reaction mantles on ilmenite nodules. El Goresy and Yoder (*Year Book* 73, pp. 359–371) reported a similar occurrence in melilite nephelinites where most of the perovskite occurs as reaction mantles around titanomagnetite. The final stages of crystallization of kimberlitic magma are characterized by reactions between its residual fluids and early-formed phenocrysts and xenocrysts (Boyd and Clement, *Year Book* 76, pp. 485–493; Boctor and Boyd, *Year Book* 77, pp. 870–876). The pattern of distribution of REE in kimberlitic minerals could be influenced by interaction between these minerals and the residual fluids of kimberlitic magma. Recent experimental investigations on partitioning of REE between silicate and carbonate melts and CO<sub>2</sub> vapor (Wendlandt and Harrison,

1979), and between minerals of garnet peridotite and H<sub>2</sub>O vapor (Mysen, 1979), support this possibility.

Four kimberlite localities that differ in their mode of emplacement and in the abundance of primary carbonates were selected: layered carbonate-kimberlite sills from Benfontein, kimberlite from the main fissure at Bellsbank, kimberlite rich in carbonate segregations from the Monastery diatreme, and hardebank depleted in carbonate from the De Beers pipe.

The distribution of REE in perovskite was determined using the electron microprobe. The standards used were silicate glass containing minor amounts of REE elements that were prepared by Drake and Weill (1972). The concentrations of REE in the standards were independently checked by neutron activation analysis. A special version of the Magic IV computer program (Colby, 1971) was used to correct for interferences between characteristic x-ray spectra of the REE and other elements, in addition to the standard corrections for deadtime, background atomic number, absorption, and fluorescence factors. Although the accuracy of the microprobe analyses of the REE that are present in trace amounts is much lower than that of neutron activation analyses, electron microprobe analysis seems to be the only feasible technique for determination of REE in perovskite from kimberlite because of difficulty in separating pure concentrates of this mineral for analysis by other methods. It is also possible to study grain-to-grain variation within individual specimens by using the electron microprobe.

The abundance of REE in perovskite from kimberlite varies widely from 3.1 to 13.4 wt % (Table 31). Perovskite from kimberlitic dikes and sills is more enriched in REE relative to perovskite from diatremes. Also, perovskite from carbonate-depleted diatremes (e.g., De Beers) has a lower REE content than perovskite from carbonate-rich diatremes (e.g., Monastery). Perovskite from kim-



TABLE 31. Electron Microprobe Analyses of Perovskite from Kimberlites

	Bellsbank		Benfontein		Monastery		De Beers	
	1	2	3*	4†	5‡	6§	7	8
SiO <sub>2</sub>	0.27	0.32	n.d.	n.d.	0.05	0.05	n.d.	0.07
TiO <sub>2</sub>	50.49	50.21	53.96	52.49	55.28	54.54	54.50	54.89
FeO	1.90	1.70	1.46	1.38	1.52	1.20	0.77	0.77
MgO	0.79	0.99	n.d.	1.18	0.26	0.01	0.68	0.89
CaO	28.69	27.91	36.82	35.63	36.04	35.79	38.57	38.86
Na <sub>2</sub> O	1.82	1.84	0.43	0.44	1.02	0.59	0.41	0.44
Y <sub>2</sub> O <sub>3</sub>	0.05	0.01	n.d.	n.d.	n.d.	n.d.	n.d.	0.02
La <sub>2</sub> O <sub>3</sub>	3.20	2.41	0.81	0.71	0.30	0.59	0.49	0.11
Ce <sub>2</sub> O <sub>3</sub>	6.53	6.66	3.10	2.95	2.48	2.64	1.57	1.45
Pr <sub>2</sub> O <sub>3</sub>	0.50	0.75	0.32	0.56	0.45	0.22	n.d.	n.d.
Nd <sub>2</sub> O <sub>3</sub>	1.75	1.53	1.28	1.24	1.02	1.37	1.05	0.91
Sm <sub>2</sub> O <sub>3</sub>	0.13	n.d.	0.09	0.37	n.d.	0.23	n.d.	n.d.
Eu <sub>2</sub> O <sub>3</sub>	0.29	0.28	0.12	0.17	n.d.	0.27	0.03	n.d.
Gd <sub>2</sub> O <sub>3</sub>	0.74	0.65	0.45	0.57	0.52	0.29	0.05	0.29
Tb <sub>2</sub> O <sub>3</sub>	n.d.	n.d.	n.d.	0.06	n.d.	n.d.	0.09	n.d.
Dy <sub>2</sub> O <sub>3</sub>	n.d.	n.d.	n.d.	n.d.	n.d.	n.d.	n.d.	n.d.
Ho <sub>2</sub> O <sub>3</sub>	n.d.	n.d.	n.d.	n.d.	n.d.	0.09	0.02	n.d.
Er <sub>2</sub> O <sub>3</sub>	0.14	0.20	0.20	n.d.	0.14	0.18	n.d.	0.11
Tm <sub>2</sub> O <sub>3</sub>	n.d.	n.d.	n.d.	n.d.	n.d.	n.d.	n.d.	n.d.
Yb <sub>2</sub> O <sub>3</sub>	n.d.	0.02	n.d.	n.d.	n.d.	n.d.	n.d.	n.d.
Lu <sub>2</sub> O <sub>3</sub>	0.09	0.13	0.03	0.14	n.d.	0.10	0.23	0.37
Cr <sub>2</sub> O <sub>3</sub>	0.44	0.42	n.d.	n.d.	0.10	0.09	0.05	0.11
Nb <sub>2</sub> O <sub>5</sub>	2.52	2.96	1.34	1.06	0.77	1.04	0.77	0.77
Totals	100.32	99.00	100.48	99.02	100.02	99.29	99.06	99.29
ΣRE <sub>2</sub> O <sub>3</sub>	13.42	12.84	6.40	6.77	4.91	6.18	3.53	3.13
ΣLRE <sub>2</sub> O <sub>3</sub>	11.98	11.35	5.51	5.46	4.25	4.82	3.11	2.47

\* Analysis 3: perovskite from kimberlite layer.  
† Analysis 4: perovskite from carbonate layer.  
‡ Analysis 5: perovskite from hardebank.  
§ Analysis 6: perovskite from carbonate segregation.  
|| n.d.: not detected.

berlite shows remarkable enrichment of the light rare earth elements (LREE) relative to the heavy rare earth elements (HREE).

The LREE, La, Ce, Pr, and Nd, account for 78–89% of the total REE content of perovskite. Because perovskite is an abundant mineral in the groundmass in some kimberlites, e.g., Likhobong kimberlite (Boctor and Boyd, *Year Book* 77, pp. 870–876), its REE distribution pattern could influence the whole-rock REE pattern.

The common association between perovskite and calcite in the groundmass

of kimberlites has led to the suggestion that the enrichment of perovskite in REE is related to the separation of an immiscible carbonate liquid from the kimberlitic magma. Experimental investigation of REE partitioning between coexisting silicate and carbonate liquids (Wendlandt and Harrison, 1979) showed that partitioning of REE favors the carbonate melts, especially for HREE. When a CO<sub>2</sub> vapor is present, however, the LREE are fractionated preferentially into the vapor relative to the carbonate melt. The enrichment of REE in CO<sub>2</sub> vapor relative to carbonate and silicate

melts is 3–4 orders of magnitude greater than that in water vapor at 5 kbar and is approximately the same as that in water vapor at 20 kbar (Wendlandt and Harrison, 1979). Therefore, the observed REE patterns in perovskite from kimberlites can be interpreted in two possible ways: (1) partitioning of REE between perovskite and immiscible carbonate liquid with enrichment of perovskite in the LREE, or (2) equilibration of perovskite with a CO<sub>2</sub>-rich vapor en-

riched in LREE. Mysen (1979) has shown that equilibration of the minerals of garnet peridotite with H<sub>2</sub>O vapor enriched in LREE can give rise to a wide range of absolute REE content and of light REE enrichment. An experimental investigation of the partitioning of REE between perovskite, CO<sub>2</sub> vapor, and carbonate melt is needed, however, in order to assess which of the two mechanisms is responsible for the enrichment of perovskite in REE.

## DIFFUSION AND KINETICS

### SELF-DIFFUSION OF Ca IN DIOPSIDE

*Robert H. McCallister, John B. Brady,  
and Bjørn O. Mysen*

Calcium, because of its relatively large ionic radius, can limit the diffusion kinetics associated with important processes in pyroxenes, such as exsolution and homogenization. Previous attempts to obtain major element diffusion data for clinopyroxenes from interdiffusion experiments and solution-exchange experiments have been unsuccessful. New measurements of the self-diffusion of Ca in clinopyroxene using <sup>45</sup>Ca and a beta-track mapping technique (Mysen and Seitz, 1975) are reported here.

Clear crystals of colorless diopside from Natural Bridge, New York, were obtained from the Smithsonian Institution (USNM 117733; Ca<sub>1.00</sub>Mg<sub>0.99</sub>Fe<sub>0.01</sub>Si<sub>1.99</sub>O<sub>6</sub>). Rectangular solids were cut from these crystals, each with one side parallel to (001) so that diffusion parallel to the C\* axis could be measured. Approximately  $4 \times 10^{-5}$  mCi of <sup>45</sup>Ca were deposited on each crystal by evaporation of a <sup>45</sup>Ca-bearing CaCl<sub>2</sub> solution on a polished (001) surface 2 mm square. The crystals were preannealed at 830°C for 72 hr to implant the tracer, then annealed for various times at higher temperatures in air.

After each experiment, the diopside crystal was mounted in epoxy, cross sectioned parallel to the diffusion direction [perpendicular to (001)], polished flat, and exposed to a K-5 (Ilford) nuclear emulsion. Diffusion profiles were obtained from the emulsions using an optical densitometer (slit height, 80 μm; slit width, 1 μm) at the Department of Terrestrial Magnetism with the generous assistance of N. Thonnard. Data from the densitometer were integrated over 10-μm intervals and normalized to a maximum density of 1.

It was hoped that the beta-track profiles could be analyzed using the "thin-film" solution to the diffusion equation (Shewmon, 1963, p. 7). This approach was not possible, however, owing to the considerable penetration range observed for <sup>45</sup>Ca beta particles (0.26 MeV) in diopside. Beta-track profiles obtained for a "zero-time" experiment (preanneal only) exhibited a nearly gaussian distribution of tracks, decreasing from a peak at the treated surface to background levels at a depth of about 100 μm in the diopside (Fig. 74). The profile extends even further in the direction away from the crystal, because the mounting epoxy is less opaque to the beta particles than the diopside. The zero-time profile in the diopside is



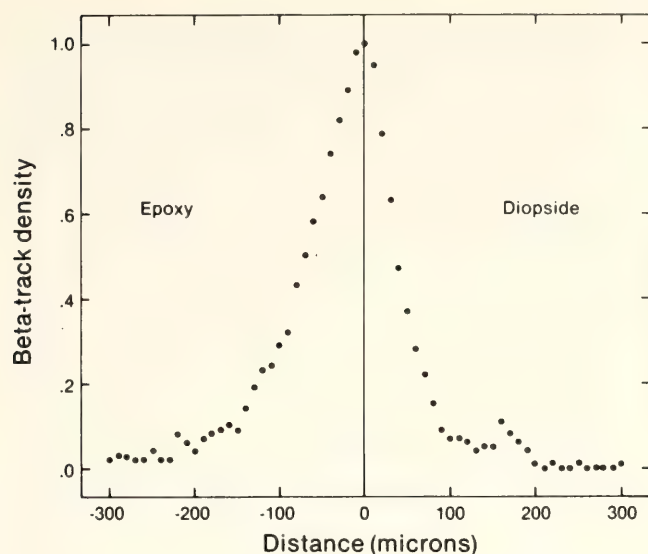


Fig. 74. A beta-track profile for a “zero-time” diffusion experiment showing the effective range of  $^{45}\text{Ca}$  beta particles in diopside and epoxy.

closely described by the equation  $\rho = \exp(-Bx^2)$  where  $\rho$  is the beta-track density,  $x$  is the distance from the treated surface in centimeters, and  $B \cong 3 \times 10^4 \text{ cm}^{-2}$ .

To interpret the diffusion runs it was necessary to consider the effect of the long range of the beta particles on the observed profiles. Calculated beta-track profiles that include this range effect were obtained by (1) taking an ideal  $^{45}\text{Ca}$  profile that would be produced by the thin-film boundary conditions for an assumed diffusion coefficient (Fig. 75A), (2) dividing the profile into small intervals ( $2 \mu\text{m}$  was found to be adequate) representing slices of the crystal parallel to (001), (3) scaling a gaussian beta-track density distribution to the  $^{45}\text{Ca}$

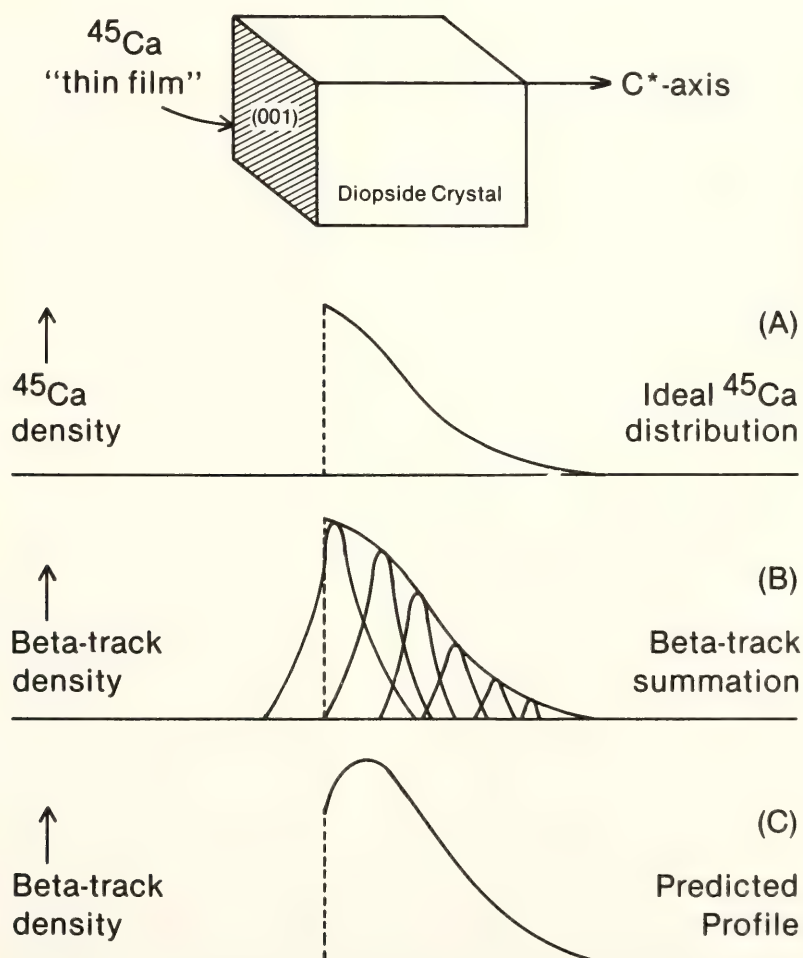


Fig. 75. A diagrammatic representation of the steps followed in calculating beta-track profiles for a thin-film diffusion experiment using a tracer that emits “long-range” beta particles. See text for details.

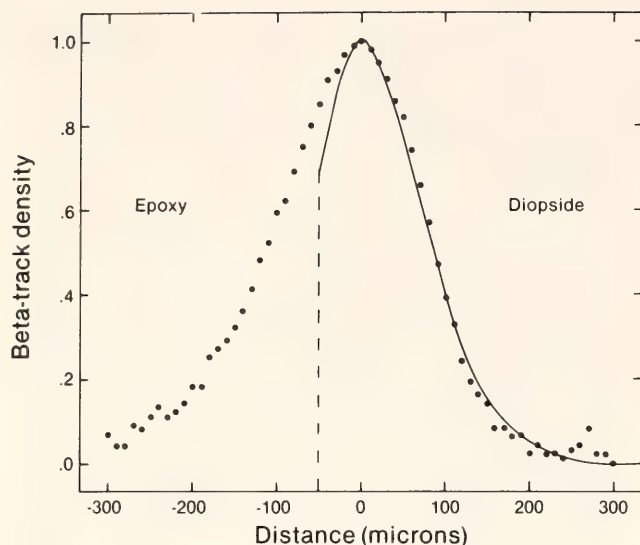


Fig. 76. A comparison of observed and calculated beta-track profiles. The observed profile for a  $1300^{\circ}\text{C}$  run of  $1.9 \times 10^6$  sec is shown by the crosses. A calculated summation profile for an assumed diffusion coefficient of  $2 \times 10^{-11}$   $\text{cm}^2/\text{sec}$  is shown by the solid line. The dashed vertical line indicates the calculated location of the crystal surface relative to the profile.

density in each slice (Fig. 75B), and (4) summing the beta-track density distributions for all the intervals to obtain a predicted profile (Fig. 75C). Calculated profiles could then be compared with the observed profiles.

An observed beta-track profile is shown in Fig. 76 along with a calculated profile for comparison. Agreement is found between the observed and calculated profiles except near the crystal edge. The discrepancy at the edge may result from anomalous  $^{45}\text{Ca}$  densities at the crystal surface due to defects introduced by polishing or to the effect on the observed profile of any rounding at the edge of the crystal surface contacting the flat emulsion. An additional complication in especially long runs is the loss of  $^{45}\text{Ca}$  from the initial "thin film" owing to surface diffusion around the diopside cube. This effect modifies the boundary conditions and may be responsible for a slightly nongaussian tail on the profile observed in some instances.

Results have been obtained for runs at  $1300^{\circ}\text{C}$  for periods of 3 weeks and 3

months. Diffusion coefficients determined are, respectively,  $1.6\text{--}2.2 \times 10^{-11}$   $\text{cm}^2/\text{sec}$  and  $6.9\text{--}8.6 \times 10^{-12}$   $\text{cm}^2/\text{sec}$ , where the range in each case refers to bounding calculated profiles that bracket the observed profile. The relatively close agreement between these two values supports the method and represents the first known laboratory determination of a major element diffusion constant in pyroxenes. A run at  $1200^{\circ}\text{C}$  for 56 days produced a profile nearly indistinguishable from the zero-time profile. Because of the magnitude of the zero-time profile, the above summation procedure returns the zero-time profile for all values of  $Dt$  less than about  $1 \times 10^{-5}$   $\text{cm}^2$ , where  $D$  ( $\text{cm}^2/\text{sec}$ ) is the diffusion constant and  $t$  (sec) is the time required for the diffusion anneal. The Ca self-diffusion constant at  $1200^{\circ}\text{C}$  is thus limited by the data to values below about  $2 \times 10^{-12}$   $\text{cm}^2/\text{sec}$ . Combined with the  $1300^{\circ}\text{C}$  data, the latter observation means that the activation energy for Ca self-diffusion in diopside is greater than 50 kcal/mole and perhaps as much as 100 kcal/mole.

The Ca self-diffusion coefficients obtained for diopside are very close to values reported by Lindner (1955) for Ca self-diffusion in pressed pellets of wollastonite. Because the pyroxene used in this study is virtually iron-free, and the M2 site contains only Ca and a trace of Na, the data probably represent minima for Ca diffusion in clinopyroxenes. Recent interdiffusion calculations of Sanford and Huebner (1979), based on pyroxene textures in lunar basalts, suggest a marked effect on the bulk diffusivity when the M2 site contains Fe and Mg (they calculated a minimum interdiffusion coefficient of  $4 \times 10^{-11}$   $\text{cm}^2/\text{sec}$  at  $1050^{\circ}\text{C}$ ). Both sets of data, however, are in sharp contrast to the diffusion coefficients ( $2.3\text{--}6.6 \times 10^{-19}$   $\text{cm}^2/\text{sec}$  at  $1125^{\circ}\text{C}$ ) predicted by Miyamoto and Takeda (1977) from kinetic data on the exsolution (McCallister and Yund, *Year Book* 74, pp. 433–436) and



homogenization (Fernandez-Moran *et al.*, 1971) of submicroscopic intergrowths of coherent clinopyroxene lamellae. Availability of diffusion data for pyroxenes places on a much firmer footing model calculations such as those attempted by Miyamoto and Takeda (1977) and Huebner *et al.* (1975). As a consequence, it should be possible to place time constraints on a variety of important geologic processes, from the emplacement of kimberlites to the cooling associated with the uplift of an orogenic belt.

#### INTERGRANULAR DIFFUSION IN QUARTZ-PERICLASE REACTION COUPLES

*John B. Brady*

Values of the diffusivities of major elements in crystalline rocks are crucial to the quantitative evaluation of metasomatic processes. Because an intergranular aqueous film may be present, possible diffusivities in crystalline rocks under crustal conditions are strictly bounded only by the values of diffusivities in aqueous solutions ( $10^{-4}$  —  $10^{-5}$  cm<sup>2</sup>/sec) and in common minerals (typically  $<<10^{-12}$  cm<sup>2</sup>/sec). Laboratory measurements of element diffusivities in outcrop samples of metamorphic or igneous rocks would almost certainly be sensitive to the internal stress history of the rock as reflected by the density of microcracks introduced (see Brace, 1972; Nur and Simmons, 1970). Therefore, although possibly relevant to near-surface processes, diffusion measurements using outcrop samples (for example, Kovalev, 1972) are not applicable to the processes of regional metamorphism where microcracks would be only transient phenomena. Similarly, available measurements on synthetic polycrystalline oxides (see Kingery, 1974a,b) are not applicable to crustal processes because of the scrupulous exclusion of water in those experiments (cf. Cabine, 1962; Tiernan, 1969).

This report summarizes a series of ex-

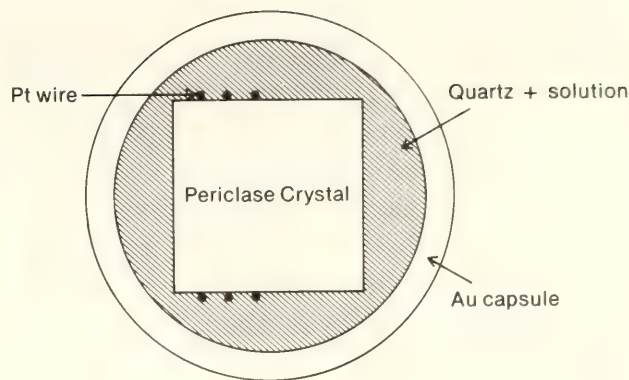


Fig. 77. Starting configuration for the diffusion experiment.

periments designed to measure the intergranular diffusivity of silica through crystalline rocks that have not suffered the stresses produced by cooling and decompression. The basic plan of the experiment is quite simple: surround a single crystal of one mineral with the powder of an incompatible mineral in the presence of an aqueous fluid. The two minerals should react to form one or more product minerals that would grow, for a judicious choice of minerals and solution, as "armoring" zones or coronas around the central single crystal. The rate of growth of the reaction rim should be a measure of the rate of diffusion of one or more chemical species across the rim. If the reaction zones have low porosities, they may adequately model microcrack-free rocks during the experiment. Thus, diffusion coefficients obtained may be applicable to material transfer during regional metamorphism.

The actual experimental geometry used is shown in Fig. 77. One or more cleaved crystals of synthetic periclase (1–2 mm rectangular solids) were sealed in 3-mm gold tubing along with natural quartz powder and water or a sodium chloride solution. In some instances the periclase crystals were wrapped with platinum wire to serve as an inert marker. The charge was then annealed in a horizontally or vertically mounted, cold-seal pressure vessel at a pressure of 1 or 2 ( $\pm 0.05$ ) kbar and a temperature



of 600°–750°C ( $\pm 10^\circ$ ) for a period of 3 hr to 8 weeks. (The experiments were initiated in the Hoffman Laboratory of Harvard University and completed at the Geophysical Laboratory.) At the conclusion of each run the pressure vessel was quenched in air. The gold capsule was carefully “peeled” from around the charge, which was then mounted in epoxy, cross sectioned by grinding, and examined in reflected light.

As desired, in every run reaction rims were formed around the periclase crystal. Forsterite was one of the product minerals in all runs. Brucite and talc were produced in a few runs. No chain silicate was positively identified in any run. On the basis of exploratory runs, the great majority of experiments were conducted

at 1 kbar and 650° or 700°C where forsterite was the only mineral product. A photomicrograph of the result of a typical run is shown in Fig. 78. The forsterite rims are polycrystalline with sufficient density to take a high polish locally. The grain size of the forsterite, observed with a scanning electron microscope, is 1  $\mu\text{m}$  or less. In many instances the forsterite rim is separated from the periclase crystal by a small gap; however, the congruency of the rim and the periclase crystal suggests that separation occurred either during the quench or during the mounting procedures. The fact that the forsterite invariably surrounds periclase (inside the platinum wires) rather than quartz and the probable high concentration of silicon relative to magnesium in these solutions (see Frantz, *Year Book* 73, pp. 380–384) suggest that the main diffusive flux across the forsterite zone was of silicon, rather than magnesium.

Although preliminary results suggested that the rims grew by diffusion (Brady, 1977), one can infer from the data in Fig. 79 that *no* measurable growth of the reaction rims occurred after the first few hours of the experiment. Because the forsterite zone is present but does not appear to thicken with run time, two conclusions seem inescapable. (1) The forsterite rim must grow rapidly at the start of the experiment by diffusion of silica from the quartz to the periclase. (2) Early in each run, presumably because of plugging of the connected porosity of the reaction rim, diffusion rates are reduced below the sensitivity of this type of measurement. These conclusions mark, respectively, the success and failure of the experiment. The success was the production of a polycrystalline reaction rim with “tight” grain boundaries early in the experiment across which a diffusion potential exists. The failure was an inability to measure diffusion rates across this rim, due in part to the initial great thickness of the rim. Even though no rim growth was observed with

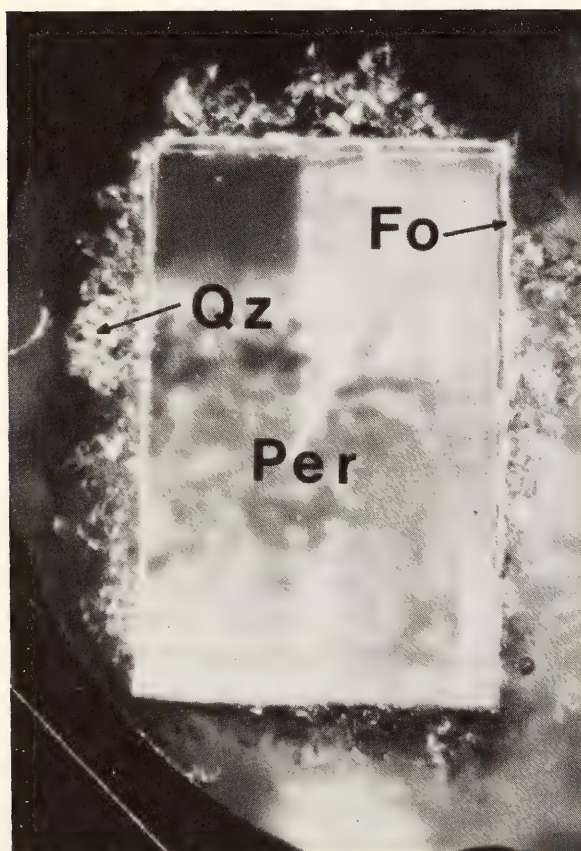


Fig. 78. A photomicrograph of a cross section of a diffusion run of two weeks at 1 kbar and 700°C. The central periclase crystal (1.7  $\times$  2.6 mm) is surrounded successively by a uniform rim (0.02 mm thick) of polycrystalline forsterite and clusters of quartz crystals. The whole assemblage is set in epoxy in a circular holder. Shadows mottle the periclase crystal.



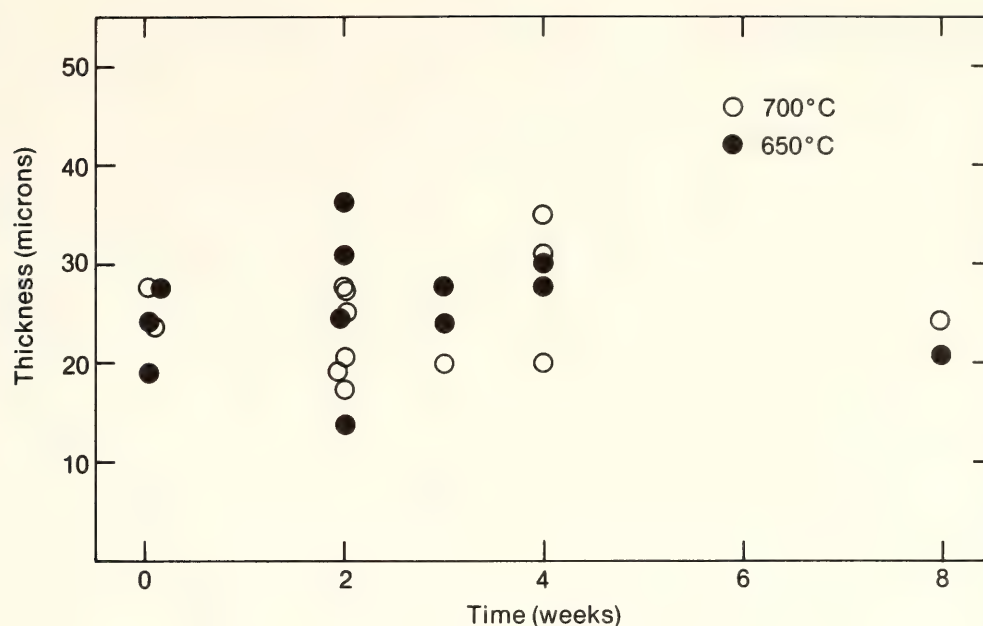


Fig. 79. Results of the diffusion runs expressed in terms of the thickness of the forsterite reaction rims as a function of the run duration. The uncertainty of each point in terms of observed variations in rim thickness is generally about  $\pm 5 \mu\text{m}$ .

run duration, a diffusion potential existed. Thus, diffusion rates must be lower than the detection limit, and an upper bound to the diffusivity may be calculated.

A maximum effective intergranular diffusion coefficient for silica was determined from the data using the following assumptions. (1) The diffusive flux of silicon is much greater than the flux of magnesium. (2) All diffusion occurred along intergranular paths in which the concentration of silica approximates the concentration of silica in water for the same value of the chemical potential of silica. (3) The polycrystalline forsterite zone approaches the density of forsterite single crystals. Equation (3) of Booth (1948) is the appropriate solution of the diffusion equation for these boundary conditions:

$$L^2 = 2D^*_{\text{SiO}_2} t (\rho^{\text{soln}}_{\text{SiO}_2} / \rho^{\text{Fo}}_{\text{SiO}_2})$$

where  $L$  (cm) is the thickness of the reaction rim,  $t$  (sec) is the duration of the anneal,  $(\rho^{\text{soln}}_{\text{SiO}_2} / \rho^{\text{Fo}}_{\text{SiO}_2})$  is the ratio of the density of  $\text{SiO}_2$  in the quartz-saturated solution to the density of  $\text{SiO}_2$  in forsterite, and  $D^*_{\text{SiO}_2}$  is the "effective"

intergranular diffusion coefficient of silica. The term  $D^*_{\text{SiO}_2}$  implicitly includes any contributing effects of intergranular porosity and tortuosity and would change if either of those variables changed. The average thickness of the observed forsterite rims is about  $25 \mu\text{m}$ . If one assumes that the rims formed during the first few minutes of the experiment and that a 50% increase in thickness would be detected, no observed growth in eight weeks leads to a maximum diffusivity of  $1 \times 10^{-9} \text{ cm}^2/\text{sec}$  using the expression

$$D^*_{\text{SiO}_2} < \frac{L^2(t) - L^2(t_0)}{t (\rho^{\text{soln}}_{\text{SiO}_2} / \rho^{\text{Fo}}_{\text{SiO}_2})}$$

Data used to evaluate the density ratio were taken from Robie *et al.* (1978), Walther and Helgeson (1977), and Burnham *et al.* (1969).

An upper bound for the effective intergranular diffusivity of silica is potentially quite useful. Assuming that the intergranular region of the forsterite zones produced, adequately models that of crystalline rocks, one can use the upper bound to place lower limits on the length of time needed to grow diffusion textures observed in rocks, such as meta-

somatic zones. For example, to grow a pure talc zone 1 m thick from pure forsterite at the contact of an ultramafic body with a wet, siliceous country rock would require more than 400 m.y. by intergranular diffusion of silica. Growth of a 1-mm talc zone would require at least 400 years. To the extent that the physical properties of the intergranular film are like those of a liquid, the diffusivities of most other major elements should be similar to that of silicon and less than  $10^{-9}$  cm<sup>2</sup>/sec. Effective diffusion distances for specific examples may differ from those given above owing to variations in the density ratio term. It is clear, however, that intergranular diffusion is not an adequate mechanism for extensive mass transfer, even on a geologic time scale, in rocks of low porosity.

#### INTERDIFFUSION OF S AND Se IN TIEMANNITE

*Nabil Z. Boctor and John B. Brady*

In addition to being the main anion in sulfide-type minerals, sulfur is a common element in sulfoselenide and sulfosalt minerals. Most of the studies on sulfur diffusion so far have been concerned with the self-diffusion of this element in sulfide minerals such as pyrrhotite ( $\text{Fe}_{1-x}\text{S}$ , Condit *et al.*, 1974), sphalerite ( $\text{ZnS}$ , Gobrecht *et al.*, 1967), wurtzite ( $\text{ZnS}$ , Blount *et al.*, 1967), and hawleyite ( $\text{CdS}$ , Kumar and Kroger, 1971; Sysoev *et al.*, 1969). The mineral tiemannite,  $\text{HgSe}$ , commonly contains minor amounts of sulfur in solid solution that substitute for Se in its structure. In some cases, however, the isomorphous substitution of S for Se is very extensive. Almost the entire range of  $\text{HgSe-HgS}$  compositions has been observed in nature, as in the Lucky Boy Mine, Marysvale District, Utah (Bethke, 1957; Boctor, 1976). Tiemannite was selected for investigation of sulfur diffusion in selenide-type minerals because (1) equilibrium relations in the  $\text{Hg-S-Se}$  system are well known

(Boctor, 1976) and (2) high-purity single crystals of  $\text{HgSe}$  grown by the vapor-transport method (Laboratory for Crystal Growth, Purdue University) were readily available.

Polished rectangular slabs of a mercury-saturated single crystal of tiemannite were completely surrounded by tightly-packed powdered synthetic  $\text{HgS}$  ( $<0.063$   $\mu\text{m}$  in diameter) and placed in silica tubes with closely fitting silica rods to reduce the vapor volume. The silica tubes were evacuated, sealed under vacuum, and annealed at 700°, 600°, and 500°C, respectively, for periods of 168, 288, and 408 hr. The vapor pressure over the charges was that of the system, and no attempts were made to control the sulfur or selenium fugacities. In each experiment, the tiemannite crystal retained its form and polished surfaces and was easily separated from the  $\text{HgS}$  powder after the run. Compositional profiles were determined with the electron microprobe from polished cross sections of each tiemannite crystal. For Hg analyses  $\text{M}\alpha$  radiation was used; for S and Se analyses,  $\text{K}\alpha$  radiation was used. Synthetic  $\text{HgSe}$  was used as a standard for Se and Hg. The  $\text{HgS}$ , provided by Materials Research Company, was used as a standard for S. Atomic number, absorption, and fluorescence corrections of raw electron microprobe data were performed using the MAGIC IV computer program of Colby (1971).

Typical sulfur compositional profiles are shown in Fig. 80 along with curves previously fitted to the data on probability paper (cf. da Silva and Mehl, 1951, p. 161). Within the limits of accuracy of the electron microprobe ( $\pm 2\%$  of the measured concentration), the tiemannite crystals have remained binary ( $\text{S} + \text{Se} = \text{constant}$ ,  $\text{Hg} = \text{constant}$ ) during the diffusion experiments. Therefore, although data were not obtained for the selenium distribution in the  $\text{HgS}$  powder, the sulfur penetration data may be analyzed using the Boltzmann-Matano solution (Matano, 1933) to the



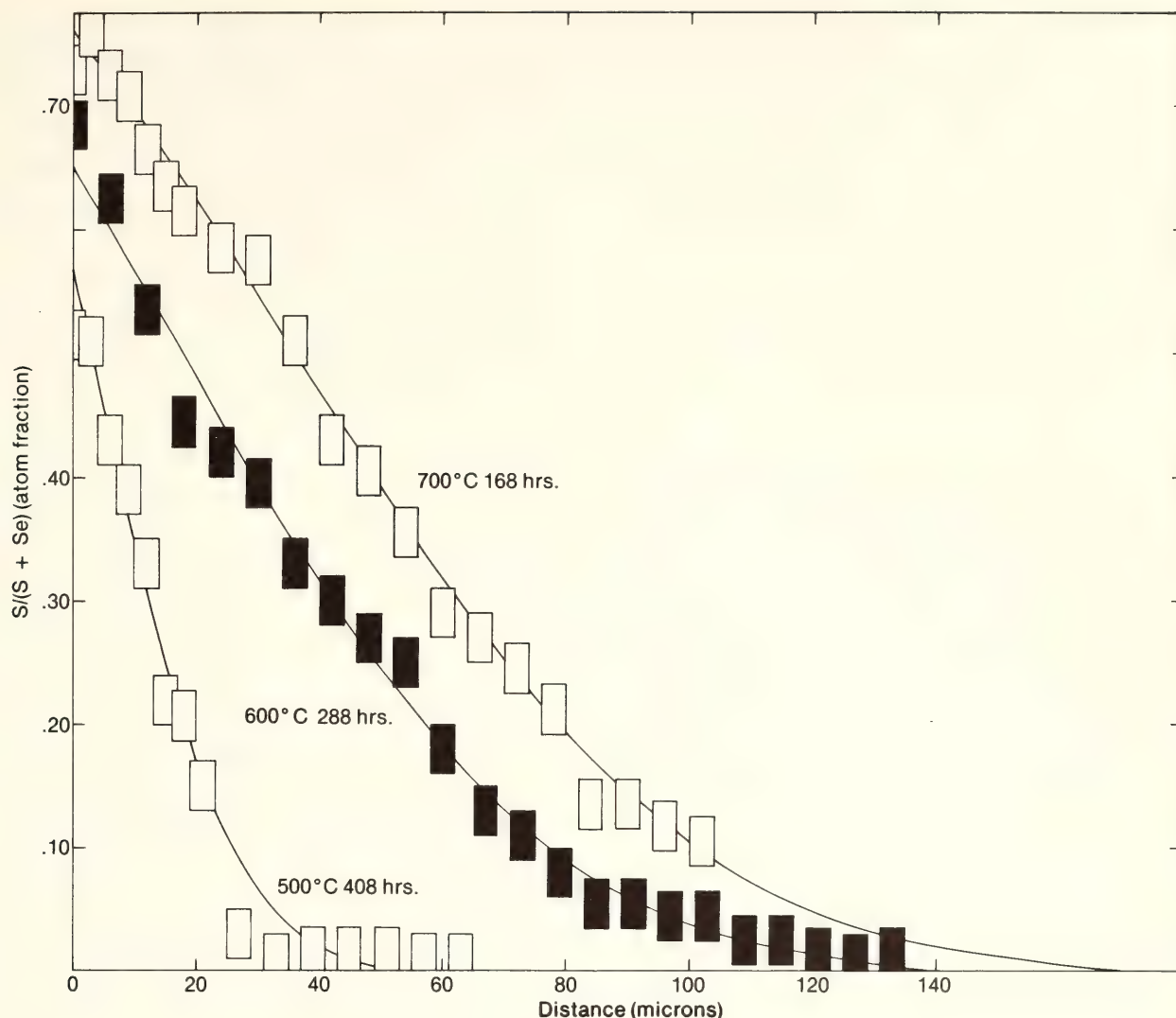


Fig. 80. Compositional profiles measured with the electron microprobe of the sulfur content of the tiemannite crystals with respect to distance from the crystal surface. The curves are a best fit of the data obtained using probability graph paper.

diffusion equation with the Boltzmann-Matano interface at the tiemannite crystal surface. A discontinuity in physical properties at the interface between the tiemannite single crystal and the HgS powder does not preclude the use of the Boltzmann-Matano solution (Jost, 1950; Appel, 1968). Slopes and areas were obtained graphically from the compositional profiles and used to compute the diffusion coefficients listed in Table 32. Uncertainties are based on the reproducibility of electron microprobe and graphical determinations. No concentration dependence of the interdiffusion coefficients can be verified within the limits of precision, although it appears that more

sulfur-rich compositions yield slightly higher diffusivities. Because the variation of molar volume with composition is not known, the diffusion coefficients could not be corrected for possible volume effects.

An activation energy for S-Se interdiffusion of  $105 (\pm 12)$  kJ/mole may be derived from the data. This value is within the range reported by Stevenson (1973, table 7.1) for similar minerals. The interdiffusion coefficients determined for tiemannite are larger than sulfur self-diffusion coefficients in sulfides with the same structure, such as sphalerite (Gobrecht *et al.*, 1967). This result is consistent with the suggestion of Steven-

TABLE 32. Interdiffusion Coefficients for S and Se in Tiemannite

<i>T</i> , °C	S/(S+Se)	<i>D</i> (cm <sup>2</sup> /sec)
700	0.5	$3.5 (\pm 1.0) \times 10^{-11}$
700	0.2	$2.7 (\pm 1.0) \times 10^{-11}$
600	0.5	$0.9 (\pm 0.8) \times 10^{-11}$
600	0.2	$1.1 (\pm 1.0) \times 10^{-11}$
500	0.5	$1.2 (\pm 0.5) \times 10^{-12}$
500	0.2	$1.1 (\pm 0.5) \times 10^{-12}$

son (1973, p. 435) that interdiffusion coefficients for the chalcogenides are expected to be much larger than the self-diffusion coefficients. These conclusions represent a first step in understanding diffusion kinetics in the tiemannite-metacinnabar series and in further characterizing these minerals for possible industrial applications as semiconductors.

#### KINETICS AND MECHANISM OF THE METACINNABAR TO CINNABAR TRANSITION

*N. Z. Boctor and R. H. McCallister*

In the majority of mercury ores, metacinnabar, a high-temperature polymorph of mercury sulfide, coexists with the low-temperature polymorph cinnabar. The phase relations in the condensed Hg-S system (Kullerud, *Year Book* 64, pp. 193–195; Potter, 1973), however, indicate that metacinnabar of stoichiometric composition is not a stable phase in the system below 345°C. In nature, metacinnabar always contains minor amounts of Fe, Zn, or Se in solid solution. Dickson and Tunell (1959) found that the presence of minor (unspecified) amounts of Fe and Zn, respectively, in solid solution lowers the temperature of the cinnabar to metacinnabar transition to 305° and 240°C. Potter (1973) found that 0.5 wt % ZnS in solid solution with HgS is sufficient to lower its transition temperature to at least 237° ± 3°C.

To evaluate the role of impurities in

retarding the metacinnabar ⇌ cinnabar transition, isothermal rate studies were undertaken on synthetic HgS doped with 0.3 wt % ZnS, 0.5 wt % ZnS, 0.6 wt % FeS, and 1.0 wt % FeS at 200° and at 100°C. The rate of transition was measured by monitoring the x-ray intensities of the (200) reflection of metacinnabar and (102) reflection of cinnabar. Thirty milligrams was used to prepare a smear mount of each sample, and eight oscillations between 30° to 32° 2θ were measured. The fraction transformed,  $\xi$ , was determined from a calibration curve prepared by monitoring the intensities of the (200) reflection of metacinnabar and (102) reflection of cinnabar for synthetic mixtures of both minerals. The ratios of the intensity of the cinnabar reflection to the sum of the intensities of the metacinnabar and cinnabar reflections  $I_{(102)\text{cin}}/I_{(102)\text{cin}} + I_{(200)\text{mc}}$  are plotted vs. the weight fraction of metacinnabar in the mixtures (Fig. 81). The solid line in Fig. 81 represents a least-squares fit for the data points, and the dashed lines represent 1 standard deviation from the mean.

#### Experimental Results

The results of the isothermal rate studies performed on Zn- and Fe-doped mercury sulfide, respectively, are shown in Figs. 82 and 83. The fractions transformed in both cases decrease with increase of impurity content. For example, the fractions transformed of metacinnabar doped with 0.6 wt % FeS and 1.0 wt % FeS after annealing for 550 hr at 100°C are, respectively, 38.5% and 20.2%. For the same impurity content, the fraction transformed increases with increase in temperature. For example, an increase in temperature from 100° to 200°C for metacinnabar doped with 1% FeS increases the fraction transformed from 20.2 to 27.5% for the same annealing time of 550 hr. Therefore, it seems that the impurity content of metacinnabar plays a more critical role in retard-



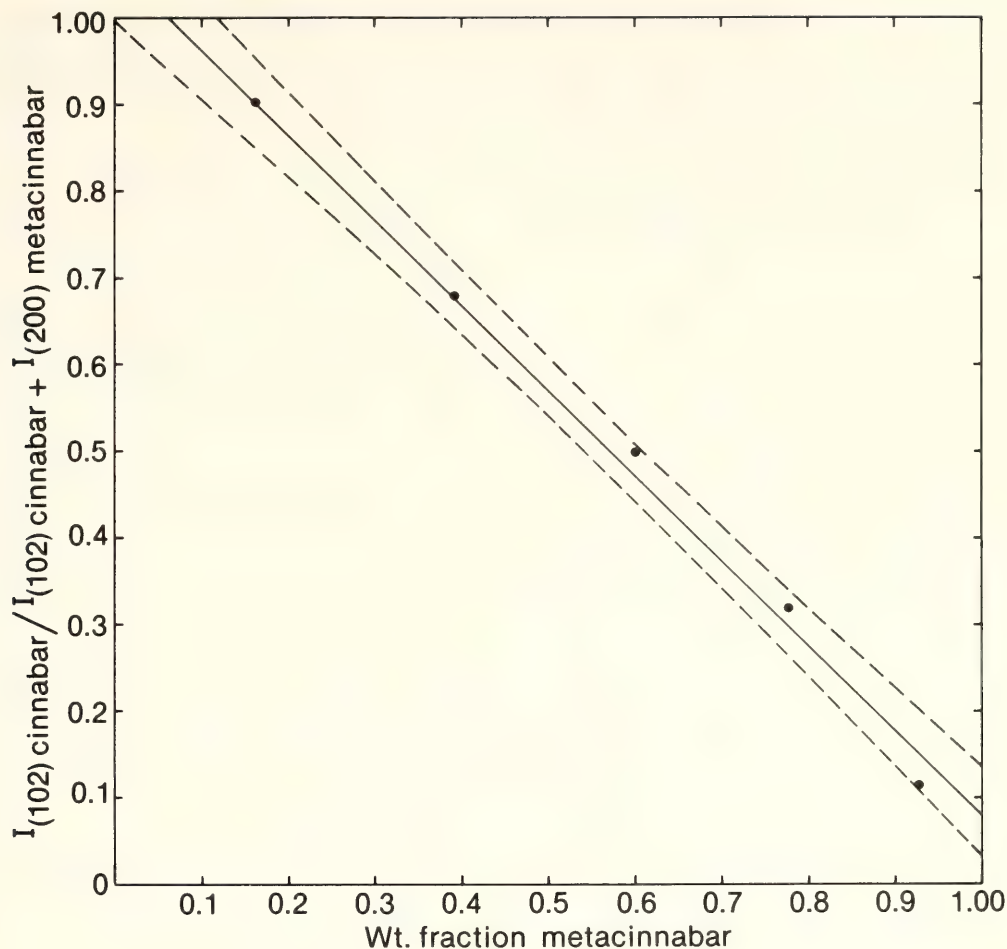


Fig. 81. A plot of the intensity of the (102) reflection of cinnabar/the intensity of the (102) reflection of cinnabar + the intensity of the (200) reflection of metacinnabar vs. weight fraction of metacinnabar in cinnabar-metacinnabar mixtures. Solid line is the best-line fit for the data points, and the dashed lines represent 1 standard deviation.

ing its transition to cinnabar than that of temperature.

The isothermal rate data on the metacinnabar  $\rightleftharpoons$  cinnabar transition can be analyzed theoretically using the relation proposed by Avrami (1941),

$$\xi = 1 - \exp(-Kt^n),$$

where  $K$  is a constant,  $t$  is time, and the value of  $n$  is dependent on the nucleation and growth rates as well as the type and distribution of nucleation sites. This relation is theoretically valid only for diffusion-controlled growth for small values of  $t$ . It is approximately valid, however, for values of  $\xi$  up to 0.9 (Christian, 1965). The slopes of the lines when  $\log \ln 1/(1 - \xi)$  is plotted vs.  $\log t$  correspond to the value of  $n$ . For both polymorphic transitions and interface-

controlled growth, theoretical values of 1 and 2 for the slope suggest, respectively, grain-boundary and grain-edge nucleation. The values of the slopes of  $\log \ln 1/(1 - \xi)$  vs.  $\log t$  plots produced by linear regression of the data obtained in this study range between 0.7 and 1.5 and are mostly closer to 1 than to 2. These values suggest that grain-boundary nucleation is the dominant type of nucleation during the metacinnabar  $\rightleftharpoons$  cinnabar transition. The analysis of the data also suggests that the cinnabar nuclei formed in the early stages of the transition because the value of  $n$  should be 4 for constant nucleation rate and  $>4$  for an increasing nucleation rate.

Microscopic investigation of Zn- and Fe-doped metacinnabar annealed for various periods of time shows that nuclei

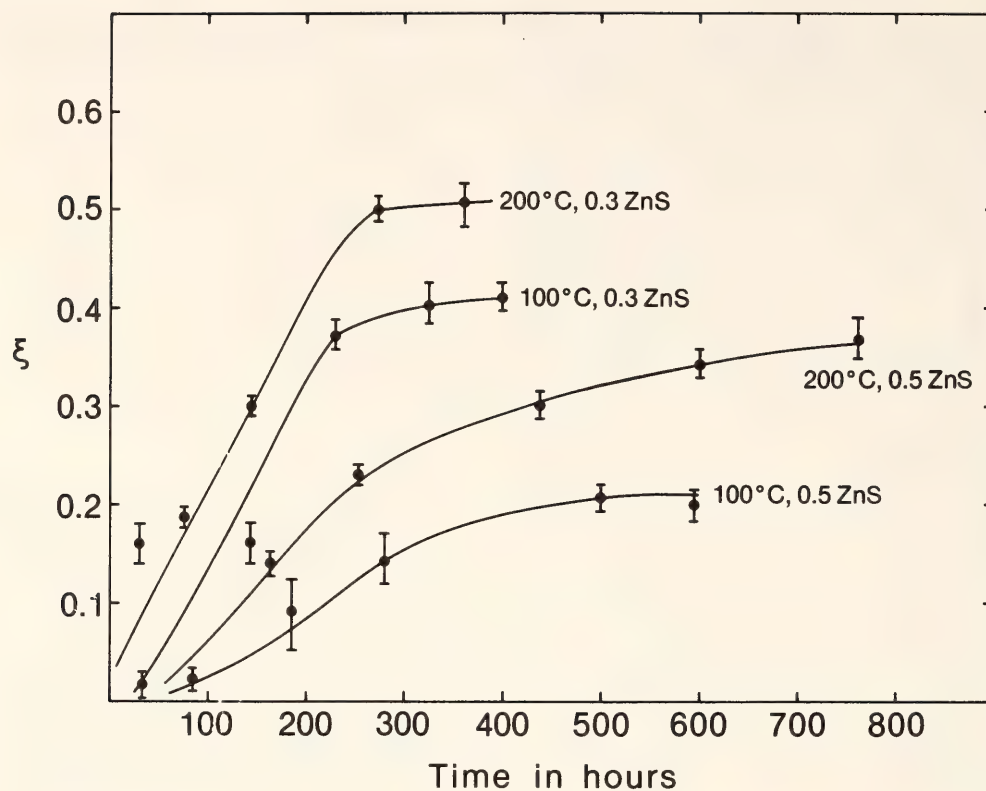


Fig. 82. A plot of the fraction transformed,  $\xi$ , as a function of time for Zn-doped HgS at 200° and 100°C.

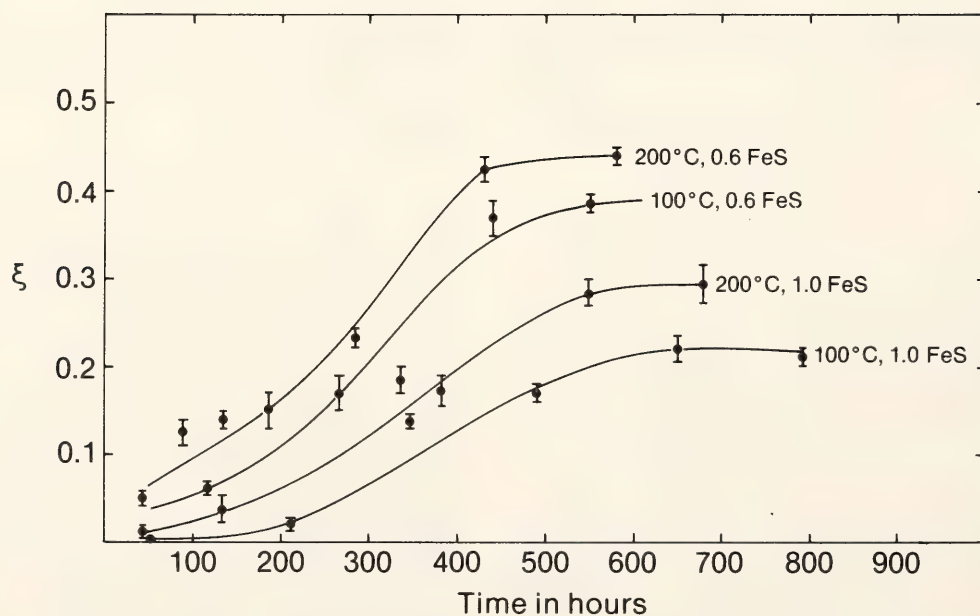


Fig. 83. A plot of the fraction transformed,  $\xi$ , as a function of time for Fe-doped HgS at 200° and 100°C.

of cinnabar appear at the early stages of transition on grain boundaries along twinning planes and along cracks induced during the transition because of the volume difference between the two poly-

morphs. The transition is propagated by growth of the nucleated cinnabar. Both the isothermal rate studies and microscopic investigation, however, indicate that the transition never goes to com-



pletion, and the maximum percentage of transformation reached during the course of this investigation was 50.5%.

### *Discussion*

In the present study, it has been demonstrated that very small amounts of Zn and Fe in solid solution can retard the metacinnabar-cinnabar transition considerably in the temperature range between 100° and 200°C. Most mercury ores form within this temperature range (Dickson, 1964; Tugarinov and Naumov, 1972). Metacinnabar from mercury ores, however, shows higher concentrations of impurities (up to 3 wt % Fe and 4.5 wt % Zn) than those used in the experiments. Such high concentrations of impurities are expected to severely retard or prohibit the transition of metacinnabar to cinnabar in nature and are responsible for the metastable coexistence of these two phases through geologic time.

In phase transformations that proceed by a nucleation and growth mechanism, such as the metacinnabar-cinnabar transition, the transformation is initiated by formation of nuclei of the new phase in the matrix and growth of the transformed phase by slow migration of the interface boundaries. Impurities in solid solution, even in minute quantities, can profoundly reduce the migration rates of these boundaries. Rath and Hu (1972) found that the activation energy for boundary migration increased from 16 kcal/mole for zone-refined Al containing up to 50 ppm Mg in solid solution to 34 kcal/mole when the impurity content was increased to 250 ppm. During phase transitions, impurities tend to segregate to grain boundaries because of an interaction force between the impurity and the boundary, and if the impurities at the boundary diffuse slowly, they exert a drag effect on the boundary that reduces its mobility (Chan, 1962; Lücke and Stüwe, 1971; Lücke *et al.*, 1972).

For the "impurity drag effect," as discussed above, it is assumed that grain boundaries are planar in configuration and that impurity concentrations remain uniform in the plane of the boundary for all boundary velocities. Roy and Bauer (1975) found that for nonplanar grain boundaries, nonplanar distribution of impurities takes place. Thus, certain regions in the boundary will be depleted in impurities, whereas other regions will acquire an excess of impurities, and non-uniform drag on the boundary will result. Therefore, the boundary migrates in a discontinuous manner as impurity clusters are produced, and the clusters later dissolve in the matrix.

Although it was not possible to study the distribution of impurities in the run products because of their fine-grained nature, data on the distribution of impurities in partially transformed metacinnabar from mercury ores (Boctor, 1976) suggest that they behave in a manner similar to that predicted by the "impurity drag effect." In the ores studied, no complete transformation of metacinnabar to cinnabar was observed, and the concentration of impurities in metacinnabar is always higher at the interface than at the center of the crystals. The concentration of impurities in metacinnabar relies in highly transformed crystals shows a higher impurity content than metacinnabar in grains showing a small degree of transformation, even when these grains occur in the same polished section. In all cases studied, the cinnabar phase produced during the transition is almost free of any impurities. Apparently impurities segregated to the grain boundaries during the transition, exerting a drag effect on its mobility, which reduced or prohibited the growth of the already nucleated cinnabar. Progressive diffusion of impurities into metacinnabar with progress of the transition led to the enrichment of its relics in impurities.

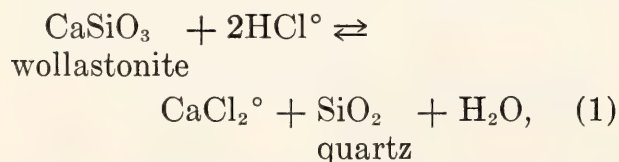
## HYDROTHERMAL SOLUTIONS AND METASOMATISM

AN EXPERIMENTAL STUDY OF MINERAL SOLUBILITIES AND THE THERMODYNAMIC PROPERTIES OF AQUEOUS  $\text{CaCl}_2$  IN THE SYSTEM  $\text{CaO-SiO}_2\text{-H}_2\text{O-HCl}$ 

R. K. Popp and J. D. Frantz

It is well known that chemical transport in many geological systems occurs by means of dissolved species in an intergranular aqueous fluid phase. If such processes are to be identified and modeled, it is first necessary to understand the equilibrium relations between mineral assemblages and coexisting aqueous fluids. The purpose of this study is to extend knowledge of mineral solubilities and thermodynamic properties of aqueous metal species in chloride-bearing fluids for geologically relevant systems. An initial report (Frantz and Popp, 1979) was concerned with the solubilities of magnesium silicates in supercritical aqueous chloride solutions and with complexing of aqueous magnesium chloride. A similar study in the system  $\text{CaO-SiO}_2\text{-H}_2\text{O-HCl}$  is reported here.

Dehydration equilibria in the system  $\text{CaSiO}_3\text{-H}_2\text{O}$  were experimentally investigated in the range  $250^\circ\text{--}450^\circ\text{C}$  and 10,000–30,000 psi by Buckner *et al.* (1960). Recently, Gunter and Eugster (1978) determined wollastonite solubility represented by the reaction



in the range 1–2 kbar and  $750^\circ\text{--}850^\circ\text{C}$  using the silver-silver chloride buffering technique (Frantz and Eugster, 1973). This study is an investigation of the same reaction to considerably lower temperatures in the range of metamorphic processes, using a modified Ag-AgCl buffering technique.

*Experimental Procedures*

The general experimental techniques and procedures used in this study are essentially the same as those described by Frantz and Popp (1979). All runs were made in rapid-quench, cold-seal, hydrothermal pressure vessels with argon as the pressure medium. Temperature gradients within the pressure vessels were previously determined at pressure. Temperatures were measured with sheathed chromel-alumel thermocouples within an uncertainty of  $\pm 5^\circ\text{C}$ . Pressure was measured with a precision of  $\pm 20$  bars, by means of a 7.7-kbar Heise bourdon-tube gauge.

*Ag + AgCl Buffer Technique.* The experimental technique used in this study consists of equilibration of the mineral assemblage wollastonite + quartz with aqueous calcium chloride solutions at elevated temperature and pressure. Determination of the concentrations of total dissolved calcium and associated  $\text{HCl}^\circ$  in the fluid in equilibrium with the solids is required to provide information on the calcium species in the fluid and calculate the free energy of such species. All runs were made using the Ag-AgCl buffer technique without an external oxygen buffer, i.e., the so-called “unbuffered” method described by Frantz and Popp (1979).\*

*Starting Materials.* The wollastonite used in all runs was synthesized hydrothermally at  $775^\circ\text{C}$  and 2 kbar for 5 days from fired CaO (Fisher Lot 765885) and cristobalite, prepared by firing silicic acid (Fisher Lot 722134). Natural quartz from a pegmatite (Lisbon, Maryland) was used in all runs.

*Analytical Techniques.* After quench, capsules were punctured with a stainless

\* A detailed description of the method and comparison with the standard or “buffered” method is given in the reference.

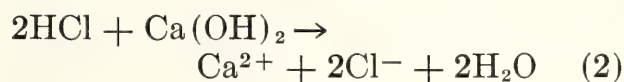


steel needle and solutions were extracted using Corning micropipettes. Suspended solids were removed by centrifuging. Calcium concentration in the fluid from the outer capsule was measured by atomic absorption spectrometry using a 500-ppm  $\text{SrCl}_2$  matrix. Chloride concentration from the outer capsule was measured using a Buchler chloridometer, whereas chloride in the fluid from the inner capsules was measured using a flow-cell colorimetric technique (Popp *et al.*, *Year Book* 77, pp. 913–917). The precision of all methods is  $\pm 5\%$ . Solid products were examined by x-ray and optical methods.

### Experimental Results

Experiments were run at 2 kbar at temperatures between  $425^\circ$  and  $600^\circ\text{C}$ , and at 1 kbar between  $450^\circ$  and  $600^\circ\text{C}$  for from 1 to 16 days.

Interpretation of the experimental results requires knowledge of the calcium complexes in the fluid at the temperature and pressure of the runs. As discussed by Gunter and Eugster (1978) in relation to their investigation of this equilibrium at higher temperatures, hydroxide-bearing species can be ruled out as the major species in the fluid because the concentration of chloride in the fluid from the outer capsule is twice that of total calcium ( $\text{Ca}_T$ ) after quench. The concentration of  $\text{HCl}^\circ$  is very small compared with that of  $\text{Ca}_T$ , so that titrations of the type



on quench cannot produce sufficient quantities of chloride. Furthermore, hydroxide species were not observed in the quenched solid products by x-ray or optical methods. It is concluded, therefore, that the predominant calcium species in the fluid under the run conditions must be  $\text{CaCl}_2^\circ$ ,  $\text{CaCl}^+$ ,  $\text{Ca}^{2+}$ , or a combination of these species.

Increasing association of aqueous electrolytes with increasing temperature has

been well documented from conductance measurements (e.g., Franck, 1956a, b; Quist and Marshall, 1968). On the basis of hydrothermal experiments on talc + quartz in equilibrium with aqueous magnesium chloride solutions, Frantz and Popp (1979) concluded that the transition from dissociated  $\text{Mg}^{2+}$  and  $\text{Cl}^-$  ions to completely associated  $\text{MgCl}_2^\circ$  occurs between approximately  $400^\circ$  and  $550^\circ\text{C}$  at 2 kbar. A similar analysis of the relationship between the concentrations of total calcium and  $\text{HCl}^\circ$  in the experiments of this study can provide information about calcium speciation.

The measurement of total calcium in the fluid after quench reflects the total concentration of all calcium species present under the  $P$ - $T$  conditions of the runs. From theoretical considerations similar to those discussed in Frantz and Popp (1979) in relation to Mg speciation, it can be shown that if  $\text{CaCl}_2^\circ$  is the only calcium species in the fluid,

$$\frac{\partial \log (m_{\text{Ca}_T} \cdot X_{\text{H}_2\text{O}})}{\partial \log m_{\text{HCl}^\circ}} = 2,$$

whereas if  $\text{CaCl}^+$  is the only calcium species,

$$\frac{\partial \log [m_{\text{Ca}_T} \cdot (X_{\text{H}_2\text{O}})^{1/2}]}{\partial \log m_{\text{HCl}^\circ}} = 1,$$

and if  $\text{Ca}^{2+}$  is the only calcium species,

$$\frac{\partial \log [m_{\text{Ca}_T} \cdot (X_{\text{H}_2\text{O}})^{1/3}]}{\partial \log m_{\text{HCl}^\circ}} = 2/3.$$

A plot of  $\log (m_{\text{Ca}_T} \cdot X_{\text{H}_2\text{O}})$  vs.  $m_{\text{HCl}^\circ}$  for the 2-kbar runs is shown in Fig. 84. Each pair of points at a given calcium value represents the concentrations of  $\text{HCl}^\circ$  obtained from each of the two inner capsules. The circles with crosses represent identical values of  $\text{HCl}^\circ$  in both capsules. The curves represent linear least-squares fits of the data. To avoid confusion, data points have been omitted from the  $550^\circ$  and  $450^\circ\text{C}$  curves. Slopes of the least-squares fits, along with their standard deviations, are summarized in Table 33.

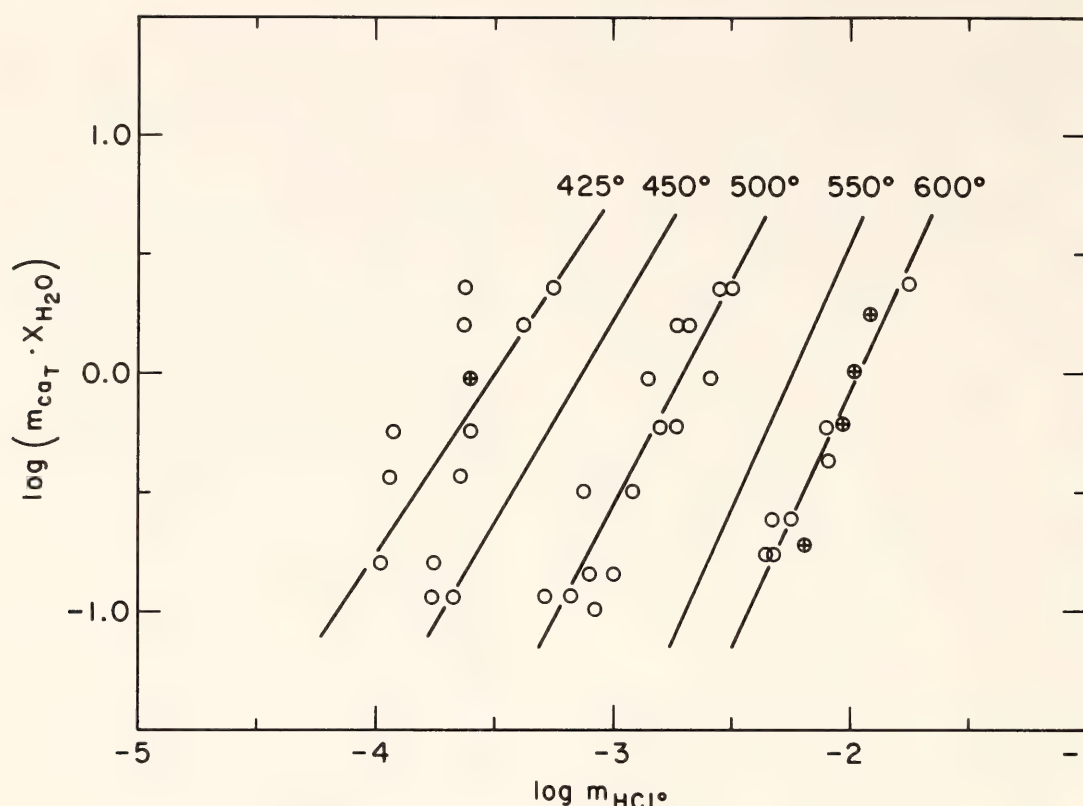


Fig. 84. Plot of  $\log (M_{CaT} \cdot X_{H_2O})$  vs.  $\log m_{HCl^\circ}$  for solutions in equilibrium with the assemblage wollastonite + quartz at 2 kbar. Circles with crosses indicate identical concentrations of  $HCl^\circ$  in both inner capsules. Analytical errors are approximately the same size as circles. Straight lines represent least-squares regressions. Data points for 550° and 450°C lines have been omitted from the plot to avoid confusion.

On the basis of the comparison of the slopes in Table 33 with the theoretical slopes discussed above, it is concluded that at 2 kbar, associated  $CaCl_2^\circ$  is the predominant species in the fluid at temperatures greater than approximately 500°C. The slopes at lower temperatures are inconclusive. Even though there is a trend toward slopes less than 2, the errors are quite large (Table 33). At these lower temperatures, the decreased rate of hy-

drogen diffusion through the Pt membranes results in poor reversibility of the  $HCl^\circ$  concentrations.

Equilibrium constants for reaction 1 (i.e., if all calcium occurs as  $CaCl_2^\circ$ ) are plotted vs.  $1/T$  in Fig. 85. The solid symbols in Fig. 85 represent equilibrium constants determined by Gunter and Eugster (1978) at higher temperature using the Ag-AgCl buffer in conjunction with an external hematite-magnetite oxygen buffer. The agreement between the two approaches is excellent, but the advantages of the "unbuffered" technique are evident from Figs. 84 and 85. The reaction can be investigated to much lower temperatures, and information concerning the calcium species in the fluid can be obtained.

The error of the 2-kbar and 425°C equilibrium constant in Fig. 85 is relatively large, but despite this fact the point falls off the major trend in the

TABLE 33. Least-Squares Slope of  $\log (m_{CaT} \cdot X_{H_2O})$  vs.  $\log m_{HCl^\circ}$  for Runs at 2 kbar

$T, ^\circ C$	Slope	$\sigma$
600	2.18	0.21
550	2.30	0.40
500	1.87	0.22
450	1.66	0.35
425	1.49	0.53



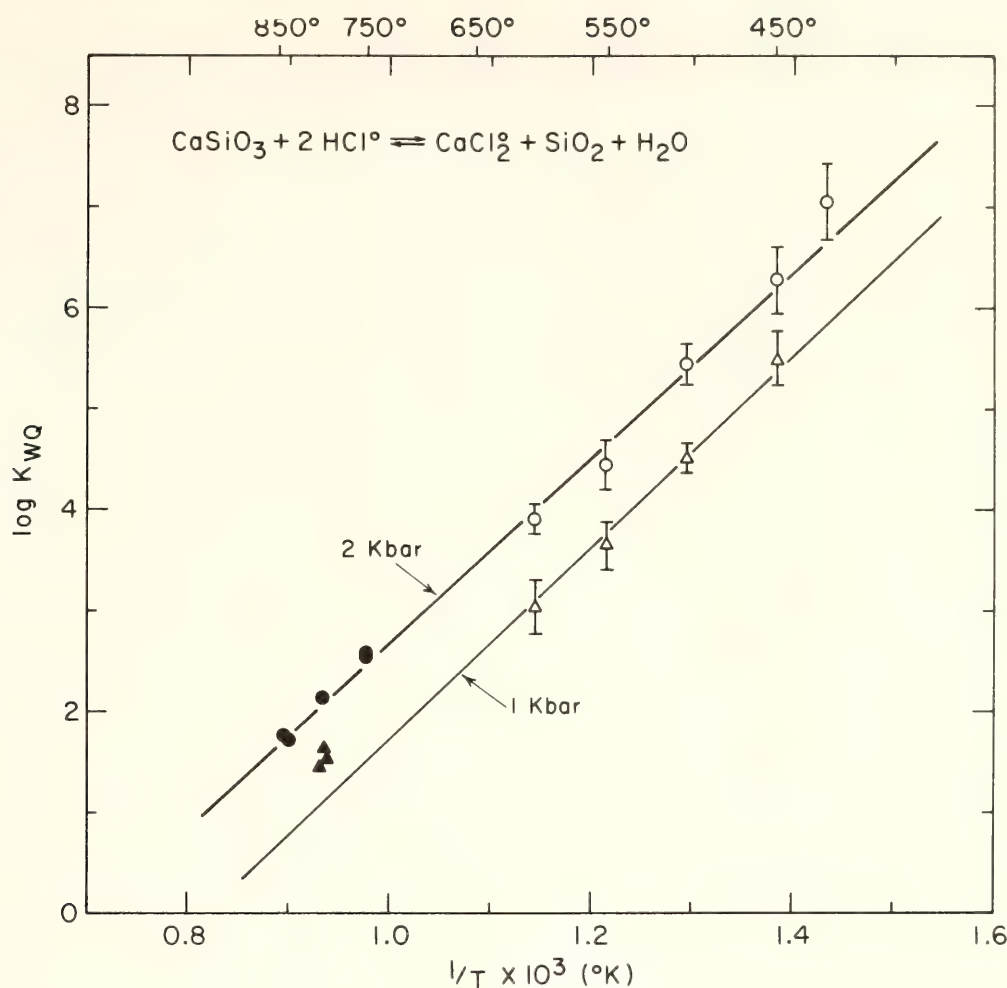


Fig. 85. Plot of  $\log K_{wq}$  expressed as in Equation 3 vs.  $1/T$  for 1- and 2-kbar data. Open symbols are from this study; error bars represent one standard deviation. Solid symbols are from Gunter and Eugster (1978). Straight lines are from linear regression of data.

direction of excess calcium. Such an excess of calcium is expected if additional Ca species are present in the fluid. Thus the data may indicate significant dissociation to  $\text{CaCl}^+$  or  $\text{Ca}^{2+}$  at  $425^\circ\text{C}$ .

Linear least-squares fits of  $\log K_{wq}$  vs.  $1/T$  ( $^\circ\text{K}$ ) yield:

$$\text{for 1 kbar: } \log K_{wq} = -7.847(0.798) + 9560.9(641.0)/T(^\circ\text{K});$$

$$\text{for 2 kbar: } \log K_{wq} = -6.440(0.300) + 9126.0(264)/T(^\circ\text{K}).$$

Numbers in parentheses represent one standard deviation of the intercept and slope, respectively. Data for the 2-kbar results were all weighted equally. For the 1-kbar results, the higher temperature data of Gunter and Eugster (1978) were

weighted as 1/2 the lower temperature data.

#### Thermodynamic Calculations

For the reaction in Equation 1, at equilibrium,

$$\begin{aligned} \Delta G_r^\circ &= G_f^\circ(\text{CaCl}_2^\circ) + G_f^\circ(\text{qtz}) \\ &+ G_f^\circ(\text{H}_2\text{O}) - G_f^\circ(\text{wo}) - 2G_f^\circ(\text{HCl}^\circ) = \\ &= -RT \ln K_{wq}, \end{aligned} \quad (3)$$

where the standard states of  $\text{H}_2\text{O}$  and the solids are pure phases at temperature and pressure, and the standard states of aqueous  $\text{CaCl}_2^\circ$  and  $\text{HCl}^\circ$  are hypothetical 1-molal solutions at temperature and pressure. Standard-state free energies of formation [ $G_f^\circ(i)$ ] refer to the

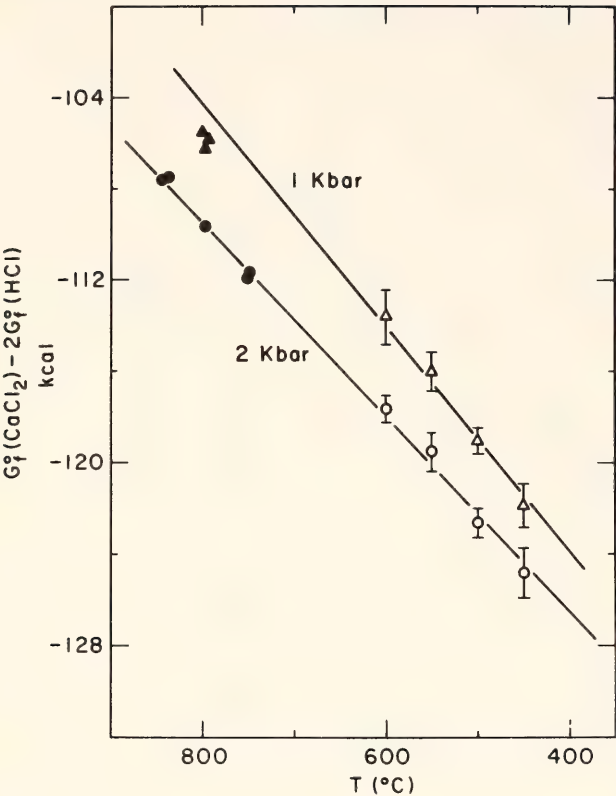


Fig. 86. Plot of the difference in free energy of formation between associated aqueous  $\text{CaCl}_2^\circ$  and  $\text{HCl}^\circ$ . Symbols and curves are the same as in Fig. 85.

free energy of formation of the phases in their standard states (i.e., at  $T$  and  $P$ ) from the elements at  $25^\circ\text{C}$  and 1 atm, where the enthalpies of the elements are zero at  $25^\circ\text{C}$  and 1 atm. The difference in free energy of formation between aqueous  $\text{CaCl}_2^\circ$  and  $\text{HCl}^\circ$  [i.e.,  $G^\circ_f(\text{CaCl}_2^\circ) - 2G^\circ_f(\text{HCl}^\circ)$ ] can be calculated from Equation 3, using values of  $K_{wq}$  obtained from the experiments, values of  $G^\circ_f(i)$  for wollastonite and quartz calculated from the data of Helgeson *et al.* (1978), and  $G^\circ_f(\text{H}_2\text{O})$  from Fisher and Zen (1971) corrected to the standard state defined above. Figure 86 shows the results of the calculations using the 1- and 2-kbar data. Least-squares fits of the free-energy difference vs.  $T$  ( $^\circ\text{K}$ ) yield:

for 1 kbar:

$$G^\circ_f(\text{CaCl}_2^\circ) - 2G^\circ_f(\text{HCl}^\circ) = -156.9(2.7) + 0.0490(0.0033) T \quad (^\circ\text{K}) \text{ kcal;}$$

for 2 kbar:

$$G^\circ_f(\text{CaCl}_2^\circ) - 2G^\circ_f(\text{HCl}^\circ) = -155.4(1.0) + 0.0428(0.0011) T \quad (^\circ\text{K}) \text{ kcal.}$$

Values for one standard error of the slope and intercept are given in parentheses. Weighting of the data is the same as for the  $\log K_{wq}$  vs.  $1/T$  fits discussed above. Errors in the free energies of the solids and  $\text{H}_2\text{O}$  are neglected. Calculation of solubility constants for minerals that do not contain chloride always involves  $\text{CaCl}_2^\circ$  and  $\text{HCl}^\circ$  in the ratio 1:2; therefore, the free energy of aqueous  $\text{CaCl}_2^\circ$  alone was not computed.

Solubility constants for Ca-bearing minerals in the system  $\text{MgO-CaO-SiO}_2\text{-HCl-CO}_2$  were calculated using the following free-energy data: aqueous  $\text{CaCl}_2^\circ$  and  $\text{MgCl}_2^\circ$ , respectively, from this study and Frantz and Popp (1979); mineral phases calculated from the data of Helgeson *et al.* (1978);  $\text{H}_2\text{O}$  from Fisher and Zen (1971) corrected to the standard state employed here; aqueous silica from Walther and Helgeson (1977); and  $\text{CO}_2$  calculated from the data of Holloway (1977). Table 34 summarizes the calculated solubility constants for the

TABLE 34. Equations for Solubility Constants\*

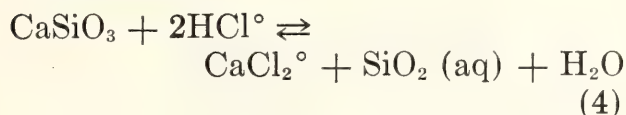
Mineral	Pressure, kbar	$a$	$b$
Wollastonite	1	- 8.197	8,748
	2	- 6.122	7,996
Diopside	1	-20.913	18,254
	2	-14.660	15,205
Tremolite	1	-77.545	63,762
	2	-51.589	50,361
Calcite	1	- 2.976	4,966
	2	- 2.303	4,854
Magnesite	1	- 7.343	7,824
	2	- 4.458	6,122
Dolomite	1	-10.159	12,260
	2	- 6.732	10,546

\*  $\log K = (a + b)/T(^\circ\text{K})$ . Temperature range  $400^\circ\text{--}600^\circ\text{C}$ .



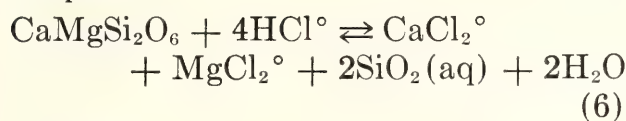
following reactions, with the assumptions that activity coefficients are unity, all solids are pure phases, and the amounts of polynuclear species such as  $\text{CaMgCl}_4^\circ$  are negligible:

*Wollastonite:*

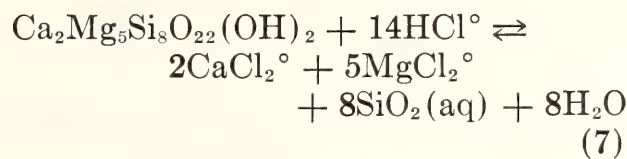


$$K = \frac{(m_{\text{CaCl}_2^\circ})(m_{\text{SiO}_2(\text{aq})})(X_{\text{H}_2\text{O}})}{(m_{\text{HCl}^\circ})^2} \quad (5)$$

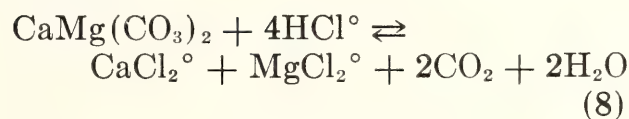
*Diopside:*



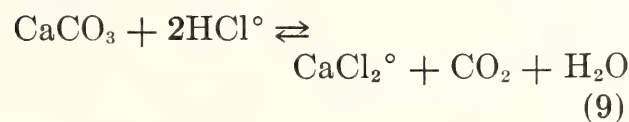
*Tremolite:*



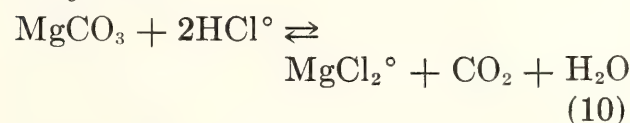
*Dolomite:*



*Calcite:*



*Magnesite:*



With these data, compositions of chloride-bearing hydrothermal fluids coexisting with minerals in the system  $\text{CaO-MgO-SiO}_2\text{-H}_2\text{O-CO}_2$  can be calculated (Frantz and Popp, this Report). Knowledge of the composition of the fluid in equilibrium with such mineral assemblages is essential if theoretical models for mass transport (e.g., Frantz and Mao, 1979) are to be extended into the realm of natural environments.

## ELECTRICAL CONDUCTANCE STUDIES OF $\text{MgCl}_2\text{-H}_2\text{O}$ AND $\text{CaCl}_2\text{-H}_2\text{O}$ SOLUTIONS

*J. D. Frantz and W. L. Marshall*

Aqueous solutions commonly consist of mixtures of ions and molecular species. Material fluxes resulting from intergranular diffusion and infiltration are highly dependent on the concentrations of these species in grain-boundary fluids. Identification of the most prevalent ions or complexes is therefore of fundamental importance to the problem of material transport.

Franck (1965a) and Quist and Marshall (1968), using electrical conductance measurements, demonstrated that in 1-1 electrolytes such as KCl and NaCl in aqueous solutions, the predominant species changes from separated hydrated ions to an electrically neutral species (ion pairs) with increasing temperature and decreasing pressure. Similar studies have not been undertaken on 2-1 electrolytes with the exception of Ritzert and Franck's (1968) investigation of  $\text{BaCl}_2$ . Frantz and Popp (1979) and Popp and Frantz (this Report) demonstrated that both  $\text{MgCl}_2$  and  $\text{CaCl}_2$  exist as molecular species above  $500^\circ\text{C}$  at 2000 bars in solutions of concentrations greater than 1 molal. In  $\text{MgCl}_2$ , evidence of dissociation was observed at temperatures between  $400^\circ$  and  $500^\circ\text{C}$  at 2000 bars. An attempt was made to compute dissociation constants for  $\text{MgCl}_2$ , but these calculations involved assumptions concerning the identity of the ionic complex and the values of activity coefficients. Because of the lack of precision of Frantz and Popp's (1979) method and the relatively high concentrations of the solutions studied, electrical conductance measurements were performed on dilute  $\text{MgCl}_2\text{-H}_2\text{O}$  and  $\text{CaCl}_2\text{-H}_2\text{O}$  solutions.

### Experimental Method

The experiments were performed at the Oak Ridge National Laboratory (ORNL) with equipment originally de-

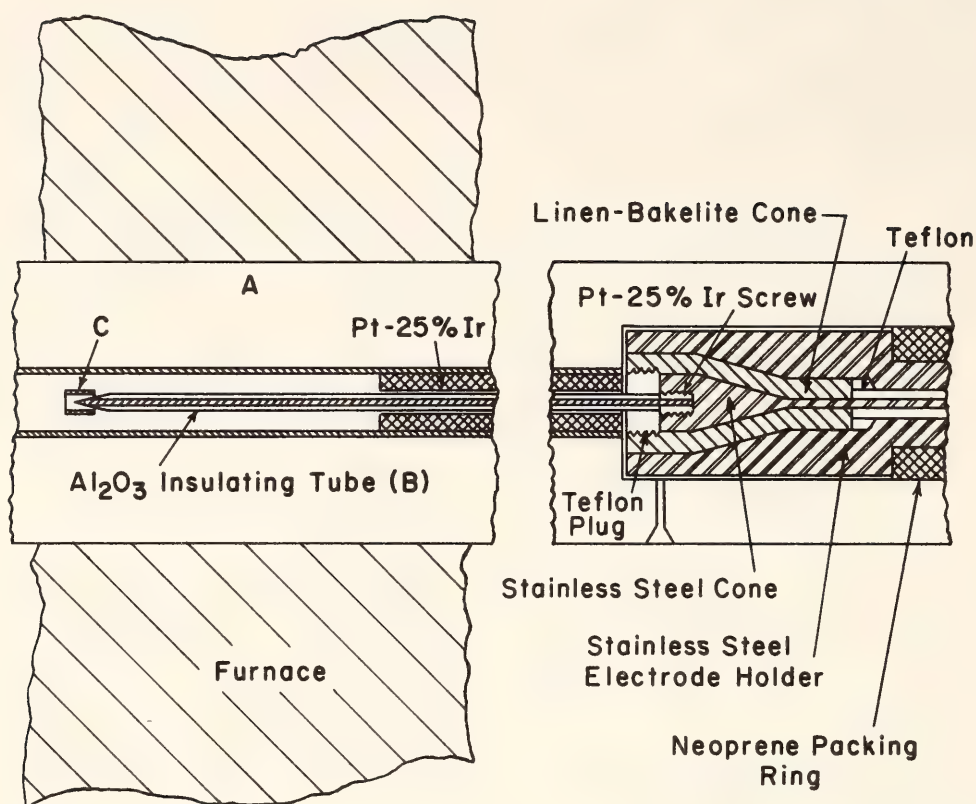


Fig. 87. Conductance apparatus: (A) pressure vessel, (B) aluminum oxide tube, (C) platinum-iridium cylinder, (D) solution entrance, (E) furnace.

signed by Franck *et al.* (1962), which was later improved by Quist and Marshall (1968).

The apparatus shown in Fig. 87 consists of a platinum-iridium-lined pressure vessel (A) with a platinum-iridium wire running from one end of the vessel through an aluminum-oxide tube (B) to a platinum-iridium cylinder (C) in the center. The wire passes out of the vessel through a Bakelite insulator. The lining of the vessel and the small cylinder (C) are both coated with platinum black and act as the electrodes.

Specific conductivity is the conductance  $[1/\text{resistance (R)}]$  of a  $1\text{-cm}^3$  cube of electrolytic solution:

$$\sigma = a/R = \frac{l}{A}/R, \quad (1)$$

where  $a$  is defined as the cell constant and equals the distance between electrodes divided by their area. The cell constants for the ORNL apparatus were obtained by measuring the conductances

of 0.1 and 0.01 demal reference solutions for which the specific conductances have been precisely determined (Jones and Bradshaw, 1933). Solutions of  $\text{MgCl}_2\text{-H}_2\text{O}$  and  $\text{CaCl}_2\text{-H}_2\text{O}$  were prepared using ultrapure crystalline material and were analyzed by gravimetrically determining chloride concentrations.

### Results

Electrical conductances were measured for three concentrations of each salt as a function of temperature and pressure. Molalities of 0.001, 0.0025, and 0.005 were chosen because the electrical conductances were well above the background values of pure water in the ORNL apparatus but still dilute enough to be analyzed by relatively simple ion-migration models (Robinson and Stokes, 1954; Fuoss *et al.*, 1965; Shedlovsky, 1938). In Figs. 88A and 88B, respectively, the specific conductances of 0.005 molal  $\text{MgCl}_2\text{-H}_2\text{O}$  and  $\text{CaCl}_2\text{-H}_2\text{O}$  solutions are plotted



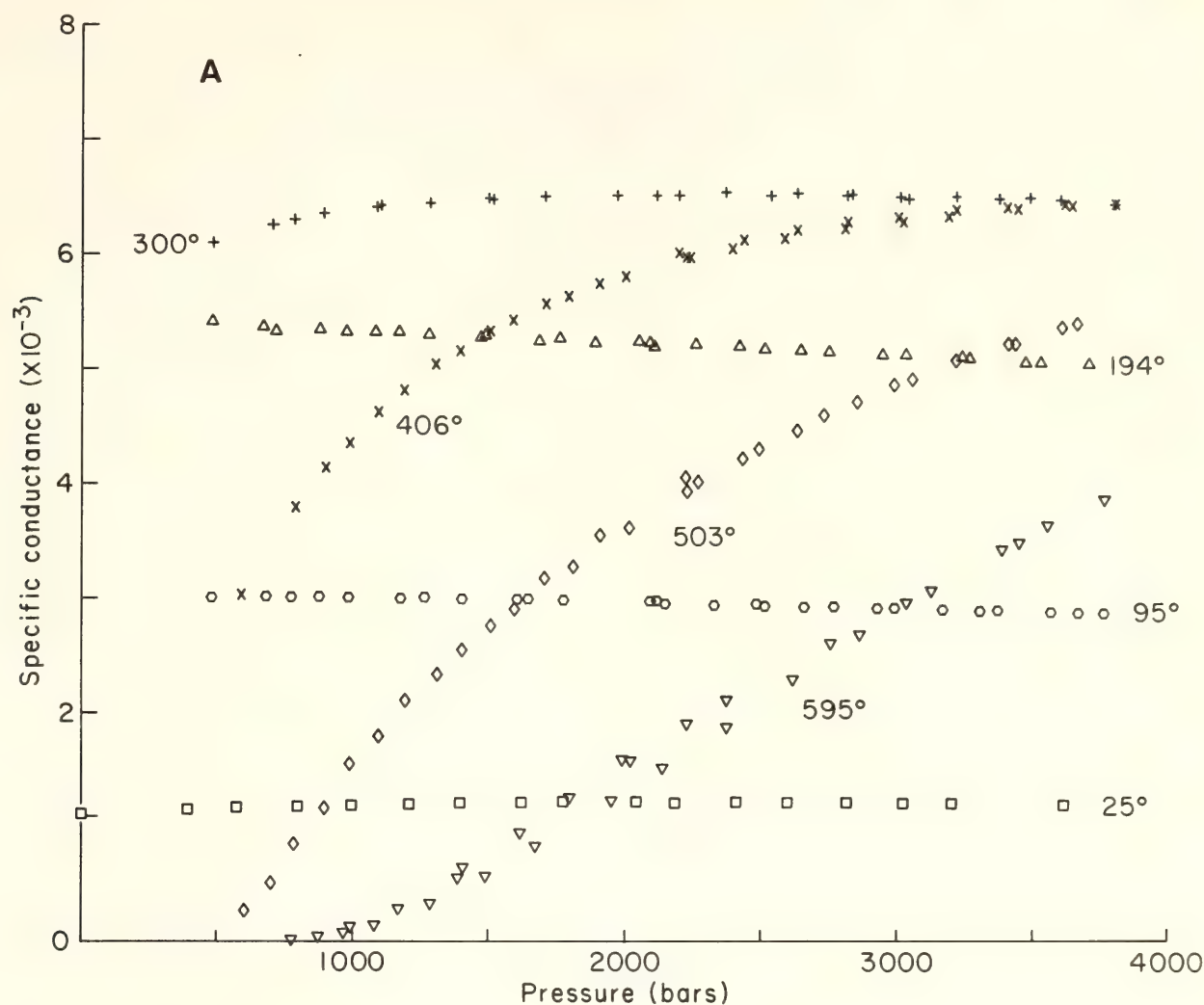


Fig. 88A. Specific conductance ( $\sigma$ ) vs. pressure for a 0.005 molal  $\text{MgCl}_2$  solution at temperatures ranging from 25° to 600°C.

against pressure for temperatures ranging from 25° to 600°C. Measurements were made by heating the apparatus to the desired temperature at 2000 bars and then changing pressure after each conductance measurement. Pressures were first increased incrementally to 4000 bars, then decreased to 500 bars, and finally increased back to the initial pressure. Very little hysteresis was observed, and the measurement error is believed to be less than 2%. Hydrolysis and subsequent hydrolytic precipitation appeared to occur in the  $\text{MgCl}_2$ - $\text{H}_2\text{O}$  system at 600°C, as can be seen by the irreversibility of the measurements at this temperature.

In Figs. 89A and 89B the specific con-

ductances of  $\text{MgCl}_2$  and  $\text{CaCl}_2$  are plotted against temperature for different densities of water. The values initially tend to increase with increasing temperature to a maximum between 300° and 400°C. Thereafter, the conductances decrease with a further rise in temperature.

These trends can be understood by considering the following expression, which relates the specific conductance ( $\sigma$ ) to the concentration ( $C_j$ ) and mobility ( $u_j$ ) of the free  $j$ th ions:

$$\sigma = F \sum_{j=1}^n Z_j C_j u_j, \quad (2)$$

where  $F$  is Faraday's constant and  $Z_j$  is the charge of the  $j$ th ion. The increase

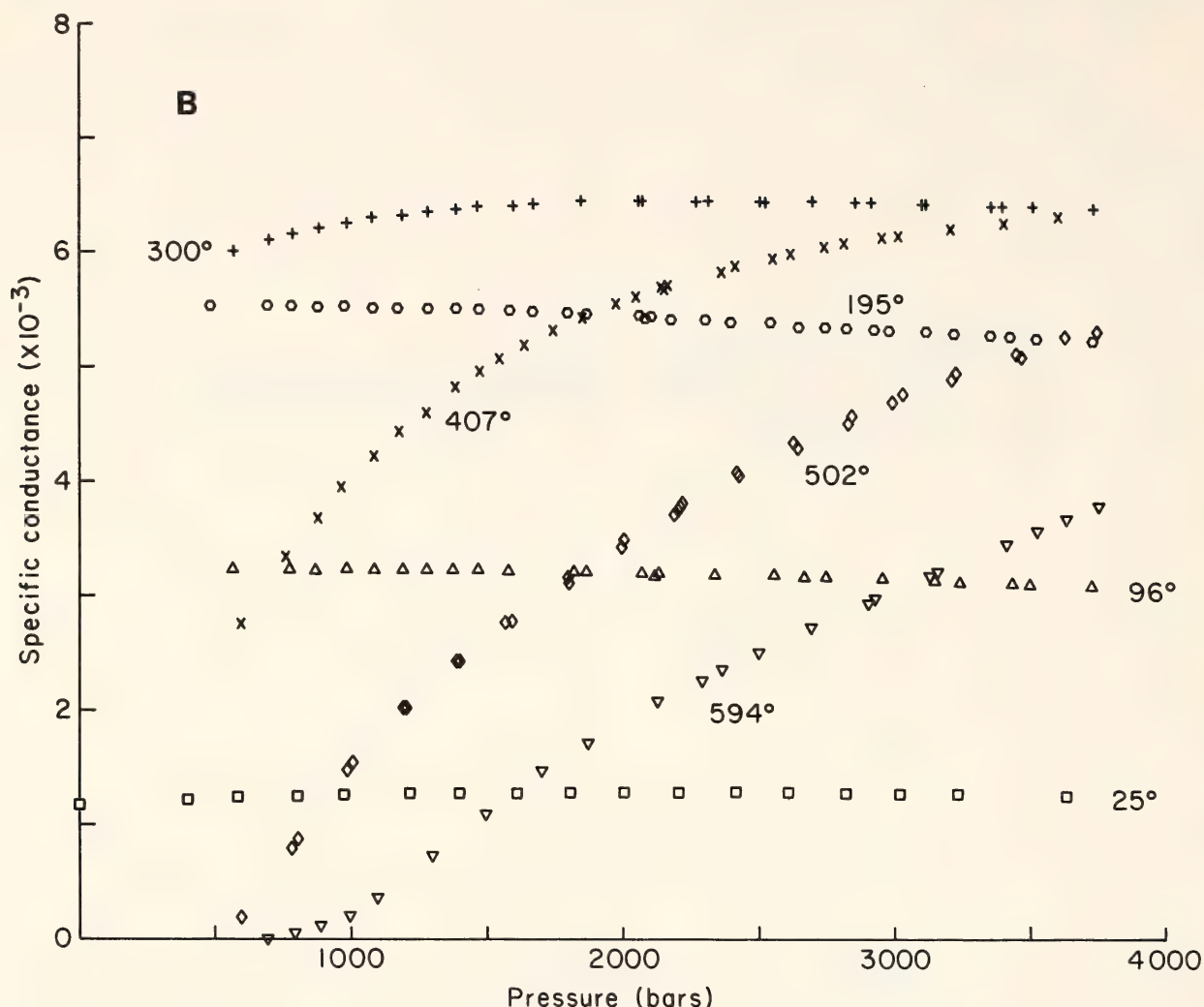


Fig. 88B. Specific conductance ( $\sigma$ ) vs. pressure for a 0.005 molal  $\text{CaCl}_2$  solution at temperatures ranging from 25° to 600°C.

of conductance with temperature below 300°C is considered first. In Fig. 90 the viscosity ( $\eta$ ) of  $\text{H}_2\text{O}$  is plotted against temperature for densities of 1.0, 0.8, and 0.6. At constant density, the viscosity decreases monotonically. The mobility of an ion can be represented as a function of the viscosity as follows (Stokes mobility):

$$u_j = Z_j e_0 / 1800 \pi r_j \eta, \quad (3)$$

where  $r_j$  is the radius of the  $j$ th ion and  $e_0$  is a unit electrostatic charge. Thus, as the temperature increases, the viscosity decreases, the mobility of the ions increases, and the specific conductance increases. The increase in specific conductance with decreasing density seen in

Figs. 89A and 89B can also be explained by changes in the  $\text{H}_2\text{O}$  viscosity. Inspection of Equation 2 suggests that at temperatures above the maxima, the decrease in specific conductance must be due to a decrease in the number of free ions and an increased degree of formation of neutral species (ion pairs). This trend is reasonable when one considers the free energy of ion-solvent interactions as a function of temperature (Born equation):

$$\Delta G_{I.S.} = \frac{(Z_j e_0)^2}{2r_j} \left( 1 - \frac{1}{\epsilon_s} \right), \quad (4)$$

where  $\epsilon_s$  is the dielectric constant of water. The dielectric constant decreases with increasing temperature and decreases



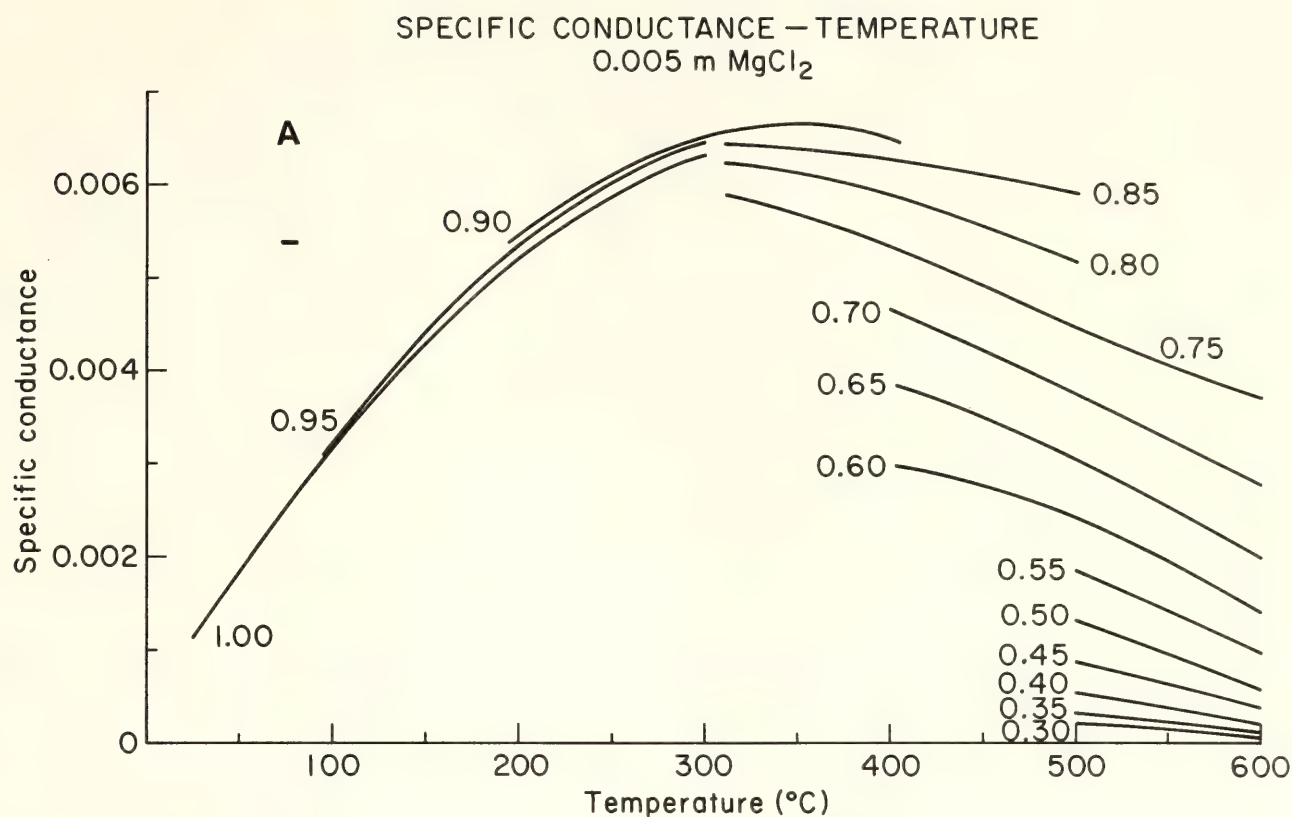


Fig. 89A. Specific conductance ( $\sigma$ ) vs. temperature for a 0.005 molal  $\text{MgCl}_2$  solution for different densities.

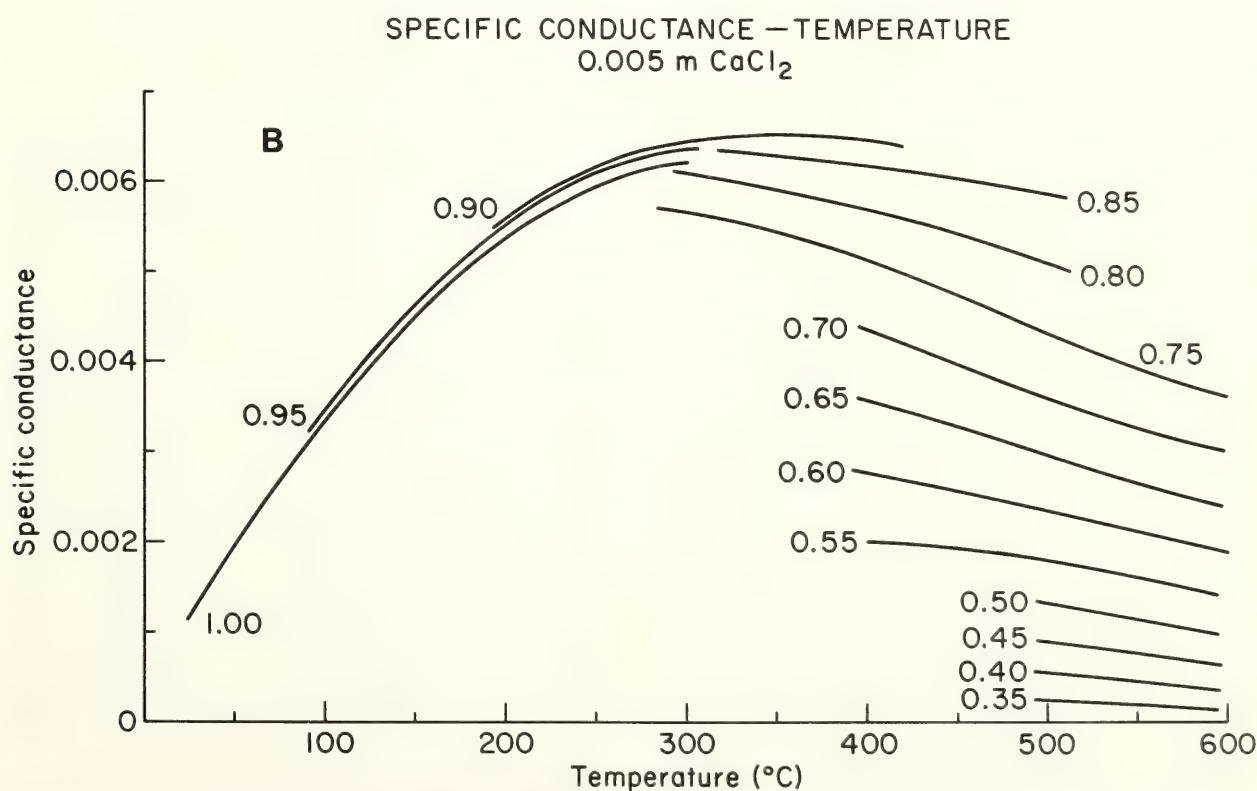


Fig. 89B. Specific conductance ( $\sigma$ ) vs. temperature for a 0.005 molal  $\text{CaCl}_2$  solution for different densities.

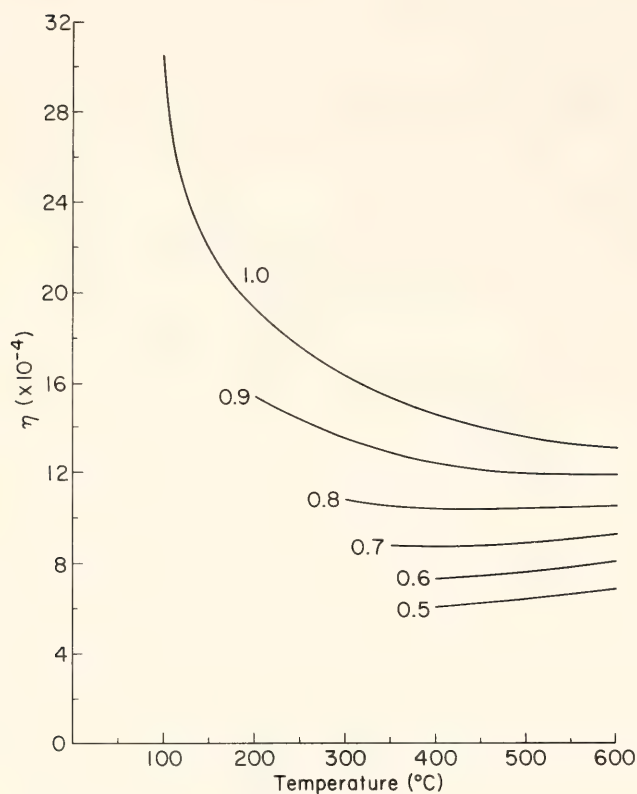


Fig. 90. Viscosity ( $\eta$ ) vs. temperature at densities of 1.0, 0.8, and 0.6 (Dudziak and Franck, 1966).

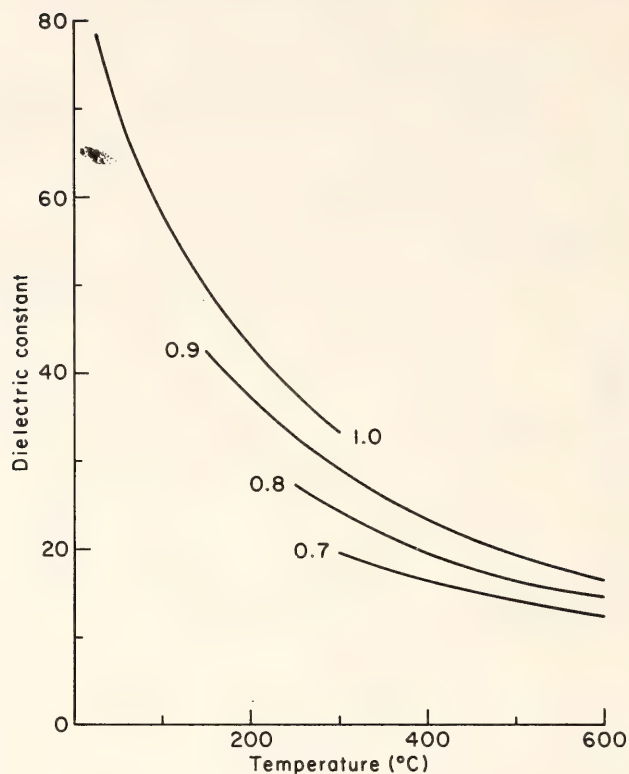


Fig. 91. Dielectric constant of water as a function of temperature at densities of 1.0, 0.8, and 0.6 (Quist and Marshall, 1965).

ing density as seen in Fig. 91. Thus, ion-solvent interactions tend to become less important, and consequently ion-ion interactions become more important as temperature increases and density decreases. The trend is also seen in 1-1 electrolytes.

### Conclusions

The trends seen by Frantz and Popp (1979) and Popp and Frantz (this Report) toward association of ions in the systems  $\text{MgCl}_2\text{-H}_2\text{O}$  and  $\text{CaCl}_2\text{-H}_2\text{O}$  at temperatures above  $400^\circ\text{C}$  at 1000 and 2000 bars are confirmed by the electrical conductance experiments. The data are now available to calculate the stepwise thermodynamic ionization constants for both salts. At temperatures above  $500^\circ\text{C}$  mass transport reactions involving concentrated solutions of 2-1 electrolytes can be written in terms of associated species because these complexes contain the bulk of the metals in the solution.

### ALTERATION OF CALCIUM-MAGNESIUM SILICATES BY CHLORIDE-BEARING HYDROTHERMAL FLUIDS

*J. D. Frantz and R. K. Popp*

The reaction products resulting from metasomatism through an intergranular fluid are dependent on the relative concentrations of the elements in the fluid. For example, the component which is least concentrated in the fluid will tend to be enriched in the solid reaction products. Recognition of large concentration differences of elements in hydrothermal fluids enables one to predict trends in metasomatic alteration. The low concentration of magnesium with respect to calcium in chloride-bearing fluids in equilibrium with  $\text{CaO-MgO-SiO}_2$  minerals is a particularly illustrative example of the enrichment process in metasomatism.

Figure 92 is a mineral-solution equilibrium diagram for a portion of the system  $\text{MgO-CaO-SiO}_2\text{-H}_2\text{O-HCl}$  at  $500^\circ\text{C}$ , 2



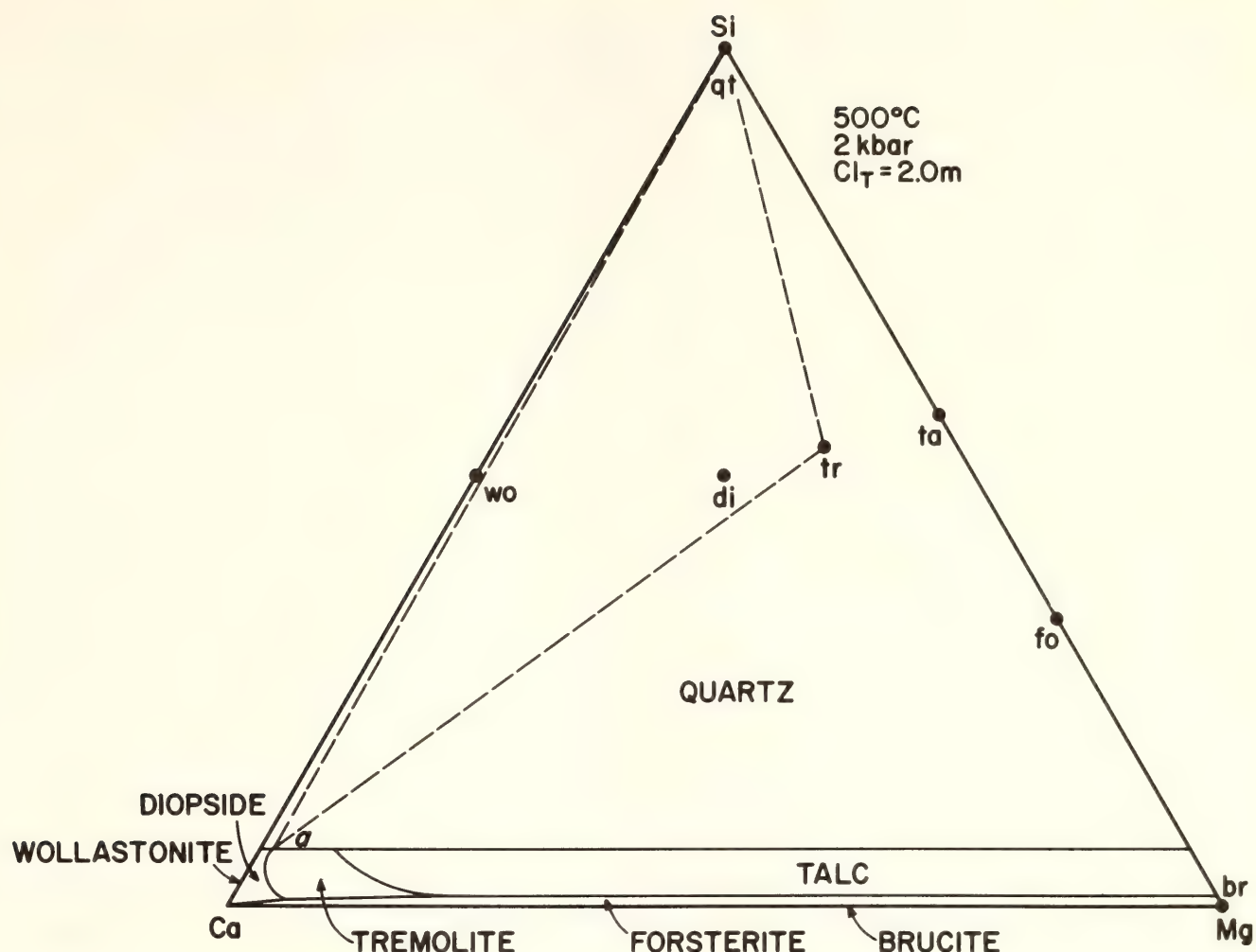


Fig. 92. Mineral-solution equilibrium diagram at 500°C, 2 kbar, and  $Cl_T = 2.0$  molal, calculated from solubility constants in Popp and Frantz (this Report) and Frantz and Popp (*Year Book 77*). The diagram shows the fields of solution compositions (in molal proportions of aqueous  $SiO_2$ ,  $MgCl_2^\circ$ , and  $CaCl_2^\circ$ ) in equilibrium with the mineral phases indicated in heavy letters. The wollastonite field is strongly compressed against the Ca-Si join; the brucite field, against the Ca-Mg join. Compositions of minerals are shown by solid circles. See text for explanation of solution-quartz-tremolite triangle (dashed lines). Abbreviations: wo, wollastonite; di, diopside; tr, tremolite; ta, talc; fo, forsterite; qt, quartz; br, brucite.

kbar, and a 2.0 molal total chloride concentration. The diagram was calculated from the solubility constants of Frantz and Popp (*Year Book 77*) and Popp and Frantz (this Report). The diagram shows the molal proportions of aqueous silica, associated  $CaCl_2^\circ$ , and associated  $MgCl_2^\circ$  in the fluid in equilibrium with the mineral assemblages shown in upper case letters. The compositions of the mineral phases themselves are shown by the solid circles. It is important to note that the diagram is a projection of the surface representing the mineral-solution equilibria in Si-Mg-Ca- $H_2O/HCl$  space onto

the Si-Ca-Mg plane from the  $H_2O/HCl$  apex. The composition of the solution in equilibrium with a three-phase mineral assemblage (e.g., quartz-talc-tremolite) is thus invariant, whereas a one-phase mineral assemblage (e.g., talc) can coexist with a divariant range of solution compositions. The striking feature in Fig. 92 is the strong shift of fluid compositions to the calcium-rich portion of the diagram relative to the compositions of the minerals.

Helgeson (1968) described a numerical method ("Path-calc") for calculating the reaction paths that a chemical system

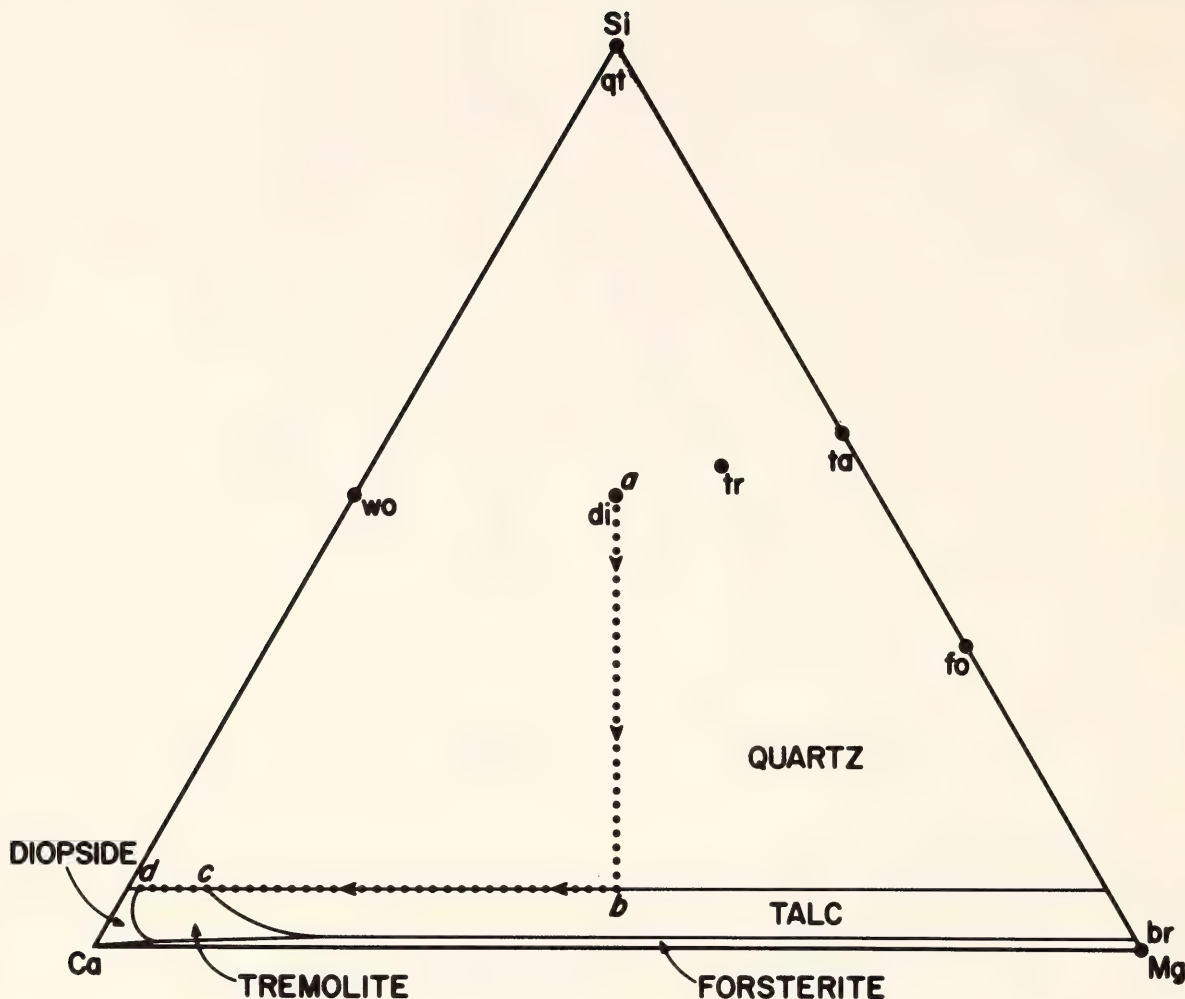


Fig. 93. Mineral-solution equilibrium diagram identical with Fig. 92 showing the reaction path occurring when successive small amounts of diopside are added to chloride solution (dotted line). Arrows show direction of the changes in the solution composition.

follows when a mineral, or minerals, are dissolved in an aqueous fluid. In his model, the fluid is assumed to be in equilibrium with all reaction products. In relatively simple systems that can be represented by ternary diagrams, analogous graphical treatments can be used to define reaction paths. Consider the repetitive additions of small amounts of diopside to an aqueous solution of composition *di* in Fig. 92 (total chloride concentration equals 2.0 molal). What will be the resulting reaction path of the fluid? Initially, diopside will dissolve congruently with the resulting solution moving along the  $H_2O/HCl$ -*di* join in the  $Ca$ - $Mg$ - $Si$ - $H_2O/HCl$  tetrahedron. At point *a* in Fig. 93, the solution will be-

come saturated with respect to quartz. As reaction proceeds, quartz precipitates and the fluid moves away from point *a* along an extension of the *qt*-*di* line on the quartz-saturation surface. At point *b* the solution becomes saturated with talc, which now begins to precipitate as addition of diopside continues. The solution now follows the peritectic talc-quartz univariant line away from talc. Talc is precipitating with the dissolution of quartz. At point *c* the solution becomes saturated with respect to tremolite, which begins to grow at the expense of talc and quartz. After all the talc has disappeared, the solution composition migrates along the tremolite-quartz peritectic precipitating tremolite and dissolv-



ing more quartz. At point *d* the solution is in equilibrium with the diopside and reaction stops.

The above model is analogous to equilibrium crystallization in igneous rocks. The independent variable is the solution-solid ratio rather than temperature as in liquidus diagrams. A model analogous to equilibrium fusion can also be considered. Consider the case in which repetitive small amounts of solution are added to a rock composed of diopside. The reaction path is exactly the reverse of the above case. Again, the solution is considered to be in equilibrium with all reaction products. Figure 94A shows the entire sequence of possible solution compositions (dotted line) and bulk solid compositions (dashed line) that can be produced by varying the initial water-diopside ratio. The arrows point in the direction of increasing water-diopside ratio. In Fig. 94B the volumes of the individual reaction minerals calculated as fractions of the volume of the unaltered host rock are plotted against the ratio of the moles of water added per mole of diopside. Thus, as the water-diopside ratio increases from an initial value of zero, solids along path *di-a'* (Figs. 94A and B) coexist with solution of composition *a*; the change in solids from *a'* to *b'* corresponds to the change in solution compositions from *a* to *b*; solids move from *b'* to *c'* while the solution composition remains fixed at *b*; solids and solution, respectively, move from *c'* to *qt* and *b* to *d*; finally the solution compositions from *d* to *di* coexist with solid of fixed composition *qt*.

The volume percentages of minerals and water-diopside (Fig. 94B) were calculated as follows. Compositional triangles can be drawn connecting the solution composition to the minerals in equilibrium with the solution. Consider the triangle connecting point *a* on the tremolite-quartz peritectic line with the reaction minerals quartz and tremolite (triangle *qt-tr-a* in Fig. 92). After all phases are normalized to four cations (the num-

ber of cations in diopside), application of the lever rule for a bulk composition on the H<sub>2</sub>O/HCl-di join (i.e., point *di* in projection) yields the number of moles of tremolite, quartz, and a hypothetical compound in the solution (Ca<sub>4X<sub>Ca</sub></sub>Mg<sub>4X<sub>Mg</sub></sub>Si<sub>4X<sub>Si</sub></sub>) produced from one mole of diopside. The volumes of the solid reaction products can then be obtained by multiplying the number of moles of the minerals times their molar volumes. The number of moles of the hypothetical solution compound represents the amounts of Ca, Mg, and Si dissolved in the coexisting solution produced per mole of diopside dissolved. Application of the lever rule in the larger triangle Si-Mg-Ca for the composition corresponding to the hypothetical "solution compound" can be written:

$$\begin{aligned} \text{moles "solution compound"} \\ = 1/4 (\text{moles}_{\text{Ca}} + \text{moles}_{\text{Mg}} \\ + \text{moles}_{\text{Si}})_{\text{in solution}}, \end{aligned} \quad (1)$$

where the 1/4 factor results from normalization of the "solution compound" to 4 cations. The amount of water that has been added to the original diopside rock can then be calculated. Because molality is the number of moles of solute per 55.5 moles H<sub>2</sub>O, Equation 1 can be rearranged to:

$$\begin{aligned} \frac{\text{moles H}_2\text{O}}{\text{mole diopside}} = \\ \frac{(4) (55.5) (\text{moles "solution compound"})}{(m_{\text{CaCl}_2} + m_{\text{MgCl}_2} + m_{\text{SiO}_2(\text{aq})})}. \end{aligned} \quad (2)$$

Mineral solution diagrams and reaction paths were calculated in a similar manner for solutions containing lower total chloride concentrations. Introduction of a solution containing 0.1 molal total chloride to a diopside rock results in the solution (dotted line) and solid (dashed line) paths shown in Fig. 95. Arrows point in the direction of increasing water-diopside ratio. With increasing water/diopside from an initial value of

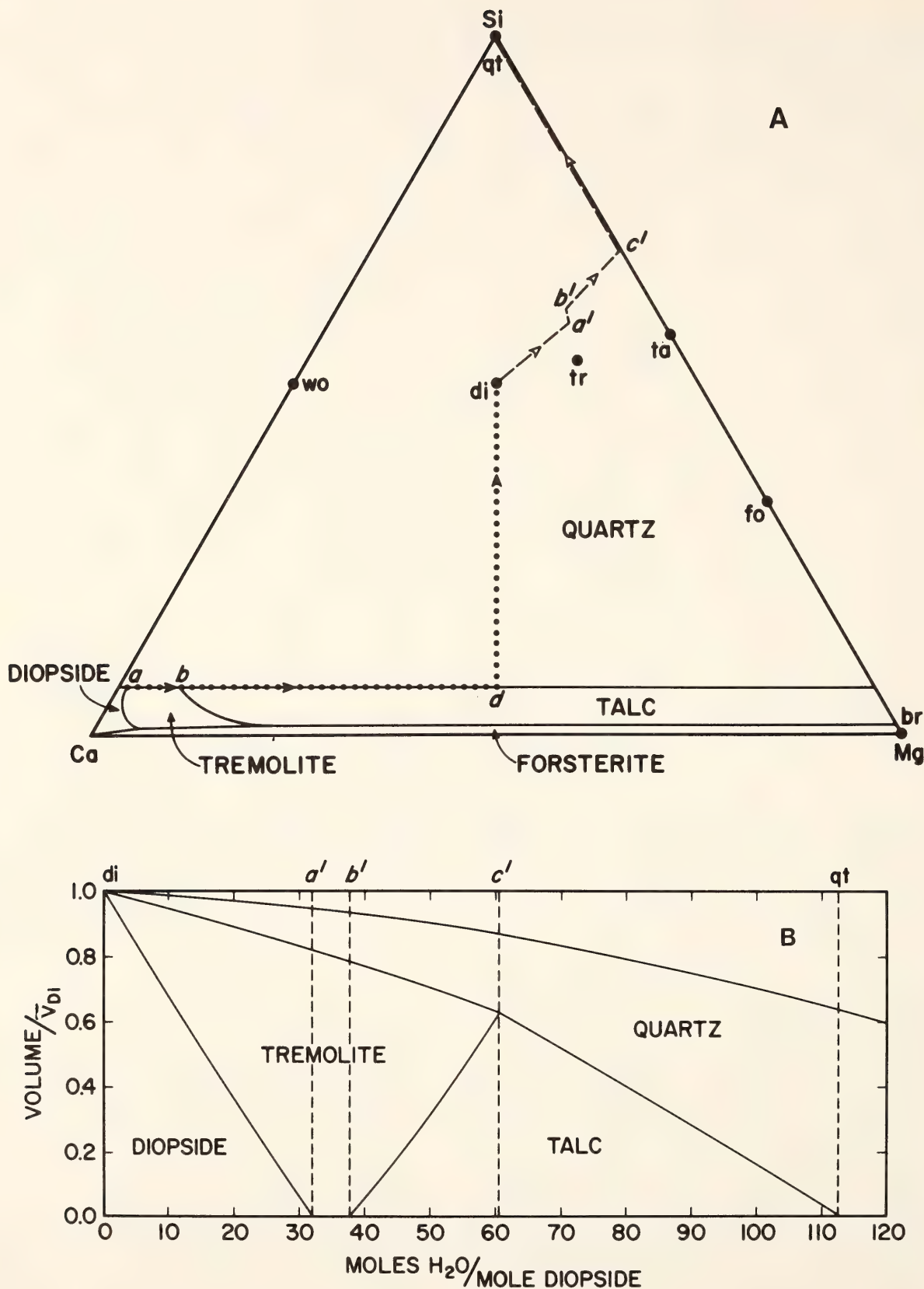


Fig. 94. (A) Mineral-solution equilibrium diagram identical with Fig. 95 (total chloride equals 2.0 molal) showing evolution of reaction products as a function of the number of moles of water (arrows are in direction of increasing ratio of  $H_2O$  to diopside). The dashed line and open arrows show evolution of the solid; the dotted line and solid arrows show evolution of the fluid. The italicized letters show corresponding fluid-solid compositions (see text). (B) Plot of the volume fraction of reaction products as a function of moles of  $H_2O$  added per mole of diopside. Italicized letters and vertical dashed lines refer to corresponding solid compositions in (A).



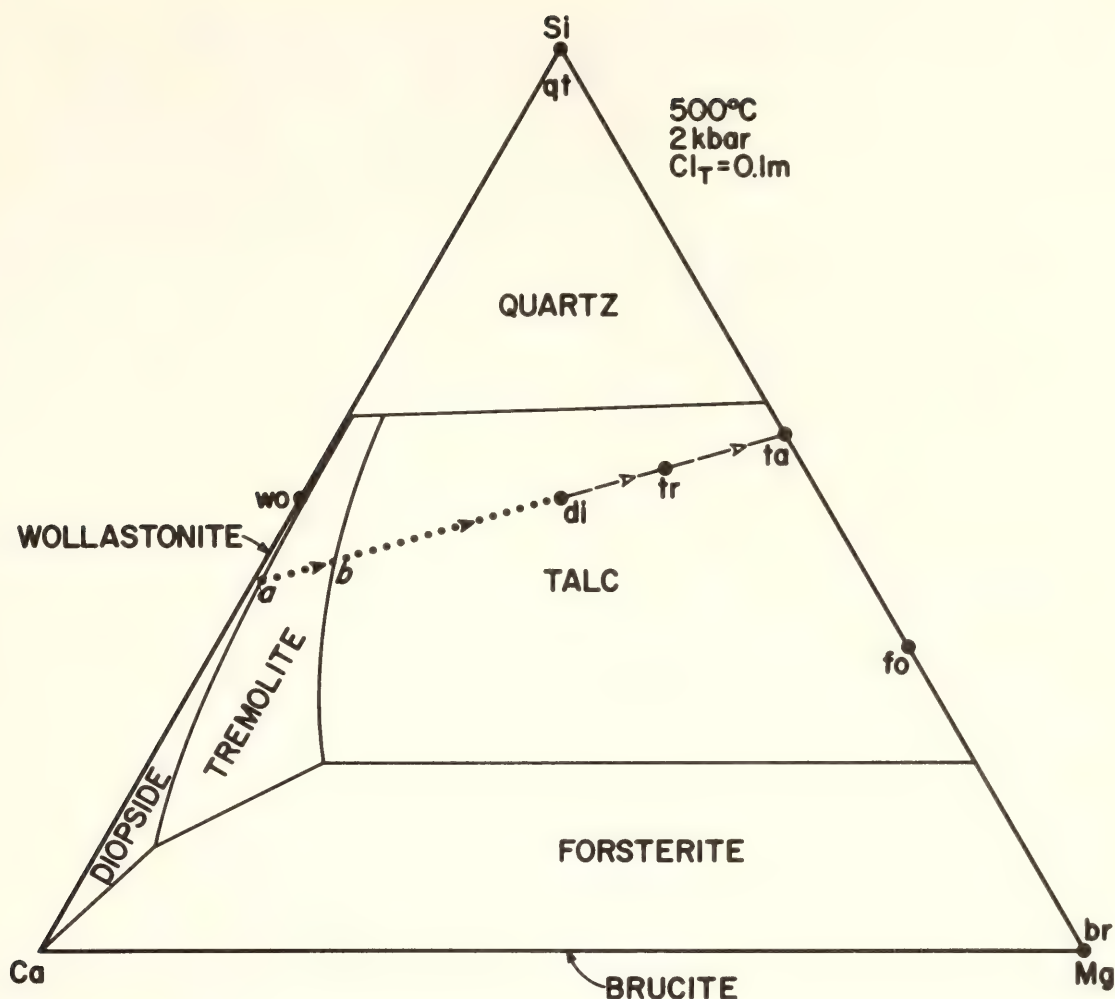


Fig. 95. Mineral-solution diagram with a total chloride concentration of 0.1 molal. See Fig. 94A for symbols, and text for description.

zero, the solids first move from *di* to *tr* while the solution remains fixed at *a*; solids then remain at *tr* while the solution changes from *a* to *b*; solids change from *tr* to *ta* with the solution remaining at *b*; and finally solutions change from *b* to *di* for fixed solid composition of *ta*. Thus, with increasing amounts of water added to the host rock, the following reaction-product assemblages appear: diopside + tremolite, tremolite, tremolite + talc, and finally talc alone. The amount of diopside dissolved per mole of  $H_2O$  is less than in the solution with total chloride equal to 2.0 molal. This decrease is apparent from inspection of Equation 2, in which smaller values for  $m_{CaCl_2}$  and  $m_{MgCl_2}$  result in a larger water-diopside ratio.

For a total chloride concentration of

0.008 molal (Fig. 96), the solids produced by alteration of diopside by increasing amounts of solution change from *di* to *fo* for a fixed solution of composition *a*, and the solutions then move from *a* to *di* for fixed solid composition of *fo*. Forsterite is, therefore, the only alteration product produced at this low concentration of total chloride.

Comparison of the results of these calculations leads to the following conclusions. In the  $CaO-MgO-SiO_2-H_2O$  system, calcium-magnesium phases dissolve incongruently in chloride-bearing hydrothermal fluids producing a more magnesium-rich solid than the host rock and enriching the fluid in calcium. This trend appears to be independent of total chloride concentration. The concentration of total chloride, however, does have

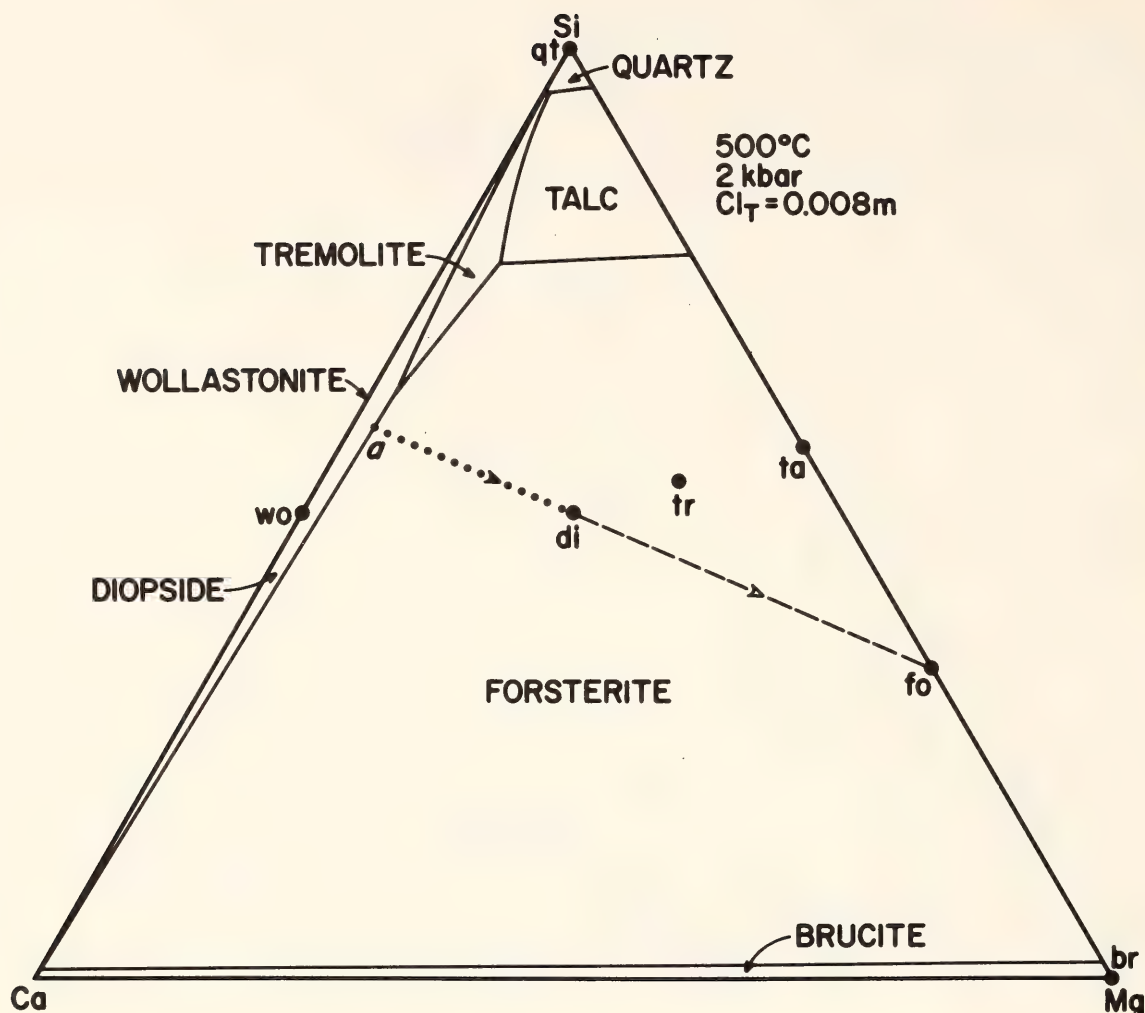


Fig. 96. Mineral-solution diagram with total chloride concentrations of 0.008 molal. See Fig. 94A for symbols, and text for description.

a bearing on the relative concentration of silicon in the alteration assemblage. At low values of total chloride, the reaction products tend to be enriched in magnesium and depleted in both calcium and silicon. At high total chloride concentrations, though, the products are enriched in *both* silicon and magnesium. The trend occurs because although the silicon concentration in the solution is independent of total chloride, the magnesium and calcium concentrations are direct functions of it. Finally, the degree of alteration of the host rock is dependent on total chloride; the greater the chloride concentration, the more alteration per mole of  $H_2O$ . When a solution contains 2.0 molal total chloride, only 32 moles of  $H_2O$  must be introduced into the host rock to convert all the diopside to re-

action products. When the solution contains only 0.1 or 0.008 molal total chloride, however, 710 or 13,500 moles, respectively, are required! The trends described in the above examples refer to a system in which the solution remains in contact with all reaction products. Calculation of alteration involving separation of the fluid from the reaction products (infiltration, diffusion) would yield different reaction paths, but trends would still be generally valid.

#### SOLUBILITY OF HEMATITE IN CHLORIDE-BEARING HYDROTHERMAL FLUIDS

*N. Z. Boctor, R. K. Popp, and J. D. Frantz*

Hematite is a common oxide mineral in the crust of the earth and a major



constituent in most iron ores. It occurs with potassium silicate wall-rock alterations associated with porphyry copper deposits and in contact aureoles around igneous plutons associated with these ores (Meyer and Hemley, 1967). Hematite is also an accessory mineral in many metamorphic rocks. The study of the solubility of hematite ( $\text{Fe}_2\text{O}_3$ ) in chloride-bearing hydrothermal solutions, therefore, would provide information bearing on the transport of iron during processes of hydrothermal alteration, ore deposition, and metamorphism. The choice of chloride solutions is reasonable in view of the presence of chloride in hydrothermal solutions, as indicated by studies of fluid inclusions.

The solubility of hematite in chloride-bearing hydrothermal fluids was determined in the temperature range 600°–400°C at 1 and 2 kbar using double capsules, rapid-quench, hydrothermal techniques, and a modification of the Ag-AgCl buffer method (Frantz and Popp, 1979). Initial solutions placed in the outer capsule varied from distilled water to  $\text{H}_2\text{O}$ - $\text{FeCl}_2$  fluids containing up to 4 molar  $\text{FeCl}_2$ . In experiments performed at 600°C and 1 and 2 kbar, either magnetite or hematite was mixed with Ag and AgCl and the fluid in the outer capsule. In experiments performed at 500°–400°C and 1 and 2 kbar, hematite was the only oxide used. Equilibration times ranged from 48 hr to 17 days. After quenching, total iron and total chlorides, respectively, were determined by atomic absorption and a Buchler chloridometer. The determination of total Fe and associated  $\text{HCl}^\circ$  in equilibrium with hematite or magnetite provides the information required to identify the predominant Fe species in the fluid. Such identification was supplemented by determination of the Cl-Fe ratio in the fluid in the outer capsule. The concentrations of associated  $\text{HCl}^\circ$  were calculated from the values for total quench chloride in the inner capsule by using the following relation,

derived by Frantz and Popp (*Year Book* 77, pp. 823–826):

$$m_{\text{Cl}} - (25^\circ\text{C}, 1 \text{ atm}) = m_{\text{HCl}^\circ}(T_e, P_e) + \sqrt{[m_{\text{HCl}^\circ}(T_e, P_e)][K_{\text{HCl}}]} \quad (1)$$

The molalities of total Fe ( $m_{\text{Fe}}$ ) and associated hydrogen chloride  $m_{\text{HCl}^\circ}$  for experiments in the temperature range 600°–400°C are shown in Figs. 97 and 98, respectively, for pressures of 1 and 2 kbar. Interpretation of the experimental data and calculation of the free energy of Fe in chloride-bearing aqueous fluids require a knowledge of the speciation of Fe in the fluid. Total Fe measured in the experiments represents the total concentration of all Fe species present at the temperature and pressure of the experiments. Possible species of Fe in chloride-bearing hydrothermal fluids include  $\text{FeCl}_2^\circ$ ,  $\text{FeCl}_3^\circ$ ,  $\text{FeCl}^+$ , and  $\text{Fe}^{2+}$ . According to Chou and Eugster (1977),  $\text{FeCl}_2^\circ$  is the dominant iron species in

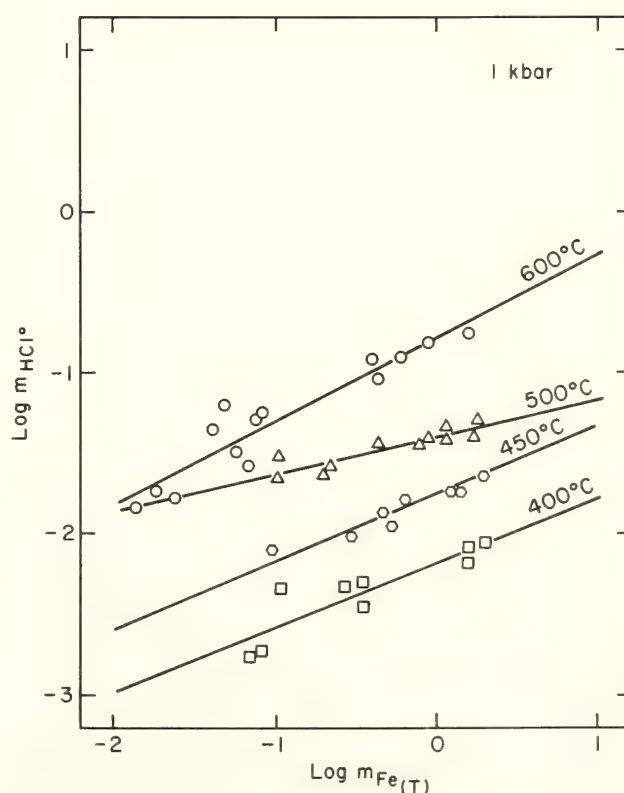


Fig. 97. Variation of  $\log m_{\text{Fe}}$  vs.  $\log m_{\text{HCl}}$  in the temperature range 600°–400°C at 1 kbar. Lines are least-squares best fits.

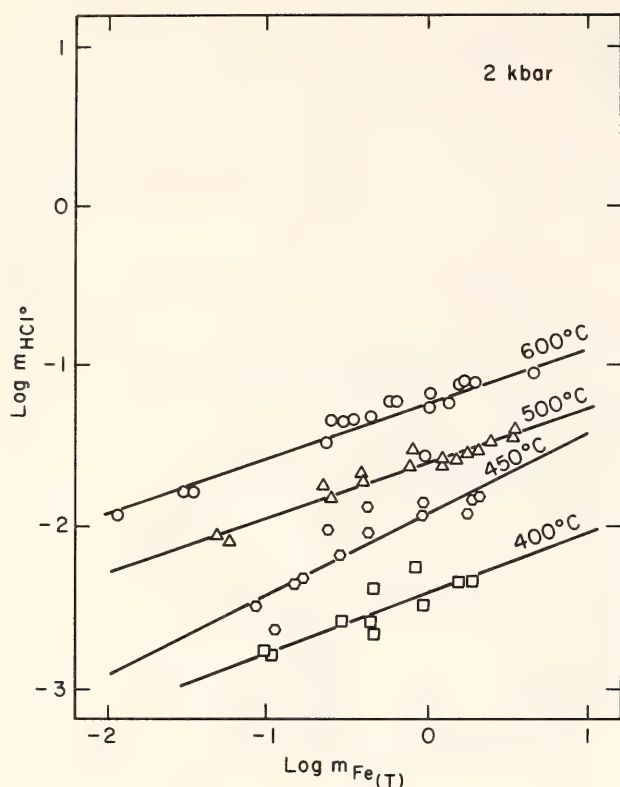
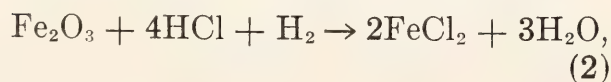


Fig. 98. Variation of  $\log m_{\text{Fe}}$  vs.  $\log m_{\text{HCl}^\circ}$  in the temperature range 600°–400°C at 2 kbar. Lines are least-squares best fits.

solutions in equilibrium with magnetite. They also suggested that  $\text{FeCl}_2^\circ$  will still be the predominant iron-bearing species for oxygen fugacities close to the hematite-magnetite equilibrium. Crerar *et al.* (1978) found that the data they obtained on the solubility of the buffer assemblage magnetite-pyrite-pyrrhotite in NaCl solutions were best represented by the species  $\text{FeCl}^+$  and  $\text{FeCl}_2^\circ$  at 300°C and by  $\text{Fe}^{2+}$  and  $\text{FeCl}_2^\circ$  at 350°C. In the present study, direct determination of Cl/Fe in the fluids in equilibrium with either hematite or magnetite gives a value  $\simeq 2$ , which suggests that  $\text{FeCl}_2$  is the dominant species in chloride-bearing hydrothermal fluids in equilibrium with these minerals. The relation between total Fe and HCl could therefore be described by the following reaction:



$$K = \frac{(m_{\text{FeCl}_2})^2 (x_{\text{H}_2\text{O}})^3}{(m_{\text{HCl}})^4 \cdot f_{\text{H}_2}}, \quad (3)$$

if the activity coefficients are equal to unity and the solids are pure phases. If  $\text{FeCl}_2$  is the predominant species, then  $m_{\text{FeCl}_2^\circ} \simeq m_{\text{Fe}_T}$  and

$$K = (m_{\text{Fe}_T})^2 (x_{\text{H}_2\text{O}})^3 / (m_{\text{HCl}})^4 \cdot f_{\text{H}_2}. \quad (4)$$

For the reaction



$$K_1 = \frac{(m_{\text{H}_2})^{1/2}}{(m_{\text{HCl}})}. \quad (6)$$

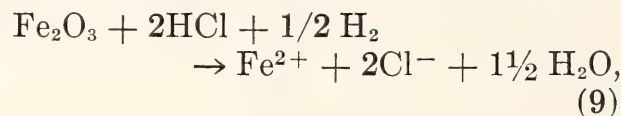
By substituting in Equation 4 ( $x_{\text{H}_2\text{O}} \simeq 1$ )

$$K = (m_{\text{Fe}_T})^2 / (m_{\text{HCl}^\circ})^4 \cdot (K_1)^2 (m_{\text{HCl}^\circ})^2. \quad (7)$$

The equilibrium constant should be independent of Fe and HCl concentrations and mole fraction of water and

$$\partial \log (m_{\text{Fe}_T}) / \partial \log (m_{\text{HCl}^\circ}) \simeq 3. \quad (8)$$

If  $\text{Fe}^{2+}$  is the predominant species, the reaction (Equation 2) can be written as



and the equilibrium constant

$$K' = \frac{(m_{\text{Fe}^{2+}}) (m_{\text{Cl}^-})^2 (x_{\text{H}_2\text{O}})^{3/2}}{(m_{\text{HCl}})^2 \cdot (f_{\text{H}_2})^{1/2}}. \quad (10)$$

Because the concentration of Fe is much greater than any positive ion, the concentration of  $\text{Cl}^-$  would be twice that of  $\text{Fe}^{2+}$  and

$$K' = 4(m_{\text{Fe}^{2+}})^3 (x_{\text{H}_2\text{O}})^{3/2} / (m_{\text{HCl}^\circ})^2 \cdot (f_{\text{H}_2})^{1/2}. \quad (11)$$

If Equation 6 is used to substitute for  $(f_{\text{H}_2})^{1/2}$  and if it is noted that  $x_{\text{H}_2\text{O}} \simeq 1$ , then

$$K' = 4(m_{\text{Fe}^{2+}})^3 / (m_{\text{HCl}^\circ})^2 \cdot (K_1)(m_{\text{HCl}^\circ}) \quad (12)$$

and

$$\partial \log (m_{\text{Fe}_T}) / \partial \log (m_{\text{HCl}^\circ}) \simeq 1.00. \quad (13)$$



The same approach can be used to show that the theoretical slopes of  $\log (m_{\text{FeT}})$  vs.  $\log (m_{\text{HCl}^\circ})$  are  $\simeq 3$  and  $\simeq 1.5$  if the predominant iron species are, respectively,  $\text{FeCl}_3^\circ$  and  $\text{FeCl}^+$ .

The experimental results show that  $\text{FeCl}_2$  is the predominant species from  $600^\circ$  to  $400^\circ\text{C}$  at 1 and 2 kbar. The equilibrium constant (Equation 7) is independent of concentration, and the slopes of  $(\log m_{\text{FeT}})$  as a function of  $\log m_{\text{HCl}^\circ}$  (Fig. 97) are  $2.87 \pm 0.032$ ,  $2.94 \pm 0.024$ ,  $1.97 \pm 0.079$ , and  $2.66 \pm 0.077$ , respectively, at  $600^\circ$ ,  $500^\circ$ ,  $450^\circ$ , and  $400^\circ\text{C}$  and 2 kbar. In a similar way, the slopes of  $(\log m_{\text{FeT}})$  vs.  $\log m_{\text{HCl}^\circ}$  are  $1.99 \pm 0.049$ ,  $4.38 \pm 0.043$ ,  $2.35 \pm 0.091$ , and  $2.50 \pm 0.0776$ , respectively, for  $600^\circ$ ,  $500^\circ$ ,  $450^\circ$ , and  $400^\circ\text{C}$  and 1 kbar (Fig. 98). Although a slope of  $\simeq 3$  is consistent with associated Fe in the form of  $\text{FeCl}_2^\circ$  or  $\text{FeCl}_3^\circ$ , determination of Cl/Fe in the fluid ( $\simeq 2$ ) suggested that  $\text{FeCl}_2^\circ$  is the dominant species in equilibrium with hematite or magnetite in chloride-bearing aqueous solutions. Deviations from the theoretical value of the slope ( $\simeq 3$ ) are attributed to possible quench reactions, as suggested by the change in the pH of the fluid over short periods of time after quenching. If the iron is dissociated, however, the slopes should be much lower than the values obtained in this study ( $\simeq 1$ – $1.5$ ).

The equilibrium constant for Equation 2 was evaluated for each experiment, and the log of  $K$  was plotted as a function of the reciprocal of temperature ( $^\circ\text{K}$ ) for 2 and 1 kbar, as shown in Fig. 99. The vertical bars represent one standard deviation of the linear regression, and the lines represent least-squares fits of the data points.

At equilibrium, the Gibbs free energy of the reaction at Equation 2 is:

$$\begin{aligned} G(\text{reaction 2}) &= 2G(\text{FeCl}_2)_{P,T} \\ &+ 3G(\text{H}_2\text{O})_{P,T} - 4G(\text{HCl})_{P,T} \\ &- G(\text{Fe}_2\text{O}_3)_{P,T} - G(\text{H}_2) \\ &= -RT \ln K. \end{aligned}$$

If the standard state of  $\text{Fe}_2\text{O}_3$  is that of

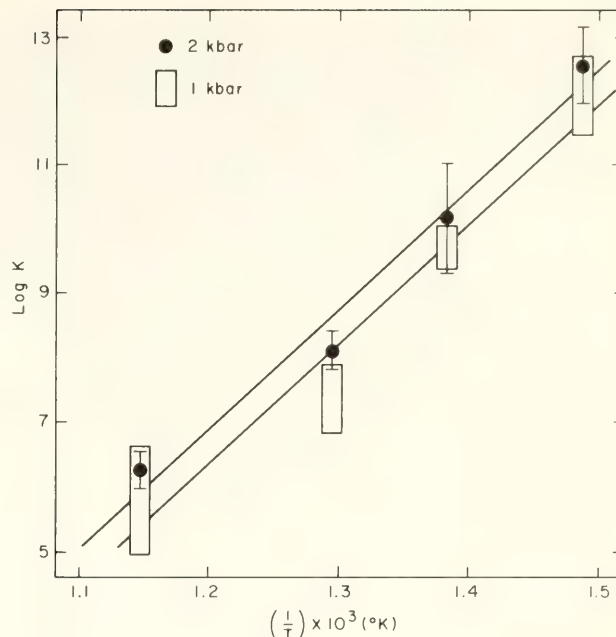


Fig. 99.  $\log K$  vs.  $1/T^\circ\text{K}$  at 1 and 2 kbar; the line is a least-squares best fit, and the vertical bars represent 1 standard deviation.

the pure solid at the temperature and pressure of interest, that of  $\text{H}_2\text{O}$  is pure  $\text{H}_2\text{O}$  at temperature and pressure, and that of  $\text{H}_2$  is pure  $\text{H}_2$  at temperature and 1 bar, and if  $\text{FeCl}_2^\circ$  and  $\text{HCl}^\circ$  are hypothetical 1-molal solutions at temperature and pressure, then the difference in the free energies of formation of standard state 1-molal  $\text{FeCl}_2^\circ$  and  $\text{HCl}^\circ$  at temperature and pressure from the elements at  $25^\circ\text{C}$ , 1 bar, can be calculated from the following relation:

$$\begin{aligned} G_f^\circ(\text{FeCl}_2^\circ) - 2G_f^\circ(\text{HCl}^\circ) \\ = 1/2[G_f^\circ(\text{Fe}_2\text{O}_3) + G_f^\circ(\text{H}_2) \\ - 3G_f^\circ(\text{H}_2\text{O}) - RT \ln K]. \end{aligned} \quad (14)$$

Values of  $G_f^\circ(\text{FeCl}_2^\circ) - 2G_f^\circ(\text{HCl}^\circ)$  as a function of temperature were calculated at 1 and 2 kbar and are plotted as a function of the reciprocal of temperature ( $^\circ\text{K}$ ) in Fig. 100.

The presence of  $\text{FeCl}_2^\circ$  as the dominant species in equilibrium with  $\text{Fe}_2\text{O}_3$  is significant because it enhances the solubility of  $\text{Fe}^{3+}$ -bearing oxides in aqueous solutions and can account for the mobility of iron in hydrothermal environments. In the temperature and pres-

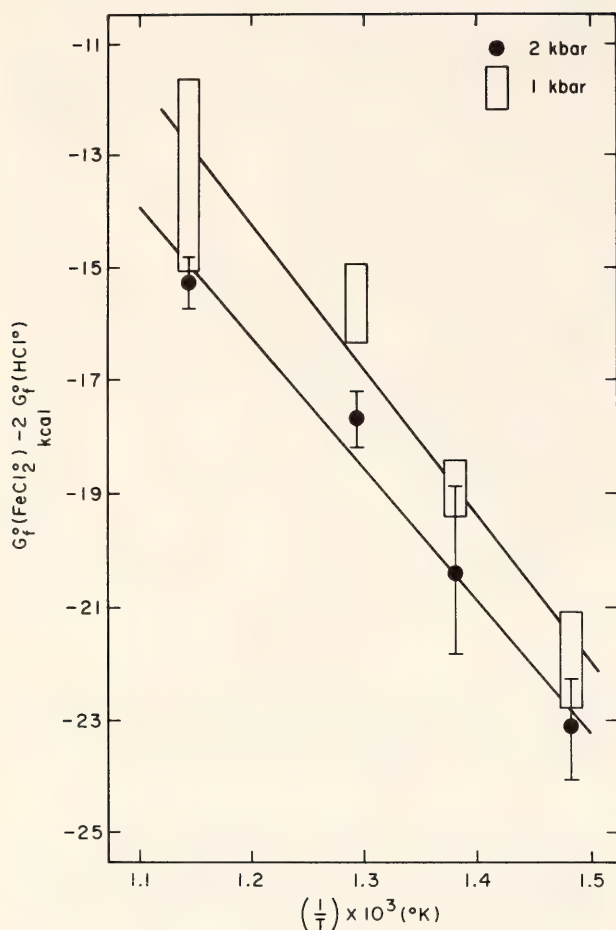


Fig. 100. Plot of  $G_f^\circ(\text{FeCl}_2^\circ) - 2G_f^\circ(\text{HCl}^\circ)$  vs.  $1/T^\circ\text{K}$  at 1 and 2 kbar. The lines are least-squares best fits.

sure range of the experiments, the speciation of iron in chloride-bearing hydrothermal fluids differs from that of Mg, an element that is commonly associated with  $\text{Fe}^{2+}$  during interaction between rock-forming minerals and hydrothermal fluids. In the temperature range  $600^\circ$ – $550^\circ\text{C}$  and 2 kbar,  $\text{MgCl}_2^\circ$  is the predominant species in Cl-bearing hydrothermal fluids, whereas between  $550^\circ$  and  $400^\circ\text{C}$  at 2 kbar, both associated  $\text{MgCl}_2^\circ$  and dissociated  $\text{Mg}^{2+}$  are present (Frantz and Popp, 1979). Below  $400^\circ\text{C}$ ,  $\text{Mg}^{2+}$  is the predominant species in the fluid. The implication of the difference in speciation of Fe and Mg at low temperatures is that for a given molality of HCl, the concentration of Mg in chloride solutions will be higher than that of iron for temperatures at which Mg exists as dissociated species.

Thus, at these temperatures, chloride-bearing hydrothermal solutions will transport more Mg than Fe.

#### SOLUTION OF A NEW HIGH-PRESSURE PHASE IN $\text{Ca}(\text{OH})_2\text{-H}_2\text{O}$

*P. Baur and A. Van Valkenburg*

The solubility of a compound in a liquid at ambient temperature generally decreases with increasing pressure (see Hildebrand and Scott, 1964, p. 295). There are, however, a few compounds whose solubilities increase with increasing pressure that are of interest to geochemists. For example, gypsum ( $\text{CaSiO}_4 \cdot 2\text{H}_2\text{O}$ ) and calcite ( $\text{CaCO}_3$ ) have a great increase in solubility with pressure (Van Valkenburg *et al.*, *Year Book 70*, pp. 233–237). A third calcium compound,  $\text{Ca}(\text{OH})_2$ , has recently been studied, and this compound also exhibits greater solubility in water at higher pressures. Another factor related to the solubility of these compounds is that the solubility increases with decreasing temperature.

Weir (1955) studied  $\text{Ca}(\text{OH})_2$  in water at ambient temperatures and pressures up to 9 kbar using a piston-cylinder apparatus. He observed a large volume discontinuity at 2.8 kbar and concluded that the discontinuity may be the formation of a new compound with a possible formula of  $\text{Ca}(\text{OH})_2 \cdot n\text{H}_2\text{O}$ . The volume discontinuity was always recorded on pressure release, as measurements were not reliable on the increase of pressure. Weir did not measure the solubility of  $\text{Ca}(\text{OH})_2$  at elevated pressures, but visual evidence obtained microscopically in a diamond-window, high-pressure cell in the present study indicates a significant precipitation of  $\text{Ca}(\text{OH})_2$  from solution at approximately 2.8 kbar.

Reagent-grade calcium hydroxide and distilled water mixed in various proportions were placed in a gasketed diamond-window, high-pressure cell, and pressures were elevated up to the freezing point of water (ice-6, 9.2 kbar,  $25^\circ\text{C}$ , Bridgman,



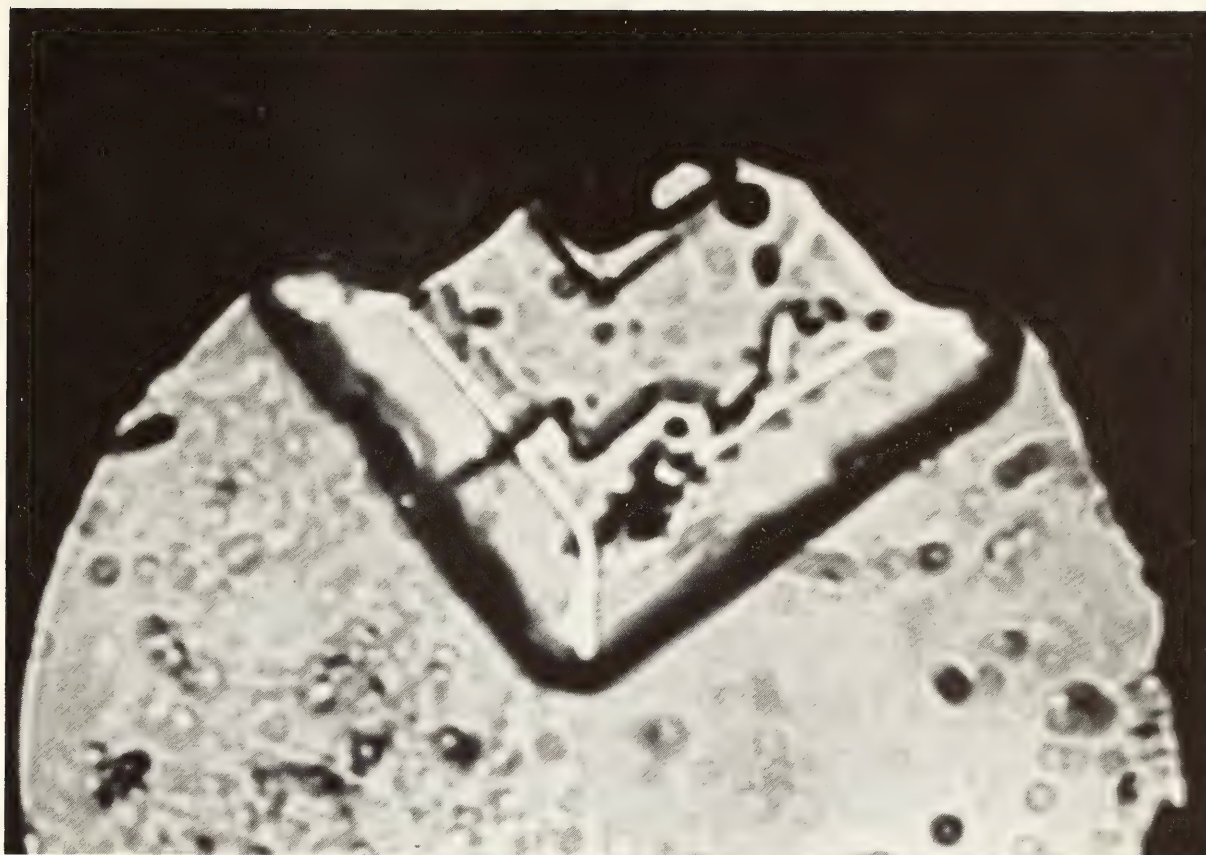


Fig. 101. Single crystal of high-pressure form of  $\text{Ca}(\text{OH})_2 \cdot n\text{H}_2\text{O}$  at 6.5 kbar ( $\times 500$ ).

1937) at ambient temperatures. Pressures were measured with the ruby fluorescent technique (Barnett *et al.*, 1973). With increasing pressure it was noted under the microscope that the  $\text{Ca}(\text{OH})_2$  dissolves readily at pressures above 1 kbar.

At a pressure of 6.5 kbar a new high-pressure compound forms from a solution of  $\text{Ca}(\text{OH})_2$ . It crystallizes from the liquid and probably has the formula  $\text{Ca}(\text{OH})_2 \cdot n\text{H}_2\text{O}$ , as suggested by Weir (Fig. 101). The crystals are rectangular in shape and birefringent. When the pressure was increased to the point of crystallization of ice-6, no significant optical change was observed in the crystals. When the pressure was slowly released the crystals dissolved into the liquid at approximately 6 kbar. When the pressure was lowered to approximately 3.0 kbar a sudden precipitation of portlandite,  $\text{Ca}(\text{OH})_2$ , from solution was observed. The visual observation is dramatic because the field of view under the microscope appears to explode into

solid spheroids from a clear solution (Fig. 102). This event is probably the volume change that Weir observed in his piston-cylinder apparatus at 2.8 kbar. If pressure is released quickly to ambient pressures after the high-pressure phase has formed, one can observe the dynamic breakdown of this phase into  $\text{Ca}(\text{OH})_2$ . In several experiments a few needle-like crystals with high birefringence were observed to precipitate from solution at approximately 5.0 kbar. Attempts to increase their growth or increase their numbers by changing pressure or temperature failed. On slow release of pressure to 1 atm, the crystals did not undergo an immediate change, nor did they readily go into solution. They are presumed to have formed metastably as a result of some impurity in  $\text{Ca}(\text{OH})_2$  such as  $\text{CO}_2$  or possibly as some varietal form of  $\text{Ca}(\text{OH})_2 \cdot n\text{H}_2\text{O}$ .

The concentration of  $\text{Ca}(\text{OH})_2$  in water is apparently an important factor in nucleating the high-pressure phase. It



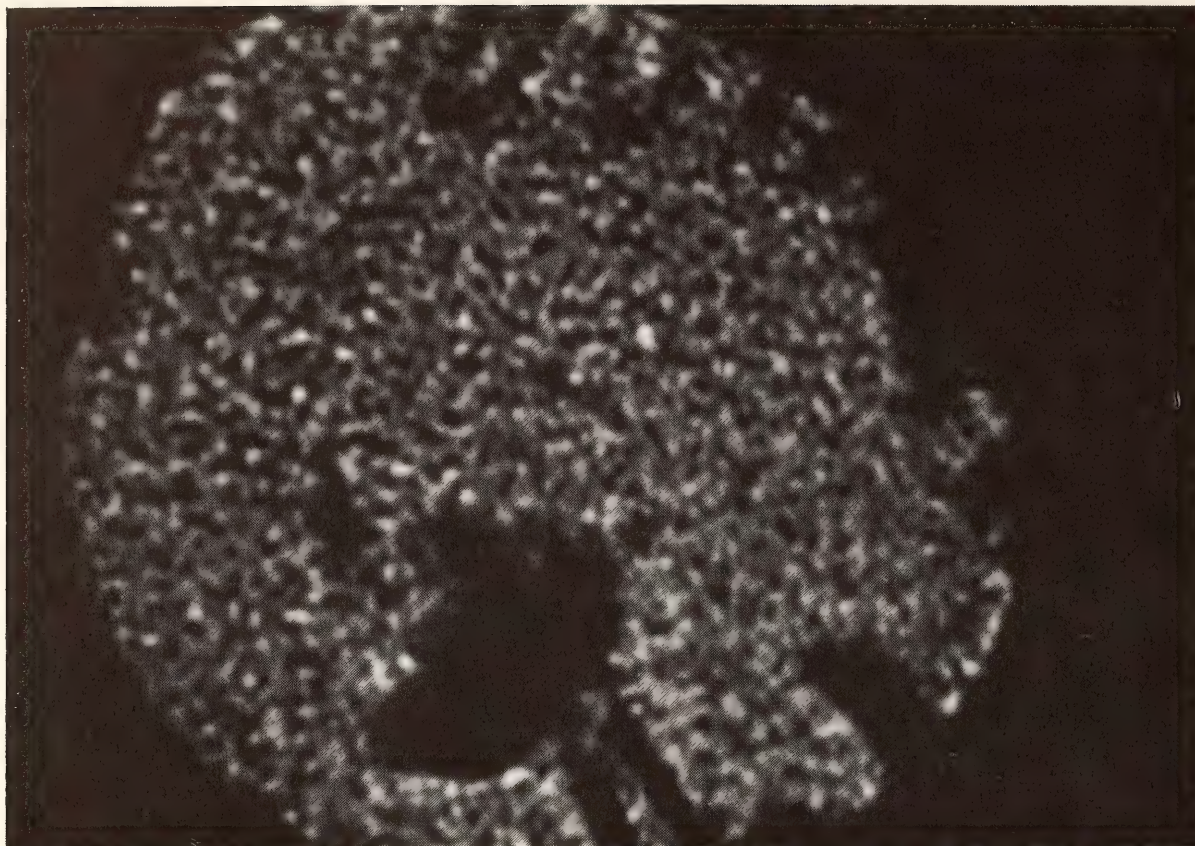


Fig. 102. Precipitate of  $\text{Ca}(\text{OH})_2$  at 2.8 kbar from clear solution ( $\times 500$ ).

was estimated visually that 10% or more by volume of  $\text{Ca}(\text{OH})_2$  had to be in solution at room temperature before the high-pressure phase would crystallize. In lesser concentrations no precipitation was observed before the appearance of ice-6. Also by visual observations, it was estimated that 20% by volume of  $\text{Ca}(\text{OH})_2$  will go into solution at a pressure of 6 kbar and room temperature. Geochemically, this is a significant amount of solution that must be considered along with gypsum,  $\text{CaSO}_4$ , and calcite,  $\text{CaCO}_3$ , when the nature of solutions at depth in the earth's crust is studied.

#### ROCK PERMEABILITY DURING METAMORPHISM

*D. Rumble III and T. C. Hoering*

Rock permeability is an important factor during metamorphism because it is this variable, together with fluid viscosity, pressure gradients, and the

amount of available fluid, that determines the magnitude of fluid flow. This flow, in turn, is one of a number of controls on the amount of heat and mass transported through rocks. In this work a method of qualitatively assessing relative variations in rock permeability during metamorphism is presented. The method has been applied to two natural examples, and a positive correlation between intensity of devolatilization reactions and rock permeability has been discovered. Such a correlation is to be expected because experiments have shown that rock permeability and pore pressure are directly related (Brace, 1972).

Rock permeability and the attainment of chemical and isotopic equilibrium between fluid components and rocks are related because a transfer of material or a flow of fluid between different mineral assemblages is required to achieve equilibrium. Such fluid flow is controlled, according to Darcy's law, by fluid viscosity, pressure gradients, and perme-



ability. Fluid viscosity is a function of  $P$  and  $T$ ; thus for rocks metamorphosed under similar conditions, variations in viscosity are not expected. Pressure gradients are primarily due to decreasing weight of overburden upward. Localized pressure gradients due to nonhydrostatic stress occur but do not exceed a few hundred bars stress difference under metamorphic conditions. Therefore, rocks metamorphosed under similar  $P$  conditions are likely to have experienced similar pressure gradients. According to this analysis, the most important variable controlling fluid flow through rocks metamorphosed under similar  $P$ ,  $T$  is permeability. The transfer of matter required to achieve equilibrium may be accomplished by grain-boundary diffusion rather than fluid flow, but the diffusive mechanism cannot be effective over distances of more than a meter according to experiments of Brady (this Report). It is concluded that the degree to which chemical and isotopic equilibrium between fluid components and rocks has been achieved is a measure of rock permeability.

Suppose that there are two outcrops, each containing three different rock layers. The rocks are of the same stratigraphic age and were metamorphosed at the same time under similar  $P$ ,  $T$  conditions. Each rock layer is characterized by its own distinctive assemblage of minerals that is uniform throughout the layer. In both outcrops the mineral assemblages of each rock layer are in local equilibrium; the identity of minerals in the assemblage and mineral proportions and compositions vary from layer to layer but the fractionation of elements between minerals is constant. Furthermore, the premetamorphic protoliths of each layer are such that they are known to have had different chemical compositions and different oxygen isotopic contents prior to metamorphism. By supposition, the outcrops are similar in most of their general properties. They differ, however, in the size of rock volumes that

have reached chemical and isotopic equilibrium with fluid components. In outcrop *A* the mineral assemblages in all three rock layers were in equilibrium during metamorphism with a fluid of uniform  $^{18}\text{O}/^{16}\text{O}$  and uniform  $\mu_{\text{H}_2\text{O}}$ . Outcrop *B*, in contrast, had three fluids of different  $^{18}\text{O}/^{16}\text{O}$  and  $\mu_{\text{H}_2\text{O}}$  in equilibrium, respectively, with the three mineral assemblages\*. According to the interpretation adopted in this work, the rocks of outcrop *A* were more permeable to fluid flow than those of outcrop *B*, for otherwise the assemblages of *B* would have equilibrated with a uniform fluid.

The writers have investigated two contrasting occurrences that demonstrate the feasibility of estimating relative values of rock permeability. The rocks of both outcrops are Siluro-Devonian in stratigraphic age and were metamorphosed at the same time during the Acadian Orogeny under similar  $P$ ,  $T$  conditions. The protoliths of each rock type differed in chemical and oxygen isotopic composition prior to metamorphism. Petrologic investigation shows that local equilibrium was attained in each mineral assemblage at both localities. It may be seen that the two occurrences are in accord with the general conditions of the hypothetical example described above.

The first occurrence is located at Black Mountain, Moosilauke quadrangle, New Hampshire (Rumble, 1978). The rock types exposed are predominantly quartzite; however, also present are micaceous pods, lenses, and layers of sedimentary origin ranging in size from centimeters to meters in thickness. These layers contain a variety of assemblages of aluminous silicate and Fe-Ti oxide minerals. Chemical analyses of coexisting minerals, obtained using the electron microprobe analyzer, indicate that attainment of

\* An alternative interpretation of outcrop *B* is that no free fluid was present in any of the rock layers. The absence of fluid would not change the classification of *B* as impermeable rock, because a fluid-free rock would be even less permeable than one containing fluid.

chemical equilibrium among minerals was limited to single sedimentary beds. Silicate and oxide minerals vary sympathetically in chemical composition from bed to bed. Fe-rich silicate assemblages occur with magnetite and ilmenite in which ilmenite is poor in  $\text{Fe}_2\text{O}_3$ ; whereas Mg-rich silicates occur with oxide pairs in which ilmenite is rich in  $\text{Fe}_2\text{O}_3$ . Graphic and algebraic analyses of coexisting minerals demonstrate no crossing tie lines between mineral assemblages from rocks of different bulk chemical content. Minor components such as Mn are partitioned systematically between minerals. These observations are consistent with the attainment of isothermal, isobaric chemical equilibrium between minerals in single sedimentary beds in the Black Mountain rocks. Minerals from separate rock layers, however, failed to attain equilibrium. Likewise, oxygen isotopic analyses of coexisting quartz and magnetite show that the attainment of isotopic exchange equilibrium was limited to single sedimentary beds. Quartz from a single rock layer is uniform isotopically but varies over a range of 2.5‰ from layer to layer. The fractionation of  $^{18}\text{O}$  and  $^{16}\text{O}$  between quartz and magnetite is the same for all samples despite the variation in  $\delta^{18}\text{O}$  of the minerals. These observations are consistent with the attainment of isothermal isotopic exchange equilibrium between mineral pairs in single sedimentary beds. Equilibrium was not achieved, however, between minerals from different rock layers.

Intergranular fluid phases likely to have been present during the metamorphism of the Black Mountain rocks could not have been chemically and isotopically homogeneous and also in equilibrium with each mineral assemblage. The oxygen isotopic composition of an aqueous solution would have varied over a range of 2.5‰ in  $\delta^{18}\text{O}$  if it were in equilibrium with each analyzed mineral pair. The sympathetic variation of silicate Fe/Mg and oxide  $\text{Fe}^{2+}/\text{Fe}^{3+}$ ,

described above, records variations in equilibrium fluid composition from a reduced composition containing 75%  $\text{H}_2\text{O}$  and 25%  $\text{H}_2$  to an oxidized composition consisting of nearly pure  $\text{H}_2\text{O}$ . An estimate of the minimum water-rock ratio (Taylor, 1977, pp. 523–524) that would have been required to bring the rock layers into isotopic equilibrium is obtained as follows: If it is assumed that the reactants are the *most*  $^{18}\text{O}$ -rich quartz from the locality and the  $\text{H}_2\text{O}$  in equilibrium with the *least*  $^{18}\text{O}$ -rich quartz and that the products are quartz whose  $\delta^{18}\text{O}$  value is that of the average for the locality and  $\text{H}_2\text{O}$  in isotopic equilibrium with it, then a value of 1.10 for water/rock (ratio of number of water oxygens to number of quartz oxygens) is obtained. The ratio so calculated gives the minimum fluid/rock required for isotopic equilibration that was *not* achieved.

An occurrence that stands in contrast to that at Black Mountain is located 12 km to the east at Beaver Brook, Moosilauke quadrangle, New Hampshire (Rumble *et al.*, *Year Book* 77, pp. 826–830). Previous study showed that decarbonation of partially silicified brachiopods had released  $^{18}\text{O}$ -enriched  $\text{CO}_2$ . The  $\text{CO}_2$  moved laterally, parallel to bedding, and contaminated a cross-cutting quartz monzonite dike. The result is that the dike rock now contains graphite and has been enriched in  $^{18}\text{O}$ . New data given in Fig. 103 show the remarkable extent to which isotopic equilibrium has been achieved despite the great disparity in premetamorphic isotopic compositions. The  $\text{CO}_2$ -rock ratio necessary to bring the isotopic composition of quartz of the dike from igneous to metamorphic values was calculated by choosing as reactants (1)  $\text{CO}_2$  (+31‰) in equilibrium with calcite (+24‰) before decarbonation of the fossils and (2) quartz having the average value of quartz (+10‰; Taylor, 1968) from granitic plutons. Products were (1) quartz (+14‰) as it is observed in the dike and (2)  $\text{CO}_2$  (+21‰) in equilibrium with such quartz. For a



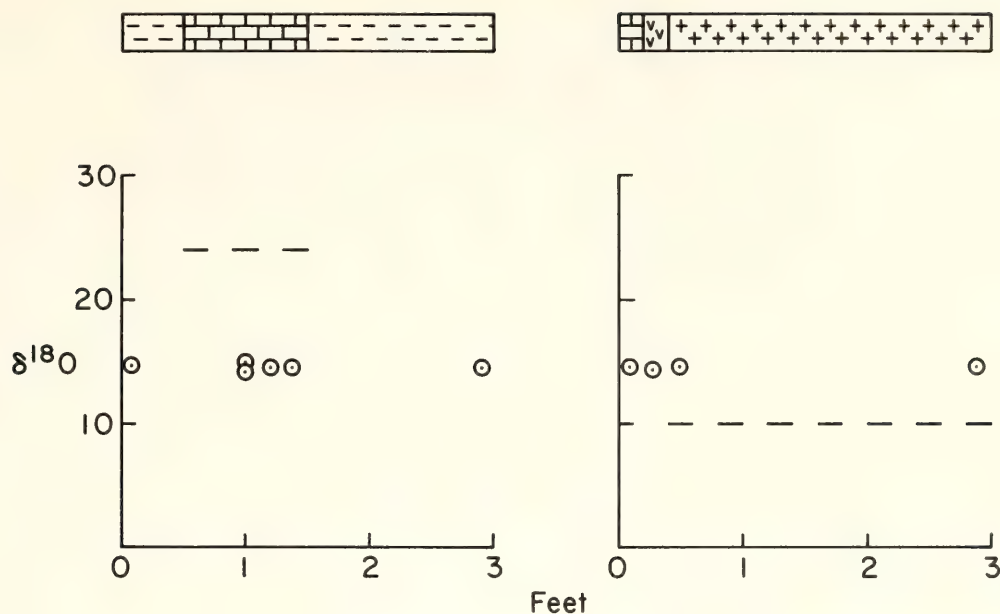


Fig. 103. Two profiles of  $\delta^{18}\text{O}$  values for quartz across contacts between different rock types at Beaver Brook locality. Rock types shown in bar graphs at top of figure: dash pattern is mica schist; brickwork pattern is fossiliferous calc-silicate; the v pattern is anorthosite alteration zone; the + pattern is quartz-monzonite. The dashed line on the left profile shows the assumed composition of calcite in fossil shells prior to metamorphism. The dashed line on the right profile gives the assumed composition of quartz in the dike prior to metamorphism.

temperature of  $600^{\circ}\text{C}$ , the result is a  $\text{CO}_2/\text{rock}$  of 0.4 (ratio of oxygen in  $\text{CO}_2$  to oxygen in quartz).

Contamination of the granitic dike at Beaver Brook by  $\text{CO}_2$  shows that fluid moved a distance of several meters during metamorphism. Preservation of isotopic and chemical disequilibrium of fluid components at Black Mountain is evidence that fluid did not move freely over similar distances. At both localities the fluid-rock interaction required to achieve isotopic equilibrium is similar—0.4 for Beaver Brook and 1.10 for Black Mountain. According to the criteria discussed above, the Beaver Brook rocks are classified as more permeable and those of Black Mountain as less so. The disparity in permeability is directly correlated with the intensity of devolatilization reactions experienced at each locality. At Black Mountain, sandstone and shale protoliths lost most of their  $\text{H}_2\text{O}$

during compaction and silica cementation. By the time the rocks reached conditions of  $400^{\circ}\text{C}$  or hotter, only 5% by weight, or less, of  $\text{H}_2\text{O}$  would have been left to expel and that expulsion would have taken place continually over a range of  $100^{\circ}\text{C}$ . The partially silicified brachiopod shells of Beaver Brook stored approximately 25% by weight of  $\text{CO}_2$  up to a temperature of  $500^{\circ}\text{--}600^{\circ}\text{C}$ , the breakdown temperature of calcite + quartz in a  $\text{CO}_2\text{--CH}_4\text{--H}_2\text{O}$  fluid (Ohmoto and Kerrick, 1977). Thus, metamorphism of Beaver Brook rocks was accompanied by copious release of volatiles, whereas much less fluid was evolved at Black Mountain. Evidently, permeability and intensity of devolatilization are correlated variables during metamorphism, a result in keeping with experiments showing the direct relationship between permeability and pore pressure (Brace, 1972).

ULTRAHIGH-PRESSURE EXPERIMENTS

LATTICE PARAMETERS AND SPECIFIC  
VOLUME FOR THE PEROVSKITE PHASE OF  
ORTHOPYROXENE COMPOSITION,  
(Mg,Fe)SiO<sub>3</sub>

*T. Yagi, H. K. Mao, and P. M. Bell*

It is necessary to define accurately the compositions of solid solutions with increasing concentrations of the iron end member of perovskite in the system MgSiO<sub>3</sub>-FeSiO<sub>3</sub> because of their direct application to geochemical models of the earth's interior (Mao, Bell, and Yagi, this Report). In this study the lattice parameters of Pv-(Mg,Fe)SiO<sub>3</sub> (see Yagi, Mao, and Bell, this Report) were measured to construct determinative composition curves.

The lattice parameters of Pv-(Mg,Fe)SiO<sub>3</sub> solid solutions increase with increasing amounts of iron (Table 35); hence the unit cell volume increases as well (Figs. 104 and 105). The ratio *c:b:a* is 1.4438:1.0318:1 for perovskite of pure enstatite composition, and reduces to 1.4422:1.0295:1 for perovskite of Mg<sub>0.8</sub>Fe<sub>0.2</sub>SiO<sub>3</sub> composition. The iron-rich orthorhombic perovskite structure is slightly closer, therefore, to the "cubic" perovskite structure, for which the ratio would be 1.4142:1:1. The unit cell volume is related to the mole fraction of

the FeSiO<sub>3</sub> component (*X*<sub>FeSiO<sub>3</sub></sub>) by the formula

$$V(\text{\AA}^3) = 162.76(3) + 5.0(2) X_{\text{FeSiO}_3} \tag{1}$$

The most significant result of this study is that the solid solution of Pv-(Mg,Fe)SiO<sub>3</sub> extends only to 20 mole % FeSiO<sub>3</sub>. Starting compositions more iron-rich than this produced perovskite with lattice parameters the same as those for a single phase of composition Mg<sub>0.8</sub>Fe<sub>0.2</sub>SiO<sub>3</sub>. Furthermore, the more iron-rich compositions always resulted in multi-phase assemblages in which the perovskite phase coexisted with stishovite and magnesiowüstite.

The raw data obtained in this study are within the uncertainty limits of the earlier data by Liu (1976*a*); however, Liu's uncertainty limits were too great to distinguish the changes in lattice parameters of perovskites in the compositional range En<sub>100</sub>-En<sub>80</sub>Fs<sub>20</sub>. Furthermore, the important observation that silicate perovskites are limited in composition to 20 mole % of the ferrosilite component at these pressures cannot be deduced from the results of Liu (1976*a*) or Sawamoto (1977), which were based on x-ray measurements of the three-phase assemblage.

TABLE 35. Unit Cell Parameters and Volume of Quenched (Mg,Fe)SiO<sub>3</sub> Perovskite at 1 bar, 25°C

Starting Material	<i>a</i> , Å	<i>b</i> , Å	<i>c</i> , Å	<i>V</i> , Å <sup>3</sup>
En 100	4.780(1)	4.933(1)	6.902(1)	162.75(3)
Fs 11	4.790(1)	4.935(1)	6.910(1)	163.33(3)
Fs 17	4.793(1)	4.937(1)	6.915(1)	163.60(3)
Fs 21	4.797(1)	4.936(1)	6.916(1)	163.75(3)



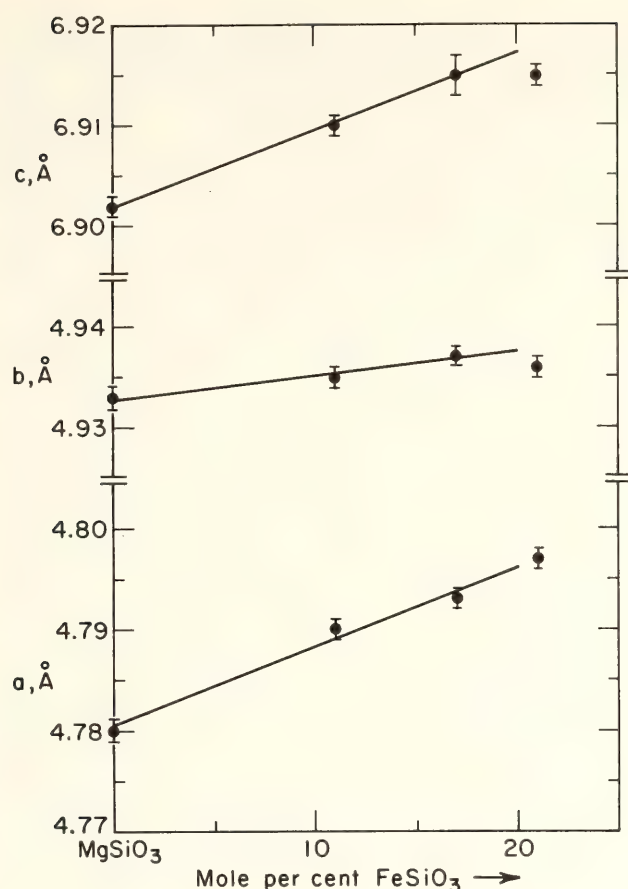


Fig. 104. Unit cell parameters vs. composition of silicate perovskite in the system  $\text{MgSiO}_3$ - $\text{FeSiO}_3$ .

#### HYDROSTATIC COMPRESSION OF $\text{MgSiO}_3$ OF PEROVSKITE STRUCTURE\*

T. Yagi, H. K. Mao, and P. M. Bell

Silicates that crystallize under high pressure in the orthorhombic (pseudocubic) perovskite structure are now known to be predominant minerals in the deep mantle of the earth (Yagi, Bell, and Mao, this Report). Data on their elastic properties are needed to interpret the density-pressure functions that are essential in relating laboratory experiments to seismic observations of the deep mantle.

The bulk modulus of  $\text{Pv-MgSiO}_3$  has been unobtainable because of stringent requirements for the precision of meas-

\* Referred to as  $\text{Pv-MgSiO}_3$ , meaning a solid solution predominantly of  $\text{MgSiO}_3$  composition having one of the perovskite structures (Yagi *et al.*, 1978).

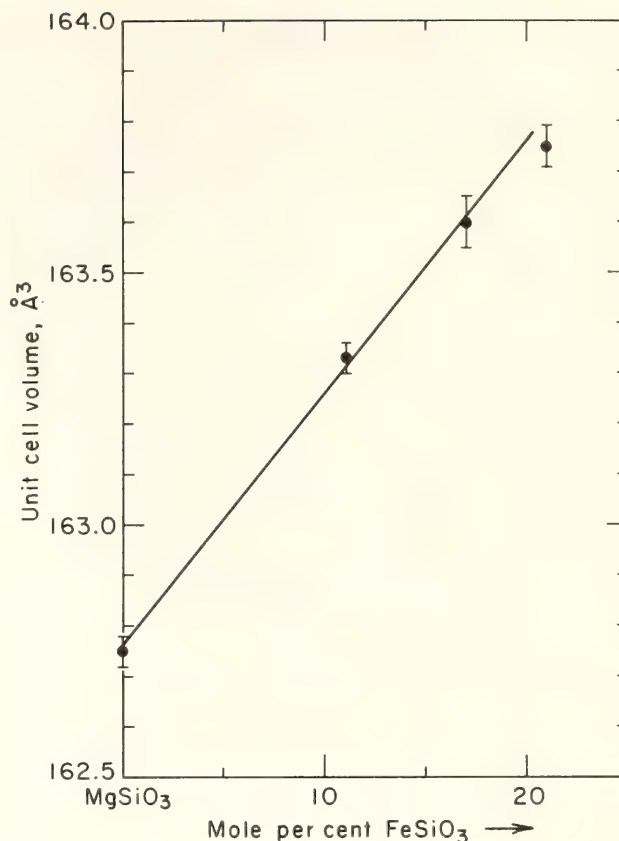


Fig. 105. Unit cell volume of perovskite in the system  $\text{MgSiO}_3$ - $\text{FeSiO}_3$ . The experimental products plotted for a bulk composition of 21 mole %  $\text{FeSiO}_3$  had traces of more than one phase. The pyroxene composition lies close to the curve, but was not used for calculation of Equation 1.

urement. The  $\text{Pv-MgSiO}_3$  phase is relatively incompressible, and x-ray data are difficult to obtain because of its low symmetry. Experiments were conducted in megabar pressure cells (MBC-X and MBC-Y; Mao and Bell, *Year Book* 77, pp. 904-908) in which precision results could be obtained. A  $\text{Pv-MgSiO}_3$  was first synthesized and then subjected to hydrostatic pressures of 40-75 kbar in separate experiments. In this pressure range a mixture of methanol and ethanol (4:1) is fluid and nonreactive, and thus is a suitable pressure medium for precise measurements. Two sets of experiments were required to determine the axial ratios and the specific volumes.

The  $\text{Pv-MgSiO}_3$  phase was synthesized both from clinoenstatite ( $\text{MgSiO}_3$ ) and from forsterite ( $\text{Mg}_2\text{SiO}_4$ ), employing the

laser heating technique (Yagi *et al.*, 1978). The initial synthesis conditions were approximately 400 kbar and 1000°C. Quenched samples are almost pure Pv-MgSiO<sub>3</sub> (from clinoenstatite) or a mixture of Pv-MgSiO<sub>3</sub> and MgO periclase (from forsterite) with a minor amount of unreacted starting material and a trace of finely divided platinum powder that was added as an absorber of laser radiation. The MgO in the latter sample forms an intimate mixture with Pv-MgSiO<sub>3</sub>, so it could be used as an internal standard for x-ray diffraction measurements (Mao and Bell, *Year Book* 76, pp. 519–522). Unit cell dimensions of the Pv-MgSiO<sub>3</sub> and MgO determined at 1 bar were found to be identical with previous values (Yagi *et al.*, 1978).

To determine the orthorhombic unit cell, 19 lines that were free from overlap were used for least-squares refinement. All the observed and calculated  $d$  values are in agreement within an error of  $\pm 0.15\%$ .

The variation of both  $b/a$  and  $c/a$  is small, increasing slightly with pressure. Based on these observations, the following equations are proposed:

$$\begin{aligned} b/a &= 1.032 + 0.04P \text{ (Mbar)}; \\ c/a &= 1.444 + 0.07P \text{ (Mbar)}. \end{aligned}$$

This relation indicates that the  $a$  axis is more compressible than either the  $b$  or  $c$  axis. If orthorhombic perovskite is to shift to an ideal cubic perovskite,  $a$ ,  $b$ , and  $c$  must satisfy the relation  $a = b = c/\sqrt{2}$ . With increase in pressure,  $c/b$  approaches the cubic value whereas  $b/a$  and  $c/a$  depart from it, so whether or not there is a change in the degree of distortion is inconclusive.

A Birch-Murnaghan equation of state was fitted to these data for various values for  $dK_0/dP$ . If  $dK_0/dP = 4$ , the best fit obtained is  $K_0 = 2.58$  Mbar; and  $K_0$  varies from 2.62 to 2.55 Mbar for  $dK_0/dP$  between 3 and 5. The bulk sound velocity calculated from these values is 8.0 km/sec.

Liebermann *et al.* (1977) studied the

elastic properties of aluminate, titanate, stannate, and germanate compounds with the perovskite structure by the ultrasonic method. Relationships such as that in which the modulus  $K_s$  is inversely proportional to the volume, or  $v_\phi \bar{M} = \text{constant}$  ( $v_\phi$  is the bulk sound velocity and  $\bar{M}$  is the mean atomic weight) in isostructural compounds, appear to apply to these various perovskite-type compounds. The values  $K_s = 2.5 \pm 0.3$  Mbar and  $v_\phi = 7.9 \pm 0.4$  km/sec were predicted for Pv-MgSiO<sub>3</sub>. The present experimental results yielded the value  $K_T = 2.6 \pm 0.2$  Mbar and  $v_\phi = 8.0$  km/sec for Pv-MgSiO<sub>3</sub>, in agreement with these predictions.

The fact that the elasticity relationships appear to apply to a variety of perovskite phases suggests that the bulk elastic properties are insensitive to distortion of the cation site. It is evident that the relatively short O-O distances in silicate perovskite (2.48 Å minimum) do not affect the bulk elastic properties.

The bulk modulus of Pv-MgSiO<sub>3</sub> measured by x-ray diffraction *in situ* at high pressure to 80 kbar is  $K_0 = 2.6 \pm 0.2$  Mbar if  $dK_0/dP$  is between 3 and 5. This value can be used as a boundary condition in models of the earth's lower mantle. Comparison of the elastic properties of various compounds with perovskite structure indicates that the proposed relationships between bulk modulus and molar volume, and between bulk sound velocity and mean atomic weight, are valid for Pv-MgSiO<sub>3</sub>.

#### PHASE RELATIONS IN THE SYSTEM MgO-FeO-SiO<sub>2</sub> BETWEEN 150 AND 700 KBAR AT 1000°C

*T. Yagi, P. M. Bell, and H. K. Mao*

Phases in the system MgO-FeO-SiO<sub>2</sub> that are stable at ultrahigh pressures are thought to be the predominant minerals in the earth's lower mantle (Mao *et al.*, *Year Book* 76, pp. 502–504), and it is important to ascertain their stability



relations. Experiments with the laser-heated, megabar-pressure cell (MBC-H; Mao and Bell, *Year Book* 77, pp. 904–908) were required to accomplish this objective for the conditions 150–700 kbar (corresponding to the depth range in the earth of approximately 500–1600 km). These experiments involved placing a sample of pure synthetic starting material in a cell designed to produce a pressure gradient so that the phase boundaries could be observed visually with an optical microscope. Pressures were measured with the ruby fluorescence method (Mao *et al.*, 1978). After they were quenched, the experimental charges were removed from the cell, separated as well as possible along the equilibrium boundaries, and then analyzed by x-ray diffraction.

Results of this study are important in formulating mineralogical models of the deep mantle because of the extensive stability range of the  $(\text{Mg,Fe})\text{SiO}_3$  perovskite phase (190 to at least 700 kbar), and because of the partitioning of iron between perovskite and magnesio-wüstite (Bell, Yagi, and Mao, this Report). Perovskite is believed to be the most dominant mineral in the deep mantle. The partitioning of iron from the perovskite phase to the magnesio-wüstite phase could be involved in a major process in the distribution of iron between the upper and lower mantle and the core (Mao, Bell, and Yagi, this Report).

The cell configuration, designed to produce a radial pressure gradient in the sample, included use of a stainless steel gasket with a hole of relatively large diameter to confine the sample (Fig. 106). The highest pressure was located in the center. Fine-grained ruby powder was placed on the sample surface before the cell was sealed. When at pressure, the sample was heated to approximately  $1000^\circ\text{C}$  by focused laser beam, and a sharp boundary appeared between the low- and high-pressure assemblages. Pressures in the ruby grains were meas-

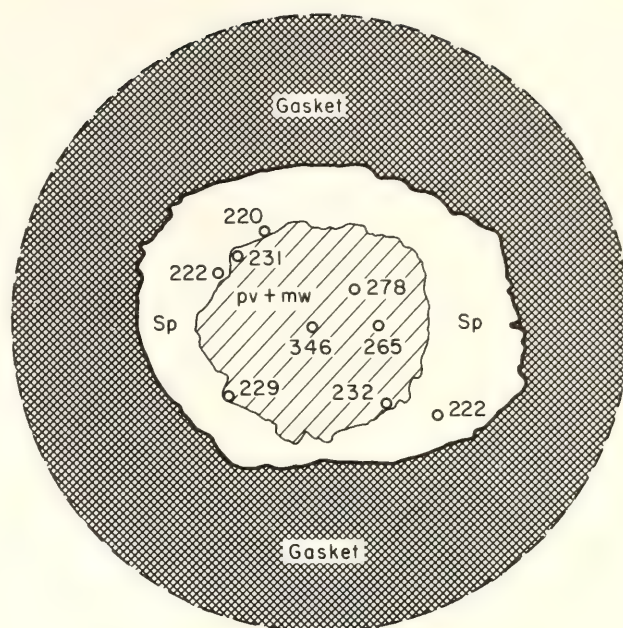


Fig. 106. Sketch of a view under microscope of a sample at pressure in the diamond-window, high-pressure cell, Run No. 104-4, Fa15. In this experiment, spinel (sp, of olivine composition) in the pressure zone has been converted to perovskite (pv, of pyroxene composition) plus magnesio-wüstite (mw). The sample diameter, approximately  $300\ \mu\text{m}$ , is relatively large, resulting in a radial pressure gradient. The highest pressure is in the center. Numbers are pressure values in kilobars, measured by the ruby fluorescence technique.

ured with the fluorescence technique, and thus it was possible to bracket the boundary. In some instances it was possible to locate ruby grains exactly on a boundary, and the specific boundary pressure could be determined.

In these experiments, the sample is viewed at a range of pressures as depicted in Fig. 106. The pressure of each assemblage was measured as close as possible to the boundary. The advantage of this technique is that the phase boundary can be seen visually and determined accurately over a pressure range in a single experimental assembly. By adjusting the load, the maximum pressure in the center and the gradient toward the edges of the sample can be raised or lowered, and thus the boundary can be made to move toward the edges (designated "up" in Table 36) or toward the

TABLE 36. Phase Boundary Determination Based on *in-situ* Observation

Starting Material*	Run No.	Pressure Cycle	Pressure Measured Close to Boundary ( $P_T$ ), kbar		
			Low†	High†	Estimated $P_T$
<i>Spinel = perovskite + magnesiowüstite transition</i>					
Fo 100	105-2	up	239	269	255 ± 10 kbar
	106-1	up	261	282	
	107-1	up	243	266	
	108-1	up	261	266	
Fa 7	103-2	up	247	257	240 ± 10 kbar
	103-4	up	236	257	
	103-6	down	222	236	
Fa 15	104-3	up	224	228	225 ± 10 kbar
	104-4	up	222	229	
	104-5	down	203	215	
	104-6	up	223	258	
	109-1	up	226	246	
<i>Spinel = magnesiowüstite + stishovite</i>					
Fs 100	113-1	up	153	168	155 ± 10 kbar
	114-1	up	153	164	
	114-2	down	126	157	
	115-1	up	156	175	
	115-2	up	163	184	
<i>Spinel = perovskite + magnesiowüstite + stishovite</i>					
Fa 51	116-1	up	191	191	200 ± 10 kbar
	116-2	up	209		
	118	up	210	210	
<i>β-phase = spinel</i>					
En 100	119	up	162	162	160 ± 10 kbar

\* Starting compositions: Fa, Fe<sub>2</sub>SiO<sub>4</sub>; Fo, Mg<sub>2</sub>SiO<sub>4</sub>; Fs, FeSiO<sub>3</sub>; En, MgSiO<sub>3</sub> (with mole fractions).

† Low = low-pressure side of the boundary; high = high-pressure side of the boundary. When the low = high, a ruby grain was found exactly on the boundary.

center (designated “down” in Table 36). This shift of the boundary constitutes reaction reversal that would require numerous experimental assemblies in experiments where the sample is under uniform pressure, or where the pressure distribution in the sample cannot be measured.

This technique is useful for pressure-dependent reactions and for invariant boundaries and univariant boundaries where the divariant fields are small. The boundaries that were distinguished using the *in situ* technique are (at constant  $T$ , Table 36)

univariant:

$$\text{Sp} = \text{Pv} + \text{Mw}, \tag{1}$$

binary invariant:

$$\text{Fe}_2\text{SiO}_4\text{Sp} = \text{Mw} + \text{St}, \tag{2}$$

ternary invariant:

$$\text{Sp} = \text{Pv} + \text{Mw} + \text{St}, \tag{3}$$

unary invariant:

$$\beta\text{Mg}_2\text{SiO}_4 = \text{Sp}, \tag{4}$$

where Sp is spinel, (Mg,Fe)<sub>2</sub>SiO<sub>4</sub>; Pv, perovskite, (Mg,Fe)SiO<sub>3</sub>; Mw, magnesiowüstite, (Mg,Fe)O; St, stishovite, SiO<sub>2</sub>; β, β phase, (Mg,Fe)<sub>2</sub>SiO<sub>4</sub>. For these re-



actions, the pressure determinations (Table 36) are accurate to  $\pm 5$  kbar.

Sample charges were quenched from temperature and then from pressure. In the type of experiment described above, the low- and high-pressure assemblages were separated to determine the phases present by x-ray diffraction. The results were used to confirm the pressure-sensitive boundaries that are optically sharp. Forty-two additional experiments of the more conventional type that minimize the pressure gradient were run at pressures between 150 and 700 kbar within the stable fields. These experiments were done for the purpose of mapping the fields. The quenched charges were analyzed in the same way.

A third type of experiment was made to determine composition-sensitive boundaries. Such boundaries are not sharp because they tend to parallel the pressure axis or have broad, multiple-phase fields. Compositions of the coexisting phases were determined by measuring lattice parameters.

Phase diagrams for the  $\text{MgO-FeO-SiO}_2$  system were constructed on the basis of the boundary determinations. Data on the Fe-Mg distribution (Bell, Yagi, and Mao, this Report) were used in conjunction with the observed boundaries. In general, plotted boundaries have an uncertainty of  $\pm 10$  kbar in pressure, and  $\pm 0.05$  (Mg end) to  $\pm 0.1$  (Fe end) mole fraction in composition.

Figures 107 and 108 are the pseudobinary diagrams for the pyroxene  $[(\text{Mg, Fe})\text{SiO}_3]$  and olivine  $[(\text{Mg, Fe})_2\text{SiO}_4]$  joins, plotted between 100 and 500 kbar. Above 100 kbar, neither pyroxene nor olivine is a stable phase, both having inverted or broken down to the  $\beta$  phase or spinel (plus stishovite for pyroxene composition). The small field for ilmenite (of pyroxene composition) is limited in pressure and composition. The ilmenite phase was not observed with olivine starting compositions nor with pyroxene starting compositions with  $\text{FeSiO}_3$  mole fractions greater than 0.2.

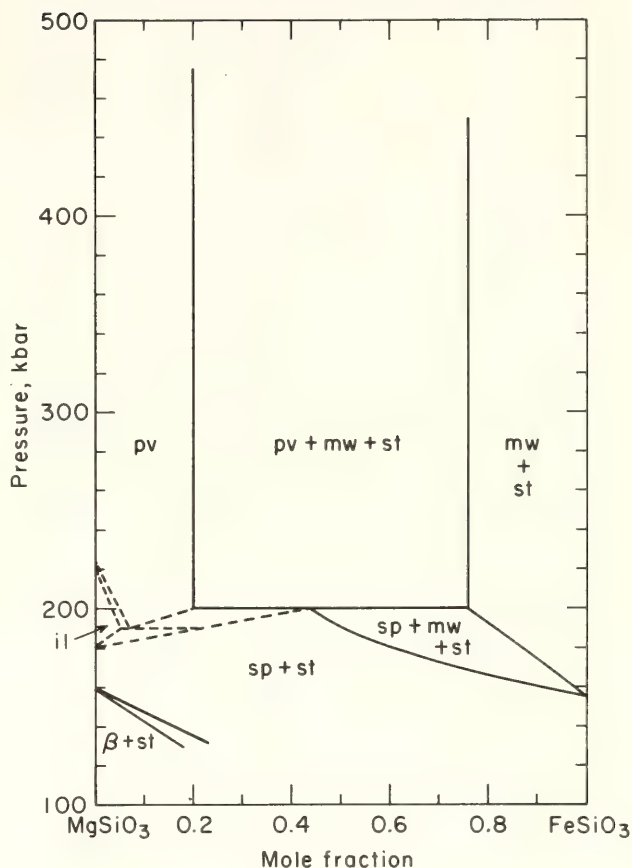


Fig. 107. Pseudobinary diagram for pyroxene composition. Abbreviations: pv, perovskite; mw, magnesiowüstite; st, stishovite; sp, spinel;  $\beta$ ,  $\beta$  phase (of olivine composition); il, ilmenite.

The boundaries for the ilmenite field are dashed in Fig. 107 because they were not resolved in detail.

In both pseudobinary joins it should be noted that the  $(\text{Mg, Fe})\text{SiO}_3$  perovskite field is extensive. Perovskite is stable in the olivine and pyroxene bulk compositional range from the pure magnesium end member to 76 mole % of the iron end member, although the composition of the perovskite phase itself ranges only to 20 mole % of the  $\text{FeSiO}_3$  end member. It is significant, also, that a relatively iron-poor perovskite can coexist with a relatively iron-rich magnesiowüstite.

Perovskite stability first appears at an intermediate composition (Fig. 107; Fig. 109, 195-kbar section). This relationship is maintained in the pressure range approximately 190–210 kbar as the composition of perovskite expands toward the

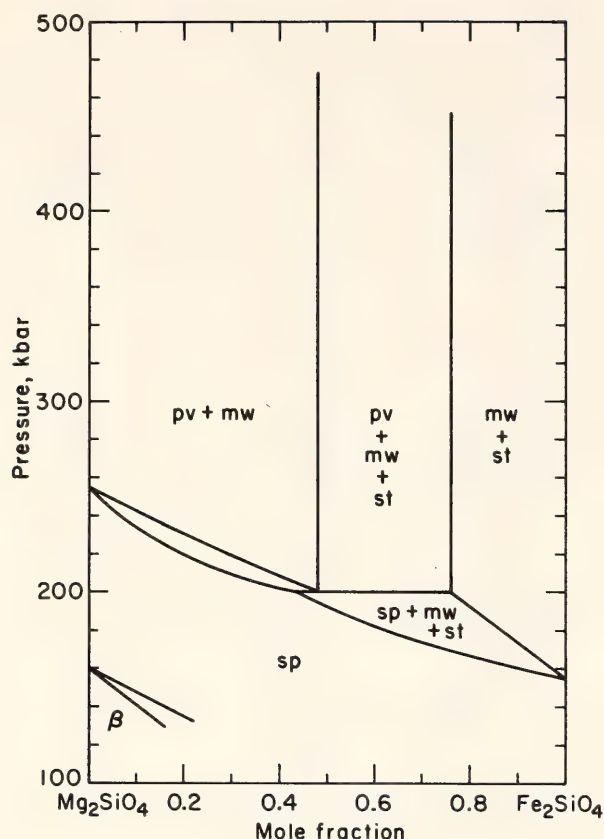


Fig. 108. Pseudobinary diagram for olivine composition. Abbreviations as in Fig. 107.

magnesium end member and to 20 mole % of the iron member.

The effects of the appearance of the perovskite field can be seen in the ternary sections (Fig. 109). In conjunction with these sections, the pressure-composition diagram for  $(\text{Mg,Fe})_2\text{SiO}_4$  (Fig. 108) shows the perovskite field with divariant boundaries to a pressure of 200 kbar, where the boundary becomes invariant. The three-phase fields stishovite-perovskite-spinel and stishovite-spinel-magnesiowüstite intersect, and the perovskite-spinel-magnesiowüstite field shifts away from the iron end of the system and diminishes with increasing pressure. Spinel disappears when the pressure reaches 255 kbar.

The formation of Pv- $(\text{Mg,Fe})\text{SiO}_3$  and its transitions from spinel between 190 and 255 kbar can occur over a relatively small pressure range, depending on composition. This narrow transitional zone would correspond to the seismic discon-

tinuity in the mantle observed at a depth of approximately 650 km. At greater depths, extending from at least 650 to 1600 km, the perovskite-magnesiowüstite assemblage is dominant. Thus, the major portion of the mantle is possibly formed of these minerals.

#### IRON-MAGNESIUM DISTRIBUTION COEFFICIENTS BETWEEN SPINEL [ $(\text{Mg,Fe})_2\text{SiO}_4$ ], MAGNESIOWÜSTITE [ $(\text{Mg,Fe})\text{O}$ ], AND PEROVSKITE [ $(\text{Mg,Fe})\text{SiO}_3$ ]

*P. M. Bell, T. Yagi, and H. K. Mao*

It was demonstrated by the phase relations in the system  $\text{FeO-MgO-SiO}_2$  at high pressure (Yagi, Bell, and Mao, this Report) that there was significant Fe and Mg partitioning between the perovskite and oxide phases (the magnesiowüstite series). This report includes a description of the observations and results of measurements of the distribution coefficients, which are limited to the experimental results on eight synthetic bulk compositions for the assemblages spinel [ $(\text{Mg,Fe})_2\text{SiO}_4$ ] + magnesiowüstite [ $(\text{Mg,Fe})\text{O}$ ] and perovskite [ $(\text{Mg,Fe})\text{SiO}_3$ ] + magnesiowüstite [ $(\text{Mg,Fe})\text{O}$ ]. The partitioning could have significant influence on geochemical models of the earth (Mao, Bell, and Yagi, this Report).

Lattice parameters of each phase in the multiphase, polycrystalline charges were determined by x-ray diffraction ( $\text{CuK}\alpha$  radiation). The relation between volume and composition (mole fraction  $\text{FeSiO}_3$  component) was used for analysis of the perovskite phases (Yagi, Mao, and Bell, this Report). For spinel (of olivine composition), the relation between volume and composition determined by Akimoto *et al.* (1976) was used. The procedure for the analysis of magnesiowüstite was similar, but complicated by the nonstoichiometry of these phases (when coexisting with metallic iron; Mao and Bell, *Year Book* 70, pp. 176–



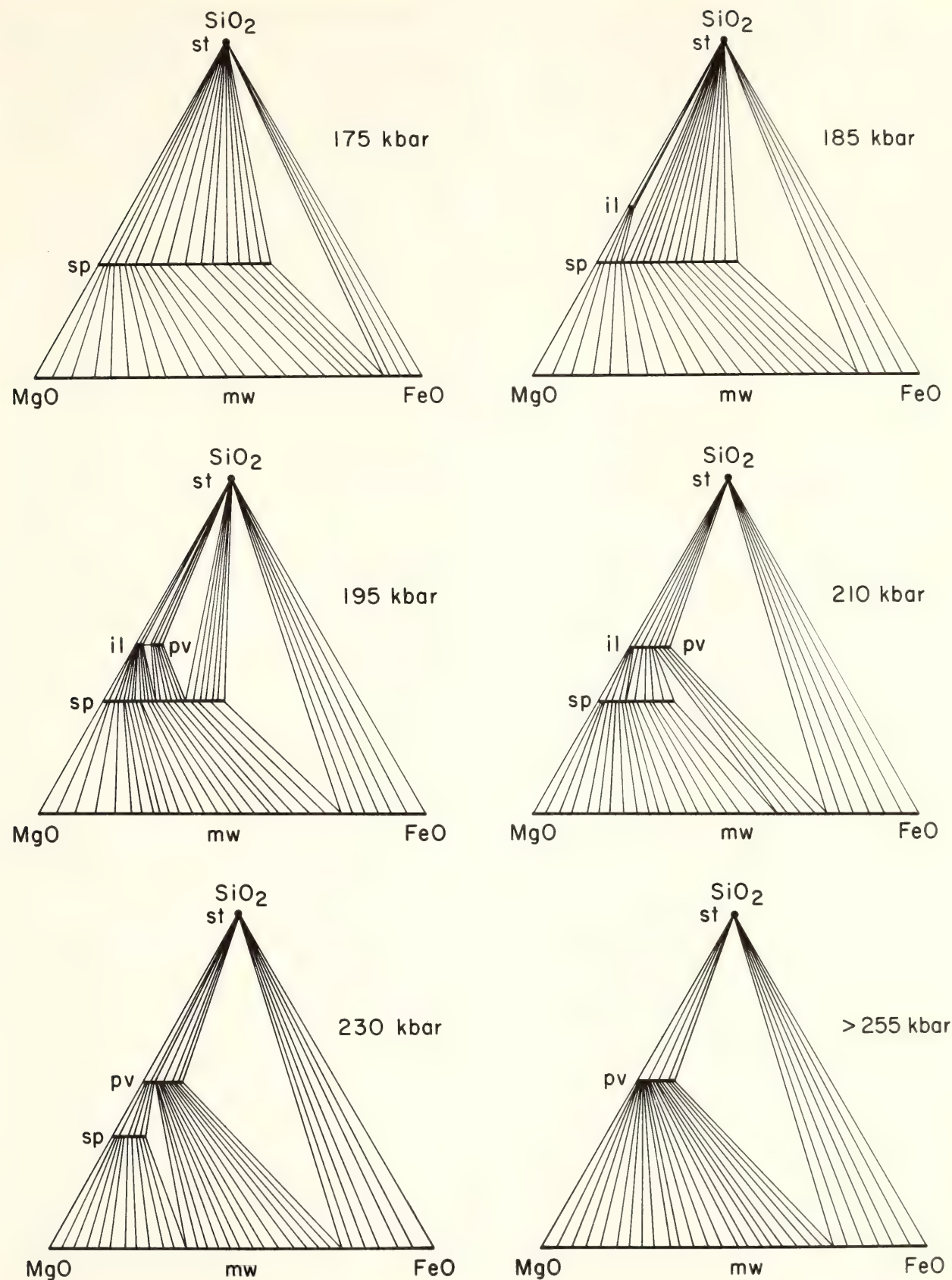


Fig. 109. Compositional ternary phase diagrams for the system SiO<sub>2</sub>-MgO-FeO (projected through oxygen at 1000°C).

178; Bassett and Ming, 1972; Liu, 1976b), which consequently affected the lattice parameter. Rosenhauer *et al.* (Year Book 75, pp. 513–515) determined the relationship between volume and Mg-Fe ratio of magnesiowüstite at 1 bar,

TABLE 37. Unit Cell Parameters and Compositions of Coexisting Phases\*

Starting Material	Perovskite		Magnesiowüstite		Spinel	
	$\bar{V}, \text{\AA}^3$	$X_{\text{FeSiO}_3}, \%$	$a, \text{\AA}$	$X_{\text{FeO}}, \%$	$a, \text{\AA}$	$X_{\text{Fe}_2\text{SiO}_4}, \%$
<i>Pyroxene</i>						
Fs29	164.0(3)	25(5)	4.293(5)	76(8)		
Fs29	163.7(1)	18(2)	4.296(5)	80(8)		
Fs39	163.6(2)	17(4)	4.294(5)	77(8)		
Fs50			4.29(1)	71(10)	8.140(5)	40(5)
Fs91			4.31(1)	100(10)	8.216(3)	87(3)
<i>Olivine</i>						
Fa7	162.5(3)	-4(6)	4.229(2)	13(2)	8.085(5)	6(3)
Fa15	163.1(1)	7(3)	4.246(3)	26(3)		
Fa41	163.8(1)	20(2)	4.294(3)	78(3)		
Fa51			4.296(2)	80(4)	8.149(3)	47(3)

\*Starting compositions: Fs, FeSiO<sub>3</sub>; Fa, Fe<sub>2</sub>SiO<sub>4</sub> (with mole fractions).

and it was assumed that their results are applicable to the present data. Possible errors attached to this assumption will have no measurable effect for compositions with less than 70 mole % FeO.

Analysis of the data (Table 37, Fig. 110) was made to determine the Fe-Mg distribution coefficient,  $K$ , defined as follows:

$$K_{A-B} = (X_{\text{Fe}}/X_{\text{Mg}})_A / (X_{\text{Fe}}/X_{\text{Mg}})_B, \tag{1}$$

where  $X$  is the mole fraction in the coexisting phases,  $A$  and  $B$ . In this case of ideal solutions,  $K$  is the equilibrium constant (Nafziger and Muan, 1967). The results are

$$\begin{aligned} K_{\text{Pe-Mw}} &= 0.08(3); \\ K_{\text{Sp-Mw}} &= 0.25(10); \\ K_{\text{Pe-Sp}} &= 0.32(5). \end{aligned}$$

Variation of  $K$  with pressure and temperature was within the uncertainty of

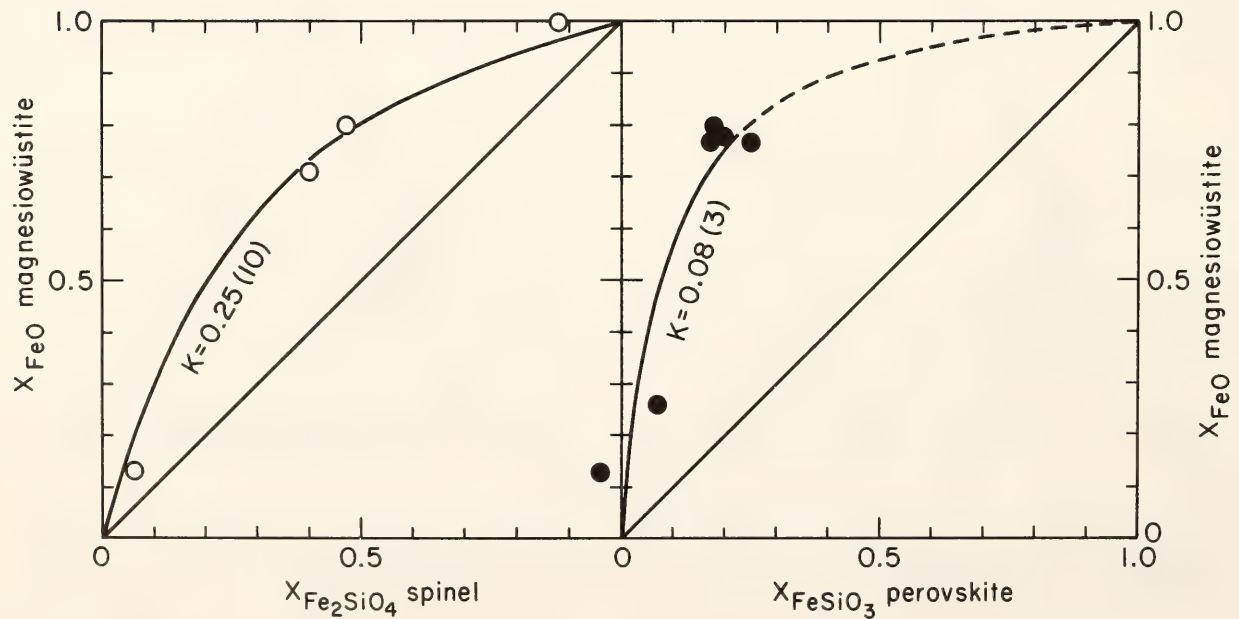


Fig. 110. Partition coefficients for magnesiowüstite + spinel and magnesiowüstite + perovskite assemblages. Curved lines were drawn to fit data points on the assumption of ideal solution.



the determination of composition and was not calculated.

These results could be significant geochemically because of the strong partitioning of iron, relative to magnesium, into magnesiowüstite or spinel that causes strong depletion of iron in the silicate perovskite phase. For example, spinel of 10 mole % iron would be in equilibrium with perovskite of 3 mole % iron and magnesiowüstite of 30 mole % iron. Iron, therefore, is separated from perovskite into the oxide or silicate spinel phase at high pressure.

#### IRON-MAGNESIUM FRACTIONATION MODEL FOR THE EARTH

*H. K. Mao, P. M. Bell, and T. Yagi*

The partitioning of iron and magnesium in the earth at a primitive stage could have played an important role in the formation of the core, the mantle, and the crust. Data on partitioning of iron and magnesium in mineral assemblages that replace the common rock-forming minerals at high pressure (Bell, Yagi, and Mao, this Report) suggest that such a role may have been important in the earth's formation and may have been important since that time in maintaining the iron-magnesium balance throughout the earth. The importance lies in the strong partitioning of iron and magnesium between the phases perovskite (of pyroxene composition) and magnesiowüstite. The density difference between the two follows the iron distribution, which creates an ideal circumstance for gravitational differentiation. This type of differentiation, which could occur in the deep mantle, is analogous to calcium-magnesium partitioning between the earth's crust and mantle.

The strong Fe-Mg partitioning for perovskite and magnesiowüstite persists over an extensive pressure range. In recent experiments between 200 and 450 kbar (Bell, Yagi, and Mao, this Report), the partitioning does not appear to

change significantly. In the earth, this range of pressure includes a portion of the mantle greater than the crust and upper mantle combined.

#### *Density Considerations*

Densities of three different pairs of coexisting magnesiowüstites and perovskites at 25°C show the effects of Fe partitioning (Fig. 111). The geochemical model of the earth described below is constrained not only by the reactions that produce the high-pressure assemblage, but also by the density-composition relationships. The Pv-(Mg,Fe)SiO<sub>3</sub> composition is limited to an iron content of 20 mole % FeSiO<sub>3</sub>, but the coexisting magnesiowüstite, whose iron content is 76 mole % FeO, is 1.5 g/cm<sup>3</sup> denser.

With a bulk composition between (Mg,Fe)SiO<sub>3</sub> and (Mg,Fe)<sub>2</sub>SiO<sub>4</sub> having  $X_{\text{Fe}} > 0.2$  ( $X$  is the mole fraction of iron end member; for example, chondrites have  $X \leq 0.5$ ), earth accretion would have produced the perovskite-magnesiowüstite assemblage. Because the perovskites are limited to  $X_{\text{Fe}} = 0.2$ , magnesiowüstite might separate gravitationally.

In a plot of differential density vs. the equilibrium iron contents of each of the coexisting pairs at 1 bar, 250 kbar, and 450 kbar (Fig. 112), magnesiowüstite is not always denser than the coexisting perovskite. At the magnesium-rich end, perovskite is denser. The line of zero density difference is close to  $X_{\text{Fe}} = 0.02$  (perovskite) and  $X_{\text{Fe}} = 0.2$  (magnesiowüstite). Gravity separation would cease close to this limit, but it is useful to note that the composition of the final, limiting assemblage is equivalent to the bulk composition of olivine with  $X_{\text{Fe}} = 0.11$  or pyroxene with  $X_{\text{Fe}} = 0.02$ , or any bulk composition between the two.

Figure 113 is a rectilinear plot of a portion of the experimentally determined equilibrium diagram in the ternary system. The shaded zones are zones of close to zero density difference ( $\pm 0.1$  g/cm<sup>3</sup>)

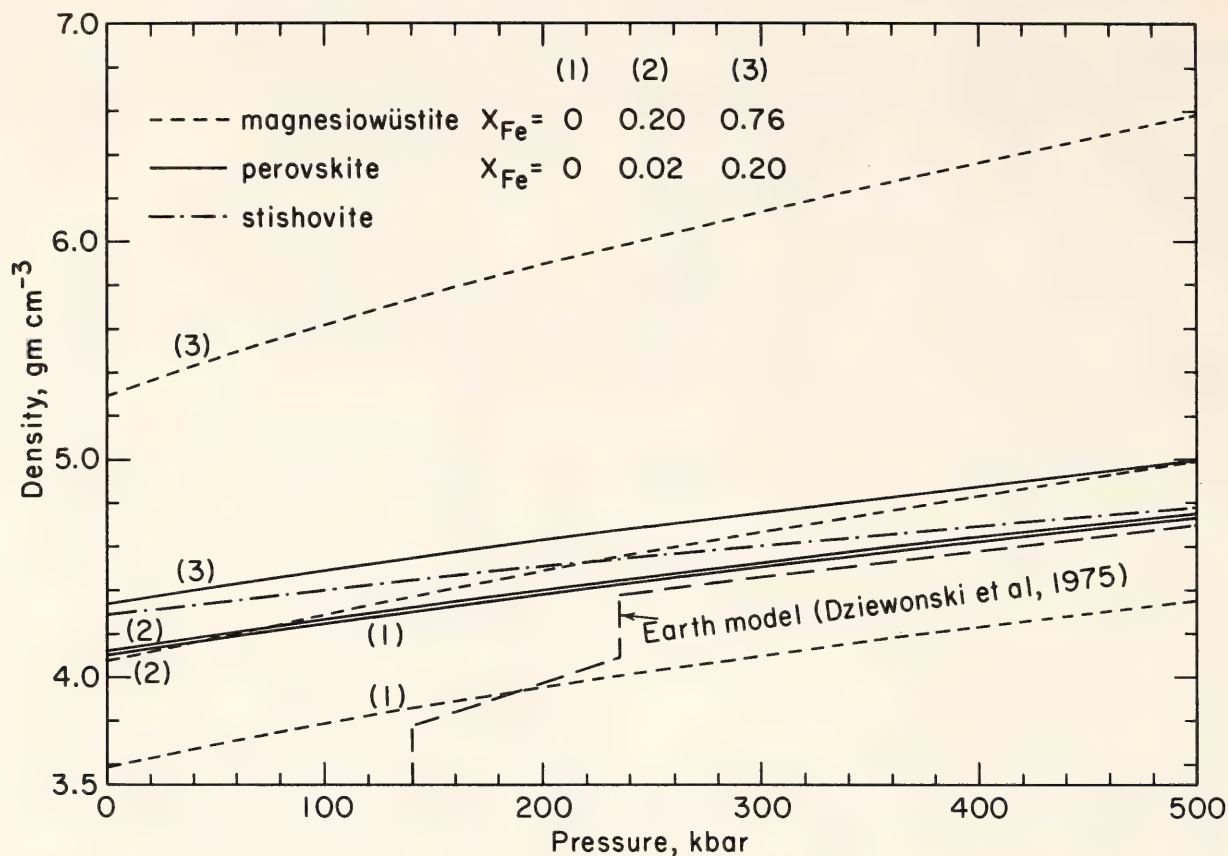


Fig. 111. Density vs. pressure for three coexisting compositions of magnesiowüstite and silicate perovskite (in the system  $MgSiO_3$ - $FeSiO_3$ ) and for stishovite.  $X_{Fe} = Fe/(Fe + Mg)$  in moles. Also shown is the model density distribution for the earth of Dziewonski *et al.* (1975).

between the coexisting phases. The initial composition for the process to become operative in the earth is not critical as long as the composition was at least as iron-rich as the present-day mantle. Differentiation of the primitive earth would presumably occur within the intermediate zone bounded by the two shaded zones and the tie line between  $SiO_2$  and  $X_{FeO}$  (magnesiowüstite) = 0.20. The final stages of differentiation would end in the area between the pyroxene and olivine compositional lines and the tie lines between  $SiO_2$  and  $X_{FeO}$  (magnesiowüstite) = 0.02 and 0.20, close to the shaded zone.

#### *The Differentiation Process*

The combined effects of the phase equilibria, compositions, and bulk moduli described above are based on equilibrium

experimental data, and thus constitute fundamental thermodynamic requirements or constraints for this chemical system, and for the earth, with considerable latitude in the nature of the bulk composition. If the bulk composition of the primitive earth were within the shaded zone described above, then the assemblage would have been gravitationally stable and would not have differentiated. If, however, the bulk composition were outside the shaded zone, the assemblage would have been unstable, and by a process of repeated fractionation and reequilibration, the stable compositional configuration would have developed.

Steps in the possible approach to the stable distribution follow.

1. If the process began at a primitive stage in earth formation with a bulk composition mainly in the  $MgO$ - $FeO$ -



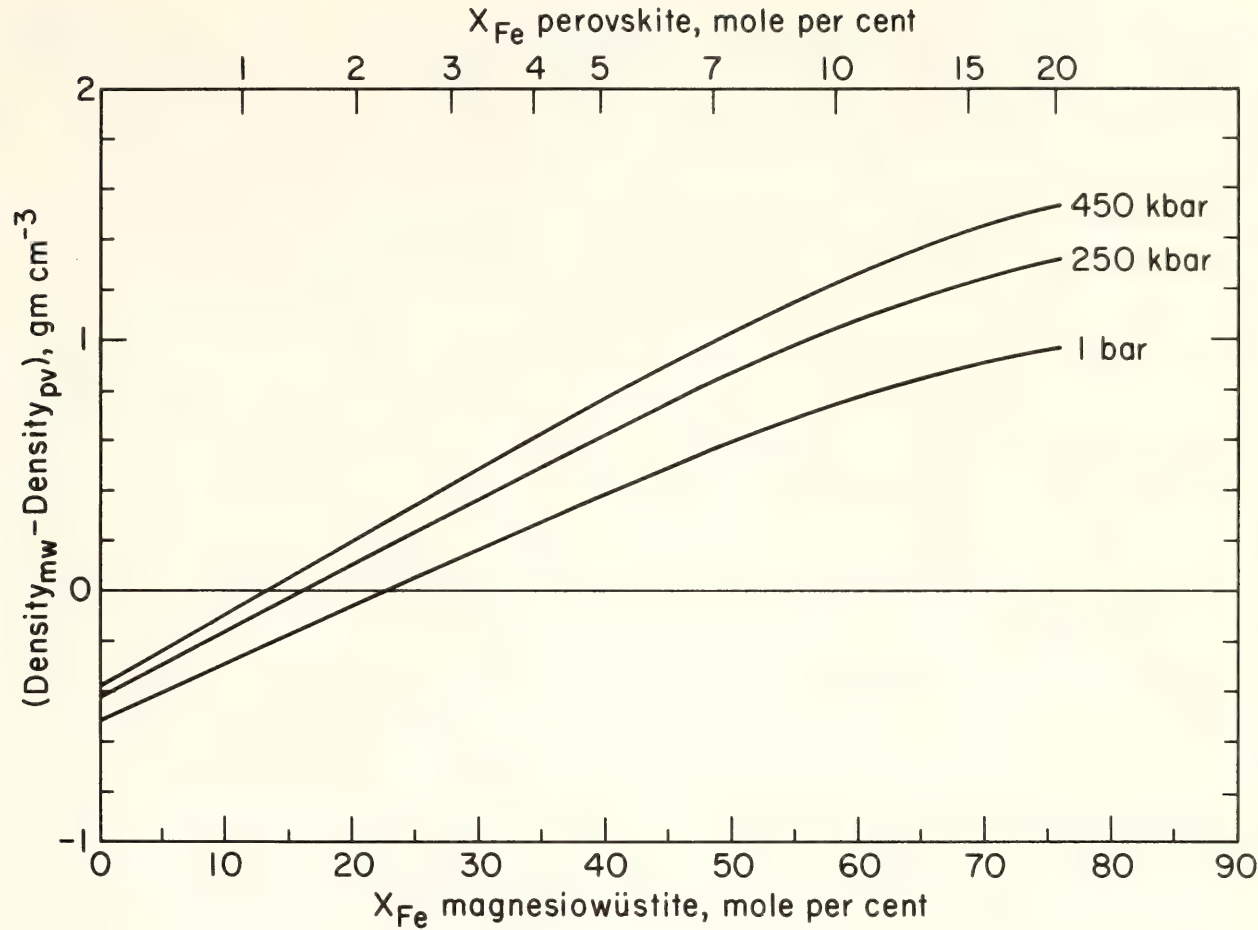


Fig. 112. Plot of the density difference between magnesiowüstite and silicate perovskite at 1 bar, 250 kbar, and 450 kbar as functions of composition ( $X$  is the mole fraction of  $\text{FeSiO}_3$ ).

$\text{SiO}_2$  system with  $X_{\text{Fe}} \geq 0.2$  and between ol and py, which are subjected to sufficient pressure and temperature, iron would partition to the silicate and oxide phases, with  $X_{\text{py}}^{\text{Fe}} = 0.2$ ,  $X_{\text{mw}}^{\text{Fe}} = 0.76$  (where  $X$  is the mole fraction). In a solid with low viscosity (or even a partial melt), the assemblage would be gravitationally unstable; the denser phase sinking toward the center.

2. The heavier magnesiowüstite would be concentrated near the core. The iron-rich magnesiowüstite could lose a portion of its iron to the core, by a process such as chemical reduction, direct solution of  $\text{FeO}$  in metallic iron (Ringwood, 1977), or chemical disproportionation (Mao and Bell, 1977).

3. The residual magnesiowüstite phase would be less iron-rich and could float or convect to be remixed and reequilibrated with the silicate perovskite layer.

4. Reequilibration would shift the equilibrium pair to a more magnesium-rich tie line (see Bell, Yagi, and Mao, this Report), and the gravitational and separation processes could again occur.

5. As the density difference became less in each cycle, the process eventually would become inefficient and would cease.

*Effect of a Possible Phase Transition in Magnesiowüstite*

A phase transition has been observed in wüstite at approximately 700 kbar. No such transition occurs at the magnesium end (at least to 1.2 Mbar, Jeanloz *et al.*, 1979), and hence it is suggested that a two-phase assemblage would form at the iron-rich end. If this reaction occurs, a more iron-rich and denser oxide phase would be produced, enhancing the differentiation process with perovskite.

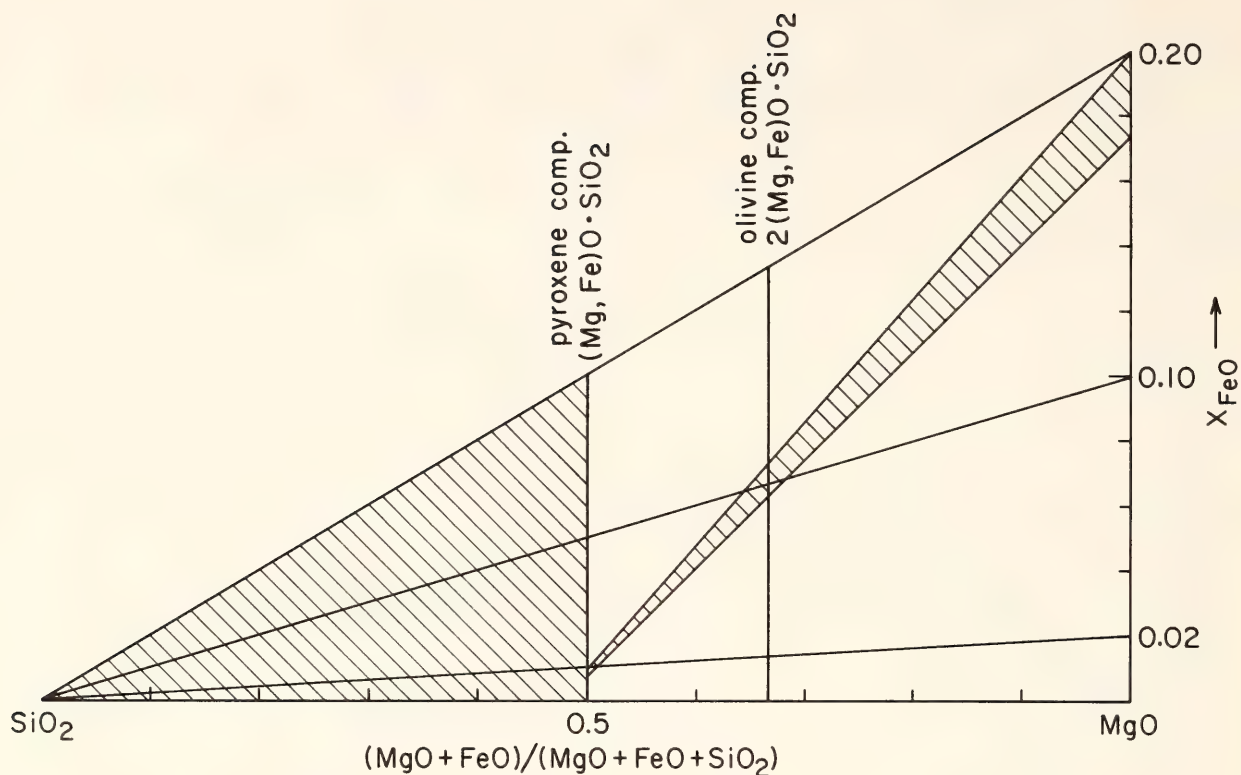


Fig. 113. Portion of the composition diagram for the system  $\text{SiO}_2\text{-FeO-MgO}$  in rectilinear coordinates ( $X$  is the mole fraction of  $\text{FeSiO}_3$ ). Shaded zones are close to zero density difference ( $\pm 0.1 \text{ g/cm}^3$ ) between the coexisting phases. At the pressures under consideration (above 195 kbar),  $\text{SiO}_2$  is represented as stishovite, pyroxene as perovskite, olivine as spinel, and the system  $\text{MgO-FeO}$  as magnesiowüstite.

#### *Application to Models of the Present Earth*

The thermodynamic requirements or constraints that are superimposed on the earth's interior as a consequence of the reactions that yield the silicate-oxide assemblage at high pressure, and the major partitioning of iron and magnesium that would be present in this assemblage, may affect the formation of the earth regardless of the nature of the original accretion or coalescence stages. Furthermore, the postulated process, or a modified version (including other components such as Ca and K), would constrain the major elemental distribution in the evolved earth. This supposition is consistent with current geophysical models based on seismic and astronomic data and on theory, such as the model proposed by Dziewonski *et al.* (1975), shown in Fig. 111. To compare the

measured density curves with the present-day earth model, the density curves of the latter require reduction to the  $25^\circ\text{C}$  isotherm. (The model curves were constructed for the geotherm.) With this reduction, the model curves are raised in density by approximately  $0.1 \text{ g/cm}^3$ , bringing them into agreement with the experimental curves. The phases located within the stable zone of Fig. 113 (described above) have densities within  $\pm 0.1 \text{ g/cm}^3$ . This band agrees with the reduced present-day geophysical model within the combined uncertainties of the data and the models.

The sharp phase transition, spinel = perovskite + magnesiowüstite, occurs at a bulk olivine composition with  $X_{\text{Fe}} = 0.1$  (the stable zone in Fig. 113) and at a pressure of 235 kbar, which corresponds to the equally sharp seismic discontinuity at approximately 650 km, shown in Fig. 111. If the transition



actually occurs in the earth at that depth, the corresponding bulk composition of the mantle there will be predominantly that of olivine ( $\text{Fo}_{0.9}\text{Fa}_{0.1}$ ). This bulk composition will yield an assemblage of perovskite of  $X_{\text{Fe}} = 0.02$  and magnesio-wüstite of  $X_{\text{Fe}} = 0.2$ , the density of which agrees with the model of Dziewon-ski *et al.* (Fig. 111).

#### HIGH-PRESSURE WÜSTITE: CELL PARAMETERS AND MÖSSBAUER SPECTRA

*B. Simons and F. Seifert*

Wüstite could be a principal phase in the lower mantle (Mao and Bell, 1977) or in the outer core (Jeanloz *et al.*, 1979), and its composition is therefore important. At atmospheric pressure, wüstite is known to be a cation-deficient phase (in equilibrium with metallic iron) (Darken and Gurry, 1945), although Katsura *et al.* (1967) reported that wüstite becomes stoichiometric at pressures above 36 kbar at 770°C. Non-stoichiometric wüstite ( $\text{Fe}_{0.91-0.97}$ ) (plus metallic iron plus stishovite) forms as a product of the disproportionation of spinel ( $\text{Fe}_2\text{SiO}_4$ ) at 250 kbar and 750°C (Mao and Bell, *Year Book 70*, pp. 176–178; see also Bassett and Ming, 1972; Liu, 1976). These changes in composition of wüstite with pressure have been related to changes in the molar volume of metallic iron and the partial molar volume of iron in wüstite that could be important in the mantle (Mao and Bell, 1977), so a careful analysis of wüstite composition under high pressures and high temperatures has been undertaken to clarify the relationships.

#### Experiments

Equimolar mixture of ferric oxide and metallic iron were homogenized and pressed into iron crucibles. These samples were then subjected to high pressures and high temperatures in a solid-media, high-pressure apparatus (Boyd and England, 1960). The products were examined by x-ray powder diffraction us-

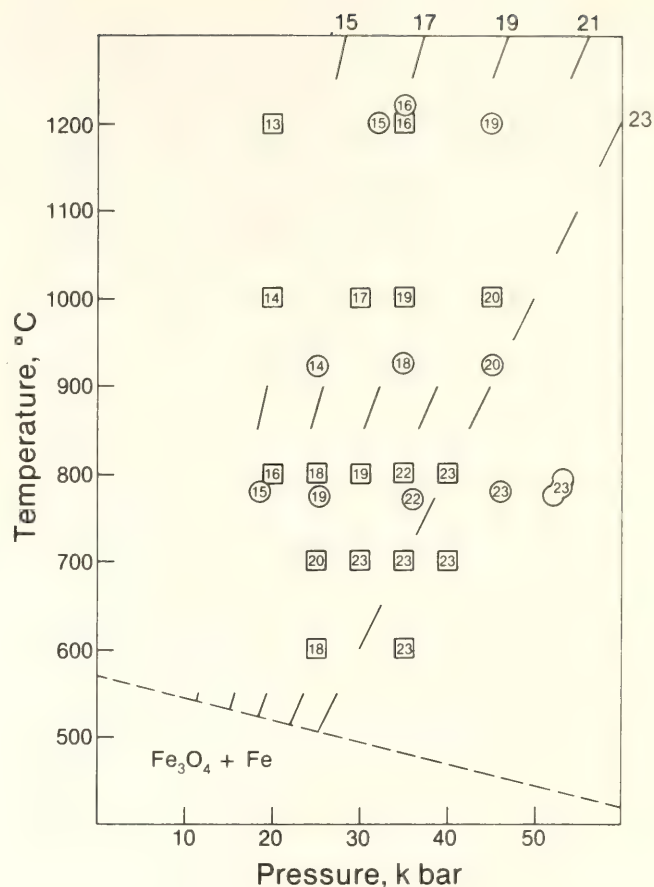


Fig. 114. Variation of the cell parameter  $a_0$  of wüstite with pressure and temperature. The digits in squares (circles: data after Katsura *et al.*, 1967) are 1/100 and 1/1000 of an angstrom; added to 4.3 Å, they give the  $a_0$  value. The values are accurate to  $\pm 0.001$  Å.

ing  $\text{CuK}\alpha$  radiation and silicon as an internal standard. The cell parameters of wüstite are functions of both temperature and pressure but increase linearly with pressure (Fig. 114) and approach a constant value of 4.323 Å, identical with the value reported by Katsura *et al.* (1967). Their data near 920°C, however, are inconsistent with the results described below.

The Mössbauer spectrum of wüstite of maximum cell size consists visually of a single but asymmetric peak. This envelope thus may be composed of a superposition of several peaks that are responsible for its large half-width (about 0.8 mm/sec) and non-Lorentzian shape. If the wüstite were exactly stoichiometric, only a single peak of  $\text{Fe}^{2+}$  would be expected (0.40 mm/sec, Greenwood and

Howe, 1972). The large line width (0.78 mm/sec) and misfit parameter ( $0.93 \pm 0.04\%$ , Ruby, 1973), as well as the existence of wüstites with much narrower line width of a single line, disprove the existence of undistorted sites only for Fe. If the wüstite were nonstoichiometric, the introduction of both vacancies and  $\text{Fe}^{3+}$  atoms into the structure would distort the environment of  $\text{Fe}^{2+}$  atoms sufficiently to result in the observed pattern. The intensity of the quadrupole-split doublet relative to the  $\text{Fe}^{2+}$  singlet is a function of defect concentration and the type of defect clustering (see Greenwood and Howe, 1972, fig. 5). The simplest structural model for which  $\text{Fe}^{2+}$  is assumed to be associated with a defect requires a four-line fit to the observed data (Fig. 115;  $\text{Fe}^{3+}_{\text{unsplit}}$ ,  $\text{Fe}^{2+}_{\text{split}}$ ,  $\text{Fe}^{2+}_{\text{unsplit}}$ ). The composition of the wüstites could be determined theoretically from the ratio of areas of the unsplit vs. the split  $\text{Fe}^{2+}$  absorption and from the area of the  $\text{Fe}^{3+}$  line relative to the total absorption. The area ratio of the two different  $\text{Fe}^{2+}$  absorptions gives a compositional range from 0.982 (random defects) to 0.950 (four-fold cluster model) Fe per formula unit (Greenwood and Howe, 1972, fig. 5).

Wet chemical analysis (Maxwell, 1968) of the same sample led to the formula  $\text{Fe}_{0.97}\text{O}$  with a standard deviation of 0.01. Thus it appears that the wüstites prepared at high pressure in the presence of metallic iron are more iron rich than those prepared at atmospheric pressure, but at least up to 40 kbar the phases do not become stoichiometric. These wüstites are less stoichiometric than those prepared metastably by disproportionation of quenched samples of  $\text{Fe}_{1-x}\text{O}$  (Greenwood and Howe, 1972). The constant lattice parameter of wüstite observed at pressures above 35 kbar at  $750^\circ\text{C}$  (4.323 Å) suggests that at higher pressures there will be only a slight increase in iron content. At significantly higher pressures (above 100 kbar) the iron content decreases (Liu, 1976), as

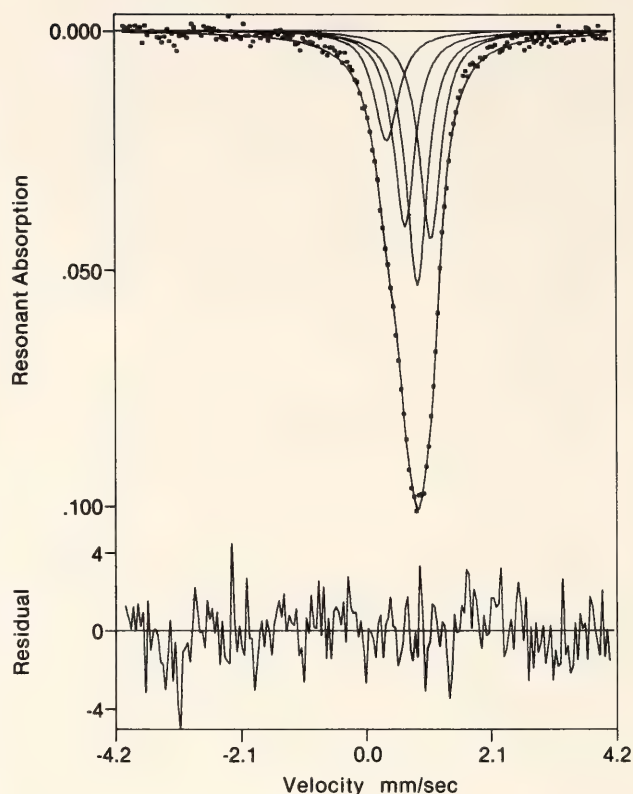


Fig. 115. Mössbauer spectrum of wüstite prepared in the presence of metallic iron at 40 kbar,  $750^\circ\text{C}$ . The envelope is an unconstrained least-squares fit to the data, for which four Lorentzians are assumed (12 line variables, 1 background variable). The individual lines (from left to right) are assigned to  $\text{Fe}^{3+}$ , quadrupole-split  $\text{Fe}^{2+}$ , low-velocity component,  $\text{Fe}^{2+}$  unsplit, and quadrupole-split  $\text{Fe}^{2+}$ , high-velocity component.

predicted by Mao (*Year Book* 73, pp. 510–518). It is therefore considered unlikely that stable wüstite becomes stoichiometric under any conditions of pressure and temperature.

#### MELTING OF $\text{CoSiO}_3$ AND ITS RELATIONSHIP TO THE STABILITY OF PYROXENOIDS

*B. Simons*

The polymorphic change from pyroxene to pyroxenoid structures is commonly observed in metasilicates with divalent cations. The molar volumes of these structures decrease with increasing periodicity (the repeat number of  $\text{SiO}_4$  tetrahedra in a chain), assuming the pyroxene structure has infinite periodic-



ity. Structures with higher periodicity, therefore, are favored by increased pressure, and the pyroxene structure is the most stable single-chain structure under high pressure (Simons, 1978). For all transformations observed so far the slope of the  $P$ - $T$  curve is positive; thus, the structures with lower periodicity are favored by increased temperature. In general, the sequence of possible transformations is correlated with the average size of the divalent cations. In certain cases, however, the influences of electronegativity and crystal-field effects have to be taken into account.

The pyroxenoid with the highest periodicity observed so far is ferrosilite III ("Neunereinfachkette"), where the average divalent cation size—in this case the ionic radius of  $\text{Fe}^{2+}$ —approaches the lowest value for pyroxenoids. All metasilicates with cations of lower radii studied thus far have pyroxene structures. The composition  $\text{CoSiO}_3$  has been studied previously only in its subsolidus region (Akimoto *et al.*, 1965), and thus it was important to determine the melting relations of the  $\text{CoSiO}_3$  metasilicate to observe whether  $\text{CoSiO}_3$  might have a pyroxenoid structure under temperature-pressure conditions qualitatively similar to those where ferrosilite III is stable. Because  $\text{Co}^{2+}$  is chemically similar to  $\text{Fe}^{2+}$ , the electronegativities and crystal-field effects are comparable; however, the  $\text{Fe}^{2+}$  ion is 5% larger than  $\text{Co}^{2+}$  (Shannon and Prewitt, 1969).

The bulk composition  $\text{CoSiO}_3$  was prepared by homogenizing equimolar mixtures of  $\text{Co}_3\text{O}_4$  (Fisher C-382),  $\text{Co}$  (Fisher C-363), and  $\text{SiO}_2$  (prepared by dehydrating  $\text{H}_2\text{SiO}_3 \cdot n\text{H}_2\text{O}$ , Fisher A-288) under acetone for 0.5 hr. The dried sample was sealed in a 1/2-inch Pyrex-sleeve graphite furnace assembly and run in a solid-media, high-pressure apparatus (Boyd and England, 1960) by the piston-in technique. Temperature was recorded by a Pt10Rh90 thermocouple, and the run duration varied between 1 and 4 hr. No corrections of the calcu-

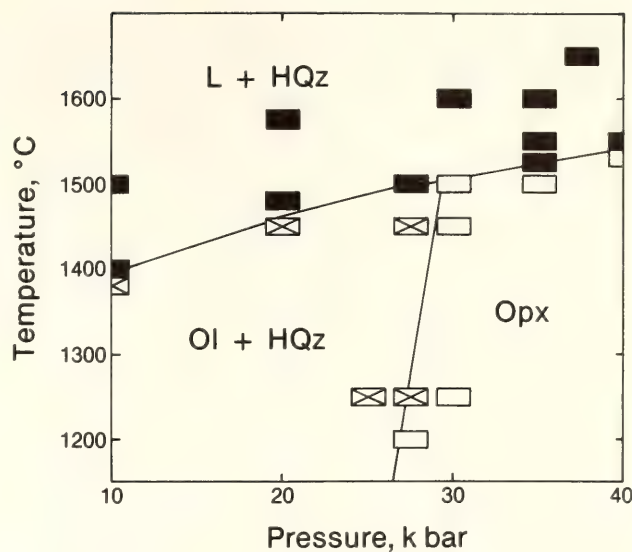


Fig. 116. Liquidus diagram of  $\text{CoSiO}_3$  composition. Size of symbol represents estimated error in pressure and temperature. Open symbols, orthopyroxene (Opx); closed symbols, liquid (L); crossed symbols, olivine +  $\text{SiO}_2$  = OI + high quartz (HQz).

lated pressure for friction losses or for the pressure effect on the electromotive force of the thermocouple have been made.

The boundary of the reaction olivine +  $\text{SiO}_2 \rightleftharpoons$  orthopyroxene (Fig. 116) is higher than originally reported by Akimoto *et al.* (1965). Akimoto *et al.* (1977) later suggested that previously reported pressure values were underestimated, possibly because of frictional losses. Orthopyroxene is stable in the entire temperature-pressure range studied here, and no pyroxenoid phase for the composition  $\text{CoSiO}_3$  was observed. Consequently, a limit for the stability of pyroxenoid structures was found to be between the radii for  $\text{Fe}^{2+}$  and  $\text{Co}^{2+}$ .

#### THE B1/B2 TRANSITION IN $\text{CaO}$ FROM SHOCK-WAVE AND DIAMOND-CELL EXPERIMENTS

*R. Jeanloz,\* T. J. Ahrens,\* P. M. Bell, and H. K. Mao*

There is considerable interest in B1/B2 transitions in theoretical studies of

\* California Institute of Technology, Seismological Laboratory, Pasadena, California, 91125.

oxide structures (Tosi and Arai, 1966; Cohen and Gordon, 1976; Demarest *et al.*, 1977), and interest also in their possible occurrence in the earth's lower mantle. Volume and crystal-structure data obtained by both dynamic shock-wave and static diamond-cell techniques indicate that CaO transforms from the B1 (NaCl-type) to the B2 (CsCl-type) structure at 0.6–0.7 Mbar with a volume decrease of 11%. The shock-wave Hugoniot data on CaO agree closely with ultrasonic measurements (Son and Bartels, 1972; Chang and Graham, 1977) on the B1 phase and also agree satisfactorily with equations of state de-

rived from *ab initio* calculations. The implication of the discovery of this B1/B2 transition is that calcium components may be included in the earth's lower mantle, consistent with theories of inhomogeneous accretion. These data are the first documentation of the B2 structure in an oxide compound that may be abundant in the earth's mantle.

### Shock-Wave Data

The shock-wave experimental data (Fig. 117) are for the shock Hugoniot not reduced to the isotherm. Initial density and elastic parameters (Table

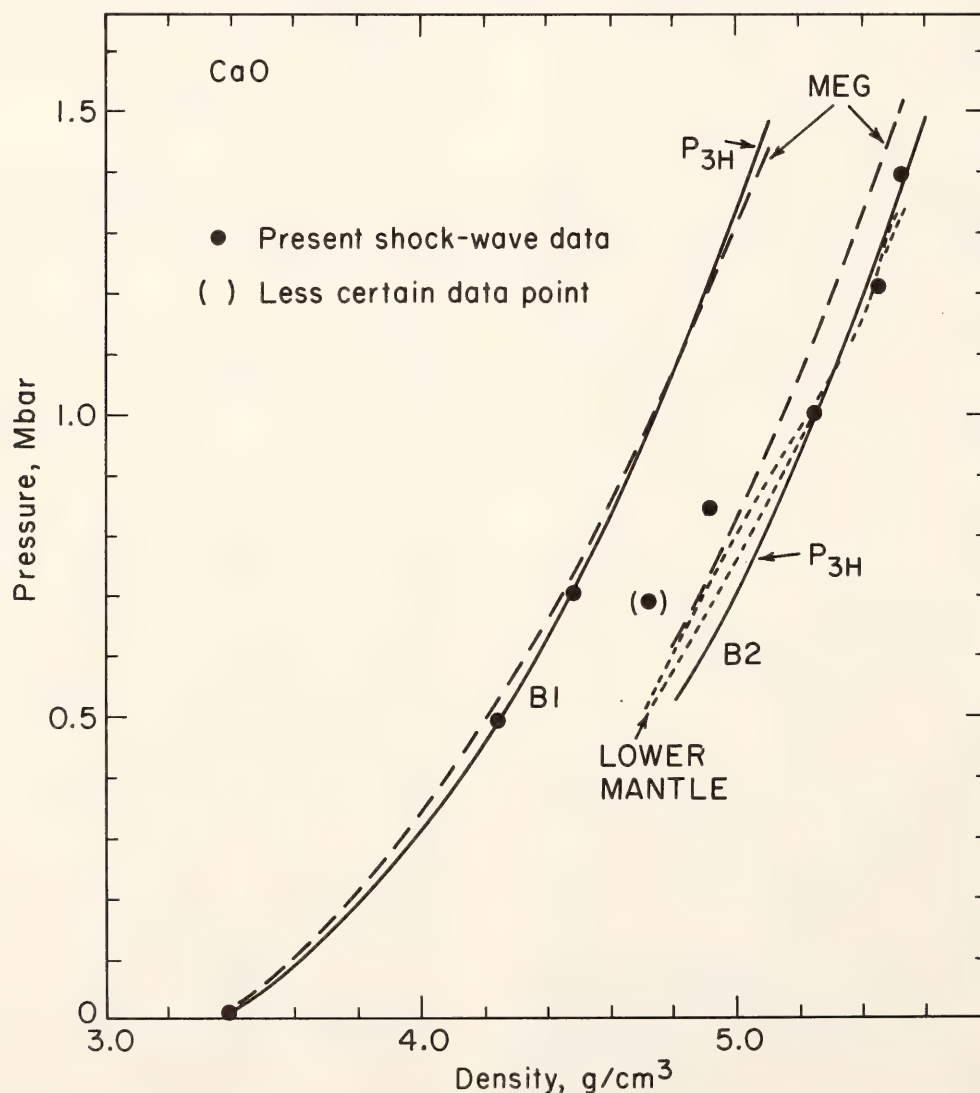


Fig. 117. New shock-wave Hugoniot data for CaO plotted with theoretical Hugoniot curves based on finite strain theory ( $P_{3H}$ ) and *ab initio* MEG calculations. Also shown are plots of two seismological models for the earth's lower mantle (Dziewonski *et al.*, 1975; Hart *et al.*, 1977).



TABLE 38. Parameters\* for CaO Used in Theoretical Hugoniot Calculations

<i>B1 phase</i> (ultrasonic data of Chang and Graham, 1977)	
$\rho_0 = 3.345 \text{ g/cm}^3$ , $K_{0s} = 1.125 \text{ Mbar}$ , $K'_0 = 4.79$ , $\gamma_0 = 1.505$ ( $\gamma/V = \text{constant}$ )	
<i>B2 phase</i> (estimated; see text)	
$\rho_0 = 3.76 \text{ g/cm}^3$ , $K_{0s} = 1.14 \text{ Mbar}$ , $K'_0 = 5$ , $E_{tr} = 65 \text{ KJ/mol}$ , $\gamma_0 = 1.51$ ( $\gamma/V = \text{constant}$ )	

\*  $\rho_0$ , density at 1 atm;  $K_{0s}$ , isentropic bulk modulus;  $K'_0 = (\partial K / \partial P)_{P=0}$ ;  $\gamma_0$ , Gruneissen parameter;  $V$ , volume;  $E_{tr}$ , enthalpy of transition.

38) determined from ultrasonic measurements by Chang and Graham (1977) for the 1-atm B1 phase of CaO were used to construct a theoretical Hugoniot curve based on third-order finite strain theory (Davies and Gaffney, 1973). This theoretical Hugoniot curve is an excellent fit to the shock-wave data to 700 kbar. A separate curve, derived in the same way but using estimates of the elastic parameters for the B2 phase based on elasticity relationships (Table 38), is a reasonable fit to the points in the pressure range approximately 1–1.4 Mbar (both curves are labeled  $P_{3H}$  in Fig. 117). Points falling between the two curves probably represent the B1-B2, two-phase assemblage that extends over a range in pressure owing either to a sluggish reaction rate, or to the temperature dependence of the reaction rate.

Theoretical Hugoniot curves (Fig. 117) were obtained from *ab initio* calculations for the B1 and B2 phases [after the Modified Electron Gas (MEG) theory of Cohen and Gordon (1976)]. In these calculations, the estimated thermal properties were used, as in the  $P_{3H}$  model, and the theoretical bulk moduli were corrected according to the methods of Hite and Kearney (1967) and Bartels and Vetter (1972). The resulting MEG curves are close to the experimental points and to the  $P_{3H}$  curves. The combined agreement of the experimental shock-wave data with the theoretical curves fitted to properties of the two phases suggests a phase transition at 0.6–0.7 Mbar.

### Static Data

Experiments with CaO were conducted between 0.60 and 0.67 Mbar and measured by the ruby fluorescence technique (Mao and Bell, *Year Book* 77, p. 910) in the megabar-pressure cell (MBC-Y; see Mao and Bell, *Year Book* 77, pp. 904–908). X-ray diffraction data on the pressurized sample (Table 39) indicated the presence of both the known B1 phase and the B2 phase predicted from the shock-wave results. The mixture is indicative of a small two-phase region caused by uniaxial stresses on the sample (Mao and Bell, *Year Book* 77, pp. 842–848).

The static experiments indicate that the transition takes place at 0.60 Mbar on the ruby-fluorescence pressure scale (Mao and Bell, *Year Book* 77, p. 910).

TABLE 39. Static Results on CaO

Pressure,* Mbar	Molar Volume,† $\text{cm}^3$		Relative Intensity,† $I(\text{B1})/I(\text{B2})$
	B1 Phase	B2 Phase	
0.605	12.44	11.10	1.7
0.610	12.36	11.06	0.7
0.635	12.26	10.90	0.5
0.635	12.28	10.87	0.5
0.670	12.18	10.91	0.2

\* Precision of  $\pm 0.02$  Mbar; calibration is within 6%.

† Based on 200 and 110 x-ray lines, respectively, for B1 and B2 patterns; estimated precision of molar volume is about  $\pm 0.7\%$ . Relative intensities of x-ray lines based on visual estimates.

and at room temperature (295°K). The shock-wave data indicate a slightly higher transition pressure, 0.63–0.70 Mbar at approximately 1350°K. A volume change of 11% ( $\pm 1\%$ ) was found for the transition in both sets of experiments. This change is in agreement with the data on B1/B2 transitions in halides (Jamieson, 1977; Demarest *et al.*, 1977) and provides additional support for applying such relationships to oxides.

Similar B1/B2 transitions possibly exist in (Mg,Fe)O solid solutions, and such phases may be present in the lower mantle. From simple, ionic-radius concepts (Wells, 1975), the B1 monoxides might be expected to transform at successively higher pressures in the following order (ratios of cation-anion radii in parentheses): BaO (0.97), SrO (0.83), CaO (0.71), MgO (0.51). Barium oxide is known to transform from a B1- to a B2-related structure at about 0.14 Mbar (Liu, 1971; Liu and Bassett, 1972), and hence SrO is expected to transform at about 0.45 ( $\pm 0.1$ ) Mbar, and MgO above 1.0–1.1 Mbar. These predictions are made on the basis of experimental results on CaO combined with crystal-chemical concepts. No transitions have been found in SrO to 0.34 Mbar and MgO to 0.95 Mbar or higher. The only other oxide for which a B1/B2 transition is known is EuO, but the transition occurs *after* EuO undergoes an electronic transition (Jayaraman, 1972). Hence, CaO appears to be the only oxide for which an uncomplicated B1/B2 transition has been found to date. Theoretical characterization of B1/B2 transitions is still imperfect. The data disagree with the B1/B2 transition pressures expected either from *ab initio* calculations (1.2–2.4 Mbar) or from a semi-empirical, lattice-instability model in which a transition pressure between 0.28 and 0.40 Mbar is predicted (Cohen and Gordon, 1976).

There is a possibility that the B2 form of CaO may dissolve in FeO within the earth's lower mantle, at least below a

depth of about 1550 km (corresponding to 0.65 Mbar). The seismologically derived pressure-density relation for the lower mantle (Fig. 117) specifies densities that are within 1–2% of the Hugoniot data at a given pressure for the B2 phase of CaO. The reduction of this Hugoniot to estimated mantle temperature results in only a small correction that slightly improves the comparison (Stacey, 1977). Although calcium might occur in a complex oxide or silicate mineral (perhaps with a perovskite structure), rather than in the simple-oxide mixture often used in modeling the properties of the lower mantle (Birch, 1952), the present results demonstrate that calcium's coordination with oxygen is at least eight-fold (as in the B2 structure) in the lower mantle.

#### OBSERVATIONS OF THE FREEZING POINT AND DENSITY OF HYDROGEN IN THE PRESSURE RANGE FROM 1 BAR TO 0.65 MBAR AT 25°C

*H. K. Mao and P. M. Bell*

Hydrogen as a solid, in the molecular and metallic states, is postulated to be a major constituent of Jupiter and the outer planets, and some form of hydrogen conceivably could be a constituent of the earth's core. Theoretical studies of solid hydrogen at 0°K have been used to predict its density-pressure curve and the nature of conversion to the metallic state (Ross and Shishkevish, 1977). As a result of the predicted high Debye temperature for hydrogen in the metallic state, metallic hydrogen may be an elevated temperature (in this instance 25°C is considered "elevated") superconductor, a possibility that could have significant implications for models of planetary interiors and for practical uses of metallic hydrogen as an efficient conductor of electricity.

Many experimental difficulties had to be overcome before observations could be made to test this hypothesis. First, there is the problem of containing a sufficient volume of hydrogen that must ulti-



mately be brought to what for hydrogen is a relatively high density. Then it must be possible to exert on the hydrogen enormous pressures that are accurately known. Finally, it must be possible to observe the pressure effects directly or indirectly. In the present study, experiments were designed to seal liquified hydrogen into a diamond-anvil, high-pressure cell at cryogenic temperatures. Then the cell was removed from the assembly and brought to room temperature. A minimal sealing pressure was sufficient to prohibit escape of the compressed gas. At room temperature, pressure on the hydrogen could then be further increased, and its effects could be observed.

The diamond-anvil, high-pressure cell was a logical choice for these experiments because of the relative ease with which gases, liquids, and solid phases are contained and because of the extremely high and accurately calibrated pressure range that can be sustained. The experimental concept was tested successfully with liquid nitrogen and liquid helium.

The observations reported here were reproduced numerous times per run in four separate experimental assemblies.

Small ruby crystals (10–20  $\mu\text{m}$  in diameter) that had been placed in the sample chamber were used for pressure measurement with reference to the calibrated pressure shift of the fluorescent  $R_1$  line (Mao *et al.*, 1978). The hydrogen sample was viewed through one of the diamond windows by microscope. At approximately 57 kbar and 25°C, hydrogen was observed to solidify to a mass of transparent crystals.

Figure 118 is a photomicrograph of a closed-circuit television image of solid hydrogen crystals at the freezing point in the cell. A minor amount of liquid is present at the junctions and boundaries at equilibrium between the hexagonal-shaped crystals, but at 25°C and 57 kbar solidification was rapid and reversible. As the pressure was increased slightly, individual crystals rapidly merged into a single, clear, transparent solid with no visible grain boundaries.

As the pressure was increased above

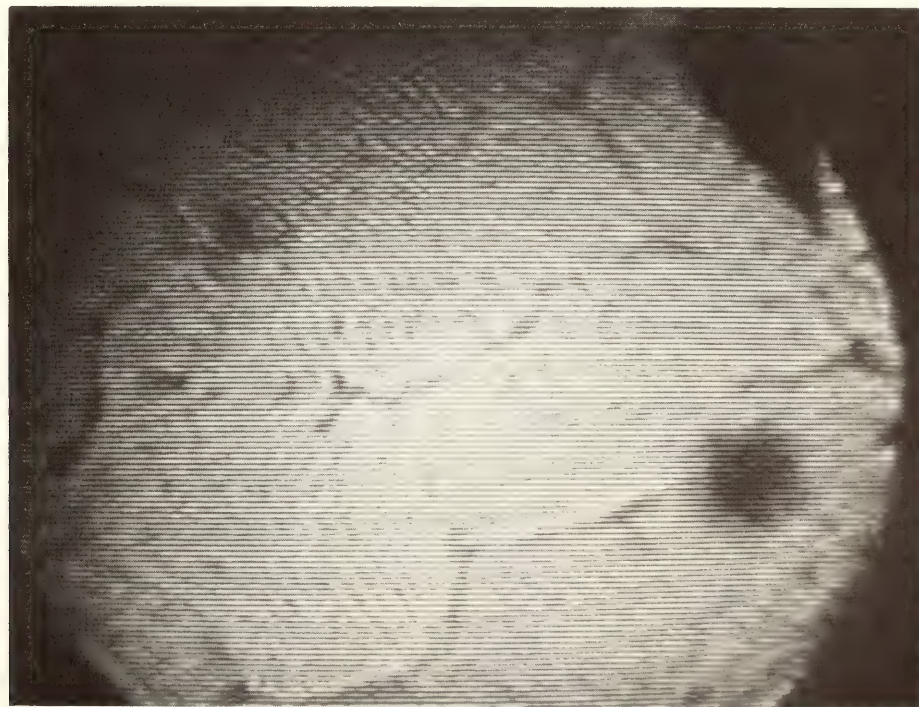


Fig. 118. Closed-circuit television image of solid hydrogen at 57 kbar, 25°C. Field of view, 300  $\mu\text{m}$ ; dark object in upper right-hand corner is ruby crystal; defocused objects are dust grains, not in contact with hydrogen.

57 kbar, the high-pressure phase became compressed and its refractive index increased. The visible boundary line between ruby and high-pressure hydrogen crystals disappeared at 360 kbar; thus, the refractive indices of the two materials had become the same. Accordingly, the results of calculations indicate that the density of the high-pressure hydrogen crystals had increased. A calculation of the specific gravity based on estimates of the average refractive index of this high-pressure phase gives 0.6–0.7 at 360 kbar. Between 360 and 650 kbar, no further changes were noted, except a continuous increase in the index of refraction of the crystalline hydrogen phase relative to ruby.

The solidification is not observed to have the type of hysteresis associated with order-disorder transformations due to varying proportions of the ortho- and para-spin states of molecular hydrogen. Nevertheless, it is probable that both liquid and solid phases of hydrogen contain a mixture of states, possibly disordered.

The solidification point (57 kbar) observed at room temperature in this study is very close to that predicted (Liebenberg *et al.*, 1978). The specific-gravity value of 0.6–0.7 for the high-pressure phase at 360 kbar agrees within the uncertainty with the values for generalized models of solid hydrogen calculated from theory by Liberman (1971) and Ross and Shishkevish (1977).

There is no direct evidence in the present experiments on which to base a choice of the physical process by which hydrogen will become (1) conducting in the molecular state or (2) a superconducting metal.

The liquid and the new high-pressure phase of hydrogen can be further characterized by measurement of the Raman spectra (see Sharma, Mao, and Bell, this Report), visible and near-infrared spectra, and electrical and magnetic properties. A separate set of experiments will be required for the generation of pressures on solid hydrogen above 650 kbar.

## HIGH-PRESSURE CRYSTALLOGRAPHY AND SPECTROSCOPY

### STUDIES IN HIGH-PRESSURE CRYSTALLOGRAPHY

*R. M. Hazen and L. W. Finger*

Temperature, pressure, and composition are the three most important variables in modeling the solid earth. An understanding of the variation of atomic arrangements with these three criteria provides important information regarding the nature and magnitudes of interatomic forces, as well as the origins of many physical properties including density, molar volume, compressibility, and thermal expansivity. Numerous crystal structures have been determined at elevated temperature, but fewer than 20

high-pressure crystallographic studies of minerals have been published (Finger and Hazen, 1979). An emphasis has been placed in current studies, therefore, on the variation of structure as a function of pressure.

Approximately 15 minerals and mineral-like compounds have been investigated at high pressure during the past year using a miniature, diamond-anvil pressure cell (Merrill and Bassett, 1974). This small, versatile cell has been modified by revision of the guide-pin arrangement for improved alignment. The two guide pins, originally 1/16 inch in diameter and 1/2 inch long, are replaced by three pins 1/8 inch in diameter and



5/8 inch long. This simple change has increased the operating range of the cell by at least 15 kbar, to a maximum pressure of 75 kbar.

Data on the compression of bonds, obtained from x-ray experiments on single crystals in the diamond cell, may be used to develop empirical models of the variation of crystal structures with pressure, as well as to constrain formulations of the repulsive potential of bonding. The high-pressure behavior of dense oxide structures is of special interest to geophysicists because atomic arrangements in these compounds may be similar to those deep within the earth. High-pressure studies of  $RO_2$  and  $R_2O_3$  oxides have therefore been undertaken.

Because silicon dioxide transforms to stishovite, a rutile isomorph, under mantle conditions of high pressure and temperature, compounds with the rutile structure are important materials for high-pressure study. Compressibilities and high-pressure crystal structures of rutile-type  $TiO_2$  (USNM 136751),  $SnO_2$  (USNM 136749),  $GeO_2$  (J. Mammone), and  $RuO_2$  (IBM Watson Research Laboratory) were determined on synthetic single crystals. All of these tetragonal compounds exhibit highly anisotropic compression, the  $a$  axis being more than twice as compressible as the  $c$  axis. The

only variable atomic positional parameter,  $x$  of oxygen, is invariant with pressure for all four compounds. Compression of  $R$ -O bonds within the (001) plane is greater, therefore, than compression of  $R$ -O bonds with a  $c$ -axis component. Bulk moduli of the four rutile-type oxides, if a Birch-Murnaghan second-order equation of state (EOS) with  $K' = 4$  is assumed, are 2.22(2), 2.24(2), 2.65(5), and 2.70(6) Mbar, respectively, for  $TiO_2$ ,  $SnO_2$ ,  $GeO_2$ , and  $RuO_2$ .

Uraninite,  $UO_2$ , has the cubic fluorite-type structure in which each U atom is surrounded by a cube of eight oxygen atoms. All atomic positional parameters are fixed so a single variable, the unit-cell edge, defines the structure. Pressure-volume data for  $UO_2$  thus may be used to determine the compressibility of U-O bonds. Unit-cell parameters of synthetic uraninite (USNM 136404), with 99.99+ %  $^{238}U$ , were determined at room pressure ( $a = 5.4687 \text{ \AA}$ ) and at several pressures to 50 kbar. Both film and diffractometer single-crystal techniques were used to measure unit-cell parameters, which are recorded in Table 40. These data yield EOS parameters  $K_0 = 2.30(8)$  Mbar and  $K' = 3.7(3.6)$  using either Murnaghan or Birch-Murnaghan second-order EOS. This bulk modulus is slightly larger than the 2.13 Mbar value

TABLE 40. Lattice Parameters of  $UO_2$

Pressure, kbar	$a$ , Å	$a/a_0$	Method*	Volume, Å <sup>3</sup>
0.001	5.4687(3)	1.0000	F + D	163.55(2)
3.4(5)	5.466(2)	0.9995	F	163.3(1)
10.9(5)	5.4600(3)	0.9984	D	162.77(2)
12.0(5)	5.459(2)	0.9983	F	162.68(10)
27.3(5)	5.448(2)	0.9962	F	161.7(1)
32.1(5)	5.444(2)	0.9955	F	161.34(10)
37.4(5)	5.4406(2)	0.9949	D	161.04(2)
38.4(5)	5.438(2)	0.9944	F	160.8(1)
46.2(5)	5.434(2)	0.9937	F	160.46(10)
49.1(5)	5.4315(2)	0.9932	D	160.24(2)
50.7(5)	5.430(2)	0.9930	F	160.1(1)

\* F, film; D, diffractometer.

reported by Wachtman *et al.* (1965), although the two bulk moduli probably agree within errors of the earlier work.

Sesquioxides of aluminum, iron, chromium, and vanadium may occur in the dense corundum structure. High-pressure crystal structures and compressibilities of hematite ( $\text{Fe}_2\text{O}_3$ , from G. P. Espinosa, North American Rockwell Corp.), eskolaite ( $\text{Cr}_2\text{O}_3$ , USNM 739S), and karelianite ( $\text{V}_2\text{O}_3$ , USNM 137007), were determined from data on synthetic single crystals. The high-pressure behavior of  $\text{Cr}_2\text{O}_3$  and  $\text{Fe}_2\text{O}_3$  is similar to that reported by Finger and Hazen (1978) for corundum, in which the structure compresses in a relatively uniform fashion. The structure of  $\text{V}_2\text{O}_3$ , on the other hand, compresses nonuniformly; the axial ratio  $c/a$  increases, and the distortion of the  $\text{VO}_6$  octahedron also changes with pressure.

In addition to the  $\text{RO}_2$  and  $\text{R}_2\text{O}_3$  oxides described above, high-pressure crystal structures have recently been completed on zircon (Hazen and Finger, 1979a) and on nickel and iron silicate spinels (Finger *et al.*, 1979). Linear compressibilities of sodium nitrite and sodium nitrate (Hazen and Finger, 1979b) and two analcites (Hazen and Finger, 1979c) have also been determined so that reversible phase transitions and sodium-site compressibilities in these materials could be documented. These data, combined with previous high-pressure structural information, have led to the recognition of general trends in the high-pressure response of minerals.

A major objective of this research is the development of empirical models that lead to the prediction and explanation of crystal response to high pressure. An empirical polyhedral bulk modulus-volume relationship has been developed that successfully models bond compression in a wide range of compounds including oxides, silicates, halides, sulfides, phosphides, and carbides (Hazen and Finger, 1979d), as illustrated in Fig. 119. In the equation shown in that figure,  $K_0$

is the polyhedral bulk modulus;  $\langle d \rangle$  is the mean cation-anion distance;  $z_c$  and  $z_a$ , respectively, are the formal charge of the cation and anion; and  $S^2$  is an empirical ionicity defined as 0.5 for oxides and adjusted for other types of anions. The equation fits more than 100 compounds for which bond compressibilities are known in more than 20 different structure types. It is significant that cation-anion bond compression is independent of structure in most cases. The only known deviation is for the CsCl structure (open circles) where the second nearest neighbor distance is similar to the cation-anion distance.

This simple relationship can be used to predict cation-anion compression, but polyhedral linkages are also important in bulk compression. In structures with corner-linked polyhedra such as quartz, perovskite, and feldspar, bending of cation-anion-cation bonds contributes to compression. In structures with extensive edge- and face-sharing of polyhedra, bulk moduli more closely approximate moduli of component polyhedra. The empirical compression relationships will be tested on highly constrained structures (garnets and spinels) in which the number of polyhedra exactly equals the number of structural variables. The variation of these structures with pressure should be predicted completely by the bulk modulus-volume relationship noted above.

The systematic trends of a common group of reversible phase transitions called "polyhedral tilt transitions" (Hazen and Finger, 1979b) constitute another general result from high-pressure structural studies. These transformations occur in structures with corner-linked polyhedra that form cavities or channels, which may contain large cations. In many such compounds including feldspars, zeolites, quartz, and perovskite, the size of the large site may control the symmetry of the corner-linked array. A small cation may result in a "collapsed" or "tilted" framework of lower sym-



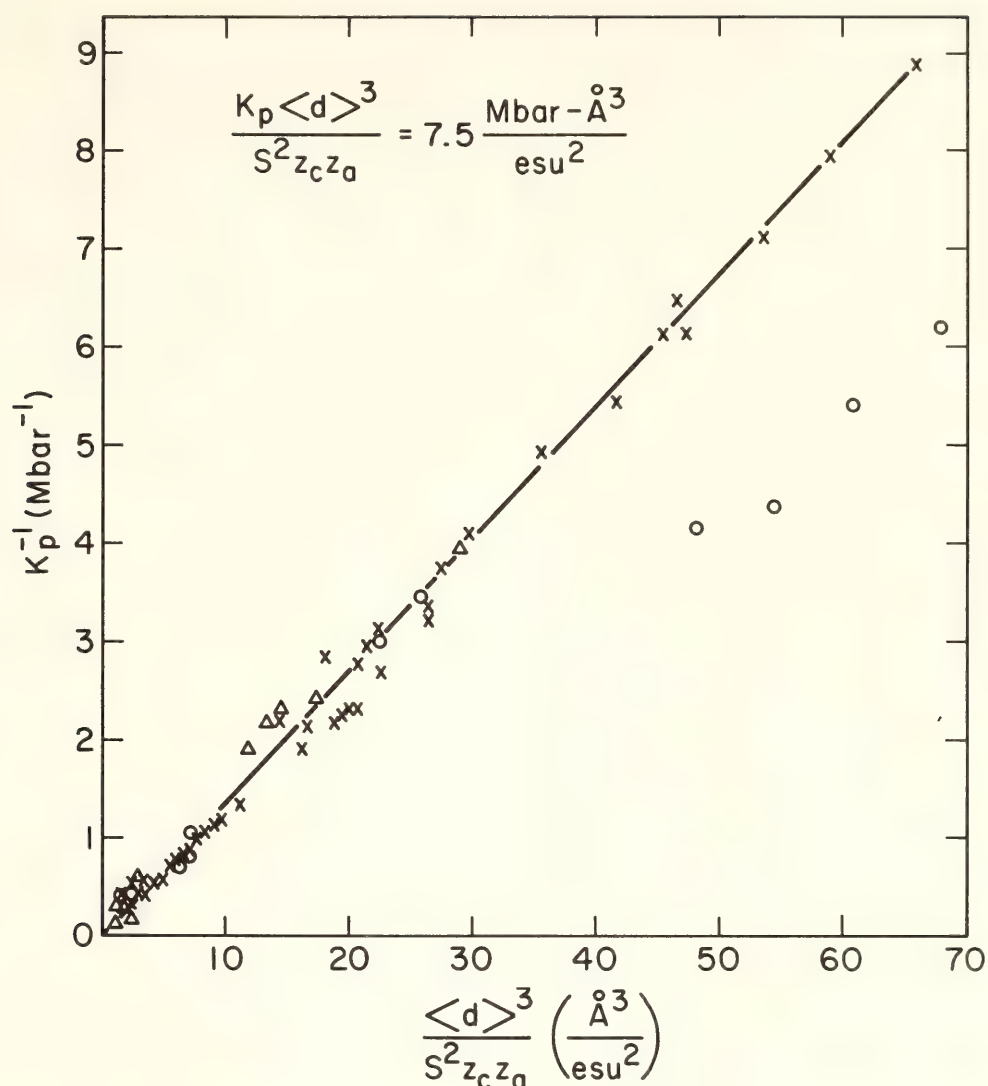


Fig. 119. The bulk modulus-volume relationship for cation-anion bonds in oxides, silicates, halides, chalcogenides, carbides, phosphides, and other compounds.

metry, whereas a larger cation may support an "untilted" form of higher symmetry. Changes in temperature and pressure may also induce transitions by changing the relative sizes of the large site and framework. On the basis of this geometrical model of polyhedral tilt transitions, the  $P$ - $T$ - $X$  transition surface of alkali feldspars has been predicted (Hazen, 1977).

Reconstructive transformations may also be related to geometrical aspects of a crystal structure. Hazen and Finger (1978) demonstrated that many transformations involving a change from tetrahedrally to octahedrally coordinated silicon occur at high pressure when the mean Si-O distance compresses to ap-

proximately 1.59 Å on the basis of known room-pressure crystal structures, Si-O bond compressibilities, and pressures of  $^{\text{IV}}\text{Si} \rightarrow ^{\text{VI}}\text{Si}$  transformations. The lower two thirds of the mantle transition zone of high-density gradient (500–900 km) corresponds to the predicted range of this transformation. The 10% density increase of this zone at zero pressure is attributed primarily to the change in silicon coordination. All silicon below 900 km is predicted to be in octahedral or greater coordination. The concept of polyhedral stability fields, due to minimum or maximum size limits at which a given cation polyhedron is stable, may prove useful in predicting possible high-pressure and high-temperature phases.

# RAMAN STUDY OF $\text{TiO}_2$ UNDER HIGH PRESSURES AT ROOM TEMPERATURE

*J. F. Mammone\* and S. K. Sharma*

Interest in the high-pressure behavior of rutile-type compounds has been stimulated by the synthesis of the rutile form of  $\text{SiO}_2$  (Stishov and Popva, 1961) and by Birch's (1952) hypothesis that the lower mantle consists mainly of dense oxide phases. Jamieson (1977) studied metal difluorides to determine available structures for  $\text{SiO}_2$  at high pressures. Others have observed high-pressure transformations in the dioxides— $\text{PbO}_2$  (Syono and Akimoto, 1968),  $\text{SnO}_2$  (Liu, 1974),  $\text{MnO}_2$  (Liu, 1976c), and  $\text{TiO}_2$  (Bendeliani *et al.*, 1966; Liu, 1978)—which may provide better models for  $\text{SiO}_2$  in the mantle. The very high pressure experiments done on  $\text{SiO}_2$  itself have proved inconclusive, so far. In a shock-wave experiment in the pressure range 700–900 kbar (German *et al.*, 1975),  $\text{SiO}_2$  was recovered in the  $\alpha$ - $\text{PbO}_2$  structure; however, Liu *et al.* (1978) have synthesized a high-pressure form of  $\text{SiO}_2$  that was indexed as a modified niccolite structure. High-pressure transformations of  $\text{TiO}_2$  may also be useful as an indicator of meteorite impact on the earth's surface (McQueen *et al.*, 1967). The behavior of rutile under hydrostatic pressures was studied, therefore, by laser Raman spectroscopy.

## Experimental

$\text{TiO}_2$  crystals (tetragonal, space group  $D_{4h}^{14}$ ;  $Z = 2$ ) were supplied by the U.S. National Museum (No. 136751). Samples were loaded in a steel gasket with a 4:1 mixture of methanol and ethanol as the pressure-transmitting medium (Piermarini *et al.*, 1973) and compressed in a diamond-window, high-pressure cell designed by Mao and Bell (*Year Book* 77,

pp. 904–908). Pressures were calculated by measuring the shift in the ruby  $R_1$  fluorescence line (Mao *et al.*, 1978). Diamond anvils, cut from low-fluorescent, type-IIb diamonds selected according to the criteria suggested by Adams and Sharma (1977), were used in the present work. Raman spectra were obtained with an argon laser using 448.0-nm excitation. The spectra were recorded at room temperature with a J-Y double monochromator (HG-2S) utilizing photon-counting detection (Sharma, *Year-Book* 77, pp. 902–904). Scattered radiation was collected in the forward direction using a  $90^\circ$  off-axis ellipsoidal mirror (Adams *et al.*, 1977; Sharma, this Report).

## Results and Discussion

The Raman spectra of rutile  $\text{TiO}_2$  at several pressures are shown in Fig. 120. Frequencies of observed Raman bands and their spectral characteristics in the spectra of  $\text{TiO}_2$  at various pressures are summarized in Table 41. The pressure dependence of the various Raman active phonons in rutile  $\text{TiO}_2$  is depicted in Fig. 121.

The results on  $\text{TiO}_2$  at 1 atm (Table 41) are in agreement with those of Porto *et al.* (1967). At 1 atm,  $\text{TiO}_2$  gives an anomalously strong, broad band at about  $235\text{ cm}^{-1}$  (Fig. 120, Table 41). The band is so strong that it was first assigned to a fundamental process (Krishnan and Russell, 1966), but after examination of the scattering tensor, Porto *et al.* (1967) proposed that it was a second-order process exhibiting considerable structure. On the basis of Raman and neutron diffraction experiments, Hara and Nicol (1979) proposed that the  $\text{TiO}_2$  lattice is disordered and that this strong band is disorder-induced. The intensity of this band decreases with increasing pressure and could indicate increased ordering.

The appearance of a number of new sharp and strong Raman lines in the spectrum of  $\text{TiO}_2$  at pressures greater

\* Work carried out under a cooperative predoctoral fellowship program between the Geophysical Laboratory and the University of California, Los Angeles.



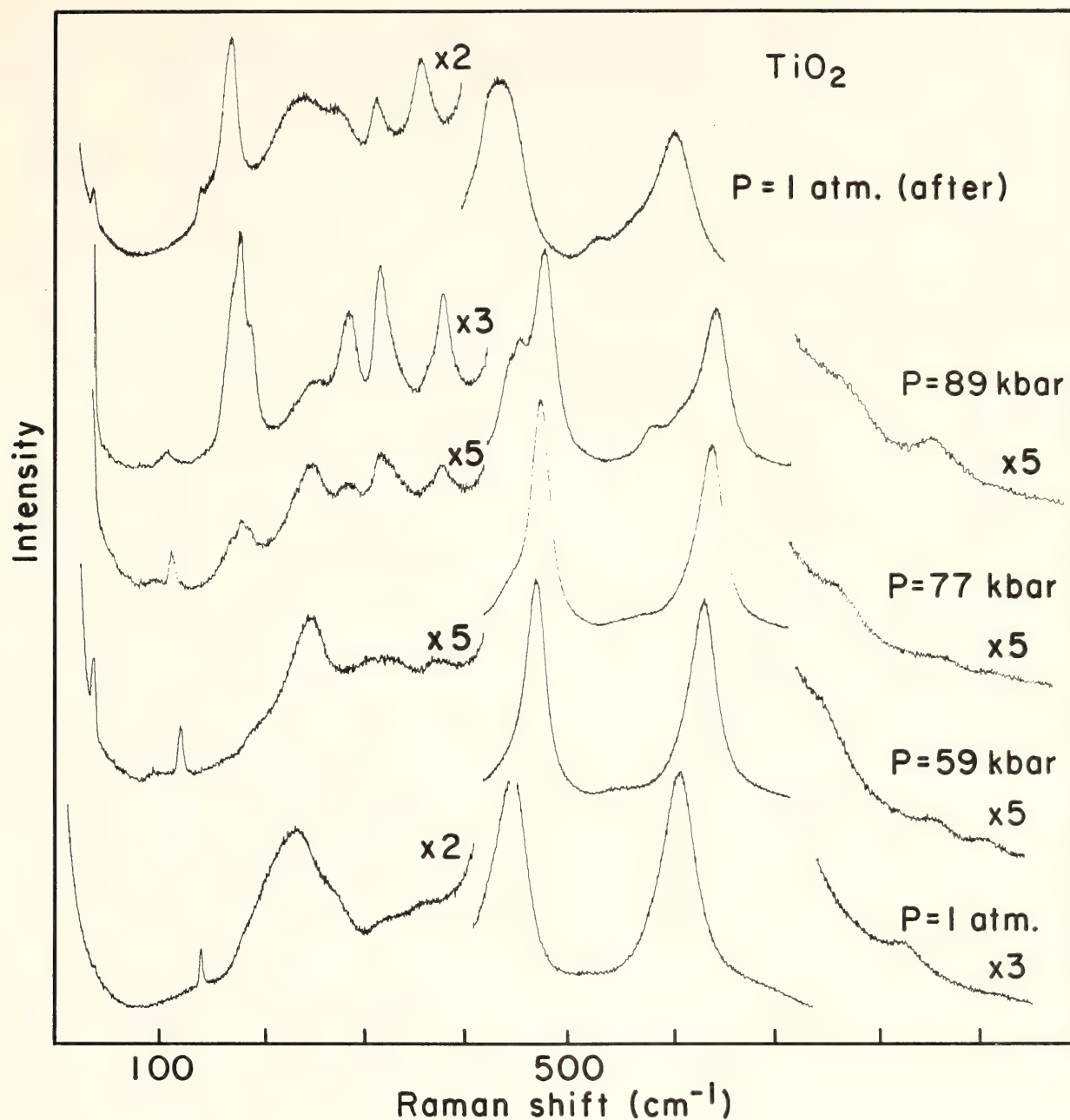


Fig. 120. Raman spectra of  $\text{TiO}_2$  at room temperature and various pressures (laser 488.0-nm line of  $\text{Ar}^+$  ion, 300 mW at the sample, spectral width  $\sim 6 \text{ cm}^{-1}$ ).

than 64 kbar indicates a phase transition. In repeated experiments on different samples of  $\text{TiO}_2$ , the transition pressure varied from sample to sample. By carefully repeating the experiment on different samples, all of which were subjected to high pressure for the first time, the transition pressure was found to be  $70 \pm 5$  kbar. Navrotsky *et al.* (1967) estimated the equilibrium transition pressure at room temperature to be  $60 \pm 20$  kbar from thermochemical data. When

the pressure was increased beyond the transition pressure, the intensities of the new Raman lines increased, whereas the intensity of the  $B_{1g}$  mode of the rutile phase decreased. The strong  $A_{1g}$  and  $E_g$  modes of the rutile phase did not show any appreciable decrease in their intensities at these pressures. Similar behavior of the intensities of the Raman bands was observed by Nicol and Fong (1971). The strong bands observed at 474 and  $640 \text{ cm}^{-1}$  at 77 kbar, which are associ-

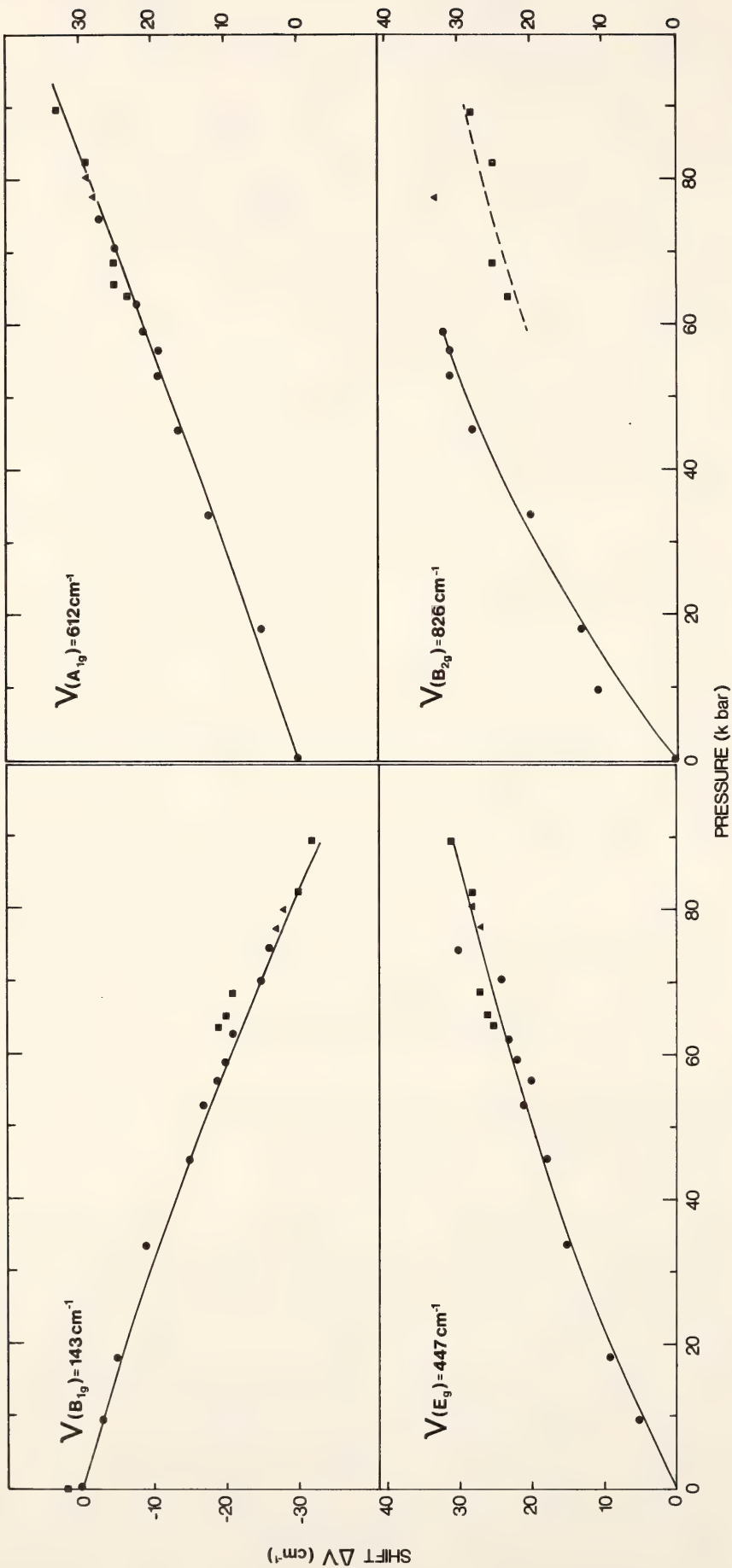


Fig. 121. Pressure dependencies of various Raman active mode frequencies for rutile  $\text{TiO}_2$  at room temperature. Circles, rutile  $\text{TiO}_2$ ; squares,  $\text{TiO}_2\text{-II}$ ; triangles, intermediate between rutile  $\text{TiO}_2$  and  $\text{TiO}_2\text{-II}$  (new bands beginning to appear).



TABLE 41. Raman Frequencies ( $\text{cm}^{-1}$ )\* of  $\text{TiO}_2$  at Different Pressures

Assign- ment	Pressure, kbar				
	0.001 (before)	59	77	89	0.001 (after)
$B_{1g}\dagger$	143w	123w	116w 174m(sh) 183m 189m(sh) 252m(bd)	111w 175vs(sh) 183vs 192vs(sh) 256m(bd)	145w(sh)  176vs  243s(bd) 278s(sh)
	235s(bd)‡ ~275s(sh)‡	249s(bd)‡	286m	288s	
	~322vw(bd)‡ ~359vw(bd)‡	~316w(bd)‡ ~371w(bd)‡	319m 387m	319s 380s 446s(sh) 453s(sh)	318s 361s
$E_g\dagger$	447vs	469vs	474vs	478vs 582m ~610m(sh)	437vs(bd) 533m ~563m(sh)
$A_{1g}\dagger$	612vs	633vs	640vs 762vw(bd)	646vs 768vs(bd)	609vs
$B_{2g}\dagger$	826vw(bd)	858vw(bd)	863vw(bd)	854vw(bd)	831vw(bd)

\*Measurement accuracy:  $\pm 1 \text{ cm}^{-1}$  for sharp and strong bands;  $\pm 5 \text{ cm}^{-1}$  for weak and broad bands. vs, very strong; s, strong; m, medium; w, weak; vw, very weak; bd, broad; sh, shoulder.

† Assignment in rutile  $\text{TiO}_2$ .

‡ Second-order Raman bands (see text).

ated, respectively, with the  $E_g$  and  $A_{1g}$  modes, shift to 478 and  $646 \text{ cm}^{-1}$  at 89 kbar without any appreciable intensity change and therefore must be associated with the new high-pressure phase.

The high-pressure phase of  $\text{TiO}_2$ , which coexists with the rutile phase in the diamond-anvil cell at pressures greater than  $70 \pm 5$  kbar, shows similar Raman bands, as observed by Nicol and Fong (1971) in the spectrum of  $\text{TiO}_2$  at pressures greater than 30 kbar. Thus, the two high-pressure phases of  $\text{TiO}_2$  may have similar structures. The difference in the transition pressure seems to be related to the amount of shear stress present. Nicol and Fong (1971) detected new Raman lines at 30 kbar in the spectra of rutile crystals that were oriented with the crystallographic  $c$  axis perpendicular to the axis of their high-pressure, Drickamer-type cell, in which

$\text{NaCl}$  is used as a pressure-transmitting medium. Thus, relatively large shear stresses, which are expected to be present in the Drickamer-type cell, probably stabilize the transition in  $\text{TiO}_2$  at lower pressures.

There has been some controversy over the structure of the high-pressure phase of  $\text{TiO}_2$ . Nicol and Fong (1971) tentatively assigned their new high-pressure phase as  $\text{TiO}_2\text{-II}$  ( $\alpha\text{-PbO}_2$  structure). Nagel and O'Keeffe (1971), on the other hand, suggested that the new phase may have a  $\text{CaCl}_2$  structure because of the softening of the  $B_{1g}$  mode. Factor group analysis indicates that the  $\alpha\text{-PbO}_2$  form (space group  $D_{2h}^{14}$ ;  $Z = 4$ ) of  $\text{TiO}_2$  can have as many as 18, and the  $\text{CaCl}_2$  form (space group  $D_{2h}^{12}$ ;  $Z = 2$ ) can have as many as six nondegenerate Raman active modes. If the bands at 111, 256, and  $854 \text{ cm}^{-1}$  in the spectrum of  $\text{TiO}_2$  (Table

41) at 89 kbar are considered to be due to the rutile structure, then the number of Raman bands that belong to  $\text{TiO}_2\text{-II}$  is at least 13. Nicol and Fong (1971) reported 14 Raman lines belonging to the  $\text{TiO}_2\text{-II}$  structure. Because the number of observed lines far exceeds the number of expected Raman lines for the  $\text{CaCl}_2$ -type structure, it is clear that  $\text{TiO}_2\text{-II}$  cannot have the  $\text{CaCl}_2$ -type structure. The presence of 13 Raman active modes in  $\text{TiO}_2\text{-II}$  is consistent, however, with the  $\alpha\text{-PbO}_2$  type structure for this polymorph. The other bands may not be seen because they may be too weak or overlap with other bands. Also, the bands at 319 and  $380\text{ cm}^{-1}$  appear asymmetric in shape, and this asymmetry suggests that coincidental degeneracies may be responsible for the observation of fewer Raman bands than expected from group theoretical calculations on the  $\alpha\text{-PbO}_2$  structure. No new low-frequency bands were observed in the  $40\text{--}100\text{ cm}^{-1}$  region. The new bands in the high-pressure phase appear in the low-frequency region  $100\text{--}450\text{ cm}^{-1}$  and would therefore reflect a change in the long-range order, such as a restacking of  $\text{TiO}_2$  octahedra, rather than a change in the primary coordination number, which is consistent with a transition to an  $\alpha\text{-PbO}_2$  phase.

The pressure dependence of the Raman active phonons is shown in Fig. 121. The data are consistent with the work of Samara and Peercy (1973) who made measurements up to only 4 kbar in a hydrostatic high-pressure cell. The frequencies of the  $A_{1g}$  and  $E_g$  modes increase with pressure. There appears to be a discontinuity in the shift of the frequency of the  $B_{2g}$  mode that would indicate a transition. An interesting feature is the negative pressure dependence of  $\nu(B_{1g})$ . Such a softening may indicate a displacive phase transition at some higher pressure. The ionic displacements associated with the  $B_{1g}$  mode consist of rotating the oxygen ions about the  $C_4$  axis. Thus, the negative  $[\partial\nu(B_{1g})/\partial P]_T$  is consistent with the idea that

rutile and  $\text{TiO}_2\text{-II}$  are related by a restacking of  $\text{TiO}_6$  octahedra. In  $\text{SrTiO}_3$  (cubic perovskite) there is a softening of the triply degenerate  $F_{2u}(\Gamma_{25})$  mode, which also consists of rotation of  $\text{TiO}_6$  octahedra about the  $C_4$  axis. As a result, a temperature-induced phase transition is observed at  $110^\circ\text{K}$  in this antiferroelectric perovskite (Fleury *et al.*, 1968).

In conclusion,  $\text{TiO}_2$  undergoes a high-pressure phase transition at  $70 \pm 5$  kbar under nearly hydrostatic conditions in the diamond-anvil, high-pressure cell. The presence of shear stresses can lower the transition pressure considerably (to 30 kbar). The structure of the new high-pressure phase is not that of  $\text{CaCl}_2$ , but at present appears to be the  $\alpha\text{-PbO}_2$  type structure. *In-situ*, powder x-ray diffraction experiments on  $\text{TiO}_2$  at high pressures ( $\sim 100$  kbar) are currently being performed to clarify its structure.

#### RAMAN STUDY OF $\text{GeO}_2$ IN CRYSTALLINE AND GLASSY STATES AT HIGH PRESSURES

*J. F. Mammone\* and S. K. Sharma*

High-pressure properties of  $\text{GeO}_2$  in the glassy and crystalline states can be used to infer analogous properties of  $\text{SiO}_2$  under mantle conditions. Sharma *et al.* (Year Book 77, pp. 665–672) studied the Raman spectra of  $\text{GeO}_2$  glasses quenched from  $\text{GeO}_2$  melt at various pressures. The spectra of these high-pressure quenched melts were similar to that of the melt quenched at 1 atm. This observation suggests that at least some of the effects of pressure on the melt structure were not quenched. In order to obtain information about the effect of pressure on the melt structure, the Raman spectra of crystalline and glassy  $\text{GeO}_2$  must be compared under pressure. Unfortunately, glasses typically give weak Raman spectra, and no data have

\* Work carried out under a cooperative predoctoral fellowship program between the Geophysical Laboratory and the University of California, Los Angeles.



been reported on the Raman spectra of glasses under pressure. One reason for selecting  $\text{GeO}_2$  is that the Raman cross section of  $\text{GeO}_2$  glass is nine times greater than that of  $\text{SiO}_2$  glass (Galeener *et al.*, 1978). An attempt was made, therefore, to study the Raman spectrum of  $\text{GeO}_2$  glass under pressure in a diamond-anvil, high-pressure cell.

### Experimental

Powdered  $\text{GeO}_2$  (hexagonal) was obtained from Alfa Products (Danvers, Massachusetts). Glassy  $\text{GeO}_2$  was prepared by heating the crystalline  $\text{GeO}_2$  (melting point,  $1116^\circ\text{C}$ ) to  $1200^\circ\text{C}$  in a platinum capsule at 1 atm for 1 hr and

subsequent quenching in mercury. Pressures were calibrated by measuring the shift in the ruby  $R_1$  fluorescence line (Mao *et al.*, 1978). Low-fluorescence, type-IIb diamond anvils were used, and Raman spectra were obtained with a Spectra Physics model 164 argon laser with 448.0-nm excitation. Spectra were recorded at room temperature with a J-Y double monochromator (HG-2S) using photon-counting detection (Sharma, *Year Book* 77, pp. 902–904). Scattered radiation was collected in the forward direction by using a  $90^\circ$  off-axis ellipsoidal mirror (Adams *et al.*, 1977; Sharma, this Report).

A 4:1 mixture of methanol:ethanol was used as a pressure-transmitting fluid

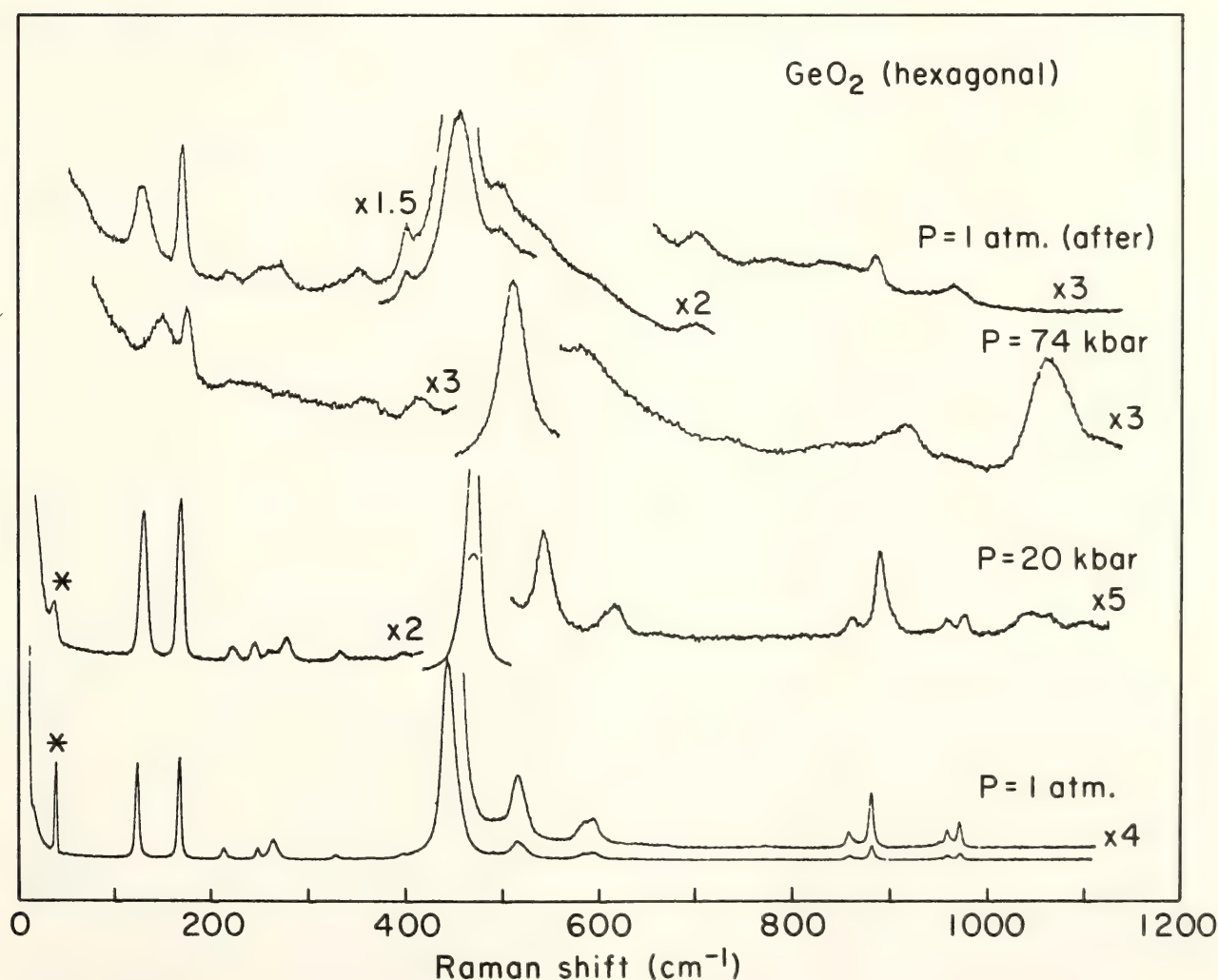


Fig. 122. Raman spectra of hexagonal  $\text{GeO}_2$  at room temperature and various pressures (laser 448.0-nm line of  $\text{Ar}^+$  ion; 350 mW at the sample; spectral width  $\sim 7 \text{ cm}^{-1}$ ); asterisk marks a plasma line from the laser.

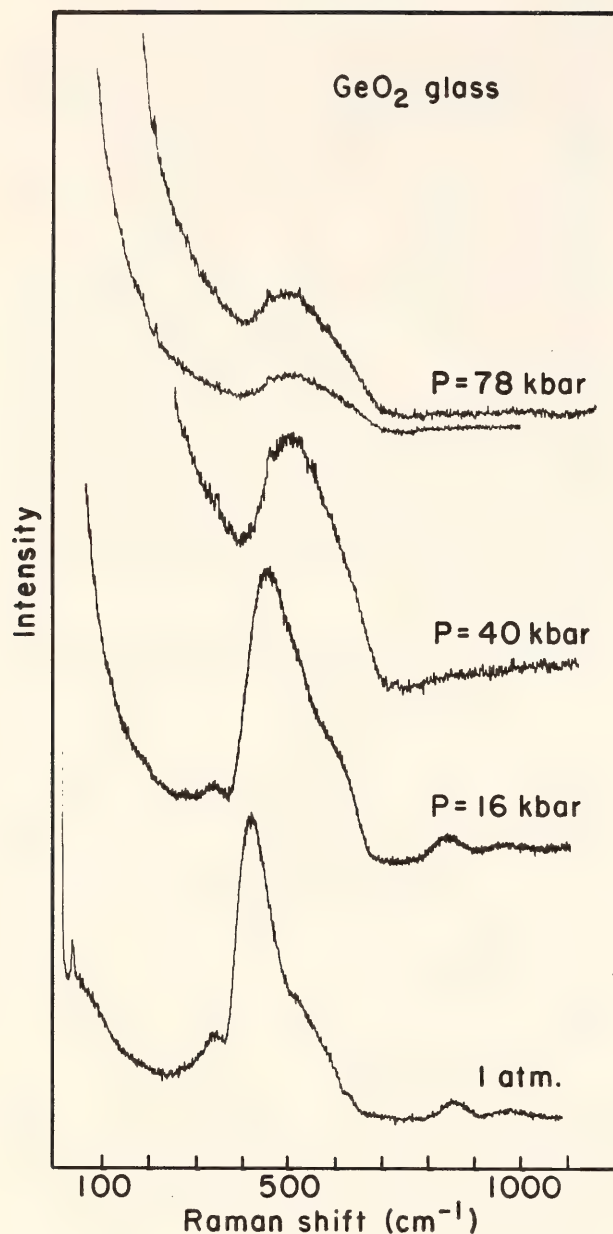


Fig. 123. Raman spectrum of vitreous  $\text{GeO}_2$  at room temperature and various pressures (laser 488.0-nm line of the  $\text{Ar}^+$  ion; 400 mW at the sample; spectral width  $\sim 6 \text{ cm}^{-1}$ ).

with hexagonal  $\text{GeO}_2$ , but pressure was applied directly to the gasketed  $\text{GeO}_2$  glass sample. This procedure was necessary because  $\text{GeO}_2$  glass reacted with the  $\text{MeOH}:\text{EtOH}$  mixture under pressure, as evidenced by the appearance of several sharp lines superimposed on the glass spectrum. Other, more inert liquids were tried with  $\text{GeO}_2$  glass (e.g., mineral oil) but the weak glass spectrum was obscured with increasing pressure at the large Rayleigh tail of the liquid.

### Results and Discussion

Raman spectra of hexagonal and glassy  $\text{GeO}_2$  at various pressures are shown in Figs. 122 and 123. The spectral characteristics of the various bands are summarized in Tables 42 and 43.

A model for silica and germania glass was put forward by Zachariasen (1932), who proposed that the glass consisted of a three-dimensional network of tetrahedra with each oxygen shared by a different neighboring tetrahedral unit. The disorder arises from a variation in the orientation of adjacent tetrahedra. In an ordered crystal the discrete character of the Raman spectrum is a direct consequence of the conservation of momentum and energy. In a glass that is disordered, the crystal momentum or wave vector ( $k$ ) conservation restraint is relaxed, and the entire energy spectrum of vibrational modes is observed (Brodsky, 1975; Solin, 1976). Breakdown of the  $k = 0$  selection rule in the glass is responsible for observed broad Raman bands in the spectrum of  $\text{GeO}_2$  glass (Fig. 123) in contrast to sharp Raman lines in the spectrum of crystalline  $\text{GeO}_2$ . Broad bands in glass spectra are actually envelopes consisting of several bands (Bell and Dean, 1972) and represent the phonon density of states.

With increasing pressure the intensity of the Rayleigh tail increased relative to the glass spectrum (Fig. 123). This increase is indicative of increasing disorder with pressure. Bridgman and Simon (1953) observed that under uniaxial compression, glasses such as silica deform nonisotropically in the direction of compression. This effect could cause a spreading out of the phonon density of states resulting in the further broadening of bands and a large Rayleigh tail. The effect is expected to be less in glasses that are more sodic, which flow more in a direction normal to the axis of compression.

In the spectrum of hexagonal  $\text{GeO}_2$  loaded in the alcohol mixture a strong band gradually appears with increasing



TABLE 42. Observed Raman Frequencies (cm<sup>-1</sup>)\* at Various Pressures and Room Temperature for Hexagonal GeO<sub>2</sub>

Assignment	Pressure, kbar				
	0.001†	20‡	74‡	0.001‡	0.001§
<i>E</i>	120s	129s	144s(bd)	125s(bd)	123s(bd)
<i>E</i>	163s	167s	171s	166s	165s
<i>A</i> <sub>1</sub>	212w	221w		214w	212w
	246w	244w		243w(bd)	~249w(bd)
<i>A</i> <sub>1</sub>	262w	276w		266w(bd)	~262w(bd)
<i>E</i>	328w	331w			
			356w	347w	~343w(bd)
			409w	396w	~398w(sh)
<i>A</i> <sub>1</sub>	442vs	468vs	506vs	450vs	443vs
				491w	
<i>E</i>	514w	540w			~516w(bd)
<i>E</i>	590w	613w			~584w(bd)
			~731vw(bd)	696w	
<i>E</i>	856vw	858w	890vw(bd)		
<i>A</i> <sub>1</sub>	876w	886w	912w(bd)		879w
<i>E</i>	954vw			} 959w(bd)	
<i>E</i>	958w	972w			962w(bd)
		1048w(bd)	1055s(bd)		

\* Measurement accuracy: ±1 cm<sup>-1</sup> for sharp and strong bands; ±5 cm<sup>-1</sup> for weak and broad bands. vs, very strong; s, strong; w, weak; vw, very weak; bd, broad; sh, shoulder.  
† Pressure-transmitting fluid was 4:1 MeOH:EtOH mixture.  
‡ Spectra measured after compression in 4:1 MeOH:EtOH mixture.  
§ Pure sample compressed directly (not in Fig. 122), and spectra measured after pressure was released.  
|| See text.

pressure ( $\nu = 1055\text{ cm}^{-1}$  at 74 kbar) and disappears upon release of pressure (Fig. 122). When pure powdered hexagonal GeO<sub>2</sub> was compressed to a similar pressure, no new band appeared in

TABLE 43. Observed Raman Frequencies (cm<sup>-1</sup>)\* at Various Pressures and Room Temperature for Vitreous GeO<sub>2</sub>

0.001 kbar	16 kbar	40 kbar	78 kbar
339w	338w		
416vs	458vs	476vs	527vs(bd)
~510w(sh)			
848w	840w	835vs(bd)	
964vs(bd)	966vw(bd)		

\* Measurement accuracy: ±1 cm<sup>-1</sup> for sharp and strong bands; ±5 cm<sup>-1</sup> for weak and broad bands. vs, very strong; s, strong; m, medium; w, weak; vw, very weak; bd, broad; sh, shoulder.

the same region. A corresponding peak was also found in the spectrum of the glass when it was loaded in only the 4:1 MeOH:EtOH mixture. This band, therefore, is attributed to the presence of the fluid. Hibben (1936) assigned bands in this region in methanol and ethanol as C-O stretching.

The pressure dependence of the frequency of the very strong *A*<sub>1</sub> mode ( $\nu = 442\text{ cm}^{-1}$  at 1 atm) is shown in Fig. 124. This band shifts more with pressure than the others. Such a shift is normal because totally symmetric stretching modes represent volume pulsations, which are more pressure-sensitive. In the glass, however, the data are more scattered. Bridgman and Simon (1953) observed an approximate threshold pressure for the onset of densification in silica glass. The existence of pressure gradients and other

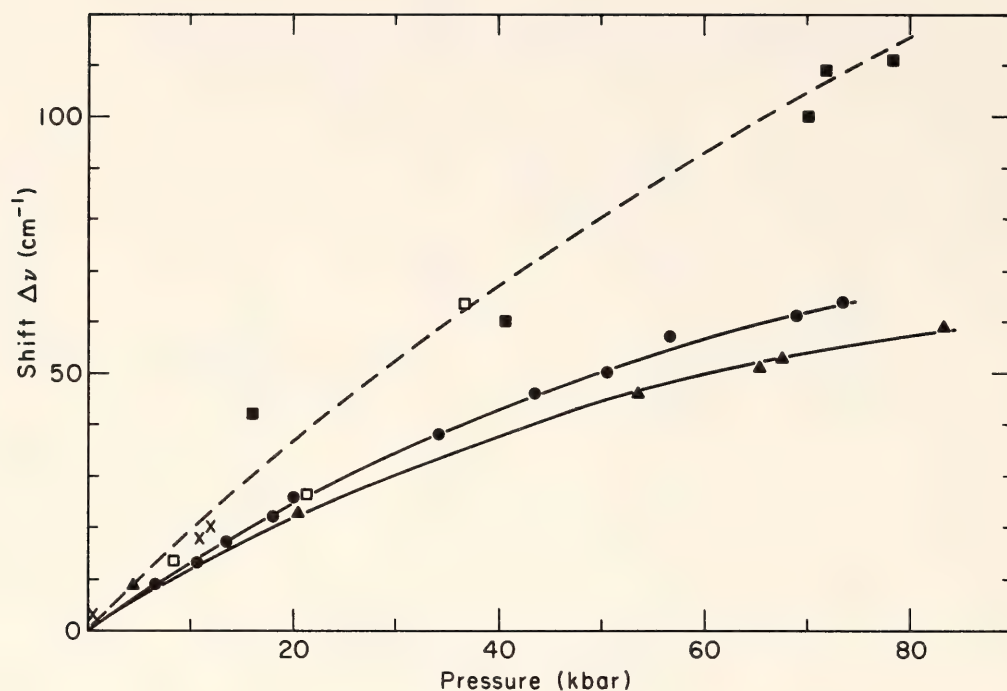


Fig. 124. Pressure dependencies of the very strong  $A$  mode for hexagonal  $\text{GeO}_2$  and corresponding band in vitreous  $\text{GeO}_2$  at room temperature. Solid triangles, hexagonal  $\text{GeO}_2$  (nonhydrostatic); solid circles, hexagonal  $\text{GeO}_2$  in 4:1  $\text{MeOH}:\text{EtOH}$ ; solid squares,  $\text{GeO}_2$  glass (nonhydrostatic); open squares,  $\text{GeO}_2$  glass quenched under pressure (nonhydrostatic); crosses,  $\text{GeO}_2$  glass quenched under pressure in 4:1  $\text{MeOH}:\text{EtOH}$ .

factors affecting the kinetics throughout the sample can initiate densification at different points in different experiments and may explain the increase in scatter and possible discontinuities in the pressure dependence of the frequency of the Raman band. The band in  $\text{GeO}_2$  glass shifts approximately twice as much as the corresponding band in the hexagonal crystal. This shift may be due to the more open structure of glass, which is therefore more compressible.

The Raman spectrum of crystalline  $\text{GeO}_2$  recorded after the pressure was released (Fig. 122) exhibits features similar to those of the original spectrum at 1 atm. A small permanent deformation, however, was induced in the crystalline  $\text{GeO}_2$ , as can be seen by the general broadening of the bands [especially  $\nu(E) = 120 \text{ cm}^{-1}$  at 1 atm] and the appearance of two weak, broad bands in the frequency range  $340\text{--}410 \text{ cm}^{-1}$  (Fig. 122; Table 42). A very weak, broad band appears in the 74-kbar spectrum at  $\sim 731$

$\text{cm}^{-1}$ , and after the pressure is released a weak band is observed at  $696 \text{ cm}^{-1}$  (Fig. 122). The strongest Raman band (symmetry  $A_{1g}$ ) in rutile  $\text{GeO}_2$  appears at  $700 \text{ cm}^{-1}$  (Sharma *et al.*, *Year Book* 77, pp. 655–672); the weak bands may therefore be attributed to the transformation of some  $\text{GeO}_2$  from the hexagonal to the rutile structure. Even though rutile  $\text{GeO}_2$  is the stable form (Navrotsky, 1971; Jackson, 1976), the transition from hexagonal to rutile  $\text{GeO}_2$  is quite sluggish at room temperature. At high pressure, however, there is a tendency for conversion of  $\text{GeO}_2$  to the rutile structure. This tendency is probably responsible for straining the lattice of hexagonal  $\text{GeO}_2$ , as reflected by the observed broadening of the doubly degenerate mode at  $120 \text{ cm}^{-1}$ .

Upon release of pressure the Raman spectrum of  $\text{GeO}_2$  glass resembled the high-pressure spectrum, and this result indicates that the glass was permanently densified. Densification of glasses under



pressure was also observed by Cohen and Roy (1961); however, no major changes in the Raman spectra that could be attributed to a phase change under pressure were observed for  $\text{GeO}_2$  glass. At room temperature the available thermal energy is apparently too slight to overcome kinetic barriers. In one experiment where  $\text{GeO}_2$  glass was compressed to  $\sim 140$  kbar, faint lines in the positions of the three strongest Raman bands in hexagonal  $\text{GeO}_2$  were observed, indicating a slight crystallization but no change in coordination number of Ge.

#### RAMAN STUDY OF $n\text{-H}_2$ UNDER VERY HIGH PRESSURES AT ROOM TEMPERATURE

*S. K. Sharma, H. K. Mao, and P. M. Bell*

Raman spectra of hydrogen have been measured for the first time in the pressure range 0.2–631 kbar at  $25^\circ\text{C}$ , to study the changes in the molecular H-H bond and the rotational modes. This study was possible because of a recent new design of the diamond-window, high-pressure cell that could be used at cryogenic temperatures (Mao and Bell, this Report) and independently coupled with a Raman spectrometer (Adams *et al.*, 1977). Raman measurements on gaseous hydrogen at room temperature and on solid hydrogen at cryogenic temperatures had been limited previously to pressures below 15 kbar with conventional apparatus (Stoicheff, 1957; Allin *et al.*, 1967; Vu *et al.*, 1975).

#### *Results and Discussion*

The pressure cell used in these experiments has a sample volume of the order of 0.25 nl, approximately one million times smaller than the volume of hydrogen required for Raman spectral measurements in conventional experiments (Stoicheff, 1957; Allin *et al.*, 1967; Thiery *et al.*, 1974; Vu *et al.*, 1975). The

high sensitivity of the technique is exemplified in the measurements of these small sample volumes of hydrogen made at 200 bars. The spectrum was recorded in approximately 3 hr, compared with  $\sim 30$  hr required with the relatively large sample volumes of conventional techniques (Stoicheff, 1957).

The hydrogen gas sample used in this study is ultrapure (99.999% hydrogen, Linde Corporation). The hydrogen molecules of the sample at the start of the experiments are in the normal ratio of spin states ( $n\text{-H}_2$ ), which is a 3:1 mixture of the parallel (ortho,  $o\text{-H}_2$ ) and antiparallel (para,  $p\text{-H}_2$ ) isomers.

The positions of the four pure rotational lines [ $S_0(J)$  ( $\Delta v = 0$ ;  $J = 0, 1, 2, 3$ )] and four Q-branch lines [ $Q_1(J)$  ( $\Delta v = 1$ ;  $\Delta J = 0$ ;  $J = 0, 1, 2, 3$ )] of the vibrational bands of hydrogen observed at  $\sim 200$  atm (Table 44) are in agreement with values previously reported (Stoicheff, 1957; Allin *et al.*, 1967). In the forward scattering geometry, used in the present experiments, both the rotational and the vibrational lines of  $n\text{-H}_2$  are narrow because the Doppler broadening is minimized (Weber, 1973).

In the present experiments at low pressures the observed line widths were broader than the natural line width of the band (Cooper *et al.*, 1968; Murray and Javan, 1969). In Table 44 the half-widths of only those lines whose widths exceeded the slit width of the spectrometer are given. It is seen from Fig. 125 that in the fluid phase the rotational lines broaden with increasing pressure. The broadening also occurs in the  $Q_1(1)$  vibrational lines (Fig. 126) although to a lesser extent than in the rotational lines (Table 44). The intensity of the Rayleigh tail also increases with increasing pressure and interferes with the rotational bands due to collision broadening (Fig. 125) (Jammu *et al.*, 1960; Weber, 1973).

At the solidification pressure (55 kbar at  $22^\circ\text{C}$ ) strong Rayleigh interference is

TABLE 44. Frequencies (cm<sup>-1</sup>) of Raman Bands of *n*-H<sub>2</sub> at Various Pressures and Room Temperature

Pressure	Pure Rotational Bands				Vibrational Bands			
	S <sub>0</sub> (0)	S <sub>0</sub> (1)	S <sub>0</sub> (2)	S <sub>0</sub> (3)	Q <sub>1</sub> (0)	Q <sub>1</sub> (1)	Q <sub>1</sub> (2)	Q <sub>1</sub> (3)
1-2 atm*	354.381	587.055	814.406	1034.651	4161.134	4155.201	4143.387	4125.832
200 atm†	354.8m‡	588.4s	814.5w	1034.2w	4161.6w	4155.9m	4144.2w	4126.6w
5 kbar	355.0m (ω=12.0)	590.8s (ω=13.0)	817.4w (ω=11.6)	1036.3w (ω=10.6)	...§	4163.3m	...§	...§
9 kbar	357.0m (ω=12.1)	592.4s (ω=28.8)	820.9w (ω=20.2)	1040.0w (ω=20.7)	...§	4165.5m	...§	...§
24 kbar	354.8m 369.0vw(sh)	529.5w 564.5vw(sh) 596.2s	824.7w (ω=22.7)	1044.4w (ω=20)	...§	4183.8m (ω=13.1)	...§	...§
40 kbar	360.7 (ω=27.3)	601.5s (ω=51.5)	832.0w (ω=33.8)	1051.2 (ω=32.3)	...§	4200.7m (ω=14.1)	...§	...§
55 kbar	...vw,bd	594.9w,bd 613.4w,bd	782vw,bd 837vw,bd	...vw,bd	...§	4205.0m (ω=5.7)	...§	...§

\* From Stoicheff (1957); the positions of rotational bands within ± 0.02 cm<sup>-1</sup> and of Q-branch vibrational bands within ± 0.05 cm<sup>-1</sup>.  
† Measurement accuracy ± 0.5 cm<sup>-1</sup>.  
‡ vw, very weak; w, weak; m, medium; bd, broad; sh, shoulder; ω, full width at half maximum height.  
§ Bands not detected.



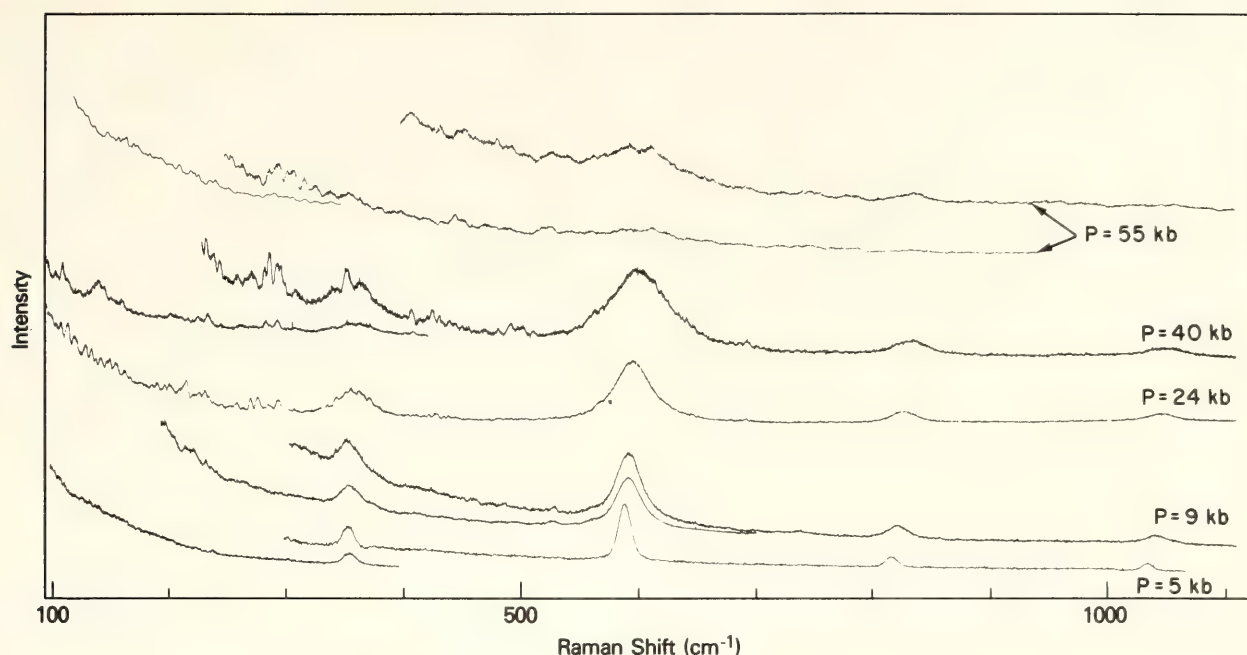


Fig. 125. Raman spectra of  $n\text{-H}_2$  in the region of rotational modes at different pressures (488.0-nm  $\text{Ar}^+$  laser excitation, 200 mW at the sample). Spectral slit width  $10\text{ cm}^{-1}$ . The lower traces of the Raman spectra at different pressures were recorded with an amplification of  $\times 0.5$ . The lowest trace in the low-frequency region in the spectrum of hydrogen at 55 kbar was recorded with a slit width of  $5\text{ cm}^{-1}$ .

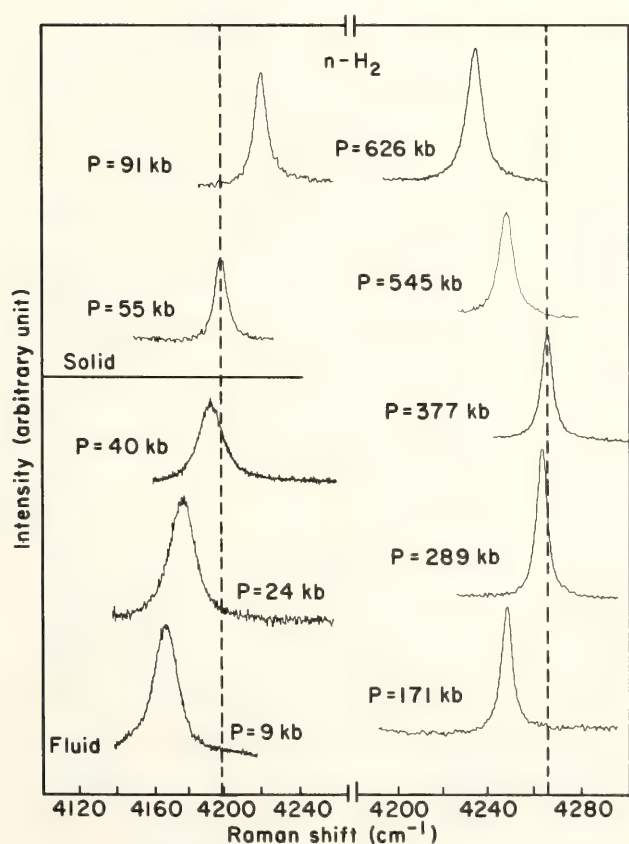


Fig. 126. The  $Q_1(1)$  Raman active mode of  $n\text{-H}_2$  at different pressures. Spectral slit width  $5\text{ cm}^{-1}$  for fluid spectra and  $3.5\text{ cm}^{-1}$  for spectra of solid  $n\text{-H}_2$  (488.0-nm excitation, 400 mW at the sample).

observed, the  $S_0(0)$ ,  $S_0(1)$  and other rotational bands become diffuse and broad (Fig. 125), and they appear to split. The existence of strong Rayleigh interference implies that the  $\text{H}_2$  molecules in the high-pressure solid are randomly oriented and that their rotation is hindered. The  $k = 0$  selection rule is relaxed because of this disorder, and the Raman spectrum shows the phonon density of states rather than the optic phonon at  $k = 0$ . The presence of a strong Rayleigh tail may be responsible for the observed interference fringes both in fluid and solid  $n\text{-H}_2$ . The large broadening and splitting of the observed  $S_0(0)$  and  $S_0(1)$  rotational bands of para- and ortho- $\text{H}_2$ , respectively, in  $\text{H}_2$  on freezing is due to delocalization of the rotational excitations by anisotropic interactions that create bands of rotational excitations in the solid (Van Kranendonk, 1959).

The  $Q_1(1)$  vibrational band in the  $n\text{-H}_2$  fluid at room temperature shifts to higher frequency with increasing pressure. The pressure dependence of the

shift ( $\Delta\nu$ ,  $\text{cm}^{-1}$ ) of this band in the fluid is empirically expressed as

$$\Delta\nu = 1.553P - 0.0115P^2 \quad (P \leq 55 \text{ kbar}).$$

At the freezing pressure (55 kbar,  $T = 22^\circ\text{C}$ ) the  $\nu[Q_1(1)]$  exhibits a small decrease ( $1.8 \text{ cm}^{-1}$ ) in frequency. In  $n\text{-H}_2$  at low temperatures the frequency of the  $Q_1(1)$  band is observed to decrease by  $9.3 \text{ cm}^{-1}$  at the liquid-to-solid transition (Bhatnagar *et al.*, 1962). The decrease in the frequency of the  $Q_1(1)$  band at the transition point is attributed to the superposition of three effects: (1) a shift ( $\Delta d$ ) due to dispersion forces, (2) a shift ( $\Delta r$ ) due to repulsive forces, and (3) a vibrational coupling effect ( $\Delta c$ ). The small decrease in the frequency of the  $Q_1(1)$  band ( $1.8 \text{ cm}^{-1}$ ) observed at the freezing pressure indicates that the repulsive forces are significant in the compressed solid at room temperature. The decrease in the half-width of the  $Q_1(1)$  band from 15 to  $5.6 \text{ cm}^{-1}$  at the fluid-to-solid transition (Fig. 126) is caused by the reduction of collision-induced broadening in the solid state. The observed large decrease in the half-width of the  $Q_1(1)$  band can be used in determining the phase boundary between fluid and solid  $\text{H}_2$  at elevated temperatures and pressures.

England *et al.* (1976) calculated from theory the effect of pressure on the rotational motion of hydrogen isotopes. According to these calculations the rotation of  $\text{H}_2$  molecules is expected to cease at  $\sim 375$  kbar. In the present study, the low-frequency ( $50\text{--}100 \text{ cm}^{-1}$ ) Raman spectra were featureless at the highest pressures studied (631 kbar). The half-width of the  $Q_1(1)$  band, however, decreased from 5.7 to  $4.5 \text{ cm}^{-1}$  at 175 kbar. It is not clear whether this reduction of half-width of the  $Q_1(1)$  band is due to a lessening of rotational motion of the hydrogen molecules or to some other second-order transition. When the pressure was increased above 200 kbar the half-width of the  $Q_1(1)$  band slightly increased. At 544 kbar the half-width of the  $Q_1(1)$

band is, however,  $6.1 \text{ cm}^{-1}$  and increases rapidly with increasing pressure ( $\omega = 7.6 \text{ cm}^{-1}$  at 626 kbar). The increase in half-width of the  $Q_1(1)$  band at very high pressure, where the  $Q_1(1)$  band frequency decreases (see below), indicates considerable interaction between hydrogen molecules at these pressures.

The pressure dependence of the shift of the  $Q_1(1)$  band from its value at 2 atm ( $4155.2 \text{ cm}^{-1}$ ) and room temperature, in the range 55 to 631 kbar, is empirically expressed as

$$\begin{aligned} \Delta\nu = & 14.61 + 0.780P - 0.220 \\ & \times 10^{-2}P^2 + 0.296 \times 10^{-5}P^3 \\ & - 0.165 \times 10^{-8}P^4 \\ & (\Delta\nu \text{ cm}^{-1}; P, \text{ kbar}). \end{aligned}$$

Initially the  $Q_1(1)$  band shifts toward higher frequency, which is caused by compression of the H-H bonds. The initial rate of shift,  $\sim 0.5 \text{ cm}^{-1}/\text{kbar}$  in the solid  $n\text{-H}_2$  at room temperature at pressures above 55 kbar, is much smaller than the reported value of  $\sim 2 \text{ cm}^{-1}/\text{kbar}$  in solid  $n\text{-H}_2$  at  $4.2^\circ\text{K}$ , in the pressure range 1 bar to 8 kbar (Thiery *et al.*, 1974). The rate of shift of the  $Q_1(1)$  band is reduced to only  $0.1 \text{ cm}^{-1}/\text{kbar}$ , and the frequency reaches a maximum at 330 kbar (Fig. 127). On increasing the pressure above 330 kbar the  $Q_1(1)$  band frequency decreases from its maximum value of  $4264.7 \text{ cm}^{-1}$  at 330 kbar. The band appears at  $4234.5 \text{ cm}^{-1}$  at 631 kbar, the maximum pressure used in the present experiments.

### Summary

The main observations of this study are related to actual rotation of the hydrogen molecules and their frequency of H-H stretch. The rotational Raman bands, initially sharp and distinct in the fluid phase at low pressure, became broad at moderate pressure and then split at the onset of solidification (55 kbar,  $22^\circ\text{C}$ ). As the pressure was increased in the solid, the rotational bands became diffuse and indistinguishable. Appar-



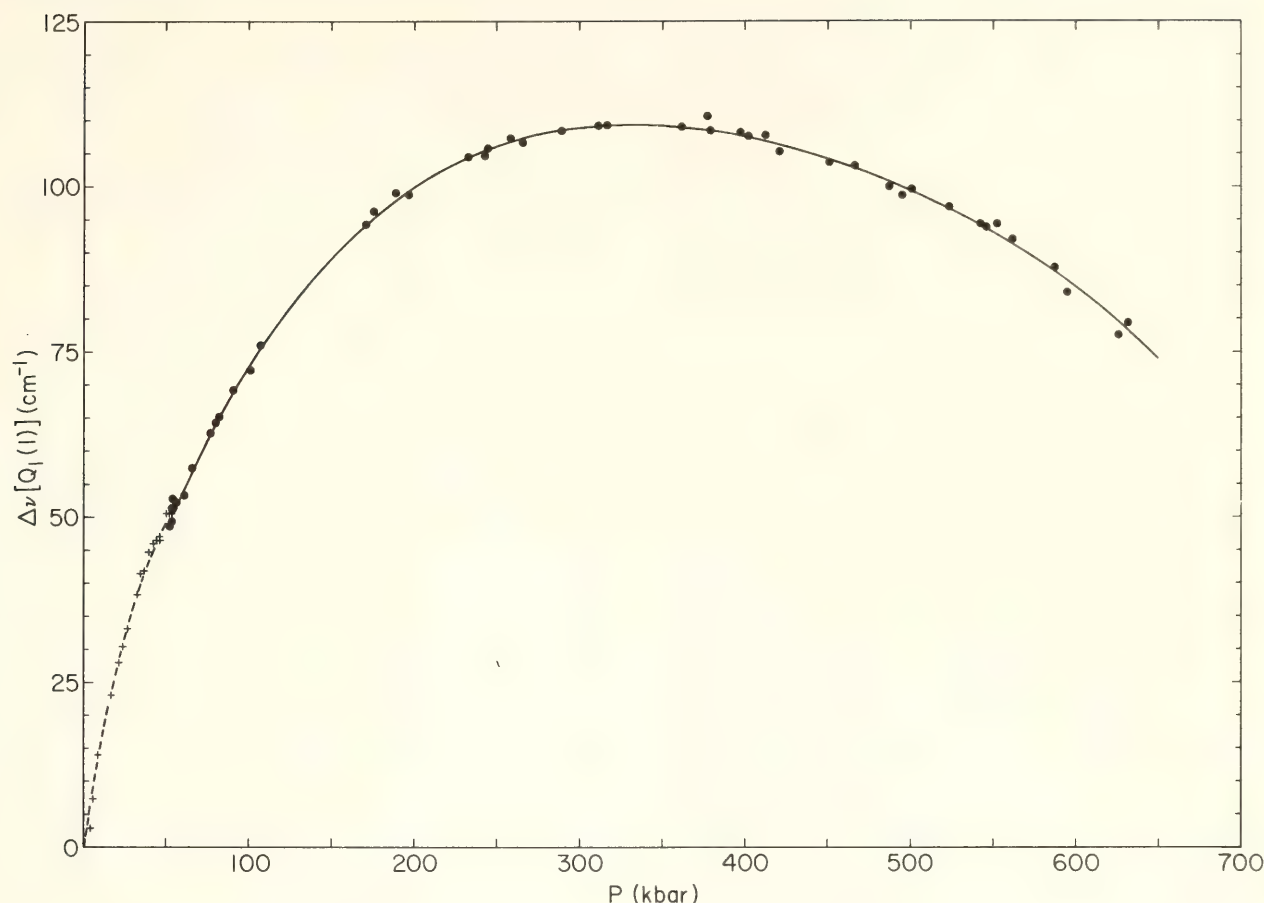


Fig. 127. The shift  $\Delta\nu[Q_1(1)]$  as a function of pressure in  $n\text{-H}_2$  at room temperature ( $26^\circ \pm 4^\circ\text{C}$ ).

ently, rotation of the molecules is greatly hindered in the disordered form of solid hydrogen.

The vibrational Raman spectra are a measure of the stretching within the diatomic hydrogen molecule and thus are of critical importance in determining whether hydrogen will change to the metallic state. The observed changes in the shape and frequency of the hydrogen Raman line indicate that interaction and significant changes of the molecular bonds have already begun to occur in the pressure range 330–631 kbar. The vibrational Raman band was broad in fluid hydrogen but became sharper in the solid. At 171 kbar the vibrational band was observed to sharpen further and then to broaden again slightly at 200 kbar. When the pressure on hydrogen had been raised to 626 kbar, the vibrational line had become approximately

2  $\text{cm}^{-1}$  broader than at 171 kbar (4.5  $\text{cm}^{-1}$ ).

In the same pressure range, 55–624 kbar, the frequency of the vibrational band shifted. The shift was first to higher frequency, gradually leveling off at approximately 330 kbar, and then falling as the pressure was increased to 626 kbar. The rise in frequency was a direct response of the hydrogen molecule to compression. This effect is observed in many polyatomic molecules (Whalley, 1975). The leveling off and then the decrease in frequency with pressure indicate that the molecular bond was softening. The implication is that the hydrogen molecules are interacting and forming new bonds. These phenomena are consistent with hydrogen solids undergoing a structural change (possibly to the metallic state) that will be complete at higher pressure.

## BIOGEOCHEMISTRY

STABLE HYDROGEN ISOTOPE  
FRACTIONATION DURING MIXOTROPHIC  
GROWTH OF *Chlorella*, A UNICELLULAR  
GREEN ALGA

Marilyn L. F. Estep

Plants grown under controlled conditions fractionate hydrogen isotopes reproducibly, indicating a strict control in the pathways of fixing hydrogen into the organic matter in cells (Estep and Hoering, *Year Book* 77, pp. 886–891). This reproducibility facilitates the use of precision isotope-ratio mass spectrometry in performing tracer experiments. There are indications that hydrogen isotopes may be useful as tracers in studying the biological source of organic matter in sedimentary rocks (Hoering, *Year Book* 73, pp. 590–595). It is necessary to understand the biochemical reactions affecting hydrogen isotopes in living organisms in order to interpret hydrogen isotope phenomena in ancient organic matter. Hydrogen isotope fractionation in biochemical pathways was studied by manipulating growth conditions of the alga *Chlorella sorokiniana* strain TX-71105 (1) by changing the wavelength of the light source for photosynthesis (autotrophic growth), (2) by transferring the algae from the light into the dark and adding an organic substrate (heterotrophic growth), (3) by growing the algae in various amounts of light and adding an organic substrate (photoheterotrophic growth), and (4) by adding inhibitory compounds that are known to affect only certain biochemical pathways. The organic matter of plants has a  $\delta D$  approximately 100 lower than the water used during growth (Estep and Hoering, *Year Book* 77, pp. 886–891). Analytical results are reported as parts per thousand difference in the D-H ratio

as compared with a standard reference material:

$$\delta D = \left[ \frac{(D/H)_x - (D/H)_s}{(D/H)_s} \right] 1000,$$

where  $x$  refers to the unknown and  $s$  refers to a standard reference material, the Standard Mean Ocean Water from the International Atomic Energy Agency, Vienna. The isotope fractionation,  $\Delta D$ , is defined as the  $\delta D$  of organically bonded hydrogen minus the  $\delta D$  of water in the growth medium.

The major hydrogen isotope fractionation in plants is due to both the light reactions (Nos. 1, 2, 3, Fig. 128) and the dark reactions (Nos. 4, 5, Fig. 128) of photosynthesis. Some of the hydrogen isotope fractionation occurs during the reduction of 3-phosphoglyceric acid (PGA), the first product of photosynthesis (reaction 4, Fig. 128) by the enzyme 3-phosphoglyceraldehyde dehydrogenase (reaction 5, Fig. 128). Blue light inhibits this enzyme in *Chlorella*, and presumably some of the PGA is transferred directly into the pathway of glycolysis with little alteration, when *Chlorella* is illuminated with blue light (Miyachi *et al.*, 1978). When *Chlorella* was grown in blue light (Plexiglas filter 2424), the isotope fractionation,  $\Delta D$ , was only  $-75$ . In contrast, when *Chlorella* was grown in either red light (Plexiglas filter 2423) or white light (Daylight or Cool-white fluorescent bulbs, see Estep and Hoering, *Year Book* 77, pp. 886–891), the  $\Delta D$  was approximately  $-115$ .

Additional fractionation of hydrogen isotopes occurs during biosynthesis. Acetyl-coenzyme A is one of the first reactants in the steps toward the synthesis of fatty acids, a group of compounds with very negative  $\delta D$  values (Hoering, 1977). The major fractionation is believed to occur previous to or



## Chloroplast

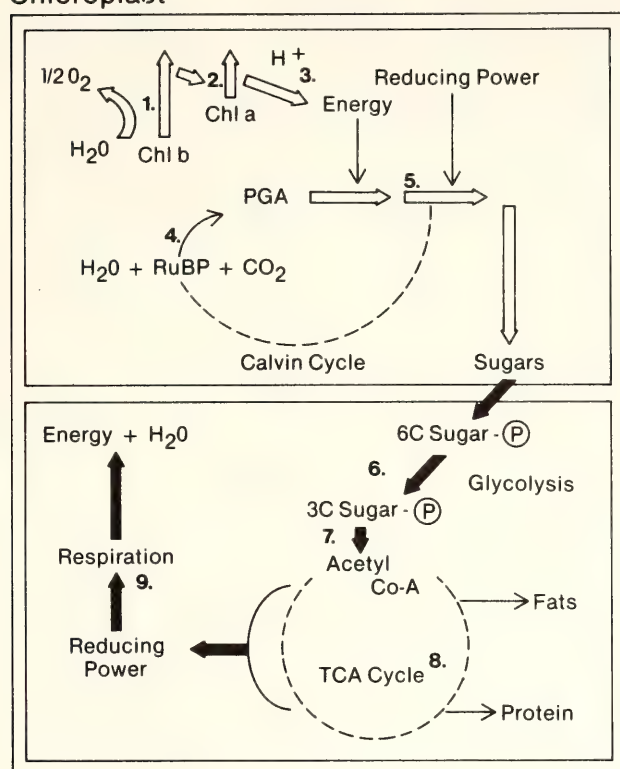


Fig. 128. Biochemical pathways involved in hydrogen isotope fractionation in plants. Pathways stimulated by light are indicated by white arrows, whereas pathways activated in the dark are indicated by black arrows. Enzymatic reactions are numbered 1 to 9. 1: Light reaction of photosynthesis. The splitting of water and the absorption of light by chlorophyll *b* (Chl *b*). 2: Light reaction of photosynthesis. The formation of biochemical energy in the compound adenosine triphosphate (ATP) and the absorption of light by chlorophyll *a* (Chl *a*). 3: Light reaction of photosynthesis. Photosynthetic electron transport coupled with the production of reducing power in the form of reduced nicotinamide adenine dinucleotide phosphate (NADPH). 4: Dark reaction of photosynthesis. Carbon dioxide fixation by the enzyme ribulose 1,5-bisphosphate (RuBP) carboxylase. 5: Dark reaction of photosynthesis. The reduction of phosphoglyceric acid (PGA) by the enzymes 1,3-bisphosphoglycerokinase and 3-phosphoglyceric aldehyde dehydrogenase. 6: Glycolysis. The breakdown of six carbon sugar phosphates formed during photosynthesis to three carbon sugar phosphates. 7: Glycolysis. Additional reactions resulting in the formation of acetyl-coenzyme A. 8: Tricarboxylic acid cycle. Organic acids are oxidized, while reducing power in the form of reduced nicotinamide adenine dinucleotide (NADH) is produced. Acetyl-coenzyme A is introduced into cell biosynthesis via malate synthase, an enzyme in the glyoxylate shunt off this pathway. 9: Dark respiration. The reducing power, NADH, is

during the formation of acetyl-coenzyme A (reaction 6 or 7, Fig. 128). Lipids were extracted from a heterotrophically grown *Chlorella* culture with glucose added. The difference between the  $\delta D$  of lipid hydrogen and that of total organic hydrogen was  $-100$  (experiments A and B, Table 45). When *Chlorella* was grown on acetate, however, the  $\delta D$  of lipids extracted from these cells was nearly identical with the  $\delta D$  of the total organically bonded hydrogen (experiment C, Table 45). The  $\delta D$  of the organic hydrogen in cells grown on acetate was always more positive than the  $\delta D$  of the acetate hydrogen by  $+40$  (experiments C-G, Table 45). The  $\delta D$  of water in the growth medium had only a slight effect on the  $\delta D$  of these cells. Acetate is known to be quickly converted to acetyl-coenzyme A and taken up via side reactions of the tricarboxylic acid cycle, which will allow acetate to be converted to carbohydrates (reaction 8, Fig. 128). One of three acetate hydrogens is lost during this reaction, perhaps causing this peculiar hydrogen isotope effect.

Small amounts of light stimulate hydrogen isotope fractionation in photoheterotrophic cells. *Chlorella* grown on glucose in darkness with  $\frac{1}{2}$  hr of light (experiment H, Table 45) showed a considerably more negative isotope fractionation than cells grown similarly in complete darkness (experiment A) (Estep and Hoering, *Year Book* 77, pp. 886-891). Moreover, cells grown with glucose in green light (Plexiglas filter 2092; some red light near 675 nm is transmitted), which is absorbed by cytochromes, show a similar negative isotope effect. The

oxidized via an electron-transport system that is coupled with the formation of biochemical energy (ATP). Oxygen is reduced to water.

Abbreviations: Chl *b*, Chlorophyll *b*; Chl *a*, chlorophyll *a*; RuBP, ribulose 1,5-bisphosphate; PGA, phosphoglyceric acid; 6C sugar-(P), six carbon sugar phosphate; 3C sugar-(P), three carbon sugar phosphate; TCA cycle, tricarboxylic acid cycle; acetyl Co-A, acetyl coenzyme A.

TABLE 45. Hydrogen Isotope Fractionation in *Chlorella*

	Experiment	$\delta D$ Water	$\delta D$ Cells	$\Delta D$	$\delta D$ Lipids
<i>Heterotrophic Growth</i>					
Glucose ( $\delta D = -18$ )	A	- 60	- 30	+30	-128
	B	- 20	- 14	+ 6	-136
Acetate ( $\delta D = -150$ )	C	- 67	-103	-36	-117
	D	- 95	- 99	- 4	
	E	-119	-113	+ 6	
	F	-123	- 97	+26	
	G	-145	-117	+28	
<i>Photoheterotrophic Growth</i>					
Glucose + $\frac{1}{2}$ hr light	H	- 60	- 87	-27	
Glucose + 24 hr green light	I	- 60	- 91	-31	
<i>Inhibitors</i>					
Glucose, DCMU, + 24 hr light	J	- 60	- 93	-33	
Glucose, DCMU, + $\frac{1}{2}$ hr light	K	- 60	- 34	+26	

additional fractionation cannot be explained by photosynthetic carbon dioxide fixation because green light and small bursts of light are insufficient in activating the total photosynthetic reactions. It is postulated that light may be activating a cytochrome involved in electron transport in either photosynthesis or respiration, or both (reactions 3 and 9, Fig. 128) (Van Baalen and Pulich, 1973; Jones and Myers, 1963). Electron transport stimulates the formation of proton gradients, which may cause hydrogen isotope fractionation by building pools of hydrogen used in biosynthesis or respiration.

The compound DCMU, 3-(3,4 dichlorophenyl) 1,1' dimethyl urea, inhibits photosynthesis by totally inhibiting oxygen evolution (reaction 1, Fig. 128) and energy production (reaction 2, Fig. 128), and hence, carbon dioxide fixation (reactions 4 and 5, Fig. 128). Photosynthetic electron transport is active, but crippled in photoheterotrophic algae inhibited with DCMU (reaction 3, Fig. 128) (Wiessner and Fork, *Year Book 69*, pp. 695-699). *Chlorella* was grown photoheterotrophically on glucose with  $10^{-5}M$  DCMU (experiment J, Table 45). The  $\delta D$  of these cells was strikingly similar to the  $\delta D$  of cells grown photohetero-

trophically without DCMU. Photosynthetic electron transport may still be operating and providing reducing power and electrons for biosynthesis or for the activation of electron transport during respiration (Van Baalen and Pulich, 1973). Continuous light is needed for this hydrogen isotope effect, as  $\frac{1}{2}$  hr of light plus DCMU did not stimulate any additional fractionation above that seen in the dark (experiment K, Table 45).

In summary, two light effects stimulate hydrogen isotope fractionation by activating different reactions in photosynthesis. Red light activates PGA reduction, which accounts for part of the isotope effect. Photosynthetic electron transport is also responsible for another portion of the hydrogen isotope fractionation, perhaps by generating a source of hydrogen used in biosynthesis. Additional fractionation occurs in the dark during the breakdown of glucose to form the precursors of fatty acids.

#### THE STABILITY OF ORGANICALLY BONDED HYDROGEN ATOMS IN MICROALGAE TOWARD ISOTOPIC EXCHANGE WITH WATER

*M. L. F. Estep and T. C. Hoering*

A study of hydrogen isotopes in living organisms is necessary to link the exten-



sive body of knowledge on stable hydrogen isotopes in the hydrogeological cycle with that on organic molecules in a geochemical environment. Stable hydrogen isotopes are of interest because they may be useful as tracers for the biological and geographical sources of organic matter in sedimentary rocks. There is, however, some indication that hydrogen isotopes in organic geochemicals may exchange slowly with those in ground waters (Hoering, 1977). Some hydrogen in simple organic molecules is labile and exchanges rapidly with water; for example, hydrogen bonded to oxygen, nitrogen, or sulfur (see Table 46). In general, hydrogen bonded directly to carbon is less reactive and exchanges slowly (Roginsky, 1956). The question of interest in this study is whether or

not the hydrogen bonded into natural macromolecules of living cells exchanges more slowly than it does in simple organic substances.

To determine the stable hydrogen isotope composition of organic matter before exchange and diagenesis occur, Estep and Hoering (*Year Book* 77, pp. 886-891) investigated stable hydrogen isotopes in living organisms, primarily microalgae, by studying the  $\delta D$  of the total organically bonded hydrogen vs. the  $\delta D$  of hydrogen in the water of the algal growth medium. They found the  $\delta D$  (Estep, this Report) to be a reproducible value depending on the mode of algal growth. Others have contended that the  $\delta D$  of the total organically bonded hydrogen (exchangeable plus nonexchangeable) in a plant is a variable,

TABLE 46. Hydrogen Isotope Exchange in Isolated Compounds

	Compound Class	Relative Exchange Rate
<i>Acid-Base Catalyzed Exchange Reactions</i>		
$\begin{array}{c} \text{O} & & \text{O} \\    & &    \\ \text{R}-\text{C}-\text{OH} + \text{HDO} \rightleftharpoons & \text{R}-\text{C}-\text{OD} + \text{H}_2\text{O} \end{array}$	acid	extremely fast
$\text{R}-\text{OH} + \text{HDO} \rightleftharpoons \text{R}-\text{OD} + \text{H}_2\text{O}$	alcohol	very fast
$\text{R}-\text{NH}_2 + \text{HDO} \rightleftharpoons \text{R}-\text{NHD} + \text{H}_2\text{O}$	amine	very fast
$\text{R}-\text{SH} + \text{HDO} \rightleftharpoons \text{R}-\text{SD} + \text{H}_2\text{O}$	thiol	very fast
$\text{C}_6\text{H}_6 + \text{HDO} \rightleftharpoons \text{C}_6\text{H}_5\text{D} + \text{H}_2\text{O}$	aromatic hydrogen	intermediate
$\begin{array}{c} \text{O} & & \text{O} \\    & &    \\ \text{R}-\text{C}-\text{CH}_3 + \text{HDO} \rightleftharpoons & \text{R}-\text{C}-\text{CH}_2\text{D} + \text{H}_2\text{O} \end{array}$	ketone	intermediate
<i>Hydrogen Atom Transfer Exchange Reaction</i>		
$\text{R}-\text{CH}_3 + \text{HDO} \rightleftharpoons \text{R}-\text{CH}_2\text{D} + \text{H}_2\text{O}$	methyl hydrogen	slow
$\begin{array}{c} \text{H} & \text{H} & & \text{H} & \text{D} \\   &   & &   &   \\ \text{R}-\text{C}=\text{C}-\text{R} + \text{HDO} \rightleftharpoons & \text{R}-\text{C}=\text{C}-\text{R} + \text{H}_2\text{O} \end{array}$	olefinic hydrogen	slow
$\begin{array}{c} \text{H} & & \text{D} \\   & &   \\ \text{R}-\text{C}-\text{R} + \text{HDO} \rightleftharpoons & \text{R}-\text{C}-\text{R} + \text{H}_2\text{O} \\   & &   \\ \text{R} & & \text{R} \end{array}$	tertiary hydrogen	slow
$\text{R}-\text{CH}_2-\text{R} + \text{HDO} \rightleftharpoons \text{R}-\text{CHD}-\text{R} + \text{H}_2\text{O}$	secondary hydrogen	very slow

TABLE 47. The Exchangeability of Organically Bonded Hydrogen Isotopes during the Washing and Drying Procedures and in Disrupted Suspensions of the Alga *Anacystis nidulans*

Experiment	Experiment No.	$\delta D$ Organically Bonded Hydrogen
Control*	1	-257
Control washed with "heavy" water†	2	-256
Sonicated suspension incubated for 0 hr at 39°C	3	-263
Sonicated suspension incubated for 3 hr at 39°C	4	-259
Sonicated suspension incubated for 6 hr at 39°C	5	-263
Sonicated suspension incubated for 24 hr at 56°C	6	-175

\* *Anacystis nidulans* strain TX20 was grown in culture medium, CG-10, which contained the regular components (Van Baalen, 1967) with the following constituents increased in concentration: 3 g  $\text{NaNO}_3/\text{l}$  and 0.2 g  $\text{KH}_2\text{PO}_4/\text{l}$ . The chamber was continuously gassed with  $1 \pm 0.1\%$   $\text{CO}_2$  mixed with air. The  $\delta D$  of the growth medium and the wash water was -65.

† The  $\delta D$  of the "heavy" water used in washing and sonication was +140.

uncontrollable entity (Epstein *et al.*, 1976). This variability may reflect (1) the plant's chemical composition, (2) the ratio of exchangeable to nonexchangeable hydrogens, (3) the accessibility of the plant to water, and (4) an artifact of the methods used for drying the plant tissue. The study focuses on experiments with algae that aid in the interpretation of the  $\delta D$  of exchangeable and nonexchangeable hydrogen bonded into macromolecules in living organisms.

A unicellular blue-green alga, *Anacystis nidulans* strain TX20, was grown at 39°C in a glass water-jacketed growth chamber (Bellco Glass Inc., Vineland, New Jersey) with a working volume of 250 ml. The culture chamber design is an adaptation of an apparatus originally designed for the continuous culture of algae (Myers and Clark, 1944). When the algae were harvested, the cell yield was approximately 1.1 mg dry weight algae/ml growth medium/day.

*Anacystis nidulans*, collected after several days' growth in the culture chamber, was harvested by centrifugation, washed once with distilled water, recentrifuged, and suspended in distilled water. An aliquot of cells was washed

with distilled water having a  $\delta D$  value equal to the  $\delta D$  of the water in the growth medium. These cells were resuspended in 1 ml of water with a  $\delta D$  of -65 and frozen immediately (Table 47, experiment 1). The remainder of the algae were washed with distilled water that was enriched in deuterium and had a  $\delta D$  value of +140 (experiments 2-6). An aliquot of this batch was resuspended in 1 ml of water with a  $\delta D$  of +140 and frozen immediately (experiment 2). The remaining portion of cells, suspended in the heavier water, was ruptured by 2 min of sonication at 4°C with a Branson ultrasonifier operated at full power. Under these conditions, cell walls and membrane were broken, and the cell contents released without denaturation. The sonicated mixture was examined microscopically to ensure that at least 95% of the cells were disrupted.

The broken cell suspension in the "heavy" water was then incubated at either 39° or 56°C in the dark in air for the time periods indicated in Table 47. After 24 hr at 56°C, the sonicated suspension was denatured, as indicated by a distinct color change in the solution from bluish purple (from the blue-green



algal pigment, phycocyanin) to a dark green. The whole, frozen cells and the sonicated suspensions were freeze-dried, placed in an oven overnight at 100°C, and stored over P<sub>2</sub>O<sub>5</sub> in a desiccator until constant weight was reached (Estep and Hoering, *Year Book* 77, pp. 886–891).

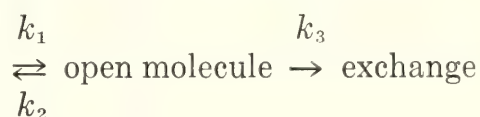
The results of experiments 1 and 2 in Table 47 indicate that the washing and drying procedure have no effect on the  $\delta D$  of total organic hydrogen. If there had been hydrogens exchanging during these manipulations, the  $\delta D$  of organic hydrogen in experiment 2 should have had a more positive  $\delta D$  than those in experiment 1. These control experiments show that the  $\delta D$  values reported by Estep and Hoering (*Year Book* 77, pp. 886–891) are not artifacts due to the washing and drying procedures.

The results of experiments 3–6 show that hydrogen in organic matter, freely in contact with water of different  $\delta D$  than that used during growth, does not exchange rapidly unless subjected to higher temperatures. Hydrogen bonded to oxygen, nitrogen, or sulfur in organic compounds of macromolecules does not exchange readily. Using tritium, Welch and Fasman (1974) have shown the exchange rate of amide hydrogens in polypeptides to be very slow (a half-life of approximately 10<sup>5</sup> min). Solvent accessi-

bility (steric considerations) and local environmental effects on the protein (pH and the binding of substrates and metal ions) account for part of the slowness of the exchange. Moreover, the tertiary or quaternary structure of organic macromolecules involves relatively rigid hydrogen bonds. These hydrogens exchange extremely slowly while in this bound form. The rate of exchange depends on the amount of time the molecule spends in a shielded, bound form vs. the time the molecule is open and hydrogen bonds are broken.

This relationship is described by the following equation:

hydrogen-bound shielded molecule



This study shows that the hydrogens bonded into macromolecules (proteins and polysaccharides) of living cells exchange much more slowly than they do when bonded into free, simple organic molecules. It is only after the cellular contents have been denaturated and their tertiary and quaternary structures are destroyed that the hydrogen atoms can exchange freely with water. In the other major class of cellular organic matter, the lipids, most hydrogen is bonded directly to carbon, and such atoms are known to exchange slowly.

## NEW TECHNIQUES: APPARATUS AND CALIBRATION

### A NEW APPROACH TO THE RESOLUTION OF OPTICAL ISOMERS: USE OF CHIRAL ELUANTS IN LIQUID CHROMATOGRAPHY

*P. E. Hare and E. Gil-Av\**

Many organic compounds can exist in one of two possible mirror-image structures called enantiomers. Their physical properties are identical except for the

rotation of polarized light in opposite directions, and their chemical properties are identical except as they interact with other optically active compounds. Con-

\* Department of Organic Chemistry, Weizmann Institute of Science, Rehovot, Israel. Some of the experiments on this project were carried out at the Weizmann Institute with the participation of Drs. A. Tishbee and S. Weinstein.

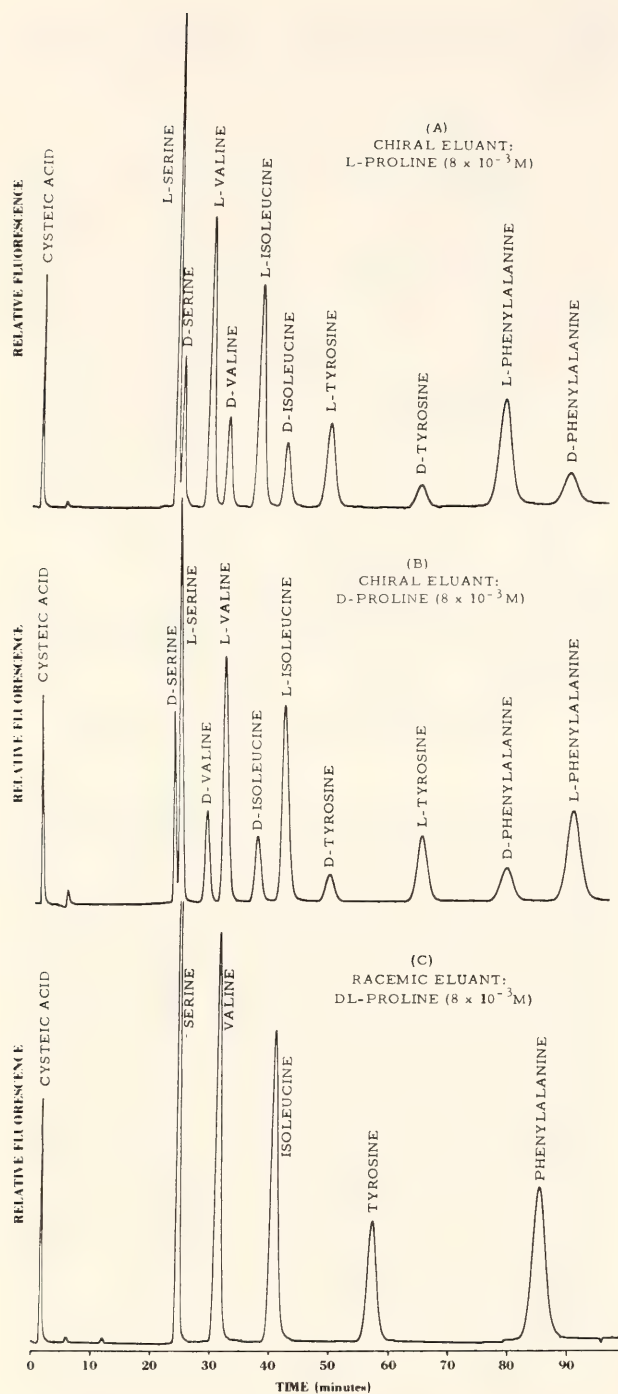


Fig. 129. Three chromatograms from the same column showing the effect of the eluant on the separation of D and L amino acid enantiomers by ligand-exchange chromatography. A mixture of five pairs of amino acid enantiomers containing 0.5 nanomole of each amino acid (0.375 nanomole L-form, 0.125 nanomole D-form) was added in each run. A solution of 0.05 N sodium acetate buffered at pH 5.5 containing  $4 \times 10^{-3}$  M copper sulfate was used in each run, with proline added as indicated. The column was  $12 \times 0.2$  cm I.D. packed with DC 4a resin. The eluant flow rate was 10 ml/hr, the reagent *o*-phthalaldehyde, flow rate was 10 ml/hr, the column pressure was 200 bars, and

sequently, the separation of enantiomers has presented a unique challenge to analytical chemists since the discovery of optical isomers by Pasteur a century ago. The present study resulted in a surprisingly simple chromatographic system that resolves the majority of the common amino acids, without prior derivatization, into their respective enantiomers. The novel feature of the system is that an optically active organic compound (L-proline), capable of coordinating with a metal ion ( $\text{Cu}^{2+}$ ), is dissolved in the aqueous *mobile* phase. This chiral ligand forms diastereomeric complexes with the D and L amino acids that are readily separable on existing chromatographic stationary phases. Compared with the related approach of resolution via a support to which a metal ion is coordinated through a covalently linked chiral ligand, the procedure developed is both simpler and more efficient.

In the initial phase of the study (Hare and Gil-Av, 1979) an ion-exchange column was equilibrated with a sodium acetate buffer containing an optically active ligand formed by the addition of L-proline and  $\text{CuSO}_4$ . Figure 129 shows the separation resulting from such a system and the reversal of elution order when L-proline is replaced by D-proline. Operating details are in the figure legend.

More recently, columns containing silica gel with an octadecyl group covalently linked (C-18 "reversed-phase" column) and essentially the same eluant have been used. This combination resulted in a marked increase in the efficiency of separation of the enantiomers.

the column temperature was  $75^\circ\text{C}$ . In (A) L-proline ( $8 \times 10^{-3}$  M) was added to the sodium acetate buffer, and effected the separation of all five pairs of enantiomers, with the L-enantiomers eluting before the corresponding D-enantiomers. In (B) D-proline ( $8 \times 10^{-3}$  M) was added, and reversed the order of elution, with the D-enantiomers eluting before the corresponding L-enantiomers. In (C) D,L-proline ( $8 \times 10^{-3}$  M) was added, and none of the pairs of enantiomers were separated.



TABLE 48. Separation Factors and Adjusted Retention Times for 19 Pairs of Amino Acid Enantiomers Chromatographed on a Reversed-Phase C-18 Column, 15 × 0.46 cm (Supelco LC-18)

Amino Acid	Form	$t'R(\text{min})$	Separation Factor $r = t'(2)/t'(1)$
(Cysteic acid)		(0) 3.75	
Aspartic acid	D	0.08	1.00
	L	0.08	
Glutamic acid	D	0.46	1.98
	L	0.91	
Serine	D	0.17	1.00
	L	0.17	
Threonine	D	0.62	1.00
	L	0.62	
Allothreonine	D	0.40	4.50
	L	1.83	
Alanine	D	0.20	2.92
	L	0.58	
$\alpha$ -Amino- <i>n</i> -butyric acid	D	1.07	3.29
	L	3.52	
Valine	D	3.80	4.82
	L	18.3	
Norvaline	D	4.3	3.07
	L	13.2	
Isoleucine	D	13.7	4.53
	L	62.0	
Alloisoleucine	D	13.8	4.38
	L	60.4	
Leucine	D	15.9	2.56
	L	40.7	
Norleucine	D	17.4	3.51
	L	61.0	
Methionine	D	9.4	2.41
	L	22.7	
Tyrosine	D	16.3	2.28
	L	37.2	
3,4-Dihydroxy-phenylalanine	D	8.7	2.24
	L	19.6	
Lysine	D	0.14	2.29
	L	0.32	
Histidine†	D	2.73	0.74
	L	2.02	
Arginine	D	1.07	1.85
	L	1.98	

\* Mobile phase: aqueous solution of copper acetate (0.008 *M*) and L-proline (0.017 *M*), pH 5. Flow rate: 0.5 ml per minute. Temperature: 25°, Pump pressure: 30 atm. Retention time of cysteic acid is taken as the approximate column void volume.

† The reversal of the order of emergence for the histidine enantiomers is ascribed to the different structure of the copper complexes formed, involving an imidazoline nitrogen coordinated to metal in the case of histidine (Österberg, 1974), as contrasted with an  $\alpha$ -amino nitrogen for the other amino acids.

Separation factors ( $r$ )<sup>†</sup> of greater than 4 have been obtained for some amino acids using this reversed-phase system, as contrasted with a maximal  $r$  value of 1.28 (for tyrosine) in the ion-exchange experiments. Table 48 lists the separation factors,  $r$ , for a series of amino acids on a C-18 column 15 cm long (Supelco LC-18). Several amino acids that were not resolved by ion exchange were readily separated on the reversed-phase columns; for example, asparagine, glutamic acid, glutamine, lysine, histidine, and arginine.

It is of interest to note that the amino acid enantiomers are eluted in reverse sequence compared with the ion-exchange system, with the D isomers preceding the L isomers when an eluant containing L proline is used. The exceptional case of histidine is discussed in the second footnote in Table 48.

In the reversed-phase system, on the other hand, it is possible that in addition to the difference of stability of the copper-coordinated species, stereoselectivity is governed in part by the partitioning of the intact diastereomeric complexes between the support and the eluant.

It is believed that such a method will have considerable impact in the study of the occurrence and role of D-amino acids in nature (Davies, 1977). Such studies have been hampered in the past by the rather cumbersome procedures required for enantiomeric analysis. Future studies might involve investigation of the possible occurrence of D-amino acids under pathological conditions and on aging. The increased interest in enantiomeric analysis in connection with nutritional problems, as well as biogeochemical studies, indicates the broad scope and need for the analytical tools being developed.

<sup>†</sup> Separation factors,  $r$ , are defined as the ratio of the corrected retention times of the two enantiomers.

## A HIGH-TEMPERATURE DIAMOND PRESSURE CELL FOR SINGLE-CRYSTAL STUDIES

*R. M. Hazen and L. W. Finger*

The miniature single-crystal, diamond-anvil pressure cell of Merrill and Bassett (1974), as modified by Hazen and Finger (*Year Book* 76, p. 655; this Report), has been adapted for high-temperature crystallographic studies at high pressure. In this device a resistance heater of 0.4-cm diameter is placed around the diamond and the gasketed sample. The heater is wound with platinum and platinum-10-rhodium thermocouple wire with the junction in the center of the two-loop winding. The furnace is operated in the manner described by Ohashi and Hadidiacos (*Year Book* 75, p. 828) in which power is applied to the winding during half the cycle of the alternating current power source. The electromotive force of the thermocouple junction is sensed during the other half of the cycle and is thus used to control power to the furnace.

The triangular steel supports of the miniature cell require no modification. Beryllium supports for the diamonds are replaced by boron carbide disks, owing to softening of beryllium metal above 200°C. Pyrophyllite insulating rings and mica disks are placed between the miniature furnace and steel components of the pressure cell, thus reducing power requirements and increasing the protection of the single-crystal diffractometer from damage caused by heating.

In the Merrill and Bassett design, three screws are tightened to apply the load. These screws are lengthened by 0.6 cm in the high-temperature design, and four Belleville spring washers of 1.0-cm diameter are inserted next to the screw heads. This modification reduces the effects of heating on the load screws.

The expected maximum temperature at 50 kbar is 700°C, on the basis of preliminary calibration experiments. It will thus soon be possible to study the



structural equations of state of minerals under conditions equal to those in the earth's crust and upper mantle.

# DESIGN OF THE DIAMOND-WINDOW, HIGH-PRESSURE APPARATUS FOR CRYOGENIC EXPERIMENTS

*H. K. Mao and P. M. Bell*

The adaptation of the megabar-cell design (*Year Book* 77, pp. 904–908) for experimentation at cryogenic temperatures had two basic requirements. One was to design the cell to be operational at temperatures close to absolute zero, where many of the metals and epoxy cements used in the cell fail because of low-temperature inversions or simply because of thermal shock. The second requirement was for a remote-controlled mechanism by which the cell could be adjusted from outside an enclosing adiabatic envelope. An additional requirement for special experiments was that it should be feasible for the cell to be operated at a range in temperature from close to absolute zero to room temperature or higher. This additional requirement arose for experiments with liquefied gases, such as hydrogen (Mao and Bell, this Report), or for experiments that might employ gas as a pressure medium.

The material requirements were satisfied by using hardened stainless maraging steel, which has no low-temperature transition (Vanadium Corporation, Vascomax steel, Rockwell hardness = C 55). The epoxy (Emerson and Cummings, Inc., Stycast-2850 FT plus catalyst 212V) used to cement the diamond anvils has a sufficiently low contraction to avoid shattering when cooled close to 0°K.

Figure 130 is a diagrammatic view of the basic apparatus. Spring-loaded screws that rotate in opposition (to avoid generating torque on the system) are used to advance the piston, which in turn forces the two diamond anvils together. The diamond anvils, cemented in place,

are shown with the rigidly mounted sample gasket in Fig. 131. The sample chamber can be filled simply by immersing the assembly in liquefied gas and then advancing the piston to seal the chamber. The stress distribution must be such that the pressure on the compressed portion of the gasket is slightly higher than on the sample.

Figure 132 shows the entire apparatus suspended in the liquid helium cryostat that was used for the liquefaction and filling of hydrogen in the cell. The cryostat and mechanical linkage were designed after apparatus of P. Chu (personal communication). Metered flow of pure hydrogen gas was first passed through a liquid nitrogen trap and then pumped into a metal cup surrounding the cell. The cell was suspended at a distance from the liquid helium (4.2°K) where the temperature was 17°K. After the liquid-hydrogen level in the cup was high enough to fill the sample chamber, remote control shafts connected to the advancing screws were rotated to seal the sample chamber and pressurize the gas at approximately 10 kbar.

After the sample chamber was filled, the entire assembly was withdrawn from the cryostat, and the cell (Fig. 130) was detached from the remote control shafts. The cell, still under pressure, could then be placed into a standard lever-arm block such as the one shown in Fig. 133. With this lever assembly it was possible to apply more force to the cell than could be applied with the advancing screws.

The procedure is the same if a gas is used as a pressure medium for a solid sample, which would be located in the sample chamber in advance. Helium (freezing pressure approximately 120 kbar at 25°C) could be used as the medium, for example, because even as a solid, helium is very weak and could be used as a nearly hydrostatic pressure medium. Figure 134 shows spectra of the ruby  $R_1$  fluorescence emission line measured in air at 1 bar and in the cell surrounded by a pressure medium of solid

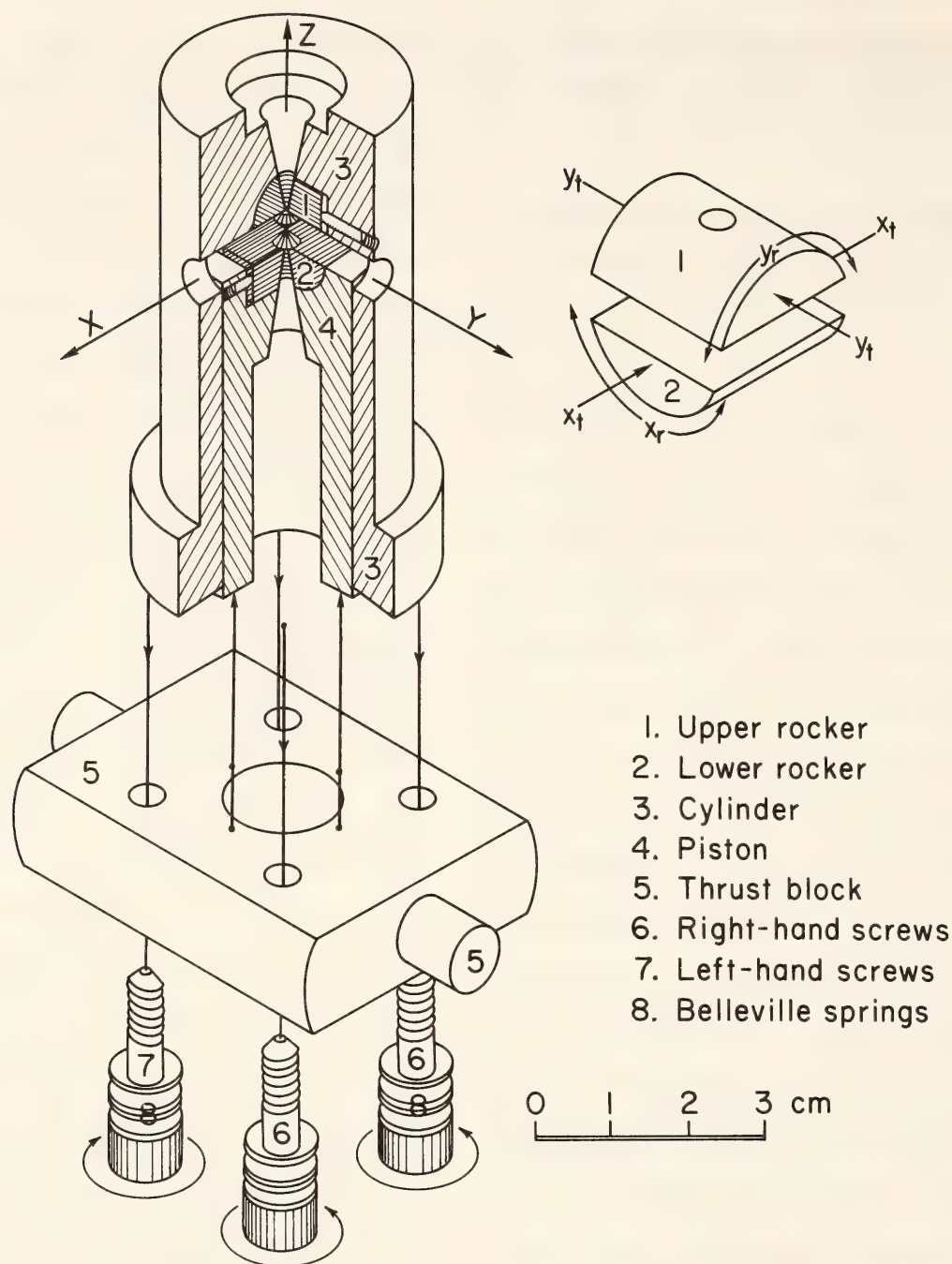


Fig. 130. Diamond-window, high-pressure cell for cryostatic experiments (see text). Inset to the right is an expanded view of the tungsten carbide support pieces (1 and 2), showing directions of translation and rotation for alignment of the diamond anvils. This cell as shown will operate to pressures of approximately 150 kbar by advancing the precision screws (6 and 7). Opposing screw directions are used to avoid torque on the remote-control system that could rupture the high-vacuum cryostat (Fig. 132).

hydrogen at 628 kbar. There is no loss of resolution or line broadening, and this result suggests that solid hydrogen is extremely weak.

The cryostatic cell will also be useful for measuring infrared and Mössbauer spectra at low temperatures, using an optical window in the cryostat.

#### RAMAN SPECTROSCOPY AT VERY HIGH PRESSURES

*S. K. Sharma*

The diamond-anvil, high-pressure cell is a device particularly well suited for spectroscopic studies at extremely high pressures. It is relatively simple in design



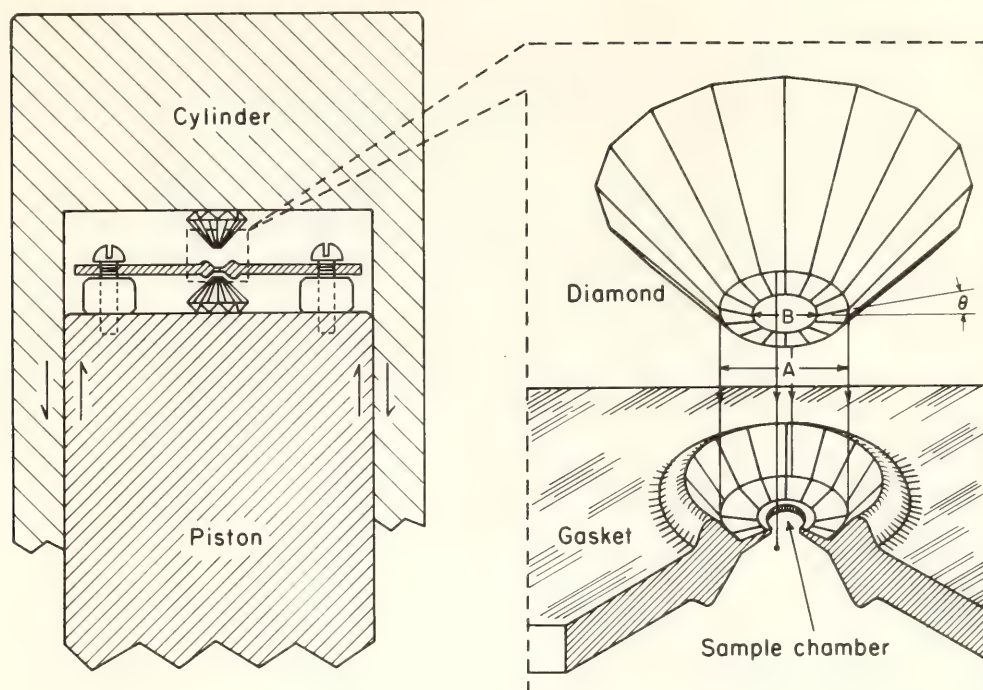


Fig. 131. Cross section of the diamond-window, high-pressure cell. Inset shows expanded view of diamond-anvil pressure face ( $A = 370 \mu\text{m}$ ;  $B = 175 \mu\text{m}$ ;  $\theta = 1.5^\circ$ ; only the upper diamond is shown).

and operation and has been used down to  $0.03^\circ\text{K}$  (Webb *et al.*, 1976), and up to  $\sim 3000^\circ\text{K}$  (Bell and Mao, *Year Book* 74, pp. 399–403; Ming and Bassett, 1974; Liu and Bassett, 1975). Recent improvements in the cell design have resulted in pressures believed to be in excess of 1.7 Mbar (Bell and Mao, *Year Book* 77, pp. 908–912; Mao and Bell, 1978). In the past ten years, spectroscopy in the cell on small samples has revealed a few problems: (1) fluorescence from the diamonds, (2) low intensities of Raman signals due to small sample volume, and (3) small numerical aperture ( $\leq 0.25$  is common) resulting in further reduction in the intensity of the Raman signal from the sample in the cell (Adams *et al.*, 1977). This report describes some solutions to these problems.

An important first step for high-pressure Raman spectroscopy in the cell is to select diamonds that exhibit low fluorescence. The fluorescence characteristics of 100 cut and uncut stones were examined while they were radiated with a 488.0- and a 514.5-nm  $\text{Ar}^+$  ion laser

beam. Of these diamonds, 48 were type I, cut for high-pressure anvils, 16 were uncut type-IIa stones, and 36 were uncut type-IIb stones. These stones were obviously preselected and do not represent average abundances in a random lot.

Fluorescence measurements on the first set of type-IIb stones failed to show any second-order spectra. All of them give a strong, single triply degenerate ( $F_{2g}$ ) first-order Raman mode at  $1333 \pm 1 \text{ cm}^{-1}$ . The fluorescence intensities in different diamonds were quantified by comparing the relative intensities of the diamond first-order Raman line with fluorescence maximum  $N = C_{1333}/C_{f,\text{max}}$  and minimum  $N_2 = C_{1333}/C_{f,\text{min}}$ , where  $C_{f,\text{max}}$  and  $C_{f,\text{min}}$ , respectively, refer to the number of counts per second at the peak positions of the first-order Raman diamond line, at the fluorescence or second-order phonon maxima and at the fluorescence minima (i.e., minimum background). The ratios  $N_1$  and  $N_2$ , respectively, thus provide a relative intensity of the  $1333 \text{ cm}^{-1}$  line with respect to maximum and minimum background.

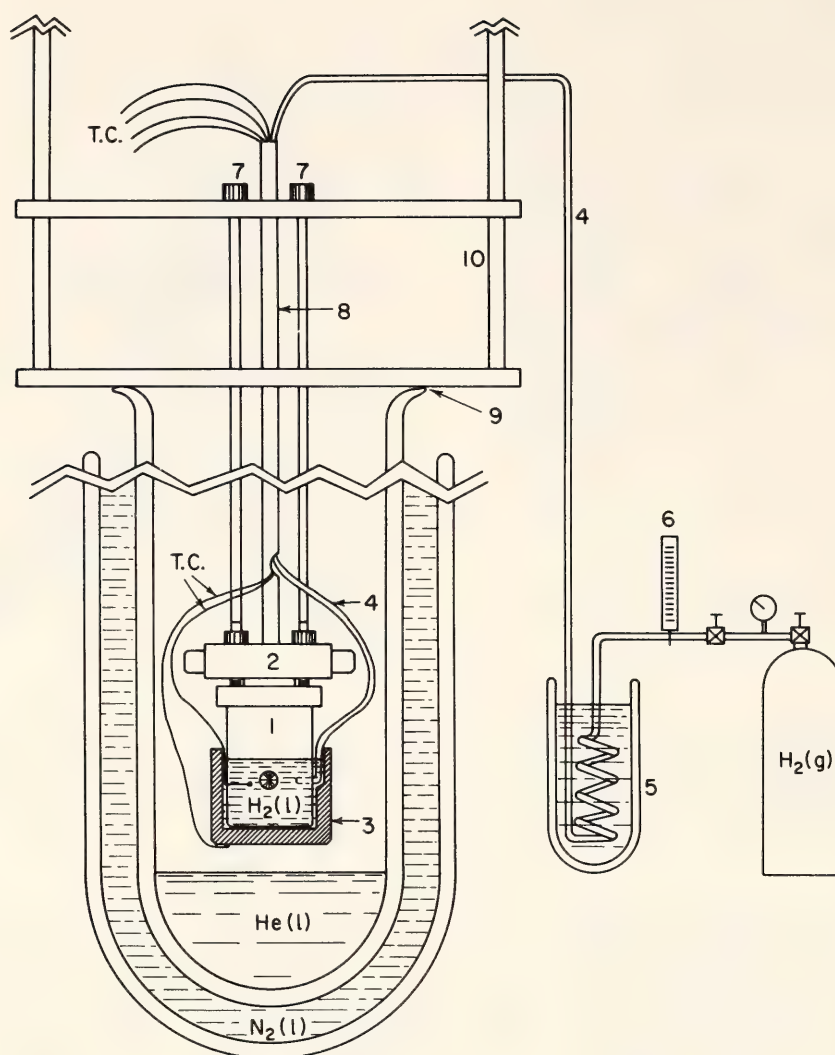


Fig. 132. Diamond-window pressure cell (1 and 2) held in liquid helium crystal (9) for hydrogen experiments (see Mao and Bell, this Report), by remote-control mechanism (7 and 8). Also shown are surrounding cup (3), gas liquification and filler tube (4), liquid N<sub>2</sub> cold traps (5), and gas-flow gauge (6).

All yellowish type-I diamonds, in general, exhibited very strong fluorescence ( $N_1 \approx 4.0$  and  $N_2 \approx 3$ ). Of 48 type-I anvils, only three showed fluorescence sufficiently low that the second-order Raman spectrum was detected. The values of  $N_1$  and  $N_2$  were in the ranges 195–132 and 1600–320. Of 16 type-IIa uncut stones, only two exhibited low fluorescence characteristics, with  $N_1 = 384$ –242 and  $N_2 = 1500$ –2180. In type-IIb diamonds, the fluorescence levels were generally lower, but some of them produced a strong and sharp fluorescence band at 500 nm because of some unknown defect or impurity in the diamond.

Of 36 type-IIb uncut stones, only 13 stones were satisfactory. These low-fluorescence diamonds can be further subdivided into two classes: (1) nine stones with lowest level of fluorescence ( $N_1 = 448$ –305,  $N_2 = 4050$ –2050) had a fluorescence background lower in intensity than the second-order diamond Raman spectrum and satisfied the criterion suggested by Adams and Sharma (1977), and (2) four stones ( $N_1 = 306$ –239,  $N_2 = 1300$ –1880) were suitable for use with strong Raman scatterers.

Thus, the acceptable type-I diamonds examined in the present study had a background 2.5 times stronger than the



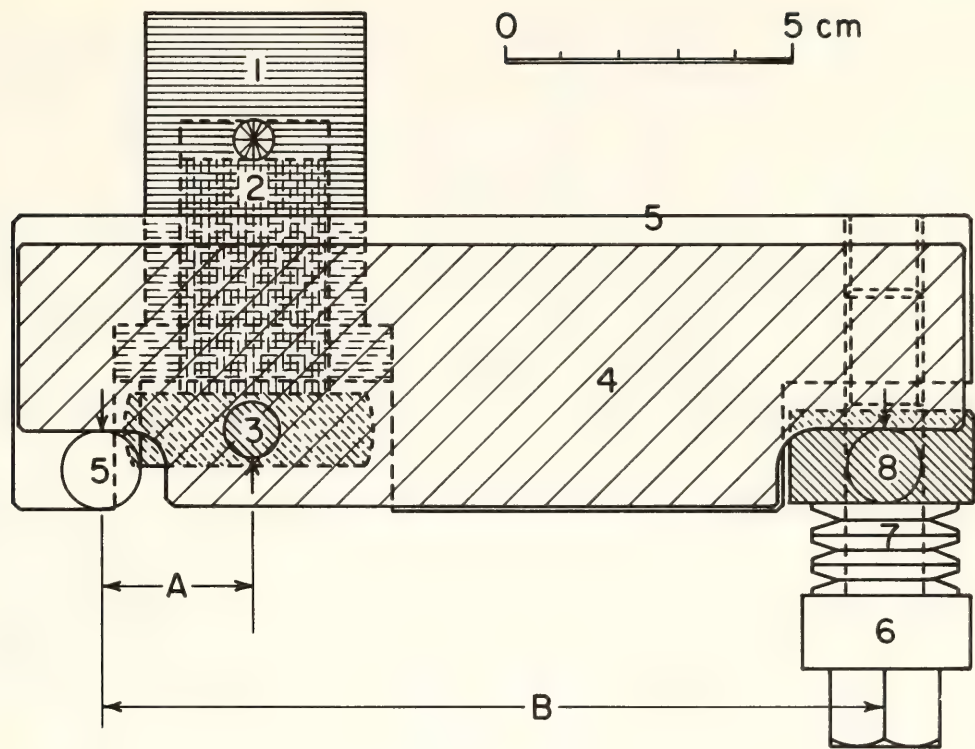


Fig. 133. Diamond-window, high-pressure cell (Fig. 130) shown assembled in lever-arm apparatus used to apply additional load on the cell. 1, cylinder; 2, piston; 3, thrust block; 4, lever arm, second class; 5, solid steel block and fulcrum; 6, advancing screw; 7, Belleville springs; 8, lever thrust block; A and B, lever factors.

acceptable type-IIb diamonds. The results of the present study support the observation of Adams and Payne (1974)

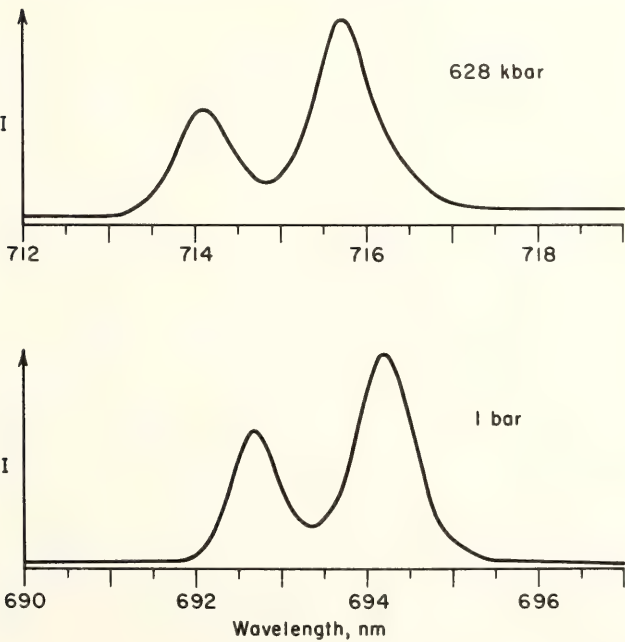


Fig. 134. Fluorescence spectra of ruby crystals at 1 bar in air and at 628 kbar in solid hydrogen. There is little loss of resolution, and it is therefore suggested that solidified gases such as hydrogen transmit pressure essentially as a hydrostatic fluid.

that type-IIb diamonds, in general, fluoresce less. The first-order Raman line in low-fluorescence type-IIb diamonds is estimated to be  $\sim 450$  times stronger than the second-order maximum. Only anvils that were free from micro-cracks and inclusions and had low birefringence patterns due to strain (Wilks, 1976; Bell and Mao, *Year Book* 77, pp. 908–913) were used for high-pressure work.

With laser radiation, diamonds usually exhibit a relatively weaker fluorescence background when excited with radiation in the red region of the spectrum than in the blue. The intensity of scattered radiation, however, is proportional to  $\lambda^{-4}$ , where  $\lambda$  is the wavelength of the exciting radiation. Because most silicates are generally weak Raman scatterers, it is advantageous to use shorter wavelength excitation radiation; only diamonds having low fluorescence background with blue (488.0-nm) excitation are satisfactory.

A 90° off-axis ellipsoidal mirror

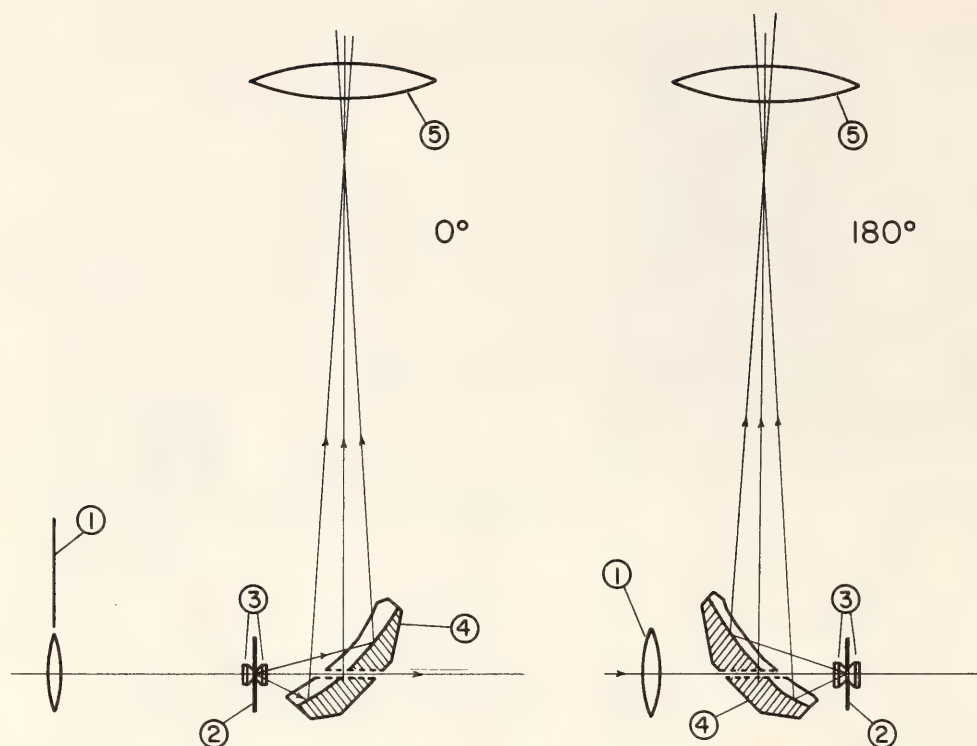


Fig. 135. Schematic diagram showing use of 90° off-axis ellipsoidal mirror in 0° and 180° high-pressure Raman experiment. 1, laser focusing lens; 2, metal gasket; 3, diamond anvils; 4, off-axis ellipsoidal mirror; 5, collecting lens.

(Perkin Elmer model 186-0110) was used to couple the cell more efficiently with the present Raman spectrometer (Sharma, *Year Book* 77, pp. 902-904) in 0° geometry. A hole of 2-mm diameter was drilled through the glass in the mirror, and a hole of 4-mm diameter through the steel mount along the axis of the steel mounting pillar bonded to its rear surface. The laser beam was thus able to pass through the hole in the mirror in either 0° or 180° scattering geometry (Fig. 135). Because the laser beam does not pass through the monochromator, relatively high laser power could be used to excite the sample without degrading performance of the spectrometer at smaller Raman shifts near the exciting line. In order to achieve higher laser power at the sample, it was necessary to use a prism premonochromator (model 300-S, Anaspec, U.K., ~85% T in a band pass of ~0.4 nm).

The original sample compartment (35.5 cm long  $\times$  26.5 cm wide) of the Ramanor (HG.2S) spectrometer was modified to improve optical coupling of

the diamond-anvil, high-pressure cell with the Jobin-Yvon monochromator. The modified sample compartment shown in Fig. 136 is 45 cm wide. In the new front plate an entrance hole for the laser beam was drilled at the position of the original hole, and a second entrance hole, used in high-pressure Raman measurement, was drilled 11 cm away from the first entrance hole. These modifications of the sample compartment made it possible to use the original facilities (i.e., the laser focusing lens mount and the X, Y, and Z sample stage) in the sample compartment as well as the modified sample position. In the modified sample position a laser focusing lens was mounted in the lens holder of a five-axis lens positioner (Fig. 136). It was possible to align the laser beam accurately with the sample by using the fine adjustments on the lens positioner.

A dual-axis translational stage was used for mounting the transfer plate of the off-axis ellipsoid (Fig. 136). The diamond-anvil, high-pressure cell was mounted on an L-shaped stand (Fig.



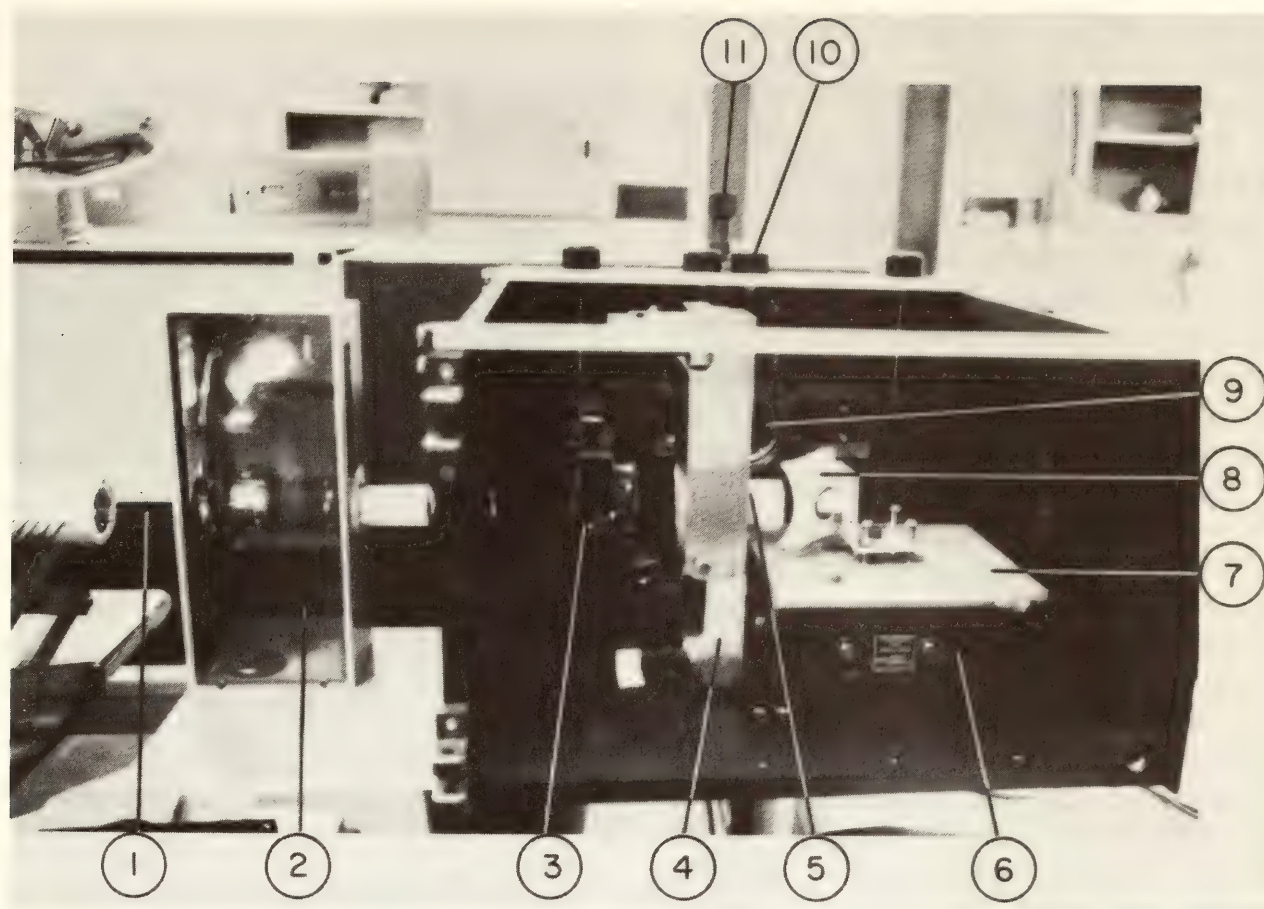


Fig. 136. The diamond-anvil, high-pressure cell and 90° off-axis ellipsoidal mirror in the modified sample compartment of the Raman spectrometer. 1, laser beam; 2, premonochromator; 3, focusing lens in a five-axis lens mount; 4, cell stand; 5, cell; 6, X-Y translational stage; 7, mirror transfer plate; 8, 90° off-axis ellipsoid; 9, collecting lens; 10, collecting lens vertical adjustment; 11, periscope viewer.

136), which could be fixed to the base plate with two bolts. By mounting the off-axis ellipsoidal mirror on the X-Y stage it was possible to focus the collected scattered radiation from the sample on the slit of the monochromator. The periscope (Fig. 136) was used to optimize the optical alignment. The strong, sharp diamond line at  $1333\text{ cm}^{-1}$  was used to make the final coupling of the cell with the spectrometer.

In this fashion it was possible to measure the Raman spectra of weak scatterers, such as  $\text{GeO}_2$  glass under pressure (Mammone and Sharma, this Report), as well as hydrogen in a thin (0.1-mm) metal gasket with a very small (0.08-mm-diameter) sample up to 630 kbar (Sharma, Mao, and Bell, this Report).

In addition, a krypton ion laser (Con-

trol Laser Corporation model 550) was added to the existing Raman facility for studying colored samples, especially iron-bearing glasses and hydrothermal solutions. Both  $\text{Ar}^+$  ion and  $\text{Kr}^+$  ion lasers are mounted on a sliding carriage to facilitate a simple, quick interchange of laser sources.

#### ABSOLUTE PRESSURE MEASUREMENTS AND THEIR COMPARISON WITH THE RUBY FLUORESCENCE ( $R_1$ ) PRESSURE SCALE TO 1.5 MBAR

*P. M. Bell and H. K. Mao*

Calibration of the ruby fluorescence pressure scale to 1 Mbar is based entirely on correlation with accurate data on shock-wave equation of state (*Year Book 77*, pp. 908–913). At pressures

above 1 Mbar, however, the scale is extrapolated. In a joint study with K. J. Dunn, R. M. Chrenko, and R. C. DeVries of the General Electric Company to analyze the observed flow in diamonds at pressures above 1.7 Mbar (Dunn *et al.*, this Report) measurements of the force, area, and pressure distribution in the diamond pressure cell were made in three experiments (13C1, 13C2, 13C3), from which the absolute pressure could be determined. These values are independent and are useful for comparison with the more precise ruby fluorescence scale to 1 Mbar. It should be practical to use the absolute measurements as a calibrated extension of the extrapolated ruby scale to 1.5 Mbar.

Measurements taken under the microscope during the increase and release of pressure of the effective area of the pressure surface were combined with values of the force on the pressure surface measured using the lever factor and the calibrated spring constant (provided by the Associated Spring Corporation) to obtain accurate values of the absolute pressure in the cell. The absolute pressure thus determined is completely independent of the ruby pressure scale and its calibration. In the present experiments, the spectral shift ( $\Delta\lambda$ ) with pressure of the ruby  $R_1$  line was used only to determine a distribution function of the pressure on the diamond face, and for this purpose the only assumption made about ruby fluorescence was that  $\Delta\lambda$  is a monotonically increasing function of pressure.

Figure 137 shows an enlarged cross section and plan view of the experimental design in the region of the sample and diamond high-pressure faces. Ruby crystals were imbedded in stainless steel located along the pressure face of the upper diamond. The plan view shows the locations where the ruby spectral shift was measured at various mean pressures (small circles) along the flat portion of the pressure surface (radius  $B$ ) and along the beveled portion (the

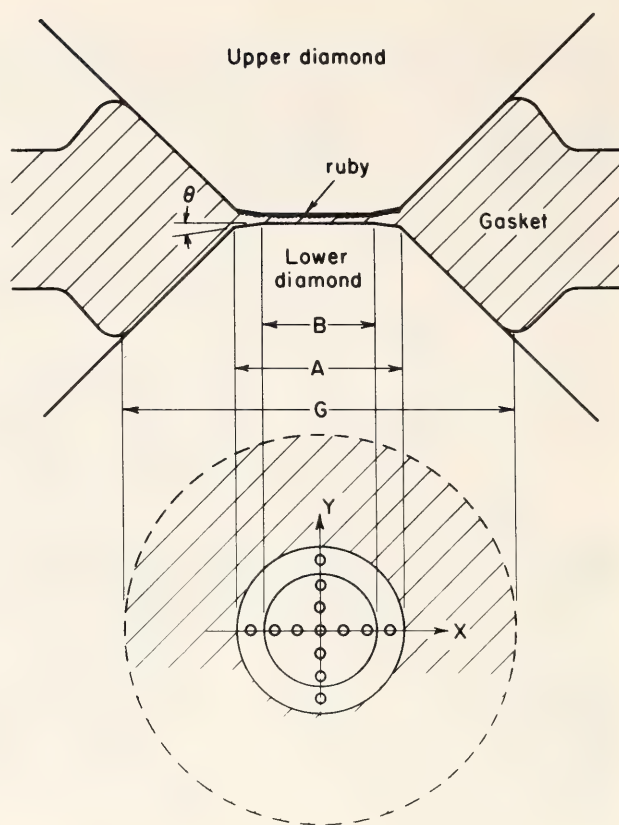


Fig. 137. Enlarged cross-sectional diagram of the diamond pressure faces in contact with the ruby sample and work-hardened stainless steel gasket assembly:  $B$ , main pressure surface, approximately  $200\ \mu\text{m}$ ;  $A$ , main pressure surface plus bevel, approximately  $300\ \mu\text{m}$ ;  $G$ , gasket contact surface, approximately  $800\ \mu\text{m}$ ;  $\theta$ , bevel half-angle,  $\sim 1.5^\circ$ . Small circles along  $X$  and  $Y$  (approximately  $20\ \mu\text{m}$  in diameter) indicate points upon which the laser beam was focused to excite fluorescence in the pressurized ruby crystals.

circular ring between the flat pressure face and the steep faceted pavilion region of the diamond).

The dimensions and positions of each point where ruby  $R_1$  spectra were taken were determined at high pressure through the microscope with a micrometer ocular; thus it was possible to obtain the areal distribution of pressure accurately. In addition, the total load divided by the area gives the average pressure independently, which can be compared directly with the ruby spectral shift.

Figures 138, 139, and 140 show plots of the spectral shift of the ruby  $R_1$  line ( $\Delta\lambda$ , nm) as a function of distance from the center of the pressure face. Figure



140 shows  $\Delta\lambda$  profiles across the pressure face in experimental run 13C3 in which the highest peak pressure was reached. The arrows indicate that  $\Delta\lambda$ , a function of pressure, increased in successive steps numbered 1–3. In step 4 (Fig. 140B) the load was increased above that of step 3 (Fig. 140A), but  $\Delta\lambda$  fell slightly in the central area of the face, whereas  $\Delta\lambda$  at the margins rose. This change in gradient was apparently caused by the onset of flow of the diamond in the central region. In succeeding steps (5–7) the load was released and  $\Delta\lambda$  fell in response.

The average  $\Delta\lambda$  per unit area was obtained for each step by integration over and division by the entire circular area of diameter  $A$  (Fig. 137). The in-

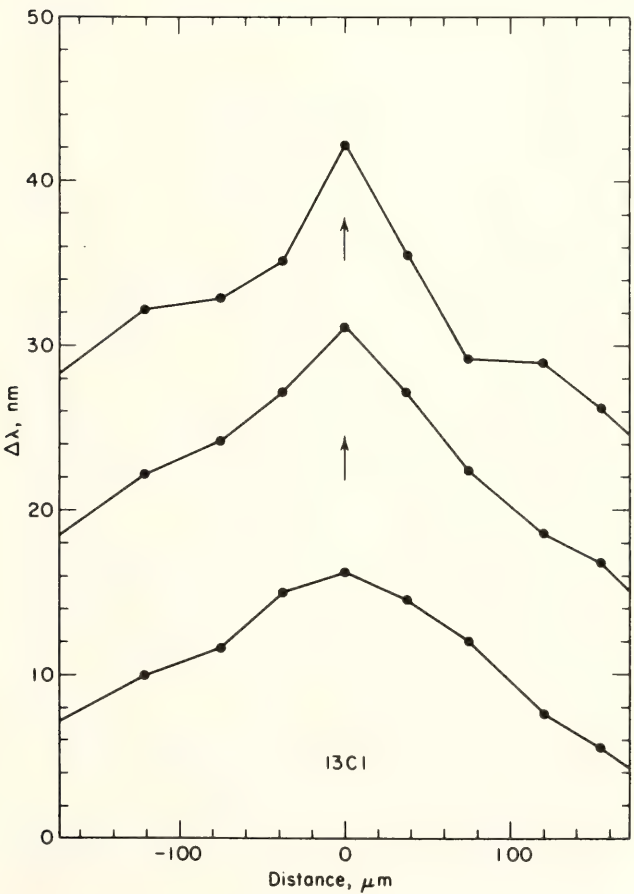


Fig. 138. Spectral shift ( $\Delta\lambda$ , nm) of the ruby  $R_1$  fluorescence line from its wavelength value at 1 bar. The  $\Delta\lambda$  were measured at points along the X direction shown in Fig. 137. These profiles were measured in experiment 13C1 at increasing loads 1, 2, and 3. One of the diamond anvils failed as the load was increased above step 3.

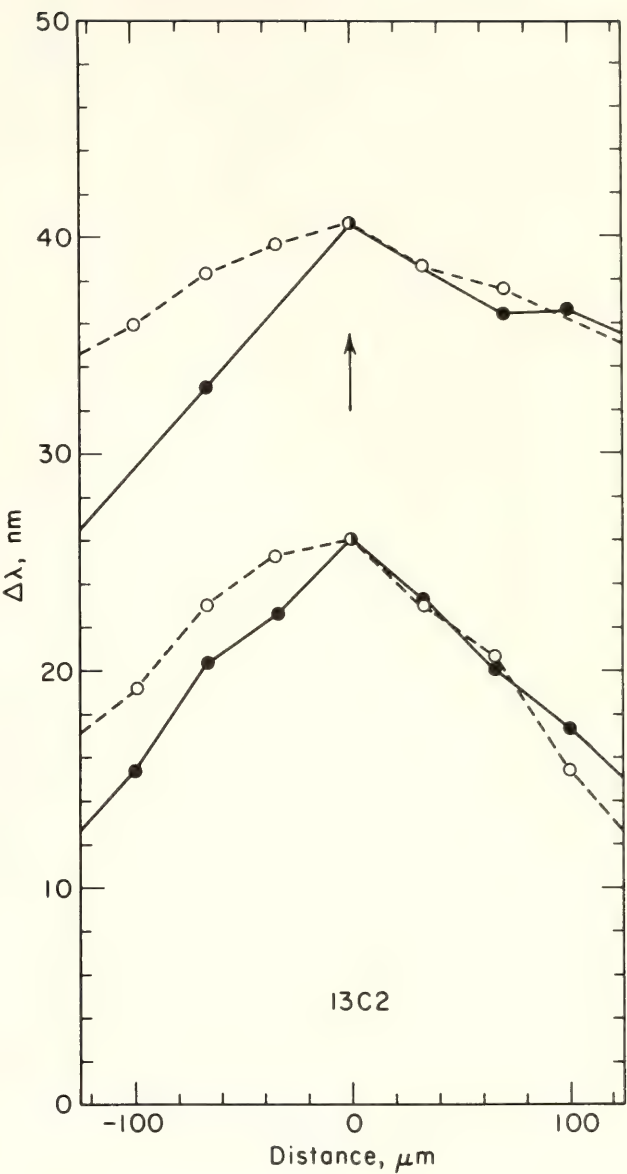


Fig. 139. Spectral shift ( $\Delta\lambda$ , nm) of the ruby  $R_1$  fluorescence line from its wavelength value at 1 bar. The  $\Delta\lambda$  were measured at points along the X (solid line and circles) and Y (dashed line and open circles) directions indicated in Fig. 137. These profiles were measured in experiment 13C2 at increasing loads 1 and 2. Further increase in load resulted in failure of one of the diamonds.

tegration required interpolation of  $\Delta\lambda$  measurements made along the X and Y directions (Fig. 137) to a smooth curved surface.

The average  $\Delta\lambda$  is plotted against the average pressure in Fig. 141 for comparison of the measured pressure (as defined by the actual load divided by the circular area of diameter  $A$ , Fig. 137) with the pressure calibration curve

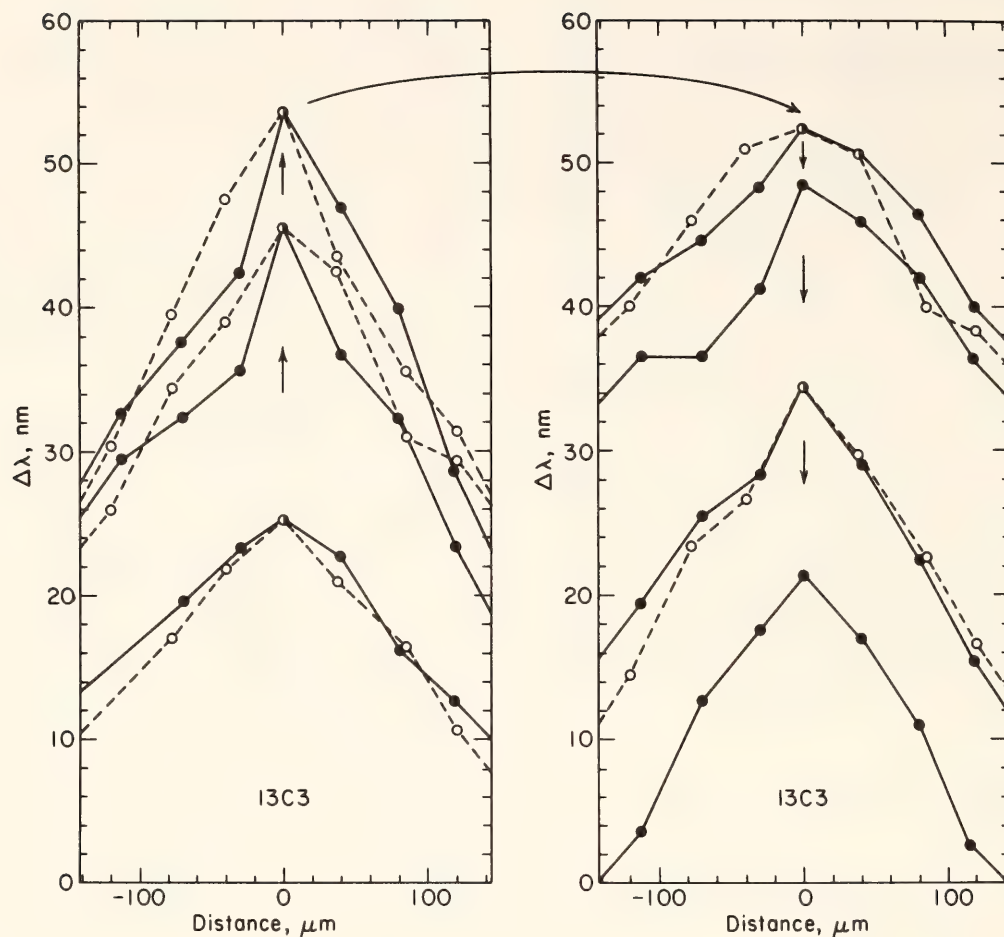


Fig. 140. Spectral shift ( $\Delta\lambda$ , nm) profiles for experiment 13C3 (similar to those shown in Figs. 138 and 139 for experiments 13C1 and 13C2). (left diagram) The load was increased in incremented steps 1, 2, and 3, corresponding to the three profiles. (right diagram) Step 4 increase in load produced no increase in the peak  $\Delta\lambda$  but did result in a change in the radial distribution of  $\Delta\lambda$ . In steps 5, 6, and 7 the load was being released.

(dashed line, Fig. 141). The random error in average  $\Delta\lambda$  is estimated to be  $\pm 15\%$ , resulting from the combined errors of positional measurement ( $\pm 20 \mu\text{m}$ ) and of areal interpolation. Random errors in the average pressure ( $\pm 0.1 \text{ Mbar}$ ) result from uncertainty in the spring constant and spring hysteresis (15%), and in the measurements of the spring length.

Systematic errors due to reversible piston-cylinder friction are negligible, on the basis of load measurements (made without the diamonds in place). Other systematic errors are caused by losses of force to the gasket region (the circular ring between diameters  $A$ , 0.29 mm, and  $G$ , 0.9 mm, Fig. 137, measured at pressure by micrometer). The pressure increase in the unsupported gasket is limited by its strength to less than 0.02 Mbar and

would therefore cause a maximum error of  $+0.1 \text{ Mbar}$  in the pressure measurements. This error is always positive in sign. It is almost constant in magnitude at pressures greater than 0.2 Mbar, at which the gasket almost ceases to flow further and thus the dimension  $G$  does not increase further. It is observed that at higher pressures there are only minor displacements in the sample and gasket regions. The systematic error is constant and therefore is a large percentage error at low pressure but only a small percentage error at pressures in the megabar region.

The curves of the average measured pressure shown in Fig. 141 lie parallel to the calibrated pressure curve, the approximately constant difference being due to the systematic error referred to above.



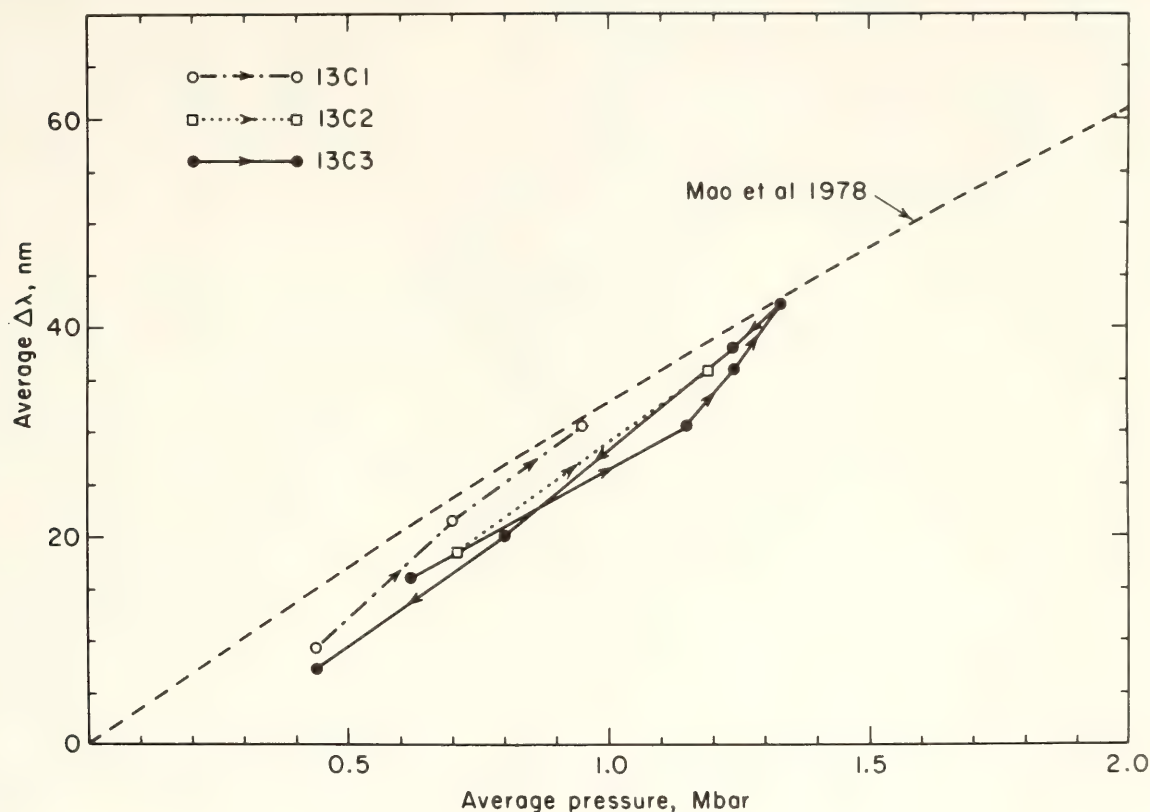


Fig. 141. Plot of the average  $\Delta\lambda$  obtained by integrating  $\Delta\lambda$  at the points shown in Figs. 138–140 over the circular area of diameter  $A$  (Fig. 137) vs. the average pressure, obtained by dividing the force by the circular area of diameter  $A$ . Dashed line is from the pressure calibration curve of Mao *et al.* (1978).

This difference is relatively small if one considers the errors. The statistical random error will be greatly reduced when a significant number of experiments at these extreme pressures are conducted. The uncertainty of the measured pressure relative to the calibrated pressure is within 10%, which is within the gross uncertainty of the calibration curve and its extrapolated extension.

#### ACCURATE CHARACTERIZATION OF THE MACROSCOPIC FLOW PRODUCED IN DIAMONDS AT 1.7 Mbar

*K. J. Dunn,\* R. M. Chrenko,\* R. C. DeVries,\*  
P. M. Bell, and H. K. Mao*

In experiments recently reported at pressures of 1.7 Mbar, plastic flow occurred in one of the diamond anvils, a

phenomenon never before observed at 25°C (Bell and Mao, *Year Book* 77, pp. 908–913). Changes in the pressure distribution reflected the resulting smoothly deformed zone, which owing to the permanent nature of the flow, could be preserved for examination and measurement on release of the pressure and removal of the diamond.

Properties of both diamonds from the 1.7-Mbar experiment and other diamonds that survived experiments in the range 1.3–1.7 Mbar were analyzed and characterized in an attempt to reveal properties that influence their strength at high pressures. These findings may prove useful in guiding the selection of diamonds and in designing future experiments at pressures above 1 Mbar.

#### *Analysis of the Diamonds*

The surface profiles on the high-pressure faces of the diamond anvils used

\* General Electric Company, Corporate Research and Development, Schenectady, New York 12301.

in the experiments were measured with a profilometer (Model 3, Talysurf, manufactured by Taylor and Hobson, England). The profilometer has a diamond stylus of  $2.5\text{-}\mu\text{m}$  diameter and a maximum sensitivity for detecting surface variations as small as  $130\text{ \AA}$ . The surfaces of the diamonds in experiments at pressures below 1.7 Mbar, measured before and after the experiments, showed no detectable changes that would have indicated plastic deformation. The results of measurements of the diamonds after use in the experiment at 1.7 Mbar are shown in Fig. 142 at three different scales. It can be observed that both diamond-anvil faces are beveled with an angle of about  $1\text{--}2^\circ$  and diameters of approximately  $300\text{ }\mu\text{m}$ . The central flat pressure face has a diameter of  $150 \pm 1\text{ }\mu\text{m}$ . At the most sensitive scale, a permanent bell-shaped depression can be observed at the center of the upper diamond with a depth of more than

$2300\text{ \AA}$  relative to the periphery of the center flat face.

The opposing (lower) diamond did not show measurable deformation. The surface irregularities shown on the most sensitive scale are within  $300\text{ \AA}$  and appear to be grinding marks left from the final surface-polishing process that were deeper than those of the upper diamond.

#### *Nomarski Interference Micrographs*

Nomarski interference photomicrographs of the pressure faces of the two diamonds taken after the experiment at 1.7 Mbar are shown in Figs. 143 and 144. Figure 143A shows the deformed surface of the upper diamond; Fig. 143B shows a magnification of the central part of Fig. 143A. In Fig. 143A the deformed portion of the originally flat pressure face can be seen. The depression and face appear to have parallel ridges, but at higher magnification of the same area (Fig. 143B) the surface appears smooth and without observable cracks; hence it is suggested that the cause of the image contrast of the ridges is beneath the surface. The direction of the ridges was determined by cathodoluminescence to be parallel to the  $\{111\}$  planes. The contrast could have been caused by large strains beneath the surface associated with a high density of dislocations generated by the plastic deformation.

Figure 144A shows the surface of the pressure face of the lower diamond at a magnification of  $\times 300$ , and Fig. 144B shows the center part of Fig. 144A at a magnification of  $\times 750$ . Several sets of parallel lines are present on the center flat face (Fig. 144A,B). They are believed to be grinding marks left from the final polishing process.

Figure 145 is a pressure-temperature diagram showing the observed threshold of plastic deformation of diamond crystals, based mainly on relatively high-temperature experiments (DeVries, 1975). It is interesting, and possibly

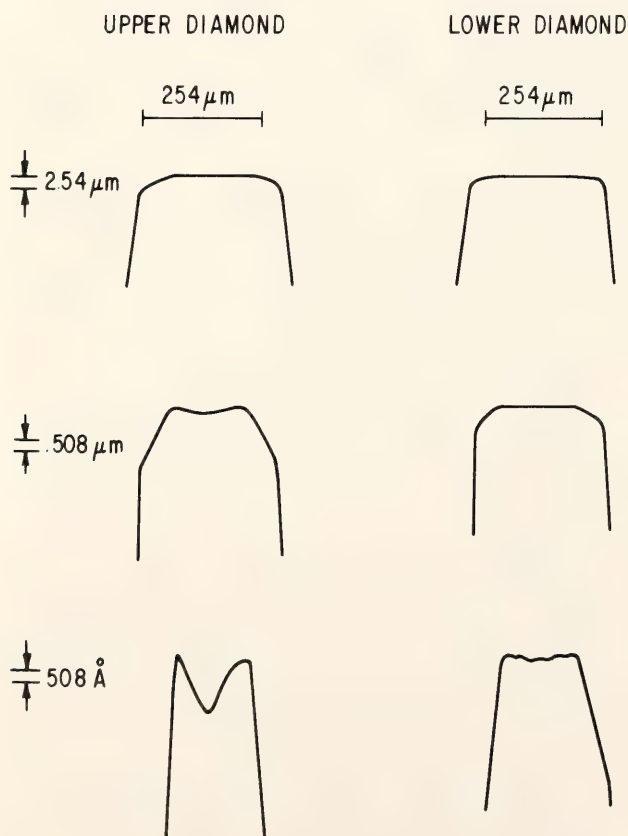


Fig. 142. Surface profiles measured on the two diamonds recovered from experiment 13C3.



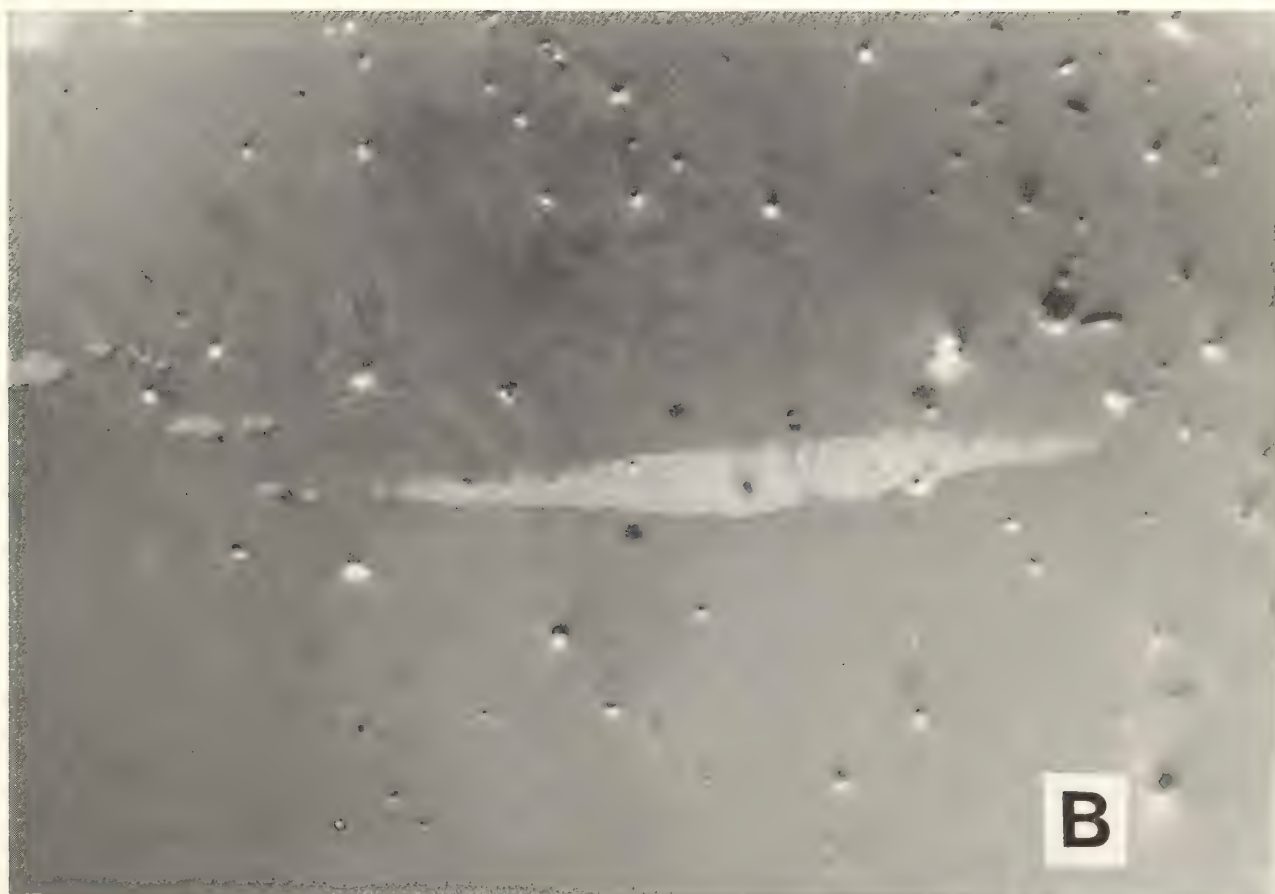


Fig. 143. Nomarski interference photomicrographs of the pressure face of the upper diamond used in experiment 13C3. Note: Remnants of the gold-palladium coating used for an electron microscope study can be observed. (A) Deformed pressure face at  $\times 300$ . (B) Magnification at  $\times 1500$  of a portion of the central area shown in A.

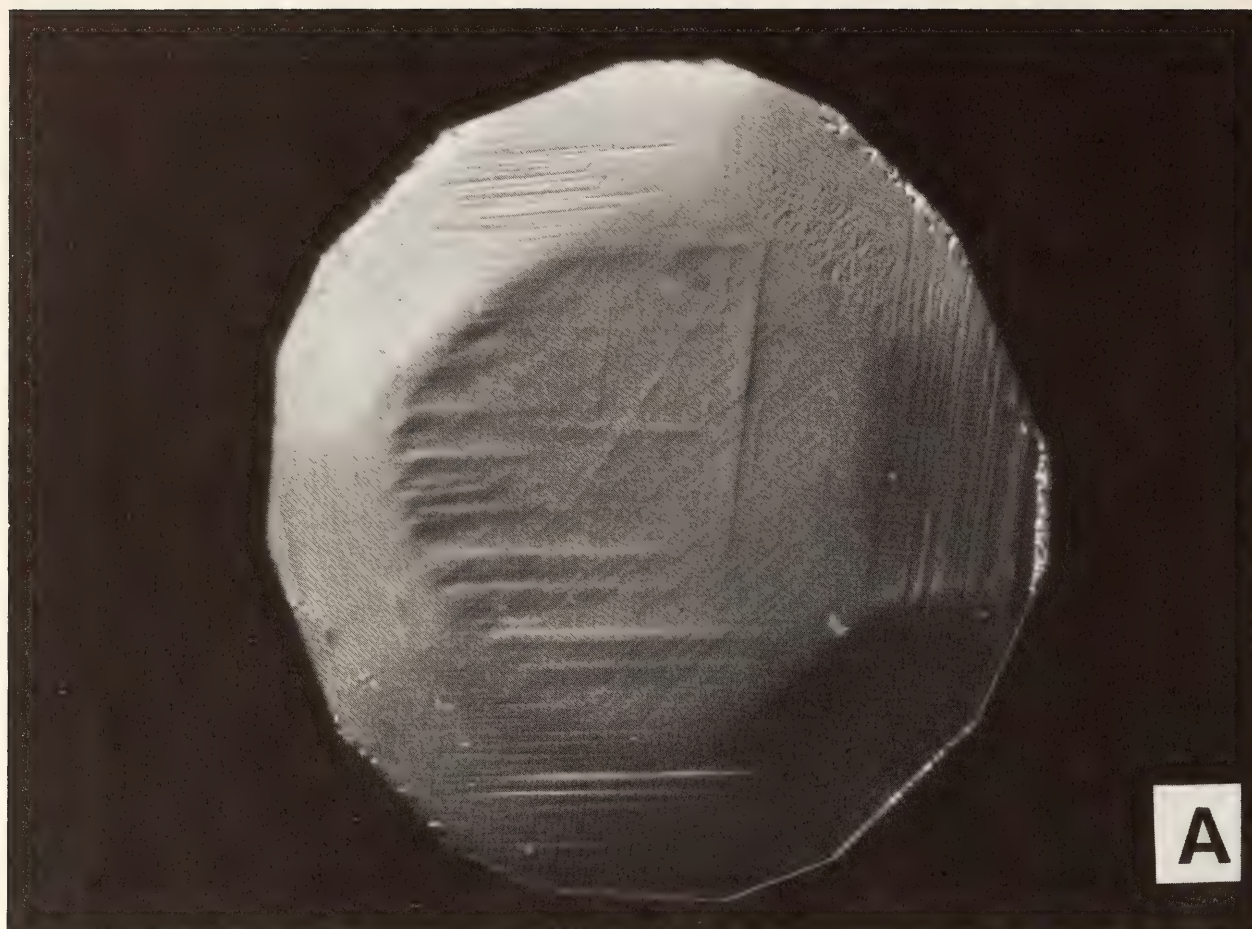


Fig. 144. Nomarski interference photomicrographs of the lower, undeformed diamond used in experiment 13C3 at two magnifications: (A)  $\times 300$ ; (B)  $\times 750$ .



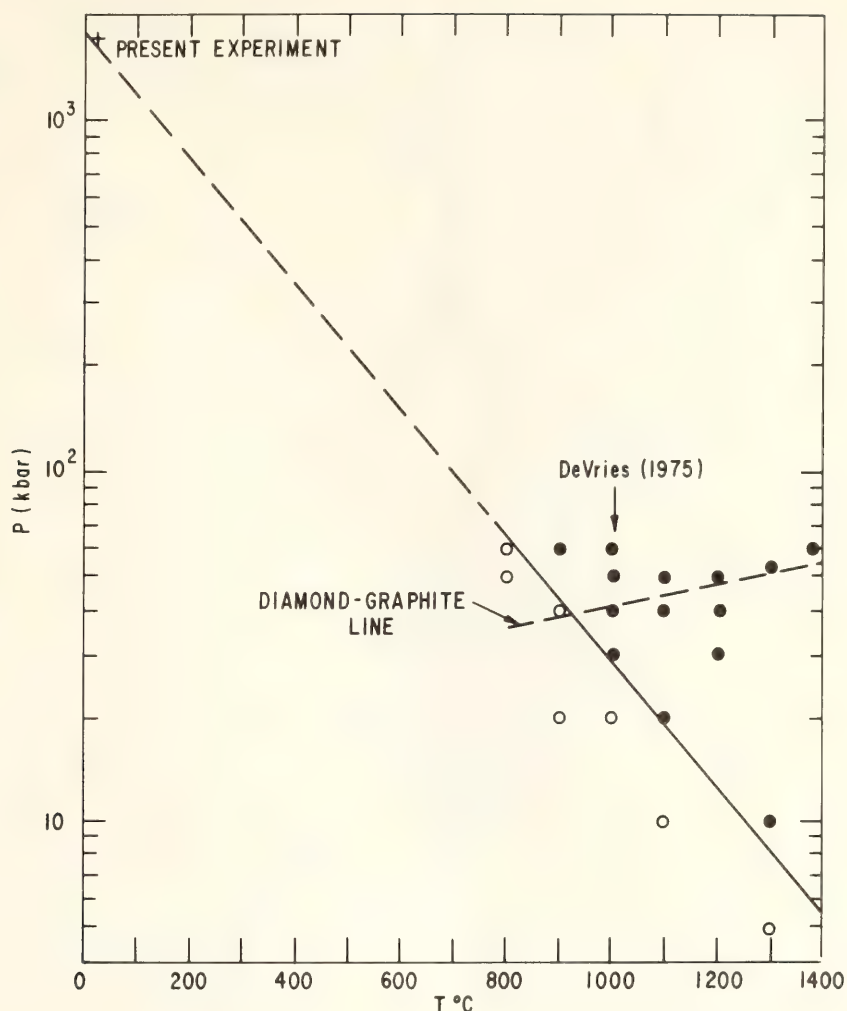


Fig. 145. Pressure-temperature diagram for plastic deformation of diamond showing the data of DeVries (1975) (open circles, no deformation; solid circles, deformation occurred) and the present experiments (plus sign).

significant, that a linear extrapolation of the threshold line to room temperature is consistent with the pressure of 1.7 Mbar at which plastic deformation occurred in one of the diamonds. To establish firmly the true threshold in that region, several more definitive results at lower temperatures would be required.

#### *Cathodoluminescence*

The two diamond anvils used in the experiment at 1.7 Mbar were also examined by the cathodoluminescence technique. A 30-keV electron beam was focused upon an area approximately 200  $\mu\text{m}$  in diameter. The beam current was approximately 9  $\mu\text{A mm}^{-2}$ . The resulting

luminescence in the pressure face of the lower diamond was observed as a homogeneous blue background without pattern. This emission is the commonly observed band A cathodoluminescence from diamond whose uniformity indicates a lack of structural deformation. The cathodoluminescence image of the upper anvil that was deformed contains bright lines on a deep-blue background. These lines could arise from the H3 emission system with the zero phonon line at 503 nm, which was observed to be associated with slip traces or dislocations in natural diamonds by Hanley *et al.* (1977).

The surface normal of the pressure face of the upper diamond was determined to be close to [741]. Figure 146

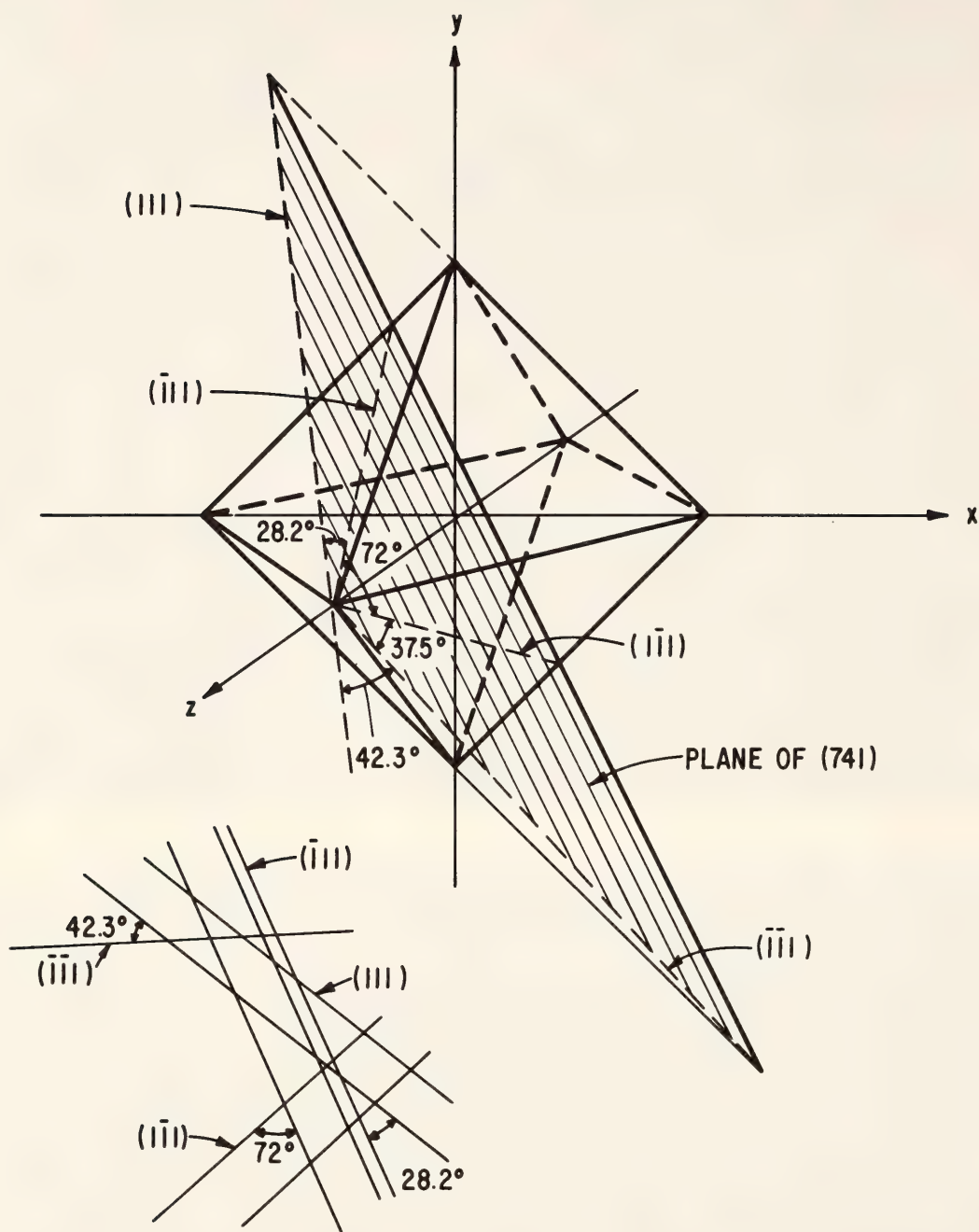


Fig. 146. Geometric construction of the (741) plane in the diamond structure on which are shown  $\{111\}$  plane intersections.

shows a geometric construction of the (741) plane on which the intersection of the  $(\bar{1}11)$  and  $(11\bar{1})$  planes is approximately  $28^\circ$ . Certain lines on the cathodoluminescence image of the pressure face of the deformed diamond appear to correspond to  $(1\bar{1}1)$  and  $(\bar{1}\bar{1}1)$ . This geometric coincidence suggests that the lines could originate from slip traces or deformation, some of which may have been present in the diamond before the experiment.

### *Infrared Absorption*

In order to determine whether the various diamond anvils had physical properties that could influence their behavior under high pressure, infrared absorption spectra were measured on all the diamonds that survived the experiments. The maximum absolute transmissions observed with a Perkin Elmer 521 spectrophotometer were only about 4%, yet the expanded spectra were of suffi-



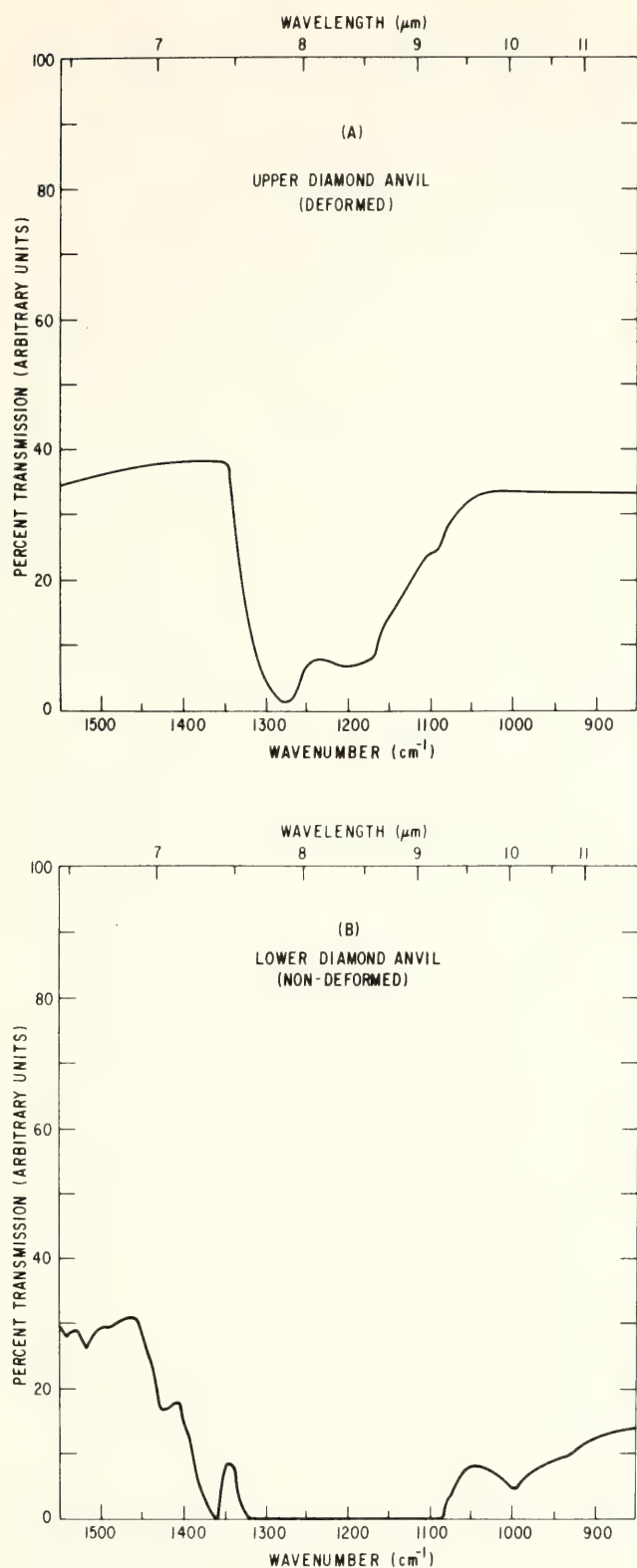


Fig. 147. Infrared absorption spectra of (A) the upper, deformed and (B) lower, non-deformed diamond anvils after being used in experiment 13C3.

cient quality to show differences among the diamonds. The relevant portions of the spectra ( $900\text{--}1500\text{ cm}^{-1}$ ) for the upper, deformed and the lower, nonde-

formed diamonds from the experiment at 1.7 Mbar are shown in Fig. 147A,B.

These spectra show that both diamonds belong to the type-Ia classification and that the deformed diamond contains approximately 500 ppm of nitrogen, as determined from the absorption at  $1280\text{ cm}^{-1}$ . The nondeformed diamond had complete absorption in the region  $1100\text{--}1300\text{ cm}^{-1}$  and contains appreciably more nitrogen impurity.

Another difference is that the spectrum of the deformed diamond contains no absorption at  $1370\text{ cm}^{-1}$  whereas the spectrum of the nondeformed diamond has complete absorption at  $\sim 1370\text{ cm}^{-1}$ . This absorption band has been related to nitrogen platelets observed in type-Ia diamonds. The plastic deformation of the upper diamond, which contains few or no platelets, and the lack of plastic deformation of the lower diamond, which contains platelets, are consistent with the results of a study on the plastic bending of diamond. Namely, type-I diamonds that contained platelets of nitrogen were more resistant to plastic deformation than diamonds that contained no platelets, in that higher stresses were needed to deform the type-I diamonds. Moreover, when the type-I diamonds did deform, the deformation was confined almost exclusively to the platelet-free regions. Transmission electron microscope results showed that the movement of dislocations was efficiently blocked by the platelets (Wild *et al.*, 1967). Infrared absorption spectra of the two nondeformed diamonds that survived pressures below 1.7 Mbar also showed strong absorption at approximately  $1370\text{ cm}^{-1}$ , indicating the presence of platelets in these crystals as well.

The presence of dislocations and perhaps large amounts of nitrogen may also influence plastic deformation of diamonds. On the basis of the present results, however, it appears that the observation of the absorption band at  $1370\text{ cm}^{-1}$ , related to the presence of platelets, is an indication that such a diamond

would be less prone to plastic deformation in a high-pressure experiment.

The fact that one of the diamonds flowed plastically on a macroscopic scale while its opposing diamond did not flow in the 1.7-Mbar experiment appears to be related to the concentration of platelets as impurity constituents. The diamond that flowed was free of platelets, on the basis of its infrared spectrum. The diamond that did not flow had a high concentration of platelets. These results are consistent with past studies on the plastic bending of diamond.

The observed plastic deformation appears as a smooth indentation centered in a zone of high birefringence. On the 100–500 Å scale, the deformation is also observed as smooth flow, similar to the plastic deformation observed in diamonds at temperatures above 1500°C (Evans and Wild, 1965). This is the first reported evidence of plastic flow in a single-crystal diamond resulting only from high pressure at room temperature. This type of deformation is distinguished from previous reports (Ruoff, 1977), where only fracture was determined to have occurred in observations on the 100-Å scale.

#### A MICROANALYTICAL TECHNIQUE FOR DETERMINATION OF ALUMINUM IN AQUEOUS SOLUTIONS

*John B. Brady and John D. Frantz*

Among the major elements of the earth's crust, aluminum is noted for its low concentrations in natural and experimental aqueous solutions equilibrated with common minerals. Special analytical techniques are available to detect aluminum concentrations on a parts-per-billion level (for example, May *et al.*, 1979), but these require a relatively large volume (100 ml) of solution. In order to study aluminum in aqueous solutions at crustal temperatures and pressures using cold-seal pressure vessels,

it was necessary to develop an analytical technique that could measure low aluminum concentrations in microliter samples. The flow-cell colorimetric method developed by Frantz and Hare (*Year Book* 72, pp. 704–706) for measurement of silicon and used by Popp and Frantz (1979) for measurement of chlorine has been successfully modified for measurement of aluminum. The modification is based on the colorimetric determination of aluminum hydroxyquinolate in a carefully buffered and mixed "ferron" solution.

The flow-cell colorimetric method entails (1) injecting and mixing of a small volume of sample into a continuously flowing stream of reagent to produce a colored reaction product, (2) passing of the sample-reagent mixture through the low-volume optical cell of a flow-cell colorimeter, (3) integrating the observed absorption over the time interval of the sample spike, and (4) comparing the integrated absorption with that of standard solutions. The advantages of this type of colorimetry include the following: (1) a relatively small volume of sample is required because of the small volume of the absorption cell, (2) multiple determinations of samples and standards are facilitated by the ease of sample introduction, and (3) any time dependency of sample-reagent reactions is overcome because of the dynamic nature of the measurement. As a result of recent developments in liquid chromatography, nearly all the required equipment is now available commercially.

The details of the flow-cell system are shown in Fig. 148. An aluminum-complexing reagent solution is pumped with approximately equal flow rates through two plastic tubes that are ultimately joined downstream. A compressed-air-operated double switch on one of the flow lines directs the flow to either a sample loop or a bypass loop. Samples are introduced by means of a specially constructed pipette holder (see inset, Fig. 148). When a 1-μl sample



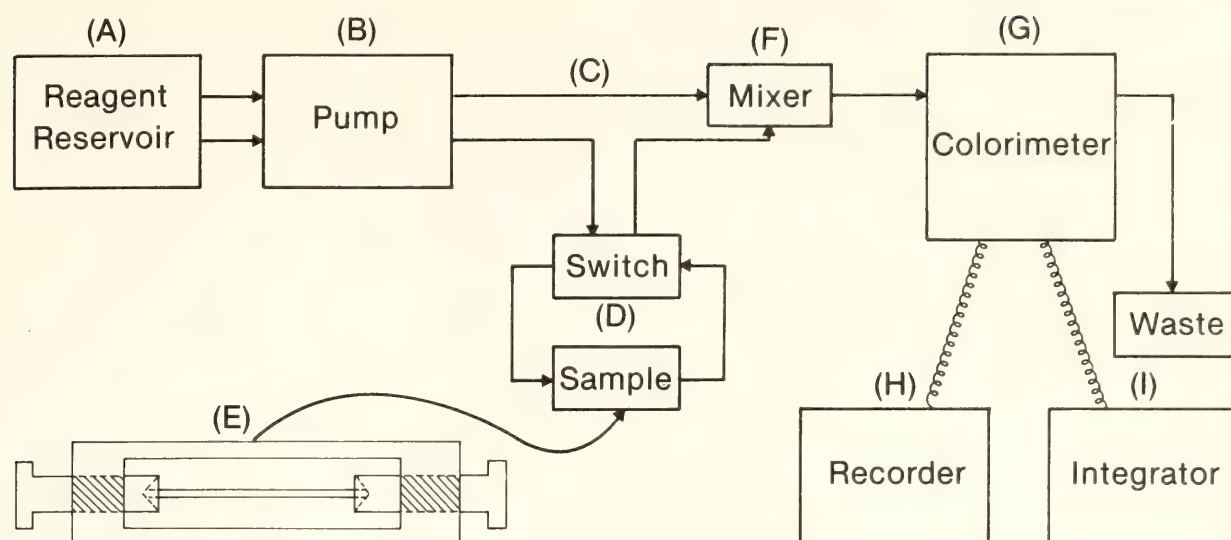


Fig. 148. Schematic diagram of the colorimeter flow system. Details of the sample pipette holder are shown in the inset. (A) Reagent is "ferron," sodium acetate, and acetic acid. (B) Gilson Minipuls 2 peristaltic pump, 0.030-in pump tubing, pump setting = 300. (C) Zeus Industrial Products 32-gauge Teflon tubing. (D) Chromatronix Inc. PA-875 switches in tandem. (E) Dade Volupette pipette P4521-1. (F) Mixer and other junctions made with Gilson polypropylene connectors. (G) Gilson Holochrome UV Monitor HM/HLPC. (H) Hewlett-Packard Recorder 7132A. (I) Spectra-Physics Autolab Minigrator.

pipette is in place, the switch can direct reagent flow through the sample pipette carrying the sample solution to the mixer where the two flow lines are joined. The flow passes on through a colorimeter and through enough additional tubing to assure a reasonable back pressure. Absorption is monitored at 370 nm by a chart recorder and an electronic integrator.

The complex-forming reaction between aluminum and "ferron" (8-hydroxy-7-iodo-5-quinoline sulfonic acid) is pH sensitive. Therefore, to ensure accurate results, it is necessary to buffer the ferron solution in the neighborhood of pH=5. Because of the relatively high HCl concentrations used in the aluminum solutions studied, a concentrated buffer solution (2M sodium acetate, 0.2M acetic acid) was mixed with an equal volume of the ferron solution (0.25 g/l). With this buffered ferron solution, a difference in HCl concentration between an unknown and the standards of an order of magnitude introduces an error of only about 2%. Because of the formation of iron hydroxyquinolate, the tech-

nique will not work (without iron extraction) for iron-bearing solutions if the iron content is unknown.

Although the absorption peak height is a function of aluminum concentration, peak area has proved to be a more reliable parameter. Typical peaks from a sequence of standard solutions are shown in Fig. 149. The peaks last for 60–90 sec and have been spaced at intervals of about 150 sec. One standard deviation from the mean of a series of replicate measurements of the same sample solution is generally less than 2–3% of the peak area. In practice, four or five 1- $\mu$ l samples of an unknown are alternated with the same number of each of two to four bracketing standard solutions. Although the time-integrated absorption appears to be strictly linear with concentration only for aluminum concentrations below 5 mM, a linear approximation is followed up to at least 40 mM for closely bracketing standard solutions. A representative standard curve is shown in Fig. 150. The high density of the buffered ferron solution leads to addi-

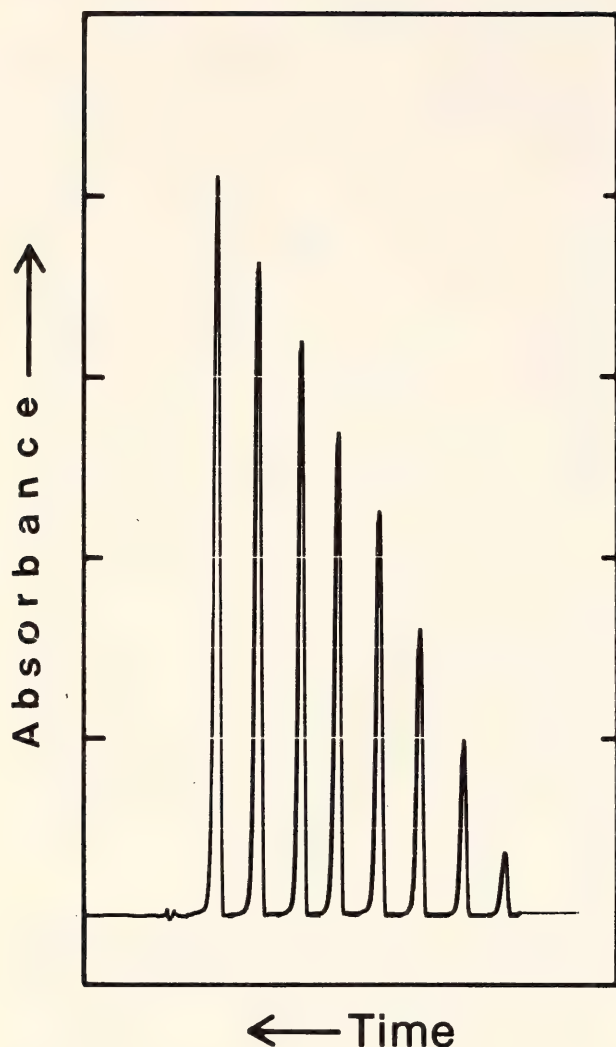


Fig. 149. Absorption peaks for 1- $\mu$ l samples containing (from right to left) 1, 3, 5, 7, 9, 11, 13, and 15 millimolar (mM) solutions of aluminum in 0.5M HCl. A distilled water sample is shown at the extreme left.

tional absorption owing to optical interference fringes at both ends of a sample spike (see distilled water peak in Fig. 149). This additional absorption limits the sensitivity of the technique to aluminum concentrations above 0.2 mM. Within this limit, however, measurement of less than a *nanomole* of aluminum in a 1- $\mu$ l sample is obtainable.

Two potential problems with regard to the sample injection procedure require comment. (1) When the sample micropipette is inserted between the funnel-shaped connectors to the plastic flow line (inset, Fig. 148), an air bubble may

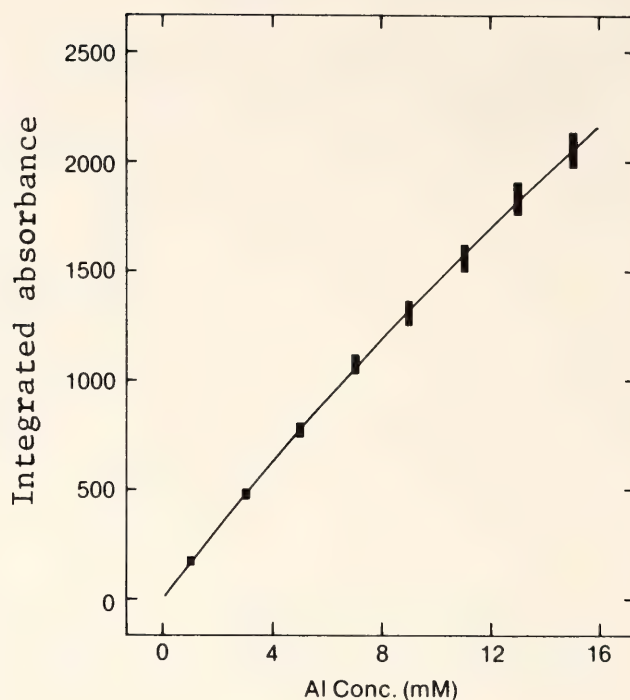


Fig. 150. A standard curve obtained from five replicate determinations of the integrated absorption of the eight standards used for Fig. 149. The curve is a second-order fit to the data. The error bars indicate one standard deviation from the mean of the measured absorption for each sample.

appear in the pipette. The air bubble signifies that some of the sample solution has been sucked from the pipette because of contact with a drop of reagent solution on the connector surface or because of an overfilled pipette. In such cases, anomalous results are obtained, mainly because there is no assurance that all the unknown solution entered the flow line. This problem can be avoided by thoroughly cleaning the connector surfaces with a blast of air or Freon between samples and by cleaning any excess solution from the sample pipette. (2) Deformation of the connectors with repeated use can increase the resistance of the sample flow line, decreasing the flow rate in that line. Periodic replacement of the connectors and monitoring of the time interval from injection to peak can prevent problems of this nature. Slight variations in the sample line resistance, for example due to variations in



pipette centering, are probably responsible for a significant part of the observed scattering of data.

The capability of analyzing aluminum at submicrogram levels is an important step toward the experimental determination of the nature of dissolved aluminum in hydrothermal fluids. Using the analytical method presented here in conjunction with techniques similar to those developed by Frantz and Eugster (1973) and Popp and Frantz (1979), one can determine both the concentration and speciation of aluminum in equilibrium with aluminum-bearing minerals at high temperatures and pressures.

#### SODIUM LOSS FROM SODIUM METASILICATE MELTS IN CO<sub>2</sub> AND CO ATMOSPHERES

*F. Seifert, D. Virgo, and B. O. Mysen*

Sodium silicate melts are stable at high temperature if SiO<sub>2</sub>:Na<sub>2</sub>O equals or exceeds 1 (Kracek, 1930). It has been found that sodium metasilicate melts can be kept in air at 1400°C for 1 hr as beads on Pt wire loops without notable changes in composition, as evidenced by the Raman spectra of quenched melt of Na<sub>2</sub>O·SiO<sub>2</sub>, which agreed with the spectra reported by Brawer and White (1975) and Sharma *et al.* (*Year Book* 77, pp. 649–652). The Raman spectra of samples held under the same conditions in CO<sub>2</sub> or CO atmospheres, however, exhibited an increase of the Raman band at ~1090 cm<sup>-1</sup>, particularly in the sample exposed to CO (Fig. 151C). This band cannot be assigned to a CO<sub>3</sub><sup>2-</sup> vibration that occurs at ~1040 cm<sup>-1</sup> because the other high-frequency modes typical of CO<sub>3</sub><sup>2-</sup> are absent (Mysen and Virgo, unpublished data). On the other hand, the band at ~1090 cm<sup>-1</sup> is typical of glasses more siliceous than Na<sub>2</sub>SiO<sub>3</sub> composition on the join Na<sub>2</sub>O-SiO<sub>2</sub>, such as Na<sub>2</sub>O·2SiO<sub>2</sub> glass (Fig. 151D). The band at ~1090 cm<sup>-1</sup> is characteristic of Si-O

stretch vibrations for SiO<sub>4</sub> tetrahedra containing on the average one nonbridging oxygen atom (Brawer and White, 1975). Concomitant with the increase of the ~1090-cm<sup>-1</sup> band, a decrease in the intensity of the ~850-cm<sup>-1</sup> band is observed (Fig. 151B,C). The 850-cm<sup>-1</sup> band is assigned to Si-O stretch vibrations in isolated SiO<sub>4</sub> tetrahedra (Brawer and White, 1975). It can therefore be inferred from the Raman spectra that the quenched melts became more polymerized (i.e., more SiO<sub>2</sub>-rich) after equilibration with CO<sub>2</sub> and CO gas compared with melts quenched in air.

Further evidence in support of this conclusion was obtained by crystallizing a glass of Na<sub>2</sub>O·SiO<sub>2</sub> composition that had been held at 1400°C in a gas mixture consisting of 67 vol % and 33 vol % CO for 1 hr. After crystallization at 800°C for 16 hr in air it consisted of subequal amounts of sodium disilicate and sodium metasilicate, as evidenced by optical examination of the charges and examination of x-ray powder patterns. Thus, about 10 wt % Na<sub>2</sub>O was lost from the melt within 1 hr.

Although the mechanism of reaction of sodium loss is not understood, it is clear that CO and to a minor extent also CO<sub>2</sub> can promote removal of Na from melts at elevated temperatures. Experimentalists studying phase equilibria involving a Na<sub>2</sub>O component in gas-mixing furnaces using CO<sub>2</sub>/CO mixtures as reducing agents are therefore cautioned.

#### QUENCH FURNACE CONTROLLER

*C. G. Hadidiacos*

High-temperature quench furnaces used in experimental petrology are heated typically between 400° and 1500°C. The heating element in this type of furnace is commonly constructed of platinum wire 0.08 mm O.D. × 8.5 m long (Greig, 1927). The resistance properties of plati-

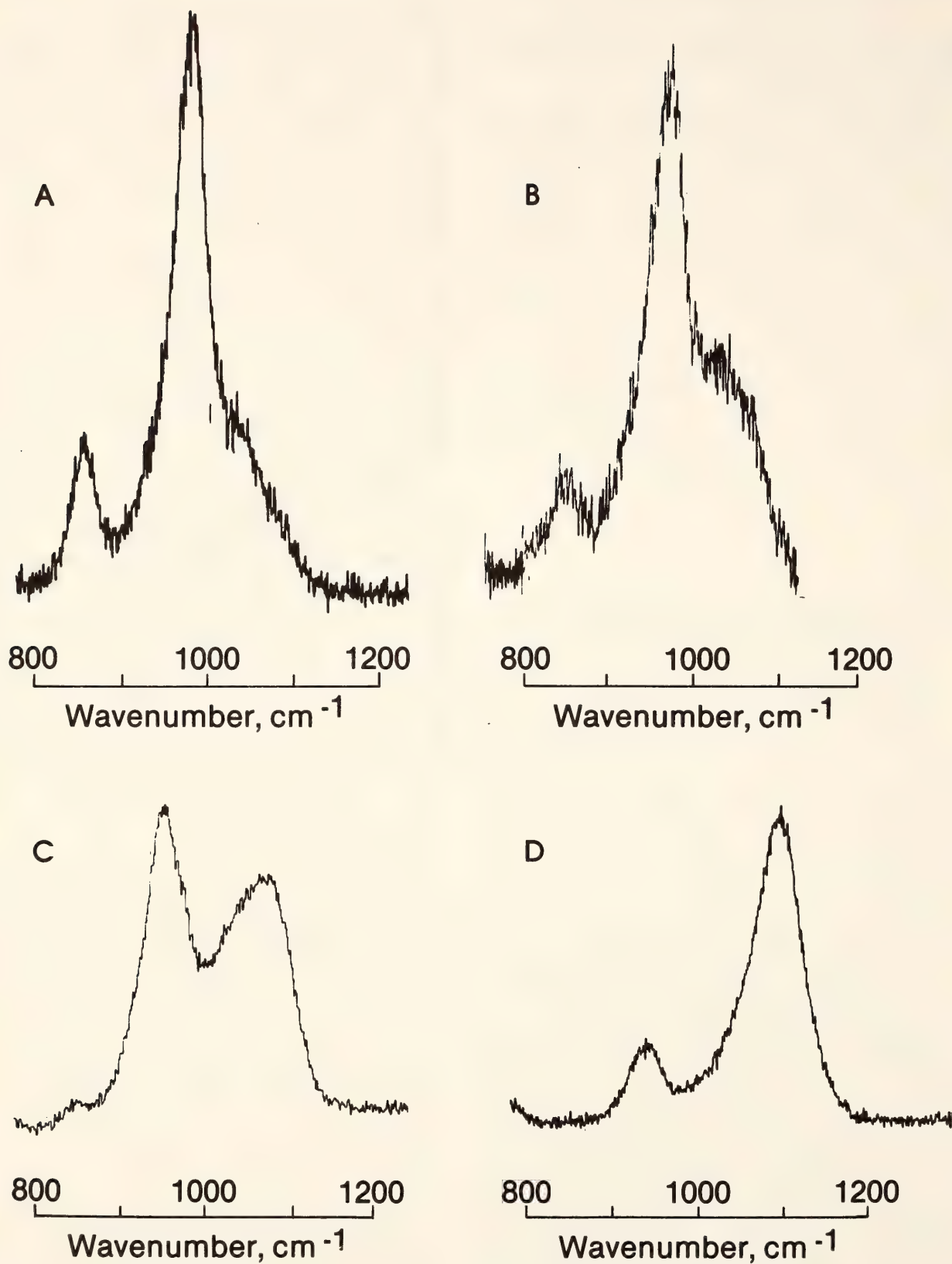


Fig. 151. High-frequency part of the unpolarized Raman spectra of  $\text{Na}_2\text{O}\cdot\text{SiO}_2$  glass held for 1 hr at  $1400^\circ\text{C}$  (A) in air, (B) in a  $\text{CO}_2$  atmosphere, (C) in a  $\text{CO}$  atmosphere. (D) High-frequency part of the Raman spectrum of a  $\text{Na}_2\text{O}\cdot 2\text{SiO}_2$  glass.



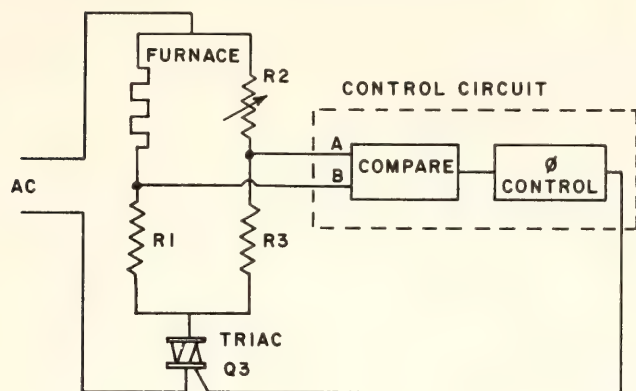


Fig. 152. Wheatstone bridge controller using the furnace as its own sensor.

num increase at a rate of  $0.0039 \text{ ohm}/^{\circ}\text{C}$  for each ohm of resistance. For example, at  $20^{\circ}\text{C}$  the resistance is 2 ohms, and at  $1200^{\circ}\text{C}$  the resistance is 10 ohms. By means of this predictable relationship the furnace temperature can be controlled with the circuit shown in Fig. 152.

With the furnace winding placed as one leg of a Wheatstone bridge, resistors R1, R2, and R3 are used to complete the circuit in Fig. 152. By comparing the magnitude of the potential at points A and B, a null point can be obtained. As potentiometer R2 is changed, the comparator circuit changes the phase-control circuit and gates Triac Q3 to apply the appropriate amount of power to the furnace winding in order to restore the null point.

#### *Control Circuit*

The control circuit is shown in Fig. 153. The potential present on pins 2, 3 and 8, 9 is applied to amplifiers A1 and A2. The output of these amplifiers is the absolute value of their input. The positive output of A1 sets the reference point at which the controller will operate. Amplifier A2 gives an output that is proportional to the temperature of the furnace. These two outputs are compared in A3, and the resulting difference is a measure of the error present between the

reference and the desired temperature. The error potential is then applied to the phase-control circuit comprised of transistors Q1 and Q2 (General Electric Company, 1964). The trigger pulse generated by Q2 is synchronized to the power-line frequency via the bridge rectifier and zener diode CR1. With a large temperature error, Q1 charges C1 rapidly, resulting in an early trigger pulse from Q2. This pulse then switches on Triac Q3 allowing nearly full AC power to be supplied to the furnace. As the temperature approaches the set point the error signal decreases, slowing down the charge rate on C1 and thus retarding the trigger signal supplied to Q3. This action then completes the feedback control loop maintaining the furnace temperature at the value determined by the temperature-select potentiometer.

If full power is applied to a cold platinum furnace, currents of up to 40 amp would flow and cause localized heating, damaging the platinum wire by volatilization. To prevent this damage, amplifier A4 measures the voltage drop across resistor R1 via A2. In comparing this voltage drop with the value set by the current limit potentiometer, A4 clamps the output of the comparator A3. The trigger pulse to Q3 is retarded and lowers the voltage supplied to the furnace. The supply voltage is limited to maintain a current of less than 12 amp.

The inherent, regenerative turn-on action of the Triacs results in rapid changes in current rise that create electrical noise on the supply line. To eliminate these high frequencies, choke coil L1 is placed in series with Triac Q3, which slows the current supplied to the furnace during the turn-on of the Triac.

These temperature regulators, on seven furnaces ranging from  $400^{\circ}$  to  $1500^{\circ}\text{C}$ , have been in service maintaining  $\pm 1^{\circ}\text{C}$  for well over a year. With the furnace winding acting as its own temperature sensor, power-line changes are immediately corrected without the necessity of a controlling thermocouple.

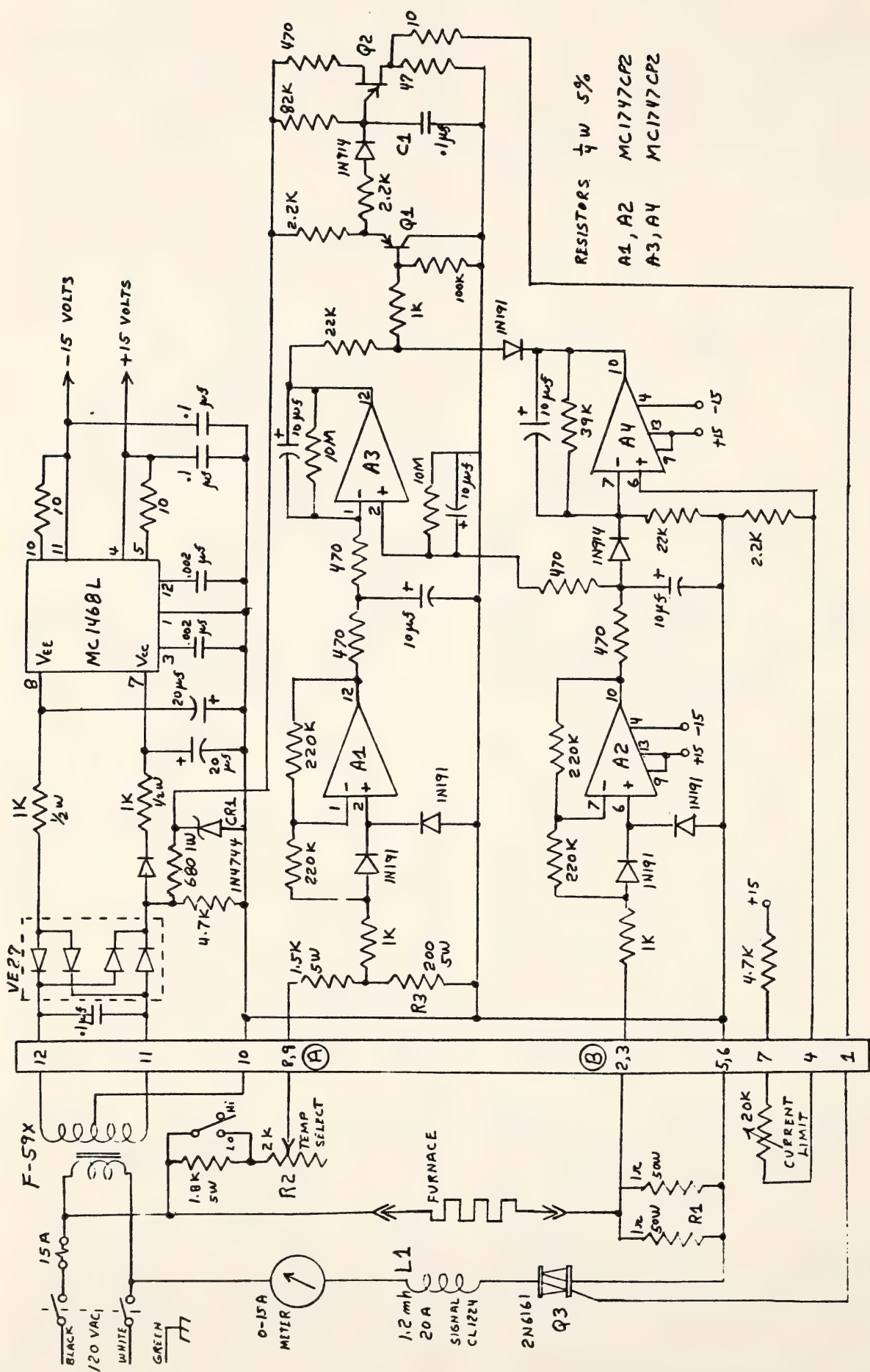


Fig. 153. Complete quench-furnace controller circuit used in experimental petrology.



## STAFF ACTIVITIES

*Workshop on Heating the Diamond-Anvil, High-Pressure Cell*

Sixty researchers from Europe, Australia, The People's Republic of China, and North America met at the Geophysical Laboratory on May 30, 1979, to discuss methods of heating and calibrating the diamond-anvil, high-pressure cell. The workshop, held in conjunction with the Spring Annual Meeting of the American Geophysical Union, was convened by Robert M. Hazen (Geophysical Laboratory) and Charles T. Prewitt (SUNY, Stony Brook). The session was divided into two sections, with lectures and discussions followed by a tour of the Laboratory's diamond-cell facilities.

Samples in the diamond-anvil, high-pressure cell must be heated if information about the earth's interior is to be gained. Both resistance furnaces and lasers have been employed successfully in heating minerals in diamond-cell experiments. External resistance furnaces can be used to provide uniform temperature for long time periods; however, temperatures are restricted to less than about 1000°C owing to graphitization of the diamonds. Furthermore, an inert atmosphere is required above 700°C to avoid oxidation of diamond. A variety of furnace configurations have been attempted, including miniature windings around the diamonds, large furnaces in which the entire cell is heated, and intermediate-sized, cylindrical furnaces that heat the piston-cylinder portion of a lever-arm diamond cell (*Year Book* 74, p. 403). In addition, some investigators have attempted to heat the metal gasket directly by applying current across the gasket itself or by using internal strip heaters. These procedures include the use of complicated resistance elements and commonly have proved less successful

because of the rapid conduction of heat by the diamonds away from the sample area.

Lasers are used to provide a method of heating samples to temperatures significantly greater than the diamond-graphite curve. The sample, which absorbs the laser energy or is mixed with an absorber, may be heated to several thousand degrees centigrade, while the transparent diamonds remain relatively cool because of their high thermal conductivity. A difficulty with this technique is that complex thermal gradients are produced in the sample because the laser is normally focused to a small spot (approximately 10–20  $\mu\text{m}$  in diameter) and is rastered across the sample. It is difficult, therefore, to define the temperature and pressure at which a laser experiment has taken place. It was suggested that the use of a longer wavelength, such as that produced by a CO<sub>2</sub> laser, in conjunction with diamonds that absorb this energy, might provide an efficient heater with a more uniform temperature distribution. As with the resistance furnaces, this laser technique would be limited to temperatures below the decomposition curve of diamond.

Perhaps the most difficult problem confronting researchers in high-temperature, diamond-cell research is calibration. The ruby fluorescence lines used to calibrate the diamond cell at high pressure and room temperature become diffuse and, therefore, unsatisfactory for calibration above 200°C. It was suggested that line-broadening and the thermal relaxation time might be used to measure pressure and temperature simultaneously. In some applications high-temperature diamond cells have no optical access during heating, and an internal calibration is required. Perhaps the most promising calibration procedure is a combination of a

thermocouple, outside the sample chamber but in contact with the diamond near the gasket area, and an internal standard with cubic symmetry such as gold. The temperature is read from the thermocouple, and the unit-cell edge of the cubic material is used to estimate the pressure.

In some experiments, such as with a laser or a miniature resistance furnace, the external thermocouple calibration could prove erroneous, and two internal x-ray standards may be required. The use of a uniaxial material with axes of greatly differing linear thermal expansivities and compressibilities was suggested as a possible pressure-temperature standard in diffraction experiments. Another possible internal calibration of temperature and pressure might be based on measurements of both position and shape of absorption or Raman emission lines. In the case of very high temperature heating of the sample with a laser, optical pyrometry using several different wavelengths of emitted light may provide a quantitative estimate of the maximum temperature, subject to the uncertainties introduced by thermal gradients in the sample. It is likely, because of the great variety of experimental configurations and the large range of temperatures and pressures available, that multiple calibration procedures will be required.

After lectures and discussions, participants in the workshop were given a tour of the Geophysical Laboratory's high-temperature, diamond-cell facilities. *Bell* and *Mao* demonstrated the conversion of olivine ( $\text{Fo}_{89}$ ) in a diamond cell to perovskite plus magnesiowüstite at 250 kbar and high temperature, using a YAG laser. This type of experimental system is capable of reaching  $2000^\circ\text{C}$  at pressures greater than 1 Mbar. *Bell* and *Mao* also showed an externally wound resistance heater that can be used with a lever-arm cell to  $800^\circ\text{C}$ . *Van Valkenburg* used a different type of lever-arm, heated cell to observe the triple point of water and the growth of single crystals of ice

VII. This pressure cell, which can be heated to  $400^\circ\text{C}$ , has an extremely sensitive pressure control and is ideal for observing the solution behavior of minerals at hydrothermal crustal conditions. *Hazen* and *Finger* demonstrated a miniature high-temperature diamond cell that is used for computer-controlled, single-crystal, x-ray studies to 50 kbar at temperatures to  $700^\circ\text{C}$ . This cell will be used to determine the structural equations of state of minerals.

The workshop on heating the diamond pressure cell illustrated the great potential of this technique for studying minerals under conditions equivalent to those in the earth's crust and mantle. With appropriate heating and calibration procedures, the diamond-anvil, high-pressure cell can be used to determine phase equilibria and physical properties not otherwise obtainable.

#### *Petrologists' Club*

Eight meetings were held during the 68th year of the Petrologists' Club, and the following lectures were presented:

"Recent developments in the thermodynamics of minerals," by Robert C. Newton (University of Chicago), October 10, 1978.

"Mantle differentiation and generation of the earth's crust," by R. K. O'Nions (Lamont Doherty Geological Observatory, Columbia University), November 21, 1978.

"Processes of ore deposition in hydrothermal environments," by George Brimhall (University of California, Berkeley), December 12, 1978.

"The composition of Ni sulfide ores with particular reference to their Pt group element contents and some constraints on genetic models," by A. J. Naldrett (University of Toronto), January 16, 1979.

"Geologic and petrologic studies of the Columbia River basalt," by T. L. Wright and D. E. Swanson (U.S. Geological Survey), February 6, 1979.



"The role of a supernova in the origin of the solar system," by R. N. Clayton (University of Chicago), February 27, 1979.

"Volatiles in the mantle beneath the North Atlantic," by J.-G. Schilling (University of Rhode Island), March 20, 1979.

"Inferences on silicate melt structure from studies on silicate glasses," by Gordon E. Brown (Stanford University), April 24, 1979.

### *Washington Crystal Colloquium*

The Washington Crystal Colloquium, an informal group of crystallographers from the Washington area, met six times during the report year. The following lectures were presented:

"Stereochemical restraints on positional and thermal parameters in least-squares refinement of large structures," by John Konnert (Naval Research Laboratory), October 13, 1978.

"The crystal structure of djurleite,  $\text{Cu}_{1.94}\text{S}$ , and crystal chemical implications," by Howard Evans (U. S. Geological Survey), November 17, 1978.

"Triplet invariants," by Jerome Karle (Naval Research Laboratory), December 15, 1978.

"The structure of tropomyosin," by E. Lattman (Johns Hopkins University Medical School), January 19, 1979.

"New x-ray detectors for structure analysis," by D. J. Nagel (Naval Research Laboratory), March 16, 1979.

"Implementation and use of BILDER at the NIH," by Gerson Cohen and Rick Bott (National Institutes of Health), April 20, 1979.

### *Seminar Series*

The seminar series met eleven times during the report year. The following lectures were presented:

"Solid state reactions in chain silicates," by David R. Veblen (Arizona State University), December 8, 1978.

"Experimental studies of scapolite and application to high-grade metamorphism," by Bruce Aitken (Stanford University), December 19, 1978.

"The thermal history of the earth," by R. St. J. Lambert (University of Alberta), January 25, 1979.

"Thermodynamics of water in cordierite," by Steve Lonker (Harvard University), January 31, 1979.

"The influence of cation properties on the structure of high-polymer silicate anions: Results and consequences from a regression analysis," by F. Liebau (Mineralogisches Institut der Universität Kiel, Germany), February 14, 1979.

"Steady state diffusion and local equilibrium in the growth of reaction zones between ultramafic bodies and siliceous country rock," by Richard F. Sanford (U.S. Geological Survey, Reston, Virginia), March 22, 1979.

"Fluid dynamics of magma mixing," by A. R. McBirney (University of Oregon), April 12, 1979.

"Siliceous carbonates metamorphosed in the aureole of the monzonite intrusion of Monzoni, N. Italy (dolomites)," by L. Masch (Mineralogisch-Petrograph Institut, Munich, West Germany), April 12, 1979.

"X-ray, spectroscopic, and molecular orbital studies of silicate glasses," by Gordon E. Brown (Stanford University), April 25, 1979.

"Some recent work on silicate glasses," by A. Navrotsky (Arizona State University), May 18, 1979.

"Transition electron microscopy study of ringwoodite," by Jean Paul Poirer (Institute de Physique du Globe de Paris), June 4, 1979.

### *Lectures and Symposia*

During the report year staff members and fellows presented lectures and participated in symposia and other extracurricular activities:

Bell lectured on "Geophysical research at high pressures" at the Thomas J.

Watson Research Center, Yorktown Heights, New York; on "Recent experimental results relevant to the geophysics of the earth's mantle to 650 kilobars pressure" at the Potomac Geophysical Society; on "Recent results in the experimental study of earth and planetary interiors" at the Department of Terrestrial Magnetism; and on "Experimental geochemistry of the mantle" at the City University of New York (CUNY), Brooklyn. He served as a member of the NASA Lunar Sample Planning Team and as Associate Editor of *Journal of Physics and Chemistry of Minerals*. In June 1979 Bell received the Apollo Principal Investigator's Award from NASA in Washington, D.C.

*Brady* gave an invited lecture on metasomatic zoning in metamorphic rocks at the Lamont-Doherty Geological Observatory and also lectured at the University of California at Los Angeles, University of Southern California, Arizona State University, and the Geological Society of Washington.

As chairman of International Geological Correlation Project 163, *Chayes* organized and conducted a Project workshop held in conjunction with the annual Geostatistical "Chatauqua" at Syracuse University; he delivered a paper entitled "Electronic computation and bookkeeping in igneous petrology" at a symposium sponsored by the Project at the Geological Society of America convention in Toronto. He attended the ordinary meeting of the International Union of Geological Sciences Subcommittee on Systematics in Petrology in Padua, Italy, as an observer, and has recently been named a member of the Subcommittee.

*Davis* presented a paper at the Fourth International Conference on Geochronology, Cosmochronology, and Isotope Geology held at Aspen, Colorado, August 20-25, 1978.

*Estep* lectured on the "Biogeochemistry of hydrogen isotopes" at the Geological Society of Washington; at the American Chemical Society meeting at

Corpus Christi, Texas, at a Symposium on Organic Geochemistry of Coastal Environments; and at the Marine Science Institute, University of South Carolina. She also gave an invited paper on "Application of stable hydrogen and carbon isotopes to microbiology" at a Branch Meeting of the American Society of Microbiology at Fort Detrick, Maryland.

*Finger* presented a paper at the Eleventh International Congress of Crystallography held August 3-12, 1978, in Warsaw, Poland, and then spent three weeks as a Guest Investigator at the Max-Planck-Institut für Kernphysik, Heidelberg, Germany. He also attended the International Conference on Modulated Structures, cosponsored by the American and Japanese Crystallographic Associations, at Kona, Hawaii, and gave an invited paper with Hazen on "Response of oxide structures to changes in pressure, temperature, and composition" at the American Crystallographic Association meeting at Honolulu. Finger served as Secretary of the Mineralogical Society of America and was elected a member of the Crystallographic Computing Committee of the American Crystallographic Association.

*George* held an appointment as Lecturer on the faculty of the Department of Earth and Planetary Sciences, Johns Hopkins University, in connection with a joint cooperative program with the University for the purpose of teaching a graduate course in the use of the electron microprobe at the Geophysical Laboratory.

*Gil-Av* lectured on "Enantiomer separation" at the Weizmann Institute of Science, Israel, April 1979; at the Fourth International Symposium on Column Liquid Chromatography at Boston, May 7-10, 1979; and at the joint meeting of the Centre National de la Recherche Scientifique (France) and the National Council for Research and Development (Israel) at Milly-La-Forêt, France, May 29-30, 1979.

*Hare* presented three papers and



helped organize the First International Conference on Biogeochemistry of Amino Acids at Airlie House, Virginia, October 29–November 1, 1978. He also gave invited lectures in March 1979 at the International Archaeometry Conference in London and the Chemistry Department, University of Maryland. He served as a Visiting Scientist at the Weizmann Institute of Science, Rehovot, Israel, in April 1979 and gave lectures on “Applications of organic geochemistry to geological problems” and “Enantiomer separation.”

*Hazen* lectured on “High-pressure crystal chemistry” at Cornell University and the University of Chicago in April 1979. His book *Early Writings on North American Geology* was published in April 1979 by Dowden, Hutchinson, and Ross. He served as Secretary of the U.S. National Committee on the History of Geology and on the Program Committee of the Mineralogical Society of America.

*Hoering* gave invited lectures on “Organic constituents of fossil mollusc shells” at the First International Symposium on the Biogeochemistry of Amino Acids, Airlie House, Virginia, October 29–November 1, 1978, and on “Biological fractionation of the stable hydrogen isotopes” at a symposium on Stable Isotopes in Oceanography at the annual meeting of the American Society of Limnology and Oceanography, State University of New York at Stony Brook, June 20–21, 1979; he presented a paper at the Fourth International Conference on Geochronology, Cosmochronology, and Isotope Geology. He also served on the Panel on Planetary Biology, National Aeronautics and Space Administration.

*Irvine* participated in a visiting lecture series program sponsored for Canadian universities by the Canadian Institute of Mining and Metallurgy. He spoke on “Magmatic density currents, cumulus processes, and the origin of chromite deposits in layered intrusions” at the universities of Manitoba, Brandon, Saskatchewan, and Alberta. Irvine also ad-

ressed the Geological Society of Washington on magmatic density currents.

*Mao* lectured on “High-pressure research” at the General Electric Company, Schenectady, New York, April 1979, and at the Department of Geology, Washington University, St. Louis, May 1979; and on “The physics of hydrogen at high pressures to 650 kbar” at the U.S. Army Watervliet Arsenal, Rensselaerville, New York, June 1979. He also served as an Advisory Editor of *Physics of the Earth and Planetary Interiors*.

*Osborn* served as chairman of the newly established Advisory Committee on Mining and Mineral Resources Research, advisory to the Secretary of the Interior; and as chairman of the Workshop on Continental Drilling for Scientific Purposes, held at Los Alamos, New Mexico, July 17–21, 1978. He delivered two lectures at the Pennsylvania State University on experimental phase equilibria as applied to the origin of subalkaline volcanic rocks. He presented testimony on Title III of the Surface Mining Control and Reclamation Act of 1977 before the Interior Subcommittee of the House Appropriations Committee. He attended meetings as a member of the Materials Advisory Committee, Office of Technology Assessment, Congress of the United States; he chaired the panel on Mineral Accessibility on Federal Lands and served as a member of the panel on Nonfederal Mineral Accessibility.

*Osborn* also served on the Geosciences Advisory Panel, Los Alamos Scientific Laboratory, U.S. Department of Energy; the Pennsylvania Science and Engineering Foundation Board (Commonwealth of Pennsylvania, Harrisburg); the Pennsylvania Research Corporation Board of Directors (Pennsylvania State University); the Geisinger Medical Center Board of Directors, Danville, Pennsylvania; and the Board of Directors of the Institute for Medical Education and Research at Geisinger Medical Center.

*Popp* gave invited lectures on the “Geochemistry of chloride-bearing hy-

drothermal solutions" at the Department of Geological Sciences, Virginia Polytechnic Institute and State University, and the Department of Geology, University of Illinois at Chicago Circle.

*Rumble* lectured on "Fluid phase of metamorphism" at the University of Wisconsin, the University of Minnesota, and the University of Pennsylvania. He also presented a paper at the Fourth International Conference on Geochronology, Cosmochronology, and Isotope Geology. *Rumble* shared second prize with A. J. Boucot for the best paper presented to the Geological Society of Washington in 1978.

*Van Valkenburg* lectured on "High-pressure optics" at a meeting of the Geological Society of Washington. He also served as Program Director of Geochemistry at the National Science Foundation during the period January through March 1979.

*Yagi* presented a paper on "Static high-pressure experiments to megabar region" at the Gordon Research Conference on Physics and Chemistry at High Pressure held August 7–11, 1978, at Meriden, New Hampshire. He also served on a Ph.D. examination committee at the State University of New York at Stony Brook and gave a lecture entitled "Structure and crystal chemistry of silicate perovskite."

*Yoder* presented his views on the "Tec-

tonophysics of melting in the mantle" at the Department of Geology and Geophysics, Woods Hole Oceanographic Institution, on July 28, 1978. He lectured on "Magma generation, aggregation, and extrusion" at a Scientific Colloquium at NASA Goddard Space Flight Center on November 17, 1978. He also lectured on "Magma sequences and thermal models" at Pennsylvania State University on March 27, 1979; and on "Thermal models and magma generation" at the Department of Geology, University of Reading, England, on June 1, 1979. *Yoder* was elected to the American Philosophical Society, April 20, 1979; to Fellowship of the American Academy of Arts and Sciences, May 9, 1979; and a Fellow of "The Explorers Club," New York, June 1979. On May 30, 1979, he was presented the Wollaston Medal, the senior award of the Geological Society of London, at its annual meeting. He sponsored a petition before the National Research Council for the formation of a Panel to investigate the "Geochemistry of fibrous materials related to health risks." One of its purposes is to identify which, if any, fibrous minerals broadly grouped under the commercial term "asbestos" are carcinogens or carcinogenic agents. *Yoder* completed his fourth year of service on the Committee on Science and Public Policy of the National Academy of Sciences.

## BIBLIOGRAPHY

- Bell, P. M., H. K. Mao, R. M. Hazen, and A. L. Mao, The Luna 24 sample from Mare Crisium: new structural features in lunar glasses deduced from a study of crystal-field spectra, in *Mare Crisium: The View from Luna 24*, R. B. Merrill and J. J. Papike, eds., Pergamon Press, New York, pp. 265–280, 1978 (G.L. Paper 1753).
- Bell, P. M., *see also* Hazen, R. M.; Mao, H. K.; Yagi, T.
- Boyd, F. R., and P. H. Nixon, Ultramafic nodules from the Kimberley pipes, South Africa, *Geochim. Cosmochim. Acta*, 42, 1367–1382, 1978 (G.L. Paper 1742).
- Boyd, F. R., *see also* Nixon, P. H.; Pasteris, J. D.
- Chayes, F., Electronic computation and book-keeping in igneous petrology, *Episodes*, 1979, no. 1, 16–19, 1979 (G.L. Paper 1764).
- Chayes, F., and J. Trochimezyk, An effect of closure on the structure of principal components, *Math. Geol.*, 10, 323–333, 1978 (G.L. Paper 1747).



- Eggler, D. H., Stability of dolomite in a hydrous mantle, with implications for the mantle solidus, *Geology*, 6, 397-400, 1978 (G.L. Paper 1749).
- Eggler, D. H., I. Kushiro, and J. R. Holloway, Free energies of decarbonation reactions at mantle pressures: I. Stability of the assemblage forsterite-enstatite-magnesite in the system  $\text{MgO-SiO}_2\text{-CO}_2\text{-H}_2\text{O}$  to 60 kbar, *Amer. Mineral.*, 64, 288-293, 1979 (G.L. Paper 1762).
- Eggler, D. H., M. E. McCallum, and C. B. Smith, Megacryst assemblages in kimberlite from northern Colorado and southern Wyoming: petrology, geothermometry-barometry, and areal distribution, in *The Mantle Sample: Inclusions in Kimberlites and Other Volcanics* (Proc. 2d Int. Kimberlite Conf., Vol. 2), F. R. Boyd and H. O. A. Meyer, eds., American Geophysical Union, Washington, D.C., pp. 213-226, 1979 (G.L. Paper 1766).
- Eggler, D. H., B. O. Mysen, T. C. Hoering, and J. R. Holloway, The solubility of carbon monoxide in silicate melts at high pressures and its effect on silicate phase relations, *Earth Planet. Sci. Lett.*, 43, 321-330, 1979 (G.L. Paper 1763).
- Eggler, D. H., and R. F. Wendlandt, Experimental studies on the relationship between kimberlite magmas and partial melting of peridotite, in *Kimberlites, Diatremes, and Diamonds: Their Geology, Petrology, and Geochemistry* (Proc. 2d Int. Kimberlite Conf., Vol. 1), F. R. Boyd and H. O. A. Meyer, eds., American Geophysical Union, Washington, D.C., pp. 330-338, 1979 (G. L. Paper 1765).
- Ferry, J. M., Fluid interaction between granite and sediment during metamorphism, south-central Maine, *Amer. J. Sci.*, 278, 1025-1056, 1978 (G.L. Paper 1746).
- Finger, L. W., and R. M. Hazen, Crystal structure and compression of ruby to 46 kbar, *J. Appl. Phys.*, 49, 5823-5826, 1978 (G.L. Paper 1741).
- Finger, L. W., see also Hazen, R. M.
- Frantz, J. D., and H. K. Mao, Bimetasomatism resulting from intergranular diffusion: II. Prediction of multimineralic zone sequences, *Amer. J. Sci.*, 279, 302-323, 1979 (G.L. Paper 1758).
- Gil-Av, E., see Hare, P. E.
- Hare, P. E., and E. Gil-Av, Separation of D and L amino acids by liquid chromatography: use of chiral eluants, *Science*, 204, 1226-1228, 1979 (G.L. Paper 1769).
- Hazen, R. M., P. M. Bell, and H. K. Mao, Effects of compositional variation on absorption spectra of lunar pyroxenes, *Proc. Lunar Planet. Sci. Conf. 9th*, 2919-2934, 1978 (G.L. Paper 1752).
- Hazen, R. M., and L. W. Finger, Crystal chemistry of silicon-oxygen bonds at high pressure: implications for the earth's mantle mineralogy, *Amer. Mineral.*, 201, 1122-1123, 1978 (G.L. Paper 1748).
- Hazen, R. M., and L. W. Finger, Crystal structure and compressibility of zircon at high pressure, *Amer. Mineral.*, 64, 196-201, 1979 (G. L. Paper 1756).
- Hazen, R. M., and D. R. Wones, Predicted and observed compositional limits of tri-octahedral micas, *Amer. Mineral.*, 63, 885-892, 1978 (G. L. Paper 1745).
- Hazen, R. M., see also Bell, P. M.; Finger, L. W.
- Hoering, T. C., see Eggler, D. H.
- Holloway, J. R., see Eggler, D. H.
- Kushiro, I., see Eggler, D. H.; Mysen, B. O.
- Mao, A. L., see Bell, P. M.
- Mao, H. K., and P. M. Bell, Observations of hydrogen at room temperature (25°C) and high pressure (to 500 kilobars), *Science*, 203, 1004-1006, 1979 (G.L. Paper 1761).
- Mao, H. K., P. M. Bell, J. Shaner, and D. Steinberg, A system of pressure calibration for the range 0.05-1.0 Mbar based on shock wave equations of state for Cu, Mo, Pd, and Ag, in *High-Pressure Science and Technology*, Vol. 1, K. D. Timmerhaus and M. S. Barber, eds., Plenum Publishing Corp., New York, pp. 739-747, 1979 (G.L. Paper 1751).
- Mao, H. K., see also Bell, P. M.; Frantz, J. D.; Hazen, R. M.; Yagi, T.
- McCallum, M. E., see Eggler, D. H.
- Mysen, B. O., Experimental determination of rare earth element partitioning between hydrous silicate melt, amphibole and garnet peridotite minerals at upper mantle pressures and temperatures, *Geochim. Cosmochim. Acta*, 42, 1253-1263, 1978 (G.L. Paper 1740).
- Mysen, B. O., Trace-element partitioning between garnet peridotite minerals and water-rich vapor: experimental data from 5 to 30 kbar, *Amer. Mineral.*, 64, 274-287, 1979 (G.L. Paper 1760).
- Mysen, B. O., and I. Kushiro, Pressure dependence of nickel partitioning between for-

- sterite and aluminous silicate melts, *Earth Planet. Sci. Lett.*, **42**, 383–388, 1979 (G.L. Paper 1757).
- Mysen, B. O., and D. Virgo, Influence of pressure, temperature, and bulk composition on melt structures in the system  $\text{NaAlSi}_2\text{O}_6\text{--NaFe}^{3+}\text{Si}_2\text{O}_6$ , *Amer. J. Sci.*, **278**, 1307–1322, 1978 (G.L. Paper 1744).
- Mysen, B. O., *see also* Eggler, D. H.
- Nixon, P. H., and F. R. Boyd, Garnet bearing lherzolites and discrete nodule suites from the Malaita alnoite, Solomon Islands, S.W. Pacific, and their bearing on oceanic mantle composition and geotherm, in *The Mantle Sample: Inclusions in Kimberlites and Other Volcanics* (Proc. 2d Int. Kimberlite Conf., Vol. 2), F. R. Boyd and H. O. A. Meyer, eds., American Geophysical Union, Washington, D.C., pp. 400–423, 1979 (G.L. Paper 1768).
- Nixon, P. H., *see also* Boyd, F. R.; Pasteris, J. D.
- Pasteris, J. D., F. R. Boyd, and P. H. Nixon, The ilmenite association at the Frank Smith Mine, R.S.A., in *The Mantle Sample: Inclusions in Kimberlites and Other Volcanics* (Proc. 2d Int. Kimberlite Conf., Vol. 2), F. R. Boyd and H. O. A. Meyer, eds., American Geophysical Union, Washington, D.C., pp. 265–278, 1979 (G.L. Paper 1767).
- Shaner, J., *see* Mao, H. K.
- Smith, C. B., *see* Eggler, D. H.
- Steinberg, D., *see* Mao, H. K.
- Trochimczyk, J., *see* Chayes, F.
- Virgo, D., *see* Mysen, B. O.
- Watson, E. B., Calcium diffusion in a simple silicate melt to 30 kbar, *Geochim. Cosmochim. Acta*, **43**, 313–322, 1979 (G.L. Paper 1754).
- Wendlandt, R. F., *see* Eggler, D. H.
- Wones, D. R., *see* Hazen, R. M.
- Yagi, T., H. K. Mao, and P. M. Bell, Structure and crystal chemistry of perovskite-type  $\text{MgSiO}_3$ , *Phys. Chem. Minerals*, **3**, 97–110, 1978 (G.L. Paper 1743).

## REFERENCES CITED

- Adams, D. M., and S. J. Payne, Laser-stimulated fluorescence of diamond, *J. Chem. Soc. Faraday Trans. II*, **70**, 1959–1966, 1974.
- Adams, D. M., and S. K. Sharma, Spectroscopy at very high pressures: Part 12. Criteria for selection of diamonds for infrared and Raman spectroscopy, *J. Phys. E*, **10**, 680–682, 1977.
- Adams, D. M., S. K. Sharma, and R. Appleby, Spectroscopy at very high pressures. 14 Laser Raman scattering in ultrasmall samples in a diamond anvil cell, *Appl. Opt.*, **16**, 2572–2575, 1977.
- Akimoto, S., and H. Fujisawa, Olivine-spinel solid solution equilibria in the system  $\text{Mg}_2\text{SiO}_4\text{--Fe}_2\text{SiO}_4$ , *J. Geophys. Res.*, **73**, 1467–1479, 1968.
- Akimoto, S., T. Katsura, Y. Syono, H. Fujisawa, and B. Komada, Polymorphic transition of pyroxenes  $\text{FeSiO}_3$  and  $\text{CoSiO}_3$  at high pressures and temperatures, *J. Geophys. Res.*, **70**, 5269–5278, 1965.
- Akimoto, S., Y. Matsui, and Y. Syono, High-pressure crystal chemistry of orthosilicates and the formation of the mantle transition zone, in *The Physics and Chemistry of Minerals and Rocks*, R. G. J. Strens, ed., John Wiley and Sons, Inc., New York, pp. 327–363, 1976.
- Akimoto, S., T. Yagi, and K. Jnoe, High temperature-pressure phase boundaries in silicate systems using in situ x-ray diffraction, in *High-Pressure Research: Applications in Geophysics*, M. H. Manghnani and S. Akimoto, eds., Academic Press, New York, pp. 585–602, 1977.
- Allin, E. J., A. D. May, B. P. Stoicheff, J. C. Stryland, and H. L. Welsh, Spectroscopy research at the McLennan Physical Laboratories of the University of Toronto, *Appl. Optics*, **6**, 1597–1608, 1967.
- Anderson, D. L., Phase changes in the upper mantle, *Science*, **157**, 1165–1173, 1967.
- Anderson, D. L., The deep structure of continents, *J. Geophys. Res.*, in press, 1979.
- Anderson, D. L., and H. Spetzler, Partial melting and the low-velocity zone, *Phys. Earth Planet. Inter.*, **4**, 62–64, 1970.
- Annersten, H., and U. Hålenius, Ion distribution in pink muscovite: a discussion, *Amer. Mineral.*, **61**, 1045–1050, 1976.



- Annersten, H., and M. Olesch, Distribution of ferrous and ferric iron in clintonite and the Mössbauer characteristics of ferric iron in tetrahedral coordination, *Can. Mineral.*, 16, 199–204, 1978.
- Appel, M., Solution for Fick's 2nd law with variable diffusivity in a multi-phase system, *Scr. Met.*, 2, 217–222, 1968.
- Arndt, J., and F. Häberle, Thermal expansion and glass transition temperatures of synthetic glasses of plagioclase-like compositions, *Contrib. Mineral. Petrol.*, 39, 175–183, 1973.
- Avrami, M., Kinetics of phase change. 3. Granulation, phase change and microstructures, *J. Chem. Phys.*, 9, 177–184, 1941.
- Barnett, J. D., S. Block, and G. J. Piermarini, An optical fluorescence system for quantitative pressure measurement in the diamond-anvil cell, *Rev. Sci. Instrum.*, 44, 1–9, 1973.
- Bartels, R. A., and V. H. Vetter, The temperature dependence of the elastic constants of CaO and SrO, *J. Phys. Chem. Solids*, 33, 1991–1992, 1972.
- Bassett, W. A., and L. C. Ming, Disproportionation of  $\text{Fe}_2\text{SiO}_4$  to  $2\text{FeO} + \text{SiO}_2$  at pressures up to 250 kbar and temperatures up to 3000°C, *Phys. Earth Planet. Interiors*, 5, 154–160, 1972.
- Basu, A. R., Origin of kimberlites and carbonatites explained by Nd isotopes (abstract), *GAC/MAC, Abstr. with Programs*, 3, 364, 1978.
- Bates, J. B., R. W. Hendricks, and L. B. Shaffer, Neutron irradiation effects and structure of non-crystalline  $\text{SiO}_2$ , *J. Chem. Phys.*, 61, 4163–4176, 1974.
- Bell, R. J., and P. Dean, Localization of phonons in vitreous silica and related glasses, in *International Conference on the Physics of Non-Crystalline Solids*, 3rd, University of Sheffield, 1970, R. W. Douglas and B. Ellis, eds., Wiley-Interscience, London, pp. 443–452, 1972.
- Bendeliani, N. A., S. V. Popva, and L. F. Vereschagin, New modification of titanium dioxide obtained at high pressures, *Geochem. Int.*, 3, 387–390, 1966.
- Best, M. G., H. L. Henage, and J. A. S. Adams, Mica peridotite, wyomingite, and associated potassic igneous rocks in northeastern Utah, *Amer. Mineral.*, 53, 1041–1048, 1968.
- Bethke, P. M., The sulfoselenides of mercury and their occurrence at Marysvale, Utah, Ph.D. thesis, Columbia University, 1957.
- Bhargava, S. C., J. E. Knudsen, and S. Mørup, Mössbauer study of spin-spin relaxation of  $\text{Fe}^{3+}$  ions in the presence of other paramagnetic ions, *J. Phys. Chem. Solids*, 40, 45–53, 1979.
- Bhatnagar, S. S., E. J. Allin, and H. L. Welsh, The Raman spectra of liquid and solid  $\text{H}_2$ ,  $\text{D}_2$ , and HD at high resolution, *Can. J. Chem.*, 40, 9–23, 1962.
- Binns, R. A.,  $(\text{Mg},\text{Fe})_2\text{SiO}_4$  spinel in a meteorite, *Phys. Earth Planet. Interiors*, 3, 156–160, 1970.
- Birch, F., Elasticity and constitution of the earth's interior, *J. Geophys. Res.*, 57, 227–286, 1952.
- Birch, F., Density and composition of the upper mantle: first approximation as an olivine layer, in "The Earth's Crust and Upper Mantle," P. J. Hart, ed., *Geophys. Monogr. Amer. Geophys. Union*, 13, 18–36, 1969.
- Blount, H. G., G. A. Marlor, and H. B. Richard, Self diffusion of S in ZnS, *J. Appl. Phys.*, 38, 3995, 1967.
- Bockris, J. O'M., and E. Kojonen, The compressibilities of certain molten alkali silicates and borates, *J. Amer. Chem. Soc.*, 82, 4493–4497, 1960.
- Bockris, J. O'M., J. D. Mackenzie, and J. A. Kitchner, Viscous flow in silica and binary liquid silicates, *Trans. Faraday Soc.*, 51, 1734–1748, 1955.
- Boctor, N. Z., The mercury selenium sulfur system and its geological implications, Ph.D. thesis, Purdue University, 1976.
- Boctor, N. Z., and H. O. A. Meyer, Oxide and sulfide minerals in kimberlite from Green Mountain, Colorado, in *Kimberlites, Diatremes, and Diamonds: Their Geology, Petrology, and Geochemistry* (Proc. 2d Int. Kimberlite Conf., Vol. 1), F. R. Boyd and H. O. A. Meyer, eds., American Geophysical Union, Washington, D.C., pp. 217–228, 1979.
- Boettcher, A. L., J. R. O'Neill, K. E. Windom, D. C. Stewart, and H. G. Wilshire, Metasomatism of the upper mantle and the genesis of kimberlites and alkali basalts, in *The Mantle Sample: Inclusions in Kimberlites and Other Volcanics* (Proc. 2d Int. Kimberlite Conf., Vol. 2), F. R. Boyd and H. O. A. Meyer, eds., American Geophysical Union, Washington, D.C., pp. 173–182, 1979.
- Bond, W. L., Making small spheres, *Rev. Sci. Instrum.*, 22, 344–345, 1951.
- Boon, J. A., and W. S. Fyfe, The coordination numbers of ferrous iron in silicate glasses, *Chem. Geol.*, 10, 287–298, 1972.

- Booth, F., A note on the theory of surface diffusion reactions, *Trans. Faraday Soc.*, 44, 796-801, 1948.
- Bottinga, Y., and D. F. Weill, The viscosity of magmatic silicate liquids: a model for calculation, *Amer. J. Sci.*, 272, 438-475, 1972.
- Bowen, N. L., J. F. Schairer, and H. W. V. Willems, The ternary system:  $\text{Na}_2\text{SiO}_3\text{-Fe}_2\text{O}_3\text{-SiO}_2$ , *Amer. J. Sci.*, 20, 405-455, 1930.
- Boyd, F. R., A pyroxene geotherm, *Geochim. Cosmochim. Acta*, 37, 2533-2546, 1973.
- Boyd, F. R., and J. L. England, Apparatus for phase equilibrium measurements at pressures up to 50 kilobars and temperatures up to 1750°C, *J. Geophys. Res.*, 65, 741-748, 1960.
- Boyd, F. R., and R. H. McCallister, Densities of fertile and sterile garnet peridotites, *Geophys. Res. Lett.*, 3, 509-512, 1976.
- Boyd, F. R., and P. H. Nixon, Ultramafic nodules from the Kimberley pipes, South Africa, *Geochim. Cosmochim. Acta*, 42, 1367-1382, 1978.
- Brace, W. F., Pore pressure in geophysics, in "Flow and Fracture in Rocks," H. C. Heard, I. Y. Borg, N. L. Carter, and C. B. Raleigh, eds., *Geophys. Monogr. Amer. Geophys. Union*, 16, 265-273, 1972.
- Brady, J. B., Experimental reaction zones between quartz and periclase and intergranular diffusion of silica (abstract), *Eos*, 58, 520, 1977.
- Brawer, S. A., and W. B. White, Raman spectroscopic investigation of the structure of silicate glasses. I. The binary alkali silicates, *J. Chem. Phys.*, 63, 2420-2432, 1975.
- Brawer, S. A., and W. B. White, Raman spectroscopic investigation of the structure of silicate glasses. II. Soda-alkali earth-alumina ternary and quaternary glasses, *J. Non-Cryst. Solids*, 23, 261-278, 1977.
- Brett, R., and P. M. Bell, Melting relations in the Fe-rich portion of the system Fe-Fs at 30 kb pressure, *Earth Planet. Sci. Lett.*, 6, 479-482, 1969.
- Bridgman, P. W., *The Physics of High Pressure*, Bell, London, 1931.
- Bridgman, P. W., The phase diagram of water to 45,000 kg/cm<sup>2</sup>, *J. Chem. Phys.*, 5, 964-966, 1937.
- Bridgman, P. W., and I. Simon, Effects of very high pressure on glass, *J. Appl. Phys.*, 24, 405-413, 1953.
- Briggs, J., Thermodynamics of the glass transition temperature in the system  $\text{CaO-MgO-Al}_2\text{O}_3\text{-SiO}_2$ , *Cent. Glass Ceram. Res. Inst. Bull.*, 22, 73-82, 1975.
- Brodsky, M. H., Raman scattering in amorphous semiconductors, in *Light Scattering in Solids*, M. Cardona, ed., Springer-Verlag, Berlin, pp. 205-251, 1975.
- Brown, G. E., K. D. Keefer, and P. M. Fenn, Extended x-ray absorption fine structure (EXAFS) study of iron-bearing silicate glasses: iron coordination environment and oxidation state (abstract), *Abstr. with Programs (Geol. Soc. Amer.)*, 10, 373, 1978.
- Buckner, D. A., D. M. Roy, and R. Roy, Studies in the system  $\text{CaO-Al}_2\text{O}_3\text{-SiO}_2\text{-H}_2\text{O}$ . II. The system  $\text{CaSiO}_3\text{-H}_2\text{O}$ , *Amer. J. Sci.*, 258, 132-147, 1960.
- Buddington, A. F., and D. H. Lindsley, Iron-titanium oxide minerals and synthetic equivalents, *J. Petrology*, 5, 310-357, 1964.
- Burnham, C. W., Thermodynamics of melting in experimental silicate-volatile systems, *Geochim. Cosmochim. Acta*, 39, 1077-1084, 1975.
- Burnham, C. W., J. R. Holloway, and N. F. Davis, Thermodynamic properties of water to 1000°C and 10,000 bars, *Geol. Soc. Amer. Spec. Pap.*, 132, 96 pp., 1969.
- Cabine, J., La diffusion intergranulaire et la structure des joints intergranulaires dans les halogénures alcalins, *J. Chim. Phys. Physicochim. Biol.*, 59, 1123-1141, 1962.
- Cabri, L. J., and J. H. LaFlamme, Rhodium, platinum, and gold alloys from the Stillwater Complex, *Can. Mineral.*, 12, 399-403, 1974.
- Cabri, L. J., J. M. Stewart, J. F. Rowland, and T. T. Chen, New data on some palladium arsenides and antimonides, *Can. Mineral.*, 13, 321-335, 1975.
- Cabri, L. J., T. T. Chen, J. M. Stewart, and J. H. LaFlamme, Two new palladium-arsenic-bismuth minerals from the Stillwater Complex, Montana, *Can. Mineral.*, 14, 410-413, 1976.
- Carter, N. L., Steady state flow of rocks, *Rev. Geophys. Space Phys.*, 14, 301-360, 1976.
- Carter, N. L., C. B. Raleigh, and P. S. DeCarli, Deformation of olivine in stony meteorites, *J. Geophys. Res.*, 73, 5439-5461, 1968.
- Cathles, L. M., III, *The Viscosity of the Earth's Mantle*, Princeton University Press, Princeton, New Jersey, 1975.



- Chan, J. W., The impurity drag effect in grain boundary motion, *Acta Met.*, 10, 789-798, 1962.
- Chang, Z. P., and E. K. Graham, Elastic properties of oxides in the NaCl-structure, *J. Phys. Chem. Solids*, 38, 1355-1362, 1977.
- Chayes, F., Alkaline and subalkaline basalts, *Amer. J. Sci.*, 264, 128-145, 1966.
- Chayes, F., On translating petrographic information into bits and bytes, in *Geomathematics: Past, Present, and Prospects*, D. W. Merriam, ed., *Syracuse Univ. Geol. Contrib.*, 5, 19-22, 1978a.
- Chayes, F., Card format for copy submitted on version JAN78 of the IGBA coding form, *Circ. 78-3D, IGCP-163-IGBA*, 13 pp., 1978b.
- Chayes, F., IGBACD—a prototype card and card-image processor for use by IGCP Project 163, *Circ. 78-6B, IGCP-163-IGBA*, 7 pp., 1978c.
- Chayes, F., Major results of the Syracuse Workshop, *Circ. 78-7, IGCP-163-IGBA*, 9 pp., 1978d.
- Chayes, F., Notes on the use of program KRDKON, *Circ. 79-1, IGCP-163-IGBA*, 6 pp., 1979a.
- Chayes, F., Organizational status of Project 163-IGBA as of 1 March 1979: an interim report to the IGCP Board, *Circ. 79-3, IGCP-163-IGBA*, 5 pp., 1979b.
- Chayes, F., Electronic computation and book-keeping in igneous petrology, *Episodes*, 1979-1, 16-19, 1979c.
- Chayes, F., and F. Mutschler, Explanatory notes for version 5FEB79 of data forms for the igneous data base designed by Project 163, *Circ. 79-2, IGCP-163-IGBA*, 13 pp., 1979.
- Chou, I. M., and H. P. Eugster, Solubility of magnetite in supercritical chloride solutions, *Amer. J. Sci.*, 277, 1296-1314, 1977.
- Christian, J. W., *The Theory of Transformations in Metals and Alloys*, Pergamon Press, London, 1965.
- Cohen, A. J., and R. G. Gordon, Modified electron-gas study of the stability, elastic properties, and high-pressure behavior of MgO and CaO crystals, *Phys. Rev. B*, 14, 4593-4605, 1976.
- Cohen, H. M., and R. Roy, Effects of ultra-high pressures on glass, *J. Amer. Ceram. Soc.*, 44, 523-524, 1961.
- Colby, J. W., MAGIC IV, a computer program for quantitative electron microprobe analysis, Bell Telephone Laboratories, Allentown, Pennsylvania, 1971.
- Colthup, N. B., L. H. Daly, and S. E. Wiberley, *Introduction to Infrared and Raman Spectroscopy*, 2d ed., Academic Press, New York, 1975.
- Condit, R. H., R. R. Hobbins, and C. E. Birchenall, Self-diffusion of iron and sulfur in ferrous sulfide, *Oxid. Met.*, 8, 409-455, 1974.
- Cooper, V. G., A. D. May, E. H. Hara, and H. F. P. Knapp, Dicke narrowing and collisional broadening of the  $S_0(0)$  and  $S_0(1)$  Raman line of  $H_2$ , *Can. J. Phys.*, 46, 2019-2023, 1968.
- Crerar, D. A., N. J. Susak, M. Borsik, and S. Schwartz, Solubility of the buffer assemblage pyrite + pyrrhotite + magnetite in NaCl solutions from 200 to 350°C, *Geochim. Cosmochim. Acta*, 42, 1427-1438, 1978.
- Cullers, R. L., L. G. Medaris, and L. A. Haskin, Experimental studies of the distribution of rare earths as trace elements among silicate minerals and liquids with water, *Geochim. Cosmochim. Acta*, 37, 1499-1512, 1973.
- Danchin, R. V., Mineral and bulk chemistry of garnet lherzolite and garnet harzburgite xenoliths from the Premier Mine, South Africa, in *The Mantle Sample: Inclusions in Kimberlites and Other Volcanics (Proc. 2d Int. Kimberlite Conf., Vol. 2)*, F. R. Boyd and H. O. A. Meyer, eds., American Geophysical Union, Washington, D.C., pp. 104-126, 1979.
- Darken, L. S., and R. W. Gurry, The system iron-oxygen. I. The wüstite field and related equilibria, *J. Amer. Chem. Soc.*, 67, 1398-1412, 1945.
- Davies, G. F., and E. S. Gaffney, Identification of high-pressure phases of rocks and minerals from Hugoniot data, *Geophys. J. Roy. Astron. Soc.*, 33, 165-183, 1973.
- Davies, J. S., Occurrence and biosynthesis of D-amino acids, in *Chemistry and Biochemistry of Amino Acids, Peptides, and Proteins*, Vol. 4, B. Weinstein, ed., Marcel Dekker, Inc., New York, pp. 1-27, 1977.
- Davis, G. L., The ages and uranium contents of zircons from kimberlites and associated rocks, *Extended Abstracts, Second International Kimberlite Conference*, Santa Fe, New Mexico, 1977.
- Dawson, J. B., and J. B. Hawthorne, Magmatic sedimentation and carbonatitic differentiation in kimberlite sills at Benfontein, South Africa, *J. Geol. Soc. London*, 129, 61-85, 1973.

- Demarest, H. H., Jr., R. Ota, and O. L. Anderson, Prediction of high-pressure phase transitions by elastic constant data, in *High-Pressure Research: Applications in Geophysics*, M. H. Manghnani and S. Akimoto, eds., Academic Press, New York, pp. 281-301, 1977.
- de Silva, L. C. C., and R. F. Mehl, Interface and marker movements in diffusion in solid solutions of metals, *Trans. AIME*, **191**, 155-173, 1951.
- Deüser, W. G., Iron-magnesium-aluminum relationship in achondrites, *Chem. Geol.*, **3**, 81-87, 1968.
- DeVries, R. C., Plastic deformation and "work-hardening" of diamond, *Mater. Res. Bull.*, **10**, 1193-1200, 1975.
- Dickson, F. W., Stability of cinnabar in  $\text{Na}_2\text{S}$  solutions at 50 to 250°C and 1-1800 bars with geologic applications, *Econ. Geol.*, **59**, 625-635, 1964.
- Dickson, F. W., and G. Tunell, The stability relations of cinnabar and metacinnabar, *Amer. Mineral.*, **44**, 471-487, 1959.
- Drake, M. J., The oxidation state of europium as an indicator of oxygen fugacity, *Geochim. Cosmochim. Acta*, **39**, 55-64, 1975.
- Drake, M. J., and D. F. Weill, New rare earth element standards for electron microprobe analysis, *Chem. Geol.*, **10**, 179-181, 1972.
- Dudziak, K. H. von, and E. U. Franck, Messungen der Viskosität des Wassers bis 560°C und 3500 bar, *Ber. Bunsenges. Phys. Chem.*, **70**, 1120-1128, 1966.
- Dziewonski, A. M., A. L. Hales, and E. R. Lapwood, Parametrically simple earth models consistent with geophysical data, *Phys. Earth Planet. Interiors*, **10**, 12-48, 1975.
- Eggler, D. H., and M. Rosenhauer, Carbon dioxide in silicate melts: II. Solubilities of  $\text{CO}_2$  and  $\text{H}_2\text{O}$  in  $\text{CaMgSi}_2\text{O}_6$  (diopside) liquids and vapors at pressure to 40 kb, *Amer. J. Sci.*, **278**, 64-94, 1978.
- Eggler, D. H., and R. F. Wendlandt, Experimental studies on the relationship between kimberlite magmas and partial melting of peridotite, in *Kimberlites, Diatremes, and Diamonds: Their Geology, Petrology, and Geochemistry (Proc. 2d Int. Kimberlite Conf., Vol. 1)*, F. R. Boyd and H. O. A. Meyer, eds., American Geophysical Union, Washington, D.C., pp. 330-338, 1979.
- England, W., J. C. Raich, and R. D. Etters, Rotational motion under pressure in the solid molecular hydrogen, *J. Low Temp. Phys.*, **22**, 213-222, 1976.
- English, S., The effect of various constituents on the viscosity of glass near its annealing temperature, *J. Soc. Glass Technol.*, **7**, 25-45, 1923.
- Epstein, S., C. J. Yapp, and J. H. Hall, The determination of the D/H ratio of non-exchangeable hydrogen in cellulose extracted from aquatic and land plants, *Earth Planet. Sci. Lett.*, **30**, 241-251, 1976.
- Etchepare, J., Study by Raman spectroscopy of crystalline and glassy diopside, in *Amorphous Materials*, R. W. Douglas and B. Ellis, eds., John Wiley and Sons, Inc., New York, pp. 337-346, 1972.
- Evans, T., and R. K. Wild, Plastic bending of diamond plates, *Phil. Mag.*, **12**, 479-489, 1965.
- Fernandez-Moran, H., M. Ohtsuki, and A. Hibino, Correlated electron microscopy and diffraction of lunar clinopyroxenes from Apollo 12 samples, in *Proc. Second Lunar Sci. Conf.*, 109-116, 1971.
- Fesq, H. W., E. J. D. Kable, and J. J. Gurney, Aspects of the geochemistry of kimberlites from the Premier Mine and other selected South African occurrences with particular reference to the rare earth elements, *Phys. Chem. Earth*, **9**, 687-708, 1975.
- Finch, C. B., G. W. Clark, L. A. Harris, and C. S. Yust, Czochralski growth and characterization of single-crystal akermanite ( $\text{Ca}_2\text{MgSi}_2\text{O}_7$ ), *J. Crystal Growth*, **23**, 295-298, 1974.
- Finger, L. W., and R. M. Hazen, Crystal structure and compressibility of ruby to 46 kbar, *J. Appl. Phys.*, **49**, 5823-5826, 1978.
- Finger, L. W., and R. M. Hazen, Response of oxygen-based structures to changes in pressure, temperature, and composition, *Trans. Amer. Crystallogr. Assoc.*, **15**, in press, 1979.
- Finger, L. W., R. M. Hazen, and T. Yagi, Crystal structures and electron densities of nickel and iron silicate spinels at elevated temperature or pressure, *Amer. Mineral.*, **64**, in press, 1979.
- Fisher, J. R., and E.-A. Zen, Thermodynamic calculations from hydrothermal phase equilibrium data and the free energy of  $\text{H}_2\text{O}$ , *Amer. J. Sci.*, **270**, 297-314, 1971.
- Fitch, F. J., and J. A. Miller, Potassium-argon radioages of Karoo volcanic rocks from Lesotho, *Bull. Volcanol.*, **35**, 64-84, 1971.
- Fleury, P. A., J. F. Scott, and T. M. Worlock, Soft phonon modes and the 110°K phase transition in  $\text{SrTiO}_3$ , *Phys. Rev. Lett.*, **21**, 16-19, 1968.



- Fodor, R. V., and K. Keil, A komatiite-like lithic fragment with spinifex texture in the Eva meteorite: origin from a supercooled impact-melt of chondritic parentage, *Earth Planet. Sci. Lett.*, 29, 1-6, 1976.
- Fong, M. Y., and M. Nicol, Raman spectrum of calcium carbonate at high pressures, *J. Chem. Phys.*, 54, 579-585, 1971.
- Franck, E. U., Hochverdichteter wasserdampf. III. Ionendissoziation von HCl, KOH und H<sub>2</sub>O in überkritischem wasser, *Z. Phys. Chem.*, 8, 192-206, 1956a.
- Franck, E. U., Hochverdichteter wasserdampf. I. Electrolytische Leitfähigkeit in KCl-H<sub>2</sub>O-lösungen bis 750°C, *Z. Phys. Chem.*, 8, 92-106, 1956b.
- Franck, E. U., J. E. Savolainen, and W. L. Marshall, Electrical conductance cell assembly for use with aqueous solutions up to 800°C and 4000 bars, *Rev. Sci. Instrum.*, 33, 115-117, 1962.
- Frantz, J. D., and H. P. Eugster, Acid-base buffers: use of Ag + AgCl in the experimental control of solution equilibria at elevated pressures and temperatures, *Amer. J. Sci.*, 267, 268-286, 1973.
- Frantz, J. D., and H. K. Mao, Bimetasomatism resulting from intergranular diffusion. II. Prediction of multiminerale zone sequences, *Amer. J. Sci.*, 279, 302-323, 1979.
- Frantz, J. D., and R. K. Popp, Mineral solution equilibria: I. An experimental study of complexing and thermodynamic properties of aqueous MgCl<sub>2</sub> in the system MgO-SiO<sub>2</sub>-H<sub>2</sub>O-HCl, *Geochim. Cosmochim. Acta*, in press, 1979.
- Frey, F. A., and M. Prinz, Ultramafic inclusions from San Carlos, Arizona: petrologic and geochemical data bearing on their petrogenesis, *Earth Planet. Sci. Lett.*, 38, 129-176, 1978.
- Frey, F. A., L. A. Haskin, and M. A. Haskin, Rare earth abundances in some ultramafic rocks, *J. Geophys. Res.*, 76, 2057-2070, 1971.
- Frey, F. A., D. H. Green, and S. D. Roy, Integrated models of basalt petrogenesis: a study of quartz tholeiites to olivine melilitites from southeastern Australia utilizing geochemical and experimental petrological data, *J. Petrology*, 19, 463-513, 1978.
- Fudali, R. F., Oxygen fugacities of basaltic and andesitic magmas, *Geochim. Cosmochim. Acta*, 29, 1063-1075, 1965.
- Fuoss, R. M., L. Onsager, and J. F. Skinner, The conductance of symmetrical electrolytes. V. The conductance equation, *J. Phys. Chem.*, 69, 2581-2594, 1965.
- Furukawa, T. S., and W. B. White, Raman spectroscopic investigation of the structure of silicate glasses. III. Alkali-silico-germanates, *Progress Report to the U. S. Department of Energy*, February 1979, Appendix 4.2, 1979.
- Furukawa, T., S. Brawer, and W. B. White, The structure of lead silicate glasses determined by vibrational spectroscopy, *J. Mater. Sci.*, 13, 268-282, 1978.
- Galeener, F. L., J. C. Mikkelsen, Jr., R. H. Geils, and W. J. Mosby, The relative Raman cross sections of vitreous SiO<sub>2</sub>, GeO<sub>2</sub>, B<sub>2</sub>O<sub>3</sub>, and P<sub>2</sub>O<sub>5</sub>, *Appl. Phys. Lett.*, 32, 34-36, 1978.
- Garlick, G. D., I. D. MacGregor, and D. E. Vogel, Oxygen isotope ratios in eclogites from kimberlites, *Science*, 172, 1025-1026, 1971.
- Gast, P. W., Trace element fractionation and the origin of tholeiitic and alkaline magma types, *Geochim. Cosmochim. Acta*, 32, 1057-1086, 1968.
- Geller, S., Crystal chemistry of the garnets, *Z. Kristallogr.*, 125, 1-47, 1967.
- General Electric Company, *GE Transistor Manual*, 7th ed., General Electric Company, Electronics Park, Syracuse, New York, pp. 301-347, 1964.
- German, V. N., N. N. Orlova, L. A. Tarasova, and R. T. Trunin, Obtaining of orthorhombic phase of SiO<sub>2</sub> in conditions of dynamic compression, *Izv. Acad. Sci. USSR Phys. Solid Earth*, 7, 50-56, 1975.
- Gobrecht, H., H. Nelkowski, J. W. Baars, and M. Weigt, Self diffusion of sulfur in zinc sulfide, *Solid State Comm.*, 5, 777-778, 1967.
- Gagnani, R., Le vulcaniti melilitiche di Cupaello (Rieti), *Rend. Soc. Ital. Mineral. Petrologia*, 28, 165-189, 1972.
- Greenwood, N. N., and A. T. Howe, Mössbauer studies of Fe<sub>1-x</sub>O. Part II. Disproportionation between 300 and 700K, *J. Chem. Soc. Dalton Trans.*, 116-121, 1972.
- Greig, J. W., Immiscibility in silicate melts, Part 1, *Amer. J. Sci.*, 13, 2-44, 1927.
- Griffith, W. P., Raman spectroscopy of minerals, *Nature (London)*, 224, 264-266, 1969.
- Grutzeck, M., S. Kridelbaugh, and D. Weill, The distribution of Sr and REE between diopside and silicate liquid, *Geophys. Res. Lett.*, 1, 273-275, 1974.

- Gunter, W., and H. P. Eugster, Wollastonite solubility and free energy of supercritical aqueous  $\text{CaCl}_2$ , *Contrib. Mineral. Petrol.*, **66**, 271–281, 1978.
- Haggerty, S. E., Luna 16. An opaque mineral study and a systematic examination of compositional variation of spinels from Mare Fecunditatis, *Earth Planet. Sci. Lett.*, **93**, 328–352, 1972.
- Haggerty, S. E., Spinel of unique composition associated with ilmenite reaction mantles in the Lihobong kimberlite pipe, Lesotho, in *Lesotho Kimberlites*, P. H. Nixon, ed., Lesotho National Development Corporation, Maseru, Lesotho, pp. 149–158, 1973.
- Haggerty, S. E., The chemistry and genesis of opaque minerals in kimberlites, *Phys. Chem. Earth*, **9**, 295–307, 1975.
- Haggerty, S. E., R. B. Hardie III, and B. M. McMahon, The mineral chemistry of ilmenite nodule association from the Monastery diatreme, in *The Mantle Sample: Inclusions in Kimberlites and Other Volcanics* (Proc. 2d Int. Kimberlite Conf., Vol. 2), F. R. Boyd and H. O. A. Meyer, eds., American Geophysical Union, Washington, D.C., pp. 249–256, 1979.
- Hanley, P. L., I. Kiflawi, and A. R. Lang, On topographically identifiable sources of cathodoluminescence in natural diamonds, *Phil. Trans. Roy. Soc. London*, **284A**, 329–368, 1977.
- Hara, Y., and M. Nicol, Raman spectra and the structure of rutile at high pressures, *Phys. Stat. Sol. B*, **94**, in press, 1979.
- Hare, P. E., and E. Gil-Av, Separation of D and L amino acids by ligand chromatography: use of chiral eluants, *Science*, **204**, 1226–1228, 1979.
- Hart, R. S., D. L. Anderson, and H. Kanamori, The effect of attenuation on gross earth models, *J. Geophys. Res.*, **82**, 1647–1654, 1977.
- Hart, S. R., and K. E. Davis, Nickel partitioning between olivine and silicate melt, *Earth Planet. Sci. Lett.*, **40**, 203–220, 1978.
- Harte, B., Rock nomenclature with particular relation to deformation and recrystallization textures in olivine-bearing xenoliths, *J. Geol.*, **85**, 279–288, 1977.
- Haskin, L. A., F. A. Frey, M. A. Haskin, R. F. Schmitt, and R. H. Smith, Meteorite, solar and terrestrial abundances of rare earth distribution, *Phys. Chem. Earth*, **7**, 167–321, 1966.
- Hass, M., Raman spectra of vitreous silica, germania, and sodium silicate glasses, *J. Phys. Chem. Solids*, **31**, 415–422, 1970.
- Hazen, R. M., Temperature, pressure and composition: structurally analogous variables, *Phys. Chem. Minerals*, **1**, 83–94, 1977.
- Hazen, R. M., and L. W. Finger, Crystal chemistry of silicon-oxygen bonds at high pressure: implications for the earth's mantle mineralogy, *Science*, **201**, 1122–1123, 1978.
- Hazen, R. M., and L. W. Finger, Crystal structure and compressibility of zircon at high pressure, *Amer. Mineral.*, **64**, 196–201, 1979a.
- Hazen, R. M., and L. W. Finger, Polyhedral tilting: a common type of displacive phase transition and its relation to analcite at high pressure, *Phase Transitions*, **1**, 1–22, 1979b.
- Hazen, R. M., and L. W. Finger, Linear compressibilities of  $\text{NaNO}_2$  and  $\text{NaNO}_3$ , *Appl. Phys. Lett.*, in press, 1979c.
- Hazen, R. M., and L. W. Finger, Bulk modulus-volume relationship for cation-anion polyhedra, *J. Geophys. Res.*, in press, 1979d.
- Helgeson, H. C., Evaluation of irreversible reactions in geochemical processes involving minerals and aqueous solutions. I. Thermodynamic relations, *Geochim. Cosmochim. Acta*, **32**, 853–877, 1968.
- Helgeson, H. C., J. M. Delany, H. W. Nesbitt, and D. K. Bird, Summary and critique of the thermodynamic properties of rock-forming minerals, *Amer. J. Sci.*, **278A**, 1–229, 1978.
- Herzberg, G., *Molecular Spectra and Molecular Structure*, Vol. 2, D. Van Nostrand Company, New York, 1945.
- Hess, H. H., Stillwater Igneous Complex, Montana—a quantitative mineralogical study, *Geol. Soc. Amer. Mem.*, **80**, 230 pp., 1960.
- Hess, P. C., Structure of silicate melts, *Can. Mineral.*, **15**, 162–178, 1977.
- Hey, M. H., *Catalogue of Meteorites*, The British Museum of Natural History, London, Publication No. 464, 1966.
- Hibben, J. H., Raman spectra in organic chemistry, *Chem. Rev.*, **18**, 1–236, 1936.
- Hildebrand, J. H., and R. L. Scott, *The Solubility of Nonelectrolytes*, Dover Publications, New York, 1964.
- Hite, H. E., and R. J. Kearney, Elastic constants of  $\text{CaO}$  in the temperature range 80°–270°K, *J. Appl. Phys.*, **38**, 5424–5425, 1967.
- Hoering, T. C., Stable isotopes of hydrogen in Precambrian organic matter, in *Chemical Evolution of the Early Precambrian*, C. Ponamperuma, ed., Academic Press, New York, pp. 81–85, 1977.



- Holloway, J. R., Fugacity and activity of molecular species in supercritical fluids, in *Thermodynamics in Geology*, D. G. Fraser, ed., Reidel Publishing Co., Dordrecht, Holland, pp. 161–181, 1977.
- Huang, C. K., and P. F. Kerr, Infrared study of the carbonate minerals, *Amer. Mineral.*, **45**, 311–324, 1960.
- Hubbert, M. K., Theory of scale models as applied to the study of geologic structures, *Geol. Soc. Amer. Bull.*, **48**, 1459–1520, 1937.
- Huebner, J. S., M. Ross, and N. Hickling, Significance of exsolved pyroxenes from lunar breccia 77215, in *Proc. Sixth Lunar Sci. Conf.*, 529–546, 1975.
- Irvine, T. N., Rocks whose compositions are determined by crystal sorting and accumulation, in *Evolution of the Igneous Rocks: Fiftieth Anniversary Perspectives*, H. S. Yoder, Jr., ed., Princeton University Press, Princeton, New Jersey, pp. 245–306, 1979.
- Irvine, T. N., and W. R. A. Baragar, A guide to the chemical classification of the common volcanic rocks, *Can. J. Earth Sci.*, **8**, 523–548, 1971.
- Irvine, T. N., and C. H. Smith, Ultramafic rocks of the Muskox intrusion, in *Ultramafic and Related Rocks*, P. J. Wyllie, ed., John Wiley and Sons, Inc., New York, pp. 38–49, 1967.
- Irving, A. J., A review of experimental studies of crystal/liquid trace element partitioning, *Geochim. Cosmochim. Acta*, **42**, 743–771, 1978.
- Irving, A. J., and F. A. Frey, Distribution of trace elements between garnet megacrysts and host volcanic liquids of kimberlitic to rhyolitic compositions, *Geochim. Cosmochim. Acta*, **42**, 771–789, 1978.
- Jackson, E. D., Primary textures and mineral associations in the Ultramafic zone of the Stillwater Complex, Montana, *U.S. Geol. Surv. Prof. Pap.*, **358**, 106 pp., 1961.
- Jackson, E. D., Ultramafic cumulates in the Stillwater, Great Dyke, and Bushveld intrusions, in *Ultramafic and Related Rocks*, P. J. Wyllie, ed., John Wiley and Sons, Inc., New York, pp. 20–38, 1967.
- Jackson, E. D., The chromite deposits of the Stillwater Complex, Montana, in *Ore Deposits of the United States, 1933–1967 (Graton-Sales Volume)*, **2**, American Institute of Mining, Metallurgical and Petroleum Engineers, 1505 pp., 1968.
- Jackson, E. D., The cyclic unit in layered intrusions—a comparison of the repetitive stratigraphy in the ultramafic parts of the Stillwater, Muskox, Great Dyke, and Bushveld Complexes, *Geol. Soc. S. Afr. Spec. Publ.*, **1**, 391–424, 1970.
- Jackson, E. D., and T. L. Wright, Xenoliths in the Honolulu volcanic series, Hawaii, *J. Petrology*, **11**, 405–430, 1970.
- Jackson, I., Melting of silica isotopes  $\text{SiO}_2$ ,  $\text{BeF}_2$ , and  $\text{GeO}_2$  at elevated pressures, *Phys. Earth Planet. Interiors*, **13**, 218–231, 1976.
- Jamieson, J. C., Phase transitions in rutile-type structures, in *High-Pressure Research: Applications in Geophysics*, M. H. Manghnani and S. Akimoto, eds., Academic Press, New York, pp. 209–218, 1977.
- Jammu, K. S., G. E. St. John, and H. L. Welsh, Pressure broadening of the rotational Raman lines of some simple gases, *Can. J. Phys.*, **44**, 797–814, 1960.
- Jayaraman, A., Pressure-induced electronic collapse of semiconductor-to-metal transition in  $\text{EuO}$ , *Phys. Rev. Lett.*, **29**, 1674–1676, 1972.
- Jeanloz, R., T. J. Ahrens, and M. Somerville,  $\text{FeO}$ : equation of state to 200 GPa (2 Mbar) (abstract), *Eos*, **60**, 387, 1979.
- Jerome, D. Y., and G. G. Goles, A reexamination of relationships among pyroxene-plagioclase achondrites, in *Activation Analysis in Geochemistry and Cosmochemistry*, A. O. Brunfelt, ed., Universitetsforlaget, Oslo, pp. 261–266, 1971.
- Johns-Manville Corporation, Ongoing Projects, *Eng. Mining J.*, **179**, 148, 1978.
- Jones, G., and B. C. Bradshaw, The measurement of the conductance of electrolytes. V. A redetermination of the conductance of standard potassium chloride solutions in absolute units, *J. Amer. Chem. Soc.*, **55**, 1780–1800, 1933.
- Jones, L. W., and J. Myers, A common link between photosynthesis and respiration in a blue-green alga, *Nature (London)*, **199**, 670–672, 1963.
- Jones, W. R., J. W. Peoples, and A. L. Howland, Igneous and tectonic structures of the Stillwater Complex, Montana, *U.S. Geol. Surv. Bull.*, **1071-H**, 287 pp., 1960.
- Jordan, T. H., The deep structure of the continents, *Sci. Amer.*, **240**, 92–107, 1979.
- Jost, W., Bemerkung zur mathematischem Behandlung komplizierter Diffusionsprobleme, *Z. Phys.*, **127**, 163–167, 1950.
- Kable, E. J. D., H. W. Fesq, and J. J. Gurney, The significance of the inter-element rela-

- tionships of some minor and trace elements in South African kimberlites, *Phys. Chem. Earth*, **9**, 709–733, 1975.
- Katsura, T. B., I. Iwasaki, and S. Kimura, High-pressure synthesis of the stoichiometric compound FeO, *J. Chem. Phys.*, **47**, 4559–4560, 1967.
- Kay, R. W., and P. W. Gast, The rare earth content and origin of alkali-rich basalts, *J. Geol.*, **81**, 653–682, 1973.
- Keith, M. L., and R. Roy, Structural relations among double oxides of trivalent elements, *Amer. Mineral.*, **39**, 1–23, 1954.
- Kennedy, C. S., and G. C. Kennedy, The equilibrium boundary between graphite and diamond, *J. Geophys. Res.*, **81**, 2467–2470, 1976.
- Kingery, W. D., Plausible concepts necessary and sufficient for interpretation of ceramic grain-boundary phenomena: I. Grain-boundary characteristics, structure, and electrostatic potential, *J. Amer. Ceram. Soc.*, **57**, 1–8, 1974a.
- Kingery, W. D., Plausible concepts necessary and sufficient for interpretation of ceramic grain-boundary phenomena: II. Solute segregation, grain-boundary diffusion, and general discussion, *J. Amer. Ceram. Soc.*, **57**, 74–83, 1974b.
- Kirkpatrick, R. J., Kinetics of crystal growth in the system  $\text{CaMgSi}_2\text{O}_6\text{--CaAl}_2\text{SiO}_6$ , *Amer. J. Sci.*, **274**, 215–242, 1974.
- Kovalev, G. N., Diffusion along grain boundaries in rock in the presence of water, *Int. Geol. Rev.*, **197**, 176–178, 1972.
- Kracek, F. C., The system sodium oxide-silica, *J. Phys. Chem.*, **34**, 1583–1598, 1930.
- Krishnan, R. S., and J. P. Russell, The first-order Raman spectrum of magnesium fluoride, *Brit. J. Appl. Phys.*, **17**, 501–503, 1966.
- Kumar, V., and F. A. Kroger, Self diffusion and the defect structure of CdS, *J. Solid State Chem.*, **3**, 387–400, 1971.
- Kuno, H., Differentiation of basalt magmas, in *Basalts*, H. H. Hess and A. Poldervaart, eds., John Wiley and Sons, Inc., New York, pp. 623–688, 1968.
- Kuno, H., and K. Aoki, Chemistry of ultramafic nodules and their bearing on the origin of basaltic magmas, *Phys. Earth Planet. Interiors*, **3**, 273–301, 1970.
- Kurkjian, C. R., P. K. Gallagher, W. R. Sinclair, and E. A. Sigety, The absorption and fluorescence spectra of trivalent europium in silicate glasses, *Phys. Chem. Glasses*, **4**, 239–246, 1963.
- Kushiro, I., Changes in viscosity and structure of melt of  $\text{NaAlSi}_2\text{O}_6$  composition at high pressures, *J. Geophys. Res.*, **81**, 6347–6350, 1976.
- Kushiro, I., Phase transformation in silicate melts under upper-mantle conditions, in *High-Pressure Research: Applications in Geophysics*, M. H. Manghnani and S. Akimoto, eds., Academic Press, New York, pp. 25–37, 1977.
- Kushiro, I., Viscosity and structural changes of albite ( $\text{NaAlSi}_3\text{O}_8$ ) melt at high pressures, *Earth Planet. Sci. Lett.*, **41**, 87–90, 1978.
- Kushiro, I., and H. S. Yoder, Jr., Anorthite-forsterite and anorthite-enstatite reactions and their bearing on the basalt-eclogite transformation, *J. Petrology*, **7**, 337–362, 1966.
- Kushiro, I., H. S. Yoder, Jr., and B. O. Mysen, Viscosities of basalt and andesite melts at high pressures, *J. Geophys. Res.*, **81**, 6351–6356, 1976.
- Lauer, H. V., and R. V. Morris, Redox equilibria of multivalent ions in silicate glasses, *J. Amer. Ceram. Soc.*, **60**, 443–451, 1977.
- Lazarev, A. N., *Vibrational Spectra and Structure of Silicates*, Consultants Bureau, New York, 1972.
- Leeman, W. P., Experimental determination of partitioning of divalent cations between olivine and basaltic liquid, Part 2 of Ph.D. thesis, University of Oregon, 1974.
- Liberman, D. A., Equation of state of molecular hydrogen at high pressure, *Los Alamos Scientific Laboratory Report*, LA-4727-MS, 1971.
- Liebenberg, D. H., R. L. Mills, and J. C. Bronson, Measurement of  $P$ ,  $V$ ,  $T$  and sound velocity across the melting curve of  $n\text{-H}_2$  and  $n\text{-D}_2$  to 19 kbar, *Phys. Rev. B*, **18**, 4526–4532, 1978.
- Liebermann, R. C., L. E. A. Jones, and A. E. Ringwood, Elasticity of aluminite, titanate, stannate, and germanate compounds with the perovskite structure, *Phys. Earth Planet. Interiors*, **14**, 165–178, 1977.
- Lindner, R., Studies on solid state reactions with radiotracers, *J. Chem. Phys.*, **23**, 410–411, 1955.
- Lindsley, D. H., and S. S. Dixon, Coexisting diopside and enstatite at 20 kbar and 900–1200°C, *Amer. J. Sci.*, **276**, 1285–1301, 1976.



- Liu, L. G., A dense modification of BaO and its crystal structure, *J. Appl. Phys.*, **42**, 3702–3704, 1971.
- Liu, L. G., Synthesis of a new high-pressure phase of tin dioxide and some geophysical implications, *Phys. Earth Planet. Interiors*, **9**, 338–343, 1974.
- Liu, L. G., Orthorhombic perovskite phases observed in olivine, pyroxene and garnet at high pressures and temperatures, *Phys. Earth Planet. Interiors*, **11**, 289–298, 1976a.
- Liu, L. G., The high-pressure phases of  $\text{FeSiO}_2$  with implications for  $\text{Fe}_2\text{SiO}_4$  and  $\text{FeO}$ , *Earth Planet. Sci. Lett.*, **33**, 101–106, 1976b.
- Liu, L. G., Synthesis of a new high-pressure phase of manganese dioxide, *Earth Planet. Sci. Lett.*, **29**, 104–106, 1976c.
- Liu, L. G., A fluorite isotype of  $\text{SnO}_2$  and a new modification of  $\text{TiO}_2$ : implications for the earth's lower mantle, *Science*, **199**, 422–424, 1978.
- Liu, L. G., and W. A. Bassett, Effect of pressure on the crystal structure and the lattice parameters of BaO, *J. Geophys. Res.*, **77**, 4934–4937, 1972.
- Liu, L., and W. A. Bassett, The melting of iron up to 2000 kbar, *J. Geophys. Res.*, **80**, 3777–3782, 1975.
- Liu, L. G., W. A. Bassett, and J. Sharpy, New high pressure modifications of  $\text{GeO}_2$  and  $\text{SiO}_2$ , *J. Geophys. Res.*, **83**, 2301–2305, 1978.
- Louisnathan, S. J., The crystal structure of synthetic soda melilite,  $\text{CaNaAlSi}_2\text{O}_7$ , *Z. Kristallogr.*, **131**, 314–321, 1970.
- Low, W., and E. L. Offenbacher, Electron spin resonance of magnetic ions in complex oxides. Review of ESR results in rutile perovskites, spinel and garnet structures, *Solid State Phys.*, **17**, 137–193, 1965.
- Lücke, K., and H. P. Stüwe, On the theory of impurity controlled grain boundary motion, *Acta Met.*, **14**, 1087–1099, 1971.
- Lücke, K., R. Rixen, and F. W. Rosenbaum, On the theory of grain boundary motion, in *The Nature and Behavior of Grain Boundaries*, H. Hu, ed., Plenum, New York, pp. 245–283, 1972.
- Macdonald, G. A., and T. Katsura, Chemical composition of Hawaiian lavas, *J. Petrology*, **5**, 82–133, 1964.
- MacGregor, I. D., The system  $\text{MgO-Al}_2\text{O}_3\text{-SiO}_2$ : solubility of  $\text{Al}_2\text{O}_3$  in enstatite for spinel and garnet peridotite compositions, *Amer. Mineral.*, **59**, 110–119, 1974.
- Mao, H. K., and P. M. Bell, Disproportionation equilibrium in iron-bearing systems at pressures above 100 kbar with applications to chemistry of the earth's mantle, in *Energetics of Geological Processes*, S. K. Saxena and S. Bhattacharji, eds., Springer-Verlag New York Inc., New York, pp. 236–249, 1977.
- Mao, H. K., and P. M. Bell, High-pressure physics: sustained static generation of 1.36 to 1.73 megabars, *Science*, **200**, 1145–1147, 1978.
- Mao, H. K., P. M. Bell, J. W. Shaner, and D. J. Steinberg, Specific volume measurements of Cu, Mo, Pd, and Ag and calibration of the ruby  $R_1$  fluorescence pressure gauge from 0.06 to 1 Mbar, *J. Appl. Phys.*, **49**, 3276–3283, 1978.
- Mason, B., Olivine composition in chondrites, *Geochim. Cosmochim. Acta*, **27**, 1011–1023, 1963.
- Matano, C., On the relation between the diffusion coefficients and concentrations of solid metals, *Jap. J. Phys.*, **8**, 109–113, 1933.
- Maxwell, J. A., *Rock and Mineral Analysis*, John Wiley and Sons, Inc., New York, 1968.
- May, H. M., P. A. Helmke, and M. L. Jackson, Determination of mononuclear dissolved aluminum in near-neutral water, *Chem. Geol.*, **24**, 259–269, 1979.
- Mazzullo, L. J., S. A. Dixon, and D. H. Lindsay,  $T$ - $f_{\text{O}_2}$  relationships in Mn-bearing compositions (abstract), *Abstr. with Programs (Geol. Soc. Amer.)*, **7**, 1192, 1975.
- McBirney, A. R., and K. Aoki, Petrology of the Galápagos Islands, in *The Galápagos; Proceedings of the Symposia of the Galápagos International Scientific Project*, R. I. Bowman, ed., University of California Press, Berkeley and Los Angeles, pp. 71–77, 1966.
- McCallum, I. S., L. D. Radaeke, and E. A. Mathez, Investigations of the Stillwater Complex. Pt. I. Stratigraphy and structure of the banded zone, *Amer. J. Sci.*, Jackson vol., in press, 1979.
- McCarthy, T. S., A. J. Erlank, J. P. Willis, and L. H. Ahrens, New chemical analyses of six achondrites and one chondrite, *Meteoritics*, **9**, 215–224, 1974.
- McMahon, B. M., and S. E. Haggerty, The Oka carbonatite complex: magnetite compositions and the related role of titanium in pyrochlore, in *Kimberlites, Diatremes, and Diamonds: Their Geology, Petrology, and Geochemistry (Proc. 2d Int. Kimberlite Conf., Vol. 1)*, F. R. Boyd and H. O. A. Meyer,

- eds., American Geophysical Union, Washington, D.C., pp. 382-392, 1979.
- McQueen, R. G., J. C. Jamieson, and S. P. Marsh, Shock-wave compression and x-ray studies of titanium dioxide, *Science*, **155**, 1401-1404, 1967.
- Mercier, J.-C. C., Peridotite xenoliths and the dynamics of kimberlite intrusion, in *The Mantle Sample: Inclusions in Kimberlites and Other Volcanics (Proc. 2d Int. Kimberlite Conf., Vol. 2)*, F. R. Boyd and H. O. A. Meyer, eds., American Geophysical Union, Washington, D.C., pp. 197-212, 1979.
- Merrill, L., and W. Bassett, Miniature diamond anvil pressure cell for single crystal x-ray diffraction studies, *Rev. Sci. Instrum.*, **45**, 290-294, 1974.
- Meyer, C., and J. J. Hemley, Wall rock alteration, in *Geochemistry of Hydrothermal Ore Deposits*, H. L. Barnes, ed., Holt, Rinehart, and Winston, pp. 166-235, 1967.
- Milton, D. J., and P. S. DeCarli, Maskelynite: formation by explosive shock, *Science*, **140**, 670-671, 1963.
- Ming, L., and W. A. Bassett, Laser heating in the diamond anvil press up to 2000°C sustained and 3000°C pulsed at pressures up to 260 kbar, *Rev. Sci. Instrum.*, **45**, 1115-1118, 1974.
- Mitchell, R. H., Composition of spinels in micaceous kimberlites from the Upper Canada Mine, Kirkland Lake, Ontario, *Can. Mineral.*, **16**, 591-595, 1978a.
- Mitchell, R. H., Manganoan magnesian ilmenite and titanium clinohumite from the Jacupiranga carbonatite, São Paulo, Brazil, *Amer. Mineral.*, **63**, 544-547, 1978b.
- Mitchell, R. H., Mineralogy of the Tunraq kimberlite, Somerset Island, N.W.T., Canada, in *Kimberlites, Diatremes, and Diamonds: Their Geology, Petrology, and Geochemistry (Proc. 2d Int. Kimberlite Conf., Vol. 1)*, F. R. Boyd and H. O. A. Meyer, eds., American Geophysical Union, Washington, D.C., pp. 161-169, 1979.
- Mitchell, R. H., and D. B. Clark, Oxide and sulfide mineralogy of the Penyuk kimberlite, Somerset Island, N.W.T., Canada, *Contrib. Mineral. Petrol.*, **56**, 157-172, 1976.
- Mitchell, R. H., D. A. Carswell, and A. O. Brunfelt, The Monastery kimberlite pipe. 1. Mineralogy and rare earth geochemistry of an ilmenite-pyroxene xenolith from the Monastery Mine, in *Lesotho Kimberlites*, P. H. Nixon, ed., Lesotho National Development Corporation, Maseru, Lesotho, pp. 224-229, 1973.
- Miyachi, S., S. Miyachi, and A. Kamiya, Wavelength effects on photosynthetic carbon metabolism in *Chlorella*, *Plant Cell Physiol.*, **19**, 277-288, 1978.
- Miyamoto, M., and H. Takeda, Evaluation of a crust model of eucrites from the width of exsolved pyroxene, *Geochem. J.*, **11**, 161-169, 1977.
- Mockovciak, S., J. Pantoficek, and K. Patek, Crystal field calculations of transition probabilities in Nd<sup>3+</sup> in glass, *Phys. Status Solidi*, **11**, 401-405, 1965.
- Molnar, P., and J. Oliver, Lateral variation of attenuation in the upper mantle and discontinuities in the lithosphere, *J. Geophys. Res.*, **74**, 2648-2682, 1969.
- Morris, R. V., Electron paramagnetic resonance study of the site preferences of Gd<sup>3+</sup> and Eu<sup>2+</sup> in polycrystalline silicate and aluminate minerals, *Geochim. Cosmochim. Acta*, **39**, 631-634, 1975.
- Moynihan, C. T., A. J. Easteal, and M. A. DeBolt, Dependence of the fictive temperature of glass on cooling rate, *J. Amer. Ceram. Soc.*, **59**, 12-16, 1976a.
- Moynihan, C. T., H. Sasabe, and J. Tucker, Kinetics of the glass transition in a calcium-potassium nitrate melt, in *Proceedings of International Symposium on Molten Salts*, J. P. Pemsler *et al.*, eds., Electrochemical Society, Inc., Princeton, New Jersey, pp. 182-194, 1976b.
- Muehlenbachs, K., and R. N. Clayton, Oxygen isotope studies of fresh and weathered submarine basalts, *Can. J. Earth Sci.*, **9**, 172-184, 1972.
- Murase, T., and A. R. McBirney, Properties of some common igneous rocks and their melts at high temperatures, *Geol. Soc. Amer. Bull.*, **84**, 3563-3592, 1973.
- Murray, J. R., and A. Javan, Motion narrowing in hydrogen Raman scattering, *J. Mol. Spectrosc.*, **29**, 502-504, 1969.
- Myers, J., and L. B. Clark, Culture conditions and the development of the photosynthetic mechanism. II. An apparatus for the continuous culture of *Chlorella*, *J. Gen. Physiol.*, **28**, 103-112, 1944.
- Mysen, B. O., The solubility of H<sub>2</sub>O and CO<sub>2</sub> under predicted magma genesis conditions and some petrological and geophysical implications, *Rev. Geophys. Space Phys.*, **15**, 351-361, 1977a.



- Mysen, B. O., Solubility of volatiles in silicate melts under the pressure and temperature conditions of partial melting in the upper mantle, in "Magma Genesis; Proceedings of the American Geophysical Union Chapman Conference on Partial Melting in the Earth's Upper Mantle," *Oreg. Dep. Geol. Miner. Ind. Bull.*, 96, 1-14, 1977b.
- Mysen, B. O., Experimental determination of rare earth element partitioning between hydrous silicate melt, amphibole and garnet peridotite minerals at upper mantle pressures and temperatures, *Geochim. Cosmochim. Acta*, 42, 1253-1263, 1978a.
- Mysen, B. O., Experimental determination of nickel partition coefficients between liquid, pargasite, and garnet peridotite minerals and concentration limits of behavior according to Henry's law at high pressure and temperature, *Amer. J. Sci.*, 278, 217-243, 1978b.
- Mysen, B. O., Limits of solution of trace elements in minerals according to Henry's law: review of experimental data, *Geochim. Cosmochim. Acta*, 42, 871-885, 1978c.
- Mysen, B. O., Trace element partitioning between garnet peridotite minerals and water-rich vapor: experimental data for 5 to 30 kbar, *Amer. Mineral.*, 64, 274-288, 1979.
- Mysen, B. O., and J. R. Holloway, Experimental determination of rare earth fractionation patterns in partial melts from peridotite in the upper mantle, *Earth Planet. Sci. Lett.*, 34, 231-237, 1977.
- Mysen, B. O., and I. Kushiro, Compositional variations of coexisting phases with degree of melting of peridotite in the upper mantle, *Amer. Mineral.*, 62, 843-865, 1977.
- Mysen, B. O., and I. Kushiro, The effect of pressure on the partitioning of nickel between olivine and aluminous silicate melt, *Earth Planet. Sci. Lett.*, 42, 383-389, 1979.
- Mysen, B. O., and M. G. Seitz, Trace element partitioning determined by beta-track mapping: an experimental study using carbon and samarium as examples, *J. Geophys. Res.*, 80, 2627-2635, 1975.
- Mysen, B. O., and D. Virgo, Influence of pressure, temperature, and bulk composition on melt structures in the system  $\text{NaAlSi}_2\text{O}_6$ - $\text{NaFe}^{3+}\text{Si}_2\text{O}_6$ , *Amer. J. Sci.*, 278, 1307-1322, 1978.
- Nafziger, R. H., and A. Muan, Equilibrium phase compositions and thermodynamic properties of olivine and pyroxenes in the system  $\text{MgO}$ - $\text{FeO}$ - $\text{SiO}_2$ , *Amer. Mineral.*, 52, 1364-1385, 1967.
- Nagel, L., and M. O'Keeffe, Pressure and stress induced polymorphism of compounds with rutile structure, *Mater. Res. Bull.*, 6, 1317-1320, 1971.
- Nakamoto, K., *Infrared and Raman Spectra of Inorganic and Coordination Compounds*, 3d ed., Wiley-Interscience, New York, 1978.
- Navrotsky, A., Enthalpies of transformation among the tetragonal, hexagonal and glassy modifications of  $\text{GeO}_2$ , *J. Inorg. Nucl. Chem.*, 33, 1119-1124, 1971.
- Navrotsky, A., J. C. Jamieson, and O. J. Kleppa, Enthalpy of transformation of a high-pressure polymorph of titanium dioxide to the rutile modification, *Science*, 158, 388-389, 1967.
- Nicholls, I. A., Petrology of Santorini volcano, Cyclades, Greece, *J. Petrology*, 12, 67-119, 1971.
- Nicol, M., and M. Y. Fong, Raman spectrum and polymorphism of titanium dioxide at high pressures, *J. Chem. Phys.*, 54, 3167-3170, 1971.
- Nixon, P. H., and F. R. Boyd, Petrogenesis of the granular and sheared ultrabasic nodule suite in kimberlites, in *Lesotho Kimberlites*, P. H. Nixon, ed., Lesotho National Development Corporation, Maseru, Lesotho, pp. 48-56, 1973a.
- Nixon, P. H., and F. R. Boyd, The Lihobong intrusion and kimberlitic olivine composition, in *Lesotho Kimberlites*, P. H. Nixon, ed., Lesotho National Development Corporation, Maseru, Lesotho, pp. 141-148, 1973b.
- Nixon, P. H., and F. R. Boyd, Garnet-bearing lherzolites and discrete nodule suites from the Malaita alnoite, Solomon Islands, S.W. Pacific, and their bearing on oceanic mantle composition and geotherm, in *The Mantle Sample: Inclusions in Kimberlites and Other Volcanics (Proc. 2d Int. Kimberlite Conf., Vol. 2)*, F. R. Boyd and H. O. A. Meyer, eds., American Geophysical Union, Washington, D.C., pp. 400-423, 1979.
- Nur, A., Tectonophysics: the study of relations between deformation and forces in the earth, in *Advances in Rock Mechanics*, Vol. 1, Part A, National Academy of Sciences, Washington, D.C., pp. 243-317, 1974.
- Nur, A., and G. Simmons, The origin of small cracks in igneous rocks, *Int. J. Rock Mech. Min. Sci.*, 7, 307-314, 1970.
- O'Hara, M. J., Is there an Icelandic mantle plume? *Nature*, 253, 708-710, 1975.

- Ohmoto, H., and D. Kerrick, Devolatilization equilibria in graphitic systems, *Amer. J. Sci.*, **277**, 1013-1044, 1977.
- O'Reilly, J. M., Effect of pressure on amorphous polymers, in *Modern Aspects of the Vitreous State*, Vol. 3, J. D. MacKenzie, ed., Butterworths, London, pp. 59-89, 1964.
- Osborn, E. F., Role of oxygen pressure in the crystallization and differentiation of basaltic magma, *Amer. J. Sci.*, **257**, 609-647, 1959.
- Osborn, E. F., Origin of calc-alkali magma series of Santorini volcano type in the light of recent experimental phase-equilibrium studies, in *Proceedings of the International Congress on Thermal Waters, Geothermal Energy and Vulcanism of the Mediterranean Area*, Athens, October 1976, **3**, 154-167, 1976.
- Osborn, E. F., The reaction principle, in *The Evolution of Igneous Rocks (Fiftieth Anniversary Perspectives)*, H. S. Yoder, Jr., ed., Princeton University Press, Princeton, New Jersey, pp. 133-169, 1979.
- Österberg, R., Models for copper-protein interaction based on solution and crystal structure studies, *Coord. Chem. Rev.*, **12**, 309-347, 1974.
- Page, N. J., Stillwater Complex, Montana: rock succession, metamorphism, and structure of the complex and adjacent rocks, *U.S. Geol. Surv. Prof. Pap.*, **999**, 79 pp., 1977.
- Peltier, W. R., Glacio-isostatic adjustment. II. The inverse problem, *Geophys. J. Roy. Astron. Soc.*, **46**, 669-706, 1976.
- Philpotts, J. A., C. C. Schnetzler, and H. H. Thomas, Petrogenic implications of some geochemical data on eclogite and ultrabasic inclusions, *Geochim. Cosmochim. Acta*, **36**, 1131-1166, 1972.
- Piermarini, G. J., S. Block, and J. D. Barnett, Hydrostatic limits in liquids and solids to 100 kbar, *J. Appl. Phys.*, **44**, 5377-5382, 1973.
- Pinckney, L. R., and D. H. Lindsley, Effects of magnesium on iron-titanium oxides (abstract), *Abstr. with Programs (Geol. Soc. Amer.)*, **8**, 1051, 1976.
- Pisárčik, M., I. Proks, and V. Jansta, Infrared spectra of the system akermanite-diopside, *Silikaty*, **3**, 207-212, 1976.
- Poirier, J. P., and M. Madon, Transmission electron microscopy of natural  $(\text{Mg}_{0.74}\text{Fe}_{0.26})_2\text{SiO}_4$  spinel (abstract), *Eos*, **60**, 370, 1979.
- Popp, R. K., and J. D. Frantz, Mineral solution equilibria: II. An experimental study of mineral solubilities and the thermodynamic properties of aqueous  $\text{CaCl}_2$  in the system  $\text{CaO-SiO}_2\text{-H}_2\text{O-HCl}$ , *Geochim. Cosmochim. Acta*, in press, 1979.
- Porto, S. P. S., P. A. Fleury, and T. C. Damen, Raman spectra of  $\text{TiO}_2$ ,  $\text{MgF}_2$ ,  $\text{ZnF}_2$ ,  $\text{FeF}_2$ , and  $\text{MnF}_2$ , *Phys. Rev.*, **154**, 522-526, 1967.
- Potter, R. W., II, The systematics of polymorphism in binary sulfides, Ph.D. thesis, Pennsylvania State University, 1973.
- Quist, A. S., and W. L. Marshall, Estimation of the dielectric constant of water to 800°, *J. Phys. Chem.*, **69**, 3165-3167, 1965.
- Quist, A. S., and W. L. Marshall, Electrical conductances of aqueous sodium chloride solutions from 0° to 800° and at pressures to 4000 bars, *J. Phys. Chem.*, **72**, 684-703, 1968.
- Rath, B. B., and H. Hu, Influence of solutes on the mobility of tilt boundaries, in *The Nature and Behavior of Grain Boundaries*, H. Hu, ed., Plenum, New York, pp. 405-436, 1972.
- Reynolds, R. W., L. A. Boatner, C. B. Finch, A. Chatelain, and M. M. Abraham, EPR investigations of  $\text{Er}^{3+}$ ,  $\text{Yb}^{3+}$ , and  $\text{Gd}^{3+}$  in zircon-structure silicates, *J. Chem. Phys.*, **56**, 5607-5625, 1972.
- Richter, F. M., and B. Parsons, On the interaction of two scales of convection in the mantle, *J. Geophys. Res.*, **80**, 2529-2541, 1975.
- Riebling, E. F., Structural similarities between a glass and its melt, *J. Amer. Ceram. Soc.*, **51**, 143-149, 1968.
- Ringwood, A. E., *Composition and Petrology of the Earth's Mantle*, McGraw-Hill Book Company, New York, 1975.
- Ringwood, A. E., Composition of the core and implications for the origin of the earth, *Geochem. J.*, **11**, 111-135, 1977.
- Ritzert, G. von, and E. U. Franck, Elektrische Leitfähigkeit wässriger Lösungen bei hohen Temperaturen und Drucken. I.  $\text{KCl}$ ,  $\text{BoCl}_2$ ,  $\text{Bu}(\text{OH})_2$  und  $\text{MgSO}_4$  bis 750°C und 6 kbar, *Ber. Bunsenges. Phys. Chem.*, **72**, 798-808, 1968.
- Robie, R. A., B. S. Hemingway, and J. R. Fisher, Thermodynamic properties of minerals and related substances at 298.15K and 1 bar (10 Pascals) pressure and at higher temperatures, *U.S. Geol. Surv. Bull.*, **1452**, 456 pp., 1978.
- Robinson, C. C., Multiple sites for  $\text{Er}^{3+}$  in alkali silicate glasses. I. The principal sixfold coordinated site of  $\text{Er}^{3+}$  in silicate glass, *J. Non-Cryst. Solids*, **15**, 1-10, 1974a.



- Robinson, C. C., Multiple sites for  $\text{Er}^{3+}$  in alkali silicate glasses. II. Evidence of four sites for  $\text{Er}^{3+}$ , *J. Non-Cryst. Solids*, 15, 11–29, 1974b.
- Robinson, R. A., and R. H. Stokes, The variation of equivalent conductance with concentration and temperature, *J. Amer. Chem. Soc.*, 76, 1991–1994, 1954.
- Roginsky, S. Z., *Theoretical Principles of Isotope Methods for Investigating Chemical Reactions*, Academy of Sciences USSR Press, Moscow, 1956.
- Ross, M., and C. Shishkevish, *Molecular and Metallic Hydrogen*, R-2056-ARPA, Rand Corporation, Santa Monica, California, 1977.
- Roy, A., and C. L. Bauer, Effect of impurities on the stability of a moving grain boundary, *Acta Met.*, 23, 957–963, 1975.
- Roy, R., Magnesium in fourfold coordination in the glass, *J. Amer. Ceram. Soc.*, 72, 3307–3308, 1950.
- Ruby, S., Why misfit when you already have  $X^2$ ? *Mössbauer Effect Methodology*, 8, 263–276, 1973.
- Rumble, D., III, Mineralogy, petrology, and oxygen isotopic geochemistry of the Clough Formation, Black Mountain, western New Hampshire, U.S.A., *J. Petrology*, 19, 317–340, 1978.
- Ruoff, A. L., The fracture and yield strengths of diamond, silicon and germanium, *Cornell Univ. Mater. Sci. Center Quart. Rep.*, 44, 44–45, 1977.
- Rutt, H. N., and J. H. Nicola, Raman spectra of carbonates of calcite structure, *J. Phys. C.*, 7, 4522–4528, 1974.
- Sakka, S., and J. D. MacKenzie, High pressure effects on glass, *J. Non-Cryst. Solids*, 1, 107–142, 1969.
- Samamoto, H., Orthorhombic perovskite ( $\text{Mg}, \text{Fe}$ ) $\text{SiO}_3$  and constitution of the lower mantle, in *High-Pressure Research: Applications in Geophysics*, M. H. Manghnani and S. Aki-moto, eds., Academic Press, New York, pp. 219–244, 1977.
- Samara, G. A., and P. S. Peercy, Pressure and temperature dependence of the static dielectric constants and Raman spectra of  $\text{TiO}_2$  (rutile), *Phys. Rev. B*, 7, 1131–1148, 1973.
- Sanford, R. F., and J. S. Huebner, Reexamination of diffusion processes in 77115 and 77215 (abstract), in *Lunar and Planetary Science*, X, Lunar and Planetary Science Institute, Houston, Texas, pp. 1052–1054, 1979.
- Scarfe, C. M., Viscosity of basic magmas at varying pressure, *Nature (London)*, 241, 101–102, 1973.
- Scarfe, C. M., Viscosity of a pantellerite melt at one atmosphere, *Can. Mineral.*, 15, 185–189, 1977a.
- Scarfe, C. M., Viscosity of some basaltic glasses at one atmosphere, *Can. Mineral.*, 15, 190–194, 1977b.
- Scarfe, C. M., D. K. Paul, and P. G. Harris, Melting experiments at one atmosphere on two ultramafic nodules, *Neues Jahrb. Mineral. Monatsh.*, 469–476, 1972.
- Schairer, J. F., and H. S. Yoder, Jr., The nature of residual liquids from crystallization, with data on the system nepheline-diopside-silica, *Amer. J. Sci.*, 258A, 273–284, 1960.
- Schneider, S. J., R. S. Roth, and J. L. Waring, Solid state reactions involving oxides of trivalent cations, *J. Res. Nat. Bur. Stand., Sect. A*, 65, 345–374, 1961.
- Schreiber, H. D., T. Thanyashiri, J. J. Lach, and R. A. Legere, Redox equilibria of Ti, Cr and Eu in silicate melts: redox potentials and mutual interactions, *Phys. Chem. Glasses*, 19, 126–140, 1978.
- Segerstrom, K., and R. R. Carlson, Preliminary geologic map of the upper zones of the western end of the Stillwater Complex, Park and Sweetgrass Counties, Montana, *U.S. Geol. Surv. Open File Rep.*, 77–370, 1977.
- Seifert, F., and M. Olesch, Mössbauer spectroscopy of grandidierite,  $(\text{Mg}, \text{Fe})\text{Al}_3\text{BSiO}_8$ , *Amer. Mineral.*, 62, 547–553, 1977.
- Seifert, F., and W. Schreyer, Synthesis and stability of micas in the system  $\text{K}_2\text{O}-\text{MgO}-\text{SiO}_2-\text{H}_2\text{O}$  and their relations to phlogopite, *Contrib. Mineral. Petrol.*, 30, 196–215, 1971.
- Shannon, R. D., and C. T. Prewitt, Effective ionic radii in oxides and fluorides, *Acta Crystallogr.*, B25, 925–946, 1969.
- Sharma, S. K., D. Virgo, and B. O. Mysen, Raman study of the structure and coordination of aluminum in jadeite ( $\text{NaAlSi}_2\text{O}_6$ ) composition glasses quenched at low and high pressure, *Amer. Mineral.*, in press, 1979.
- Shartsis, L., S. Spinner, and W. Capps, Density, expansivity, and viscosity of molten alkali silicates, *J. Amer. Ceram. Soc.*, 35, 155–160, 1952.
- Shaw, D. M., Trace element fractionation during anatexis, *Geochim. Cosmochim. Acta*, 34, 237–243, 1970.

- Shaw, H. R., Obsidian-H<sub>2</sub>O viscosities at 1000 and 2000 bars in the temperature range 700° to 900°C, *J. Geophys. Res.*, **68**, 6337-6343, 1963.
- Shedlovsky, T., The computation of ionization constants and limiting equivalent conductances from conductivity measurements, *J. Franklin Inst.*, **225**, 739-743, 1938.
- Shewmon, P. G., *Diffusion in Solids*, McGraw-Hill Book Company, New York, 1963.
- Shimizu, N., Rare earth elements in garnets and clinopyroxenes from garnet lherzolite nodules in kimberlites, *Earth Planet. Sci. Lett.*, **25**, 26-32, 1975.
- Shimizu, N., and R. J. Arculus, Rare earth element concentrations in a suite of basanitoids and alkali olivine basalts from Grenada, Lesser Antilles, *Contrib. Mineral. Petrol.*, **50**, 231-240, 1975.
- Shimizu, N., and I. Kushiro, The partitioning of rare earth elements between garnet and liquid at high pressures: preliminary experiments, *Geophys. Res. Lett.*, **2**, 413-416, 1975.
- Simon, I., Infrared studies of glasses, in *Modern Aspects of the Vitreous State*, J. D. Mackenzie, Butterworth, Washington, D.C., pp. 120-151, 1960.
- Simons, B., Pyroxen-Pyroxenoid-Umwandlungen im System FeSiO<sub>3</sub>-MnSiO<sub>3</sub>-MnGeO<sub>3</sub>-FeGeO<sub>3</sub> unter hohen Drucken und hohen Temperaturen, Ph.D. thesis, Rheinisch-Westfälische Technische Hochschule Aachen, 1978.
- Simpson, J. E., A comparison between laboratory and atmospheric density currents, *Quart. J. Roy. Meteorol. Soc.*, **95**, 758-765, 1969.
- Smith, A. L., and I. S. E. Carmichael, Quaternary lavas from the Southern Cascades, western U.S.A., *Contrib. Mineral. Petrol.*, **19**, 212-238, 1968.
- Snee, L. W., and T. J. Ahrens, Shock induced deformation features in terrestrial peridot and lunar dunite, *Proc. Sixth Lunar Sci. Conf.*, Vol. 1, 833-842, 1975.
- Solin, S. A., Optical probes of vibrational excitations and structure of amorphous solids, in *International Conference on Structure and Excitations of Amorphous Solids*, Williamsburg, Va., 1976, G. Luconsky and F. L. Galeener, eds., American Institute of Physics, New York, pp. 205-216, 1976.
- Son, P. R., and R. A. Bartels, CaO and SrO single crystal elastic constants and their pressure derivatives, *J. Phys. Chem. Solids*, **33**, 819-828, 1972.
- Stacey, F. D., A thermal model of the earth, *Phys. Earth Planet. Inter.*, **15**, 341-348, 1977.
- Stern, R. G. J., The common chain, ribbon, and ring silicates, in *Infrared Spectra of Minerals*, V. C. Farmer, ed., Mineralogical Society, London, pp. 305-330, 1974.
- Stevenson, D. A., Diffusion in the chalcogenides of Zn, Cd, and Pb, in *Atomic Diffusion in Semiconductors*, D. Shaw, ed., Plenum Press, New York, pp. 431-542, 1973.
- Stishov, S. M., and S. V. Popva, A new dense modification of silica, *Geokhimiya*, **10**, 837-839, 1961.
- Stocker, R. L., and R. B. Gordon, Velocity and internal friction in partial melts, *J. Geophys. Res.*, **80**, 4828-4836, 1975.
- Stöffler, D., Deformation and transformation of rock forming minerals by natural and experimental shock processes. I. Behavior of minerals under shock compression, *Fortschr. Mineral.*, **44**, 50-113, 1972.
- Stoicheff, B. P., High resolution Raman spectroscopy of gases. IX. Spectra of H<sub>2</sub>, HD and D<sub>2</sub>, *Can. J. Phys.*, **35**, 730-741, 1957.
- Syono, Y., and S. Akimoto, High pressure synthesis of fluorite-type PbO<sub>2</sub>, *Mater. Res. Bull.*, **3**, 153-158, 1968.
- Sysoev, L. A., A. Y. Gel'fam, A. D. Kovaleva, and N. G. Kravchenko, Measurements of the coefficients of self diffusion of sulfur in CdS microcrystals, *Izv. Akad. Nauk SSSR Neorg. Mater.*, **5**, 2208-2209, 1969.
- Tarte, P., The determination of cation coordination in glasses by infrared spectroscopy, in *Physics of Non-Crystalline Solids; Proceedings of the International Conference, Delft, 1964*, North Holland, Amsterdam, pp. 550-565, 1965.
- Tarte, P., M. J. Pottier, and A. M. Proce, Vibrational studies of silicate and germanates. V. Infrared and Raman spectra of pyrosilicates and pyrogermanates with linear bridge, *Spectrochim. Acta*, **29A**, 1017-1027, 1973.
- Taylor, H. P., Jr., The oxygen isotope geochemistry of igneous rocks, *Contrib. Mineral. Petrol.*, **19**, 1-71, 1968.
- Taylor, H. P., Jr., Water/rock interactions and the origin of H<sub>2</sub>O in granitic batholiths, *J. Geol. Soc. London*, **133**, 509-558, 1977.
- Taylor, H. P., Jr., and R. W. Forester, Low-<sup>18</sup>O igneous rocks from the intrusive complexes of Skye, Mull, and Ardnamurchan, western Scotland, *J. Petrology*, **12**, 465-497, 1971.



- Taylor, H. P., Jr., and B. Turi, High- $^{18}\text{O}$  igneous rocks from the Tuscan Magmatic Province, Italy, *Contrib. Mineral. Petrol.*, **55**, 33–54, 1976.
- Taylor, M., and G. E. Brown, Structure of mineral glasses. I. The feldspar glasses  $\text{NaAlSi}_3\text{O}_8$ ,  $\text{KAlSi}_3\text{O}_8$ ,  $\text{CaAl}_2\text{Si}_2\text{O}_8$ , *Geochim. Cosmochim. Acta*, **43**, 61–77, 1979.
- Taylor, T. D., and G. E. Rindone, Properties of soda aluminosilicate glasses. V. Low-temperature viscosities, *J. Amer. Ceram. Soc.*, **53**, 692–695, 1970.
- Thiery, M. M., D. Fabre, M. Jean-Louis, H. Vu, and B. Vodar, Physique moléculaire—spectres de diffusion Raman de l'hydrogène normal solide à 4.2K comprimé jusqu'à 9 kbar, *C.R. Acad. Sci., Ser. B*, **278**, 731–734, 1974.
- Tiernan, R. J., Diffusion of thallium chloride into single crystals and bicrystals of potassium chloride, Ph.D. thesis, Massachusetts Institute of Technology, 1969.
- Toksoz, M. N., and P. Bird, Formation and evolution of marginal basins and continental plateaus, in *Island Arcs, Deep Sea Trenches and Back-Arc Basins*, M. Talwani and W. C. Pitman III, eds., American Geophysical Union, Washington, D.C., pp. 162–174, 1977.
- Tosi, M., and T. Arai, Stability of solids under pressure, *Advan. High Pressure Res.*, **1**, 265–325, 1966.
- Tugarinov, A. I., and N. B. Naumov, The physicochemical parameters of hydrothermal mineral formation, *Geochem. Int.*, **9**, 161–167, 1972.
- Turner, W. E. S., and F. Winks, Thermal expansion of glass. II. Glasses of the series sodium metasilicate-silica, *J. Soc. Glass Technol.*, **14**, 110–126, 1930.
- Urey, H. C., and H. Craig, The composition of stony meteorites and the origin of meteorites, *Geochim. Cosmochim. Acta*, **4**, 36–82, 1953.
- Usselman, T. M., Experimental approach to the state of the core: Part 1. The liquidus relations of the Fe-rich portion of the Fe-Ni-S system from 30 to 100 kbar, *Amer. J. Sci.*, **275**, 278–290, 1975.
- Van Baalen, C., Further observations on growth of single cells of coccoid blue-green algae, *J. Phycol.*, **3**, 154–157, 1967.
- Van Baalen, C., and W. Pulich, Heterotrophic growth of the microalgae, *Crit. Rev. Microbiol.*, **2**, 229–255, 1973.
- Van Kranendonk, J., Rotational and vibrational energy bands in solid hydrogen, *Physica*, **25**, 1080–1094, 1959.
- Van Schmus, W. R., The mineralogy and petrology of chondritic meteorites, *Earth Sci. Rev.*, **3**, 145–184, 1969.
- Van Schmus, W. R., and J. A. Wood, A chemical-petrologic classification for the chondritic meteorites, *Geochim. Cosmochim. Acta*, **31**, 747–765, 1967.
- Vergano, P. J., D. C. Hill, and D. R. Uhlmann, Thermal expansion of feldspar glasses, *J. Amer. Ceram. Soc.*, **50**, 59–60, 1967.
- Verweij, H., and W. L. Konijnendijk, Structural units in  $\text{K}_2\text{O-PbO-SiO}_2$  glasses by Raman spectroscopy, *J. Amer. Ceram. Soc.*, **59**, 517–521, 1976.
- Verweij, H., H. Van Den Boom, and R. E. Breemer, Raman scattering of carbonate ions dissolved in potassium silicate glasses, *J. Amer. Ceram. Soc.*, **60**, 529–534, 1977.
- Verweij, H., H. Van Den Boom, and R. E. Breemer, Raman spectroscopic study of the reaction in potassium carbonate-silica glass forming batch, *J. Amer. Ceram. Soc.*, **61**, 118–121, 1978.
- Vu, H., M. Jean-Louis, M. M. Thiery, D. Fabre, S. Avriller, and P. Khatibi, Infrared and Raman spectra of simple molecular solids up to 15 kbar at 4.2K, in *Proceedings of the Fourth International Conference on High Pressure*, J. Osugi, ed., The Physicochemical Society of Japan, Kyoto, pp. 348–353, 1975.
- Wachtman, J. B., Jr., M. L. Wheat, H. J. Anderson, and J. L. Bates, Elastic constants of single crystal  $\text{UO}_2$  at 25°C, *J. Nucl. Mater.*, **16**, 39–41, 1965.
- Wager, L. R., G. M. Brown, and W. J. Wadsworth, Types of igneous cumulates, *J. Petrol.*, **1**, 73–85, 1960.
- Walther, J. V., and H. C. Helgeson, Calculation of the thermodynamic properties of aqueous silica and the solubility of quartz and its polymorphs at high pressures and temperatures, *Amer. J. Sci.*, **277**, 1315–1351, 1977.
- Watson, E. B., Two-liquid partition coefficients: experimental data and geochemical implications, *Contrib. Mineral. Petrol.*, **56**, 119–134, 1976.
- Watson, E. B., Partitioning of manganese between forsterite and silicate liquid, *Geochim. Cosmochim. Acta*, **41**, 1363–1374, 1977.

- Webb, A. W., D. U. Gubser, and L. C. Towle, Cryostat for generating pressures to 100 kbar and temperatures to 0.03K, *Rev. Sci. Instrum.*, **47**, 59–62, 1976.
- Weber, A., High resolution Raman studies of gases, in *The Raman Effect*, Vol. 2, A. Anderson, ed., Marcel Dekker, Inc., New York, pp. 543–757, 1973.
- Weill, D. F., and G. A. McKay, The partitioning of Mg, Fe, Sr, Ce, Sm, Eu and Yb in lunar igneous systems and a possible origin of KREEP by equilibrium partial melting, *Proc. Sixth Lunar Sci. Conf.*, 1143–1158, 1975.
- Weir, C. E., The system lime-water at 21°C and high pressures, *J. Res. Nat. Bur. Stand.*, **54**, 37–40, 1955.
- Welch, W. H., and G. D. Fasman, Hydrogen-tritium exchange in polypeptides. Models of  $\alpha$ -helical and  $\beta$ -conformations, *Biochemistry*, **13**, 2455–2466, 1974.
- Wells, A. F., *Structural Inorganic Chemistry*, 4th ed., Oxford Press, Oxford, 1975.
- Wendlandt, R. F., and W. J. Harrison, Rare earth partitioning between immiscible carbonate and silicate liquids and CO<sub>2</sub> vapor: results and implications for the formation of light rare earth-enriched rocks, *Contrib. Mineral. Petrol.*, in press, 1979.
- Whalley, E., High pressure Raman spectroscopy, in *Proceedings of the Fourth International Conference on High Pressure*, J. Osugi, ed., The Physico-Chemical Society of Japan, Kyoto, pp. 37–43, 1975.
- White, W. B., The carbonate minerals, in *The Infrared Spectra of Minerals*, V. C. Farmer, ed., Mineralogical Society, London, pp. 227–284, 1974.
- Whittaker, E. J. W., and R. Muntus, Ionic radii for use in geochemistry, *Geochim. Cosmochim. Acta*, **34**, 945–956, 1970.
- Wilcox, R. E., Petrology of Parícutin volcano, Mexico, *U.S. Geol. Surv. Bull.*, **965-C**, 281–353, 1954.
- Wild, R. K., T. Evans, and A. R. Lang, Birefringence, x-ray topography and electron microscope examination of the plastic deformation of diamond, *Phil. Mag.*, **15**, 267–279, 1967.
- Wilks, E. M., Optical methods to select diamonds of very high lattice perfection, *Nature (London)*, **262**, 570–571, 1976.
- Wong, J., and C. A. Angell, *Glass Structure by Spectroscopy*, Marcel Dekker, New York, 1976.
- Yagi, T., H. K. Mao, and P. M. Bell, Structure and crystal chemistry of perovskite-type MgSiO<sub>3</sub>, *Phys. Chem. Minerals*, **3**, 97–110, 1978.
- Yoder, H. S., Jr., High-low quartz inversion up to 10,000 bars, *Trans. Amer. Geophys. Union*, **31**, 827–835, 1950.
- Yoder, H. S., Jr., Melilite stability and paragenesis, *Fortschr. Mineral.*, **50**, 140–173, 1973.
- Yoder, H. S., Jr., *Generation of Basaltic Magma*, National Academy of Sciences, Washington, D.C., 1976.
- Yoder, H. S., Jr., and C. E. Tilley, Origin of basalt magmas: an experimental study of natural and synthetic rock systems, *J. Petrology*, **3**, 342–532, 1962.
- Young, T. F., L. F. Maranville, and H. M. Smith, Raman spectral investigation of ionic equilibria in solution of strong electrolytes, in *The Structure of Electrolytic Solutions*, W. J. Hamer, ed., John Wiley and Sons, Inc., New York, pp. 35–63, 1959.
- Zachariasen, W. H., The atomic arrangement in glass, *J. Amer. Chem. Soc.*, **54**, 3841–3851, 1932.
- Zussman, J., The crystal chemistry of the micas, *Bull. Mineral.*, **102**, 5–13, 1979.



## PERSONNEL

*Scientific Staff*

*Director:* H. S. Yoder, Jr., *Petrologist*

*Emeritus Research Associate:* E. G. Zies,  
*Chemist*

*Emeritus Distinguished Professor, CIW:*  
E. F. Osborn, *Petrologist*

*Emeritus Isotope Geochemist:* G. L. Davis

*Systematic Petrologist:* F. Chayes

*Petrologists:* F. R. Boyd, Jr., T. N. Irvine,  
I. Kushiro,<sup>1</sup> D. Rumble III, F. A. Seifert<sup>2</sup>

*Physical Chemists:* J. D. Frantz, T. C.  
Hoering

*Geophysicists:* P. M. Bell, H. K. Mao

*Organic Geochemist:* P. E. Hare

*Crystallographer:* L. W. Finger

*Solid State Geochemist:* D. Virgo

*Geochemists:* J. B. Brady,<sup>3</sup> B. O. Mysen

*Experimental Mineralogist:* R. M. Hazen<sup>4</sup>

*Mineralogist:* R. H. McCallister<sup>5</sup>

*Volcanologist:* T. Murase<sup>6</sup>

*Postdoctoral Research Associates:* R. K. Popp, Virginia Polytechnic Institute and State University;<sup>7</sup> B. A. Simons, Rheinisch Westfälische Technische Hochschule Aachen, West Germany;<sup>8</sup> T. Yagi, University of Tokyo<sup>9</sup>

<sup>1</sup> Appointment through August 31, 1978; on leave of absence at University of Tokyo from September 1, 1978.

<sup>2</sup> Temporary appointment from January 16 through April 15, 1979.

<sup>3</sup> Temporary appointment from September 1, 1978.

<sup>4</sup> Temporary appointment from July 1, 1978.

<sup>5</sup> Temporary appointment from December 1, 1978 through February 28, 1979.

<sup>6</sup> Temporary appointment through August 31, 1978 and from June 16, 1979.

<sup>7</sup> Appointment from January 1, 1979.

<sup>8</sup> Appointment from December 1, 1978.

<sup>9</sup> Appointment terminated November 30, 1978, to accept position as Research Associate at the Institute of Solid State Physics, Tokyo University.

*Postdoctoral Fellows:* N. Z. Boctor, Purdue University; Marilyn L. F. Estep, Marine Science Institute, University of Texas at Port Aransas;<sup>10</sup> A. A. Finnerty, University of California at Los Angeles;<sup>11</sup> H. Fukuyama, University of Tokyo;<sup>12</sup> R. K. Popp, Virginia Polytechnic Institute and State University;<sup>13</sup> S. K. Sharma, University of Leicester, England; B. A. Simons, Rheinisch Westfälische Technische Hochschule Aachen, West Germany;<sup>14</sup> F. S. Spear, University of California at Los Angeles;<sup>15</sup> E. Takahashi, University of Tokyo;<sup>16</sup> R. F. Wendlandt, Pennsylvania State University<sup>17</sup>

*Predocctoral Fellows:* Wendy J. Harrison, University of Manchester, England; J. D. Hoover, University of Oregon;<sup>18</sup> R. H. Kingsley, University of Rhode Island;<sup>12</sup> C. A. Lawson, Princeton University;<sup>19</sup> J. F. Mammone, University of California at Los Angeles;<sup>20</sup> Shirley A. Rawson, University of Oregon<sup>20</sup>

*Fellowship Trainees:* Pamela R. Baur, University of Connecticut;<sup>21</sup> Heather D. Boek, Duke University;<sup>21</sup> Julia A. Carey,

<sup>10</sup> Appointment terminated June 30, 1979, to accept position as Temporary Staff Member (Biochemist).

<sup>11</sup> Appointment terminated August 31, 1978, to accept position as Planetary Geologist, Jet Propulsion Laboratory, Pasadena, California.

<sup>12</sup> Appointment from June 16, 1979.

<sup>13</sup> Appointment terminated December 31, 1978, to accept position as Postdoctoral Research Associate.

<sup>14</sup> Appointment from October 1 through November 30, 1978, terminated to accept position as Postdoctoral Research Associate.

<sup>15</sup> Appointment terminated August 31, 1978, to accept position as Assistant Professor, Department of Earth and Planetary Sciences, Massachusetts Institute of Technology.

<sup>16</sup> Appointment from May 16, 1979.

<sup>17</sup> Appointment terminated August 31, 1978, to accept position as Geologist at the U.S. Geological Survey, Reston, Virginia.

<sup>18</sup> Appointment terminated August 31, 1978.

<sup>19</sup> Appointment terminated December 31, 1978.

<sup>20</sup> Appointment from September 1, 1978.

Duke University;<sup>21</sup> Julia D. Pasteris, Yale University;<sup>22</sup> Noreen C. Tuross, Bryn Mawr College<sup>23</sup>

*Executive High School Intern:* J. K. Powell, Bethesda-Chevy Chase High School<sup>24</sup>

*Guest Investigators:* J. Brandle, University of Madrid, Spain; J. M. Ferry, Arizona State University; E. Gil-Av, Weizmann Institute, Rehovot, Israel; Hillary Hutchison, Oberlin College; R. K. Kotra, University of Maryland; S. A. Margolis, National Bureau of Standards; W. L. Marshall, Oak Ridge National Laboratory; G. H. Miller, University of Colorado; J. Myers, Johns Hopkins University; L. Pratt, University of Toledo; C. S. Rai, University of Hawaii at Manoa; R. Ralph, University of Washington; C. Redding, West German Geological Survey, Hanover, West Germany; M. Rosenhauer, University of Frankfurt, West Germany; M. Rubenach, Johns Hopkins University; C. M. Scarfe, University of Alberta, Edmonton, Canada; D. Schissel, Johns-Manville Corporation; Y. N. Shieu, Purdue University; A. Shimoyama, University of Maryland; Ann Sigleo, University of Maryland; Agnes Stix, Smithsonian Institution; D. M. Stothers, University of Toledo; S. G. Todd, Johns-Manville Corporation; G. C. Ulmer, Temple University; A. Van Valkenburg, U. S. Bureau of Mines (re-

tired); Danielle Velde, Université Pierre et Marie Curie, Paris, France; W. J. Verwoerd, University of Stellenbosch, South Africa; D. W. Von Endt, Smithsonian Institution; R. W. G. Wyckoff, University of Arizona; Kathy Zoon, National Institutes of Health

### *Operating and Maintenance Staff*

*Executive Officer:* A. D. Singer

*Editor and Librarian:* Dolores M. Thomas

*Stenographers:* Marjorie E. Imlay, Mabel B. Mattingly

*Typist-Accounting Clerk:* Barbara B. Jones

*Typist-Clerk:* Joan F. Facchina<sup>25</sup>

*Clerk and Technician:* H. J. Lutz

*Electronics Technicians:* D. J. George, C. G. Hadidiacos

*Shop Foreman and Instrument Maker:* C. A. Batten

*Laboratory Technician and Instrument Maker:* G. E. Speicher

*Instrument Makers:* C. Brown, J. W. Schwartz

*Building Engineer:* H. L. Moore

*Custodian and Painter:* M. Ferguson

*Custodian and Thin-Section Technician:* D. Ratliff, Jr.

*Custodian and Mechanic:* L. B. Patrick

<sup>25</sup> Resigned March 15, 1979.

<sup>21</sup> Appointment terminated August 4, 1978.

<sup>22</sup> Appointment terminated July 14, 1978.

<sup>23</sup> Appointment terminated July 25, 1978.

<sup>24</sup> Appointment from September 11, 1978 through January 25, 1979.



# *Hale Observatories*

Operated by Carnegie Institution of Washington  
and California Institute of Technology

*Pasadena, California*

Maarten Schmidt  
*Director*

## OBSERVATORY COMMITTEE

Maarten Schmidt, *Chairman*

Halton C. Arp

James E. Gunn

Gerry Neugebauer

George W. Preston

Allan Sandage

Wallace L. W. Sargent

*Carnegie Institution of Washington Year Book 78, 1978-1979*



# Contents

Introduction . . . . .	713	The Galaxy . . . . .	739
Observing Conditions . . . . .	716	The galactic nuclear bulge . . . . .	739
Physics of the Sun . . . . .	717	Galactic mass distribution . . . . .	739
Synoptic observations at Mount Wilson . . . . .	717	Survey for low-metal-abundance stars . . . . .	739
Rotation of the Sun . . . . .	718	Galaxies . . . . .	740
Large-scale velocity fields . . . . .	718	Globular clusters in the Magellanic Clouds . . . . .	740
Active regions . . . . .	719	Globular clusters in M31 . . . . .	740
Solar axis elements . . . . .	719	Rotation in the nuclear bulge of M31 . . . . .	741
Big Bear Solar Observatory . . . . .	719	Stellar content of M33 . . . . .	741
Instruments . . . . .	719	Search for Cepheids in nearby resolved galaxies . . . . .	744
Blue continuum in flares . . . . .	720	Spectrophotometry of the nuclear region of M51 . . . . .	745
Thermal x-ray plasma in solar flares . . . . .	720	The Las Campanas survey of bright galaxies . . . . .	745
Solar System . . . . .	721	Warped dust planes . . . . .	746
Solar system studies . . . . .	721	Dust arms alone . . . . .	747
Jupiter imaging at 5 $\mu\text{m}$ . . . . .	721	The morphology of Sa galaxies . . . . .	748
Jupiter magnetosphere . . . . .	722	Smooth-arm Sa . . . . .	748
Infrared observations of planets . . . . .	723	Sa outer-arm structures . . . . .	749
The diameter of Pluto . . . . .	723	Kinematics and structure of disk galaxies . . . . .	750
Stellar Spectroscopy . . . . .	724	H II regions in galaxies . . . . .	752
Stellar chromospheres . . . . .	724	Luminosity classification . . . . .	752
Magnetic Ap star . . . . .	725	Nonequilibrium companions of spiral galaxies . . . . .	752
Dwarf novae . . . . .	725	Dwarf irregular galaxies in nearby groups . . . . .	752
Variable stars . . . . .	726	The radio galaxies NGC 6251 and M87 . . . . .	754
Binary stars . . . . .	727	M87 jet . . . . .	755
Stellar coronas . . . . .	728	Seyfert galaxies . . . . .	756
Red giants in old disk clusters . . . . .	728	Clusters of Galaxies . . . . .	759
Lower main sequence . . . . .	728	Populations . . . . .	759
Degenerate stars . . . . .	730	Dynamics . . . . .	760
A rotating magnetic white dwarf . . . . .	731	Space distribution of Abell clusters . . . . .	761
Interstellar Matter . . . . .	732	Quasars and Quasi-Stellar Objects . . . . .	762
Molecular hydrogen in Orion . . . . .	732	Continuum energy distribution . . . . .	762
Globular Clusters . . . . .	734	Millimeter photometry . . . . .	766
Radial gradients . . . . .	734	X-ray quasars . . . . .	767
CN/CH anomalies . . . . .	736	Palomar bright quasar survey . . . . .	768
Radial velocities . . . . .	736	IUE observations of quasars . . . . .	768
Metallicity in globular clusters . . . . .	737	Absorption lines . . . . .	769
Infrared studies of $\omega$ Centauri . . . . .	737	Quasars near bright galaxies . . . . .	770
Optical Identifications . . . . .	738		
Optical candidate for the binary pulsar 1913+16 . . . . .	738		
Identification of 3C sources . . . . .	738		
The HEAO-2 deep x-ray survey . . . . .	738		

Observational Cosmology . . . . .	771	Infrared photometer for the Swope Telescope . . . . .	778
The velocity field of nearby bright galaxies . . . . .	771	Infrared Fabry-Perot spectrometer .	778
Calibration of largest H II regions in galaxies . . . . .	776	Prime-focus universal extragalactic instrument . . . . .	779
The Tully-Fisher relation . . . . .	776	FORTH language software develop- ment . . . . .	779
Theoretical Studies . . . . .	776	Fabry-Perot spectrometer . . . . .	779
Gravitational separation of elements	776	Wide field/planetary camera for Space Telescope . . . . .	780
A universal helium and deuterium abundance? . . . . .	777		
Instrumentation . . . . .	777	Guest Investigators . . . . .	781
The du Pont Telescope . . . . .	777	Bibliography . . . . .	793
Santa Barbara Street computing facility . . . . .	778	Personnel . . . . .	798
Direct image tube camera for Las Campanas . . . . .	778		



## INTRODUCTION

This report of the scientific activity of the Hale Observatories reflects the large range of interests of the staff, students, and visitors. While there is a gradual shift of emphasis toward more distant objects such as galaxies and quasars, continuing and important research is reported on objects in our solar system. Space science related research is playing an increasing role: several investigators have observed with the International Ultraviolet Explorer, usually in connection with concurrent ground-based observations. Also, ground-based observations of x-ray sources detected with the HEAO-2 Einstein Observatory yield optical identifications that are of interest for x-ray and optical astronomers alike.

In the next few paragraphs, I summarize some of the results reported this year. This part is intended for the general reader who wants a brief overview of the work done at the Observatories. Astronomers will, of course, want to consult the detailed reports given in the later sections.

Terrile and Westphal have undertaken a program of imaging Jupiter at a wavelength of  $5\ \mu$  with the Hale 5-meter Telescope. The purpose of the program was to support imaging and infrared radiation experiment targeting on board the Voyager Spacecraft during its encounter with Jupiter. Plans for the spacecraft observations, which had to be fixed at least one month before encounter, were critical, since the  $5\text{-}\mu$  appearance of Jupiter changes rapidly. The coordinated program worked well: spacecraft observations were successfully targeted for the hottest areas and, therefore, for the deepest regions of Jupiter's atmosphere. The combination of high-quality ground-based data recorded during the Voyager 1 encounter and the high-resolution

spacecraft imaging results is expected to resolve many details of the vertical cloud structure of Jupiter.

Almost 30 years ago, Dr. Gerard P. Kuiper of Yerkes Observatory used the Hale Telescope on a night of particularly good seeing to make a new determination of the diameter of Pluto. The value obtained, 0.23 seconds of arc, was about one half of the best previous determination (*Year Book 49*, p. 20). A new determination was undertaken by Arnold, Boksenberg, and Sargent on March 28, 1978, with Boksenberg's Image Photon Counting System and speckle camera at the Cassegrain focus of the Hale Telescope. The diameter obtained is about 0.15 seconds of arc, or 3200 km. Combined with an estimate of Pluto's mass obtained from the motion of the recently discovered satellite, a low mean density of  $0.5\ \text{gm cm}^{-3}$  is derived for the planet. The observations suggest also that Pluto shows strong surface mottling or that it exhibits a bright central spot, as would be produced by a semi-specular surface. The average albedo of the planet is around 0.3, consistent with a covering of methane frost on the planet.

The presence of solid methane on the surface of Pluto was demonstrated entirely independently of spectral reflectivity measurements near  $2\ \mu$  obtained with the Hale Telescope by Soifer, Matthews, and Neugebauer. As they note, this is surprising, since methane is not expected to survive on Pluto over the lifetime of the solar system.

Olin Wilson has published his observations of chromospheric Ca II H and K emission fluxes in 91 late-type main-sequence stars obtained over the period 1966–1977. All the program stars show evidence of variations on a wide variety of time scales. About a quarter of the stars appear to have completed a cycle

of variation during the period of observation. Vaughan and Preston are continuing the observations in the hope of obtaining further complete cycles.

Vaughan and Preston are engaged in a complete survey of H and K emission fluxes in main-sequence F–M type stars in the solar neighborhood. Since chromospheric activity declines with age on a time scale of a few billion years, the survey should yield an observational estimate of the ages of field stars in the solar neighborhood and, hence, information on past rates of formation of late-type main-sequence stars in the disk of our Galaxy.

Zinn completed his investigations of the integrated colors of globular clusters with the 1-meter Swope and 2.5-meter du Pont Telescopes at Las Campanas. He used a narrow- and intermediate-band photometric system that allows interstellar reddening and metallicity of the clusters to be obtained with high precision. He finds that metal-rich clusters (those with metal abundance at least 20% of the solar value) occupy a relatively small region of space near the nucleus of the Galaxy, while metal-poor clusters are found both in the nuclear region and at galactocentric distances as large as 100 kpc. The nuclear clusters show a decrease of metal abundance with increasing height above the galactic plane. Little gradient of metal abundance is seen in clusters in the halo.

Beck, Lacy, and Townes of the University of California at Berkeley, in collaboration with Geballe, continued their study of the central parsec of our Galaxy with the 2.5-meter du Pont Telescope at Las Campanas. They used 12.8- $\mu$  emission from Ne II to detect many small clouds of ionized gas. There appears to be a collective motion of the clouds in the central parsec, which is described most simply as a rotation, with a period of around 20,000 years. The orientation of the axis is unexpected in that it is about perpendicular to the axis of rota-

tion of the galactic disk. This suggests that the nuclear region is a separate structure, independent of its galactic surroundings.

Rotation velocities of moderately flattened elliptical galaxies are much lower than their flattening would suggest. Since the nuclear bulges of spiral galaxies exhibit radial light distributions and flattenings similar to those of small elliptical galaxies, it is of considerable interest to investigate their rotation velocities. Sheetman and Richstone have measured the nuclear bulge of the Andromeda Nebula, which has a flattening comparable to an E3 elliptical galaxy. They used a photometer with a narrow-band interference filter centered near the Ca II H and K lines that can be tilted to measure the Doppler shift. Along the major axis of the galaxy, they found a rotation velocity rising gradually to 85 km s<sup>-1</sup> at 1 kpc from the center. This rotation velocity is sufficient to account for its flattening, unlike that of most elliptical galaxies.

A similar result has been found within the central arcminute of the nucleus of the S0 galaxy NGC 3115. Using a Fourier spectral-analysis program written by Rose to analyze data obtained with the SIT digital spectrograph, Searle and Rose found the bulge of NGC 3115 to be in rapid rotation, of the same order as the velocity dispersion. The result is consistent with the idea that the bulge, which has an axial ratio of 3 to 1, is a rotationally supported oblate spheroid. Perhaps, as noted by Searle and Rose, the spheroidal components of disk galaxies have kinematic properties that sharply differentiate them from ellipticals.

In 1974, Sandage and Tammann discovered that the absolute visual magnitude  $M_v$  for the brightest red supergiants in resolved galaxies of morphological types Sc, Sd, Sm, and Im appeared to be constant at  $-7.9 \pm 0.1$ , independent of the absolute magnitude of the parent



galaxy itself. This is potentially a very powerful distance indicator that permits precise distances to be determined to larger distances than provided by Cepheid variables (which cover the range  $M_v = -2$  to  $-6$ ). One of the goals of the collaborative effort by Sandage and Humphreys, as described in *Year Book 77* (p. 178), is to provide an independent calibration of  $M_v$  for the brightest red supergiants in M33. Since M33 is so close, its angular size is large and the separation of its brightest red stars from the numerous foreground M dwarfs in our Galaxy is tedious. Humphreys obtained spectra of many of the candidate stars by using the Kitt Peak 1.2-meter and 4-meter reflectors, and so identified those belonging to M33. The three brightest red supergiants have  $M_v = -8.1$ ,  $-7.8$ , and  $-7.8$ , which confirms the 1974 calibration from other galaxies.

Sandage and Brucato are continuing their photographic survey of bright galaxies with the 2.5-meter du Pont Telescope and the 5-meter Hale Telescope. The purpose is to improve the morphological classification of all galaxies in the Shapley-Ames catalog (published in 1932) for which the existing plate material is inadequate. New Hubble classifications, together with luminosity classes, will be published in the Revised Shapley-Ames Catalog (RSA). Most of the survey at Las Campanas was concentrated on S0 and Sa galaxies in an attempt to understand the morphological relations between these types. In the course of this work, a new type of Sa galaxy was discovered which exhibits spiral arms consisting purely of dust and no indication of recent star formation along any of the dust lanes.

Of considerable interest, too, are the smooth-armed Sa galaxies where the spiral features are defined by old stars alone, in contrast to Sb and Sc Hubble types where the arms are delineated by young supergiants, H II regions, and

dust. Many smooth-armed Sa galaxies are found among field galaxies. Since collisions among the latter are rare, it appears unlikely that the lack of gas, dust, and young stars in smooth-armed Sa galaxies can be due to environmental stripping, and must instead be a phenomenon associated with galaxy formation and evolution.

Last year (*Year Book 77*, p. 185), we reported the possible detection of a massive black hole in M87. This year, similar evidence has been collected for the elliptical galaxy NGC 6251, which is a strong radio source with a total linear extent of 3 Mpc. Young, Sargent, Kristian, and Westphal used charge-coupled device cameras at the Kitt Peak 4-meter telescope and the Palomar 5-meter telescope to obtain exposures that show a luminosity profile that cannot be found by a King model, unlike that of Coma cluster galaxies which were also observed. The profile of NGC 6251 can be fitted by a King model together with a central point mass and a central mass concentration, probably of around  $2 \times 10^9$  solar masses.

Dressler has used the large  $50 \times 50$  cm plates obtained with the 2.5-meter du Pont Telescope to determine Hubble types and approximate magnitudes of some 6000 galaxies in 55 clusters. He has found that, regardless of the type of cluster (regular, irregular, or x-ray), there is an excellent correlation between the types of galaxies present and the local galaxy density. The fractions of S0 and elliptical galaxies rise almost linearly with the logarithm of the local galaxy density. The fraction of these galaxies that are observed outside clusters of galaxies also fits well onto this relation. On the basis of this relationship, Dressler argues against the hypothesis that S0 galaxies are produced when spiral galaxies lose their gas by ram pressure sweeping or evaporation. Instead, he proposes that S0's may be produced by internal processes such as gas removal by galactic

winds or gas exhaustion through star formation.

Gunn and Thuan have finished a study of a complete sample of Abell clusters of galaxies. They constructed the space distribution of these clusters and found them to be highly clustered. Significant correlation structure is seen to exist to distances in excess of 60 Mpc. Hoessel has studied the distribution of surface brightness of the brightest galaxies in the clusters. He finds that the gradient of the luminosity profile is strongly correlated with the absolute magnitude of the galaxy, in agreement with predictions by Ostriker and Hausman for dynamical friction-induced cannibalism.

Oke, Neugebauer, Becklin, and Matthews are reporting on continuum energy distributions of quasars in the wavelength range 0.3–10  $\mu$ . They find that, while in a gross sense the energy distributions follow a power law, no single power law applies to the entire wavelength range. The slopes in the rest frame are flatter from 0.3–1  $\mu$  than from 1–3  $\mu$ . They state that, on the basis of the rapid variations observed and the shape of the energy distributions, the dominant radiation mechanism has to be non-thermal. However, thermal radiation from dust cannot be ruled out as a contributing source.

Schmidt and Green have obtained

almost all spectroscopic observations needed to complete the Bright Quasar Survey. Over an area of some 10,000  $\square^\circ$ , around 3000 blue starlike objects—all brighter than  $B \approx 16.2$  mag—were observed. At least 100 quasars were found, of which at least 75 are new. Comparison with surveys to fainter magnitudes shows an exceedingly steep rise in quasar counts, by a factor of 8.5–9 per magnitude. Such a slope is incompatible with local hypotheses of quasars. In the cosmological hypothesis, it corresponds to a steep increase of quasar space density with redshift, by a factor of around 100,000 at redshift 2.

One of the powerful ways to measure the deceleration parameter  $q_0$  is to determine the effect of gravity on the velocity field of nearby galaxies. The application of this method is based on measuring the dynamical effect of the density excess in the northern galactic hemisphere anomaly on the local expansion field. Sandage, Tammann, and Yahil have undertaken an analysis of the Revised Shapley-Ames Catalog to produce accurate measurements of the density contrast of the anomaly and of the velocity perturbation. In an extensive study, detailed in the report below, they conclude that  $q_0$  is no larger than 0.06.

*Maarten Schmidt*

## OBSERVING CONDITIONS

The 2.5-meter Hooker Telescope on Mount Wilson was used for observations on 211 complete nights and 94 partial nights for a total of 2187 observing hours. The 1.5-meter telescope was in regular use. At Mount Wilson, the total rainfall for the year was 712 mm, and total snowfall was 2700 mm.

The 5-meter Hale Telescope on Palomar Mountain was used for a total

of 2762 nighttime hours (see Table 1). In addition, 260 hours of daylight or twilight observations were carried out at infrared wavelengths. The 5-meter mirror was aluminized in September. The Palomar 1.5-meter telescope was in constant use, while the 1.2-meter and 0.46-meter Schmidt telescopes were in regular use except during the light of the Moon. Total rainfall at Palomar was 1052 mm



TABLE 1. Observations with the Hale Telescope

Month	Complete Nights	Partial Nights	Hours of Nighttime Observing
July	30	1	265
August	28	2	264
September	22	3	226
October	23	4	273
November	16	10	245
December	21	3	256
January	6	15	147
February	14	8	211
March	14	3	161
April	27	3	261
May	27	2	230
June	25	4	223
Total	253	58	2762

and total snowfall 2100 mm. Maximum temperature was 34°C in July 1978 and June 1979; minimum was -12°C in December 1978.

Public visitors at the Palomar Observatory totaled 120,000 for the year.

The 2.5-meter du Pont Telescope at the Las Campanas Observatory was used for 215 full nights and 72 partial nights for a total of 2448 observing hours. The 1-meter Swope Telescope was used on 186 nights for a total of 1346 hours. The maximum temperature during the year was 26°C; the minimum, 1°C. Total rainfall amounted to 2.5 mm; total snowfall was 0 mm.

PHYSICS OF THE SUN

*Synoptic Observations at Mount Wilson*

Fundamental synoptic observations of the Sun continue to provide the basis for the Mount Wilson solar research effort. This long-term program, supervised by Howard, includes the following observations in the interval June 1, 1978, to June 30, 1979:

Direct photographs	292
H $\alpha$ spectroheliograms, 9-meter focus	508
K2 spectroheliograms, 9-meter focus	504
Full-disk magnetograms	308
Integrated-light magnetic field measurements	235
Sunspot drawings	310
Sunspot magnetic field measurements	299

Observations of the Sun were made on 339 days during this period.

The daily full-disk magnetograms, along with sunspot data, are published monthly by the National Oceanic and Atmospheric Administration in the bulletin *Solar-Geophysical Data*. The mag-

netic synoptic charts are published by the International Astronomical Union in the *Quarterly Bulletin on Solar Activity*. Partial support for the observing programs and for the solar research at Mount Wilson comes from the Office of Naval Research, the National Aeronautics and Space Administration, and the National Science Foundation.

The magnetograph at the 150-foot Tower Telescope at Mount Wilson has produced digital data since late 1966. These data have been preserved on magnetic tape. A large project involving the rereduction of all these data has been in progress for over two years and should be completed within the next year. The reduction programs, which are also being used for current data, provide a good background velocity field representation so that "residual" velocities may be determined accurately for studies of surface velocity fields. In addition, the new reduction programs assemble and preserve on tape various derived quantities such as the latitude dependence of the solar rotation. Condensed arrays of mag-

netic field strength and residual velocities are also preserved. This condensed data set has already seen much use in studies of large-scale velocity and magnetic fields. It is continually updated and will serve as an invaluable tool in future studies of solar convection and activity.

### *Rotation of the Sun*

From a study of magnetic features seen on magnetograms in polar latitudes, Howard has concluded that polar magnetic fields rotate at significantly ( $\sim 12\%$ ) lower rates than does the photosphere and at lower rates than similar features measured in the 1950's. Since the equatorial rotation rates appear to change very little, this suggests a large latitude gradient of rotation that could presage a very active solar cycle 21, based on current ideas concerning the solar dynamo.

Previous studies using the Mount Wilson solar data have shown differences between the rotation rates of magnetic and nonmagnetic gas in the solar photosphere (Wilcox and Howard, *Solar Phys.*, 13, 251, 1970). The rotation of the nonmagnetic gas is measured using Doppler wavelength shifts of spectrum lines, a method which does not work well for the magnetic gas because the magnetic fields occupy only very small areas on the solar surface. The magnetic rotation rate is measured from the proper motions of individual features. The reality of the difference in rotation rates can be questioned because of the use of different measurement techniques. LaBonte performed an experiment designed to test for a rotation difference in a consistent way. Daily velocity maps of the whole Sun were reduced twice: once including and once excluding the magnetic regions. The difference in rotation rates found in the two reductions of the same data was then due to the magnetic gas. In all cases, the fractional change in rotation was less than 0.5%. However, the fractional change was proportional

to the amount of magnetic flux present on the solar surface and, in the sense that the magnetic gas rotates faster than the nonmagnetic, was consistent with the old result. The magnitude of the rotation difference is model dependent but is also consistent with the old result.

In March, an informal meeting was held at the Santa Barbara Street offices to discuss instrumental effects on magnetograph measures of Doppler shifts. Thirteen participants attended, representing all the major solar observatories in this country. Howard and LaBonte presented the results of some experiments carried out at the 150-foot Tower Telescope. Scattered light just off the solar limb is generally less than 1% of the disk center brightness. This number varies with the condition of the sky and of the optics. This means that the resulting variation in the measured solar rotation rate is less than  $\frac{1}{2}\%$ . A polarizing crystal (KD\*P), in use between 1976 and 1978, was found to introduce interference fringes in the spectrum at the magnetograph. This affected rotational velocities and dispersion measurements, although average rotational velocities were not affected. This fringe pattern, and its effect on the measured rotational velocity, varied systematically with temperature in the observing room. It has therefore been possible to correct all the rotational velocities during this interval for the effects of the fringes. When this is done, the daily variations in the measured rotational velocities decrease by a factor of two.

### *Large-Scale Velocity Fields*

Residual velocities over the solar surface from the condensed magnetograph data set have been studied by Howard and LaBonte. Using a technique that isolates horizontal east-west motions, they have examined seven years of data and found a characteristic pattern, faintly visible above the background noise at times. This pattern, which is



stronger in the earlier data (before 1975), consists of alternating east-west features, each full (double) cell being  $60^\circ$  in both hemispheres. Velocity amplitudes are about 10 m/s, which puts these features only barely above various sources of solar and instrumental noise. The pattern appears in general not to repeat well from one rotation to the next. Preliminary attempts to correlate this apparent cellular motion with various manifestations of solar activity have led to null results.

### *Active Regions*

One continuing project has been the measurement and classification of magnetic regions using the daily full-disk magnetograms. Early results from these data were given by Smith and Howard (*Int. Astron. Union Symp.*, 35, 33, 1967). Since that time a full sunspot cycle has elapsed, and the quality of the magnetic data has greatly increased. LaBonte is now making a new study of the magnetic regions.

It has been found that regions present early in the sunspot cycle have larger areas than those occurring later. The latitudes of region location (Spörer's Law) during sunspot cycle 20 showed three phases, with rapid equatorward drift at both the beginning and end of the cycle. The position angle of regions was discovered to be a function of latitude, with higher latitude regions being more inclined to the equator.

Inverted regions, those violating the Hale polarity law, are particularly interesting. It was found that there was an excess of inverted regions over the number expected from a normal distribution of position angles, and that the latitude distribution of inverted regions was the same as that of normal regions, on average. These all indicate that inverted regions must be treated as a well-defined part of the magnetic cycle rather than as random accidents.

### *Solar Axis Elements*

Given the observed differences between the magnetic and nonmagnetic areas on the solar surface, it might be thought that these are two independent systems. They might even have different axes of rotation. LaBonte has tested this idea using the Mount Wilson velocity data to determine the rotation of the axis of the nonmagnetic gas. A differential procedure was used in which the rotation axis was assumed to be that of the magnetic features, and residual error velocity patterns were then examined. Amplitudes of the velocity patterns were 5 to 15 m s<sup>-1</sup> and imply that the rotation axis of the gas is identical with that of the magnetic field to within  $0.14^\circ$ . This accuracy equals that of the magnetic determinations of the rotation axis direction.

### *Big Bear Solar Observatory*

Observations were carried out under the supervision of Patterson for 300 days; 346 rolls of film, comprising 2,768,000 photos, were taken. With the upswing in solar activity, a number of new observations were obtained, including blue flashes in flares, D2 and D3 emission and absorption in flares, and their line spectra. Special attention was paid to observations of prominences and of the brightness of plages at the extreme limb.

### *Instruments*

A number of instrumental improvements were made. The Universal Birefringent Filter was brought under computer control, so a flare may be scanned in many wavelengths at the push of two or three buttons. The Zeiss tunable filter was modified for microprocessor control by Richard Goeden, assisted by Steve Eaton, a Caltech undergraduate. It can now carry out a number of preprogrammed scanning routines at the push

of a button. We hope this year to integrate these routines with a flare sensor that will initiate them upon detecting a brightening.

A new Quantex digital subtraction system was obtained with a grant for support of the Solar Maximum Mission. It replaces the videodisk and other hardware in the videomagnetograph, allowing successive subtraction of digitized magnetic television pictures. The first magnetograms, obtained with this system in May, suggest substantial improvement over the previous system.

### *Blue Continuum in Flares*

In 1972, Zirin and Tanaka observed small bright flashes lasting 5–10 seconds at the footpoints of flare loops. The emission, observed in a 15 Å band at 3835 Å, was attributed to the Balmer line H9, because hard electrons cannot penetrate to the level of formation of the continuum here. In July 1978 and again in the spring of 1979, these flashes were observed in impulsive flares. Zirin studied three flares occurring on July 9 and 10, 1978, which were observed simultaneously in green and red continua. The flashes are at least twice as bright at 3835 Å than at 5233 Å, and they are not seen in the red at all. Furthermore, in this case a filter 50 Å wide was used at 3835 Å, so the emission there cannot be attributed to H9. H $\alpha$  observations show the bright flashes to have been at the two ends of the bright H $\alpha$  loop marking the flare; successive flashes occurred at the footpoints of other loops. It is concluded that energetic flare particles heat the atmosphere at a level transparent to the green and red light. Although electrons do not reach this depth, protons can. Unfortunately, the source of opacity is not clear; continuum opacity is lower at 3800 Å than in the green. Although there are many strong lines, these should either disappear in the flare or appear in emission, neither of

which has yet been observed. It is interesting that the same blue continuum is seen in dMe flare stars.

Zirin also studied a flare of July 10, 1978, which showed a ring of absorption in the He D3 line before it erupted. He thinks the ring is the projection of a shell that has formed along a current sheet separating the flare from the overlying magnetic field. When the flare broke out, He D3 and continuum emission formed at another lower place, with higher density, and the shell broke up as material flowed through it.

### *Thermal X-Ray Plasma in Solar Flares*

Every H $\alpha$  flare is accompanied by a burst of soft x rays ( $h\nu < 10\text{keV}$ ). The spectra of these bursts show that these x rays are emitted from thermal plasmas at temperatures of the order of  $10^7\text{ K}$ . The soft x rays are therefore referred to as “thermal x rays,” and the  $T \sim 10^7\text{ K}$  plasma is called the “thermal x-ray plasma.” Flares also commonly emit an impulsive burst of hard x rays ( $h\nu < 10\text{ keV}$ ) during the fast rise phase of the soft x-ray burst. Whereas the thermal x-ray burst develops in step with the H $\alpha$  flare through rise, maximum, and decay, the impulsive hard x rays, which are thought to be emitted by nonthermal high-energy electrons, are detectable only during the rise phase of the H $\alpha$  and soft x-ray flare. Therefore, the maximum phase and decay phase together are often referred to as the “thermal phase” of the flare.

Moore, as leader of the Thermal Phase Team of the Skylab Solar Workshop on Solar Flares, in collaboration with the other 15 members of the Team, has carried out an extensive study of the physical state and evolution of the thermal x-ray plasma in flares. The central physical problem of the thermal phase of flares is that of the thermal x-ray plasma, that is, the physics of the formation and evolution of the thermal



x-ray loops. The Thermal Phase Team investigated this component of the flare by carrying out detailed studies of selected large two-ribbon flares and very small compact flares that were especially well observed from Skylab.

The main results follow.

1. In compact flares (linear extent  $L \leq 10^9$  cm) the density of the x-ray plasma at flare maximum is in the range  $10^{11}$ – $10^{12}$  cm $^{-3}$ , an order of magnitude higher than in very large flares ( $L \sim 10^{10}$  cm).

2. In large two-ribbon flares there is continued flare energy release and heating of new x-ray plasma far into the decay phase.

3. In compact flares there is probably less continued heating in the decay phase than in large two-ribbon flares.

4. The  $T \sim 10^7$  K plasma cools roughly equally by radiation and by conduction in flares of all sizes.

5. The bulk of the mass of the x-ray

plasma is supplied from the chromosphere during the rise phase, probably by upflow from the feet of the x-ray loops.

The observations of the studied flares and the above results have been interpreted to imply that (1) the mass of the x-ray plasma is supplied mainly by conduction-driven evaporation, (2) the basic flare mechanism that generates the x-ray plasma is magnetic field reconnection at a large-scale current sheet, and (3) most of the energy released onto the closed field lines goes directly into a very high temperature ( $T \sim 10^8$  K) plasma at the top of the flare arch rather than first going into beamed nonthermal electrons that impinge on the chromosphere. A full account of this research has been prepared by Moore and will appear later this year as a chapter in *Solar Flares, A Monograph from Skylab Solar Workshop II* (P. A. Sturrock, ed., Colorado Associated Universities Press).

## SOLAR SYSTEM

### *Solar System Studies*

Kowal has continued his "Solar System Survey" with the Palomar 1.2-meter Schmidt telescope. Two thirds of the ecliptic zone has been photographed, as well as 10% of the planned zones to the north of the ecliptic. During the period of this report, comet Jackson-Neujmin and the Apollo-type asteroid 1975 YA were recovered. Both objects now have well-determined orbits. An unusual Trojan asteroid (1978 TB) was discovered in October 1978. This object was more than  $100^\circ$  from Jupiter at the time of discovery, a record distance for Trojans. A new comet (P/Kowal 2  $\equiv$  1979a) was discovered on plates taken for other purposes. This comet has a period of seven years. The Solar System Survey is under the general direction of

P. Goldreich and is supported by NASA Grant NGL 05-002-140.

### *Jupiter Imaging at 5 $\mu$ m*

A coordinated program to observe Jupiter at high spatial resolution in the 5- $\mu$ m wavelength region was undertaken by Richard J. Terrile, Caltech graduate student, and Westphal to support Voyager imaging and infrared radiation experiment targeting. Voyager afforded an opportunity to make spectroscopic and radiometric observations with high spectral resolution and sufficient spatial resolution to include individual hot regions. In order to predict the global 5- $\mu$ m appearance of Jupiter at the time of Voyager encounter and the location of specific hot spots for spacecraft observations, Terrile and Westphal undertook

a program of  $5\text{-}\mu\text{m}$  imaging of the planet in September 1978 with the Hale 5-meter Telescope and continued the observations through the second Voyager encounter. Terrile found that the gross appearance of Jupiter changes from year to year, and that while some regions of enhanced  $5\text{-}\mu\text{m}$  emission have lifetimes of several months, others form and dissipate on a time scale of days. Planning and sequencing considerations for spacecraft observations at near encounter required that  $5\text{-}\mu\text{m}$  hot spot targets be established with a high degree of certainty as to position and expected degree of "activity" at least one month in advance of the encounter dates.

Observations at  $5\text{ }\mu\text{m}$  for both Voyager 1 and Voyager 2 encounters were extremely successful. Predictions of feature locations were good and the spacecraft observations were successfully targeted for the hottest areas and, therefore, the deepest regions in the Jovian atmosphere.

Excellent quality ground-based data were recorded during Voyager 1 encounter and are providing a very powerful data set when combined with the high spatial resolution, spacecraft-imaging results. The combination of these ground-based results with the Voyager data is expected to resolve many details of the vertical cloud structure of Jupiter.

### *Jupiter Magnetosphere*

Trauger, in collaboration with Dr. Guido Münch of the Max Planck Institute for Astronomy, Heidelberg, and Dr. F. L. Roesler of the University of Wisconsin, used the 2.5-meter Hooker Telescope and the 5-meter Hale Telescope to obtain new observations of [S II] in the Jovian magnetosphere and the first ground-based observations of Jovian [S III]. These measurements will contribute to a more complete picture of

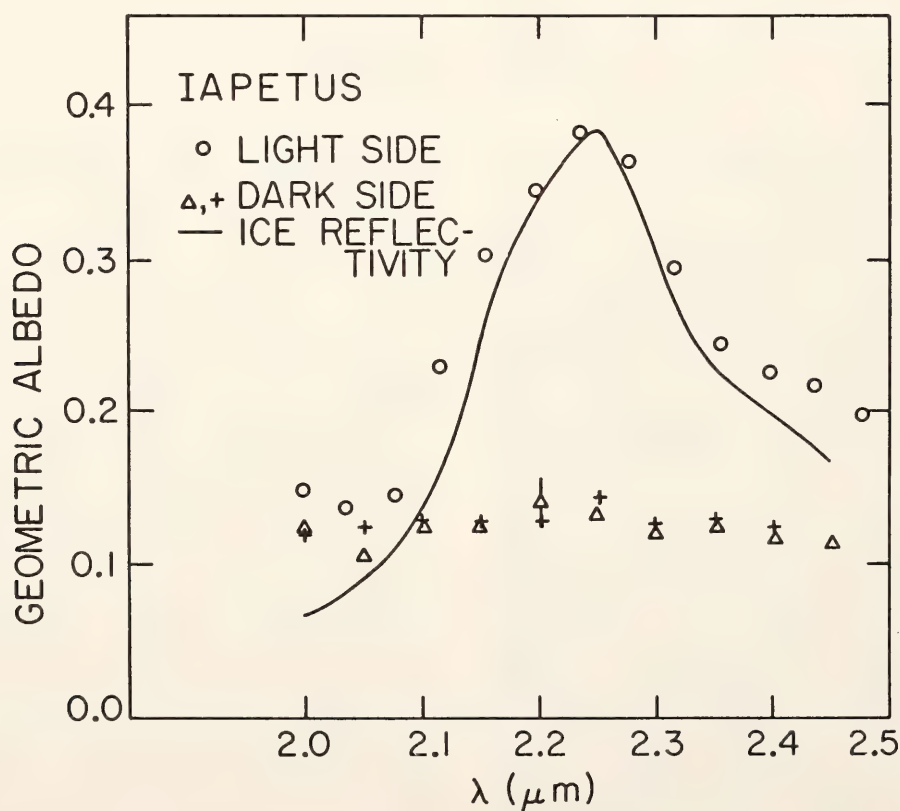


Fig. 1. The geometric albedos of the bright and dark faces of Iapetus in the  $2.0\text{--}2.5\text{ }\mu\text{m}$  wavelength range. The circles represent the bright side albedo, while the triangles and squares represent the dark side albedo. The solid line shows the reflectivity of water ice.



ion evolution and plasma conditions in the Jovian magnetosphere.

### *Infrared Observations of Planets*

Soifer, Matthews, and Neugebauer have begun using the technique of near-infrared spectroscopy to analyze the surface constituents of solar system objects. In particular, they have obtained spectra of the bright and dark faces of Iapetus and Pluto.

Iapetus, one of the satellites of Saturn, is distinguished by its peculiar property of strong bright and dark faces. The spectra from 2.0–2.45  $\mu\text{m}$  of the bright and dark faces of Iapetus were obtained at western and eastern elongation with the Mount Wilson 2.5- and 1.5-meter telescopes. These fluxes have been converted to normalized spectral reflectivity by dividing each flux by the flux of a solar spectrum. The reflectivity spectrum (Fig. 1) of the bright side shows the characteristic reflectivity peak of water ice that was first reported for Iapetus by Fink *et al.* (*Astrophys. J. [Lett.]*, 207, L63, 1976). The spectrum of the dark side is substantially different from that of the bright side, showing a dominant gray reflectivity with perhaps evidence for a slight amount of ice reflectivity. Since the leading face of Iapetus in its orbit around Saturn is the dark face, we interpret these data as proving that the dark face of Iapetus has been coated with debris in its orbit. The debris, as suggested by Pollack *et al.* (*Icarus*, 36, 271, 1978), could come from the outer, dark satellite Phoebe.

In Fig. 2, the spectral reflectivity of Pluto derived from a near-infrared spectrum of Pluto obtained on the 5-meter telescope at Palomar Mountain is shown. Also shown is the reflectivity of a combination of gray reflectivity and solid methane ( $\text{CH}_4$ ). The agreement between the two is sufficiently good to demonstrate that there is a significant amount of solid methane on the surface of Pluto. This result is very surprising,

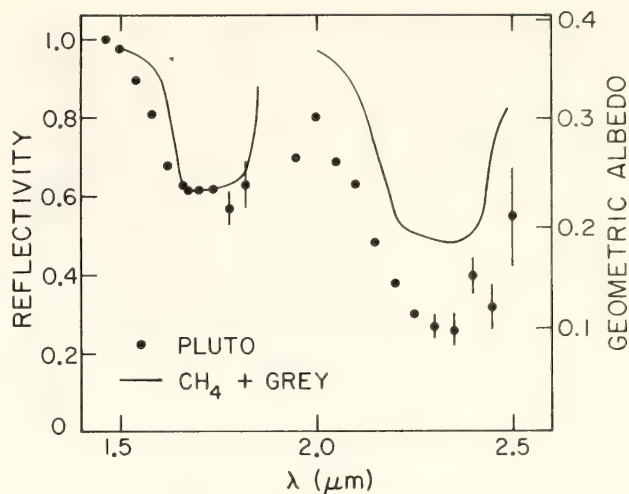


Fig. 2. The reflectivity spectrum of Pluto from 1.5–2.5  $\mu\text{m}$ . The solid line represents a combination of methane ice and neutral reflectivity, compared to the data.

since methane is not expected to be stable on Pluto over the lifetime of the solar system at the distance of Pluto (Lebofsky, *Icarus*, 25, 205, 1975).

### *The Diameter of Pluto*

During a short run in March 1978, Sargent joined A. Boksenberg and graduate student S. J. Arnold of University College London in making observations of a variety of objects with Boksenberg's speckle camera. This device is similar to the one described by Blazit *et al.* (*Astrophys. J. [Lett.]*, 214, L79, 1977) and employs a concave holographic grating both as a tunable filter and as an atmospheric dispersion compensator. The instrument was mounted at the Cassegrain focus of the Hale Telescope. Boksenberg's Image Photon Counting System (IPCS) was used as detector in the form of an array of  $256 \times 256$  pixels framing at  $50 \text{ s}^{-1}$  and covering a field  $1''$  square. The addresses of photon events were recorded frame by frame directly on digital magnetic tape for subsequent processing off line.

Observations of Pluto (magnitude  $V = 15.1$ ) were made on March 28, 1978, with Pluto at a distance of 29.44 AU,

near opposition. The data consisted of 168,616 frames with roughly 3.5 photon events per frame. These speckle images were analyzed by means of a technique that was introduced and demonstrated by Worden *et al.* (*Icarus*, 32, 450, 1977). In this method it is asserted that the autocorrelation of the diffraction-limited image can be derived from the difference between the mean autocorrelation of the individual speckle frames and the mean cross-correlation of pairs of frames in the same set of data.

For the diameter of Pluto, Arnold, Boksenberg, and Sargent obtained values of  $0''.14 \pm 0''.02$ , assuming no limb darkening, and  $0''.17 \pm 0''.02$ , assuming a cosine limb darkening. These values translate to linear diameters of  $3000 \pm 400$  km and  $3600 \pm 400$  km, respectively. The detailed autocorrelation functions show high-frequency features that indicate the presence of surface structure

on Pluto. The possible interpretations of the measurements are strong surface mottling, a strong central bright spot (as would be produced by a semi-specular surface), or both. Values for the average geometric albedo are  $0.36 \pm 0.14$  (no limb darkening), or  $0.25 \pm 0.08$  (limb darkening included), consistent with a large covering of methane frost on the planet. Combined with an estimate of Pluto's mass obtained from the motion of the recently discovered satellite, a very low density  $0.5 \pm \frac{0.3}{0.2} \text{ gm cm}^{-3}$  was obtained for the planet.

This work has lead to the first accurate estimate of the diameter of Pluto; it has also shown that the speckle technique can give information on the angular structure of objects as faint as 15 mag. References to further speckle work are contained in the section on galaxies.

## STELLAR SPECTROSCOPY

### *Stellar Chromospheres*

In 1966, Wilson began observing the fluxes in 1-angstrom bands at the centers of the H and K lines in 91 main-sequence stars extending from about F5 down to and including one star of spectral type M2. The observing on this project terminated in July 1977, and the results have been published in the *Astrophysical Journal* (226, 379, 1978). The purpose was to investigate possible changes in the chromospheric emission components of H and K and, in particular, to look for cyclical variations analogous to those seen in the Sun during the course of the solar sunspot cycle.

The results show that probably no main-sequence stellar chromospheres are constant; variations on a wide variety of time scales are clearly evident in all the program stars. In addition, a total

of about two dozen stars either have completed a cycle of variation during the period of observation, or probably would have done so if the observations had been extended. This survey, not surprisingly, also raises a number of questions that can be answered only by further observation. For details, the interested reader should consult the publication noted above.

Vaughan and Preston have continued their observational study of chromospheric Ca II H and K emission fluxes in main-sequence stars. The flux measurements for this work are made with the HK Photometer (*Year Book* 76, p. 134) on the 1.5-meter telescope at Mount Wilson. During the past year, the project has included two primary programs: (1) the continuation of Wilson's survey of stellar analogs of the solar activity cycle in a sample of about 90 main-sequence



stars, and (2) a complete survey of H-K fluxes in main-sequence F-G-K-M stars located in the solar neighborhood defined by the 1970 *Greenwich Catalog of Stars Within Twenty-Five Parsecs of the Sun*. Thus far, the solar neighborhood survey has been confined to the northern half of the catalog down to  $V = 12$  mag, comprising some 685 objects of which about 55% have been observed one or more times as of June 1979. Completing the survey to the level of at least two observations per star will occupy another year or two. In conjunction with this work, observations of nearby galactic stars were also undertaken during the past year. These observations (to be continued in 1979-1980) should permit the calibration of the decline of chromospheric activity in main-sequence stars as a function of age. Thus, it is hoped that the survey will yield an observational estimate of the ages of field stars in the solar neighborhood and hence give a direct indication of past rates of formation of lower-main-sequence stars in the disk of the Galaxy.

While definitive interpretation of the survey must await completion of the scheduled observations, several interim results of interest have emerged. Of 117 stars of type F5-G9 observed so far, about one third have H-K fluxes roughly comparable with Hyades-age stars, and two thirds have fluxes roughly similar to that of the Sun (as judged from Wilson's observations of sunlight reflected from the Moon). A significant fraction (perhaps half) of the latter group have H-K fluxes that are even weaker than that of the quiet Sun, suggesting that not only the prevalence of active regions but also the chromospheric network emission may be a declining function of age, on a time-scale of a few billion years. On the basis of plausible assumptions (which remain to be tested) about the relation between chromospheric activity and age, and with allowance for dilution due to the higher  $z$ -motions of the older stars, the "observed" age distribution of F5-G9 stars

in the solar neighborhood appears to be in tolerable agreement with the assumption of a constant initial mass function implicit in the Simple Model of star formation in the Galaxy. On the other hand, this is not so obviously the case for late K- and M-type stars, which exhibit a small velocity dispersion as a group and show a marked deficiency of chromospherically weak (presumably very old) stars.

A small number of the 90 stars now being observed routinely for cyclical behavior have completed a cycle in 1978-1979. Of notable interest is the K5 star HD 32147. From a minimum in mid-1968, the H-K flux of this star increased by almost 40% to a maximum 1.5 years later, then declined nearly linearly with time until mid-1977 when it began "recovery," again reaching a maximum by late 1978. The marked sawtooth asymmetry of its cycle is thus similar to that frequently exhibited by the Sun.

### *Magnetic Ap Star*

Dr. Sidney C. Wolff of the University of Hawaii and Preston have found a period of 3.86 days for the Ap star 52 Herculis. The  $V$  magnitude and  $b - y$  color are very nearly constant: the period was determined by use of well-marked variations of the equivalent width of Ca II K and the Strömgren  $m_1$  and  $c_1$  indices. The magnetic field is fairly large ( $\sim 1.5$  kilogauss), but the range is small relative to the observational errors. The latter arise because of unusual profile variations during the cycle that are not readily explicable.

### *Dwarf Novae*

Graduate students Kirk Borne and Richard Wade continued a program of spectroscopy of cataclysmic variable stars, using Shectman's Varo-Reticon detector at the coudé focus of the Mount Wilson 2.5-meter telescope. One of the stars studied is U Geminorum, for which

three long series of short (1% of the orbital period) integrations in the near infrared have been obtained. In a preliminary analysis of one of these series, Wade found strong evidence for radial velocity variations in the Na-absorption doublet at  $\lambda 8183$  and  $\lambda 8195$ , at the orbital frequency and with the orbital phase appropriate for the M5-type secondary star. A tentative value for the radial velocity semiamplitude  $K_2$  is  $290 \text{ km s}^{-1}$ , subject to refinement when all the data have been analyzed. A first attempt to detect the neutral potassium line at  $\lambda 7699$  was unsuccessful. Detection of the Na doublet in absorption makes U Gem only the second cataclysmic variable to be both a double-lined spectroscopic binary and an eclipsing binary. A reanalysis of the emission-line radial velocities, using new data obtained by Oke with the SIT digital spectrograph at the 5-meter Hale telescope, will permit a new determination of the component masses of U Gem.

Greenstein and Wade obtained ultraviolet spectra of the dwarf nova YZ Cancri, using the International Ultraviolet Explorer (IUE) during the December 1978 "supermaximum" outburst of the star. Coincidentally, Oke observed YZ Cancri during the same outburst in the course of an ongoing program to obtain multichannel scanner observations of cataclysmic variables with the 5-meter Hale telescope. The combined visual and ultraviolet data permit study of the bolometric magnitude and spectral energy distribution over an exceptionally large range in wavelength. First results indicate that stellar atmosphere models near  $\log g = 2.0$  and  $T_{\text{eff}} = 14,000 \text{ K}$  represent the visual data better than single-temperature blackbody or power-law distributions. In the ultraviolet, the continuum distribution can be represented by a power-law spectrum ( $f_\nu = \text{constant}$ ) or by a stellar atmosphere model near  $\log g = 4.0$  and  $T_{\text{eff}} = 16,000 \text{ K}$ . Flux distributions from recently published accretion disk models

rise too steeply toward shorter wavelengths, presumably because the outer radius of the disk is chosen too small in the models, artificially moving the flux from the cooler outer regions of the disk. The ultraviolet spectrum shows C IV in emission with P Cygni-type absorption of the short wavelength edge and absorption at N V, Si III, and Si IV. The estimated flux at the time of Oke's observation is  $2 \times 10^{33} \text{ erg s}^{-1}$  in the 900–10,000 Å interval if YZ Cnc is 100 pc distant.

### *Variable Stars*

Donald P. Schneider, a Caltech graduate student collaborating with Greenstein, has analyzed some data taken in July 1978 during an eclipse of the classical nova DQ Herculis (1934). In this system, an accretion disk has a hot spot fed from an invisible main-sequence M star; the period is 16,740 seconds, and eclipse of the hot spot and disk produces a deep minimum during which the system drops by 4 mag in the blue, 2 mag at  $1 \mu$ . The total eclipse duration is only 3000 seconds, so that spectrophotometry at intervals of  $120^s$  was possible only by using the multichannel at a fixed wavelength setting and obtaining 34 observations giving light curves at the 30 different wavelengths of each channel observed simultaneously, from 3200 to 11,000 Å. (Previous attempts to obtain higher wavelength resolution by spectral scanning had failed because of the rapidity of changes of light level.) At minimum, the flux steeply decreases toward the blue, resembling a dM star, has a flat blue region, and a Balmer emission continuum. However, these low-resolution spectra (360 Å in the red, 160 Å in the blue) do not show recognizable TiO bands. An upper limit of  $m_V = 19$  can be set to the dM. To complicate the situation, there is an 18-mag visual companion (late F)  $4''$  distant and also the background expanding emission nebula. A small aperture was used to elimi-



nate the optical companion. SIT spectra help to eliminate the emission lines of the nebula. The red dwarf that eclipses the ring cannot be on the main sequence; its color and absolute luminosity require a spectral type later than M4 (mass  $\leq 0.3 M_{\odot}$ ), while dynamical arguments (Roche lobe overflow) indicate a mass of  $0.6 M_{\odot}$ . The light curves and the He II  $\lambda 4686/H\beta$  ratio show the disk to be very asymmetric, with a bright spot on the side of the disk eclipsed last. Since the white dwarf, inner disk, and hot spot are completely hidden, the residual red light must come from a larger region surrounding the white dwarf. A power law fitted to the observed fluxes shows large variation in slope. If it is optically thin, the electron temperature of this outer region is about 35,000 K, and the electron density  $10^{12}$  to  $10^{13} \text{ cm}^{-3}$ . The hot spot produces a strong asymmetry in the eclipse and a sharp drop at phase 0.98 (conjunction occurring near 0.96). X-ray observations during eclipse would be valuable.

Mochnecki observed Nova Vulpeculae 1979 shortly after it was first reported. Coudé Varo-Reticon scans showed that only  $H\alpha$  was in emission, with the rest of the visible region spectrum resembling an A4 supergiant. The  $H\alpha$  line had a P Cygni profile, with the emission and absorption components separated by about  $50 \text{ km s}^{-1}$ , a very small amount. Mochnecki and Ake are continuing to monitor this unusual object, which probably is not a classical nova but a very slow recurrent novalike variable.

### *Binary Stars*

Contact binaries of late spectral type (W Ursae Majoris stars) are thought to evolve by a combination of nuclear processes and angular momentum loss by gravitational radiation. Mochnecki has recently completed spectroscopic observations of one unusual system, FG Hydrae, whose evolution has possibly been strongly influenced by gravitational

radiation. An accurate knowledge of its mass is required to model its evolution. Mochnecki has also begun a program of observing the contact binaries in the old galactic clusters M67 and NGC 188, in collaboration with Dr. John Whelan of Cambridge University.

Mochnecki has compiled data obtained by modern synthesis methods for contact binaries. Densities and minimum periods have been computed for these systems, using accurate determinations of their Roche figures. Estimates of masses and absolute magnitudes have also been obtained. Mochnecki has computed a theoretical grid of evolutionary models, which agrees well with the observational data on many systems but disagrees with others. This suggests that the origins and evolution of contact binaries are more complex than hitherto thought. For example, some initially detached systems may eventually evolve into contact, and mechanisms of angular momentum loss other than gravitational radiation may be important. Data on contact binaries that are members of clusters will help to answer these questions.

Infrared observations of the unusual RS Canum Venaticorum stars, a class of late-type binary stars whose light curves exhibit asymmetric minima, unequally bright maxima, and large period changes, have been carried out by Graham Berriman, a Caltech graduate student.

The principal result is of a negative character: none of the stars measured shows an infrared excess at any wavelength at any orbital phase observed. This result contradicts previously published photometry such as that of Hall and Atkins (1972), who claimed excesses of 0.5 mag at  $1.2 \mu\text{m}$ ,  $2.2 \mu\text{m}$ , and  $3.5 \mu\text{m}$  in five of six objects observed. The mass-loss rates implied by the period changes are very large:  $10^{-6}$ – $10^{-7} M_{\odot} \text{ yr}^{-1}$ . The mass is believed to be lost through flaring activity on one component, which gives rise to a hot stellar wind ( $T \sim 10^7 \text{ K}$ ) and is responsible for the production of soft x rays. The

mass-loss rate required to produce the observed x-ray emission is only  $10^{-10} \mathcal{M}_{\odot} \text{ yr}^{-1}$ .

Infrared free-free emission is expected as the ejected material expands and cools; the observed lack of infrared emission places upper limits of  $10^{-8}$ – $10^{-9} \mathcal{M}_{\odot} \text{ yr}^{-1}$  on the mass-loss rates—clearly consistent with x-ray data but inconsistent with values obtained from period changes. Either the purported period changes are erroneous or they originate by some mechanism other than mass loss, such as the presence of third bodies of low mass. A more detailed interpretation of the data will account for the relative roles of adiabatic and radiative cooling and of conduction in a hot plasma.

### *Stellar Coronas*

Zirin has continued his observations of various stars in the He I 10830 line, which is a tracer of soft x-ray and *XUV* flux and hence of a stellar corona. This year, most of the brighter RS CVn stars were surveyed: most of them showed strong 10830; some did not and may be variable in *XUV* flux. Since many close binaries show such activity, a random survey of binaries has been started to determine the dependence of coronal activity on period and spectral class. For the first time, spectra of several T Tauri stars were obtained; all show strong 10830 P Cygni-type emission.

The star  $\theta$  Herculis returned to emission in 10830; previous periods of emission occurred in 1966, 1971, and 1975, with absorption or no line at all in the intervening times. It thus appears to have a four-year “period,” at the end of which a hot shell is expelled. The emission cannot be due to *XUV* excitation because that radiation cannot penetrate to the depth at which He emission is formed; however, *XUV* could play a role in the excitation of an expanding shell—but the shell would probably cool the stellar corona.

### *Red Giants in old Disk Clusters*

Cottrell and Da Costa have derived carbon and nitrogen abundances in red giant stars in the old open cluster M67. The program stars covered more than two magnitudes, from  $M_{\text{bol}} + 1.7$  to  $-0.5$ . The data was acquired using the “Shectograph” attached to the 32-inch camera of the Mount Wilson 100-inch coudé. The wavelength interval covered was  $\lambda\lambda 4100$ – $4600$  with a resolution of  $\sim 1.2\text{\AA}$ . Preliminary results indicate that, within the errors of the determination, solar carbon and nitrogen abundance ratios (relative to the metals for which we adopt  $[\text{metals}/\text{H}] = -0.3$ ) were obtained for the stars. This contrasts with the results that have been obtained in many globular clusters (e.g., 47 Tucanae, NGC 6397, and NGC 6752) where nitrogen has been shown to be enhanced relative to the other metals. Recent theoretical work on meridional mixing in red giants (Sweigart and Mengel, *Astrophys. J.*, 229, 624, 1979) provided an explanation for some of the observed CH- and CN-band anomalies in globular clusters. However, their theory also predicts that the onset of meridional mixing in M67 would occur at  $M_{\text{bol}} = +0.7$ . Since no such anomalies appear to exist, either the threshold of one of the mixing parameters has not been attained or this theory is not at all applicable to this system.

### *Lower Main Sequence*

Stefan Mochnacki has observed six emission-line K and M dwarfs in a search for magnetic fields. The Varo-Reticon photon-counting spectrometer was adapted for use with the circularly polarizing optics of Vaughan and Borra. No Zeeman effects greater than the  $3\sigma$  level were detected at  $H\alpha$ . For the dMe flare star EQ Pegasi, the upper limit on the effective field in  $H\alpha$  was 1 KGauss. These results are further evidence against



the existence of extensive, easily observable strong magnetic fields in M dwarfs.

Mochnacki and Schommer are continuing their program of monitoring K and M dwarfs for radial velocity variations, and reductions are under way.

Ake has completed the study of the parallax M dwarf and subdwarf stars observed by Greenstein with the multichannel spectrometer. The work will lead to improved photometric parallaxes and the spectrophotometric identification of metal-poor M dwarfs for studies of space motions and densities.

To calibrate the M-dwarf main sequence with respect to abundance differences, the multichannel scans were used to choose a color system unaffected by either composition differences or spectral indices known to be metallicity dependent. Five continuum points were selected to avoid both stellar and terrestrial features, and comparison of the photometry with Mould's dM models demonstrates that these points are composition independent. Measures of CaH, MgH, TiO, and Ca I  $\lambda 4227$ , the traditional spectroscopic M subdwarf criteria, were selected as metallicity indicators. Problems with the Mould models precluded derivations of abundances by fitting the models to the multichannel scans. Instead, high-dispersion spectra taken with the coude Varo-Reticon at the 2.5-meter telescope will be compared with synthetic spectra to calibrate the multichannel indices with metal abundance.

The behavior of the spectral indices with composition depends on temperature, except for TiO, which is always weak for the subdwarfs. For metal-poor stars of color equivalent to K7-M0, all features are weak; MgH, however, quickly strengthens and becomes too strong for its color by M0.5. By type M1, CaH and Ca I  $\lambda 4227$  are enhanced over the normal dM stars so that the extreme subdwarfs are easily recognized as having strong hydrides and  $\lambda 4227$  but weak TiO. They are not found redder than color equivalent type M3. The old-

disk subdwarfs, which lie on the lower envelope of the main sequence, exhibit the subdwarf characteristics except for having normal TiO and can be found from type M2 to M4.5.

For the M dwarfs of solar composition, the multichannel colors alone do no better than broadband colors for deriving photometric absolute magnitudes, that is,  $\sigma_{M_v} = \pm 0.5$  mag. The additional use of the spectral indices, however, reduces the error to  $\pm 0.3$  mag, while also segregating the subdwarfs independently of kinematical criteria. The subdwarfs are separated from the main sequence by a gap of 0.5 mag, but on the average fall 1.5 mag below the mean main sequence. While the main sequence extends to  $M_V = 19$ , no TiO weak subdwarf fainter than  $M_V = 12.5$  was found.

Comparison of the multichannel colors with  $M_{bol}$  and  $T_{eff}$  calibrations of Johnson (1966), Veeder (1974), and Mould and Hyland (1976), yields bolometric magnitudes to  $\pm 0.07$  mag and temperatures to  $\pm 100$  K, although the temperature scales are quite different. The fundamentally derived temperatures of YY Geminorum and CM Draconis indicate that the Veeder scale is best. Radii obtained from the  $M_{bol}$  and  $T_{eff}$  derivations indicate that if the mass-radius relation is independent of composition, unlike the mass-luminosity relation, the parallax subdwarf of latest spectral type has a mass comparable to a normal M5 type, or  $\sim 0.1 M_{\odot}$ .

Work has been started on analyzing the nonparallax stars to derive space motions and densities for the normal and subdwarf M groups separately. The observations include all Giclas stars with proper motions larger than  $1'' \text{ yr}^{-1}$ . Preliminary results indicate that the genuine subdwarfs have total velocities exceeding  $180 \text{ km s}^{-1}$  and  $W$  components greater than  $100 \text{ km s}^{-1}$ , while the old-disk subdwarfs are high-velocity stars confined to the galactic plane. The ratio of halo/disk stars in the solar neighborhood is  $\sim 1/250$ . Although Greenstein



preferentially observed stars with large, reduced proper motions to increase the likelihood of discovering the intrinsically faintest subdwarfs, only two possible candidates have been identified below the M3,  $M_V = 12.5$  cutoff so far.

### *Degenerate Stars*

Much effort to improve the temperature scale was based on multichannel observations by Greenstein, supplemented by observations with the International Ultraviolet Explorer (IUE) by Greenstein and Oke. The major result of the IUE observations is that model atmospheres can be fitted to the observations from 11,000 to 1150 Å. Eight hydrogen-atmosphere DA's have been so observed, with effective temperatures from 7000 K to 60,000–70,000 K at the hot end. The photometry from space gives surprisingly accordant results with that from the ground. Since most white dwarfs have nearly the same radius ( $\approx 0.0127 R_\odot$ ), this sample covers the range of bolometric magnitudes from +4.2 to +14.2; two of the hottest have been observed in the extreme ultraviolet from Apollo-Soyuz. No metallic lines were found in any DA star. Two helium-line DB stars also have temperatures accordant with ground-based data; the hotter is just below 25,000 K and no  $\text{Ly}\alpha$  is seen. One rapid variable, HZ 29, which is dominated by broad He I absorption in the optical region, apparently has an accretion disk with a flat spectrum, superposed on which are deep P Cygni-type N V, C IV, Si IV, Si III, and He II absorption lines, with possible weak emission components. Thus the material from an invisible companion contains only He, C, N, Si, and not hydrogen; the N V line is strongest, suggesting a hydrogen-deficient hot plasma rather similar to that seen in quasar absorption lines. The single DB (metallic) star GD 40 has a strong Mg II absorption, continuing the tendency found in many DB stars to have metals absent in DA stars.

The magnetic (polarized) stars are much more difficult to fit, since model atmospheres are lacking. However, Feige 7, DBAP, fits a composite He and H model and does show  $\text{Ly}\alpha$  absorption; it may have  $\lambda 1640$  of He II, not expected at its low temperature. The fascinating star Grw +70° 8247, however, continues to be mysterious. The ultraviolet has several discontinuities, all unidentified, and cuts off sharply at  $\lambda 1400$ ; it can be fitted with a blackbody of 15,000 K, with large deviations. Its parallax is known, and the radius as derived is then the smallest known for any degenerate star ( $0.0062 \pm 0.0008 R_\odot$ ), i.e., smaller and therefore more massive than Sirius B.

An extensive analysis by Greenstein of data on 162 DA stars observed with the multichannel spectrometer includes temperature determinations and the first comparison of Balmer-line equivalent widths with theory. This analysis was based on the grids of hydrogen model atmosphere fluxes kindly made available by Dr. D. Koester, Institute for Theoretical Physics, Kiel, West Germany, and Dr. H. Shipman, University of Delaware. In addition, SIT measurements of equivalent widths were available from a study by G. Vauclair and Greenstein; these were used to calibrate multichannel measurements. The major conclusion is that present model atmospheres permit internally consistent temperature determinations from multichannel colors. The mean surface gravity cannot be as accurately determined as the effective temperature, but it must exceed  $\log g = 7$  and possibly be near or slightly above  $\log g = 8$ . Metals and helium cannot be detected in DA stars and must have low abundance. The frequency of observed stars, selected by various initial criteria, is not ideal for a determination of their frequency in space. But when their numbers are binned in groups by  $\log T \pm 0.05$ , the counted numbers have a flat maximum from  $\log T = 3.85$ –4.25. If we assume all have the same mean



radius, these limits correspond to the bolometric luminosity of the most commonly observed DA star, covering a range of 40 ( $13.2 \leq M_{\text{bol}} \leq 9.2$ ). The extreme range,  $15.2 \leq M_{\text{bol}} \leq 4.2$ , shows that stars classified as DA have a range of 25,000 in luminosity—one of the largest ranges of any type of star known. An approximate correction for volume of space surveyed, down to a limiting apparent magnitude, yields the relative space densities for comparison with the numbers expected if white dwarfs shine only by converting internal heat into radiated energy. The observed slope of the number density appears to be slightly steeper than expected from the cooling law (possibly because of the intensity of the search for degenerate stars of very low luminosity). Neglecting this selection effect, the cooling law, lifetime proportional to  $L^{-5/7}$ , is substantiated down to 5500°K. This provides the first test of the  $L^{-5/7}$  law for a large sample of stars of known temperature,  $N \approx T^{-20/7}$ .

As mentioned in *Year Book 77* (p. 172), Ross 640 (EG 119) DFp has been observed with the IUE by Greenstein and Oke. Cottrell and Greenstein have used these data and the observations of Liebert (*Astron. Astrophys.*, 60, 101, 1977) to derive Mg, Si, Ca, and Fe abundances, using spectrum synthesis techniques. Helium-rich white dwarf model atmospheres were obtained from Liebert and atomic line lists were constructed for calculation of the synthetic spectra. Using Liebert's model with  $T_{\text{eff}} = 8800$  K,  $\log g = 8.0$ , and metals ( $\mathcal{M}$ ) deficient by  $10^4$ , Cottrell and Greenstein derived the following abundance ratios  $[\text{Mg}/\mathcal{M}] = +1.5$ ,  $[\text{Si}/\mathcal{M}] = +1.0$ ,  $[\text{Ca}/\mathcal{M}] = +0.6$ , and  $[\text{Fe}/\mathcal{M}] = -0.2$ . The errors are approximately  $\pm 0.5$  dex. A detailed fit was not obtained to the observed spectrum, especially in the core of the Mg II line at  $\lambda 2800$ . Some changes in the atmospheric structure of the model may be required to fit the observations more precisely.

To interpret the above abundance ratios, one can postulate that the combined effects of accretion (of interstellar matter) followed by thermal diffusion (within the atmosphere) provide a reasonable explanation. This more complex theory has to be favored over simple diffusion processes, which predict that all the metals would have settled out of a helium-rich atmosphere on time scales much less than the cooling lifetime of the white dwarf.

### *A Rotating Magnetic White Dwarf*

The star PG 1015+01 was discovered to be a magnetic variable in work reported by Green and Schmidt, in collaboration with Drs. H. S. Stockman, R. P. Angel, and J. W. Liebert of Steward Observatory, I. Thompson and J. D. Landstreet of the University of Western Ontario, and E. A. Beaver of the University of California at San Diego. Selected for its ultraviolet excess in the PG survey for blue stellar objects, the star showed variable, broad absorption features on 5-meter Hale Telescope image-tube spectrograms, as well as on UCSD Digicon spectra from the Steward 2.3-meter telescope. Such a spectrum is characteristic of magnetic white dwarfs. This identification was confirmed by the presence of circular polarization, varying from +1.1% to -1.5% with a 99-minute period.

The spectra do not match theoretical spectra of hydrogen and helium for magnetic fields  $\leq 50$  MG, and the field is probably stronger. The object was followed through an entire rotation period with the Hale SIT spectrograph; the principal features vary dramatically in both total strength and profile, and are consistent with variation in phase with the magnetic field. This white dwarf is the only known example with such a strong field that rotates to exhibit different spectral features.

## INTERSTELLAR MATTER

*Molecular Hydrogen in Orion*

Since the discovery of  $\text{H}_2$  emission in Orion, the nature of the mechanism responsible for its excitation has attracted the attention of both theoretical and experimental workers. Since hydrogen is the major constituent of the universe,  $\text{H}_2$  should dominate the composition of molecular clouds. On the other hand, its high energy of excitation and low rate of formation impose strong constraints on the physical conditions that can make it observable. Early observations at Caltech were centered on high spatial resolution studies of  $\text{H}_2$  with low spectral resolution. Daniel Nadeau, a graduate student in the infrared group, together with Geballe, has recently made observations that combine high spectral and high spatial resolution, using a piezo-electrically scanned Fabry-Perot interferometer with a resolution of  $20 \text{ km s}^{-1}$ .

Observations made in November 1978 of the  $2.12 \mu\text{m } v=1-0 \text{ S}(1)$  line of  $\text{H}_2$  are shown in Figs. 3A and 3B. The former shows spectra of the  $\text{H}_2 v=1-0 \text{ S}(1)$  line in Orion after sky subtraction. The numbers on the left-hand side of the spectra refer to the corresponding position in Fig. 3B. The relative intensities of the lines of different spectra are accurate to 10%. The uncertainty on the calibration of the origin of the velocity scale is  $\pm 5 \text{ km s}^{-1}$ , and the relative velocities of the lines of different spectra are accurate to  $\pm 2 \text{ km s}^{-1}$ . Figure 3B

shows the positions of the spectra presented on the  $13''$  map of the  $\text{H}_2 v=1-0 \text{ S}(1)$  line emission. The size of the circles corresponds to the  $10''$  spatial resolution used in the measurements. Pointing uncertainties are typically  $\pm 3''$ .

These observations show that (1) the full widths at half maximum of the observed  $\text{S}(1)$  lines vary between 18 and  $58 \text{ km s}^{-1}$ , (2) a small fraction of the observed  $\text{H}_2$  gas is moving at a velocity of approximately  $-100 \text{ km s}^{-1}$  with respect to the bulk of the molecular cloud, (3) the region of emission is probably undergoing differential expansion from a center roughly along the line of sight to the BN-KL infrared sources, (4) the  $\text{H}_2$  emission is probably associated with the "plateau" sources seen in the emission of other molecules, and (5) although collisional excitation is the likely cause of the  $\text{S}(1)$  emission, the excitation is not produced by a single shock front moving at low velocity ( $v < 24 \text{ km s}^{-1}$ ) through the molecular cloud.

Many of these results were totally unexpected on the basis of both the theoretical models and previous observations. Further analysis of the data presented here, together with some new data obtained in February 1979, should provide a strong basis for a model of the excitation of molecular hydrogen in Orion and, hence, of the internal dynamics of the molecular cloud in the region where  $\text{H}_2$  is observed.



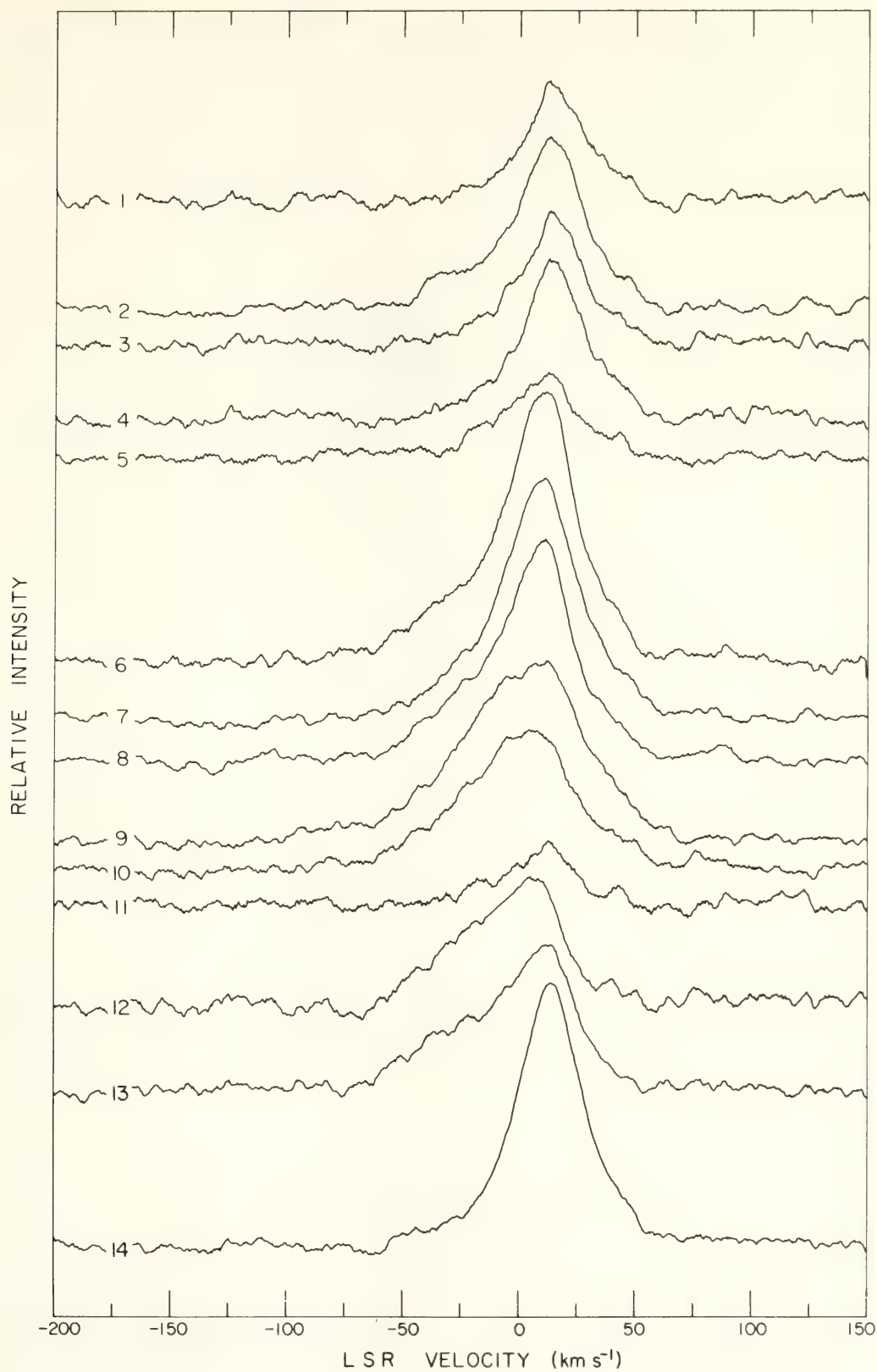


Fig. 3A. Spectra of the  $\text{H}_2$   $v = 1-0$  S(1) line in Orion after sky subtraction. The spectral resolution is  $20 \text{ km s}^{-1}$ . The noise level should be judged from each baseline individually, as different integration times were used on different spectra. See text (p. 732) for further explanation.

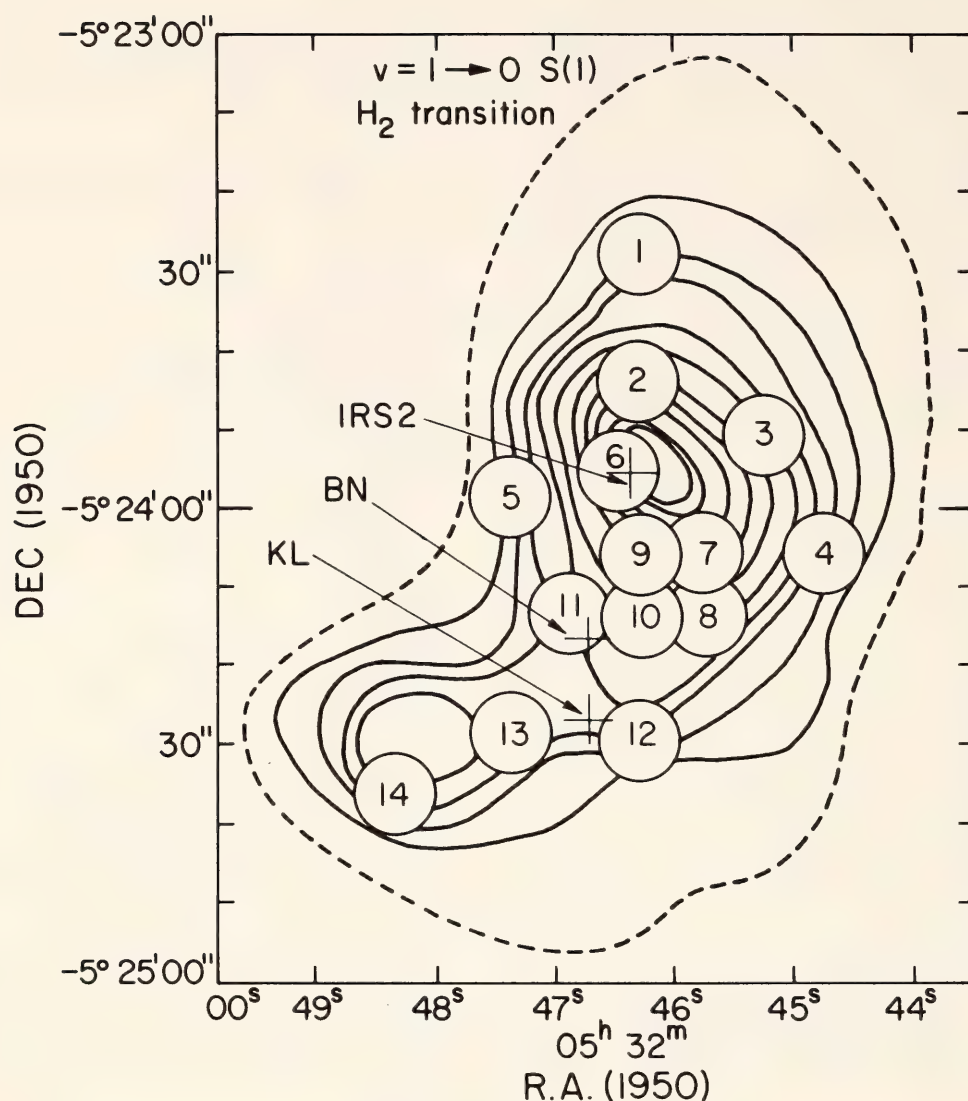


Fig. 3B. The positions of the spectra presented in Fig. 3A are shown on the 13" map of the  $\text{H}_2$   $v = 1-0$  S(1) line emission from Beckwith *et al.* (*Astrophys. J.*, 223, 464, 1978). The size of the circles corresponds to the 10" spatial resolution used in the measurements. Pointing uncertainties are typically  $\pm 3''$ .

## GLOBULAR CLUSTERS

### *Radial Gradients*

Globular clusters are generally regarded as being spatially homogeneous: in the vast majority of clusters, quantities such as the mean metal abundance are not thought to vary with distance from the cluster center. Recent work by Chun and Freeman (*Astrophys. J.*, 227, 93, 1979), however, appears to indicate that this "standard picture" may not be correct. Using concentric aperture meas-

urements, they determined the integrated *UBV* colors of 23 globular clusters as a function of distance from the cluster center. They found that while 16 clusters had radially uniform colors, the colors of the remaining seven became redder toward the cluster centers. Further, they found that the presence of a color gradient correlated with the central relaxation times of the clusters: the clusters with color gradients all had central relaxation



times longer than  $10^8$  years. This correlation led them to suggest that the radial color gradients reflected a radial gradient in some cluster parameter, possibly metal abundance, set up at the time of the cluster's formation; for the clusters with shorter relaxation times, there has been enough time for these primordial gradients to diffuse away.

The origin of these radial color gradients has been investigated by Da Costa using frames taken with the SIT direct camera attached to the 1.5-meter telescope at Palomar. Frames were obtained of three clusters that have central color gradients (according to Chun and Freeman) and of four that do not. It is immediately apparent from these frames that the central regions of the three clusters with color gradients are more clearly resolved into individual bright giants than are the central regions of the other clusters. In this situation, the colors measured through the smaller of Chun and Freeman's apertures (9", 12", and 15" diameter) will be, for the resolved clusters, critically dependent on where the apertures are centered. If the apertures are centered on one of the bright giants, then this star will contribute a substantial fraction of the measured signal through the smaller apertures, leading to apparently redder integrated colors. For the other four clusters, however, the degree of resolution is considerably less, and even in the smallest apertures the measured light is not dominated by any individual bright red star. Hence it appears likely that the integrated color gradients found by Chun and Freeman result from the centering of their apertures on bright cluster giants rather than from more fundamental causes.

Evidence that supports this explanation is provided by the following correlation: of the 11 clusters with core radii greater than 15", six have color gradients, while only one cluster of the 12 with core radii less than 15" has a color gradient. In other words, all but one of the clusters showing color gradients have

core radii significantly larger than the radii of the smaller apertures used in the measurements. This correlation with core radius also explains the correlation with central relaxation time,  $T_R$ , found by Chun and Freeman. Since  $T_R \propto r_c^{3/2}$ , the clusters with larger apparent core radii will tend to have larger values of  $T_R$ , inducing a correlation between  $T_R$  and the presence of a color gradient. If, however, as suggested here, the color gradients are the result of centering the smaller apertures on bright cluster giants, then this correlation with  $T_R$  is merely a secondary effect from which no inference should be drawn.

Continuing his investigation of this problem, Da Costa has obtained concentric aperture photometry of a number of globular clusters with the Las Campanas 1-meter Swope Telescope. The clusters in this sample have small core radii and high central surface brightness so that the centering problems that marred the Chun-Freeman measurements are avoided. The photometric system used is the metal-abundance-sensitive system of Zinn. For all clusters measured so far, the photometry is consistent with the "standard picture"—the mean metal abundance does not change with radius. The upper limit to any such change is less than 0.2 in  $[\text{Fe}/\text{H}]$  in most cases.

Two other globular clusters have been singled out for special study. They are  $\omega$ Centauri, where a large, presumably primordial abundance range is present, and 47 Tucanae, where radial gradients in integrated colors in the CN-band strength of the giants and possibly in overall metal abundance have been reported. The proximity and high intrinsic luminosity of these clusters make it possible to obtain photometry with relatively high spatial resolution out to large radial distances. The observations for 47 Tuc are not yet complete, but for  $\omega$ Cen the observations indicate that the mean metal abundance does not, to within  $\pm 0.1$  in  $[\text{Fe}/\text{H}]$ , change out to at least 8' ( $\sim 4$  core radii) from the cluster cen-

ter. Since the relaxation time in this cluster is very long, any radial gradient set up at the time of the cluster's formation should still be present. Consequently, the observed lack of any metal-abundance gradient may have important implications for understanding the formation of  $\omega$ Cen, and for the origin of the large abundance range seen in this cluster. These possibilities are currently being investigated.

### *CN/CH Anomalies*

A spectroscopic survey of the giant branch of the southern globular cluster NGC 6752 has been carried out by Drs. J. E. Norris and K. C. Freeman of Mt. Stromlo and Siding Spring Observatory and by Da Costa. The observations have been obtained both in Australia and with the Sheckman photon-counting image-intensifier/Reticon system ("Sheckograph") attached to the Cassegrain spectrograph of the du Pont Telescope at Las Campanas Observatory. Briefly, the survey has shown that on the first giant branch in this cluster, the distribution of strengths of the CN molecular band at  $\lambda 3883$  is bimodal; stars appear to be either "CN strong" or "CN weak." Further, the strength of this CN band is anticorrelated with that of the G-band (CH); the CN-weak stars have in general stronger G-bands than the CN-strong stars. This anticorrelation suggests that the CN-strong stars result from the mixing of processed material into the atmospheres of the stars.

In order to aid the interpretation of the observations of this cluster, Da Costa and Cottrell have analyzed the relatively high resolution Sheckograph spectra, using spectrum-synthesis techniques. This analysis has enabled the determination of quantitative carbon and nitrogen abundances for stars in both the CN-strong and CN-weak groups. It appears that the CN-strong stars are enhanced in nitrogen by  $0.8 \pm 0.3$  dex and depleted in carbon by  $0.3 \pm 0.2$  dex relative to

the CN-weak stars. These abundance changes are consistent with the carbon- and nitrogen-abundance changes that occur in the interior of stars during CNO-cycle processing. Thus the results of the spectrum-synthesis analysis strongly support the hypothesis that the mixing of processed material into the surface layers is responsible for the band-strength variations seen in this cluster.

A second result obtained from spectrum-synthesis analysis is that the CN-weak stars in this cluster, which presumably have not undergone any mixing, appear to have approximately solar carbon-to-iron and nitrogen-to-iron abundance ratios. The result for carbon agrees with the predictions of models of nucleosynthesis, but the result for nitrogen does not; the models predict that nitrogen should be significantly depleted relative to iron in metal-poor stars. The observed lack of such a depletion in this cluster indicates that a significant fraction of the nitrogen in NGC 6752 must have been produced by primary processes rather than by the secondary processes assumed in the nucleosynthesis models.

### *Radial Velocities*

A program to investigate the dynamics of selected southern hemisphere globular clusters has been initiated by Da Costa. This program uses spectra obtained with the Las Campanas Sheckograph, and the eventual aim is the determination of such quantities as the variation of cluster velocity dispersion with radius, and the size and extent of any cluster rotation. The success of this program depends critically on the accuracy with which radial velocities can be determined from the (digital) Sheckograph spectra. Consequently, much effort has been expended this year in determining this accuracy.

The velocities are determined by cross-correlating the spectra with those of radial velocity standards of similar spectral types, using a modified version of the Fourier transform cross-correlation pro-



gram originally written by Rose. Typically, four independent sections of 512 pixels (Spectograph spectra have 3744 pixels) are used in the correlation, and the resulting velocities are averaged. Repeated observations of many globular cluster stars over several nights have shown that, for spectra obtained with a dispersion of  $0.3 \text{ \AA/pixel}$  ( $30 \text{ \AA mm}^{-1}$ ), the rms accuracy of a single observation is  $3 \text{ km s}^{-1}$ . This is of sufficient accuracy for the cluster dynamics program, and further observations are planned.

### *Metallicity in Globular Clusters*

During the report year, Zinn completed his investigations of the integrated colors of globular clusters. In 1977 and 1978, Zinn obtained measurements of 79 clusters with a narrow- and intermediate-band photometric system that enables the interstellar reddening and metallicities of the clusters to be estimated with high precision ( $\sigma E[B - V] = \pm 0.03$  and  $\sigma [\text{Fe}/\text{H}] = \pm 0.1$ ). The 1-meter Swope and 2.5-meter du Pont Telescopes were used to make the majority of these observations. These measurements have significantly improved the earlier distance and metallicity determinations for the majority of the clusters; consequently, the trends of metallicity with position in the Galaxy that are seen in the globular cluster system are now better documented. The most salient features of these trends are (1) the metal-rich clusters (i.e.,  $[\text{Fe}/\text{H}] > -1$ ) occupy a relatively small region of space near the galactic nucleus, whereas the metal-poor clusters are found in the nuclear regions and also at galactocentric distances ( $R$ ) as large as 100 kpc; (2) among the nuclear clusters there is a gradient of the mean metal abundance with distance above or below the galactic plane; and (3) in the outer halo ( $R > 9 \text{ kpc}$ ), there is roughly a factor of 10 range in metal abundance, but at most a small gradient of the mean metal abundance with distance from the galactic center or from

the galactic plane. These observations are consistent with the picture that the outer regions of the proto-Galaxy underwent a free-fall collapse, but the collapse became highly dissipative in the nuclear regions and eventually led to the formation of the galactic disk.

Cohen has determined the metal abundances of four members of M71. Although the results for the light elements are within a factor of five of solar, the iron-group elements are deficient by a factor of approximately 15 in M71. The metallicity of M71 is much lower than was anticipated; this cannot result from a problem in the method, as analyses of four M67 giants and two members of NGC 2420 give abundances satisfyingly close to solar. The implications of this unexpected result are being evaluated.

### *Infrared Studies of $\omega$ Centauri*

The program of infrared photometry of globular cluster red giants to determine energy distributions, bolometric luminosities, and CO and  $\text{H}_2\text{O}$  absorption strengths, was continued by Persson and Cohen in collaboration with Dr. Jay A. Frogel of Cerro Tololo Inter-American Observatory. In addition to the demonstration of variations in metallicity on the upper giant branch of  $\omega$ Cen discussed in *Year Book 77* (p. 176), analysis of observations of 82 stars in this cluster indicates that there are two sequences of stars distinguished by CNO/Fe ratios. Defining Fe metallicity by the position of the giants in the luminosity-effective temperature plane, they find that the group of stars that have "normal" CO absorption for their metallicity ("normal" means lying on a sequence defined by behavior of the M92, M13, M71, and field giants) comprises less than 50% of the  $\omega$ Cen stars. Most have CO considerably stronger than would be expected, as do the stars in M3 compared to those in M13. This latter difference led Cohen, Frogel, Persson, and others to suggest that the CNO/Fe ratio was the "second

parameter" that determines the population structure of the horizontal branch in globular clusters. If the apparent CNO/Fe variations with  $\omega$ Cen and between M3 and M13 are primordial, then the  $\omega$ Cen data argue against CNO/Fe as the second parameter. This is because  $\omega$ Cen contains few red horizontal-branch stars, and the analogy between  $\omega$ Cen and

M3/M13 breaks down. On the other hand, if mixing is important in altering the surface C, N, and O abundances, then it may be very difficult to use data on the CN, CH, and CO bands to decide whether CNO/Fe is the second parameter. In this case, a better understanding of the mixing process(es) will be prerequisite.

## OPTICAL IDENTIFICATIONS

### *Optical Candidate for the Binary Pulsar 1913+16*

Observations are continuing on the candidate discovered by Kristian and Westphal, as reported in *Year Book* 77 (p. 175). Improved position measurements place the candidate within  $0.3''$  of the radio position, but its  $V$  magnitude of 22.5 is more than three magnitudes brighter than published limits for visible pulsed radiation. If it is associated with the pulsar system, therefore, it is more likely to be the previously unseen binary companion of the pulsar. Preliminary reduction of a spectrum of the candidate, taken with the SIT/prism spectrograph by Kristian and Westphal, shows a red continuum, with no easily visible lines either in emission or absorption.

### *Identification of 3C Sources*

Gunn, with Drs. M. Perryman and M. S. Longair of Mullard Radio Astronomy Observatory, Cambridge, has investigated the few remaining unidentified spring high-latitude 3C sources with the new PFUEI (see section on Instrumentation, below) CCD camera. For the 12 fields for which data were obtained, five somewhat doubtful previous identifications have been confirmed, four new ones are proposed, one remains empty, one is provisionally identified with an object

off the radio source axis, and one is obscured by glare from a bright star. Essentially all the identifications at the faint level ( $R \sim 22.5$ ) are galaxies, as expected. The work will continue this fall on the southern hemisphere part of the sample.

### *The HEAO-2 Deep X-Ray Survey*

One of the prime objectives of the HEAO-2 x-ray observatory, which was launched in November 1978, is to study the microstructure of the x-ray background radiation. The principal question is, To what extent can the extragalactic x-ray background be accounted for by discrete sources such as QSO's and active galaxies? In order to answer this question, a sizable fraction of the observing time on HEAO-2 is committed to the Deep Survey, in which exposures of 100,000 seconds are to be made on eight areas of the sky, each with a diameter of about  $1^\circ$ , at high galactic latitudes. Sargent has collaborated extensively with Dr. R. Giacconi and his associates at the Center for Astrophysics, Harvard-Smithsonian Observatories, in doing optical studies to complement the x-ray observations. First, Sargent and Kowal have obtained deep photographs of the accessible deep survey fields on IIIaJ and IIIaF emulsions with the 1.2-meter



Schmidt telescope. Second, Sargent has obtained deep photographs of four of the fields (Ursa Minor, Corona Borealis, and two Draco fields) with the Kitt Peak 4-meter telescope, which has a field of 58'. The first three fields to be observed by HEAO-2 were those in UMi, Eridanus, and Draco. Some of the plate material described above has been used by Giacconi and his colleagues to identify the x-ray sources found in these areas.

Sargent, using the SIT spectrograph at the Cassegrain focus of the Hale Telescope, has obtained spectra of 11 supposed identifications out of 20 sources detected in the Draco field. Of these, two are 17.5 mag QSO's with redshifts of 1.59

and 2.0, respectively. Several of the sources are identified with galactic stars as faint as 16 mag. It is concluded that 10 of the sources in the Draco field are extragalactic; most of these are yet unidentified. On this basis, a preliminary impression has been reached that most of the x-ray background is produced by discrete sources, mostly QSO's.

At the time of this report, work was just beginning on the UMi deep survey field. However, one source, IE 1412+7303, was identified with a blue 18-mag starlike object. A spectrum obtained by Sargent showed that this object has a blue continuum with a single, fairly sharp emission line at  $\lambda 4000$ .

## THE GALAXY

### *The Galactic Nuclear Bulge*

Using the 2.5-meter du Pont Telescope, Mould has begun a study of the characteristics of the stellar population in the spheroidal nuclear bulge of the Galaxy. Very deep, fine-grain plates have been obtained with the Cassegrain camera in Baade's Window and other, higher-latitude fields. These plates will be analyzed in collaboration with Dr. H. R. Butcher of Kitt Peak National Observatory to seek the main-sequence mass function in the nuclear bulge. If successful, this will place important constraints on the luminosity evolution of spheroidal systems.

In addition, Mould has obtained spectra of 50 of the very late M giants found in large numbers in Baade's Window by V. M. Blanco of Cerro Tololo Inter-American Observatory. These stars are strongly concentrated toward the galactic center. The excellent dimensional stability of the intensified-Reticon spectrograph should allow an accurate velocity dispersion to be derived for these stars.

### *Galactic Mass Distribution*

Dr. G. Knapp of the California Institute of Technology and Gunn have continued their work on a general rediscussion of the mass distribution in the Galaxy, particularly for the region interior to the Sun. Both northern and southern hemisphere rotation curves show an unambiguous feature that cannot be explained without a density maximum near  $R \sim 0.5 R_0$ . This dynamical evidence, plus the data on the distribution of molecular emission, pulsars, and the  $2.4\text{-}\mu$  galactic background, suggest very strongly that the Galaxy is of the barred-ring variety exemplified by NGC 1398. The conflicting criteria, which have long suggested that the Galaxy is of early type on the basis of the bulge (whereas the disk suggests a much later type), may thus be resolved.

### *Survey for Low-Metal-Abundance Stars*

Preston and Shectman have extended their objective-prism search for low-

metal-abundance stars to the southern hemisphere by use of the Curtis Schmidt telescope at the Cerro Tololo Inter-American Observatory. The combination of HK interference filter and  $4^\circ$  prism ( $180 \text{ \AA mm}^{-1}$  at H and K) yields a limiting magnitude of  $B \sim 15\text{--}16$ . Scans of 22 anticentral fields ( $\sim 500 \square^\circ$  in the intervals  $-60^\circ < b^{\text{II}} - 40^\circ$ ,  $150 < l^{\text{II}} < 230$ ) have produced approximately 40

low-metal candidates and a finding list of some 500 AB stars, most of which can be expected to be BHB stars. Additional observations of many more fields, well distributed in longitude and latitude, are planned. Follow-on observations of the AB stars found in this survey should provide detailed information about the density distribution and kinematics of the BHB component of the galactic halo.

## GALAXIES

### *Globular Clusters in the Magellanic Clouds*

Among the red globular clusters of the Magellanic Clouds, there are a number with giant branches that reach very red values of  $B - V$  at the tip. Mould and Dr. Marc Aaronson of the University of Arizona have published the results of a spectroscopic survey done at the tip of the giant branch in these clusters. Numerous carbon stars whose luminosities place them on the upper asymptotic giant branch (well above the first giant branch tip) were found. Mould and Aaronson argue that such stars can only be produced by clusters considerably younger than the globular clusters of our own Galaxy. The age of the clusters is estimated at three billion years (within a factor of two). Although the Magellanic Cloud globulars split into two groups by color, the existence of a number of intermediate-age clusters among the red group is consistent with a picture of continuous cluster formation in the Clouds. The existence of large numbers of carbon stars in the field of the Clouds would suggest a star formation history quite different from the Galaxy, the rate of star formation being much less strongly peaked in the past.

### *Globular Clusters in M31*

Infrared photometry of 35 globular clusters in M31 has been analyzed by

Persson and Cohen in collaboration with Dr. Jay A. Frogel of the Cerro Tololo Inter-American Observatory, using reddening corrections provided by Searle. In addition to a well-defined correlation between  $V - K$  and metal abundance (as given by Searle's measure of the strength of Ca absorption), there is good correlation between  $V - K$  and  $U - V$ . This latter correlation fits the stellar synthesis models of Aaronson, Cohen, Mould, and Malkan (*Astrophys. J.*, 223, 824) extremely well. The implied value for the initial mass function slope is  $\leq 2.5$  (the Salpeter mass function is  $s = 2.35$ ). The scatter of the colors around the theoretical lines is extremely small and is consistent with the observational errors; furthermore, it is much less than the scatter of galactic globulars around the theoretical predictions. Because theory and observation agree so well, an attempt was made to fit the models to similar observations of elliptical galaxies. The nuclei of the most-luminous galaxies are definitely not on an extension of the globular-cluster sequence, and no combination of clusters of different metallicity can alleviate the problem. It seems most likely that a population of extremely red giant stars is altering the infrared energy distribution of elliptical galaxies. Narrow band  $2\text{-}\mu\text{CO}$  and  $\text{H}_2\text{O}$  observations of a faint dwarf elliptical galaxy in Virgo show a similar effect: compared to M31 globular clusters of the



same  $U - V$  color, the dwarf galaxy has stronger indices. This probably indicates a population of cool stars whose presence is detected most easily in the near-infrared.

### *Rotation in the Nuclear Bulge of M31*

The nuclear bulge of the Andromeda Nebula and the halo of our own Galaxy are the nearest examples of the roughly spherical stellar systems that typically accompany the flat disks of spiral galaxies. The radial light distributions in spiral galaxy bulges suggest that they are similar to small elliptical galaxies. While the material in spiral-galaxy disks rotates in roughly circular fashion, the rotational velocities of moderately flattened elliptical galaxies are typically a factor of five lower than in spirals. The rotation of ellipticals seems to be too low to account for their flattening. In an attempt to understand how the nuclear bulges of spiral galaxies fit into this picture, Shectman and Dr. Douglas O. Richstone of the University of Pittsburgh have measured velocities in the nuclear bulge of M31, which has a flattening comparable to an E3 elliptical. The measurements are of the Doppler shift in scans made of the Ca II H and K lines by tilting a narrow-band interference filter in a specially constructed photometer. This instrument, which is used at the prime focus of the 5-meter Hale Telescope, accumulates information rapidly because it can be used with much larger entrance apertures—of up to  $3\Box'$ —than are practical in a conventional spectrograph.

Along the minor axis of the nuclear bulge, where the measurements extend 600 parsecs from the nucleus, there is no evidence for velocities in excess of  $20 \text{ km s}^{-1}$ . Along the major axis, the rotational velocity appears to rise gradually in the inner kiloparsec to a value of  $85 \pm 16 \text{ km s}^{-1}$ . This rotational velocity, when scaled to an elliptical galaxy the size of the nuclear bulge of M31, is at the very

upper end of the range of rotational velocities exhibited by ellipticals. The nuclear bulge of M31 is exceptional in that its rotational velocity is sufficiently high to account for its flattening. It will be of interest to extend these measurements to the nuclear bulges of other spirals in order to understand the dynamical structure of these systems and the relation between spiral and elliptical galaxies.

### *Stellar Content of M33*

Sandage and Dr. Roberta Humphreys of the University of Minnesota brought to completion their collaborative effort, described in *Year Book* 77 (p. 178), on the brightest red and blue stars in M33. One of the goals of the work was to locate, and to obtain spectroscopy and photometry of, the brightest red supergiants in M33 so as to provide an important further calibration of the absolute  $V$  magnitude for the brightest red supergiants in the Sc, Sd, Sm, and Im highly resolved galaxies. In 1974, Sandage and Tammann (*Astrophys. J.*, 191, 603, 1974) discovered that  $\langle M_v \rangle$  for red supergiants with colors of  $(B-V)_0 > 2.0$  was remarkably constant at  $\langle M_v \rangle = -7.9 \pm 0.1$  in all resolved galaxies whose distances had been determined by them at that time and where the necessary data on individual stars were available. They further showed that, remarkably, the  $M_r$  of the brightest red stars is *independent* of the absolute magnitude of the parent galaxy itself. The galaxies involved were NGC 6822, IC 1613, LMC, and SMC in the Local Group and Ho II, IC 2574, and NGC 2403 in the M81/NGC 2403 group.

The importance of the result, if true, is that a very powerful new distance indicator is available that permits precise distances to be determined over a larger span of distances than is provided by Cepheid variables, because  $M_v = -8.0$  is so much brighter than the range of  $M_v \simeq -2$  to  $-6$  provided by the variables. Furthermore, the very small in-

trinsic dispersion of the relation ( $\sigma \simeq 0.1$  mag in the first calibration in 1974) has a very powerful advantage in removing most of the selection effects of observational bias (such as the Malmquist effect) in any larger sample of galaxies to which the brightest-red-star criteria will eventually be applied.

A great deal of effort is currently being put forth to obtain as strong a calibration of  $M_v$  (brightest red supergiant) as is possible. M33 is an important calibrator galaxy because its distance from Cepheids will soon be well known. However, because this galaxy is so close, its angular

size on the plane of the sky is very large (diameter  $\simeq 1^\circ$ ), and the isolation of the brightest red stars in M33, separated from the numerous field M dwarfs in our Galaxy projected over the M33 face, is tedious and requires much attention to detail. Hence, M33 was not among the original calibrators.

Sandage and Humphreys first prepared a color-magnitude diagram for  $\sim 1000$  of the brightest red and blue stars over the face of M33, which they had found by blinking pairs of 103aO+GG13, 103aD+GG11, and IVN+RG8 plates. These plates of the major area of M33

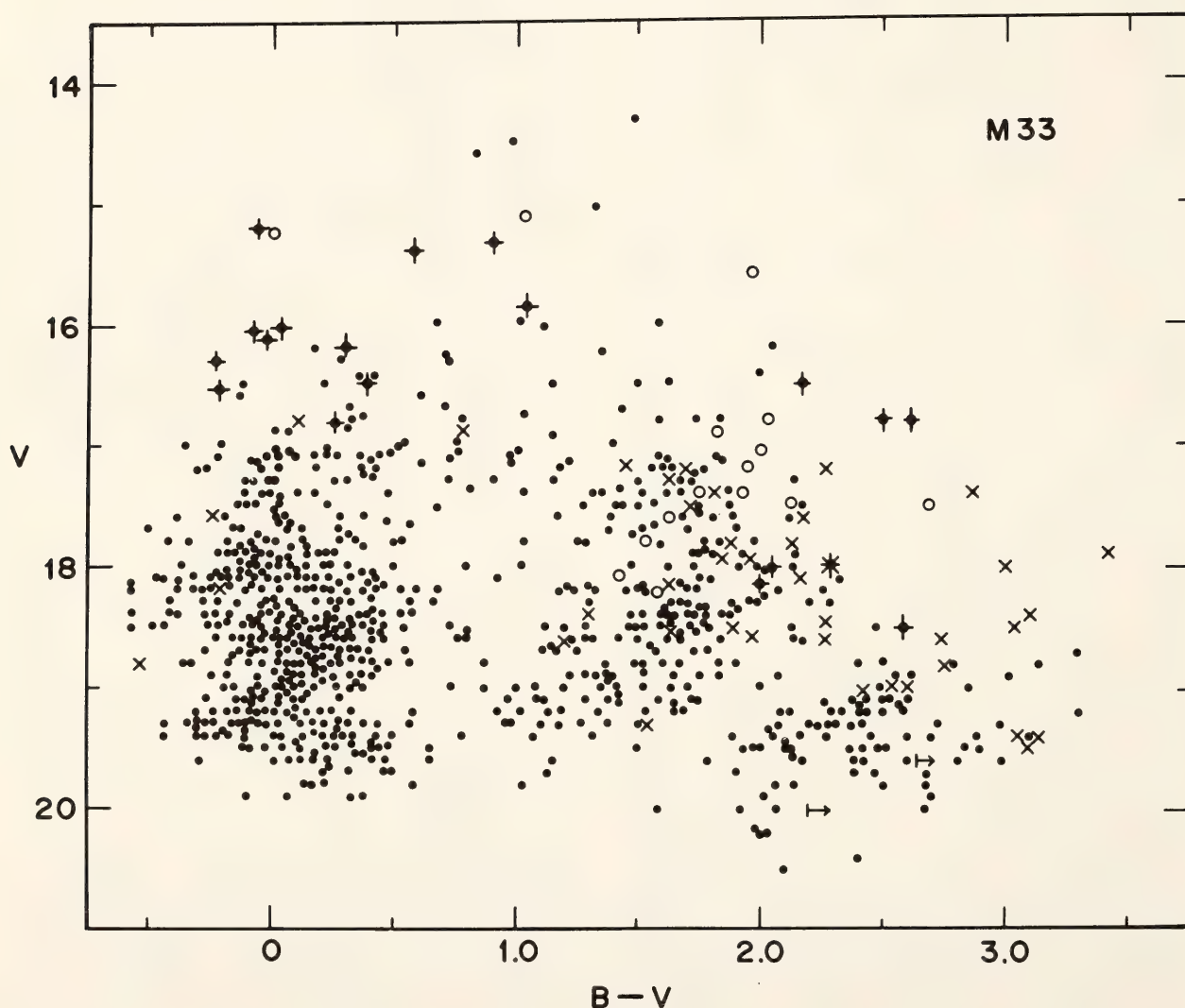


Fig. 4. Color-magnitude diagram for the red and blue stars measured by step-scale photometry over the face of M33. Most of the blue stars ( $B - V \lesssim 0.3$ ) are certainly supergiants in M33. Many of the red stars are superposed K and M foreground dwarfs in our Galaxy. Crosses are variable stars and therefore almost certainly M33 members; dots with vertical crosses are stars for which Humphreys has spectra and that are supergiants; open circles are foreground dwarfs as determined from Humphreys's spectra.



( $\sigma \simeq 25'$ ) had been obtained in the late 1950's for seven plate centers using the Hale 5-meter reflector, and in 1977 using the Kitt Peak 4-meter reflector. The  $B$  and  $V$  magnitudes were measured using the Argelander step-scale method with a specially made scale plate, calibrated frequently with the photoelectric sequence set up previously for this purpose (*Astrophys. J.*, 191, 63, 1974). The resulting color-magnitude diagram for all stars measured is shown in Fig. 4. The symbols are explained in the figure caption.

Most of the red stars in this color-magnitude diagram are foreground field stars from our own Galaxy, as shown by a special study of the expected contamination in the nearby Selected Area 45,

where a color-magnitude diagram in  $B$  and  $V$  has been constructed during the report year by Katem, to  $V = 22$  mag. The contamination can also be seen by comparing Fig. 4 with Fig. 5, which is the color-magnitude diagram only for stars inside the associations that are identified along the arms in the photograph in last year's Report (*Year Book* 77, p. 180, fig. 2).

Humphreys then obtained spectra of many of the candidate red and blue stars, using the Kitt Peak 1.2-meter and 4-meter reflectors, and these spectrograms unequivocally located the red and blue supergiants belonging to M33. These stars are shown by vertical crosses on certain dots in Figs. 4 and 5.

The principal result is that the three

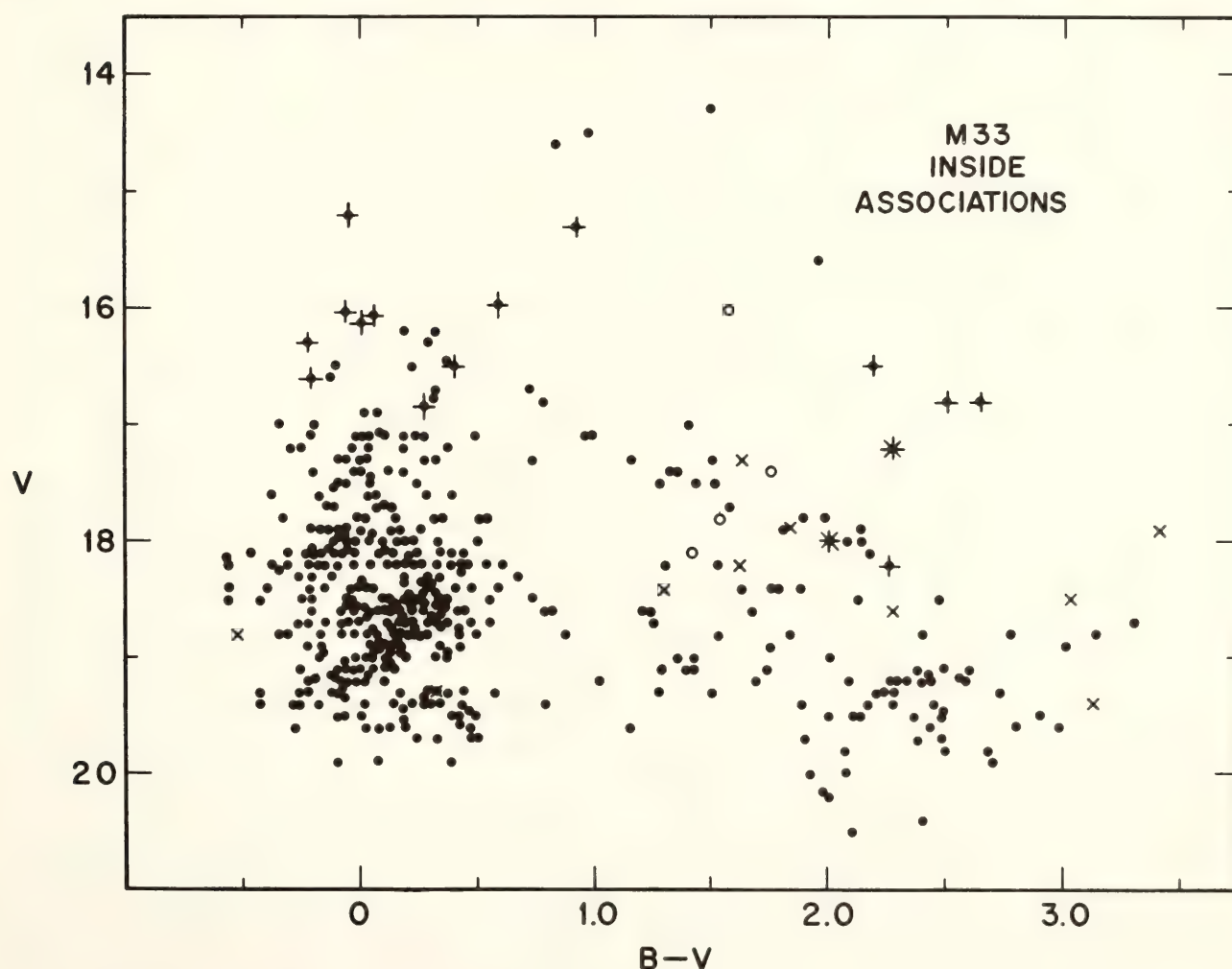


Fig. 5. Color-magnitude diagram for stars inside the marked boundaries of the M33 associations. Symbols are the same as in Fig. 4. The four brightest red supergiants are at  $V = 16.5, 16.8, 16.8$ , and  $17.2$ . The last is a variable star.

brightest red supergiants in M33 occur in associations (Nos. 12, 17, and 100 on the photograph shown in *Year Book* 77, p. 180) at apparent magnitudes of  $V = 16.5$ ,  $16.8$ , and  $16.8$ . Humphreys' spectra show the spectral types to be M0 Ia, M1 Ia, and M1 Ia. Since the apparent distance modulus of M33 is  $(m - M)_v = 24.6$ , the absolute magnitudes of the three red supergiants are  $M_v = -8.1$ ,  $-7.8$ , and  $-7.8$ , which confirms and strengthens the 1974 calibration from other galaxies.

The brightest star so far isolated in M33 is an F0-F5I intermediate supergiant in association 116 at  $V = 15.3$  ( $M_v = -9.3$ ), and/or an A5e Ia blue supergiant in association 67 at  $V = 15.2$  ( $M_v = -9.4$ ).

The upper limit for red supergiants seems well defined at  $M_v \simeq -8.0$  in M33. There is a growing theoretical understanding why such a sharply defined upper limit should exist for red supergiants. Evolutionary models for very massive stars with  $M > 20 M_\odot$  by Chiosi, Nasi, and Screenwasan (*Astron. Astrophys.*, 63, 103, 1978) show that mass loss in the form of stellar winds, as first observed in the late 1960's by D. C. Morton for upper main-sequence stars, prevents massive stars from proceeding far to the right in the CM diagram. They cannot reach the Hayashi red limit near  $\log T_e = 3.6$  at all for  $M \gtrsim 50 M_\odot$ , but do succeed in reaching that limit for stars of lower mass where the rate of mass loss is lower. The Chiosi *et al.* models predict explicitly that no red supergiants should exist brighter than a limit that is near  $M_v = -8$ .

With this theoretical understanding of what at first seemed such a remarkable observational result, the next step is to attempt a definitive calibration using all other galaxies where Cepheids can be found to provide the principal fundamental distances. Despite contrary claims in the literature, Cepheids provide the only reliable fundamental distance indicator of small intrinsic dispersion whose

calibration can be done within the Galaxy by reliable methods. For this reason it is still believed that Cepheids form the strongest foundation upon which to build the calibration of the new brightest-red-star indicator.

### *Search for Cepheids in Nearby Resolved Galaxies*

To strengthen the calibration of the brightest-red-supergiant distance indicator, Sandage has begun a systematic search for Cepheids in four highly resolved nearby stellar systems just beyond the Local Group. He has been accumulating plates on some of these systems since 1950 with the Hale 5-meter telescope, and more recently has begun a program on southern resolved galaxies with the du Pont 2.5-meter reflector.

A long series of plates of the Wolf-Lundmark-Mellotte (WLM) system taken with the Hale 5-meter reflector is now available. A trial blinking of a single pair of plates has yielded 22 variables (18 of them definite), of which most will be Cepheids. A red and blue pair has also been blinked to find the red supergiants. A photoelectric sequence to  $V = 22$  has been measured and a CM diagram suggests  $m - M \simeq 26.0$ , as mentioned in *Year Book* 75, p. 300.

A series of plates has been obtained with the du Pont 2.5-meter reflector at Las Campanas during 1977, 1978, and 1979 on NGC 247 and NGC 300 of the South Polar group, NGC 3109 (a nearby isolated dwarf), Sextans A, and Sextans B. All have supergiants that are easily isolated from foreground K and M field stars because of their concentration in the arms or associations.

Trial blinking of a single pair of plates has yielded 6 definite variables in Sextans B, 8 in Sextans A, and 20 in NGC 3109, of which 15 are certain. J. A. Graham's finding of many Cepheids in NGC 300 shows this to be a first-class calibrating galaxy as well.



Photoelectric sequences have been measured to  $V \simeq 17.5$  in the outlying regions of NGC 3109, Sextans A, and Sextans B, and these have been extended to  $V = 22.5$  via Racine Wedge plates.

In anticipation of using the brightest-red-star distance indicator extensively, red and blue Racine Wedge plates of the Pegasus dwarf, Leo A, Ho IX, IC 4182, NGC 4395, NGC 4214, NGC 4190, and several other members of the CVn I group have also been obtained. Photoelectric sequences have also been determined for stars near each of the listed galaxies to  $V = 17.5$ , which again can be extended to  $V = 22.5$  via the Racine Wedge plates.

These studies are expected to be completed within the year to further map the regularity of the Hubble flow in the very local region by using the more accurate distances found from the brightest-red-supergiant indicator.

#### *Spectrophotometry of the Nuclear Region of M51*

It has been known for some time that within the nuclear regions of some apparently normal spiral galaxies and of M51 in particular, the emission-line spectra exhibit striking peculiarities, such as a sudden reversal in the  $[\text{N II}]/\text{H}\alpha$  ratio (see Burbidge and Burbidge, *Astrophys. J.*, 135, 694, 1962). Rose has recently obtained long-slit spectrophotometry of M51, using the SIT Vidicon digital spectrograph of the Hale 5-meter telescope, in order to study the source of ionization of the gas in the nuclear regions of this Galaxy and to investigate the distribution and kinematics of the ionized gas.

Within the central  $15''$ – $20''$  in diameter, the emission-line spectra show numerous peculiarities in addition to the breadth of the lines ( $\text{FWHM} \sim 400 \text{ km s}^{-1}$ ). A preliminary analysis of the data indicates that the ionization in the nuclear regions is provided by a nonthermal power-law central ionizing source. This

conclusion is based on theoretical ionization models, developed by Caltech graduate student Stephen Kent, which show that gas photoionized by a nonthermal continuum provides an excellent fit to the emission-line spectrum throughout the nuclear regions of M51. Radial gradients in the observed emission-line intensity ratios are well reproduced by the theoretical models. The abundances of the heavy elements must be greater than solar, and nitrogen, in particular, must be enhanced by a factor of 10. Ionization of the gas by either hot young stars or shock heating and preionization can almost certainly be ruled out.

The distribution and kinematics of the ionized gas are still poorly understood. The emission lines are broad throughout the nuclear regions, where the peculiar emission-line spectrum dominates. For the most part, the line widths decrease radially from the nucleus. However, the broadest lines are found in an area  $\sim 4''$  from the nucleus.

#### *The Las Campanas Survey of Bright Galaxies*

The photographic survey of bright galaxies described in *Year Book* 77 (p. 179) has been continued by Sandage and Brucato with the du Pont 2.5-meter reflector and with the Hale Palomar 5-meter telescope. The purpose is to rephotograph all galaxies in the Shapley-Ames Catalog for which inadequate plate material now exists, so as to improve the morphological classifications. Plates for 400 galaxies, often taken under good-to-excellent seeing, were obtained during the report year. The new Hubble classifications, together with luminosity classes, were used to update the provisional classifications in the Revised Shapley-Ames Catalog (RSA), and are the last to be included before the first edition of the RSA is sent to press toward the end of 1979.

The large scale of the Las Campanas and Palomar plates and the truly supe-





Fig. 6. The intermediate Sa galaxy NGC 1350 taken with the du Pont 2.5-meter reflector. The reproduction is printed to emphasize the dust pattern across the interior central lens and its asymmetrical character, stronger on the right side of the major axis than on the left.

rior seeing at the Las Campanas site have revealed details of galaxy morphology that have only seldom been seen before.

#### *Warped Dust Planes*

Based on the new plate material, Sandage and Brucato have begun a study of the distribution of dust in galaxies along the Hubble sequence of spirals, together with the internal ring pattern in  $SO_3$  galaxies. The most usual dust feature, known for years, is the asymmetry of the dust pattern over the face of inclined galaxies. In this normal asymmetry, the dust is more sharply silhouetted against the near side than against the far side of the light distribution. The ratio of extinction between the near and far sides depends on the bulge-to-disk ratio, and a family of models is being constructed

by Brucato in an attempt to explain this classical asymmetry pattern and its variation along the Hubble sequence in terms of the relative size of the halos of the galaxies involved.

But the new phenomenon, which occurs in about one quarter of the sample, is an asymmetry in the dust extinction between halves of the galaxy separated by the minor axis. In these cases, the extinction is stronger in one quadrant of the image than in a symmetrical quadrant where, in the simplest model in which the dust is confined to a plane coincident with the luminous disk, the extinction should have been symmetrical. An example is the Sa galaxy NGC 1350 where, in the illustration of Fig. 6, the dust extinction is seen to be stronger along the right-hand part of the major axis than along the left. A conclusion from a study of a number of



such cases is that the dust layer in these galaxies must lie *out* of the luminous plane (albeit by only a few degrees). In those places of a given galaxy where the dust lies above the plane (i.e., closer to the observer), it is sharply silhouetted against the luminous disk. Where the dust lies below the plane, the foreground stars of the disk reduce the contrast. As the nodes of the warping of the dust plane have no relation to the major axis of the projected image (the inclination axis of the galaxy to the line of sight), the dust asymmetry due to a warped plane will not, in general, show symmetry upon reflection about the minor axis. A study of this interesting new phenomenon is expected to become a major part of the Las Campanas Survey as more plates of Sa, Sb, and Sc galaxies are taken.

### *Dust Arms Alone*

During the report year, most of the Las Campanas Survey was concentrated on S0 and Sa galaxies in an attempt to understand the morphological relations between these types. Among the new phenomena found were galaxies having pure dust spiral arms but no indication of recent star formation along any of these dust lanes. The dust arms are clearly arranged in a spiral pattern about the nucleus.

The two clearest examples of galaxies of this type are NGC 2855 [called S0<sub>3</sub>/Sa (r) in *The Hubble Atlas of Galaxies*] and NGC 7377, shown in Fig. 7 here. The spiral pattern is defined by the dust as it winds outward through an otherwise featureless lens of luminous material. The asymmetry in the dust pattern can be seen in Fig. 7; it is not clear if the asym-



Fig. 7. NGC 7377, which is the type example of a new class of Sa galaxies where the spiral pattern is composed of dust lanes only. No recent star formation associated with the dust is present. The dust pattern, clearly organized about the nucleus, defines the spiral structure in this and in similar galaxies of the type. The photograph was taken with the du Pont 2.5-meter reflector as part of the Las Campanas Survey of bright galaxies.



metry is due to a warped dust plane or to the normal situation of silhouetting against the more extended halo on the near side.

### *The Morphology of Sa Galaxies*

A special study of the morphology of the 141 Sa galaxies listed in the RSA was begun by Sandage. Its purpose is to provide optical data to aid in the interpretation of the 21-cm radio survey of S0 and Sa galaxies being made by Huchtmeier and Tammann with the 100-meter Bonn reflector.

Adequate plate material now exists for most Sa and S0 galaxies in the RSA. A special effort was made on these systems during the past two years of the Las

Campanas and the Palomar photographic surveys. A list of all Sa, Sba, and S0/a galaxies has been prepared from the RSA so as to subclassify the Sa systems as early (E), intermediate (I), or late (L), according to the resolution into stars and the prominence of the central bulge. Dust classes have also been assigned according to the presence or absence of dust. Preliminary analysis shows that the 21-cm flux (reduced to unit distance) correlates well with the dust and morphological subclass. The radio flux is greatest for the L and for the dusty systems.

### *Smooth-Arm Sa*

Of particular interest in themselves are the smooth-armed Sa galaxies, where the

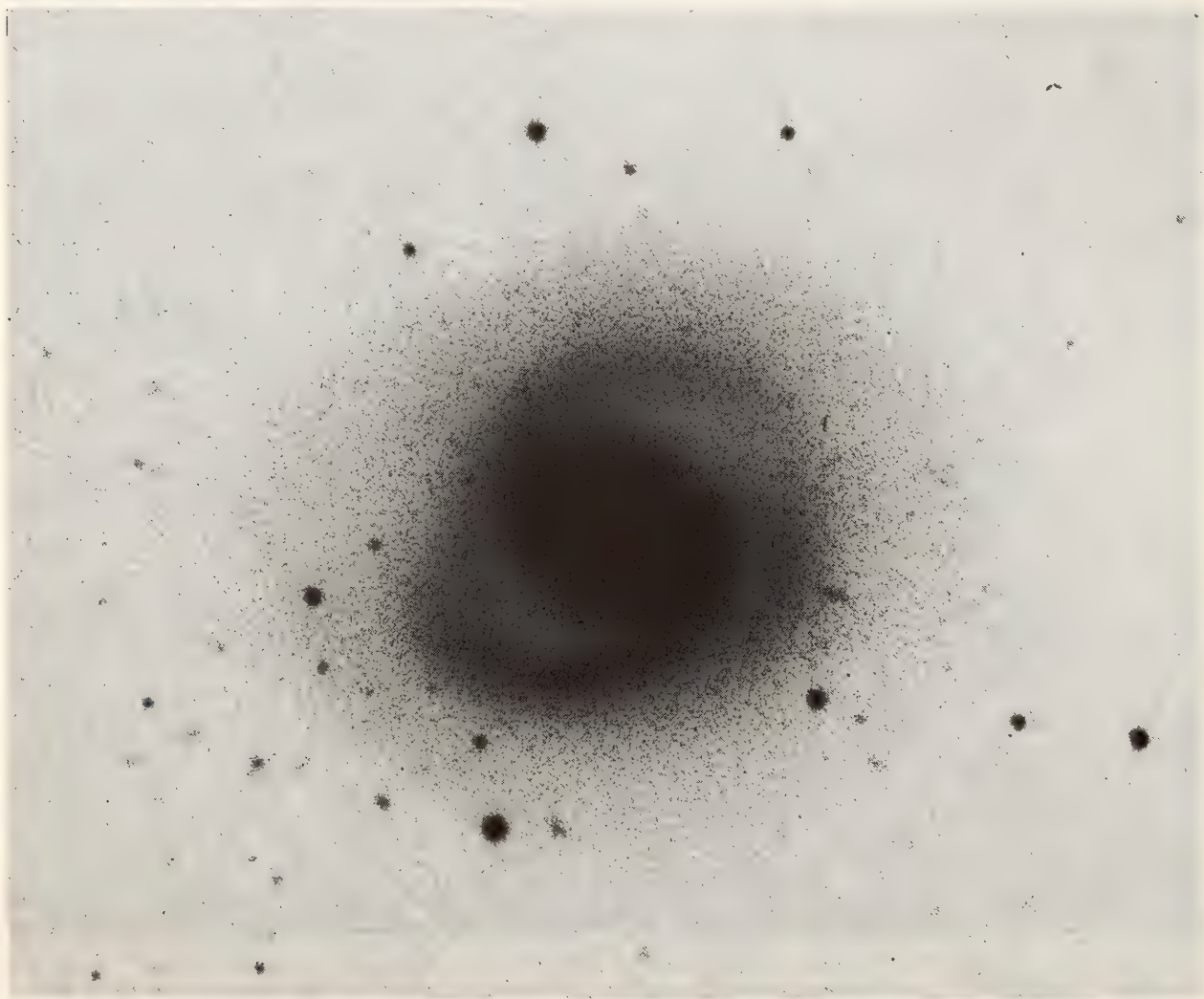


Fig. 8. High-contrast negative print of NGC 718 showing the smooth star arms in this early Sa field galaxy. The arms are composed of old stars with no evidence for H II regions or recently formed OB young stars. Palomar 5-meter reflector plate.





Fig. 9. Smooth-armed Sa galaxy NGC 4260 in the Virgo cluster region. Palomar 5-meter reflector plate.

spiral features are defined by old stars alone, not by dust, H II regions, or newly formed O, B, and A supergiants, as in the later Sb and Sc Hubble types. Smooth-armed Sa galaxies are a common type, found throughout the general field. They are important because they *exist among the field galaxies*. Hence their lack of gas, H II regions, dust, and young stars is not a result of environmental effects, such as ram-pressure stripping in clusters or galaxy-galaxy collisions, but rather is a phenomenon associated with galaxy formation and with the reason any galaxy finds itself at a particular place along the Hubble sequence. The existence of smooth-armed Sa galaxies in the general field provides a case against “environmental stripping” as the mode of their formation.

Several known examples of smooth-armed spirals shown in the *Hubble Atlas* are NGC 718 (Sa, *Atlas*, p. 11), NGC 4314 (SBa, *Atlas*, p. 44), and NGC 7743 (SBa, *Atlas*, p. 43). A deeper reproduction of NGC 718 (a type example) than is given in the *Hubble Atlas* is shown in Fig. 8. A further example is NGC 4260 (in the Virgo Cluster), shown in Fig. 9, where the presence of some dust is seen at the outer boundary of the lens.

#### *Sa Outer-Arm Structures*

One of the most unexpected features of Sa galaxies revealed by the Las Campanas Survey is that star formation is going on in the very extended outer, almost detached and isolated arms, far from the central regions. A good example



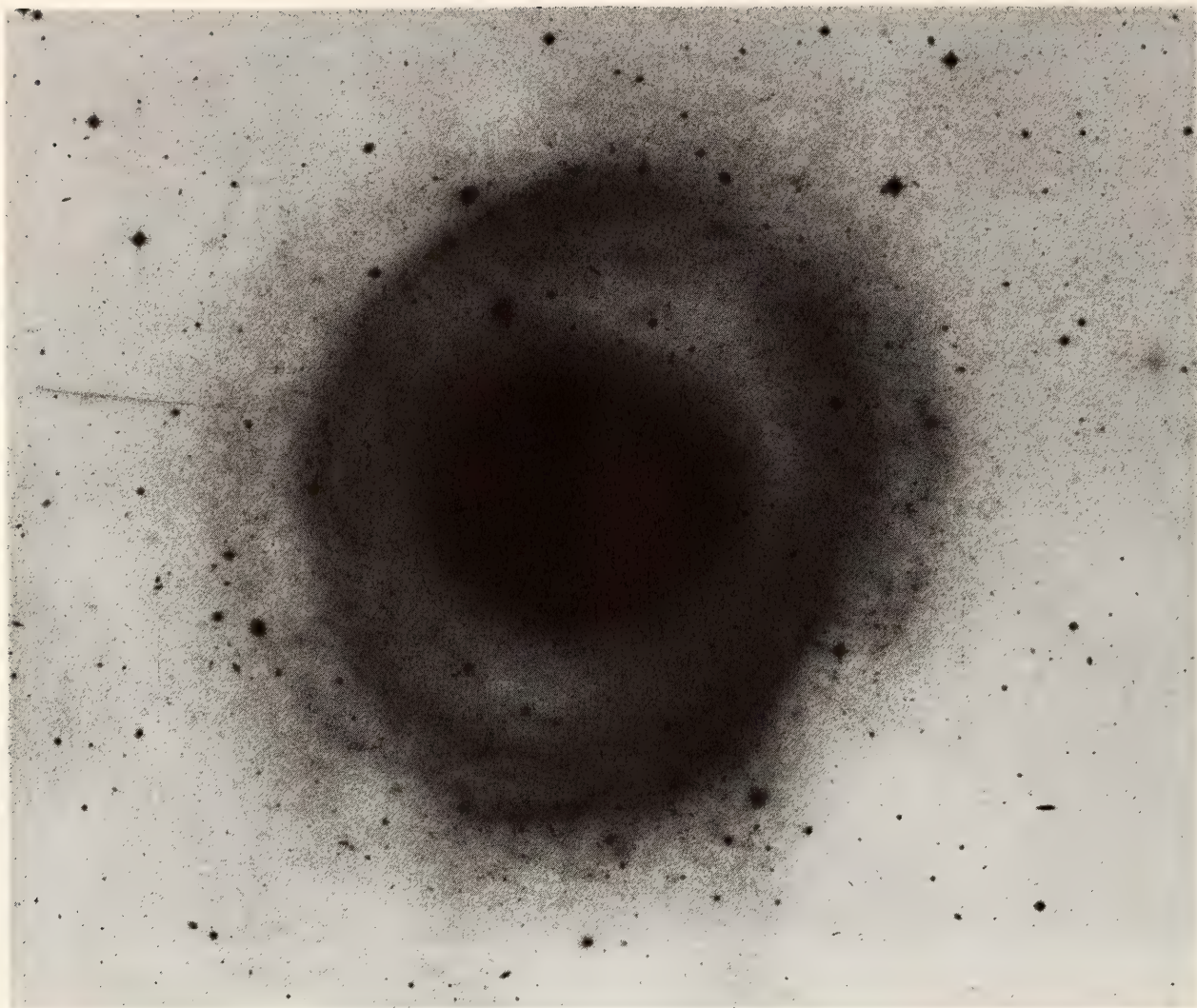


Fig. 10. High-contrast negative print of the Sa galaxy NGC 1291 made from a du Pont 2.5-meter plate. The outer ring is composed of individual segments of spiral arms. Star formation is occurring in these outer arm fragments rather than in the smooth inner lens and bar regions.

is NGC 1291, originally called an RSO galaxy but now an Sa because of its clear system of thin outer arms where star formation is now occurring. A negative print of NGC 1291 from a du Pont 2.5-meter plate is shown in Fig. 10. Similar structures are shown by NGC 2217 in Fig. 11, printed at high contrast to show the faint-surface-brightness outer arms. This plate, taken with the du Pont reflector at Las Campanas, can be compared with the lighter print of NGC 2217 taken with the Mount Wilson 2.5-meter reflector and shown in the *Hubble Atlas* (p. 43).

#### *Kinematics and Structure of Disk Galaxies*

A Fourier spectral-analysis program written by Rose has been used to analyze data taken by Searle and Rose with the SIT digital spectrograph. The aim of this program is to map the velocity field and velocity-dispersion field in the central regions of a number of S0 and spiral galaxies. The observations also provide a map of the isochromes (lines of constant average chemical composition). This program will be continued for some years in order to provide fundamental data relevant to the problem of the for-





Fig. 11. A high-contrast print of NGC 2217, which is similar to NGC 2191 but somewhat later in the Sa sequence. Las Campanas 2.5-meter du Pont plate.

mation and chemical evolution of disk galaxies.

In the course of checking out the observing and reduction procedures for this program, numerous galaxies previously studied for velocity-dispersion were re-examined and, in most cases, the agreement was excellent. Of particular interest is the confirmation of the velocity dispersion gradient in the central regions of M87 reported in *Year Book 77* (p. 185) by Sargent and co-workers. Rose and Searle find that the velocity dispersion is everywhere about 15% higher than previously reported.

In their program on the kinematics of disk galaxies, Rose and Searle have paid

particular attention this year to mapping the region within an arcminute of the nucleus of NGC 3115. In contrast to Illingworth's recent finding that ellipticals are rotating much less rapidly than their flattening suggests, the central bulge of this S0 galaxy is found to be in rapid rotation; a typical value of the ratio of rotation velocity-to-velocity dispersion is unity. The axial ratio of the bulge is about 3 to 1, and the result is consistent with the idea that the bulge is a rotationally supported oblate spheroid. Unexpectedly, it begins to look as though the spheroidal components of disk galaxies have kinematic properties that sharply differentiate them from ellipticals.



### *H II Regions in Galaxies*

Kennicutt has completed a photographic survey of over 100 spiral galaxies, taken with a set of 20-Å-wide  $H\alpha$  interference filters and image-tube cameras at Las Campanas and at Kitt Peak National Observatory. In collaboration with Dr. Paul Hodge of the University of Washington, he is publishing an atlas of H II regions in galaxies. The atlas will include photographs, identifications, and positions of all H II regions visible on the plates, and should enable a rich variety of investigations concerning the spiral structure and star formation in such galaxies to be undertaken.

Kennicutt and Hodge themselves are concentrating their interest on a comparison of the observed properties of spiral arms with theoretical models and on the measurement of the luminosity function of H II regions in galaxies of various Hubble types and luminosities.

### *Luminosity Classification*

Kennicutt is studying the correlations between spiral structure and luminosity on which the van den Bergh luminosity classification is based. This classification is one of the few distance-independent indicators of a galaxy's luminosity, and serves as a foundation for most calibrations of the extragalactic distance scale and the Hubble constant. There exists mounting evidence, however, for a large luminosity scatter in the existing classes and, subsequently, sampling biases in many of the samples used.

The new study is based upon  $H\alpha$  material obtained over the last four years at Kitt Peak and Las Campanas. H II regions often define spiral structure much more unambiguously than the blue photographs that have been used in the past. The goal is to determine which of van den Bergh's classification criteria are strong-luminosity dependent and which (if any) are extraneous, in order to ascertain whether present inconsistencies are

due to classification error or to a genuine diversity of spiral structure among galaxies of a given type and mass.

### *Nonequilibrium Companions of Spiral Galaxies*

For a number of years, Arp has been studying the neighborhoods of large spiral galaxies. Three years ago, Dr. Jack W. Sulentic joined Arp in studying a specific kind of object: nonequilibrium companion galaxies in the neighborhood of large spirals. The study was an international United States-Italy cooperative research program, aided on the Italian side by Padova University and Dr. Graziella di Tullio. The study has now been completed and the catalog of nonequilibrium companions has been published (Sulentic, Arp, and di Tullio, *Astrophys. J.*, 220, 47, 1978). Further analysis and interpretations of the companions—based on the spectra and photometry obtained in the final year of the project—are now under way. It is expected that the velocity, spectral composition, brightness, and color data will shed light on the puzzling nature of these disturbed companions and particularly on the question how these companions were formed.

### *Dwarf Irregular Galaxies in Nearby Groups*

As reported in *Year Book 76* (p. 157), Sargent is collaborating with Dr. K.-Y. Lo, Senior Research Fellow in Radio Astronomy at Caltech, in a search for intergalactic neutral hydrogen clouds via observations of nearby groups of galaxies at the 21-cm line. The results of an extensive survey of the M81, CVn I, and NGC 1023 groups were already published (*Astrophys. J.*, 227, 756, 1979). In this work, the discovery of four faint dwarf irregular galaxies of very low surface brightness, made with the Bonn 100-meter radio telescope, was reported.

During the summer of 1978, Sargent visited the Kapteyn Laboratory at the



University of Groningen, The Netherlands, in order to study the neutral hydrogen structure of the most extreme of these dwarf galaxies, M81 dw A. This galaxy, which lies 29' from the irregular Ho II, has  $M_v = -9$ ; its mass-to-light ratio is  $M_H/L_{pg} = 25$ , which is abnormally large for an irregular galaxy. In collaboration with Drs. R. Sancisi of Groningen and Lo, a full 21-cm synthesis map of M81 dw A was obtained with the Westerbork array. The map has a resolution of 25'', and it shows that the neutral hydrogen in M81 dw A is distributed in the form of a lumpy ring with diameter 2 kpc surrounding the visible galaxy. The position angle of the optical major axis of M81 dw A is roughly 45°. The measured maximum projected rotation amplitude lies along this direction but is only  $2.5 \pm 1 \text{ km s}^{-1}$ . If the system is flat and axisymmetric, its inclination to the plane of the sky would also be about 45°, leading to a true maximum rotation amplitude of only  $3.5 \pm 1 \text{ km s}^{-1}$ .

M81 dw A is deduced by Sancisi, Sargent, and Lo to be the first gas-rich galaxy to have been discovered that is supported by turbulence (to account for the observed 21-cm line width of 19 km s<sup>-1</sup>) and not by rotation. The total mass of hydrogen in the galaxy is estimated from the 21-cm line flux to be  $1.1 \pm 0.1 \times 10^7 M_\odot$ , whereas the total mass estimated from its kinematical properties is  $2 \pm 1 \times 10^7 M_\odot$ . Thus, the observations are entirely consistent with the notion that most of the mass of M81 dw A is in the form of neutral hydrogen and that this is why the value of  $M/L$  is so high.

The dynamical properties of M81 dw A raise interesting theoretical problems. Following a suggestion by P. Goldreich, Sancisi, Sargent, and Lo are exploring the possibility that the neutral hydrogen clouds in M81 dw A are immersed in, and supported by, a more tenuous gas with an electron temperature  $T_e = 10^4 \text{ }^\circ\text{K}$ . This gas is, in turn, presumably heated by hot stars in the galaxy. In this view, star formation itself regulates the

consumption of interstellar gas to form further stars. Sargent, in particular, advocates the view that simple dwarf irregular galaxies like M81 dw A are the astronomical equivalent of single cells in biology, and that they are ideal objects by which to study the physics of star formation, unencumbered by the complications of such large-scale phenomena as density waves in spiral galaxies.

The optical work which accompanied the discovery of M81 dw A led to the idea that a deeper optical survey of nearby groups of galaxies would be a more economical way of finding these gas-rich, low-surface brightness systems than the laborious 21-cm searches. Accordingly, a IIIaJ survey of the M81, CVn I, and NGC 1023 groups was commenced in 1976. Because of bad weather, progress on this survey has been slow. However, in the NGC 1023 group, photographs have been obtained by Kowal of six ( $6^\circ \times 6^\circ$ ) fields, which have yielded 35 faint dwarf galaxies, most of them newly discovered. In the M81 group, photographs were obtained of 20 out of 29 program fields. Here about 150 dwarfs were found, of which 110 are new. No progress was made on the CVn I group. However, observations were made of 10 control fields in the summer sky; in these fields, which are at a similar galactic latitude to the program fields, there are on average only 0.7 dwarfs per field.

In both the M81 group and the NGC 1023 group, the dwarf galaxies are distributed in a highly clumpy manner. Some but not all of the prominent concentrations of dwarfs are around the bright galaxies in the groups. For example, there is an obvious concentration of dwarfs around the triple system containing M81 and M82. This fact, together with the lack of dwarfs in the control fields, would indicate that most of them are group members. If this is the case, the prospect opens of using the dwarf galaxies in the nearby groups to study such questions as the extent and the internal dynamics of the groups, with a rea-

sonably large number of test particles. In order to follow up this possibility, Lo and Sargent were assigned 12 days on the National Radio Astronomy Observatory 300-foot telescope in March 1979 to try to measure 21-cm velocities of the M81 group dwarfs. Unfortunately, only about 20 out of 100 dwarfs were detected. These were among the optically brighter objects, and few of them have the redshift appropriate to the M81 group.

In addition to the IIIaJ survey of the M81, CVn I, and NGC 1023 groups, Sargent, Lo, and Kowal began a similar survey of the Local Group, beginning with fields in the general vicinity of M31 and M33. During this work, three probably new, Local Group galaxies were discovered. These objects were later observed with the 21-cm system on the Arecibo dish by Dr. T. X. Thuan of the University of Virginia. Thuan found that Kowal, Lo, and Sargent's object, LGS 3, has a velocity similar to those of M31 and M33. LGS 3 has resolved 21-mag stars and is the faintest known member of the Local Group.

#### *The Radio Galaxies NGC 6251 and M87*

The 14-mag elliptical galaxy NGC 6251 was recently identified as a strong radio source of unusually large angular size, corresponding to a linear extent of 3 Mpc. Part of the source consists of a straight, thin jet 200 kpc long. Recent VLBI studies by the Caltech group have shown that there is a much smaller jet, about 1.7 pc long and pointing in almost exactly the same direction as the larger jet. NGC 6251 lies on the edge of the cluster Zw Cl 1609.0+8112.

Sargent, together with de Bruyn and Dr. Anthony C. S. Readhead of the Owens Valley Radio Observatory, obtained spectra of 17 of the galaxies brighter than 15.7 mag within the cluster boundary. The redshifts show that NGC 6251 is in the cluster, which has a mean redshift  $\langle cz \rangle = 7110 \text{ km s}^{-1}$ . The velocity dispersion of the cluster is  $\sigma_v = 525 \text{ km s}^{-1}$  and the virial mass is  $\mathcal{M}_c = (7.8 \pm$

$1.3) \times 10^{13} \mathcal{M}_\odot$ . The resulting mass-to-light ratio is estimated to be  $\mathcal{M}/L = 51 \pm 25$ . If the relationship between x-ray luminosity  $L_x$  and  $\sigma_v$  found for more optically luminous clusters is extrapolated downward to the luminosity of the NGC 6251 cluster, then it is predicted that the cluster has  $L_x = 10^{43} \text{ ergs s}^{-1}$ . The electron density of the hot gas in the cluster would then be  $n_e \sim 10^{-5} \text{ cm}^{-3}$ , leading to a thermal pressure  $n_e kT = 3 \times 10^{-14} \text{ dynes cm}^{-2}$ . It is interesting that considerations of the radio-source structure lead to a pressure in the intergalactic medium around NGC 6251 of about  $2 \times 10^{-14} \text{ dynes cm}^{-2}$ .

In May 1978, Young and Sargent obtained CCD pictures of NGC 6251 together with the two central supergiant ellipticals in the Coma cluster, NGC 4874 and NGC 4889, all galaxies at a redshift of about  $7000 \text{ km s}^{-1}$ . These observations were obtained during a run on the Kitt Peak 4-meter telescope, which was devoted to tests of a CCD camera made at Jet Propulsion Laboratory. The Kitt Peak data were supplemented by a single short CCD observation of NGC 6251 made by Kristian, Westphal, and Young at the prime focus of the Hale Telescope in excellent seeing.

It was found from the accurate photometry that the optical minor axis of NGC 6251 is at  $\text{PA} = 289^\circ \pm 0.5^\circ$ . This is significantly different, but only by a few degrees, from the values  $296.5^\circ \pm 0.5^\circ$  and  $300.5^\circ \pm 2^\circ$  found by radio astronomers for the outer and inner jets, respectively. This observation adds some credence to the growing belief that the axis of ejection in radio sources is the axis of rotation of a massive central object, possibly a black hole.

It was also found that, while NGC 4874 and NGC 4889 have radial luminosity profiles that are well represented by King models, NGC 6251 has a luminosity profile that cannot be fitted by a King model, either with or without an additional central point luminosity source. The profile of NGC 6251 can,



however, be well fitted by a King model together with a central point luminosity source and a central mass concentration. In this respect, NGC 6251 is very similar to M87, in which arguments for the existence of a central point mass were presented in *Year Book 77* (p. 186). The velocity dispersion of the stars in NGC 6251 has not been measured; efforts to do this in April 1978 by Boksenberg, Sargent, and Young were unsuccessful. However, if one adopts a plausible value of  $\sigma_v = 220 \text{ km s}^{-1}$  for the central velocity dispersion in NGC 6251, then the resulting black-hole mass required to fit the photometry is  $M_H = 2 \times 10^9 M_\odot$ . This is very close to the value obtained for M87.

The work on M87 and NGC 6251 has emphasized that, because of the low stellar densities in the centers of normal giant elliptical galaxies, a central point mass as large as  $10^9 M_\odot$  results in a considerable distortion in the luminosity profile inside the core radius of the galaxy. Such distortions can be measured with very accurate photometry for galaxies out to distances of about 100 Mpc from the ground. The effects inside  $0''.1$  are very pronounced and should be easily observed with the Space Telescope.

Black holes as massive as  $3 \times 10^9 M_\odot$  have a mean density inside the Schwarzschild radius, which is about the density of air. Consequently, stars captured by the black hole would ride to their doom virtually undistorted. The absence of spectacular optical activity in the very centers of NGC 6251 and M87 may be a natural consequence of this inferred large mass for the central energy source.

Observations with Boksenberg's speckle camera to determine the angular diameter of Pluto were described in the section devoted to the Solar System. During the same run, Sargent, Boksenberg, and Arnold made speckle observations of the center of M87 and of the brightest knot (A) in the optical jet of M87 in order to determine the light distributions in these objects to the diffraction limit

of the Hale Telescope, namely,  $1/50''$ . Preliminary results indicate that both the center of M87 and knot A are unresolved. At the end of the report year, attempts were being made to fit a power law of the form expected for the stellar distribution around a black hole to the observed luminosity distribution near the center of M87.

Drs. F. Bertola of the Astronomical Observatory, Padova, and A. Holm of Goddard Space Flight Center, and Oke have made a study of M87, using both visual and *IUE* ultraviolet spectrophotometry. It is found that the *IUE* fluxes continue the visual fluxes smoothly into the ultraviolet. The flux decreases rapidly toward the *UV* and reaches a minimum at  $2200 \text{ \AA}$ . Below  $2200 \text{ \AA}$ , the flux rapidly increases again at least as far as  $1250 \text{ \AA}$ . Observations of cool stars rule out any scattered light problems. The turnup in flux in the *UV*, similar to that reported from OAO (Orbiting Astronomical Observatory) observations, could be caused in this object by the central massive source (the jet is not in the aperture used) or by hot horizontal-branch stars. Since the profile on the sky of this  $1250$ – $2200 \text{ \AA}$  radiation is extended on the basis of the *IUE* data, this appears to rule out the central massive object as the source and strongly suggests that the radiation is from hot horizontal-branch stars.

### *M87 Jet*

Past spectroscopic studies of the jet of M87 have revealed only that it radiates with a featureless blue continuum. In 1956, Baade showed that some of the condensations in the jet were polarized. A few years ago, Arp and Lorre showed that the jet consisted of six very well aligned, small discrete knots. Last year, Sulentic and Arp continued the study of the jet by repeating, under the same conditions and with the same equipment, the Baade plates of 1956. By calibrating accurately with field stars, Sulentic and Arp were able to show that the brightest knot in the jet had varied by about 0.4 mag



in the 22-year interval. The polarization direction appeared to stay roughly the same, but the strength of polarization and total brightness of the knot had unmistakably changed.

This result, combined with other known properties of the condensations in the jet, led Sulentic and Arp to suggest that the knots phenomenologically resembled BL Lacertae objects. The two authors list all the properties of the jet and compare them to known properties of the quasar-like BL Lac objects. An investigation into the distribution of BL Lac objects in general showed some evidence for their being more numerous in the vicinity of bright galaxies.

Sulentic and Arp also made new measures on the nucleus of M87 with the SIT spectrograph on the 5-meter Hale reflector. They detected some very weak emission lines, such as  $H\beta$  and [O III],  $\lambda\lambda 4959, 5007$ , which had not previously been seen. But they detected no emission lines in any knots of the jet, and were able to place an upper limit of less than 15% of the continuum emission for any emission lines in the jet.

During the past year, Arp published a chapter entitled "Ejection From Galaxies and Galaxy Formation" in *Problems of Physics and Evolution of the Universe* (Academy of Sciences of Armenian SSR, Yerevan, pp. 65–80, 1978). This article reviewed observations on many kinds of active galaxies, including M87. In the paper, Arp emphasized that work by many different astronomers on many different galaxies had established the fact that a wide range of galaxies exhibited ejection phenomena, that luminous as well as radio-emitting material was connected with this ejection, and that the nature or state of the ejected material was very mysterious. It must be concluded that some very powerful cosmic force is at work in the centers of many galaxies. It is clear that physical conditions exist in the observed material, such as in M87, of which we have very little understanding.

### *Seyfert Galaxies*

Infrared, visual, and *IUE* ultraviolet observations of NGC 1068 have been obtained by Dr. E. Daltabuit, Instituto de Astronomía, Mexico, D.F.; Matthews; Dr. D. C. Morton, Princeton University Observatory; Neugebauer; Oke; Persson; Dr. A. M. Smith, Goddard Space Flight Center; and Soifer. This is the first Type II Seyfert to be studied using *IUE* data. The interstellar reddening can be measured using many line ratios, namely  $L\alpha/H\beta$ ,  $H\alpha/H\beta$ ,  $P\alpha/H\beta$ ,  $B\gamma/H\beta$ , He II 1640/4686, and [S II] 10320/4072. It is found that all these line ratios are consistent with a standard interstellar reddening law but without the  $\lambda 2175$  feature, and a value of  $E_B - V = 0.40$  provided the He II and hydrogen lines are formed by pure Case B recombination. One of the ratios, namely that of [S II], is independent of physical conditions, while the others could depend on physical conditions in different ways. There does not appear to be any discrepancy in the  $L\alpha/H\beta$  ratio such as is found in Type I Seyferts and quasars. This suggests that the discrepancy in these latter objects occurs because the electron densities are  $10^{10} \text{ cm}^{-3}$  rather than  $10^6 \text{ cm}^{-3}$ , as in Type II Seyferts.

Oke and Zimmerman have used *IUE* as well as MCSP and SIT digital spectrograph data to analyze two Type I Seyferts, 3C120 and Markarian 79. In both objects the continua show an excess of flux in the neighborhood of 3000 Å, similar to that found in quasars. In both objects there is a depression in the continuum near 2200 Å, which is probably caused by the interstellar absorption feature centered at 2175 Å. The strength of this feature suggests  $E_B - V$  of 0.22 for Markarian 79 and 0.38 for 3C120. Adopting these reddening values brings the  $L\alpha/H\beta$  intensity ratio very close to the recombination value in 3C120 and within a factor four of the recombination value for Markarian 79. The C IV/ $L\alpha$  line ratio is abnormally high in these objects



compared with the ratio of quasars. Although both objects have strong Fe II lines in the visual, there is no Fe II absorption or emission at the position of the ultraviolet resonance lines; this is consistent with the current cloud picture of quasars and Seyferts.

Oke, Sargent, and Readhead have combined all available spectroscopic and spectrophotometric observations of 3C120 taken during the last 10 years. There is excellent evidence for a dramatic change in the spectrum that occurred between November 1974 and November 1975. It is found that the intensity of  $H\beta$  has been changing approximately in synchronism with the continuum, the equivalent width having remained essentially constant over the decade. At the same time, the [O III] forbidden line intensities have remained constant over the same interval. This shows that the overall dimension of the permitted line region is less than 1 light year, whereas the size of the forbidden line region is at least an order of magnitude larger.

In last year's Report (*Year Book* 77, p. 189), some preliminary results were reported on an exploratory program to study spectrum variability in Seyfert galaxies with the multichannel spectrometer. The complete results of this successful program have now been analyzed by de Bruyn and are nearly ready for publication. A total of 43 spectrum scans of 15 Type I Seyfert galaxies were used in the analysis. The typical time interval between successive scans on the same object is about one year. All spectrum scans were taken through a 10" circular diaphragm and care was taken to minimize observational and calibration errors (see de Bruyn and Sargent, *Astron. J.*, 83, 1257, 1978). From the total of 43 scans, 28 difference scans were obtained by subtracting successive scans of each individual object. A particularly nice result was obtained on NGC 5548 and is shown in Fig. 12. It embodies all of the variability characteristics that have been observed in the various program galaxies.

Some of the most interesting, and often not anticipated, results of the variability analysis follow (and most of these can be verified in the NGC 5548 spectra).

1. Strong variability of all broad emission lines (H I, He I, He II, possibly O I  $\lambda 8446$ ). Within the Balmer series, the relative variations are larger for the higher members, resulting in a more "normal" Balmer decrement when the line (and continuum) intensity is high. This suggests that self-absorption and collisional excitation effects strongly influence the Balmer line intensities, in agreement with recent work by Netzer.

2. Statistically, within each object, the  $H\alpha$  line intensity varies as about the  $+1/3$  power of the continuum intensity as measured at 3500 Å. This is the same proportionality as found by Baldwin between the C IV  $\lambda 1549$  line luminosity and the local continuum luminosity for a sample of (mainly) flat-spectrum radio quasars. It provides yet another argument for the fundamental similarities in the structure and ionization of the broad line region in active nuclei whose luminosities may differ by up to a factor of 1000.

3. The optical light variations in Seyfert galaxy nuclei are caused by the dimming and brightening of an approximately flat continuum. In the light of recent infrared work on Seyfert galaxies, these observations take away most of the arguments for the presence of a nonthermal power-law continuum dominating the optical and near-infrared spectra. (In the violently variable and strongly polarized QSO's and BL Lacertae-type objects, such a nonthermal component, however, is definitely present.) It seems an attractive hypothesis to identify the flat continuum with the *thermal* spectrum of an accretion disk. The mysterious violet bump in the spectra of Seyferts and QSO's appears connected with the variable continuum, and may result from the Balmer recombination continuum from a hot ( $T_e \sim 20,000$  K) inner disk.

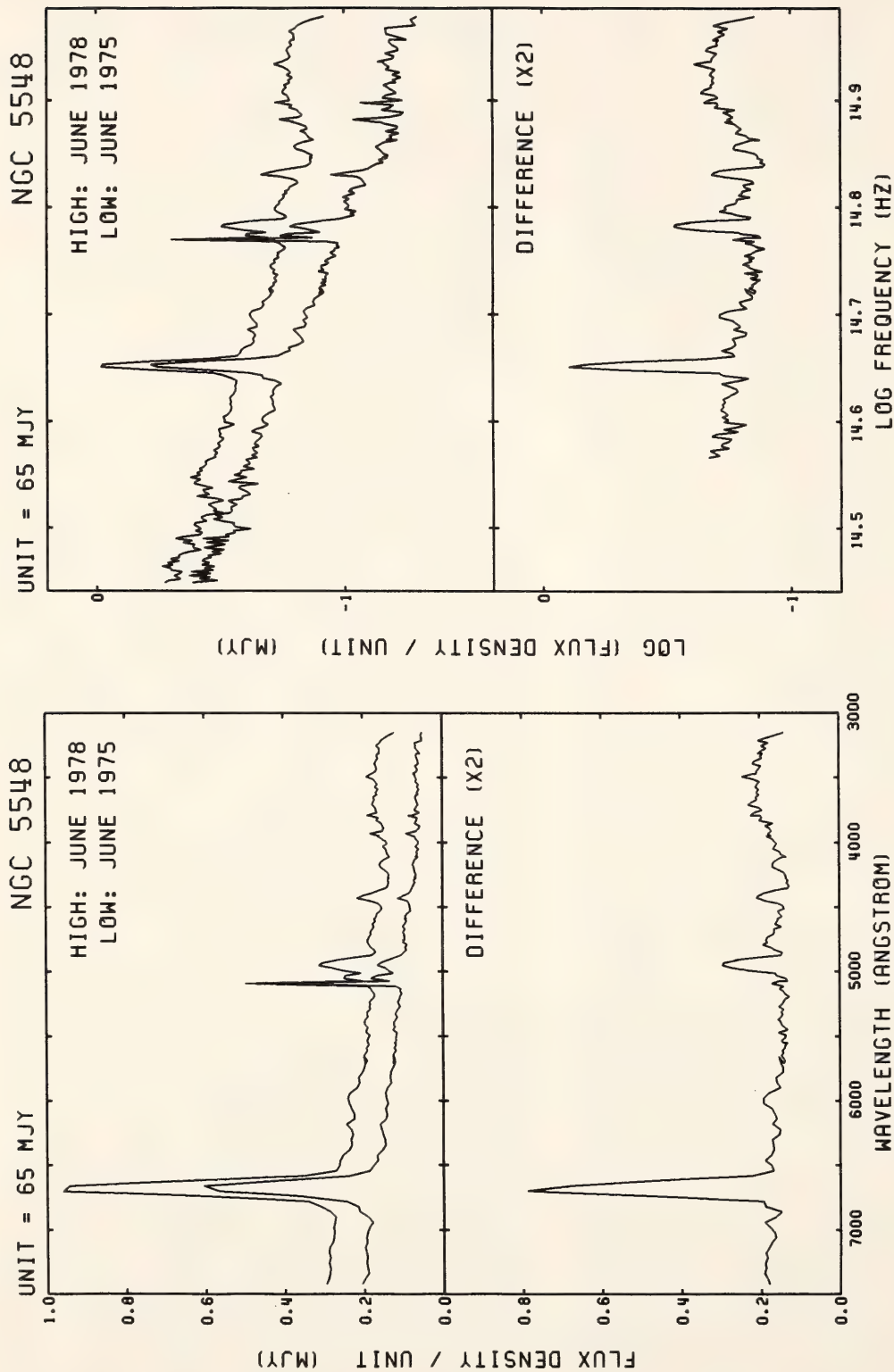


Fig. 12. Spectra of the Seyfert galaxy NGC 5548 taken with the multichannel spectrometer on the 5-meter Hale Telescope on dates three years apart. Both linear ( $f_\nu - \lambda$ ) and logarithmic ( $\log f_\nu - \log \nu$ ) presentations of the data are shown. The top parts of each figure show the individual spectral scans without displaced zero; the difference spectrum, multiplied by 2, is shown underneath. The intensity variation in the violet corresponds to a magnitude change of 1.1, one of the largest recorded thus far in the program. Note the perfect cancellation of the intense narrow [O III]  $\lambda\lambda 4959, 5007$  lines in the difference spectrum.



## CLUSTERS OF GALAXIES

*Populations*

Dressler has completed a study of the morphological populations of rich clusters of galaxies. High-scale 50-cm du Pont plates have been used to determine the Hubble types and approximate magnitudes of  $\sim 6000$  galaxies distributed among 55 clusters. With these data, Dressler has investigated relationships between galaxy type and environment or cluster type. Specifically, he finds that regardless of cluster type (e.g., regular, irregular, x-ray) there is an excellent correlation between the types of galaxies represented and the local galaxy density (Fig. 13). The fractions of S0 and elliptical galaxies rise almost linearly with the logarithm of the local galaxy density along with a complementary decrease in the spiral content. Further, the fractional representation of *field* galaxies fits well this density/morphological type relation. Thus the populations vary smoothly and monotonically over five orders of magnitude in space density.

Dressler uses this relationship to raise two objections to the hypothesis that S0 galaxies are produced when spiral galaxies lose their gas by ram-pressure sweeping or evaporation. (1) Both of these processes are highly density dependent so that they should be unimportant in the outer regions of clusters that are 1000 times less dense than the cores of rich, concentrated clusters like Coma. Yet in such regions S0 galaxies are common, composing  $\sim 30\%$  of the population. Thus the slow dependence of population on density is an argument against gas removal as an S0 production mechanism. (2) The relationship between density and morphological type holds in *both* regular, concentrated clusters and loose irregular clusters. If, as has been suggested by Butcher and Oemler, the regular concentrated clusters have under-

gone violent relaxation, then only they will have an intergalactic medium of sufficient density and temperature for significant gas removal from spiral galaxies. Since the relative abundance of S0 and spiral galaxies is not a function of *global* cluster morphology but only of *local* galaxy density, global characteristics, such as a cluster's dynamical history or the nature of the intergalactic medium, cannot be primarily responsible for galaxy differentiation.

Dressler also finds that S0's in clusters have significantly larger and brighter bulges (spheroidal components) than cluster spirals, as has been suggested for field galaxies. Since the tightly bound inner bulge would remain unaffected when gas is removed from a spiral, this argues strongly against the (external) gas removal mechanism of S0 production.

Alternative explanations for galaxy differentiation are indicated by Dressler's data. He cites recent suggestions that disks of galaxies may form over rather long time scales ( $T \gtrsim 10^9$  years). If so, disk building may be interrupted in regions where galaxy density has increased substantially and encounters are more frequent (collapsing clusters), which could explain the dearth of spiral galaxies in such environments. S0's may also be produced by internal processes, such as gas removal by galactic winds or gas exhaustion through star formation, which are likely to be more prevalent in larger bulge galaxies. Dressler's data suggest that large-bulge systems are more common in regions of high galaxy density, which could then account for the dominance of ellipticals and S0 galaxies in such regions. This in turn suggests that in the early Universe, large-amplitude high-frequency density perturbations, which grow into concentrated galaxies (E's and S0's), may have been coupled

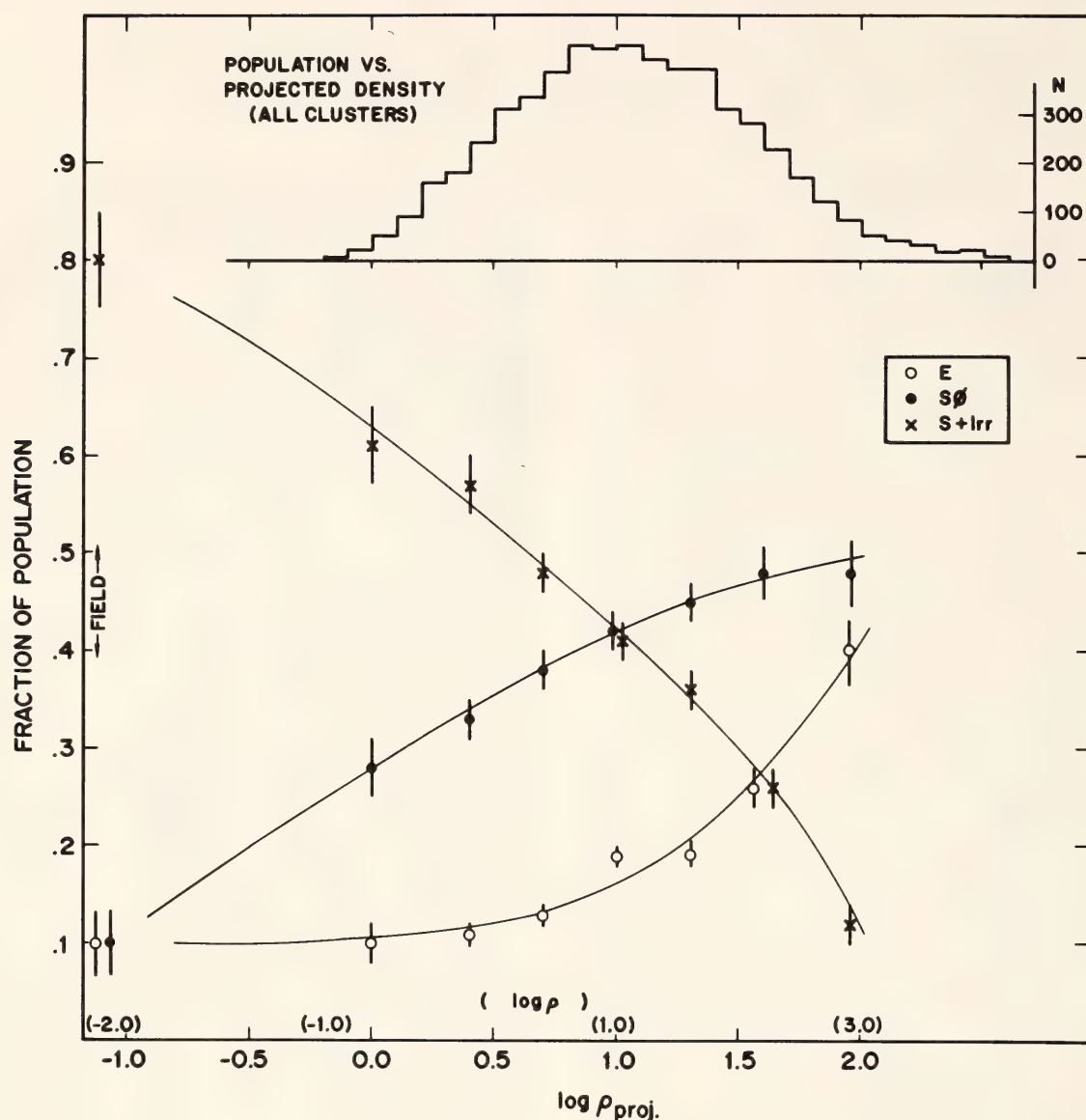


Fig. 13. The fraction of E, S0, and S+Irr galaxies as a function of the log of the projected density in galaxies  $\text{Mpc}^{-2}$ . The data shown are for all cluster galaxies in the sample and for the field. Also shown is an estimated scale of true space density in galaxies  $\text{Mpc}^{-3}$ . The upper histogram shows the number distribution of the galaxies over the bins of projected density.

to large-amplitude low-frequency perturbations, which were destined to become rich, concentrated clusters.

### Dynamics

Dressler has completed his study of the dynamics of the stellar envelope of the cD galaxy in A2029. As reported in *Year Book 77* (p. 191), he finds that the velocity dispersion rises with increasing radius, in contrast with normal elliptical galaxies (Fig. 14). This is to be expected, however, if the material in the envelope is

feeling the gravitational effect of the "missing mass" that binds the cluster. Dressler has built a computer model of a cD galaxy that sits at the center of a rich cluster bound together by high  $M/L$  material which has been torn from cluster members. This model predicts the rise in velocity dispersion seen in the cD and is thus consistent with the hypothesis that galaxies lose their dark, massive halos through collisions, and that this material forms a smoothly distributed superstructure that binds the cluster.

Dressler and Shectman are presently



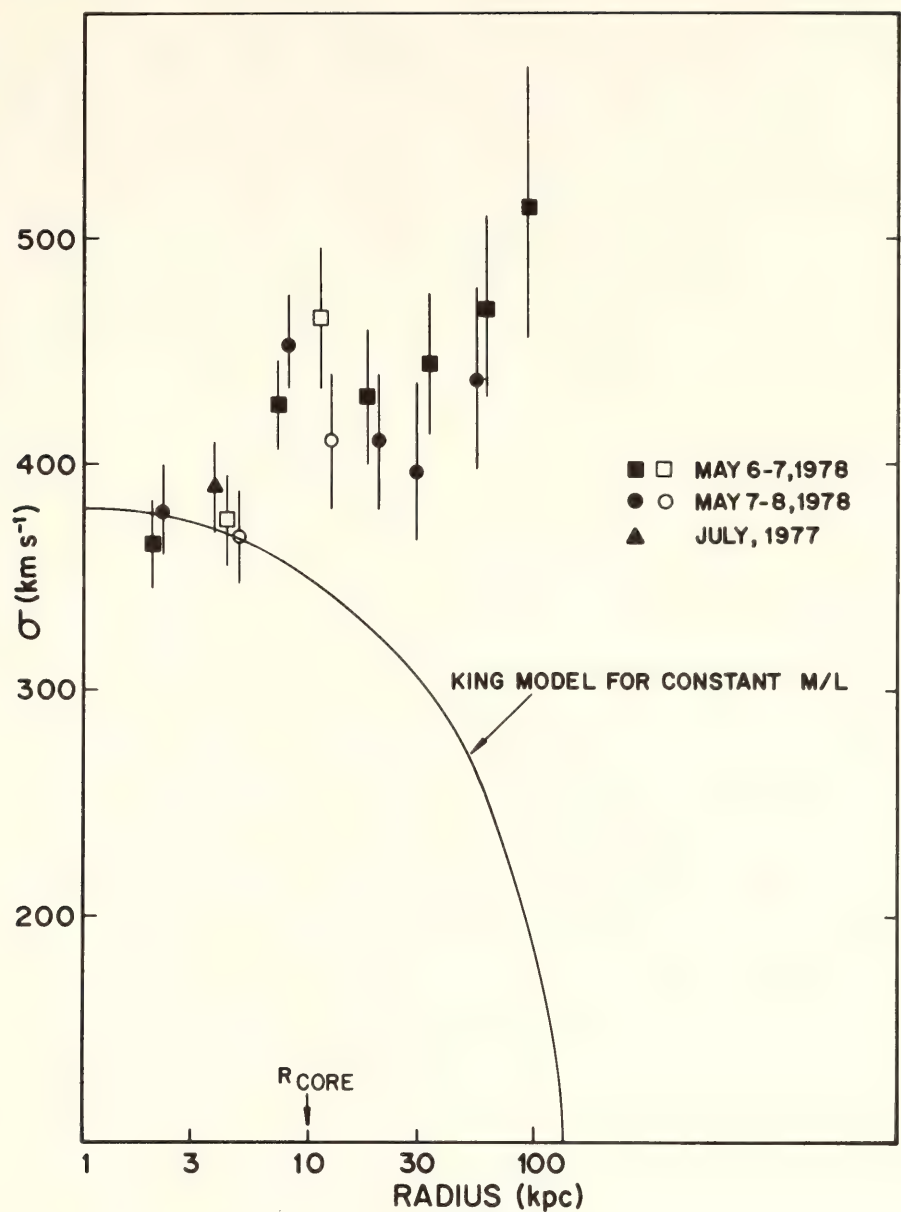


Fig. 14. The run of the velocity dispersion as a function of radius for the May 1978 data. Also indicated is the nuclear value determined from the July 1977 data provided by Sackett. The open symbols are points to the NE; closed symbols are points to the SW. The solid curve is the run of  $\sigma$  for a constant  $M/L$  King model with  $R_{\text{cor}} = 10$  kpc.

working with the SIT and Reticon spectrographs to obtain large numbers of redshifts in A2029 and other rich clusters. With  $\sim 100$  velocities per cluster, one should be able to investigate the different dynamical histories of clusters (i.e., pre-relaxation vs. post-relaxation clusters) and evaluate the importance of interactions and subclustering.

*Space Distribution of Abell Clusters*

Gunn and Dr. Trinh X. Thuan of the University of Virginia have completed a

survey of redshifts of a complete sample of 107 Abell clusters (richness class 1 or greater; distance class 4 or smaller;  $|b| = 30^\circ$ ). The data allow construction of the space distribution of these objects, and it is found that the centers of clusters are themselves very highly clustered with an amplitude much larger than the galaxy-galaxy correlation structure; significant correlation exists to distances in excess of 60 Mpc. These data, along with similar data on field galaxies recently obtained by Schechter, Oemler, and

Kirshner, suggest strongly that the fluctuation spectrum of irregularities in the early Universe contained much more power on large scales than the usually supposed white-noise spectrum.

Work is continuing on the sample to attempt to extract dynamical information from comparison of the correlations in "distance" (redshift) with the angular correlations. In principle, distortions of the redshift correlations brought about by gravitationally induced peculiar motions of the clusters provide a powerful test for the mean mass density in the Universe; in practice, a larger sample will certainly be required before any conclusions can be drawn.

Caltech graduate student John Hoessel, with Thuan and Gunn, has recently completed *gr* photometry of the brightest members of the clusters in this sample. The raw dispersion in the absolute magnitudes for the sample referred to the Gunn-Oke standard radius of 16 Mpc is 0.36 mag at 5556 Å rest, and the mean is about 0.1 mag brighter than the heterogeneous low-redshift sample of Gunn and Oke.

Hoessel has studied the surface brightness distribution of these objects, for which most of the photometry has been obtained with the SIT Vidicon on the Palomar 1.5-meter telescope. He finds that the absolute magnitude is strongly correlated with the slope of the logarithmic growth curve  $\alpha_0 = (d \ln L / D \ln r)_{r_0}$  at 16 kpc. The quantity  $\alpha$  can be directly

related to the core radius of an equivalent Hubble law profile. The results are in striking agreement with the predictions of Ostriker and Hausman for dynamical friction-induced cannibalism. Furthermore, the " $\alpha$ -correction" seems to be the only correction required; the richness and Bautz-Morgan corrections arise through correlations of  $\alpha$  with these quantities. If  $\alpha$  really measures the dynamical state of a composite system, then dynamical evolution can be corrected for explicitly by measuring  $\alpha$  for distant cluster galaxies. Work on this, using high signal-to-noise CCD images, has been underway for the past two years by Hoessel and Gunn; some results should be in hand shortly.

One of the most remarkable structures in the sample of 107 clusters is a super-cluster at  $15^h30^m, +30^\circ$ , which contains seven Abell clusters and many smaller groups. The dynamics of this aggregate is being studied by Gunn and Dressler, again with an eye to obtaining the mass density in the region.

The SIT spectrograph has made it possible to investigate the dynamics of quite distant clusters; since all the very rich clusters are also distant, one can for the first time study the dynamical state of these systems. Gunn and Dressler have obtained data for A665, the only richness 5 cluster in the Abell catalog, and A2218, a remarkably symmetric  $R = 4$  cluster that is an x-ray source and for which the Zel'dovich microwave background cooling may have been measured.

## QUASARS AND QUASI-STELLAR OBJECTS

### *Continuum Energy Distribution*

This year marked the conclusion of a decade of observations of the continuum energy distributions of quasars from a collaborative effort among Oke, Neugebauer, Becklin, and Matthews. More than 20 quasars were measured from 0.3  $\mu\text{m}$

to 10  $\mu\text{m}$ ; line intensities have been obtained for 36. Figure 15 shows the energy distributions of the quasars. During the past year, the observations have been analyzed with special emphasis on the relation between the infrared and visual data and between the infrared/visual data and those at radio wavelengths. The



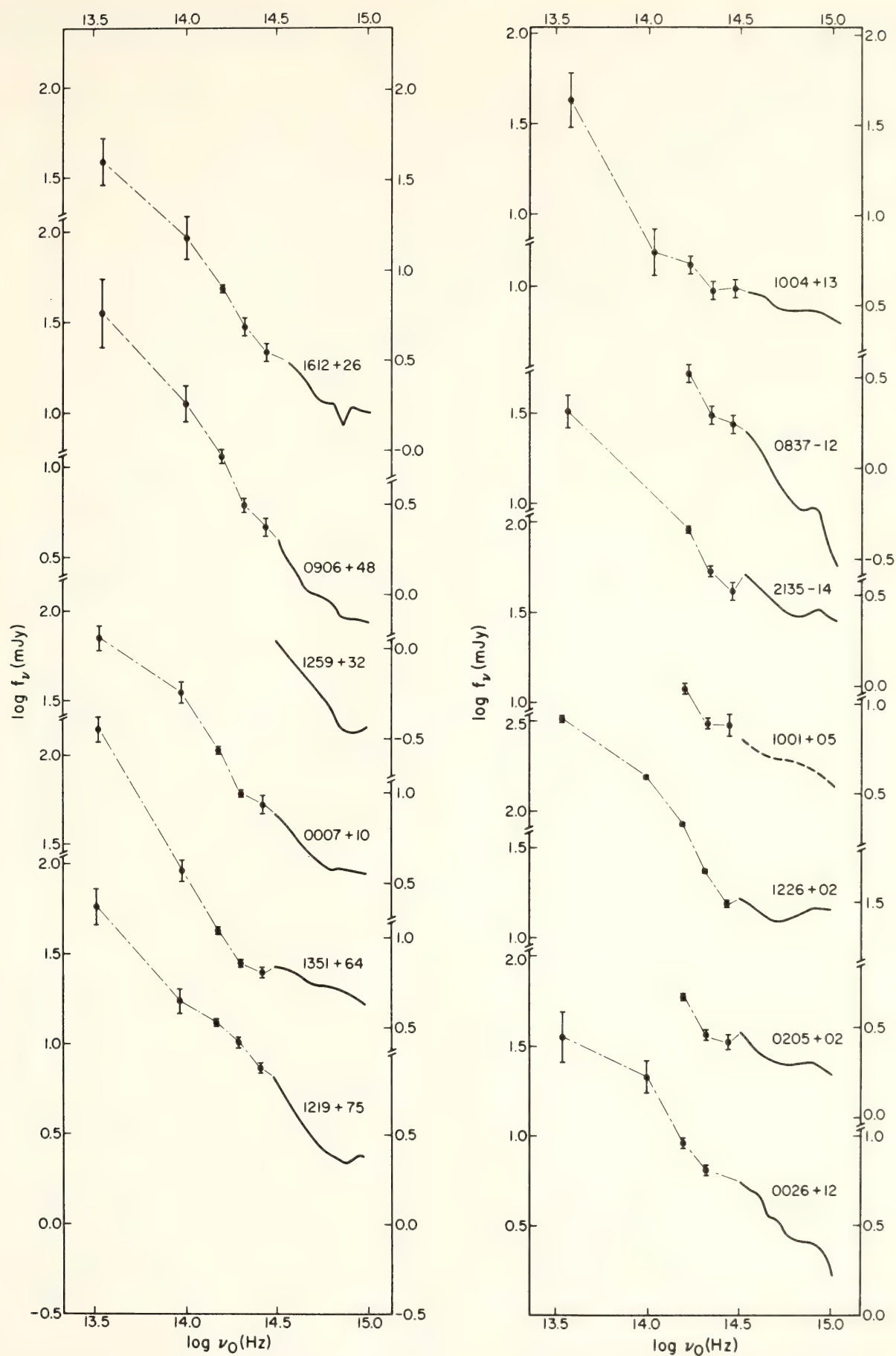


Fig. 15A. The observed flux densities of the objects studied as a function of the frequency in the rest frame of the quasar. The solid line represents the visual continuum with the emission lines removed. In some cases, variability may have produced a discontinuity between the infrared and visual data. All limits are  $3\sigma$ . The redshifts,  $z$ , on the left frame run from 0.070 (bottom) to 0.131 (top); those in the right frame run from 0.142 (bottom) to 0.240 (top).

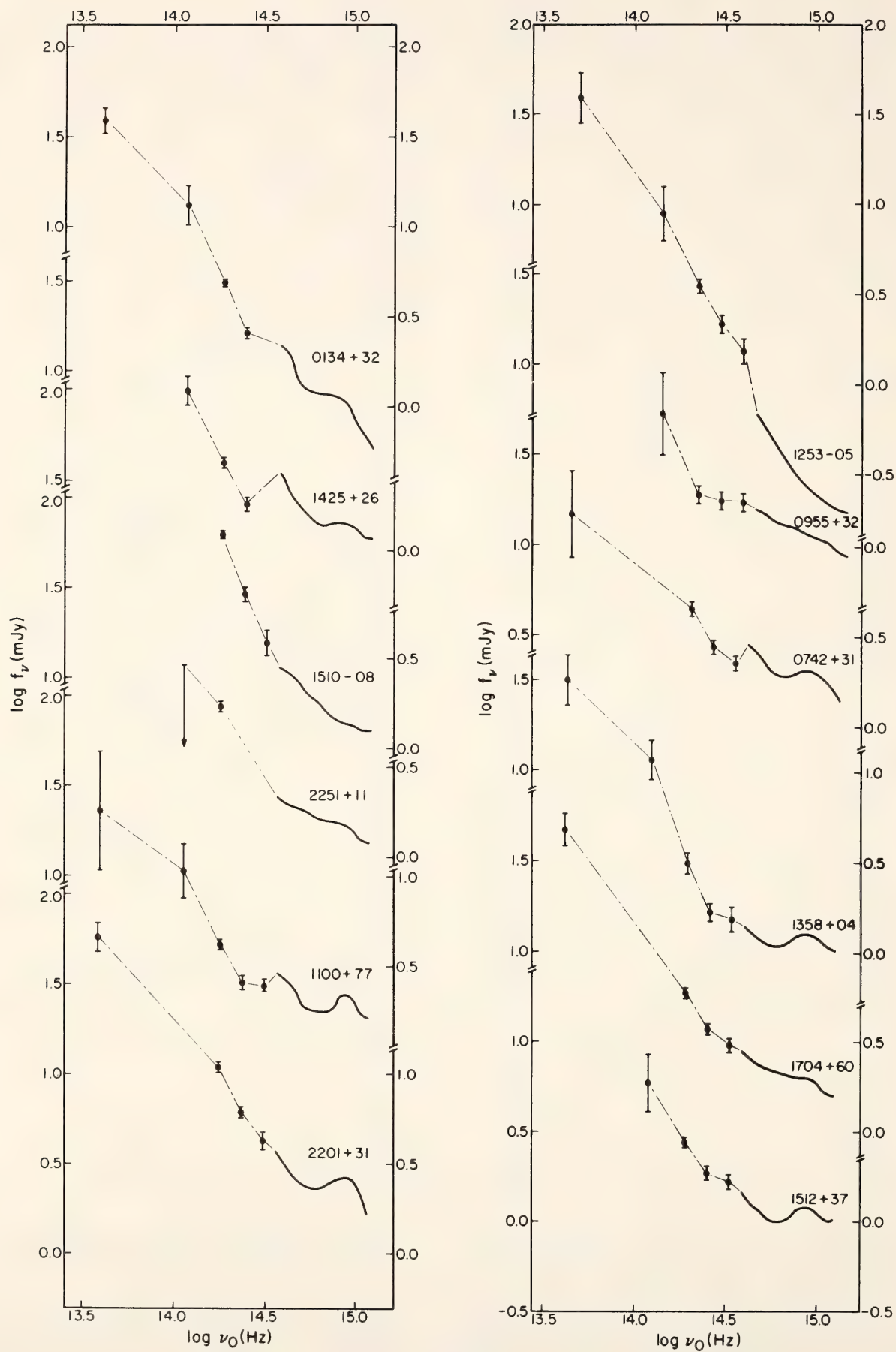


Fig. 15B. The same as Fig. 15A but  $0.297 \leq z \leq 0.367$  (left frame) and  $0.371 \leq z \leq 0.538$  (right frame).



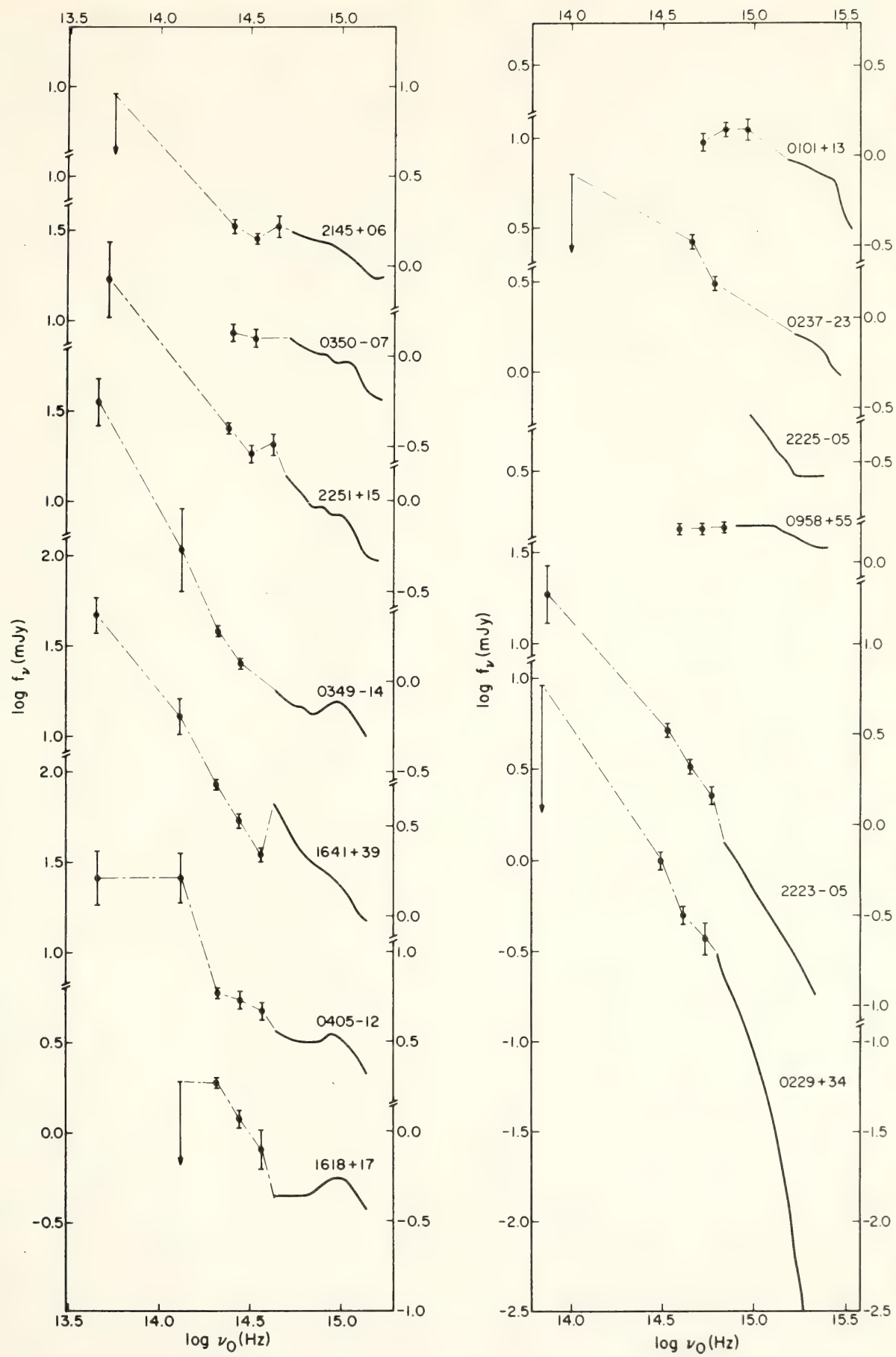


Fig. 15C. The same as Fig. 15A but  $0.555 \leq z \leq 0.990$  (left frame) and  $1.238 \leq z \leq 2.690$  (right frame).

cogent points obtained from the data can be summarized as follows:

1. In a gross sense, the energy distributions follow a power law from the visible through the near-infrared, but no single power law describes the energy distributions over the entire wavelength range. For the sample measured, the slopes in the rest frame are flatter from 0.3 to 1  $\mu\text{m}$  than from 1 to 3  $\mu\text{m}$ .

2. The luminosity around 0.3  $\mu\text{m}$  of the quasars studied is similar to that around 3  $\mu\text{m}$  and is significantly larger than around 1  $\mu\text{m}$ .

3. No strong correlation is observed between the strength of the radio continuum and the infrared fluxes.

4. The ratio of intensities of ( $\text{H}\alpha + [\text{N II}]/\text{H}\beta$ ) is on the average significantly larger than the case B recombination ratio for  $\text{H}\alpha/\text{H}\beta$ . The  $[\text{O III}] \lambda\lambda 4959 + 5007$  lines can be twice as strong as  $\text{H}\beta$ .

5. For those quasars that are highly variable, the variations in the infrared and visible are correlated.

6. The dominant radiation mechanism producing the visible and near-infrared flux in many quasars is nonthermal, on the basis of the rapid time variations and the shape of the energy distribution. Thermal radiation from dust cannot be ruled out as a contributing source. In particular, there is evidence for an excess at 3  $\mu\text{m}$  in some quasars, which might be attributed to thermal radiation from heated dust.

One additional result of these data, obtained from a comparison of the radio and infrared properties of the quasars with those of Seyfert galaxies, is that there are many similarities between the bulk of the Seyfert galaxies and the radio-quiet galaxies. If, in fact, Seyfert galaxies and quasars are related in an evolutionary sense, this may provide a clue to how the energetics evolve. More observations are necessary to understand whether the apparent correlations are real or are artifacts of selection effects.

### *Millimeter Photometry*

As an extension of the program of understanding the nature of the infrared continuum of quasars, emphasis by Werner, Ennis, and Neugebauer has been placed on 1-mm photometry of quasars during this observing season. Observations were performed at the prime focus of the 5-meter Hale Telescope on Palomar Mountain. Under good atmospheric water vapor conditions, the detection system has a noise level of  $\sim 0.3$  Jy in one hour of integration time. The purpose of these observations is to gain a better understanding both of the total continuum energy distribution of the quasars and of the physical processes connecting the observed energy fluxes in different frequency bands. Specifically, in order to investigate the relationship between near-infrared and 1-mm flux densities of quasars, a sample chosen for study consisted of all quasars with a 10- $\mu\text{m}$  flux density greater than 32 mJy. Quasars in this group were observed whether they had been detected at radio wavelengths or not. Of the 16 quasars satisfying this criteria, 14 have been looked for and 5 have been detected. Three-sigma upper limits for the remaining objects are  $\sim 1$  Jy. The data imply no correlation between the 10- $\mu\text{m}$  and 1-mm flux densities.

Millimeter observations of specific radio-quiet quasars were also carried out. One millimeter is the shortest radio wavelength at which attempts at detection of radio-quiet quasars have been made. None of the six quasars were detected to a level of 1 Jy. These objects are among a sample of radio-quiet quasars recently observed at a wavelength of 6 cm by Dr. James Condon of the National Radio Astronomy Observatory. Of the six we observed, he detected three, and set upper limits of 1 mJy for the rest. Combining these results will constrain the range of possible radio spectral indices  $\alpha [F_\nu \propto \nu^\alpha]$  allowed for radio-quiet quasars. The millimeter upper limits will be especially sensitive to the high, positive



spectral indices associated with thermal or self absorption of synchrotron radiation.

Millimeter measurements of three of the optically brightest high redshift quasars were also attempted. The existence of dust in quasars has been proposed as an explanation for the discrepancy between the observed hydrogen-line ratios and the predictions of standard recombination theory. If there exists thermal radiation from a suitable amount of cold dust associated with these quasars, part of the infrared energy distribution of this dust will be redshifted into the bandpass of our millimeter system. None of the three were detected to a level of a few Jy.

A program to monitor the 1-mm emission from five bright extragalactic sources known to be variable at radio wavelengths continued through this season. Three of the sources—3C273, 3C279, and 3C84—have shown no significant variability in their emission. This is consistent with temporal data for these objects obtained during the last four years. On the other hand, no fluxes were detected from BL Lacertae and 3C120, whereas in previous epochs they were easily measured.

Two objects, OJ287 and III Zw2, were chosen for investigation because of recent increases in their radio emission. This year, OJ287 has had a 1-mm flux density on the order of 5 Jy, contrasting with an upper limit ( $3\sigma$ ) of  $\sim 4$  Jy set in 1975. The millimeter emission from OJ287 has been measured during four separate months this winter and spring. Only a small amount of variability, if significant at all, is apparent.

Since the emission outburst of III Zw2 observed last year, the radio spectrum can be fitted with a spectral index  $\alpha = +1.5$  for frequencies between 1 and 90 GHz. An extrapolation of this steeply rising energy distribution to 300 GHz predicts a flux of  $\sim 13$  Jy. By contrast, the measured 1-mm flux density is  $2.0 \pm 0.6$  Jy. This observed flattening of the energy distribution is presumably representative of a transition from an optically

thick to an optically thin region of the spectrum. The optically thick emission could be due to synchrotron self-absorption or thermal absorption of the synchrotron radiation.

In addition to the five sources in our monitoring program, five other radio sources have been detected at a wavelength of 1 mm this season. Combined with the measurements of OJ287 and III Zw2, we thus have 1-mm data on a sample of 12 of the brighter extragalactic radio sources. Coordinated photometry at three radio wavelengths of these 12 sources has been carried out by Dr. L. Rudnick of the National Radio Astronomy Observatory. By combining these 1-mm measurements with the corresponding data at wavelengths of 6 cm, 2 cm, and 3 mm, an investigation of the high-frequency region of the synchrotron emission is possible. For most of the objects, the 1-mm data agree with a smooth extrapolation from the data at the lower radio frequencies. High-energy electrons emitting synchrotron radiation primarily at a wavelength of 1 mm must be present in these sources. The high-frequency cutoff in the synchrotron spectrum—a consequence of the high-energy cutoff in the electron's energy spectrum—must be at frequencies greater than 300 GHz.

### *X-Ray Quasars*

Photometric and spectrophotometric observations of the recently discovered x-ray quasars 0241+622 and 2251-178 have been made in the near infrared by Soifer, Matthews, and Neugebauer. The infrared energy distributions of both of these quasars follow quite closely that of 3C273 and are indistinguishable from the energy distributions of the sample of low-redshift quasars discussed in *Year Book 77* (p. 192). The spectrum of 0241+622 in the 2- $\mu$ m atmospheric window was reobserved to confirm the detection of  $P\alpha$  at 1.96  $\mu$ m. This line is only marginally present, the major hindrance to its

detection being the strong atmospheric extinction at these wavelengths. The most significant result of this study is that the three known x-ray quasars, 3C273, 0241+622, and MR 2251-178, are the three brightest optical quasars. This strongly suggests that the new generation of x-ray telescopes will be a powerful tool for discovering new low-redshift quasars.

### *Palomar Bright Quasar Survey*

Schmidt and Green have essentially completed spectroscopic observations of all ultraviolet-excess candidates selected from two-color exposures with the Palomar 46-cm Schmidt telescope. The final list consists of nearly 3000 spectra taken with the SIT spectrographs on the Hale 5-meter and Palomar 1.5-meter telescopes. The resulting sample is expected to be statistically complete down to an average limiting  $B$  magnitude of 16.0-16.2 over 10,000 square degrees above galactic latitude  $30^\circ$ . About 25% of the candidates were halo F and G subdwarfs, assuring that the expected color limit of  $U - B \leq -0.4$  was well covered within the measuring errors.

The resulting sample contains some 100 quasars, of which 12 were known radio sources and 13 were discovered in other optical surveys. Comparison with surveys to fainter magnitudes, by Dr. A. Braccesi of the Radioastronomy Laboratory, Institute of Physics, Bologna, and by Sandage and Dr. P. Usher, Pennsylvania State University, shows that the number of quasars rises very steeply, by a factor of 8.5-9 per magnitude. This slope is incompatible with that of a factor of 4 per magnitude, which should be observed if quasars had a uniform space distribution in the local part of the Universe. This constitutes one of the strongest arguments against the so-called local hypothesis of quasars.

The steep gradient of quasar counts corresponds to a co-moving space density of quasars that rises steeply, as  $e^{18\tau}$ ,

where  $\tau$  is the look-back time expressed in the age of the Universe. At redshift  $z = 2$ , or  $\tau = 0.67$  (two thirds of the age of the Universe back in time), quasars were 100,000 times as numerous as they are at redshift zero (i.e., at present). There are indications that the density variation for quasars of the highest absolute luminosity is much steeper yet. The density increase for optically selected quasars is much steeper than that found previously for radio quasars. Apparently, the fraction of quasars exhibiting radio emission is now larger than it was in the past.

### *IUE Observations of Quasars*

Spectra of six quasars have been obtained with the International Ultraviolet Explorer Satellite by Schmidt, Green, and Caltech graduate student Jeffrey Piér, in collaboration with Drs. Frank B. Estabrook, Arthur L. Lane, and Hugo D. Wahlquist of the Jet Propulsion Laboratory. Five of the six quasars show no evidence for strong  $\text{Ly}\alpha$  absorption between the redshifted and rest wavelengths for  $0.23 \leq z_{\text{em}} \leq 1.72$ . In addition, the quasar PG 1115+080 at  $z = 1.72$  shows no evidence for strong He I absorption from the resonance transition at  $\lambda 584$ . These results confirm that the intergalactic medium must be both tenuous and hot enough to produce an optical depth  $< 0.1$  in neutral hydrogen and helium. The absence of a continuum depression also indicates that the lines of sight to these quasars contain far fewer discrete hydrogen absorption clouds than are typically seen toward quasars of higher redshift. In no case was the Lyman edge detected in absorption near the emission redshift, implying a covering factor for intrinsic optically thick clouds of  $0.00 \pm 0.45$ , or, combined with the tally of 11 high-redshift quasars by Osmer and Smith (*Astrophys. J. [Lett.]*, 215, L47, 1977), a covering factor of  $0.13 \pm 0.25$ .

Three of the objects, PG 0953+415, 3C351, and PKS 0405-123, show an



average  $L\alpha/H\beta$  intensity ratio of 6.0, in disagreement with the theoretical prediction for Case B optically thick recombination of 30. The C IV/ $L\alpha$  intensity ratio ranges from 0.39 in PG 0953+415 to 0.15 in the more luminous PKS 1302-102, bracketing the "typical" value of 0.25. The ratio of [C III] to C IV ranges from 1.7 to 0.6, and that of  $(L\beta + O\text{ VI})/L\alpha$  from 0.28 to less than 0.02. The  $L\alpha$  emission line in 3C351 shows the identical asymmetry observed in the Balmer lines, implying a common transfer process for both sets of photons.

The two higher redshift objects merit further comment. PG 1115+080 shows a featureless continuum down to an observed wavelength of 1150 Å, corresponding to an emitted wavelength of 423 Å. On the one hand, this observation puts an upper limit of  $<5$  Å on the equivalent widths of such important resonance transitions as C III  $\lambda 977$  and He I  $\lambda 584$ . On the other hand, it indicates that the ionizing spectrum, with  $f_{\nu} a\nu^{-1.89}$ , persists beyond 2 Rydbergs.

The quasar PG 1247+268 with  $z = 2.038$  displays two interesting properties. The  $(L\beta + O\text{ VI})/L\alpha$  intensity ratio is the highest observed of the six objects, and there is evidence for the detection of  $L\gamma$  in emission, with an observed equivalent width of 37 Å. This detection would again call into question the validity of the line transfer assumptions in Case B recombination. At  $\lambda 2697$ , a strong absorption line is observed with a core reaching 0 intensity. Further, no net flux was detected to the violet of  $\lambda 2000$  down to the observed limit at 1150 Å, even though PG 1115+080 with a lower measured flux at  $\lambda 2100$  and a steeper spectral index was detected at the  $5\sigma$  level in the same integration time. This result is interpreted as absorption in  $L\alpha$  and the Lyman edge at  $z = 1.218$ . Evidence for  $L\beta$  absorption is weak because of the low signal-to-noise ratio. Optical spectra taken with the Palomar 1.5-meter and SIT spectrograph show no evidence for C IV or Mg II absorption in the same system. The ten-

tative conclusion is that the line of sight intersects a metal-poor cloud with  $\tau \gtrsim 1$  in the Lyman continuum at  $(1 + z_{\text{em}})/(1 + z_{\text{abs}}) = 1.37$ .

### Absorption Lines

Sargent, Young, Dr. A. Boksenberg of University College London, and their collaborators completed for publication their statistical work on the absorption lines in the QSO's observed at high spectral resolution at Palomar and at the Anglo-Australian Observatory during the past five years. As summarized in *Year Book* 77 (p. 194), it was concluded that the large number of single  $L\alpha$  lines in QSO spectra are associated with intergalactic clouds, while the heavy-element redshift systems are due to intervening galaxies.

Further work on the consequences of these hypotheses was done by Sargent and Young, together with Boksenberg and Dr. David Tytler, University College London. It was concluded that the  $L\alpha$  clouds have densities of ionized plus neutral hydrogen in the range from  $10^{-4}$  to  $4 \times 10^{-3} \text{ cm}^{-3}$ , temperatures near  $3 \times 10^4 \text{ K}$ , and diameters in the range  $10^{20}$ - $10^{23} \text{ cm}$ . (All estimates pertain to a redshift  $z = 2.5$ , the mean of the range covered.) The clouds are photoionized by the integrated radiation from the general distribution of QSO's and are highly ionized, with  $n_{\text{H II}}^e/n_{\text{H I}}^e \sim 10^5$ . The clouds cannot be gravitationally bound, but must be supported by some external pressure. This pressure is most plausibly provided by a general intergalactic medium. Such a medium could range in density from  $n_H^M = 10^{-5} \text{ cm}^{-3}$  ( $\Omega = 0.1$ ) to  $10^{-4} \text{ cm}^{-3}$  ( $\Omega = 1$  with  $H_0 = 60 \text{ km s}^{-1} \text{ Mpc}^{-1}$ ) and may have a temperature from  $T^M = 3 \times 10^5 \text{ K}$  to  $10^7 \text{ K}$ . The very existence of the clouds appears to rule out an intergalactic medium with  $\Omega = 1$  and  $T = 2 \times 10^8 \text{ K}$ , which would be required in order for the x-ray background radiation to be produced by thermal bremsstrahlung.

If the current theory of the evaporation of cool clouds immersed in a hot medium is correct, then the limits quoted above can be considerably sharpened. The clouds would have  $D = 10^{23}$  cm, and  $n_H = 10^{-4}$  cm $^{-3}$ . The general confining medium would have  $T = 3 \times 10^5$  K and  $n_H^M = 10^{-5}$  cm $^{-3}$ . In any case, the clouds themselves have a trifling cosmological density, with  $\Omega_{\text{cloud}} \sim 10^{-3}$ .

It should be emphasized that these results are only a first attempt to realize the hope that observations of QSO's would eventually lead to direct studies of the physical properties of matter in intergalactic space at large redshifts. The authors have shown that considerably more insight could be obtained from observations of QSO continua in the vicinity of the He I and He II resonance lines at  $\lambda 584$  and  $\lambda 303$ , respectively. They estimate that the calculated QSO radiation should be unable to ionize the He II in a general intergalactic medium unless  $n_H^M < 10^{-5}$  cm $^{-3}$ , a rather low value at  $z = 2.44$ . This is quite unlike the situation for hydrogen, where the QSO radiation is able to ionize H I in a medium of any reasonable density. Thus, the Gunn-Peterson test applied to He II promised to yield important constraints on the physical properties of the intergalactic medium. Observations from above the atmosphere would be required.

Boksenberg and Sargent used the IPCS detector at the coudé focus of the Hale Telescope in October 1978 in order to survey the spectra of 12 low-redshift QSO's for Mg II absorption. A wavelength region 350 Å in extent, with the Mg II emission line near the red end, was observed in each case. With these high-resolution observations, Mg II absorption was found in one object, 2128—123. This QSO has  $z_{\text{em}} = 0.501$ ; the absorption system is at  $z_{\text{abs}} = 0.43$ . The density of Mg II absorption systems in these low-redshift objects is thus about 1 per  $\Delta z = 1$  interval. This is comparable to the density of Mg II absorptions found in

high-redshift QSO's, as it should be on the intervening hypothesis.

Sargent also collaborated with Boksenberg, Dr. M.A.J. Snijders of University College London, Dr. Michael V. Penston of ESA Villafranca Satellite Tracking Station, Madrid, and Dr. Theodore R. Gull of the National Aeronautics and Space Administration in making *IUE* observations of QSO absorption lines. The principal work was a 14-hour exposure of 3C232, a 16-mag QSO with  $z = 0.53$ , which is 1.7' from the galaxy NGC 3067 on the plane of the sky. In earlier work, Boksenberg and Sargent found Ca II H and K absorption lines in the spectrum of the QSO at the redshift  $cz = 1406$  km s $^{-1}$  of NGC 3067. The *IUE* observations revealed absorption lines identified at  $L\alpha$  and Si II  $\lambda 1264$  also at the redshift of NGC 3067 and at zero redshift. Weaker absorption lines of Fe II and Mg II at the redshift of NGC 3067 were also found.

In other *IUE* work, a very long exposure was made on 3C273 with the high-dispersion camera in order to search for weak absorption lines. None were found in a preliminary examination of the data.

### *Quasars Near Bright Galaxies*

Arp has been systematically searching for ultraviolet-excess objects in fields around companions to a large number of bright galaxies, many of which upon spectroscopic investigation turn out to be quasars. He summarized recent work in a paper entitled "Quasars Near Companion Galaxies and the Problem of the Absolute Magnitude of Quasars," presented at the Ninth Texas Symposium on Relativistic Astrophysics in Munich, December 1978. The paper catalogued 44 quasars near 22 companion galaxies or large galaxies.

The alignment or concentration of the quasars near galaxies makes Arp believe that these objects must be associated with the galaxies in question. Since the quasars have large redshifts, Arp con-



cludes that the redshifts cannot be of cosmological origin. This subject is controversial, since many astronomers believe on the basis of other grounds that the redshift of quasars is cosmological indeed. They would argue that it makes no better sense to search for an alignment of quasars and galaxies than it is to seek one between galactic stars and galaxies. Statistical arguments about the expected number of coincidental alignments between quasars and galaxies should eventually resolve the matter one way or the other. The complexity of the statistical situation has initially only led to a heightening of the controversy.

In the course of this work, Arp found

1. Five quasars near companions of the galaxies NGC 936, 615, 2549, and 2681. The quasars have magnitudes of 18.5–19.6 and redshifts 1.1–2.4.

2. Ten quasars roughly in a line  $\pm 20'$  on either side of the companion of NGC 2639. The quasars tend to pair across the companion with redshifts of  $z = 0.303$ ,  $0.305$ ;  $z = 1.52$ ,  $1.53$ ; and  $z = 2.03$ ,  $2.12$ .

3. Three high-redshift quasars, each near a different one of the four companions of NGC 2859.

4. Five quasars within a circle of  $8'$

diameter in a field at  $11^{\text{h}}46^{\text{m}} + 11^{\circ}12'$  (1950), with redshifts of 0.86, 1.010, 1.011, 1.10, and 2.12. This field is one of two jointly investigated by Arp and Dr. C. Hazard of Cambridge University on the basis of objective-prism plates taken with the U.K. Schmidt telescope at Siding Springs.

5. In a second field, at  $11^{\text{h}}30^{\text{m}} + 10^{\circ}40'$  (1950), two cases of a pair of faint quasars exactly aligned across a bright quasar. The redshifts are, in the one case,  $z = 0.54$  for the bright quasar and 1.61 and 2.12 for the faint ones; and in the other case, 0.51, 1.72, and 2.15, respectively.

Arp has selected a control field at  $15^{\text{h}}48^{\text{m}} + 49^{\circ}$  (1950), far from bright or nearby galaxies, to obtain the surface density of quasars to  $B = 20$  mag. The field covers about  $20 \square^{\circ}$  and registers some 200 ultraviolet-intense objects. Measures of about a dozen of the objects lead to the expectation that about half of them are quasars. In a very rough, preliminary way, this would lead to around 5 quasars per square degree to  $B = 20$  mag, to be compared to  $7 \pm 4$  reported last year (*Year Book* 77, p. 176) in a different field.

## OBSERVATIONAL COSMOLOGY

### *The Velocity Field of Nearby Bright Galaxies*

In the early 1970's, it was realized that one of the powerful ways to measure the deceleration parameter  $q_0$  is to determine the effect of gravity on the velocity field of very nearby galaxies. This method measures the dynamical effect of the density contrast of the North Galactic density anomaly on the local expansion field. Sandage, Tammann, and Hardy (*Astrophys. J.*, 172, 253, 1972) argued that since no measurable velocity perturbations due to the Virgo complex could be detected greater than  $\sim 200 \text{ km s}^{-1}$ ,

the effect of gravity is small compared to the kinetic energy of the expansion, and hence  $q_0$  must be small ( $< 0.5$ ). Silk (*Astrophys. J.*, 193, 525, 1974), who made the method more explicit by giving the first theoretical estimate of the expected size of the velocity perturbation produced by various density contrasts of the Virgo cluster for various  $q_0$  values, reached the same conclusion.

But what was needed for a convincing determination of  $q_0$  by this local method were two observational facts, largely missing in 1975: (1) an accurate measurement of the density contrast of the North Galactic anomaly relative to the

average global density of the universe, and (2) an accurate measurement of the velocity perturbation about an ideal Hubble flow caused by this density anomaly.

Completion of the velocity coverage of the Revised Shapley-Ames Catalog (RSA) as well as completion of the Catalog itself, discussed in *Year Book 77* (p. 198), has provided the observational data from which these two numbers can be calculated.

Sandage, Tammann, and Yahil have undertaken an analysis of the RSA to solve a number of problems associated with mapping these very local density and velocity fields. Their results, to be discussed in a projected series of six papers, were partially completed during the report year, and the first three papers of the series were submitted for publication. The work has entailed a very extensive series of calculations to obtain such necessary distribution functions as the luminosity functions of galaxies of all types in the RSA (E, S0, Sa, Sb, Sc, with the later spirals separated into luminosity classes I to V), as well as functions  $f(m)$  that describe the completeness of the RSA compared with a true complete catalog at every apparent magnitude  $m$ . These functions, along with the velocity distribution functions  $N(v)$  in various directions, are needed to calculate the density of local galaxies toward and away from the Virgo complex, and hence to evaluate the density contrast of the north galactic anomaly.

The luminosity functions are also needed to evaluate the observational bias caused by the apparent magnitude-limited nature of the RSA so as to obtain proper photometric distances for all RSA galaxies freed from systematic bias errors in the calculation of the velocity field.

It is shown in Paper I of the series that the concept of a constant  $\langle M \rangle_v$  does not apply to the RSA sample, that  $\langle M \rangle_v = -23$  at  $v \simeq 6000 \text{ km s}^{-1}$  to  $\langle M \rangle_v = -19$  at  $v \simeq 500 \text{ km s}^{-1}$ , and that this variation must be taken into account in

any analysis of photometric distances. It is shown that the  $\langle M \rangle_v$  variation is expected in the present RSA sample because of the very broad luminosity function and the very narrow range of apparent magnitude encompassed by the RSA.

In Paper II, the luminosity functions of galaxies of all types are calculated using the method of maximum likelihood on the data for the RSA galaxies. The principal result is the very large overlap in absolute luminosities of spiral galaxies of different luminosity classes. For example, the brightest Sc III galaxies are fully 2 mag brighter than the faintest Sc I galaxies, and the overlap of the distributions is substantial. These results are illustrated in the accompanying two figures. Figure 16 shows the variation of  $M_B$  with redshift for Sc galaxies in the RSA sample. This variation, as just explained, is caused by the wide luminosity function  $\phi(M)$  and the magnitude limit of the Catalog at  $B \simeq 13.2$ . Figure 17 shows a composite of the luminosity functions for the separate galaxy types in the RSA, calculated with no correction for internal absorption (CIA) applied to the spirals. Clearly, with this large range in luminosities within any given luminosity class, and with the large overlap between the classes, the luminosity class of a galaxy is not correlated primarily with absolute magnitude. Hence, the concept of luminosity class may have largely lost its original meaning.

In Paper III, the  $\phi(M)$  functions have been used, together with the observed distribution of velocities  $N(v)$ , to calculate the density contrasts in various directions from the Virgo complex and hence to calculate the acceleration that the Local Group should experience toward the Virgo center due to the unbalanced forces. The principal conclusions are the following:

1. The well-known concentration of galaxies in the north galactic hemisphere is present for all galaxy types and is centered near the core of the Virgo cluster proper.



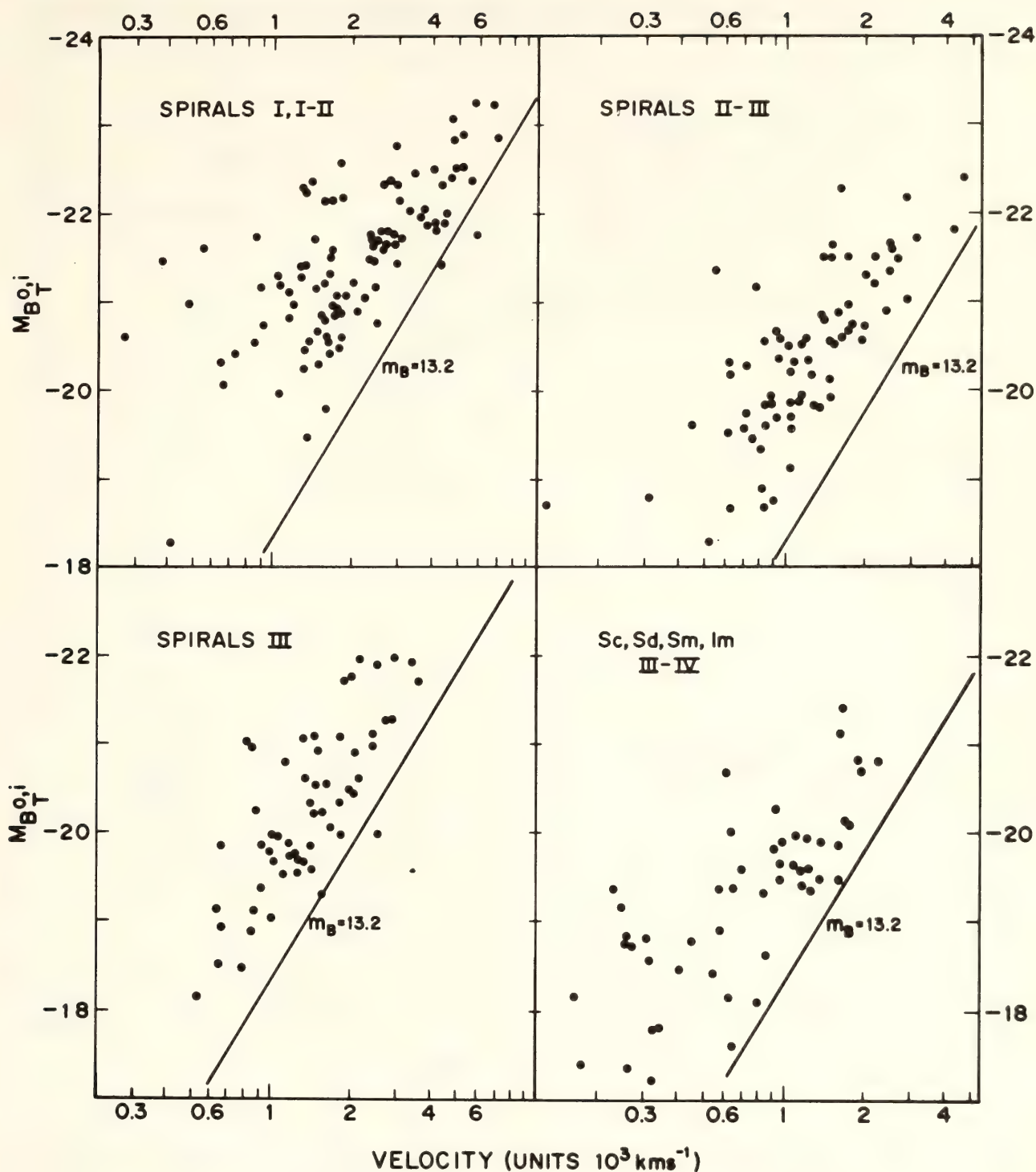


Fig. 16. Various differential luminosity functions for spirals, E, and S0 galaxies in the RSA. The normalization is such that  $\phi(M)$  is the number of galaxies at  $M$  in the absolute magnitude interval from  $M + \frac{1}{2}$  to  $M - \frac{1}{2}$  per cubic Mpc. Note that although the bright ends of  $\phi(M)$  do move faintward with increasing luminosity class, the overlap in  $M_B$  between the classes is large.

2. The density anomaly can be described as a distribution that extends to  $\sim 20$  Mpc in all directions from the Virgo cluster center as an envelope about the core. The Local Group is at the edge of the anomaly. Figure 18 illustrates this

density structure: the north galactic hemisphere is plotted toward the right; the south galactic hemisphere is toward the left.

3. The contrast between the density averaged over the anomaly from its cen-

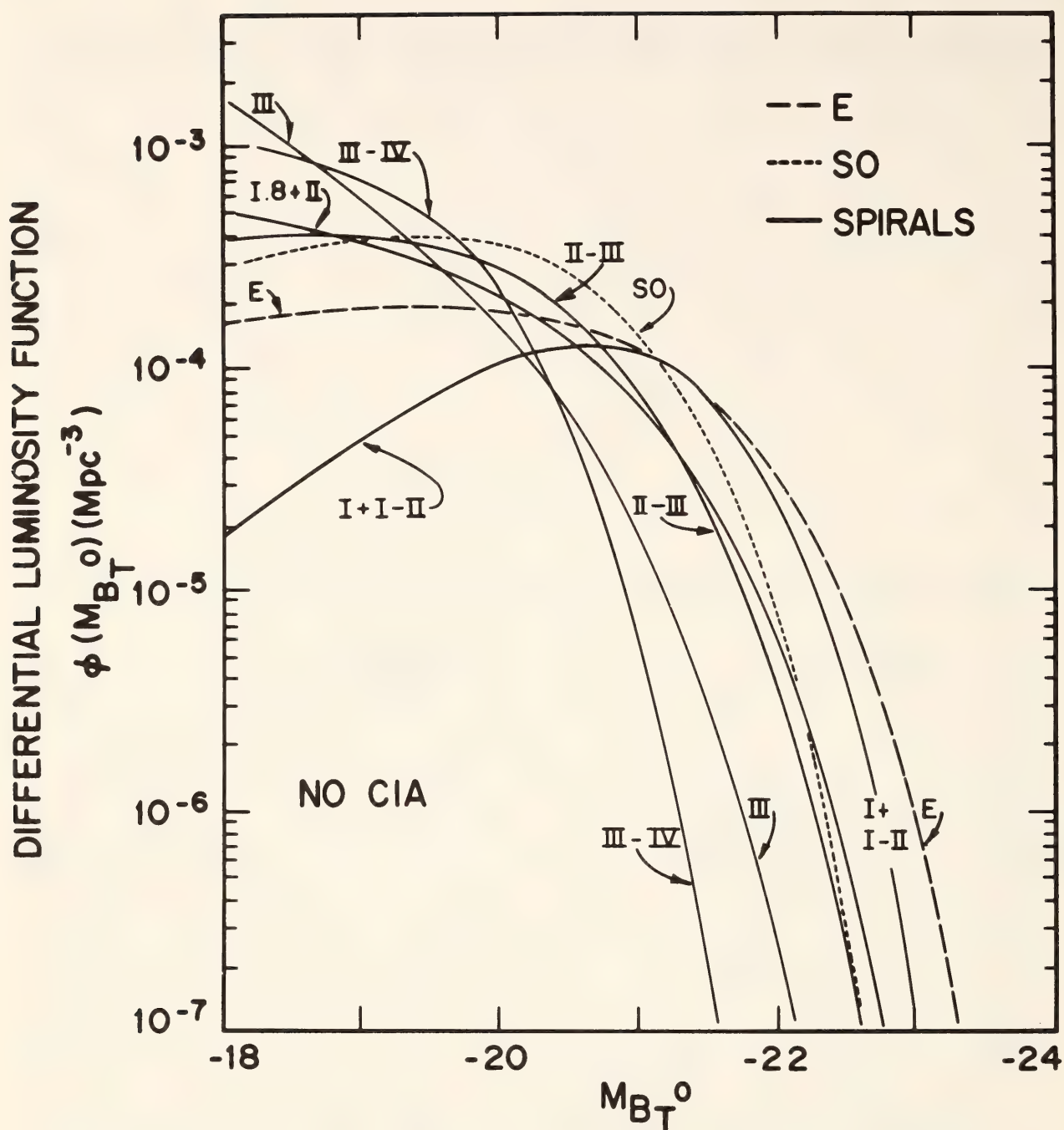


Fig. 17. Variation of absolute magnitude with redshift for spirals of different luminosity classes in the Revised Shapley-Ames Catalog. The magnitude limit of the Catalog at  $B = 13.2$  is shown in each frame. The principal features to note are (1) the wide range in  $M_B$  within any given luminosity class and (2) the large overlap in  $M_B$  between various classes.

ter to the position of the Local Group and the density that is close to the global mean is  $\langle D \rangle / \langle D(\text{global}) \rangle = 4$ .

4. Galaxies within the anomaly are somewhat concentrated toward the plane described by de Vaucouleurs, but the concentration largely disappears for Virgocentric distances greater than  $\sim 20$  Mpc ( $1000 \text{ km s}^{-1}$ ). Hence, the super-

galactic plane is a local phenomenon peculiar only to the local envelope of the Virgo complex and has no significance in the south galactic hemisphere.

5. The gravitational field generated by the north galactic anomaly is expected to pull the Local Group toward Virgo, resulting in a peculiar velocity at the present epoch of  $3700 q_0 \text{ km s}^{-1}$ . Since



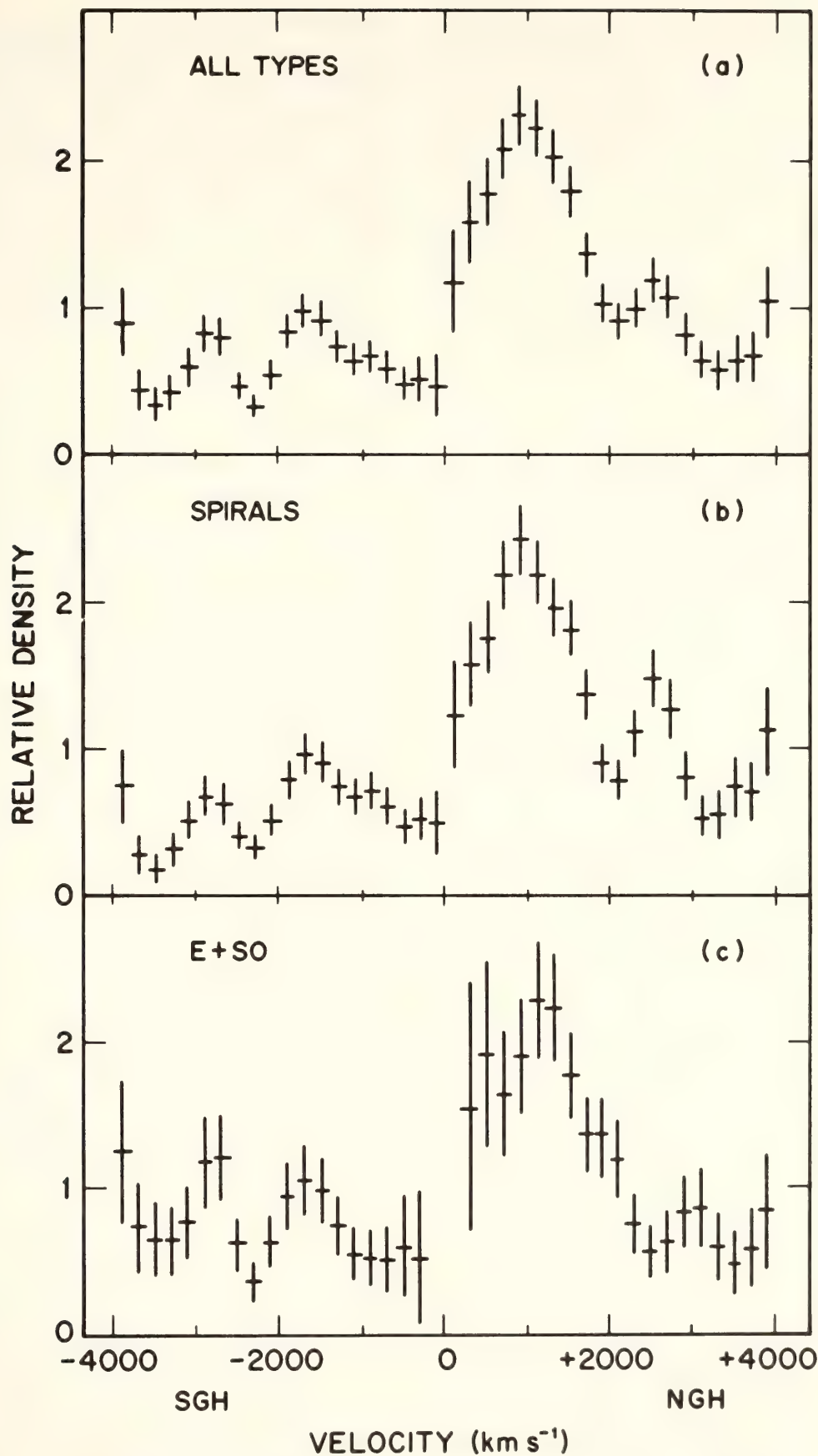


Fig. 18. Calculated densities of E, S0, and spirals averaged over the north and south galactic hemispheres. The principal feature is the large density contrast toward the center of the Virgo cluster at  $v \simeq 1000 \text{ km s}^{-1}$ . The Virgo complex consists of Virgo cluster core surrounded by an envelope whose radius is  $\sim 20 \text{ Mpc}$  (i.e.,  $1000 \text{ km s}^{-1}$ ). The Local Group is at the edge of this envelope.

all indications are that our peculiar motion toward Virgo is at most  $200 \text{ km s}^{-1}$  (as newly determined and as summarized from others in Paper II of the series), a well-determined value of  $q_0 \lesssim 0.06$  results. Note that this value is independent of corrections for evolution and other uncertainties possessed by look-back methods. Hence, providing that any local unseen matter is distributed in the same way as the visible galaxies, the Universe is open and the expansion will continue forever.

Papers IV and V are expected to treat the formal solutions for the perturbed motions of the local galaxies. Paper VI will treat the recalculation of the Hubble constant, using the methods of treating the bias that have been developed in Papers I and II. Preliminary calculations show that  $H_0 = 50 \text{ km s}^{-1} \text{ Mpc}$  will not be changed drastically by the new methods.

#### *Calibration of Largest H II Regions in Galaxies*

The diameters and luminosities of the largest H II regions in galaxies are important in the calibration of the extragalactic distance scale and the determination of the Hubble constant by Sandage and Tammann (*Year Book* 73, p. 155). Despite recent improvements in the H II region measurements by Kennicutt, distances to galaxies determined from H II regions possess a large uncertainty. Only nearby dwarf galaxies are available for calibrating the H II regions, and the existing calibration for the giant galaxies is a highly uncertain extrapolation.

Kennicutt is now attempting to solve this problem by directly measuring the shape of the entire H II region versus

galaxy luminosity calibration.  $H\alpha$  photographs and SIT photometry have been obtained for the largest H II regions in 20 Virgo cluster spirals, ranging from faint M33-type dwarfs to giant Sc I systems. Tying the upper end of H II region calibration from Virgo to the local (dwarf-based) calibration should yield considerably better distances to spiral galaxies in the field as well as to the Virgo cluster itself.

#### *The Tully-Fisher Relation*

Mould has followed up his collaborative work with Dr. Marc Aaronson of the University of Arizona and Dr. John Huchra of the Center for Astrophysics, Harvard-Smithsonian Observatory, on the relation between the luminosity of spiral galaxies and their 21-cm velocity widths. Radio studies have been carried out at Arecibo for a number of clusters in the  $3000 < v < 7000 \text{ km s}^{-1}$  range by Drs. Woodruff T. Sullivan and Robert Schommer of the University of Washington; reddening-free infrared magnitudes have been measured at Mount Wilson by Mould and Berriman and at Kitt Peak by Aaronson and Huchra. Distances to several clusters outside the Local Supercluster can now be derived. Preliminary results indicate a high Hubble ratio ( $80\text{--}100 \text{ km s}^{-1} \text{ Mpc}^{-1}$ ) outside the Virgo mass concentration (contrasting with  $60 \text{ km s}^{-1} \text{ Mpc}^{-1}$  found for Virgo in the earlier work). These results are now being prepared for publication in a series of papers on a Tully-Fisher-based distance scale. Work is in progress on a field sample and on a number of southern clusters, the latter in collaboration with Persson and Dr. Robert J. Dickens of the Royal Greenwich Observatory.

## THEORETICAL STUDIES

#### *Gravitational Separation of Elements*

During their year's stay at Caltech, Drs. Gerard and Sylvie Vauclair ex-

plored the mechanisms that may separate the chemical elements in the atmosphere of a white dwarf. Under the intense gravitational field, if the atmosphere is



stable against rotational meridional circulation and convection, diffusive separation occurs—elements of higher atomic weight settle, hydrogen floats on top of helium, the metals fall rapidly. Time scales are from  $10^2$  to  $10^5$  years, dependent on whether the atmosphere is opaque (appreciable hydrogen) or transparent (helium). Further effects are radiation-pressure support of certain elements whose strong lines or continua fall in a region of high stellar radiative flux. An element subject to radiation pressure in its dominant ionization stage may evaporate. The only realistic possibility for changing atmospheric composition of a white dwarf, after gravitational separation has occurred, is accretion of material of normal composition from the interstellar medium. Convection operates only in a limited temperature range, and rotation is negligible. Greenstein has obtained considerable evidence that only in helium-dominated atmospheres is there any appreciable metal content (most white dwarfs having less than  $10^{-5}$  the solar abundance of metals). This is partly caused by the low opacity of helium, partly explained by a recent accretion event.

#### *A Universal Helium and Deuterium Abundance?*

While on leave at the Niels Bohr Institute, Greenstein critically examined evidence for early nucleosynthesis of  $^2\text{D}$  and

$^4\text{He}$ , in preparation for the conference on The Universe at Large Redshifts. An elaborate discussion will be included in the report of that conference to be published in *Physica Scripta*. In brief, no objects can be found from studies of stellar atmospheres and gaseous nebulae in which a very low current abundance of helium is suggested. Study of stellar interiors always requires an initial value that is not zero. This is a result indicating that when the oldest known stars were formed, the mass fraction of helium,  $Y$ , was not much less than in the contemporary interstellar gas, covering for globular clusters a time span of 90–95% of the age of our Galaxy, and for individual old stars (half as old), the same. No evidence yet exists concerning pre-stellar phenomena. In gas-rich galaxies in which star formation is greatly retarded (like the small Magellanic Cloud) or in the compact intergalactic H II regions studied by Searle and Sargent, the gas may have 20% less helium. None have  $Y = 0$ ; it is probable that  $0.22 < Y < 0.30$  represents an extreme range. The only knowledge of deuterium is in the major planets and in nearby interstellar gas. The abundances of  $^2\text{D}$  agree, giving  $X(^2\text{D}) \approx 2 \times 10^{-5}$ . This local value is very sensitive to initial conditions during the Big Bang. It is consistent with the more widespread value for helium in indicating a nearly empty universe, with  $\Omega_0 h_0^3 \approx 0.02$ . No stellar sources synthesizing  $^2\text{D}$  are known.

## INSTRUMENTATION

### *The du Pont Telescope*

Because of the good seeing and the high quality of its optics, the du Pont Telescope is capable of yielding photographs with star images at least as small as 60 microns or  $2/3''$  on a substantial number of nights per year. It is therefore

of interest to investigate the way in which diffraction effects and seeing degrade the quality of the images. Babcock has developed a minicomputer program to produce the diffraction pattern of a star, in the absence of seeing effects, taking account of the presence of the secondary mirror and of its four supporting

webs. Another such program convolves the diffraction pattern with varying degrees of seeing.

Babcock continued to supervise the project for completion of the coudé optical system of the du Pont Telescope, although progress has been limited by shortage of technical manpower. Loomis is working on the figure of the optical flat. He states that the figure is better than  $\frac{1}{2}$  wavelength and that the mirror should be ready soon for its acceptance test.

#### *Santa Barbara Street Computing Facility*

A new computer has been installed at the Santa Barbara Street offices to aid in the growing volume of data reduction associated with new electronic instrumentation. The computer, a PDP-11/34, provides a factor of 20 increase in computational speed compared to the Raytheon computer, which it will gradually replace. In addition, the PDP-11 provides for simultaneous access to the machine by several users, which makes the computer far more convenient and less time consuming to use.

#### *Direct Image Tube Camera for Las Campanas*

Construction was completed on a direct image tube camera for Las Campanas. The camera, designed by Brucato, utilizes a 90-mm ITT Model F-4092 image tube, a single-stage magnetically focused device. Initial tests of the camera were made by Rose on the Swope Telescope and by Kennicutt on the du Pont. The image tube exhibits excellent uniformity and resolution. Image size on the du Pont Telescope remains seeing-limited to less than an arcsecond, the best seeing encountered during the observations. The effective gain in the visual is typical of single-stage devices. An extended red MA3 photocathode was selected, however, which extends the usable sensitivity of the camera to beyond 8000 Å, where

it will be particularly useful for near-infrared studies of faint objects. To date, all applications of the camera have been at  $H\alpha$ , and a pair of 100-mm interference filters is available for that purpose. Additional *UBVRI* wideband filters, especially selected to suppress the red leak with the image tube, are now being fabricated.

#### *Infrared Photometer for the Swope Telescope*

An infrared photometer was built for the 1-meter Swope Telescope at Las Campanas. Persson and Mould first used the system in April 1979 to make observations of spiral galaxies at  $1.65\ \mu$ . The observations were made as part of a large program of extending the 21-cm line width/IR luminosity correlation to a number of southern groups and clusters. The device can also be used with a photomultiplier for optical photometry.

#### *Infrared Fabry-Perot Spectrometer*

An infrared Fabry-Perot and grating spectrometer is being designed and constructed by Geballe and Persson. The spectrometer will consist of two 10-cm first order gratings cooled to solid nitrogen temperature, located inside a dewar, and a warm, piezoelectrically scanned Fabry-Perot interferometer outside of the dewar. An indium antimonide photovoltaic device inside the dewar will serve as the detector. The two gratings cover the spectral region  $1.5\text{--}5\ \mu\text{m}$ ; interchangeable Fabry-Perot mirrors will cover portions of this region. The maximum resolving power (without overlapping orders of the Fabry-Perot within the grating bandpass), using an aperture of diameter corresponding to a few arcseconds in the plane of the sky, will be  $\sim 3 \times 10^4$ . Thus the instrument, when used with a large telescope, will be capable of studying small wavelength intervals at high resolution and with high sensitivity. It is being designed for use



at the Cassegrain and is expected to be completed during the next year.

### *Prime-Focus Universal Extragalactic Instrument*

Gunn, in collaboration with Westphal (who is primarily responsible for the CCD detector), has constructed a prime-focus CCD instrument for imaging and spectroscopy at the Hale Telescope, called PFUEI (prime-focus universal extragalactic instrument). The instrument uses a  $500 \times 500$  Texas Instruments CCD, one of the prototype devices for the  $800 \times 800$  Space Telescope sensor program. The CCD is thinned and back-illuminated, and is characterized by very high quantum efficiency ( $\sim 70\%$  in the red and near-infrared) and low noise ( $\sim 15$  electrons per pixel RMS). Since the pixels in the device are so small ( $15\text{-}\mu\text{-square}$ ), it is necessary to image on to the CCD with a very fast optical system for efficient sampling. This is accomplished with a pair of commercially available Nikon lenses: a 135-mm f/2 Xero-Nikkor as collimator and a 55-mm f/1.2 Nikkor as camera. The combination yields a scale with the f/3.52 Wynne Corrector of  $0.4''$  pixels and a field about  $3'$  square. The total detective quantum efficiency of the instrument is near  $30\%$ . Since there is space available in the parallel beam between the camera and collimator and since the primary focal plane is accessible, the addition of a transmission grating, a slit, and tilt adjustments convert the instrument into a spectrograph. High signal-to-noise spectra of bright elliptical galaxies at  $z > 0.5$  and a resolution of about 200 can be obtained in about an hour (Fig. 19) with the instrument. The CCD is interfaced with the PDP 11/40 at Palomar. The combination is essential for doing spectroscopy of faint objects, since accurate offsets must be calculated from CCD pictures of the field taken with the instrument immediately prior to performing the spectrograph conversion and

obtaining spectra. Zimmerman has developed the software to do this.

### *FORTH Language Software Development*

Computer programs in the FORTH language have been developed to support a number of instruments of the Hale Observatories, both in the operation and data reduction phases.

Zimmerman, under the direction of Oke and Gunn, has developed programs to operate the PDP 11/40 data acquisition system at the 5-meter Hale Telescope. Instruments controlled by this system include the digital spectrograph with SIT Vidicon and CCD detectors, Oke's Multichannel Spectrophotometer, the Griffin-Gunn radial velocity machine, and Gunn's prime-focus universal extragalactic instrument. Zimmerman has also developed FORTH software for reducing data both during and after observing (using the PDP 11/34 at the Robinson Laboratory). She also has worked with Oke to develop programs to reduce IUE satellite data and photographic spectra at the Robinson Laboratory.

Graduate student Bill Sebok has developed a comprehensive package to reduce two-dimensional SIT Vidicon, CCD, and digitized photographic images, as well as a pattern recognition system for faint galaxy classification.

Stefan Mochnacki has developed a package for the reduction of Vero-Reticon spectrometer data for use on both the PDP 11/34 and 11/40 computers. Mochnacki and Zimmerman have developed a FORTH program to operate the new PDP 11/03 telescope control computer for the 5-meter telescope. This system can display telescope positions converted to catalog coordinates for any mean equinox chosen by the observer.

### *Fabry-Perot Spectrometer*

Trauger has initiated development of a high-resolution, 100-mm Fabry-Perot

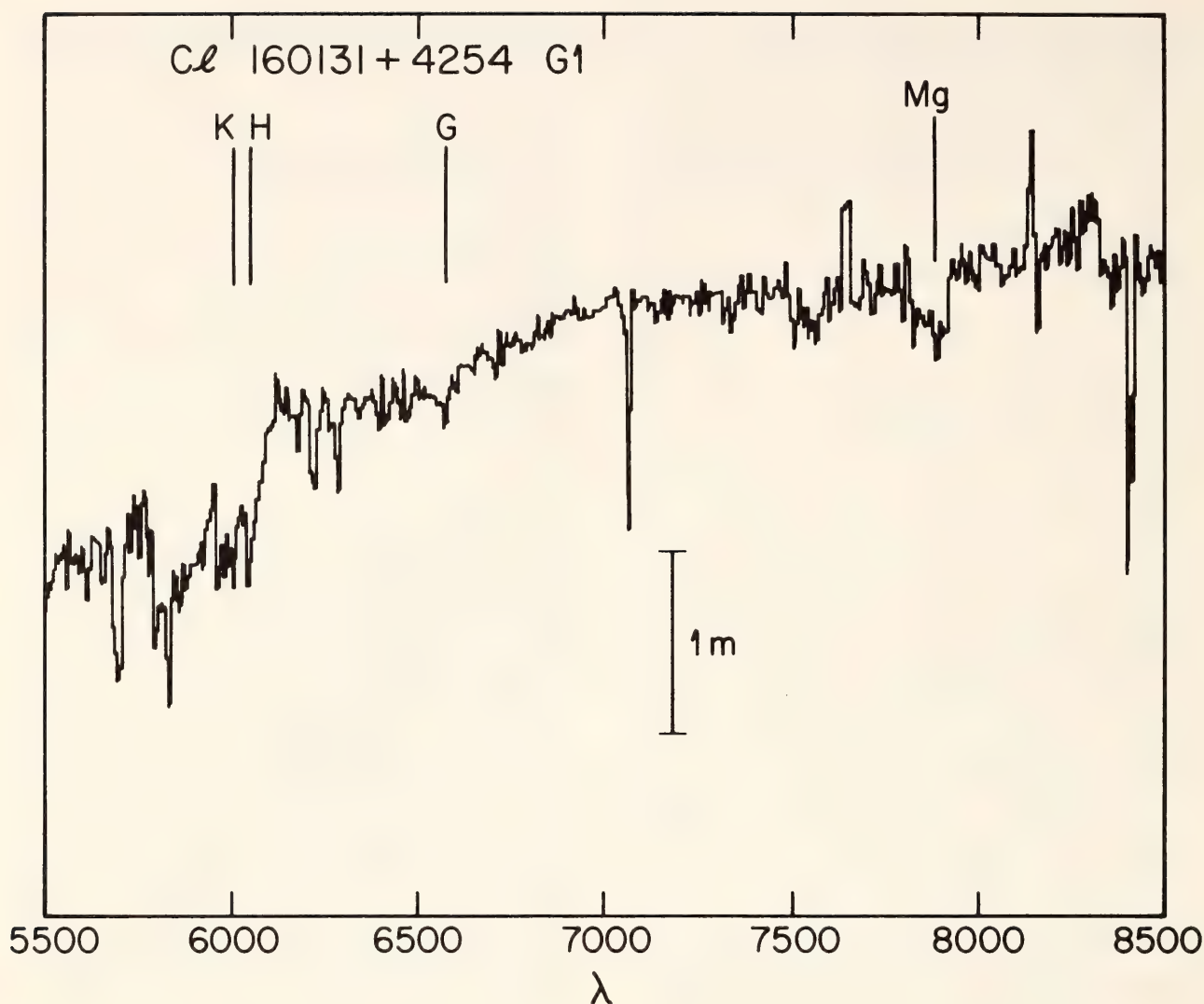


Fig. 19. PFUEI (Prime-Focus Universal Extragalactic Instrument) CCD spectrum of the brightest galaxy in C1. 160131+4254. Exposure time, 4000 seconds; redshift = 0.53.

spectrometer with NASA support. This year's effort includes machining and assembly of the spectrometer frame, acquisition of Fabry-Perot plates, and fabrication of an in-house optical coating facility; construction of a microprocessor-based data-collecting system, Fabry-Perot servocontroller, and interferometric calibrator; and the integration of existing surplus components into the spectrometer. It is expected that all of these systems will be integrated and fully functional by the end of 1979, and adapted for use at the coudé focus of either the 5-meter Hale Telescope or the 2.5-meter Hooker Telescope.

#### *Wide Field/Planetary Camera for Space Telescope*

Following a review of preliminary definitions and designs, NASA has confirmed the award of the contract for the Wide Field/Planetary Camera for Space Telescope to the California Institute of Technology. Westphal is the Principal Investigator, and general project oversight is in the hands of a team of scientists which includes Gunn, who is the Deputy-PI, and Kristian, who has primary responsibility for science data reduction. Other team members are Drs. W. A. Baum of Lowell Observatory, A. D. Code of the University of Wis-



TABLE 2. Wide Field/Planetary Camera (Space Telescope) In-Orbit Characteristics

Performance		Wide Field Mode (f/12.9)	Planetary Mode (f/30)
Angular field		2.67' × 2.67'	68.7" × 68.7"
Pixel spacing (1600×1600)		0.1"	0.043"
Throughput detective quantum efficiency	1200 Å–3000 Å 3% 3000 Å–7000 Å peak 40 % 7000 Å–10,000 Å 8%		
Filters, gratings, and polarizers	48		
Minimum intrascene dynamic range	4000		
Exposure time range	0.1 <sup>s</sup> –30 <sup>h</sup>		
Overall dynamic range		8.5 ≤ <i>m<sub>r</sub></i> ≤ 28	7.5 ≤ <i>m<sub>r</sub></i> ≤ 28
Linearity	better than 1%		
Photometric stability	better than 1%/day		
CCD readout noise	15 e <sup>−</sup> /pixel		
CCD dark current at −95°C	10 <sup>−2</sup> e <sup>−</sup> /pixel/sec		
Overall image quality		70% of a stellar image in a centered 5 pixel patch	70% of a stellar image in a centered 17 pixel patch

consin, D. G. Currie of the University of Maryland, G. E. Danielson of the California Institute of Technology, C. R. Lynds of Kitt Peak National Observatory, K. Seidelmann of the U. S. Naval Observatory, and B. A. Smith of the University of Arizona.

The camera, which is the prime instrument for Space Telescope, will be built at Caltech's Jet Propulsion Laboratory under the supervision of D. H. Swenson. In-orbit characteristics are given at Table 2.

The 2.4-meter Space Telescope will be launched in December 1983. Its location

above Earth's atmosphere will give it 0.1'' images and access to the ultraviolet and infrared regions of the spectrum. These characteristics, and the consequent order-of-magnitude increase in resolution and in signal-to-noise for faint objects, will make it a very powerful tool for extending many ground-based scientific programs. In connection with the Wide Field/Planetary Camera Project, Kristian and Westphal are assembling a computer system, based on a VAX 11/780 processor, for interactive reduction of two-dimensional data.

GUEST INVESTIGATORS

Dr. Saul J. Adelman of The Citadel used the 2.5-meter Hooker Telescope at Mount Wilson to obtain IIaO spectrograms of several Ap stars and IIaO spectrograms of several sharp-lined stars

in the Ursa Major stream and in the Scorpio-Centaurus association. Spectrophotometry taken at Palomar and other observatories in previous years was analyzed. Criteria based on photometric

indices were derived from the detection of the  $\lambda 4200$  and  $\lambda 5200$  broad, continuum features of the magnetic Ap stars. Better than 90% of the Ap stars examined have both features. About one half of the mercury-manganese stars surveyed also appeared to have these features. Spectrophotometry of 11 HgMn stars were examined in collaboration with Dr. Diane Pyper Smith. The HgMn stars exhibit a continuous range in behavior of both the  $\lambda 4200$  and  $\lambda 5200$  regions among those stars that have index values larger than the appropriate criterion of presence, and they present definite evidence for the feature among those with only a slight possibility of having such features.

Mr. Gonzalo Alcaino of Santiago, Chile, used the 2.5-meter du Pont Telescope at Las Campanas to obtain plates in *B* and *V* for his photometric program of 17 globular clusters.

Dr. Lawrence H. Aller of the University of California at Los Angeles and Dr. Stanley J. Czysak of Ohio State University, using the Varo-Reticon detector at the 2.5-meter Hooker Telescope on Mount Wilson, concentrated their studies of gaseous nebulae in particular on NGC 6572, IC 4997, and NGC 7027. They derived improved diagnostics for N I and will now be able to examine the problem of Ar IV, which heretofore has not been possible because of lack of spectral resolution.

Dr. S. C. Beck, J. H. Lacy, and Dr. C. H. Townes of the University of California at Berkeley, in collaboration with Geballe, used the 2.5-meter du Pont Telescope in two major projects. They continued study of the central parsec of our Galaxy, using an infrared emission line of  $\text{Ne}^+$ , and made observations of a pure rotational transition of molecular hydrogen in the Orion nebula. Observations of Ne II ( $12.8\text{-}\mu\text{m}$ ) emission from the galactic center over the previous two years had resolved many small clouds of ionized gas within the central parsec of the Galaxy. During this year, the galactic center was observed with a 3''

aperture and spectral resolution of  $86\text{ km s}^{-1}$ . The wavelength region scanned corresponded to velocities of  $\pm 1000\text{ km s}^{-1}$ , nearly twice the interval previously covered. The small aperture used helps define the geometry of the clouds. No new clouds at very high velocities were detected. The lack of such clouds places an important constraint on models of the galactic center. The observers have also been trying to understand the unusually low excitation state of the galactic center. This year, G05—0°1, an H II region very close to the galactic center, was mapped in Ne II and S IV, and a very low excitation was found for it as well. This raises the prospect that low excitation may be characteristic of the central region of the Galaxy and not just the innermost parsec.

The Berkeley group and Geballe detected the  $12.28\text{ }\mu\text{m}$ ,  $v = 0 \rightarrow 0$  S(2) line of  $\text{H}_2$  in the Orion nebula. This is the first detection of a pure rotational transition of  $\text{H}_2$  outside the solar system. With the  $2\text{ }\mu\text{m}$   $v = 1 \rightarrow 0$  transitions already studied by other groups, the intensity of this line is important for determining the shock velocity and the abundances of molecules that cool the shocked gas by radiation. The  $\text{H}_2$  lines were found to be broad ( $45 \rightarrow 75\text{ km s}^{-1}$  FWHM) and quite asymmetric, with strong blue wings. This result suggests that the gas is expanding asymmetrically with little or no motion into the far side of the molecular cloud.

Drs. Steven Beckwith and Ray Russell of Cornell University initiated a program of near-infrared spectroscopy which will make use of the Hale 5-meter, Hooker 2.5-meter, and the Mount Wilson 1.5-meter telescopes. The spectroscopic measurements will be obtained with a cooled grating spectrometer currently being developed at Cornell. The spectrometer uses a Cassegrain collimator with a replica grating used under near-Littrow conditions. The grating angle is adjustable for wavelength tuning. It is equipped with an InSb detector and several broad-



band interference filters for order sorting. Observations can be made between 1 and 5  $\mu\text{m}$  with a spectral resolving power of nearly 1000 ( $\lambda/\Delta\lambda$ ).

Initial observations will concentrate on two independent studies. The first is a continuation of work begun earlier by Beckwith studying line emission from molecular hydrogen. These lines have been shown to originate from  $\text{H}_2$  heated to around 2000°K near regions of ongoing star formation (Beckwith *et al.*, *Astrophys. J.*, 223, 464, 1978) and surrounding planetary nebulae (Beckwith, Persson, and Gatley, *Astrophys. J. [Lett.]*, 219, L33, 1978). The second is a study of several near-infrared emission and absorption features of unknown origin that are seen in the 3–5  $\mu\text{m}$  spectra of many objects. An understanding of these spectra should have important implications for understanding the composition of interstellar dust. Work on these studies as well as the development of the spectrometer is under way.

Dr. Jay T. Bergstralh of the Jet Propulsion Laboratory used the Mount Wilson 1.5-meter telescope to make spatially resolved spectrophotometric observations of selected areas on the planets Jupiter and Saturn, with the twofold aim of (1) determining the local reflectivities of the observed regions and (2) providing calibration for the photometric and video instruments on the Voyager 1 and 2 and Pioneer 11 spacecraft as they encounter Jupiter and Saturn, respectively.

Drs. K. H. Böhm and E. Mannery of the University of Washington used the multichannel spectrometer at the 5-meter Hale Telescope to obtain scans in the range 3100 Å  $\leq$  10,900 Å of the following Herbig-Haro objects: H-H1 SE, H-H1 NW, H-H 2G, H-H 2H, H-H 2A, H-H3, H-H7, H-H11, H-H32. The purpose of these studies is to compare the spectrophotometric data to the predictions of shock-wave models for Herbig-Haro objects. The agreement seems to be good for fairly high-excitation objects like the condensations of H-H1, H-H2, and

H-H32. The objects H-H7 and H-H11 show very low ionization and excitation with [N I]  $\lambda\lambda 5198, 5200$  stronger than  $\text{H}\beta$ , [S II]  $\lambda 6717$  much stronger (by more than a factor 3 in the case of H-H7) than  $\text{H}\alpha$ , and with very strong [Ca II]  $\lambda 7291$  line. The spectra of H-H7 and H-H11 cannot be explained by the simple shock-wave models that are presently available. Theoretical aspects of this problem are being studied now. The observations will also be used to determine Ca and Fe abundances (as has already been done for H-H1) in order to study whether these abundances have been reduced by dust formation in some H-H objects. This may give us some additional information about the properties of shock waves in H-H objects. The observations of H-H1 NW, H-H 2G, and H-H 2H (for which some earlier observations are available) will also be used to determine time changes in the electron temperature and electron density, the degree of ionization, and possibly the filling factors in these objects.

Drs. Howard E. Bond and R. Earle Luck of Louisiana State University used the 2.5-meter Hooker Telescope on Mount Wilson and the 5-meter Hale Telescope on Palomar Mountain to continue their studies of chemical abundances in Population II stars. They have completed the analysis for 10 new, extremely metal-deficient red giants discovered on Cerro Tololo objective-prism plates. The iron abundances are low by factors ranging from 30 to 500 (relative to abundances in young star clusters), with elements like zirconium and barium showing an even more extreme underabundance. Using these results, Bond and Luck used broad-based photometry to determine from a sample of 125 new metal-poor giants that the most metal-deficient known stars in the galaxies have an iron abundance that is low by a factor of 600.

Dr. E. F. Borra of the Université Laval and Dr. J. D. Landstreet of the University of Western Ontario used the

1.5-meter telescope on Palomar Mountain and the 2.5-meter du Pont Telescope at Las Campanas to complete a study of magnetic fields in bright peculiar B and A stars in both hemispheres. Field measurements were obtained using the University of Western Ontario Cassegrain Pockels cell polarimeter as a Balmer-line Zeeman analyzer. This technique allows a field measurement on a fifth magnitude star with a standard error of  $\sim 150$  gauss to be obtained in 1–2 hours, independent of the rotational velocity of the star observed. Using this technique, Borra and Landstreet have obtained more accurate magnetic curves for a number of known magnetic stars than were possible to obtain using photographic techniques, and they have resolved some outstanding difficulties in modeling the field distribution over stellar surfaces. They have also obtained data on the magnetic fields of a number of broad-lined Ap stars ( $r \sin i \geq 40 \text{ km s}^{-1}$ ) that could not previously be observed for magnetic fields. Finally, they have discovered magnetic fields in a number of helium-weak and helium-rich early B stars. (This is the first time that fields have been detected in helium-strong stars.)

Landstreet and Mr. D. N. Brown of the University of Michigan used the Griffin-Gunn radial-velocity spectrometer on the 5-meter Hale Telescope, together with a Pockels cell polarization modulator, as a 340-channel Zeeman analyzer. This instrument has been used to search for weak magnetic fields in a number of categories of late-type stars (for example, stars with Ca II or He I  $\lambda 10830$  emission, RS Canum Venaticorum stars, W Ursae Majoris stars, and dMe stars). For several stars observed, standard errors of less than 20 gauss were achieved (for stars of  $B \sim 5$  with roughly 40' integrations), making this set of measurements the most sensitive survey of cool stars for magnetic fields ever done. However, no fields were detected except in the known magnetic star  $\beta$  Coronae

Borealis, which was used to test the system.

Dr. Christine Clement of the University of Toronto used the 1-meter Swope Telescope at Las Campanas to make photographic V-band observations of the globular cluster IC 4199. The purpose of the investigation is to study the colors of the RR Lyrae variables. The work will be pursued in collaboration with Drs. R. J. Dickens and E. Bingham at the Royal Greenwich Observatory at Herstmonceux. They have recently published a study of the periods of the RR Lyrae variables in this cluster (*Astron. J.*, 84, 217, 1979), a study based mainly on observations made with the Swope Telescope in 1975. IC 4499 has the highest frequency of RR Lyrae variables for a globular cluster in the Galaxy. This is a consequence of the fact that most of the stars on the horizontal branch of its color-magnitude diagram lie in the variables in this cluster (*Astron. J.*, 84, mean periods of its RR Lyrae variables, IC 4499 belongs to Oosterhoff Group I (the short-period group). However, it is the Type I cluster whose properties are closest to those of the Type II clusters. A study of the colors of its RR Lyrae variables should prove useful to our understanding of the evolution of horizontal-branch stars.

Dr. Richard M. Crutcher of the University of Illinois used the Varo-Reticon detector on the 2.5-meter Hooker Telescope to observe the interstellar D lines toward several dozen B-type stars that are projected on a large cold cloud of neutral hydrogen detected in the 21-cm line of neutral atomic hydrogen. Detection of strong interstellar lines at the velocity of the hydrogen established that the cloud is closer than the star observed. The cloud, which extends  $40^\circ$  in galactic longitude and  $10^\circ$  in latitude in the general direction of the galactic center, was found to be at a distance of around 100 pc from the Sun.

Dr. Michael A. Dopita of the Mount



Stromlo and Siding Spring Observatories used the 1.2-meter Schmidt telescope to search for supernova remnants in M31 and M33, using deep [S II],  $H\alpha$ , and green continuum plates. Nineteen supernova remnants were found in each of M31 and M33, some of which were confirmation of earlier identifications by D'Odorico and Kumar. Twelve of the M33 candidates, one in M31, and seven low-excitation H II regions in M33, were observed spectrophotometrically between 3700 Å and 6800 Å, using the SIT spectrograph on the 5-meter Hale Telescope, and abundances were determined using shock-modeling techniques. A well-developed galactic abundance gradient in nitrogen and a somewhat less steep gradient in oxygen were found. No galactic enrichment theory is entirely successful in explaining the observations; as in earlier H II region studies, the gradient is too steep. The agreement with H II regions is very good, and the N/S gradient obtained with supernova remnants and H II regions is identical. Nitrogen is found to be produced first as a primary, but later (at higher enrichment and star-to-gas mass ratio) as a secondary nucleosynthesis element.

The high-dispersion coude spectroscopy program carried out by Dr. Michael M. Dworetzky of University College London on the Hg-Mn star Coronae Borealis (*Year Book* 77, p. 204) has shown that this star is in fact a double-lined spectroscopic binary of extremely low inclination. This result is to a great extent due to the loan of virtually all the high-dispersion spectra of this star taken at Hale Observatories during the past 25 years. Preliminary elements are  $P = 35.47$  days;  $\gamma = -20.28$  km s<sup>-1</sup>;  $K = 1.97$  km s<sup>-1</sup>;  $e = 0.44$ ;  $\omega = 151^\circ$ ;  $T = \text{JD } 2,438,019.54$ ;  $M_1/M_2 \sim 2$ . The blue-shifted asymmetries reported by Smith and Parsons (*Astrophys. J.*, 205, 430, 1976) are interpreted as blends due to the secondary star. The primary is underabundant in nitrogen and aluminum, and the weak sharp lines of these elements

show velocity shifts 180° out of phase with the primary star.

Dr. Jay Elias of the Cerro Tololo Inter-American Observatory used the infrared photometer on the 2.5-meter du Pont Telescope at Las Campanas to obtain 2- $\mu$  spectra of Herbig-Haro objects. Spectra at a resolution of 1.4% were obtained at a total of 10 positions in eight H-H objects. Emission lines of molecular hydrogen were seen in six of the eight objects, with lines visible down to a limit of approximately  $3 \times 10^{-17}$  erg cm<sup>-2</sup> s<sup>-1</sup>. No atomic hydrogen lines were visible in any of the objects down to a comparable detection limit. These results demonstrate first that molecular hydrogen is present in the vicinity of Herbig-Haro objects and, second, provide confirmation for the view that the optical emission lines from these regions are produced in shocks, since such an emission mechanism is most consistent with the absolute and relative strengths of the infrared lines.

Dr. Gilles Fontaine of the University of Montreal and Dr. Gerard P. Vauclair of Observatoire de Meudon, Paris, initiated a search for variable white dwarfs through observations at the 1.5-meter telescope at Mount Wilson. Candidate lists were made up, using the fact that known variables cluster in a definite region of the two-color diagram in Greenstein's multicolor system. White-light photometric observations were carried out for several hours, and the data were Fourier-analyzed to search for variabilities with time scales ranging from a few seconds to about an hour. A new variable white dwarf was discovered: GD385, the 13th star belonging to the ZZ Ceti class. This result was subsequently confirmed by Dr. John McGraw and co-workers at McDonald Observatory. The star appears to be singly periodic ( $\sim 256^s$ ) but with one harmonic. Follow-up observations on this star are being pursued.

Drs. R. and R. Griffin of the Cambridge Observatories, England, completed and

published their *Photometric Atlas of the Spectrum of Procyon* (1979). This work, a successor to the *Arcturus Atlas* by R. F. Griffin (published by Cambridge Philosophical Society, 1968), gives detailed spectrophotometry of Procyon over the wavelength range 3140–7470 Å. It is based on photographic spectrograms 3 mm wide taken with the coudé spectrograph of the Mount Wilson 2.5-meter reflector at dispersions of 0.7–1.7 Å mm<sup>-1</sup>.

Gunn and R. F. Griffin continued their work on radial velocities of individual stars in galactic and globular clusters with the photoelectric spectrometer at the coudé focus of the 5-meter Hale Telescope. An observing run in December 1978 was mainly concerned with the Hyades, while one in June 1979 yielded a substantial number of measurements in M13, M92, and M11.

Drs. G. Grueff and M. Vigotti, from the Laboratorio di Radioastronomia C.N.R., Bologna, and J. Wall and C. Benn, from the Mullard Radio Astronomy Laboratory, Cambridge, England, cooperating in a program of optical identification of faint radio sources, have obtained several deep plates at the 1.2-meter Schmidt telescope. Observations were begun in 1978 on two fields, centered at 12<sup>h</sup>58, +35° and 13<sup>h</sup>06, +29°. The first is the so-called Sandage-Véron field on which many optical and radio observations were already made in the past; the second field was observed only for calibration purposes, since it contains the Selected Area 57 with a photometric star sequence down to ~20 mag. Deep red and blue exposures have been obtained on Kodak IIIaF and IIIaJ emulsions, and the calibration sequence has been extended to ~23 mag, using a Racine prism especially built for the 1.2-meter telescope. At the same time, the 12<sup>h</sup>58, +35° field has been surveyed at 408 MHz with the Cambridge 1-mile Radiotelescope, obtaining a list of 246 radio sources down to 15 mJy (5C12). Magnitudes and colors of the optical

counterpart of the sources are being measured down to 23 mag, with an accuracy of about 0.1 mag. These and other data will be used to derive the cosmological evolutionary properties of faint radio sources.

Dr. Eduardo J. Hardy of Université Laval, Québec, used the 2.5-meter du Pont Telescope for a photometric study of various clusters. For the galactic cluster NGC 2243, he confirms a metallicity  $[Fe/H] = -0.7 \pm 0.2$ . For NGC 2158, he finds  $[Fe/H] = -0.8 \pm 0.2$ . These clusters thus seem to be the most metal-deficient galactic clusters known so far. Because of the position of their red giants in the C-M diagram, NGC 2158 is the closest analogue in our Galaxy to the blue "globulars" in the Magellanic Clouds. In the LMC, the photometry yields  $[Fe/H] = -0.6 \pm 0.1$  for NGC 2209, thus confirming the upper bound of the metallicity range given by other workers. It is puzzling that the red giants of a small sample located on the bar itself have solar abundances, although of course the question of their membership could still be somewhat debatable and a larger sample should be studied.

From previous photographic material obtained with the du Pont Telescope, Hardy confirms the Population II nature of the globular cluster NGC 416 in the Small Cloud. A color-magnitude diagram for the SMC cluster NGC 419 is also being constructed. From integrated photometry at the du Pont Telescope, Hardy finds for both clusters a value of  $[Fe/H] = -1.3 \pm 0.2$ .

Dr. W. A. Hiltner of the University of Michigan observed the optical counterpart of the x-ray source 2A0311–227 with the 1-meter Swope Telescope at Las Campanas. There are two maxima and two minima in visual light (5300 Å); the two minima are of nearly equal depth, but the two maxima differ by 0.4 mag. The total variation is near 1.2 mag, from  $V = 13.8$  to 15.0. The brighter maximum is in phase with the maximum



velocity of approach. In the blue (4300 Å), only one maximum is present, which again corresponds in phase to the brighter of the two maxima in the visual light curve. The total variation in the blue is about 0.6 mag. The star has pronounced flickering in both blue and yellow light. The blue-light curve at maximum light shows a very short but deep minimum that seems to repeat. This minimum is in excess of 0.5 mag but has a width at half minimum of only 2 minutes, compared with 20–25 minutes for the width of the maximum on which it occurs. The interpretation of this phenomenon is not immediately obvious, but an occultation is suggested.

Dr. Paul Hodge of the University of Washington and Schommer used the 2.5-meter du Pont Telescope with a Racine wedge to obtain plates in *B* and *V* of three rich globularlike clusters of the Large Magellanic Cloud: NGC 2121, 2133, and 2134. A photoelectric sequence was established nearby, using the 1-meter Swope Telescope. These observations are being used to produce color-magnitude diagrams in order to establish the nature of these clusters, which are probably somewhat younger than true globular clusters but have a comparable low metal abundance.

The distribution of the brightest blue and red stars, and the associations of young stars, H II regions, and dust lanes are being mapped by Dr. Roberta M. Humphreys of the University of Minnesota and Sandage to investigate the structure and content of the spiral features in the nearby spiral M33. These optical spiral tracers, when compared with existing 21-cm maps of the galaxy, will yield information on the rate of star formation in the arms and possibly some clue to the mechanisms by which the chaotic spiral features of M33 are formed and maintained. A color-magnitude diagram of the brightest blue and red stars has also been obtained. The variation of the ratio of blue to red supergiants with distance from the galactic center

reveals a gradient that correlates very well with the observed variation in the  $[O III]/H\beta$  ratio for H II regions in M33.

A team consisting of Drs. Frank P. Israel of the California Institute of Technology, Thys De Graauw, Sverre Lidholm, Brian Fitton, and John Beckman of the European Space Agency, and Hans Nieuwenhuyzen of the University of Utrecht used the Las Campanas 1-meter and 2.5-meter telescopes in conjunction with a heterodyne submillimeter receiver to observe  $^{12}CO$  ( $J = 2 \rightarrow 1$ ) emission from galactic sources. Although the weather was cloudy for most of the observing period, satisfactory maps were obtained for NGC 6334 and Orion A, with a resolution of 4'. In the Orion Molecular Cloud (OMC-1), four centers of activity were found. The resulting complicated picture seems to exclude several simple models for the Orion region.

Mr. Howard Lanning of Mount Wilson Observatory used the 1.5-meter telescope to obtain differential photometry of Nova V1500 Cygni. Several minima have been observed in order to redetermine the period of the variations. Though the 3.3-hour period decreased by  $\sim 2\%$  from 1975 to 1976, then increased 1% in 1977, it now appears to have decreased once again. These observations have been taken as a joint program with Dr. I. Semeniuk of the University of Warsaw.

Drs. M. S. Longair and N. J. Schuch of the Mullard Radio Astronomy Observatory, Cambridge, England, and Gunn have completed their spectroscopic observations at the 5-meter Hale Telescope of galaxies in the field of the supercluster associated with 5C10. A total of some 80 radial velocities were obtained. The supercluster consists of six or seven Abell clusters and a large number of weaker groups. The radial velocities obtained for each Abell cluster enabled their masses to be determined, and then, using the mean velocity of each Abell cluster, estimates of the

dynamics of the supercluster as a whole were made. The preliminary results suggest that the mean density of matter in the supercluster region is lower than the cosmological density. Another interesting result is that many of the groups turn out to be background systems rather than members of the supercluster. The investigators have also been able to evaluate the radio properties of galaxies in the supercluster and, using the velocity information, to discriminate against background systems.

Longair and Gunn, together with Drs. J. M. Riley and M. A. C. Perryman of the Mullard Radio Astronomy Observatory, Cambridge, England, used the JPL charge-coupled device (CCD) camera to pursue their program of deep optical identifications of radio sources at the 5-meter Hale Telescope. Three separate programs were involved. In the first, identifications were sought for unidentified radio sources in the 3CR catalog, and of 12 fields studied only 3 remain unidentified. The identifications are with galaxies having magnitudes in the range 20.5–23. Taking these new identifications in conjunction with our previous work, 3CR identifications are more than 95% complete for regions that have been intensively studied. The second program concerned bright radio sources selected at high frequencies. Of 11 fields studied, 7 now have identifications, again making a total identification percentage of well over 90%. This sample consists of radio sources having flux densities  $\geq 1.5$  Jy at 2.7 GHz. In the third program, deep CCD images were obtained for about 50 sources in a complete sample having flux densities between 1 and 2 Jy at 408 MHz.

Dr. Barry F. Madore of the University of Toronto used the 1-meter Swope Telescope to finish two projects concerned with calibration of the period-luminosity relation for Cepheids in the Large Magellanic Cloud. Photoelectric photometry was completed for 10 Cepheids, all with periods of seven days but

covering a wide range of amplitudes. Ultraviolet plates were secured for four fields centered on very long-period Cepheids ( $P > 80$  days) and calibrating sequences were set up to a limiting magnitude of  $B \sim 14$  mag.

Drs. Yuri Mekler and Bruce Goldberg of the Jet Propulsion Laboratory, Pasadena, used the 60-inch SIT spectrograph in an effort to record the intensities of the forbidden emission doublets of ionized sulfur ( $\lambda\lambda 4068, 4076$  and  $6716, 6730$ ) in the vicinity of Jupiter. Such observations, if successfully completed, will allow direct determinations of the thermal plasma electron temperatures. Their objective is to investigate the temperature distribution of the plasma within the inner magnetosphere of Jupiter.

Dr. H. Richard Miller of Georgia State University used the SIT spectrograph at the Palomar 1.5-meter telescope to obtain spectra for 54 galaxies in the list of Arakelian. Nine of these galaxies have been identified as emission-line galaxies similar to M51 and M82. Five additional galaxies have been classified as Seyfert galaxies. Therefore, on the basis of this limited sample of galaxies taken from the Arakelian list, it appears that Seyfert galaxies make up approximately the same percentage of this sample as they do in the Markarian lists.

The rotational periods of Uranus and Neptune have been redetermined by Drs. Guido Münch and H. H. Hippelein of the Max Planck Institute for Astronomy, Heidelberg, Germany, on the basis of a series of image-tube spectrograms obtained with the coudé spectrograph of the 5-meter Hale Telescope in January 1976 and July 1977, respectively. The apparent tilt of Fraunhofer lines has been determined from the digitized spectra by a cross-correlation technique. The corrections to the radial velocities, thus measured at different points on the apparent disk, due to seeing and guiding-image motions, have been evaluated by a semianalytical procedure rather than



numerically as done heretofore. For the case of Gaussian point-spread function, it has been shown that the continuum brightness distribution over the apparent disk contains all the information required to derive the centroid and entire shape of the reflected Fraunhofer lines. The raw measurements, when corrected in this fashion, lead to rotational periods of 15 and 11 hours, respectively, for Uranus and Neptune.

Drs. Edward P. Ney and Brian J. Hatfield of the University of Minnesota are using the 1.2-meter Schmidt telescope on Palomar Mountain to search for polarized objects, such as the "egg nebula," in the Milky Way. They take pairs of plates with the polaroid in different orientations. The material of 224 plates has not yet been systematically blinked, but two dozen polarized objects already have been identified. The "egg nebula," which has polarization exceeding 85%, is still the most polarized object, but some others, such as M2-9, come close to it.

Drs. John V. Peach, Jon G. Godwin, and K. L. Dixon of the University of Oxford have completed two-band photographic photometry of the clusters of galaxies A1367, A2197, and A2199, based on digitally-stacked Schmidt plates and leading to uniform and complete samples of galaxies from which luminosity functions and color-magnitude diagrams have been constructed. They have developed reliable automatic methods of star-galaxy discrimination to  $B_{27} \approx 20.5$ , using Schmidt plates, as well as a technique to distinguish between cluster members and the "field." They have compared their observations with models based on a variety of cosmological assumptions. Godwin and Peach have used the projected distributions of cluster galaxies with various models of three-dimensional cluster structure to predict detailed maps of x-ray bremsstrahlung emission from the intergalactic medium. From intercomparisons with earlier studies using Palomar material, they conclude

that the luminosities of the brightest members of clusters, and the spatial dependence of the luminosity functions within clusters, provide evidence consistent with mass exchange between galaxies in dense regions.

Dr. Peter Pesch of the Warner and Swasey Observatory and Lanning used the Varo-Reticon detector at the coudé focus of the 2.5-meter Hooker Telescope at Mount Wilson to observe the  $H\alpha$  emission in the Hyades binary HZ 9, which consists of a white dwarf and an M-type dwarf. The orbit is circular, the velocity amplitude  $130 \text{ km s}^{-1}$ , and the period 0.564329 days. Multi-channel spectrometer data kindly provided by Greenstein indicate a spectral type of  $\sim dM4$  for the cool companion. Photometric observations with the 1.5-meter telescope at Mount Wilson in the  $UBV$  over  $\sim 75\%$  of the orbit indicate variations of as much as  $0^m.2$ , though no eclipse has yet been observed. Observations of this new binary will continue, as well as those of the primary comparison star, which also appears to be variable.

Dr. Mark M. Phillips of the Cerro Tololo Inter-American Observatory used the intensified-reticon spectrograph on the 2.5-meter du Pont Telescope at Las Campanas to study emission-line intensities in 10 H II regions in the radio galaxy NGC 5128 (Centaurus A). The aim of this program was to obtain information on the ionization, reddening, and abundances of the numerous H II regions that lie along the dust lane in this peculiar galaxy. Also observed were the nucleus and Graham's knot X, both of which show peculiar emission-line intensity ratios, and knots A and C in the northeast radio lobe.

As a secondary program, Phillips obtained spectra of several emission-line galaxies identified by Sandage as having high-excitation nuclear gas. Among the six observed with the intensified-reticon, four were found to have emission-line ratios typical of Seyfert 2 galaxies, and



one, NGC 1019, was shown to be a Seyfert 1 galaxy with broad Balmer lines. These observations bring to 11 the number of Seyfert 2-like galaxies that Phillips has identified from Sandage's list. Most of these galaxies are relatively nearby, and the large number of them would indicate that the Seyfert 2 phenomenon is considerably more common than was previously thought.

Drs. Vera C. Rubin and David Burstein of Carnegie Institution's Department of Terrestrial Magnetism used the Palomar 1.2-meter Schmidt telescope and the Mount Wilson 1.5-meter telescope to obtain direct plates of spiral galaxies that have been studied dynamically by Rubin and her collaborators. Surface brightness profiles will be determined for these galaxies; the luminosity variation will then be correlated with mass distributions across the galaxies. Unfortunately, the poor winter weather permitted no useful observations to be obtained.

The systematic search program for new planet-crossing asteroids conducted by Dr. Eugene M. Shoemaker and Mrs. Eleanor F. Helin of the California Institute of Technology, using the 46-cm Schmidt telescope, continued at Palomar. Between July 1, 1978, and June 30, 1979, 298 independent fields were photographed and reviewed. Significant discoveries made during this time with the 46-cm Schmidt were: (2100) Ra-Shalom (Aten-type asteroid), and 1978 TA and 1979 HA (Phocaea-family asteroids). (2100) Ra-Shalom is the third member of the new class of Aten asteroids discovered by the Palomar Asteroid Survey, characterized by orbits smaller than Earth's and orbital periods less than one year. Its period of 278 days is the shortest of any known minor planet. Photometric observations suggest that (2100) Ra-Shalom is a dark, very primitive object.

A set of fields obtained with the 1.2-meter Schmidt telescope has produced 238 asteroids, which have been measured and for which orbits are being computed for identifications, classifications, and

official designations. The following 20 asteroids have been identified and designated: 1978 NC, ND, NE, NF, NG, NH, MJ, NK, MU, NM, NN; 1978 NP, NQ, NR, NS, NT, NU, NV, NW; and 1978 VA.

Dr. Richard W. Shorthill of the University of Utah Research Institute and Drs. Dale W. Smith and Paul E. Johnson of the University of Washington used the 5-meter Hale Telescope and the Oke multichannel spectrometer to observe faint objects as follows: Jovian satellites J7 Elara, J8 Himalia, J9 Sinope; Trailing Trojan asteroids 617 Patroclus, 884 Priamus, 1172 Aeneas; the main belt asteroid 14 Irene for calibration; and comet Temple 2.

Dr. Susan M. Simkin of the Mount Stromlo and Siding Springs Observatories reports that the survey of Seyfert galaxies with radial velocities less than  $5000 \text{ km s}^{-1}$ , in progress for the past three years with the 1.2-meter Schmidt telescope at Palomar and on Siding Springs, is two-thirds complete. A preliminary analysis conducted in collaboration with Drs. H. J. Su and M. P. Schwartz suggests conclusions in three areas. (1) The space density of Seyferts in this sample appears to be  $\sim 4$  times greater than that previously found for the Markarian Seyferts by Huchra and Sargent. This implies that either the true space density of Seyferts is much greater than was previously suspected or that there is an anomalously high density of Seyferts within  $\sim 100 \text{ Mpc}$  of our Galaxy. (2) The morphological structure of both Seyfert 1 and Seyfert 2 galaxies is characterized by the three-step radial-intensity distribution originally noted in Seyfert 2 objects by Khachikian and Weedman. Within this general framework, a second parameter characterizing the morphology of Seyferts is the clarity of the features in their disks. This ranges from sharp, well-defined spiral structure to completely amorphous, ringlike segments. The radial intensity distribution and progression from sharp spiral struc-



ture to amorphous rings has been reproduced in a computer model by Schwartz. In this model, the gas in a star-gas disk system is perturbed by a  $2\theta$  perturbation. For some pattern speeds and disks that have sharp increases in density toward the center, such a perturbation forces the gas to redistribute into a spiral and finally into double rings located near corotation and the outer Lindblad resonance. The significant feature of this forced redistribution is that it produces a gas inflow into the nuclear regions of  $\sim 0.5 M_{\odot} \text{ yr}^{-1}$ . (3) Plots of nuclear emission line widths versus axial ratio for this sample of Seyferts show no correlation for the Seyfert 2 objects and no correlation for the forbidden lines in the Seyfert 1 objects.

Dr. Paula Szkody of the University of Washington collaborated with graduate student Richard Wade in obtaining high-dispersion spectra of Z Camelopardalis and EX Hydrae throughout their orbital cycles with the Varo-Reticon detector at the wide focus of the 5-meter Hale Telescope at Palomar. The data are being used to obtain radial velocities and to study the distribution of material in these close binary systems. A survey of unclassified variables and novalike systems was conducted with Wade at the Palomar 1.5-meter telescope with the SIT at lower dispersion in order to determine the type of stars in the unclassified systems, and to compare the Balmer-line intensities of the novalike systems with that of dwarf novae and old novae. Finally, through the cooperation of Neugebauer and the infrared group, infrared observations of dwarf novae and novalike systems were carried on at Mount Wilson in collaboration with graduate student Graham Berriman. These measurements are being used to study the type of secondary star in the system and the flux distribution from the disk.

Line profiles from T Tauri stars for the  $H\alpha$ ,  $H\beta$ , and NaD have been observed by Dr. Roger K. Ulrich of the

University of California at Los Angeles and Dr. Gillian Knapp of the Owens Valley Radio Observatory. They used the Varo-Reticon scanner at the 2.5-meter Hooker Telescope on Mount Wilson and the 5-meter Hale Telescope at Palomar at a spectral resolution of 0.25 Å or 0.60 Å. The observed Balmer profiles are classified into six types and the NaD lines are classified as to the strength, depth, and velocity of absorption components. The NaD lines indicate the direction of gas flow while the interpretation of the Balmer lines can be ambiguous. The NaD lines indicate the gas flow can be in either direction, with a slight excess of mass-gaining stars over mass-losing stars in the present sample. The mass loss appears more sporadic than the mass accretion. Ulrich and Knapp suggest that the sporadic mass loss is due to flare activity enhanced by the accretion of some interstellar magnetic field along with the gas. The sudden brightening of FU Orionis and V1057 Cygni may be related to the general reversal of the gas flow direction by such flare activity. The apparent contradiction between the Balmer line profiles and the NaD line profiles in many of the stars can be reconciled if the accretion is nonspherically symmetric.

Dr. Peter D. Usher from the Pennsylvania State University continued research in collaboration with Sandage, on selected high-latitude fields of the north and south galactic polar caps. Using the 1.2-meter Schmidt telescope, he obtained three-color plates to search for blue-excess objects, as well as single-color plates to search for large-amplitude variables. Plates were also taken of the BL Lacertae object OJ287.

Dr. Sidney van den Bergh of the Dominion Astrophysical Observatory has continued his long-term study of bright variable stars in Local Group galaxies with the 1.2-meter Schmidt telescope. This instrument was also to push the search for northern supernova remnants

on matched pairs of  $H\alpha$  and  $[S II]$  plates to fainter limits. Intercomparison of 5-meter prime-focus plates of IC 1613 with (defocused) Curtis Schmidt plates of the Small Magellanic Cloud shows that active regions of star formation in the Small Cloud produce more star clusters than do those in IC 1613. Dr. Elmar Brosterhus, also at the Dominion Astrophysical Observatory, obtained plates with the 1-meter Swope Telescope at Las Campanas for a program aimed at the discovery and study of associations surrounding southern Cepheids with periods longer than 11 days.

Drs. Glenn J. Veeder and Dennis L. Matson of the Jet Propulsion Laboratory and Staff Associate Charles Kowal continued their study of the surface composition of selected asteroids, using simultaneous visual and infrared photometry. The bright hemisphere of Iapetus has a reflectance consistent with a surface exposure of water ice, as previously suggested. The reflectance of the dark hemisphere is too large to be compatible with previous suggestions of carbonaceous material.

Chiron was discovered at Palomar by Kowal in 1977. It is the only known minor planet whose orbit has a semi-major axis greater than that of Saturn. Observations obtained by Oke with the Cassegrain scanner at the 5-meter Hale Telescope are being reduced in collaboration with Matson and Kowal. The spectral reflectance of Chiron is essentially flat in the 3200–10,800 Å region, with a possible band near 10,000 Å. This flat spectral reflectance is consistent with either dark carbonaceous material or bright frosts. Both types of material are

found on other objects in the outer solar system.

Dr. N. V. Vidal of the Royal Greenwich Observatory continued his program of direct  $14'' \times 14''$  plates of x-ray clusters of galaxies, using the 1-meter Swope Telescope. The plates are used to determine the percentage of (E + S0) galaxies in each cluster, which then will be correlated with the observed x-ray luminosity (see *Year Book* 77, p. 212).

Dr. K. Wakamatsu of Gifu University, Japan, obtained plates with the 2.5-meter du Pont Telescope for the study of globular clusters in galaxies. Globular cluster systems beyond the Local Group are recognized as concentrations of faint stellar images toward nuclei of galaxies. To minimize contamination by faint background galaxies, 103aO emulsion was used with a Wratten 2C filter. Program galaxies are the following: NGC 1549, 1553, 3115, 3377, 3379, 3384, 4365, 4374, 4406, 4486, 4594, 4621, 4649, 4636, 4697, and 5363. These plates will be used to study (1) the radial distribution of globular clusters, (2) the flatness (ellipticity) of globular cluster systems, and (3) a correlation between the total population of globular clusters and the absolute magnitude of the spheroidal system of parent galaxies.

Dr. Alma C. Zook of the University of California at Berkeley used the 2.5-meter Hooker Telescope at Mount Wilson to obtain Varo-Reticon observations with a resolution of 0.1 Å in an attempt to see the isotopic splitting of the band heads of  $^{90}\text{ZrO}$  and  $^{91}\text{ZrO}$  near 6900 Å. She will use the results to study the apparently on-going s-process nucleosynthesis in S-type stars.



## BIBLIOGRAPHY

- Aaronson, Marc, *see* Persson, S. E.
- Arp, Halton, Ejection from galaxies and galaxy formation, in *Problems of Physics and Evolution of the Universe*, pp. 65–80, Academy of Sciences of Armenian SSR, Yerevan, 1978.
- Arp, Halton, and Jack W. Sulentic, Three quasars near the spiral arms of NGC 1073, *Astrophys. J.*, 229, 496–502, 1979.
- Arp, Halton, Jack W. Sulentic, and Graziella di Tullio, Quasars aligned across NGC 3384, *Astrophys. J.*, 229, 489–495, 1979.
- Arp, Halton, W. L. W. Sargent, A. G. Willis, and C. E. Oosterbaan, An eruptive BL Lacertae object with a high redshift, 0846+51W1, *Astrophys. J.*, 230, 68–78, 1979.
- Arp, Halton, *see also* Madore, Barry F.
- Baas, F., *see* Lacy, J. H.
- Beck, S. C., *see* Geballe, T. R.
- Becklin, Eric E., and G. Neugebauer, 2.2-micron map of the central 1° of the galactic center, *Publ. Astron. Soc. Pacific*, 90, 657–660, 1978.
- Becklin, Eric E., *see also* Beckwith, S.; Nadeau, D.; Neugebauer, G.
- Beckwith, S., S. E. Persson, and G. Neugebauer, Measurements of the extinction to the molecular hydrogen emission from the Orion Nebula, *Astrophys. J.*, 227, 436–440, 1979.
- Beckwith, S., I. Gatley, K. Matthews, and G. Neugebauer, Molecular hydrogen emission from T Tauri stars, *Astrophys. J. (Lett.)*, 223, L41–L43, 1978.
- Beckwith, S., S. E. Persson, G. Neugebauer, and E. E. Becklin, Observations of the molecular hydrogen emission from the Orion Nebula, *Astrophys. J.*, 223, 464–470, 1978.
- Bergeron, J., *see* Thuan, Trinh X.
- Boggess, A., Richard Green, J. B. Oke, Maarten Schmidt, and eight coauthors, IUE observations of the quasar 3C273, *Astrophys. J. (Lett.)*, 230, L131–L136, 1979.
- Boksenberg, A., R. F. Carswell, and W. L. W. Sargent, Multiple components in the  $z = 0.424$  absorption system in the spectrum of the BL Lacertae object Pks 0735+178, *Astrophys. J.*, 227, 370–379, 1979.
- Boksenberg, A., Maarten Schmidt, and 24 co-authors, IUE observations of extragalactic objects, *Nature*, 275, 404–414, 1978.
- Boksenberg, A., *see also* Greenstein, Jesse L.; Sargent, Wallace L. W.; Young, Peter J.
- Boroson, Todd A., *see* Sargent, Wallace L. W.
- Brucato, Robert, *see* Sandage, Allan.
- Carswell, R. F., *see* Boksenberg, A.; Sargent, Wallace L. W.; Young, Peter J.
- Cohen, Judith G., *see* Frogel, Jay A.
- Darland, Jeffrey J., *see* Schneider, Donald P.
- de Bruyn, A. G., and E. Hummel, A multi-frequency continuum study of the edge-on galaxy NGC 3556, *Astron. Astrophys.*, 73, 196–201, 1979.
- de Bruyn, A. G., and Wallace L. W. Sargent, Absolute spectrophotometry of 68 Seyfert galaxy nuclei, *Astron. J.*, 83, 1257–1292, 1978.
- de Bruyn, A. G., *see also* Katgert, P.
- di Tullio, Graziella, *see* Arp, Halton.
- Dressler, Alan, A comprehensive study of 12 very rich clusters of galaxies, II, Dynamics, *Astrophys. J.*, 226, 55–69, 1978.
- Elias, J. H., 2.2- $\mu$ m field stars at the north galactic pole, *Astron. J.*, 83, 791–794, 1978.
- Elias, J. H., A study of the IC 5146 dark cloud complex, *Astrophys. J.*, 223, 859–875, 1978.
- Elias, J. H., An infrared study of the Ophiuchus dark cloud, *Astrophys. J.*, 224, 453–472, 1978.
- Elias, J. H., A study of the Taurus dark cloud complex, *Astrophys. J.*, 224, 857–872, 1978.
- Elias, J. H., H. Lanning, and G. Neugebauer, Infrared and optical variations in  $\alpha$  Cassiopeiae (HD 4180), *Publ. Astron. Soc. Pacific*, 90, 697–702, 1978.
- Elias, J. H., *see also* Hoessel, J. G.; Nadeau, D.; Wade, R. A.
- Ennis, D., *see* Huggins, P. J.; Nadeau, D.
- Frogel, Jay A., S. E. Persson, and Judith G. Cohen, Infrared colors, CO band strengths, and physical parameters for giants in M71, *Astrophys. J.*, 227, 499–509, 1979.
- Frogel, Jay A., *see also* Persson, S. Eric.

- Gatley, I., *see* Beckwith, S.
- Geballe, T. R., J. H. Lacy, and S. C. Beck, The eight-micron band of silicon monoxide in the expanding cloud around VY Canis Majoris, *Astrophys. J. (Lett.)*, 230, L47-L51, 1979.
- Geballe, T. R., *see also* Lacy, J. H.; Nadeau, D.
- Giclas, Henry, *see* Greenstein, Jesse L.
- Goldreich, P., *see* Nicholson, P. D.
- Green, Richard F., and Michael E. Morrill, An automated technique for stellar magnitude, color, and position measurements of astronomical photographs, *Publ. Astron. Soc. Pacific*, 542, 601-606, 1978.
- Green, Richard F., D. O. Richstone, and M. Schmidt, PG1413: a white dwarf-red dwarf eclipsing binary, *Astrophys. J.*, 224, 892-898, 1978.
- Green, Richard F., T. B. Williams, and Donald C. Morton, Spectrophotometry of the galaxies and nebulosity associated with the quasar III Zw 2, *Astrophys. J.*, 226, 729-735, 1978.
- Green, Richard F., *see also* Boggess, A.; Schmidt, Maarten.
- Greenstein, Jesse L., A further list and some properties of red degenerates, XI, *Astrophys. J.*, 227, 244-251, 1979.
- Greenstein, Jesse L., and A. Boksenberg, Studies of the magnetic white dwarfs GD 229 and Feige 7, *Mon. Notic. Roy. Astron. Soc.*, 185, 823-832, 1978.
- Greenstein, Jesse L., and Henry Giclas, An emission-line proper-motion star GD 552, *Publ. Astron. Soc. Pacific*, 90, 460-462, 1978.
- Greenstein, Jesse L., and J. B. Oke, Ultraviolet spectrophotometry of degenerate stars, *Astrophys. J. (Lett.)*, 229, L141-L144, 1979.
- Greenstein, Jesse L., J. B. Oke, and Richard Wade, H2155-304, *Int. Astron. Union Circ.*, 3324, February 5, 1979.
- Greenstein, Jesse L., *see also* Heap, S. R.
- Griffin, R. F., and James E. Gunn, Spectroscopic orbits for the Hyades dwarfs van Bueren 62, 117, and 121, *Astron. J.*, 83, 1114-1118, 1978.
- Griffin, R. F., *see also* Gunn, James E.
- Gunn, James E., and R. F. Griffin, Dynamical studies of globular clusters based on photoelectric radial velocities of individual stars, I, M3, *Astron. J.*, 84, 752-773, 1979.
- Gunn, James E., *see also* Griffin, R. F.; Knapp, G. R.; Schechter, Paul L.; Tremaine, Scott.
- Hardy, Eduardo, The population structure of the Large Magellanic Cloud, II, Count-brightness ratios for the central regions, *Astrophys. J.*, 223, 98-108, 1978.
- Hauser, M. G., *see* Werner, Michael W.
- Heap, S. R., Jesse L. Greenstein, and 16 co-authors, IUE observations of hot stars: HZ43, BD+75°325, NGC 6825, SS Cygni,  $\eta$  Carinae, *Nature*, 275, 385-388, 1978.
- Hoessel, J. G., J. H. Elias, R. A. Wade, and J. P. Huchra, A near infrared photographic survey of the galactic plane, *Publ. Astron. Soc. Pacific*, 91, 41-45, 1979.
- Hoessel, J. G., *see also* Wade, R. A.
- Houck, J. R., *see* Werner, Michael W.
- Howard, Robert, Evidence for large-scale velocity features on the Sun, *Astrophys. J. (Lett.)*, 228, L45-L50, 1979.
- Howard, Robert, The rotation of the Sun, *Rev. Geophys. Space Phys.*, 16, 721-732, 1978.
- Howard, Robert, Magnetic field rotation at high solar latitudes, *Solar Phys.*, 59, 243-248, 1978.
- Huchra, J. P., *see* Hoessel, J. P.; Wade, R. A.
- Huggins, P. J., T. G. Phillips, G. Neugebauer, M. W. Werner, P. G. Wannier, and D. Ennis, The detection of the  $J = 3-2$  lines of HCN, HNC, and HCO<sup>+</sup> in the Orion molecular cloud, *Astrophys. J.*, 227, 441-445, 1979.
- Hummel, E., *see* de Bruyn, A. G.
- Hurford, G. J., *see* Marsh, K. A.; Zirin, Harold.
- Karachentsev, I. D., W. L. W. Sargent, and Barbara Zimmerman, Radial velocities and masses for 44 binary galaxies, *Astrofizika*, 15, 25-32, 1979.
- Katgert, P., A. G. de Bruyn, and A. G. Willis, Optical identification of the radio sources in the third Westerbork survey, *Astron. Astrophys., Suppl. Ser.*, 36, 213-225, 1979.
- Kent, S. M., An SIT vidicon detector system for the Palomar 1.5-meter telescope, *Publ. Astron. Soc. Pacific*, 91, 394-397, 1979.
- Kent, S. M., and W. L. W. Sargent, Ionization and excitation mechanisms in the filaments around NGC 1275, *Astrophys. J.*, 230, 667-680, 1979.
- Knapp, G. R., S. D. Tremaine, and James E. Gunn, The global properties of the galaxy,



- I, The H I distribution outside the solar cycle, *Astron. J.*, 83, 1585-1593, 1978.
- Kowal, Charles T., Periodic Comet Jackson-Neujmin (1978q), *Int. Astron. Union Circ.*, 3311, December 4, 1978.
- Kowal, Charles T., Comet Kowal (1979a), *Int. Astron. Union Circ.*, 3321, January 30, 1979; 3322, January 31, 1979.
- Kowal, Charles T., 1977 HA, *Int. Astron. Union Circ.*, 3371, June 21, 1979.
- Kowal, Charles T., W. Liller, and B. G. Marsden, The discovery and orbit of (2060) Chiron, in *Dynamics of the Solar System*, *Int. Astron. Union Symp. No. 81*, pp. 245-250, R. L. Duncombe, ed., D. Reidel Publishing Co., Dordrecht, Holland, 1979.
- Kowal, Charles T., K. Y. Lo, and W. L. W. Sargent, New galaxies of the Local Group, *Int. Astron. Union Circ.*, 3324, November 13, 1978.
- Kristian, Jerome, and James A. Westphal, Visible candidate for the binary pulsar, *Int. Astron. Union Circ.*, 3242, July 7, 1978.
- Krzeminski, W., *see* Priedhorsky, W.
- Kunth, Daniel, and Wallace L. W. Sargent, Spectrophotometry of six Seyfert galaxies from the Zwicky lists, *Astron. Astrophys.*, 76, 50-59, 1979.
- LaBonte, Barry J., Activity in the quiet Sun, I, Observations of macrospicules in H $\alpha$  and D $_3$ , *Solar Phys.*, 61, 283-296, 1979.
- Lacy, J. H., F. Baas, C. H. Townes, and T. R. Geballe, Observations of the motion and distribution of the ionized gas in the central parsec of the galaxy, *Astrophys. J. (Lett.)*, 227, L17-L20, 1979.
- Lacy, J. H., *see* Geballe, T. R.
- Lanning, Howard, *see* Elias, J.
- Lauer, T. R., *see* Oke, J. B.
- Leung, Kam-Ching, and Donald P. Schneider, Evolved contact systems of spectral type O, III, V729 Cygnus, *Astrophys. J.*, 224, 565-569, 1978.
- Leung, Kam-Ching, *see also* Schneider, Donald P.
- Liller, W., *see* Kowal, Charles T.
- Lo, K. Y., and W. L. W. Sargent, A search for intergalactic neutral hydrogen in three nearby groups of galaxies, *Astrophys. J.*, 227, 756-766, 1979.
- Lo, K. Y., *see also* Kowal, C. T.
- Madore, Barry F., and Halton Arp, Three new faint star clusters, *Astrophys. J. (Lett.)*, 227, L103-L104, 1979.
- Marsden, B. G., *see* Kowal, Charles T.
- Marsh, K. A., Ephemeral region flares and the diffusion of the network, *Solar Phys.*, 59, 105-113, 1978.
- Marsh, K. A., H. Zirin, and G. J. Hurford, VLA observations of solar flares, interpreted with optical, x-ray, and other microwave data, *Astrophys. J.*, 228, 610-615, 1979.
- Marsh, K. A., *see also* Zirin, Harold.
- Matthews, Keith, *see* Beckwith, S.; Nadeau, D.; Neugebauer, G.; Nicholson, P. D.; Priedhorsky, W.; Soifer, B. T.
- Melnick, Jorge, On the distribution of dust in giant extragalactic H II regions, *Astrophys. J.*, 228, 112-117, 1979.
- Miller, William C., From the dark ages onward, in *Modern Techniques in Astronomical Photography*, pp. 1-13, R. M. West and J. L. Heudier, eds., European Southern Observatory, Geneva, Switzerland, 1978.
- Mochnecki, Stefan, Novalike object in Vulpecula, *Int. Astron. Union Circ.*, 3350, April 24, 1979.
- Morrill, Michael E., *see* Green, Richard F.
- Morton, Donald C., *see* Green, Richard F.
- Nadeau, Daniel, and Thomas R. Geballe, Velocity profiles of the 2.1  $\mu$ m H $_2$  emission line in the Orion molecular cloud, *Astrophys. J. (Lett.)*, 230, L169-L173, 1979.
- Nadeau, Daniel, G. Neugebauer, E. E. Becklin, J. Elias, D. Ennis, K. Matthews, and K. Sellgren, The light curve at 10  $\mu$ m of Algol near secondary minimum, *Mon. Notic. Roy. Astron. Soc.*, 184, 523-525, 1978.
- Neugebauer, Gerry, J. B. Oke, E. E. Becklin, and K. Matthews, Absolute spectral-energy distribution of quasi-stellar objects from 0.3 to 10 microns, *Astrophys. J.*, 230, 79-94, 1979.
- Neugebauer, Gerry, *see also* Becklin, Eric E.; Elias, J. H.; Huggins, P. J.; Nadeau, D.; Nicholson, P. D.; Priedhorsky, W.; Soifer, B. T.; Werner, Michael W.
- Nicholson, P. D., S. E. Persson, K. Matthews, P. Goldreich, and G. Neugebauer, The rings of Uranus: results of the 1978 April 10 occultation, *Astron. J.*, 83, 1240-1248, 1978.
- Oke, J. B., Seyfert galaxies and quasars, *J. Roy. Astron. Soc. Canada*, 72, 121-137, 1978.

- Oke, J. B., and T. R. Lauer, An analysis of the spectra of the Seyfert galaxies Markarian 79 and I Zw 1, *Astrophys. J.*, 230, 360-372, 1979.
- Oke, J. B., *see also* Boggess, A.; Greenstein, J. L.; Neugebauer, G.; Racine, René; Soifer, B. T.; Thuan, Trinh X.; Yee, H. K. C.
- Oosterbaan, C. E., *see* Arp, Halton.
- Persson, S. E., H2155-304, *Int. Astron. Union Circ.*, 3324, February 5, 1979.
- Persson, S. E., Jay A. Frogel, and Marc Aaronson, Photometric studies of composite stellar systems, III, *UBVR* and *JHK* observations of E and S0 galaxies, *Astrophys. J., Suppl. Ser.*, 39, 61-87, 1979.
- Persson, S. E., *see also* Beckwith, S.; Frogel, Jay A.; Nicholson, P. D.
- Phillips, T. G., *see* Huggins, P. J.
- Preston, George W., *see* Wolff, Sidney C.
- Priedhorsky, W., K. Matthews, G. Neugebauer, M. Werner, and W. Krzeminski, Joint infrared and visual monitoring of AM Herculis, *Astrophys. J.*, 226, 397-404, 1978.
- Racine, René, J. B. Oke, and Leonard Searle, The metallicity of globular clusters in the halo of M87, *Astrophys. J.*, 223, 82-87, 1978.
- Richstone, D. O., *see* Green, Richard F.
- Ritchie, D., *see* Young, Peter J.
- Sandage, Allan, Optical redshifts for 719 bright galaxies, *Astron. J.*, 83, 904-937, 1978.
- Sandage, Allan, and Robert Brucato, The Las Campanas survey of bright southern galaxies, II, New classifications for 153 systems, *Astron. J.*, 84, 472-496, 1979.
- Sandage, Allan, and Natarajan Visvanathan, The color-absolute magnitude relation for E and S0 galaxies, II, New colors, magnitudes, types, and velocities for 405 galaxies, *Astrophys. J.*, 223, 707-729, 1978.
- Sandage, Allan, and Natarajan Visvanathan, Color-absolute magnitude relation for E and S0 galaxies, III, Fully corrected photometry for 405 galaxies: comparison of color distributions for E and S0 field and cluster galaxies, *Astrophys. J.*, 225, 742-750, 1978.
- Sargent, Wallace L. W., and Todd A. Boroson, An attempt to measure the extended Lyman- $\alpha$  emission from the absorbing regions of five QSOs, *Astrophys. J.*, 228, 712-717, 1979.
- Sargent, Wallace L. W., Peter J. Young, A. Boksenberg, R. F. Carswell, and J. A. J. Whelan, A high-resolution study of the QSOs Q 0002-422 and Q 0453-423, *Astrophys. J.*, 230, 49-67, 1979.
- Sargent, Wallace L. W., *see also* Arp, H.; Boksenberg, A.; de Bruyn, A. G.; Karachentsev, I. D.; Kent, S. M.; Kowal, C. T.; Kunth, Daniel; Lo, K. Y.; Stauffer, John; Young, Peter J.
- Schechter, Paul L., and James E. Gunn, Observations of the internal dynamics of twelve elliptical galaxies, *Astrophys. J.*, 229, 472-484, 1979.
- Schechter, Paul L., and James E. Gunn, NGC 2685: spindle or pancake? *Astron. J.*, 83, 1360-1362, 1978.
- Schmidt, Maarten, and Richard Green, Nova-like object in Vulpecula, *Int. Astron. Union Circ.*, 3350, April 24, 1979.
- Schmidt, Maarten, *see also* Boggess, A.; Boksenberg, A.; Green, Richard F.
- Schneider, Donald P., and Kam-Ching Leung, Evolved contact systems of spectral type O, II, AO Cassiopeiae, *Astrophys. J.*, 223, 202-206, 1978.
- Schneider, Donald P., Jeffrey J. Darland, and Kam-Ching Leung, Semidetached systems of spectral type B: BF Aurigae,  $\mu^1$  Scorpii, and V Puppis, *Astron. J.*, 84, 236-243, 1979.
- Schneider, Donald P., *see also* Leung, Kam-Ching; Young, Peter J.
- Searle, Leonard, and Robert Zinn, Compositions of halo clusters and the formation of the galactic halo, *Astrophys. J.*, 225, 357-379, 1978.
- Searle, Leonard, *see also* Racine, René.
- Sellgren, K., *see* Nadeau, D.
- Soifer, B. T., G. Neugebauer, and K. Matthews, Infrared observations of the x-ray quasars 0241+622 and MR 2251-178, *Nature*, 278, 231-232, 1979.
- Soifer, B. T., J. B. Oke, K. Matthews, and G. Neugebauer, The hydrogen lines in the high-luminosity quasar B2122+35, *Astrophys. J. (Lett.)*, 227, L1-L3, 1979.
- Spinrad, Hyron, *see* Stauffer, John.
- Stauffer, John, Hyron Spinrad, and W. L. W. Sargent, New redshifts for galaxies in Abell 2255, *Astrophys. J.*, 228, 379-384, 1979.
- Sulentic, Jack W., *see* Arp, Halton.
- Tanaka, Katsuo, Measurement and analysis of magnetic-field variation during a class 2B flare, *Solar Phys.*, 58, 149-163, 1978.



- Tang, Frances, Umbral flares, *Solar Phys.*, 60, 119–122, 1978.
- Thuan, Trinh X., J. B. Oke, and J. Bergeron, The emission-line spectrum of 3C48, *Astrophys. J.*, 230, 340–347, 1979.
- Townes, C. H., *see* Lacy, J. H.
- Tremaine, Scott, and James E. Gunn, The dynamical role of light neutral leptons in cosmology, *Phys. Rev. (Lett.)*, 42, 407–410, 1979.
- Tremaine, Scott, *see also* Knapp, G. R.
- Visvanathan, Natarajan, *see* Sandage, Allan.
- Wade, Richard A., A spectrophotometric parallax for U Geminorum, *Astron. J.*, 84, 559–561, 1979.
- Wade, Richard A., J. G. Hoessel, J. H. Elias, and J. P. Huchra, A two-color photometric system for the near infrared, *Publ. Astron. Soc. Pacific*, 91, 35–40, 1979.
- Wade, Richard A., *see also* Greenstein, Jesse L.; Hoessel, J. G.
- Wannier, P. G., *see* Huggins, P. J.
- Werner, M. W., G. Neugebauer, J. R. Houck, and M. G. Hauser, One-millimeter brightness temperatures of the planets, *Icarus*, 35, 289–296, 1978.
- Werner, M. W., *see also* Huggins, P. J.; Priedhorsky, W.
- Westphal, James A. *see* Kristian, Jerome.
- Whelan, J. A. J., *see* Sargent, Wallace L. W.; Young, Peter J.
- Williams, T. B., *see* Green, Richard F.
- Willis, A. G., *see* Arp, Halton; Katgert, P.
- Wilson, Olin C., Chromospheric variations in main-sequence stars, *Astrophys. J.*, 226, 379–396, 1978.
- Wolff, Sidney C., and George W. Preston, Late B-type stars: rotation and the incidence of the HgMn stars, *Astrophys. J., Suppl. Ser.*, 37, 371–392, 1978.
- Wolff, Sidney C., and George W. Preston, The magnetic, spectrum, and photometric variations of the Ap star 52 Herculis, *Publ. Astron. Soc. Pacific*, 90, 406–411, 1978.
- Yee, H. K. C., and J. B. Oke, Photoelectric spectrophotometry of radio galaxies, *Astrophys. J.*, 226, 753–769, 1978.
- Young, Peter J., and D. Ritchie, Supernova in MCG 10-16-117, *Int. Astron. Union Circ.*, 3242, July 7, 1978.
- Young, Peter J., and Donald P. Schneider, Improved infrared observations of AM Herculis, *Astrophys. J.*, 230, 502–518, 1979.
- Young, Peter J., Wallace L. W. Sargent, A. Boksenberg, R. F. Carswell, and J. A. J. Whelan, A high-resolution study of the absorption spectrum of Pks 2126–158, *Astrophys. J.*, 229, 891–908, 1979.
- Young, Peter J., *see also* Sargent, Wallace L. W.
- Zimmerman, Barbara, *see* Karachentsev, I. D.
- Zinn, Robert, The metal abundance range in the Draco dwarf galaxy, *Astrophys. J.*, 225, 790–803, 1978.
- Zinn, Robert, *see also* Searle, Leonard.
- Zirin, Harold, The ecology of prominences, in *Physics of Solar Prominences*, *Int. Astron. Union Coll. No. 44*, pp. 193–208, E. Jensen, ed., Institute of Theoretical Astrophysics, Blindern, Oslo, 1978.
- Zirin, Harold, Studies of solar flares using optical, x-ray, and radio data, *Solar Phys.* 58, 95–120, 1978.
- Zirin, Harold, G. H. Hurford, and K. Marsh, The small-scale sources of quiet-sun cm-wave radio emission, *Astrophys. J.*, 224, 1043–1047, 1978.
- Zirin, Harold, *see also* Marsh, K. A.

## PERSONNEL

*Year Ended June 30, 1979*

Dr. Judith G. Cohen was appointed a Staff Member of the Hale Observatories, effective January 15, 1979.

*Research Division**Staff Members*

Halton C. Arp  
 Horace W. Babcock  
 Judith G. Cohen<sup>1</sup>  
 Jesse L. Greenstein<sup>2</sup>  
 James E. Gunn<sup>3</sup>  
 Robert F. Howard  
 Jerome Kristian  
 Robert B. Leighton<sup>4</sup>  
 Gerry Neugebauer<sup>4</sup>  
 J. Beverley Oke<sup>3</sup>  
 S. Eric Persson  
 George W. Preston, *Assistant Director,*  
*Mount Wilson*  
 Allan R. Sandage  
 Wallace L. W. Sargent<sup>5</sup>  
 Maarten Schmidt,<sup>3</sup> *Director*  
 Leonard Searle  
 Stephen A. Shectman  
 Arthur H. Vaughan  
 James A. Westphal<sup>6</sup>  
 Harold Zirin<sup>7</sup>

*Members Engaged in Post-Retirement Studies*

Alexander Pogo  
 Henrietta H. Swope  
 Olin C. Wilson

<sup>1</sup> Associate Professor of Astronomy, California Institute of Technology.

<sup>2</sup> Lee A. DuBridge Professor of Astrophysics, California Institute of Technology.

<sup>3</sup> Professor of Astronomy, California Institute of Technology.

<sup>4</sup> Professor of Physics, California Institute of Technology.

<sup>5</sup> Professor of Astronomy and Executive Officer for Astronomy, California Institute of Technology.

<sup>6</sup> Professor of Planetary Science, California Institute of Technology.

<sup>7</sup> Chief Astronomer of Big Bear Solar Observatory; Professor of Astrophysics, California Institute of Technology.

*Staff Associates*

Robert J. Brucato<sup>8</sup>  
 Charles T. Kowal<sup>9</sup>  
 Jean J. Lorre<sup>10</sup>  
 Keith Matthews<sup>9</sup>  
 B. Thomas Soifer<sup>11</sup>  
 John T. Trauger<sup>11</sup>  
 Michael W. Werner<sup>12</sup>

*Senior Research Fellows*

Alan M. Dressler<sup>13</sup>  
 Thomas R. Geballe<sup>13</sup>  
 Ronald Moore<sup>11</sup>  
 Robert J. Zinn<sup>13</sup>

*Research Fellows*

Thomas B. Ake III<sup>14</sup>  
 Peter L. Cottrell<sup>14</sup>  
 Gary S. Da Costa<sup>15</sup>  
 A. Ger de Bruyn<sup>15, 16</sup>  
 Richard F. Green<sup>14</sup>  
 Frank P. Israel<sup>14</sup>  
 Robert C. Kennicutt, Jr.<sup>15</sup>  
 Barry J. LaBonte  
 Stefan Mochnecki<sup>14</sup>  
 Jeremy R. Mould<sup>15</sup>  
 Larry D. Petro<sup>15, 17</sup>  
 James A. Rose<sup>15, 18</sup>  
 Anneila I. Sargent<sup>14</sup>  
 Robert Schommer<sup>14, 19</sup>  
 Jack W. Sulentic<sup>20</sup>  
 Peter L. Young<sup>14</sup>

<sup>8</sup> Scientific Officer, Las Campanas Observatory.

<sup>9</sup> Member of the Professional Staff, California Institute of Technology.

<sup>10</sup> Scientist/Member of the Professional Staff, Jet Propulsion Laboratory.

<sup>11</sup> Senior Research Fellow, California Institute of Technology.

<sup>12</sup> Assistant Professor of Physics, California Institute of Technology.

<sup>13</sup> Las Campanas Observatory Fellow.

<sup>14</sup> Research Fellow, California Institute of Technology.

<sup>15</sup> Carnegie Fellow.

<sup>16</sup> Fellowship ended September 30, 1978.

<sup>17</sup> Fellowship ended July 31, 1978.

<sup>18</sup> Fellowship ended June 30, 1979.

<sup>19</sup> Fellowship ended January 31, 1979.

<sup>20</sup> Fellowship ended September 30, 1978.



*Carnegie-Chilean Fellow*

Guido Garay

*Predoctoral Fellow Trainees*

Michael Rich

Robert Shaw

*Librarians*

Joan Gantz

Helen Z. Knudsen

Nan W. Schow<sup>21</sup>*Senior Research Assistants*

Gordon J. Hurford

Grace V. Knox

*Research Assistants*

John M. Adkins

John E. Boyden

Ken D. Clardy

Basil N. Katem

Margaret Katz

Stephen P. Padilla

Frances Y. C. Tang

*Student Observers*

Graham Berriman

Kirk D. Borne

France A. Cordova<sup>22</sup>Boris Gokham<sup>23</sup>

John G. Hoessel

Keith Horne

Stephen M. Kent

Matthew Malkan

Daniel Nadeau

Jeffrey R. Pier

Douglas M. Rabin

Abhijit Saha

Donald P. Schneider

William L. Sebok

Richard A. Wade

Howard K.-C. Yee

*Photographic Department*

John R. Bedke, Photographer

*Instrument Design and Construction*

George Avera, Electronics Engineer

Lawrence E. Blakée, Supervisor, Electronic Services

Harvey Crist, Machinist

Stephen Doro, Machinist<sup>24</sup>

Earle B. Emery, Senior Research Engineer

Jerry T. Fridenberg, Senior Electronics Engineer

C. L. Friswold, Head, Design Group

Robert D. Georgen, Machinist

Richard M. Goeden, Senior Engineer

Simon Groesz, Electronics Specialist

Fred H. Harris, Associate Electronics Engineer

William H. McLellan, Senior Engineer

Roger L. Minnix, Engineer<sup>25</sup>

Nancy A. Newton, Illustrator

Frederick G. O'Neil, Shop Foreman

Paul N. Price, Electronics Technician

Orval A. Smith, Electronics Specialist<sup>26</sup>

Edward H. Snoddy, Designer

Merle R. Sweet, Senior Electronics Technician

Robert Thicksten, Senior Electronics Technician

David F. Thompson, Senior Technical Assistant

Glenn A. Toennes, Electronics Technician<sup>27</sup>*Operation and Maintenance**Mount Wilson Observatory and Offices*

Richard T. Black, Business Manager

Robert E. Cadman, Mountain Superintendent

Herman E. Carpentier, Carpenter

David M. Carr, Night Assistant

Maynard Clark, Electronics Engineer

Hugh T. Couch, Superintendent, Buildings and Grounds<sup>28</sup>

Helen S. Czaplicki, Editor

Bette DeSmet, Secretary<sup>29</sup>

James Frazer, Night Assistant

Hazel M. Fulton, Head Stewardess

Pamela Gilman, Secretary

Rhea Goodwin, Assistant to the Director

Thomas S. Gregory, Optical Technician

Joseph F. Hacker, Mechanic

Mary Hark, Stewardess

Jeanne M. Knight, Bookkeeper

Howard H. Lanning, Night Assistant

Jose Lopez-Tiana, Purchasing Clerk

Frank Perez, Assistant Mountain Superintendent

<sup>21</sup> To January 31, 1978.<sup>22</sup> Graduated June 7, 1979.<sup>23</sup> To December 31, 1978.<sup>24</sup> To June 30, 1979.<sup>25</sup> To May 31, 1979.<sup>26</sup> To October 20, 1978.<sup>27</sup> To August 4, 1978.

William D. Qualls, Chauffeur  
 Delores Sahlin, Typist-Telephone  
 Operator  
 Glen Sanger, Senior Custodian<sup>28</sup>  
 Bernard K. Simpier, Electronics Technician  
 William D. St. John, Chauffeur<sup>30</sup>  
 Larry Webster, Night Assistant  
 Gary Yanik, Electronics Engineer

*Palomar Observatory and Robinson  
 Laboratory*

Ranney G. Adams, Night Assistant<sup>31</sup>  
 Albert R. Andrews, Maintenance Mechanic  
 Charles L. D. Beishline, Maintenance  
 Mechanic  
 Jan Andriaan Bruinsma, Painter and  
 Senior Custodian  
 Maria J. Bruinsma, Housekeeping Aide<sup>32</sup>  
 Juan R. Carrasco, Senior Night Assistant  
 Lily D. Carrasco, Housekeeping Aide<sup>33</sup>  
 Bruce M. Cuney, Maintenance Mechanic  
 and Relief Night Assistant  
 Anita Dietz, Housekeeping Aide  
 Ronald B. Druliner, Maintenance  
 Mechanic  
 Rita A. Ewing, Secretary<sup>34</sup>  
 Liselotte M. Hauck, Senior Administrative  
 Assistant  
 Roger Higson, Night Assistant  
 Helen Holloway, Administrative Secretary  
 Willie D. Jones, Custodian<sup>35</sup>  
 Taras Kiceniuk, Mountain Superintendent<sup>36</sup>  
 J. Luz Lara, Maintenance Mechanic  
 Maria Alicia Lara, Housekeeping Aide  
 Isolde Lata, Administrative Secretary<sup>35</sup>  
 Charles L. Miller, Custodian

<sup>28</sup> Retired June 30, 1979.

<sup>29</sup> To September 30, 1978.

<sup>30</sup> Retired July 31, 1978.

<sup>31</sup> To March 8, 1979.

<sup>32</sup> To March 8, 1979.

<sup>33</sup> To October 24, 1978.

<sup>34</sup> To July 31, 1978.

<sup>35</sup> To September 8, 1978.

Thomas Murphy, Maintenance Mechanic  
 and Relief Night Assistant  
 Petra Ornelas, Department Clerk  
 Ruth E. Rabin, Administrative Aide  
 Marilynne J. Rice, Senior Administrative  
 Secretary  
 Spencer D. Shidner, Maintenance Mechanic  
 and Relief Night Assistant<sup>37</sup>  
 Barrett A. Staples, Night Assistant  
 Elsa-Brita Titchenell, Administrative  
 Secretary  
 Gary M. Tuton, Superintendent  
 Verdella M. Tuton, Secretary  
 Paul Van Ligten, Assistant Superintendent  
 Larry L. Wickern, Assistant  
 Superintendent<sup>38</sup>  
 David K. Williams, Maintenance  
 Mechanic<sup>39</sup>  
 Dorothy Williams, Cook  
 Barbara A. Zimmerman, Computing  
 Analyst<sup>9</sup>

*Big Bear Solar Observatory*

Alberta R. Altman, Secretary  
 Jack R. Klemroth, Solar Observer  
 Eugene H. Longbrake, Solar Observer  
 Walter M. Nagao, Custodian<sup>40</sup>  
 Alan P. Patterson, Superintendent  
 Owen Phairis, Solar Observer  
 Linda P. Zydek, Film Processor and  
 Custodian

*Las Campanas Observatory*

Ljubomir Papic, Mountain Superintendent  
 Antonio Urrutia, Administrative Staff  
 Member (part-time)  
 Manfred Wagner, Administrative Manager

<sup>36</sup> To September 4, 1978.

<sup>37</sup> Educational training leave of absence, May  
 14, 1979.

<sup>38</sup> To July 28, 1978.

<sup>39</sup> To August 17, 1978.

<sup>40</sup> Retired March 30, 1979.



## *Administrative Reports*





# Office of Administration

1530 P Street, N.W.  
Washington, D.C. 20005

## OFFICE OF THE PRESIDENT

James D. Ebert, *President*  
Montgomery S. Bradley, *Special Assistant, Corporate Sponsors Program*<sup>1</sup>  
Franklin H. Portugal, *Historian*  
Julia G. Thompson, *Secretary*  
Susan Y. Vasquez, *Assistant to the President*  
Christopher Wright, *Staff Member (Science Policy and Institutional Development)*<sup>1</sup>

## OFFICE OF THE BURSAR

James W. Boise, *Bursar*  
Candace J. Armstrong, *Secretary*<sup>2</sup>  
Patricia Gibbs, *Secretary*<sup>3</sup>  
Mary G. Hedger, *Administrative Assistant*<sup>4</sup>  
Kenneth R. Henard, *Assistant Bursar*  
Joseph M. S. Haraburda, *Assistant to the Bursar*  
Sherman L. E. Johnson, *Payroll Supervisor*  
Richard S. Kuzmyak, *Accountant*<sup>5</sup>  
Cathy D. Morningstar, *Secretary*<sup>6</sup>  
Diep T. Nguyen, *Secretary*<sup>7</sup>  
Arnold J. Pryor, *Computer Operations Supervisor*  
Terry L. Stahl, *Accountant*<sup>8</sup>

## PUBLICATIONS OFFICE

Sheila McGough, *Editor, Publications Officer*  
Ray L. Bowers, *Assistant Editor*  
Barry P. Fay, *Assistant Editor*<sup>9</sup>  
Courtland Lewis, *Assistant Editor*<sup>10</sup>

## ADMINISTRATIVE OFFICE

Richard E. Hewitt, *Administrative Officer for Services*  
Lloyd H. Allen, *Custodian*  
Don A. Brooks, *Custodian*  
Delinda Tilghman, *Secretary*<sup>11</sup>  
Helen R. Wallace, *Secretary-Receptionist*<sup>12</sup>

<sup>1</sup> From July 1, 1979.

<sup>2</sup> From June 11, 1979.

<sup>3</sup> From July 10, 1978, to September 1, 1978.

<sup>4</sup> Retired June 30, 1979.

<sup>5</sup> From October 24, 1978.

<sup>6</sup> From September 7, 1978, to September 29, 1978.

<sup>7</sup> From October 2, 1978.

<sup>8</sup> To September 25, 1978.

<sup>9</sup> From January 2, 1979.

<sup>10</sup> To November 15, 1978.

<sup>11</sup> From July 26, 1978.

<sup>12</sup> From June 14, 1979.





# Bibliography

July 1, 1978–June 30, 1979\*

## PUBLICATIONS OF THE INSTITUTION

*Carnegie Institution of Washington Year Book 77*. viii + 35 + 998 pages, 472 figures, December 1978.

*Carnegie Institution of Washington Catalogue 1979–1980*. 80 pages, 24 figures.

*Carnegie Institution of Washington Newsletter*. Issued in December 1978, April and July 1979.

*Books in Science*. 8 pages. Catalogue of in-print book titles, June 1979.

*On the Mathematical Derivation of Gibbs's Equation (98) from Experimentally Determinable Thermodynamic Relations*, Supplementary Publication 49, by George

Tunell, 58 pages, 50 copies; reprints on demand from University Microfilms International, Inc., Ann Arbor, Michigan, June 1979.

## PUBLICATIONS BY THE PRESIDENT OF THE INSTITUTION

James D. Ebert

*Mechanisms of Cell Change*, J. D. Ebert and T. S. Okada, eds., John Wiley and Sons, New York, 1979.

Retention of intact Concanavalin A and *Lens culinaris* lectin in transformed lymphoblasts during mitogenic response [with Keiko Ozato], *Cellular Immunol.*, 37, 273–284, 1978.

\* Scientific publications by Staff Members and Fellows of the Institution are listed in the reports of the several departments.





# *Report of the Executive Committee*

*To the Trustees of the Carnegie Institution of Washington*

Gentlemen: In accordance with the provisions of the By-Laws, the Executive Committee submits this report to the Annual Meeting of the Board of Trustees.

During the fiscal year ending June 30, 1979, the Executive Committee held five meetings. Printed accounts of these meetings have been or will be mailed to each Trustee.

The estimate of expenditures for the fiscal year beginning July 1, 1979, has been reviewed by the Executive Committee.

Four vacancies exist in the membership of the Board of Trustees resulting from the resignations of J. Paul Austin, Walter H. Page, William M. Roth, and James N. White. Mr. Austin's resignation also created a vacancy on the Executive Committee, which has not been filled, and Mr. Roth's resignation will create a vacancy on the Nominating Committee.

The terms of the Vice-Chairman and Secretary of the Board, all Committee Chairmen, and the following members of Committees also expire on May 1, 1979:

*Finance Committee*  
William T. Golden

*Nominating Committee*  
John Diebold

*Auditing Committee*  
Juan T. Trippe

William C. Greenough, *Chairman*

*May 1, 1979*





# *Abstract of Minutes*

## *of the Eighty-Second Meeting of the Board of Trustees*

The annual meeting of the Board of Trustees was held in the Board Room of the Administration Building on Tuesday, May 1, 1979. The meeting was called to order by Chairman Frank Stanton.

The following Trustees were present: Philip H. Abelson, John Diebold, Carl J. Gilbert, William T. Golden, Crawford H. Greenewalt, William C. Greenough, Caryl P. Haskins, William R. Hewlett, William McChesney Martin, Jr., Franklin D. Murphy, Robert M. Pennoyer, Richard S. Perkins, William M. Roth, Robert C. Seamans, Jr., Frank Stanton, and Charles H. Townes. Also present were Garrison Norton and Charles P. Taft, Trustees Emeriti, James D. Ebert, President, James W. Boise, Bursar, Marshall Hornblower, Counsel, and by special invitation, Fred Mann, Secretary and Treasurer of the Carnegie Dunfermline Trust.

The minutes of the Eighty-First Meeting were approved.

The resignations of J. Paul Austin, Walter H. Page, William M. Roth, and James N. White were accepted with regret. Mr. White was designated Trustee Emeritus.

The reports of the Executive Committee, the Finance Committee, the Employee Benefits Committee, and the Auditing Committee were accepted. On the recommendation of the latter, it was resolved that Arthur Andersen & Co. be reappointed as public accountants for the fiscal year beginning July 1, 1979.

On the recommendation of the Nominating Committee, William C. Greenough was elected Vice-Chairman of the Board and William T. Golden was elected Secretary of the Board, both for terms ending in 1982.

The following were elected for one-year terms: William C. Greenough, as Chairman of the Executive Committee; Richard S. Perkins, as Chairman of the Finance Committee; Crawford H. Greenewalt, as Chairman of the Auditing Committee; Robert C. Seamans, Jr., as Chairman of the Nominating Committee; and Carl J. Gilbert, as Chairman of the Employee Benefits Committee.

Vacancies in Standing Committees, with terms ending in 1982, were filled as follows: William T. Golden was elected a member of the Finance Committee; Lewis M. Branscomb was elected a member of the Auditing Committee; and Franklin D. Murphy was elected a member of the Nominating Committee. In addition, William R. Hewlett was elected a member of the Executive Committee for the unexpired term ending in 1981 and Robert M. Pennoyer was elected a member of the Nominating Committee for the unexpired term ending in 1981.

The annual report of the President was accepted.

To provide for the operation of the Institution for the fiscal year beginning July 1, 1979, and upon recommendation of the Executive Committee, the sum of \$9,210,300 was appropriated.





# *Financial Statement*

*for the year ended June 30, 1979*

CARNEGIE INSTITUTION OF WASHINGTON  
TEN-YEAR FINANCIAL SUMMARY, 1970-1979  
(All Figures are Thousands of Dollars)

	Total											
	Fiscal Year Ended June 30	1970-1979	1979 <sup>3</sup>	1978 <sup>3</sup>	1977 <sup>3</sup>	1976 <sup>3</sup>	1975 <sup>3</sup>	1974 <sup>3</sup>	1973	1972	1971	1970
Receipts												
Interest and dividends		\$41,273	\$ 5,256	\$ 5,019	\$ 4,675	\$ 3,958	\$ 3,295	\$ 3,356	\$ 3,647	\$ 3,863	\$ 4,127	\$ 4,077
Other		1,251	306	80	338	126	83	60	58	65	90	45
Restricted grants, expended <sup>1</sup>		8,187	1,805	1,544	1,077	772	447	484	554	470	517	517
Total		<u>\$50,711</u>	<u>\$ 7,367</u>	<u>\$ 6,643</u>	<u>\$ 6,090</u>	<u>\$ 4,856</u>	<u>\$ 3,825</u>	<u>\$ 3,900</u>	<u>\$ 4,259</u>	<u>\$ 4,398</u>	<u>\$ 4,734</u>	<u>4,639</u>
Expenditures												
Terrestrial Magnetism		\$10,243	\$ 1,000	\$ 1,106	\$ 1,209	\$ 1,046	\$ 1,188	\$ 1,025	\$ 1,022	\$ 937	\$ 909	\$ 801
Mount Wilson Observatory		10,818	1,191	1,168	1,204	1,085	1,027	1,051	1,016	992	930	1,154
Las Campanas Observatory		14,295	792	700	1,056	1,753	2,138	2,572	2,559	1,075	1,184	466
Geophysical Laboratory		10,081	1,284	1,202	1,162	1,032	1,136	964	984	770	779	768
Embryology		7,689	815	818	900	816	851	791	718	699	668	613
Plant Biology		5,363	537	530	636	620	1,270	673	330	271	252	244
Genetics Research Units		632	22	22	23	22	24	70	65	68	165	151
Research Projects, etc.		758	168	85	92	89	51	98	29	22	61	63
Office of Administration		5,683	710	602	577	500	571	520	592	583	559	469
General publications		746	62	78	59	66	78	57	79	58	98	111
Consulting fees, insurance, taxes		1,252	175	216	226	158	134	95	62	67	75	44
Employee benefits, special		1,000	143	145	117	102	81	89	97	78	77	71
Financial advisory, services		1,867	308	265	238	205	213	199	195	108	66	70
Restricted grants <sup>1</sup>		8,187	1,805	1,544	1,077	772	447	484	554	470	517	517
Total <sup>2</sup>		<u>\$78,614</u>	<u>\$ 9,012</u>	<u>\$ 8,481</u>	<u>\$ 8,576</u>	<u>\$ 8,266</u>	<u>\$ 9,209</u>	<u>\$ 8,688</u>	<u>\$ 8,302</u>	<u>\$ 6,198</u>	<u>\$ 6,340</u>	<u>\$ 5,542</u>
Restricted grants, unexpended <sup>1</sup>			(284)	\$ 777	\$ 95	\$ 430	\$ 368	\$ 21	( \$ 10)	( \$ 26)	( \$ 34)	( \$ 80)
Gifts received			998	637	241	41	146	330	377	354	611	5
Total market value of investments			86,425	84,136	89,287	92,215	93,719	98,200	124,770	128,826	113,042	89,000

SEE FOOTNOTES 1, 2, 3 ATTACHED.



CARNEGIE INSTITUTION OF WASHINGTON  
FOOTNOTES TO THE TEN-YEAR FINANCIAL SUMMARY, 1970-1979

<sup>1</sup> Restricted grants for funds received from Federal Agencies, Foundations, etc., in support of specific proposals for scientific research and educational programs.

Many restricted grants received are for the entire grant period which may not coincide with the Institution's fiscal year. Accordingly, the Ten-Year Financial Summary lists separately the portions of the grants expended and unexpended within the fiscal year.

During the report period, significant grants were received from Carnegie Corporation of New York, Helen Hay Whitney Foundation, Andrew W. Mellon Foundation, Alfred P. Sloan Foundation, National Aeronautics & Space Administration, National Science Foundation, Office of Naval Research, Public Health Service, and Department of Agriculture and Interior.

<sup>2</sup> The Institution capitalizes expenditures for land, buildings, telescopes and other significant equipment, and construction projects in progress. Expenditures for other equipment are charged to current operations as incurred, and the cost of such equipment is not capitalized. The Institution follows the policy of not depreciating its buildings, telescopes and significant equipment.

Included in the Expenditures of Appropriated Funds are purchases of capitalized equipment as follows:

1979	\$ 71,994
1978	56,526
1977	316,607
1976	2,133,374
1975	2,806,042
1974	2,048,947
1973	3,078,426
1972	11,987
1971	370,566
1970	<u>371,023</u>
TOTAL	<u>\$11,265,492</u>

During the report period, significant items of capitalized equipment were:

100" Irene duPont Telescope	\$7,881,348
Plant Biology Building Annex	952,767
60" Palomar Telescope	800,800
40" Swope Telescope	541,115
Mount Wilson Observatory	
Building Annex	261,395

<sup>3</sup> In 1974, the financial statements of the Institution were prepared on the accrual basis of accounting. In prior years, the Institution used the cash receipts and disbursements basis of accounting. The purpose of this change was to conform with Audit Guides of the American Institute of Certified Public Accountants which recommend accrual basis accounting for nonprofit institutions. The differences in the financial data on the accrual basis and on the former cash basis are not material.

ARTHUR ANDERSEN & CO.

WASHINGTON, D. C.

To the Auditing Committee of

Carnegie Institution of Washington:

We have examined the statements of assets, liabilities and fund balances of CARNEGIE INSTITUTION OF WASHINGTON (a nonprofit corporation chartered by Act of the United States Congress) as of June 30, 1979 and 1978, the related statement of income, expenses and changes in fund balances for the year ended June 30, 1979, and the supplementary schedules, which are presented on the thirteen immediately following pages. Our examinations were made in accordance with generally accepted auditing standards and, accordingly, included such tests of the accounting records and such other auditing procedures as we considered necessary in the circumstances.

In our opinion, the financial statements referred to above present fairly the assets, liabilities and fund balances of Carnegie Institution of Washington as of June 30, 1979 and 1978, and the changes in fund balances for the year ended June 30, 1979, and the supplementary schedules referred to above present fairly the information set forth therein, all in conformity with generally accepted accounting principles applied on a consistent basis.

*Arthur Andersen & Co.*

Washington, D. C.,

August 16, 1979.



CARNEGIE INSTITUTION OF WASHINGTON  
NOTES TO THE FINANCIAL STATEMENTS  
JUNE 30, 1979

*Note 1*

The financial statements of the Institution are prepared substantially on the accrual basis of accounting. The Institution follows a policy of reporting all commitments outstanding at year-end as liabilities for financial statement purposes.

*Note 2*

The Institution capitalizes expenditures for land, buildings, telescopes and other significant equipment, and construction projects in progress. Expenditures for other equipment are charged to current operations as incurred, and the cost of such equipment is not capitalized. The Institution follows the policy of not depreciating its buildings, telescopes and significant equipment.

During the year the Institution sold all of its land located at Cold Spring Harbor, New York for \$200,000. Previously, the Institution had leased all of its buildings at this facility to the Cold Spring Harbor Laboratory ("Laboratory"). The buildings were located on land owned by the Laboratory and were thus essentially conveyed to it. The buildings and land carried on the books in the amount of \$988,383 has been included in "retirements" on the Statement of Income, Expenses and Changes in Fund Balances.

*Note 3—Retirement Plan*

The Institution has a noncontributory money purchase retirement plan in which all United States personnel are eligible to participate. Voluntary contributions may also be made by employees. Actuarially determined contributions are funded currently by the Institution, and there are no unfunded past service costs. The total contributions made by the Institution were \$538,299 in 1979 and \$553,851 in 1978. Benefits under the plan upon retirement are dependent upon the investment performance of the Institution's Retirement Trust. After four years' participation, benefits are fully vested.

*Note 4—Restricted Grants*

Restricted Grants are funds received from Foundations, Individuals and Federal Agencies in support of scientific research and educational programs. The Institution follows the policy of reporting only expenditures equal to income. The Restricted Grants Statement shows all of the current grants.

*Note 5—Income Taxes*

The Institution is exempt from Federal income tax under Section 501(c)(3) of the Internal Revenue Code. Accordingly, no provision for income taxes is reflected in the accompanying financial statements. The Institution is an educational institution within the meaning of Section 170(b)(1)(A)(ii) of the Code. The Internal Revenue Service has classified the Institution as other than a private foundation as defined in Section 509(a) of the Code.

CARNEGIE INSTITUTION OF WASHINGTON  
STATEMENT OF ASSETS, LIABILITIES AND FUND BALANCES  
JUNE 30, 1979 and 1978

ASSETS

	1979	1978
<i>Current Assets</i>		
Cash .....	\$ 569,745	\$ 452,151
Grants Receivable .....	306,982	159,210
Accrued Interest .....	350,998	537,327
Advances .....	<u>26,910</u>	<u>15,282</u>
	<u>1,254,635</u>	<u>1,163,970</u>
Investments (cost)* Schedule 5:		
United States Government .....	10,217,990	2,626,600
Corporate Debt Securities .....	25,149,605	31,192,775
Loan and Collateral Pledge Agreement .....	200,000	200,000
Mortgage .....	166,500	—
Corporate Stocks—Preferred .....	1,051,316	150,000
Corporate Stocks—Common .....	<u>42,311,214</u>	<u>43,910,629</u>
	<u>79,096,625</u>	<u>78,080,004</u>
Total Current Assets .....	80,351,260	79,243,974
Land .....	869,257	899,138
Buildings .....	3,884,242	4,816,816
Equipment .....	<u>10,112,818</u>	<u>10,221,752</u>
TOTAL ASSETS .....	<u>\$95,217,577</u>	<u>\$95,181,680</u>

LIABILITIES AND FUND BALANCES

*Current Liabilities*

Appropriated

Accounts Payable and Accrued Expenses

Unrestricted .....	\$ 656,526	\$ 645,008
Restricted Grants .....	126,951	67,202
Restricted Grants, received but not expended .....	<u>369,229</u>	<u>439,061</u>
Total Current Liabilities .....	<u>1,152,706</u>	<u>1,151,271</u>

*Fund Balances*

Appropriated

Unrestricted .....	1,977,551	1,593,352
Unappropriated Funds .....	77,221,003	76,499,351
Plant Fund .....	<u>14,866,317</u>	<u>15,937,706</u>
Total Fund Balances .....	<u>94,064,871</u>	<u>94,030,409</u>
TOTAL LIABILITIES AND FUND BALANCES .....	<u>\$95,217,577</u>	<u>\$95,181,680</u>

\*Approximate market value on June 30, 1979: \$86,424,691: on June 30, 1978: \$84,135,709.

The accompanying notes are an integral part of this statement.



CARNEGIE INSTITUTION OF WASHINGTON  
STATEMENT OF INCOME, EXPENSES AND CHANGES IN FUND BALANCES  
FOR THE YEARS ENDED JUNE 30, 1979 AND 1978

	Appropriated Funds			Unappropriated Funds	Plant Fund	1979	1978
	<u>Unrestricted</u>	<u>Restricted</u>	<u>Total</u>			<u>Total</u>	<u>Total</u>
<i>Income</i>							
Investment Income							
Interest	\$2,687,057	—	\$2,687,057	\$ 38,224	—	\$ 2,725,281	\$ 2,499,208
Dividends	2,531,708	—	2,531,708	—	—	2,531,708	2,520,251
Capital Gain	—	—	—	1,752,263	—	1,752,263	(101,813)
Grants—Private & Government	—	\$1,804,568	1,804,568	—	—	1,804,568	1,544,357
Other Income	305,716	—	305,716	—	—	305,716	79,534
Gifts	—	—	—	997,919	—	997,919	637,139
Total Income	5,524,481	1,804,568	7,329,049	2,788,406	—	10,117,455	7,178,676
<i>Expenses</i>							
Salaries, fringe benefits and payroll taxes	4,399,678	554,983	4,954,661	—	—	4,954,661	4,782,146
Equipment	383,689	270,152	653,841	—	—	653,841	527,491
General expenses	2,616,994	786,108	3,403,102	—	—	3,403,102	3,172,069
Indirect costs	(193,325)	193,325	—	—	—	—	—
Total Expenses	7,207,036	1,804,568	9,011,604	—	—	9,011,604	8,481,706
Income over expenses (Deficit)	(1,682,555)	—	(1,682,555)	2,788,406	—	1,105,851	(1,303,030)
<i>Transfers</i>							
Provision for Operating Deficit	2,066,754	—	2,066,754	(2,066,754)	—	—	—
Land, buildings and equipment:							
Capitalization	—	—	—	—	\$ 71,994	71,994	56,526
Retirement	—	—	—	—	(1,143,383)	(1,143,383)	(19,052)
Total Transfers	2,066,754	—	2,066,754	(2,066,754)	(1,071,389)	1,071,389	37,474
Net Change	384,199	—	384,199	721,652	(1,071,389)	34,462	(1,265,556)
Balance, beginning of year	1,593,352	—	1,593,352	76,499,351	15,937,706	94,030,409	95,295,965
Balance, end of year	\$1,977,551	\$ —	\$1,977,551	\$77,221,003	\$14,866,317	\$94,064,871	\$94,030,409

The accompanying notes are an integral part of this statement.

CARNEGIE INSTITUTION OF WASHINGTON  
SUMMARY OF INVESTMENT TRANSACTIONS  
FOR THE YEAR ENDED JUNE 30, 1979

Cash awaiting investment, June 30, 1978 .....	\$	31,639
---	----	--------

*Sales and Redemptions*

	<i>Cost</i>	<i>Capital Gain (Net)</i>
Bonds .....	\$403,644,892	\$ (627,500)
Preferred stocks .....	305,000	(41,909)
Common stocks .....	10,705,971	2,421,672
Mortgage .....	<u>33,500</u>	<u>-0-</u>
	<u>\$414,689,363</u>	<u>\$ 1,752,263</u>

Total sales and redemptions .....		416,441,626
Gifts of securities at fair market value .....		182,419
Cash transferred to Operating Fund .....		<u>(1,017,619)</u>
Total .....		\$415,638,065

*Acquisitions*

Bonds .....	\$405,675,138	
Mortgage .....	200,000	
Preferred stocks .....	1,206,316	
Common stocks .....	<u>8,442,112</u>	
Total acquisitions .....		<u>\$415,523,566</u>

Cash awaiting investment, June 30, 1979 .....	\$	<u>114,499</u>
---	----	----------------

The accompanying notes are an integral part of this statement.



CHANGES IN UNAPPROPRIATED FUNDS

FOR THE YEAR ENDED JUNE 30, 1979

	Balance July 1, 1978	Investment Income	Grants Gifts and Other Income	Capital Gain, net	Appropriations	Transfers	Balance June 30, 1979
<i>Endowment Fund</i>							
Andrew Carnegie .....	\$22,000,000	—	—	—	—	—	\$22,000,000
Sybil & William T. Golden .....	25,000	—	—	—	—	—	25,000
Anonymous Gifts .....	443,250	—	\$ 600,000	—	—	—	1,043,250
Realized Capital Gains .....	36,296,694	—	—	\$1,353,882	—	—	37,650,576
<i>Unrestricted Capital Funds</i>							
Carnegie Corporation .....	10,000,000	—	—	—	—	—	10,000,000
Carnegie Futures .....	131,152	—	70,549	—	—	—	201,701
Vannevar Bush .....	100,000	—	—	—	—	—	100,000
Realized Capital Gains .....	6,028,783	—	—	370,289	\$2,066,754	—	4,332,318
<i>Working Capital Fund</i>							
Income .....	—	\$5,163,765	—	—	5,469,481	\$305,716	—
Sale of assets .....	—	—	9,647	—	—	( 9,647)	—
Royalties .....	—	—	24,333	—	—	( 24,333)	—
Rent .....	—	—	17,520	—	—	( 17,520)	—
Refunds .....	—	—	2,853	—	—	( 2,853)	—
Sale of land .....	—	—	200,000	—	—	(200,000)	—
University of Toronto .....	—	—	38,000	—	—	( 38,000)	—
Sale of Publications .....	—	—	13,363	—	—	( 13,363)	—
Restricted Grants .....	—	—	1,804,568	—	1,804,568	—	—
<i>Special Funds</i>							
Astronomy .....	—	4,214	140,000	197	—	—	144,411
Ira S. & Mary Bowen .....	117,544	10,661	175,229	2,460	5,000	—	300,894
Bush Gift .....	21,846	2,456	—	800	—	—	25,102
Colburn .....	250,400	16,699	—	5,439	11,900	—	260,638
Hale Relief .....	7,137	408	—	129	—	—	7,674
Harkavy .....	12,098	724	—	236	600	—	12,458
Lundmark .....	48,765	2,680	—	873	2,500	—	49,818
Morganroth .....	41,024	1,918	—	625	2,000	—	41,567
Moseley Astronomy .....	111,220	6,730	12,141	2,113	5,000	—	127,204
Special Instrumentation .....	118,692	6,345	—	2,066	—	—	127,103
Special Opportunities .....	72,585	4,783	—	1,558	—	—	78,926
Wood .....	673,161	35,606	—	11,596	28,000	—	692,363
Total .....	\$76,499,351	\$5,256,989	\$3,108,203	\$1,752,263	\$9,395,803	\$	\$77,221,003

The accompanying notes are an integral part of this statement.

CARNEGIE INSTITUTION OF WASHINGTON  
SUMMARY STATEMENT OF APPROPRIATED FUNDS  
FOR THE YEAR ENDED JUNE 30, 1979

	<i>Unexpended Appropriations July 1, 1978</i>	<i>Appropriations</i>	<i>Transfers and Allotments</i>	<i>Total Expenditures</i>	<i>Unexpended Appropriations June 30, 1979</i>
Terrestrial Magnetism .....	\$ 1,423	\$1,415,626	(\$ 4,296)	\$1,385,130	\$ 27,623
Mount Wilson Observatory .....	57,989	1,511,292	28,774	1,555,565	42,490
Las Campanas Observatory .....	4,242	773,367	39,985	807,759	9,835
Geophysical Laboratory .....	16,937	1,432,078	99,141	1,511,868	36,288
Embryology .....	—	1,422,519	( 109,448)	1,313,071	—
Plant Biology .....	—	845,021	5,399	850,420	—
Genetic Research Unit .....	—	23,500	( 2,219)	21,281	—
Research Projects, etc. ....	91,947	175,200	( 69,145)	168,167	29,835
Office of Administration .....	—	660,100	50,382	710,482	—
General publications .....	—	65,000	( 3,074)	61,736	190
Consulting fees, insurance, taxes .....	—	278,000	( 102,908)	175,092	—
Retiree benefits .....	117,000	159,900	( 33,515)	140,385	103,000
Employee benefits, special .....	—	7,700	( 5,434)	2,266	—
Financial advisory services .....	—	301,500	6,882	308,382	—
Contingent operating fund .....	—	325,000	( 295,000)	—	30,000
Unallocated appropriations .....	1,303,814	—	394,476	—	1,698,290
Total .....	<u>\$1,593,352</u>	<u>\$9,395,803</u>	<u>\$ —</u>	<u>\$9,011,604</u>	<u>\$1,977,551</u>



## CARNEGIE INSTITUTION OF WASHINGTON

## SCHEDULE 3

## RESTRICTED GRANTS

FOR THE YEAR ENDED JUNE 30, 1979

	<i>Grants</i> <i>July 1, 1978</i>	<i>New</i> <i>Grants</i>	<i>Expenditures</i>	<i>Grants</i> <i>June 30, 1979</i>
American Cancer Society . . .	\$ 920	\$ 1,000	\$ 1,920	\$ —
Atlantic Richfield Company .	—	25,000	—	25,000
Carnegie Corporation of New York . . . . .	—	90,000	89,085	915
The Andrew W. Mellon Foundation . . . . .	401,105	—	194,675	206,430
Muscular Dystrophy Association . . . . .	8,391	24,788	31,185	1,994
National Academy of Sciences . . . . .	14,975	—	—	14,975
NL Industries . . . . .	—	1,000	1,000	—
National Aeronautics & Space Administration . . . .	73,164	82,413	125,503	30,074
National Science Foundation . . . . .	518,364	398,077	556,605	359,836
New York Community Trust Kenilworth Fund . . . . .	—	5,793	—	5,793
Office of Naval Research . . . .	9,186	68,400	43,709	33,877
Public Health Service . . . . .	166,126	613,438	411,291	368,273
Richard B. T. Roberts . . . . .	—	2,500	2,500	—
Alfred P. Sloan Foundation . .	502,041	—	202,040	300,001
Whitehall Foundation . . . . .	3,254	—	3,254	—
Helen Hay Whitney Foundation . . . . .	8,375	37,760	35,469	10,666
United States Department of Agriculture . . . . .	—	110,000	68,834	41,166
United States Department of Interior . . . . .	—	60,967	37,498	23,469
	<u>\$1,705,901</u>	<u>\$1,521,136</u>	<u>\$1,804,568</u>	<u>\$1,422,469</u>
Expended—Not received . . . .	\$ 159,210			\$ 306,982
Unearned—Received . . . . .	439,061			369,229
Unearned—Not received . . . .	<u>1,107,630</u>			<u>746,258</u>
	<u>\$1,705,901</u>			<u>\$1,422,469</u>

## CARNEGIE INSTITUTION OF WASHINGTON

## SCHEDULE OF EXPENSES

FOR THE YEAR ENDED JUNE 30, 1979

	<i>Appropriated Funds</i>		
	<i>Unrestricted</i>	<i>Restricted</i>	<i>Total</i>
<i>Salaries, Fringe Benefits &amp; Payroll Taxes:</i>			
Salaries .....	\$3,536,944	\$ 448,374	\$3,985,318
Fringe Benefits .....	643,172	80,442	723,614
Payroll Taxes .....	219,562	26,167	245,729
 Total Salaries, Benefits & Payroll Taxes .....	 4,399,678	 554,983	 4,954,661
<i>Equipment:</i>			
Educational & Research .....	146,605	269,730	416,335
Administrative & Operating Funds .....	98,772	297	99,069
Library .....	79,598	125	79,723
Telescope (Improvement) .....	46,066	—	46,066
Building (Improvement) .....	12,648	—	12,648
 Total Equipment .....	 383,689	 270,152	 653,841
<i>General Expenses:</i>			
Educational & Research Supplies .....	407,914	394,325	802,239
Building Maintenance .....	585,854	—	585,854
Fellowship Grants .....	154,958	300,451	455,409
Financial Advisory Service .....	308,382	—	308,382
Administrative .....	291,326	—	291,326
Travel .....	172,661	60,188	232,849
Retiree Benefits .....	140,385	—	140,385
Insurance .....	137,441	—	137,441
Awards .....	124,458	11,824	136,282
Publications .....	105,554	19,320	124,874
Consulting Fees .....	64,924	—	64,924
Commissary .....	38,466	—	38,466
Entertainment .....	36,691	—	36,691
Shop .....	23,036	—	23,036
Rent .....	20,832	—	20,832
Taxes .....	4,112	—	4,112
 Total General Expenses .....	 2,616,994	 786,108	 3,403,102
<i>Indirect Costs</i> .....	<i>(193,325)</i>	<i>193,325</i>	<i>—</i>
 TOTAL EXPENSES .....	 \$7,207,036	 \$1,804,568	 \$9,011,604

The accompanying notes are an integral part of this statement.



## SCHEDULE 5

CARNEGIE INSTITUTION OF WASHINGTON  
INVESTMENTS, JUNE 30, 1979

<i>Description</i>	<i>Par</i>	<i>Cost</i>	<i>Approximate Market</i>
United States Government Securities			
Federal Home Loan Banks, Cons., 7.30s, 1983 .....	\$ 600,000	\$ 599,625	\$ 567,000
Federal Home Loan Banks, Cons., 7.60s, 1987 .....	600,000	605,063	552,000
Federal Home Loan Mortgage, Ctf. Series 500, Group #16035, 8.50s, 2007 .....	88,461	82,855	82,971
Federal National Mortgage Association, 7.25s, 1985 .....	600,000	594,937	551,250
United States of America, Treasury Bill, 1979 .....	1,975,000	1,880,944	1,880,944
United States of America, Treasury Bill, 1979 .....	5,500,000	5,258,220	5,258,220
United States of America, Treasury Notes, 7.375s, 1981 .....	200,000	199,784	194,624
United States of America, 8.625s, 1993 .....	1,000,000	<u>996,562</u>	<u>981,870</u>
Total United States Government Securities .....		<u>10,217,990</u>	<u>10,068,879</u>
Corporate Debt Securities			
Alcan Aluminum Corp., Prom. Note, 4.75s, 1984 .....	350,000	350,000	304,063
American Hoechst Corp., Note, 5.75s, 1986 .....	537,000	537,000	470,546
American International Group, Inc., Conv. Sub. Deb., 4s, 1997 .....	175,000	147,125	178,500
Bank of America Ctf. 9.875s, 1979 .....	1,500,000	1,500,046	1,500,046
Boeing Co., Note, 6.375s, 1986 .....	428,000	428,000	379,315
Chesapeake & Potomac Tel. Co. of Va., Deb., 9.25s, 2015 .....	395,000	396,564	393,025
Churchill Falls (Labrador) Corp., Ltd., 1st Mtg. Series A, 7.75s, 2007 .....	675,000	675,000	543,375
Columbia Broadcasting System, Inc., Prom. Note, 5.50s, 1991 .....	560,000	560,000	453,600
Commonwealth Edison Co., 1st Mtg., 8.125s, 2007 .....	400,000	400,000	346,500
Crown Zellerbach Corp. Prom. Note, 4.625s, 1981 .....	75,000	75,000	70,031
Digital Equipment, Conv. Sub. Deb., 4.50s, 2002 .....	350,000	350,000	401,625
European Investment Bank, 9.125s, 1998 .....	500,000	493,125	471,250
Four Corners Pipe Line Co., Sec. Note, 5s, 1982 .....	9,000	9,000	8,933
General Motors Acceptance Corp., Prom. Note, 9.50s, 1979 .....	1,125,000	1,125,000	1,125,000
General Motors Acceptance Corp., Prom. Note, 9.50s, 1979 .....	2,515,000	2,515,000	2,515,000

CARNEGIE INSTITUTION OF WASHINGTON

INVESTMENTS, JUNE 30, 1979

<i>Description</i>	<i>Par</i>	<i>Cost</i>	<i>Approximate Market</i>
Corporate Debt Securities — Continued			
General Motors Acceptance Corp., Deb., 8.25s, 2006 .....	250,000	\$ 250,625	\$ 226,875
General Motors Acceptance Corp., 8s, 2002 .....	500,000	489,375	438,125
GNMA, Pool #14728, 7.50s, 2007 .....	588,543	530,078	510,561
GNMA, Pool #16544, 7.50s, 2007 .....	580,066	557,325	503,207
GNMA, Pool #16944, 7.50s, 2007 .....	446,684	424,629	387,498
GNMA, Pool #30102, Series A .....	999,487	970,752	954,510
GNMA, Pool #32169, Series A .....	299,810	291,200	286,319
Government of Canada, 9.25s, 1998 .....	1,000,000	1,001,250	986,250
Home Savings & Loan Association, Ctf. 2nd Series, 9.20s, 2008 .....	496,774	481,871	463,242
IAC Ltd., Sec. Note, Series Z, 5.25s, 1982 .....	750,000	750,000	630,000
Indiana Bell Telephone Co., Inc. 8.125s, 2017 .....	500,000	495,000	438,125
Inter-American Development Bank, Note, 8.25s, 1985 .....	500,000	502,500	476,875
International Bank for Reconstruction and Development, Note, 8.15s, 1985 .....	400,000	400,000	380,500
Kaiser Aluminum & Chemical Corp., 1st Mtg., 5.50s, 1987 .....	135,000	135,000	108,000
K Mart Corp., Prom. Note, 4.875s, 1983 .....	338,333	338,333	299,002
Mountain States Tel. & Tel. Co., Deb., 8.625s, 2018 .....	375,000	354,688	350,156
New Jersey Bell Telephone, Deb. 8.25s, 2016 .....	350,000	318,500	318,500
Public Service Electric & Gas Co., 1st & Ref. Mtg., 8.45s, 2006 .....	500,000	494,875	444,375
Quebec Hydro-Electric Commission, S.F., Deb., 5s, 1988 .....	546,000	536,445	395,850
Repurchase Agreement, Secured by USA Notes 9.35s, 1979 .....	1,770,000	1,770,000	1,770,000
Repurchase Agreement Secured by Continental Illinois National Bank & Trust Co., Chicago 9.75s, 1979 .....	1,753,000	1,753,000	1,753,000
Shell Funding Corp., Collat. Tr. Series B, 4.75s, 1985 .....	389,000	389,000	337,944
Tandy, Con. Sub. Deb., 6.50s, 2003 .....	190,000	185,250	172,425
United Air Lines, Inc., Note, 5s, 1984 .....	350,000	350,000	309,750
United States Steel Credit Corp., Prom. Note, 9.65s, 1979 .....	1,440,000	1,440,000	1,440,000



CARNEGIE INSTITUTION OF WASHINGTON  
INVESTMENTS, JUNE 30, 1979

<i>Description</i>	<i>Par/Shares</i>	<i>Cost</i>	<i>Approximate Market</i>
Corporate Debt Securities — <i>Continued</i>			
Woolworth (F. W.) Company, Prom. Note, 5s, 1981 .....	<u>379,049</u>	<u>\$ 379,049</u>	<u>\$ 339,723</u>
Total Corporate Debt Securities .....		<u>25149,605</u>	<u>23,881,621</u>
Mortgage			
Cold Spring Harbor Laboratory, 1983 .....	166,500	<u>166,500</u>	<u>166,500</u>
Loan and Collateral Pledge Agreement			
James D. & Alma C. Ebert (noninterest bearing loan to president secured by real estate) .....	200,000	<u>200,000</u>	<u>200,000</u>
Corporate Stocks—preferred			
Burlington Northern Inc., 2.82 .....	3,000	150,000	158,250
Time, Conv. Pfd., 1.575 .....	9,100	293,216	265,038
United Technologies Corp. ....	12,000	<u>608,100</u>	<u>606,000</u>
Total Corporate Stocks—preferred .....		<u>1,051,316</u>	<u>1,029,288</u>
Corporate Stocks—common			
Allied Stores Corp. ....	10,000	241,675	248,750
American Home Products Corp. ....	14,025	485,484	380,428
American International Group, Inc. ....	9,700	363,000	509,250
American Telephone & Telegraph Co. ....	37,755	2,367,574	2,185,070
AMP Incorporated .....	23,000	590,029	828,000
Automatic Data Processing, Inc. ....	2,500	34,003	80,313
Avnet, Inc. ....	20,000	369,500	375,000
Avon Products, Inc. ....	15,500	752,207	732,375
Big Three Industries .....	9,000	281,928	346,500
Bristol-Myers Co. ....	12,000	400,618	387,000
Cameron Iron Works, Inc. ....	2,400	69,750	132,000
Capital Holding Corp. ....	25,000	553,700	578,125
Caterpillar Tractor Co. ....	7,250	298,378	399,656
Central Telephone & Utilities Corp. ....	20,000	298,256	520,000
Cessna Aircraft .....	19,500	354,503	297,000
Charles River Breeding Laboratories, Inc. ....	1,500	59,154	42,375
Chesebrough-Pond's, Inc. ....	10,000	186,583	227,500
Citicorp .....	15,000	268,929	376,875
Clark Equipment Co. ....	6,500	244,668	251,063
Coca-Cola Company (The) ....	10,000	80,228	382,500
Colt Industries, Inc. ....	7,500	246,675	314,063
Consolidated Edison Company of New York, Inc. ....	22,400	527,436	540,400
Consolidated Foods Corp. ....	24,500	612,503	566,563
Continental Corp. ....	11,600	293,361	320,450
Continental Illinois Corp. ....	19,600	553,173	573,300

CARNEGIE INSTITUTION OF WASHINGTON  
INVESTMENTS, JUNE 30, 1979

<i>Description</i>	<i>Shares</i>	<i>Cost</i>	<i>Approximate Market</i>
Corporate Stocks—common — <i>Continued</i>			
CPC International, Inc. ....	6,500	\$ 303,097	\$ 341,250
Cross (A. T.) Co. ....	3,000	89,250	87,375
Cummins Engine Co., Inc. ....	7,351	354,586	248,096
Data General Corporation ....	1,000	31,168	68,250
Dexter Corp. ....	6,000	122,620	126,000
Dominion Bankshares Corp. ....	14,000	220,500	227,500
Dover Corporation ....	11,500	415,595	602,313
Dow Chemical Company (The) ....	8,015	237,176	207,388
du Pont (E.I.) de Nemours & Co. ....	8,822	629,084	596,723
Eastman Kodak Company ....	9,000	281,454	514,125
Eckerd (Jack) Corp. ....	10,500	262,731	297,938
Engelhard Minerals & Chemical Corp. ....	7,500	263,350	276,563
Exxon Corporation ....	34,020	617,730	1,832,828
Farmers Group, Inc. ....	30,000	650,875	727,500
First Charter Financial Corporation ....	18,000	311,772	355,500
First Kentucky National Corp. ....	8,500	252,375	261,375
Fleming Cosmetics, Inc. ....	8,000	129,191	134,000
General Electric Co. ....	17,000	384,207	850,000
General Mills ....	3,500	84,788	87,500
General Motors Corporation ....	15,124	389,075	897,987
General Telephone & Electronics Corp. ....	18,000	566,825	486,000
Gillette Company ....	8,000	202,775	196,000
Goodyear Tire & Rubber Co. (The) ....	20,050	279,854	318,294
Great Western Financial Corp. ....	16,500	271,155	410,438
Gulf Oil Corp. ....	26,000	712,557	711,750
Halliburton Company ....	10,900	601,595	730,300
Harland (John H.) Co. ....	2,500	65,068	82,500
Hewlett-Packard Co. ....	12,600	466,016	618,975
Honeywell, Inc. ....	7,500	407,220	515,625
Household Finance Corp. ....	22,100	441,810	447,525
INA Corporation ....	18,000	811,303	841,500
INCO Limited ....	11,500	368,385	240,063
Interco, Incorporated ....	16,550	720,274	686,825
International Business Machines Corp. ....	60,376	1,337,929	4,430,090
International Paper Company ....	9,000	375,900	401,625
Interpace Corp. ....	3,750	52,018	68,906
K Mart ....	11,000	311,300	291,500
Kaiser Aluminum & Chemical Corporation ....	25,070	391,658	470,063
Malone & Hyde, Inc. ....	15,000	361,148	423,750
Marathon Oil Co. ....	15,000	420,465	570,000
MCA ....	9,500	403,055	427,500
McCormick & Co., Inc. ....	18,400	321,388	289,800
McDonalds ....	7,000	300,856	318,500
Merck & Co., Inc. ....	6,015	106,309	406,013
Minnesota Mining & Manufacturing Company ....	8,015	404,350	451,846
Monsanto Company ....	9,500	677,458	476,188
Moore McCormack Resources, Inc. ....	7,500	235,767	228,750
Motorola, Inc. ....	6,000	218,910	273,750
NALCO Chemical Co. ....	5,000	147,525	166,875
National Gypsum Co. ....	24,500	416,025	459,375
N.C.R. Corp. ....	6,500	433,225	432,250



CARNEGIE INSTITUTION OF WASHINGTON  
INVESTMENTS, JUNE 30, 1979

<i>Description</i>	<i>Shares</i>	<i>Cost</i>	<i>Approximate Market</i>
Corporate Stocks—common — <i>Continued</i>			
Northwest Industries, Inc. ....	5,000	\$ 127,941	\$ 155,000
Ocean Drilling & Exploration Co. ....	1,000	42,100	49,000
Petrie Stores Corporation ....	2,000	68,390	66,250
Pfizer, Inc. ....	12,000	338,578	367,500
Philip Morris ....	21,000	762,084	724,500
Pittston Company (The) ....	10,200	365,900	261,375
Potlatch Corporation ....	16,500	331,257	579,563
Procter & Gamble Company (The) ....	4,012	398,558	308,423
Public Service Co. of Indiana, Inc. ....	16,000	416,350	412,000
Quaker Oats Co. ....	13,000	293,100	310,375
Ralston Purina Co. ....	22,500	329,054	230,625
Revco D.S., Inc. ....	16,500	335,233	424,875
Reynolds (R.J.) Industries, Inc. ....	6,000	356,500	342,000
Royal Dutch Petroleum Co. ....	9,050	514,556	658,388
Safeway Stores, Inc. ....	9,500	409,924	351,500
Schlumberger Ltd. ....	18,750	374,302	1,387,500
Sears, Roebuck and Co. ....	12,024	649,381	231,462
Security Pacific Corp. ....	18,000	407,875	567,000
Southern California Edison ....	2,200	59,070	56,375
Squibb Corporation ....	15,600	607,909	485,550
Standard Oil Co. of California ....	24,000	983,284	1,164,000
Super Value Stores ....	5,000	90,878	111,325
Tandy Corp. ....	7,200	158,324	153,900
Tenneco, Inc. ....	29,000	1,037,455	1,011,375
Texas Gas Transmission Corp. ....	18,600	833,724	834,675
Texas Utilities ....	11,172	216,979	215,042
Transway International Corp. ....	16,500	385,688	391,875
Travelers Corp. (The) ....	12,000	368,700	459,000
Union Camp Corp. ....	6,000	264,714	281,250
Union Carbide Corp. ....	5,000	313,750	185,000
Union Pacific Corp. ....	8,050	373,763	550,419
United States Steel Corp. ....	7,500	341,250	162,188
West Point-Pepperell, Inc. ....	7,500	262,346	251,250
Waste Management ....	3,100	98,235	128,500
Total Corporate Stocks—common .....		<u>42,311,214</u>	<u>51,076,403</u>
Total Investments .....		<u>\$79,096,625</u>	<u>\$86,424,691</u>





# *Articles of Incorporation*

**Fifty-eighth Congress of the United States of America;**

**At the Second Session,**

**Begun and held at the City of Washington on Monday, the seventh day of December, one thousand nine hundred and three.**

---

## **AN ACT**

**To incorporate the Carnegie Institution of Washington.**

---

*Be it enacted by the Senate and House of Representatives of the United States of America in Congress assembled, That the persons following, being persons who are now trustees of the Carnegie Institution, namely, Alexander Agassiz, John S. Billings, John L. Cadwalader, Cleveland H. Dodge, William N. Frew, Lyman J. Gage, Daniel C. Gilman, John Hay, Henry L. Higginson, William Wirt Howe, Charles L. Hutchinson, Samuel P. Langley, William Lindsay, Seth Low, Wayne MacVeagh, Darius O. Mills, S. Weir Mitchell, William W. Morrow, Ethan A. Hitchcock, Elihu Root, John C. Spooner, Andrew D. White, Charles D. Walcott, Carroll D. Wright, their associates and successors, duly chosen, are hereby incorporated and declared to be a body corporate by the name of the Carnegie Institution of Washington and by that name shall be known and have perpetual succession, with the powers, limitations, and restrictions herein contained.*

SEC. 2. That the objects of the corporation shall be to encourage, in the broadest and most liberal manner, investigation, research, and discovery, and the application of knowledge to the improvement of mankind; and in particular—

(a) To conduct, endow, and assist investigation in any department of science, literature, or art, and to this end to cooperate with governments, universities, colleges, technical schools, learned societies, and individuals.

(b) To appoint committees of experts to direct special lines of research.

(c) To publish and distribute documents.

(d) To conduct lectures, hold meetings, and acquire and maintain a library.

(e) To purchase such property, real or personal, and construct such building or buildings as may be necessary to carry on the work of the corporation.

(f) In general, to do and perform all things necessary to promote the objects of the institution, with full power, however, to the trustees hereinafter appointed and their successors from time to time to modify the conditions and regulations under which the work shall be carried on, so as to secure the application of the funds in the manner best adapted to the conditions of the time, provided that the objects of the corporation shall at all times be among the foregoing or kindred thereto.

SEC. 3. That the direction and management of the affairs of the corporation and the control and disposal of its property and funds shall be vested in a board of trustees, twenty-two in number, to be composed of the following individuals: Alexander Agassiz, John S. Billings, John L. Cadwalader, Cleveland H. Dodge, William N. Frew, Lyman J. Gage, Daniel C. Gilman, John Hay, Henry L. Higginson, William Wirt Howe, Charles L. Hutchinson, Samuel P. Langley, William Lindsay, Seth Low, Wayne MacVeagh, Darius O. Mills, S. Weir Mitchell, William W. Morrow, Ethan A. Hitchcock, Elihu Root, John C. Spooner, Andrew D. White, Charles D. Walcott, Carroll D. Wright, who shall constitute the first board of trustees. The board of trustees shall have power from time to time to increase its membership to not more than twenty-seven members. Vacancies occasioned by death, resignation, or otherwise shall be filled by the remaining trustees in such manner as the by-laws shall prescribe; and the persons so elected shall thereupon become trustees and also members of the said corporation. The principal place of business of the said corporation shall be the city of Washington, in the District of Columbia.

SEC. 4. That such board of trustees shall be entitled to take, hold and administer the securities, funds, and property so transferred by said Andrew Carnegie to the trustees of the Carnegie Institution and such other funds or property as may at any time be given, devised, or bequeathed to them, or to such corporation, for the purposes of the trust; and with full power from time to time to adopt a common seal, to appoint such officers, members of the board of trustees or otherwise, and such employees as may be deemed necessary in carrying on the business of the corporation, at such salaries or with such remuneration as they may deem proper; and with full power to adopt by-laws from time to time and such rules or regulations as may be necessary to secure the safe and convenient transaction of the business of the corporation; and with full power and discretion to deal with and expend the income of the corporation in such manner as in their judgment will best promote the objects herein set forth and in general to have and use all powers and authority necessary to promote such objects and carry out the purposes of the donor. The said trustees shall have further power from time



to time to hold as investments the securities hereinabove referred to so transferred by Andrew Carnegie, and any property which has been or may be transferred to them or such corporation by Andrew Carnegie or by any other person, persons, or corporation, and to invest any sums or amounts from time to time in such securities and in such form and manner as are permitted to trustees or to charitable or literary corporations for investment, according to the laws of the States of New York, Pennsylvania, or Massachusetts, or in such securities as are authorized for investment by the said deed of trust so executed by Andrew Carnegie, or by any deed of gift or last will and testament to be hereafter made or executed.

SEC. 5. That the said corporation may take and hold any additional donations, grants, devises, or bequests which may be made in further support of the purposes of the said corporation, and may include in the expenses thereof the personal expenses which the trustees may incur in attending meetings or otherwise in carrying out the business of the trust, but the services of the trustees as such shall be gratuitous.

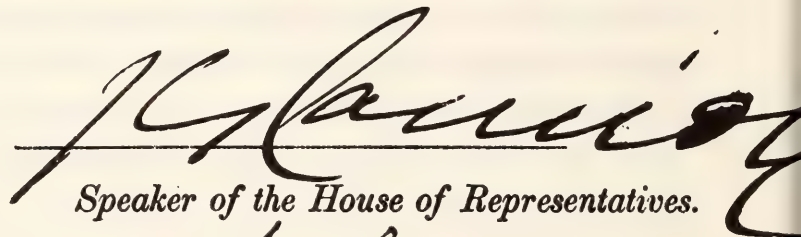
SEC. 6. That as soon as may be possible after the passage of this Act a meeting of the trustees hereinbefore named shall be called by Daniel C. Gilman, John S. Billings, Charles D. Walcott, S. Weir Mitchell, John Hay, Elihu Root, and Carroll D. Wright, or any four of them, at the city of Washington, in the District of Columbia, by notice served in person or by mail addressed to each trustee at his place of residence; and the said trustees, or a majority thereof, being assembled, shall organize and proceed to adopt by-laws, to elect officers and appoint committees, and generally to organize the said corporation; and said trustees herein named, on behalf of the corporation hereby incorporated, shall thereupon receive, take over, and enter into possession, custody, and management of all property, real or personal, of the corporation heretofore known as the Carnegie Institution, incorporated, as hereinbefore set forth under "An Act to establish a Code of Law for the District of Columbia, January fourth, nineteen hundred and two," and to all its rights, contracts, claims, and property of any kind or nature; and the several officers of such corporation, or any other person having charge of any of the securities, funds, real or personal, books or property thereof, shall, on demand, deliver the same to the said trustees appointed by this Act or to the persons appointed by them to receive the same; and the trustees of the existing corporation and the trustees herein named shall and may take such other steps as shall be necessary to carry out the purposes of this Act.

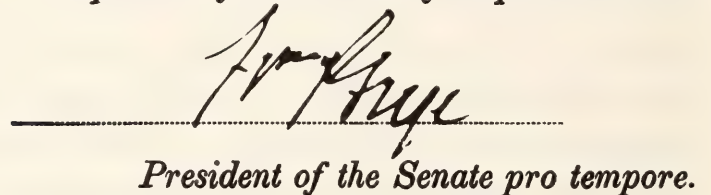
SEC. 7. That the rights of the creditors of the said existing corporation known as the Carnegie Institution shall not in any manner be impaired by the

passage of this Act, or the transfer of the property hereinbefore mentioned, nor shall any liability or obligation for the payment of any sums due or to become due, or any claim or demand, in any manner or for any cause existing against the said existing corporation, be released or impaired; but such corporation hereby incorporated is declared to succeed to the obligations and liabilities and to be held liable to pay and discharge all of the debts, liabilities, and contracts of the said corporation so existing to the same effect as if such new corporation had itself incurred the obligation or liability to pay such debt or damages, and no such action or proceeding before any court or tribunal shall be deemed to have abated or been discontinued by reason of the passage of this Act.

SEC. 8. That Congress may from time to time alter, repeal, or modify this Act of incorporation, but no contract or individual right made or acquired shall thereby be divested or impaired.

SEC. 9. That this Act shall take effect immediately.

  
Speaker of the House of Representatives.

  
President of the Senate pro tempore.

Approved.

April 28, 1904.

Theodore Roosevelt



# By-Laws of the Institution

*Adopted December 13, 1904. Amended December 13, 1910, December 13, 1912, December 10, 1937, December 15, 1939, December 13, 1940, December 18, 1942, December 12, 1947, December 10, 1954, October 24, 1957, May 8, 1959, May 13, 1960, May 10, 1963, May 15, 1964, March 6, 1967, May 3, 1968, May 14, 1971, August 31, 1972, May 9, 1974, and April 30, 1976.*

## ARTICLE I

### *The Trustees*

1. The Board of Trustees shall consist of twenty-four members with power to increase its membership to not more than twenty-seven members. The Trustees shall hold office continuously and not for a stated term.

2. In case any Trustee shall fail to attend three successive annual meetings of the Board he shall thereupon cease to be a Trustee.

3. No Trustee shall receive any compensation for his services as such.

4. All vacancies in the Board of Trustees shall be filled by the Trustees by ballot at an annual meeting, but no person shall be declared elected unless he receives the votes of two-thirds of the Trustees present.

5. If, at any time during an emergency period, there be no surviving Trustee capable of acting, the President, the Director of each existing Department, and the Executive Officer, or such of them as shall then be surviving and capable of acting, shall constitute a Board of Trustees *pro tem*, with full powers under the provisions of the Articles of Incorporation and these By-Laws. Should neither the President, nor any such Director, nor the Executive Officer be capable of acting, the senior surviving Staff Member of each existing Department shall be a Trustee *pro tem* with full powers of a Trustee under the Articles of Incorporation and these By-Laws. It shall be incumbent on the Trustees *pro tem* to reconstitute the Board with permanent members within a reasonable time after the emergency has passed, at which time the Trustees *pro tem* shall cease to hold office. A list of Staff Member seniority, as designated annually by the President, shall be kept in the Institution's records.

6. A Trustee who resigns after having served at least five years and having reached age seventy shall be eligible for designation by the Board as a Trustee Emeritus. A Trustee Emeritus shall be entitled to attend the annual meeting of the Board but shall have no vote and shall not be counted for purposes of ascertaining the presence of a quorum. A Trustee Emeritus may be invited to serve in an advisory capacity on any committee of the Board of Trustees except the Executive Committee.

## ARTICLE II

### *Officers of the Board*

1. The officers of the Board shall be a Chairman of the Board, a Vice-Chairman, and a Secretary, who shall be elected by the Trustees, from the members of the Board, by ballot to serve for a term of three years. All vacancies shall be filled by the Board for the unexpired term; provided, however, that the Executive Committee shall have power to fill a vacancy in the office of Secretary to serve until the next meeting of the Board of Trustees.

2. The Chairman shall preside at all meetings and shall have the usual powers of a presiding officer.

3. The Vice-Chairman, in the absence or disability of the Chairman, shall perform the duties of the Chairman.

4. The Secretary shall issue notices of meetings of the Board, record its transactions, and conduct that part of the correspondence relating to the Board and to his duties.

### ARTICLE III

#### *Executive Administration*

##### *The President*

1. There shall be a President who shall be elected by ballot by, and hold office during the pleasure of, the Board, who shall be the chief executive officer of the Institution. The President, subject to the control of the Board and the Executive Committee, shall have general charge of all matters of administration and supervision of all arrangements for research and other work undertaken by the Institution or with its funds. He shall prepare and submit to the Board of Trustees and to the Executive Committee plans and suggestions for the work of the Institution, shall conduct its general correspondence and the correspondence with applicants for grants and with the special advisers of the Committee, and shall present his recommendations in each case to the Executive Committee for decision. All proposals and requests for grants shall be referred to the President for consideration and report. He shall have power to remove, appoint, and, within the scope of funds made available by the Trustees, provide for compensation of subordinate employees and to fix the compensation of such employees within the limits of a maximum rate of compensation to be established from time to time by the Executive Committee. He shall be *ex officio* a member of the Executive Committee.

2. He shall be the legal custodian of the seal and of all property of the Institution whose custody is not otherwise provided for. He shall sign and execute on behalf of the corporation all contracts and instruments necessary in authorized administrative and research matters and affix the corporate seal thereto when necessary, and may delegate the performance of such acts and other administrative duties in his absence to the Executive Officer. He may execute all other contracts, deeds, and instruments on behalf of the corporation and affix the seal thereto when expressly authorized by the Board of Trustees or Executive Committee. He may, within the limits of his own authorization, delegate to the Executive Officer authority to act as custodian of and affix the corporate seal. He shall be responsible for the expenditure and disbursement of all funds of the Institution in accordance with the directions of the Board and of the Executive Committee, and shall keep accurate accounts of all receipts and disbursements. Following approval by the Executive Committee he shall transmit to the Board of Trustees before its annual meeting a written report of the operations and business of the Institution for the preceding fiscal year with his recommendations for work and appropriations for the succeeding fiscal year.

3. He shall attend all meetings of the Board of Trustees.

4. There shall be an officer designated Executive Officer who shall be appointed by and hold office at the pleasure of the President, subject to the approval of the Executive Committee. His duties shall be to assist and act for the President as the latter may duly authorize and direct.

5. The President shall retire from office at the end of the fiscal year in which he becomes sixty-five years of age.

### ARTICLE IV

#### *Meetings and Voting*

1. The annual meeting of the Board of Trustees shall be held in the City of Washington, in the District of Columbia, in May of each year on a date fixed by the Executive Committee, or at such other time or such other place as may be designated by the Executive Committee, or if not so designated prior to May 1 of such year, by the



Chairman of the Board of Trustees, or if he is absent or is unable or refuses to act, by any Trustee with the written consent of the majority of the Trustees then holding office.

2. Special meetings of the Board of Trustees may be called, and the time and place of meeting designated, by the Chairman, or by the Executive Committee, or by any Trustee with the written consent of the majority of the Trustees then holding office. Upon the written request of seven members of the Board, the Chairman shall call a special meeting.

3. Notices of meetings shall be given ten days prior to the date thereof. Notice may be given to any Trustee personally, or by mail or by telegram sent to the usual address of such Trustee. Notices of adjourned meetings need not be given except when the adjournment is for ten days or more.

4. The presence of a majority of the Trustees holding office shall constitute a quorum for the transaction of business at any meeting. An act of the majority of the Trustees present at a meeting at which a quorum is present shall be the act of the Board except as otherwise provided in these By-Laws. If, at a duly called meeting, less than a quorum is present, a majority of those present may adjourn the meeting from time to time until a quorum is present. Trustees present at a duly called or held meeting at which a quorum is present may continue to do business until adjournment notwithstanding the withdrawal of enough Trustees to leave less than a quorum.

5. The transactions of any meeting, however called and noticed, shall be as valid as though carried out at a meeting duly held after regular call and notice, if a quorum is present and if, either before or after the meeting, each of the Trustees not present in person signs a written waiver of notice, or consent to the holding of such meeting, or approval of the minutes thereof. All such waivers, consents, or approvals shall be filed with the corporate records or made a part of the minutes of the meeting.

6. Any action which, under law or these By-Laws, is authorized to be taken at a meeting of the Board of Trustees may be taken without a meeting if authorized in a document or documents in writing signed by all the Trustees then holding office and filed with the Secretary.

7. During an emergency period the term "Trustees holding office" shall, for purposes of this Article, mean the surviving members of the Board who have not been rendered incapable of acting for any reason including difficulty of transportation to a place of meeting or of communication with other surviving members of the Board.

## ARTICLE V

### *Committees*

1. There shall be the following Standing Committees, viz. an Executive Committee, a Finance Committee, an Auditing Committee, a Nominating Committee, and an Employee Benefits Committee.

2. All vacancies in the Standing Committees shall be filled by the Board of Trustees at the next annual meeting of the Board and may be filled at a special meeting of the Board. A vacancy in the Executive Committee and, upon request of the remaining members of any other Standing Committee, a vacancy in such other Committee may be filled by the Executive Committee by temporary appointment to serve until the next meeting of the Board.

3. The terms of all officers and of all members of Committees, as provided for herein, shall continue until their successors are elected or appointed.

### *Executive Committee*

4. The Executive Committee shall consist of the Chairman, Vice-Chairman, and Secretary of the Board of Trustees, the President of the Institution *ex officio*, and, in addition, not less than five or more than eight Trustees to be elected by the Board by ballot for a term of three years, who shall be eligible for re-election. Any member elected



to fill a vacancy shall serve for the remainder of his predecessor's term. The presence of four members of the Committee shall constitute a quorum for the transaction of business at any meeting.

5. The Executive Committee shall, when the Board is not in session and has not given specific directions, have general control of the administration of the affairs of the corporation and general supervision of all arrangements for administration, research, and other matters undertaken or promoted by the Institution. It shall also submit to the Board of Trustees a printed or typewritten report of each of its meetings, and at the annual meeting shall submit to the Board a report for publication.

6. The Executive Committee shall have power to authorize the purchase, sale, exchange, or transfer of real estate.

#### *Finance Committee*

7. The Finance Committee shall consist of not less than five and not more than six members to be elected by the Board of Trustees by ballot for a term of three years, who shall be eligible for re-election. The presence of three members of the Committee shall constitute a quorum for the transaction of business at any meeting.

8. The Finance Committee shall have custody of the securities of the Institution and general charge of its investments and invested funds and shall care for and dispose of the same subject to the directions of the Board of Trustees. It shall have power to authorize the purchase, sale, exchange, or transfer of securities and to delegate this power. So long as the Institution is the trustee under any retirement or other benefit plan for the staff members and employees of the Institution, it shall be responsible for supervision of matters relating to investments thereunder and for the appointment or removal of any investment manager or advisor. It shall also be responsible for reviewing the financial status and arrangements of any employee benefit plan for which the Institution is not the trustee and for appointment or removal of any plan trustee or insurance carrier. It shall consider and recommend to the Board from time to time such measures as in its opinion will promote the financial interests of the Institution and improve the management of investments under any retirement or other benefit plan. The Committee shall make a report at the annual meeting of the Board.

#### *Auditing Committee*

9. The Auditing Committee shall consist of three members to be elected by the Board of Trustees by ballot for a term of three years.

10. Before each annual meeting of the Board of Trustees, the Auditing Committee shall cause the accounts of the Institution for the preceding fiscal year to be audited by public accountants. The accountants shall report to the Committee, and the Committee shall present said report at the ensuing annual meeting of the Board with such recommendations as the Committee may deem appropriate.

#### *Nominating Committee*

11. The Nominating Committee shall consist of the Chairman of the Board of Trustees *ex officio* and, in addition, three Trustees to be elected by the Board by ballot for a term of three years, who shall not be eligible for re-election until after the lapse of one year. Any member elected to fill a vacancy shall serve for the remainder of his predecessor's term, provided that of the Nominating Committee first elected after adoption of this By-Law one member shall serve for one year, one member shall serve for two years, and one member shall serve for three years, the Committee to determine the respective terms by lot.

12. Sixty days prior to an annual meeting of the Board the Nominating Committee shall notify the Trustees by mail of the vacancies to be filled in membership of the Board. Each Trustee may submit nominations for such vacancies. Nominations so submitted shall be considered by the Nominating Committee, and ten days prior to the annual meeting the Nominating Committee shall submit to members of the Board by mail a list of the persons so nominated, with its recommendations for filling existing vacancies on the Board and its Standing Committees. No other nominations shall be received by the Board at the annual meeting except with the unanimous consent of the Trustees present.



*Employee Benefits Committee*

13. The Employee Benefits Committee shall consist of three members to be elected by the Board of Trustees by ballot for a term of three years, who shall be eligible for re-election and the Chairman of the Finance Committee *ex officio*. Any member elected to fill a vacancy shall serve for the remainder of his predecessor's term.

14. The Employee Benefits Committee shall, subject to the directions of the Board of Trustees, be responsible for supervision of the activities of the administrator or administrators of any retirement or other benefit plan for staff members and employees of the Institution, except that any matter relating to investments or to the appointment or removal of any trustee or insurance carrier under any such plan shall be the responsibility of the Finance Committee. It shall receive reports from the administrator or administrators of the employee benefit plans with respect to administration, benefit structure, operation, and funding. It shall consider and recommend to the Board from time to time such measures as in its opinion will improve such plans and the administration thereof. The Committee shall submit a report to the Board at the annual meeting of the Board.

## ARTICLE VI

*Financial Administration*

1. No expenditure shall be authorized or made except in pursuance of a previous appropriation by the Board of Trustees, or as provided in Article V, paragraph 8, hereof.

2. The fiscal year of the Institution shall commence on the first day of July in each year.

3. The Executive Committee shall submit to the annual meeting of the Board a full statement of the finances and work of the Institution for the preceding fiscal year and a detailed estimate of the expenditures of the succeeding fiscal year.

4. The Board of Trustees, at the annual meeting in each year, shall make general appropriations for the ensuing fiscal year; but nothing contained herein shall prevent the Board of Trustees from making special appropriations at any meeting.

5. The Executive Committee shall have general charge and control of all appropriations made by the Board. Following the annual meeting, the Executive Committee may allocate these appropriations for the succeeding fiscal year. The Committee shall have full authority to reallocate available funds, as needed, and to transfer balances.

6. The securities of the Institution and evidences of property, and funds invested and to be invested, shall be deposited in such safe depository or in the custody of such trust company and under such safeguards as the Finance Committee shall designate, subject to directions of the Board of Trustees. Income of the Institution available for expenditure shall be deposited in such banks or depositories as may from time to time be designated by the Executive Committee.

7. Any trust company entrusted with the custody of securities by the Finance Committee may, by resolution of the Board of Trustees, be made Fiscal Agent of the Institution, upon an agreed compensation, for the transaction of the business coming within the authority of the Finance Committee.

8. The property of the Institution is irrevocably dedicated to charitable purposes, and in the event of dissolution its property shall be used for and distributed to those charitable purposes as are specified by the Congress of the United States in the Articles of Incorporation, Public Law No. 260, approved April 28, 1904, as the same may be amended from time to time.

## ARTICLE VII

*Amendment of By-Laws*

1. These By-Laws may be amended at any annual or special meeting of the Board of Trustees by a two-thirds vote of the members present, provided written notice of the proposed amendment shall have been served personally upon, or mailed to the usual address of, each member of the Board twenty days prior to the meeting.





# Index of Names

- Aaronson, M., 740, 776  
publications, 793
- Abelson, P. H., v, vi, 14, 809
- Adelman, S. J., 781
- Ake, T. B. III, 45, 727, 798
- Alcaino, G., 782
- Aldrich, L. T., 46, 424  
publications, 421
- Aller, L. H., 782
- Anderson, D. M., 256  
studies, 244–245
- Anderson, R. O., v
- Angerer, R. C., 252, 257
- Argon, Y., 44, 7, 107  
studies, 43–44, 49–52
- Armond, P. A., 40, 46, 114, 116, 149, 152, 164, 167, 168, 199, 201, 234, 237  
publications, 231  
studies, 153–157, 168–171
- Arnold, S. J., 713, 723–724, 755
- Arp, H. C., 45, 709, 752, 755–756, 770–771, 798  
publications, 793
- Assousa, G. E., 46, 386, 387, 388, 389, 424  
publications, 421
- Atsumi, S., 44, 106
- Austin, J. P., v, 40, 809
- Babcock, H. W., 45, 777–778, 798
- Badger, M. R., 37, 40, 46, 113, 115, 234, 237  
publications, 231  
studies, 145–148, 171–175, 175–178
- Barry, A., 101, 102  
publications, 103
- Baum, W. A., 780
- Baur, P. R., 45, 444, 707  
studies, 606–608
- Bayne, E., 44, 106  
studies, 21–22, 22–27
- Beaver, E. A., 731
- Beck, S. C., 714, 782  
publications, 793
- Becklin, E., 716, 762  
publications, 793
- Beckman, J., 787
- Beckwith, S., 782–783  
publications, 793
- Belford, H. S., 38, 46, 116, 231, 234, 238  
publications, 231  
studies, 217–223
- Bell, P. M., 3, 25, 42, 44, 436, 444–445, 446–447, 448–449, 518, 546, 625, 661, 663, 665, 684, 685, 699, 707  
publications, 688  
studies, 485–488, 612–613, 613–614, 614–618, 618–621, 621–625, 627–630, 631–632, 645–650, 659–660, 665–669, 669–676
- Benn, C., 786
- Bergstrahl, J. T., 783
- Berriman, G., 45, 727, 776, 791, 799
- Berry, J. A., 37, 40, 46, 113, 114, 115, 145, 148, 153, 156, 168, 171, 184, 234, 237  
publications, 231  
studies, 149–152, 157–162, 163–168, 171–175, 175–178
- Bertola, F., 755
- Binghan, E., 784
- Birkenmeier, E. H., 44, 106  
publications, 103  
studies, 71–72, 81–82, 82–84
- Björkman, O., 8, 37, 42, 46, 113, 114, 151, 162, 166, 167, 169, 177, 178, 234–235, 237  
publications, 231–232  
studies, 145–148, 153–157
- Blatt, M. R., 46, 232, 238
- Boctor, N. Z., 31, 44, 436, 437, 441, 442, 443, 691, 707  
studies, 485–488, 492–493, 493–496, 496–498, 572–574, 580–582, 582–586, 602–606
- Boek, H. D., 45, 707
- Bopenhagen, D., 44, 78, 106  
studies, 71–72, 75, 78–80, 80–81
- Böhm, K. H., 783
- Boise, J. W., vii, 803, 809
- Boksenberg, A., 713, 723–724, 755, 769–770  
publications, 793
- Bond, H. E., 783
- Borne, K. D., 45, 725, 799
- Borra, E. F., 783
- Botchan, P., 44, 69, 106  
publications, 103
- Böving, B. G., 106
- Boyd, F. R., Jr., 44, 436, 437, 441, 442, 457, 460, 532, 547, 553, 563, 567, 625, 692, 701, 707  
publications, 688  
studies, 488–492, 493–496, 496–498, 572–574
- Bradley, M. S., 41, 803
- Brady, J. B., 44, 442, 449, 609, 686, 707  
publications, 692  
studies, 574–577, 577–580, 580–582, 676–679

- Brain, R. D., 118, 120, 122, 124, 125  
 Branscomb, L. M., v  
 Briggs, W. R., 39, 46, 117, 118, 196, 231, 235, 237  
   report of the Director, Department of Plant  
   Biology, 113-118  
   publications, 232  
   studies, 118-120, 121-125, 126-128, 129-134,  
   134-137, 138-139, 140-144  
 Britten, R. J., vii, 204, 207, 212, 217, 222, 225, 256  
   report of the Developmental Biology Re-  
   search Group, 239-257  
   publications, 256  
   studies, 247, 247-248, 248, 249, 249-250  
 Britz, S. J., 118, 120, 122, 125, 235  
   publications, 232  
 Brown, D. B., 3, 6, 8, 35, 44, 9, 56, 106  
   report of the Director, Department of Em-  
   bryology, 7-9  
   publications, 103, 104  
   studies, 71-72, 72-75, 75, 78-80, 81, 82-84  
 Brown, D. N., 784  
 Brown, J. S., 40, 46, 183-187, 235, 237  
   publications, 232  
   studies, 189-194, 202, 202-204  
 Brown, L., 28, 46, 268, 424  
   publications, 421  
   studies, 346, 353, 419-421  
 Brucato, R. J., 45, 715, 745-746, 798  
   publications, 793  
 Bugnon, M.-F., 28, 47, 268, 425  
   studies, 346-351  
 Burstein, D., 18, 47, 270, 371, 425, 790  
   publications, 421  
   studies, 373-376, 376-379  
 Bush, V., vi, 12  
 Butcher, H. R., 739, 759
- Calame, K., 255  
 Carbonetto, S. T., 44, 106  
   publications, 103, 104  
 Carey, J. D., 45, 707  
 Carney, B. W., 47, 270, 425  
   publications, 421  
   studies, 379-383  
 Catanzaro, B., 40, 115, 238  
   studies, 196-199  
 Caubergs, R., 39, 46, 117, 237  
   studies, 118-120, 121-125  
 Cebra, J., 53-55, 107  
   publications, 104  
 Chamberlin, M. E., 225, 256  
 Chatelain, P., 107  
 Chayes, F., 44, 435, 686, 693, 707  
   publications, 688  
   studies, 481-484, 484-485  
 Chrenko, 449, 666, 669-676  
 Clarke, R. S., Jr., 407, 409-413, 425  
 Clegg, K. B., 251  
 Clement, C., 784
- Code, A. D., 780  
 Coe, E. H., 64-65, 107  
 Cohen, J. G., 45, 737, 740, 798  
   publications, 793  
 Collatz, G. J., 40, 46, 115, 145, 148, 167, 235, 238  
   studies, 171-175  
 Connor, J. T., v  
 Cordova, F. A., 45, 799  
 Corner, G. W., 42  
 Costantini, J., 247, 256  
   publications, 257  
   studies, 246  
 Cottrell, P. L., 728, 731, 736, 798  
 Croce, C., 35, 44, 8, 107  
   studies, 56-61  
 Cross, J. W., 124, 125, 232  
 Crutcher, R. M., 784  
 Cuellar, R., 38, 39, 46, 116, 117, 195, 196, 207,  
   212, 223, 226, 231, 238  
   publications, 232  
   studies, 215-217  
 Cummings, M. R., 250  
 Currie, D. G., 781  
 Czysak, S. J., 782
- Da Costa, G. S., 45, 728, 735-736, 798  
 Danielson, G. E., 781  
 Davidson, E. H., 204, 207, 212, 217, 222, 225, 256  
   publications, 256  
   studies, 244, 244-245, 245, 246, 246-247, 250,  
   251, 252, 253, 254, 254-255, 255, 255-256  
 Davis, G. L., 44, 351, 426, 686, 693, 707  
 Dawid, I. B., 35, 36, 8, 9, 106  
   publications, 104  
 de Bruyn, A. G., 45, 754, 757, 798  
   publications, 793  
 De Graauw, T., 787  
 DeHaan, R. L., 106  
 Dickens, R. J., 776, 784  
 Diebold, J., v, 807, 809  
 di Tullio, G., 752  
   publications, 793  
 Dixon, K. L., 789  
 Dopita, M. A., 784  
 Downton, W. J. S., 46, 114, 237  
   studies, 157-162  
 Dressler, A. M., 45, 715, 759-761, 761-762, 798  
   publications, 793  
 Duncan, W., 31, 107  
 Dunn, 449, 666, 669-676  
 Dworetzky, M. M., 785
- Ebert, J. D., v, vii, 803, 805, 809  
   Report of the President, 3-47  
 Echeverría, L. M., 28, 47, 268, 425  
   studies, 340-344  
 Ecklund, E. T., 427  
   studies, 414-418  
 Efstratiadis, A., 255



- Ehleringer, J., 162, 177, 178, 232  
 Elias, J., 785  
     publications, 793  
 Elliott, E. J., 44, 106  
     studies, 9–12, 20  
 Ellison, J. W., 256  
     studies, 253, 254  
 Ennis, D., 766  
     publications, 793  
 Ernst, S. G., 256  
     publications, 256  
     studies, 254  
 Estabrook, F. B., 768  
 Estep, M. L. F., 29, 41, 44, 447, 686, 707  
     studies, 650–652, 652–655  
 Evans, J. R., 24, 47, 266  
     publications, 421  
     studies, 311–320
- Faber, S. M., 18, 270, 376–379, 426  
 Fambrough, D. M., 44, 7, 9, 106  
     publications, 104  
     studies, 21–22, 22–27  
 Fedoroff, N. V., 36, 44, 9, 106  
     publications, 104  
     studies, 61–65  
 Ference, M., Jr., v  
 Finger, L. W., 44, 446, 448, 490, 684, 686, 694, 696, 707  
     publications, 689  
     studies, 632–636, 658–659  
 Finnerty, A. A., 44, 437, 492, 707  
 Fitton, B., 787  
 Fontaine, G., 785  
 Forbush, S. E., 46, 424  
 Ford, G. A., 39, 40, 115, 116, 117, 196, 231, 238  
     publications, 232  
     studies, 196–199, 199–201  
 Ford, W. K., Jr., 18, 46, 269, 374, 424  
     publications, 421  
     studies, 363–373, 418–419  
 Fork, D. C., 40, 46, 115, 116, 162, 168, 169, 171, 235, 237  
     publications, 232  
     studies, 178–180, 180–182, 196–199, 199–201  
 Frantz, J. D., 31, 44, 443, 449, 578, 695, 702, 707  
     publications, 689  
     studies, 586–591, 591–596, 596–602, 602–606, 676–679  
 French, C. S., 46, 195, 202–204, 232, 237  
 Frogel, J. A., 737, 740  
     publications, 793  
 Fukuyama, H., 45, 707
- Gallagher, J. S., 18, 270, 363, 373, 376–379, 426  
 Garay, G., 45, 799  
 Gardner, J. M., 44, 107  
     publications, 104  
     studies, 21–22, 22–27  
 Gavis, E., 44, 107
- Gearhart, P., 35, 44, 8, 9, 106  
     publications, 104  
     studies, 52–56  
 Geballe, T. R., 45, 778, 782, 798  
     publications, 794  
 George, D. J., 686, 708  
 Giacconi, R., 738–739  
 Gil-Av, E., 32, 448, 655–658, 686, 708  
     publications, 689  
 Gilbert, C. J., v, 809  
 Giza, P. E., 84, 107  
 Godwin, J. G., 789  
 Goeden, R. M., 719, 799  
 Gokham, B., 45, 799  
 Goldberg, B., 788  
 Golden, W. T., v, 807, 809  
 Goldsmith, M. H., 39, 46, 117, 237  
     studies, 118–120, 121–125  
 Gorton, H., 39, 46, 117, 235, 238  
     studies, 134–137, 138–139  
 Green, R. F., 17, 45, 716, 731, 768, 798  
     publications, 794  
 Greenewalt, C. H., v, 809  
 Greenough, W. C., v, 807, 809  
 Greenstein, J. L., 45, 726, 729–731, 776, 785, 798  
     publications, 794  
 Griffin, R. E. M., 785  
 Griffin, R. F., 785–786  
     publications, 794  
 Grueff, G., 786  
 Grula, J. W., 256  
     studies, 249  
 Gull, T. R., 770  
 Gunn, J. E., 45, 379, 709, 716, 738–739, 761–762, 779, 780, 787, 788, 798  
     publications, 794  
 Gurdon, J. B., 70, 107  
     publications, 103, 104
- Hadidiacos, C. G., 449, 547, 708  
     studies, 679–682  
 Hall, T. J., 256  
     studies, 248–249, 249–250  
 Haraburda, J. M. S., vii  
 Hardy, E. J., 786  
     publications, 794  
 Hare, P. E., 32, 44, 448, 449, 676, 686–687, 696, 707  
     publications, 689  
     studies, 655–658  
 Harrison, W. J., 45, 441, 572, 573, 706, 707  
     studies, 562–568, 568–572  
 Hart, R. W., 40, 115, 238  
     studies, 202–204  
 Hart, S. R., 301, 304, 309, 313, 331, 335, 339, 344, 346  
 Harvey, G. W., 46, 115, 235, 237  
     studies, 194–196  
 Hasegawa, A., 22, 47, 265, 273, 286, 288, 425  
     studies, 276–284  
 Haskins, C. P., v, vi, 809

- Hatfield, B. J., 789  
 Hazard, C., 771  
 Hazen, R. M., 44, 446, 448, 683, 684, 687, 694, 696, 707  
   publications, 689  
   studies, 632-636, 658-659  
 Heard, O. O., 101  
 Heinze, W. D., 47, 268, 425  
   studies, 288-298  
 Helin, E. F., 790  
 Henard, K. R., vii  
 Herbst, W., 47, 269, 383-387, 388, 389, 425  
   publications, 421  
 Hertig, A. T., 106  
 Hess, J. L., 46, 152, 235-236, 237  
   studies, 168-171  
 Hewitt, R. E., vii, 803  
 Hewlett, W. R., v, 809  
 Hiesey, W. M., 46, 237  
 Hiltner, W. A., 786  
 Hippelein, H. H., 788  
 Hipskind, R. A., 44, 56, 107  
   publications, 104  
 Hiyama, T., 115  
   studies, 180-182  
 Hodge, P., 752, 787  
 Hoering, T. C., 29, 44, 339, 438, 439, 444, 447, 530, 537, 650-651, 687, 696, 707  
   publications, 689  
   studies, 492-493, 537-542, 608-612, 652-655  
 Hoessel, J., 45, 762, 799  
   publications, 794  
 Hofmann, A. W., 46, 267, 331-335, 353, 355, 356, 359, 424  
   publications, 421-422  
   studies, 335-340  
 Holm, A., 755  
 Hood, L., 55, 106, 255  
 Hoover, J. D., 45, 707  
 Hough-Evans, B. R., 225, 256  
   publications, 256  
   studies, 250, 251  
 Hornblower, M., vii, 809  
 Howard, R. F., 45, 717-719, 798  
   publications, 794  
 Huchra, J., 776, 790  
   publications, 794  
 Humphreys, R., 16, 715, 741-743, 787  
 Hunt, R. E., 126-128  
 Hurford, G. J., 799  
   publications, 794  
 Hurwitz, J., 53, 107
- Irvine, T. N., 27, 44, 433-434, 466, 467, 498, 559, 687, 697, 707  
   studies, 450-461, 461-468  
 Israel, F. P., 45, 787, 798
- Jacobs-Lorena, M., 250  
 Jambon, A., 46, 267, 425  
   studies, 352-355, 355-359
- James, D. E., 22-24, 46, 265, 266, 274, 276-278, 284, 298-300, 302, 304, 307, 335, 339, 424  
   publications, 422  
   studies, 272-276, 308-311  
 Jezek, P. A., 304-308, 426  
   publications, 422  
 Johnson, N., 55, 56, 107  
 Johnson, P. E., 790  
 Jordan, E., 71, 81, 82, 104, 107  
 Jorgensen, R. A., 38, 46, 116, 211, 217, 236, 237  
   studies, 212-214
- Kennicutt, R. C., Jr., 45, 752, 776, 778, 798  
 Kent, S. M., 45, 745, 799  
   publications, 794  
 Kingsbury, R., 56, 107  
 Kingsley, R. H., 45, 707  
 Klein, W. H., 217, 245, 256  
   publications, 257  
   studies, 246  
 Knapp, G. R., 739, 791  
   publications, 794  
 Knox, G. V., 799  
 Konigsberg, I. R., 106  
 Korn, L. J., 44, 69, 70, 78, 106  
   publications, 104  
   studies, 71-72, 75, 82-84  
 Kothari, B. K., 20, 47, 271, 425  
   publications, 422  
   studies, 399-402  
 Kowal, C. T., 42, 45, 721, 738, 754, 792, 798  
   publications, 795  
 Kristian, J., 45, 715, 738, 754, 780-781, 798  
   publications, 795  
 Krumm, N., 18, 270, 364, 367, 371, 426  
   studies, 373-376  
 Kumar, C. K., 383, 426  
 Kushiro, I., 44, 362, 426, 440, 479, 498, 501, 542, 547, 548, 551-552, 555, 563, 567, 698, 701, 707  
   publications, 689  
   studies, 559-562
- LaBonte, B. J., 45, 718-719, 798  
   publications, 795  
 Lacy, J. H., 714, 782  
   publications, 795  
 Landstreet, J. D., 731, 783-784  
 Lane, A. L., 768  
 Lanning, H., 787, 789  
   publications, 795  
 Lasky, L. A., 256  
   studies, 246-247, 253  
 Lawson, C. A., 45, 707  
 Lee, A. S., 256  
   publications, 257  
   studies, 252  
 Lee, T., 41  
 Leighton, R. B., 45, 798  
 Lev, Z., 256  
   publications, 257  
   studies, 252, 253, 254



- Levitt, J., 46, 232, 236, 237  
 Lidholm, S., 787  
 Liebert, J. W., 731  
 Linde, A. T., 46, 268, 424  
   publications, 422  
   studies, 284–288, 320–325  
 Lo, K.-Y., 752–754  
   publications, 795  
 Lockman, F. J., 47, 270, 425  
   publications, 422  
   studies, 388–389  
 Longair, M. S., 738, 787, 788  
 Lorre, J. J., 45, 755, 798  
 Luck, R. E., 783  
 Lux, R. A., 47, 425  
   publications, 422  
 Lynds, C. R., 781
- Macagno, E., 19, 107  
 Maden, B. E. H., 44, 107  
   publications, 104  
   studies, 65–67  
 Madore, B., 789  
   publications, 795  
 Magaritz, M., 23, 24, 265, 266, 299, 300, 304,  
   305, 307, 308, 311, 353, 355, 356, 359  
   publications, 422  
 Malkan, M., 45, 799  
 Malkin, S., 40, 46, 116, 199–201, 237  
   studies, 199–201  
 Mammone, J. F., 45, 446, 665, 707  
   studies, 636–640, 640–645  
 Mandoli, D. F., 39, 46, 117, 236, 238  
   studies, 140–144  
 Mannery, E., 783  
 Mao, H. K., 3, 25, 44, 436, 445, 446–447, 448–  
   449, 518, 546, 591, 625, 626, 641, 661, 663,  
   665, 684, 687, 695, 699, 706, 707  
   publications, 689  
   studies, 485–488, 612–613, 613–614, 614–618,  
   618–621, 621–625, 627–630, 630–632, 645–650,  
   659–660, 665–669, 669–676  
 Marshall, W. L., 31, 32, 443, 708  
   studies, 591–596  
 Martin, O. C., 31, 32, 107  
 Martin, W. M., Jr., v, 809  
 Matson, D. L., 792  
 Matthews, K., 45, 713, 716, 723, 756, 762, 767,  
   798  
   publications, 795  
 Mauron, A., 251  
 Mauvais, J., 61, 107  
 McCallister, R. H., 44, 442, 457, 558, 707  
   studies, 574–577, 582–586  
 McClintock, B., vii, 36, 42, 9, 61–63, 107  
 McGough, S., vii  
 McKnight, S., 35, 44, 8, 106  
   studies, 56–61  
 Mekler, Y., 788  
 Melis, A., 46, 237  
 Melnick, B., 103
- Miller, H. R., 788  
 Mochnacki, S., 45, 727–729, 779, 798  
   publications, 795  
 Moore, G. P., 217, 256  
   publications, 257  
   studies, 247, 247–248  
 Moore, R., 45, 721, 798  
 Morgan, H. S., v  
 Mose, D. G., 28, 46, 268, 425  
   studies, 344–346  
 Mould, J. R., 45, 729, 739–740, 776, 778, 798  
 Muller, K. J., 34, 44, 7, 9, 106  
   publications, 104  
   studies, 9–12, 12–13, 13–16, 16–20  
 Münch, G., 722, 788  
 Murase, T., 44, 440, 700, 707  
   studies, 559–562  
 Murata, N., 169, 171, 178–180, 197, 199  
   publications, 233  
 Murphy, F. D., v, 809  
 Murray, M. G., 38, 39, 46, 116, 117, 215, 217,  
   220, 222, 223, 236, 237  
   publications, 233  
   studies, 204–207, 208–212, 226–231  
 Mysen, B. O., 44, 267, 340, 426, 437, 438–440,  
   441–442, 530, 556, 560, 563, 567, 568, 572,  
   700–701, 703, 707  
   publications, 689–690  
   studies, 359–363, 498–502, 502–506, 506–511,  
   511–519, 519–526, 542–547, 547–551, 551–556,  
   574–577, 679
- Nadeau, D., 46, 732, 799  
   publications, 795  
 Nelson, G. A., 34, 44, 7, 51  
   publications, 105  
   studies, 43–44, 44–48  
 Neuffer, M. G., 64–65, 107  
 Neugebauer, G., 45, 709, 713, 716, 723, 756, 762,  
   766–767, 791, 798  
   publications, 795  
 Ney, E. P., 789  
 Nicholls, I. A., 304–308  
   publications, 422  
 Nieuwenhuyzen, H., 787  
 Nixon, P. H., 463, 496, 563, 567, 701  
   publications, 690  
   studies, 488–492  
 Nobs, M. A., 46, 167, 237  
 Norton, G., v, 809
- Ocola, L., 46, 425  
 Ohshima, Y., 44, 106  
   publications, 105  
   studies, 84–85, 92–96  
 Okada, H., 272–273, 276, 284, 426  
 Oke, J. B., 45, 716, 726, 730–731, 755, 756–757,  
   762, 779, 792, 798  
   publications, 795–796  
 O’Nions, R. K., 303, 305, 307, 326, 331, 333, 335

- O'Rahilly, R., 106  
 publications, 105  
 studies, 101-102
- Osborn, E. F., 44, 435, 687, 702, 707  
 studies, 475-481
- Pagano, R. E., 34, 44, 7, 9, 106  
 publications, 105  
 studies, 31-32, 32-33
- Page, W. H., v, 40, 809
- Palmer, J. D., 39, 46, 117, 205, 207, 238  
 studies, 226-231
- Pasteris, J. D., 45, 708
- Patterson, A. P., 719, 800
- Peach, J. V., 789
- Pennoyer, R. M., v, 809
- Penston, M. V., 770
- Perkins, R. S., v, 809
- Perryman, M., 738, 788
- Persson, S. E., 45, 737, 740, 756, 776, 778, 782, 798  
 publications, 796
- Pesch, P., 789
- Peters, D. L., 38, 116, 213, 238  
 studies, 208-212
- Peterson, R., 44, 8, 106  
 studies, 71-72, 72-75
- Petro, L. D., 45, 798
- Phillips, M. M., 789
- Pier, J. R., 46, 768, 799
- Pike, C. S., 46, 114, 157, 168, 171, 236, 237  
 publications, 233  
 studies, 163-168
- Pikó, L., 251, 256
- Pogo, A., 798
- Pollock, H. E. D., vii
- Popp, R. K., 31, 44, 443, 591, 596, 679, 687-688, 695, 702, 707  
 studies, 586-591, 596-602, 602-606
- Portugal, F. H., vii, 803
- Posakony, J. W., 256  
 studies, 245
- Powell, J. K., 45, 708
- Pratt, L. H., 126-128, 129-134, 137
- Preisler, R., 46, 231, 238
- Preston, G. W., 45, 709, 714, 724-725, 739, 798  
 publications, 796
- Quail, P. H., 39, 40, 46, 116, 236, 237  
 publications, 233  
 studies, 126-128, 129-134
- Rabin, D. M., 46, 799
- Rai, C. S., 437, 498-502, 708
- Raison, J. K., 46, 113, 115, 145, 148, 156, 162-168, 236-237, 238  
 publications, 233  
 studies, 149-152, 183-189
- Rajan, R. S., 20, 46, 269, 271, 412, 424  
 publications, 422-423  
 studies, 383-387, 399-402, 402-405, 405-409
- Ramsey, E. M., 106
- Ranganayaki, R. P., 47, 425
- Rawson, S. A., 45, 435, 707  
 studies, 475-481
- Readhead, A. C. S., 754, 757
- Reeder, R. H., 35, 36, 44, 8, 9, 56, 69, 106  
 publications, 105  
 studies, 65-67, 67-71
- ReVelle, D. O., 47, 425
- Rich, M., 45, 799
- Richstone, D. O., 741  
 publications, 796
- Roberts, J. W., 256
- Roberts, R. B., 46, 424  
 publications, 422
- Roberts, T., 44, 106  
 studies, 43-44
- Roesler, F. L., 722
- Rose, J. A., 42, 45, 714, 737, 745, 750-751, 778, 798
- Rosenhauer, M., 440, 619, 694, 708  
 studies, 556-559
- Roth, W. R., v, 40, 809
- Rotundo, R., 34, 44, 7, 106  
 studies, 21-22, 27-30
- Rubin, V. C., 18, 42, 46, 269, 374, 424, 790  
 publications, 422  
 studies, 363-373
- Rumble, D., III, 44, 309, 444, 688, 703, 707  
 studies, 492-493, 608-612
- Russell, R., 782
- Ryerson, F. J., 47, 267, 425  
 studies, 359-363
- Sacks, I. S., 22, 24, 46, 265, 266, 267, 424  
 publications, 422  
 studies, 272-276, 276-284, 284-288, 288-298, 311-320, 320-325
- Saha, A., 46, 799
- Sakonju, S., 44, 107  
 studies, 71-72, 75, 75-78
- Sancisi, R., 753
- Sandage, A. R., 16, 45, 369, 373, 376, 377, 379, 709, 714, 715, 716, 741-742, 745-746, 771-772, 776, 787, 798  
 publications, 796
- Sandra, A., 44, 105, 106
- Sargent, A. I., 45, 715, 798
- Sargent, W. L. W., 45, 709, 713, 723-724, 738-739, 751-755, 757, 769-770, 777, 790, 798  
 publications, 796
- Scarfe, C. M., 340, 437, 440, 505, 703, 708  
 studies, 498-502, 547-551, 551-556, 556-559
- Scheller, R. H., 217, 245, 247, 256
- Schissel, D., 434, 461-468
- Schmidt, M., 17, 42, 45, 709, 716, 731, 768, 798  
 report of the Director, Hale Observatories, 713-716  
 publications, 796



- Schneider, D. P., 46, 726, 799  
publications, 796
- Schommer, R., 45, 729, 787, 798
- Schreiber, U., 149, 152, 153, 158, 162, 233
- Schroit, A., 34, 44, 7, 106  
publications, 105  
studies, 31–32, 37–43
- Schuch, N. J., 787
- Schwartz, M. P., 790
- Scott, E. R. D., 20, 47, 271, 425  
publications, 422  
studies, 402–405, 405–409, 409–413
- Scott, S., 44, 106  
studies, 9–12, 12–13, 13–16, 16–20, 21–22
- Seamans, R. C., Jr., v, 809
- Searle, L., 45, 714, 750–751, 777, 798  
publications, 796
- Sebok, W. L., 46, 779, 799
- Seemann, J. R., 46, 114, 149, 238  
studies, 157–162
- Seidemann, K., 781
- Seifert, F. A., 44, 438, 445, 469, 703, 707  
studies, 502–506, 506–511, 511–519, 519–526, 542–547, 625–626, 626–627, 679
- Semeniuk, I., 787
- Sharma, S. K., 45, 362, 438, 439, 446–447, 448, 502, 505, 507, 509, 511, 514, 522, 525, 551, 632, 679, 703, 707  
studies, 526–532, 532–537, 537–542, 636–640, 640–645, 645–650, 660–665
- Shaw, R., 45, 799
- Shectman, S. A., 45, 739, 741, 760–761, 798
- Shelby, J. E., 267, 355–359, 426
- Shin, H., 107
- Shoemaker, E. M., 790
- Shorthill, R. W., 790
- Simkin, S. M., 790
- Simons, B. A., 44, 445, 704, 707  
studies, 625–626, 626–627
- Smith, B., 31, 107
- Smith, B. A., 781
- Smith, C. M., 40, 115, 238  
studies, 171–175
- Smith, D. P., 782
- Smith, D. W., 790
- Snijders, M. A. J., 770
- Snoke, J. A., 22, 265, 272, 282–284, 325, 426  
publications, 422
- Soifer, B. T., 45, 713, 723, 756, 767, 798  
publications, 796
- Sollner-Webb, B., 44, 8, 65–66, 106  
publications, 105  
studies, 67–71
- Somerville, D., 21, 107
- Spear, F. S., 45, 707
- Spradling, A., 37, 41, 9, 103
- Staehelin, L. A., 114, 153–157, 164, 167, 233, 237
- Stanton, F., v, 12, 809
- Stefansson, R., 268, 320–325, 426
- Stein, D. B., 38, 116  
publications, 233  
studies, 223–225
- Stockman, H. S., 731
- Struck, D., 34, 44, 7, 106  
studies, 31–32, 33–37
- Su, H. J., 790
- Sulentice, J. W., 45, 752, 755–756, 798  
publications, 796
- Sun, S.-S., 331, 332, 334, 335, 426
- Suzuki, Y., 35, 36, 44, 8, 9, 106  
publications, 105  
studies, 84–85, 86–92, 92–96, 96–100
- Swenson, D. H., 781
- Swope, H. H., 798
- Szkody, P., 791
- Taft, C. P., v, 809
- Takahashi, E., 45, 707
- Tammann, G. A., 16, 369, 373, 714, 716, 741, 748, 771–772, 776
- Tanaka, K., 720  
publications, 796
- Tera, F., 28, 46, 268, 424  
publications, 422  
studies, 346–351
- Terrile, R. J., 713, 721–722
- Thomas, B. E., 9, 12, 13, 107
- Thomas, T. L., 256  
studies, 244, 252, 253, 255, 255–256
- Thompson, I., 731
- Thompson, W. F., 37–39, 46, 109, 116, 117, 196, 237  
publications, 233  
studies, 204–207, 208–212, 212–214, 215–217, 217–223, 223–225, 226–231
- Thonnard, N., 18, 46, 269, 374, 424  
publications, 422–423  
studies, 363–373, 414–418
- Thuan, T. X., 716, 754, 761–762  
publications, 797
- Tilton, G. R., 23, 47, 265, 266, 309, 348, 351, 352, 425  
studies, 298–304
- Todd, S. G., 434, 461–468, 708
- Townes, C. H., v, 714, 782, 797, 809
- Trauger, J. T., 45, 722, 779, 798
- Trippe, J. T., v, 807
- Tsuda, M., 44, 91, 107  
studies, 84–85, 92–96, 96–100
- Tsujimoto, Y., 44, 107  
publications, 105  
studies, 84–85, 86–92
- Turner, K. C., 46, 424  
publications, 422  
studies, 383, 414–418
- Tuross, N. C., 45, 708
- Tuve, M. A., 46, 425
- Tytler, D., 769
- Ulrich, R. K., 791
- Usher, P. D., 791

- van den Bergh, S., 791  
 van Ginkel, G., 46, 115, 238  
   publications, 233  
   studies, 178-180, 183-189  
 Van Valkenburg, A., 444, 684, 688, 708  
   studies, 606-608  
 Vasquez, S., vii, 41, 803  
 Vauclair, G., 776, 785  
 Vauclair, S., 776  
 Vaughan, A. H., 45, 714, 724, 728, 798  
 Veeder, G. J., 792  
 Velde, D., 435, 708  
   studies, 468-475  
 Vidal, N. V., 792  
 Vigotti, M., 786  
 Virgo, D., 44, 267, 426, 438-440, 530, 701, 703, 707  
   publications, 690  
   studies, 359-363, 502-506, 506-511, 511-519, 542-547, 547-551, 551-556, 556-559, 679  
  
 Wade, R. A., 46, 725-726, 791, 799  
   publications, 797  
 Wahlquist, H. D., 768  
 Wahn, H., 44, 107  
   publications, 105  
 Wakamatsu, K., 792  
 Wakshull, E., 44, 107  
   studies, 21-22  
 Wall, J., 786  
 Ward, S., 34, 44, 7, 9, 106  
   publications, 105  
   studies, 43-44, 48-49  
 Wasserburg, G. J., 300, 349, 352, 387, 409  
   publications, 424  
 Watson, E. B., 435, 705  
   publications, 690  
   studies, 475-481  
 Weeks, 441  
   studies, 568-572  
 Wendlandt, R. F., 45, 470-471, 498, 563, 568, 572, 573, 694, 706, 707  
   publications, 690  
 Werner, M. W., 45, 766, 798  
   publications, 797  
 Westphal, J. A., 45, 713, 715, 721-722, 738, 754, 779, 780-781, 798  
   publications, 797  
 Wetherill, G. W., 17, 19, 21, 42, 46, 271, 272, 352, 424  
  
   report of the Director, Department of Terrestrial Magnetism, 263-272  
   publications, 424  
   studies, 389-399  
 Whelan, J., 727  
   publications, 797  
 White, J. N., v, 40, 809  
 White, W. M., 23, 24, 47, 266, 267, 339, 425  
   publications, 424  
   studies, 304-308, 325-331, 331-335  
 Whitford, D. J., 23, 24, 47, 265, 266, 311, 344, 425  
   publications, 424  
   studies, 304-308  
 Widell, U. M. S., 124  
 Williams, W., 46, 238  
 Wilson, O. C., 14, 15, 713, 724-725, 798  
   publications, 797  
 Wiser, J., 37, 9, 107  
 Wold, B. J., 255, 257  
 Wolff, S. C., 725  
   publications, 797  
 Wright, C., vii, 41, 803  
 Wright, T. L., 267, 330, 331, 334, 335-340, 426  
  
 Xin, J., 256  
  
 Yagi, T., 44, 444-445, 486-487, 688, 694, 706, 707  
   publications, 690  
   studies, 612-613, 613-614, 614-618, 618-621, 621-625  
 Yahil, A., 716, 772  
 Yee, H. K.-C., 46, 799  
 Yoder, H. S., Jr., 13, 41, 44, 355, 438, 439, 468, 471, 475, 479, 501, 502, 536, 537, 543, 558, 567, 572, 688, 698, 703, 706, 707  
   report of the Director, Geophysical Laboratory, 433-449  
   studies, 526-532, 537-542  
 Young, P. L., 45, 715, 754-755, 769, 798  
   publications, 797  
  
 Zies, E. G., 44, 707  
 Zimmerman, B., 756, 779  
   publications, 797  
 Zinn, R. J., 45, 714, 735, 737, 798  
   publications, 797  
 Zirin, H., 45, 720, 728, 798  
   publications, 797  
 Zook, A. C., 792





















